Model Calculations of the Atmospheric Effects of Supersonic Aviation Which Were Used in the IPCC Special Report on Aviation and the Global Atmosphere

Lead Author:
Debra Weisenstein, AER, Inc., U.S.A.

Technical Support:
Karen Sage, NASA Langley Research Center, U.S.A.
Donald Brown, NASA Langley Research Center, U.S.A.

Co-Authors:
Richard S. Eckman, NASA Langley Research Center, U.S.A.
Malcolm K.W. Ko, AER, Inc., U.S.A.

Contributors:
Steven L. Baughcum, Boeing Company, U.S.A.
Martyn Chipperfield, University of Cambridge, U.K.
Michael Gauss, University of Oslo, Norway
William L. Grose, NASA Langley Research Center, U.S.A.
Robert S. Harwood, University of Edinburgh, U.K.
Ivar Isaksen, University of Oslo, Norway
Charles H. Jackman, NASA Goddard Space Flight Center, U.S.A.
Douglas E. Kinnison, Lawrence Livermore National Laboratory, U.S.A.
Giovanni Pitari, University L'Aquila, Italy
Helen Rogers, University of Cambridge, U.K.
Courtney J. Scott, AER, Inc., U.S.A.
Peter F. Vohralik, CSIRO, Australia
Vicky West, University of Edinburgh, U.K.

May 1999

Rationale

This report is intended to expand upon the IPCC Special Report on Aviation and the Global Atmosphere. It provides additional detail regarding the supersonic emission scenario calculations presented in Chapter 4—Modeling the Future Atmosphere. Due to the space limitations in that document, detailed plots and discussion for a majority of the model calculations were omitted. This document is intended to fill that gap and has been compiled for two reasons: (1) to aid those called upon to review the IPCC Special Report, and (2) to archive and document the calculations performed by nine modeling groups for up to 50 scenarios each. This document does not attempt to provide a synthesis of the modeling results or draw conclusions regarding the impact of aircraft on the atmosphere. That function is provided by the IPCC report.

The model descriptions and model results presented in this document represent the state of those models in 1997 when the calculations were performed. Because models are continually evolving and undergoing further development, these results should be considered as a historical snapshot. Please do not cite results presented herein without first obtaining permission from the group which performed the calculations.

Contents

1 Model Descriptions **4**
- 1.1 Transport Formulation . . . 4
  - 1.1.1 Domain and Resolution . . . 4
  - 1.1.2 Temperature and Transport Parameters . . . 6
- 1.2 Chemistry Treatment . . . 11
  - 1.2.1 Gas-phase Chemistry . . . 11
  - 1.2.2 Heterogeneous Chemistry . . . 11
    - 1.2.2.1 Reactions on Sulfate Aerosol . . . 11
    - 1.2.2.2 Reactions on PSCs and Cold Sulfate Aerosol . . . 12
  - 1.2.3 Chemistry Solvers . . . 14
- 1.3 Sources and Sinks for Some Species . . . 14

2 Emission Scenarios **22**
- 2.1 Fuel Use . . . 22
- 2.2 HSCT Emissions . . . 23
- 2.3 Sulfur Emission Scenarios . . . 24

3 Background Atmospheres **44**
- 3.1 Scenario D Results . . . 44
- 3.2 Scenario D3 Results . . . 96
- 3.3 Scenario D4 Results . . . 101
- 3.4 Scenario D5 Results . . . 111
- 3.5 Scenario D6 Results . . . 117
- 3.6 Scenario D7 Results . . . 123
- 3.7 Scenario D8 Results . . . 129
- 3.8 Scenario D9 Results . . . 133
- 3.9 Scenario F Results . . . 141
- 3.10 Scenario G Results . . . 145

4 HSCT Perturbations for 2015 **150**
- 4.1 H_2O Perturbations . . . 152
- 4.2 NO_y Perturbations . . . 175
- 4.3 O_3 Perturbations . . . 213
  - 4.3.1 Base Scenarios (S1a-e,i,j) . . . 213
  - 4.3.2 Scenarios with Sulfur Emissions (S1f-h,k,l) . . . 286
  - 4.3.3 Scenarios with Modified Cruise Altitude (S2a-e) . . . 323
  - 4.3.4 Scenarios with Enhanced Background Aerosol (S3a-f) . . . 353
  - 4.3.5 Scenarios without PSC Formulations (S4a-c) . . . 391
  - 4.3.6 Scenarios with Different Cl_y Loadings (S5a,b, S6a,b) . . . 404
  - 4.3.7 Scenarios with Interactive Microphysics (S7a-d, S8a) . . . 425

5 HSCT Perturbations for 2050 **454**
5.1 H_2O Perturbations 456
5.2 NO_y Perturbations 460
5.3 O_3 Perturbations 467
5.3.1 Base Scenarios (S9a,b,d,g) 468
5.3.2 Scenarios with Sulfur Emissions (S9c,e,f,h) 485
5.3.3 Scenarios with Modified Cruise Altitude (S10a-d) 503
5.3.4 Scenarios with Modified Subsonic Fleets (S11a, S12a) 520

Chapter 1

Model Descriptions

Descriptions of the nine numerical models of the stratosphere used to predict perturbations to ozone due to a future fleet of supersonic aircraft are presented in this chapter. These are six two-dimensional (2-D) models and three three-dimensional (3-D) models as listed in Table 1.1. The 2-D models are the Atmospheric and Environmental Research (AER) model, the Commonwealth Scientific and Industrial Organization (CSIRO) model, and NASA Goddard Space Flight Center (GSFC) model, the Lawrence Livermore National Laboratory (LLNL) model, the University of Edinburgh (THINAIR) model, and the University of L'Aquila (UNIVAQ) model. The 3-D models are the NASA Langley Research Center (LARC) model, the University of Oslo (SCTM1) model, and the University of Cambridge (SLIMCAT) model. The scientists who comprise the research team for each model, as well as the person to contact regarding results in this report, are listed in Table 1.1.

These model descriptions refer to the models as they were in 1997 when the IPCC scenario calculations were performed. As models are continually evolving and undergoing improvements and enhancements, the following descriptions do not necessarily represent the present state of the models described, but merely a historical snapshot. For current information regarding any of these models, please contact the research team directly.

We will discuss the transport and chemical treatments of the models below with emphasis on the differences that may explain the different model predictions of aircraft impact on ozone. Model transport affects the residence time and concentration of emitted materials in the lower stratosphere. Treatment of chemistry in the model determines how the emitted pollutants will modify radical concentrations and ozone.

1.1 Transport Formulation

1.1.1 Domain and Resolution

All 2-D models have the lower boundary at the ground and most use log-pressure coordinates in the vertical with equal resolution in the troposphere and the stratosphere. The THINAIR model uses potential temperature (θ) as the vertical coordinate. Key parameters for model grid and resolution are summarized in Table 1.2. Horizontal resolution is 10^o for the AER, GSFC, THINAIR, and UNIVAQ models and 5^o for the CSIRO and LLNL models. Vertical resolution varies from 1.2 km for the AER model, 1.5 km for the LLNL model, 2 km for the CSIRO and GSFC models, 2.8 km for the UNIVAQ model, and 3.5 km for the THINAIR model. The model top boundary varies from 60 km (AER and THINAIR) to 90 km (GSFC). THINAIR has a model top boundary of 100 km for dynamics, but chemistry is explicitly calculated only up to 60 km.

Among the 3-D models, the SLIMCAT and SCTM1 models are grid point models. The LARC 3-D chemistry transport model (CTM) uses a spectral representation in the horizontal dimension with triangular truncation to zonal wavenumber 16 (T16). Constituent chemistry calculations are done in grid space using a 5.5^ox5.5^o grid that ensures alias-free evaluation of all inverse transforms (Eckman et al., 1995). Winds and temperatures are truncated from a higher resolution (T32) version of the LARC spectral GCM for input to the CTM. Sigma coordinates are used in the vertical dimension with ten layers in the troposphere and 14

Table 1.1: List of Models that Contributed Results to this Report

Model name	Institution	Model Team	contact person for model	contact person for results in this report
2-D Models				
AER	Atmospheric and Environmental Research, Inc., U.S.A.	Malcolm Ko, Debra Weisenstein, Courtney Scott, Jose Rodriguez, Run-Lie Shia, N.D. Sze	Malcolm Ko	Debra Weisenstein
CSIRO	Commonwealth Scientific and Industrial Research Organization (CSIRO), Telecommunications and Industrial Physics, Australia	Keith Ryan, Ian Plumb, Peter Vohralik, Lakshman Randeniya	Keith Ryan	Peter Vohralik
GSFC	NASA Goddard Space Flight Center, U.S.A.	Charles Jackman, David Considine, Eric Fleming	Charles Jackman	Charles Jackman
LLNL	Lawrence Livermore National Laboratory, U.S.A.	Peter Connell, Keith Grant, Douglas Kinnison, Douglas Rotman	Douglas Kinnison	Douglas Kinnison
THINAIR	University of Edinburgh, United Kingdom	Robert Harwood, Vicky West	Robert Harwood	Vicky West
UNIVAQ	University of L'Aquila, Italy	Giovanni Pitari, Barbara Grassi, Lucrezia Ricciardulli, Guido Visconti	Giovanni Pitari	Giovanni Pitari
3-D Models				
LARC	NASA Langley Research Center, U.S.A.	William Grose, Richard Eckman	William Grose	Richard Eckman
SCTM1	University of Oslo, Norway	Ivar Isaksen, Michael Gauss	Ivar Isaksen	Michael Gauss
SLIMCAT	University of Cambridge, United Kingdom	Martyn Chipperfield, Helen Rogers	Martyn Chipperfield	Helen Rogers

layers in the stratosphere. The vertical resolution is approximately 3 km in the stratosphere and decreases in the troposphere to less than 1 km near the surface.

The SCTM1 model has a horizontal resolution of 7.8^o latitude x 10^o longitude, with 29 vertical layers from the surface to 90 km. Sigma coordinates are used in the layers below 100 hPa and constant pressure coordinates above. The vertical resolution is approximately 1.5 km between 350 hPa and 21 hPa. Above 21 hPa, the vertical resolution is 5 km. The SLIMCAT model uses a horizontal resolution of 7.5^o latitude x 7.5^o longitude. The lower boundary of this model is at θ=335 K (approximately 8 km) and the upper boundary at θ=2700 K (about 60 km). There are 12 vertical layers in θ (potential temperature) coordinates, with vertical resolution in the lower stratosphere about 3 km.

Most models use temperature lapse rate to define the location of the tropopause, which changes with season and latitude. The 2-D models use temperature from climatology, except for the THINAIR model which calculates temperature interactively. The 3-D models employ a single year of temperature data. The LARC 3-D model uses temperature calculated by a T32 version of the Langley spectral GCM. The SCTM1 model uses NMC temperature data from 1990, and the SLIMCAT model uses 1992 data from the U.K. Met Office. The SCTM1 model uses a different approach to identify the model tropopause. In this model, tropospheric air is defined by an ozone mixing ratio less than 0.25 ppmv. The tropopause is constrained, however, and not allowed to rise above the 46 hPa level.

In 2-D models, the troposphere is distinguished from the stratosphere by assigning large values of K_{yy} (typically 1-1.5x10^6 m^2/sec) and K_{zz} (4-10 m^2/sec). Studies indicate that strat-trop exchange may be dominated by transport from the middle-world to the troposphere (Eluszkiewicz, 1996). In a 2-D model, this will manifest itself as eddy flux along isentropic surfaces across the boundary (Shia et al., 1993). If this is true, the model calculated residence time of aircraft emissions in the lower stratosphere would be sensitive to the horizontal and vertical resolutions of the models that determine the location and seasonal variation of the tropopause.

1.1.2 Temperature and Transport Parameters

Most results in this report are generated by the models in the chemistry-transport (CTM) mode, i.e. results are obtained using pre-calculated temperature and transport fields. The temperature is used in the models to compute temperature-dependent reaction rate constants, and, in some models, to predict the surface area of polar stratospheric clouds (PSCs). In addition, the temperature is also used in computing the winds and eddy diffusion coefficients in some of the 2-D models. The THINAIR 2-D model is the exception and calculates temperature and winds interactively along with chemical perturbations. Model characteristics related to temperature, winds, and parameterization of eddy diffusion are summarized in Tables 1.3 and 1.4. A more detailed description is given below.

The UNIVAQ 2-D model uses the zonal mean temperature and statistics for zonal asymmetry in temperature from the twelve year NMC average (1979-1990) in the chemistry calculations, but the transport parameters are computed (Pitari, 1993a) from the output of a spectral quasi-geostrophic 3-D model (Pitari et al., 1992). The residual circulation is calculated directly from velocity and temperature data of the GCM. It calculates K_{yy} as the quasi-geostrophic potential vorticity flux to gradient ratio (see Newman et al., 1986), with the dynamical data taken from the GCM. Typical values for K_{yy} in the tropical lower stratosphere are 0.1-0.5x10^5 m^2/sec. A minimum value of 2x10^5 m^2/sec is adopted outside the tropics. K_{yz} values are obtained by projecting the K_{yy} from isentropic to pressure surfaces.

The AER model uses the zonal mean temperature and statistics for zonal asymmetry in temperature from the eight year NMC average (1979-1986). It computes the vertical velocity as the ratio of the heating rate (based loosely on published results of Dopplick [1979]) to the temperature lapse rate (see e.g. Tung [1982] and references therein). The vertical velocity field is integrated to obtain a stream function with adjustments made to the heating rate to assure mass conservation (see Ko et al. [1985] for a description of the procedure). Values for K_{yy} are assigned to simulate the tropical barrier (Shia et al., 1998) guided by observed exchange time constants between midlatitudes and the tropics (Minschwaner et al., 1996; Volk et al., 1996; Schoeberl et al., 1997). Values chosen are 0.7-1.3x10^5 m^2/s for the tropics and 3-10x10^5 m^2/s elsewhere. Values of 0.1 m^2/sec are adopted for K_{zz} from the tropopause to 40 km, increasing to 1 m^2/sec above 50 km. Values of K_{yz} are obtained by projecting the K_{yy} from isentropic surfaces to pressure surfaces.

The CSIRO model uses the zonal mean temperature from the eight year NMC average (1979-1986). The

Table 1.2: Model Grid and Resolution

Model	Horizontal Resolution (lat x lon)	Vertical Resolution, Coordinate	Model Top Boundary	Tropopause
2-D Models				
AER	10^o	1.2 km log-pressure	60 km 0.2 hPa	temperature gradient from climatology
CSIRO	5^o	2 km log-pressure	80 km 0.01 hPa	temperature gradient from climatology
GSFC	10^o	2 km log-pressure	90 km 0.0024 hPa	temperature gradient from climatology
LLNL	5^o	1.5 km log-pressure	84 km 0.01 hPa	temperature gradient from climatology
THINAIR	10^o	3.5 km θ coordinates	60 km 0.2 hPa	temperature gradient from climatology
UNIVAQ	10^o	2.8 km log-pressure	70 km 0.04 hPa	temperature gradient from climatology
3-D Models				
LARC	5.5^o x 5.5^o (T16 spectral)	100 hPa interval below 100 hPa; 3 km interval above 100 hPa, sigma coordinates	65 km 0.1 hPa	temperature gradient from T32 GCM
SCTM1	7.8^o x 10^o	1.5 km between 350 hPa and 21 hPa, 5 km above 21 hPa, sigma/pressure	90 km 0.002 hPa	defined as O_3=0.25 ppmv but always below 46 hPa
SLIMCAT	7.5^o x 7.5^o	12 levels, $\sim$3 km θ coordinates	$\sim$60 km θ=2700 K	model lower boundary at θ=335 K ($\sim$8 km)

Table 1.3: Temperature, Winds and K_{yy} Used in the Models

Model	zonal mean temperature	zonal asymmetry in temperature	winds	K_{yy}
2-D Models				
AER	8 year average (1979-1986) monthly mean T from NMC	probability distribution based on statistics from NCEP (1979-1986), used in chemistry calculation only	w=Q/Γ Heating rate based loosely on Dopplick, adjusted to conserve mass	assigned values to match exchange time constant across the tropical barrier
CSIRO	8 year average (1979-1986) monthly mean T from NMC	zonal asymmetry not used.	iterative procedure to solve TEM energy equation (include dT/dt term); heating rates taken from M&M augmented by latent heat in troposphere, computed for mesosphere	computed from $\frac{EPFlux}{gradient\ of\ PV}$
GSFC	17 year average (1979-1995) monthly mean T from NCEP	probability distribution based on statistics from NCEP (1979-1995)	solve stream function using Garcia and Solomon (1983); heating rate from climatological T, O_3, and H_2O plus latent heat; forcing from 6 planetary waves and gravity wave breaking	computed from $\frac{EPFlux}{gradient\ of\ PV}$
LLNL	Fleming (private communication)	Fleming (private comm.), used in chemistry calculations and in determination of winds and K_{yy}	solve stream function using Garcia and Solomon (1983); heating rate from climatological T and calculated trace gases; forcing from 2 planetary waves, gravity wave breaking, and Rayleigh friction	computed from $\frac{EPFlux}{gradient\ of\ PV}$
THINAIR	calculated interactively	zonal asymmetry base on wave 1 in temperature	calculated interactively using 3 planetary waves and spectrum of gravity waves	computed from $\frac{EPFlux}{gradient\ of\ PV}$
UNIVAQ	12 year average (1979-1990) monthly mean T from NMC	zonal asymmetry based on statistics, used in chemistry calculations only	calculated from velocity and temperature data of 3-D GCM	computed from $\frac{EPFlux}{gradient\ of\ PV}$
3-D Models				
LARC	from T32 GCM	explicit	from T32 GCM	none
SCTM1	1990 NMC	explicit	horizontal winds from GISS GCM, vertical winds from continuity	in troposphere only, associated with convection
SLIMCAT	UKMO analysis (1992)	explicit	UKMO analysis (1992)	none

Table 1.4: Values of Eddy Diffusion Coefficients Used in the 2-D Models

Model	K_{yy}, trop (10^5 m^2/sec)	K_{zz}, trop (m^2/sec)	K_{yy}, strat (10^5 m^2/sec)	K_{zz}, strat (m^2/sec)	K_{yz}, strat (m^2/sec)
2-D Models					
AER	15	10	0.7-1.3 in tropics, 3-10 elsewhere	0.1-1	projected, typical values ± 100
CSIRO	10	4	calculated diagnostically, set to 0.1 when wind is easterly, always between 0.1 and 30	0.25 from 21 km-42 km; 0.1 elsewhere	projected, magnitude can be as large as 1000
GSFC	calculated (6 waves), minimum value of 15	tropopause: 1; at ground: 50 in tropics, 25 at poles	calculated (6 waves), minimum value 0.1	0.03 at tropopause to 0.3 at stratopause, computed in mesosphere	0
LLNL	10	4	calculated (2 waves), minimum value 0.1	calculated, with minimum value of 0.2	0
THINAIR	1	5	calculated (3 waves)	0	0
UNIVAQ	5-15	10-30	calculated from 3-D output, typically 0.1-0.5 in tropics, $\geq$2 elsewhere	calculated from 3-D output, 0.1-1.0 in stratosphere	projected, typical values ± 100

heating rates (a combination of archived stratospheric values in the M&M report [Prather and Remsberg, 1993], calculated values in the mesosphere based on climatological ozone and temperature, and latent heat in the troposphere from Dopplick) are used along with the adopted climatological zonal-mean temperature field to compute the velocities from the zonal-mean energy equation (see Solomon et al. [1986]). K_{yy} values are calculated as the ratio of the E-P flux divergence to the meridional gradient of potential vorticity where the E-P flux is determined diagnostically from the zonal-mean momentum equation using the calculated velocities and the zonal wind determined from the zonal-mean temperature (see Randeniya et. al. [1997] and Vohralik et al. [1998] for details). Values for K_{zz} in the stratosphere are taken to be 0.1 to 0.25 m^2/sec. Values of K_{yz} are obtained by projecting the K_{yy} from isentropic surfaces to pressure surfaces.

The GSFC and LLNL models use the seventeen year average (1979-1995) temperature from NCEP. Both models use the climatological 3-D temperature field to compute the zonal-mean winds and K_{yy} in a self-consistent way. The GSFC model (see Jackman et al., 1996) uses observed ozone, H_2O, and temperature to compute the diabatic heating which is augmented by the latent heat to provide the net heating in the energy equation. Mechanical forcing from planetary waves (calculated using the 3-D temperature database using six waves) and effects of gravity wave breaking provide the wave driving for the momentum equation. The stream function is obtained by solving an elliptic equation obtained by combining the zonal-mean momentum and energy equations (see e.g., Garcia and Solomon, 1983). The LLNL model solves a similar set of equations but employs different methods to compute the heating and the forcing terms. The heating rate for the LLNL model is computed from climatological temperatures and model calculated trace gases. Mechanical forcing employs 2 planetary waves, gravity wave breaking, and Rayleigh friction. Both models use the ratio of the E-P flux divergence to the gradient of potential vorticity computed using the 3-D temperature database to calculate K_{yy} (see e.g. Garcia, 1991; Randel and Garcia, 1994), and use a gravity wave breaking parameterization to calculate K_{zz}. The K_{yz} is zero in these models.

The THINAIR model is the only model which calculated temperature and winds interactively, ie. the temperature and circulation differ in each scenario based on variations in model-calculated ozone, which is itself controlled by temperature and circulation. Three planetary waves and a spectrum of gravity waves are employed in the calculation of model winds and stratospheric K_{yy} (see Kinnersley and Harwood, 1993). K_{zz} is not used in the stratosphere. The THINAIR model utilizes the "wave" approach to accounting for zonal asymmetry in temperature [see De Rudder et al., 1996; Portmann et al., 1996; Smyshlaev et al., 1998]. A wavenumber 1 modulation to the zonal mean temperature is employed to approximate the temperature fluctuations a circulating atmospheric parcel might experience as it moves around the globe. The amplitude of the modulation varies in space and time and is proportional to the calculated planetary wave amplitudes. The period of the modulation is also a spatially and temporally varying quantity, similar to the circumnavigation time of an air parcel in the atmosphere. Thus, the model temperature at some grid point can vary dramatically on short time scales and be very far from the zonal mean temperature of the grid point.

It should be noted that K_{yy} values calculated using observed temperature are sometimes negative (see e.g. Newman et al., 1986). In those cases, the models reassign a minimum value, typically about 0.1×10^5 m^2/sec. CSIRO also assigns K_{yy} values of 0.1×10^5 m^2/sec whenever the zonal wind (derived from temperature data) is easterly and resets values larger than 30×10^5 m^2/sec to that value.

Temperatures and wind fields for the LARC 3-D model are taken from the LARC T32 spectral GCM output. The SCTM1 and SLIMCAT 3-D models both employ observed temperature fields, SCTM1 using the 1990 NMC temperature field and SLIMCAT the UKMO analysis from 1992. SLIMCAT also uses horizontal winds from the 1992 UKMO analysis (Swinbank and O'Neill, 1994). SCTM1 uses horizontal winds from the GISS GCM and vertical winds from continuity. SLIMCAT generates vertical winds diagnostically using the MIDRAD radiation scheme (Shine, 1987). These 3-D models do not require eddy diffusion coefficients, though the SCTM1 models does employ K_{yy} diffusion in the troposphere in association with convective events.

While no specific study has been performed to confirm this, it is reasonable to assume that each model has checked on their own that their velocities and numerical schemes are mass conserving. Judging from the minimum value chosen for K_{yy} in the models, one would assume that numerical diffusion should not be an issue.

Given the different methods used in deriving the transport parameters in the models, it is not surprisingly that there are large differences in the calculated distributions of the trace gases. Large differences in

model simulated distributions of chemically inert tracers such as sulfur hexafluoride point to transport differences as a major contributor. The community is trying to identify a climatological database of zonal-mean distributions of trace gases that can be used to diagnose the transport parameters.

1.2 Chemistry Treatment

1.2.1 Gas-phase Chemistry

The kinetic reaction rate constants are from JPL-97 (DeMore, 1997) except SCTM1 which uses JPL-94. CSIRO, LARC and SLIMCAT assumes a 5% yield of HCl from OH+ClO. The 3-D models use the temperature at the 3-D grid points to compute the reaction rate constants. Among the 2-D models, gas phase rate constants are computed using the zonal mean temperature in the CSIRO, GSFC, and UNIVAQ models. The AER and LLNL models use rate constants weighted by the probability distribution of the zonally asymmetric temperature structure.

1.2.2 Heterogeneous Chemistry

The following seven heterogeneous reactions were identified in JPL-97 as possible reactions on sulfate aerosol and/or polar stratospheric cloud (PSC) particles.

$$N_2O_5 + H_2O(solid) \rightarrow 2HNO_3 \quad \text{(A)}$$
$$ClONO_2 + H_2O(solid) \rightarrow HNO_3 + HOCl \quad \text{(B)}$$
$$BrONO_2 + H_2O(solid) \rightarrow HNO_3 + HOBr \quad \text{(C)}$$
$$ClONO_2 + HCl(solid) \rightarrow HNO_3 + Cl_2 \quad \text{(D)}$$
$$HOCl + HCl(solid) \rightarrow Cl_2 + H_2O \quad \text{(E)}$$
$$HOBr + HCl(solid) \rightarrow BrCl + H_2O \quad \text{(F)}$$
$$N_2O_5 + HCl(solid) \rightarrow HNO_3 + ClNO_2 \quad \text{(G)}$$

Most models assume that the rate constant is in the form γvA/4, where γ is the sticking coefficient, v is the thermal velocity of the reactant, and A is the surface area of the sulfate or PSC.

1.2.2.1 Reactions on Sulfate Aerosol

For reactions on sulfate, AER, GSFC, LLNL, and SCTM1 include the first six reactions. UNIVAQ includes the first 5, CSIRO the first 3, while THINAIR and LARC includes only the first two. All models use γ=0.1 for reaction A. There are slight variations in the temperature dependence of γ for the other reactions on sulfate particles. Previous analyses (Murphy and Ravishankara, 1994; Borrmann et al., 1997; Michelsen et al., 1997) have shown that the γ for some of the reactions are very sensitive to temperature. Ignoring the zonal asymmetry in temperature by using the zonal mean temperature in calculations may underestimate the ozone impact from HSCT (Weisenstein et al., 1998). Since the sulfate surface area is specified in the calculations, the temperature dependence comes from γ and v. The AER and LLNL models use the 3-D temperature distribution to calculate a weighted γv. UNIVAQ uses the temperature distribution to calculate a weighted γ. CSIRO and GSFC use zonal mean temperature. The 3-D models explicitly employ 3-D temperature fields and so handle the temperature-dependent reaction rates more appropriately than 2-D models. A summary of the treatment of heterogeneous chemistry in the models is given in Table 1.5.

The model calculated ozone responses to HSCT will depend on the sulfate surface area density (SAD) in the atmosphere. In this study, the SAD is prescribed rather than calculated by the individual models. In the background atmosphere, the SAD from WMO (1992) corresponding to the clean background with no volcanic influence is used. Sulfur in the fuel will result in SO_2 emission from the engine, with the potential to perturb the SAD. The change in SAD depends on how much of the emitted SO_2 is converted in the plume to sulfate particles (Weisenstein et al., 1996, Danilin et al., 1997). Most results in this study use SAD changes calculated from the AER 2-D sulfate model (Weisenstein et al., 1997) with different assumptions on

Table 1.5: Treatment of Heterogeneous Chemistry in the Models

Model	Sulfate Reactions	Sulfate Reaction Rates	PSC Reactions	PSC Reaction Rates	PSC Parameterization
2-D Models					
AER	A-F	$\overline{\gamma(T)v(T)}A/4$	A,B,D,E,G on NAT A-G on ice	$\overline{\gamma(T)v(T)A(T)}/4$	thermodynamic equilibrium, no supersaturation
CSIRO	A-C	$\gamma(\overline{T})v(\overline{T})A/4$	none	NA	NA
GSFC	A-F	$\gamma(\overline{T})v(\overline{T})A/4$	A,B,D,E on NAT A-G on ice	$\gamma(\overline{T})v(\overline{T})\overline{A(T)}/4$	thermodynamic equilibrium, supersaturation ratios: 10 for NAT, 1.4 for ice
LLNL	A-F	$\overline{\gamma(T)v(T)}A/4$	A-F on STS	$\overline{\gamma(T)v(T)}A/4$	PSC surface area fixed from climatology
THINAIR	A-B	$\gamma(\overline{T})v(\overline{T})A/4$	A,B,D,G	$\gamma(\overline{T})v(\overline{T})\overline{A(T)}/4$	PSC reactions for T<195 K assume gas lifetimes of 9 hours
UNIVAQ	A-E	$\overline{\gamma(T)}v(\overline{T})A/4$	A,B,D,E on NAT A-E on ice	$\overline{\gamma(T)}v(\overline{T})\overline{A(T)}/4$	explicit microphysics with nucleation and condensation
3-D Models					
LARC	A-B	$\gamma(T)v(T)A/4$	A,B,D,E,G on NAT and ice	$\gamma(T)v(T)A(T)/4$	thermodynamic equilibrium
SCTM1	A-F	$\gamma(T)v(T)A/4$	A,B,D,E,G on NAT none on ice	$\gamma(T)v(T)A(T)/4$	thermodynamic equilibrium
SLIMCAT	A-F	$\gamma(T)v(T)A/4$	A,B,D,E,G on NAT A-G on ice	$\gamma(T)v(T)A(T)/4$	thermodynamic equilibrium

conversion in the plume. The changes in SAD from the AER model were found to be in general agreement with the results of other sulfate aerosol models (Weisenstein et al., 1998).

Both the AER and UNIVAQ models have the capability to calculate sulfate surface area interactively with a microphysics code. This capability was utilized in several scenarios, so we will describe here the microphysical processes and methodologies employed. Both models calculate aerosol size distributions by employing discrete size binning. The AER model uses 40 size bins, from 0.0004 μm to 3.2 μm by volume doubling. The UNIVAQ model uses 11 size bins, from 0.01 μm to 10.25 μm by radius doubling. Both models include the processes of homogeneous nucleation, coagulation, condensational growth, sedimentation, and evaporation. The UNIVAQ model also includes heterogeneous nucleation. A more detailed description of the AER microphysical model can be found in Weisenstein et al. (1997) and of the UNIVAQ microphysical model in Pitari et al. (1993b). A comparison of the two models is given by Weisenstein et al. (1998). The main differences between the calculated sulfate aerosol in these models result from different wind fields and the different aerosol size resolutions.

1.2.2.2 Reactions on PSCs and Cold Sulfate Aerosol

The reaction rate constants for reactions on PSCs are also in the form of γvA/4, where A is the surface area for type I PSC (assumed to be NAT) or type II PSC (assumed to be ice) or ternary sulfate particles. A summary of the PSC parameterization scheme and PSC reactions employed by each model is given in

Table 1.5. The CSIRO model does not include any reactions on PSCs or ternary sulfate. UNIVAQ includes the first 5 reactions on ice and reactions A, B, D and E on NAT. The microphysics model described in Pitari et al. (1993b) is used to compute the sulfate surface area and PSC surface area in the UNIVAQ model. The model keeps track of homogeneous nucleation, heterogeneous nucleation (H_2O and H_2SO_4 on Aiken nuclei; HNO_3 and H_2O on sulfate particles; H_2O on NAT particles); condensation (H_2O and H_2SO_4 on sulfate; HNO_3 and H_2O on NAT; H_2O on ice); coagulation (only for sulfate particles), evaporation and gravitational settling to calculate the particle size distributions for the sulfate, NAT and ice. For this report, the model calculated sulfate surface area is replaced by the assigned surface area in the calculations. Since the model explicitly calculates type I and type II PSC, transport of solid HNO_3 and H_2O are included.

GSFC and AER treat all seven reactions as surface reactions on ice and reactions A, B, D and E on NAT using the sticking coefficients as stated in JPL-97. The GSFC model adjusts the rates for reactions B, D and E to account for the dependence of these reaction rate constants on relative humidity, as suggested by Tabazadeh and Turco (1993) and Hanson and Ravishankara (1994). Both models compute the PSC surface area following the approach of Considine et al. (1994). AER assumes local thermodynamical equilibrium between gas and condensed phases for HNO_3 and H_2O with no supersaturation requirement. If the temperature is colder that the critical temperature for NAT, but warmer than the critical temperature for ice, the excess gas-phase HNO_3 and H_2O (enough to form the trihydrate) will be put into NAT particles with 0.5 μm radius and bulk density of 1.6 gm/cm^3. For temperatures colder than the critical temperature of ice, it is assumed that some of the NAT that is formed previously will be coated by ice. After the excess gas-phase HNO_3 and some of the excess H_2O is put into 0.5 μm NAT particles, the left-over excess H_2O is used to cover some of the NAT particles to form 7 μm radius type II PSC (considered as ice as far as assigning γ is concerned) with a bulk density of 0.93 gm/cm^3. As a result, both type I and type II PSCs are present in this case.

The GSFC model calculations employ supersaturation ratios of 10 for NAT and 1.4 for ice, effectively reducing the nucleation temperatures (i.e. the temperature threshold for particle formation) by 3K and 2K for type I and type II PSCs, respectively. In the GSFC model, NAT is assumed to have a bulk density of 1.6 gm/cm^3, lognormal size distribution with a mode radius of 1 μm and standard deviation of 1.8. The corresponding parameters for Type II PSC are 1.0 gm/cm^3, 10 μm radius and 1.8. Both AER and GSFC transport solid HNO_3 and solid H_2O separately with sedimentation velocities at each time step. The GSFC model takes temperature asymmetry into account when calculating surface area. The AER model uses the temperature asymmetry to calculate a weighted product for γvA.

LLNL simulates polar processing of radicals by allowing the six reactions to occur on sulfate ternary droplets. The rates are obtained from various published literature and have not been reviewed by JPL-97. A surface area density of 1 μm^2/cm^3 is imposed within 25^o of the poles when the PSC climatology of Poole and Pitts (1994) indicates a PSC frequency of occurrence exceeding 0.08. Dehydration and denitrification are represented globally (independent of the PSC surface area parameterization) by assuming that the partial pressure in excess of the saturation vapor pressure over ice (calculated using zonal mean temperatures) is removed permanently with first order time constants of 1 day for H_2O and 0.5 days for HNO_3.

The THINAIR model employs wave 1 zonal asymmetry in temperature to determine the fraction of each latitude circle which contains PSCs. Reactions A, B, D, and G are turned on for temperatures below 195 K. These reactions are assumed to remove the gas phase species with a local time constant of 9 hours.

LARC treats reactions A, B, D, E and G on PSCs using a routine supplied by Martyn Chipperfield (Univ. of Cambridge) and employing a code by Ken Carslaw to calculate rates. The parameterization calculates surface area for type I PSCs from the amount of HNO_3 condensed assuming that there are 10 NAT particles cm^{-3} and for type II PSCs from the amount of H_2O condensed assuming the radius of ice particles is 10 μm. Denitrification is triggered by the presence of type II PSCs and simulated by adopting a first order removal rate constant to remove solid phase HNO_3. Solid HNO_3 is turned back into gas-phase HNO_3 with a time constant of 1 day when the temperature is above 195 K.

The SCTM1 model employs cold heterogeneous chemistry on NAT only, using reactions A, B, D, E, and G. The occurrence of PSCs is calculated based on temperature, but is confined to latitudes higher than 47^o. Between 100 and 47 hPa, the threshold temperature is 197 K; between 47 and 22 hPa it is 193 K. The effects of PSCs are modeled in terms of the effective lifetimes of the gaseous reactants in the presence of polar stratospheric clouds. The lifetimes are calculated based on mass transfer rates taken from Turco et al. (1989). The SLIMCAT model employs cold heterogeneous chemistry on both NAT and ice particles using

the PSC scheme of Chipperfield, which is also used by the LARC model. An equilibrium calculation for NAT and ice formation is used to obtain rates for reactions A, B, D, E, and G on NAT and reactions A-G on ice.

Accounting for temperature deviations away from the zonal mean is essential to correctly representing polar heterogeneous chemistry in a 2D model. A quantitative investigation of the differences between the temperature distribution (used by AER, GSFC, LLNL, and UNIVAQ) and the temperature wave (used by THINAIR) approaches has been performed by Smyshlaev et al. (1998). They found that the wave approach utilizing at least 3 waves accurately represents 3-D temperature fluctuations. Models which use the probability distribution approach based on monthly statistics are likely to predict too long a duration for PSCs. Model which use only 1 wave are likely to underpredict PSC duration.

The above discussion shows that PSC treatments in models have not converged and are different among the models. For example, the chlorine activation rate on PSCs in the LLNL and SCTM1 models does not respond to changes in concentration of HNO_3 and H_2O due to aircraft emissions. Temperature asymmetry in 2-D models is handled differently in different models. Different sets of heterogeneous reactions are employed. Different PSC surface areas are calculated even for the same conditions.

1.2.3 Chemistry Solvers

Finally, we would like to comment on the chemistry solvers used in the 2-D models. Previous model intercomparison exercises have shown that solvers in most models calculate the same partitioning of the radicals under the same constraints (solar zenith angle, overhead ozone, and local concentrations of the long-lived species) when used as a box model. Since the 2-D models transport zonal mean concentrations, the zonal mean production and loss rates are needed in the mass continuity equations for the long-lived species in these models. Different techniques are used to obtain the zonal mean production and loss rates. These include integrating the diurnally varying concentrations of the radicals obtained by explicit time marching to obtain the zonal mean rates; and using diurnally-averaged radical concentrations calculated from average solar zenith angles corrected by pre-calculated correction factors. The AER model employs the former method, while most of the other 2-D models use some variation on the latter method. The different approaches are summarized in Table 1.6.

UNIVAQ uses 24 hour average photolysis rates to calculate 24 hour average radical concentrations and the production and loss terms for long-lived species. CSIRO and LLNL use similar techniques to obtain zonal mean production and loss rates, but they employ pre-calculated factors to correct for diurnal effects. LLNL calculates the diurnal factors for a variety of chlorine loadings and sulfate surface area densities. THINAIR calculates daytime average radical concentrations. Production and loss rates for the long-lived species are an average of the daytime rates, obtained using daytime radical concentrations, and nighttime rates, most of which are assumed to be zero. Non-zero nighttime rates mainly come from washout removal or reactions involving species which have little diurnal variation. However, the $NO_2+NO_3 \rightarrow N_2O_5$ reaction is assumed to occur only at night. The GSFC model calculates daytime average concentrations of most radical species, but performs explicit time-marching for night species, including HNO_3, NO_2, NO_3, N_2O_5, HOCl, HCl, ClO, $ClNO_3$, BrO, HOBr, and $BrNO_3$.

All models except LLNL employ family groupings to minimize the number of transported species. The transported species vary somewhat, especially for the nitrogen and chlorine species. Some models transport HNO_3, N_2O_5, and HNO_4 separately from the NO_y family, while some consider these species part of NO_y. Likewise, some models transport $ClNO_3$ and HCl separately from the Cl_y family, while others do not. Transported species for each model are listed in Table 1.6. Transport is performed with a variety of advection schemes and different time steps. The frequency with which production and loss rates for the slow species are updated also varies. This information is provided in Table 1.6 also.

1.3 Sources and Sinks for Some Species

Aircraft emissions include H_2O, oxides of nitrogen, and oxidation products from sulfur in the fuel. We will discuss how these are treated in the models.

Most 2-D models assigned tropospheric concentrations of H_2O based on relative humidity and temperature. The exception is GSFC, which uses a first order removal time constant to relax the calculated

Table 1.6: Chemistry Solvers Used in the Models

Model	solve continuity equations for:	radicals and P & L for long-lived species	time step
2-D Models			
AER	source gases, O_x, HNO_3, NO_y, Cl_y, Br_y, solid HNO_3, solid H_2O	do explicit time-marching of radical species for 24 hours; use diurnally varying radical concentrations to compute 24-hour averaged P & L for long-lived species.	no operator splitting; 6 hour time step; Smolarkiewicz scheme for advection; P & L updated daily
CSIRO	source gases, O_x, NO_y, Cl_y, Br_y	24-hour averaged zonal-mean P & L calculated using correction factors obtained from a 24-hour integration of all species;uUpdated every 10 days	use variable order Bott scheme with 6 hour time step; keep same P & L for 10 days
GSFC	source gases, O_x, NO_z, HNO_3, N_2O_5, Cl_z, $ClNO_3$, Br_y, solid HNO_3, solid H_2O	use time marching for night-species (HNO_3, NO_2, NO_3, N_2O_5, HOCl, HCl, ClO, $ClNO_3$, BrO, HOBr and $BrNO_3$); use daytime averaged J-rates and dawn values of night-species to get day-averaged values of all species; diurnal average P & L updated daily	use split operator; Lin and Rood scheme; 12 hour for advection, 3 hour for vertical diffision, 24 hour for horizontal diffusion, 24 hour for chemistry
LLNL	explicit, non-family approach	use 24-hour averaged sun and diurnal factors to time march the species with 15 minute time step; diurnal factors are calculated for each chlorine loading and sulfate surface area density	use split operator; use Smolarkiewicz with 2 hour time step to do transport for 2 days, then time march chemical species for 2 days.
THINAIR	source gases, O_x, NO_y, HNO_3, N_2O_5, HNO_4, HO_x, Cl_y, Br_y	use daytime average J-rate to calculate daytime mixing ratios; 24-hour average P & L is weighted sum of day and night rates; most night rates zero except for NO_2+NO_3 $\rightarrow$ N_2O_5	Adams-Bashforth scheme with 4 hour time step
UNIVAQ	source gases, O_x, NO_y, HNO_3, $ClNO_3$, Cl_y, Br_y	use 24-hour averaged sun to calculate 24-hour averaged radical concentrations to get P & L for long-lived species; updated every 2 hours	explicit time marching with 2 hour time step
3-D Models			
LARC	source gases, O_x, NO_y, HNO_3, N_2O_5, Cl_y, HCl, $ClONO_2$, H_2O_2, solid HNO_3	use instantaneous J-rates to calculate photochemical equilibrium concentrations of the radicals every 30 minutes	forward Euler with 30 minute time step
SCTM1	source gases, O_x, NO_x, NO_y, Cl_x, Cl_y, Br_y, HO_x	QSSA method; family approach	10 minute integration step; rate coefficients updated every 40 min
SLIMCAT	source gases, O_x, NO_x, HNO_3, HNO_4, N_2O_5, NO_3, $ClNO_3$, HCl, HOCl, OClO, ClO_x, BrO_x, HBr, HOBr, BrCl, $BrNO_3$, H_2O_2	semi-implicit symmetric method (Ramaroson et al., 1992); explicit calculation of rates every time step with no diurnal averaging	operator split; 20 min for chemical time step, 30 min for dynamical time step

Table 1.7: Parmeterization of Lightning and Rainout

Model	Lightning source, source region	species removed by washout	washout time constant
2-D Models			
AER	2 MT/yr, 4-14 km	H_2O_2, CH_3OOH, CH_3CO_3H, CH_2O, HNO_3, HCl, HBr, F_x, CF_2O	5 days at the surface, 40 days at 10 km
CSIRO	2 MT/yr, 4-14 km	NO_y, Cl_y, Br_y, H_2O_2, CH_2O, CH_3COOH	3 days at the surface, 28 days at 10 km
GSFC	2 MT/yr, 4-14 km	H_2O_2, CH_3COOH, HNO_3, HO_2NO_2, HCl, HBr, HF, CClFO, and COF_2	25 days to 100 days
LLNL	5 MT/yr, from ISCCP cloud database	N_2O_5, HNO_3, HNO_4, H_2O_2, CH_2O, ClO, HCl, HOCl, $ClONO_2$, $BrONO_2$	3 days below 4 km, 50 days near tropopause
THINAIR	none	HNO_3, HNO_4, HCl, HBr, H_2O_2, CH_2O, CH_3OOH	7 days
UNIVAQ	5 MT/yr, from ECHAM3 GCM output	HNO_3, HCl, HBr, H_2O_2, CH_3COOH, CH_2O, H_2SO_4, SO_2, aerosols	5 days at the surface, 50 days at 10 km
3-D Models			
LARC	2 MT/yr, 4-14 km	H_2O_2, HNO_4, HNO_3, HCl, HBr	Mahlman and Moxim (1978)
SCTM1	7 MT/yr, from GCM output	HNO_3, individual members of Br_y, Cl_y, and NO_x families	Isaksen and Rodhe (1978)
SLIMCAT	none due to lower boundary location (at 335 K)	HNO_3, HCl, HBr, HNO_4, H_2O_2	20 days

concentrations to a pre-assigned relative humidity in the troposphere. The concentration in the stratosphere is computed using appropriate sources (in situ oxidation from methane, transport from the troposphere, and aircraft emission along flight corridors) and sinks (removal by transport out of the stratosphere and photochemical removal) in the mass continuity equation using an assigned boundary condition at the tropopause. The LARC model uses a fixed background H_2O determined from climatology. The distribution of water emissions from aircraft is solved as a separate species and added to the background in the calculations.

To simulate the concentration of NO_y in the lower stratosphere, all models include in situ oxidation of N_2O, transport of NO_x produced by lightning in the tropical upper troposphere, and NO_x emission from aircraft along the flight corridors. To simulate the effect of lightning, the models assigned a production rate of NO in the tropical upper troposphere. The exact location and the total amount differ slightly from model to model. The AER, CSIRO, GSFC and LARC models use a total of 2 MT(N)/yr uniformly (constant in molecules/cm^3/sec) distributed between 4 and 14 km in the tropics. The LLNL and UNIVAQ models use a total of 5 MT(N)/yr. The distribution in LLNL is derived from the ISCCP cloud database. The distribution in UNIVAQ is from the ECHAM GCM output. The THINAIR model does not use a lightning source of NO. Table 1.7 summarizes the lightning treatment in the models.

Most models use first order removal rate constants to simulate washout rates for soluble species, with time constants of 3-5 days at the ground, increasing to 30-50 days at 10 km. The washout rate in GSFC is longer, ranging from 25 days to 100 days. The CSIRO model allows no washout within 3 km of the tropopause. Washout in the LARC model follows the treatment of Mahlman and Moxim (1978). The SCTM1 model follows Isaksen and Rodhe (1978). SLIMCAT uses a constant 20 day washout lifetime. It should be noted that different models pick different species for washout. Some models remove NO_y, some only HNO_3 while others include N_2O_5, HNO_4, and $ClNO_3$. These are itemized by model in Table 1.7. With efficient washout, surface sources of NO_x have little impact on stratospheric NO_y.

There are significant differences in the H_2O and NO_y distributions (both in the background and the perturbed atmosphere) simulated by the models. No observational databases have been identified as the benchmarks for the climatological mean for these species in the present day atmosphere. It remains unclear as to whether the differences among the models are due to transport differences or differences in treatment of the sources. The quadratic loss of NO_y by photolysis of NO followed by the N+NO reaction may be a significant source of model NO_y differences.

Bibliography

[1] Borrmann, S., S. Solomon, J. E. Dye, D. Baumgardner, K. K. Kelly, and K. R. Chen, Heterogeneous reactions on stratospheric background aerosols, volcanic sulfuric acid droplets, and type I PSCs: effects of temperature fluctuations and differences in particle phase, *J. Geophys. Res., 102,* 3639-3648, 1997.

[2] Considine, D. B., A. R. Douglass, and C. H. Jackman, Effects of a polar stratospheric cloud parameterization on ozone depletion due to stratospheric aircraft in a two-dimensional model, *J. Geophys. Res., 99,* 18,879-18,894, 1994.

[3] Danilin, M. Y., J. M. Rodriguez, M. K. W. Ko, D. K. Weisenstein, R. C. Brown, R. C. Miake-Lye, and M. R. Anderson, Aerosol particle evolution in an aircraft wake: Implications for the HSCT fleet impact on ozone, *J. Geophys. Res. 102,* 21,453-21,463, 1997.

[4] Dopplick, T. G., Radiative heating of the global atmosphere: Corrigendum, *J. Atmos., Sci., 36,* 1812-1817, 1979.

[5] DeMore, W. B., S. P. Sander, D. M. Golden, R. F. Hampson, M. J. Kurylo, C. J. Howard, A. R. Ravishankara, C. E. Kolb, and M. J. Molina, Chemical kinetics and photochemical data for use in stratospheric modeling, Evaluation number 12, *JPL Publication 97-4,* Jet Propulsion Laboratory, NASA, 1997.

[6] DeMore, W. B., S. P. Sander, D. M. Golden, R. F. Hampson, M. J. Kurylo, C. J. Howard, A. R. Ravishankara, C. E. Kolb, and M. J. Molina, Chemical kinetics and photochemical data for use in stratospheric modeling, Evaluation number 11, *JPL Publication 94-26,* Jet Propulsion Laboratory, NASA, 1994.

[7] De Rudder, A., N. Larsen, X. Tie, G. P. Brassuer, and C. Granier, Model study of polar stratospheric clouds and their effect on stratospheric ozone 1. Model description, *J. Geophys. Res., 101,* 12,567-12,574, 1996.

[8] Eckman, R. S., W. L. Grose, R. E. Turner, W. T. Balckshear, and J. M. Russell III, Stratospheric trace constituents simulated by a three-dimensional general circulation model: Comparison with UARS data, *J. Geophys. Res. 100,* 13,951-13,966, 1995.

[9] Eluszkiewcz, J., A three-dimensional view of the stratosphere-to-troposphere exchange in the GFDL SKYHI model, *Geophys. Res. Lett., 23,* 2489-2492, 1996.

[10] Garcia, R. R., and S. Solomon, A numerical model of the zonnally averaged dynamical and chemical structure of the middle atmosphere, *J. Geophys. Res., 88,* 1379-1400, 1983.

[11] Garcia, R. R., Parameterization of planetary wave breaking in the middle stratosphere, *J. Atmos., Sci., 48,* 1405-1419, 1991.

[12] Hanson, D. R., and A. R. Ravishankara, Reactive uptake of $ClONO_2$ onto sulfuric acid due to reaction with HCl and H_2O, *J. Phys. Chem., 98,* 5728-5735, 1994.

[13] Isaksen, I., and H. Rodhe, A two-dimensional model for the global distribution of gases and aerosol particles in the troposphere. *Report AC-47,* Department of Meteorology, University of Stockholm, 1978.

[14] Jackman, C. H., E. L. Fleming, S. Chandra, D. B. Considine, and J. E. Rosenfield, Past, present, and future modeled ozone trends with comparisons to observed trends, *J. Geophys. Res., 101,* 28,753-28,767, 1996.

[15] Kinnersley, J. S. and R. S. Harwood, An isentropic model with an interactive parameterization of dynamical and chemical planetary wave fluxes, *Quart. J. Royal Met. Soc., 119,* 1167-1193, 1993.

[16] Kinnersley, J. S., The climatology of the THIN-AIR model", *Quart. J. Royal Met. Soc., 122,* 219-252, 1996.

[17] Ko, M. K. W., K. K. Tung, D. Weisenstein, and N. D. Sze A zonal mean model of stratospheric tracer transport in isentropic coordinates: Numerical simulations for nitrous oxide and nitric acid, *J. Geophys. Res., 90,* 2313-2329, 1985.

[18] Mahlman, J. D., and W. J. Moxim, Tracer simulation using a global general circulation model: Results from a midlatitude instantaneous source experiment, *J. Atmos., Sci., 35,* 1340-1374, 1978.

[19] Michelsen, H. A., et al., Stratospheric ozone loss enhanced by aerosol reactions at temperatures above 200K, paper presented at the 1997 Conference on the Atmospheric Effects of Aviation, Virginia Beach, Virginia, 1997.

[20] Minschwaner, K. et al., Bulk properties of isotropic mixing into the tropics in the lower stratosphere, *J. Geophys. Res., 9101,* 9433-9439, 1996.

[21] Murphy, D. M., and A. R. Ravishankara, Temperature averages and rates of stratospheric reactions, *Geophys. Res. Lett., 21,* 2471-2474, 1994.

[22] Newman, P. A., M. R. Schoeberl, and R. A. Plumb, Horizontal mixing coefficients for two-dimensional chemical models calculated from National Meteorological Center data, *J. Geophys. Res., 91,* 7919-7924, 1986.

[23] Pitari, G., S. Palermi, G. Visconti, and R. Prinn, Ozone response to a CO_2 doubling: Results from a stratospheric circulation model with heterogeneous chemistry, *J. Geophys. Res., 97,* 5953-5962, 1992.

[24] Pitari, G., A numerical study of possible perturbation of stratospheric dynamics due to Pinatubo aerosols: Implications for tracer transport, *J. Atmos., Sci., 50,* 2443-2461, 1993a.

[25] Pitari, G., L. Ricciardulli, and G. Visconti, High-speed civil transport impact: Role of sulfate, nitric acid trihydrate, and ice aerosols studied with a two-dimensional model including aerosol physics, *J. Geophys. Res., 98,* 23141-23164, 1993b.

[26] Poole, L. R., and M. C. Pitts, Polar stratospheric cloud climatology based on Stratospheric Aerosol Measurement II observation from 1978 to 1989, *J. Geophys. Res., 99,* 13,083-13,089, 1994.

[27] Portmann, R. W., S. Solomon, R. R. Garcia, L. W. Thomason, L. R. Poole, and M. P. McCormick, Role of aerosol variations in anthropogenic ozone depletion in the polar regions, *J. Geophys. Res., 101,* 22,991-23,006, 1996.

[28] Prather, M. J. and E. E. Remsberg, eds., The atmospheric effects of stratospheric aircraft: Report of the 1992 Models and Measurements Workshop, *NASA Reference Publication 1292,* NASA, Washington, D.C., 1993.

[29] Ramaroson, R., M. Pirre and D. Cariolle, A boxmodel for on-line computations of diurnal variations in a 1D model: Potential for application to multidimensional cases, *Ann. Geophys, 10,* 416-428, 1992.

[30] Randel, W. J., and R. R. Garcia, Application of a planetary wave breaking parameterization to stratopsheric circulation statistics, *J. Atmos., Sci., 51,* 1157-1168, 1994.

[31] Randeniya, L. K., P. F. Vohralik, I. C. Plumb, and K. R. Ryan, Heterogeneous $BrONO_2$ hydrolysis: Effect on NO_2 columns and ozone at high latitudes in summer, *J. Geophys. Res., 102,* 23,543-23,557, 1997.

[32] Schoeberl, M. R. et al., An estimation of the dynamical isolation of the tropical lower stratosphere using UARS wind and trace gas observations of quasi-biennial oscillation, *Geophys. Res. Lett., 24,* 53-56, 1997.

[33] Shia, R.-L., M. K. W. Ko, M. Zou, and V. R. Kotamarthi, Cross tropopause transport of excess ^{14}C in a two-dimensional model. *J. Geophys. Res., 98,* 18,599-18,606, 1993.

[34] Shia, R-L, M. K. W. Ko, D. K. Weisenstein, C. Scott, and J. Rodriguez, Transport between the tropical and mid-latitude lower stratosphere: Implication for ozone response to HSCT emissions, *J. Geophys. Res.,* 103, 25,435-25,446, 1998.

[35] Shine, K. P., The middle atmosphere in the absence of dynamical heat fluxes, *Quart. J. Roy. Met. Soc., 113,* 603-633, 1987.

[36] Smyshlaev, S. P., V. L. Dvortsov, M. A. Geller, and V. A. Yudin, A two-dimensional model with input parameters fro a GCM: Ozone sensitivity to different formulations for the longitudinal temperature variation, *J. Geophys. Res., 103,* 28,373-28,387, 1998.

[37] Solomon, S., J. T. Kiehl, R. R. Garcia, and W. Grose, Tracer transport by diabatic circulation deduced from satellite observations, *J. Atmos., Sci., 43,* 1603-1617, 1986.

[38] Swinbank, R., and A. O'Neill, Quasi-biennial and semi-annual oscillations in equatorial wind fields constructed by data assimilation, *Geophys. Res. Lett., 21,* 2099-2102, 1994.

[39] Tabazadeh, A., and R. P. Turco, A model for heterogeneous chemical processes on the surfaces of ice and nitric acid trihydrate particles, *J. Geophys. Res., 98,* 12,727-12,740, 1993.

[40] Turco, R. P., O. B. Toon, and P. Hamill, Heterogeneous Physicochemistry of the Polar Ozone Hole, *J. Geophys. Res., 94,* 16,493-16,510, 1989.

[41] Tung, K. K., On the two-dimensional transport of stratospheric trace gases in isentropic coordinates, *J. Atmos., Sci., 39,* 2330-2355, 1982.

[42] Vohralik, P. F., L. K. Randeniya, I. C. Plumb, and K. R. Ryan, Use of correlations between long-lived atmospheric species in asssessment studies, *J. Geophys. Res., 103,* 3611-3627, 1998.

[43] Volk, C. M., et al., Quantifying transport between the tropical and mid-latitude lower stratosphere, *Science, 272,* 1763-1768, 1996.

[44] Weisenstein, D. K., M. K. W. Ko, N-D Sze,and J. M. Rodriguez, Potential impact of SO_2 emissions from stratospheric aircraft on ozone, *Geophys. Res. Lett., 23,* 161-164, 1996.

[45] Weisenstein, D. K., G. K. Yue, M. K. W. Ko, N-D. Sze, J. M. Rodriguez, C. J. Scott , A two-dimensional model of sulfur species and aerosol, *J. Geophys. Res., 102,* 13,019-13,035, 1997.

[46] Weisenstein, D. K., M. K. W. Ko, I. G . Dyominov, G. Pitari, L. Ricciardulli, G. Visconti, and S. Bekki, The effect of sulfur emissions from HSCT aircraft: A 2-D model intercomparison, *J. Geophys. Res., 103,* 1527-1547, 1998.

[47] World Meteorological Organization (WMO), Scientific Assessment of Ozone Depletion: 1991, Global Ozone Res. and Monit. Proj., *Rep. 25,* Geneva, Switzerland, 1992.

Chapter 2

Emission Scenarios

The future fleet of High Speed Civil Transport (HSCT) aircraft employed in these scenarios is based on the technology concept aircraft developed by the U.S. National Aeronautics and Space Administration (NASA). This developing technology is aimed at a 300 passenger aircraft with a 5000 nautical mile range cruising at Mach 2.4 at 18-20 km altitudes. Three dimensional inventories of fuel consumption and emissions based on fleets of 500 and 1000 HSCT aircraft have been developed (Baughcum and Henderson, 1998). The future date at which a viable HSCT fleet will be in operation is unknown. However, we use detailed scenarios for 2015 and 2050 in order to account for displacement of subsonic aircraft by HSCTs.

The subsonic emission scenarios for 2015 and 2050 are discussed in detail in Chapter 9 of the IPCC report. The 2015 projections were developed by NASA based on forecasts of air travel demand and aircraft technology (Baughcum et al., 1998; Mortlock and van Alstyne, 1998). The "background" scenarios with 2015 boundary conditions (Scenarios D, D3-D8) use this subsonic fleet projection. The 2050 projections were developed by the International Civil Aviation Organization Forecasting and Economic Support Group (FESG) (CAEP/4-FESG/Report-4, 1998). These long range projections are much more uncertain, and therefore three different subsonic fleet scenarios have been employed for 2050 modeling. Background Scenario D9, with 2050 boundary conditions, employs the NASA 2015 fleet projection. Scenario F employs the FESG base case projections to 2050 based on IPCC GDP Scenario IS92a, and Scenario G employs the 2050 FESG high demand projections based on IPCC GDP Scenario IS92e. Technology Scenario 1 is employed in both cases for converting passenger-kilometers to emissions.

2.1 Fuel Use

Fuel use inventories were compiled for the projected fleets as functions of latitude, longitude, and altitude on a 1^ox1^ox1 km pressure altitude grid. Seasonal variations in fleet utilization and emissions were not considered. Figure 2.1 shows vertically-integrated fuel use from the projected 2015 subsonic fleet as a function of latitude and longitude. Figures 2.2 and 2.3 show similar plots for the projected 2050 fleets under the IS92a and high demand IS92e assumptions, respectively. The flight tracks of the projected HSCT aircraft fleet are evident in Figure 2.4, which shows fuel use above 13 km by the 500 HSCT fleet. HSCT aircraft are expected to be used for intercontinental and long-distance routes primarily over water, due to the need to minimize sonic booms over populated land masses. Fuel use above 13 km by the 1000 aircraft HSCT fleet is shown in Figure 2.5 as a function of latitude and longitude. The projected 1000 HSCT fleet is not a scaled version of the 500 HSCT fleet, but a separate projection which includes a greater percentage of flights in Asia.

The HSCT scenarios, which include an "S" in the scenario descriptor, include both a subsonic and a supersonic fleet. The subsonic fleet has been reduced relative to the subsonic-only scenarios to account for passenger demand displacement from subsonic to supersonic aircraft. Fuel use by both subsonic and supersonic aircraft is shown in Figure 2.6 for the 500 aircraft HSCT fleet together with the adjusted 2015 subsonic fleet as a function of latitude and altitude. Figure 2.7 shows a similar plot for the 1000 HSCT scenario. Fuel use integrated over latitude and longitude, ie. as a function of altitude only, is shown in Figure 2.8 The 2015 subsonic only fleet, the 500 HSCT fleet, and the 1000 HSCT fleet are shown by separate bars in the histogram. Notice that the 1000 HSCT fleet at cruise altitude does not consume twice the fuel of

the 500 HSCT fleet, but only 80% more (see Baughcum and Henderson, 1995). A histogram of the vertical distribution of fuel use in 2050 for the 1000 HSCT fleet along with the IS92a subsonic scenario is shown in Figure 2.9. Figure 2.10 show a similar histogram plot using the 2050 IS92e high demand subsonic fleet. A summary of fuel use for the included scenarios is given in Table 2.1, showing total fuel use and fuel use above and below 13 km.

Table 2.1: Fuel Use Projected for the Future Aircraft Scenarios

Scenario	Total Fuel (Tg/yr)	Fuel Burned below 13 km (Tg/yr)†	Fuel Burned above 13 km (Tg/yr)
2015 Subsonic	309	307	2
2015 Subsonic + 500 HSCTs	338	282	56
2015 Subsonic + 1000 HSCTs	378	279	99
2050 Subsonic IS92a	471	469	2
2050 Subsonic IS92a + 1000 HSCTs	557	458	99
2050 Subsonic IS92e High Demand	744	742	2
2050 Subsonic IS92e + 1000 HSCTs	831	732	99

†Note that scenarios which include supersonic aircraft use a reduced subsonic fleet to account for a shift in passenger demand.

2.2 HSCT Emissions

Because the HSCT technology is still in the research and development stage, operating parameters and emission indices (EI, grams of pollutant emitted per kilogram of fuel burned) are quite uncertain, and are therefore treated parametrically in this study. Aircraft emissions of H_2O, NO_x, and sulfur are the most significant to atmospheric ozone response. Emissions of CO and hydrocarbons were included in the atmospheric modeling performed for IPCC, but their emissions do not constitute a large perturbation to their background concentrations and thus do not influence ozone to a significant extent. Emissions of CO_2 do not chemically interact with ozone. CO_2 may impact ozone indirectly by modifying atmospheric temperature and circulation, but this effect is not accounted for by most of the models used here. Emission of soot particles is also ignored.

Table 2.2 lists the pollutants considered in the current modeling study and their emissions above 13 km. Emission indices (in grams of pollutant per kg fuel burned) for the aircraft at cruise are also shown. H_2O emissions are strictly proportional to fuel use, with an EI(H_2O)=1230. The NO_x emission indices are given as grams NO_2 equivalent per kg fuel burned and are treated parametrically. Projected emission indices for CO are 2.9 and for hydrocarbons 0.3. Most models represent all the hydrocarbon emissions as CH_4, even though aircraft are known to emit a variety of hydrocarbons. Sulfur (SO_x) emissions are not included in many of the emission scenarios. Where they are included, an EI(SO_x) of 0.4 gm SO_2 per kg fuel burned is employed, which represents a 50% reduction in fuel sulfur content from the current world average. Total emissions are projected on an annual basis. The models treat this emission as a continuous input flux at a fixed rate in molecules per second per grid box volume.

The NASA technology program is aggressively pursuing a combustor with an EI(NO_x) of 5. However, the emission scenarios treat this parameter parametrically and consider three values of EI(NO_x): 5, 10, and 15. The subsonic fleet projection accounts for different values of EI(NO_x) for different engine types and operating conditions and yields a weighted average EI(NO_x) of approximately 13 gm/(kg fuel). Vertical profiles of NO_x emissions, integrated over latitude and longitude, are shown in Figure 2.11 with EI(NO_x) of 5 for the HSCT aircraft. The 2015 subsonic only fleet, the 500 HSCT fleet, and the 1000 HSCT fleet are shown by separate bars in the histogram.

Table 2.2: Emissions by Projected HSCT Fleets above 13 km

Pollutant	Emission Index	500 HSCT Fleet (Gg/yr)	1000 HSCT Fleet (Gg/yr)
H_2O	1230	66,300	119,400
NO_x	5[†]	269	486
	10[†]	539	971
	15[†]	808	1460
CO	2.9	155	279
Hydrocarbons	0.3[‡]	15.7	28.2
SO_x	0	0	0
	0.4[♯]	21.6	38.8

[†]NO_x emission index given as NO_2 equivalent.
[‡]Hydrocarbon emission index given as CH_4 equivalent.
[♯]SO_x emission index given as SO_2 equivalent.

2.3 Sulfur Emission Scenarios

Sulfur emissions are a large uncertainty in the present assessment of the impact of aircraft on the atmosphere. The total emission of sulfur from aircraft depends on the sulfur content of the fuel. Sulfur content varies widely in current fuels. Economic or environmental considerations may lead to reductions in sulfur in future fuel supplies. Among the scenarios considered for this report, most omit sulfur emissions, equivalent to assuming desulfurized fuel. Others assume an EI(SO_x) of 0.4 grams SO_2/(kg fuel) as a sensitivity study of the effects of sulfur from aircraft on atmospheric ozone. The EI(SO_x) averaged over the current subsonic fleet is about 0.8.

The fractionation of emitted sulfur species is unknown, but may include SO_3 and H_2SO_4 in addition to SO_2. The SO_3 and H_2SO_4 are expected to form sulfuric acid aerosol particles within the near-field aircraft plume. Such particles have been observed (Fahey et al., 1995; Miake-Lye et al., 1998; Anderson et al., 1998; Hagen et al., 1998) The fraction of sulfur converted to particles within the aircraft plume may be a complex function of engine type, operating parameters, fuel sulfur content, and ambient conditions. Previous studies (Weisenstein et al., 1996; Weisenstein et al., 1998) have found large sensitivities in both global sulfate aerosol surface area density (SAD) and ozone response to the assumed particle conversion fraction. Therefore this parameter is treated parametrically, with values of 0%, 10%, 50%, and 100% employed. The number of particles emitted and their size distribution are less important, as coagulation within the plume will tend to reduce the number density and increase the average diameter during plume evolution.

Because most models participating in this study did not have the capability to handle sulfur emission and calculate perturbations to sulfate aerosol, the sulfate surface area density (SAD) was specified as a scenario input. Microphysical calculations were performed by the AER 2-D model (Weisenstein et al., 1997) to calculate the SAD perturbation due to a given sulfur emission scenario. Sulfate particles formed in the plume were assumed to be 10 nm in radius. Only sulfur emissions above 13 km were used in the calculations to avoid increasing the number of subsonic scenarios and due to the greater uncertainty involved in modeling tropospheric sulfur. The calculated perturbations were added to the SA0 volcanically clean surface area density defined in WMO (1992). SAD fields were kept constant from January to June and from July to December, in accordance with the definition of SA0. Scenario definitions are presented in Table 2.3, which also includes the percent change in calculated SAD relative to the SA0 background surface area distribution in the 14-21 km, 33-90^{o}N region. Figures 2.12-2.16 shows the zonal mean SAD perturbations used by all modelers for those scenarios which include aircraft sulfur emissions.

Table 2.3: Sulfate Surface Area Density (SAD) Scenario Definitions for Various HSCT Emission Assumptions

SAD Name	HSCT Fleet Size	Cruise Altitude	SO_2 Gas to Particle Conversion	Change in SAD[†] (14-21 km, 33-90^{o}N)	Reference
SA0[‡]	-	-	-		WMO (1992)
SA1	500	Std	50%	82%	AER 2-D Model
SA2	1000	Std	50%	124%	AER 2-D Model
SA2-2km	1000	-2km	50%	57%	AER 2-D Model
SA3	500	Std	100%	111%	AER 2-D Model
SA4	1000	Std	100%	164%	AER 2-D Model
SA5	500	Std	10%	38%	AER 2-D Model
SA6	1000	Std	10%	74%	AER 2-D Model
SA6-2km	1000	-2km	10%	22%	AER 2-D Model
SA7	500	Std	0%	26%	AER 2-D Model

[†]Percent change is relative to SA0.
[‡]SA0 represents the volcanically clean background sulfate aerosol distribution without aircraft influence.

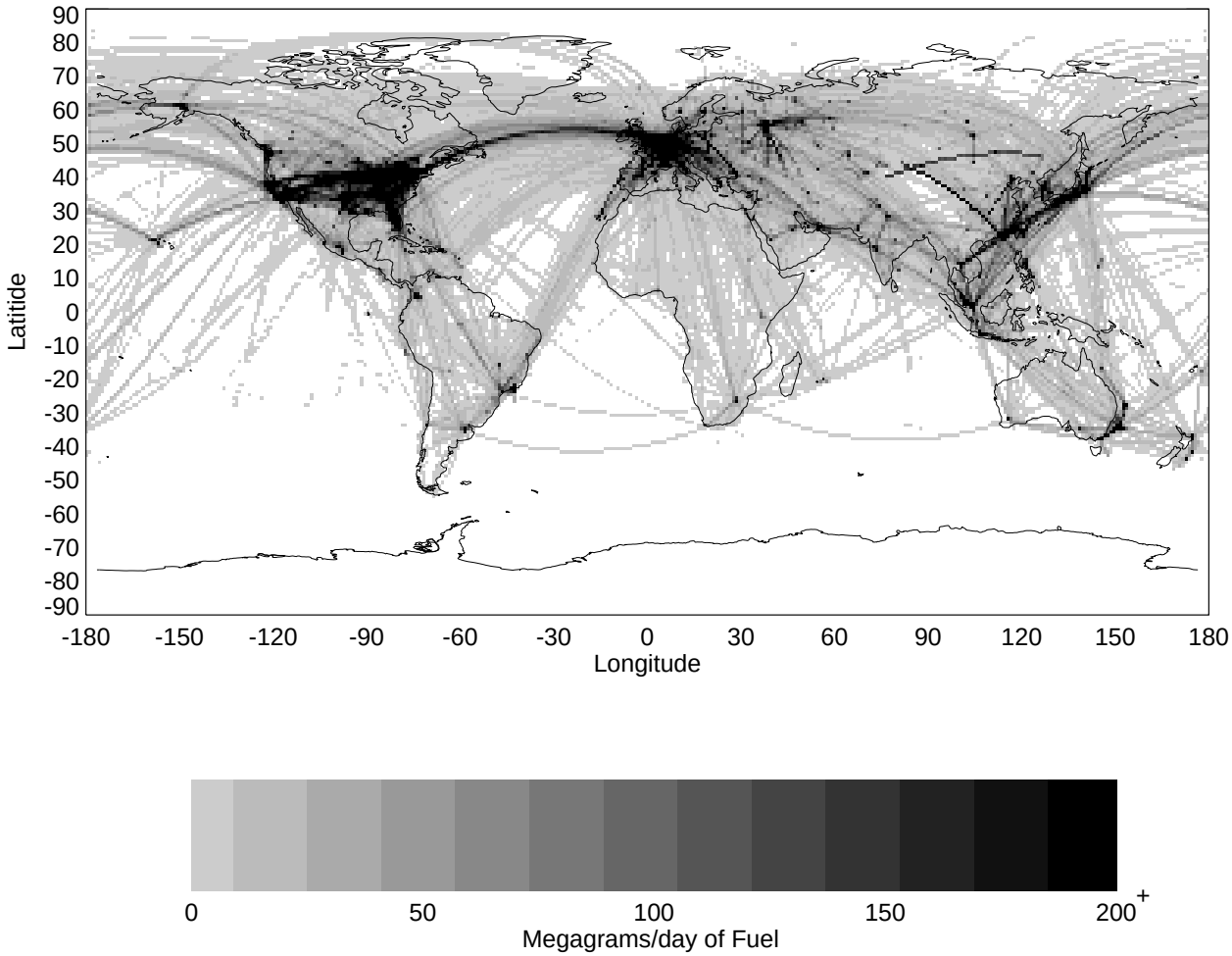

Figure 2.1: Total fuel use for the projected 2015 subsonic fleet according to the NASA emission scenario as a function of latitude and longitude.

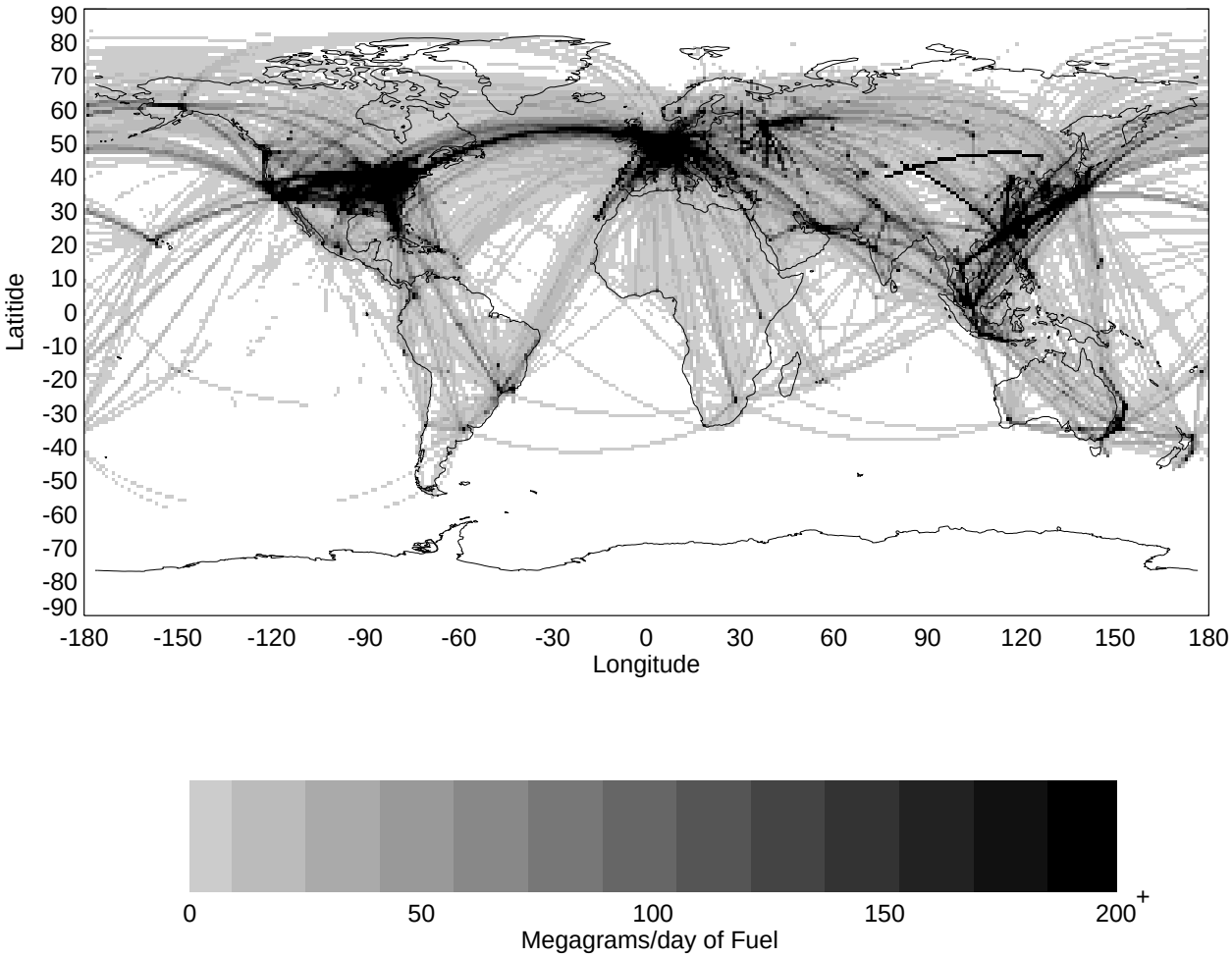

Figure 2.2: Total fuel use for the projected 2050 subsonic fleet according to the FESG IS92a scenario as a function of latitude and longitude.

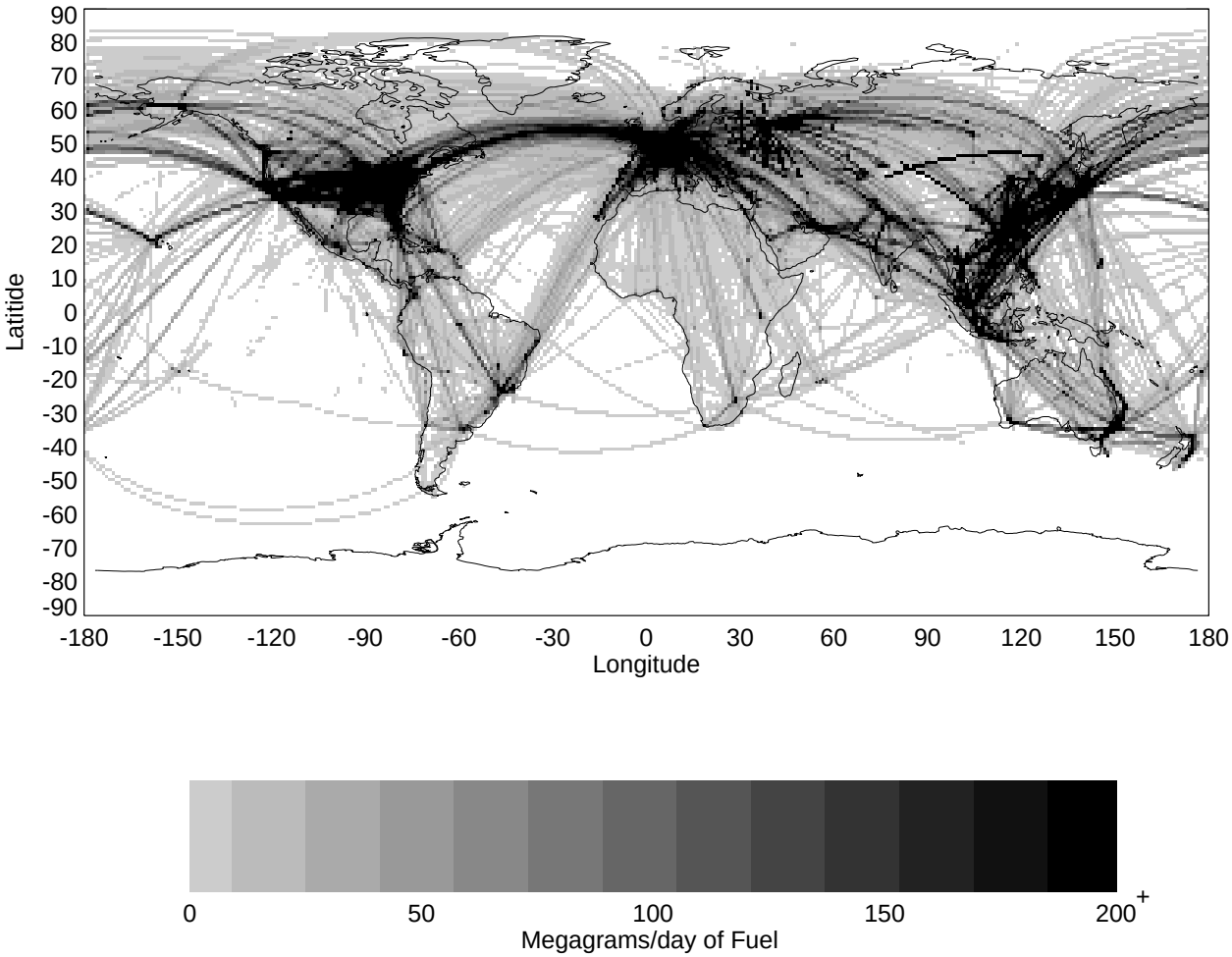

Figure 2.3: Total fuel use for the projected 2050 subsonic fleet according to the FESG IS92e high demand scenario as a function of latitude and longitude.

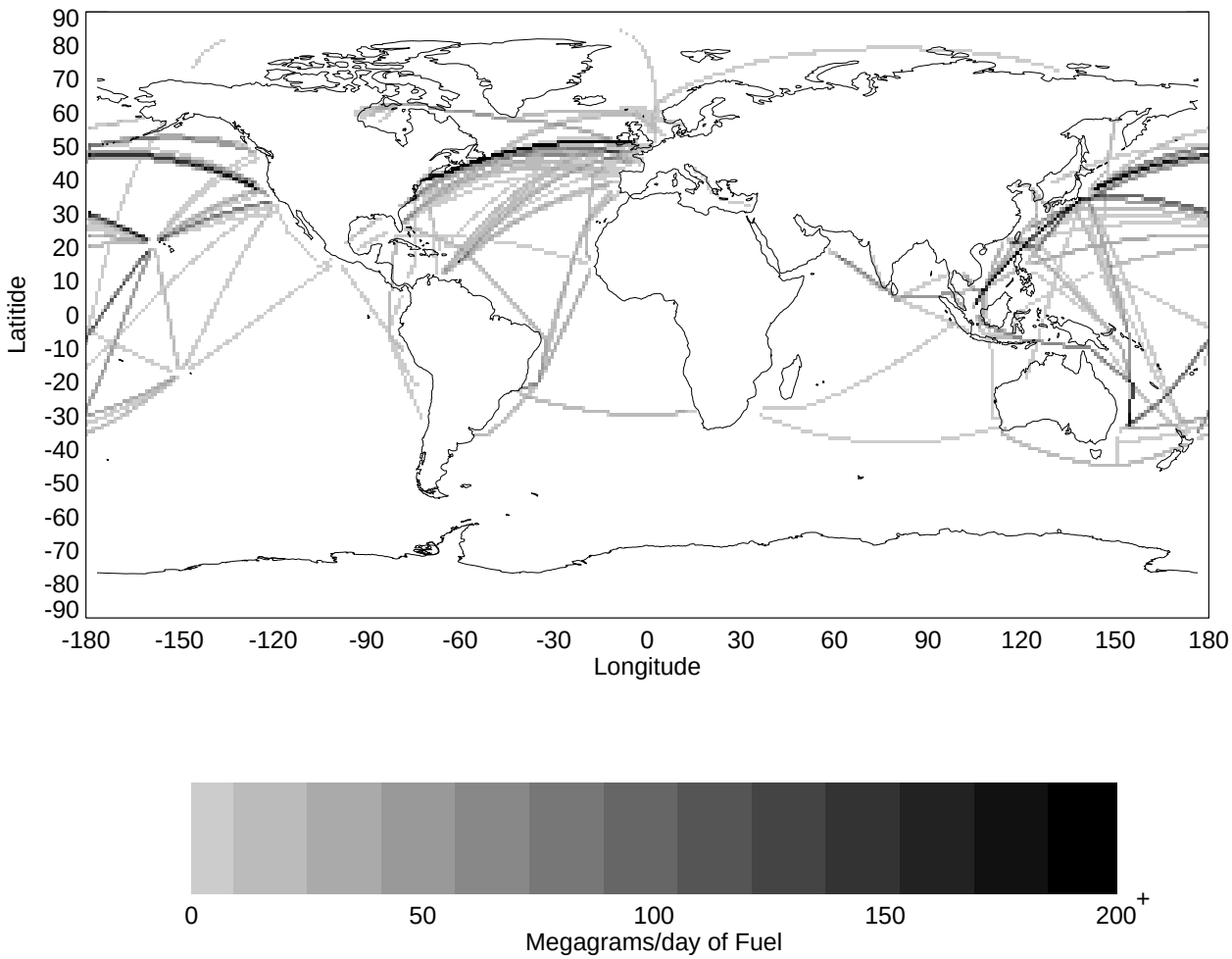

Figure 2.4: Fuel use above 13 km for the projected fleet of 500 HSCTs as a function of latitude and longitude.

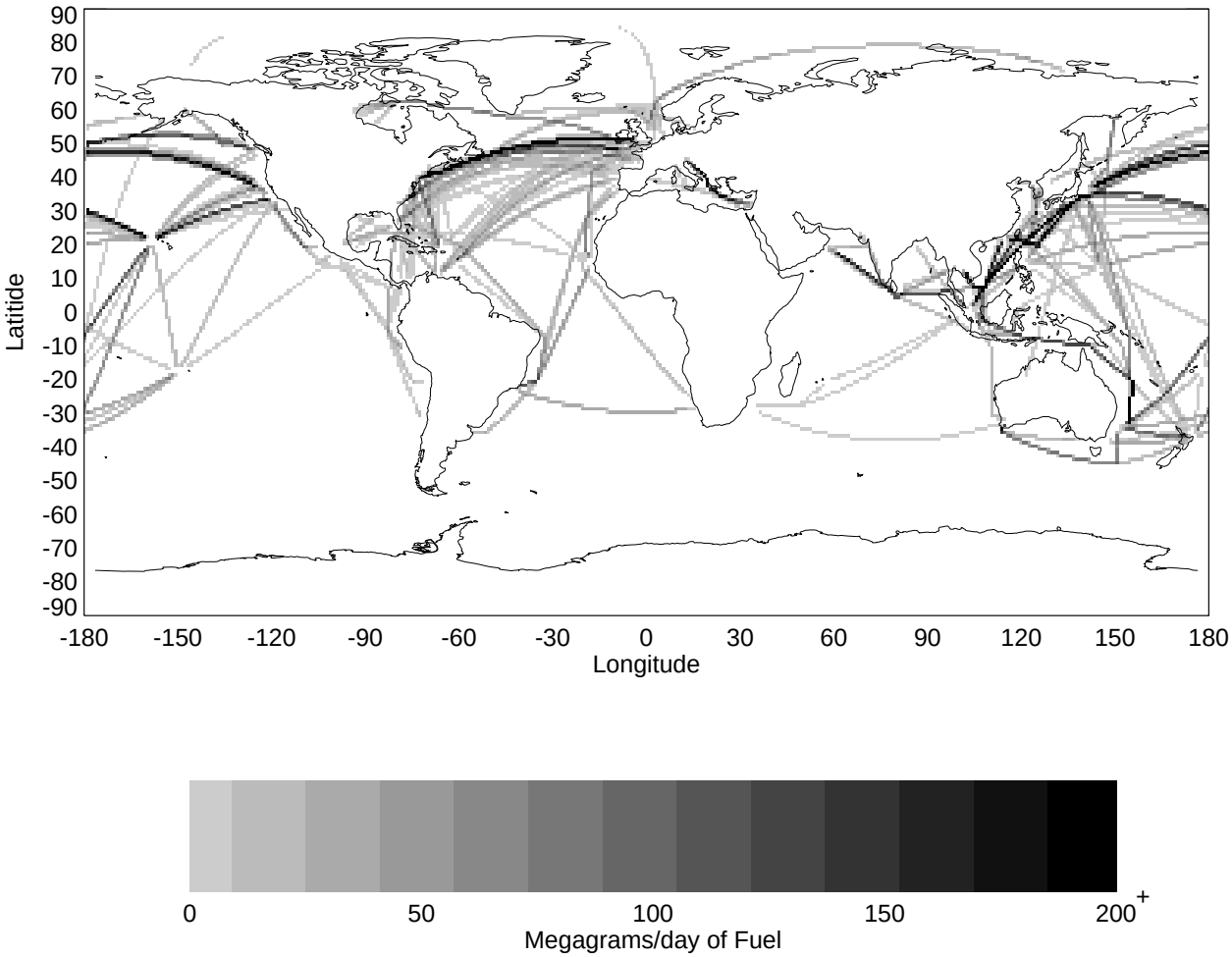

Figure 2.5: Fuel use above 13 km for the projected fleet of 1000 HSCTs as a function of latitude and longitude.

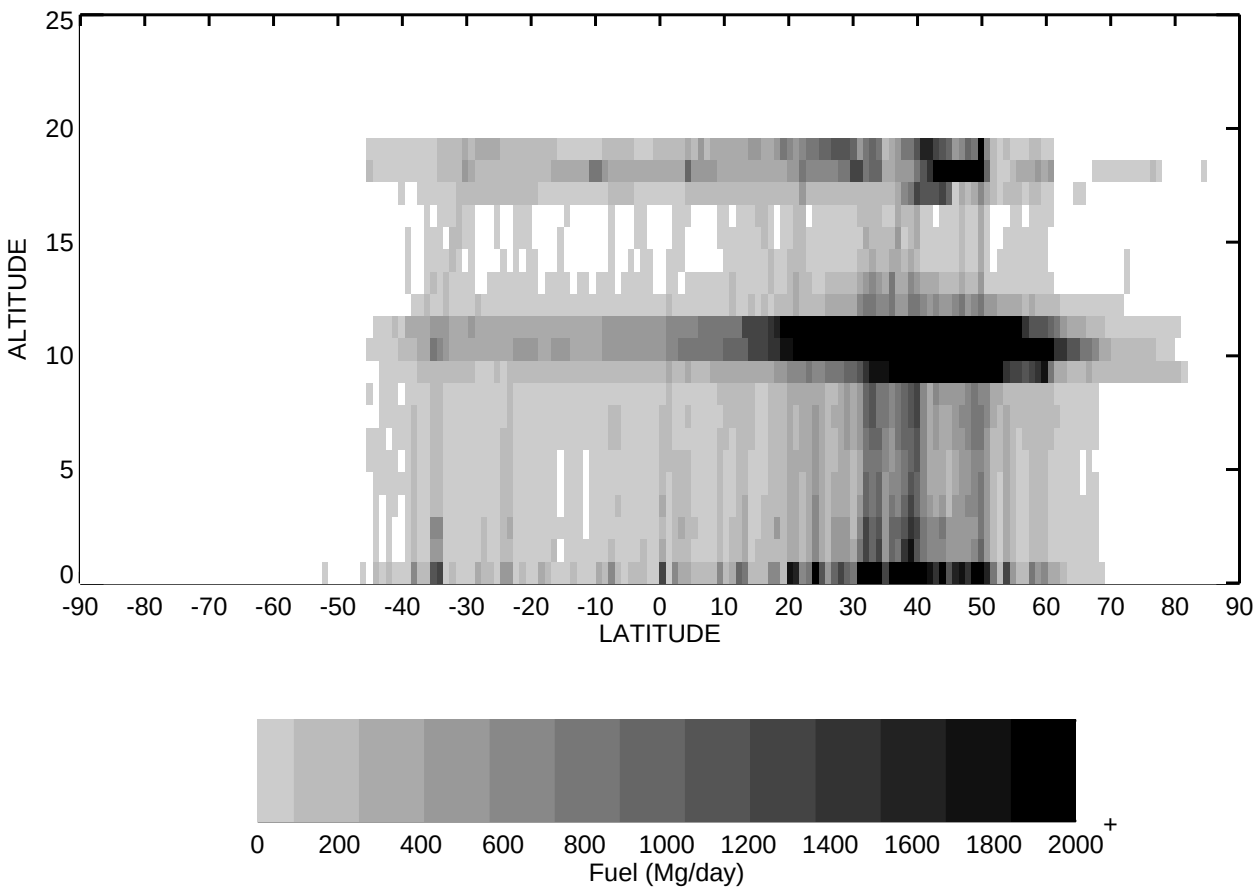

Figure 2.6: Total fuel use for the projected 500 HSCT fleet combined with the 2015 subsonic fleet as a function of latitude and altitude.

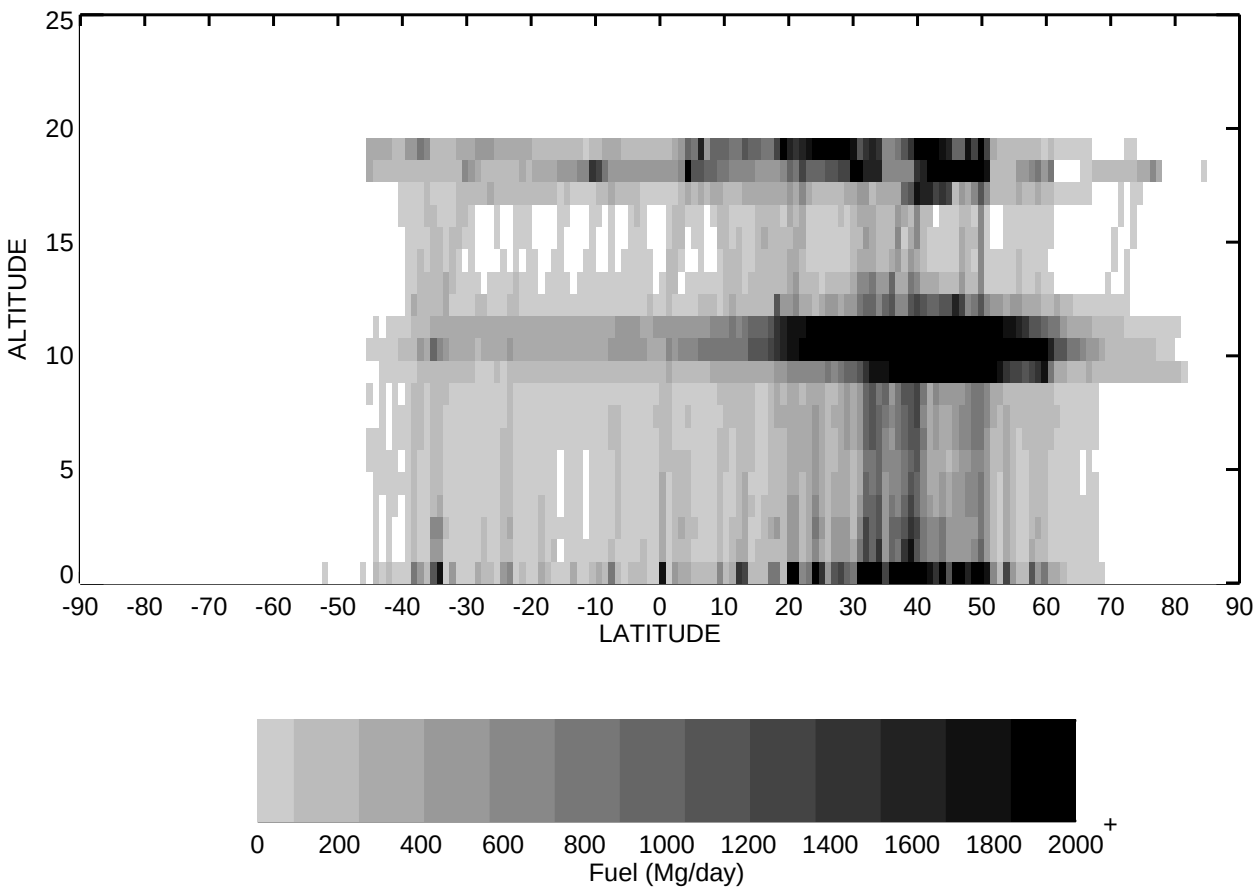

Figure 2.7: Total fuel use for the projected 1000 HSCT fleet combined with the 2015 subsonic fleet as a function of latitude and altitude.

Figure 2.8: Total fuel use as a function of altitude for the projected 500 and 1000 HSCT scenarios along with the 2015 subsonic-only scenario.

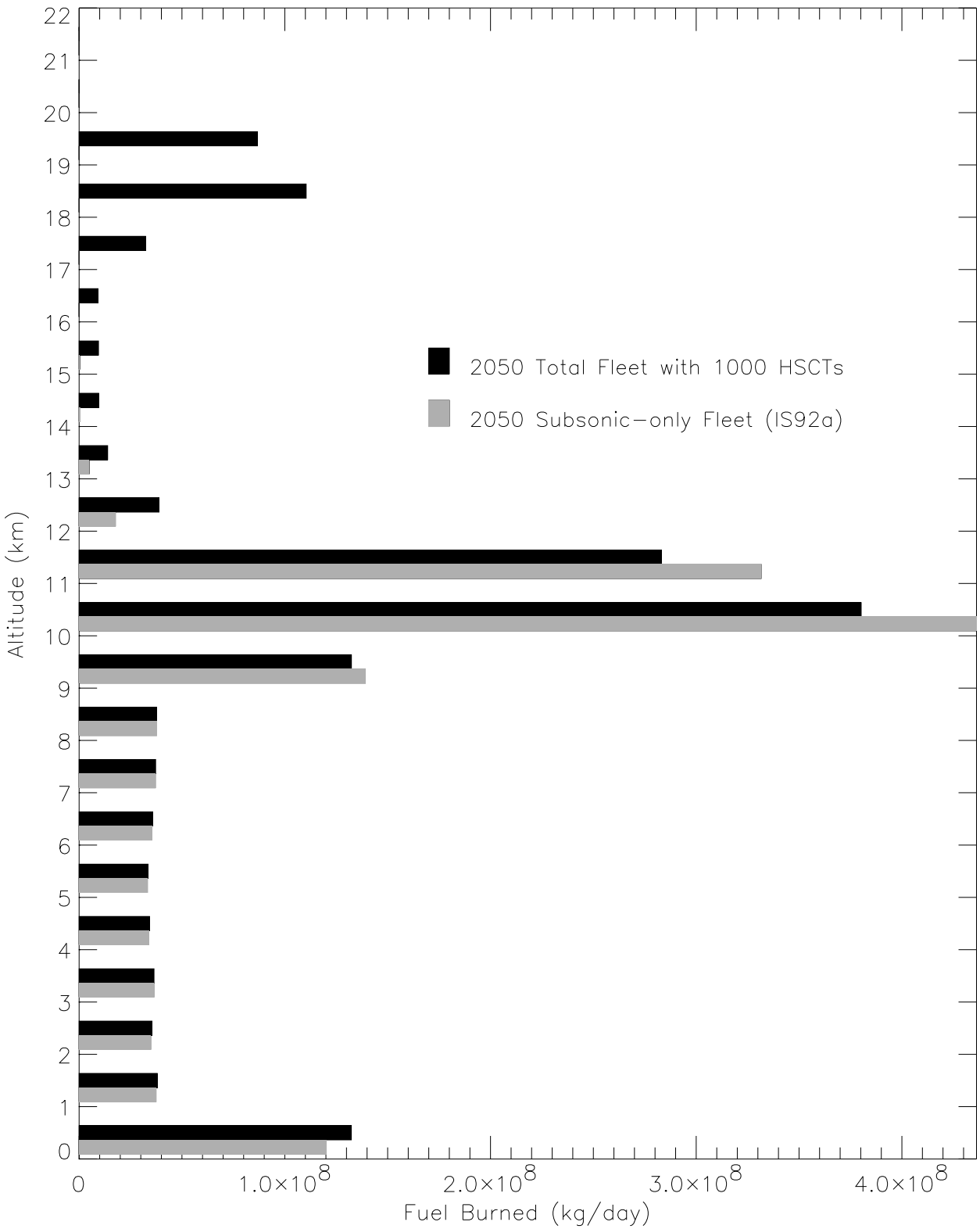

Figure 2.9: Total fuel use as a function of altitude for the projected 1000 HSCT scenario along with the 2050 IS92a subsonic-only scenario.

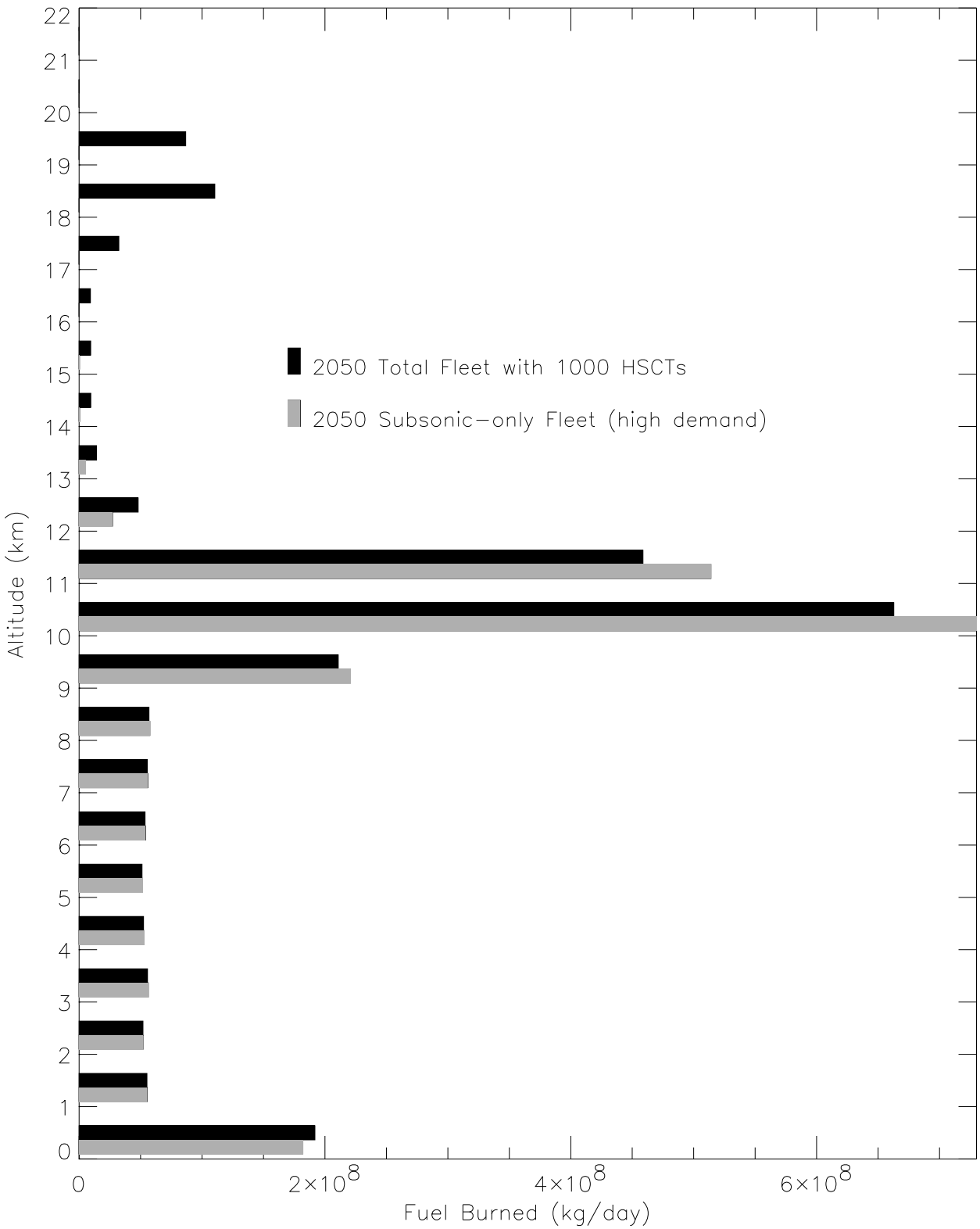

Figure 2.10: Total fuel use as a function of altitude for the projected 1000 HSCT scenario along with the 2050 IS92e high demand subsonic-only scenario.

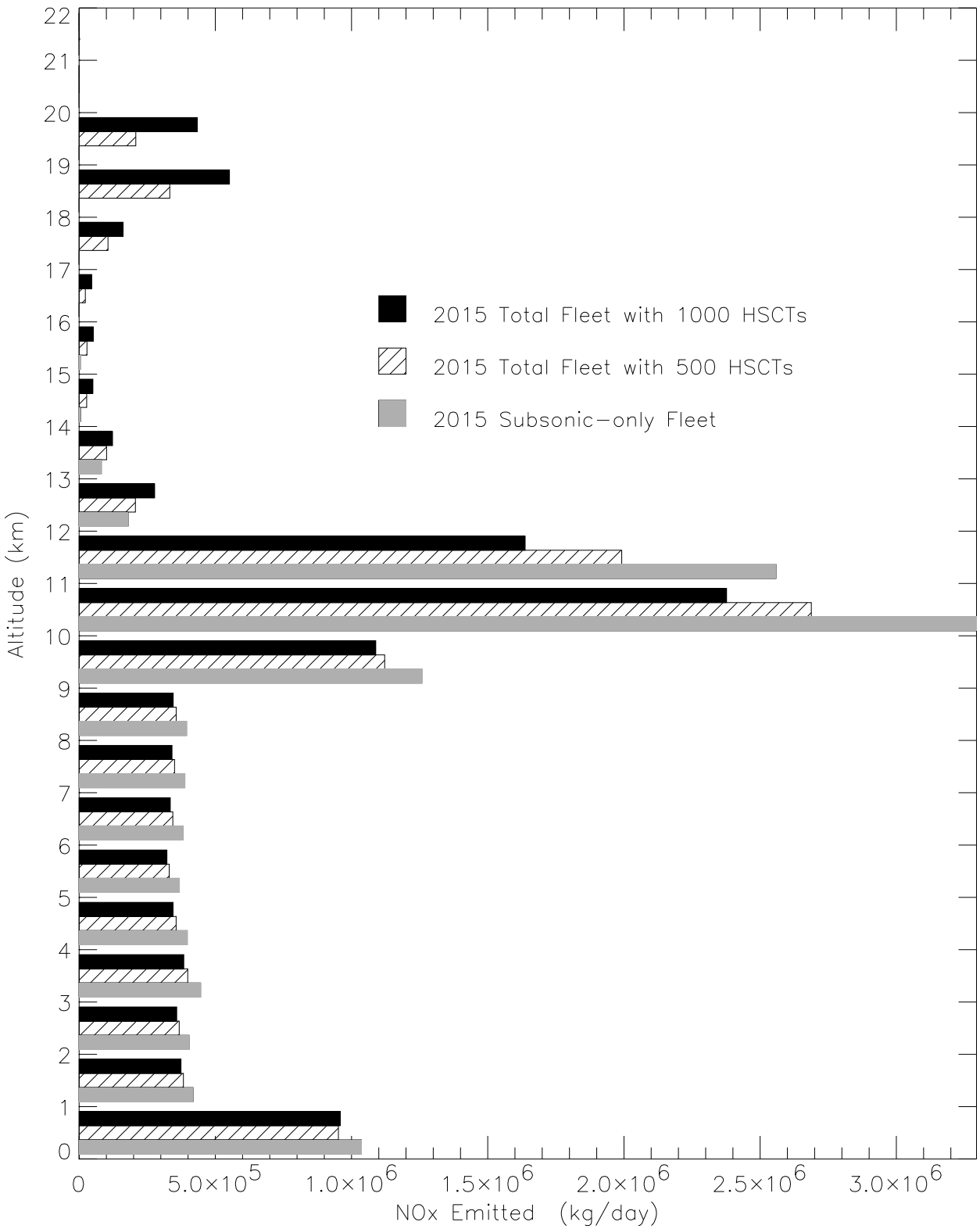

Figure 2.11: NO_x emissions for EI(NO_x)=5 as a function of altitude for the projected 500 and 1000 HSCT scenarios along with the 2015 subsonic-only scenario. .

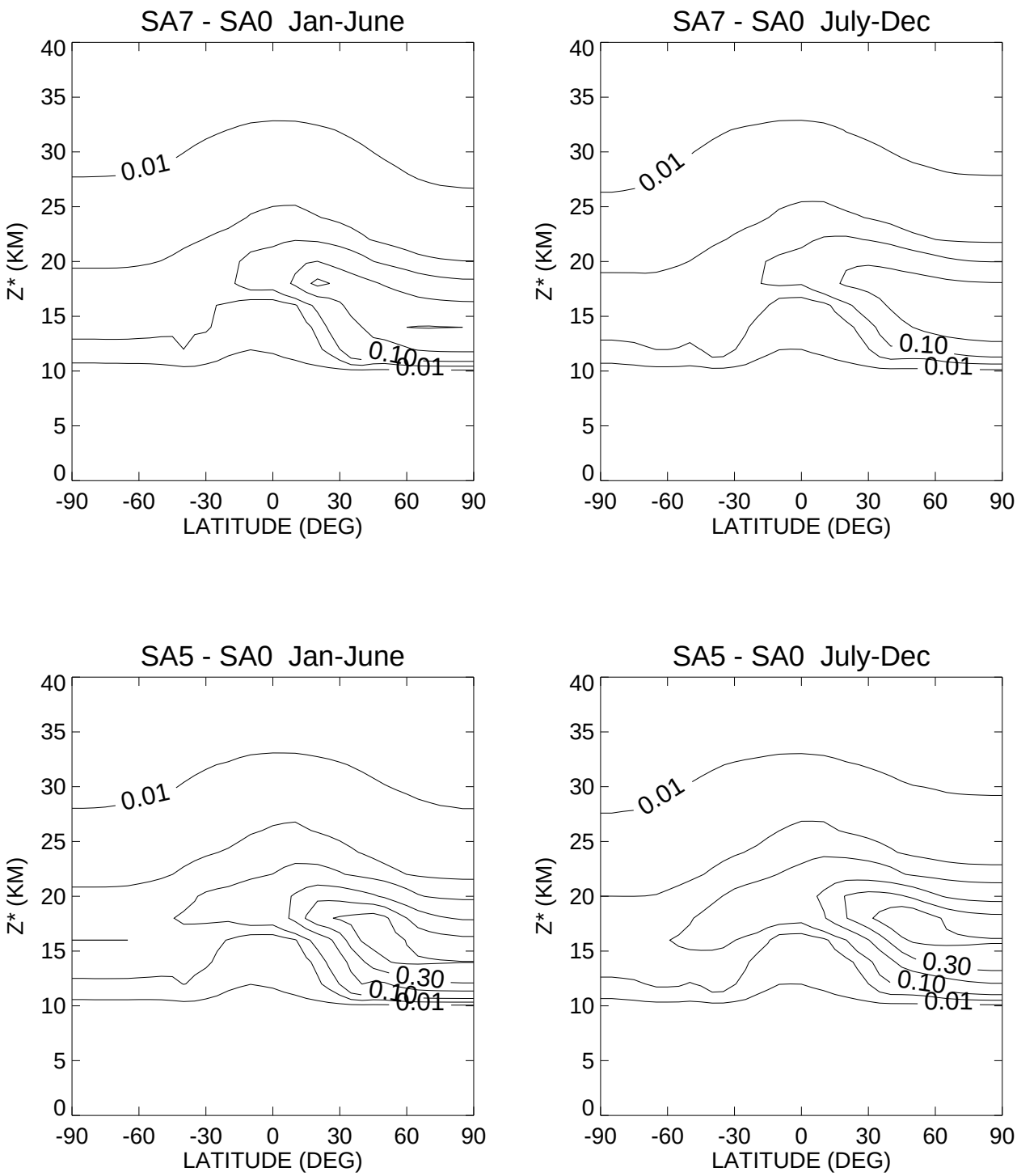

Figure 2.12: Aerosol surface area density ($\mu m^2/cm^3$) perturbations relative to SA0 as calculated by the AER 2-D sulfate aerosol model. These scenarios represent sulfur emissions from 500 HSCTs with EI(SO_2)=0.4 and 0% (for SA7) or 10% (for SA5) gas to particle conversion in the plume. Contour levels are 0.01, 0.05, 0.1, 0.2, 0.3, 0.4.

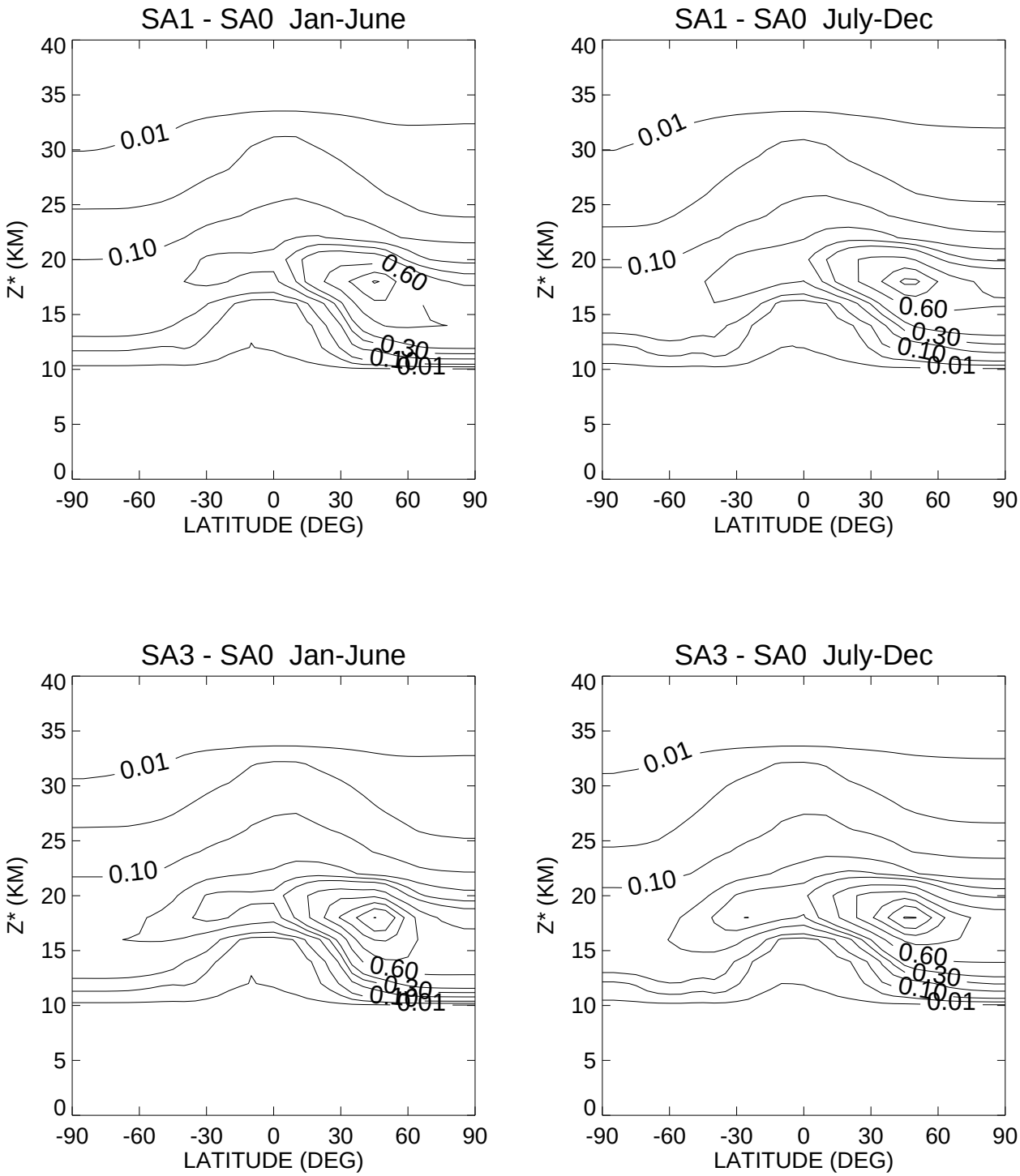

Figure 2.13: Aerosol surface area density ($\mu m^2/cm^3$) perturbations relative to SA0 as calculated by the AER 2-D sulfate aerosol model. These scenarios represent sulfur emissions from 500 HSCT with EI(SO_2)=0.4 and 50% (for SA1) or 100% (for SA3) gas to particle conversion in the plume. Contour levels are 0.01, 0.05, 0.1, 0.2, 0.3, 0.4, 0.6, 0.8, 1.0, 1.2, 1.5.

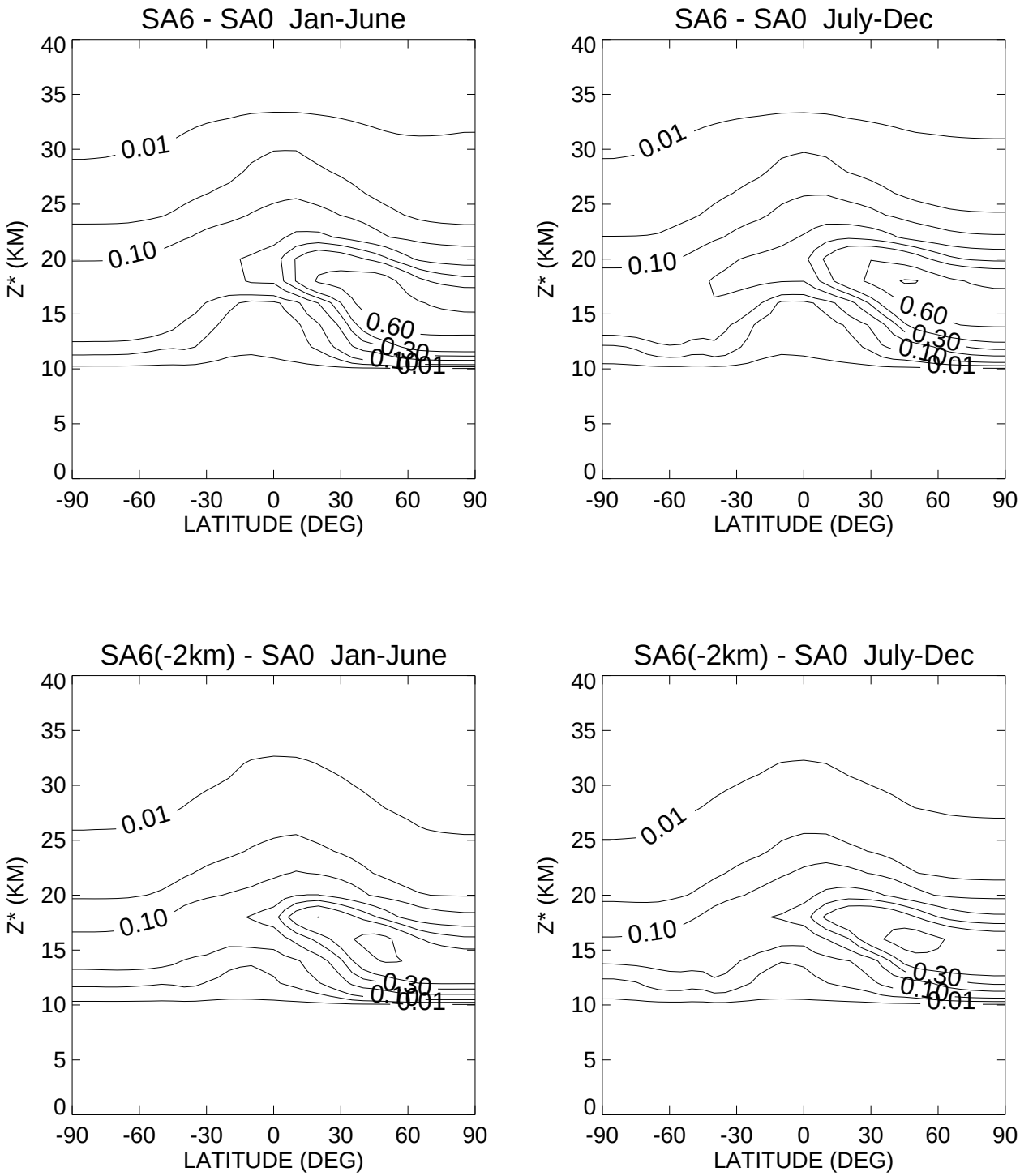

Figure 2.14: Aerosol surface area density ($\mu m^2/cm^3$) perturbations relative to SA0 as calculated by the AER 2-D sulfate aerosol model. These scenarios represent sulfur emissions from 1000 HSCT with EI(SO_2)=0.4 and 10% gas to particle conversion in the plume and standard cruise altitude (SA6) or cruise altitude decreased by 2 km (SA6-2km). Contour levels are 0.01, 0.05, 0.1, 0.2, 0.3, 0.4, 0.6, 0.8.

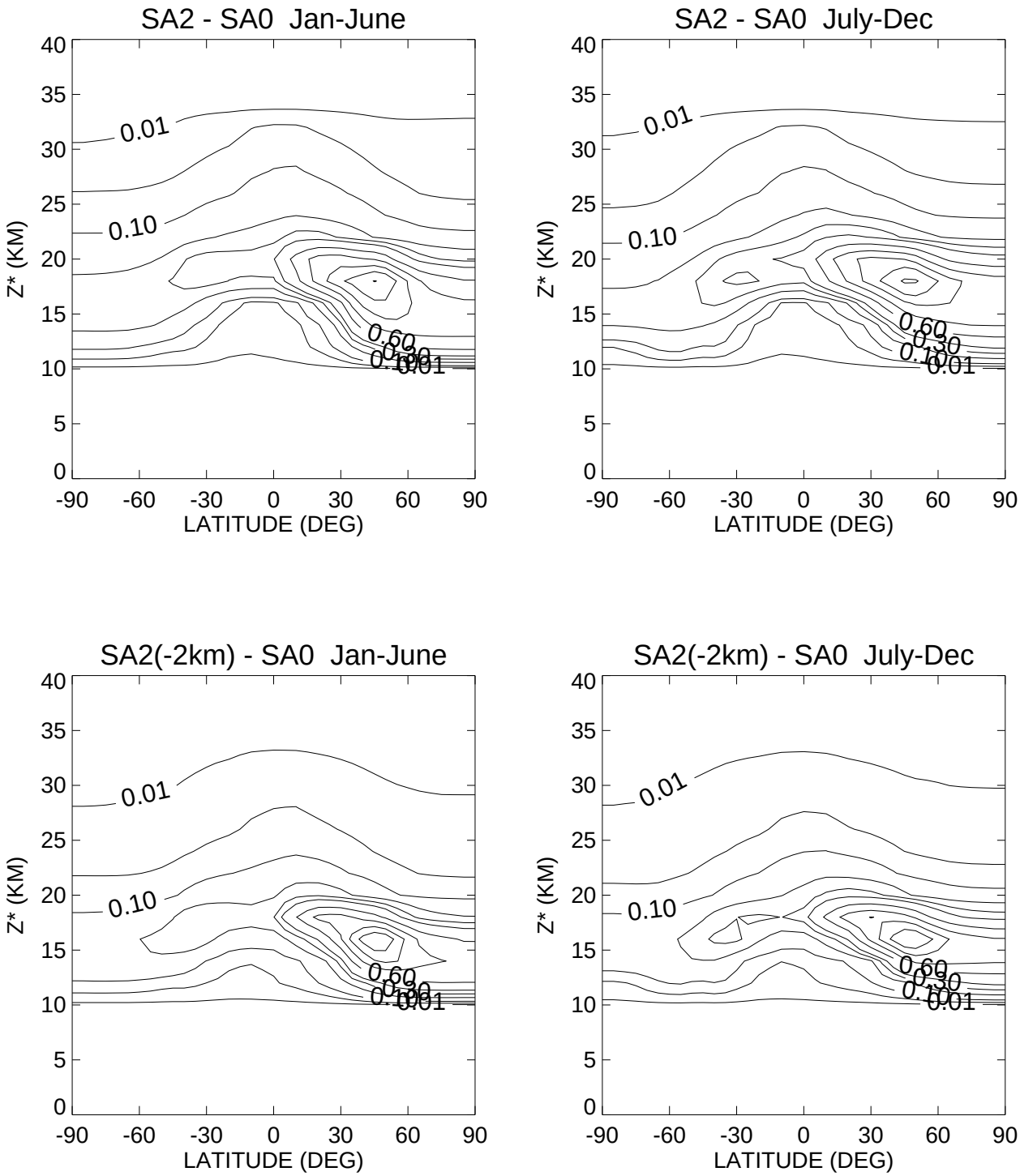

Figure 2.15: Aerosol surface area density ($\mu m^2/cm^3$) perturbations relative to SA0 as calculated by the AER 2-D sulfate aerosol model. These scenarios represent sulfur emissions from 1000 HSCT with EI(SO_2)=0.4 and 50% gas to particle conversion in the plume and standard cruise altitude (SA2) or cruise altitude decreased by 2 km (SA2-2km). Contour levels are 0.01, 0.05, 0.1, 0.2, 0.3, 0.4, 0.6, 0.8, 1.0, 1.2, 1.5.

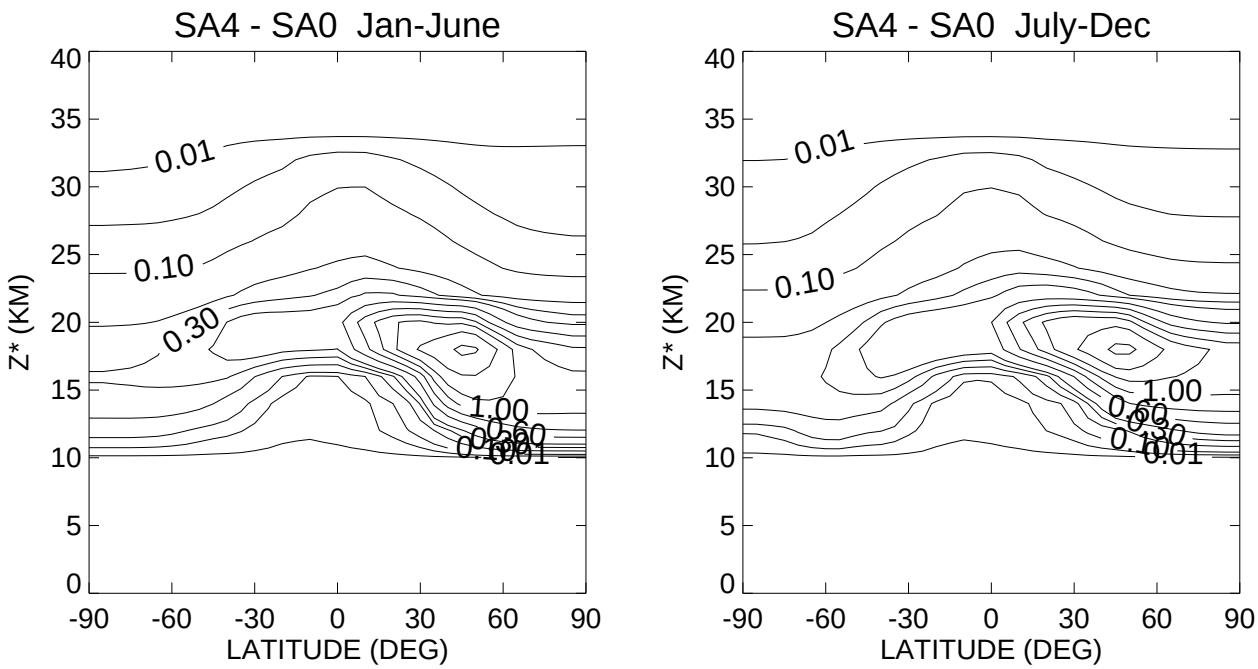

Figure 2.16: Aerosol surface area density ($\mu m^2/cm^3$) perturbations relative to SA0 as calculated by the AER 2-D sulfate aerosol model. This scenario (SA4) represents sulfur emissions from 1000 HSCTs with EI(SO_2)=0.4 and 100% gas to particle conversion in the plume. Contour levels are 0.005, 0.01, 0.05, 0.1, 0.2, 0.3, 0.4, 0.5, 1.0, 1.5, 2.0.

Bibliography

[1] Anderson, B. E., W. R. Cofer, J. D. Barrick, D. R. Bagwell, and C. H. Hudgins, Airborne observations of aircraft aerosol emissions II: Factors controlling volatile particle production, *Geophys. Res. Lett., 25,* 1693-1696, 1998.

[2] Baughcum, S. L. and S. C. Henderson, Aircraft Emission Inventories Projected in Year 2015 for a High Speed Civil Transport (HSCT) Universal Airline Network, *NASA CR-4659,* 1995.

[3] Baughcum, S. L. and S. C. Henderson, Aircraft Emission Scenarios Projected in Year 2015 for the NASA Technology Concept Aircraft (TCA) High Speed Civil Transport, *NASA CR-1998-207635,* 1998.

[4] Baughcum, S. L., S. C. Henderson, and D. J. Sutkus, Scheduled Civil Aircraft Emission Inventories Projected for 2015: Database Development and Analysis, *NASA CR-1998-207638,* 1998.

[5] CAEP/4-FESG/Report-4, Report of the Forecasting and Economic Analysis Sub-Group (FESG), *Long-Range Scenarios*, CAEP Steering Group Meeting, Canberra, January 1998.

[6] Fahey, D. W., et al., Emission measurements of the Concorde supersonic aircraft in the lower stratosphere, *Science, 270,* 70-74, 1995.

[7] Hagen, D., P. Whitefield, J. Paladino, M. Trueblood, and H. Lilenfeld, Particulate sizing and emission indices for a jet engine exhaust sampled at cruise, *Geophys. Res. Lett., 25,* 1681-1684, 1998.

[8] Miake-Lye, R. C., et al., SO_x oxidation and volatile aerosol in aircraft exhaust plumes depend on fuel sulfur content, *Geophys. Res. Lett., 25,* 1677-1680, 1998.

[9] Mortlock, A. M., and R. van Alstyne, Military, Charter, Unreported Domestic Traffic and General Aviation: 1976, 1984, 1992, and 2015 Emission Scenarios, *NASA CR-1998-207639,* 1998.

[10] Weisenstein, D. K., M. K. W. Ko, N-D Sze,and J. M. Rodriguez, Potential impact of SO_2 emissions from stratospheric aircraft on ozone, *Geophys. Res. Lett., 23,* 161-164, 1996.

[11] Weisenstein, D. K., G. K. Yue, M. K. W. Ko, N-D. Sze, J. M. Rodriguez, C. J. Scott , A two-dimensional model of sulfur species and aerosol, *J. Geophys. Res., 102,* 13,019-13,035, 1997.

[12] Weisenstein, D. K., M. K. W. Ko, I.G . Dyominov, G. Pitari, L. Ricciardulli, G. Visconti, and S. Bekki, The effect of sulfur emissions from HSCT aircraft: A 2-D model intercomparison, *J. Geophys. Res., 103,* 1527-1547, 1998.

[13] World Meteorological Organization (WMO), Scientific Assessment of Ozone Depletion: 1991, Global Ozone Res. and Monit. Proj., *Rep. 25,* Geneva, Switzerland, 1992.

Chapter 3

Background Atmospheres

Atmospheric perturbations due to emissions by supersonic aircraft are computed relative to the 2015 and 2050 atmospheres. Modeling of both future years is important because the concentrations of atmospheric chlorine and other trace gases are changing with time. HSCT perturbations are believed to be sensitive to concentrations of these background gases. Boundary conditions for 1992, 2015 and 2050 were specified for the modelers and are listed in Table 3.1. The future atmosphere boundary conditions were based on the IPCC IS92a scenario from past IPCC reports (1992, 1995). The halocarbon boundary conditions correspond to 3.7, 3.0, and 2.0 ppbv of Cl_y in the upper stratosphere in 1992, 2015, and 2050, respectively. Concentrations of Br_y in the upper stratosphere are 15, 12.5, and 11.1 pptv for the same years.

The sulfate surface area density (SAD) for the background atmosphere (designated SA0) was that given in Table 8-8 of *WMO* (1992) and is displayed in Figure 3.1. Maximum sulfate surface area density occurs in the lower stratosphere at middle to high latitudes in both hemispheres and decreases with height, with zero surface area density above 32 km. The profile is specified at two times during the year (April and October) and modelers were instructed to use the April profile for the first half of the year and the October profile for the second half. SA0 represents an atmosphere with minimal volcanic influence. To approximate the effects of an active period of volcanic eruptions (e.g., the last two decades), some scenarios employed an SAD enhanced by a factor of 4 relative to the nonvolcanic case (designated 4xSA0). The surface area of polar stratospheric clouds (PSCs) was not specified. Those models with the capability to calculate PSC surface area (AER, GSFC, UNIVAQ, SCTM1, SLIMCAT, and LARC) followed their standard treatment, while LLNL and THINAIR used an approach based on current climatology.

There were a total of seven baseline scenarios for the year 2015 and three baseline scenarios for the year 2050. These are listed, along with their scenario designations, in Table 3.2. Each includes a subsonic aircraft fleet, which was reduced in the HSCT scenarios to account for displacement of the subsonic fleet by the supersonic fleet. Scenario D is the standard 2015 baseline scenario. Scenario D3 includes a volcanically perturbed sulfate surface area density at 4xSA0. Scenario D4 has the PSC parameterizations removed. Scenarios D5 and D6 use different Cl_y amounts, 1.0 and 4.0 ppbv, respectively. Scenarios D7 and D8 include interactive sulfate aerosol microphysics. Scenario D9 uses the 2050 boundary conditions, resulting in 2.0 ppbv of Cl_y, though the subsonic aircraft fleet is the same as that used for the 2015 scenarios. Scenarios F and G also represent 2050 and employ projected subsonic fleets appropriate to 2050.

3.1 Scenario D Results

Nine models submitted results for Scenario D which employs boundary conditions appropriate to 2015, background aerosol surface area SA0, and a subsonic aircraft fleet. Figure 3.2 shows the integrated ozone column as a function of time of year and latitude expressed in Dobson Units (DU) for Scenario D. All nine models calculate the seasonal behavior of ozone in a manner consistent with observations, such as those from the TOMS instrument for 1990, shown in Figure 3.3. Features of note include the tropical minimum, reproduced in all models at approximately 260-280 DU, except in the SLIMCAT-3D model where the tropical minimum is slightly higher at 300 DU. The northern hemisphere high latitude winter/spring maximum is seen in all models, but with widely varying maximum levels, ranging from 420 DU in the CSIRO and

Table 3.1: Recommendations for Species Concentrations in 1992, 2015, and 2050

Species	1992 (3.6 ppbv Cl_y)	2015 (3 ppbv Cl_y)	2050 (2 ppbv Cl_y)
CFC-11	268 pptv	220 pptv	120 pptv
CFC-12	503 pptv	470 pptv	350 pptv
CFC-113	82 pptv	80 pptv	60 pptv
CCl_4	132 pptv	70 pptv	35 pptv
HCFC-22	100 pptv	250 pptv	15 pptv
CH_3CCl_3	135 pptv	3 pptv	0 pptv
HCFC-141b†	2 pptv	12 pptv	0 pptv
Halon-1301	3 pptv	1.4 pptv	0.9 pptv
Halon-1211	2 pptv	1.1 pptv	0.2 pptv
CH_3Cl	600 pptv	600 pptv	600 pptv
CH_3Br	10 pptv	10 pptv	10 pptv
CH_4	1714 ppbv	2052 ppbv	2793 ppbv
N_2O	311 ppbv	333 ppbv	371 ppbv
CO_2	356 ppmv	405 ppmv	509 ppmv

†For those models that cannot handle HCFC-141b, the recommendation is to put it in as CH_3CCl_3 after adjusting for the number of chlorine atoms per molecule, i.e., multiply the HCFC-141b mixing ratio by 2/3 and add to CH_3CCl_3. The stratospheric lifetimes for CH_3CCl_3 and HCFC-141b are 50 years and 75 years, respectively. These lifetimes are sufficiently close that supplementing CH_3CCl_3 with HCFC-141b should be a reasonable approximation.

Table 3.2: Specifications for Baseline Scenarios which Include a Subsonic Aircraft Fleet

Scenario	Year	Cl_y (ppbv)	Subsonic Fleet Projection	PSC Representation	SAD Representation
D	2015	3.0	2015	Included	SA0
D3	2015	3.0	2015	Included	4xSA0
D4	2015	3.0	2015	Removed	SA0
D5	2015	1.0	2015	Included	SA0
D6	2015	4.0	2015	Included	SA0
D7	2015	3.0	2015	Included	Sulfate microphysics with SO_2 gas to particle conversion of 50%
D8	2015	3.0	2015	Included	Sulfate microphysics with SO_2 gas to particle conversion of 100%
D9	2050	2.0	2015	Included	SA0
F	2050	2.0	2050 IS92a	Included	SA0
G	2050	2.0	2050 High Demand	Included	SA0

SLIMCAT-3D models to 500 DU in the AER, LLNL, UNIVAQ, and SCTM1 models. The high latitude summer decrease is seen in all models, but with widely varying rates of decrease, and minimum values from 320 to 380 DU. In the southern hemisphere, the winter/spring midlatitude maximum is simulated by all models with levels ranging from 360 DU to 500 DU. The models that include polar stratospheric chemistry (all but CSIRO) calculate a springtime minimum in southern polar ozone ranging from 240 DU to 320 DU, somewhat higher than typical present day levels.

In the zonal mean, the model O_3 fields also compare well with available observations as evidenced in Figure 3.4, showing zonal mean O_3 versus height in June. Peak ozone mixing ratios occur in the tropics near 30 km with levels of 8 to 11 ppmv. The vertical decrease through the upper stratosphere and mesosphere is similar in all models, with levels of 2 ppmv reached at 50 km in the tropics for most models, though the SLIMCAT-3D and THINAIR-2D models calculate slightly higher mesospheric ozone and the SCTM-3D model slightly lower. The SLIMCAT-3D and THINAIR-2D models both use θ as the vertical coordinate, and conversion onto the common UADP grid in log-pressure coordinates is only approximate. In addition, the SLIMCAT-3D and SCTM1-3D models have coarse vertical resolution in the upper stratosphere and mesosphere. Therefore these three models (SLIMCAT, SCTM1, and THINAIR) are expected to differ from the others in the upper stratosphere/mesosphere.

Figures 3.5, 3.6, and 3.7 shows the ozone number density profile at 45^oN, the equator, and 45^oS during June as a function of altitude. Most of the models show similar ozone maxima at approximately 25 km in midlatitudes with levels of 4-5x10^{12} molecules/cm^3. AER and LLNL, while similar to other models at 25 km, have higher concentrations (up to 5-6x10^{12} molecules/cm^3) between 15 and 25 km at 45^oN. Among other models, there is a moderate spread in calculated O_3 in the lower stratosphere. Above 28 km, all models yield similar ozone profiles, except that UNIVAQ is a bit higher. Model differences in background ozone, particularly in the lower stratosphere, are likely to yield differences in the response to HSCT emissions, particularly as HSCT emissions peak at northern midlatitudes, coincident with projected flight corridors.

The partitioning within the odd oxygen family is further illustrated in Figures 3.8 and 3.9. In Figure 3.8, zonal mean atomic oxygen mixing ratios are plotted as a function of latitude and height for June. The 2-D models reported daytime average values of atomic oxygen, while the 3-D models reported 24-hour averages. Model behavior is broadly similar in all cases. The O/O_3 ratio (Figure 3.9) shows odd oxygen partitioning in the upper stratosphere and lower mesosphere. This ratio is largely controlled by the photolysis of ozone, which is not expected to differ significantly between models because the models' photodissociation schemes have been previously benchmarked. Some differences may be due to the averaging interval used for atomic oxygen. Also, the temperature in this region (and the corresponding neutral density) may be a factor in this difference. As the mesospheric contribution to the ozone column is minimal, these differences would not be expected to have a substantial impact on stratospheric ozone levels (as evidenced in Figure 3.4).

N_2O, a longer-lived constituent, is shown in Figure 3.10. Differences are apparent between the models, which implies differences in transport. The CSIRO, GSFC and LARC models have more latitudinal variation in the upper stratosphere while the LARC and SLIMCAT N_2O fields are flatter in the lower stratosphere than others. This points to significant differences in mixing rates and transport time scales between different regions of the atmosphere. These differences in transport characteristics will impact the calculated HSCT effluent accumulation and distribution among, and thus the ozone impact.

Model water vapor fields are shown in Figure 3.11. H_2O is the principal source of atmospheric odd hydrogen which dominates ozone loss processes in the lower stratosphere and troposphere, as well as in the upper stratosphere and mesosphere. The models show similar H_2O distributions with stratospheric maxima of approximately 6 ppmv, though the THINAIR-2D model calculates a lower stratospheric maximum of only 5 ppmv. Differences are apparent in the tropical lower and middle stratosphere, with many models showing distinct local minima and others with less apparent local minima (e.g., CSIRO, SLIMCAT-3D, and THINAIR). The LARC H_2O distribution is specified from a 2D model distribution derived from an older version of the NOCAR model, rather than calculated self- consistently.

Zonal mean hydoxyl radical mixing ratio is plotted in Figure 3.12. The 3-D models reported 24-hour average values of radical species (ie. zonal means of the 3-D results), whereas the 2-D models reported daytime average values, so the OH fields in the 3-D models differ from the 2-D models by a factor of 2, roughly. Concentrations are generally similar in all models, if adjusted for averaging period. This general consistency, particularly in the lower stratosphere suggests that ozone loss rates due to odd hydrogen chemistry should be reasonably consistent among the models.

Figure 3.13 shows the model NO_y fields. Substantial differences are evident between the models. Maximum NO_y concentrations occur between 35 and 40 km with mixing ratios of between 18 and 26 ppbv. Figures 3.14, 3.15, and 3.16 show profiles of NO_y mixing ratio at 45^{o}N, the equator, and 45^{o}S in June. The large spread of model results is evident above 35 km in the tropics and at all stratospheric altitudes at midlatitudes. In the lower stratosphere, the AER, GSFC, LLNL, and THINAIR models have greater NO_y. In the upper stratosphere, the CSIRO, GSFC, LLNL, and THINAIR models have greater NO_y. As NO_y is a principal emission product of an HSCT fleet, differences in background lower stratospheric levels would have an impact on any calculated perturbations. The NO_x (or NO+NO_2) to NO_y ratio is shown in Figure 3.17. Despite the differences in total NO_y, these values are broadly similar among the models suggesting that the partitioning is similar in all cases. Large differences in NO_x/NO_y in the tropical upper troposphere likely reflect different treatments of the NO_x lightning source.

As expected by the differing peak NO_y values, the sum of NO and NO_2 (Figure 3.18) reveals differences in the maximum values, with mixing ratios from approximately 15 ppbv in the LARC model to 24 ppbv in the CSIRO, GSFC, and LLNL models. NO_2 fields are shown in Figure 3.19, with maxima from 6 to 10 ppbv at 35 km. Lower stratospheric differences are also apparent. Differences in the calculated NO_y (and NO_x) fields could have several sources: the photolysis of NO (which impacts atomic N that participates in the destruction of NO_y); the N_2O distribution (which is the principal source of NO_y); O_3 and O(1D), the latter reacting with N_2O to produce NO_y, and atmospheric transport. Such intercomparisons are beyond the scope of this document, but a more detailed study of these NO_y differences is warranted.

The odd chlorine family is examined in the next group of figures. Zonal mean Cl_y is shown in Figure 3.20 for the six models reporting this quantity. Results are similar and appropriate to the boundary conditions ($\sim$3.0 ppbv), except for the THINAIR result, which shows only 2.0 ppbv in the upper stratosphere. Figures 3.21, 3.22, and 3.23 show vertical profiles of Cl_y mixing ratio at 45^{o}N, the equator, and 45^{o}S in June. Most models yield very similar Cl_y concentrations at 60 km, exceptions being the THINAIR model which is quite low compared to the other models and the LARC and SCTM1 models which are a bit higher. Modest variation in Cl_y concentration among the models is found in the lower stratosphere.

ClO mixing ratios reveal distinct differences (Figure 3.24). Stratospheric maxima vary from levels of 0.5 ppbv (CSIRO and UNIVAQ) to 1.0 ppbv (AER and SCTM1-3D at about 40 km in the northern hemisphere. The THINAIR model shows much smaller maximum concentrations (only 0.1 ppbv) related to the smaller Cl_y concentrations in this model. Equator to pole gradients in the middle stratosphere vary from strong (AER, LLNL, SCTM1) to weak (CSIRO, UNIVAQ, SLIMCAT). Some of these differences are related to the way the models treat the reaction between OH and ClO. JPL 1997 makes no recommendation of product yields. The CSIRO, SLIMCAT, and LARC models include non-zero yields for the minor channel ClO+OH$\rightarrow$HCl+O_2. The inclusion of this channel would tend to lower the level of ClO at the peak. In the lower stratosphere, calculated mixing ratios are in better agreement, though ozone loss due to odd chlorine is a minor component in this region outside the poles. The ratio of ClO to Cl_y (Figure 3.25) also shows differences, with higher values of this ratio in the AER and SCTM1-3D models, and smaller values in the LARC and THINAIR models.

Total odd bromine (Br_y) is shown in Figure 3.26 as a function of latitude and altitude and in Figures 3.27, 3.28, and 3.29 as a function of latitude only at 45^{o}N, the equator, and 45^{o}S. Based on tropospheric boundary conditions of the organic halogens, Br_y levels in the upper stratosphere are expected to be 12.5 pptv. The AER, CSIRO, GSFC, and SCTM1 models show about 12 pptv of Br_y in the upper stratosphere, while the LARC model shows 14 pptv, the THINAIR model 20 pptv, and the SLIMCAT model 8 pptv. BrO concentrations, shown in Figure 3.30 for all nine models, have maxima near 40 km. Maximum concentrations range from 6 to 10 pptv, except for the THINAIR model which shows a maximum of 14 pptv. Lower stratospheric concentrations of BrO are in fair agreement. The ratio of BrO to Br_y is shown in Figure 3.31. Some difference in the partitioning are evident, with AER, CSIRO, and THINAIR calculating a partitioning of 70% active bromine near 40 km, GSFC and LARC calculating 60% active bromine, and SCTM1 calculating only 30-40%.

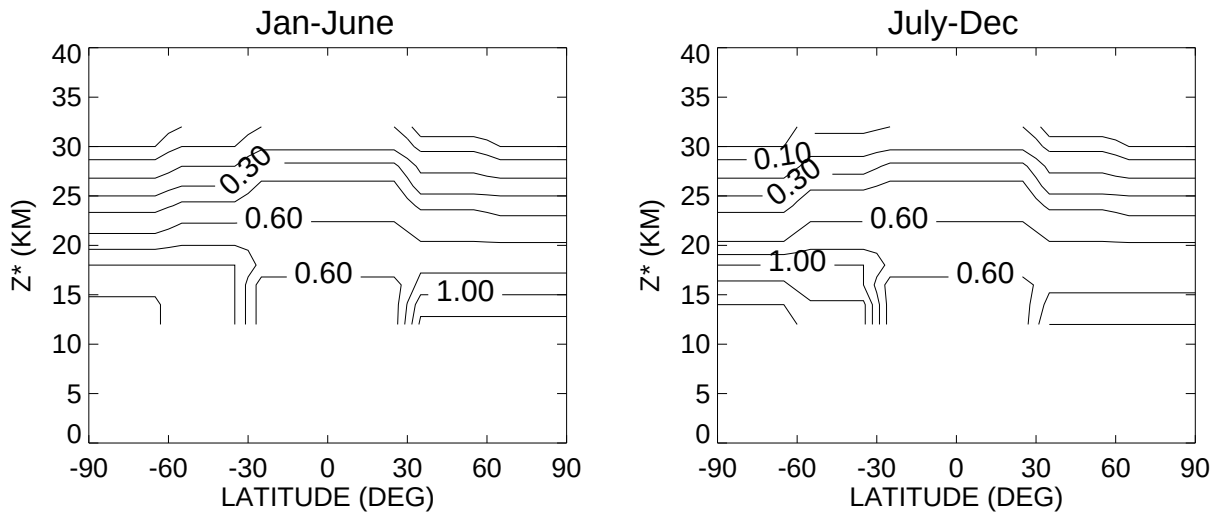

Figure 3.1: Surface area density ($\mu m^2/cm^3$) used for background atmospheres in 2015 and 2050 under volcanically clean conditions. This surface area density is designated SA0 and comes from *WMO* (1992). Contours are 0, 0.1, 0.2, 0.3, 0.4, 0.6, 0.8, 1.0, 1.2, 1.5.

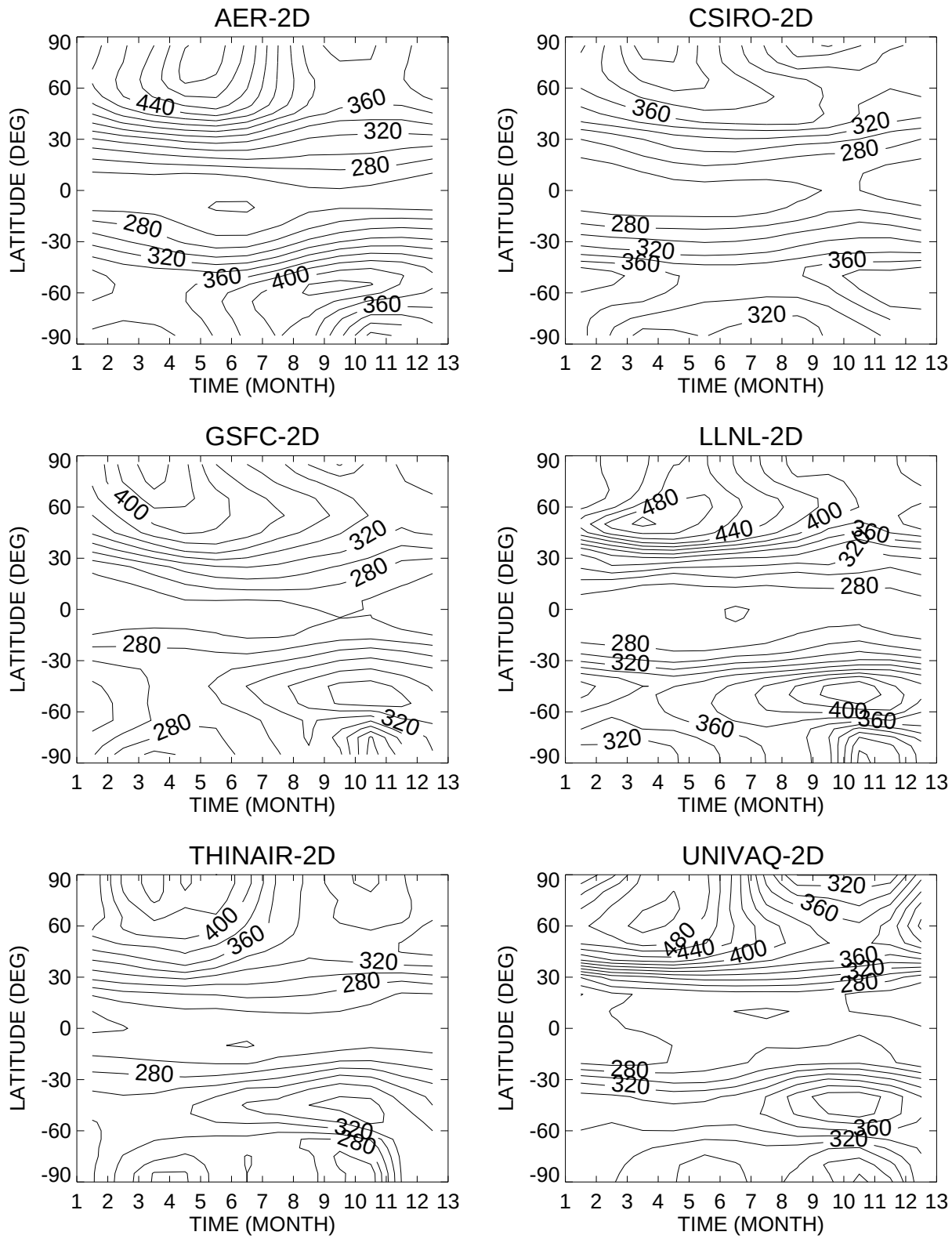

Figure 3.2: Total column ozone (Dobson Units) as a function of latitude and season calculated by the models for Scenario D, the 2015 background atmosphere with subsonic aircraft. The contour interval is 20 DU.

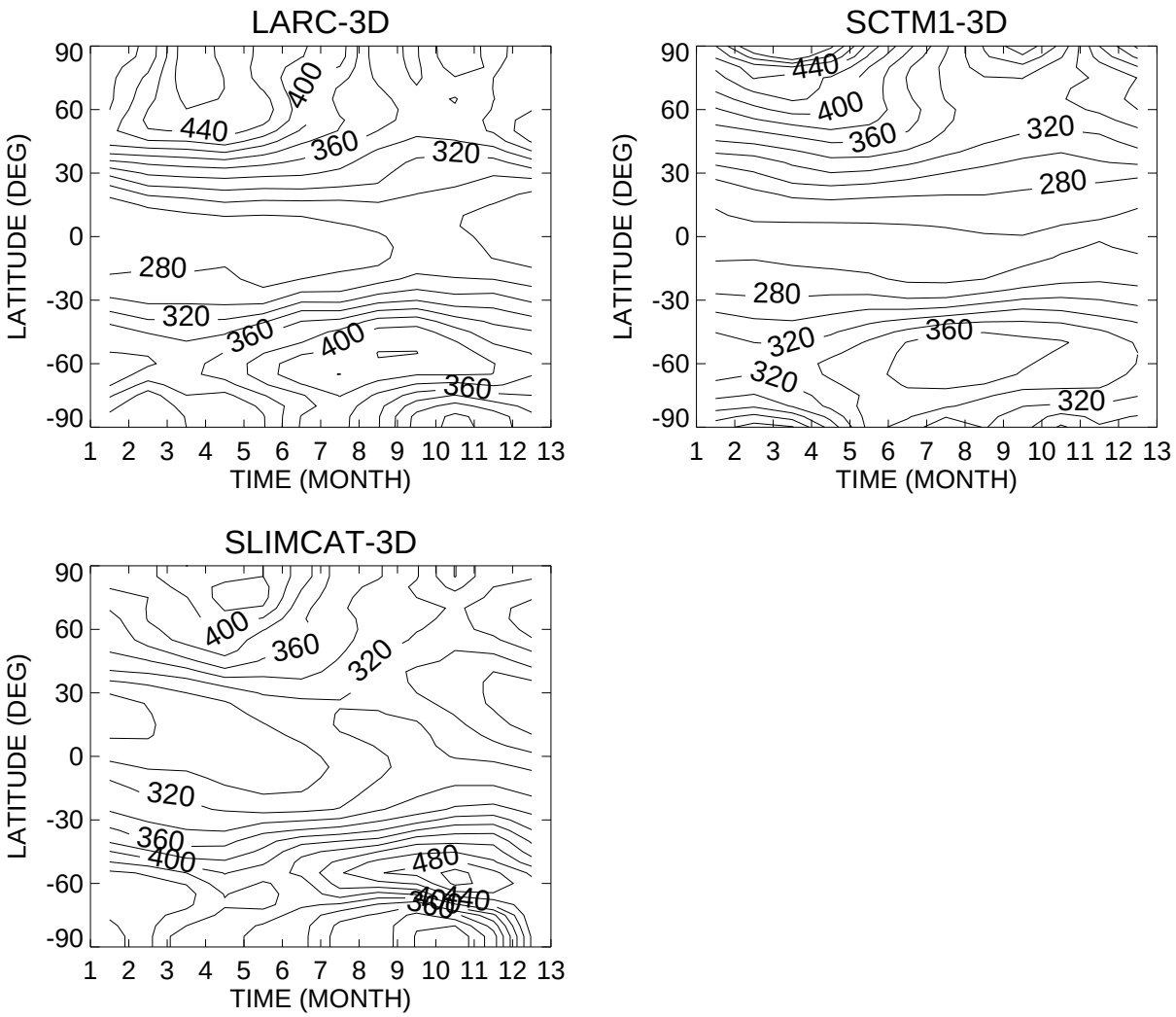

Figure 3.2: continued

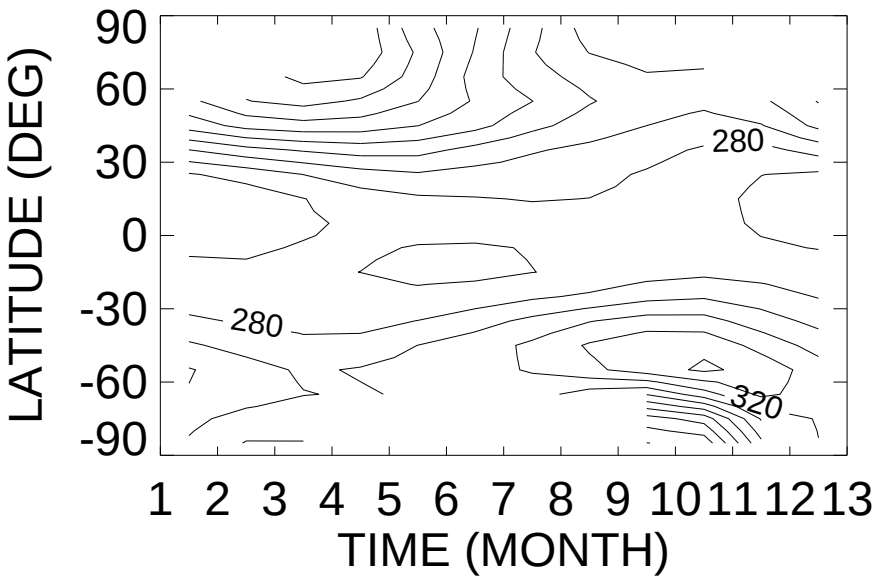

Figure 3.3: Total column ozone (Dobson Units) as a function of latitude and season for 1990 as observed by the TOMS instrument. The contour interval is 20 DU.

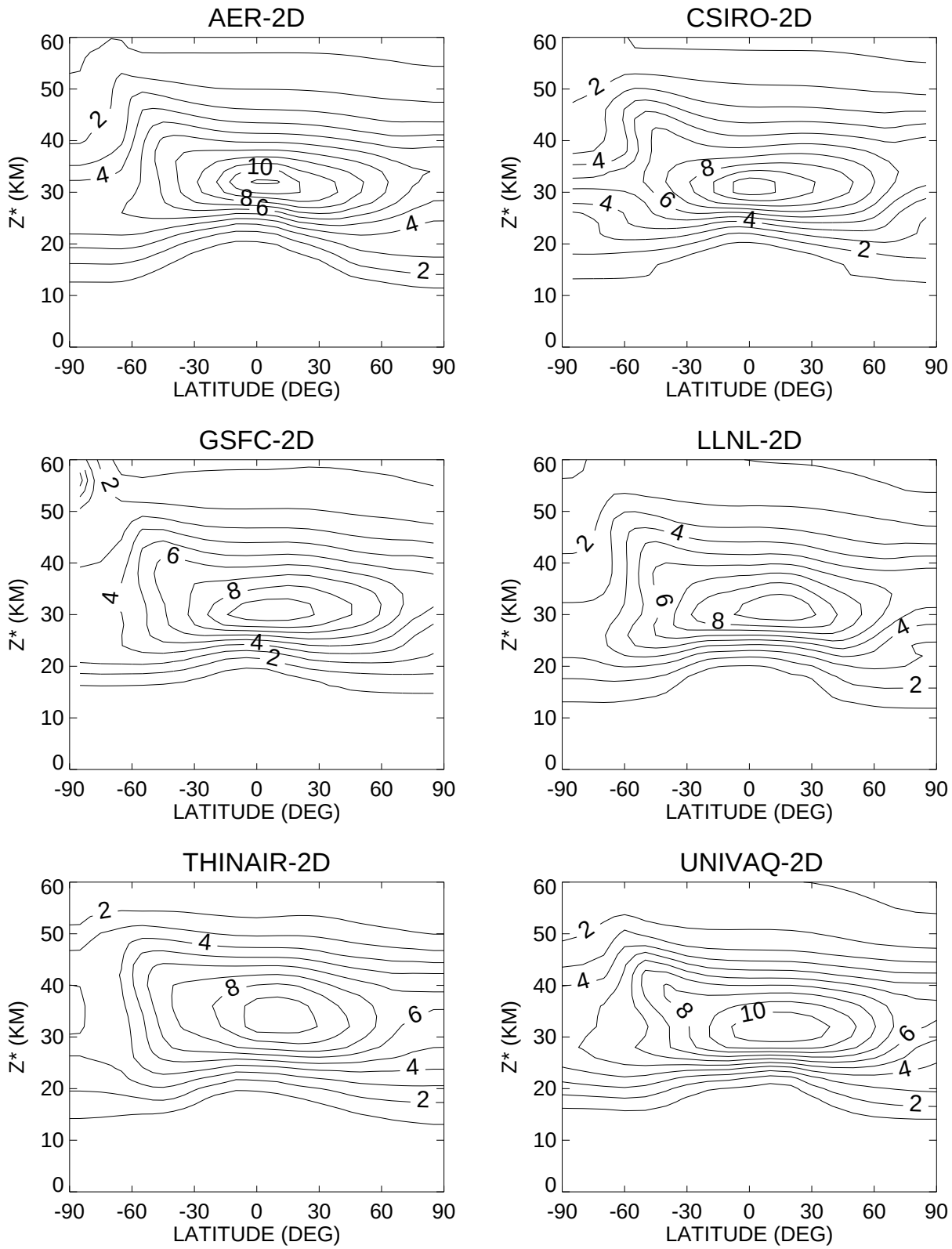

Figure 3.4: Calculated ozone mixing ratios (ppmv) as a function of latitude and altitude for Scenario D in June of 2015. The contour interval is 1 ppmv.

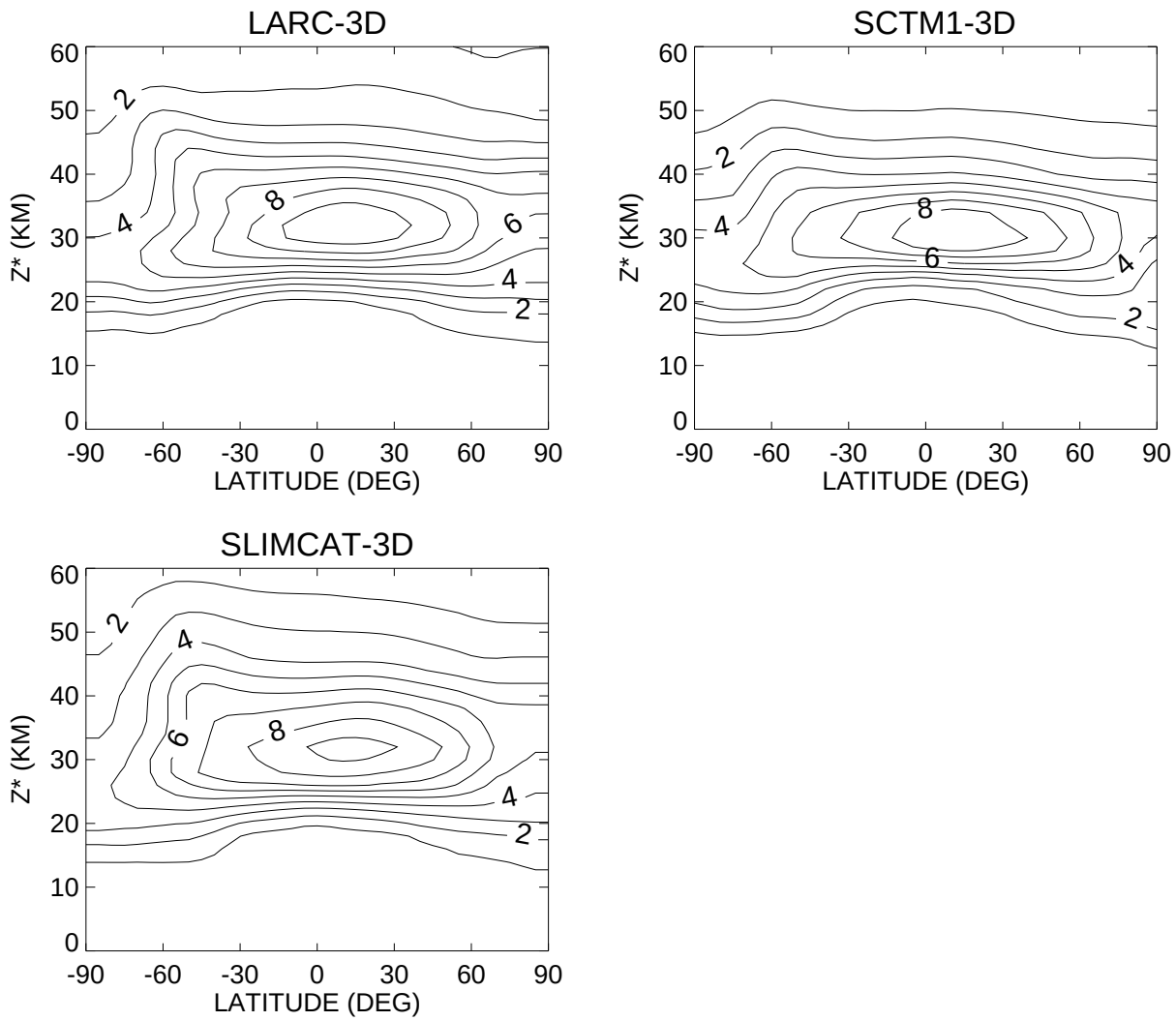

Figure 3.4: continued

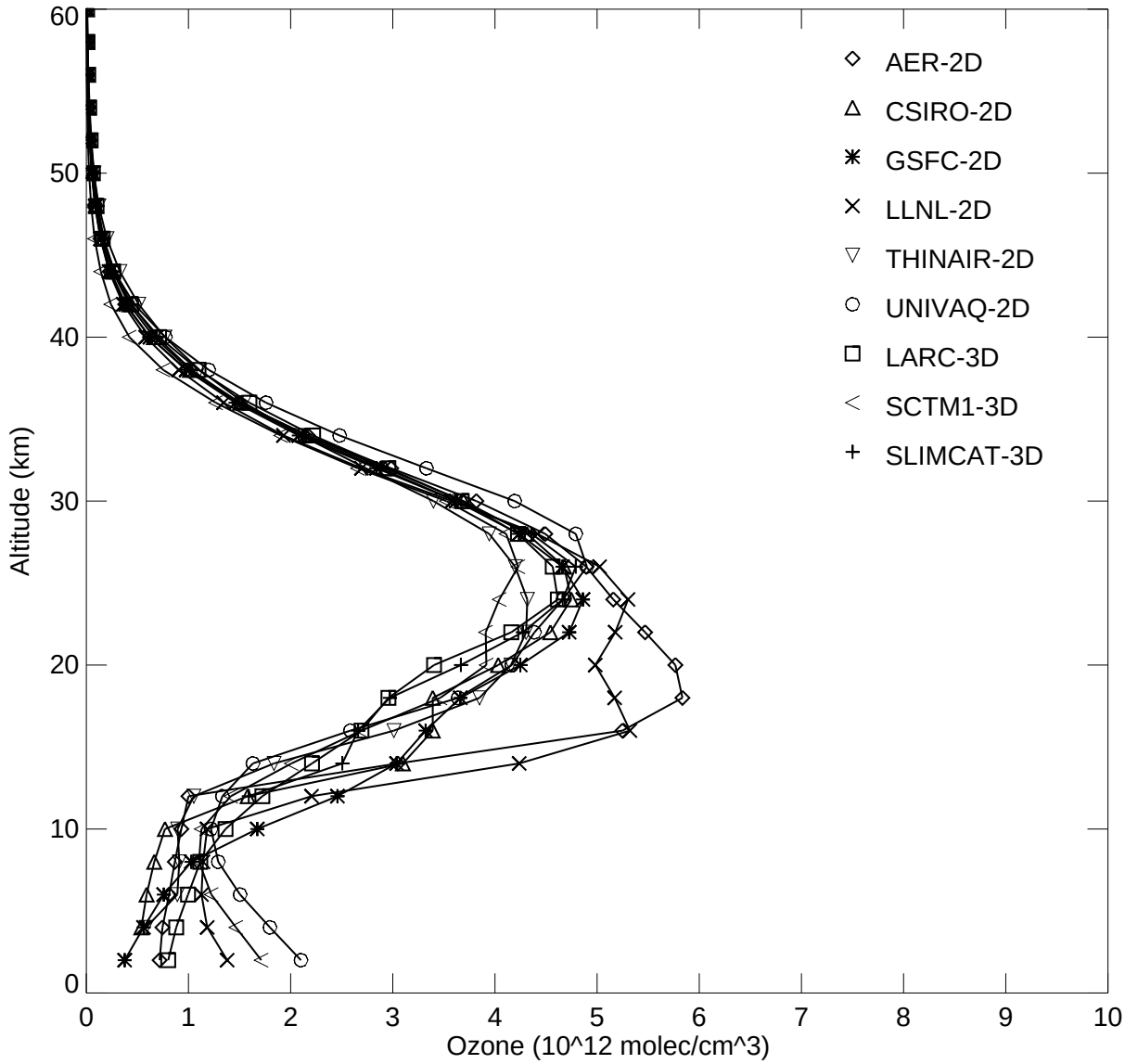

Figure 3.5: Calculated ozone concentration (molecules/cm^3) as a function of altitude for Scenario D at 45^{o}N in June.

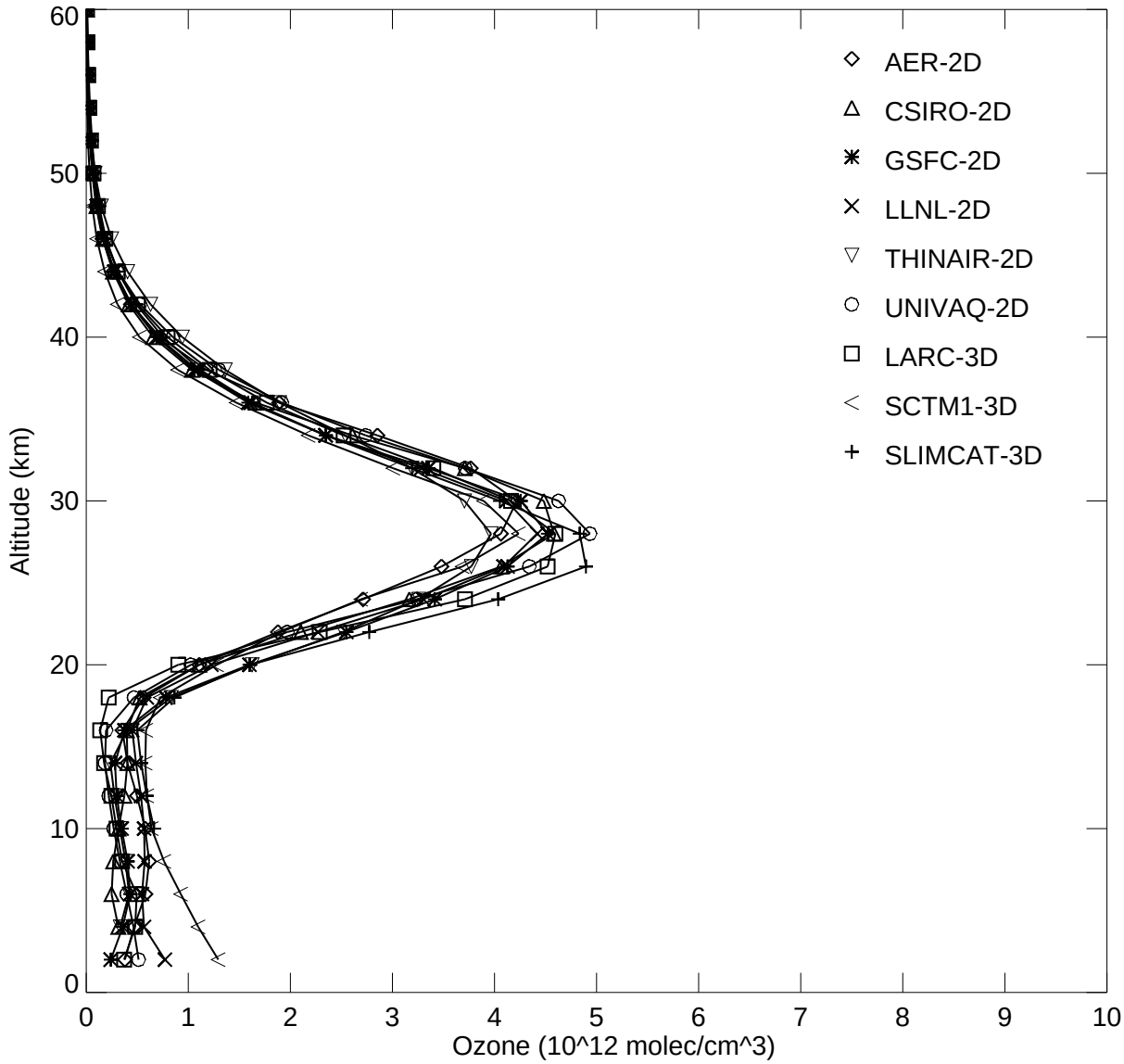

Figure 3.6: Calculated ozone concentration (molecules/cm^3) as a function of altitude for Scenario D at the equator in June.

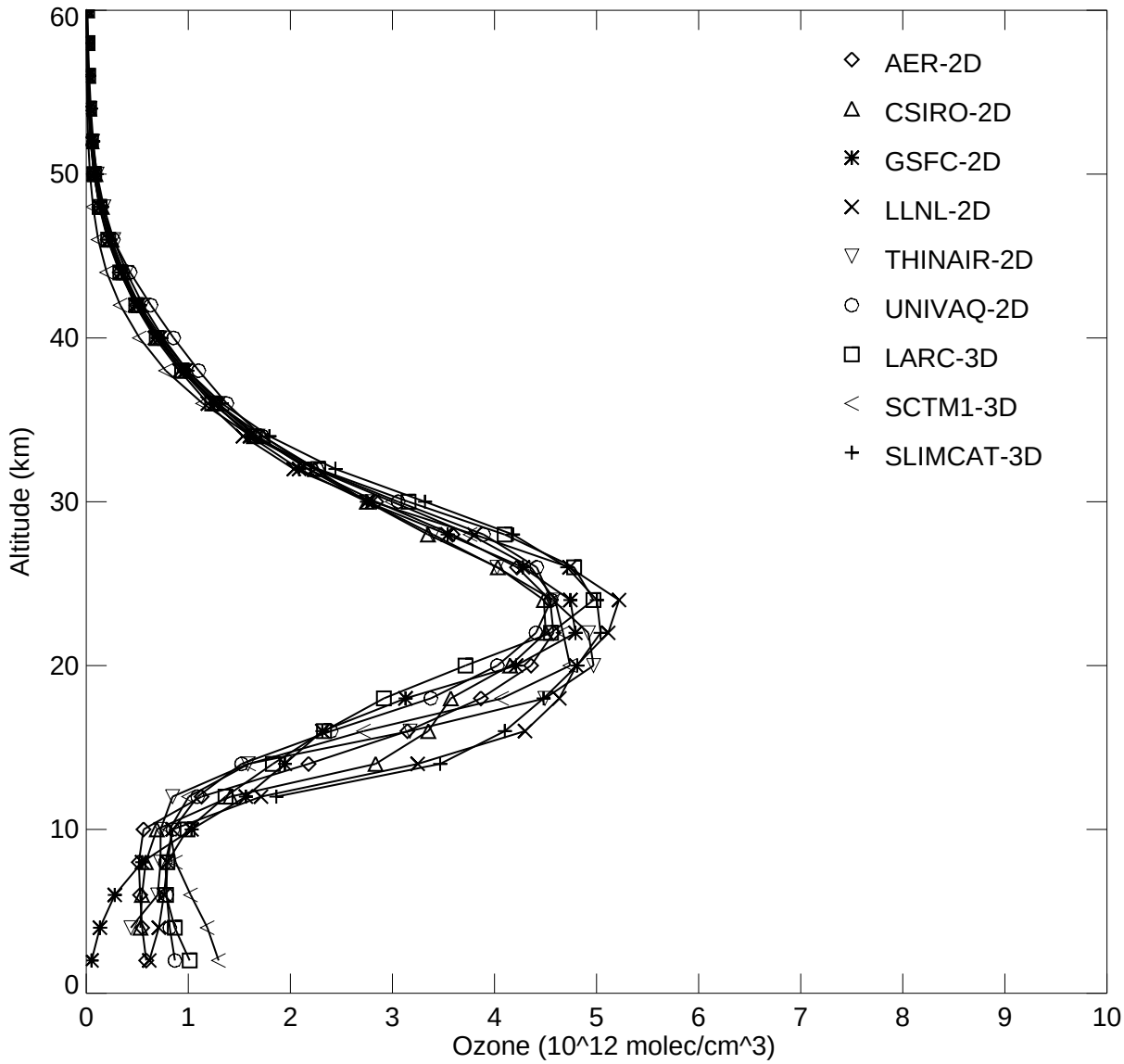

Figure 3.7: Calculated ozone concentration (molecules/cm^3) as a function of altitude for Scenario D at 45^{o}S in June.

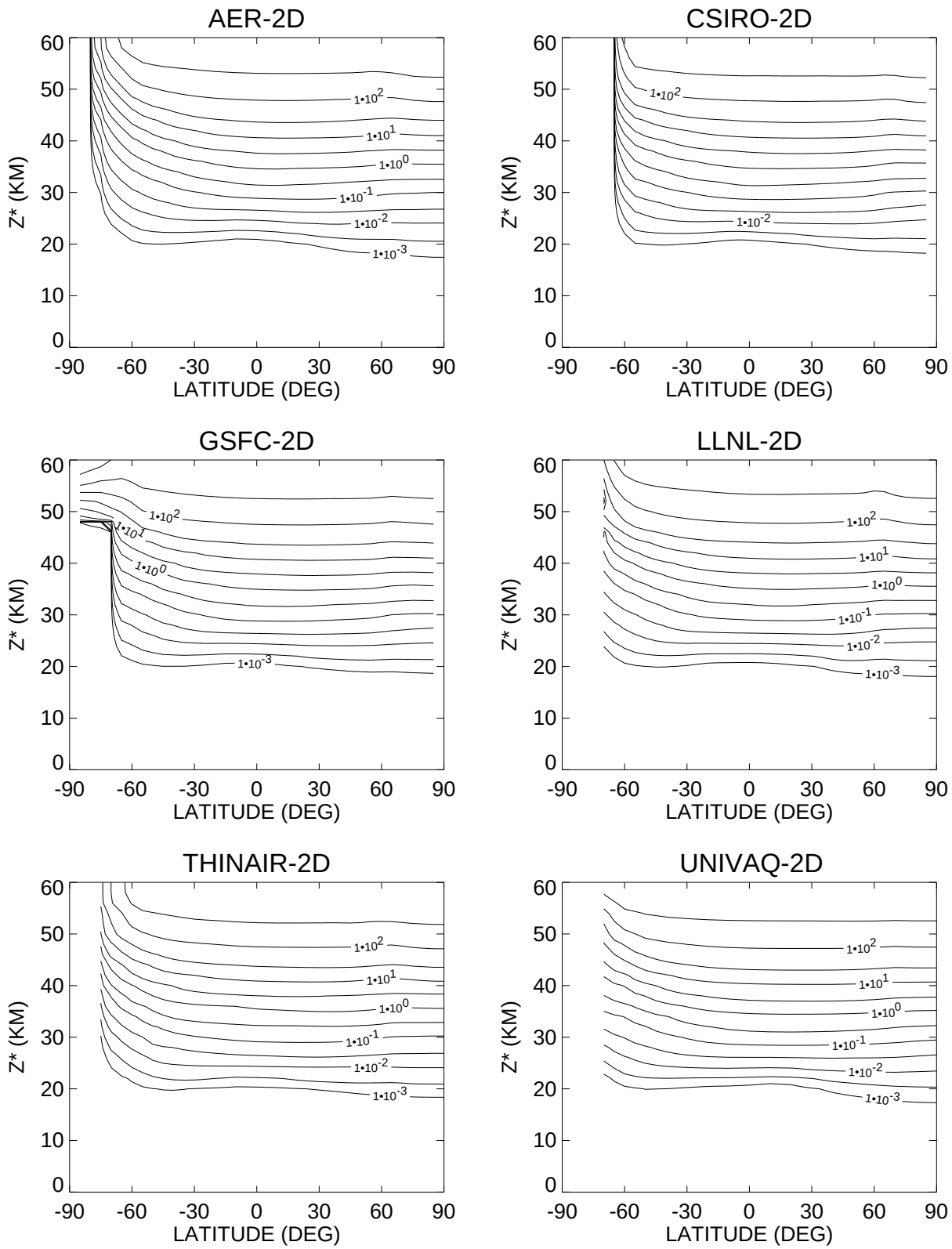

Figure 3.8: Calculated atomic oxygen mixing ratios (pptv) as a function of latitude and altitude for Scenario D in June of 2015. Daytime averages are shown for 2-D models, 24-hour averages for 3-D models. Contours are .001, .003, .01, .03, .1, .3, 1, 3, 10, 30, 100, 300, 1000 ppbv.

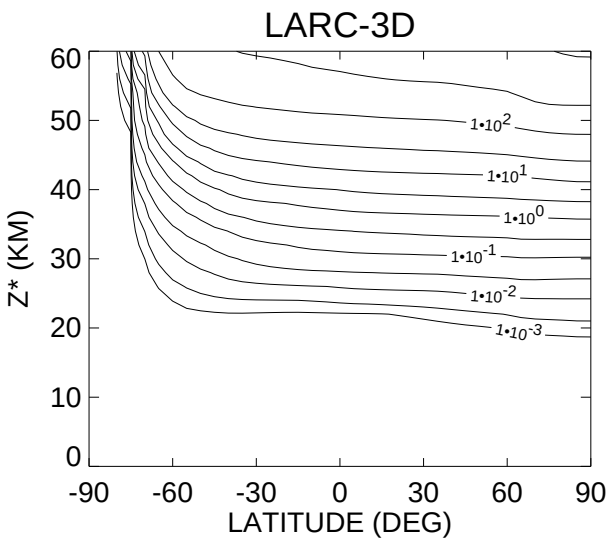

Figure 3.8: continued

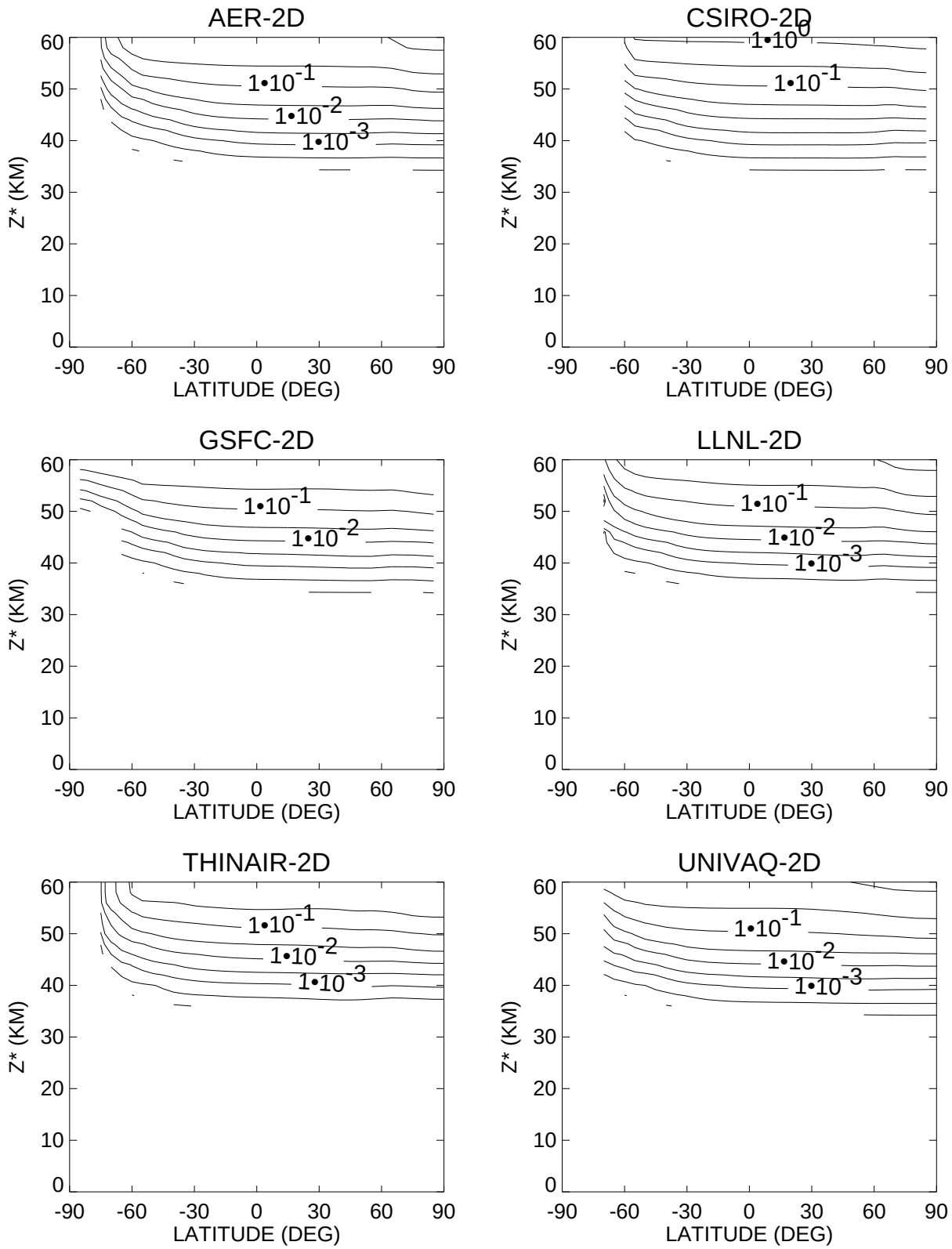

Figure 3.9: Calculated O/O_3 ratio as a function of latitude and altitude for Scenario D in June of 2015. Contours are .0001, .0003, .001, .003, .01, .03, .1, .3, 1.0.

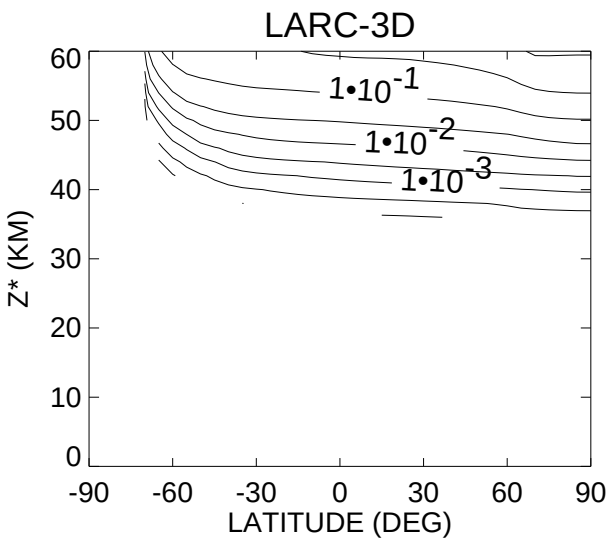

Figure 3.9: continued

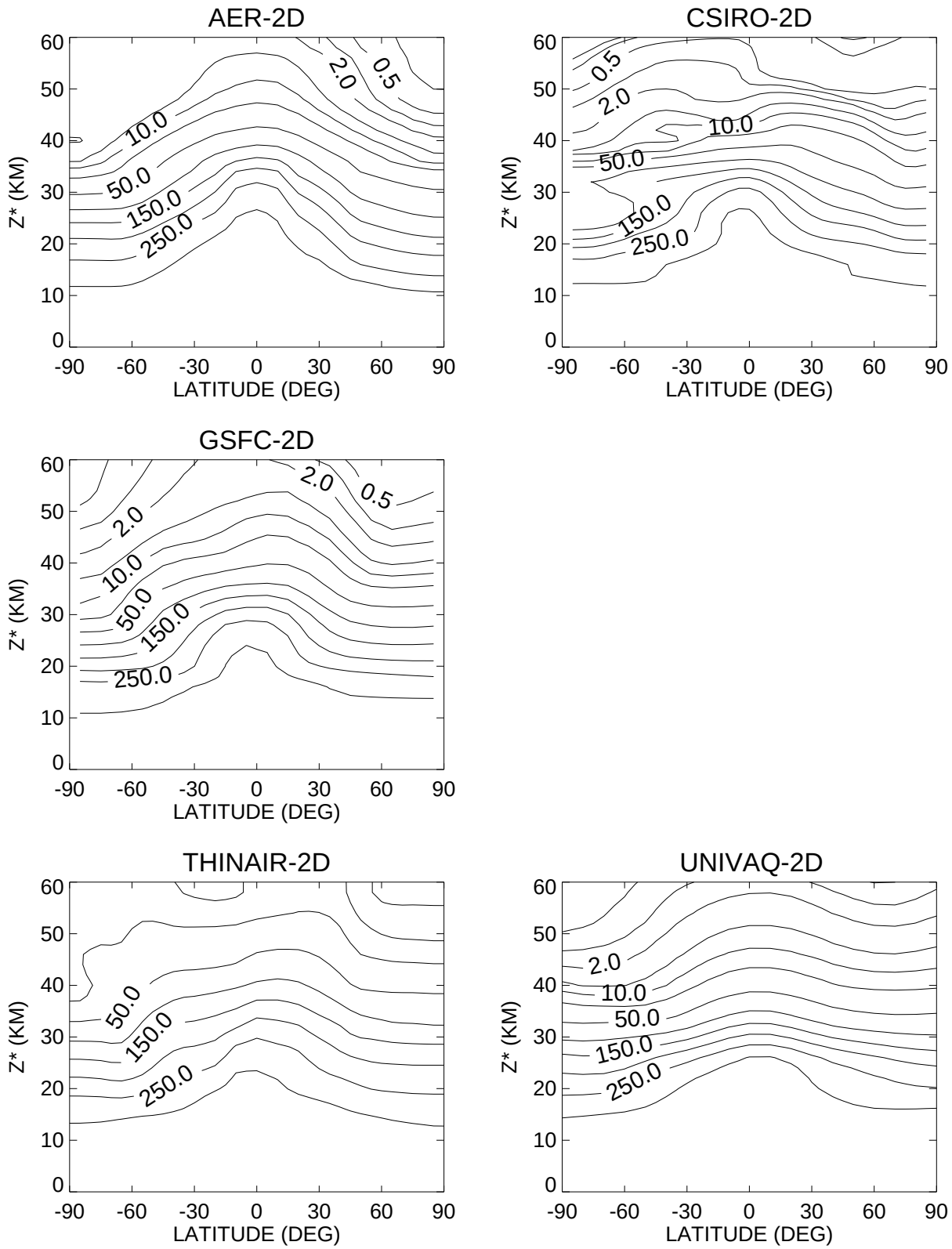

Figure 3.10: Calculated N_2O mixing ratios (ppbv) as a function of latitude and altitude for Scenario D in June of 2015. Contours are 0.1, 0.2, 0.5, 1, 2, 5, 10, 20, 50, 100, 150, 200, 250, 300 ppbv.

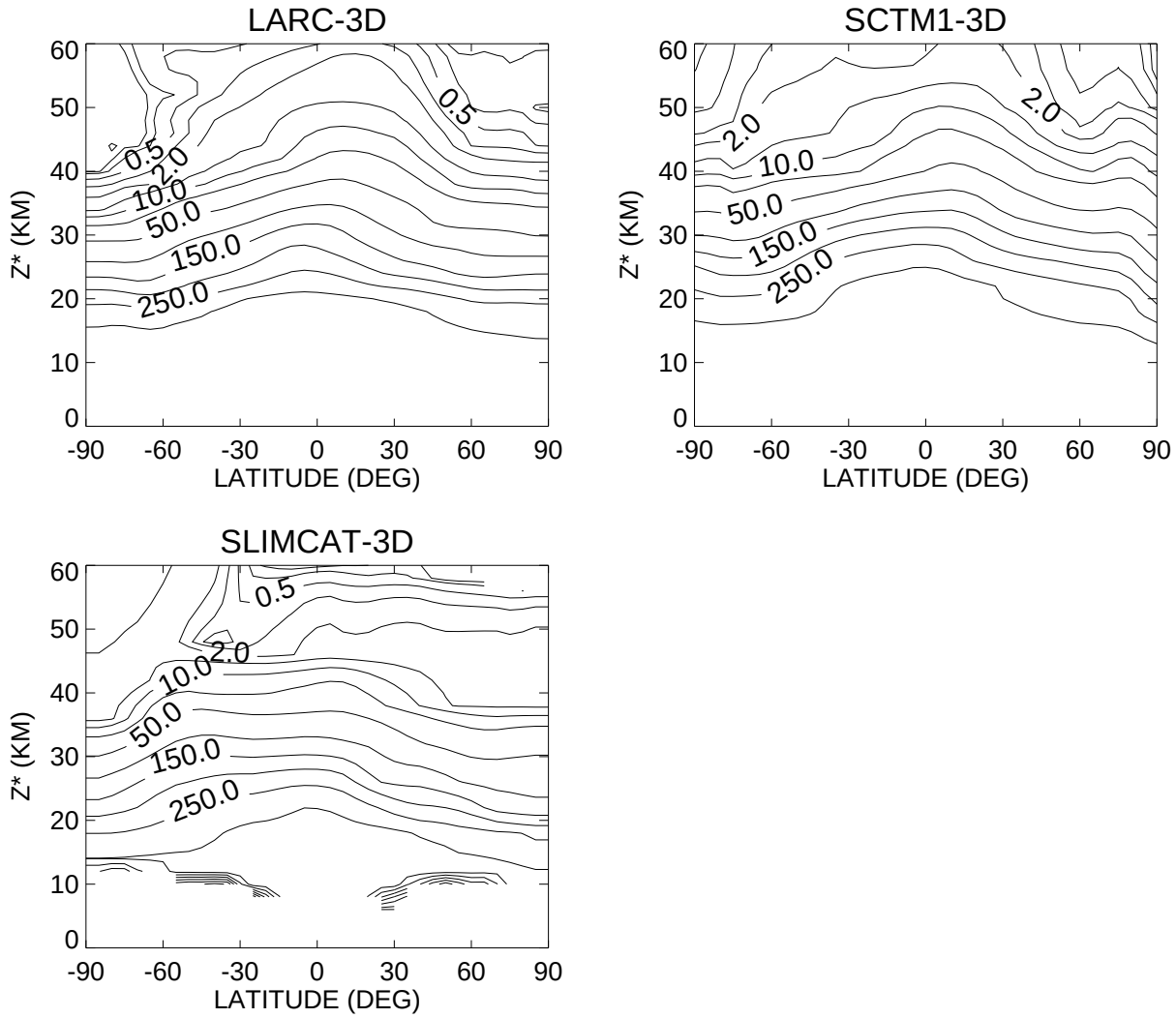

Figure 3.10: continued

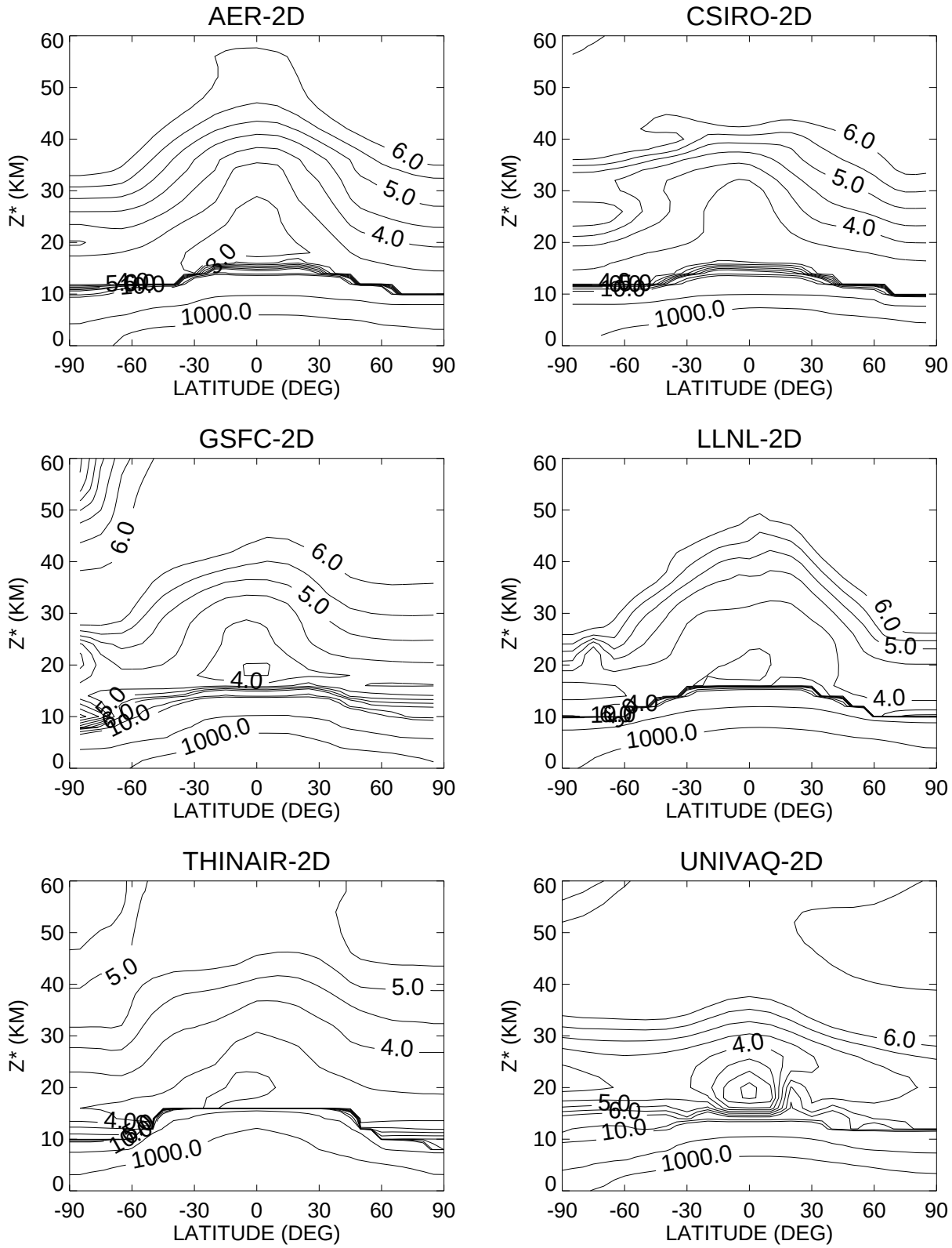

Figure 3.11: Calculated H_2O mixing ratios (ppmv) as a function of latitude and altitude for Scenario D in June of 2015. Contours are 2.5 to 6.5 by 0.5 ppmv and 10, 100, 1000 ppmv.

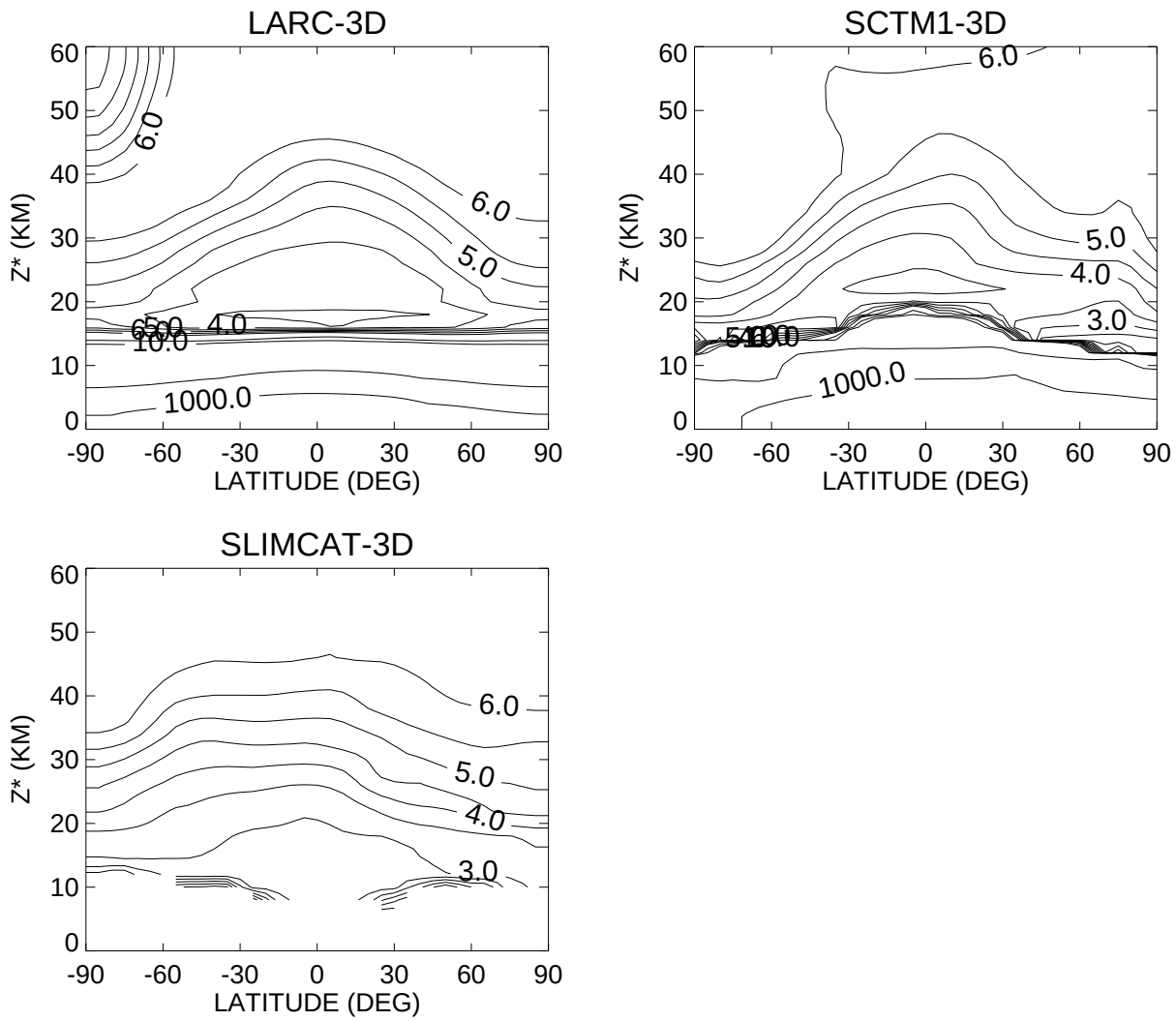

Figure 3.11: continued

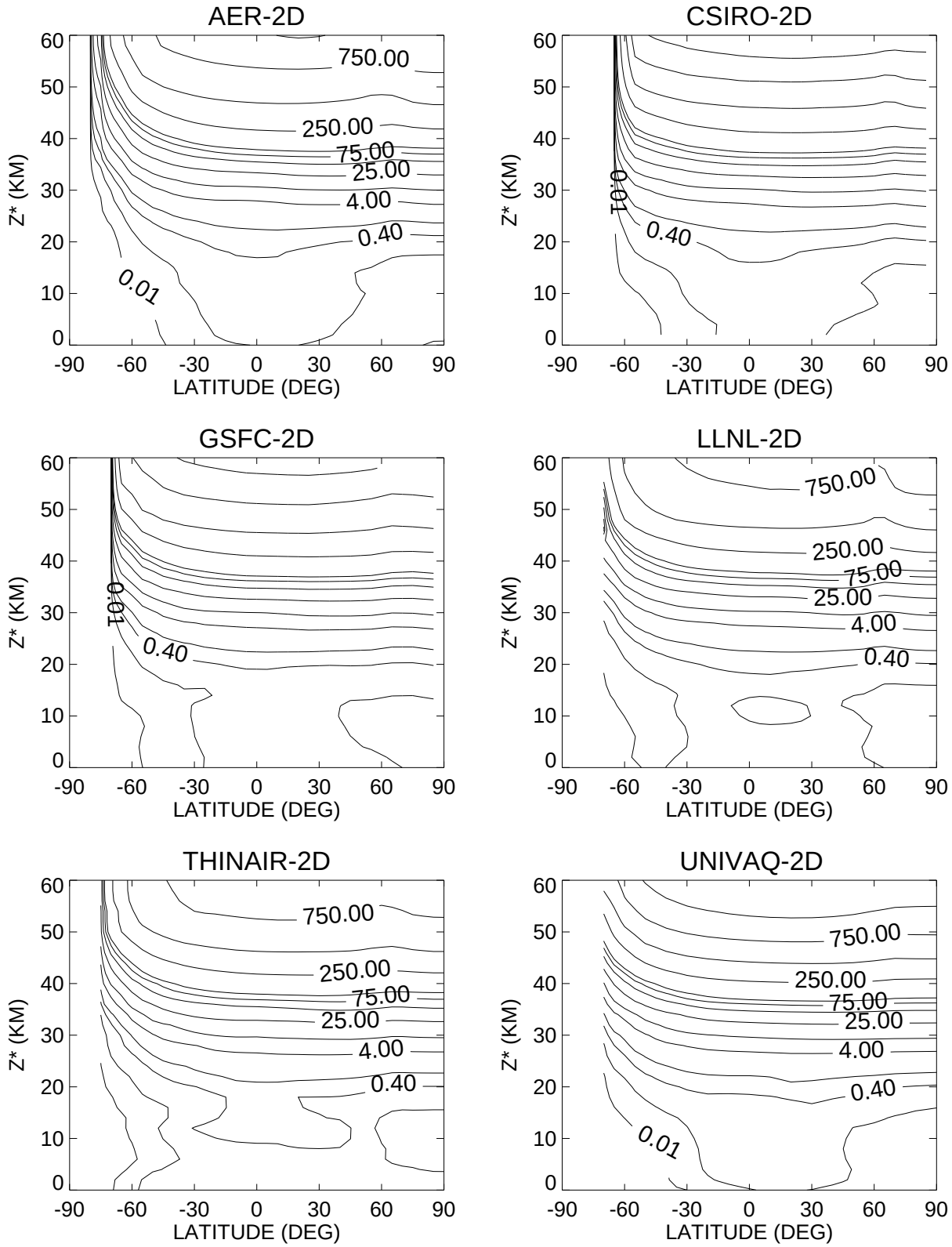

Figure 3.12: Calculated OH mixing ratios (pptv) as a function of latitude and altitude for Scenario D in June of 2015. Daytime averages are shown for 2-D models, 24-hour averages for 3-D models. Contours are .01, .1, .4, 1, 4, 10, 25, 50, 75, 100, 250, 500, 750 pptv.

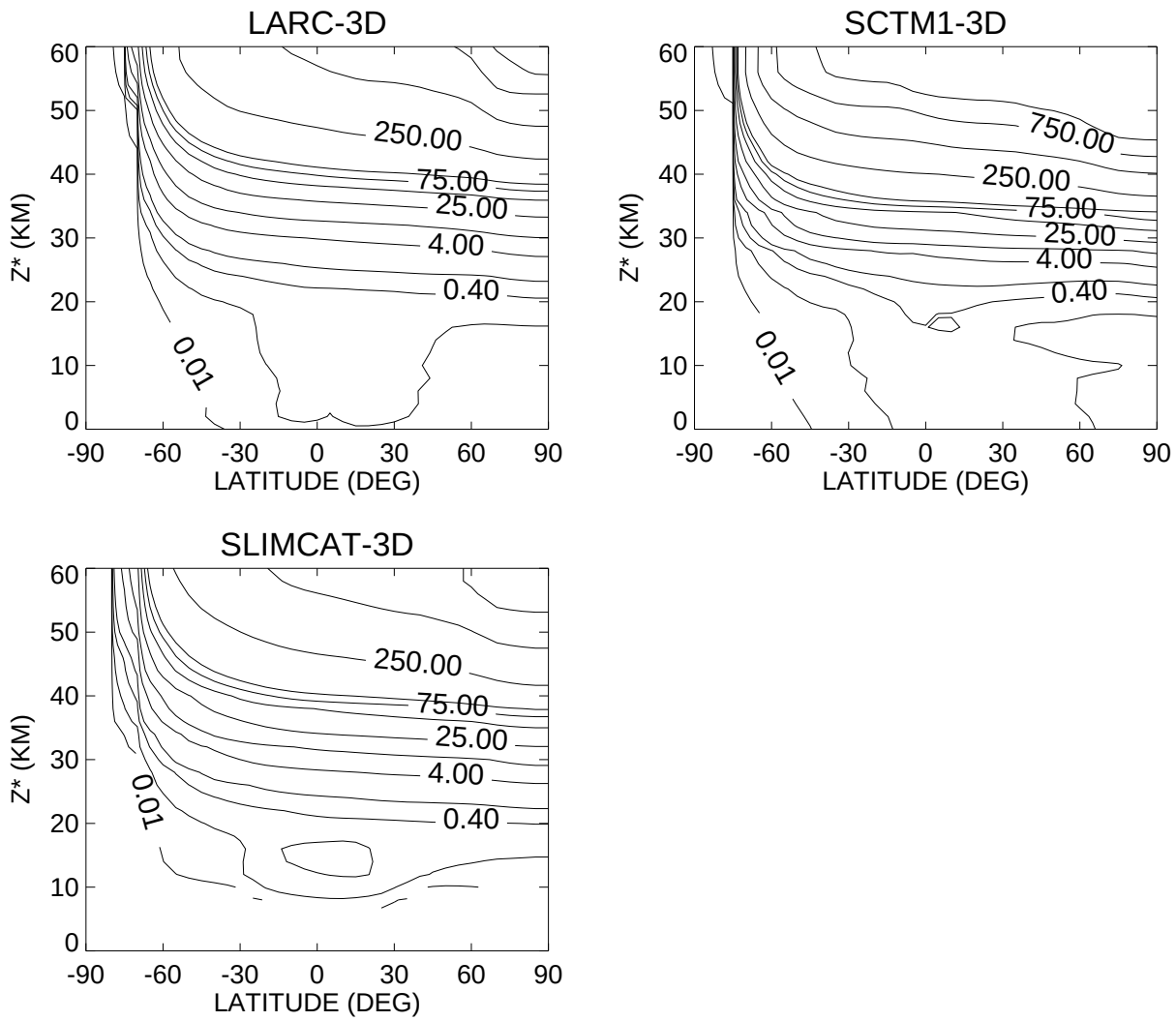

Figure 3.12: continued

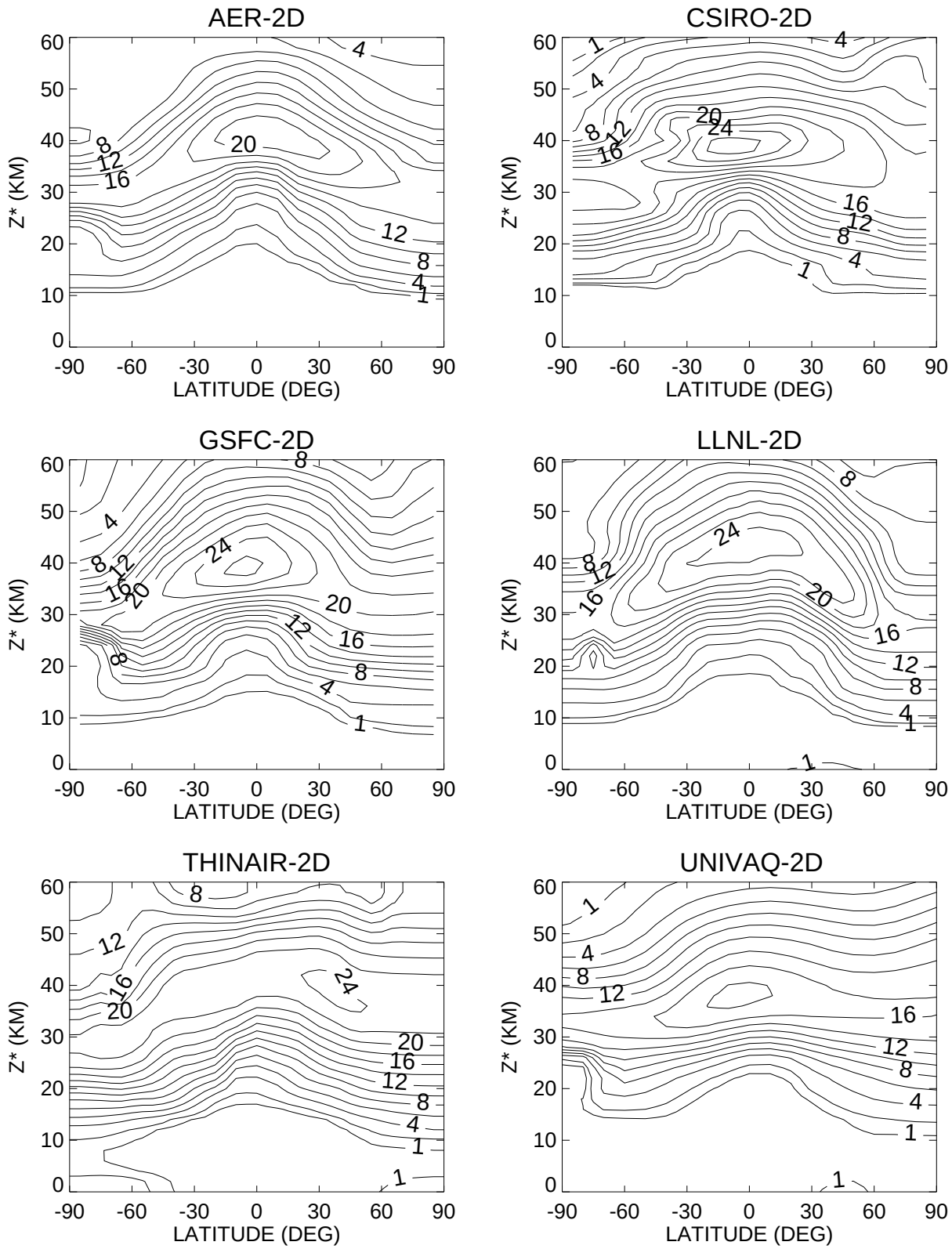

Figure 3.13: Calculated NO_y mixing ratios (ppbv) as a function of latitude and altitude for Scenario D in June of 2015. Contours are 1 ppbv and from 2 to 26 ppbv by 2 ppbv.

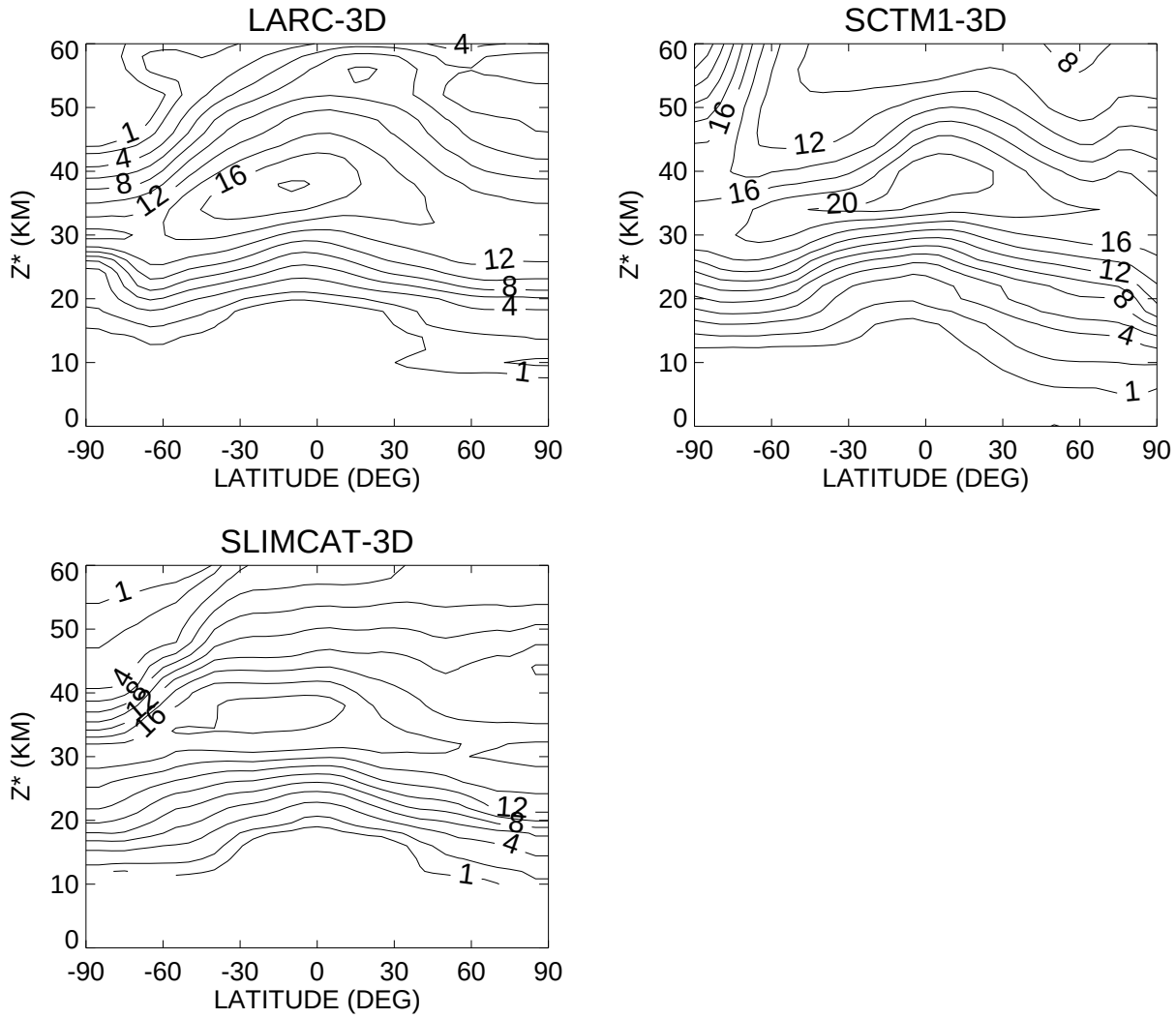

Figure 3.13: continued

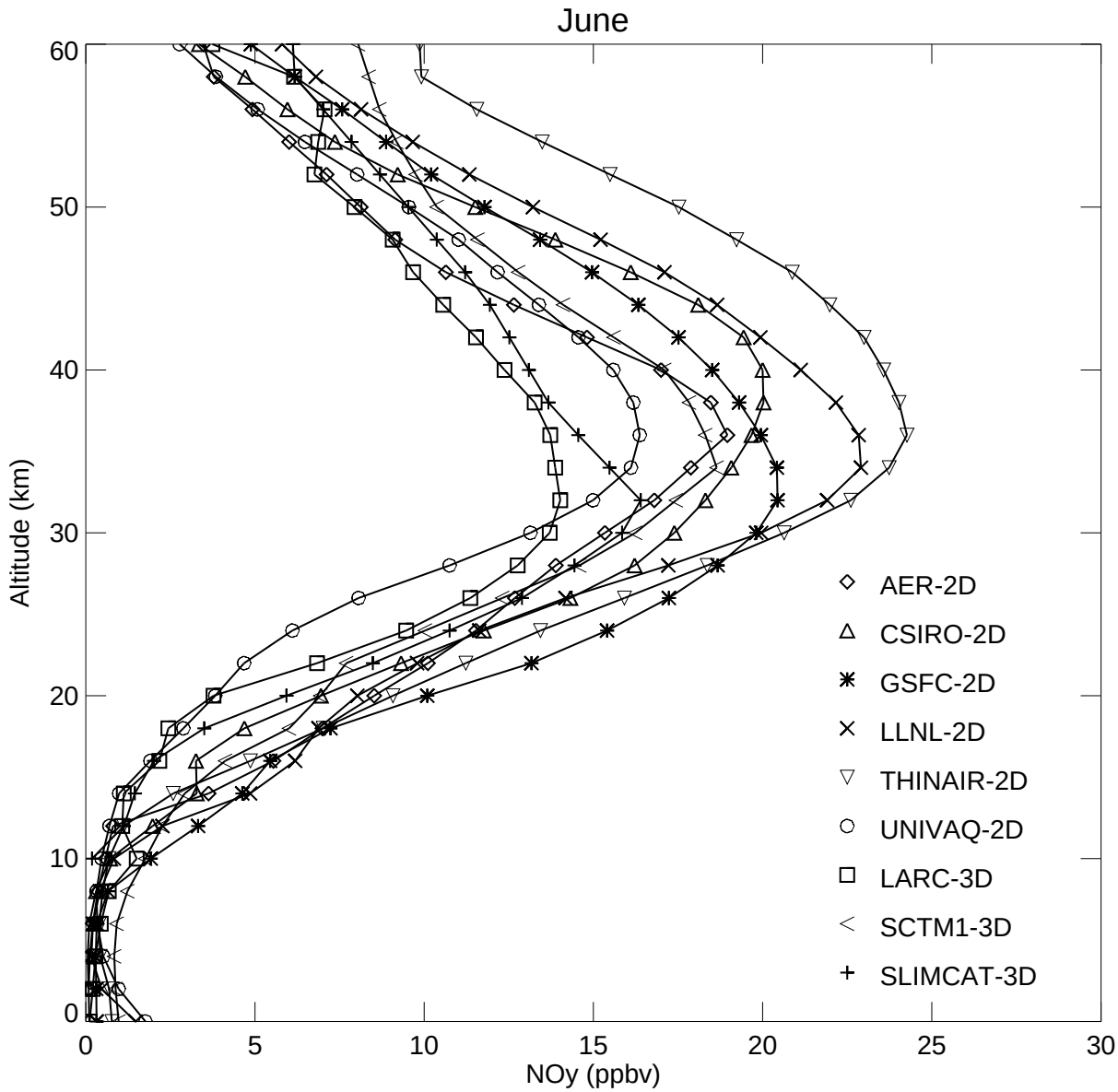

Figure 3.14: Calculated NO_y concentration (ppbv) as a function of altitude for Scenario D at 45°N in June.

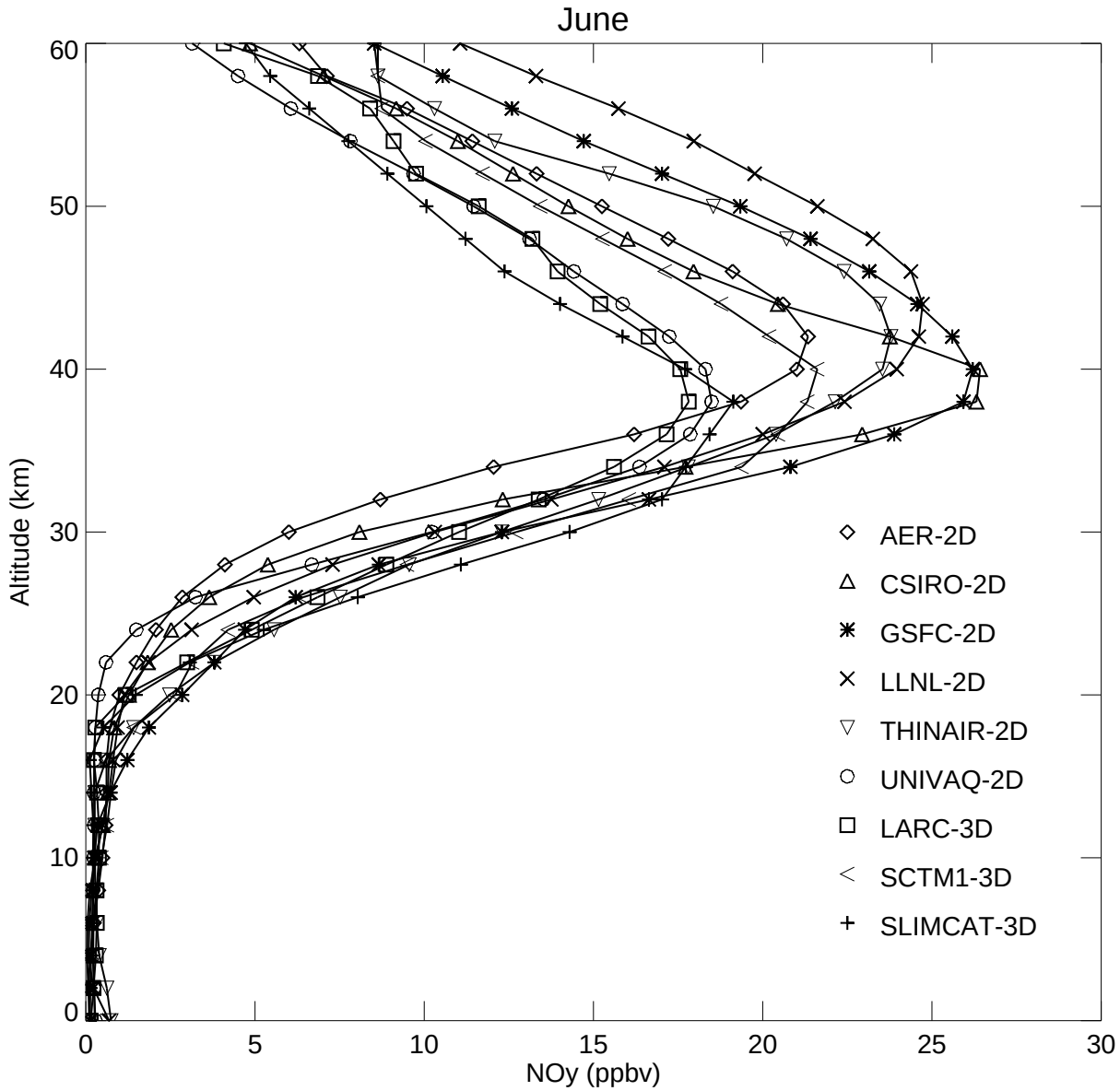

Figure 3.15: Calculated NO_y concentration (ppbv) as a function of altitude for Scenario D at the equator in June.

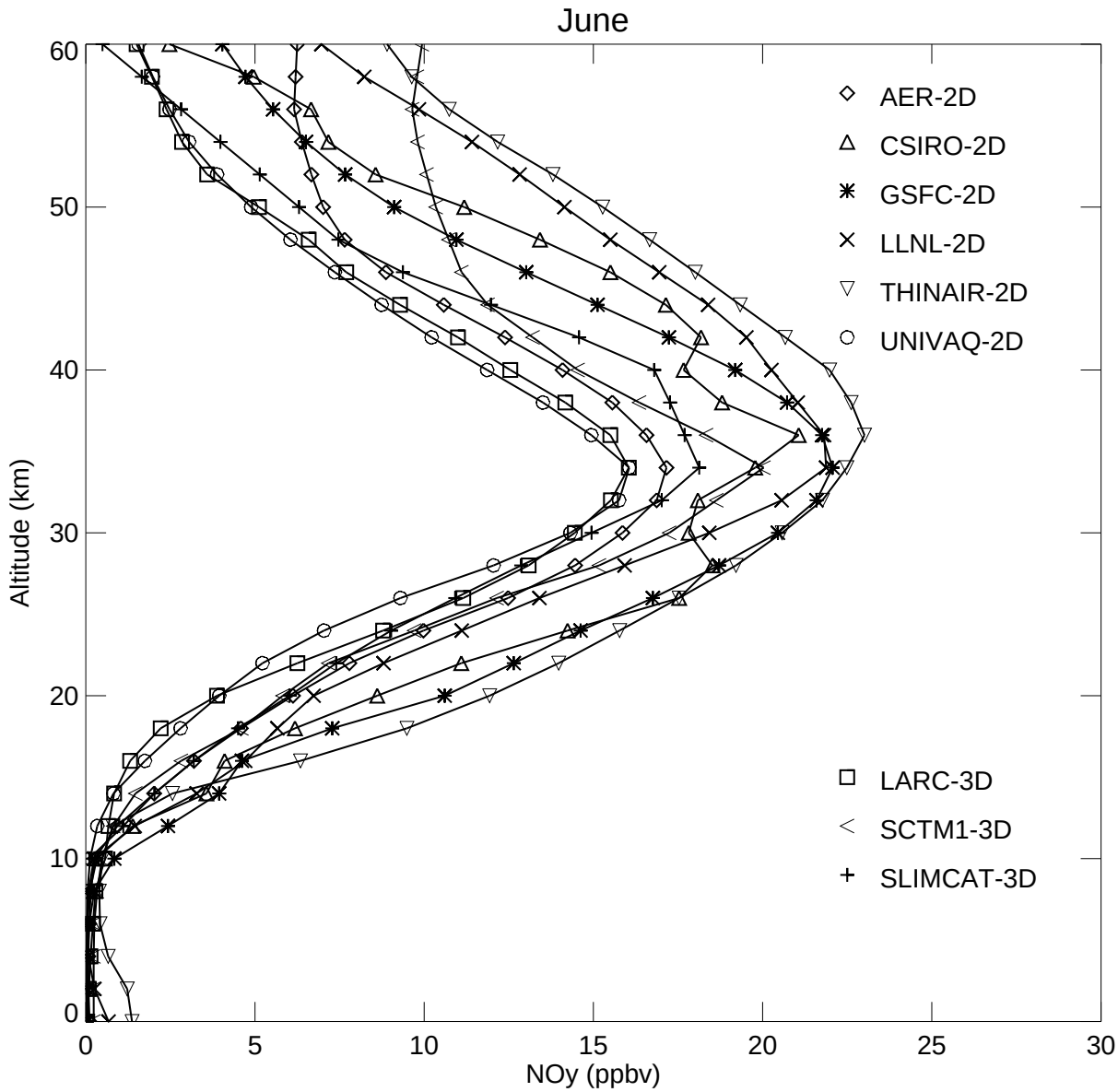

Figure 3.16: Calculated NO_y concentration (ppbv) as a function of altitude for Scenario D at 45°S in June.

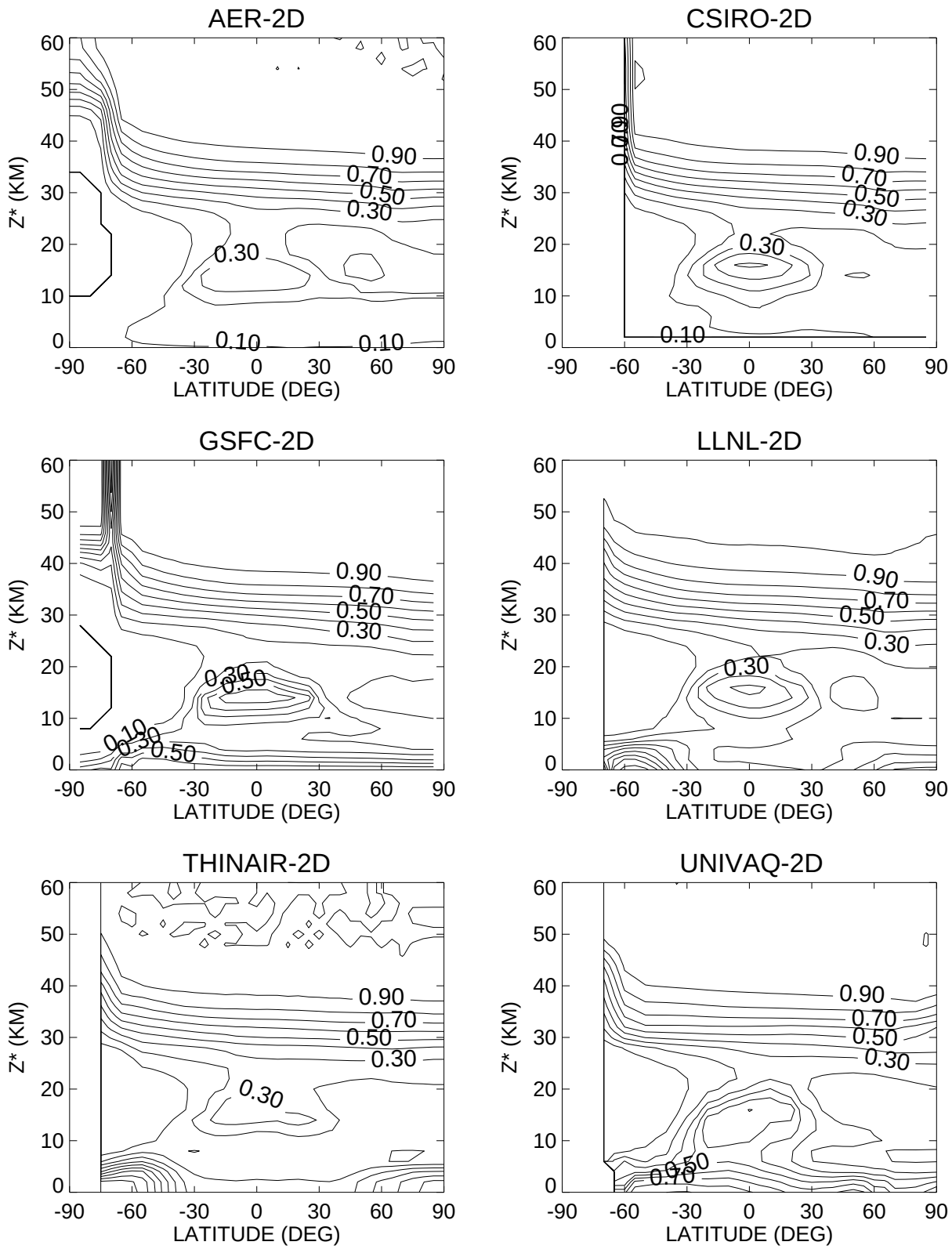

Figure 3.17: Calculated $NO_x(=NO+NO_2)/NO_y$ ratio as a function of latitude and altitude for Scenario D in June of 2015. Contour interval is 0.1.

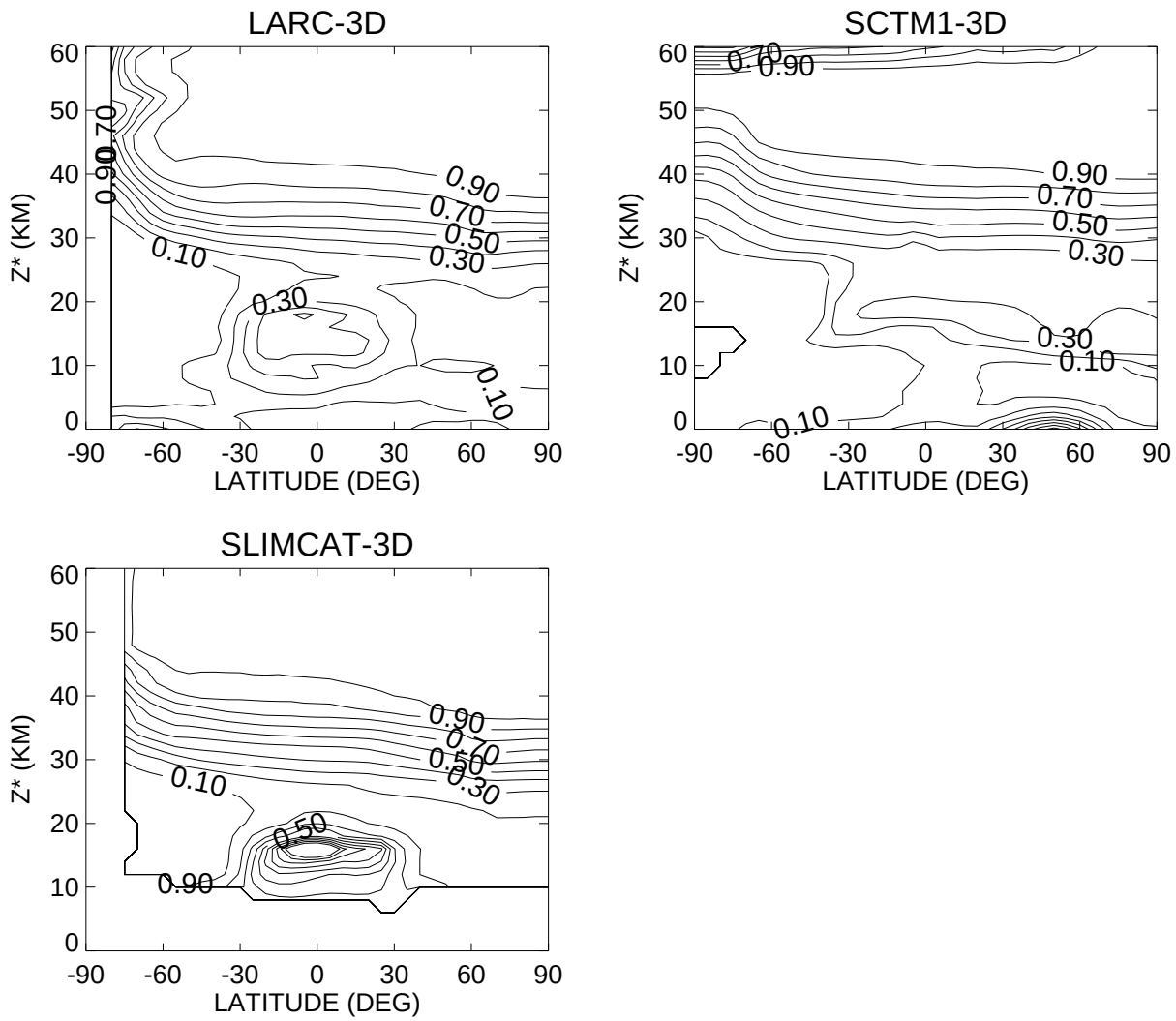

Figure 3.17: continued

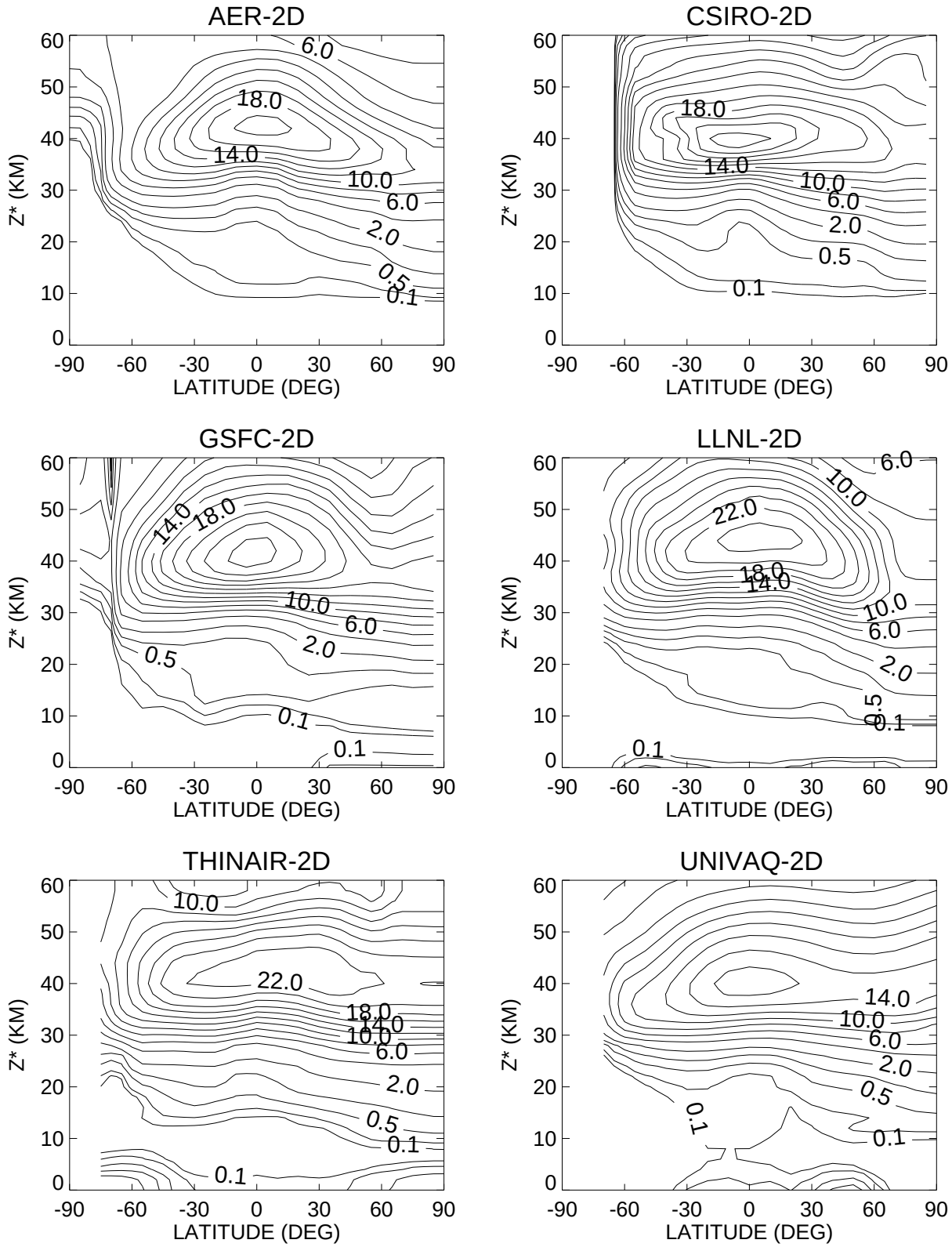

Figure 3.18: Calculated NO_x (=NO+NO_2) mixing ratios (ppbv) as a function of latitude and altitude for Scenario D in June of 2015. Daytime averages are shown for 2-D models, 24-hour averages for 3-D models. Contours are 0.1, 0.2, 0.5, 1, and 2 to 24 by 2 ppbv.

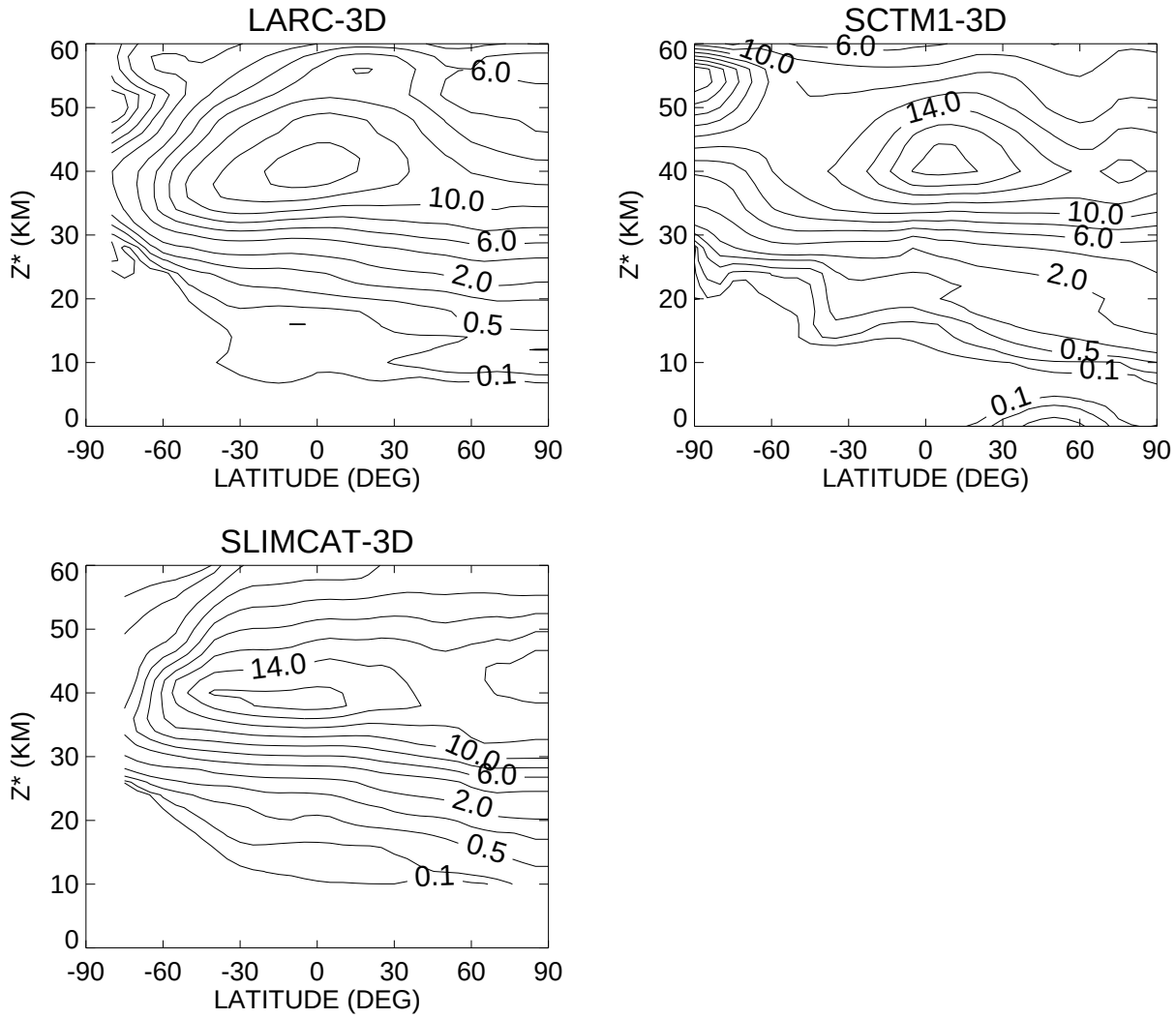

Figure 3.18: continued

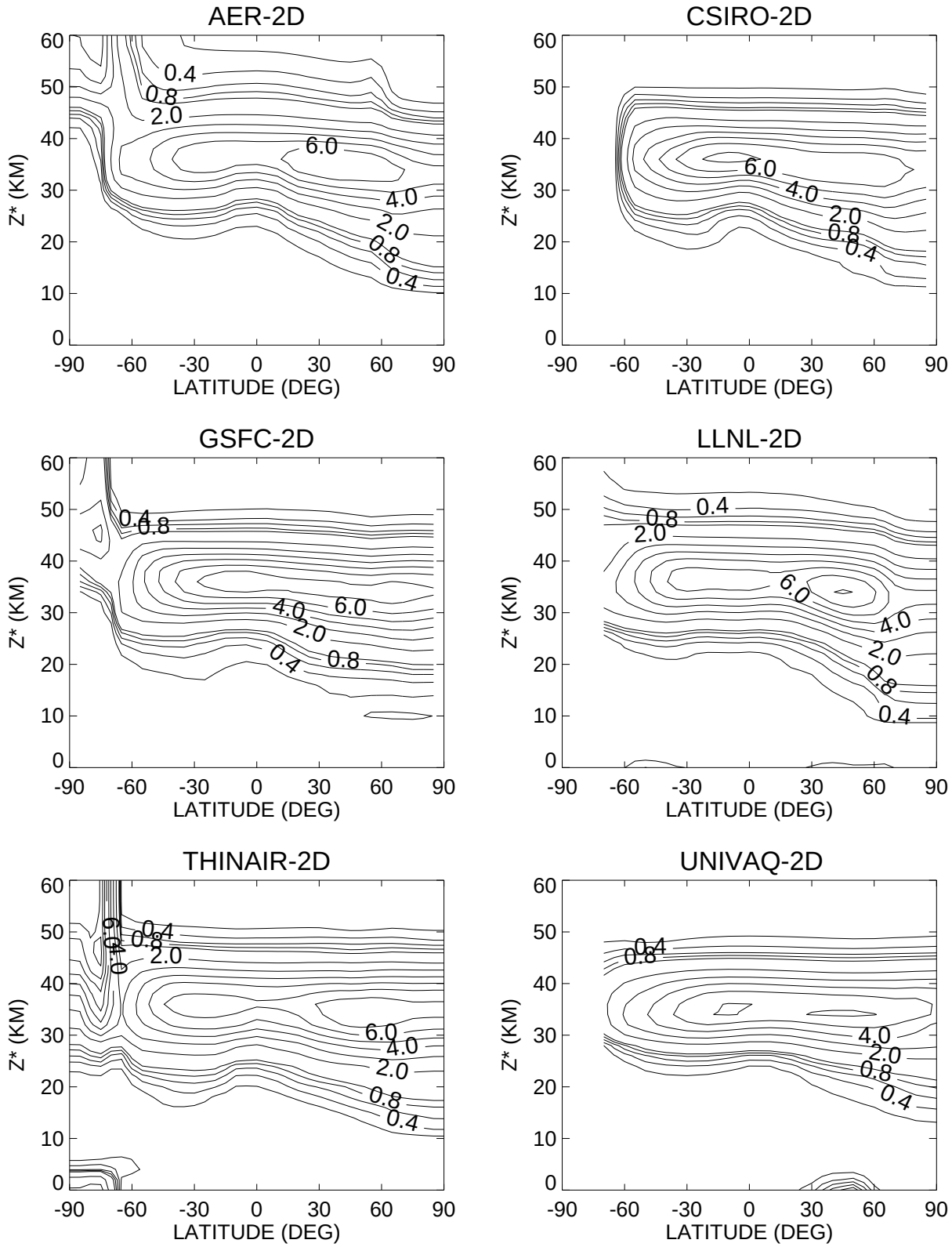

Figure 3.19: Calculated NO_2 mixing ratios (ppbv) as a function of latitude and altitude for Scenario D in June of 2015. Daytime averages are shown for 2-D models, 24-hour averages for 3-D models. Contours are .2, .4, .6, .8, and 1 to 10 by 1 ppbv.

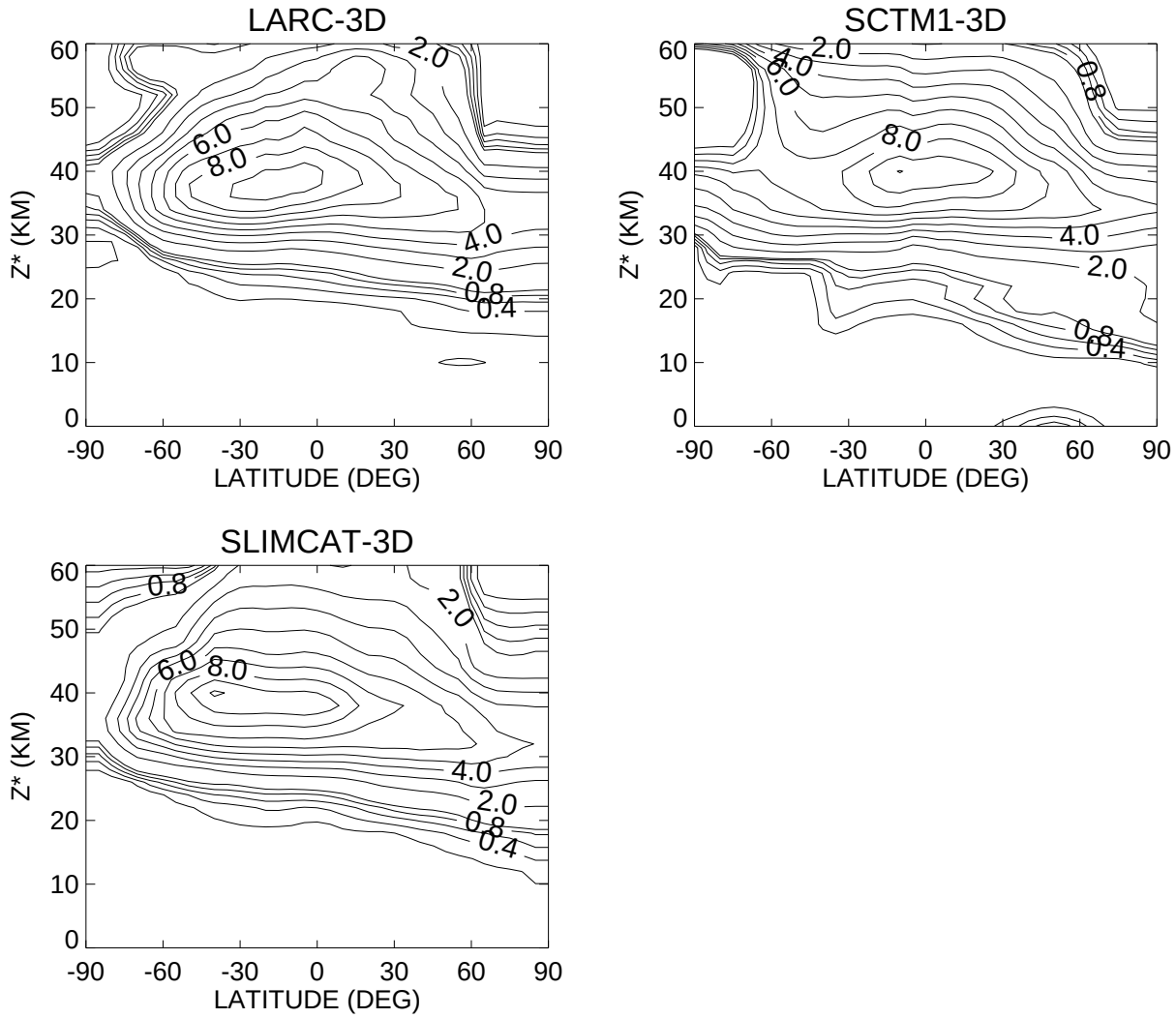

Figure 3.19: continued

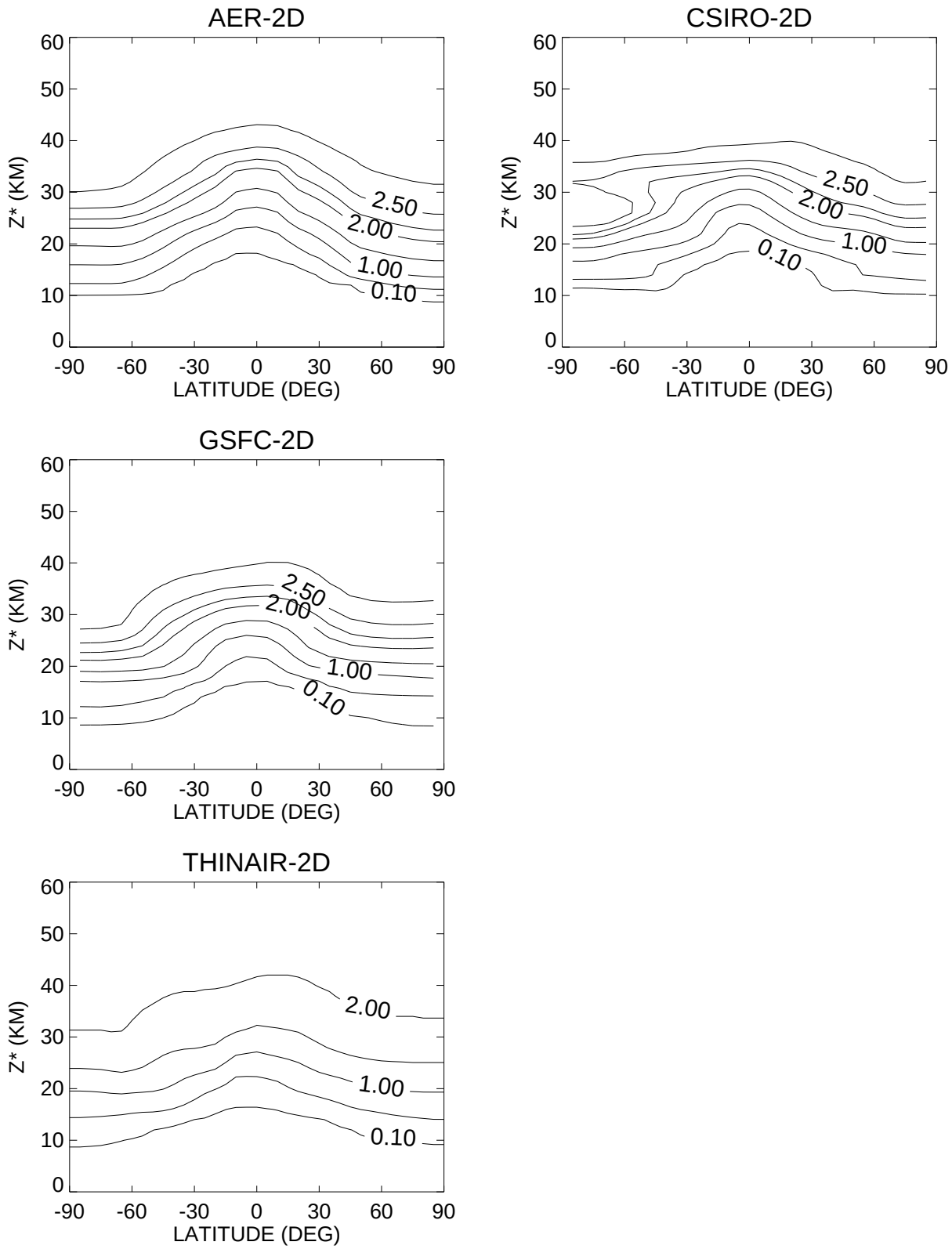

Figure 3.20: Calculated Cl_y mixing ratios (ppbv) as a function of latitude and altitude for Scenario D in June of 2015. Contours are .1, .5, 1, 1.5, 2, 2.25, 2.5, 2.75 ppbv.

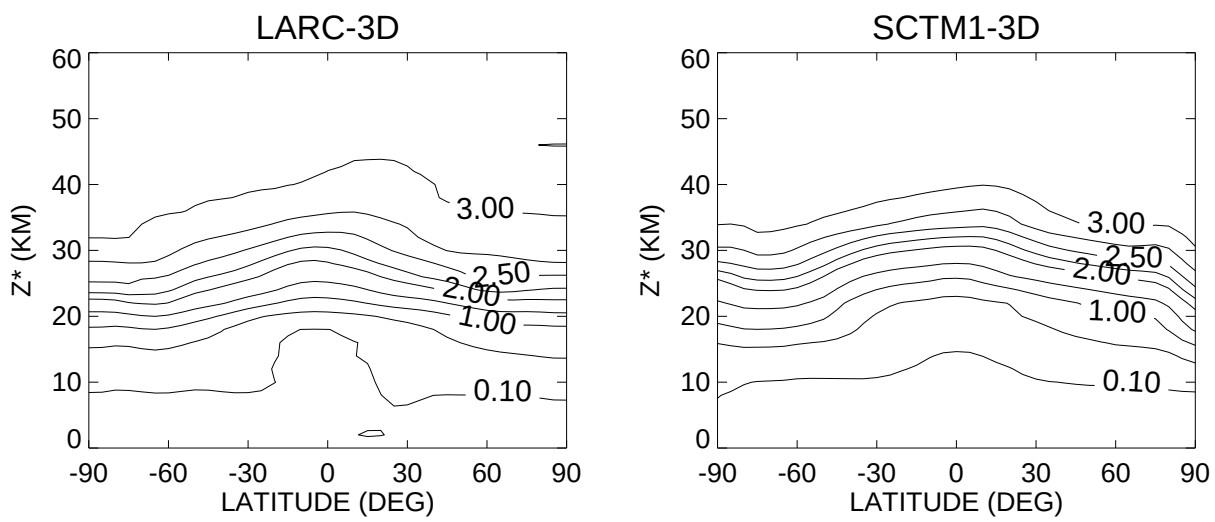

Figure 3.20: continued

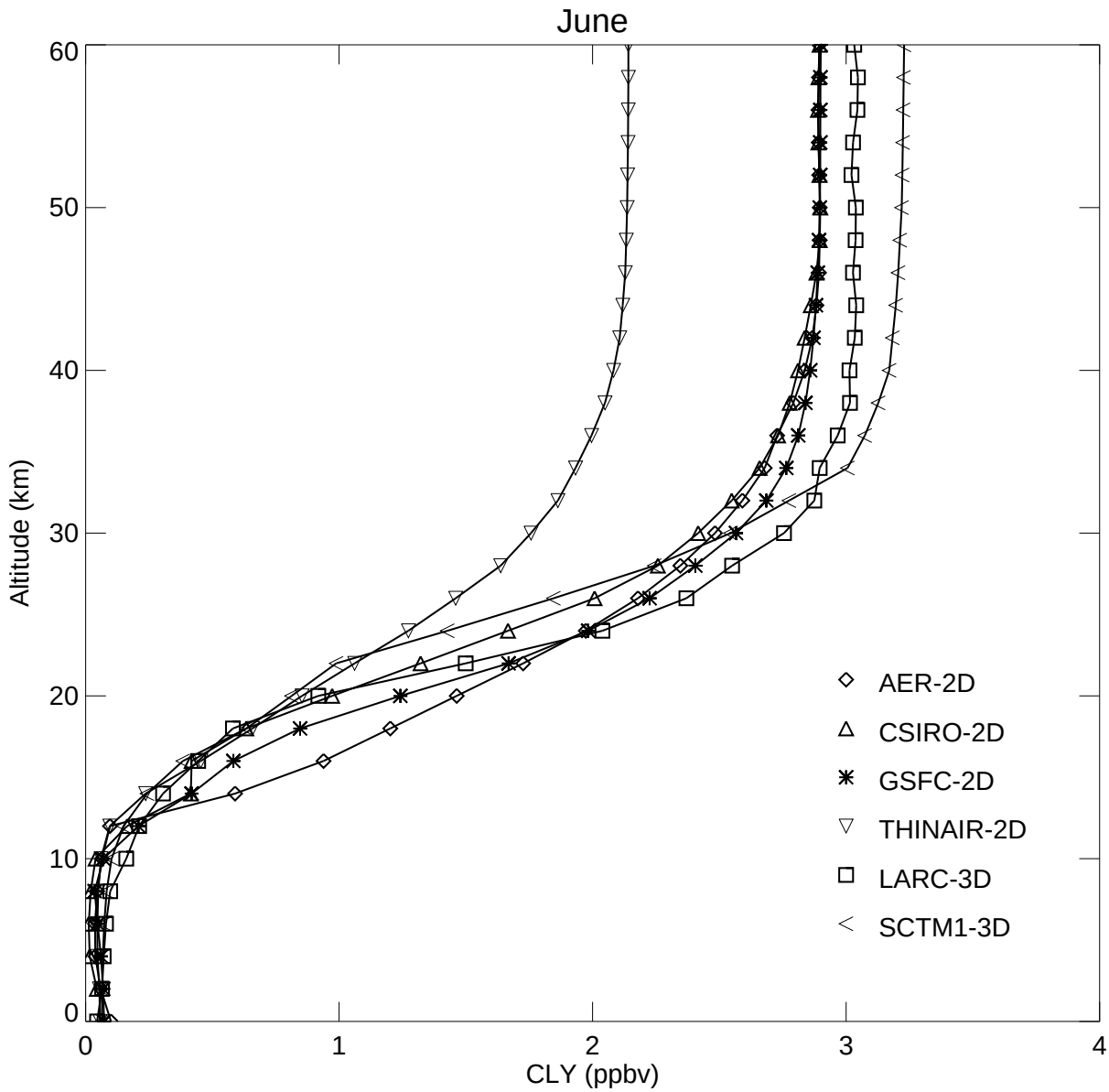

Figure 3.21: Calculated Cl_y concentration (ppbv) as a function of altitude for Scenario D at 45^oN in June.

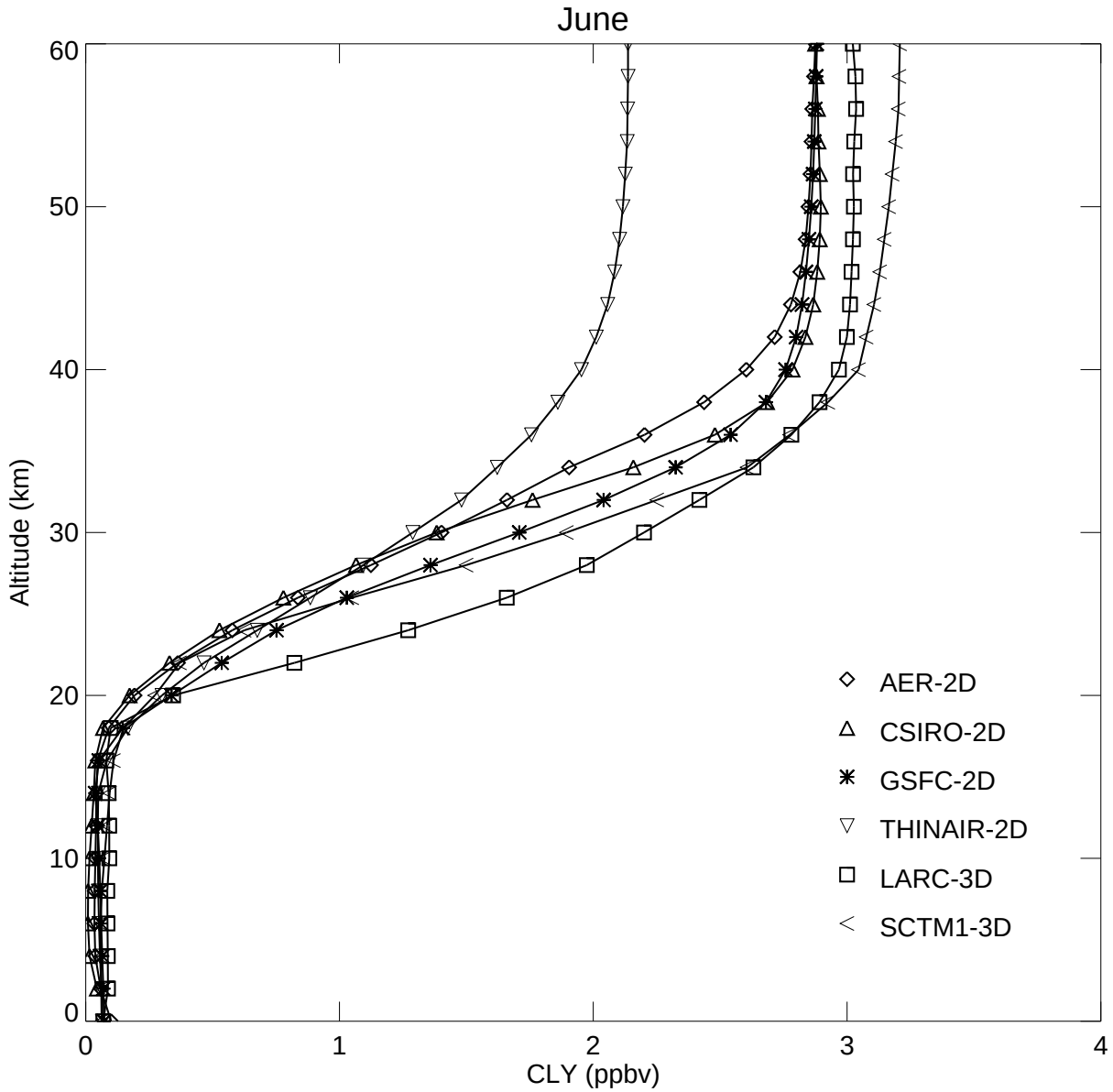

Figure 3.22: Calculated Cl_y concentration (ppbv) as a function of altitude for Scenario D at the equator in June.

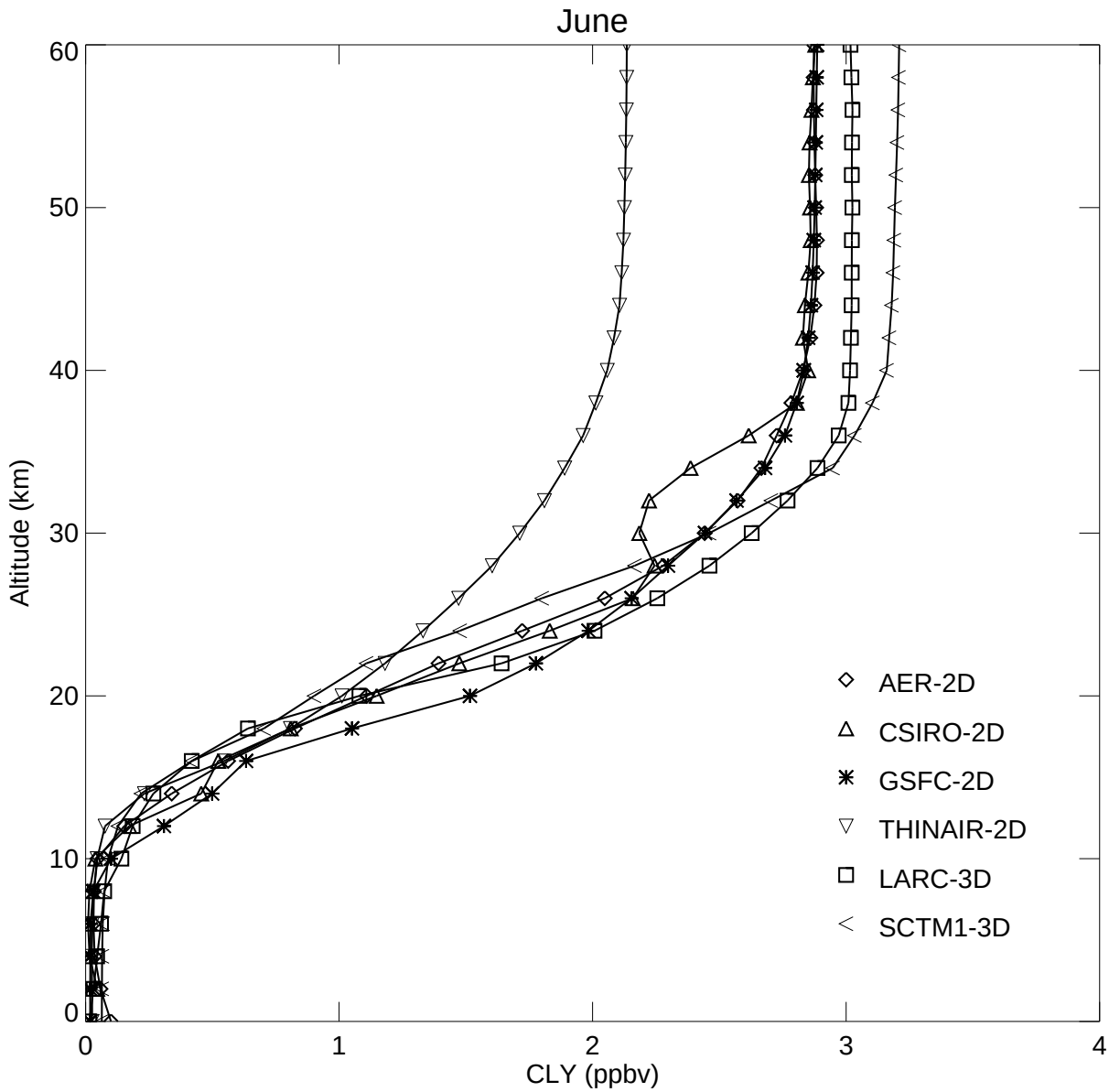

Figure 3.23: Calculated Cl_y concentration (ppbv) as a function of altitude for Scenario D at 45^oS in June.

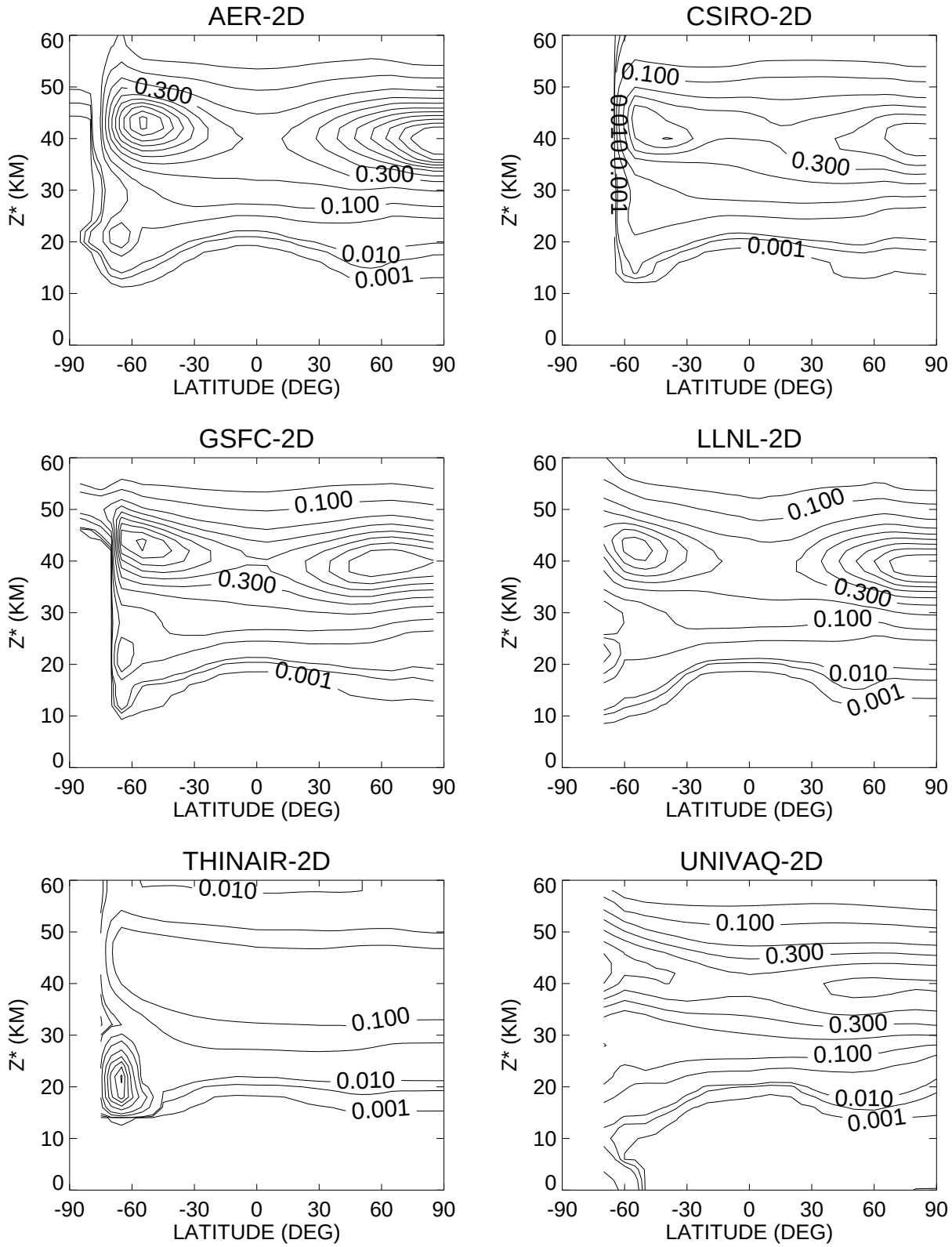

Figure 3.24: Calculated ClO mixing ratios (ppbv) as a function of latitude and altitude for Scenario D in June of 2015. Daytime averages are shown for 2-D models, 24-hour averages for 3-D models. Contours are .001, .005, .01, .05, and .1 to 1.0 by 0.1 ppbv.

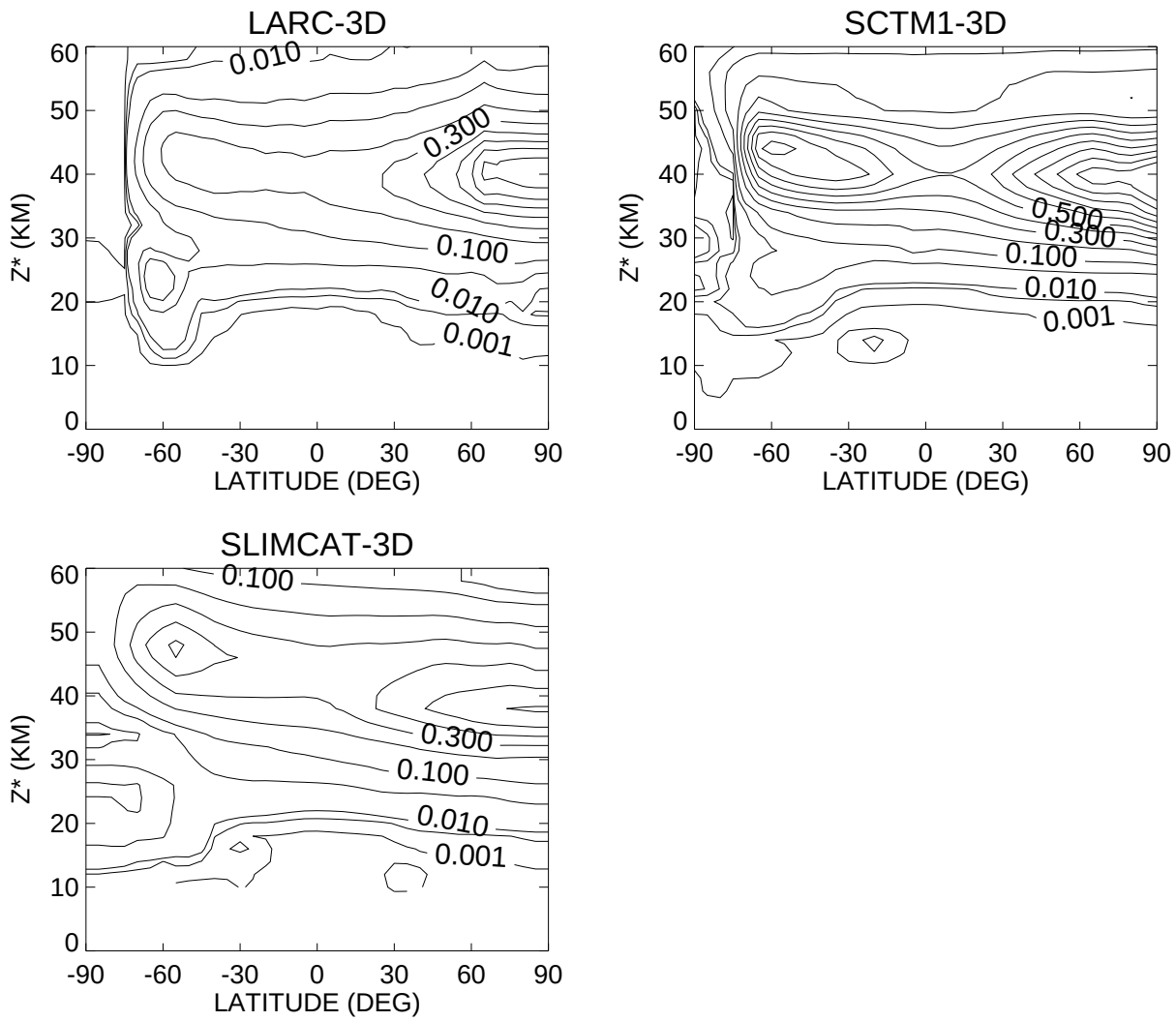

Figure 3.24: continued

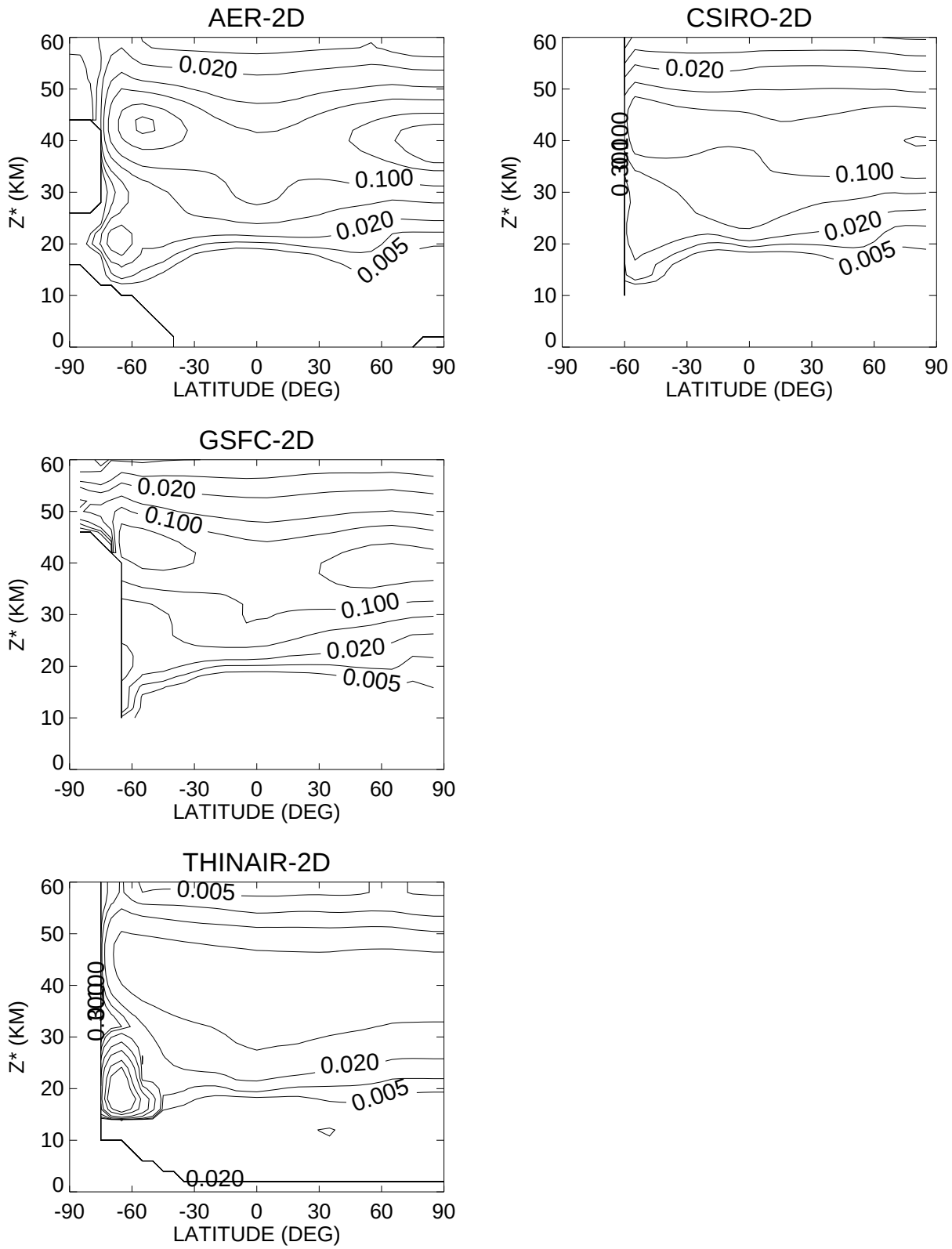

Figure 3.25: Calculated ClO/Cl_y ratio as a function of latitude and altitude for Scenario D in June of 2015. Contours are .005, .01, .02, .05, .1, .15, .2.

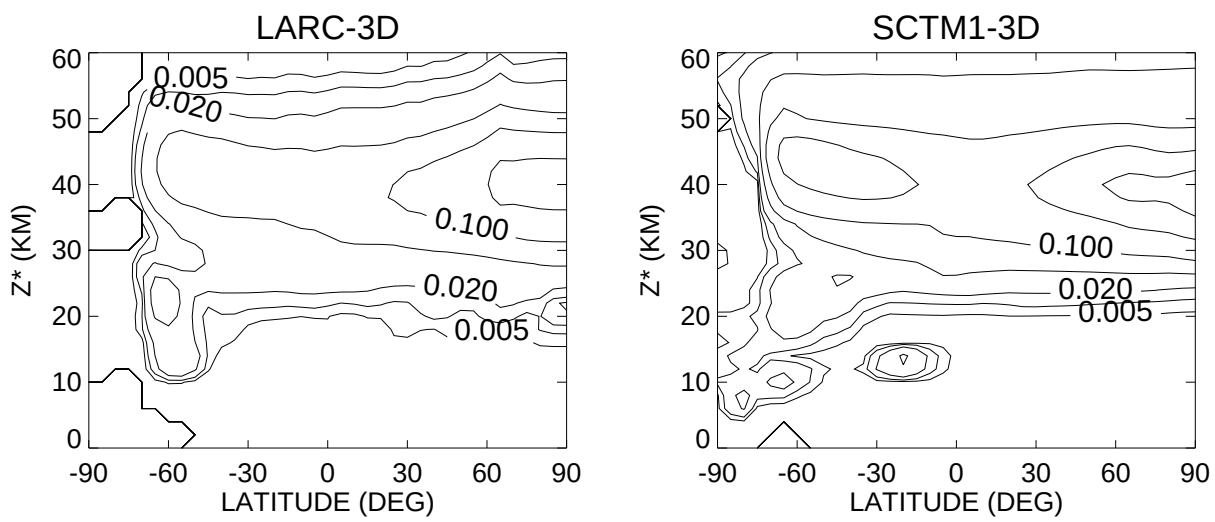

Figure 3.25: continued

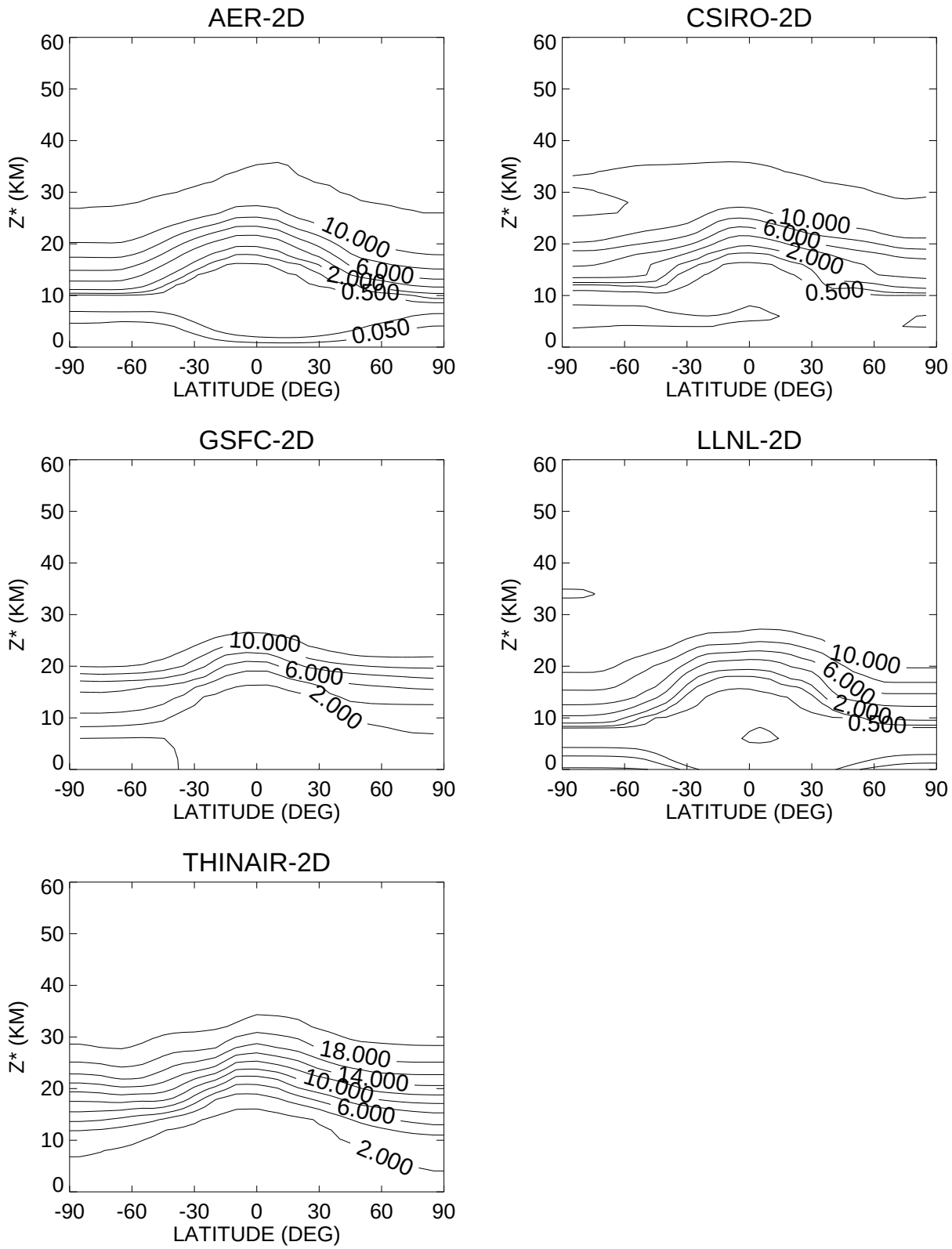

Figure 3.26: Calculated Br_y mixing ratios (pptv) as a function of latitude and altitude for Scenario D in June of 2015. Contours are .05, .01, .5, 1, and 2 to 20 by 2 pptv.

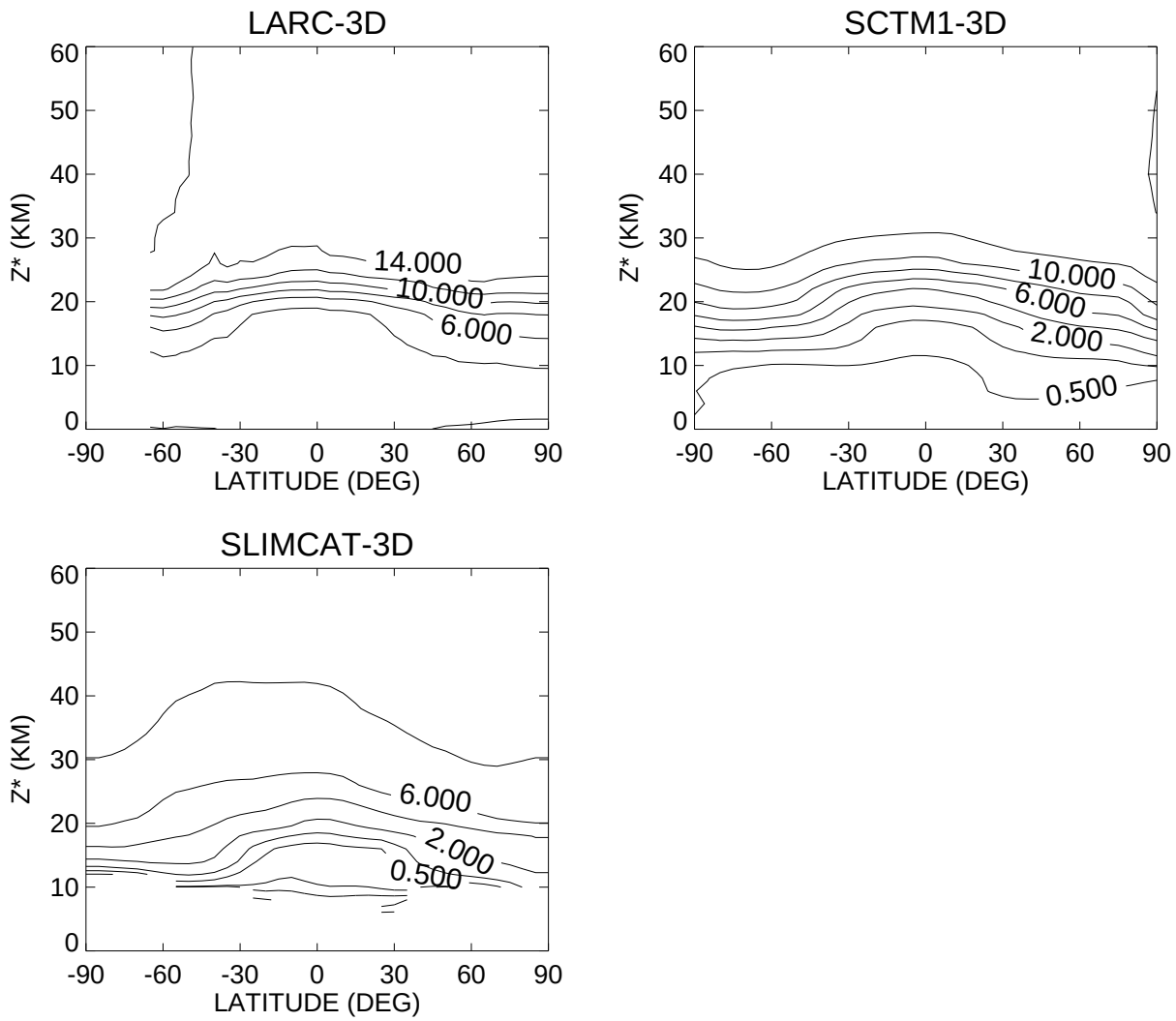

Figure 3.26: continued

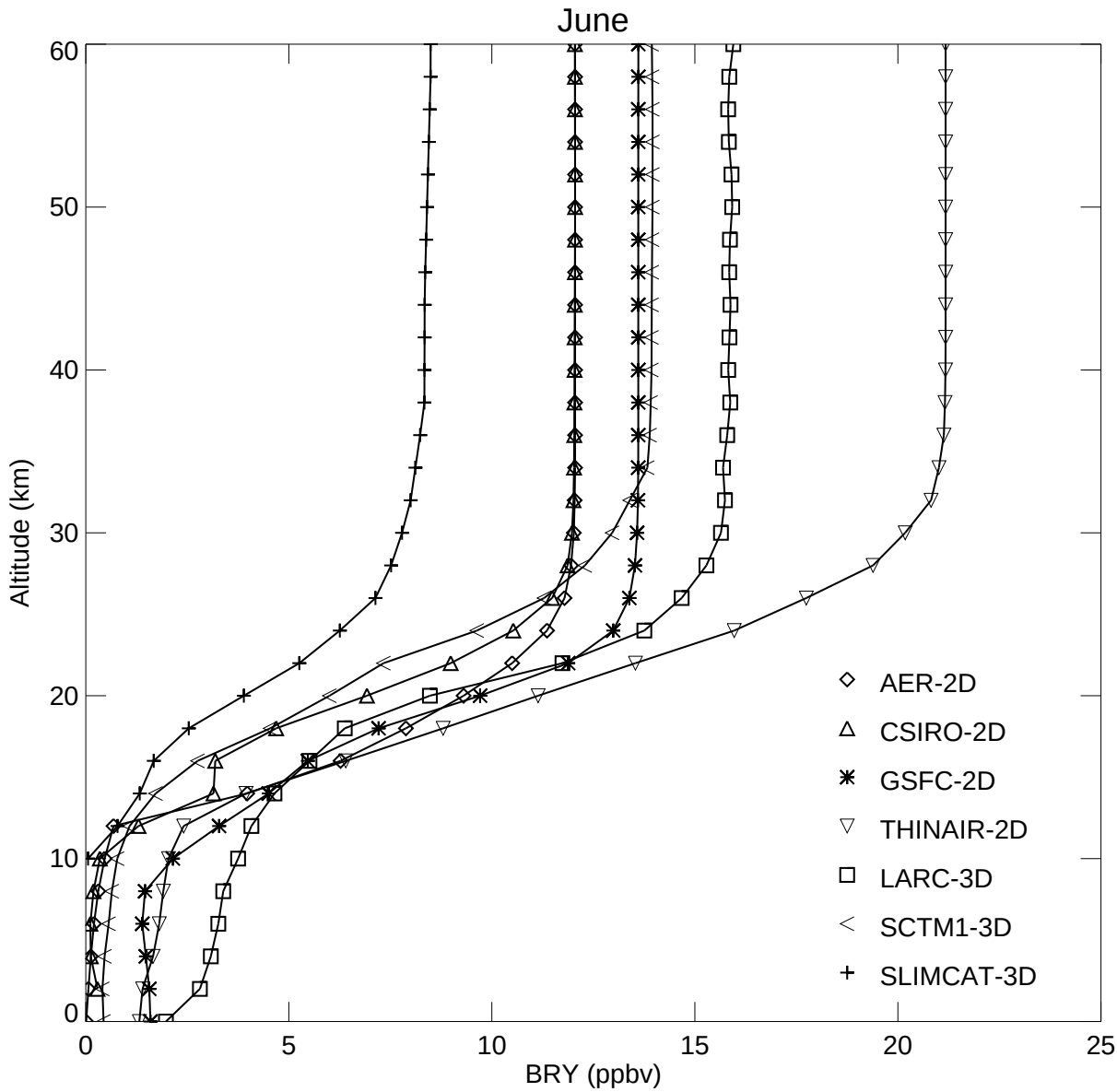

Figure 3.27: Calculated Br_y concentration (ppbv) as a function of altitude for Scenario D at 45^oN in June.

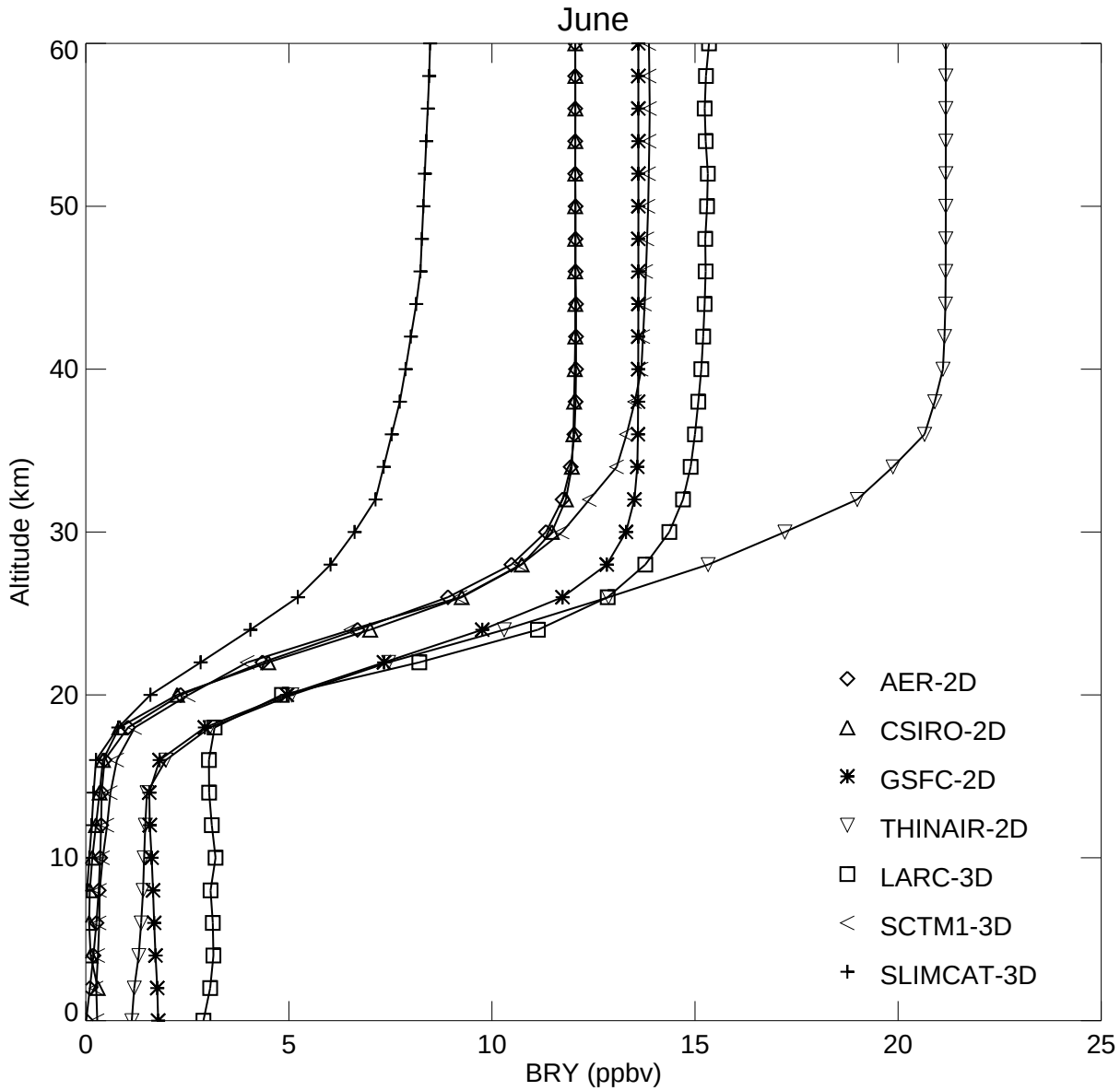

Figure 3.28: Calculated Br_y concentration (ppbv) as a function of altitude for Scenario D at the equator in June.

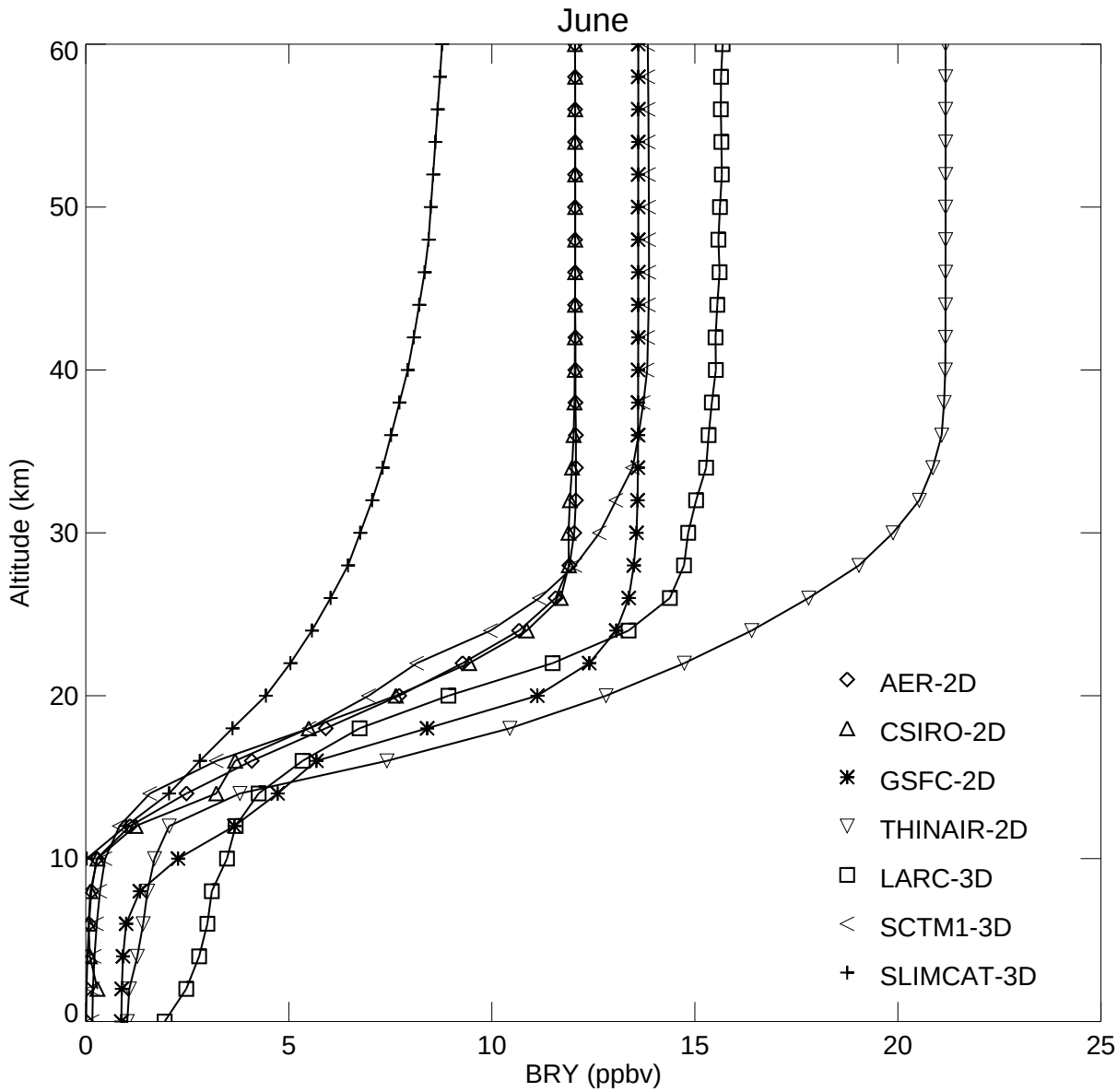

Figure 3.29: Calculated Br_y concentration (ppbv) as a function of altitude for Scenario D at 45°S in June.

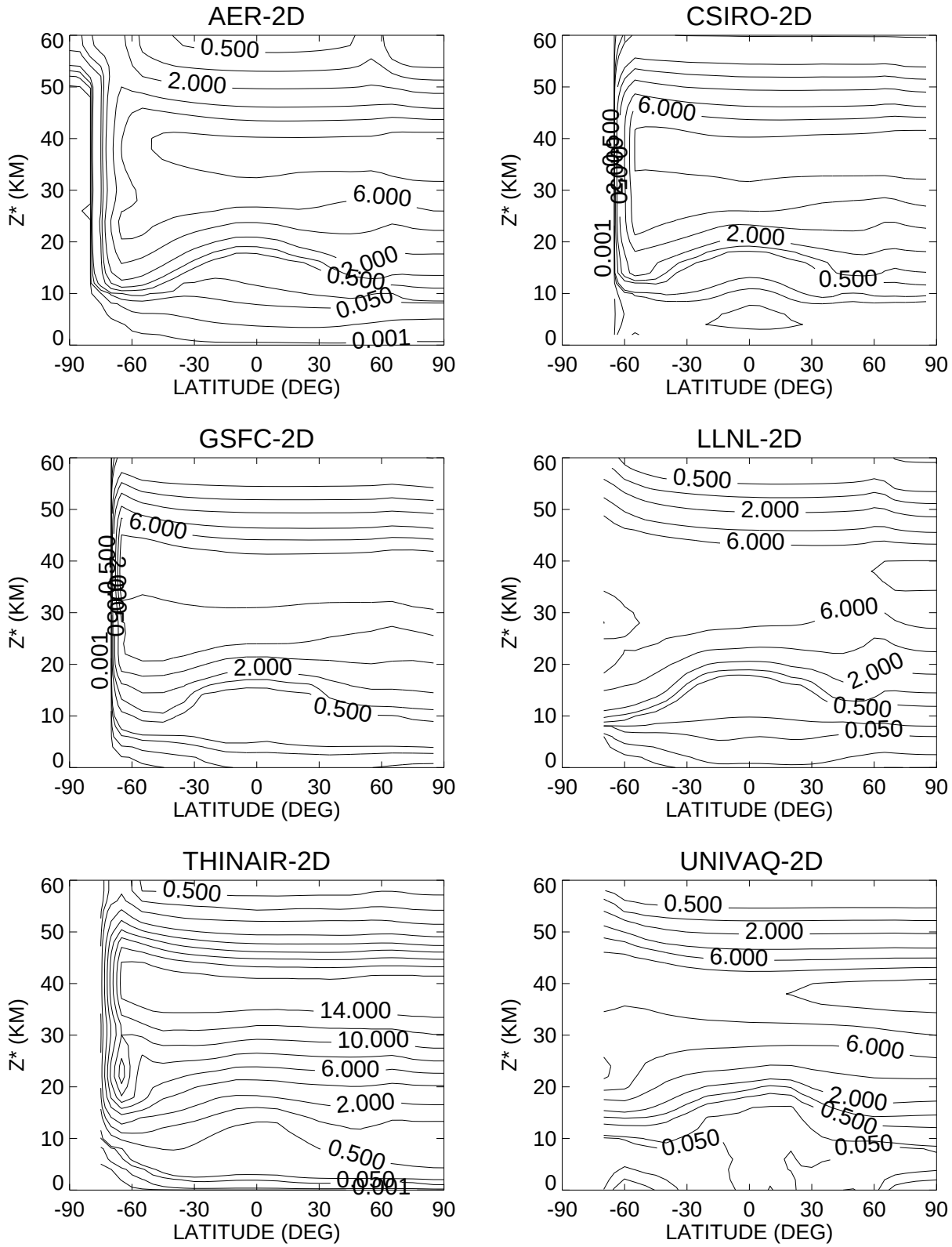

Figure 3.30: Calculated BrO mixing ratios (pptv) as a function of latitude and altitude for Scenario D in June of 2015. Daytime averages are shown for 2-D models, 24-hour averages for 3-D models. Contours are .001, .01, .05, .1, .5, 1, and 2 to 14 by 2 pptv.

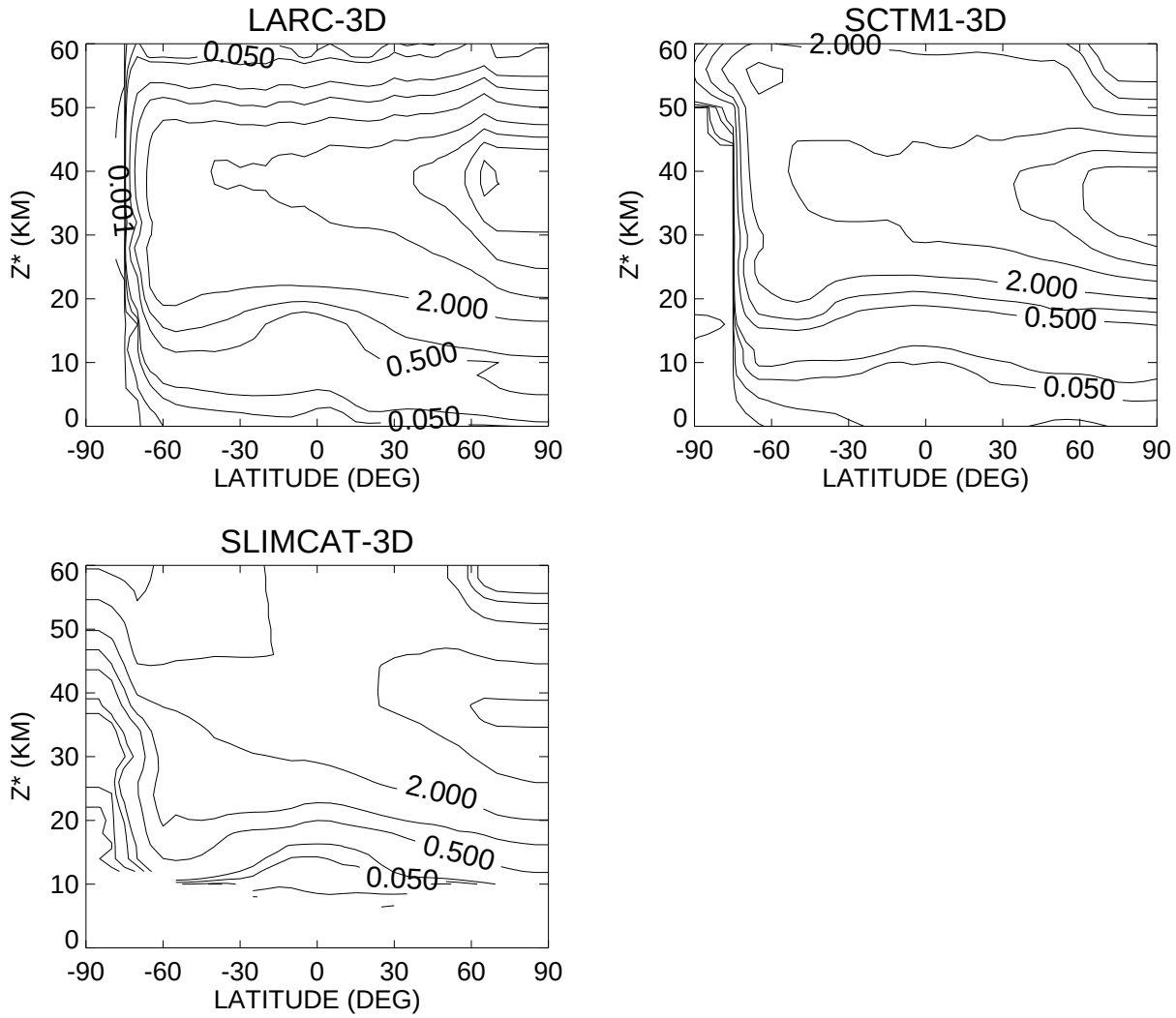

Figure 3.30: continued

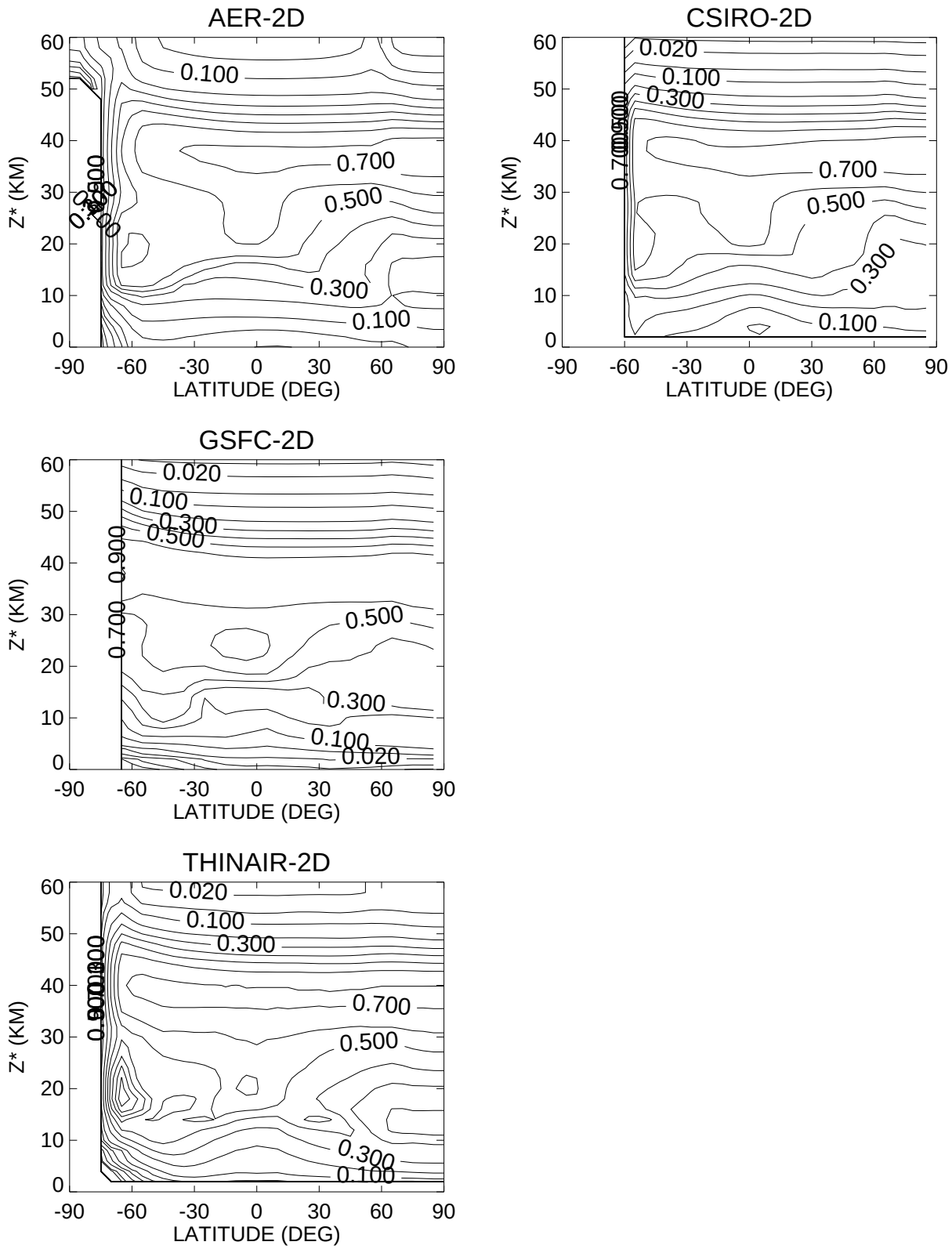

Figure 3.31: Calculated BrO/Br_y ratio as a function of latitude and altitude for Scenario D in June of 2015. Contours are .001, .002, .005, .01, .02, .05, and .1 to .7 by .1.

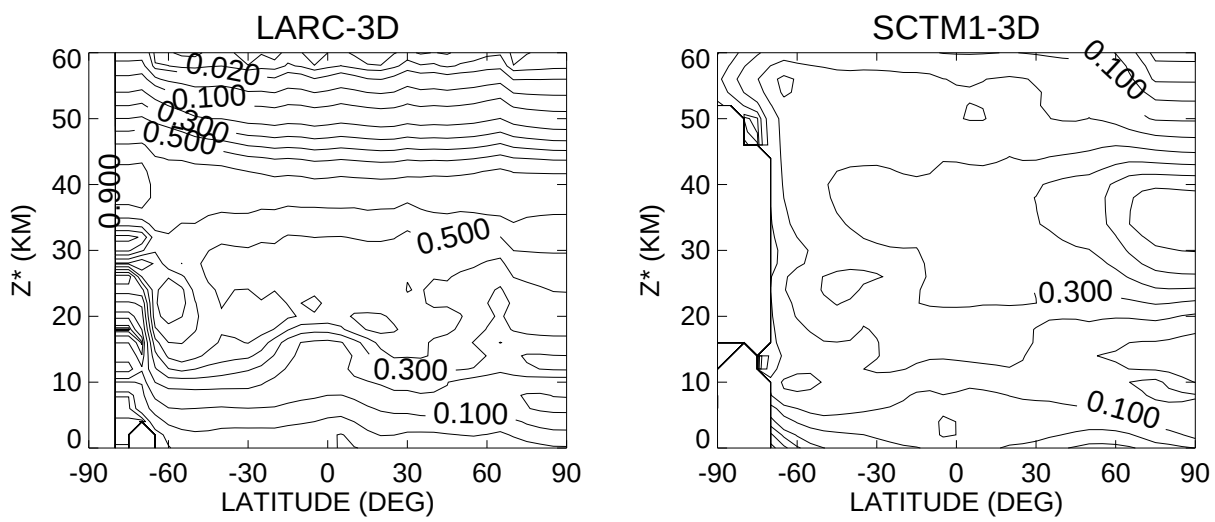

Figure 3.31: continued

3.2 Scenario D3 Results

Scenario D3 differs from Scenario D only in the aerosol SAD employed. Scenario D3 assumes an enhanced SAD due to volcanic eruptions of 4xSA0. The calculated values of total ozone column for this scenario are shown in Figure 3.32. The percent difference in ozone column between Scenario D3 and Scenario D is shown in Figure 3.33. Enhanced aerosol loading leads to reductions in ozone column of up to 3% in the AER model, 1% in the CSIRO model, 10% in the GSFC model, 15% in the LLNL model, and 4% in the UNIVAQ model. Ozone mixing ratios in June for Scenario D3 are shown in Figure 3.34. Changes in ozone mixing ratio relative to Scenario D are shown in Figure 3.35. All models show reductions in ozone below 20 km and increases from 20-30 km due to enhanced aerosol SAD.

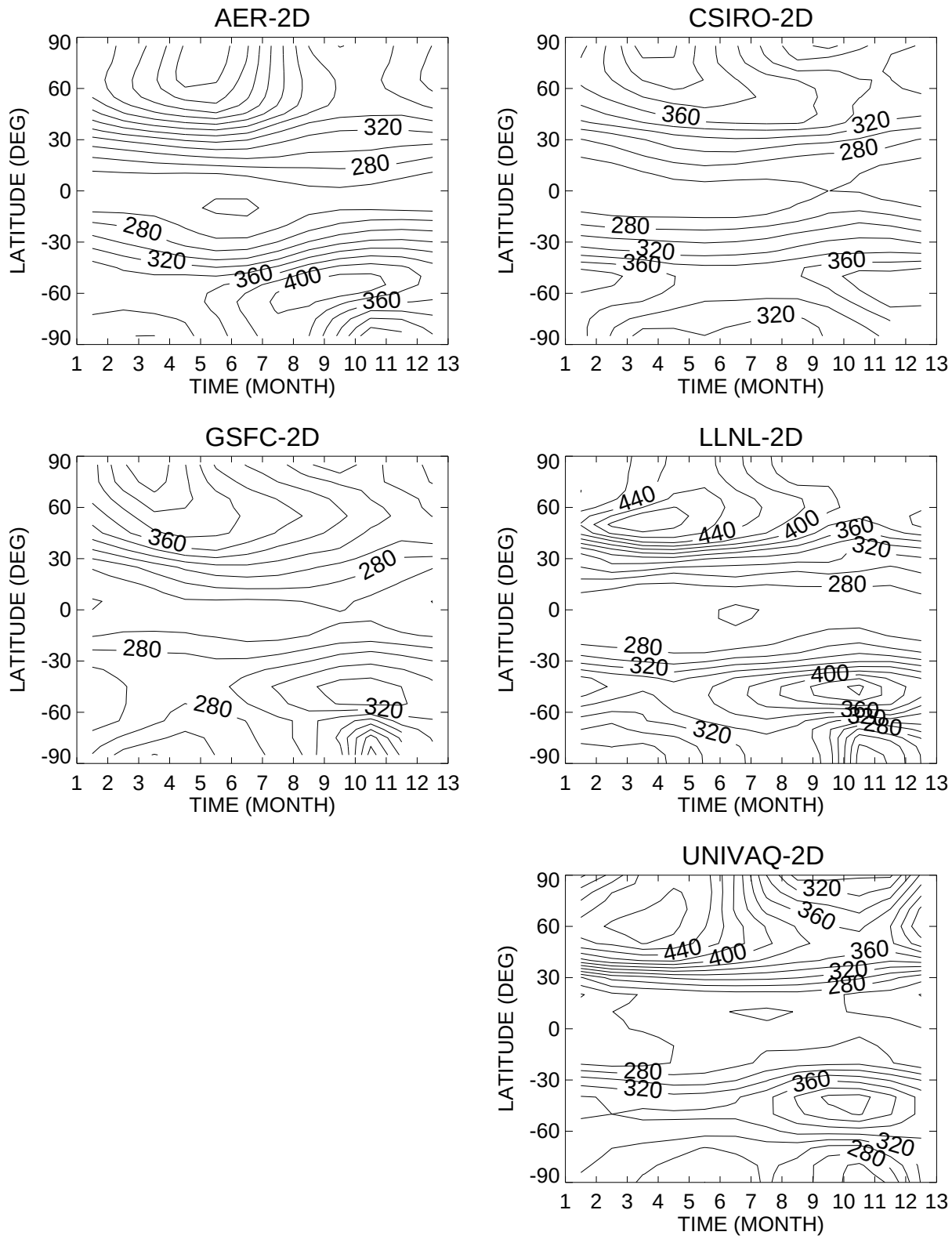

Figure 3.32: Total column ozone (Dobson Units) as a function of latitude and season as calculated by the models for Scenario D3, the 2015 background atmosphere with SAD=4xSA0 and with subsonic aircraft included. Contour interval is 20 DU.

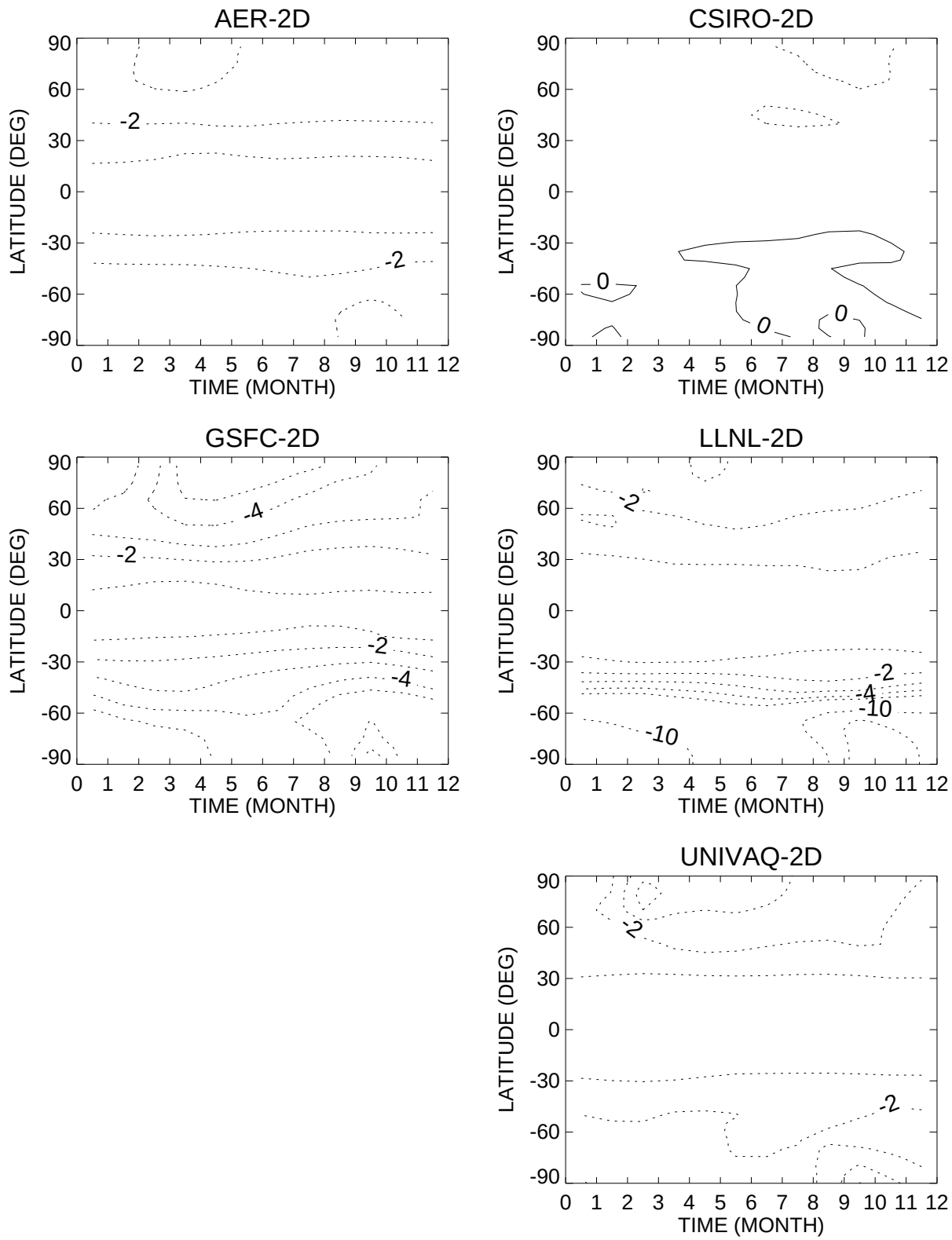

Figure 3.33: Percent change in total column ozone between Scenarios D3 and D. The difference in the scenarios is the background sulfate aerosol surface area density. Contours are -15, -10, -5, -4, -3, -2, -1, 0.

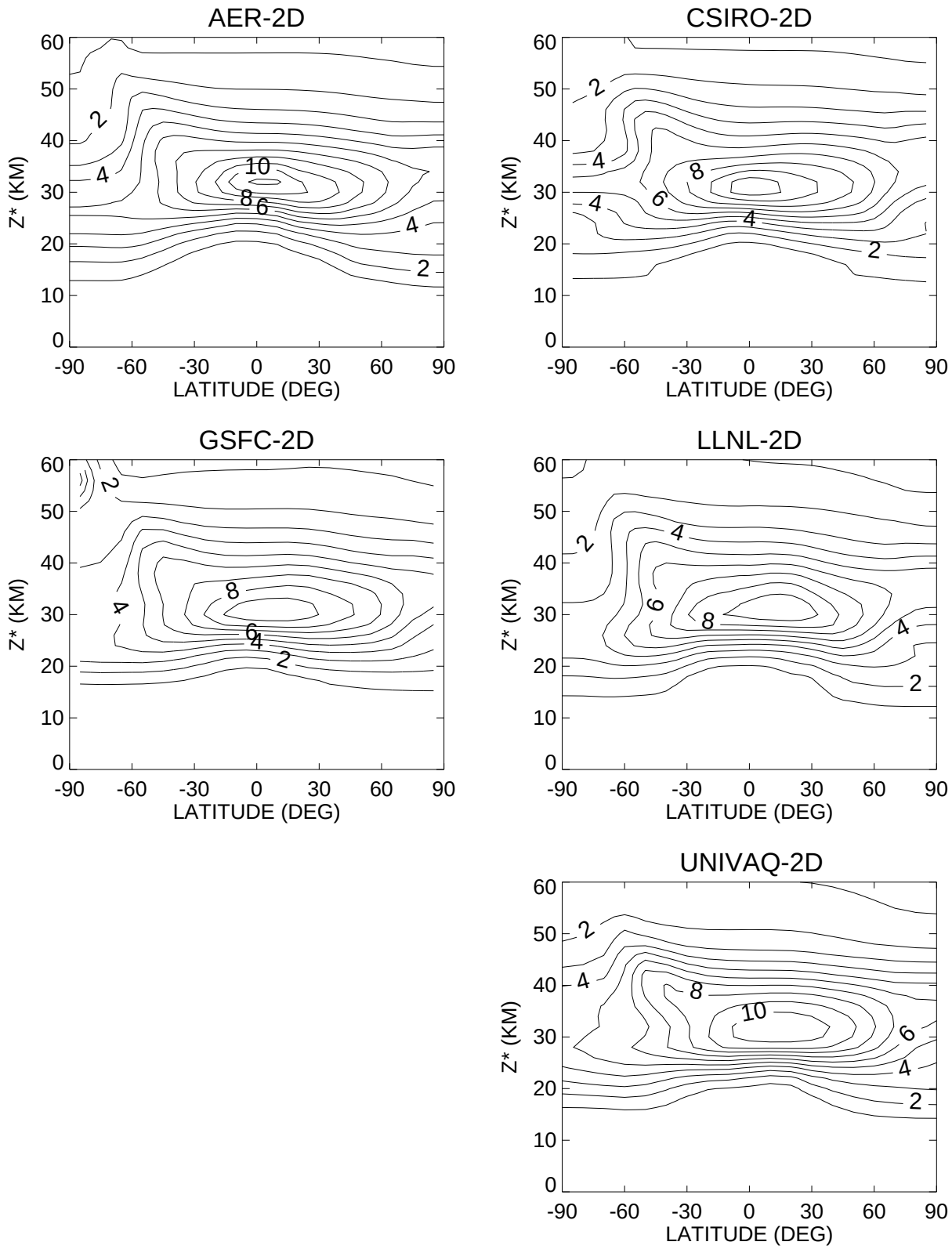

Figure 3.34: Calculated ozone mixing ratios (ppmv) as a function of latitude and altitude for Scenario D3 in June of 2015. The contour interval is 1 ppmv.

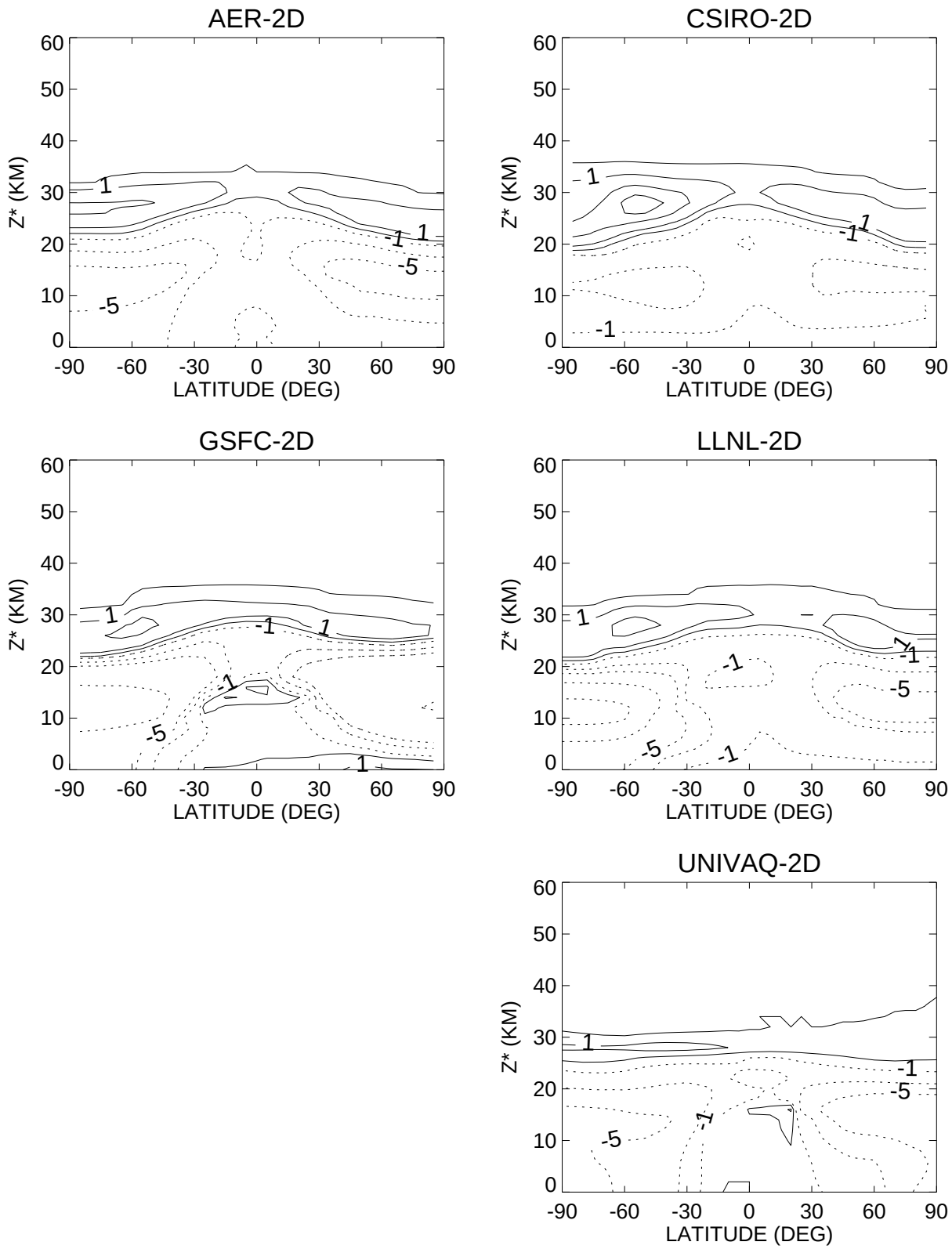

Figure 3.35: Percent change in ozone concentration between Scenarios D3 and D in June of 2015. The difference in the scenarios is the background sulfate aerosol surface area density. Contours are -15, -10, -5, -3, -1, 0, 1, 2, 3%.

3.3 Scenario D4 Results

Scenario D4 differs from Scenario D in that the PSC representation was removed from the models. Note that the CSIRO model did not include a PSC representation in any of its calculations. Therefore Scenarios D and D4 are identical for CSIRO and difference plots between D and D4 for this model are not shown. Figure 3.36 shows total ozone columns calculated by the models for Scenario D4. As seen in Figures 3.37, ozone column is increased by removing the PSC representation. In the AER model, the effect is 2% in the northern springtime polar region and 5% in the southern springtime polar region. The UNIVAQ model shows a 1% effect in the NH and a 3% effect in the SH. The GSFC model shows no effect in the northern hemisphere, but a very large effect (>30%) in the southern hemisphere. Ozone mixing ratios for June from Scenario D4 are shown in Figure 3.38. Differences in ozone mixing ratio between Scenarios D4 and D for March, June, and October are shown in Figures 3.39, 3.40, and 3.41, respectively. June differences are small for all but the GSFC model, which shows southern hemisphere differences in the lower stratosphere of up to 45%.

Differences in H_2O due to omission of the model PSC parameterization are shown in Figure 3.42 for June conditions. Southern hemisphere increases in H_2O are seen for all three models, extending to 60^{o}S in the AER and GSFC models and to 30^{o}S in the UNIVAQ model. The GSFC model also shows a small impact of PSCs from 30 to 40 km in the northern high latitudes. Differences in NO_y are shown in Figure 3.43. NO_y concentrations increase without model PSCs, ie. denitrification leads to reductions in NO_y when PSCs are included in the models. Maximum denitrification is 60% in the AER model, 80% in the GSFC model, and 97% in the UNIVAQ model southern polar region (60-90^{o}N). The UNIVAQ model shows modest denitrification in the lower stratosphere for both hemispheres in June, and the GSFC model shows some denitrification at all southern latitudes. ClO differences are shown in Figure 3.44 and show lower levels of ClO without PSCs in the southern hemisphere. The UNIVAQ model in addition shows reduced ClO in the northern hemisphere. The GSFC model also shows increased ClO in the southern midlatitudes below 15 km in June.

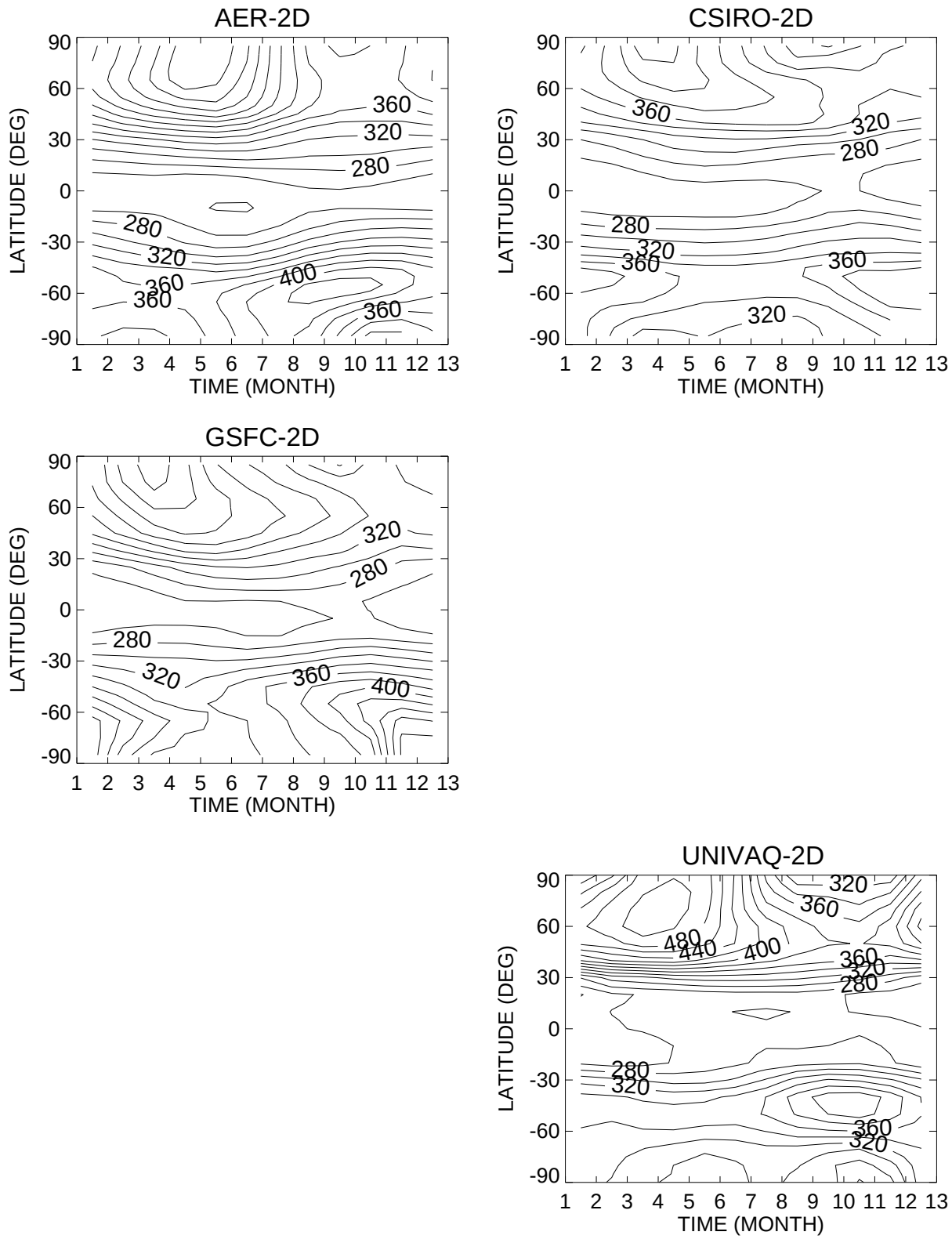

Figure 3.36: Total column ozone (Dobson Units) as a function of latitude and season as calculated by the models for Scenario D4, the 2015 background atmosphere with the model PSC representation removed. Contour interval is 20 DU.

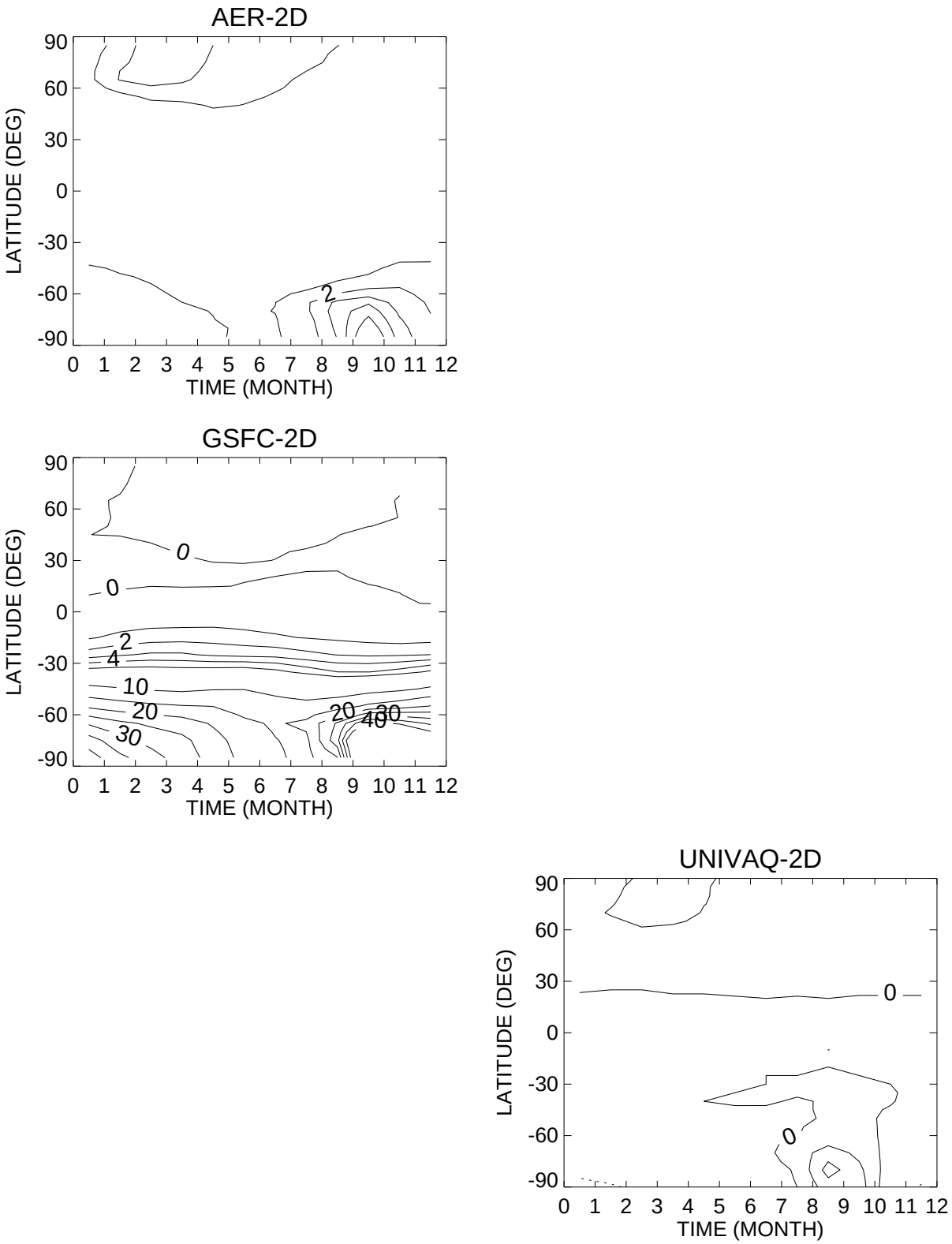

Figure 3.37: Percent change in total ozone column between Scenarios D4 and D. The difference in the scenarios is that the PSC representation is removed in Scenario D4. Contours are -1 to 5 by 1 and 10 to 30 by 5.

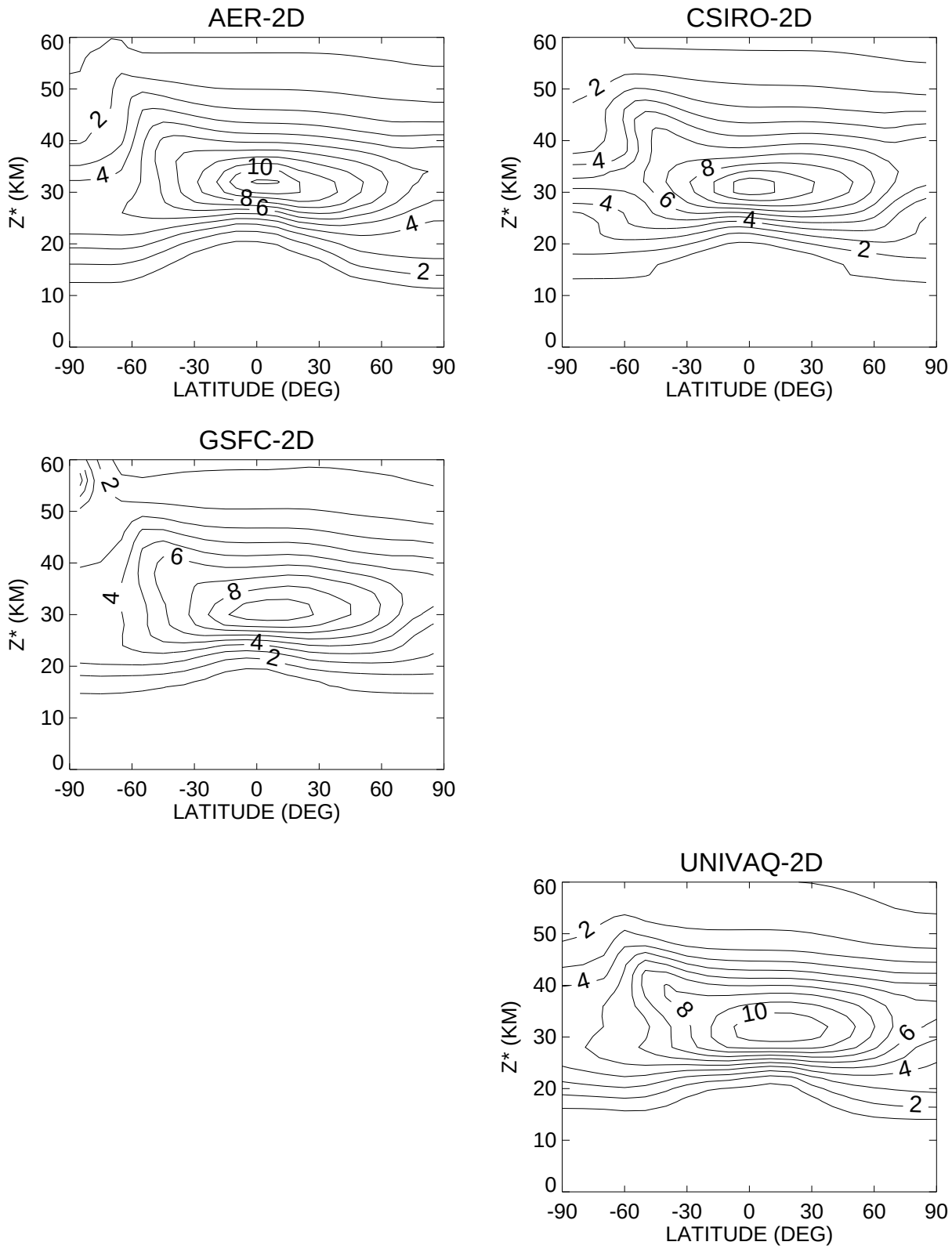

Figure 3.38: Calculated ozone mixing ratios (ppmv) as a function of latitude and altitude for Scenario D4 in June of 2015. The contour interval is 1 ppmv.

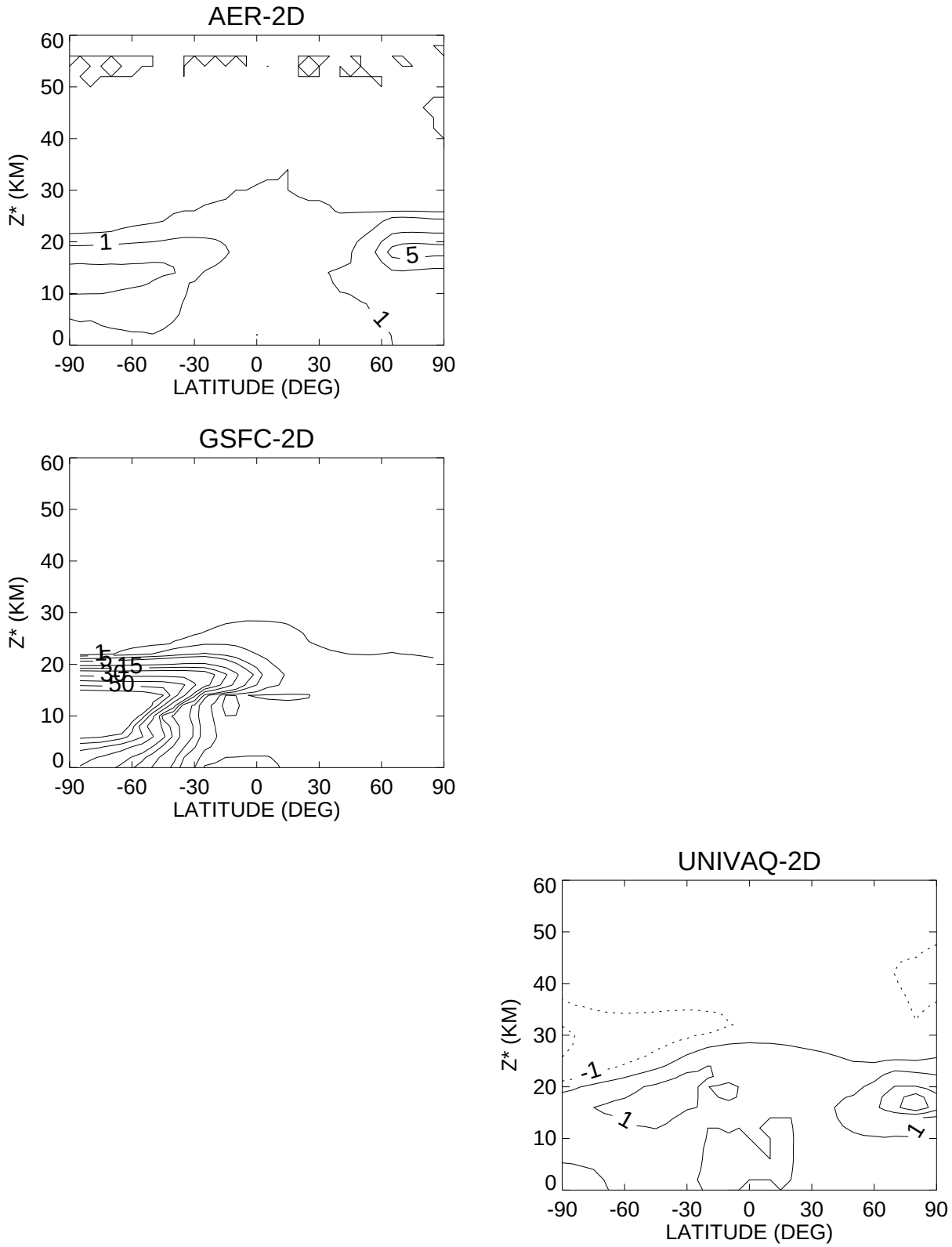

Figure 3.39: Percent change in ozone concentration between Scenarios D4 and D in March of 2015. The difference in the scenarios is that the PSC representation is removed in Scenario D4. Contours are -1, 0, 1, 3, 5, 10, 15, and 20 to 60 by 10.

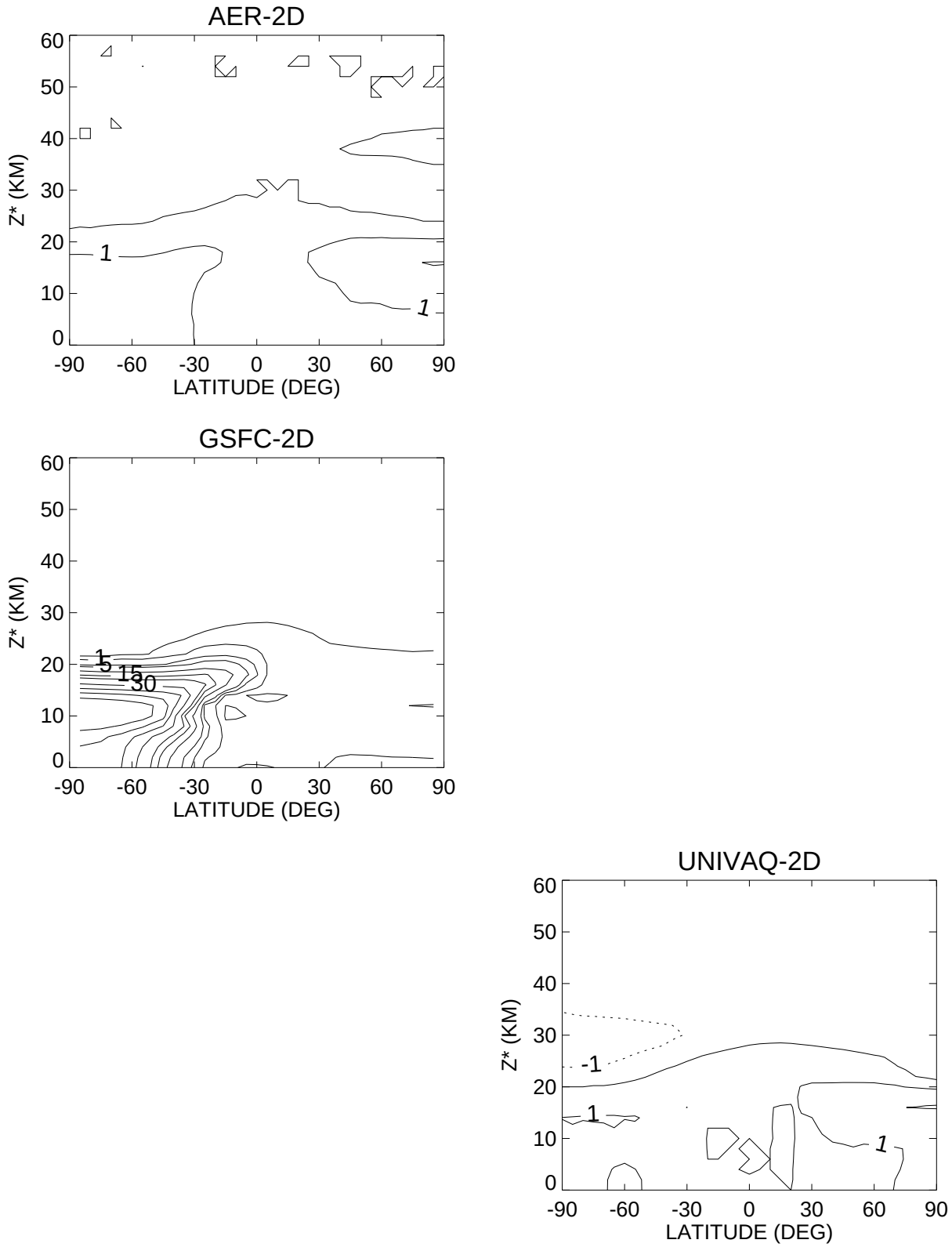

Figure 3.40: Percent change in ozone concentration between Scenarios D4 and D in June of 2015. The difference in the scenarios is that the PSC representation is removed in Scenario D4. Contours are -1, 0, 1, 3, 5, 10, 15, and 20 to 60 by 10.

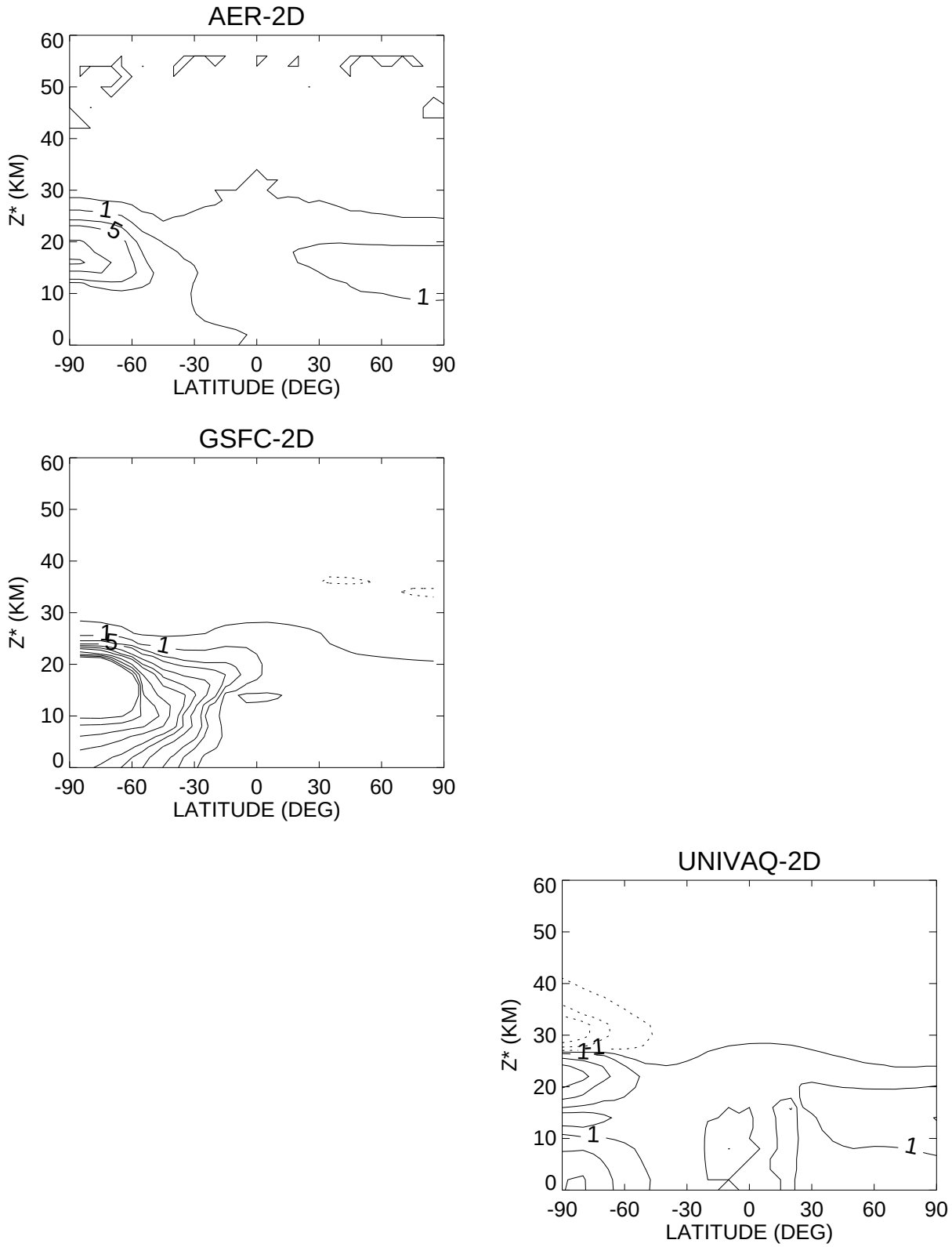

Figure 3.41: Percent change in ozone concentration between Scenarios D4 and D in October of 2015. The difference in the scenarios is that the PSC representation is removed in Scenario D4. Contours are -1, 0, 1, 3, 5, 10, 15, and 20 to 60 by 10.

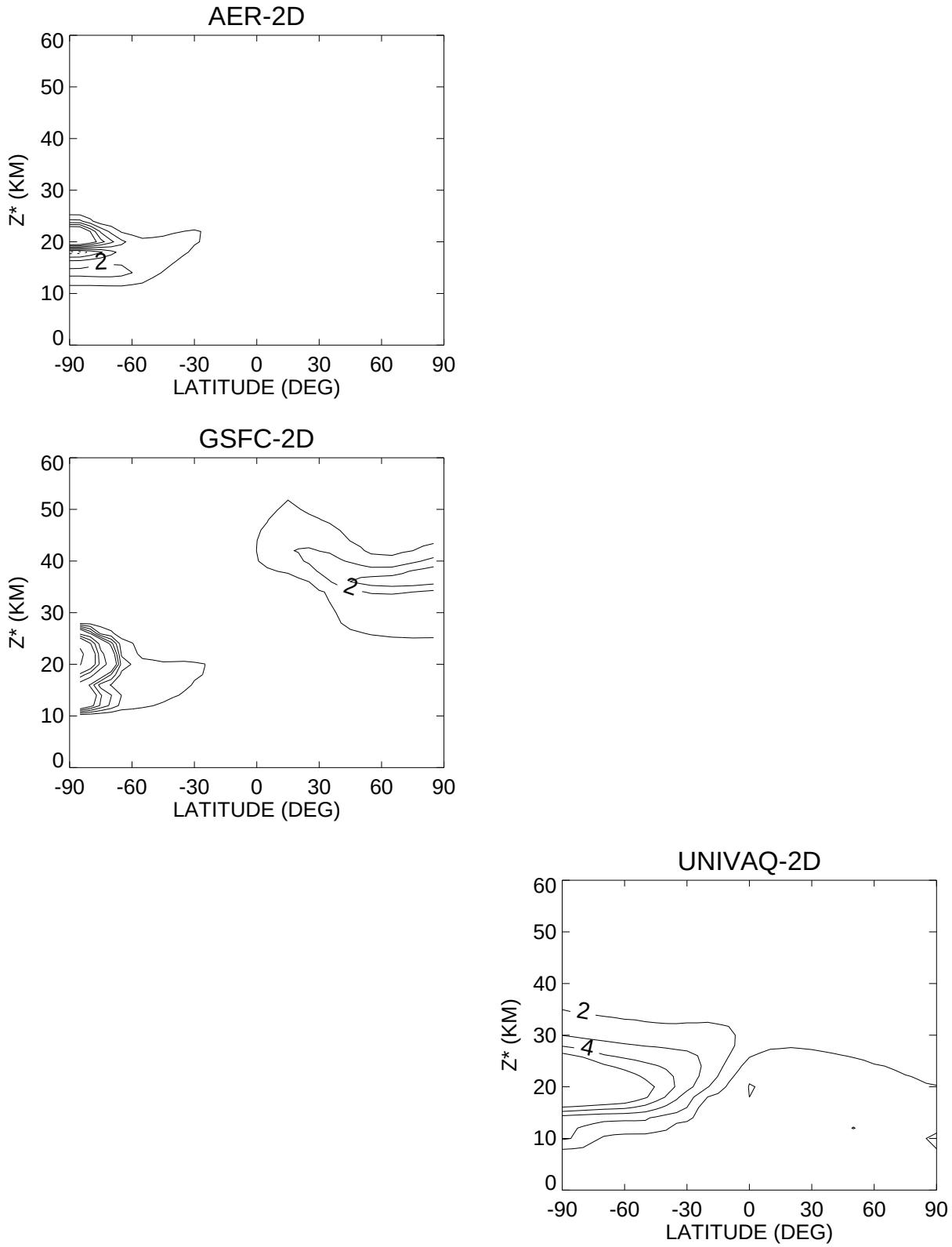

Figure 3.42: Percent change in H_2O concentration between Scenarios D4 and D in June of 2015. The difference in the scenarios is that the PSC representation is removed in Scenario D4. Contours are 1 to 5 by 1 and 10, 15, 20, 30, 40.

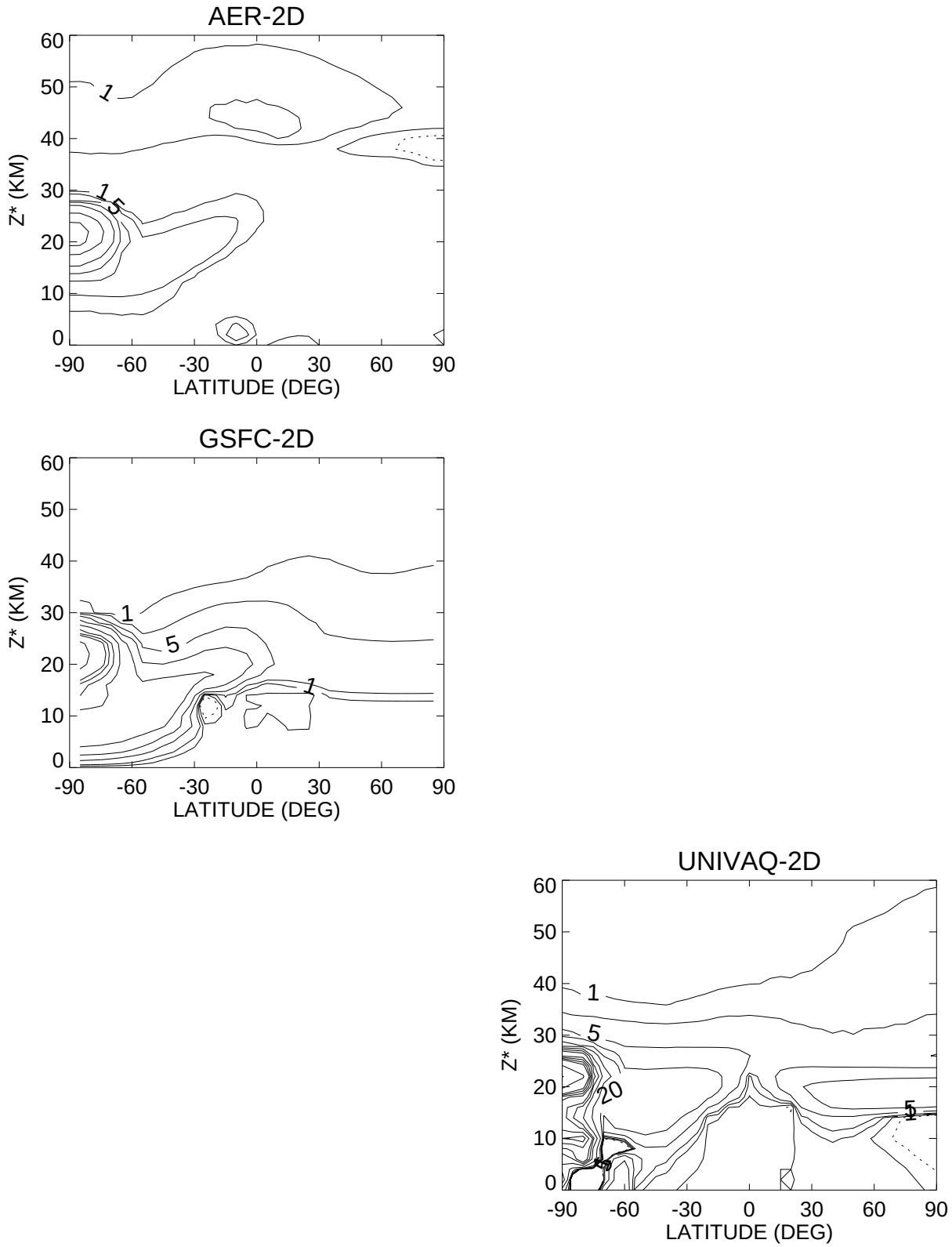

Figure 3.43: Percent change in NO_y concentration between Scenarios D4 and D in June of 2015. The difference in the scenarios is that the PSC representation is removed in Scenario D4. Contours are -1, 0, 1 2, 5, 10, 20, 50, 100, 150, 200, 400, 600, 800, 1000, 2000, 4000.

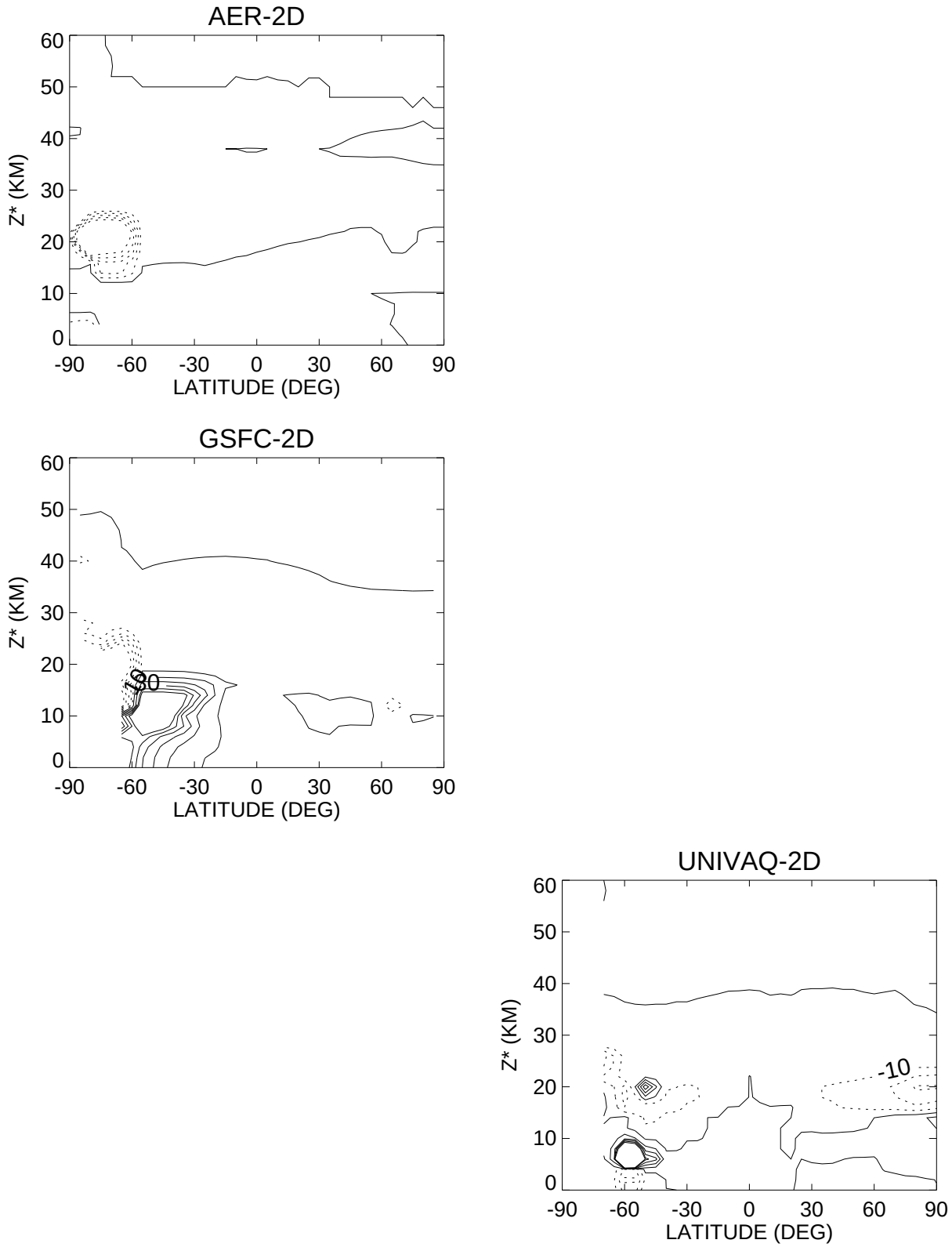

Figure 3.44: Percent change in ClO concentration between Scenarios D4 and D in June of 2015. The difference in the scenarios is that the PSC representation is removed in Scenario D4. Contours are -50 to 50 by 10.

3.4 Scenario D5 Results

Scenario D5 differs from Scenario D in the total odd chlorine loading. Boundary conditions of organic chlorine species were modified to produce approximately 1 ppbv of inorganic chlorine in the upper stratosphere. This scenario, along with D6, is used to test the sensitivity of the HSCT impact on ozone to background Cl_y concentrations. Cl_y mixing ratios as a function of latitude and altitude for June are shown in Figure 3.45. The AER model has just under 1 ppbv of Cl_y in the upper stratosphere and the GSFC model just over 1 ppbv.

Total ozone column fields for Scenario D5 are shown in Figure 3.46. Differences in total ozone between Scenarios D5 and D are shown in Figure 3.47. Ozone columns are greater with reduced Cl_y concentrations. All models show a 2% increase in tropical ozone due to reduced Cl_y. The AER model shows a 5% increase at northern high latitudes and a 5-15% increase at high southern latitudes. The GSFC model shows a 5% northern high latitude increases and greater than 30% increases at southern high latitude. The UNIVAQ model shows a 5% increases at high latitudes in both hemispheres. The GSFC changes due to reduced Cl_y are consistent with ozone change caused by removal of the PSC parameterization. Figure 3.48 shows ozone mixing ratios as a function of latitude and altitude for June from Scenario D5. Figure 3.49 shows changes in ozone mixing ratio relative to Scenario D. Large changes (15-30%) are found in the stratosphere above 30 km. The GSFC model also has large changes in the southern hemisphere lower stratosphere and troposphere due to the effects of heterogeneous chemistry.

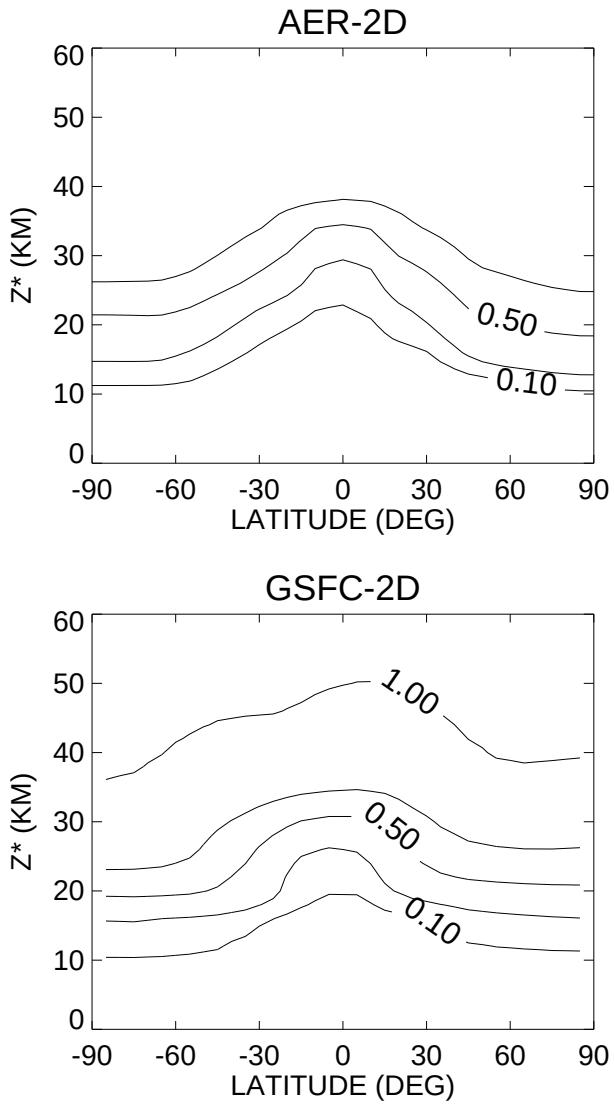

Figure 3.45: Calculated Cl_y mixing ratio (ppbv) in June for Scenario D5, the 2015 background atmosphere including subsonic aircraft and with organic chlorine boundary conditions adjusted to produce approximately 1 ppbv of inorganic chlorine. Contours are 0.1, 0.25, 0.5, 0.75 and 1.0 ppbv.

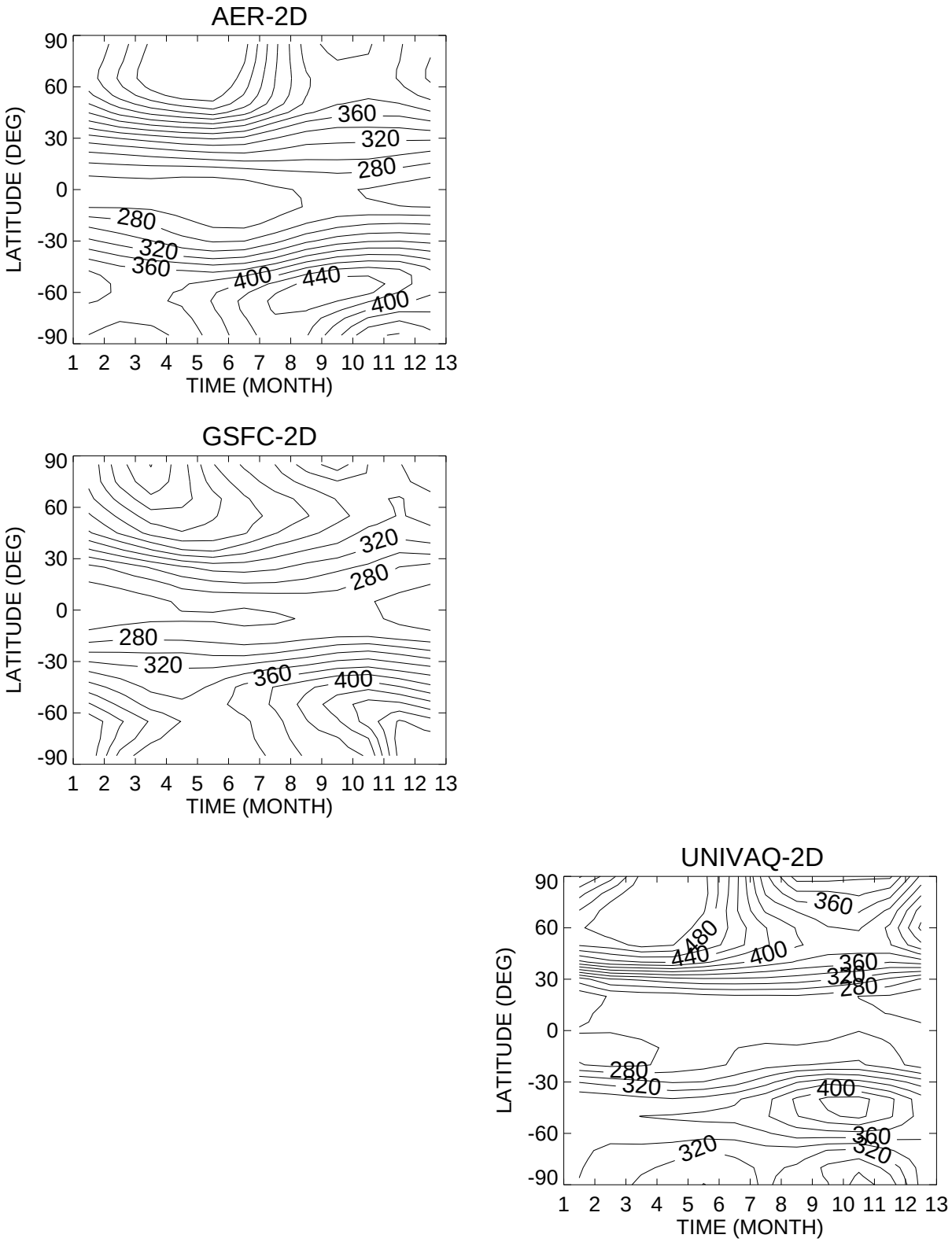

Figure 3.46: Total column ozone (Dobson Units) as a function of latitude and season as calculated by the models for Scenario D5, the 2015 background atmosphere with organic chlorine boundary conditions adjusted to produce approximately 1 ppbv of inorganic chlorine. Contour interval is 20 DU.

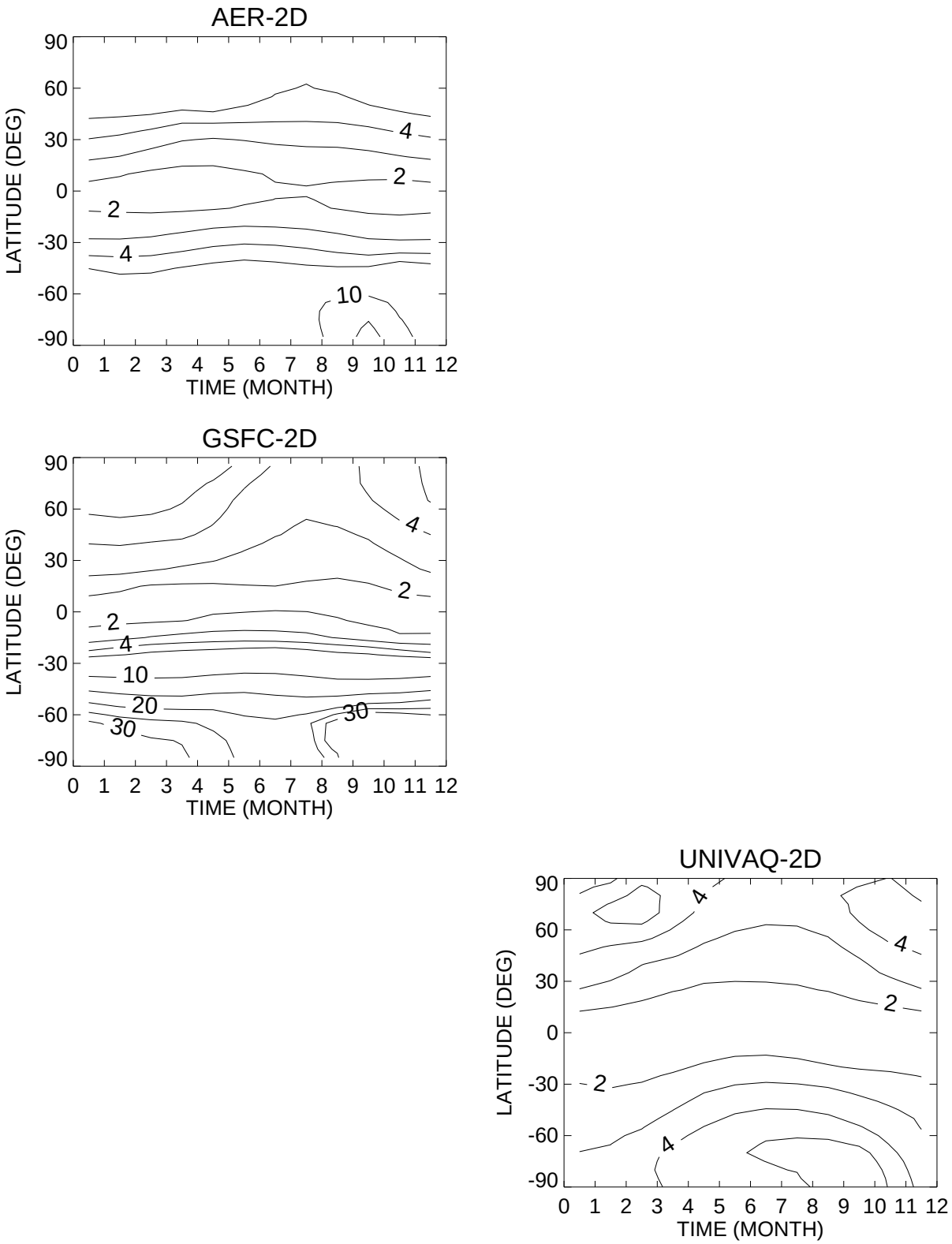

Figure 3.47: Percent change in total ozone column between Scenarios D5 and D. The difference in the scenarios is that D5 contains 1 ppbv of Cl_y and D contain 3 ppbv of Cl_y. Contours are 2, 3, 4, 5 and 10 to 30 by 5.

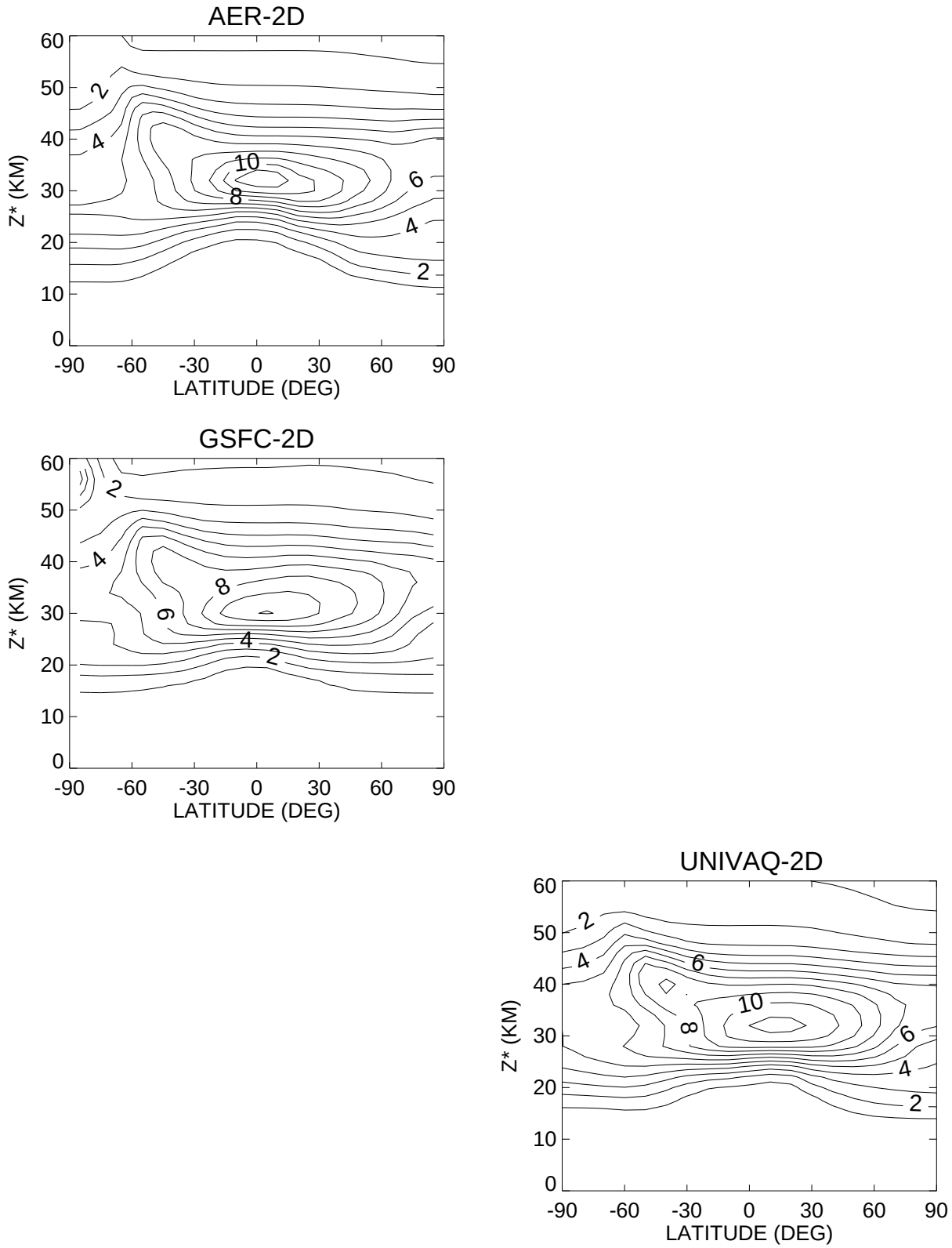

Figure 3.48: Calculated ozone mixing ratios (ppmv) as a function of latitude and altitude for Scenario D5 in June of 2015. The inorganic chlorine loading is 1 ppbv. The contour interval is 1 ppmv.

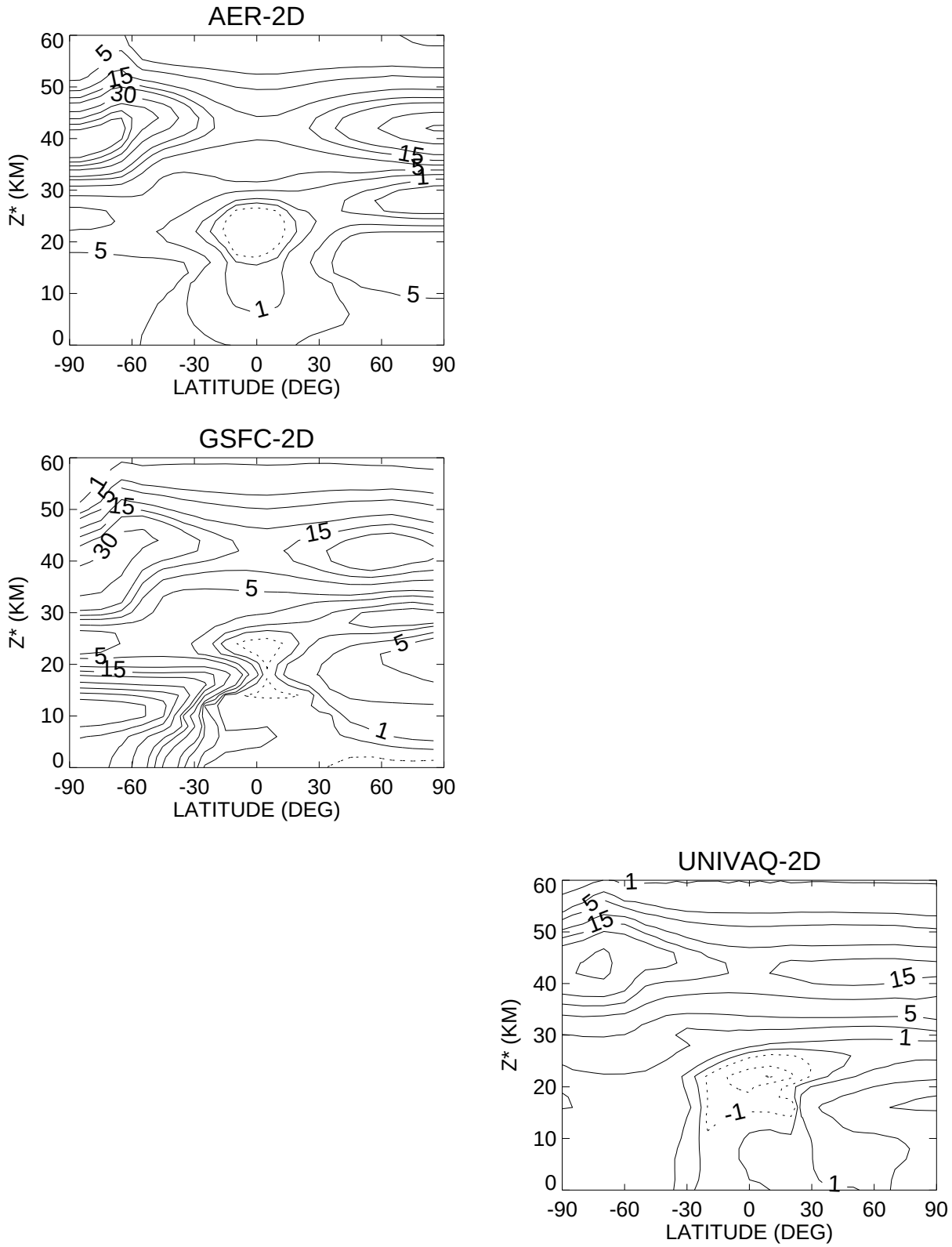

Figure 3.49: Percent change in ozone concentration between Scenarios D5 and D in June of 2015. The difference in the scenarios is that D5 contains 1 ppbv of Cl_y and D contain 3 ppbv of Cl_y. Contours are -1, 0, 1, 3, 5, 10, 15, and 20 to 60 by 10.

3.5 Scenario D6 Results

Scenario D6 contains a total odd chlorine loading of 4 ppbv. This scenario is also used to test the sensitivity of the HSCT impact on ozone to background Cl_y concentrations. Boundary conditions of organic chlorine species were modified to produce approximately 4 ppbv of inorganic chlorine in the upper stratosphere. Cl_y mixing ratios as a function of latitude and altitude for June are shown in Figure 3.50. The GSFC model has more Cl_y in the lower stratosphere than the AER model.

Total ozone column fields for Scenario D6 are shown in Figure 3.51. Differences in total ozone between Scenarios D6 and D are shown in Figure 3.52. Reduced ozone columns are calculated with larger Cl_y concentrations in the AER and GSFC models, but the UNIVAQ model shows little change between 4 ppbv of Cl_y and 3 ppbv of Cl_y. Figure 3.53 shows ozone mixing ratio for June for Scenario D6. Changes in June ozone mixing ratio relative to Scenario D are shown in Figure 3.54. Ozone is reduced above 30 km in all models due to the increase in Cl_y from 3 to 4 ppbv. The GSFC model also shows reduced ozone in the southern hemisphere lower stratosphere and troposphere, while the AER model shows some ozone reduction in the northern hemisphere lower stratosphere. In the UNIVAQ model, lower stratospheric ozone increases compensate for ozone reduction above 30 km.

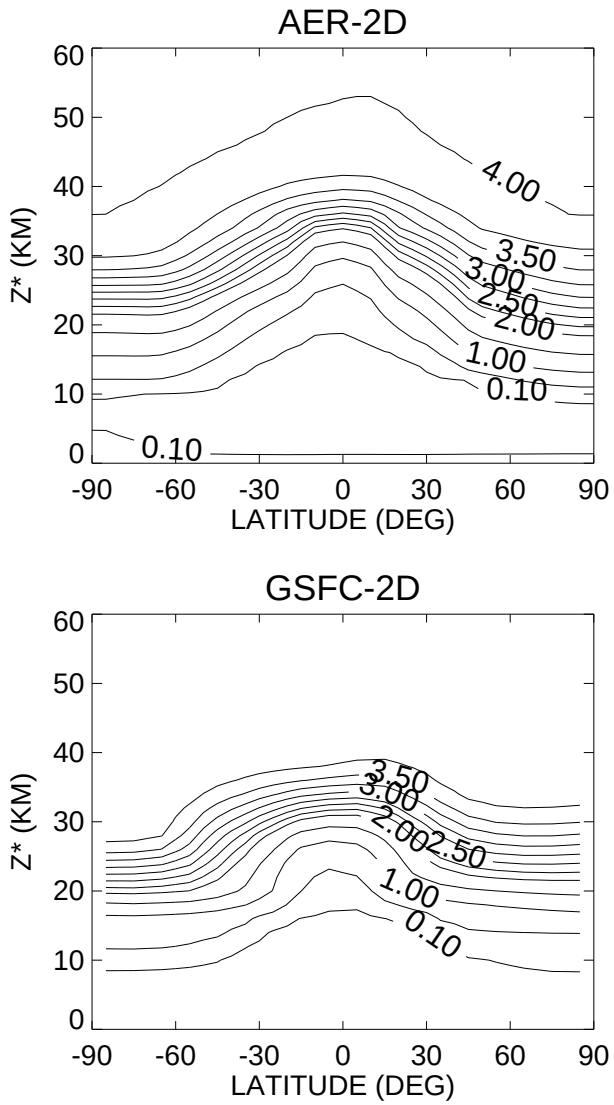

Figure 3.50: Calculated Cl_y mixing ratios (ppbv) in June for Scenario D6, the 2015 background atmosphere including subsonic aircraft and with organic chlorine boundary conditions adjusted to produce approximately 4 ppbv of inorganic chlorine. Contours are 0.1, 0.5, 1.0, 1.5, and 2.0 to 4.0 by 0.25 ppbv.

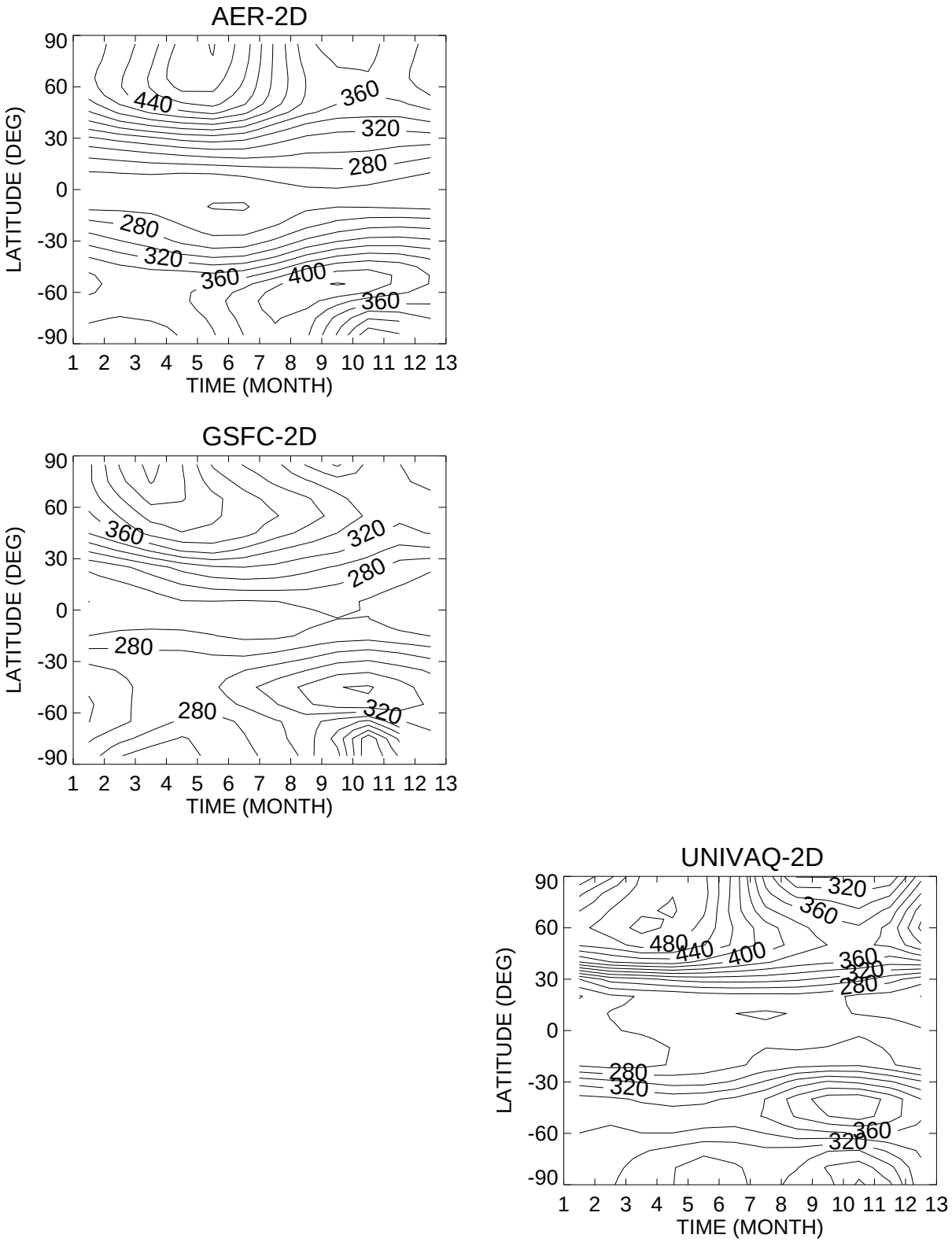

Figure 3.51: Total column ozone (Dobson Units) as a function of latitude and season as calculated by the models for Scenario D6, the 2015 background atmosphere with organic chlorine boundary conditions adjusted to produce approximately 4 ppbv of inorganic chlorine. Contour interval is 20 DU.

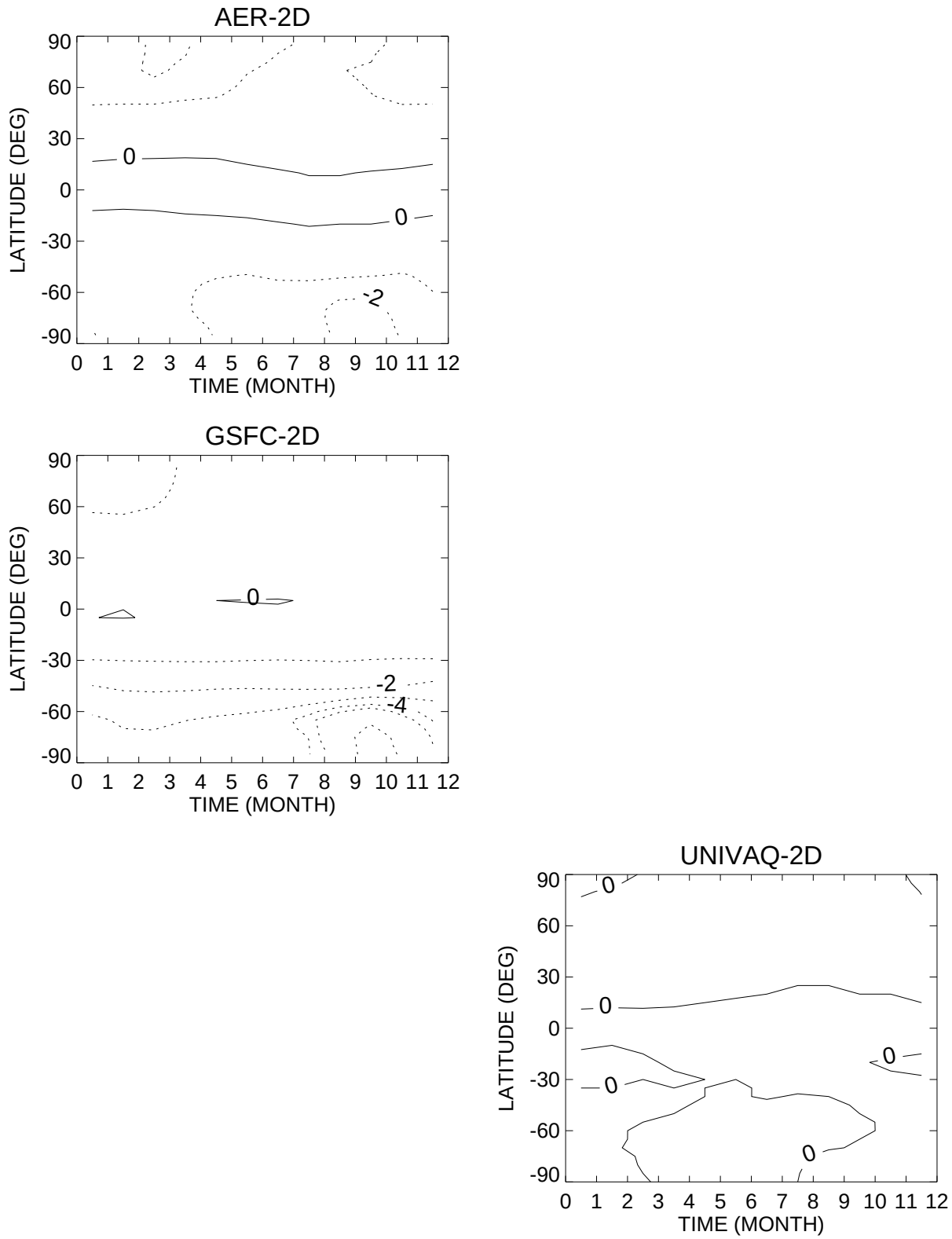

Figure 3.52: Percent change in total ozone column between Scenarios D6 and D. The difference in the scenarios is that D6 contains 4 ppbv of Cl_y and D contain 3 ppbv of Cl_y. Contours are -10, -5, -4, -3, -2, -1, 0.

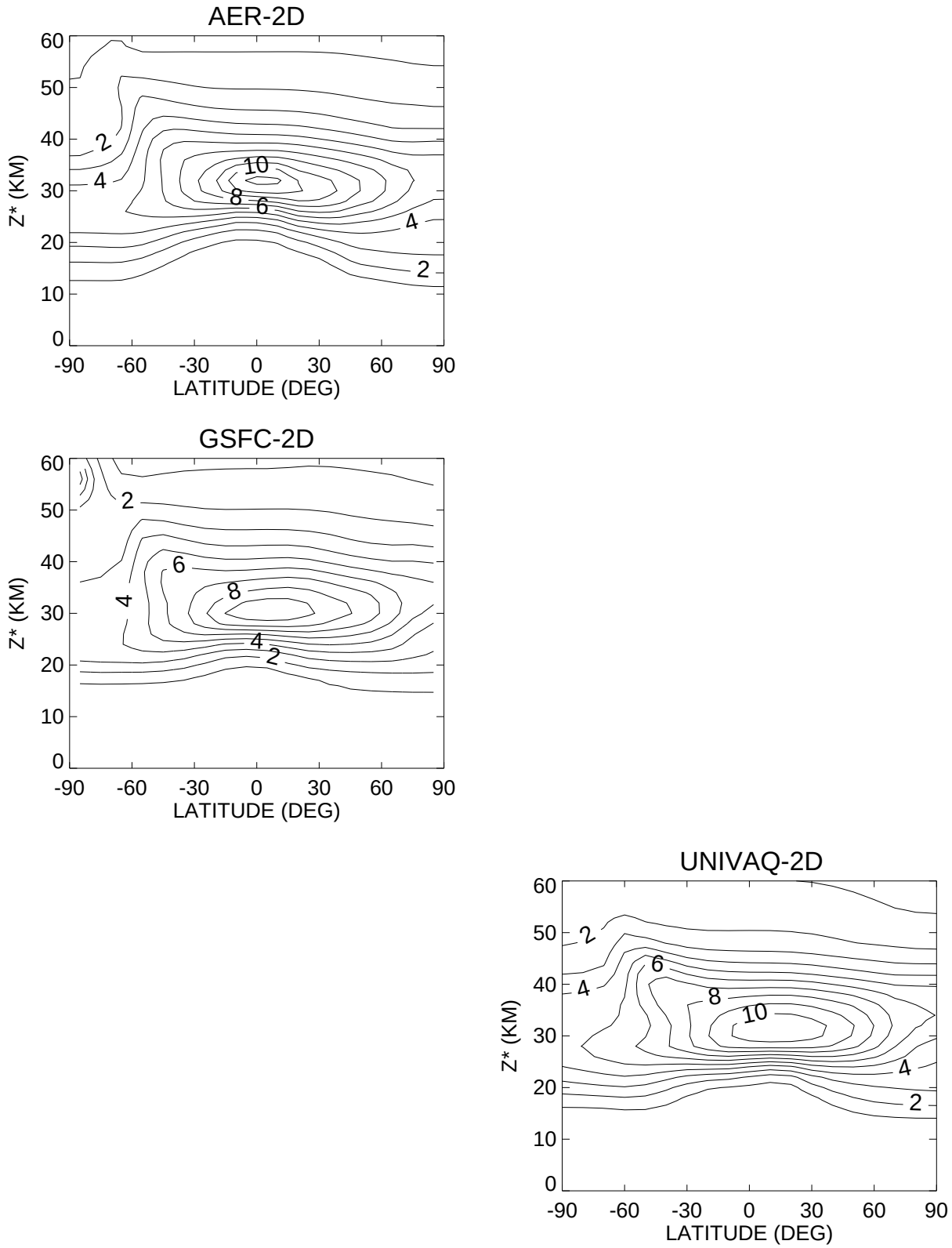

Figure 3.53: Calculated ozone mixing ratios (ppmv) as a function of latitude and altitude for Scenario D6 in June of 2015. The inorganic chlorine loading is 4 ppbv. The contour interval is 1 ppmv.

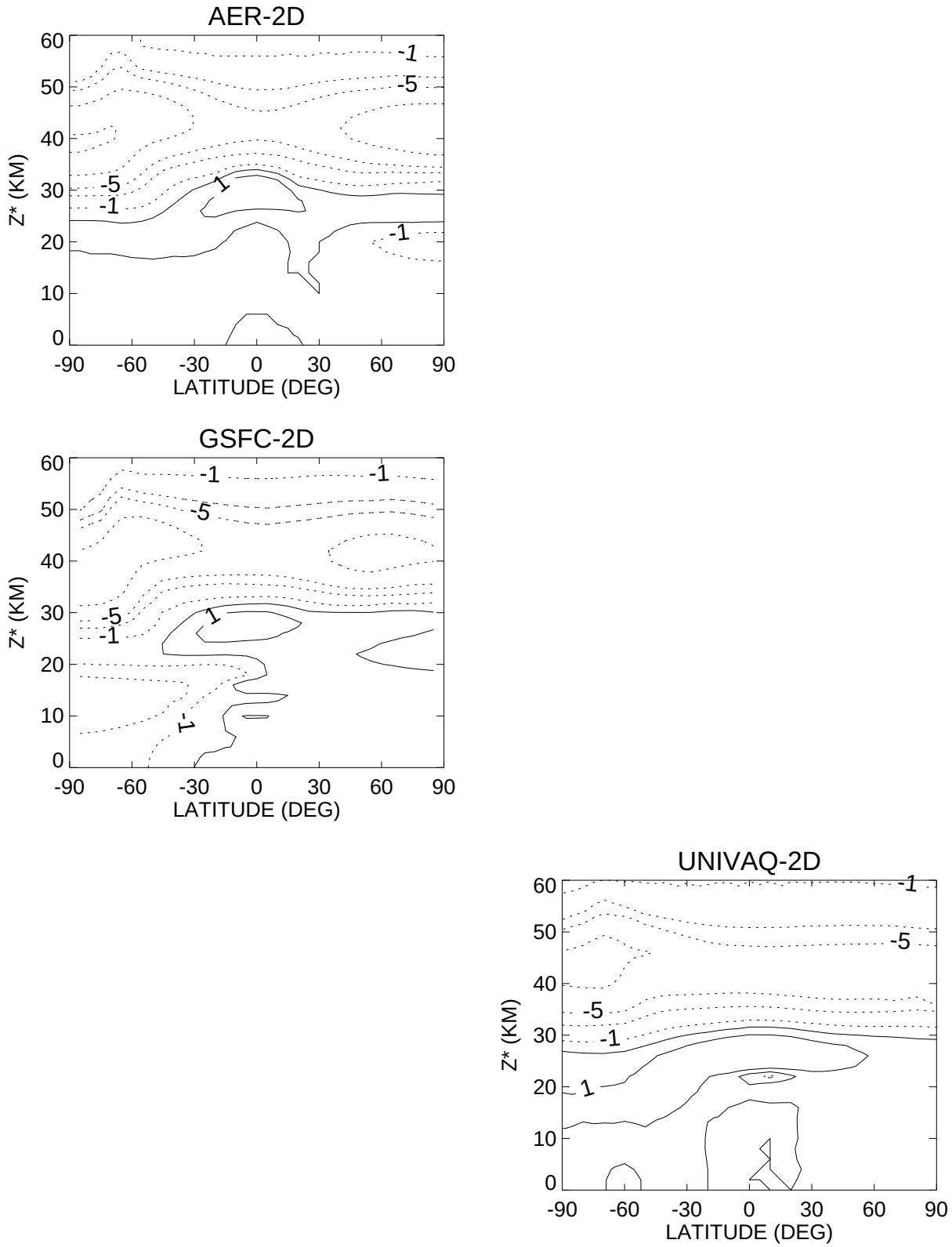

Figure 3.54: Percent change in ozone concentration between Scenarios D6 and D in June of 2015. The difference in the scenarios is that D6 contains 4 ppbv of Cl_y and D contain 3 ppbv of Cl_y. Contours are -15, -10, -5, -3, -1, 0, 1.

3.6 Scenario D7 Results

Scenario D7 did not employ the SA0 surface area density prescribed from WMO, but utilized interactive calculations of surface area density in the AER and UNIVAQ models. The UNIVAQ model included sulfur emissions for subsonic aircraft, assuming EI(SO_2)=0.4 and 50% SO_2 gas to particle conversion in the plume. The AER model did not consider sulfur emissions from subsonic aircraft and so employs a calculated non-volcanic background SAD. The SAD fields calculated by these models are shown in Figure 3.55. Note that the WMO SAD shown in Figure 3.1 includes no aerosols below 12 km. Modeling of tropospheric aerosols in 2-D models should be considered highly uncertain.

The calculated total ozone as a function of latitude and season for Scenario D7 is shown in Figure 3.56. The percent difference in total ozone relative to Scenario D is shown in Figure 3.57. Ozone column is increased by up to 1% in the AER model and up to 4% in the UNIVAQ model in the southern polar springtime due to the change in background aerosol SAD. Figure 3.58 shows ozone mixing ratios for June for this scenario. Changes in June ozone relative to Scenario D are shown in Figure 3.59. The AER model shows reduced ozone relative to Scenario D in most of the troposphere in June, but an increase above 10 km at middle and high latitudes. The UNIVAQ model show increased ozone at middle and high latitudes below 10 km in June and an ozone decrease in the northern hemisphere lower stratosphere. These calculations are provided as sensitivity analysis for understanding the effects of changes in background aerosol SAD on ozone perturbations.

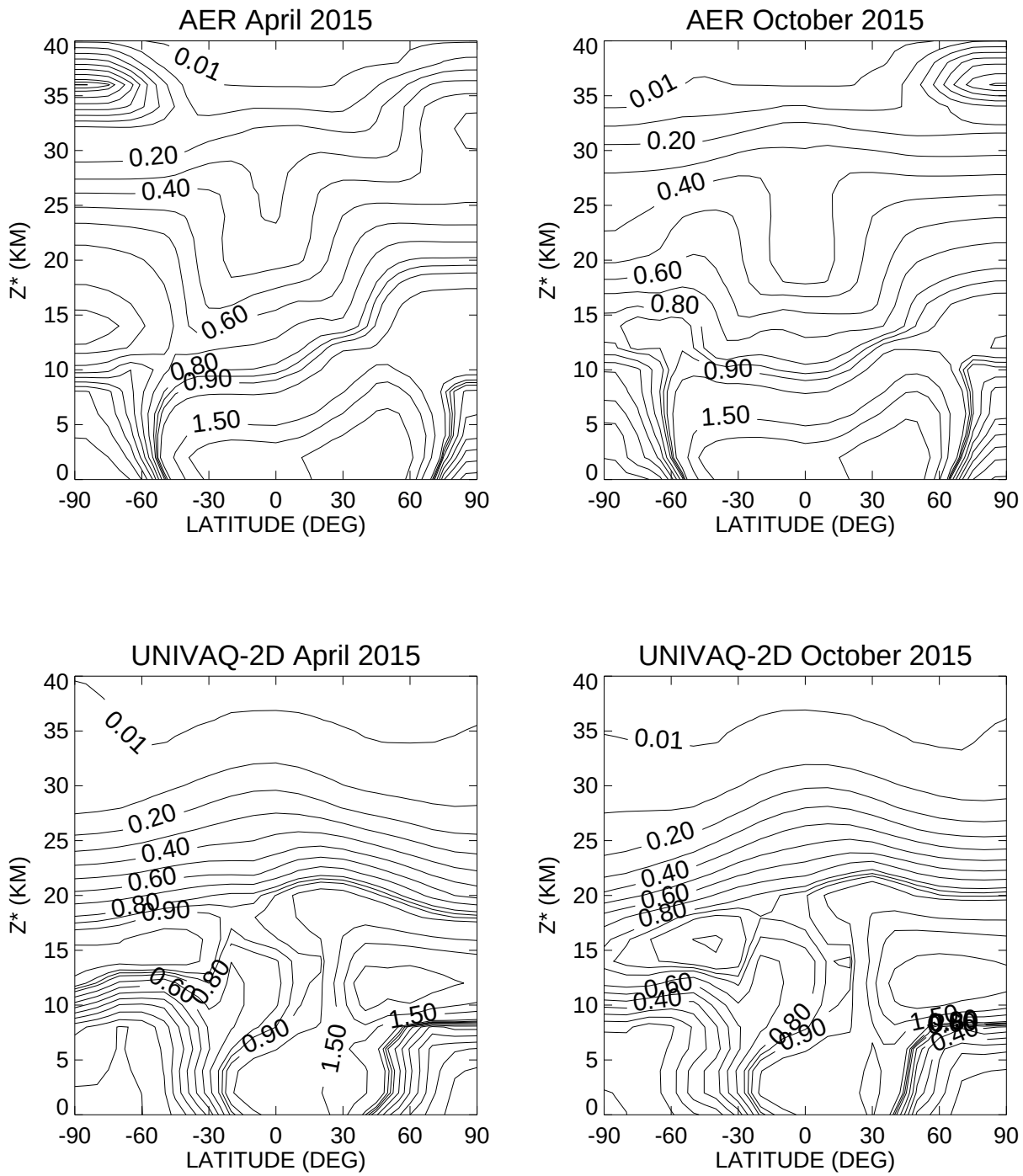

Figure 3.55: Aerosol surface area density ($\mu m^2/cm^3$) calculated by the AER and UNIVAQ models for Scenario D7, the 2015 background atmosphere including subsonic aircraft and interactive microphysics. The UNIVAQ model included sulfur emissions from subsonic aircraft assuming 50% SO_2 gas to particle conversion, while the AER model omitted subsonic sulfur. Contours are 0.01, 0.1 to 0.8 by 0.1, 0.85, 0.9, 1.0, 1.5, 2, 3.

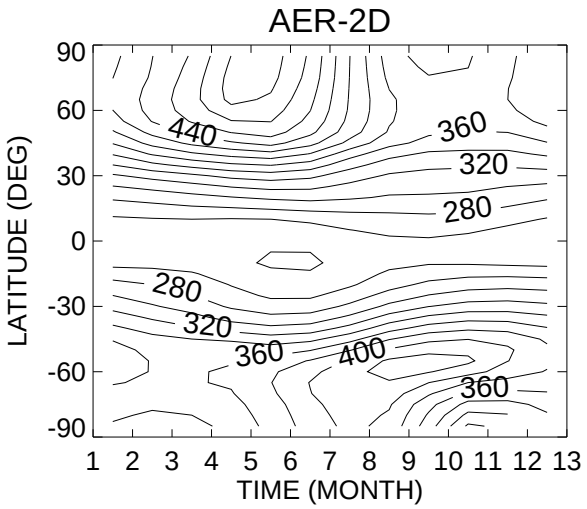

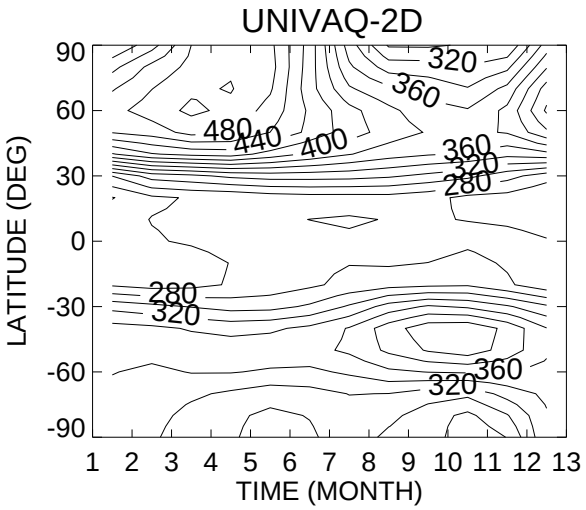

Figure 3.56: Total ozone column (Dobson Units) as a function of latitude and season as calculated by the models for Scenario D7, the 2015 background atmosphere including subsonic aircraft and interactive microphysics. The contour interval is 20 DU.

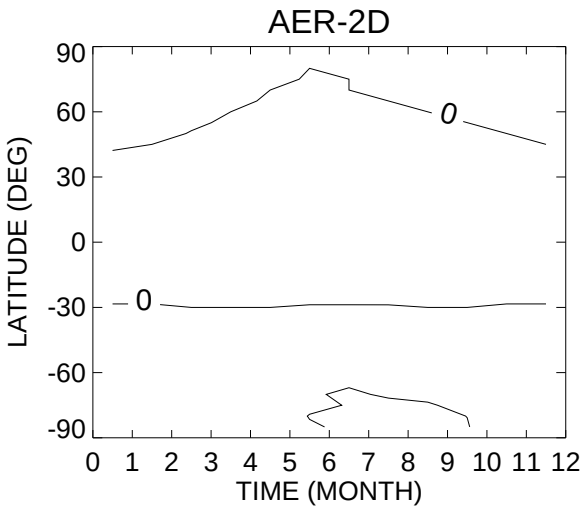

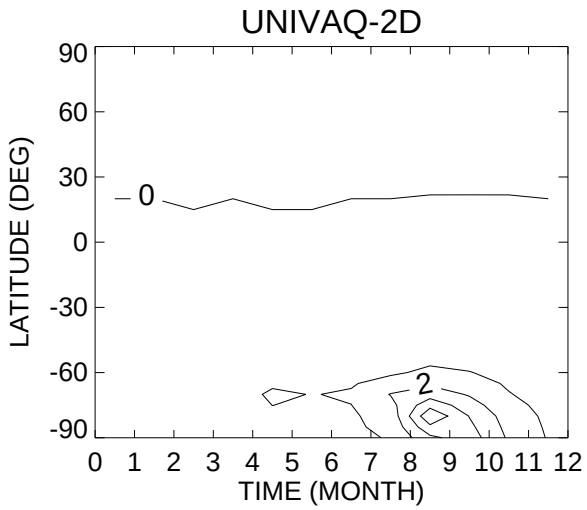

Figure 3.57: Percent change in total ozone column between Scenarios D7 and D. The difference in the scenarios is in the aerosol surface area density. Contours are 0, 1, 2, 3, 4.

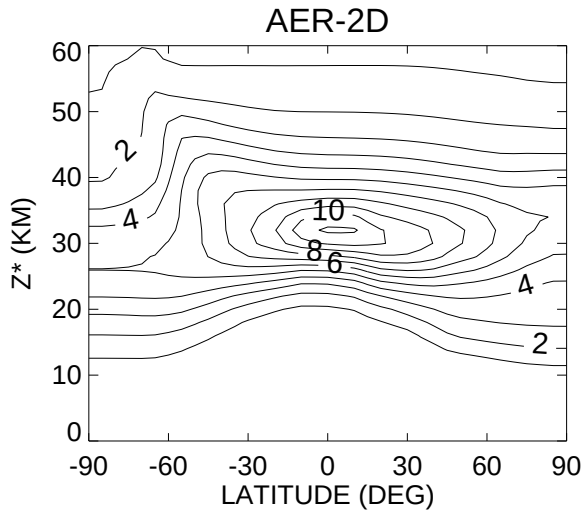

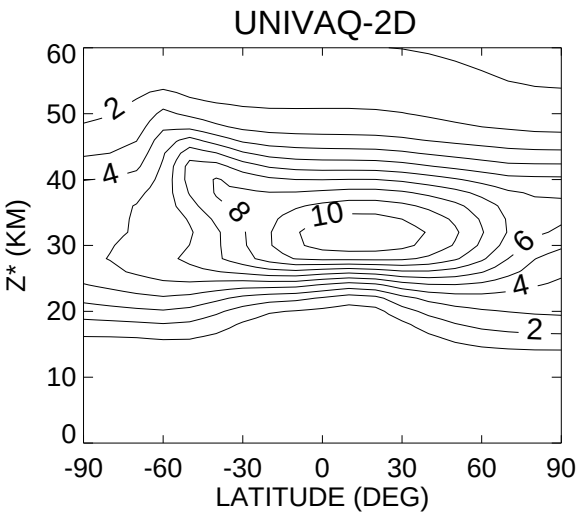

Figure 3.58: Calculated ozone mixing ratios (ppmv) as a function of latitude and altitude for Scenario D7 in June of 2015. Contour interval is 1 ppmv.

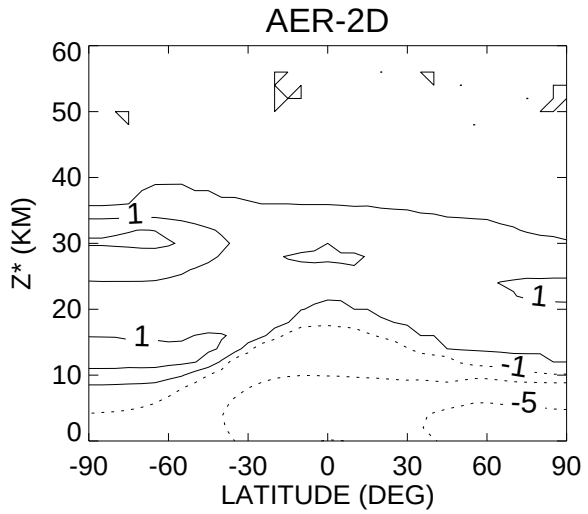

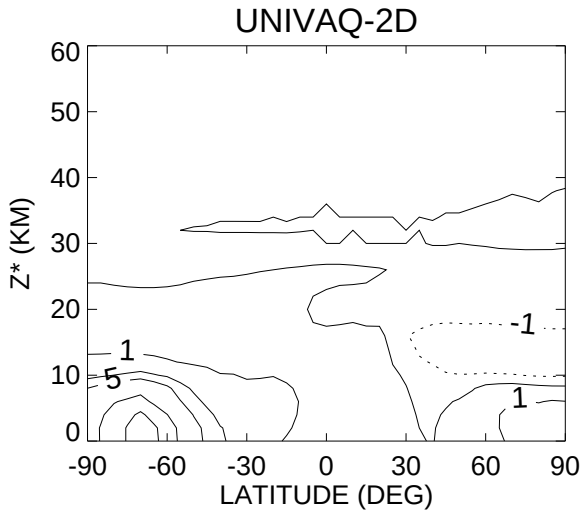

Figure 3.59: Percent change in ozone concentration between Scenarios D7 and D in June of 2015. The difference in the scenarios is in the aerosol surface area density. Contours are -5, -3, -1, 0, 1, 3, 5, 10, 15.

3.7 Scenario D8 Results

Scenario D8 is similar to Scenario D7 except that 100% SO_2 gas to particle conversion in the plume is assumed for subsonic aircraft emissions in the UNIVAQ model. The AER model did not consider sulfur emissions from subsonic aircraft, and so D7 and D8 are identical for the AER model. The SAD fields calculated for Scenario D8 are shown in Figure 3.60. Total ozone fields as a function of latitude and season are shown in Figure 3.61. Changes in total ozone relative to Scenario D are shown in Figure 3.62. Figure 3.63 shows ozone mixing ratios as a function of latitude and altitude for June, and Figure 3.64 shows changes in June ozone relative to Scenario D.

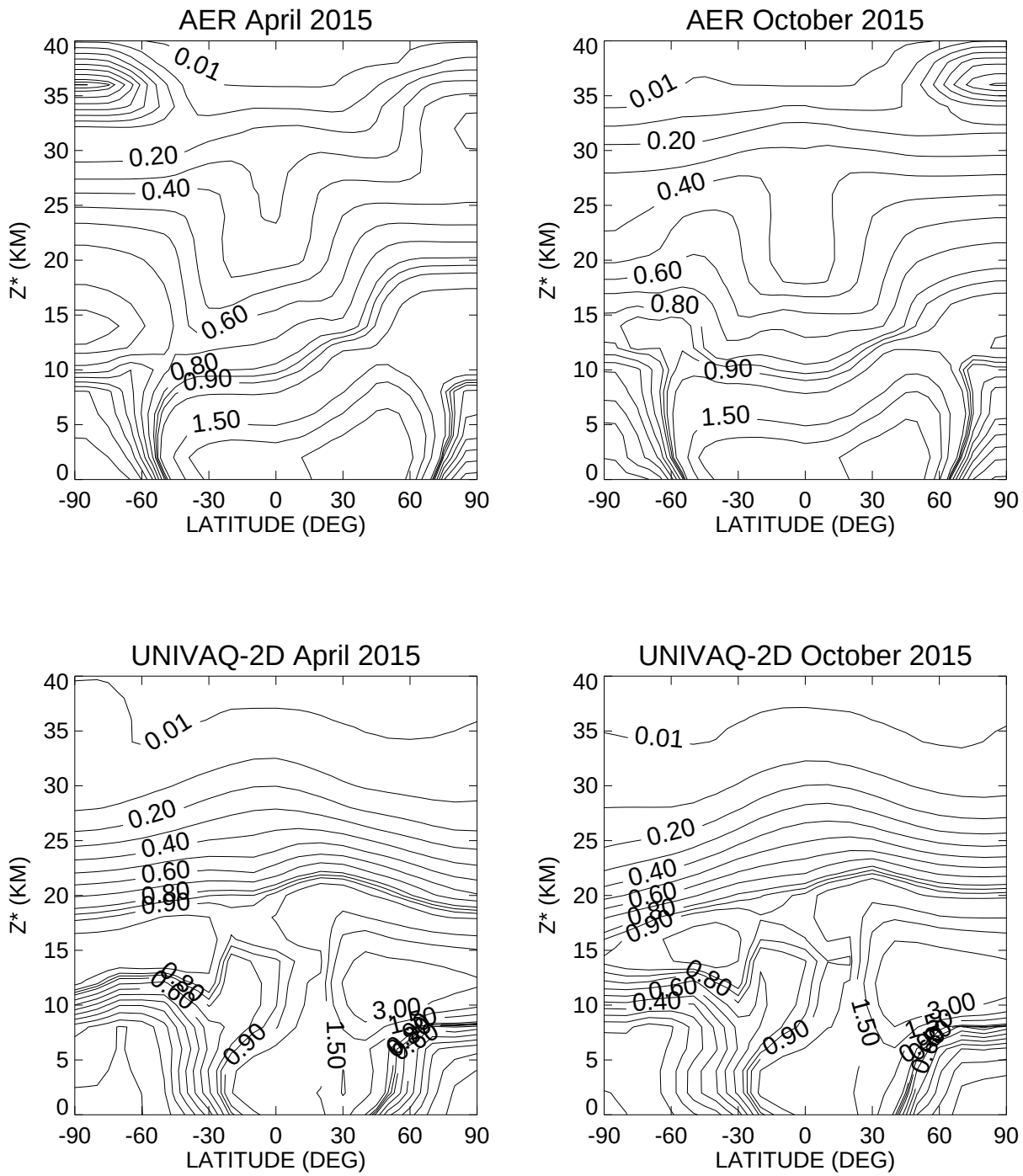

Figure 3.60: Aerosol surface area density ($\mu m^2/cm^3$) calculated by the AER and UNIVAQ models for Scenario D8, the 2015 background atmosphere including subsonic aircraft and interactive microphysics. The UNIVAQ model included sulfur emissions from subsonic aircraft assuming 100% SO_2 gas to particle conversion, while the AER model did not. Contours are 0.01, 0.1 to 0.8 by 0.1, 0.85, 0.9, 1.0, 1.5, 2, 3.

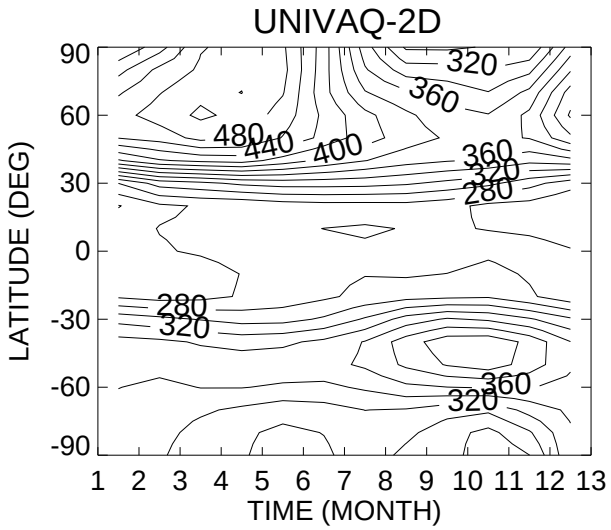

Figure 3.61: Total ozone column (Dobson Units) as a function of latitude and season as calculated by the UNIVAQ model for Scenario D8, the 2015 background atmosphere including subsonic aircraft and interactive microphysics. Contour interval is 20 DU.

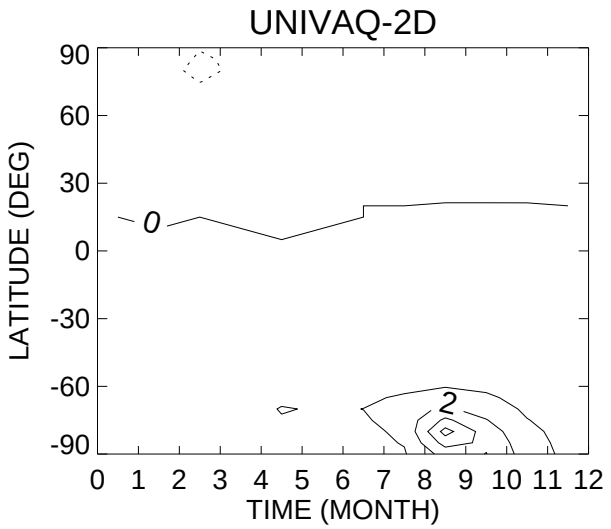

Figure 3.62: Percent change in total ozone column between Scenarios D8 and D. The difference in the scenarios is in the aerosol surface area density. Contours are 0, 1, 2, 3, 4.

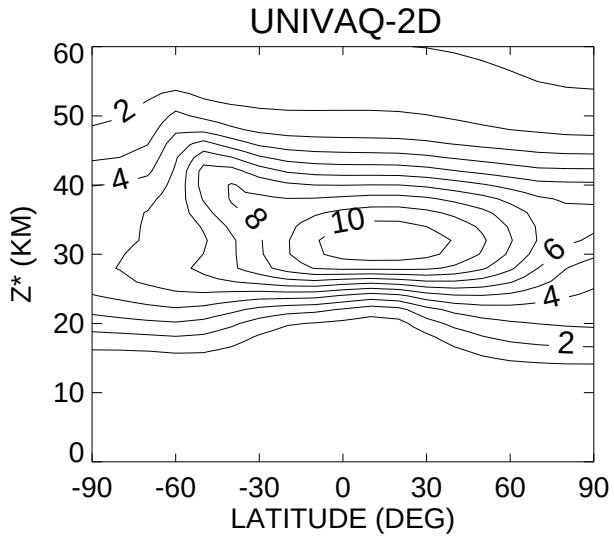

Figure 3.63: Ozone mixing ratio (ppmv) as a function of latitude and altitude as calculated by the UNIVAQ model for Scenario D8 in June on 2015. Contour interval is 1 ppmv.

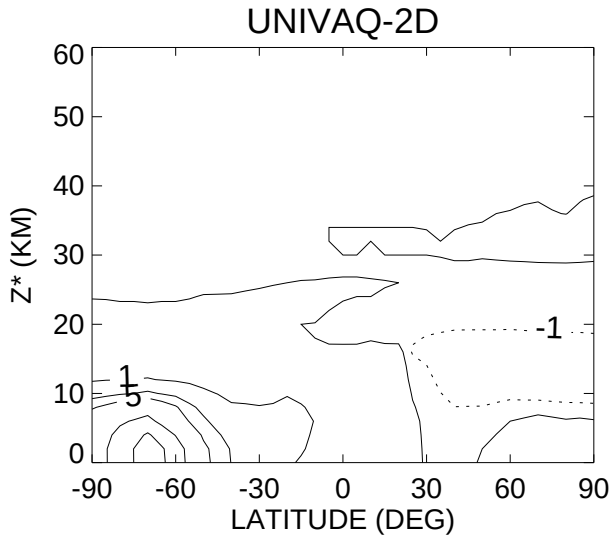

Figure 3.64: Percent change in ozone concentration between Scenarios D8 and D in June of 2015. The difference in the scenarios is in the aerosol surface area density. Contours are -1, 0, 1, 3, 5, 10, 15.

3.8 Scenario D9 Results

Scenario D9 represent the 2050 background atmosphere. Surface boundary conditions are described in Table 3.1. The nonvolcanic sulfate surface area density SA0 is used. The subsonic aircraft fleet is the same as that used in 2015. Calculated NO_y mixing ratios as a function of latitude and altitude for June are shown in Figure 3.65. The N_2O boundary condition for 2050 is 11% greater than for 2015, so NO_y concentrations are increased accordingly. Cl_y mixing ratios are shown in Figure 3.66 and Br_y fields in Figure 3.67. The surface boundary conditions provide for 2.0 ppbv of Cl_y and 11 pptv of Br_y.

Total column ozone as a function of latitude and season is shown in Figure 3.68 for Scenario D9. Figure 3.69 shows changes in total ozone relative to Scenario D, the 2015 background atmosphere. Ozone columns are larger in 2050 than in 2015 due to the reduced concentration of Cl_y and Br_y. The GSFC and LLNL models calculate total ozone increases of 10-30% in the southern hemisphere high latitudes, while the AER, CSIRO, and UNIVAQ model calculate much smaller changes. Figure 3.70 shows ozone mixing ratios for June for Scenario D9. Changes in June ozone concentration relative to Scenario D are shown in Figure 3.71. All models show significant ozone increases between 35 and 50 km. The GSFC and LLNL models also show significant ozone increases in the southern hemisphere lower stratosphere, due to the importance of PSC processes in those models.

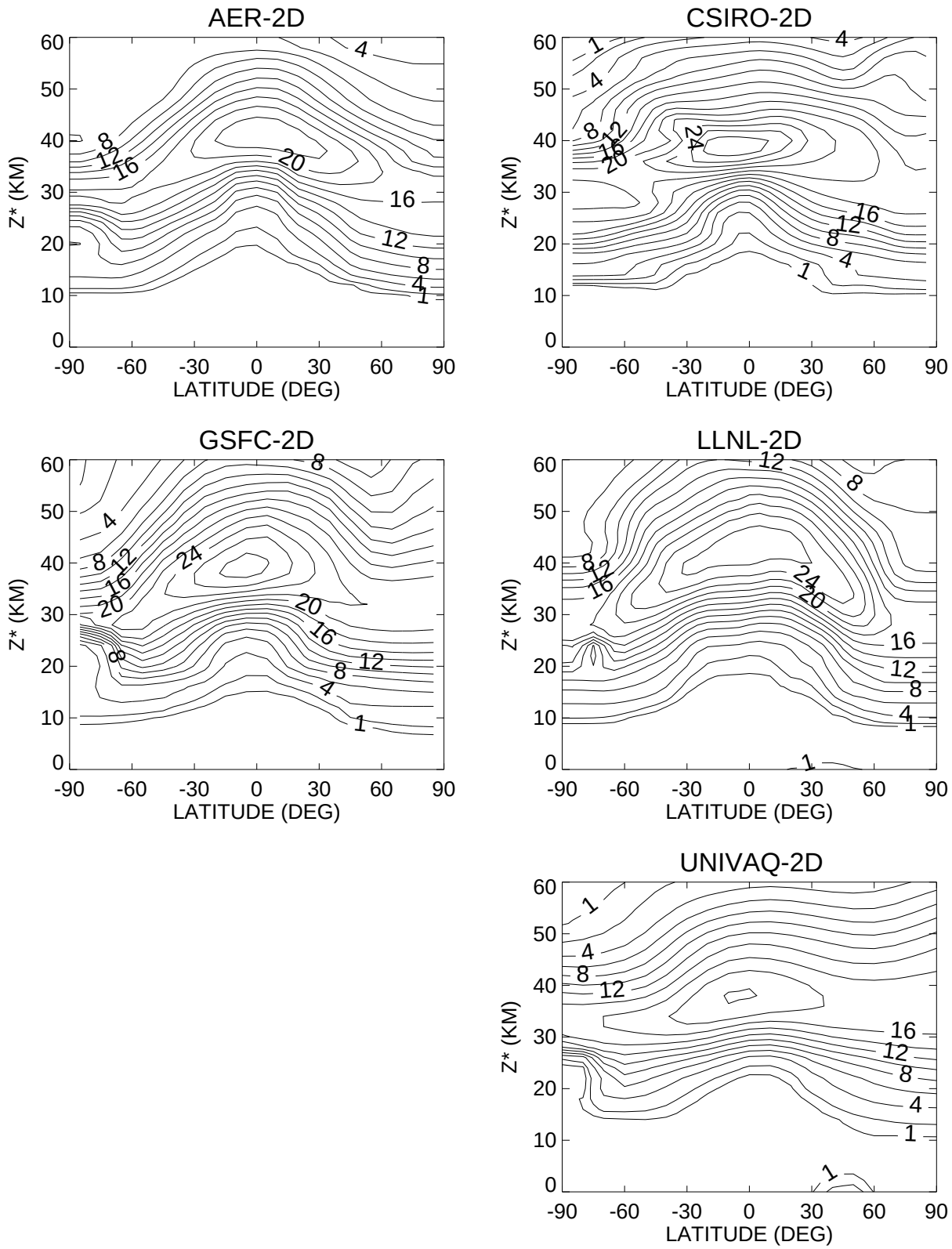

Figure 3.65: Calculated NO_y mixing ratios (ppbv) as a function of latitude and altitude in June for Scenario D9, the 2050 background atmosphere. Contours are 1 and 2 to 28 by 2 ppbv.

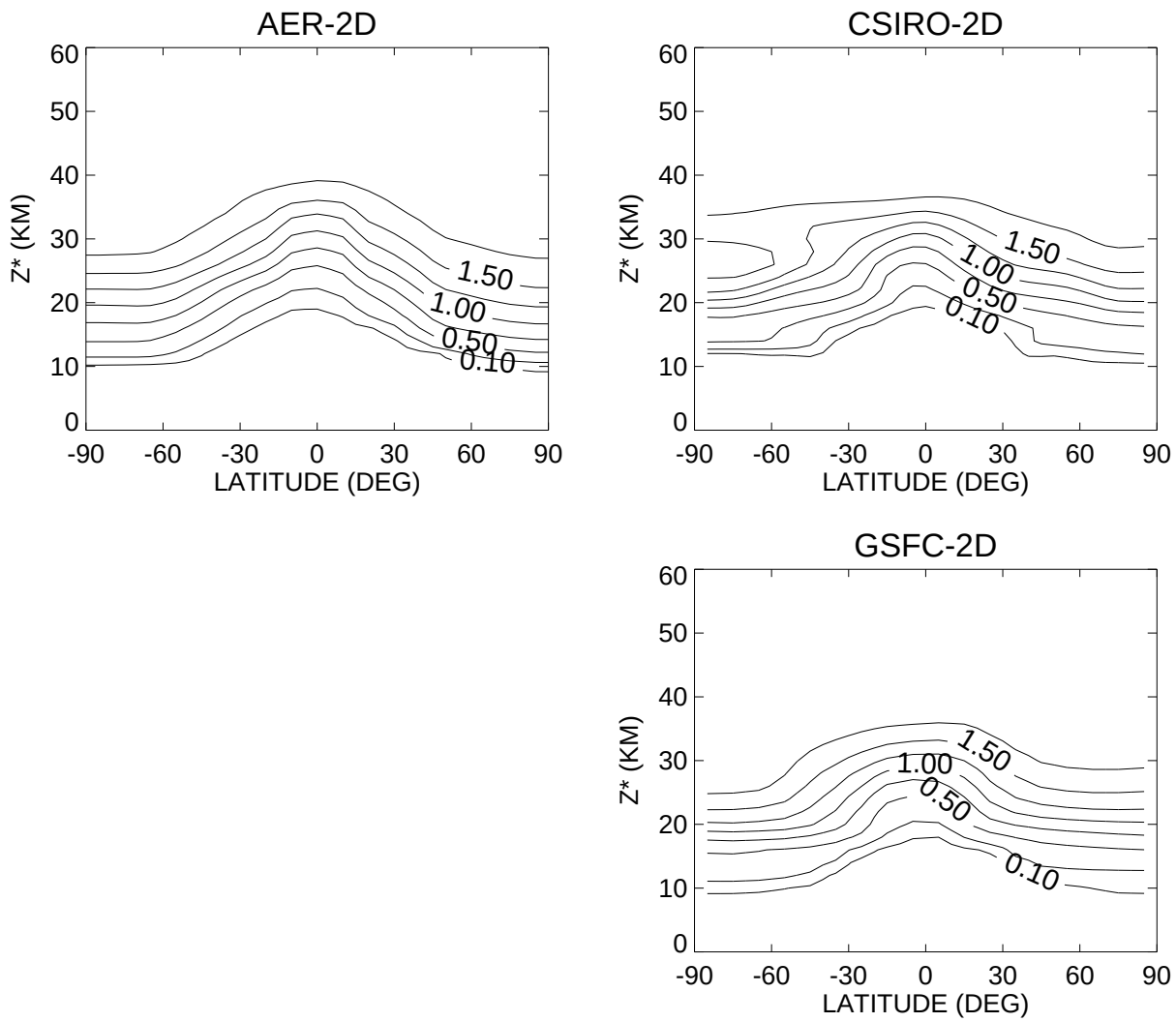

Figure 3.66: Calculated Cl_y mixing ratios (ppbv) as a function of latitude and altitude in June for Scenario D9, the 2050 background atmosphere. Inorganic chlorine loading is approximately 2 ppbv. Contours are 0.1 and 0.25 to 1.75 by 0.25 ppbv.

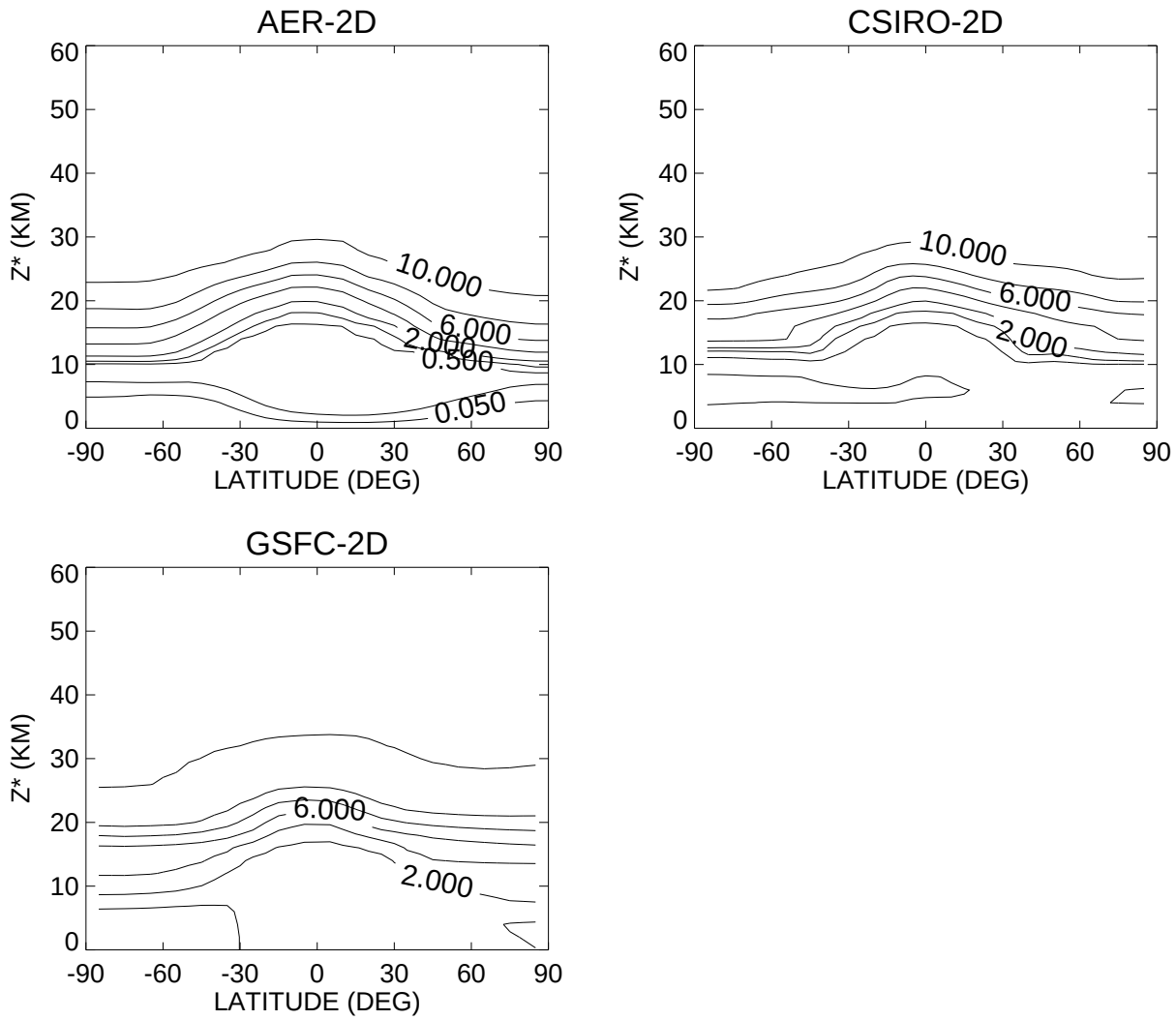

Figure 3.67: Calculated Br_y mixing ratios (ppbv) as a function of latitude and altitude in June for Scenario D9, the 2050 background atmosphere. Inorganic bromine loading is approximately 11 pptv. Contours are 0.05, 0.1, 0.5, 1.0, and 2 to 12 by 2 pptv.

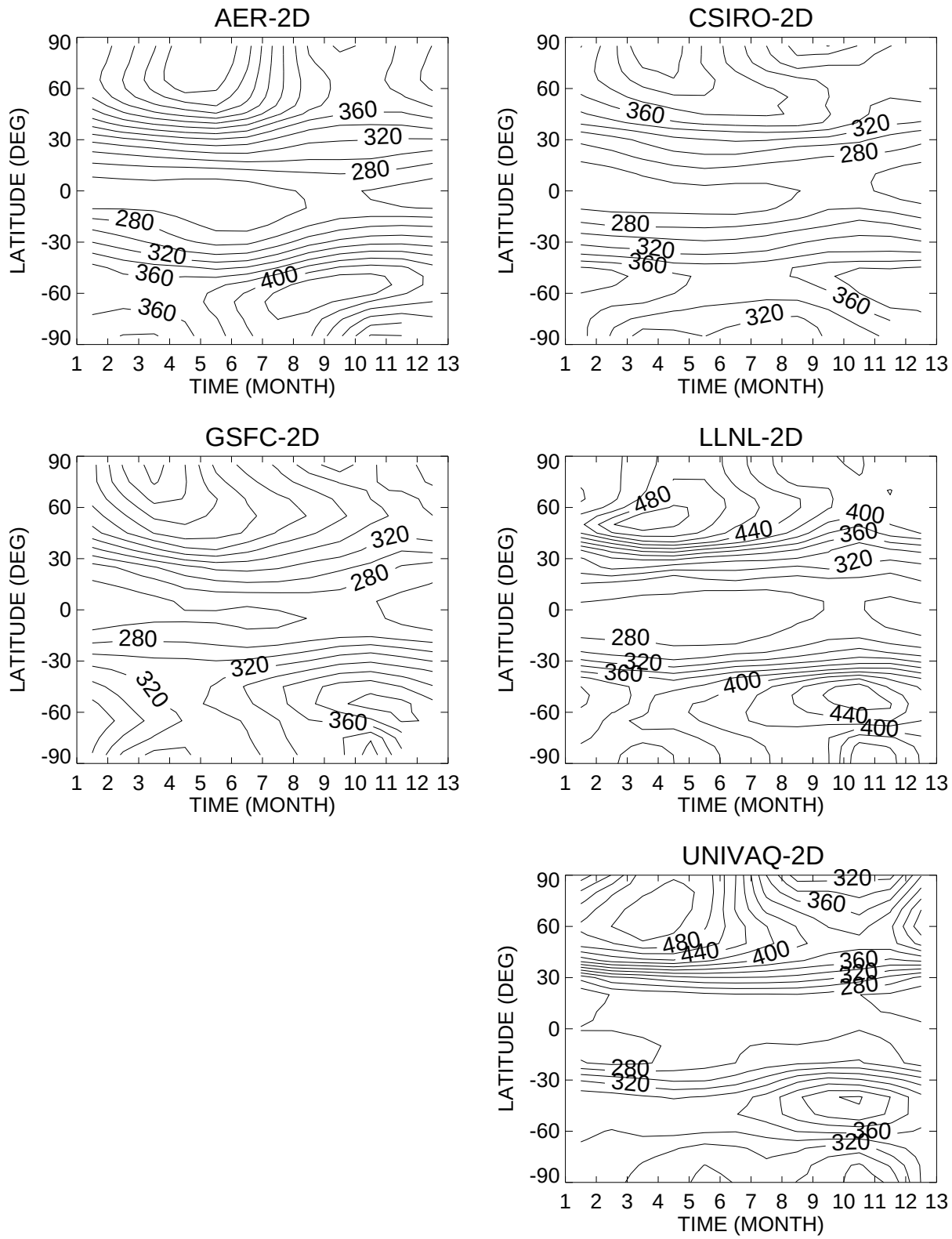

Figure 3.68: Total ozone column (Dobson Units) as a function of latitude and season as calculated by the models for Scenario D9, the 2050 background atmosphere including subsonic aircraft. Contour interval is 20 DU.

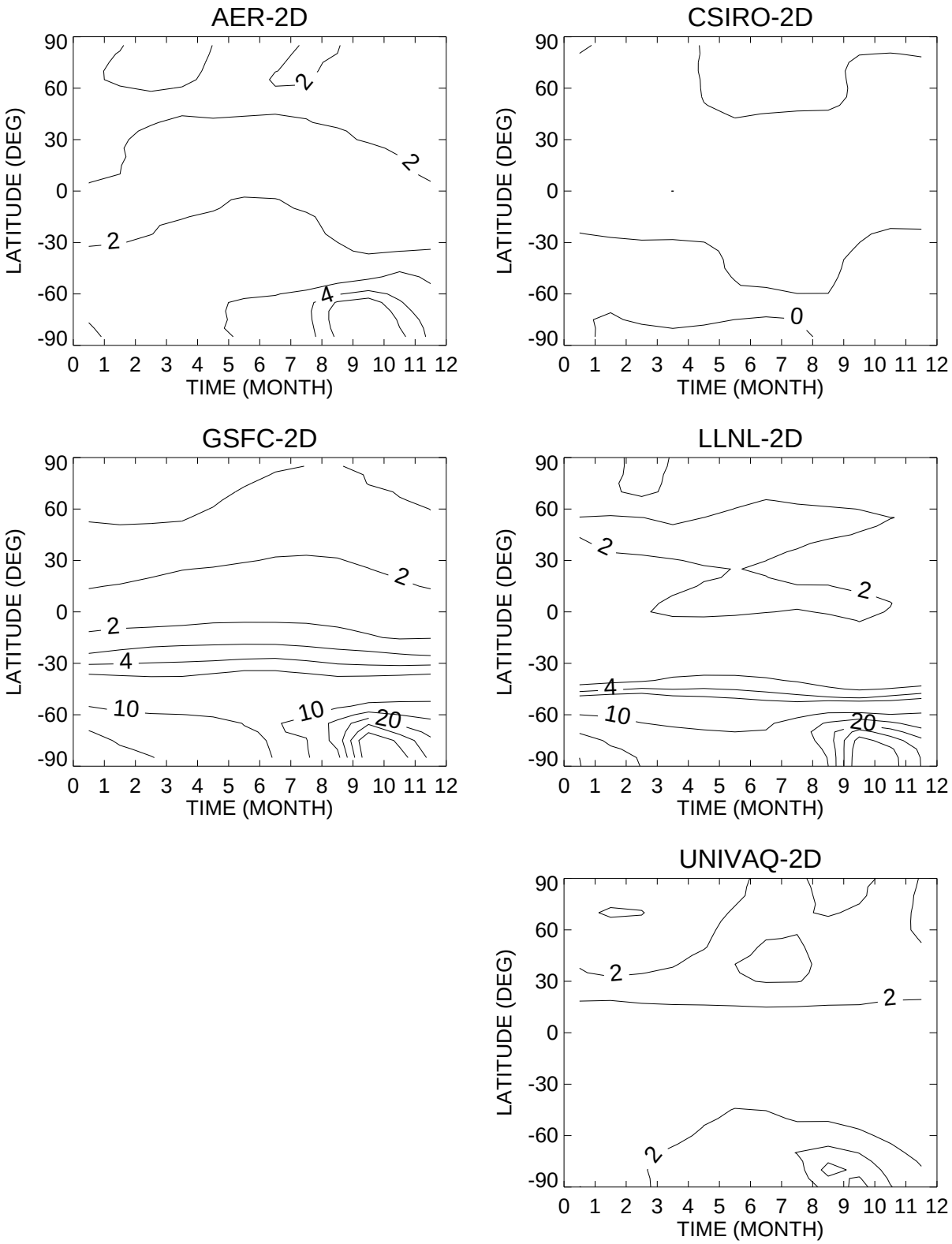

Figure 3.69: Percent change in total ozone column between Scenarios D9 and D. Scenario D9 represents 2050 and Scenario D 2015. The same subsonic aircraft fleet is included. Contours are 0 to 5 by 1 and 10 to 30 by 5.

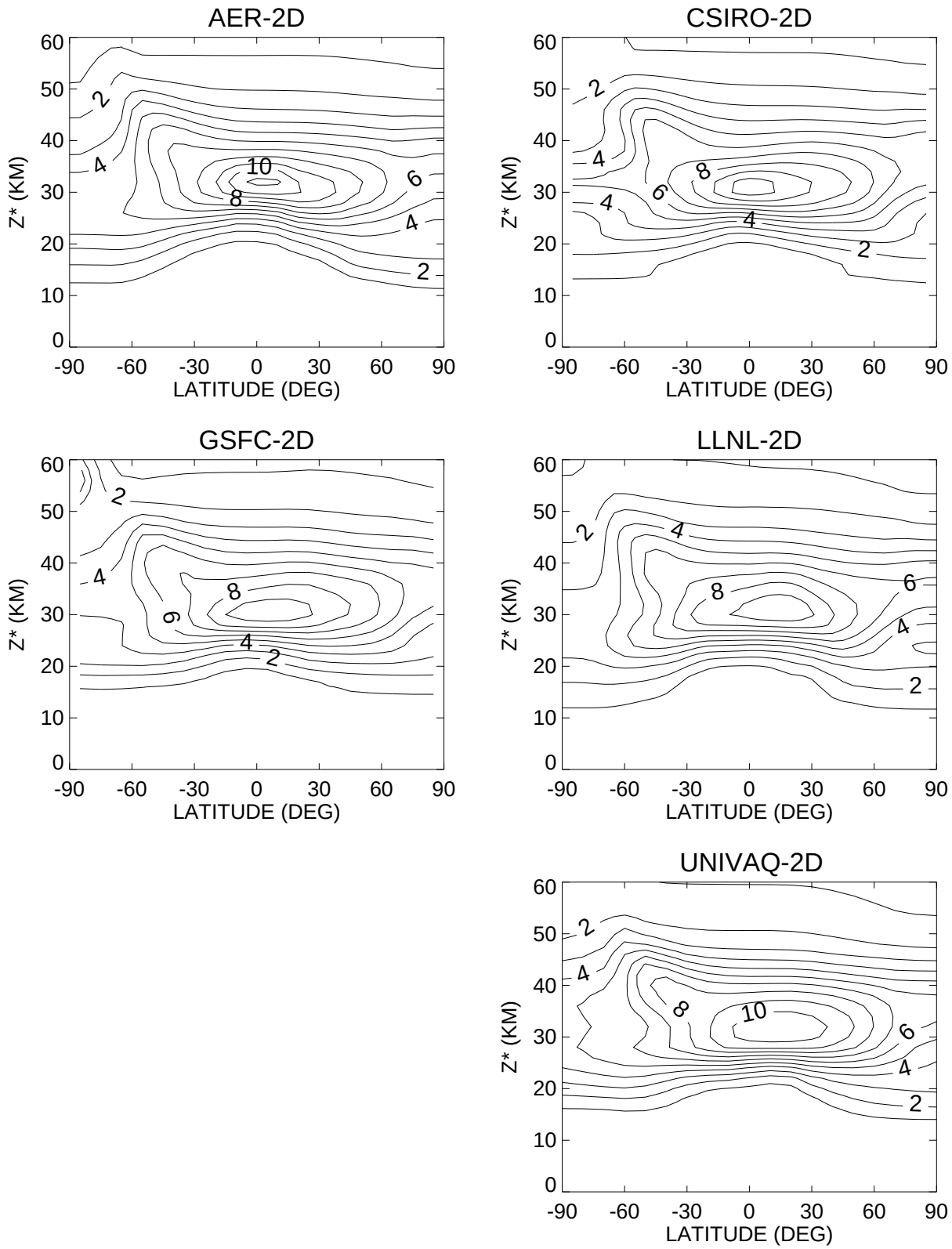

Figure 3.70: Calculated ozone mixing ratios (ppmv) as a function of latitude and altitude for Scenario D9 in June of 2050. Contour interval is 1 ppmv.

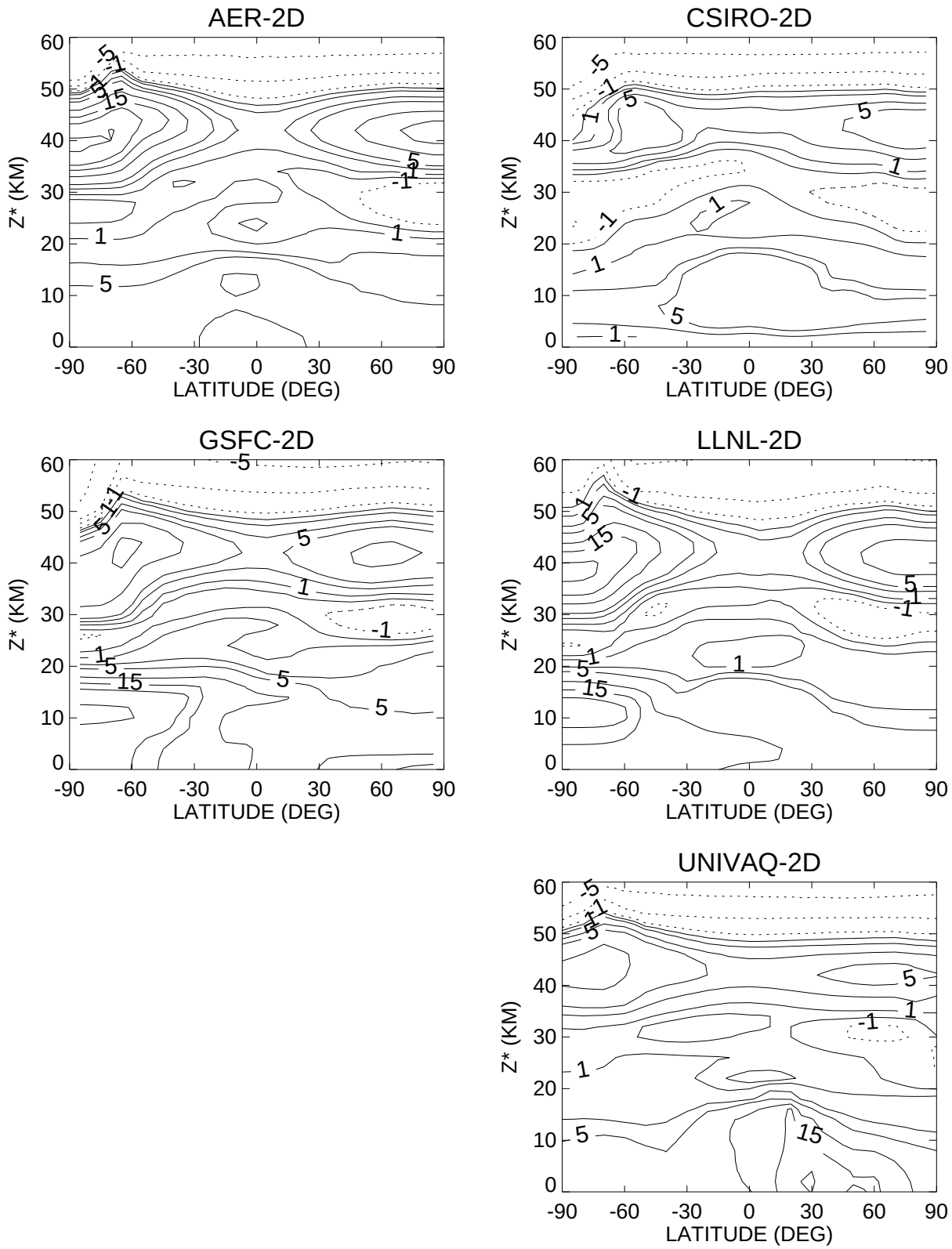

Figure 3.71: Percent change in ozone concentration between Scenarios D9 and D in June of 2015. Scenario D9 represents 2050 and Scenario D 2015. Contours are -1, 0, 1, 3, and 5 to 25 by 5.

3.9 Scenario F Results

This is an alternate 2050 background atmosphere with the subsonic fleet described by the IPCC IS92a scenario. The total fleet fuel burn is 471 Tg/yr for the 2050 IS92a scenario, compared with 309 Tg/yr for the 2015 subsonic scenario. Subsonic aircraft emissions perturb tropospheric NO_y concentrations. Figure 3.72 shows NO_y mixing ratios as a function of latitude and altitude for June for Scenario F. Figure 3.73 shows percent differences in NO_y concentration between Scenarios F and D9. NO_y concentrations in the troposphere are increased by only 0.5% due to increases in aircraft-emitted NO_y of 50%. Aircraft emissions of NO_y are small relative to other tropospheric sources, and tropospheric removal rates are large. The percent change in ozone mixing ratio for June for Scenario F relative to Scenario D9 is shown in Figure 3.74. The AER, CSIRO, and GSFC models show ozone increases of up to 5% in the troposphere, while changes in the UNIVAQ model are smaller.

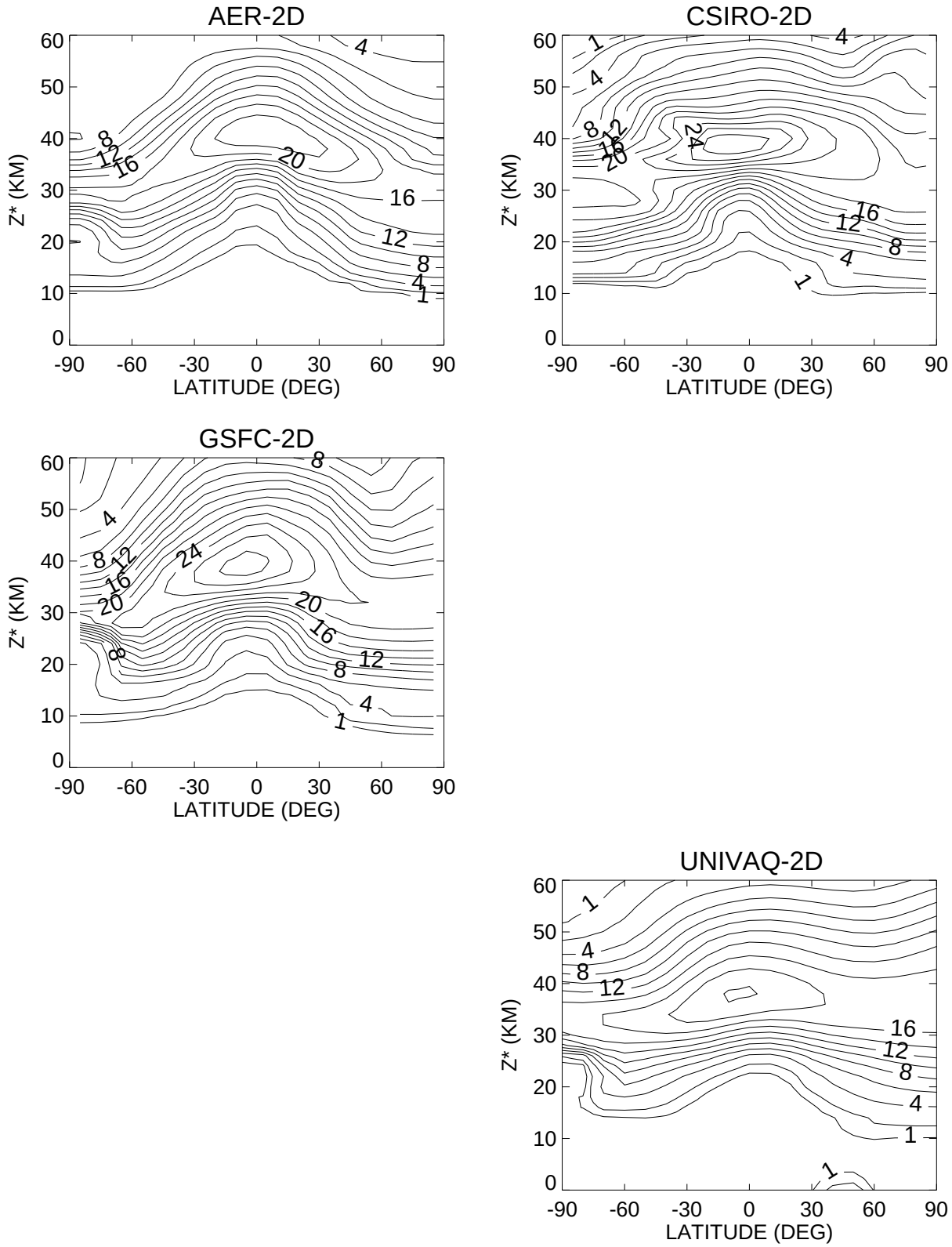

Figure 3.72: Calculated NO_y mixing ratios (ppbv) as a function of latitude and altitude in June for Scenario F, the 2050 background atmosphere with the subsonic fleet projected to 2050 using the IPCC IS92a scenario. Contours are 1 and 2 to 28 by 2 ppbv.

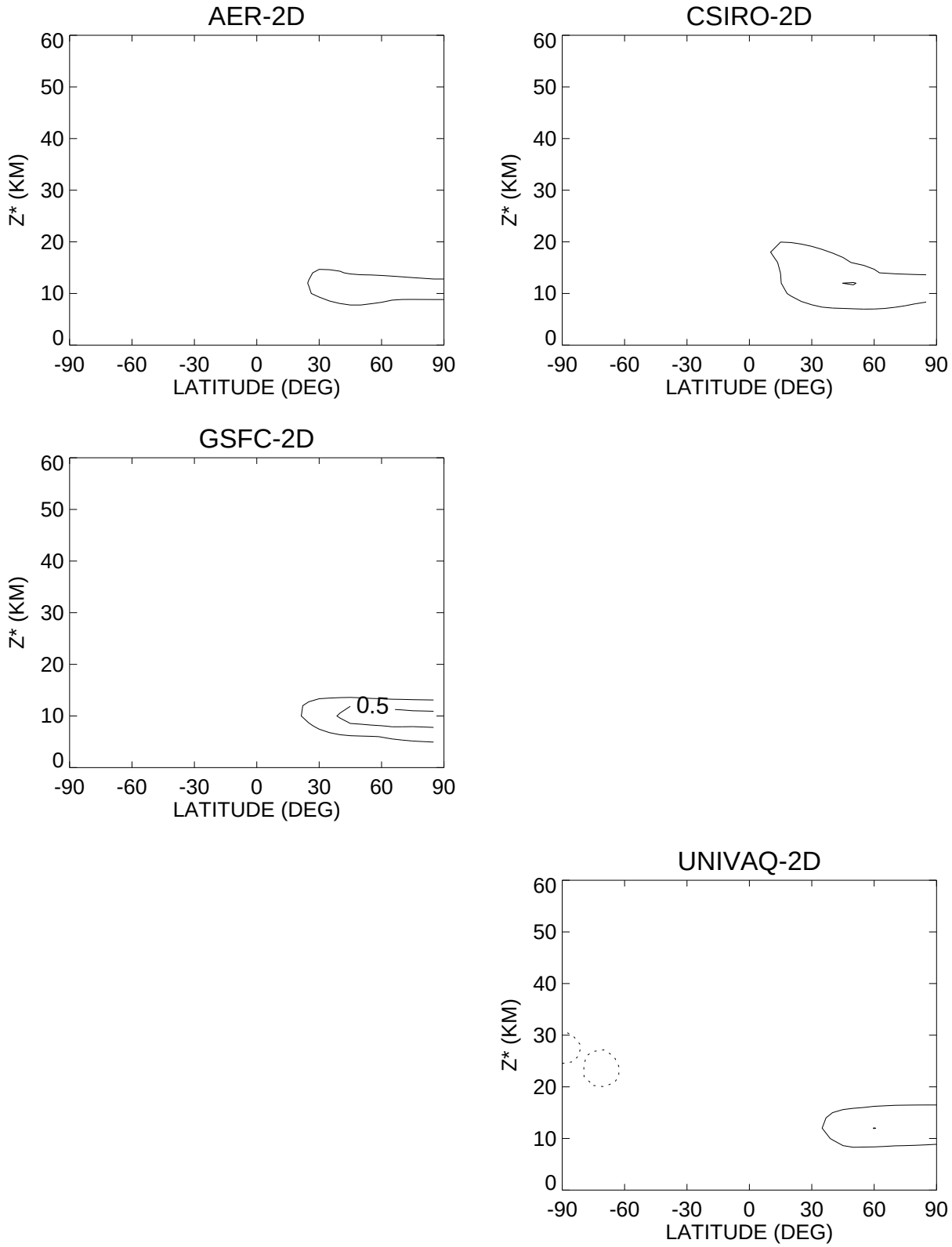

Figure 3.73: Percent change in calculated NO_y mixing ratio (ppbv) in June for Scenario F relative to Scenario D9. Scenario F uses a subsonic fleet projected to 2050 using the IPCC IS92a scenario, while Scenario D9 used the 2015 projected subsonic fleet. Contours are -0.5, 0, 0.5.

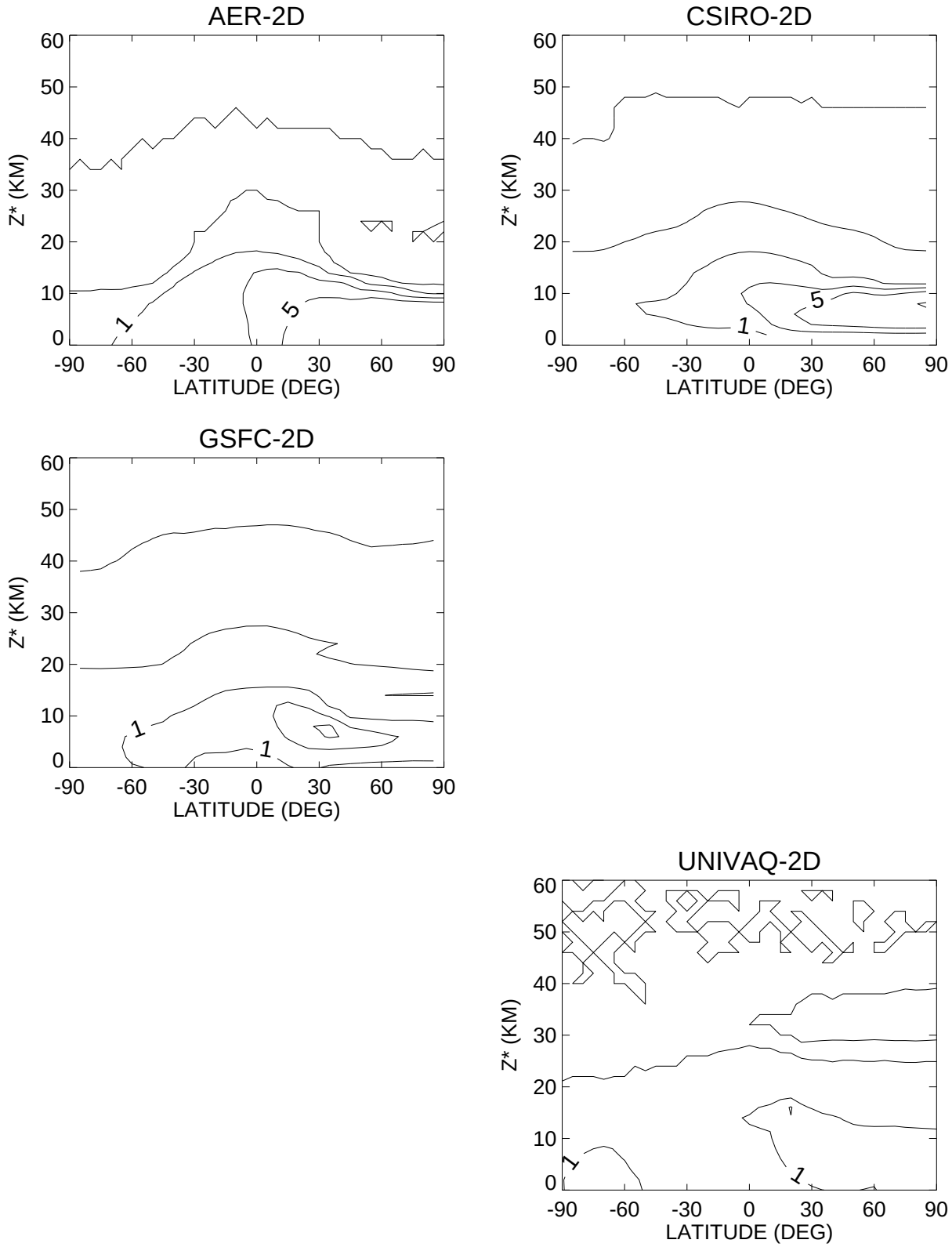

Figure 3.74: Percent change in ozone concentration between Scenarios F and D9 in June of 2015. Scenario F uses a subsonic fleet projected to 2050 using the IPCC IS92a scenario, while Scenario D9 used the 2015 projected subsonic fleet. Contours are 0, 1, 3, and 5.

3.10 Scenario G Results

This is an alternate 2050 background atmosphere with the subsonic fleet described by the IPCC IS92e high demand scenario. Total fuel burn from subsonic emission is 744 Tg/yr, an increase of 130% over the 2015 subsonic fleet. NO_y mixing ratios for June for this scenario are shown in Figure 3.75. Changes in NO_y mixing ratio relative to Scenario D9 are shown in Figure 3.76. Increases in NO_y of up to 1.5% are seen for the GSFC model and up to 1.0% for the CSIRO and UNIVAQ models. The AER model shows a smaller increase. The corresponding changes in ozone mixing ratio for June are shown in Figure 3.77. The CSIRO model shows tropospheric ozone changes as large as 20%.

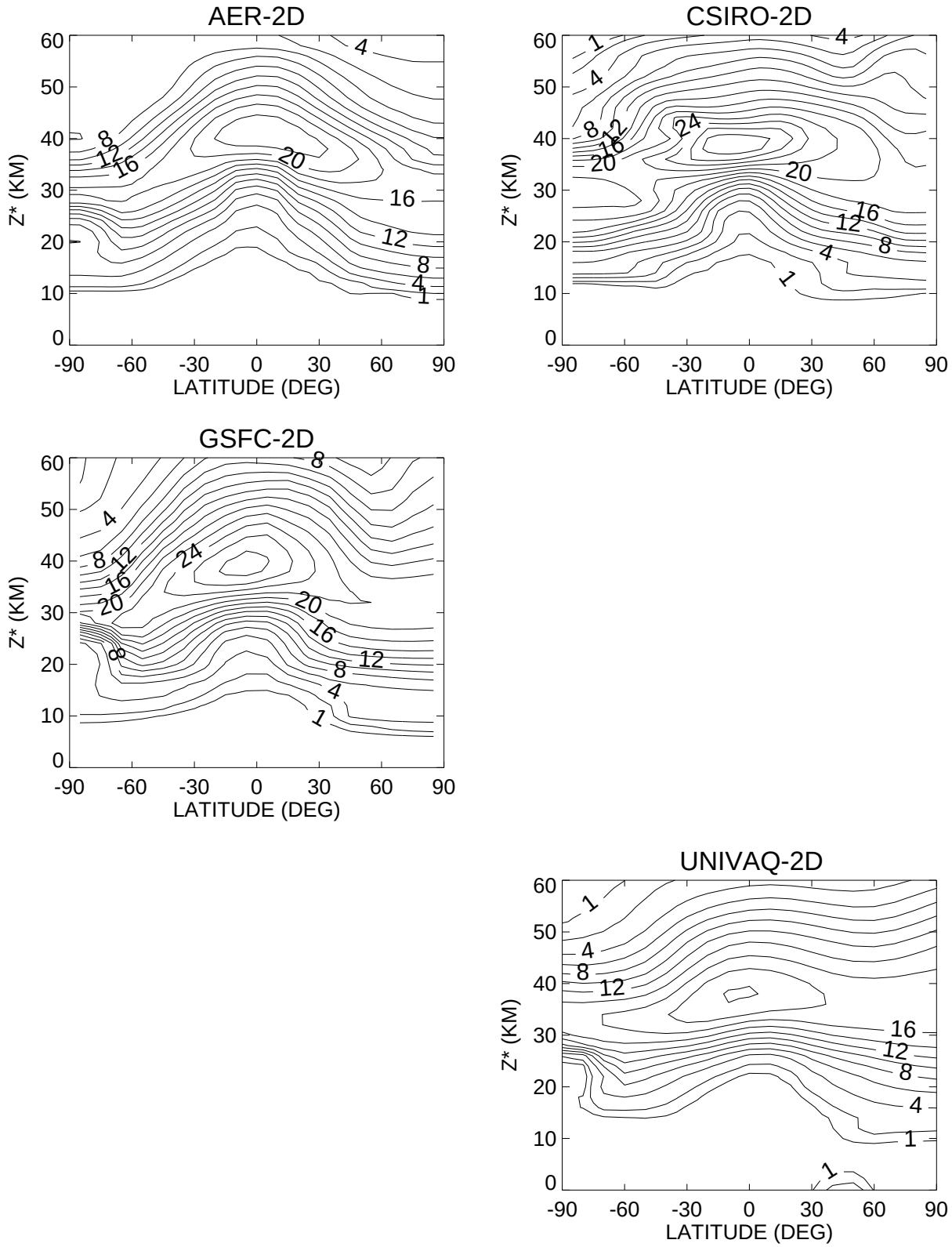

Figure 3.75: Calculated NO_y mixing ratios (ppbv) as a function of latitude and altitude in June for Scenario G, the 2050 background atmosphere with the subsonic fleet projected to 2050 using the IPCC IS92e high demand scenario. Contours are 1 and 2 to 28 by 2 ppbv.

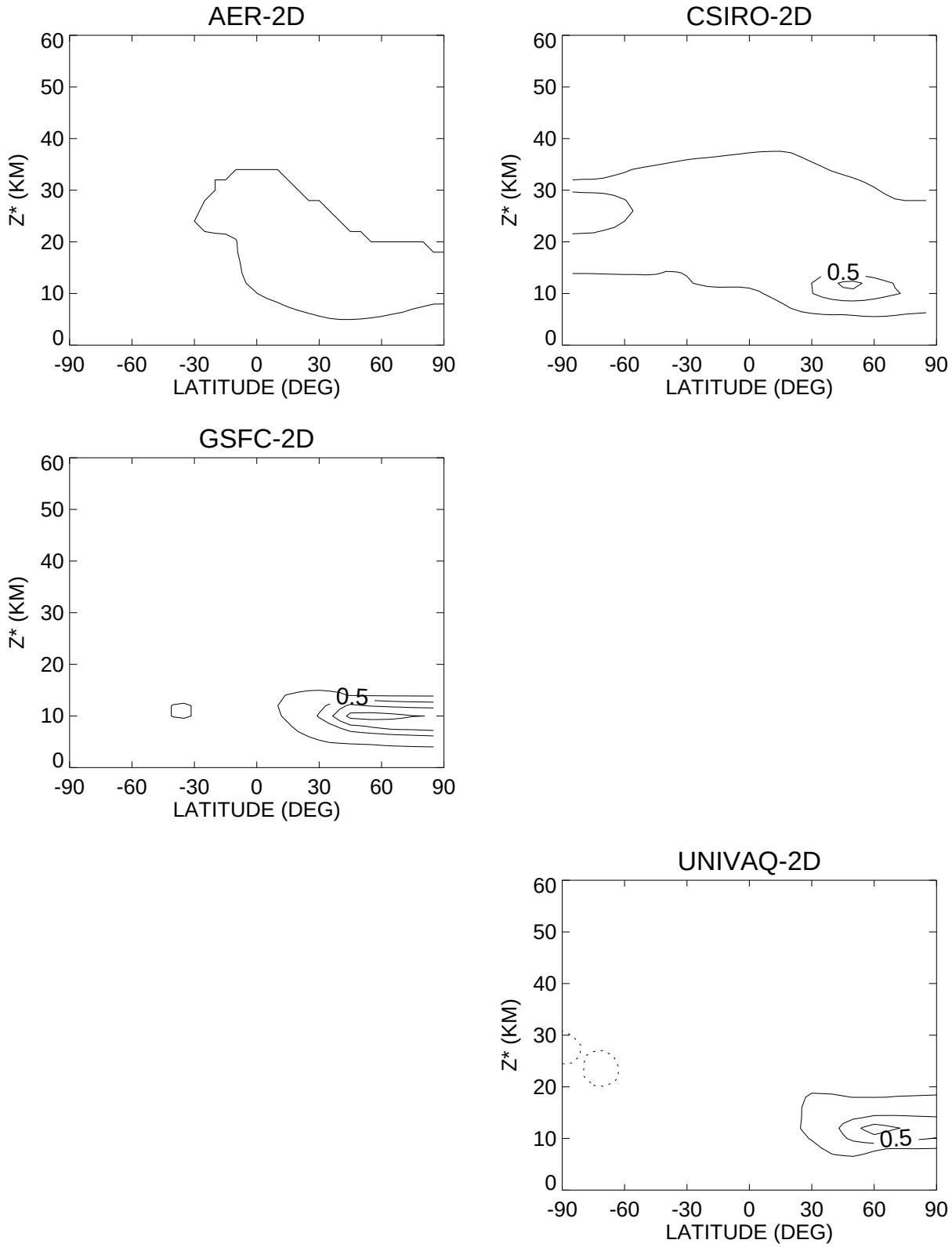

Figure 3.76: Percent change in calculated NO_y mixing ratio (ppbv) in June for Scenario G relative to Scenario D9. Scenario G uses a subsonic fleet projected to 2050 using the IPCC IS92e high demand scenario, while Scenario D9 used the 2015 projected subsonic fleet. Contours are -0.5, 0, 0.5, 1.0, and 1.5.

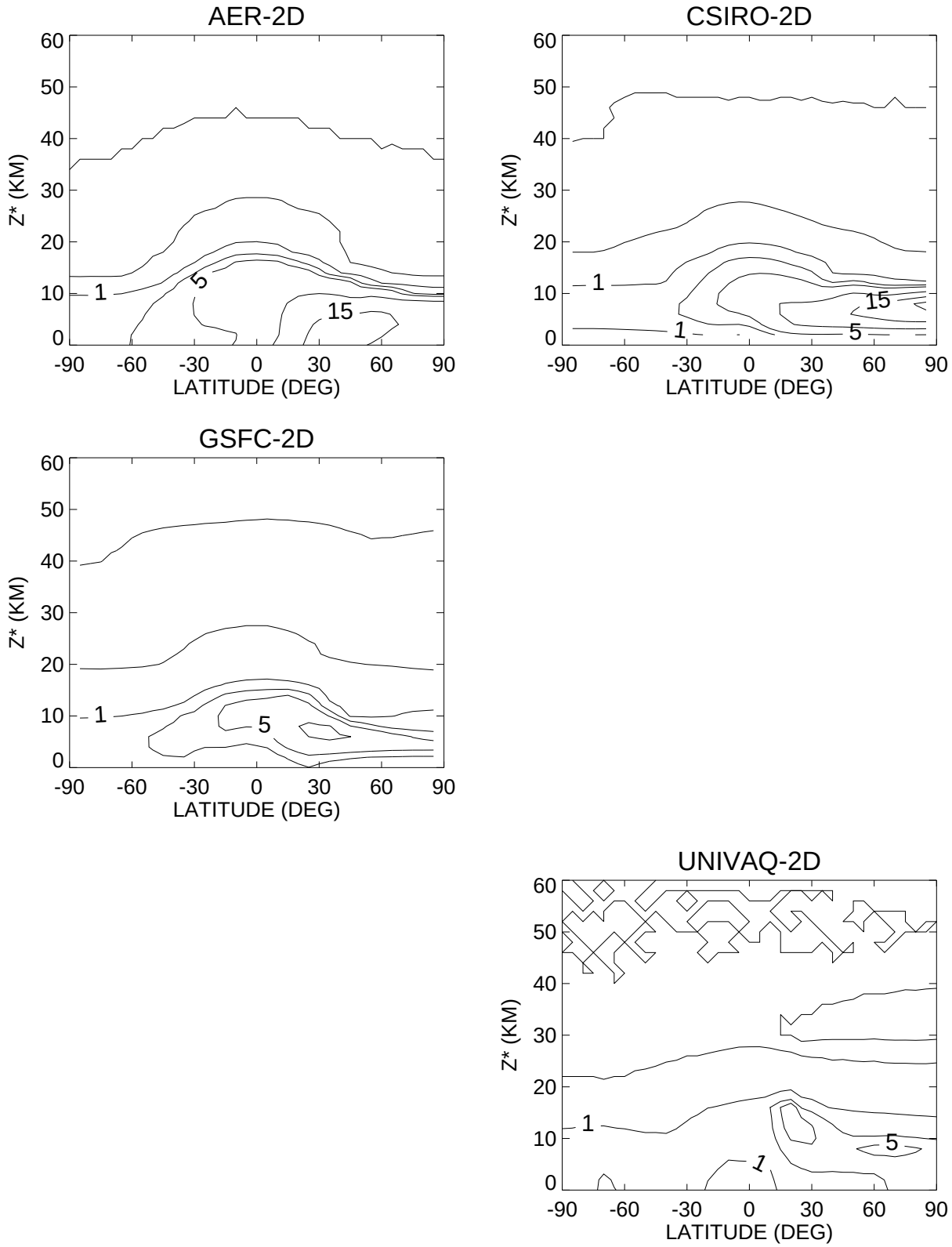

Figure 3.77: Percent change in ozone concentration between Scenarios G and D9 in June of 2015. Scenario G uses a subsonic fleet projected to 2050 using the IPCC IS92e high demand scenario, while Scenario D9 used the 2015 projected subsonic fleet. Contours are 0, 1, 3, 5, 10, 15, and 20.

Bibliography

[1] IPCC (International Panel on Climate Change), *Climate Change 1992: The Supplemental Report to the IPCC Scientific Assessment,* J. T. Houghton, B. A. Callander, and S. Varney (Eds.), Cambridge University Press, Cambridge, U.K., 1992.

[2] IPCC (International Panel on Climate Change), *Climate Change 1995: The Science of Climate Change,* J. T. Houghton, L. G. Meira Filho, B. A. Callander, N. Harris, A. Kattenberg, and K. Maskell (Eds.), Cambridge University Press, Cambridge, U.K., 1995.

[3] World Meteorological Organization (WMO), Scientific Assessment of Ozone Depletion: 1991, Global Ozone Res. and Monit. Proj., *Rep. 25,* Geneva, Switzerland, 1992.

Chapter 4

HSCT Perturbations for 2015

A total of 35 scenarios for the 2015 atmosphere were used in the IPCC supersonic aircraft assessment. Not all models performed all scenario calculations. The scenarios were chosen to explore the effects of parametric modifications in the HSCT aircraft fleet, such as EI(NO_x), fleet size, cruise altitude, EI(SO_2), and SO_2 gas-to-particle conversion fraction. The effect of modifications in the background atmosphere was also explored by varying the background aerosol surface area density, the chlorine loading level, the PSC parameterization, and the microphysical treatment. A summary of the scenarios considered, along with the scenario designations, for 2015 is given in Table 4.1. The reference atmosphere used for each scenario is listed in the table. Perturbations are given relative to the reference scenario, which includes identical boundary conditions and the same model formulation, but omits the HSCT fleet.

Table 4.1: Specifications for Supersonic Aircraft Emission Scenarios in 2015

Scenario	Cl_y (ppbv)	Fleet Size	EI(NO_x)	Cruise Altitude	SAD Description	Special	Ref. Atm.
S1a	3.0	500	5	Std	SA0	No H_2O	D
S1b	3.0	500	0	Std	SA0		D
S1c	3.0	500	5	Std	SA0		D
S1d	3.0	500	10	Std	SA0		D
S1e	3.0	500	15	Std	SA0		D
S1f	3.0	500	5	Std	SA1		D
S1g	3.0	500	10	Std	SA1		D
S1h	3.0	500	5	Std	SA3		D
S1i	3.0	1000	5	Std	SA0		D
S1j	3.0	1000	10	Std	SA0		D
S1k	3.0	500	5	Std	SA5		D
S1l	3.0	500	5	Std	SA7		D
S2a	3.0	500	5	+2 km	SA0		D
S2b	3.0	500	5	-2 km	SA0		D
S2c	3.0	500	10	-2 km	SA0		D
S2d	3.0	500	15	-2 km	SA0		D
S2e	3.0	1000	5	-2 km	SA0		D
S3a	3.0	500	0	Std	4xSA0		D3
S3b	3.0	500	5	Std	4xSA0		D3
S3c	3.0	500	10	Std	4xSA0		D3
S3d	3.0	500	15	Std	4xSA0		D3
S3e	3.0	500	5	Std	4xSA0+(SA1-SA0)		D3
S3f	3.0	500	5	Std	4xSA0+(SA3-SA0)		D3
S4a	3.0	500	0	Std	SA0	No PSCs	D4
S4b	3.0	500	5	Std	SA0	No PSCs	D4
S4c	3.0	500	5	Std	SA0	No PSCs, No H_2O	D4
S5a	1.0	500	5	Std	SA0		D5
S5b	1.0	500	5	Std	SA1		D5
S6a	4.0	500	5	Std	SA0		D6
S6b	4.0	500	5	Std	SA1		D6
S7a	3.0	500	5	Std	50% Particles	Microphysics	D7
S7b	3.0	500	5	+2 km	50% Particles	Microphysics	D7
S7c	3.0	500	5	-2 km	50% Particles	Microphysics	D7
S7d	3.0	500	10	Std	50% Particles	Microphysics	D7
S8a	3.0	500	5	Std	100% Particles	Microphysics	D8

4.1 H_2O Perturbations

Because EI(H_2O) is invariant, only modifications in fleet size and cruise altitude impact the HSCT perturbation to stratospheric water vapor. Figure 4.1 shows the change in H_2O in ppmv for June due to emission of H_2O by a fleet of 500 HSCT aircraft operating in 2015 (Scenario S1c). The maximum perturbation is located in the northern hemisphere lower stratosphere for all models. The LARC model produces the smallest maximum perturbations to H_2O of 0.2 ppmv. However, this model does not calculate H_2O mixing ratios in the stratosphere, but instead solves for the HSCT-emitted H_2O as a separate species and adds the perturbation to the otherwise fixed background H_2O. All other models calculate maximum H_2O perturbations of between 0.4 ppmv and 0.6 ppmv with the CSIRO, SCTM1, and SLIMCAT models at the lower end of this range. Differences in the way the models treat tropospheric H_2O has an impact on these calculated perturbations. Some models fix H_2O in the entire troposphere, while others fix H_2O only in the lower troposphere.

Vertical profiles of H_2O perturbation at 45^oN, the equator, and 45^oS are shown in Figures 4.2-4.4 for Scenario S1c. Profiles of all models are included in each plot to allow easy comparison. The GSFC model calculates the greatest perturbation in H_2O in the middle and upper stratosphere (above 25 km) at all latitudes and also the largest perturbation in the lower stratosphere at 45^oN. This indicates that the GSFC model has the longest residence time for the aircraft-emitted H_2O. The AER, UNIVAQ, and LLNL models have lower stratospheric H_2O perturbations at 45^oN only slightly less than the GSFC model, but much lower perturbations in the middle and upper stratosphere. The SCTM1 model calculates the lowest H_2O perturbation in the middle and upper stratosphere at all latitudes. The SLIMCAT model, though it has one of the lower perturbations at 45^oN in the lower stratosphere, has a perturbation in the middle stratosphere at the equator and 45^oS comparable with the GSFC model. This model must have a long stratospheric residence time for emitted H_2O, but rapidly transports the emitted material out of the northern hemisphere lower stratosphere.

Increases in H_2O due to emission by a fleet of 1000 HSCT aircraft in 2015 (Scenario S1i) are shown in Figure 4.5 for June conditions. Vertical profiles of this perturbation at 45^oN, the equator, and 45^oS are shown in Figures 4.6-4.8. Because the 1000 HSCT fleet is not simply scaled from the 500 HSCT fleet, but represents a different economic projection, the geographical distribution of emissions is different. This is apparent in the GSFC model results at 45^oN, which peak at 18 km for the 500 aircraft fleet and at 20 km for the 1000 aircraft fleet.

Scenario S2a represents a 500 aircraft HSCT fleet with cruise altitude adjusted upward by 2 km. H_2O perturbations for this scenario are shown in Figure 4.9 for June conditions of 2015. While the quantity of emitted H_2O is identical to that from Scenario S1c, the perturbation to H_2O is enhanced by 30-100%, depending on the model. The stratospheric residence time of emitted materials is considerably enhanced at higher emission altitudes relative to lower altitudes.

Vertical profiles of H_2O perturbation at 45^oN, the equator, and 45^oS are shown in Figures 4.10-4.12 for Scenario S2a. Compared with similar figures for Scenario S1c (Figures 4.2-4.4), it can be seen the the maximum perturbation at 45^oN occurs at 20-22 km rather than 18-20 km, and the relative perturbations between models are somewhat different. At 45^oN, the peak perturbation in the GSFC model is 30% greater than any other model for Scenario S2a, but only 15% greater than any other model for Scenario S1c.

Scenario S2b represents a 500 aircraft HSCT fleet with cruise altitude adjusted downward by 2 km. Figure 4.13 shows perturbations in H_2O for June conditions in 2015 from this emission scenario. The H_2O perturbations are reduced by 40-60% relative to the S1c-D scenario because the emissions are closer to the tropopause and more readily removed from the stratosphere. The maximum perturbations at 45^oN are 0.2 ppmv for the AER, CSIRO, and THINAIR models; 0.4 ppmv for the GSFC and LLNL models; and 0.5 ppmv for the UNIVAQ model.

Vertical profiles of H_2O perturbation at 45^oN, the equator, and 45^oS are shown in Figures 4.14-4.16 for Scenario S2b. Maximum perturbation at 45^oN occurs at 16 km for this scenario. The UNIVAQ model calculated the largest perturbation in the 12-20 km altitude region. The GSFC and UNIVAQ models calculate much larger perturbations than the other models from 8-12 km. Perturbations in the upper stratosphere are only 0.1-0.2 ppmv at 45^oN and 0.1 ppmv at the equator and 45^oS.

Figure 4.17 shows H_2O perturbations from Scenario S2e-D, representing 1000 HSCT aircraft operating at 2 km below the nominal cruise altitude. The perturbation is roughly linear with fleet size (compare with Scenario S2b). Compared with Scenario S1i (same fleet size but different cruise altitude), the H_2O

perturbations are reduced by 50% for the AER and CSIRO models and by 30% for the GSFC and LLNL models due to the lowered cruise altitude. Vertical profiles of the H_2O perturbation at 45^oN, the equator, and 45^oS are shown in Figures 4.18-4.20 for this scenario.

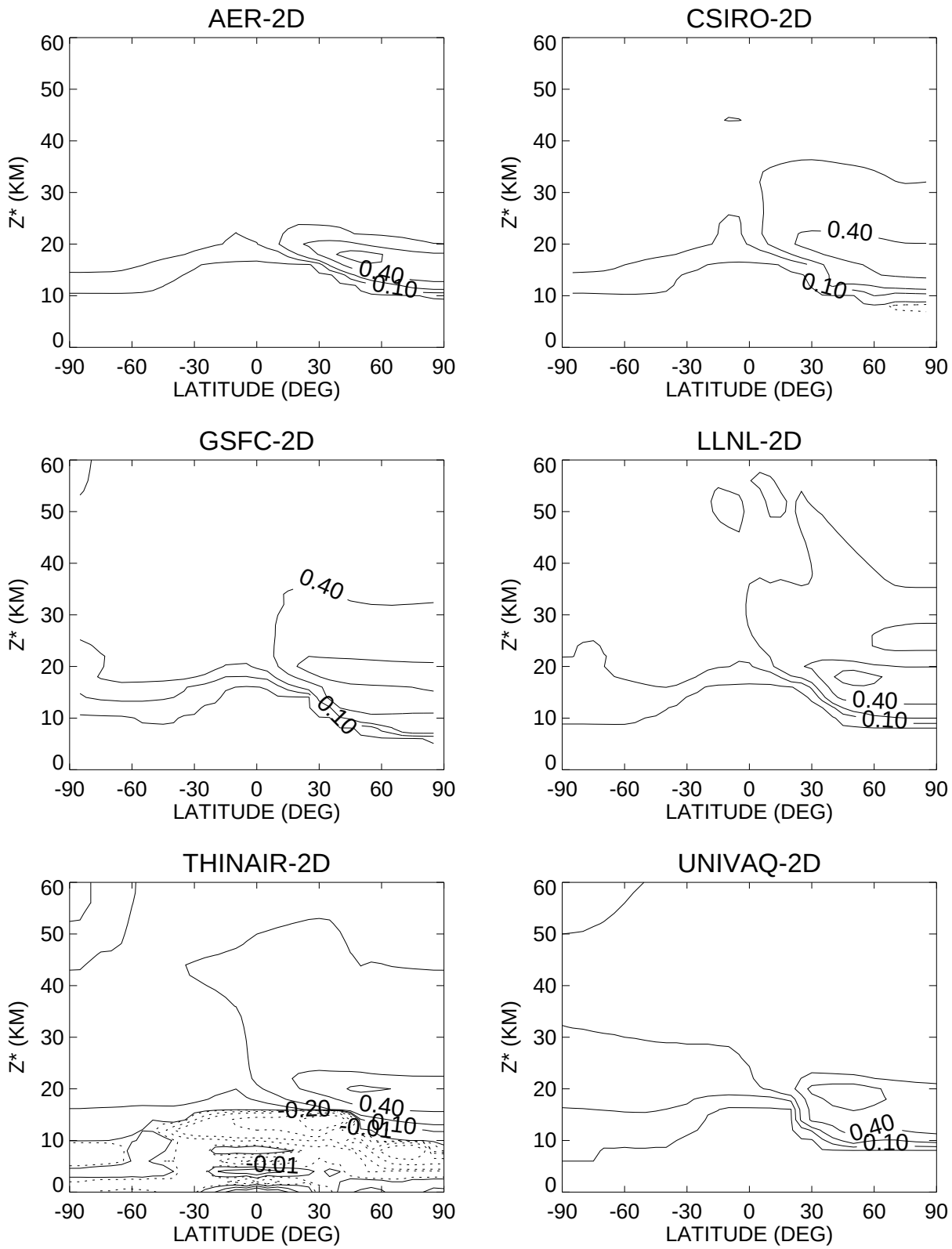

Figure 4.1: Calculated perturbation to H_2O (ppmv) as a function of latitude and altitude in June of 2015 due to H_2O emissions from a fleet of 500 HSCT aircraft under Scenario S1c relative to Scenario D. Contours are -0.6, -0.4, -0.2, -0.1, -0.01, 0.01, 0.1, 0.2, 0.4, 0.6 ppmv.

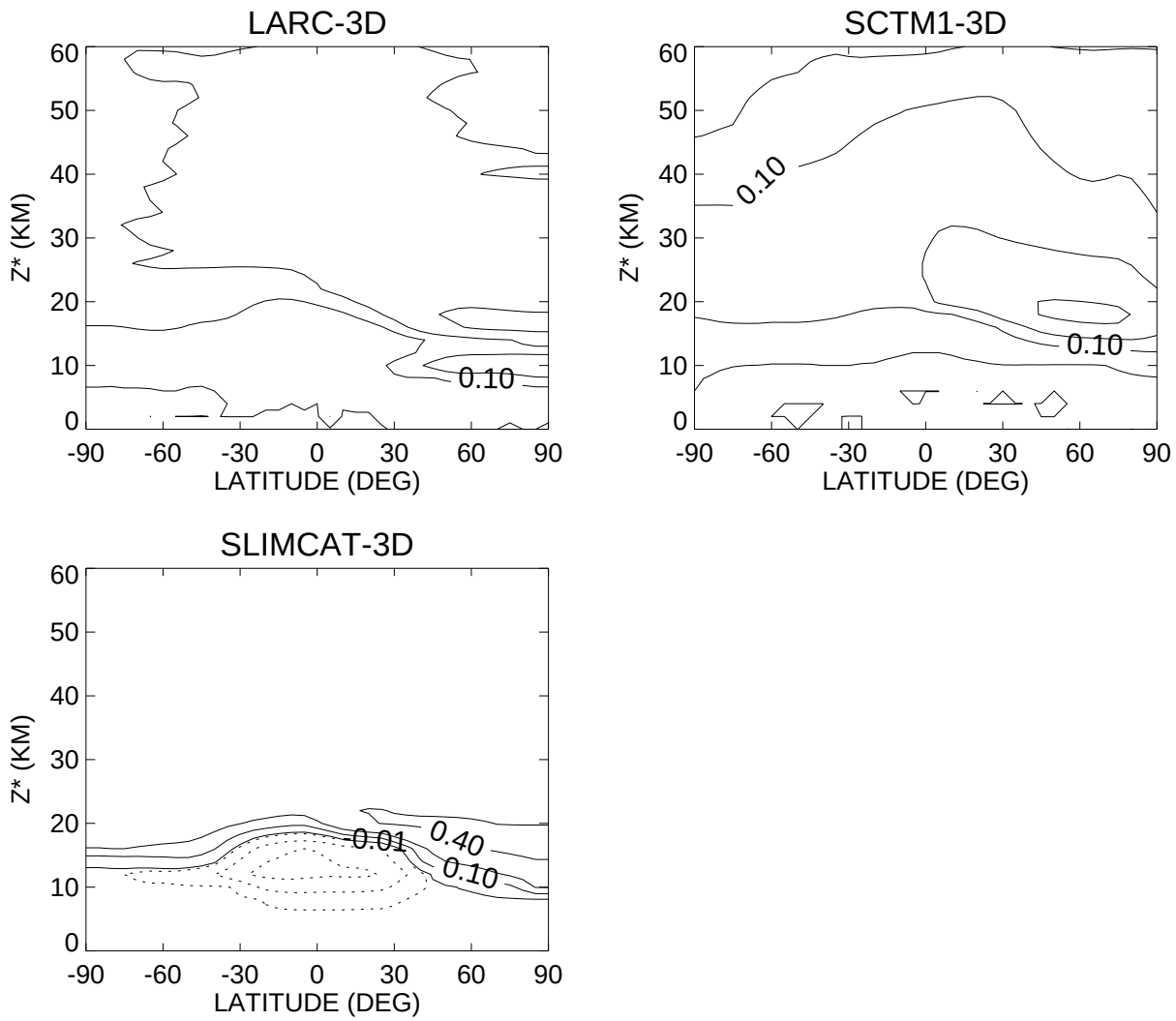

Figure 4.1: continued

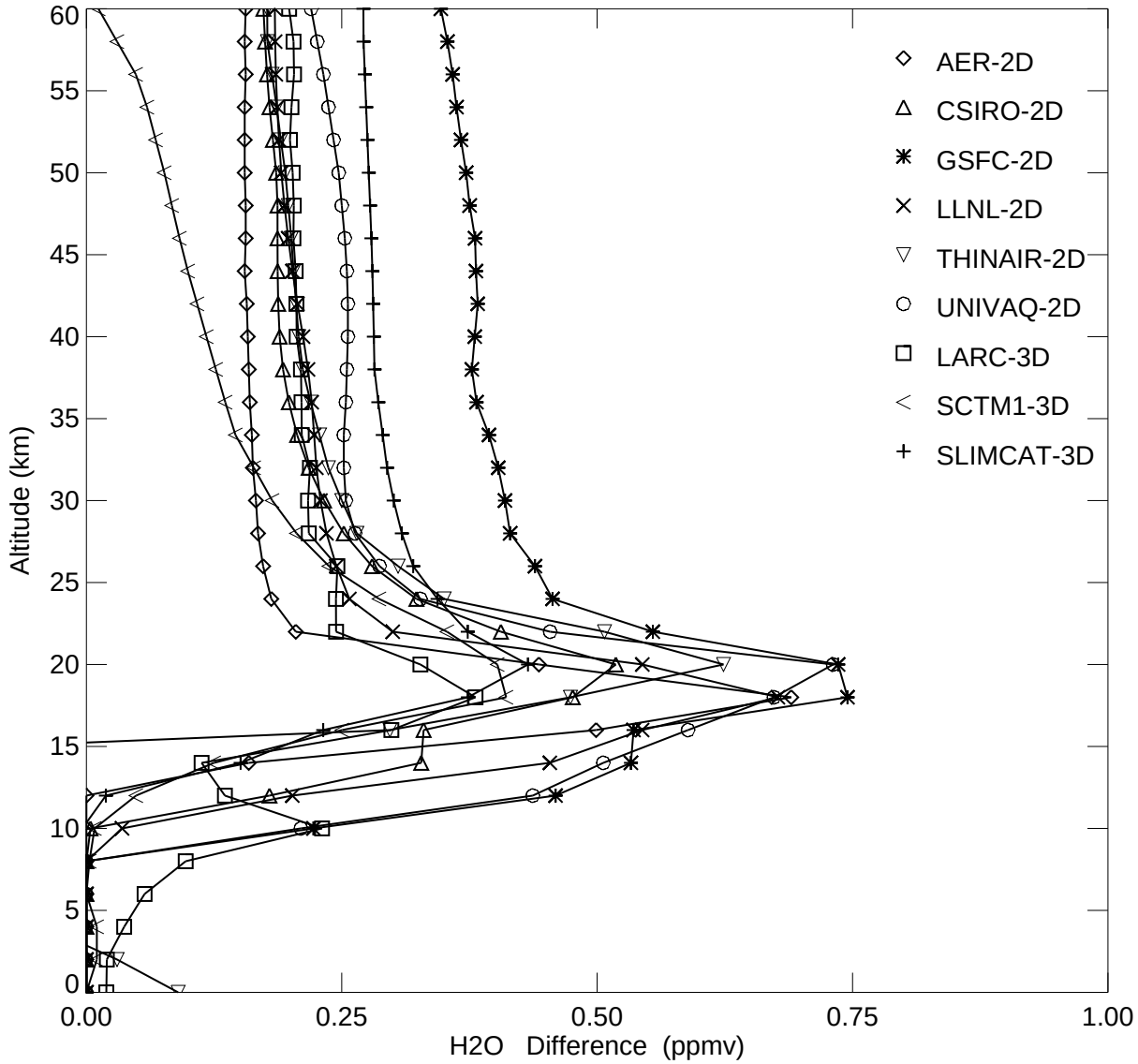

Figure 4.2: Calculated perturbations to H_2O (ppmv) as a function of altitude at 45°N in June of 2015 due to H_2O emissions from a fleet of 500 HSCT aircraft under Scenario S1c relative to Scenario D.

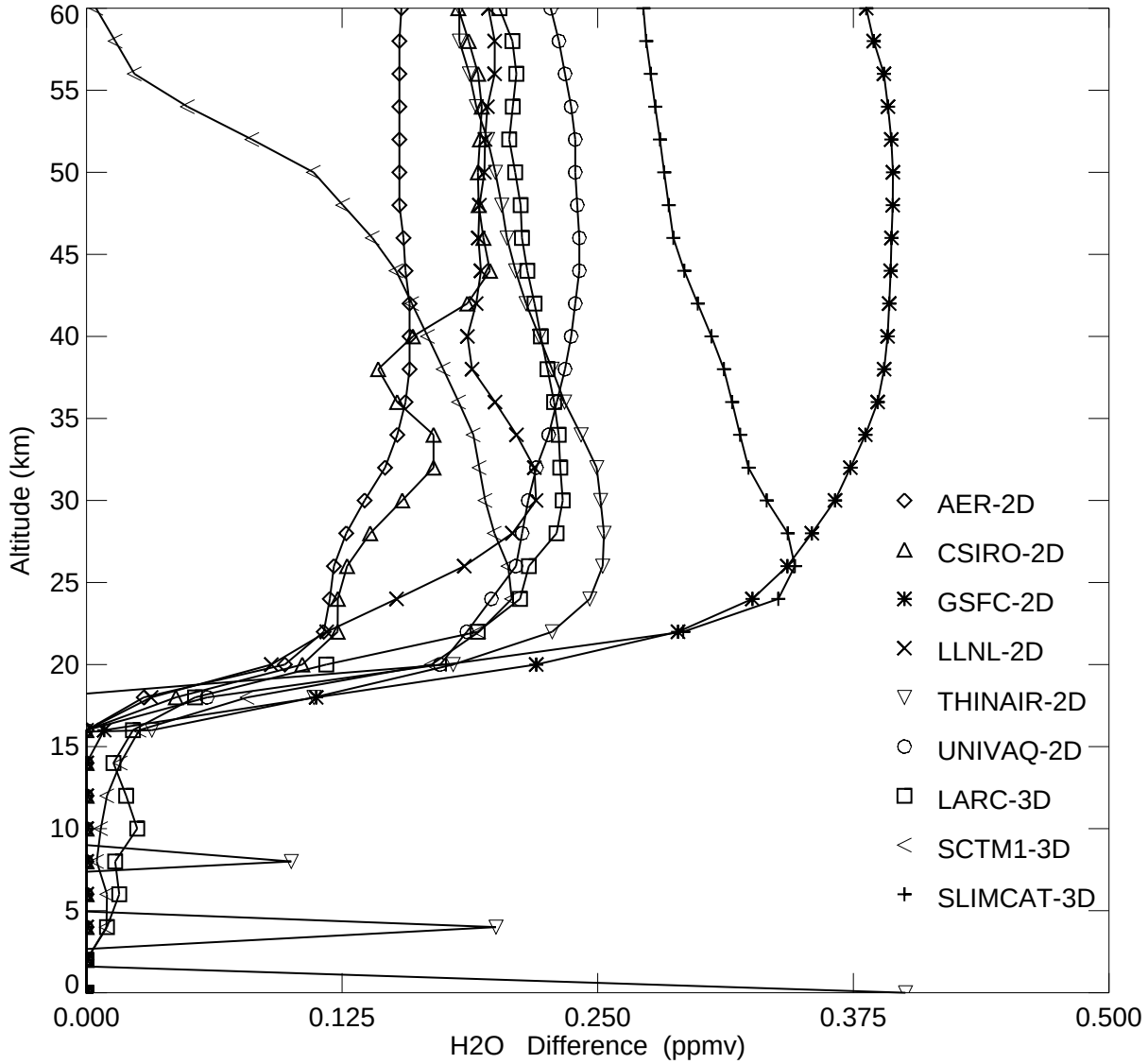

Figure 4.3: Calculated perturbations to H_2O (ppmv) as a function of altitude at the equator in June of 2015 due to H_2O emissions from a fleet of 500 HSCT aircraft under Scenario S1c relative to Scenario D.

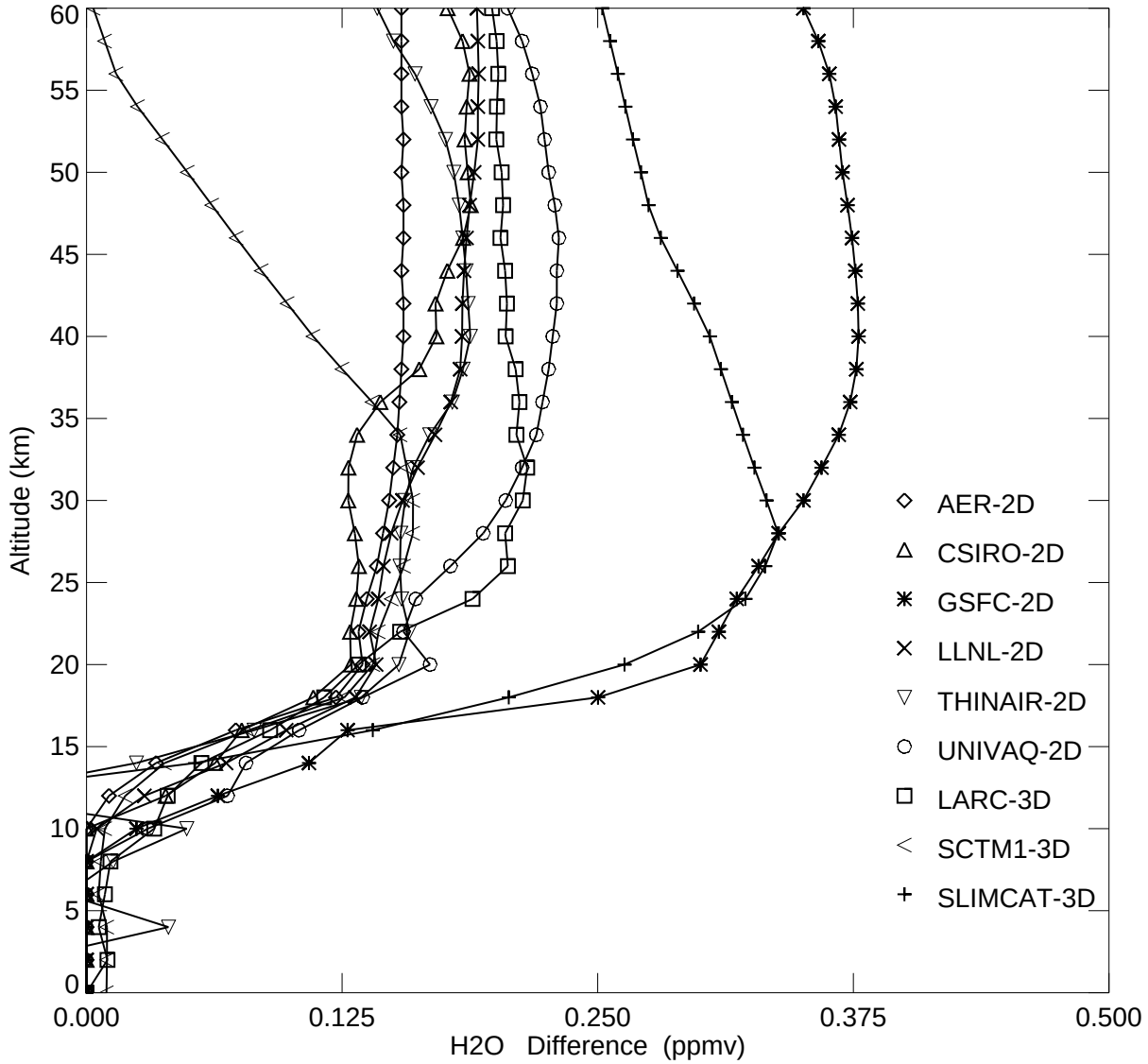

Figure 4.4: Calculated perturbations to H_2O (ppmv) as a function of altitude at 45°S in June of 2015 due to H_2O emissions from a fleet of 500 HSCT aircraft under Scenario S1c relative to Scenario D.

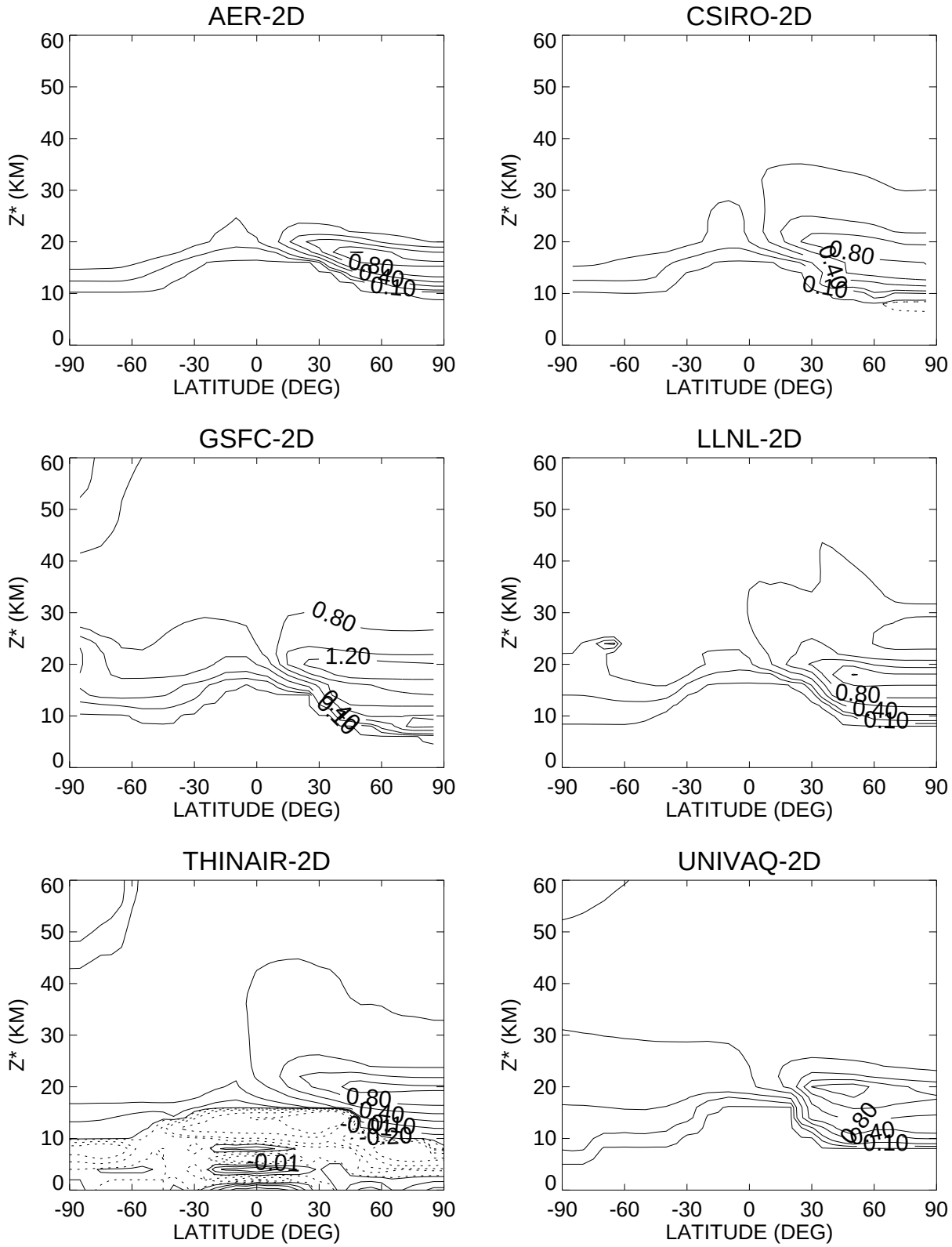

Figure 4.5: Calculated perturbations to H_2O (ppmv) as a function of latitude and altitude in June of 2015 due to H_2O emissions from a fleet of 1000 HSCT aircraft under Scenario S1i relative to Scenario D. Contours are -0.6, -0.4, -0.2, -0.1, -0.01, 0.01, 0.1, and 0.2 to 1.2 by 0.2 ppmv.

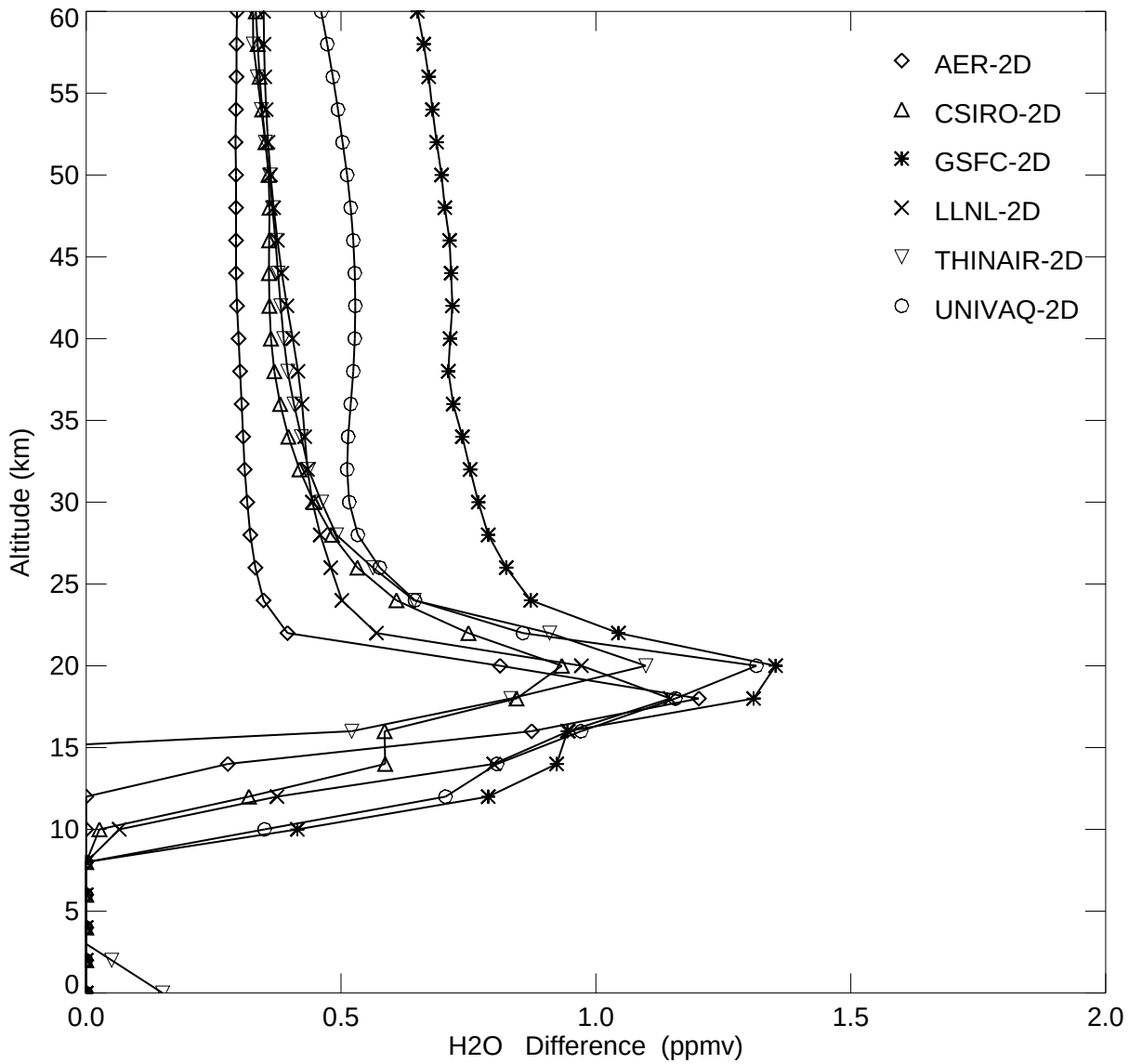

Figure 4.6: Calculated perturbations to H_2O (ppmv) as a function of altitude at 45°N in June of 2015 due to H_2O emissions from a fleet of 1000 HSCT aircraft under Scenario S1i relative to Scenario D.

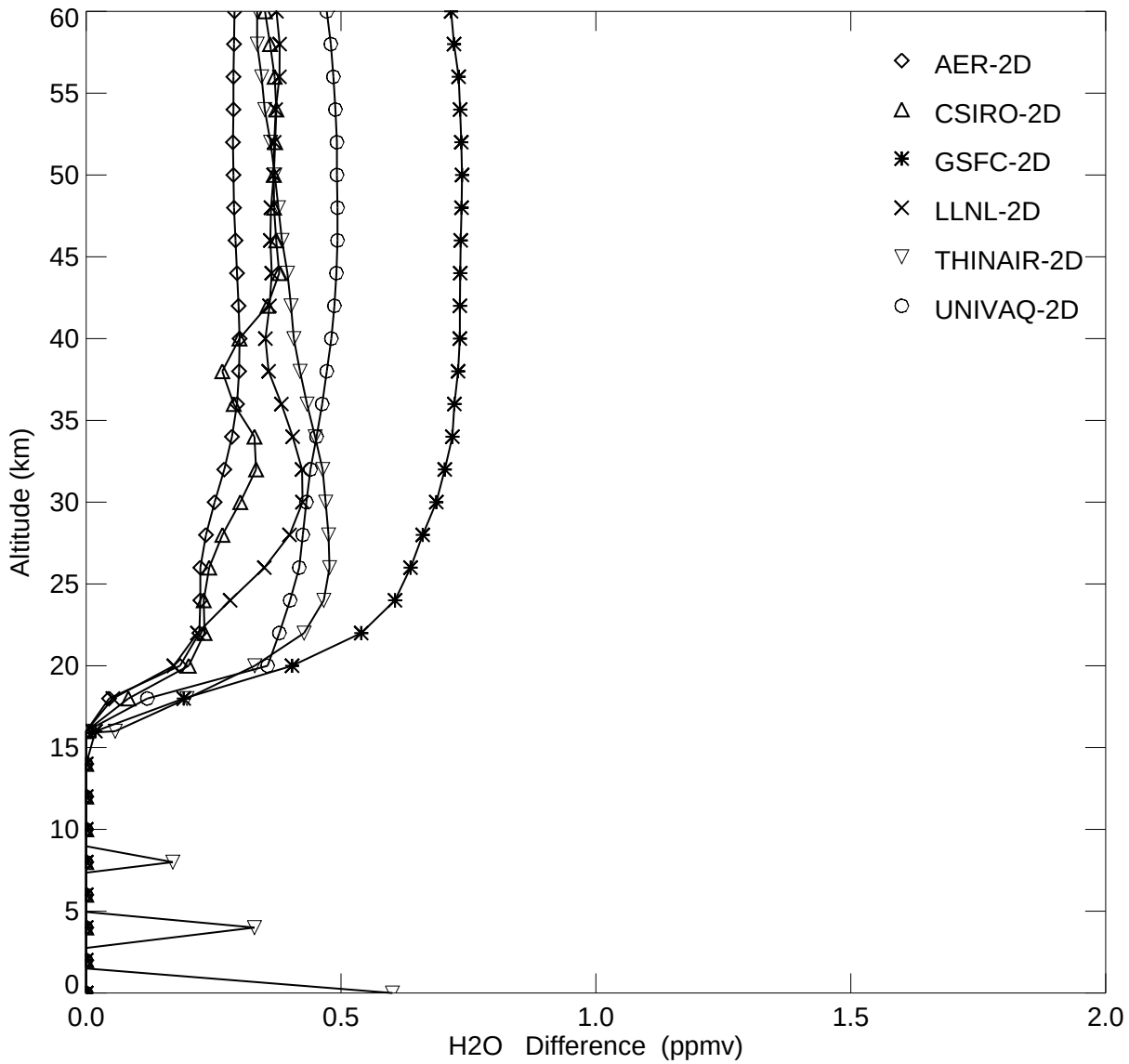

Figure 4.7: Calculated perturbations to H_2O (ppmv) as a function of altitude at the equator in June of 2015 due to H_2O emissions from a fleet of 1000 HSCT aircraft under Scenario S1i relative to Scenario D.

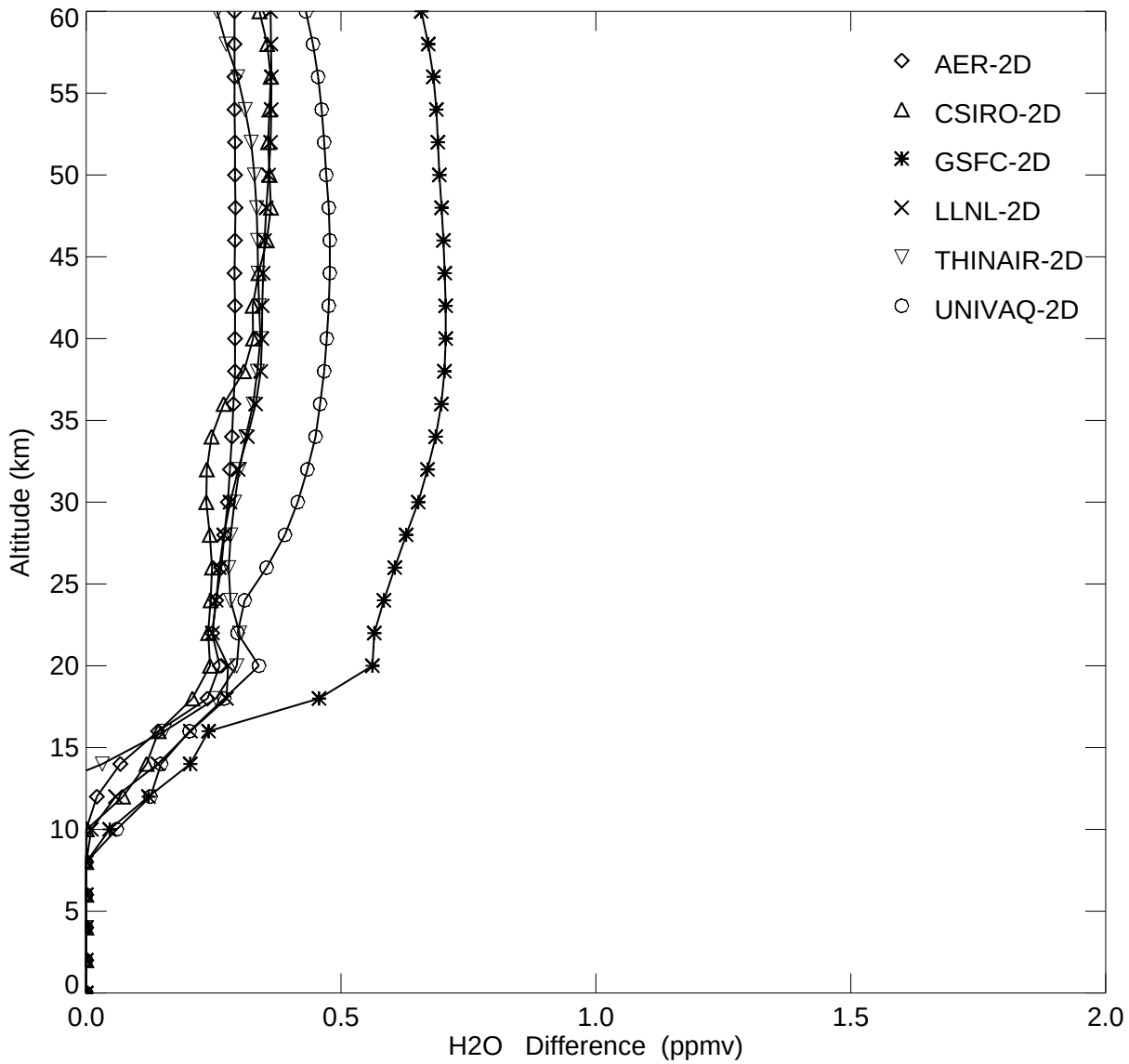

Figure 4.8: Calculated perturbations to H_2O (ppmv) as a function of altitude at 45°S in June of 2015 due to H_2O emissions from a fleet of 1000 HSCT aircraft under Scenario S1i relative to Scenario D.

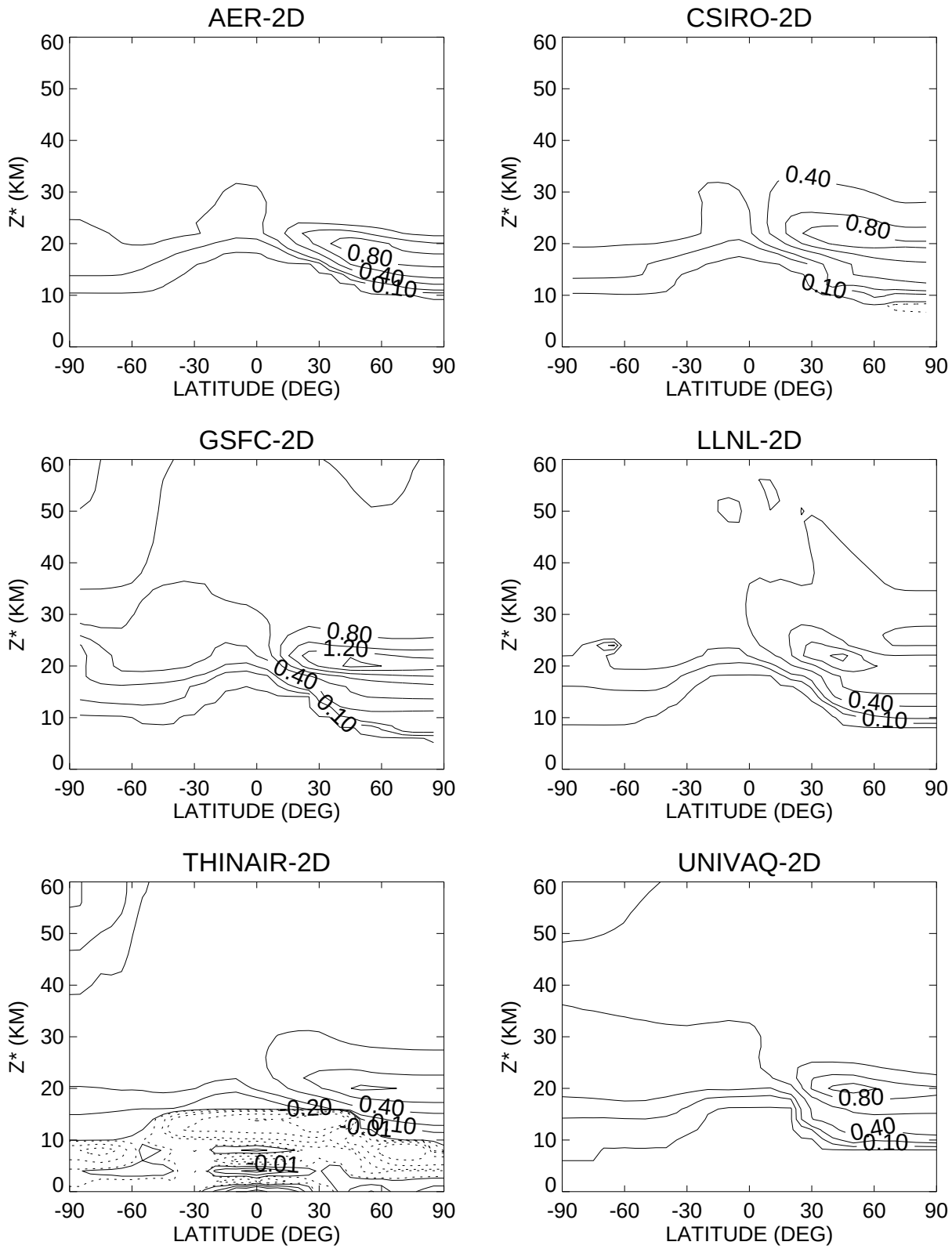

Figure 4.9: Calculated perturbations to H_2O (ppmv) as a function of latitude and altitude in June of 2015 due to H_2O emissions from a fleet of 500 HSCT aircraft operating at 2 km above nominal cruise altitude under Scenario S2a relative to Scenario D. Contours are -0.6, -0.4, -0.2, -0.1, -0.01, 0.01, 0.1, and 0.2 to 1.4 by 0.2 ppmv.

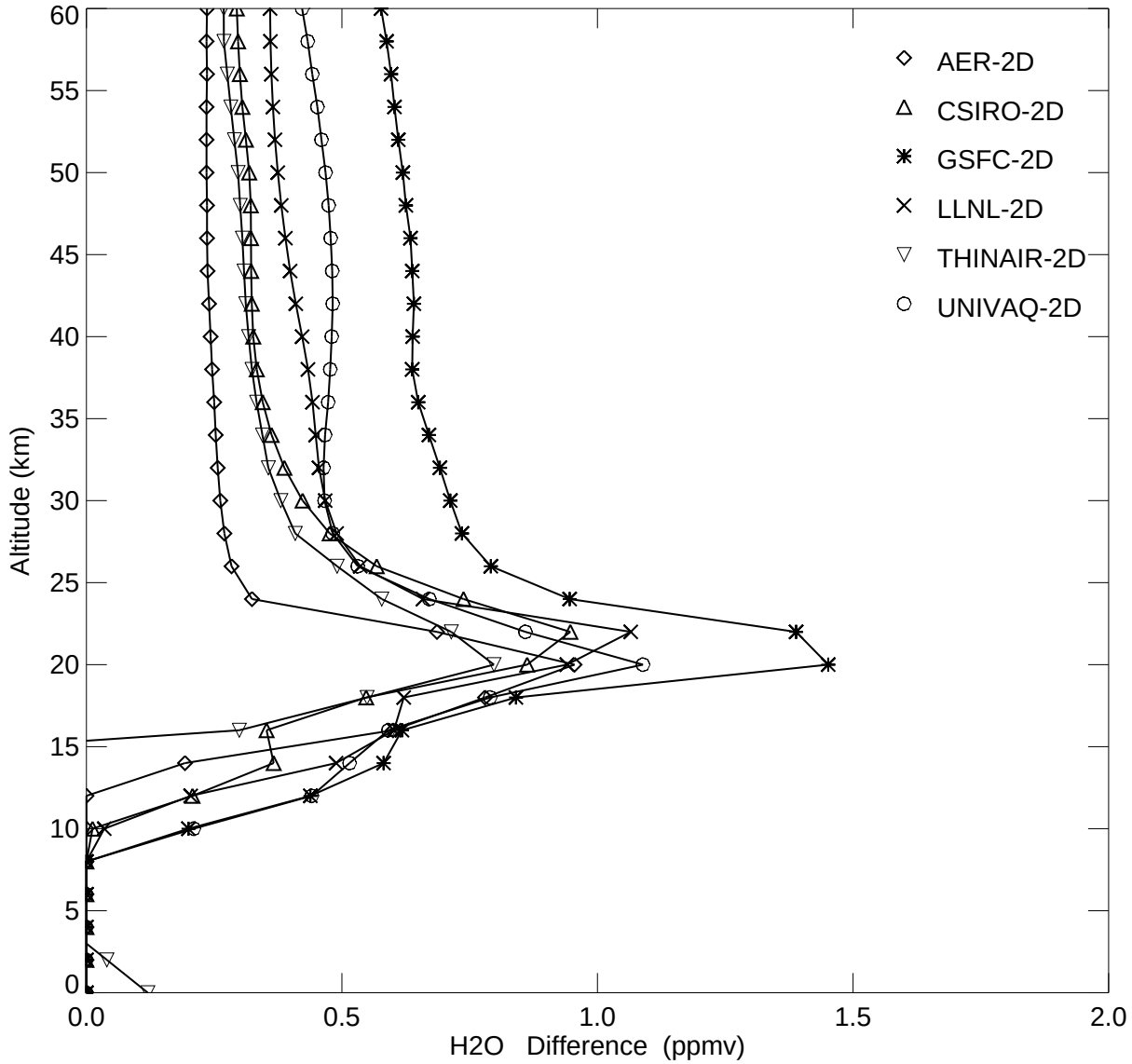

Figure 4.10: Calculated perturbations to H_2O (ppmv) as a function of altitude at 45°N in June of 2015 due to H_2O emissions from a fleet of 500 HSCT aircraft operating at 2 km above nominal cruise altitude under Scenario S2a relative to Scenario D.

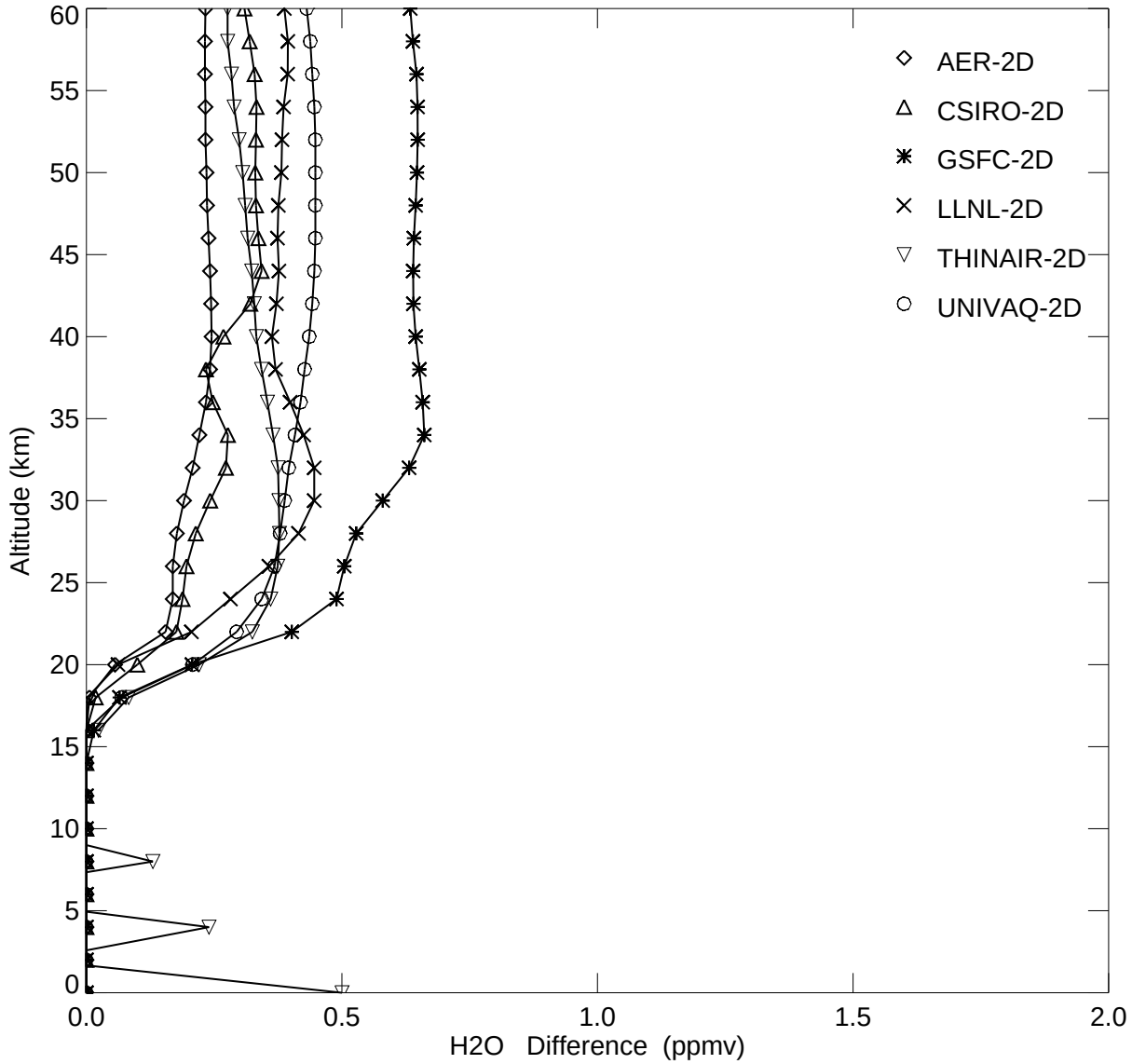

Figure 4.11: Calculated perturbations to H_2O (ppmv) as a function of altitude at the equator in June of 2015 due to H_2O emissions from a fleet of 500 HSCT aircraft operating at 2 km above nominal cruise altitude under Scenario S2a relative to Scenario D.

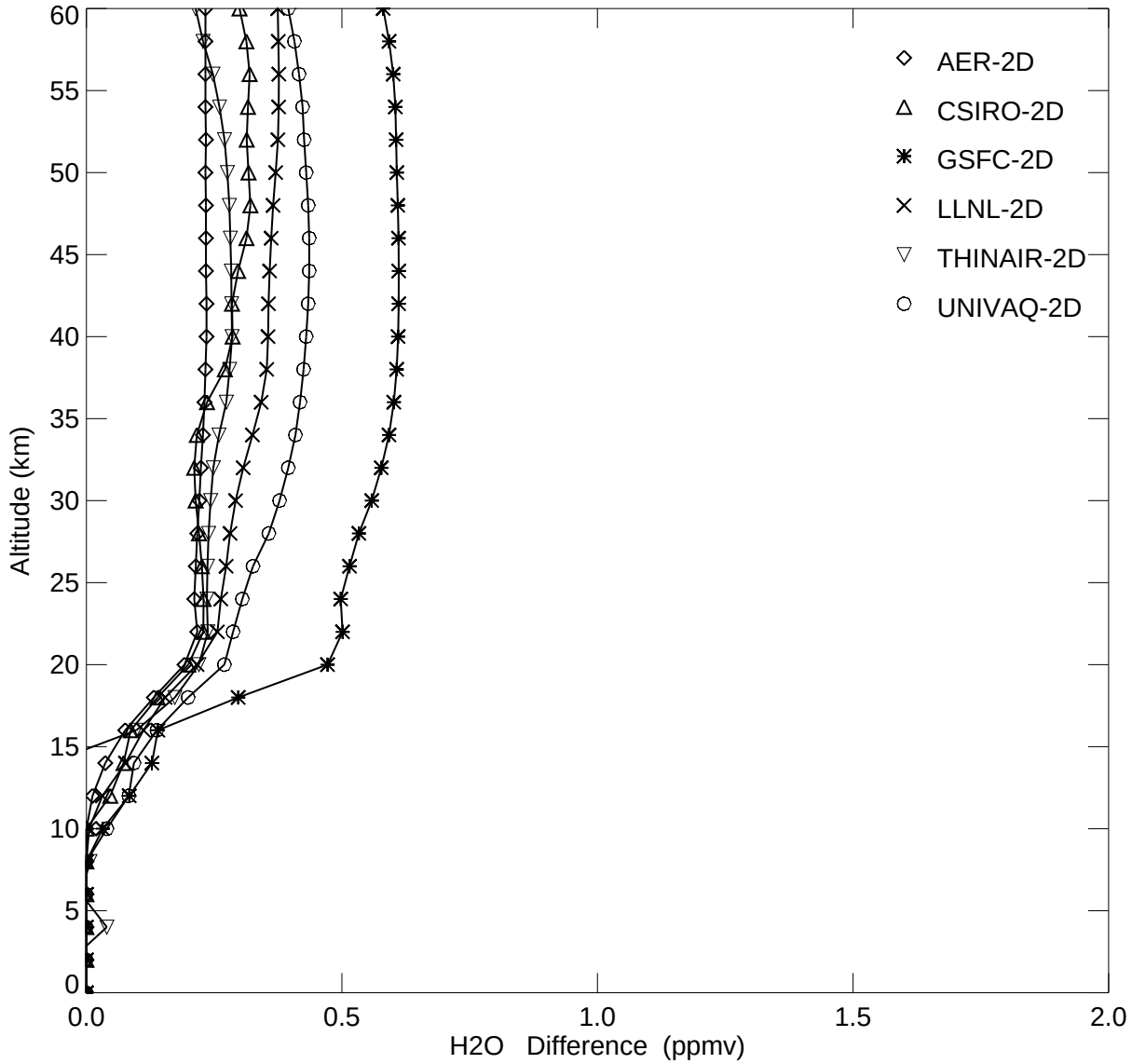

Figure 4.12: Calculated perturbations to H_2O (ppmv) as a function of altitude at 45^oS in June of 2015 due to H_2O emissions from a fleet of 500 HSCT aircraft operating at 2 km above nominal cruise altitude under Scenario S2a relative to Scenario D.

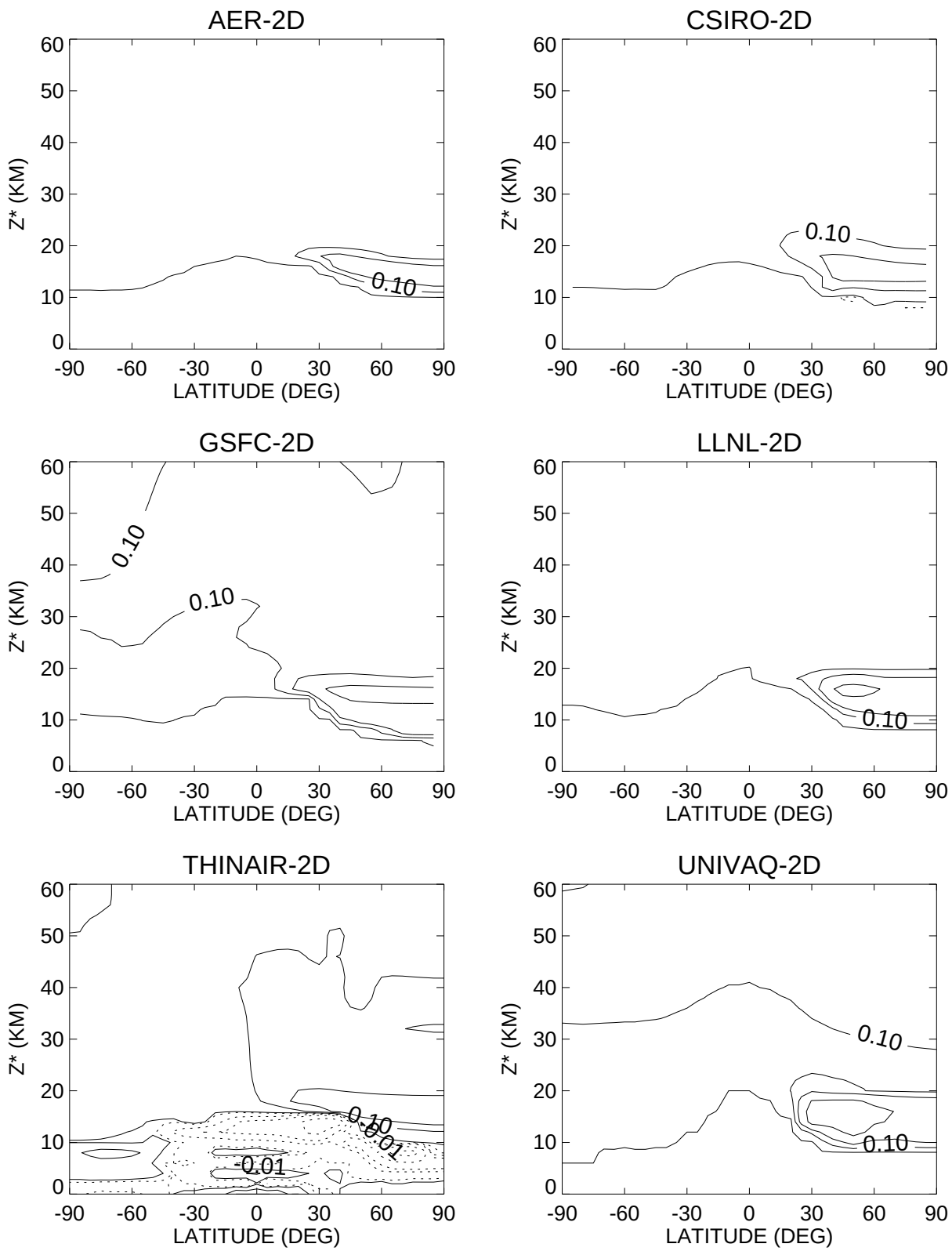

Figure 4.13: Calculated perturbations to H_2O (ppmv) as a function of latitude and altitude in June of 2015 due to H_2O emissions from a fleet of 500 HSCT aircraft operating at 2 km below nominal cruise altitude under Scenario S2b relative to Scenario D. Contours are -0.4, -0.2, -0.1, -0.01, 0.01, 0.1, 0.2, 0.4 ppmv.

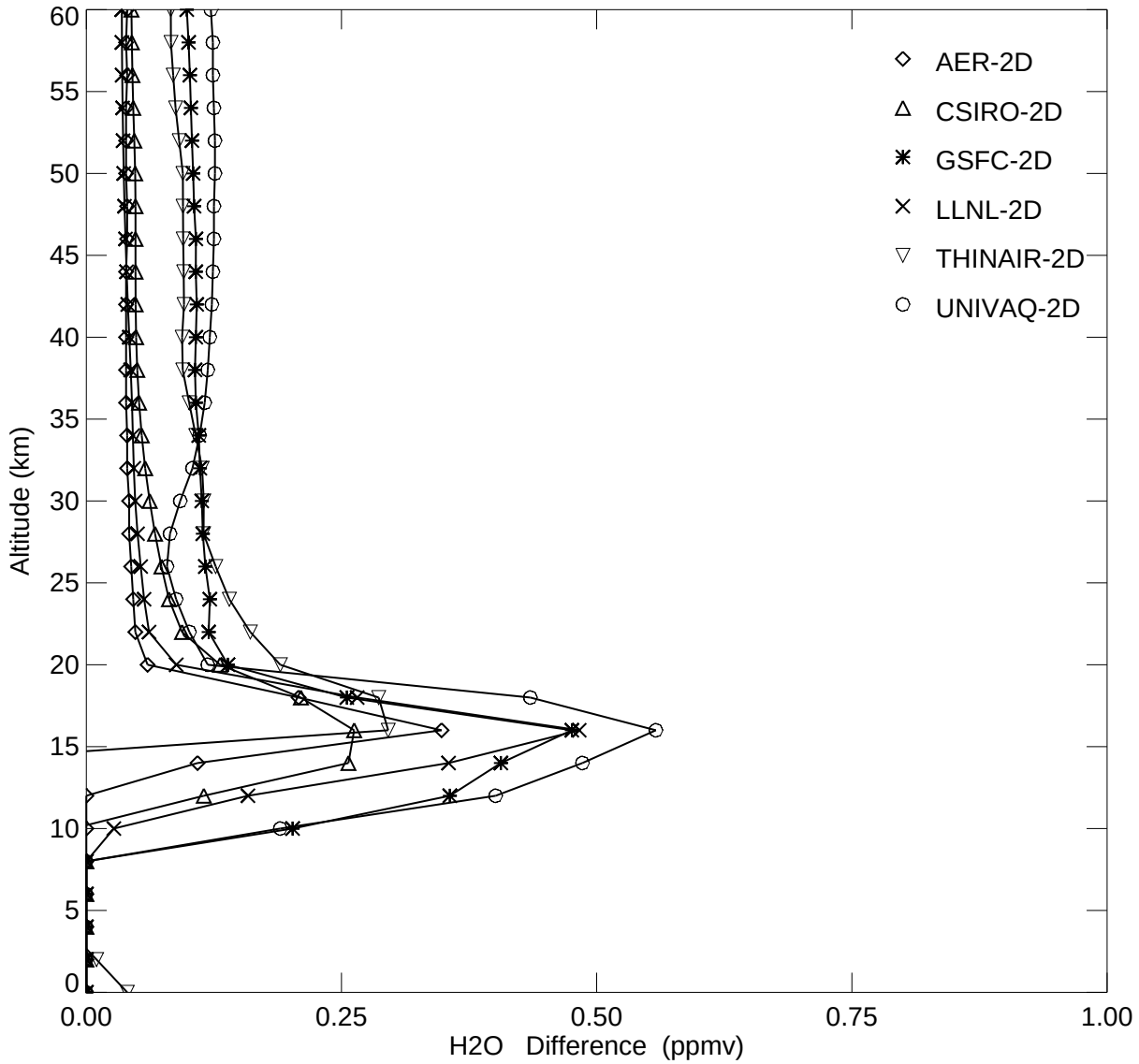

Figure 4.14: Calculated perturbations to H_2O (ppmv) as a function of altitude at 45^oN in June of 2015 due to H_2O emissions from a fleet of 500 HSCT aircraft operating at 2 km below nominal cruise altitude under Scenario S2b relative to Scenario D.

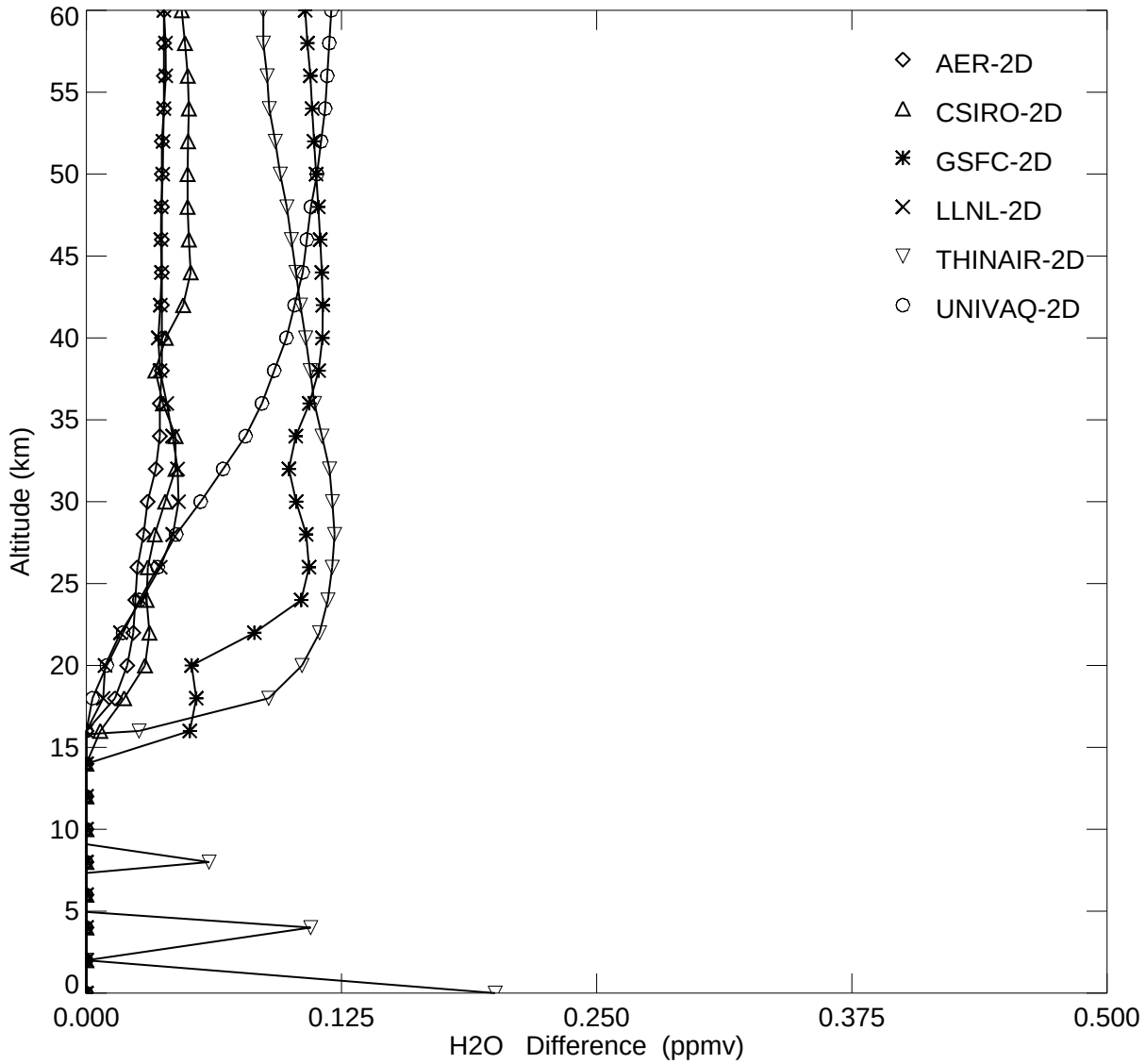

Figure 4.15: Calculated perturbations to H_2O (ppmv) as a function of altitude at the equator in June of 2015 due to H_2O emissions from a fleet of 500 HSCT aircraft operating at 2 km below nominal cruise altitude under Scenario S2b relative to Scenario D.

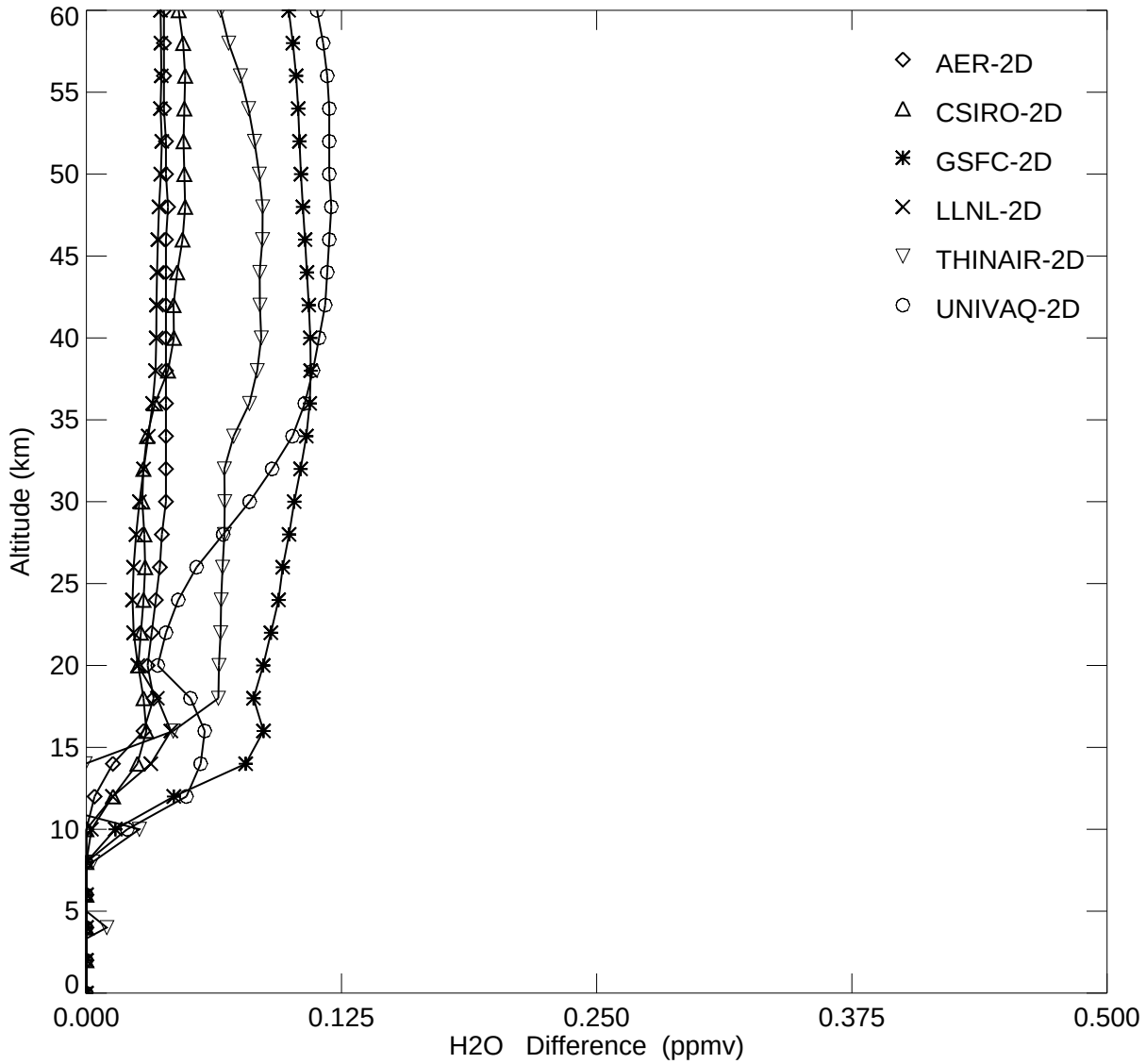

Figure 4.16: Calculated perturbations to H_2O (ppmv) as a function of altitude at 45^oS in June of 2015 due to H_2O emissions from a fleet of 500 HSCT aircraft operating at 2 km below nominal cruise altitude under Scenario S2b relative to Scenario D.

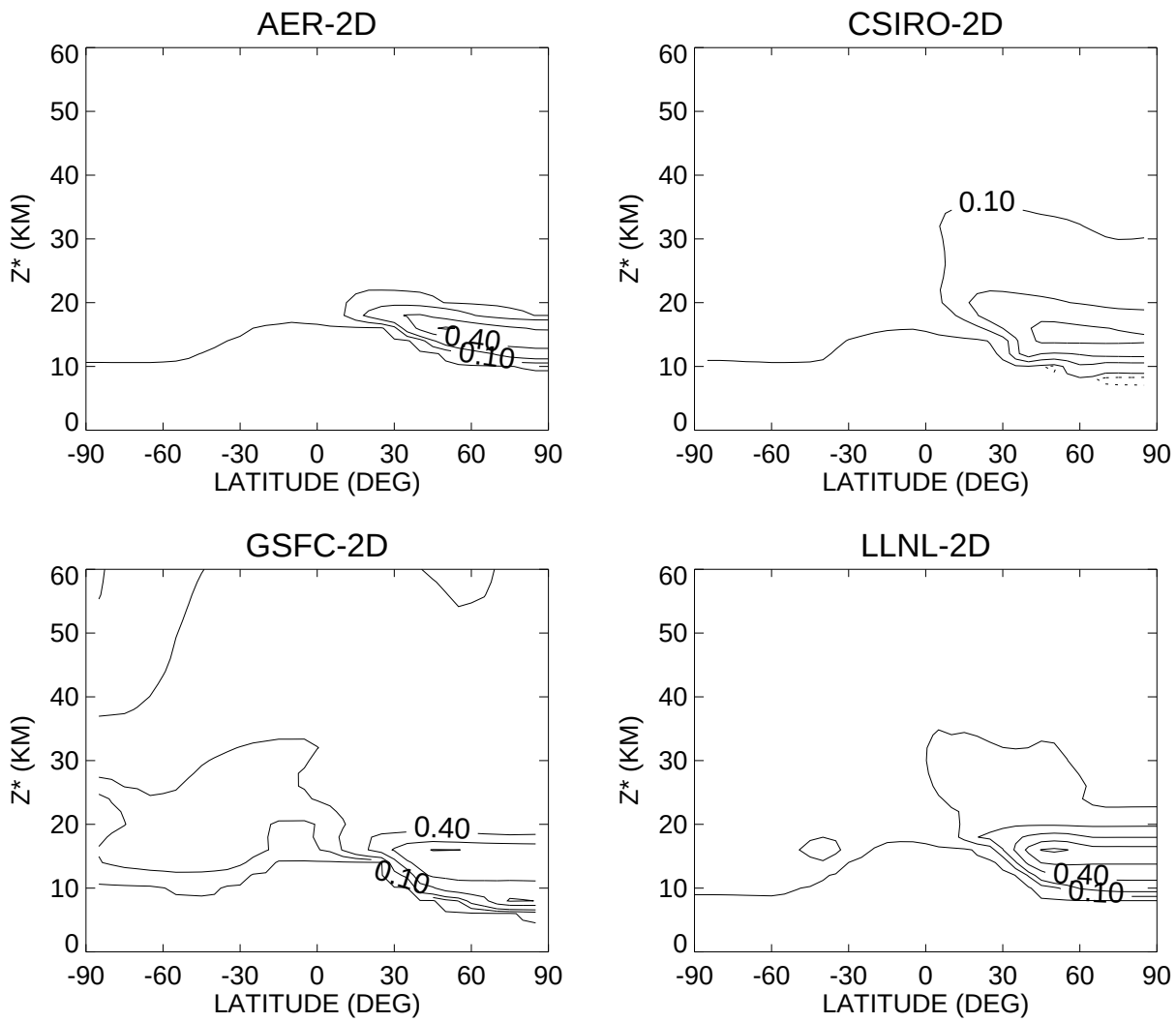

Figure 4.17: Calculated perturbations to H_2O (ppmv) as a function of latitude and altitude in June of 2015 due to H_2O emissions from a fleet of 1000 HSCT aircraft operating at 2 km below nominal cruise altitude under Scenario S2e relative to Scenario D. Contours are -0.01, 0.01, 0.1, 0.2, 0.4, 0.6, 0.8 ppmv.

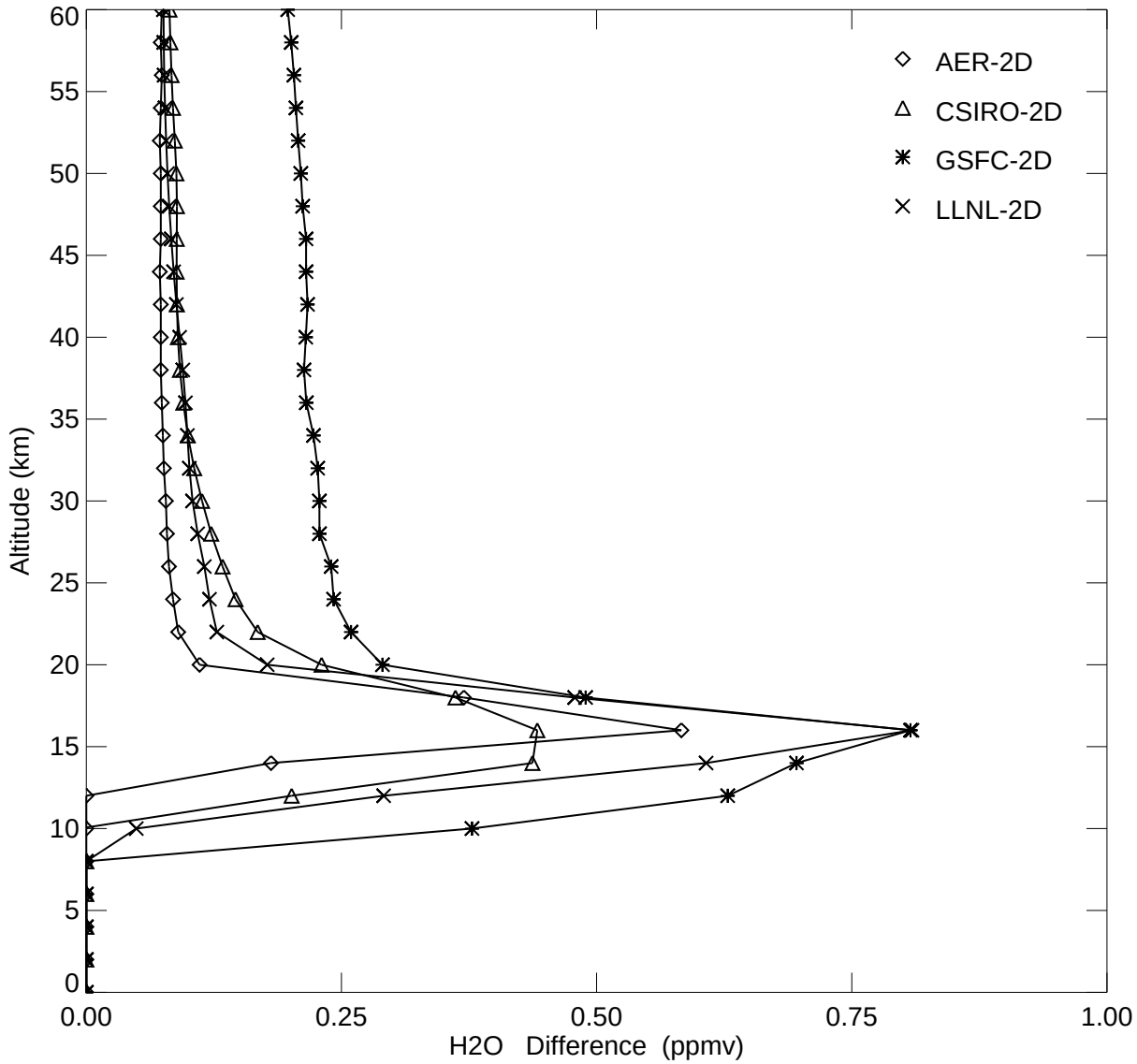

Figure 4.18: Calculated perturbations to H_2O (ppmv) as a function of altitude at 45^oN in June of 2015 due to H_2O emissions from a fleet of 1000 HSCT aircraft operating at 2 km below nominal cruise altitude under Scenario S2e relative to Scenario D.

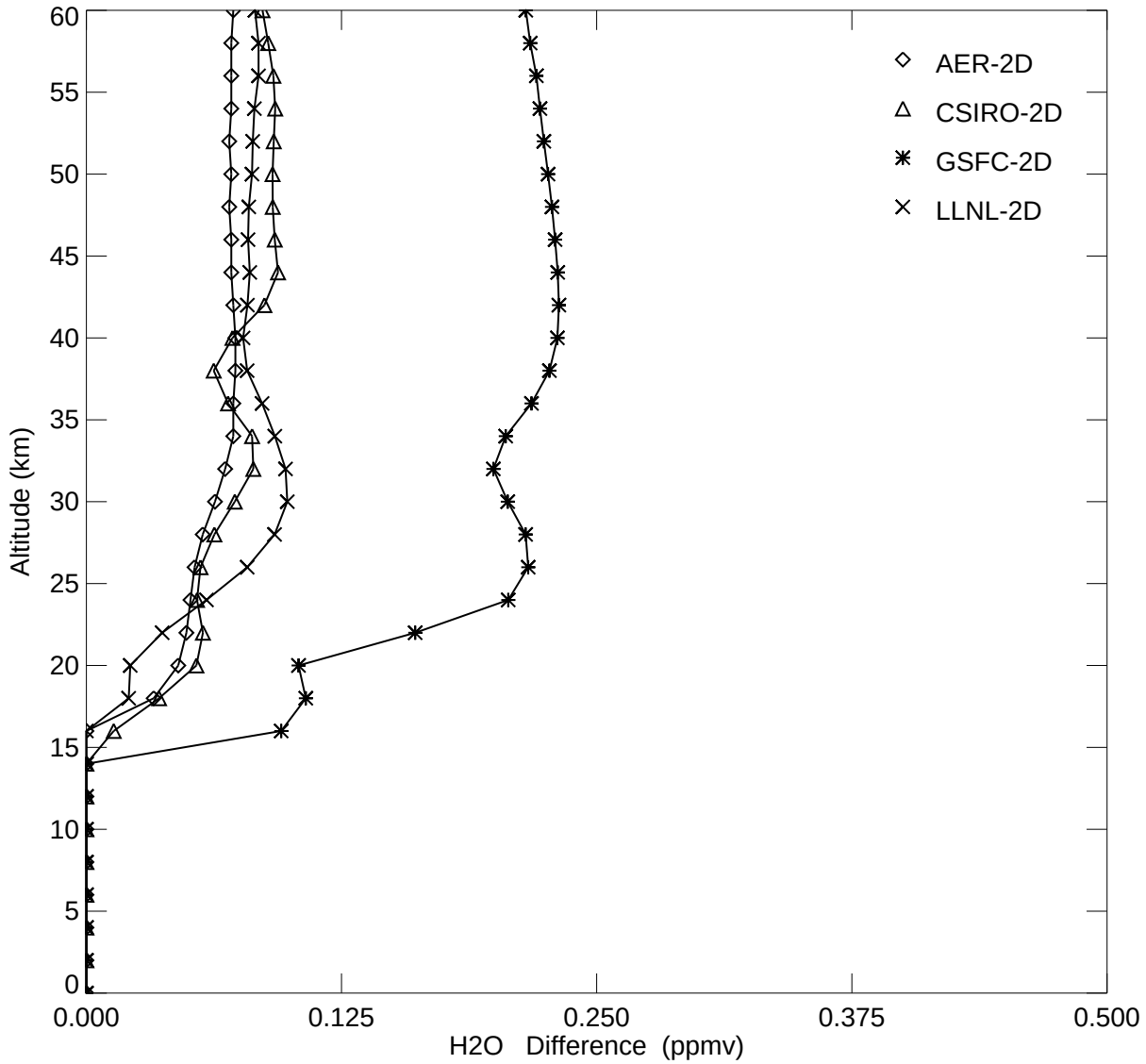

Figure 4.19: Calculated perturbations to H_2O (ppmv) as a function of altitude at the equator in June of 2015 due to H_2O emissions from a fleet of 1000 HSCT aircraft operating at 2 km below nominal cruise altitude under Scenario S2e relative to Scenario D.

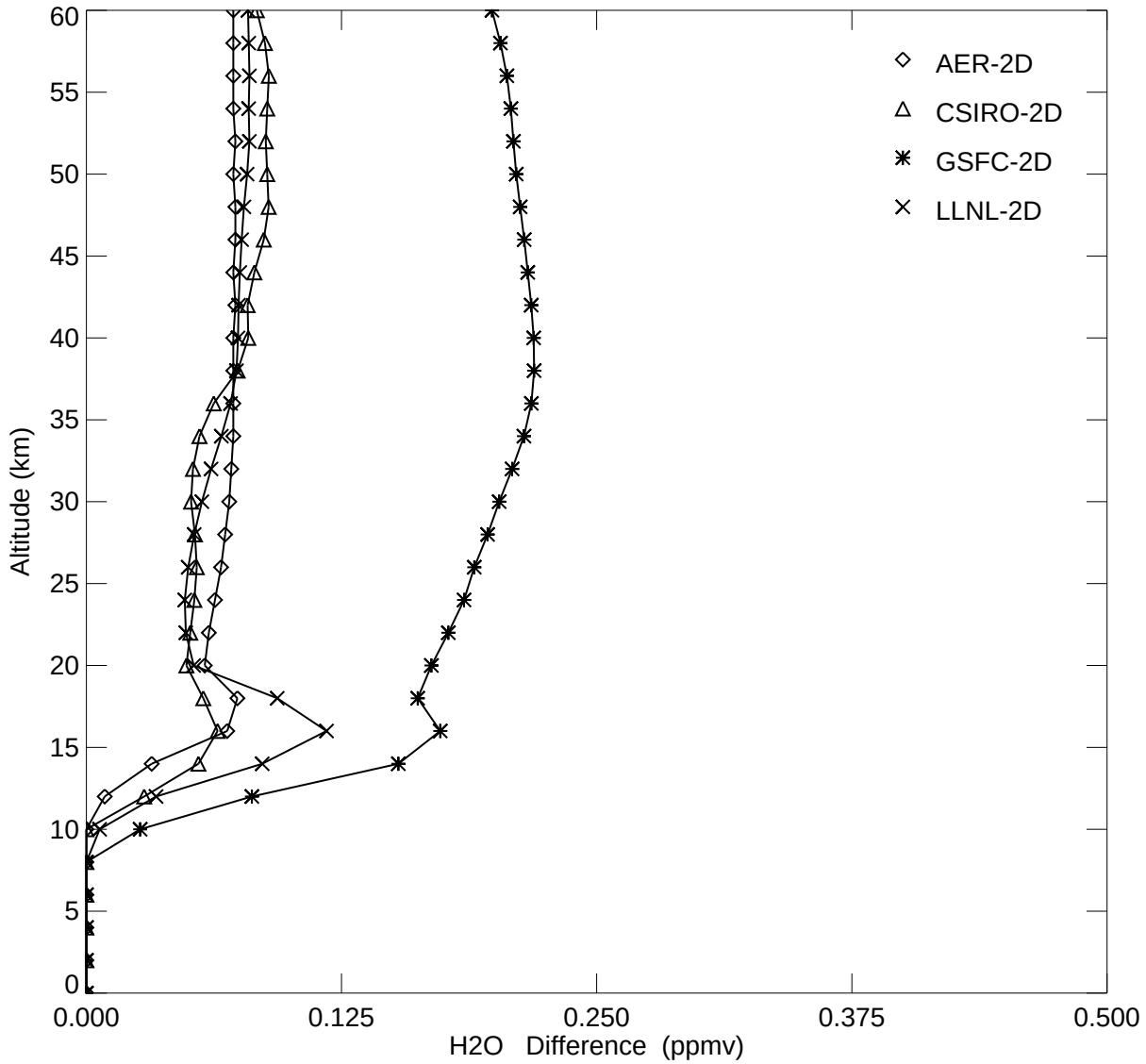

Figure 4.20: Calculated perturbations to H_2O (ppmv) as a function of altitude at 45^oS in June of 2015 due to H_2O emissions from a fleet of 1000 HSCT aircraft operating at 2 km below nominal cruise altitude under Scenario S2e relative to Scenario D.

4.2 NO_y Perturbations

Because the NO_x emission index for future HSCT engines is not known with certainty, this parameter is treated parametrically in these scenarios. The NO_x emission index is varied from 5 to 15 gm (NO_2) per kg fuel burned to cover the likely range of future engines. The engineering goal for the HSCT program is a NO_x EI of 5, so this is treated as the standard case. Other emission indices, including zero, are used to study the sensitivity of the ozone response to this parameter. Variations in fleet size and cruise altitude also modify the atmosphere's response to NO_x emissions.

The perturbations to NO_y due to aircraft emissions of NO_x under Scenario S1c are shown in Figure 4.21. This scenario represents 500 HSCT aircraft operating in 2015 with EI(NO_x)=5. Figures 4.22-4.24 show vertical profiles of NO_y perturbation at 45^{o}N, the equator, and 45^{o}S in June of 2015 for the same scenario. The maximum perturbation varies from 0.6 ppbv to 1.2 ppbv at 45^{o}N, with the GSFC model calculating the largest perturbation. Some models show negative perturbations near the south pole in June due to denitrification reactions occurring on polar stratospheric clouds in this region. These models include AER, GSFC, LLNL, and UNIVAQ.

There is a factor of two variation in calculated NO_y perturbation among the models at 45^{o}N in the lower stratosphere. The intermodel variability becomes a factor of 3 at the equator and a factor of 4-5 at 45^{o}S. Though the GSFC model shows the largest perturbation at 45^{o}N, the SLIMCAT model show a much greater perturbation at 45^{o}S. At the equator, SLIMCAT shows the largest perturbation below 27 km, while GSFC and THINAIR have larger perturbations above 30 km. The AER model shows the smallest perturbation in the 22-35 km region at all latitudes.

NO_y perturbations with EI(NO_x)=10 and 500 HSCT aircraft (Scenario S1d) are shown in Figure 4.25. The perturbations are roughly twice the magnitude of those for EI(NO_x)=5. Figures 4.26-4.28 show profiles of NO_y perturbation for this scenario. Notice that the calculated perturbations for the THINAIR model from Scenario S1d have different profile shapes than the perturbations from Scenario S1c. Because the THINAIR model calculated temperature and wind fields interactively, calculated perturbations do not simply scale with EI(NO_x) for this model.

Figure 4.29 shows NO_y perturbations for a 500 aircraft fleet with EI(NO_x)=15 (Scenario S1e). Only 6 models performed calculations for this scenario. Maximum NO_y perturbations are greater than 2 ppbv in the northern hemisphere lower stratosphere for all models, and greater than 3 ppbv for GSFC. This can be compared to background NO_y concentrations of 6-10 ppbv in the same region. Vertical profiles of NO_y perturbation are shown in Figures 4.30-4.32.

With a fleet of 1000 HSCTs and EI(NO_x)=5, the total NO_x emitted is somewhat less than with the 500 HSCT fleet and EI(NO_x)=10. The geographical distribution of fuel use is somewhat different also. The NO_y perturbations for this scenario (S1i) are shown in Figure 4.33. Vertical profiles of NO_y perturbation at 45^{o}N, the equator, and 45^{o}S are shown in Figures 4.34-4.36. Maximum perturbations at 45^{o}N range from 1.5 to 2.1 ppbv.

Scenario S1j represents a fleet of 1000 HSCT aircraft with EI(NO_x)=10. NO_y perturbations from this scenario are shown in Figure 4.37 as functions of latitude and altitude and in Figures 4.38-4.40 as functions of altitude at 45^{o}N, the equator, and 45^{o}S. Maximum NO_y perturbations range from 3.0 ppbv to 4.3 ppbv.

Several scenarios were used to examine the impact of aircraft emissions at different cruise altitudes. Scenario S2a assumes that the HSCT cruise altitude is shifted 2 km above the nominal cruise altitude of 18-20 km. Scenarios S2b-S2e assume that the HSCT cruise altitude is shifted 2 km below the nominal cruise altitude. As with the H_2O perturbation, emission at higher altitudes increases the perturbation while emission at lower altitudes decreases the perturbation.

NO_y perturbations for Scenario S2a, with 500 aircraft cruising at 20-22 km with EI(NO_x)=5, are shown in Figures 4.41-4.44. Increases relative to Scenario S1c range from 30% to 90% in the northern hemisphere lower stratosphere. Figures 4.45-4.48 show NO_y perturbations with 500 aircraft, EI(NO_x)=5, and a cruise altitude of 16-18 km. In this case, decreases in the perturbation relative to Scenario S1c range from 20% to 55%.

Scenario S2c represents 500 aircraft cruising at 2 km below the nominal cruise altitude with EI(NO_x)=10. NO_y perturbations from this scenario are shown in Figure 4.49. For the four models which calculated this scenario, the NO_y perturbation is found to be double that for Scenario S2b. The GSFC model also calculated the scenario with EI(NO_x)=15 for the same fleet size and cruise altitude (Scenario S2d). This result is shown

in Figure 4.50.

Figures 4.51-4.54 show results for Scenario S2e with 1000 HSCT aircraft cruising at 2 km below nominal cruise altitude with EI(NO_x)=5. NO_y perturbations are 70-90% greater than those from Scenario S2b. Maximum perturbations range from 0.75 ppbv to 1.5 ppbv.

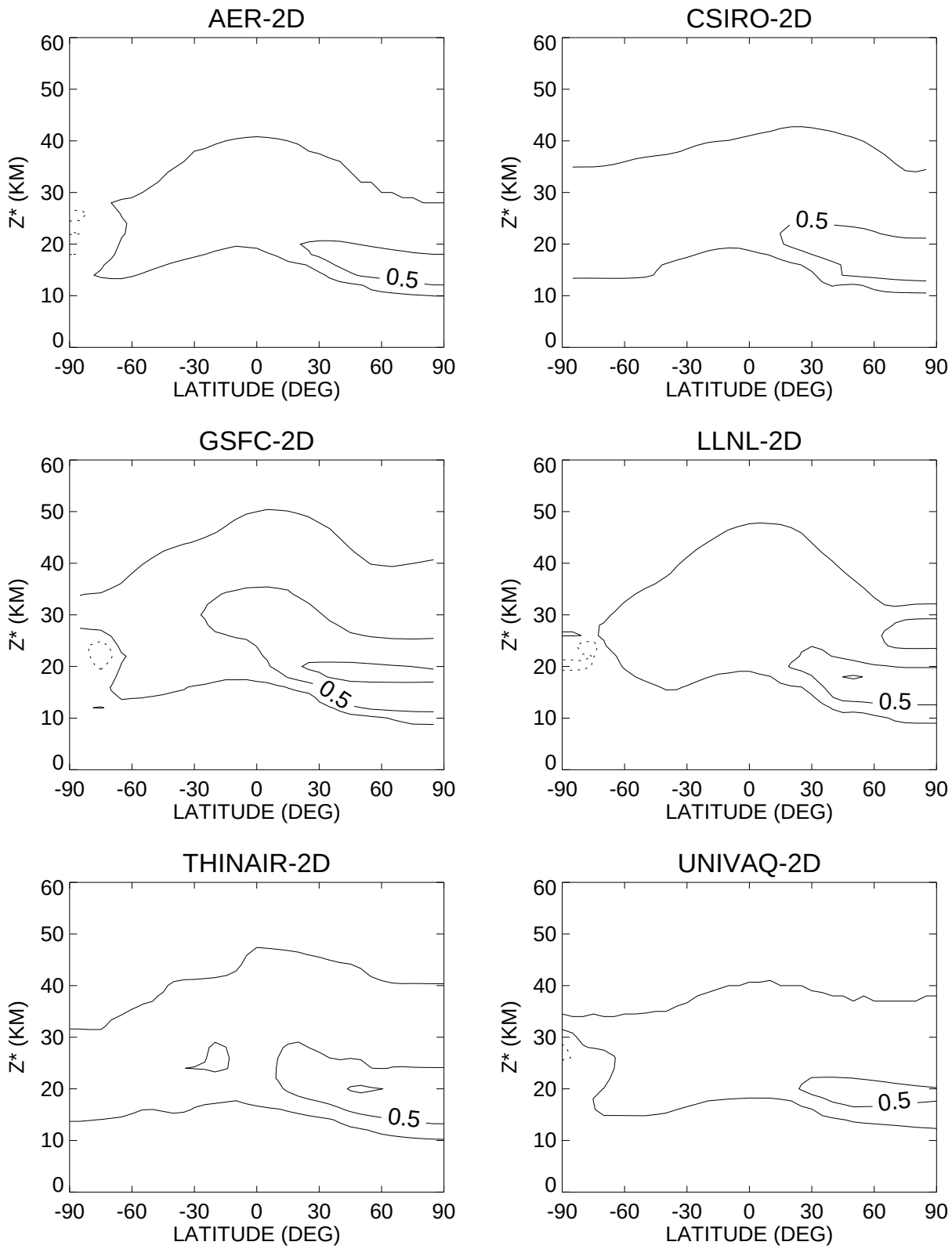

Figure 4.21: Calculated perturbations to NO_y (ppbv) as a function of latitude and altitude in June of 2015 due to NO_x emissions from a fleet of 500 HSCT aircraft with EI(NO_x)=5 under Scenario S1c relative to Scenario D. Contours are -1, -0.5, 0, 0.5, 1.0 ppbv.

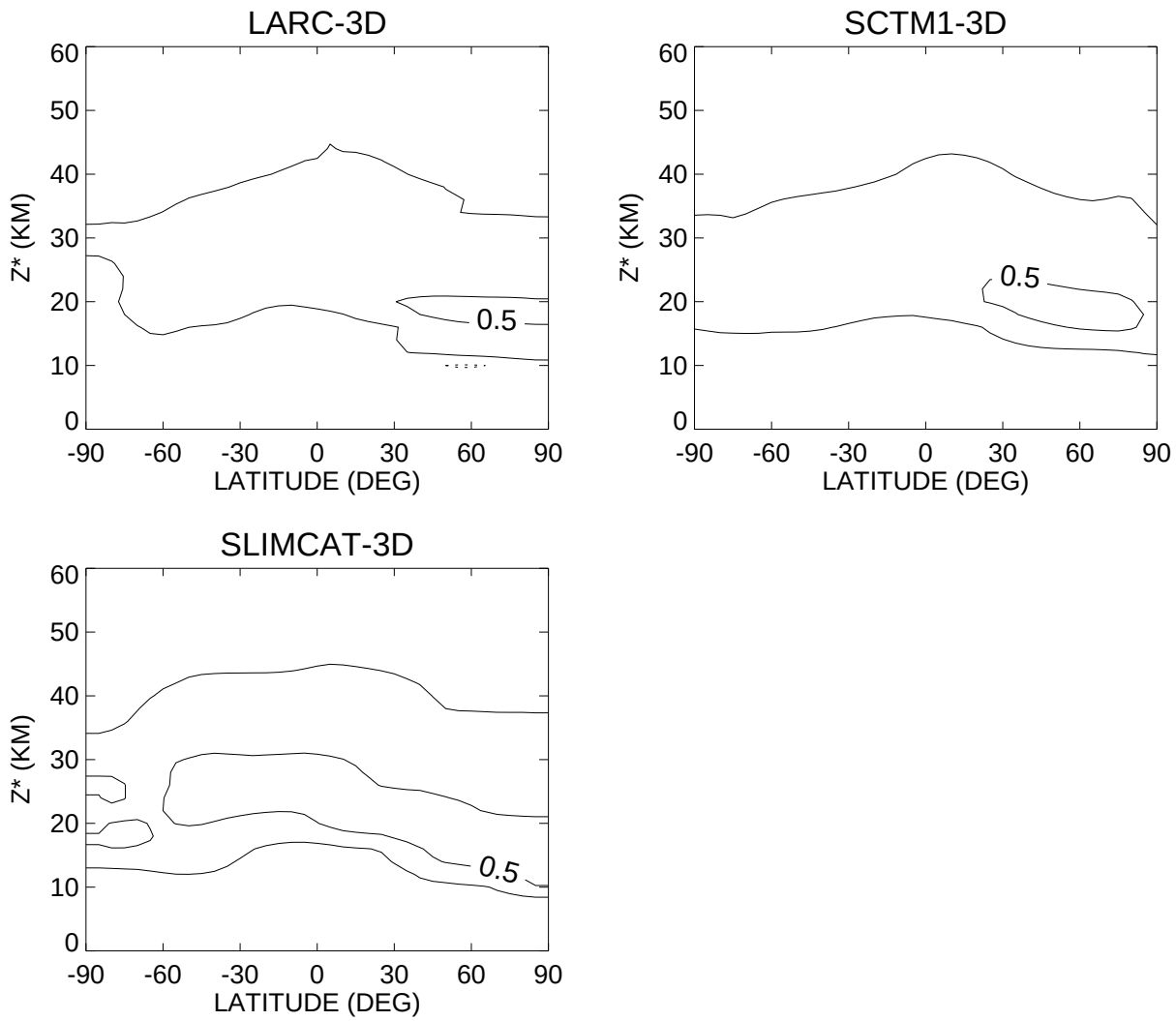

Figure 4.21: continued

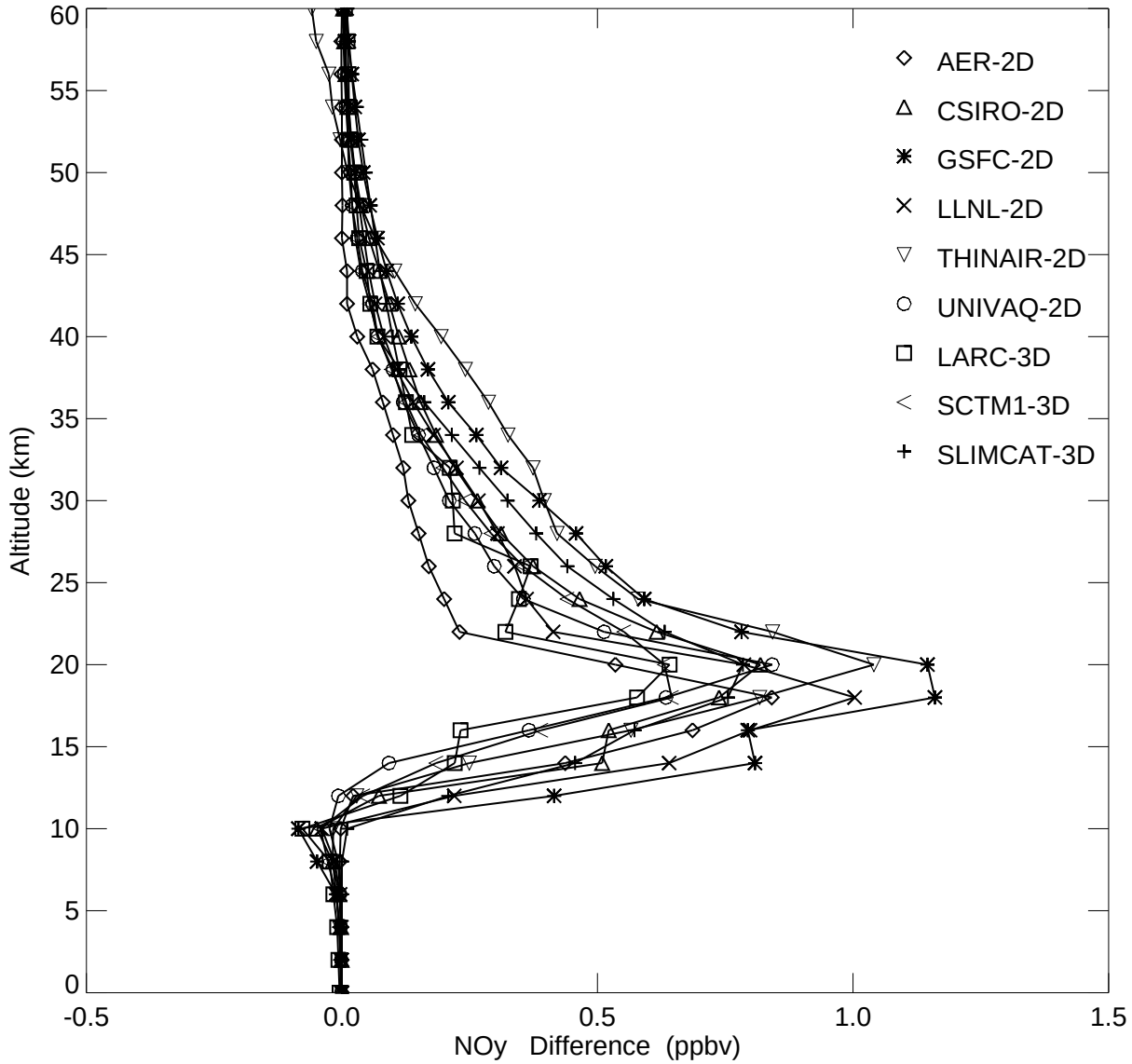

Figure 4.22: Calculated perturbations to NO_y (ppbv) as a function of altitude at 45°N in June of 2015 due to NO_x emissions from a fleet of 500 HSCT aircraft with EI(NO_x)=5 under Scenario S1c relative to Scenario D.

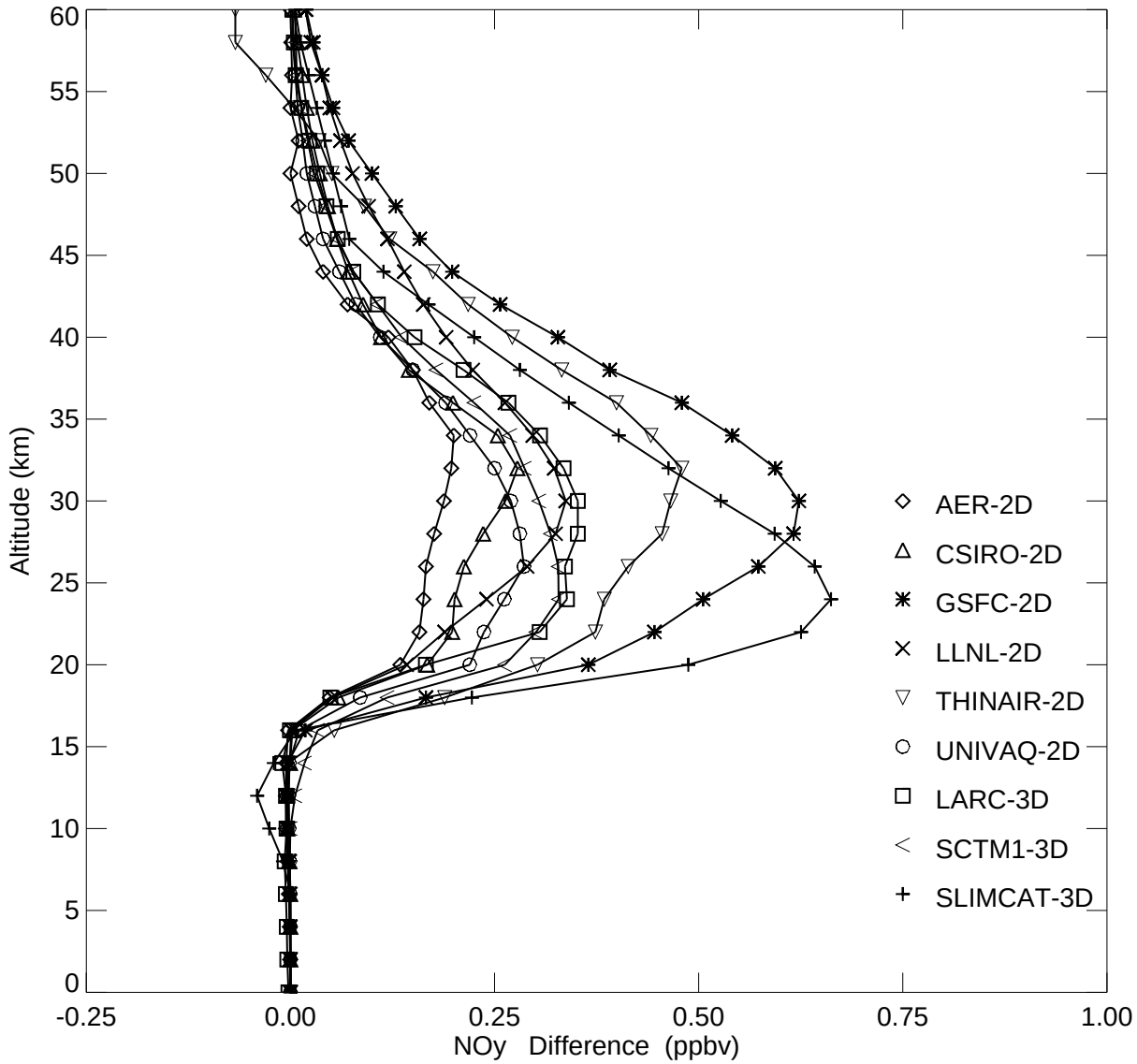

Figure 4.23: Calculated perturbations to NO_y (ppbv) as a function of altitude at the equator in June of 2015 due to NO_x emissions from a fleet of 500 HSCT aircraft with EI(NO_x)=5 under Scenario S1c relative to Scenario D.

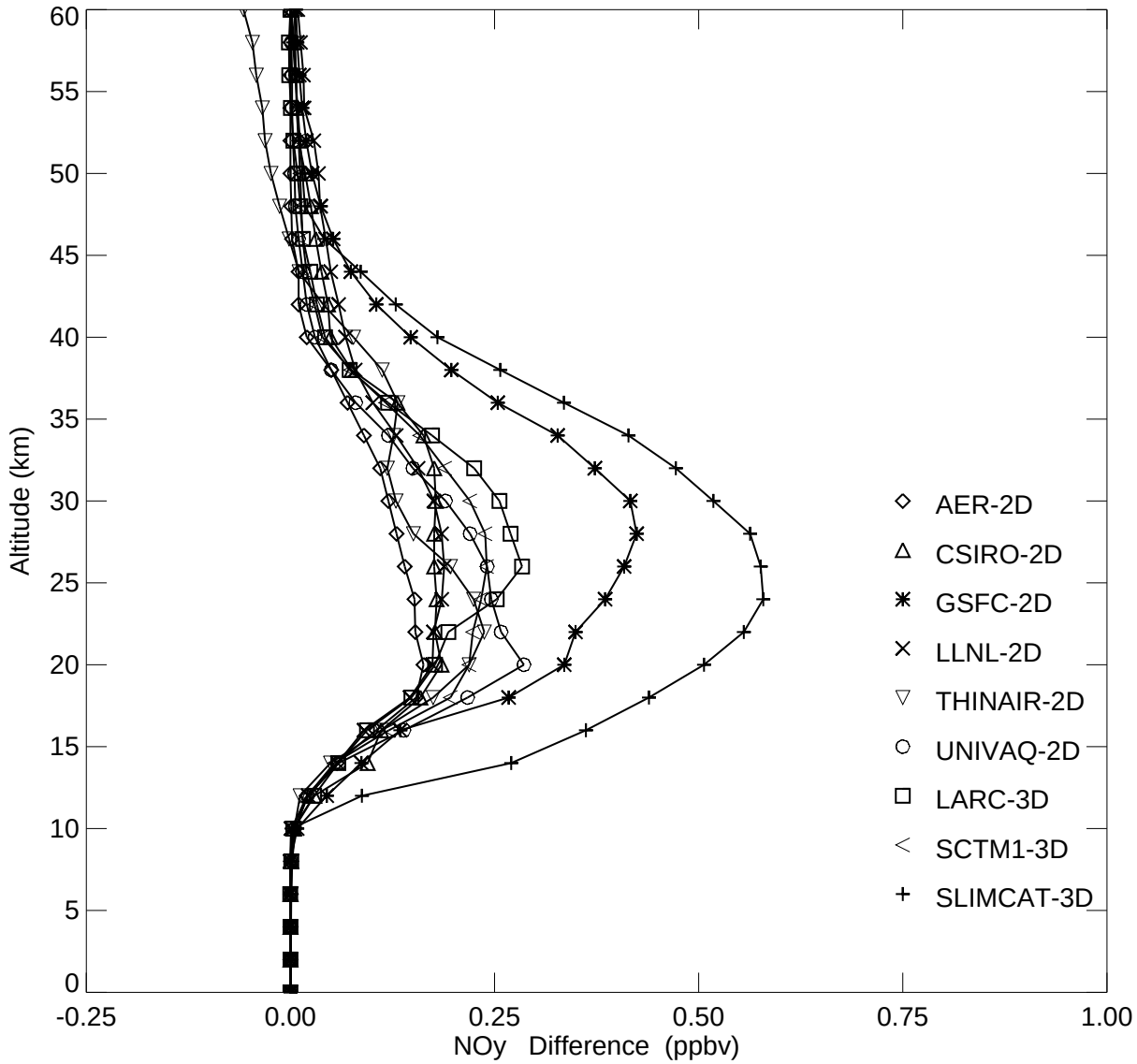

Figure 4.24: Calculated perturbations to NO_y (ppbv) as a function of altitude at 45^oS in June of 2015 due to NO_x emissions from a fleet of 500 HSCT aircraft with EI(NO_x)=5 under Scenario S1c relative to Scenario D.

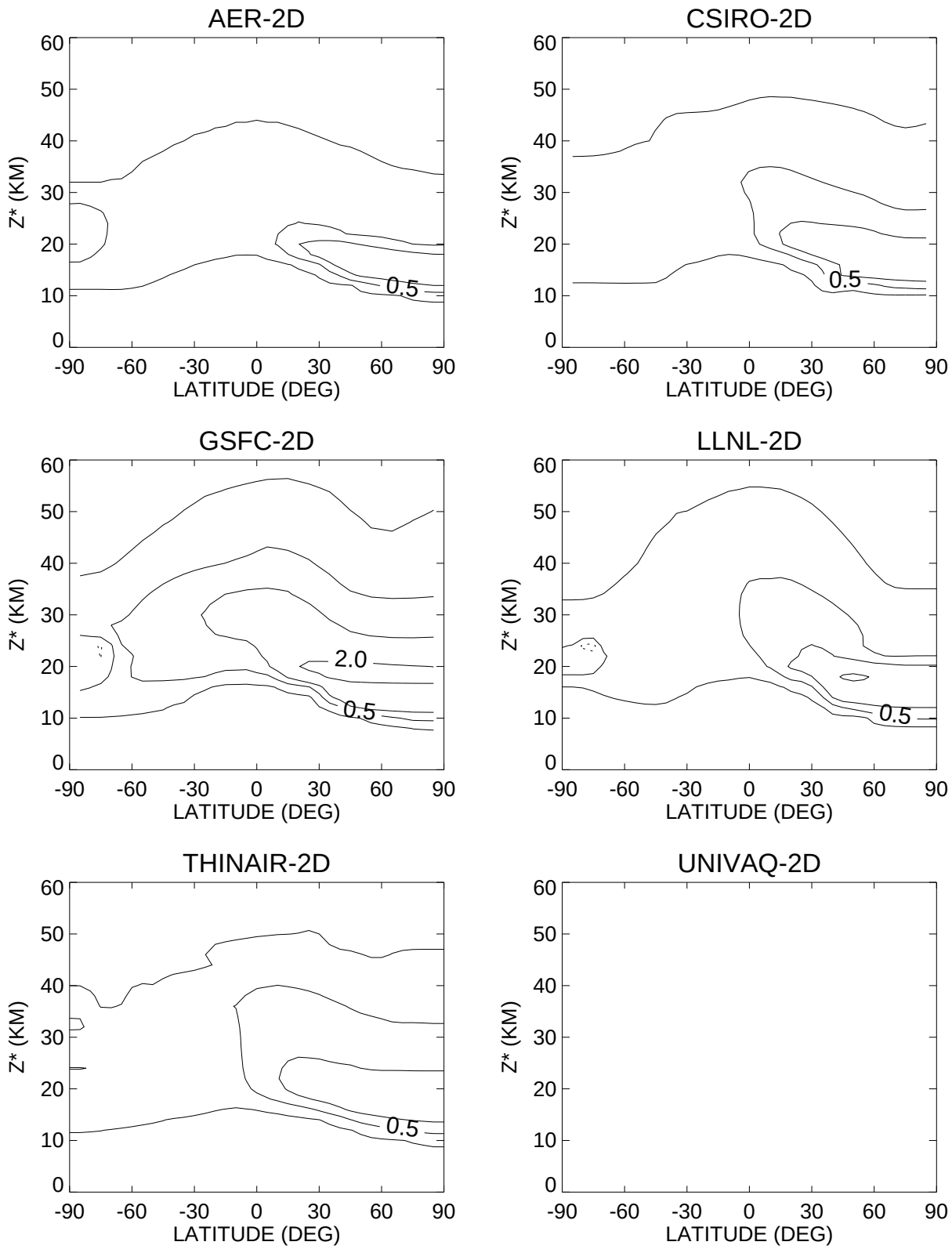

Figure 4.25: Calculated perturbations to NO_y (ppbv) as a function of latitude and altitude in June of 2015 due to NO_x emissions from a fleet of 500 HSCT aircraft with EI(NO_x)=10 under Scenario S1d relative to Scenario D. Contours are -0.5, 0, 0.5, 1.0, 2.0 ppbv.

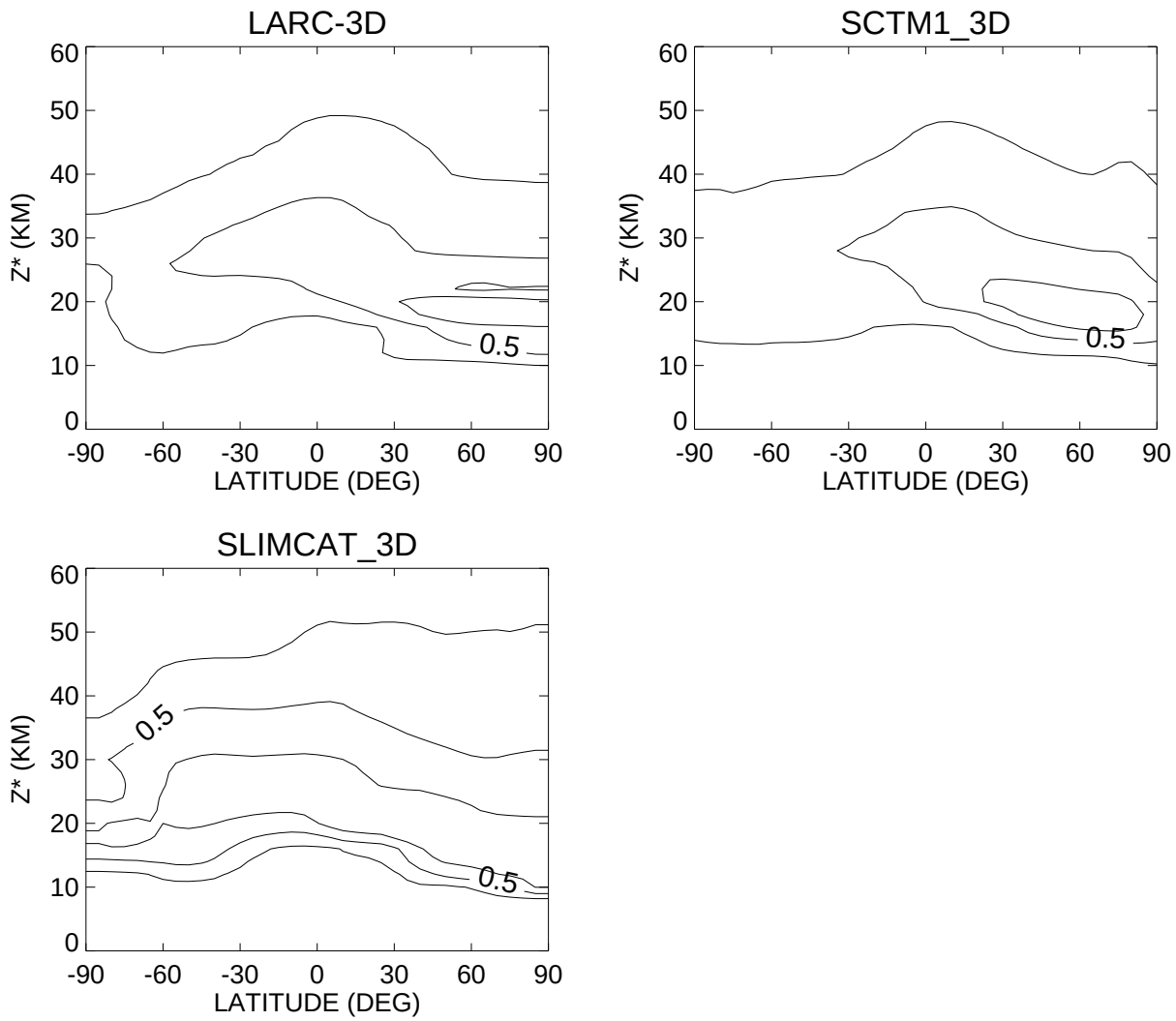

Figure 4.25: continued

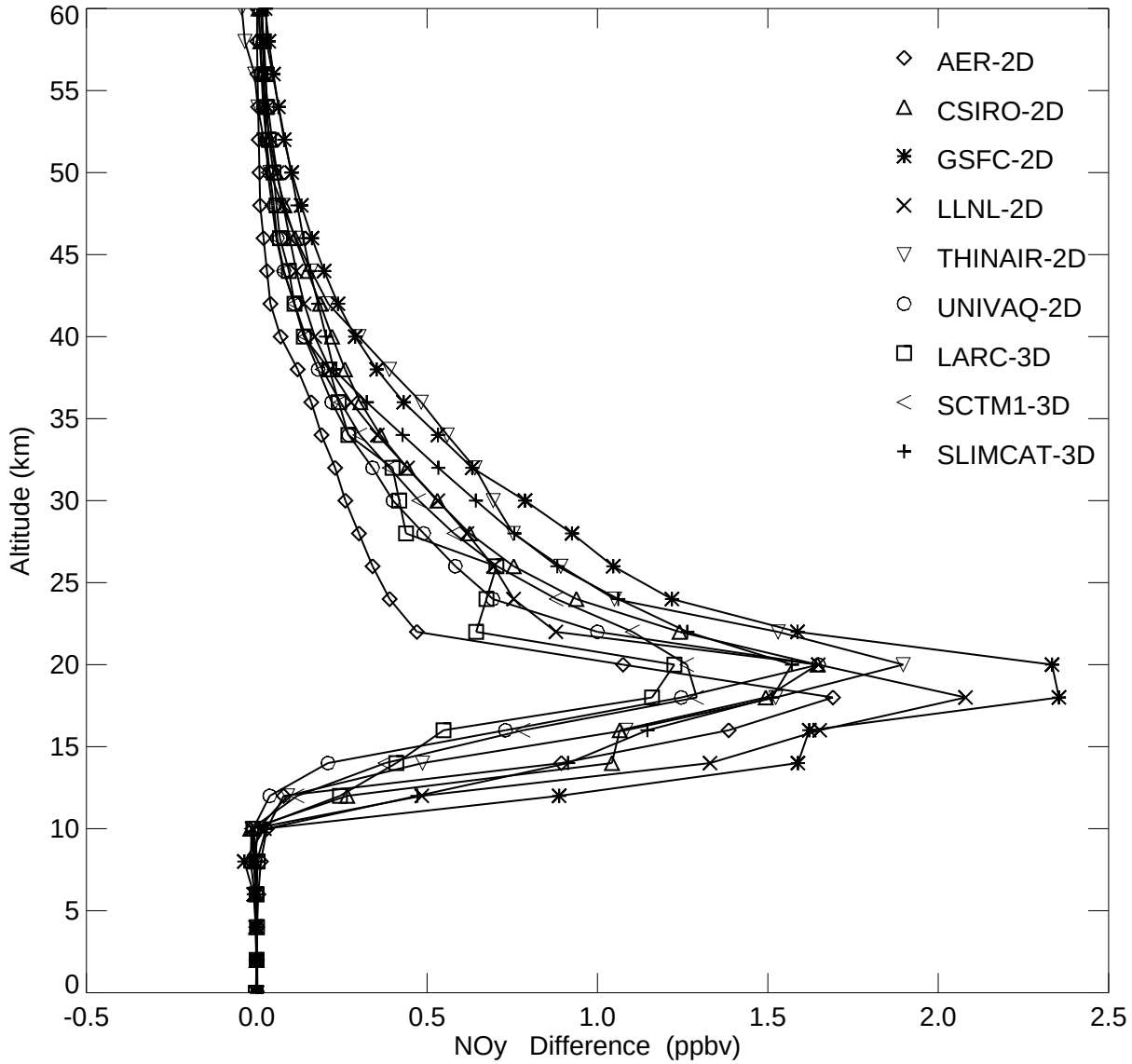

Figure 4.26: Calculated perturbations to NO_y (ppbv) as a function of altitude at 45^oN in June of 2015 due to NO_x emissions from a fleet of 500 HSCT aircraft with EI(NO_x)=10 under Scenario S1d relative to Scenario D.

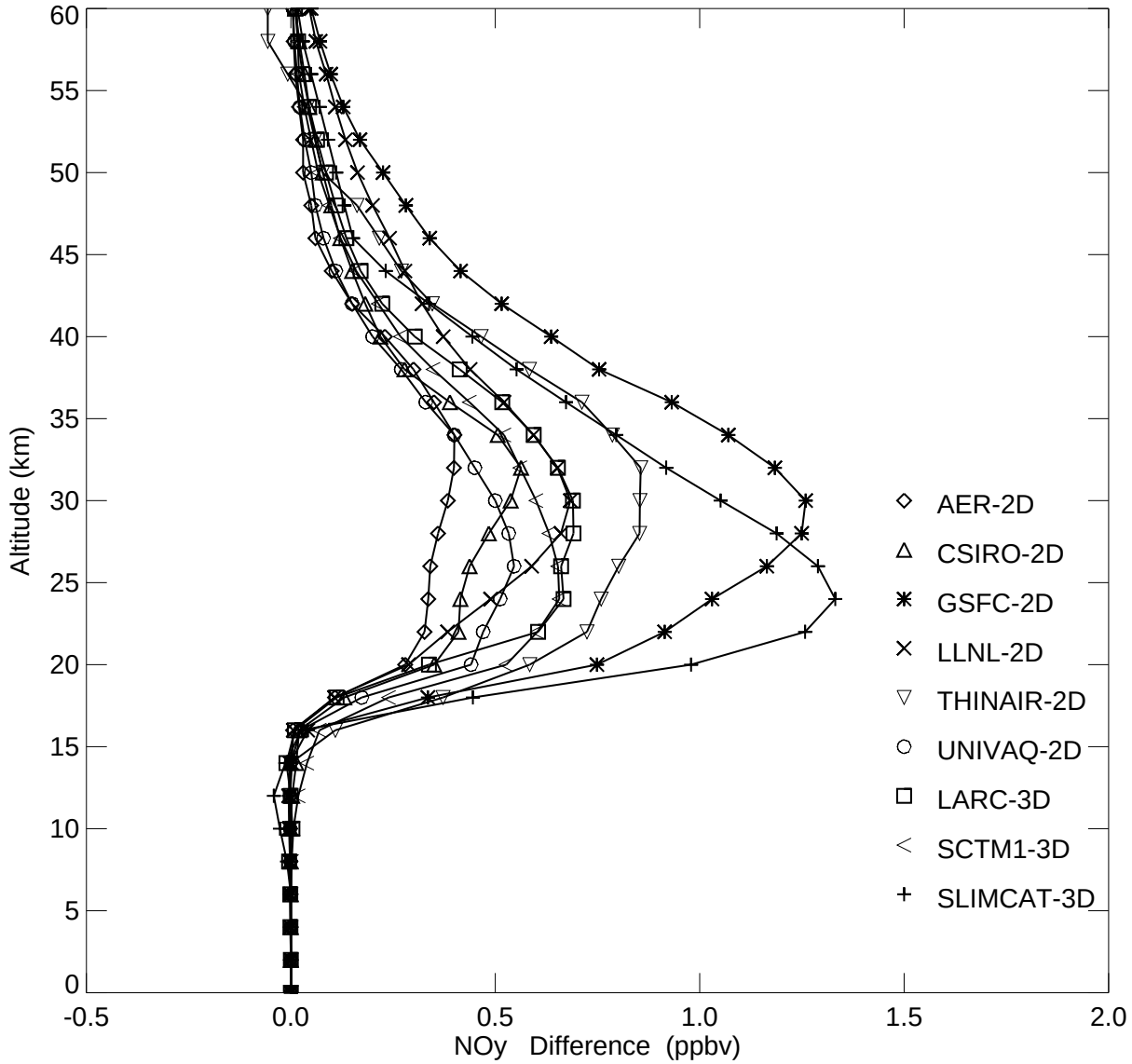

Figure 4.27: Calculated perturbations to NO_y (ppbv) as a function of altitude at the equator in June of 2015 due to NO_x emissions from a fleet of 500 HSCT aircraft with EI(NO_x)=10 under Scenario S1d relative to Scenario D.

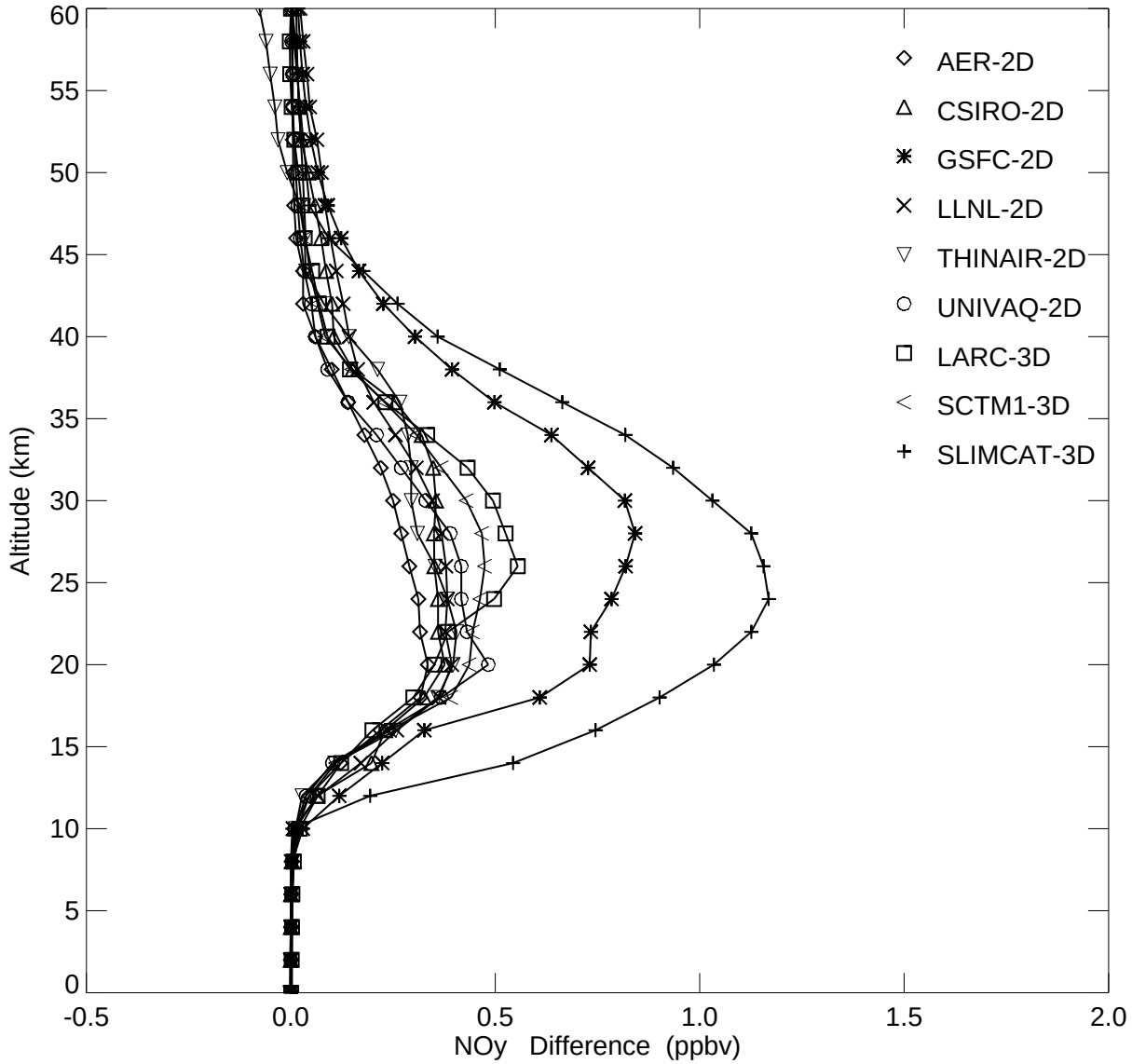

Figure 4.28: Calculated perturbations to NO_y (ppbv) as a function of altitude at 45°S in June of 2015 due to NO_x emissions from a fleet of 500 HSCT aircraft with EI(NO_x)=10 under Scenario S1d relative to Scenario D.

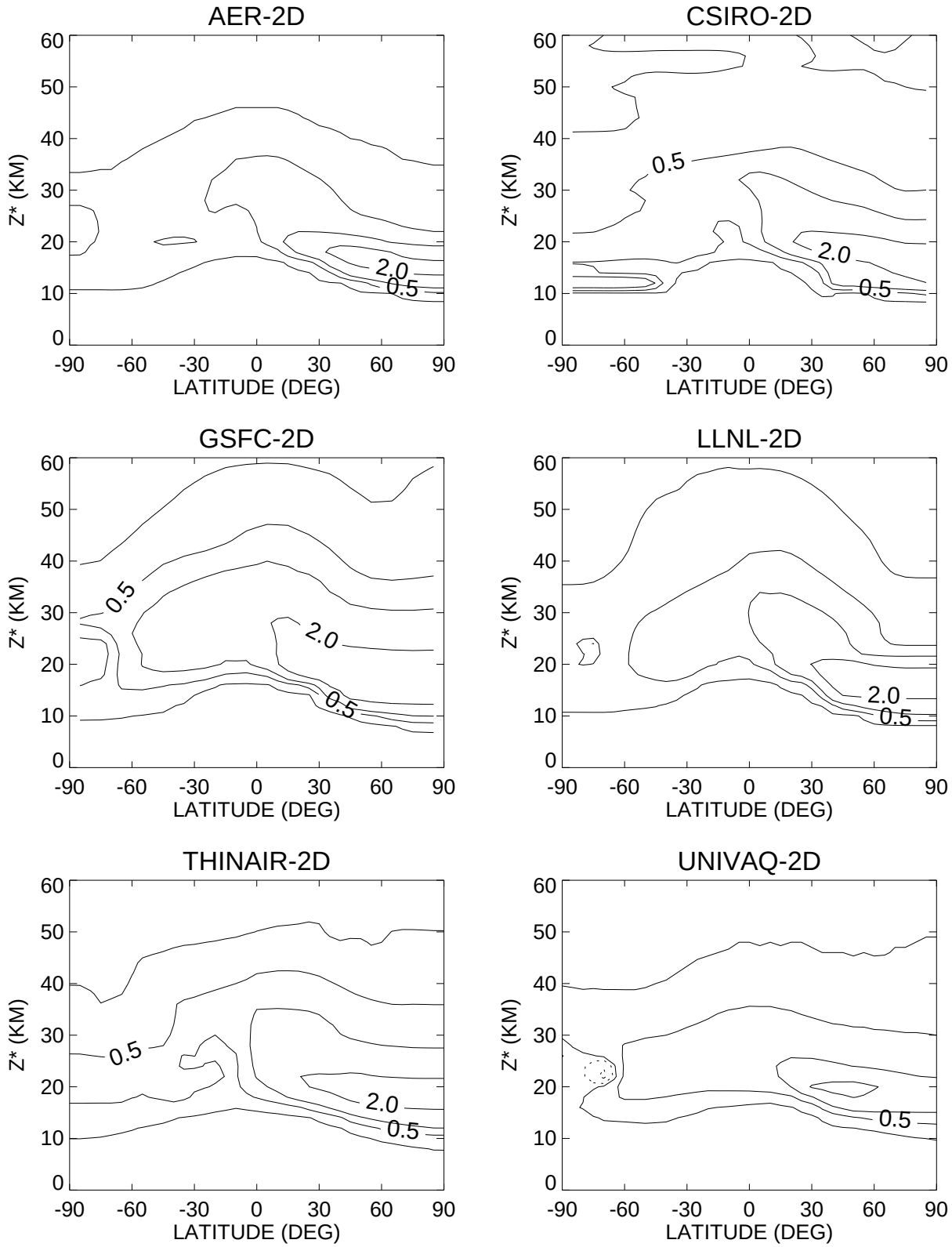

Figure 4.29: Calculated perturbations to NO_y (ppbv) as a function of latitude and altitude in June of 2015 due to NO_x emissions from a fleet of 500 HSCT aircraft with EI(NO_x)=15 under Scenario S1e relative to Scenario D. Contours are -1.0, -0.5, -0.1 0, 0.1, 0.5, 1, 2, 3 ppbv.

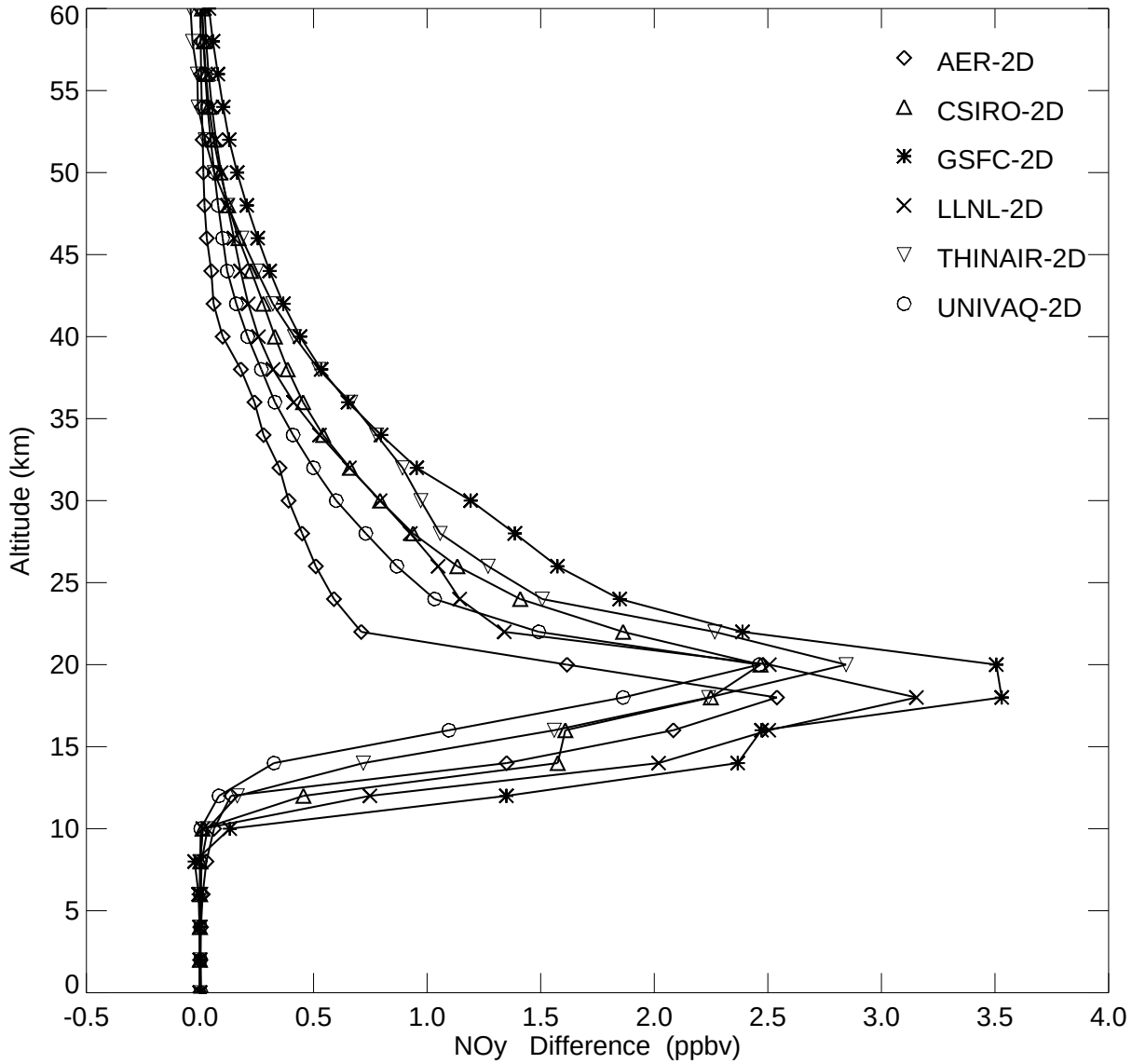

Figure 4.30: Calculated perturbations to NO_y (ppbv) as a function of altitude at 45^oN in June of 2015 due to NO_x emissions from a fleet of 500 HSCT aircraft with EI(NO_x)=15 under Scenario S1e relative to Scenario D.

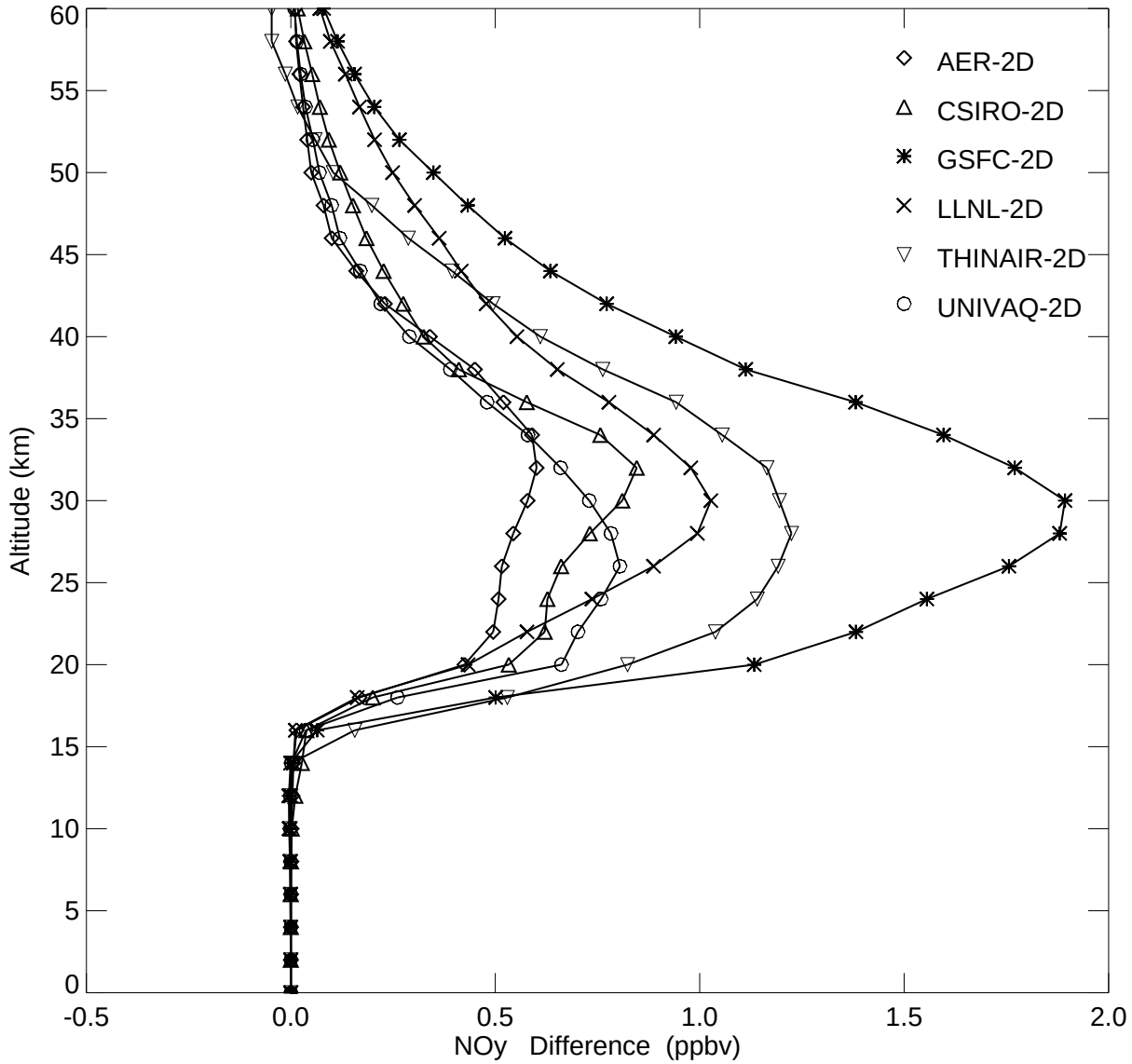

Figure 4.31: Calculated perturbations to NO_y (ppbv) as a function of altitude at the equator in June of 2015 due to NO_x emissions from a fleet of 500 HSCT aircraft with EI(NO_x)=15 under Scenario S1e relative to Scenario D.

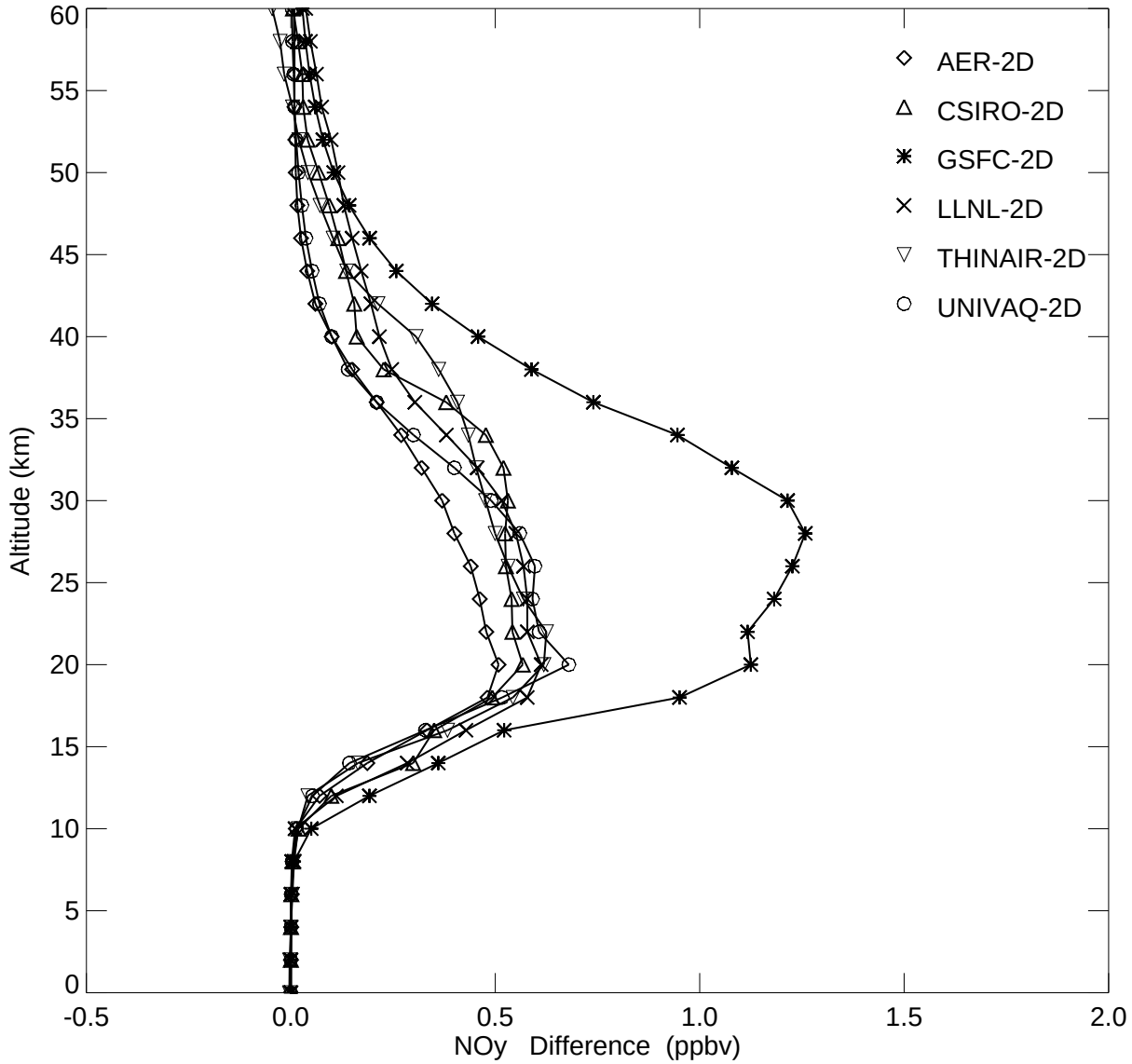

Figure 4.32: Calculated perturbations to NO_y (ppbv) as a function of altitude at 45°S in June of 2015 due to NO_x emissions from a fleet of 500 HSCT aircraft with EI(NO_x)=15 under Scenario S1e relative to Scenario D.

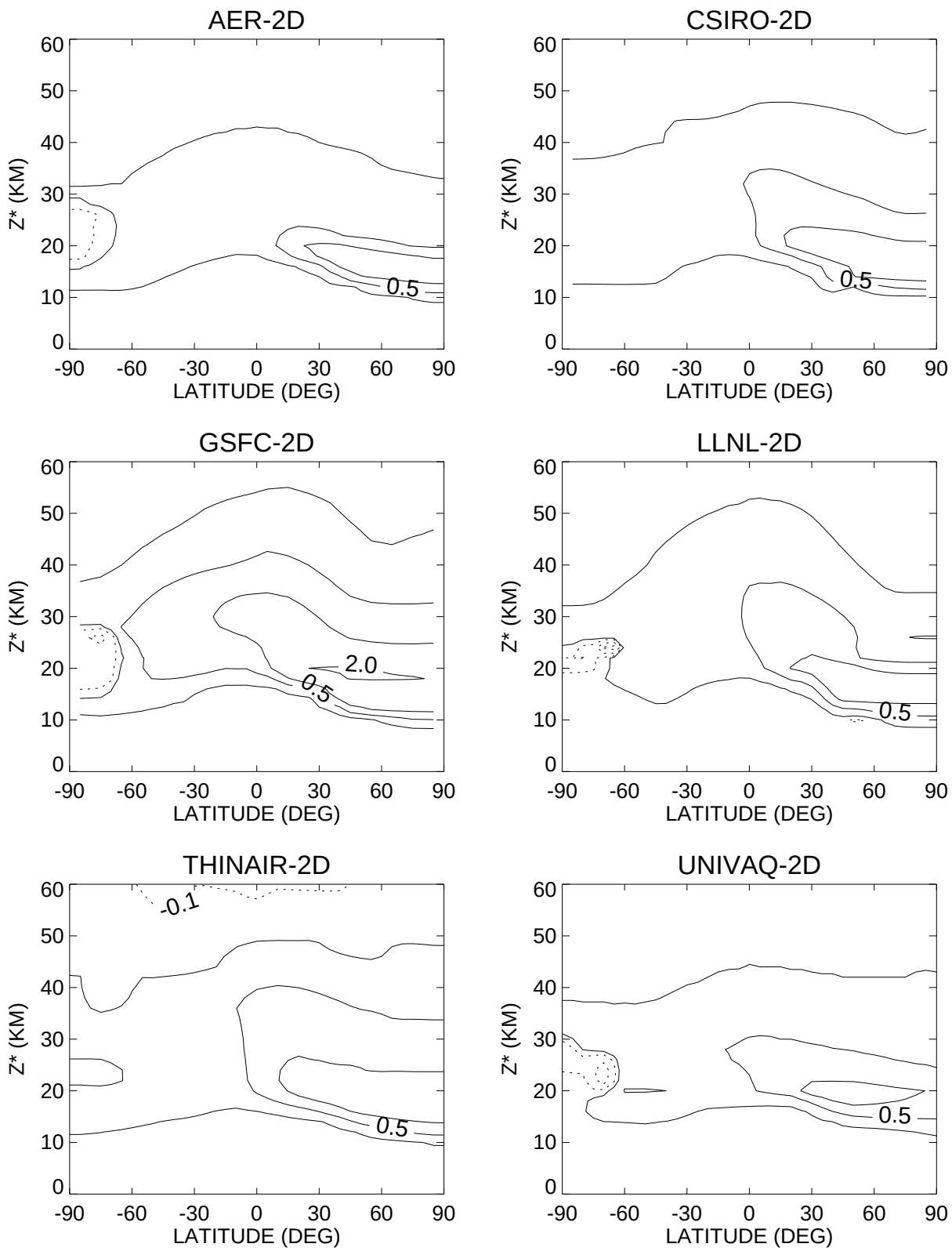

Figure 4.33: Calculated perturbations to NO_y (ppbv) as a function of latitude and altitude in June of 2015 due to NO_x emissions from a fleet of 1000 HSCT aircraft with EI(NO_x)=5 under Scenario S1i relative to Scenario D. Contours are -1.0, -0.5, 0, 0.5, 1.0, 2.0 ppbv.

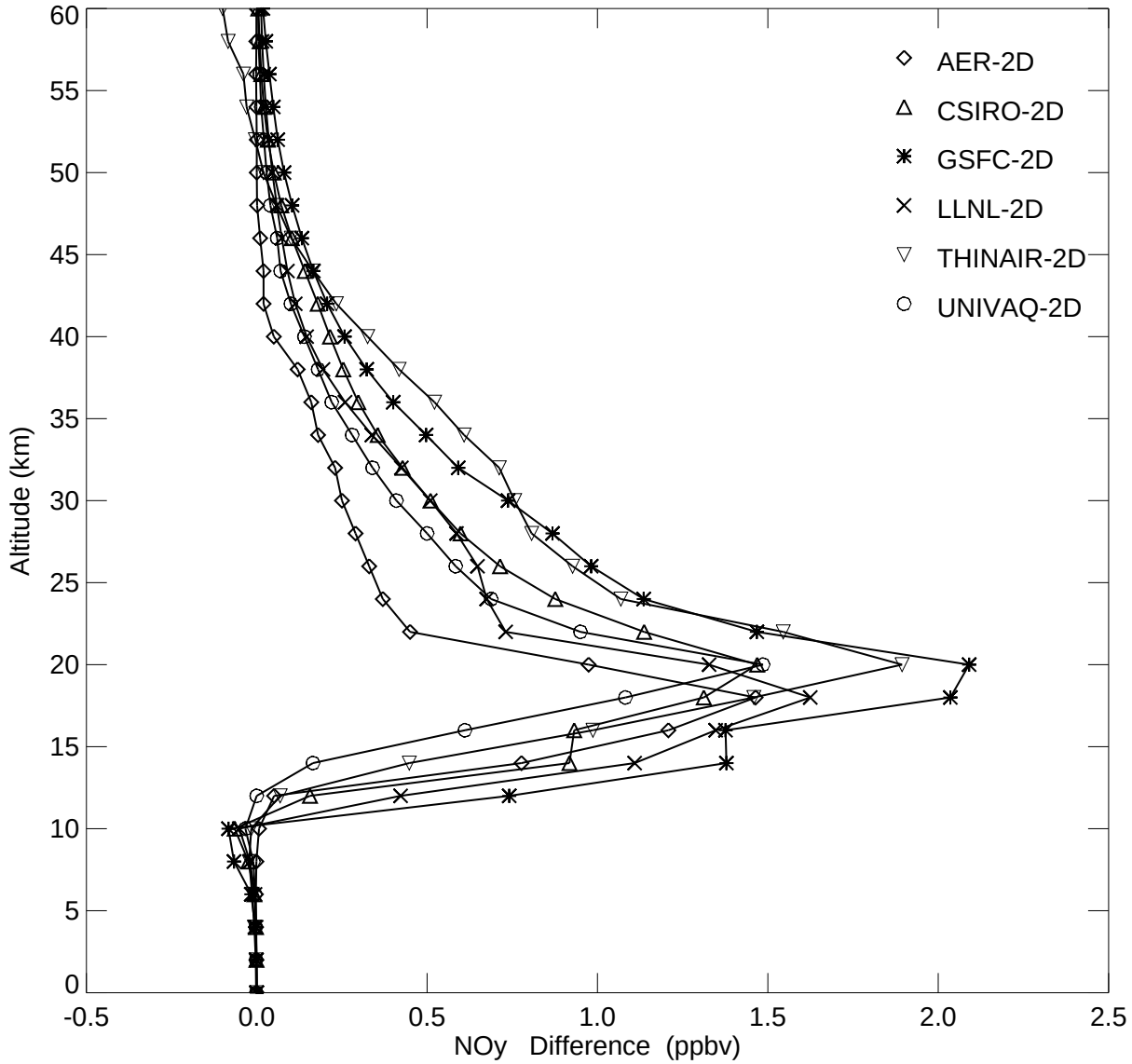

Figure 4.34: Calculated perturbations to NO_y (ppbv) as a function of altitude at 45^oN in June of 2015 due to NO_x emissions from a fleet of 1000 HSCT aircraft with EI(NO_x)=5 under Scenario S1i relative to Scenario D.

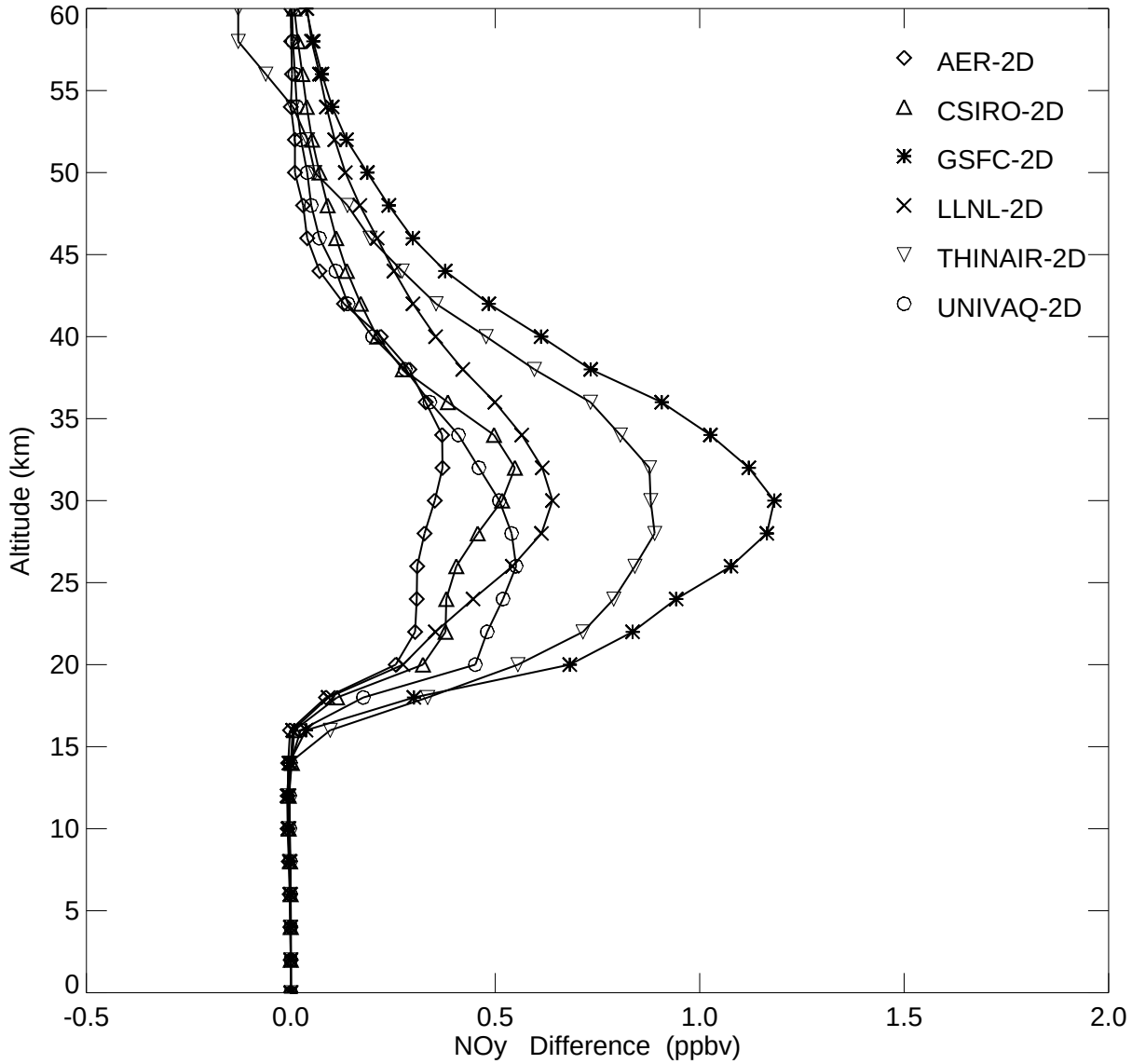

Figure 4.35: Calculated perturbations to NO_y (ppbv) as a function of altitude at the equator in June of 2015 due to NO_x emissions from a fleet of 1000 HSCT aircraft with EI(NO_x)=5 under Scenario S1i relative to Scenario D.

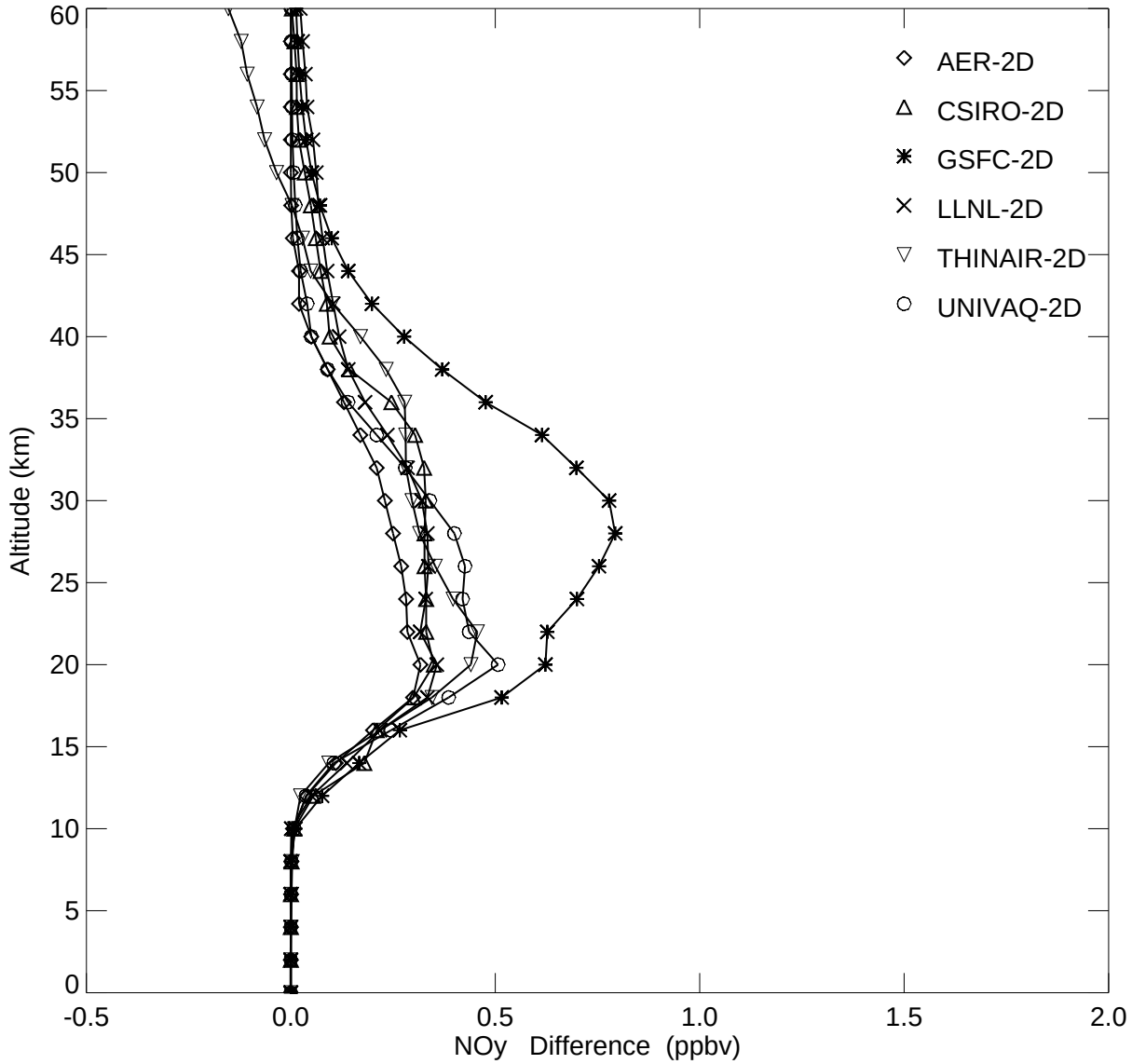

Figure 4.36: Calculated perturbations to NO_y (ppbv) as a function of altitude at 45°S in June of 2015 due to NO_x emissions from a fleet of 1000 HSCT aircraft with EI(NO_x)=5 under Scenario S1i relative to Scenario D.

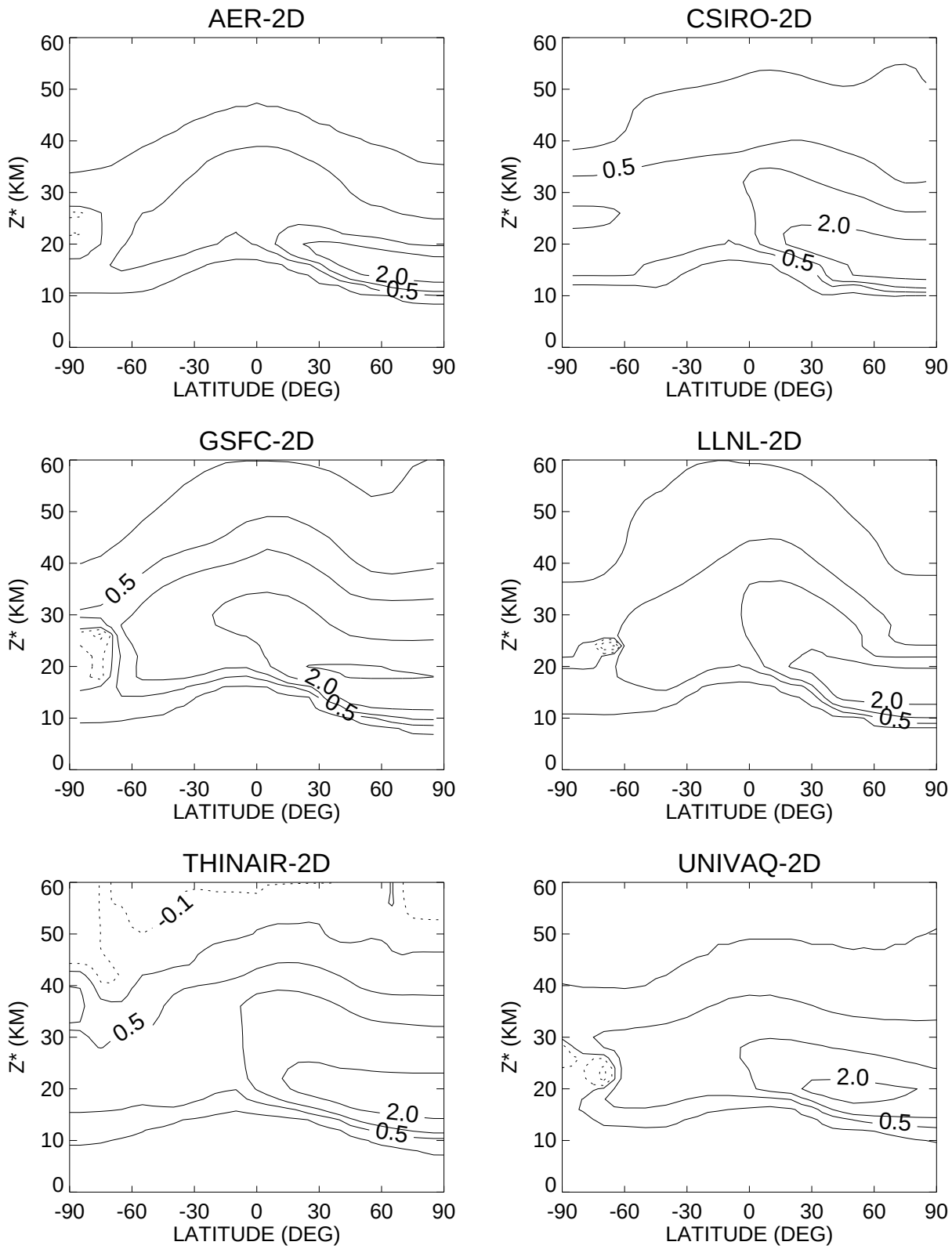

Figure 4.37: Calculated perturbations to NO_y (ppbv) as a function of latitude and altitude in June of 2015 due to NO_x emissions from a fleet of 1000 HSCT aircraft with EI(NO_x)=10 under Scenario S1j relative to Scenario D. Contours are -1, -0.5, -0.1, 0, -.1, 0.5, 1, 2, 3, 4 ppbv.

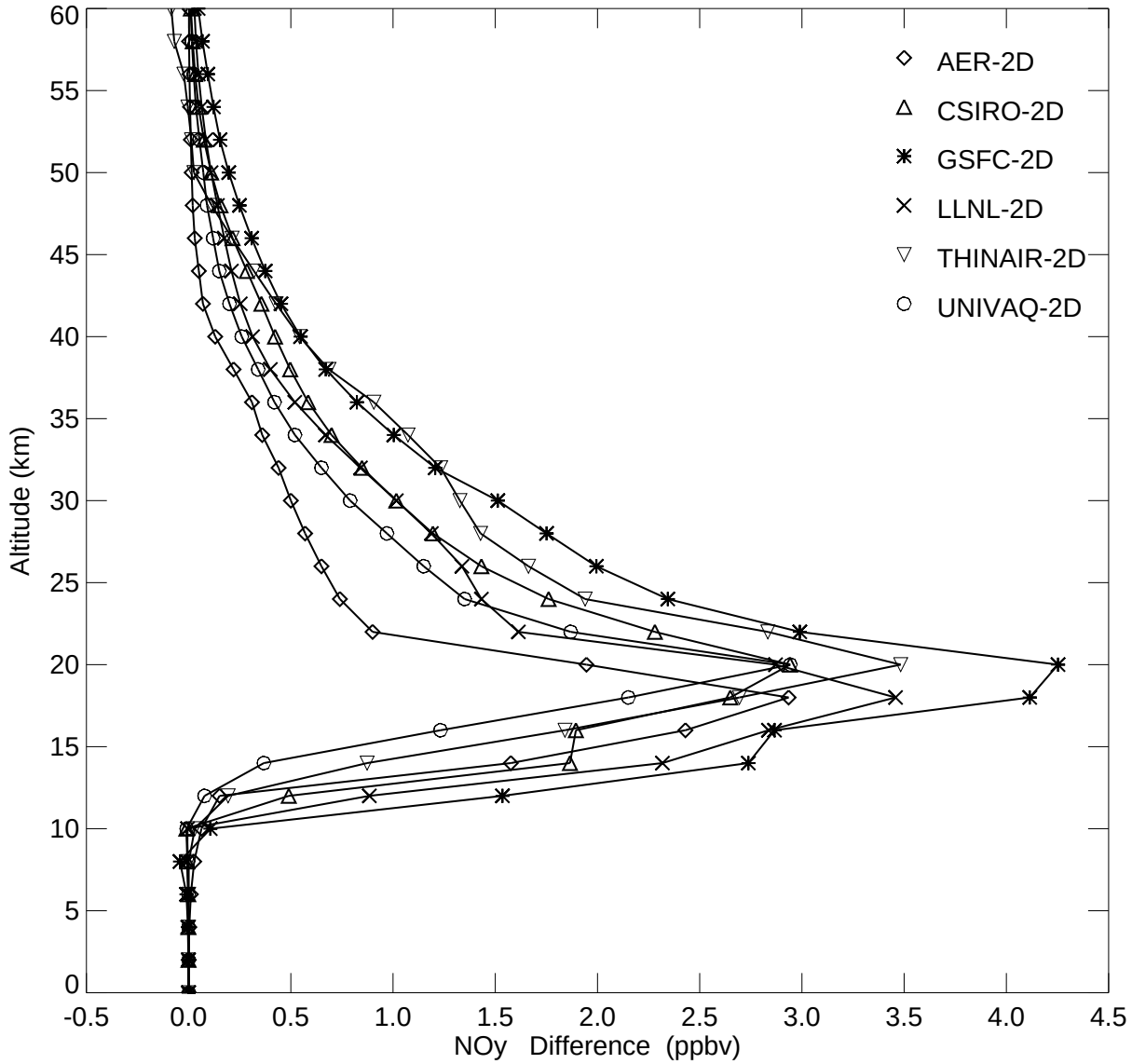

Figure 4.38: Calculated perturbations to NO_y (ppbv) as a function of altitude at 45^oN in June of 2015 due to NO_x emissions from a fleet of 1000 HSCT aircraft with EI(NO_x)=10 under Scenario S1j relative to Scenario D.

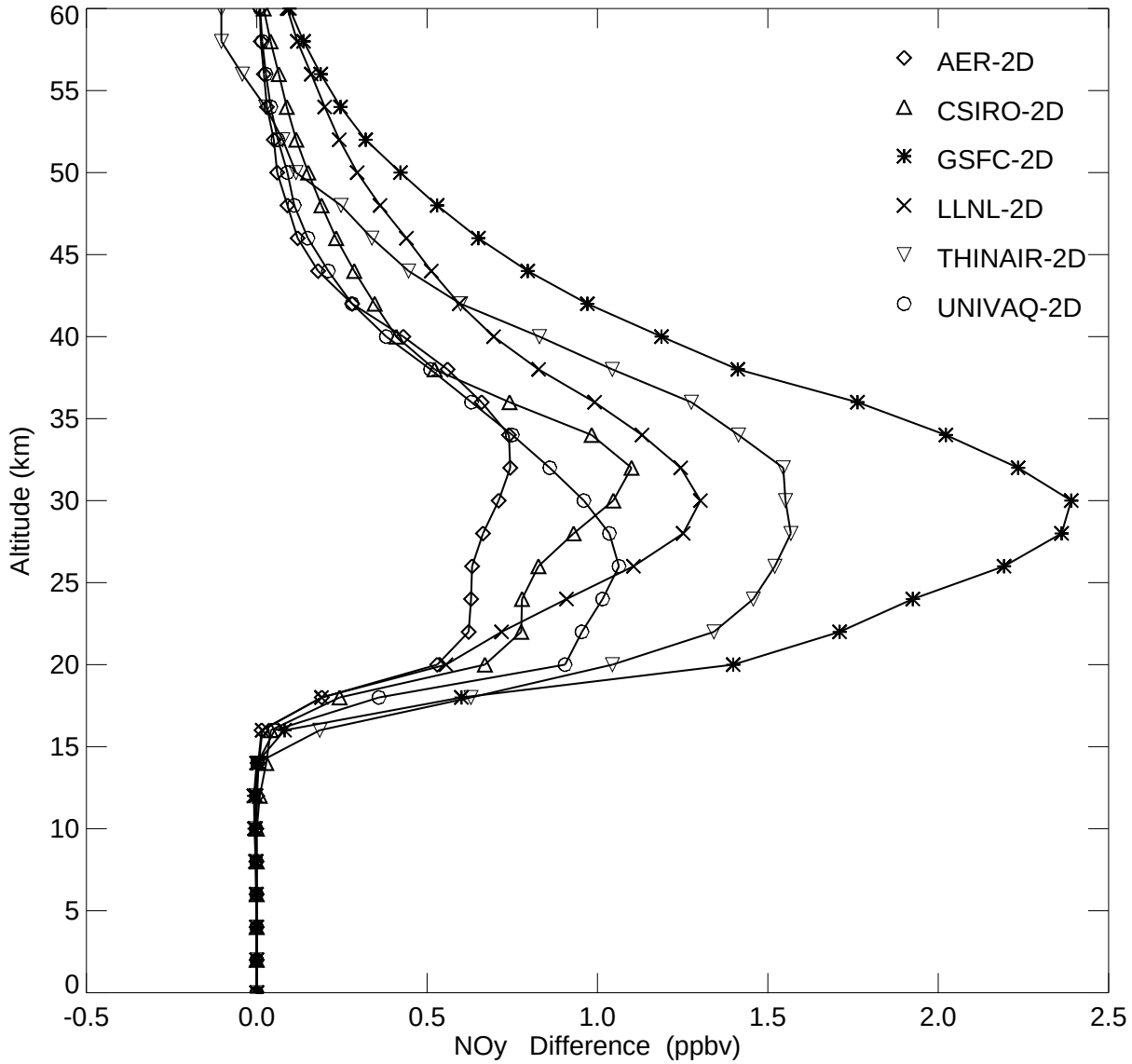

Figure 4.39: Calculated perturbations to NO_y (ppbv) as a function of altitude at the equator in June of 2015 due to NO_x emissions from a fleet of 1000 HSCT aircraft with EI(NO_x)=10 under Scenario S1j relative to Scenario D.

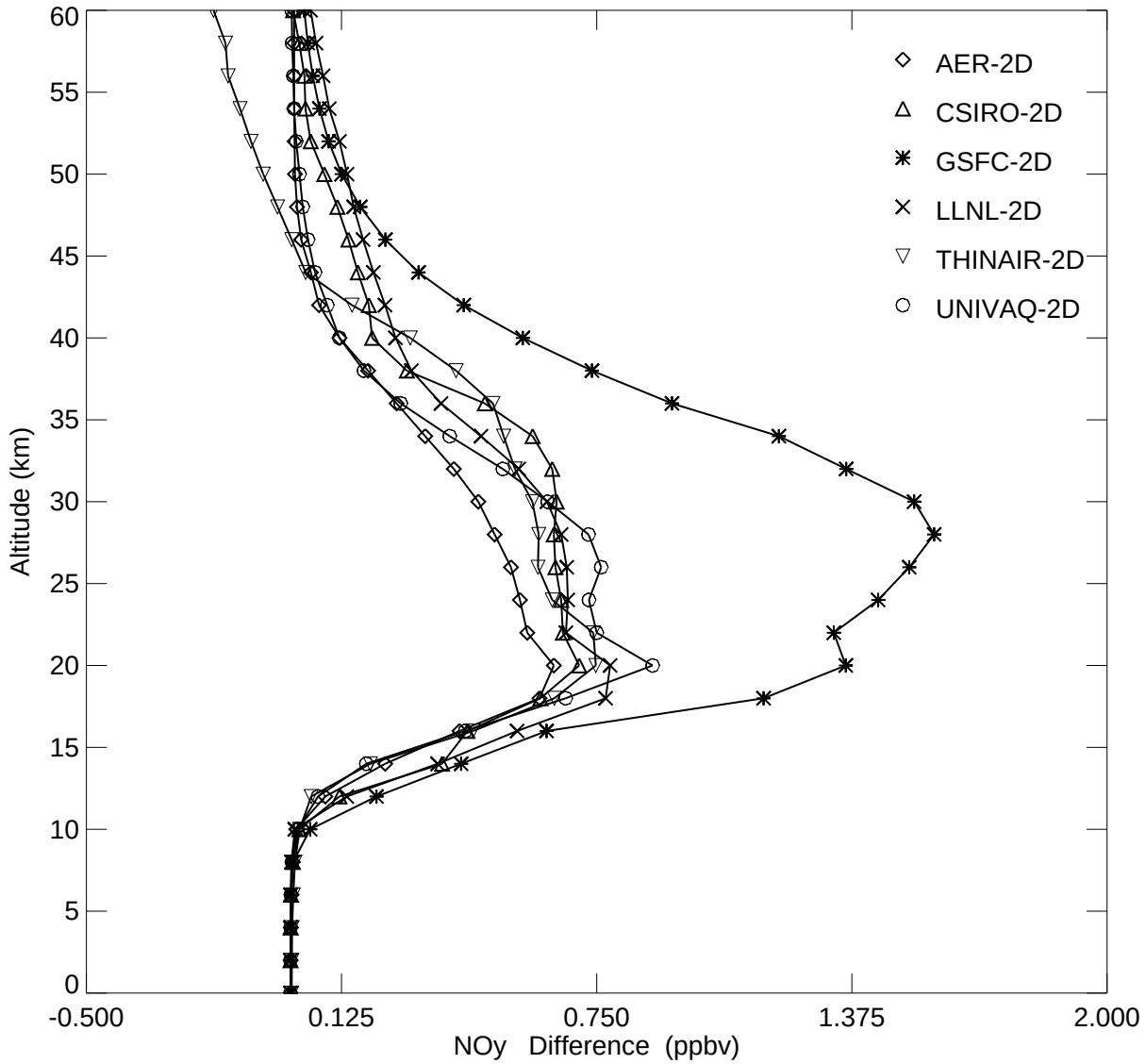

Figure 4.40: Calculated perturbations to NO_y (ppbv) as a function of altitude at 45°S in June of 2015 due to NO_x emissions from a fleet of 1000 HSCT aircraft with EI(NO_x)=10 under Scenario S1j relative to Scenario D.

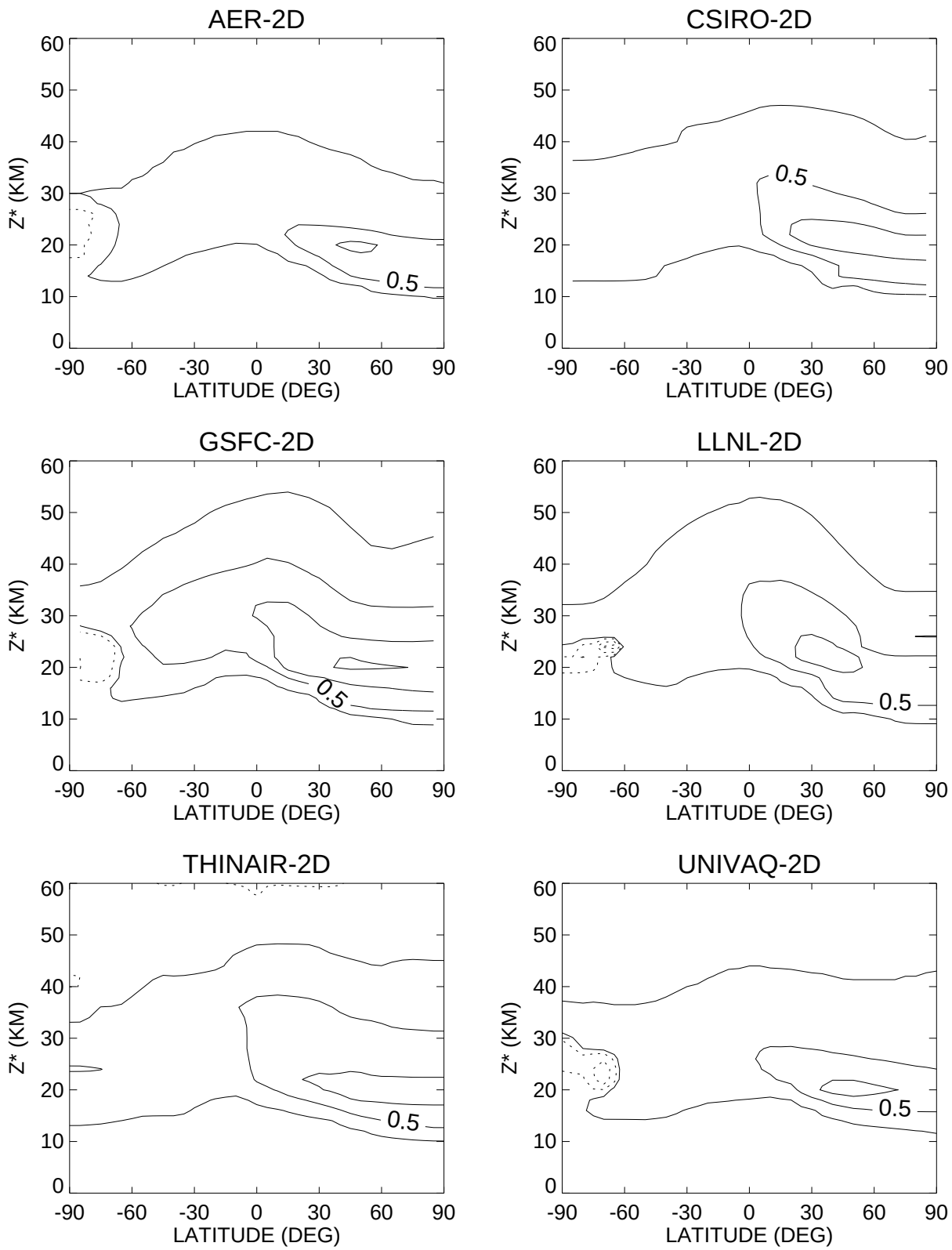

Figure 4.41: Calculated perturbations to NO_y (ppbv) as a function of latitude and altitude in June of 2015 due to NO_x emissions from a fleet of 500 HSCT aircraft operating at 2 km above nominal cruise altitude with EI(NO_x)=5 under Scenario S2a relative to Scenario D. Contours are -1.0, -0.5, 0, 0.5, 1.0, 2.0 ppbv.

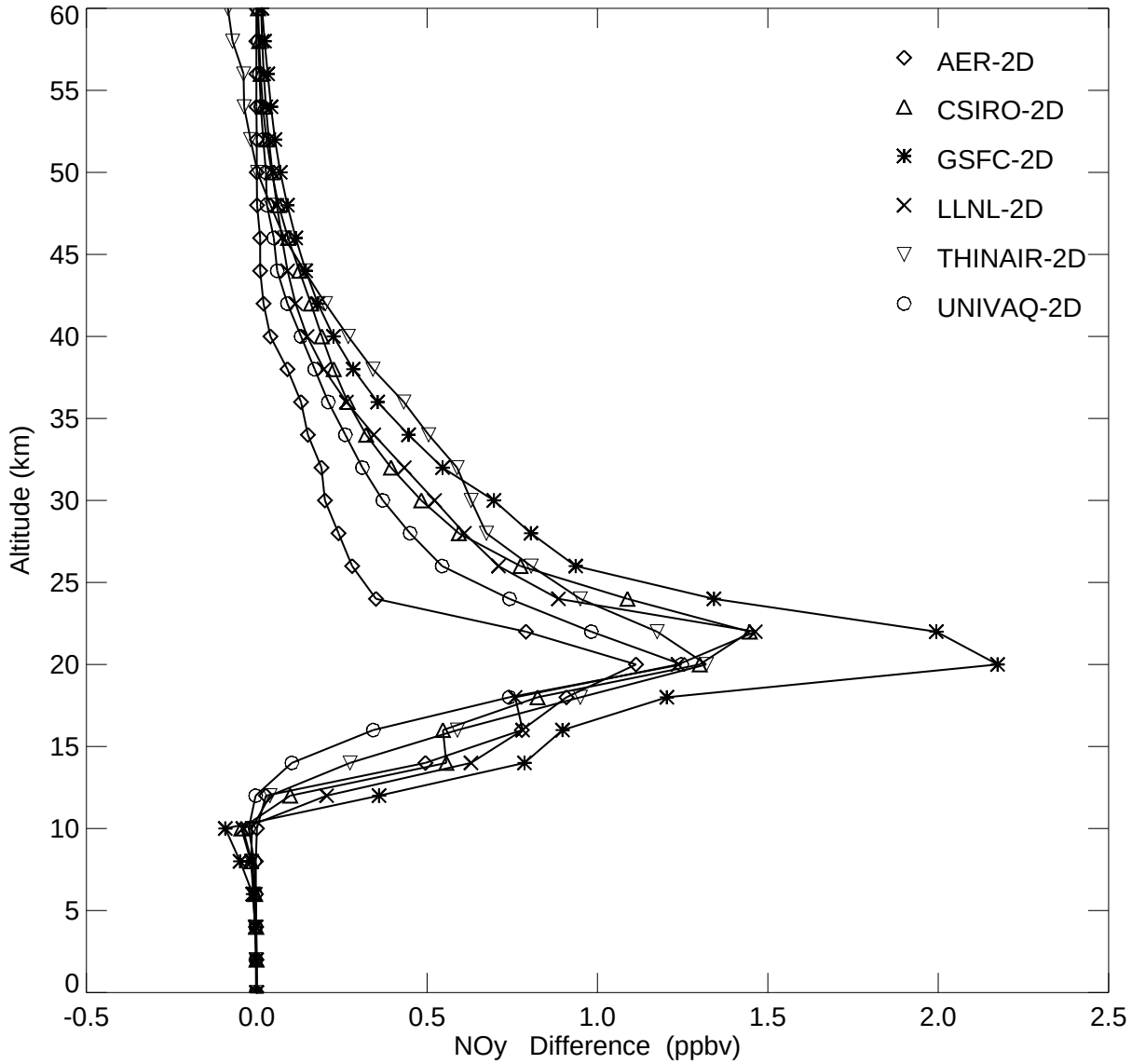

Figure 4.42: Calculated perturbations to NO_y (ppbv) as a function of altitude at 45^oN in June of 2015 due to NO_x emissions from a fleet of 500 HSCT aircraft operating at 2 km above nominal cruise altitude with EI(NO_x)=5 under Scenario S2a relative to Scenario D.

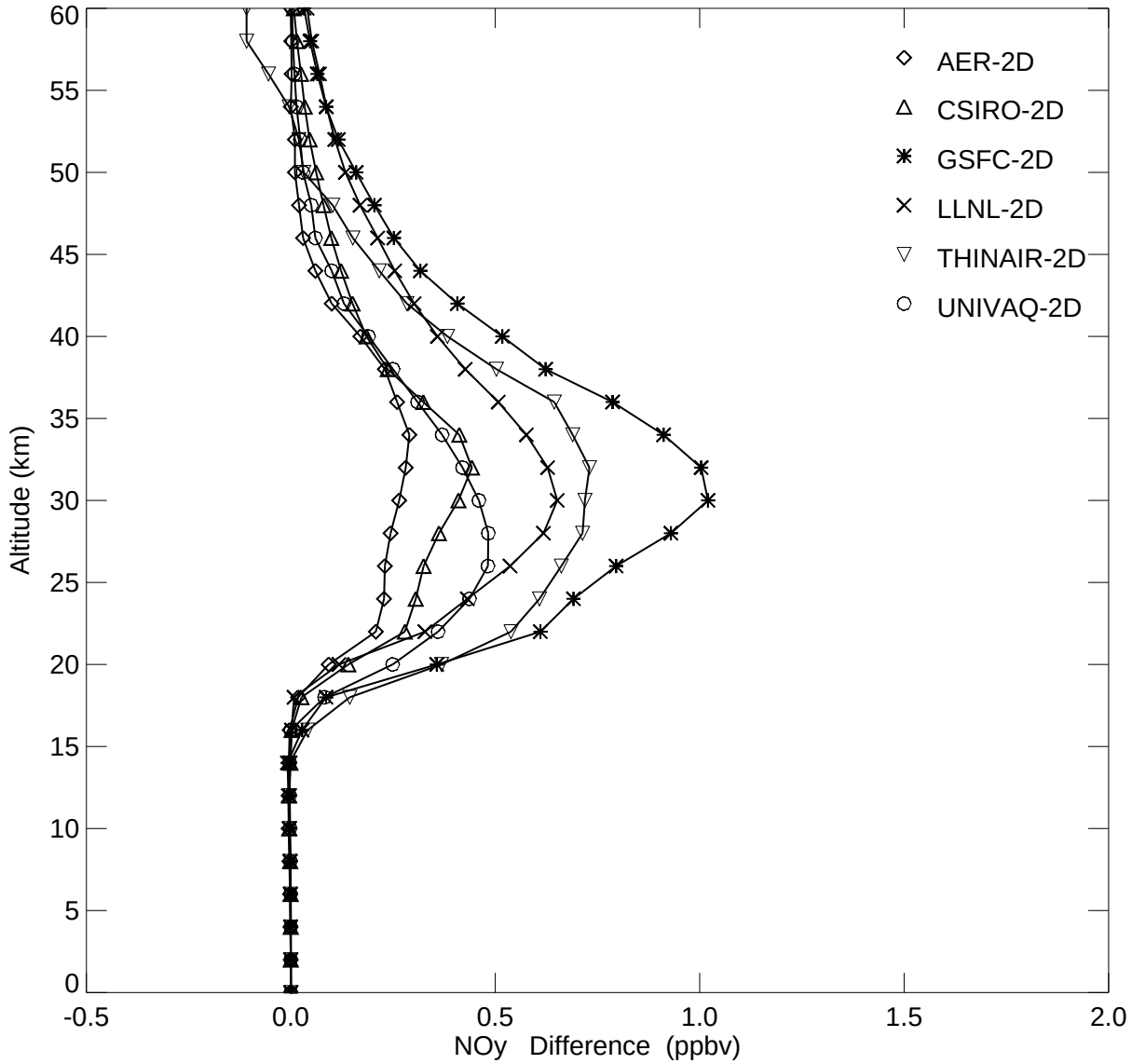

Figure 4.43: Calculated perturbations to NO_y (ppbv) as a function of altitude at the equator in June of 2015 due to NO_x emissions from a fleet of 500 HSCT aircraft operating at 2 km above nominal cruise altitude with EI(NO_x)=5 under Scenario S2a relative to Scenario D.

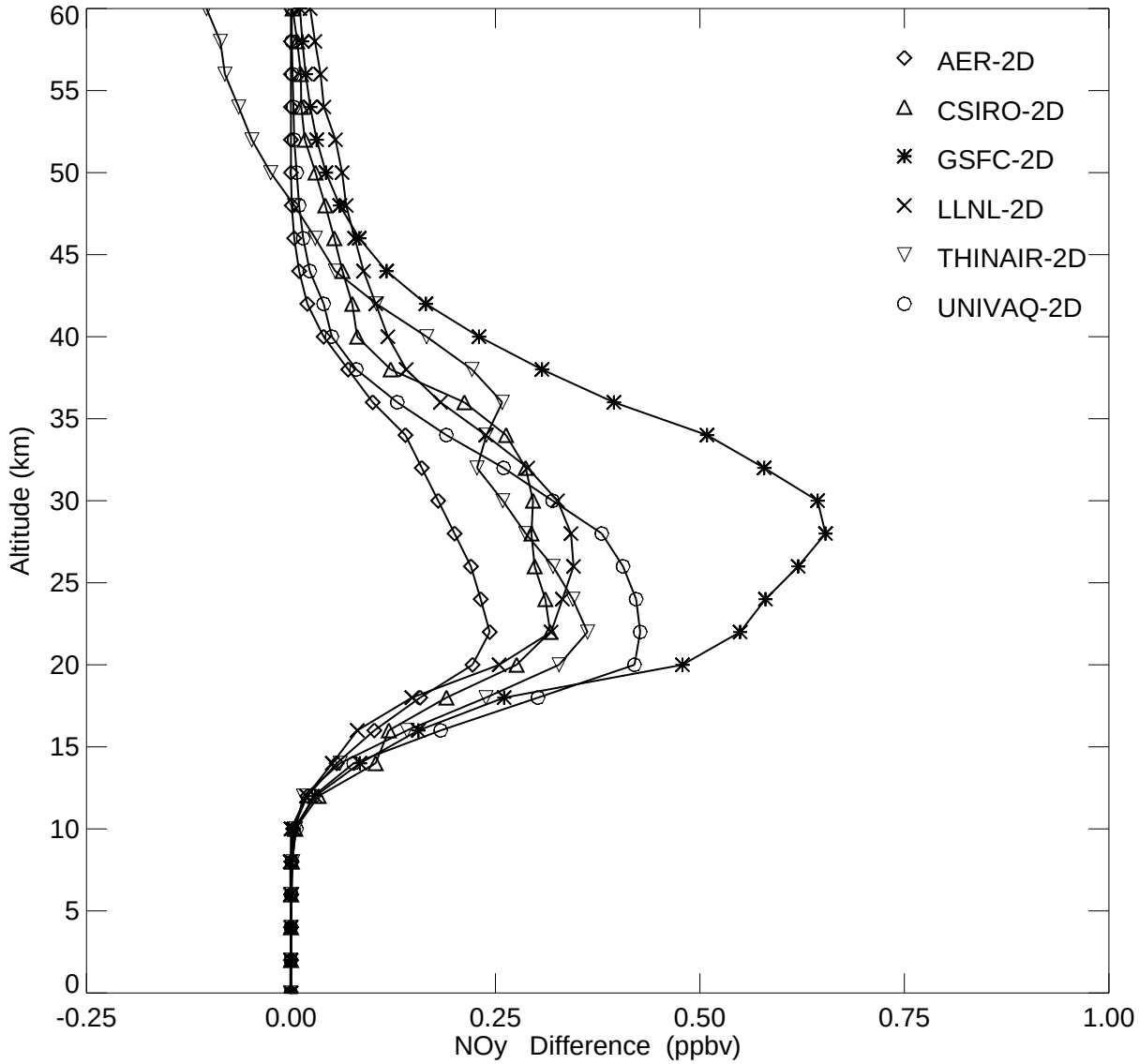

Figure 4.44: Calculated perturbations to NO_y (ppbv) as a function of altitude at 45^oS in June of 2015 due to NO_x emissions from a fleet of 500 HSCT aircraft operating at 2 km above nominal cruise altitude with EI(NO_x)=5 under Scenario S2a relative to Scenario D.

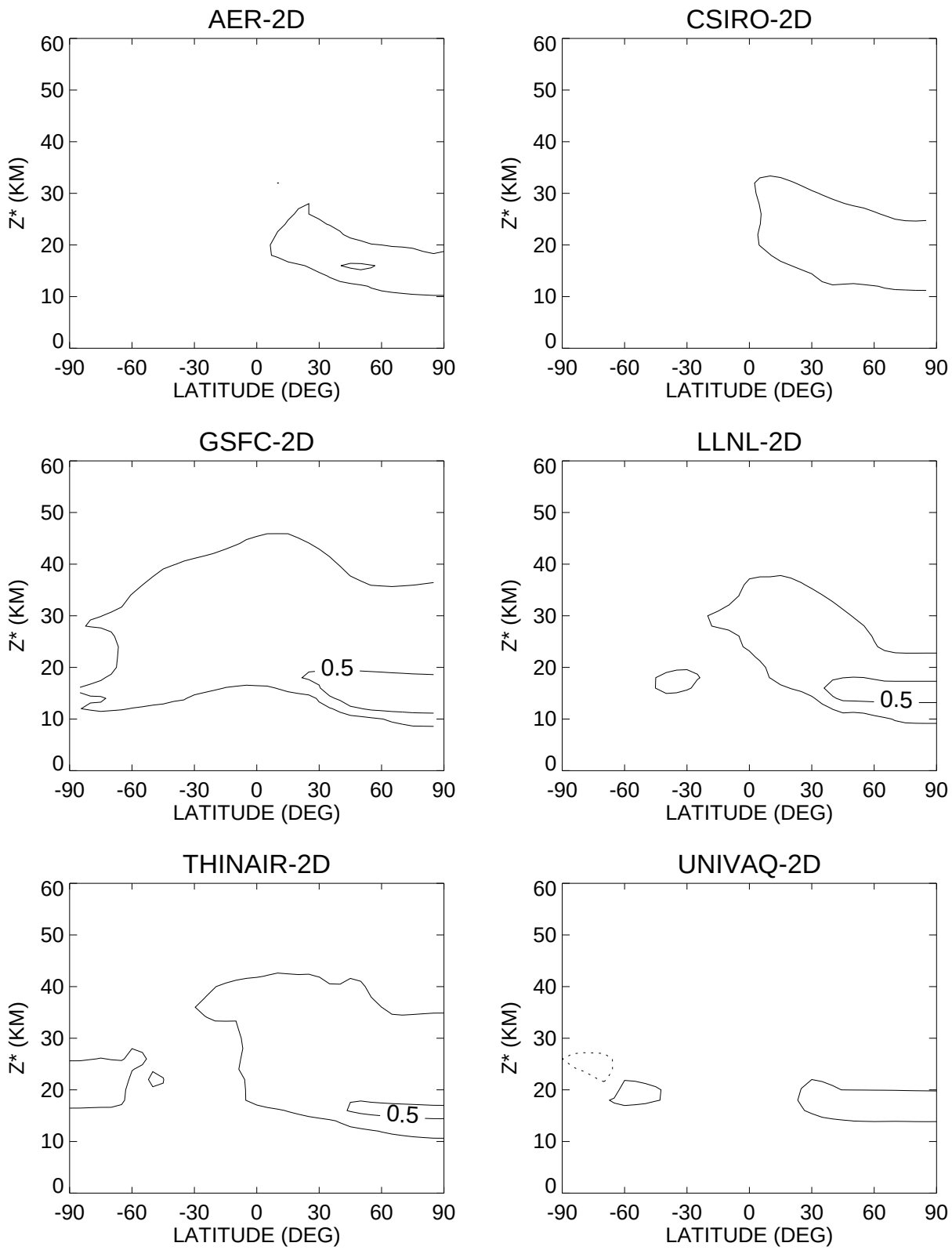

Figure 4.45: Calculated perturbations to NO_y (ppbv) as a function of latitude and altitude in June of 2015 due to NO_x emissions from a fleet of 500 HSCT aircraft operating at 2 km below nominal cruise altitude with EI(NO_x)=5 under Scenario S2b relative to Scenario D. Contours are -0.1, 0, 0.1, 0.25, 0.5, 0.75 ppbv.

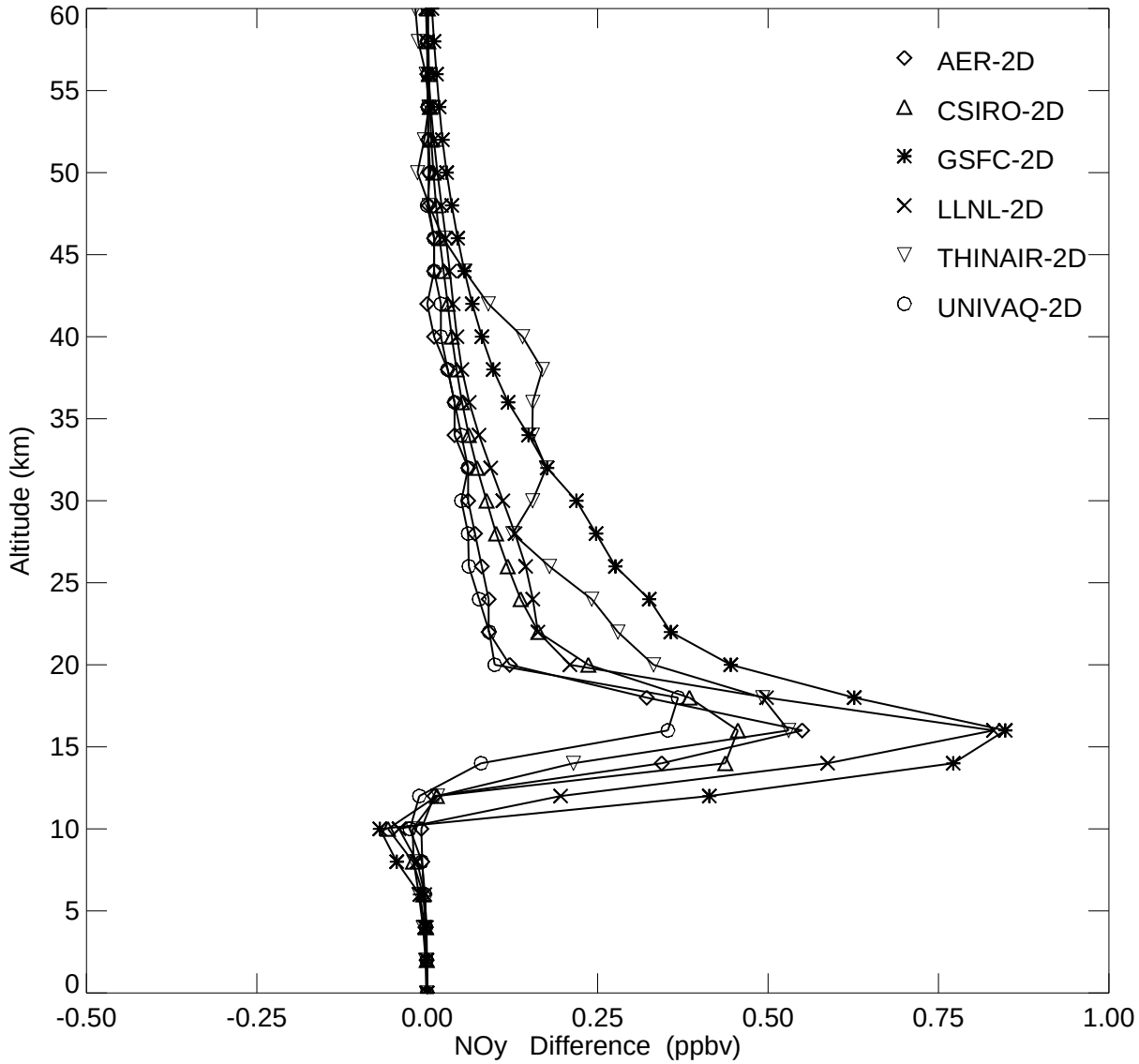

Figure 4.46: Calculated perturbations to NO_y (ppbv) as a function of altitude at 45^{o}N in June of 2015 due to NO_x emissions from a fleet of 500 HSCT aircraft operating at 2 km below nominal cruise altitude with EI(NO_x)=5 under Scenario S2b relative to Scenario D.

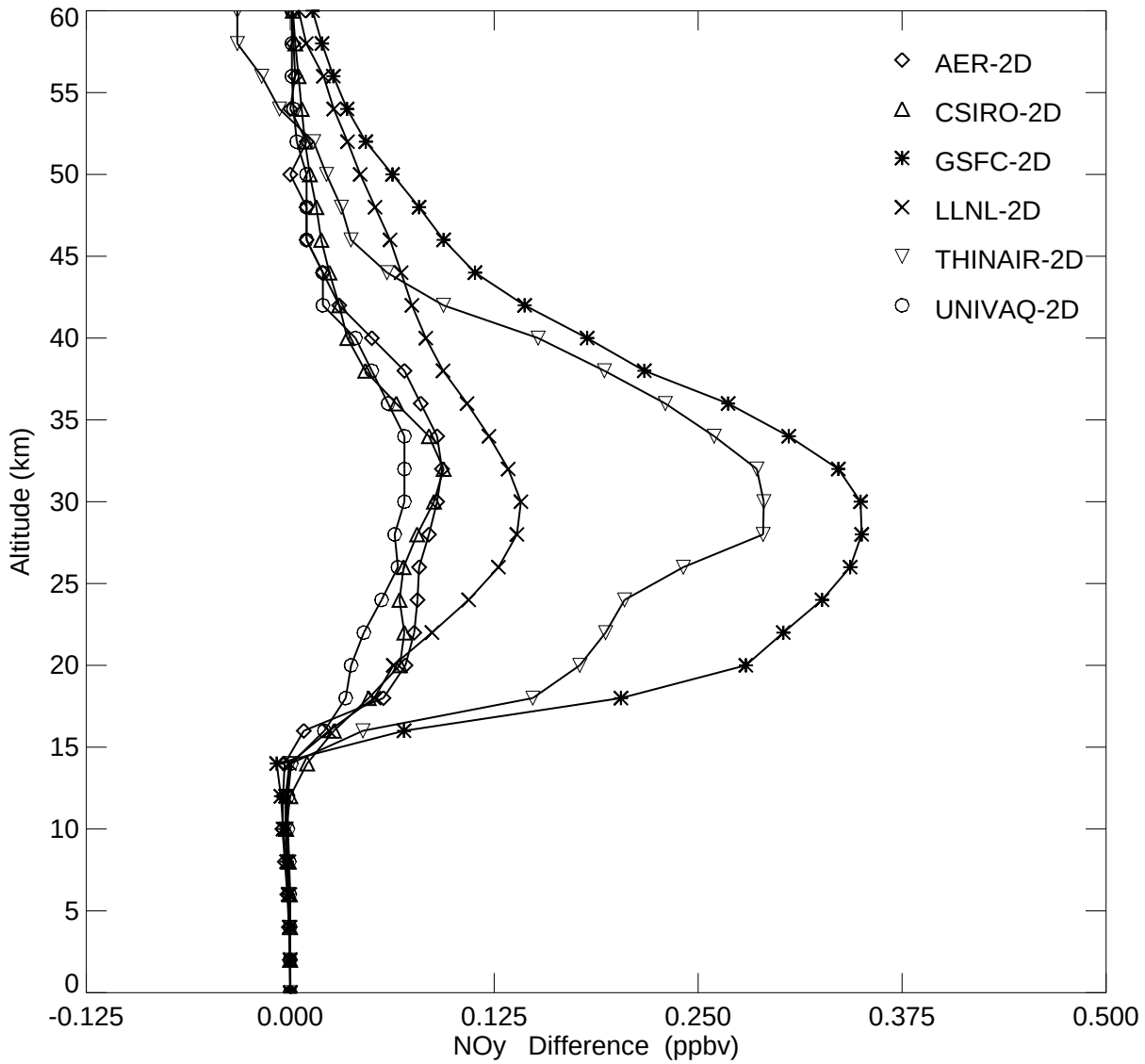

Figure 4.47: Calculated perturbations to NO_y (ppbv) as a function of altitude at the equator in June of 2015 due to NO_x emissions from a fleet of 500 HSCT aircraft operating at 2 km below nominal cruise altitude with EI(NO_x)=5 under Scenario S2b relative to Scenario D.

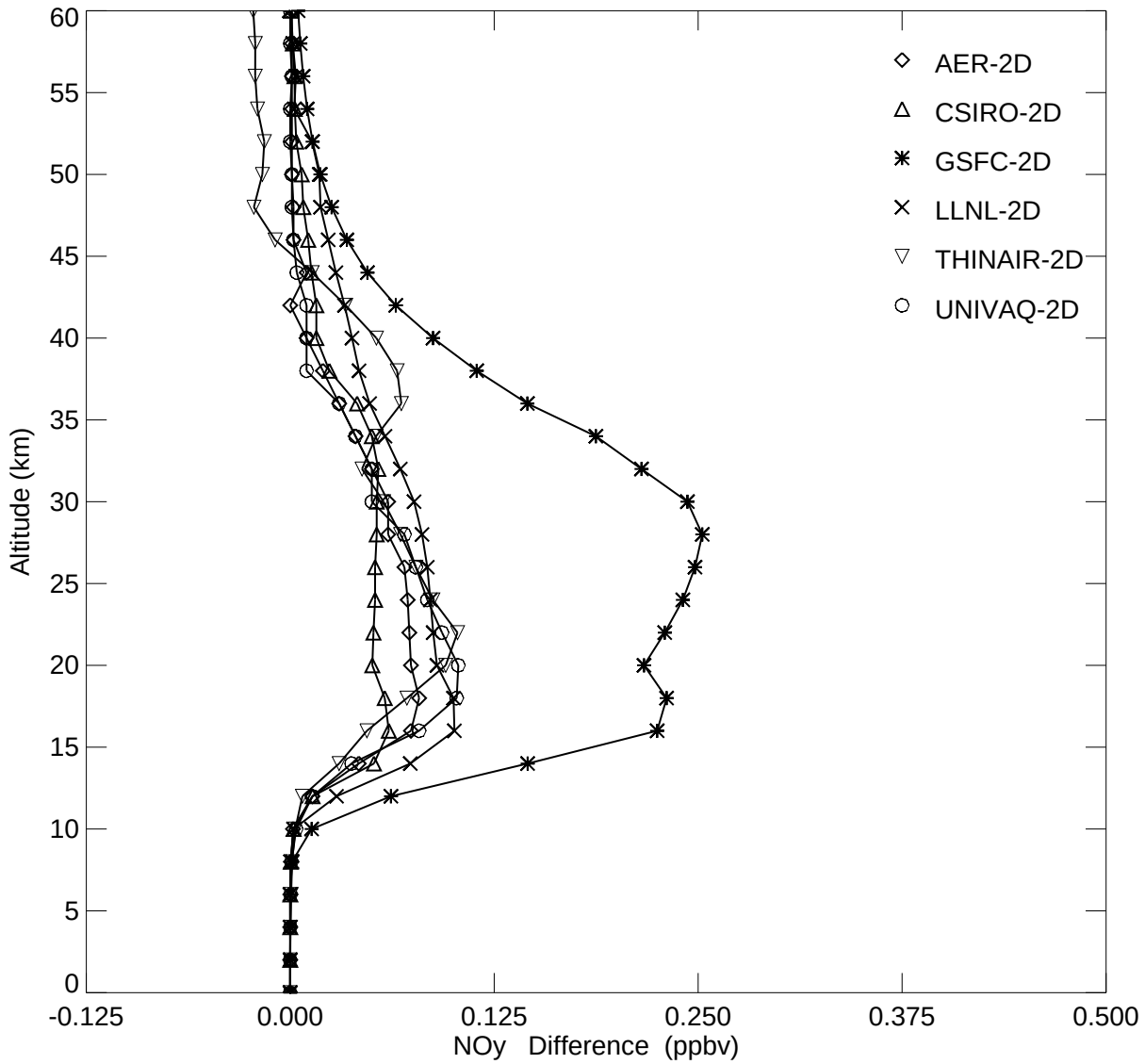

Figure 4.48: Calculated perturbations to NO_y (ppbv) as a function of altitude at 45^oS in June of 2015 due to NO_x emissions from a fleet of 500 HSCT aircraft operating at 2 km below nominal cruise altitude with EI(NO_x)=5 under Scenario S2b relative to Scenario D.

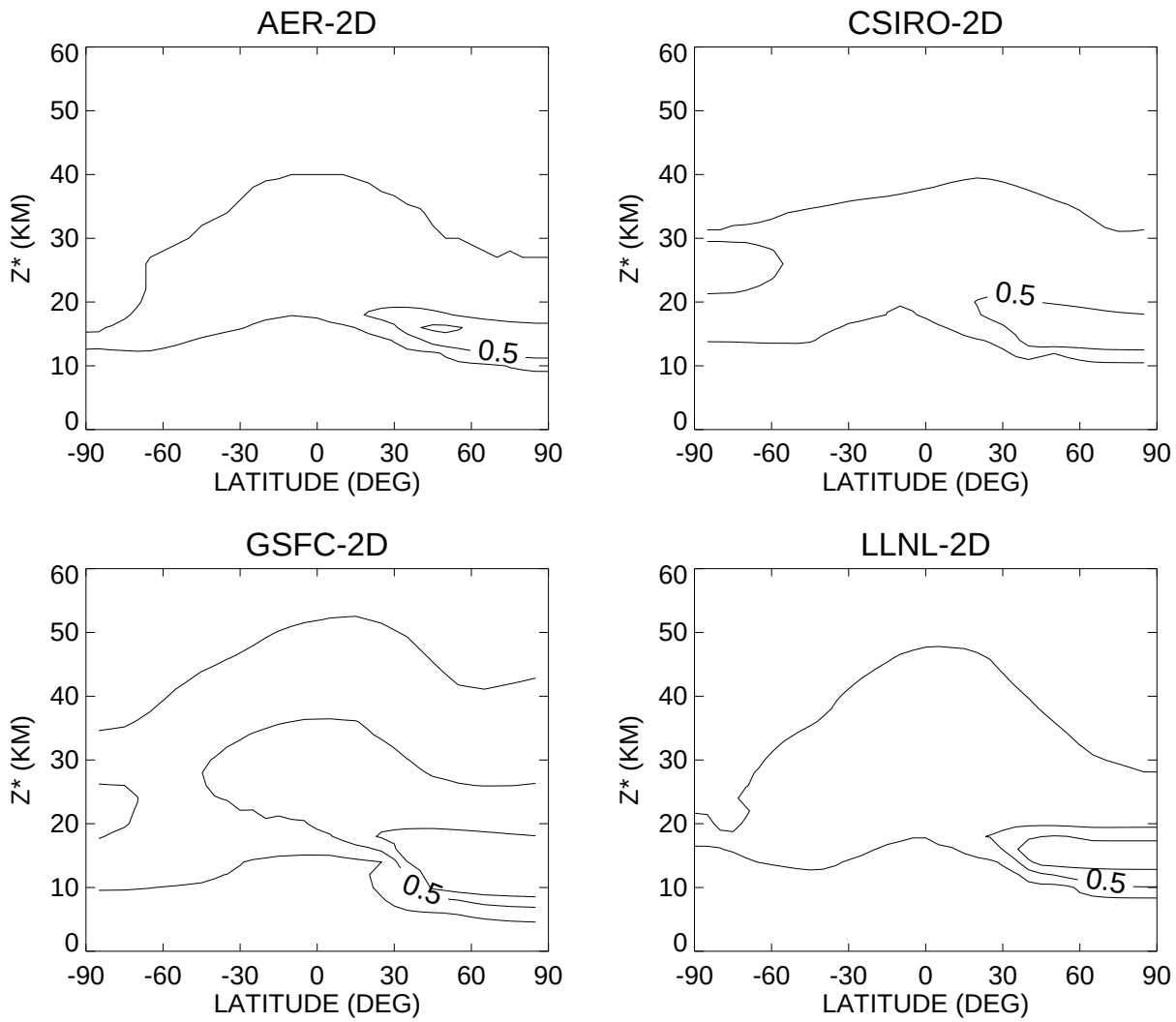

Figure 4.49: Calculated perturbations to NO_y (ppbv) as a function of latitude and altitude in June of 2015 due to NO_x emissions from a fleet of 500 HSCT aircraft operating at 2 km below nominal cruise altitude with EI(NO_x)=10 under Scenario S2c relative to Scenario D. Contours are 0, 0.5, 1.0 ppbv.

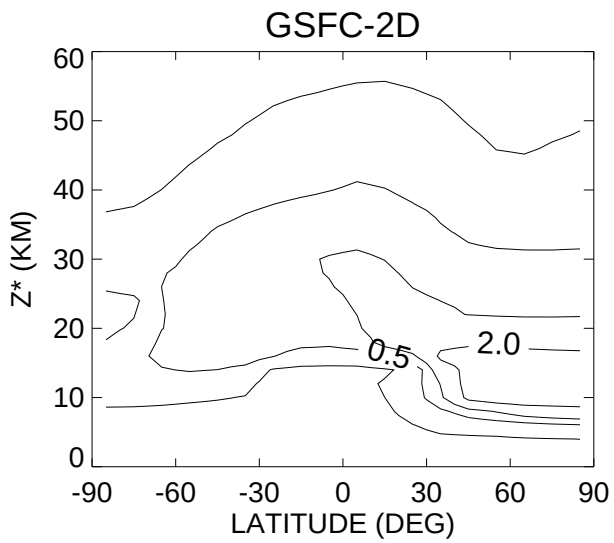

Figure 4.50: Calculated perturbations to NO_y (ppbv) as a function of latitude and altitude in June of 2015 due to NO_x emissions from a fleet of 500 HSCT aircraft operating at 2 km below nominal cruise altitude with EI(NO_x)=15 under Scenario S2d relative to Scenario D. Contours are 0, 0.5, 1.0, 2.0 ppbv.

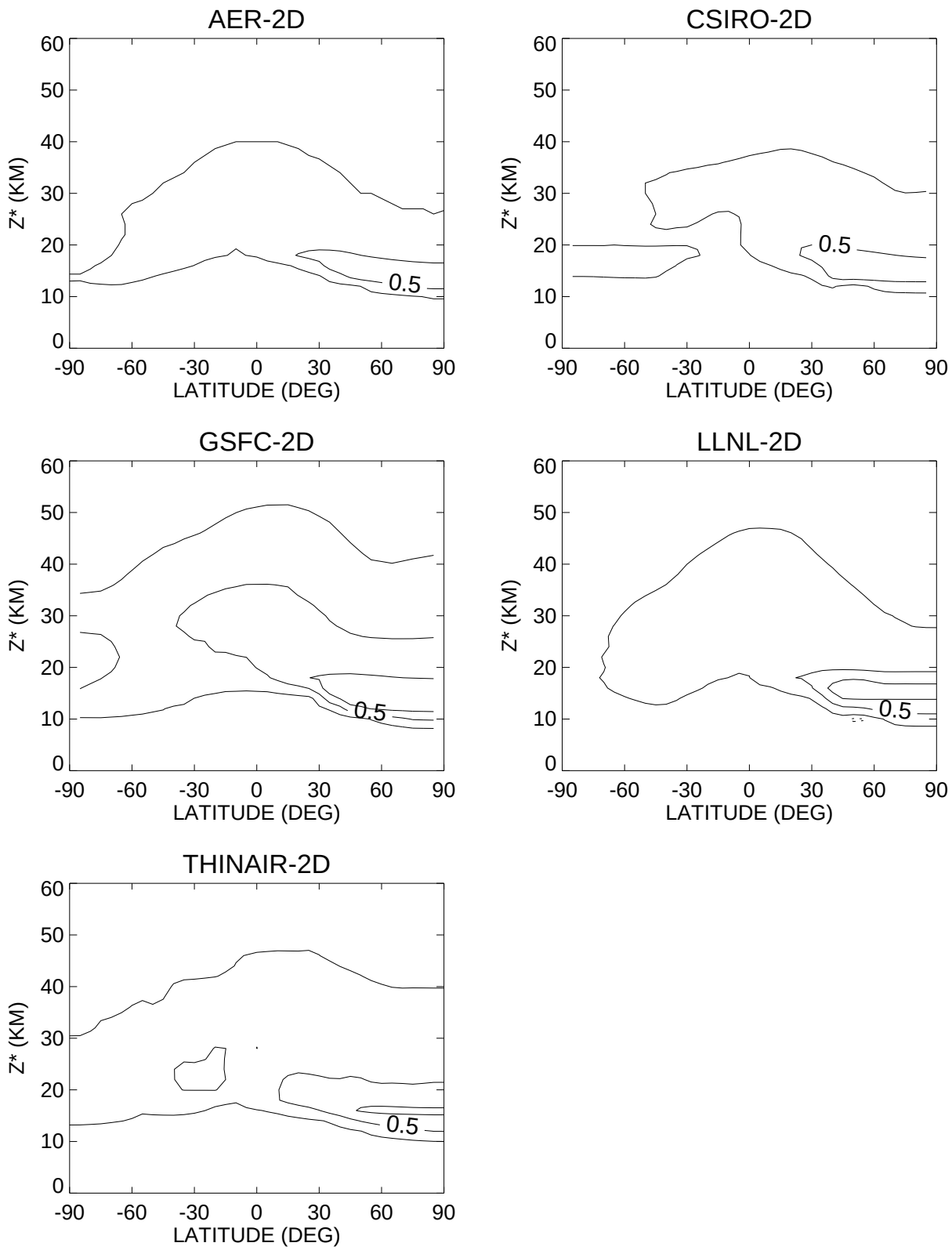

Figure 4.51: Calculated perturbations to NO_y (ppbv) as a function of latitude and altitude in June of 2015 due to NO_x emissions from a fleet of 1000 HSCT aircraft operating at 2 km below nominal cruise altitude with EI(NO_x)=5 under Scenario S2e relative to Scenario D. Contours are 0, 0.5, 1.0 ppbv.

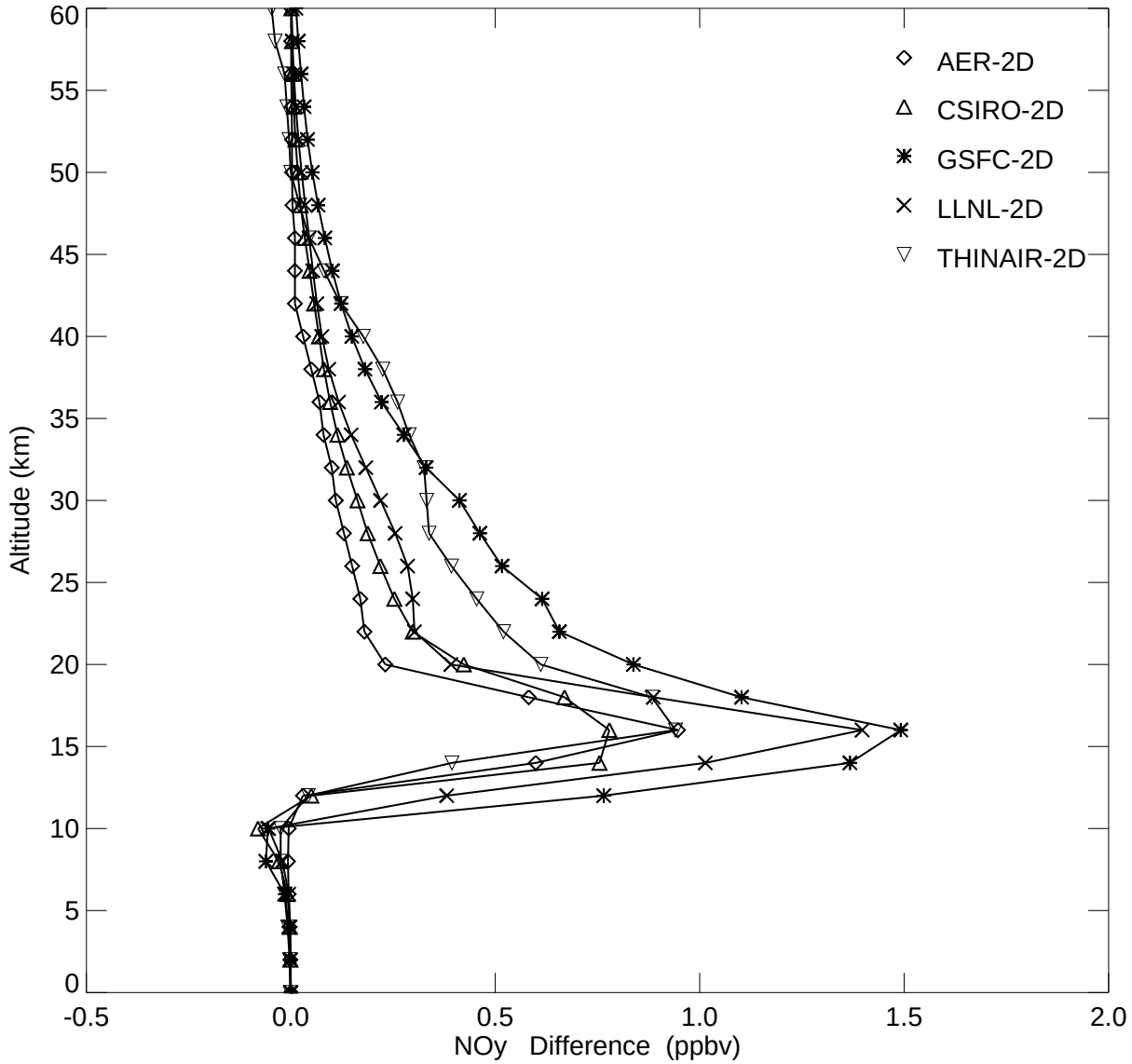

Figure 4.52: Calculated perturbations to NO_y (ppbv) as a function of altitude at 45^{o}N in June of 2015 due to NO_x emissions from a fleet of 1000 HSCT aircraft operating at 2 km below nominal cruise altitude with EI(NO_x)=5 under Scenario S2e relative to Scenario D.

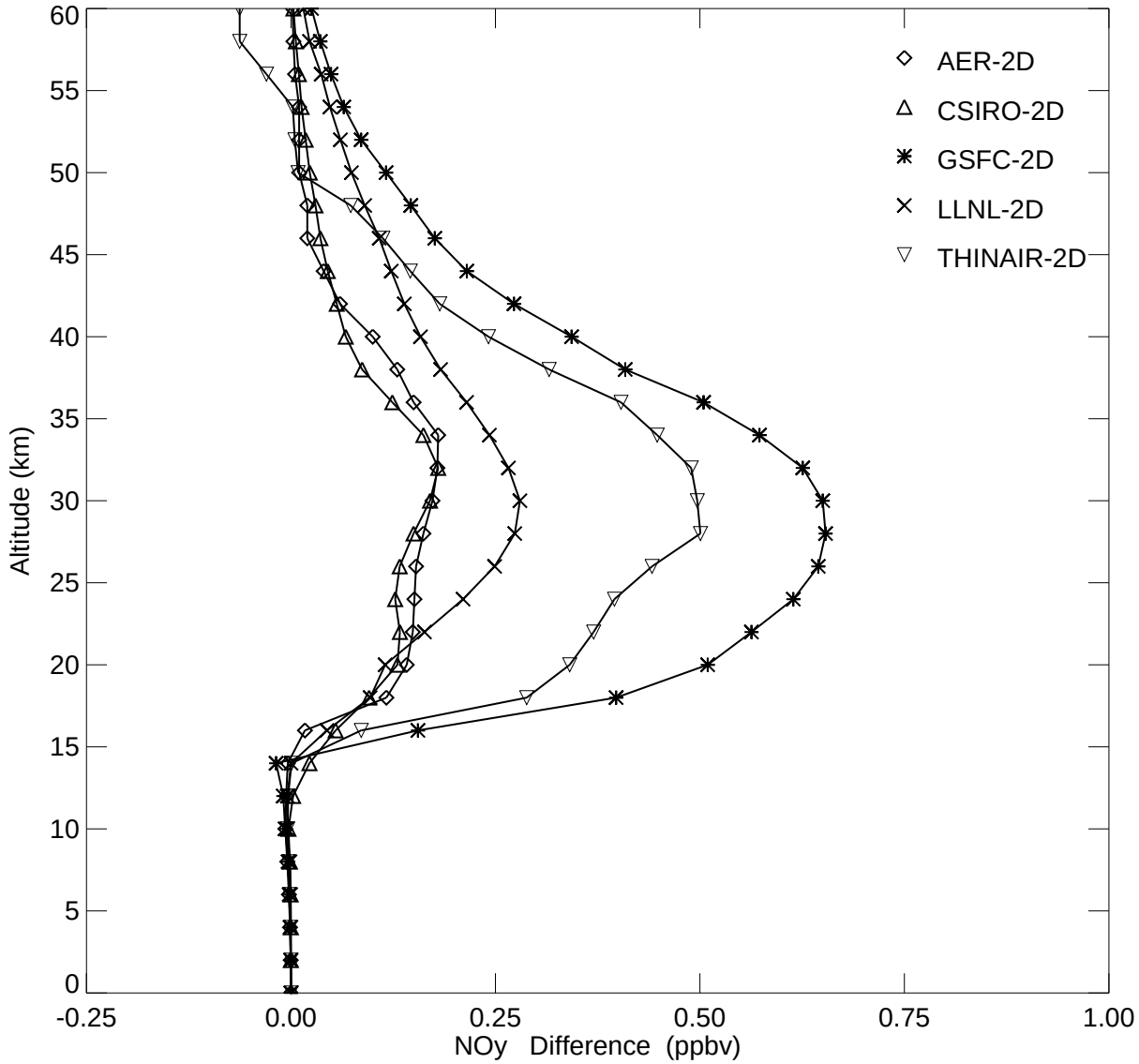

Figure 4.53: Calculated perturbations to NO_y (ppbv) as a function of altitude at the equator in June of 2015 due to NO_x emissions from a fleet of 1000 HSCT aircraft operating at 2 km below nominal cruise altitude with EI(NO_x)=5 under Scenario S2e relative to Scenario D.

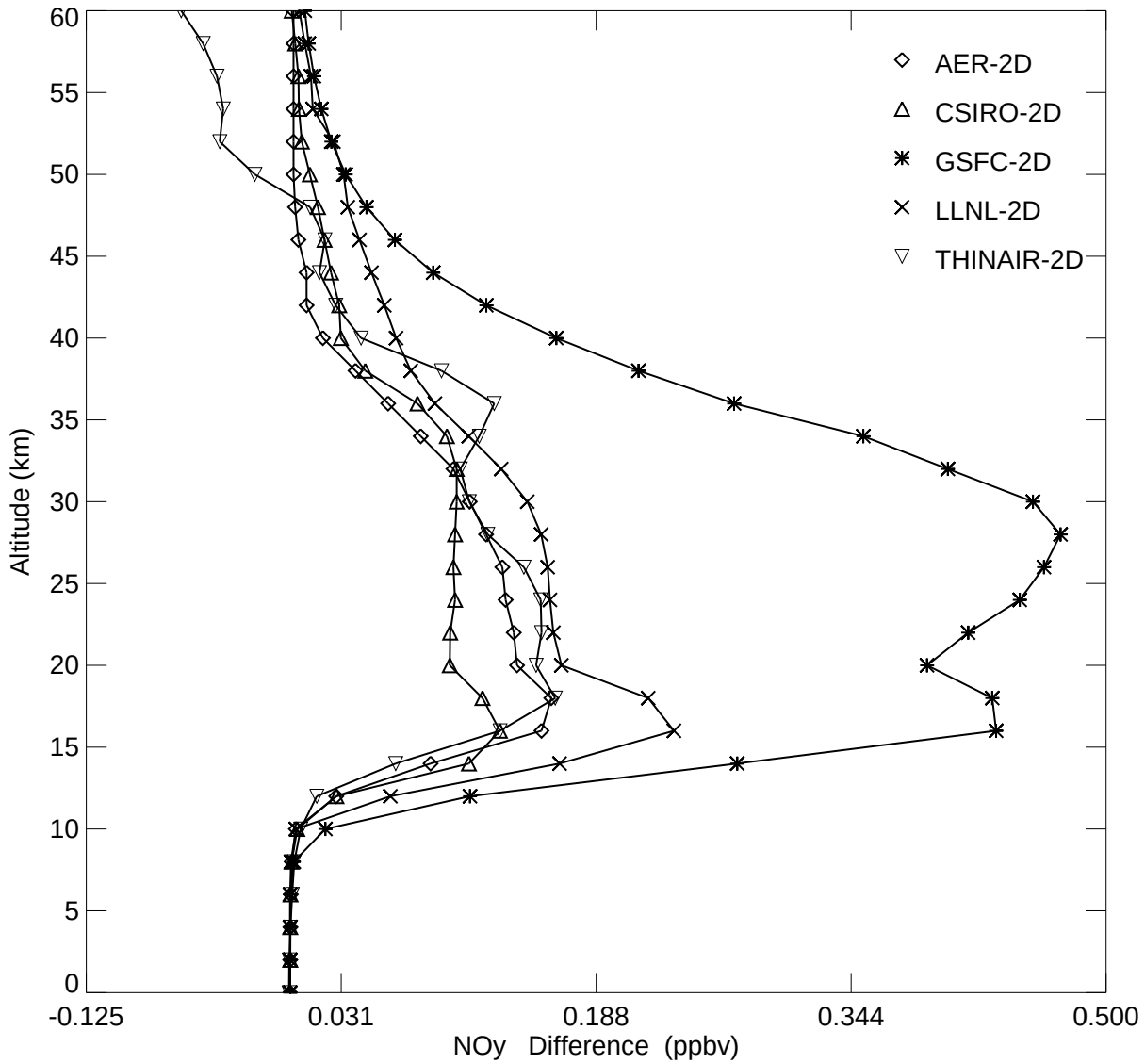

Figure 4.54: Calculated perturbations to NO_y (ppbv) as a function of altitude at 45^oS in June of 2015 due to NO_x emissions from a fleet of 1000 HSCT aircraft operating at 2 km below nominal cruise altitude with EI(NO_x)=5 under Scenario S2e relative to Scenario D.

4.3 O_3 Perturbations

Changes in ozone are related to changes in ultra-violet radiation reaching the ground. Changes in ozone would also be expected to modify the climate. Thus predicted changes in ozone are the most important results provided in Chapter 4 of IPCC. A synopsis of calculated ozone column changes is listed in Table 4.2 for the northern and southern hemispheres for each model for all of the 2015 scenarios. In the following sections, changes in ozone are plotted for each scenario. Changes in ozone as a function of altitude and latitude are shown for March, June, and October. These months were chose to present both polar regions in their respective springtimes, since the northern and southern polar regions often respond differently to perturbations in H_2O and NO_y. This is due to the colder temperatures in the southern polar region, which allows for PSC occurrence and denitrification/dehydration to occur continuously throughout the winter season.

4.3.1 Base Scenarios (S1a-e,i,j)

This set of scenarios is represented by the designations S1a-S1e and S1i-S1j. These scenarios represent variations in EI(NO_x), variations in fleet size, and sensitivity to H_2O emissions. The background atmosphere for all these scenario is D, the 2015 atmosphere with subsonic aircraft and nonvolcanic levels of sulfate aerosol (SA0). Scenarios S1a-S1e assume 500 HSCT aircraft and use the SA0 sulfate surface area density, ie. they assume no emission of sulfur from HSCT aircraft in the stratosphere. Scenarios S1i and S1j assume 1000 HSCT aircraft with EI(NO_x) of 5 or 10 and no sulfur emissions.

Scenario S1a includes NO_x emissions with emission index 5, but no emissions of H_2O. This scenario is provided as a sensitivity study to help separate the impact of NO_x and H_2O on stratospheric ozone. It is completely unrealistic, however, to assume that the aircraft engines could emit no H_2O. The change in March ozone mixing ratio in percent relative to Scenario D is shown in Figure 4.55. Most models show ozone decreases in the stratosphere above 20-30 km and in parts of the troposphere. Ozone increases are found in the lowermost stratosphere and parts of the troposphere due to smog reactions involving NO_x. Changes in zonal-mean ozone are less than 1% for most models over most of the domain. Zonal-mean ozone changes for June are shown in Figure 4.56 and for October in Figure 4.57. The GSFC model shows substantial ozone increases in the southern polar region in October due to HSCT emission of NO_x. Figures 4.58, 4.59, and 4.60 show vertical profiles of ozone change at 45^oN, the equator, and 45^oS, respectively, with all models shown in a single plot. Percentage changes in zonal-mean column ozone for Scenario S1a relative to Scenario D are shown in Figure 4.61. Calculated changes in ozone column for this scenario are quite small, though the SCTM1 model calculates depletions of 0.5% for northern polar regions in summer and fall.

Scenario S1b represents HSCT emissions with EI(NO_x)=0, ie. only emission of H_2O is included. Figures 4.62-4.64 show ozone change as a function of latitude and altitude for Scenario S1b relative to Scenario D for March, June, and October. S1b shows much larger ozone depletions than S1a, indicating that H_2O emissions have a larger impact on ozone than NO_x emissions at EI(NO_x)=5. Emission of H_2O leads to ozone depletion below 20 km and above 35 km. Upper stratospheric ozone depletion ranges from 0.5 to 2% in direct correlation to the amount of H_2O accumulated in this region. Depletion in the lower stratosphere ranges from 0.5 to 3% for most models and seasons, though GSFC shows 10% depletion in October near the south pole. Changes in ozone as a function of altitude at 45^oN, the equator, and 45^oS for June are shown in Figures 4.65-4.67. Perturbation to total ozone as a function of latitude and season are shown in Figure 4.68. Of the six models which calculated this scenario, three predict ozone depletions of 0.5% or more in parts of the northern hemisphere. The GSFC and LLNL models also predicts substantial depletion in the southern hemisphere (-4% maximum for GSFC, -1.4% for LLNL).

The case with both H_2O and NO_x emissions is represented by Scenario S1c, with 500 HSCT aircraft, EI(NO_x)=5, and no sulfur emissions. All 9 models performed this calculation. Changes in ozone for Scenario S1c relative to Scenario D are shown in Figures 4.69, 4.70, and 4.71 for March, June, and October, respectively. Changes in ozone as a function of altitude at 45^oN, the equator, and 45^oS are shown in Figures 4.72-4.74. All models show a positive ozone response in the tropical lower stratosphere, with the UNIVAQ model shows the largest positive response there. The LARC model shows a substantial positive response in the northern hemisphere lower stratosphere and upper troposphere as well. The GSFC model shows the largest ozone perturbations above 35 km and in the southern hemisphere lower stratosphere at all

Table 4.2: Annual Average Ozone Column Perturbations (in percent) for Each Model for the Northern Hemisphere (top number) and Southern Hemisphere (bottom number) in 2015

Scen -ario	Fleet Size	EI NO_x	SAD Desc.	Special	AER	GSFC	UNI-VAQ	LLNL	CSI -RO	THIN -AIR	SLIM -CAT	SCT -M1	LARC
S1a	500	5	SA0	No H_2O	-0.07	-0.1	0.2	-0.01	-0.09	-	-0.2	-0.2	-
					-0.03	0.03	0.1	0.1	-0.07	-	-0.09	-0.007	-
S1b	500	0	SA0		-0.6	-0.4	-0.4	-0.3	-0.2	-	-0.6	-	-
					-0.3	-0.8	-0.2	-0.3	-0.07	-	-0.7	-	-
S1c	500	5	SA0		-0.3	-0.4	-0.002	-0.2	-0.2	-0.2	-0.4	-0.3	-0.05
					-0.1	-0.8	0.02	-0.2	-0.1	-0.2	-0.6	-0.1	-0.1
S1d	500	10	SA0		-0.3	-0.6	0.2	-0.3	-0.3	-0.5	-0.5	-0.5	0.07
					-0.1	-0.7	0.1	-0.1	-0.2	-0.3	-0.7	-0.1	-0.03
S1e	500	15	SA0		-0.3	-0.8	0.4	-0.4	-0.5	-0.9	-	-	-
					-0.05	-0.7	0.2	-0.01	-0.3	-0.5	-	-	-
S1f	500	5	SA1		-1.0	-1.1	-0.4	-0.7	-0.5	-	-	-	-0.4
					-0.4	-1.1	-0.1	-0.5	-0.1	-	-	-	-0.3
S1g	500	10	SA1		-0.8	-1.1	-0.2	-0.7	-0.5	-	-	-	-
					-0.3	-1.0	-0.01	-0.4	-0.2	-	-	-	-
S1h	500	5	SA3		-1.1	-1.3	-0.5	-0.8	-0.5	-	-	-	-
					-0.4	-1.2	-0.2	-0.6	-0.1	-	-	-	-
S1i	1000	5	SA0		-0.7	-0.9	-0.06	-0.5	-0.5	-0.4	-	-	-
					-0.3	-1.4	0.005	-0.3	-0.2	-0.3	-	-	-
S1j	1000	10	SA0		-0.7	-1.4	0.1	-0.7	-0.7	-1.1	-	-	-
					-0.2	-1.4	0.2	-0.2	-0.3	-0.6	-	-	-
S1k	500	5	SA5		-0.8	-0.7	-0.2	-0.5	-0.4	-	-	-	-
					-0.3	-0.9	-0.05	-0.3	-0.1	-	-	-	-
S1l	500	5	SA7		-0.6	-	-	-	-	-	-	-	-
					-0.3	-	-	-	-	-	-	-	-
S2a	500	5	SA0	Cruise +2 km	-0.7	-1.0	-0.1	-0.6	-0.6	-0.3	-	-	-
					-0.2	-1.2	-0.06	-0.3	-0.2	-0.2	-	-	-
S2b	500	5	SA0	Cruise -2 km	-0.1	-0.09	0.01	-0.05	-0.05	-0.09	-	-	-
					-0.04	-0.2	0.03	-0.01	-0.03	-0.09	-	-	-
S2c	500	10	SA0	Cruise -2 km	-0.1	0.1	-	-0.03	-0.003	-	-	-	-
					-0.1	-0.06	-	0.07	-0.03	-	-	-	-
S2d	500	15	SA0	Cruise -2 km	-	0.3	-	-	-	-	-	-	-
					-	0.07	-	-	-	-	-	-	-
S2e	1000	5	SA0	Cruise -2 km	-0.3	-0.2	-	-0.1	-0.09	-0.2	-	-	-
					-0.2	-0.4	-	-0.02	-0.05	-0.2	-	-	
S3a	500	0	4xSA0		-0.5	-0.5	-0.4	-0.4	-0.3	-	-	-	-
					-0.2	-0.7	-0.1	-0.3	-0.1	-	-	-	-
S3b	500	5	4xSA0		-0.2	-0.04	0.07	-0.2	-0.09	-	-	-	-
					-0.09	-0.5	0.06	-0.2	-0.09	-	-	-	-
S3c	500	10	4xSA0		0.04	0.2	0.4	0.001	0.03	-	-	-	-
					0.02	-0.4	0.2	-0.04	-0.08	-	-	-	-
S3d	500	15	4xSA0		0.2	0.4	0.6	0.09	0.09	-	-	-	-
					0.1	-0.3	0.3	0.07	-0.07	-	-	-	-
S3e	500	5	4xSA0+ SA1-SA0		-0.5	-0.4	-0.09	-0.3	-0.2	-	-	-	-
					-0.2	-0.6	-0.01	-0.3	-0.1	-	-	-	-
S3f	500	5	4xSA0+ SA3-SA0		-0.6	-0.5	-0.2	-0.4	-0.3	-	-	-	-
					-0.2	-0.7	-0.02	-0.3	-0.1	-	-	-	-
S4a	500	0	SA0	No PSCs	-0.5	-0.4	-0.3	-	-0.2	-	-	-	-
					-0.3	-0.3	-0.1	-	-0.07	-	-	-	-
S4b	500	5	SA0	No PSCs	-0.2	-0.4	0.02	-	-0.2	-	-	-	-
					-0.1	-0.3	0.001	-	-0.1	-	-	-	-
S4c	500	5	SA0	No PSCs No H_2O	-0.1	-0.2	0.3	-	-0.09	-	-	-	-
					-0.1	-0.02	0.1	-	-0.07	-	-	-	-
S5a	500	5	SA0	Cl_y= 1.0 ppbv	-0.3	-0.5	-0.006	-	-	-	-	-	-
					-0.1	-0.5	-0.02	-	-	-	-	-	-
S5b	500	5	SA1	Cl_y= 1.0 ppbv	-0.5	-0.7	-0.3	-	-	-	-	-	-
					-0.2	-0.7	-0.1	-	-	-	-	-	-
S6a	500	5	SA0	Cl_y= 4.0 ppbv	-0.4	-0.4	0.03	-	-	-	-	-	-
					-0.1	-0.8	-0.01	-	-	-	-	-	-
S6b	500	5	SA1	Cl_y= 4.0 ppbv	-1.0	-1.1	-0.4	-	-	-	-	-	-
					-0.4	-1.0	-0.2	-	-	-	-	-	-
S7a	500	5	50% Part.	Microphysics	-1.0	-	-0.5	-	-	-	-	-	-
					-0.4	-	-0.3	-	-	-	-	-	-
S7b	500	5	50% Part.	Microphysics Cruise +2 km	-1.4	-	-0.7	-	-	-	-	-	-
					-0.5	-	-0.4	-	-	-	-	-	-
S7c	500	5	50% Part.	Microphysics Cruise -2 km	-0.6	-	-0.2	-	-	-	-	-	-
					-0.3	-	-0.1	-	-	-	-	-	-
S7d	500	10	50% Part.	Microphysics	-0.9	-	-0.2	-	-	-	-	-	-
					-0.4	-	-0.2	-	-	-	-	-	-
S8a	500	5	100% Part.	Microphysics	-1.1	-	-0.5	-	-	-	-	-	-
					-0.5	-	-0.3	-	-	-	-	-	-

seasons. Changes in total ozone as a function of latitude and season are shown in Figure 4.75. Most models show a slightly smaller ozone column response with NO_x and H_2O emissions than with H_2O emission alone. Changes in total ozone in June as a function of latitude only are shown in Figure 4.76, with all models plotted together. Hemispheric average ozone changes, which are listed in Table 4.2, range from ∼0% to -0.4% in the northern hemisphere and from ∼0% to -0.8% in the southern hemisphere.

Scenario S1d is similar to S1c but with EI(NO_x)=10. Changes in ozone as a function of latitude and altitude for March, June, and October are shown in Figures 4.77, 4.78, and 4.79. Vertical profiles of ozone change are shown in Figures 4.80, 4.81, and 4.82 for 45^{o}N, the equator, and 45^{o}S in June. Compared with Scenario S1c, most models show additional ozone depletion in the northern hemisphere middle and high latitudes between 20 and 35 km. Most models also show less ozone depletion, or a greater ozone increase, in the southern hemisphere below 20 km. Figure 4.83 shows changes in total ozone for this scenario. The CSIRO, THINAIR and SCTM1 models show larger total ozone depletion in Scenario S1d than in Scenario S1c. The UNIVAQ and LARC models shows a more positive ozone response, while the GSFC and LLNL models show more depletion in the northern hemisphere and less depletion in the southern hemisphere. AER show little change in column ozone depletion between Scenarios S1d and S1c.

Scenario S1e is similar to S1d and S1c but with EI(NO_x)=15. The model results continue the pattern seen between Scenarios S1c and S1d. The additional NO_x produced additional ozone depletion in the northern hemisphere middle and high latitudes between 20 and 35 km, and less ozone depletion in the southern hemisphere below 20 km. These results can be seen in Figures 4.84-4.89. Changes in total ozone for Scenario S1e are shown in Figure 4.90. Changes in total ozone in June as a function of latitude only are shown in Figure 4.91, with all models plotted together. The CSIRO, GSFC, and LLNL models show more northern hemisphere ozone depletion than for Scenario S1d. Only the CSIRO and THINAIR models show more ozone depletion in the southern hemisphere. The UNIVAQ model shows a more positive ozone response in both hemispheres.

Sensitivity to aircraft NO_x emissions is shown graphically in Figures 4.92 and 4.93, which plot annual average hemispheric ozone perturbation as a function of EI(NO_x) for 500 HSCT aircraft, background surface area of SA0, and no sulfur emissions. Scenarios S1b-S1e are included. For the northern hemisphere (Figure 4.92), all models show similar or less ozone depletion as the EI(NO_x) varies from 0 to 5, indicating that emission of H_2O from the aircraft plays the dominant role in ozone depletion. The UNIVAQ model shows the largest positive sensitivity in this range, while the AER and SLIMCAT models also show a positive sensitivity. The THINAIR, LARC, and SCTM1 models did not calculate the EI(NO_x)=0 case. Between EI(NO_x)=5 and EI(NO_x)=15, the GSFC, LLNL, CSIRO, THINAIR, AND SLIMCAT models show increased ozone depletion at greater EI(NO_x). The AER model shows little sensitivity to EI(NO_x) in this range, and the UNIVAQ and LARC models show less ozone depletion at greater EI(NO_x). Notice also that the range of calculated ozone perturbations among the models is narrower for smaller EI(NO_x). In the southern hemisphere (Figure 4.93), sensitivities are smaller because of the smaller amount of emitted material released or transported to the southern hemisphere. GSFC and SLIMCAT have substantially larger calculated ozone depletions in the southern hemisphere than other models, but this ozone depletion is insensitive to EI(NO_x).

Scenarios S1i and S1j include 1000 HSCT aircraft, with EI(NO_x)=5 for S1i and EI(NO_x)=10 for S1j. Figures 4.94, 4.95, and 4.96 show ozone percent changes as a function of latitude and altitude for March, June, and October for Scenario S1i relative to Scenario D. Compared with Scenario S1c, all models show substantially more ozone depletion at all seasons for extratropical latitudes. The tropical lower stratosphere shows a greater ozone increase due to the self-healing effect from ozone depletion at higher altitudes. Vertical profiles of ozone changes for Scenario S1i are shown in Figures 4.97, 4.98, and 4.99 for June at 45^{o}N, the equator, and 45^{o}S. Changes in total ozone for Scenario S1i relative to Scenario D are shown in Figure 4.100. Ozone column changes are substantially larger than for Scenario S1c. They are also substantially larger than for Scenario S1d, which has similar NO_x emissions but half the H_2O emissions, indicating the important role of H_2O emissions from HSCT aircraft in future ozone depletion. The THINAIR model differs from the rest in that S1d shows more ozone depletion than S1i, ie. the relative roles of NO_x and H_2O differ from the other models.

Changes in ozone for March, June, and October from Scenario S1j relative to Scenario D are shown in Figures 4.101, 4.102, and 4.103. Ozone depletion above 20 km is enhanced above that from Scenario S1i, while below 20 km, ozone depletion is reduced. Vertical profiles of ozone changes for Scenario S1j are shown in Figures 4.104, 4.105, and 4.106 for June at 45^{o}N, the equator, and 45^{o}S. Changes in total ozone for

Scenario S1j relative to Scenario D are shown in Figure 4.107. Northern hemisphere total ozone depletion is enhanced relative to Scenario S1i in the GSFC, LLNL, CSIRO, and THINAIR models, unchanged in the AER model, and reduced in the UNIVAQ model. In the southern hemisphere, ozone depletion is reduced in the AER, LLNL and UNIVAQ models and enhanced in the CSIRO and THINAIR models relative to Scenario S1i. The GSFC model obtains about the same southern hemisphere ozone depletion for S1j as for S1i.

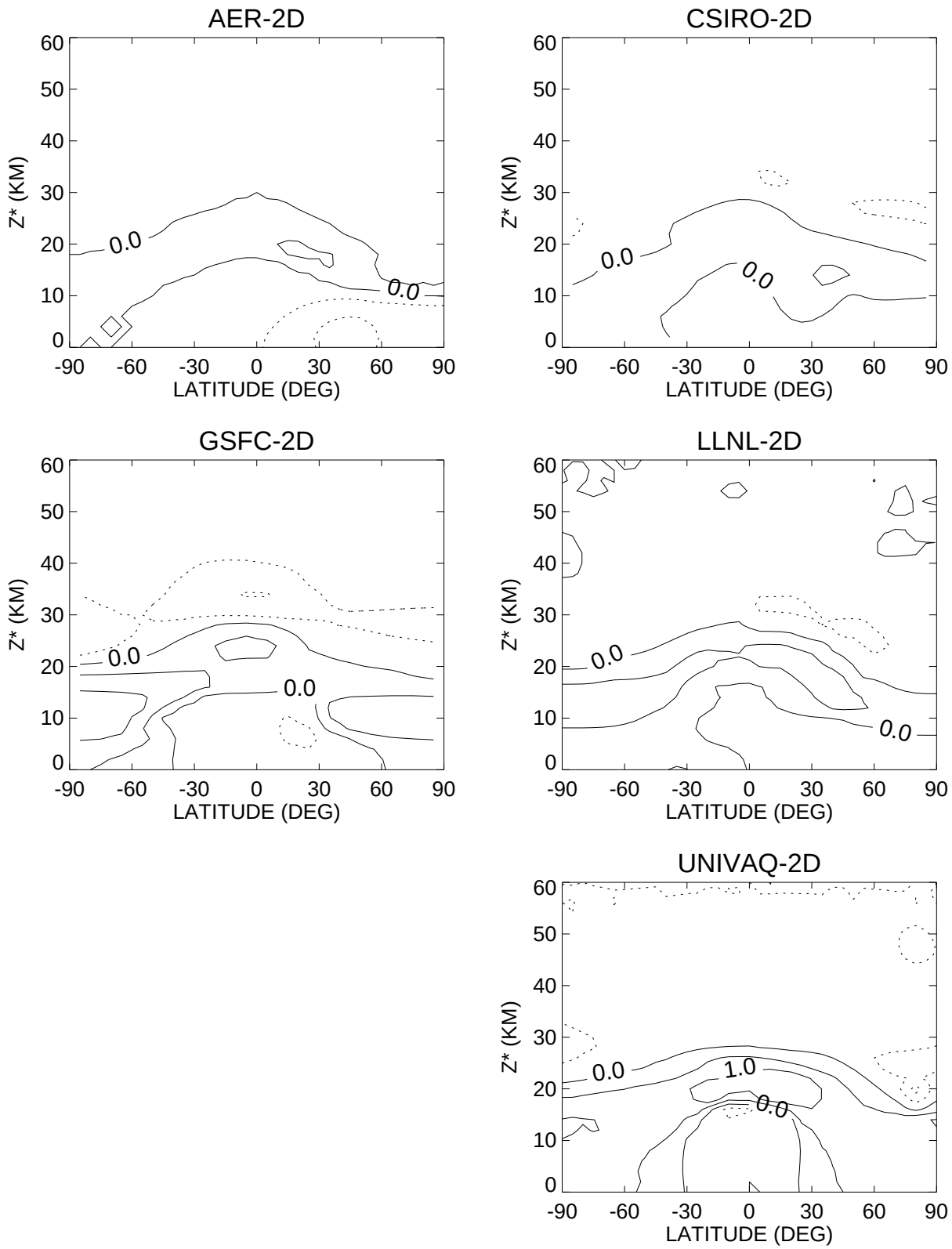

Figure 4.55: Calculated perturbations to O_3 (percent) as a function of latitude and altitude in March of 2015 due to emissions from a fleet of 500 HSCT aircraft with EI(NO_x)=5 and no H_2O emissions under Scenario S1a relative to Scenario D. Contours are -1, -0.5, 0, 0.5, 1.

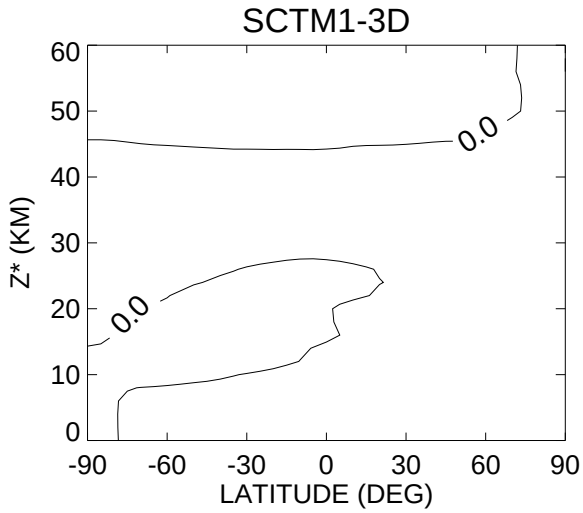

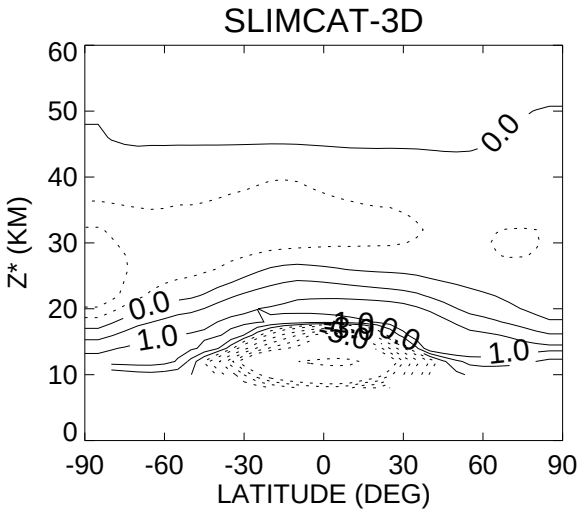

Figure 4.55: continued

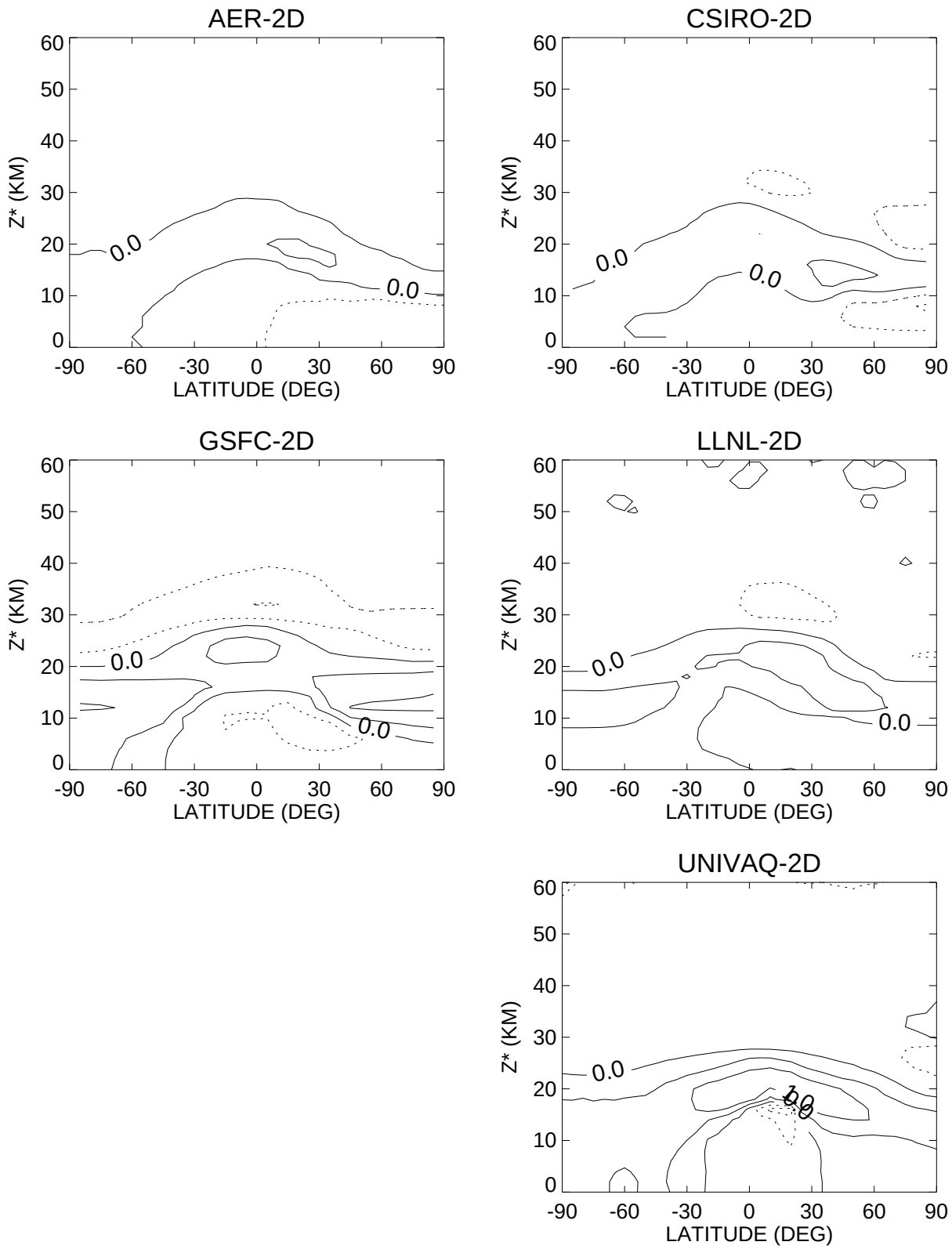

Figure 4.56: Calculated perturbations to O_3 (percent) as a function of latitude and altitude in June of 2015 due to emissions from a fleet of 500 HSCT aircraft with EI(NO_x)=5 and no H_2O emissions under Scenario S1a relative to Scenario D. Contours are -1, -0.5, 0, 0.5, 1.

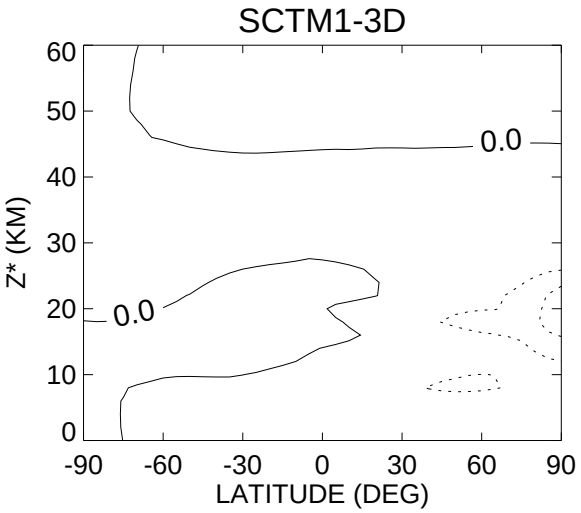

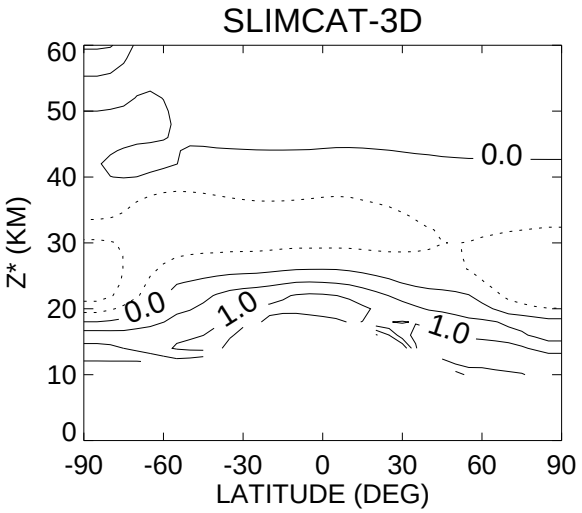

Figure 4.56: continued

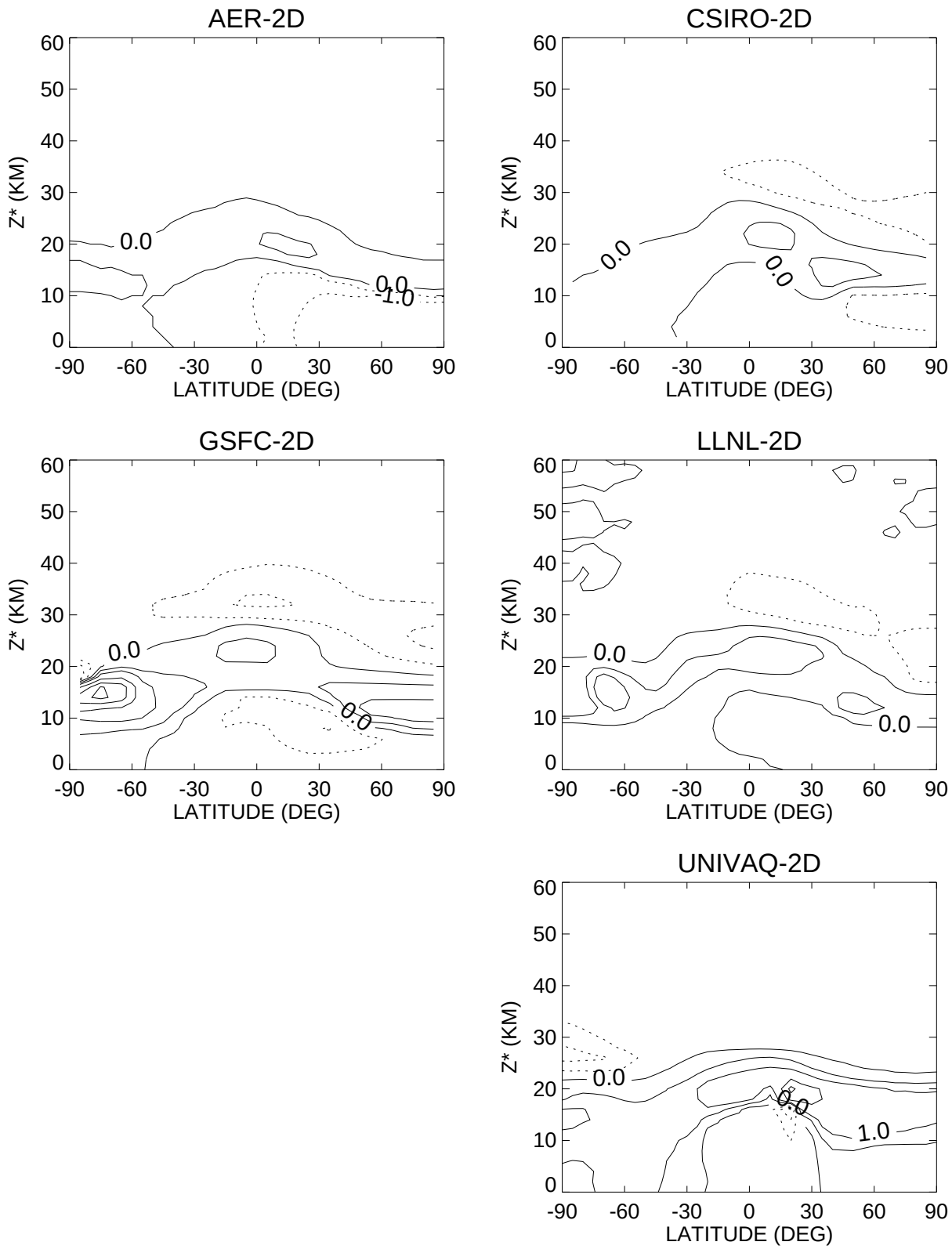

Figure 4.57: Calculated perturbations to O_3 (percent) as a function of latitude and altitude in October of 2015 due to emissions from a fleet of 500 HSCT aircraft with EI(NO_x)=5 and no H_2O emissions under Scenario S1a relative to Scenario D. Contours are -1, -0.5, 0, 0.5, 1, 2, 3.

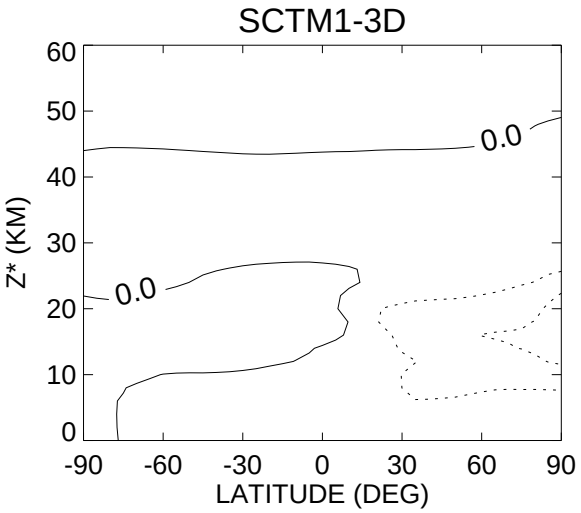

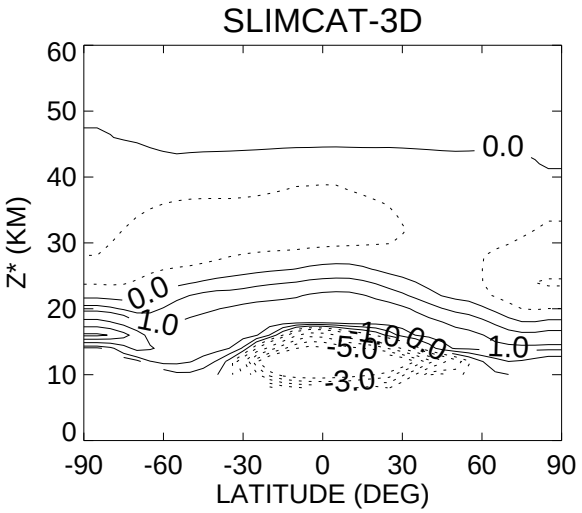

Figure 4.57: continued

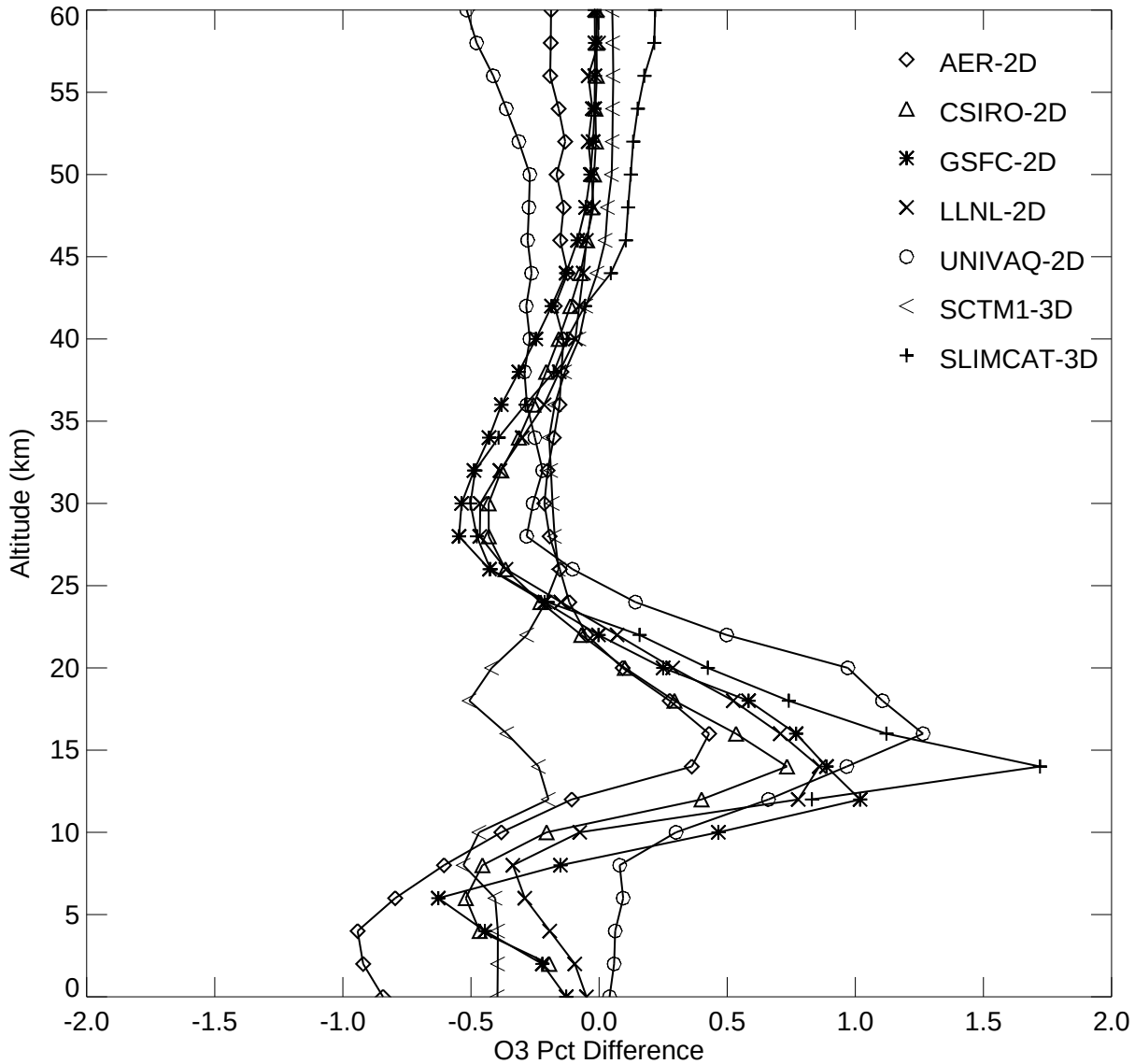

Figure 4.58: Calculated perturbations to O_3 (percent) as a function of altitude at 45°N in June of 2015 due to emissions from a fleet of 500 HSCT aircraft with EI(NO_x)=5 and no H_2O emissions under Scenario S1a relative to Scenario D.

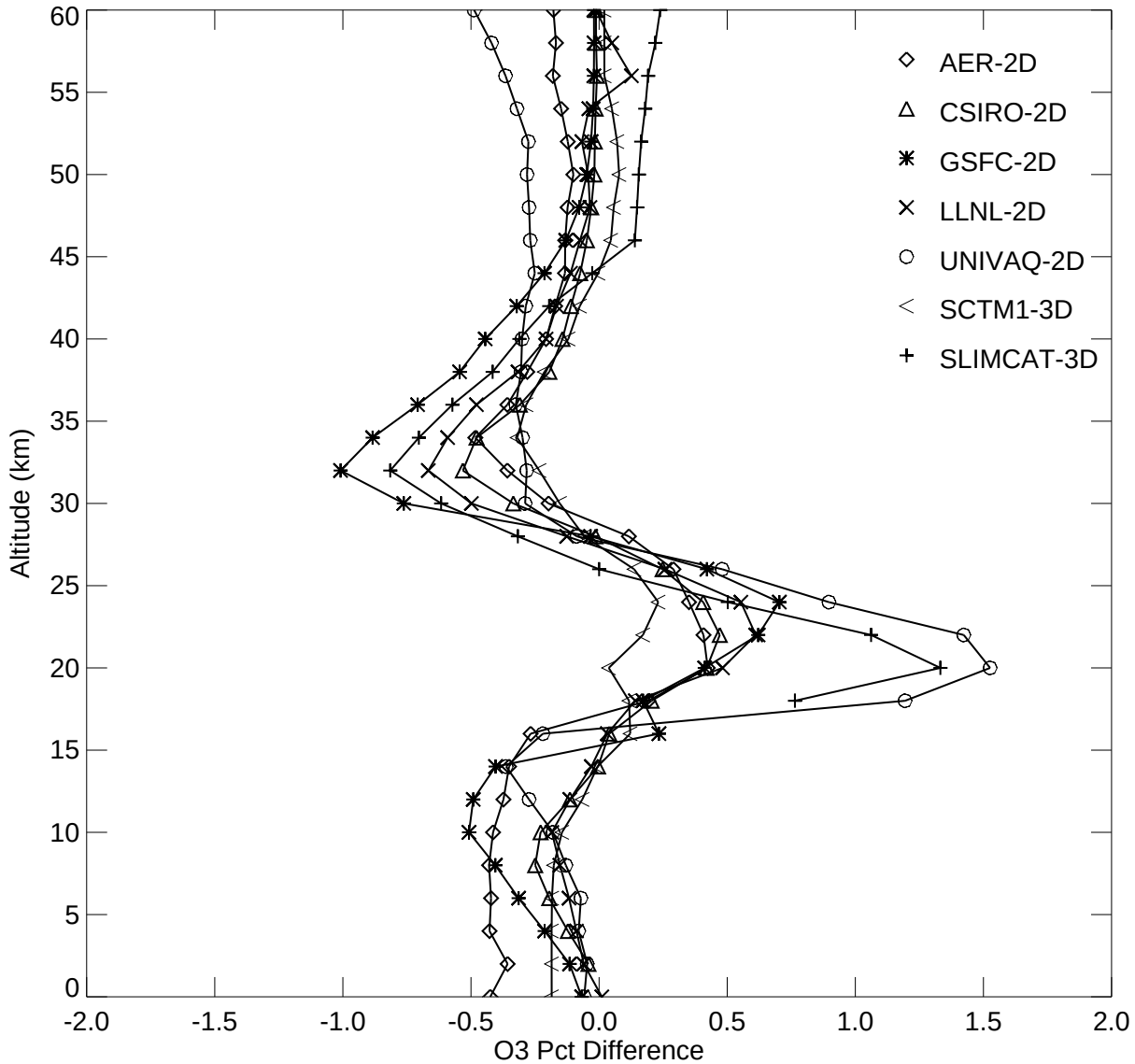

Figure 4.59: Calculated perturbations to O_3 (percent) as a function of altitude at the equator in June of 2015 due to emissions from a fleet of 500 HSCT aircraft with EI(NO_x)=5 and no H_2O emissions under Scenario S1a relative to Scenario D.

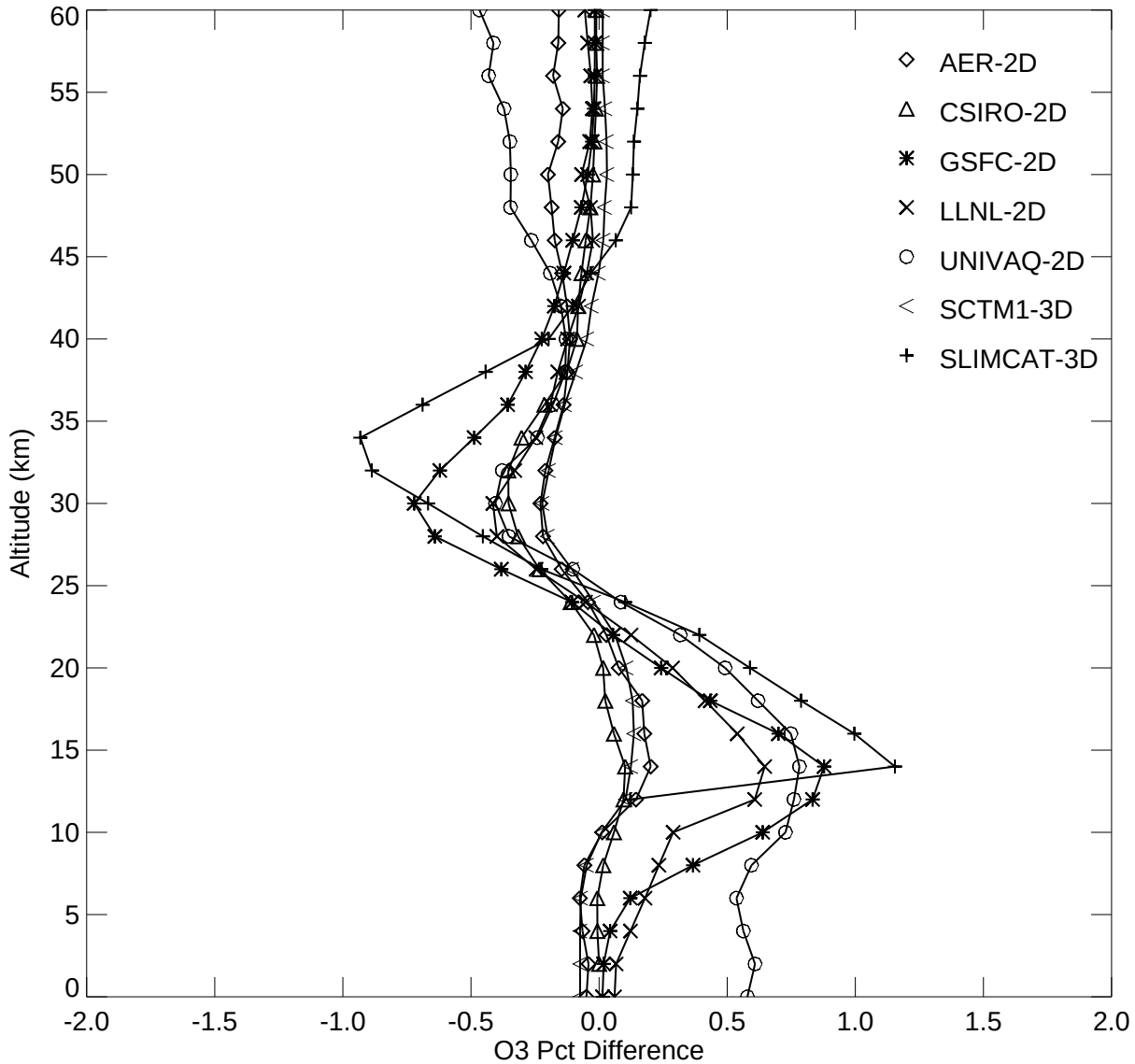

Figure 4.60: Calculated perturbations to O_3 (percent) as a function of altitude at 45^{o}S in June of 2015 due to emissions from a fleet of 500 HSCT aircraft with EI(NO_x)=5 and no H_2O emissions under Scenario S1a relative to Scenario D.

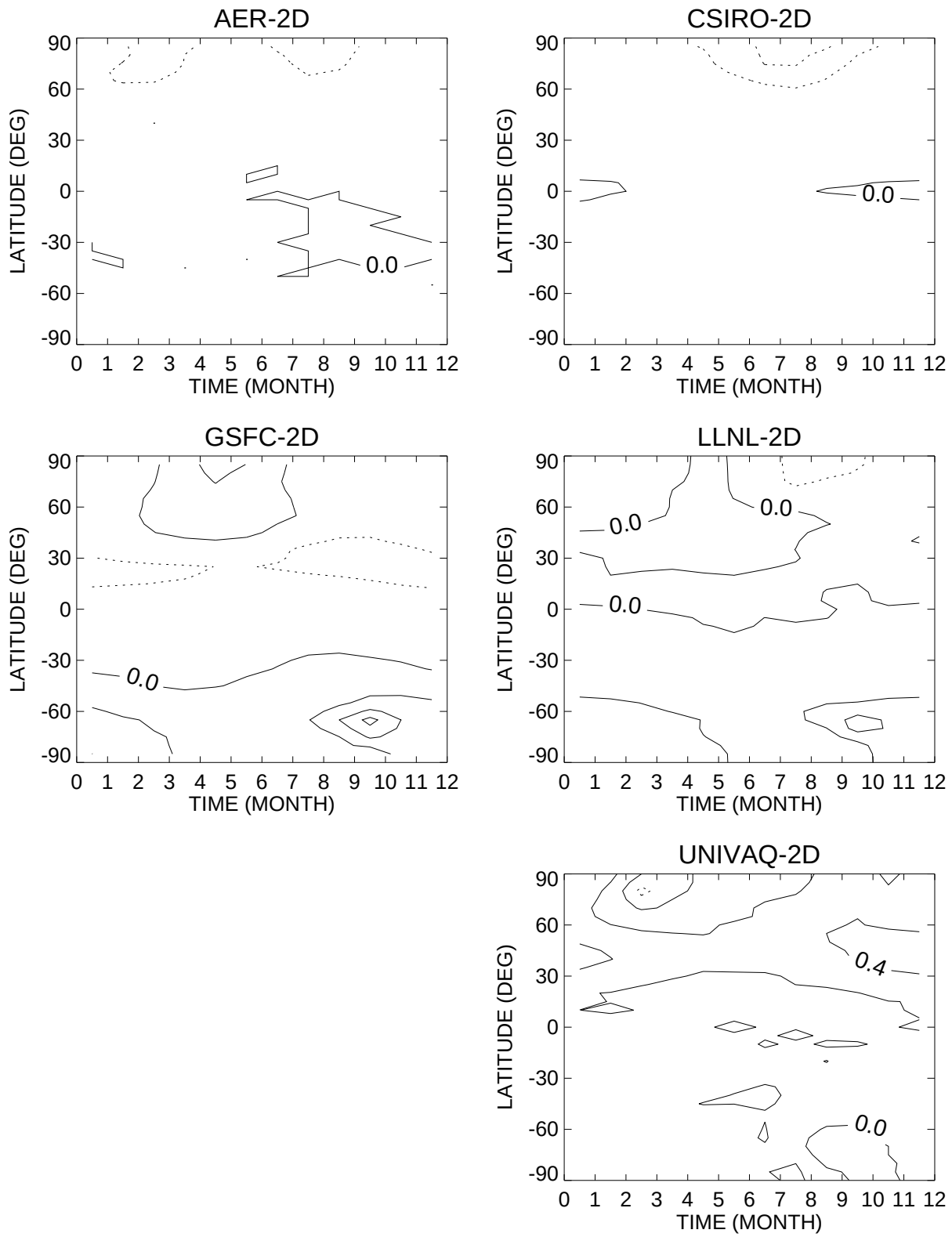

Figure 4.61: Calculated perturbations to column O_3 (percent) as a function of latitude and season in 2015 due to emissions from a fleet of 500 HSCT aircraft with EI(NO_x)=5 and no H_2O emissions under Scenario S1a relative to Scenario D. Contours are -1.2 to 0.6 by 0.2.

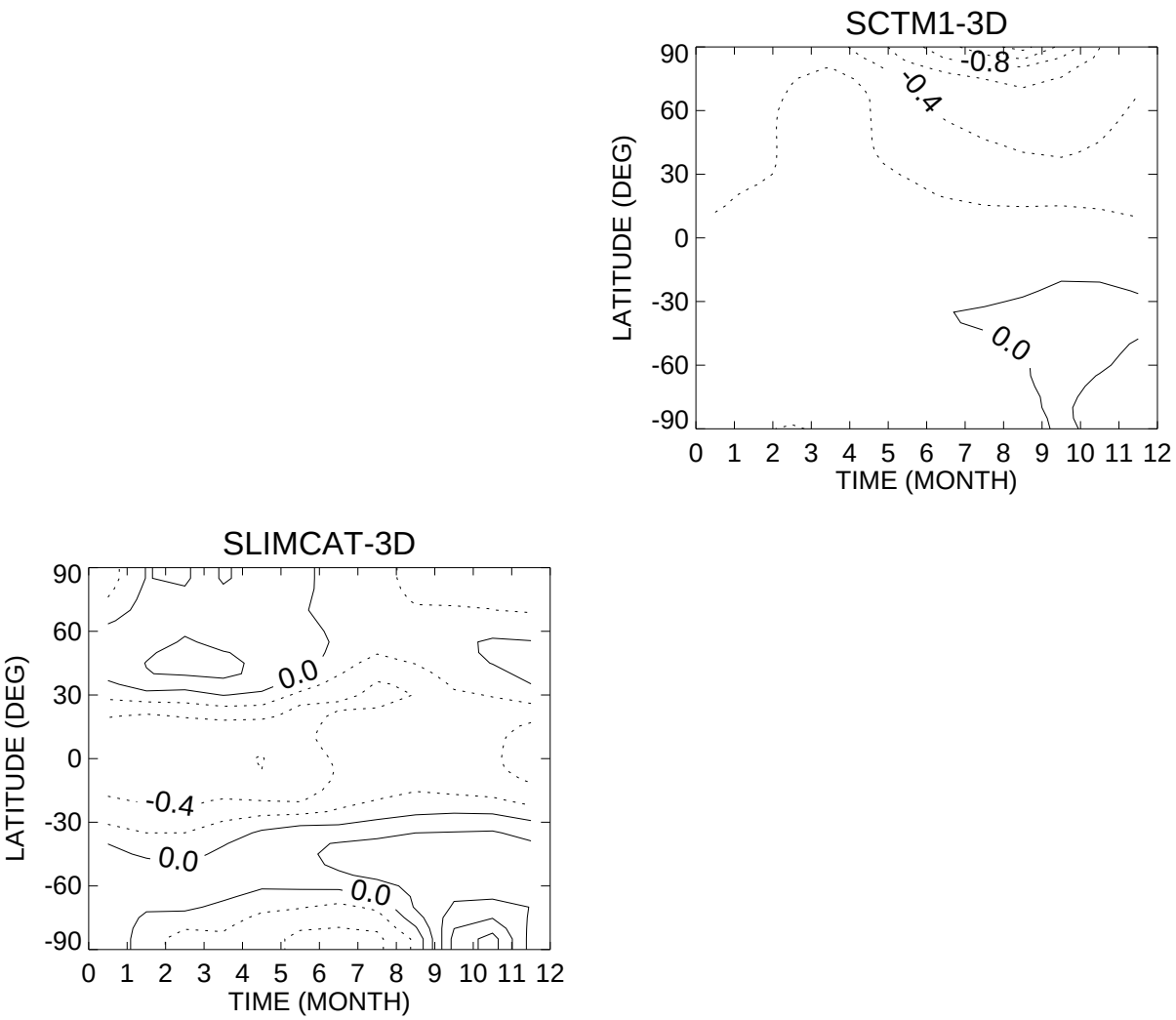

Figure 4.61: continued

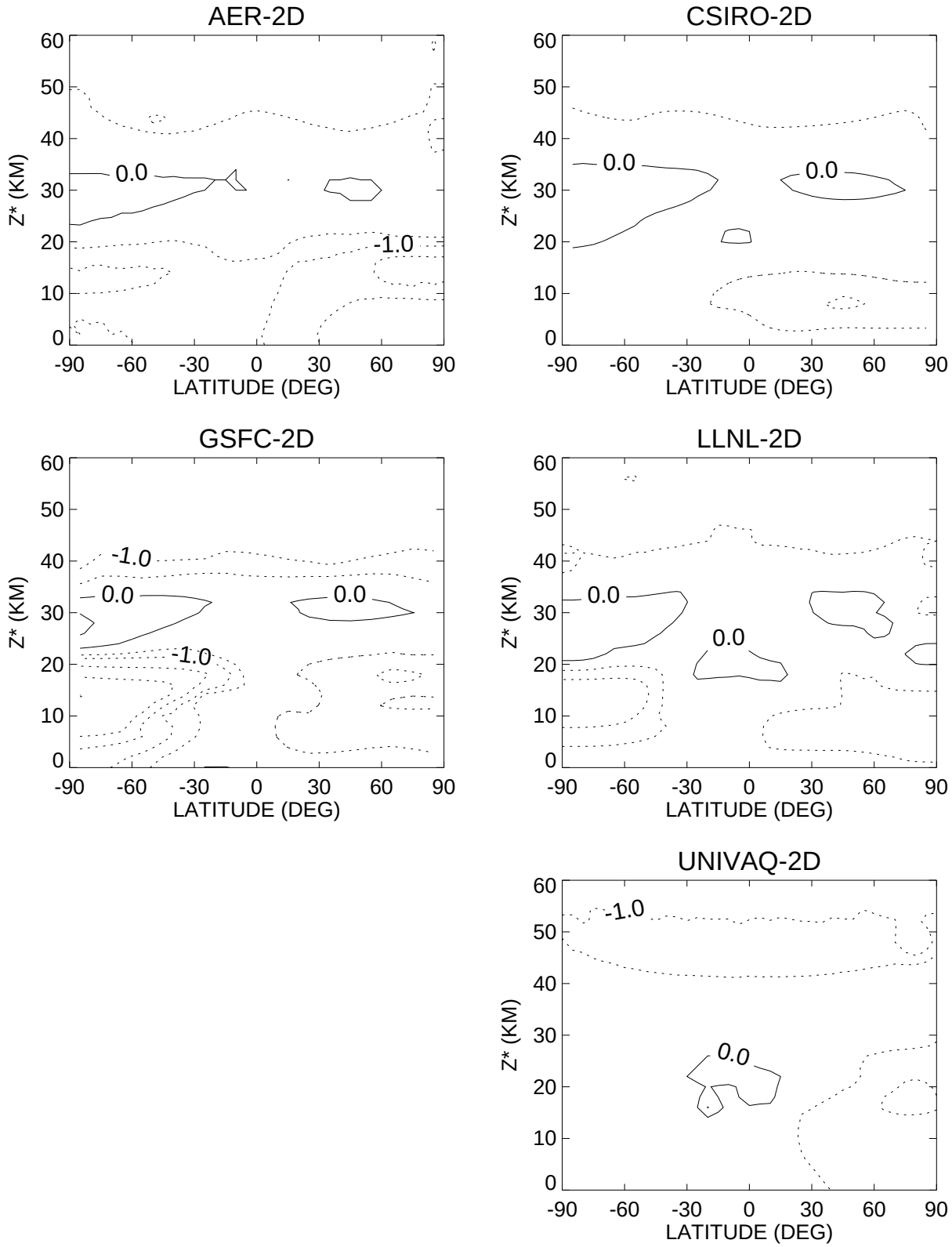

Figure 4.62: Calculated perturbations to O_3 (percent) as a function of latitude and altitude in March of 2015 due to emissions from a fleet of 500 HSCT aircraft with EI(NO_x)=0 under Scenario S1b relative to Scenario D. Contours are -3, -2, -1, -0.5, 0, 0.5.

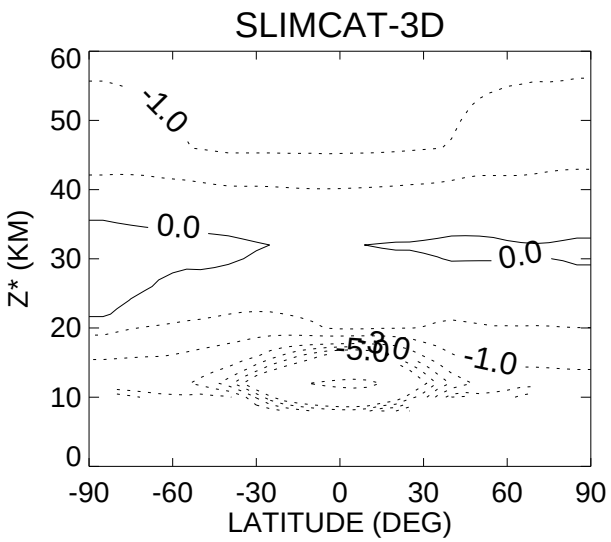

Figure 4.62: continued

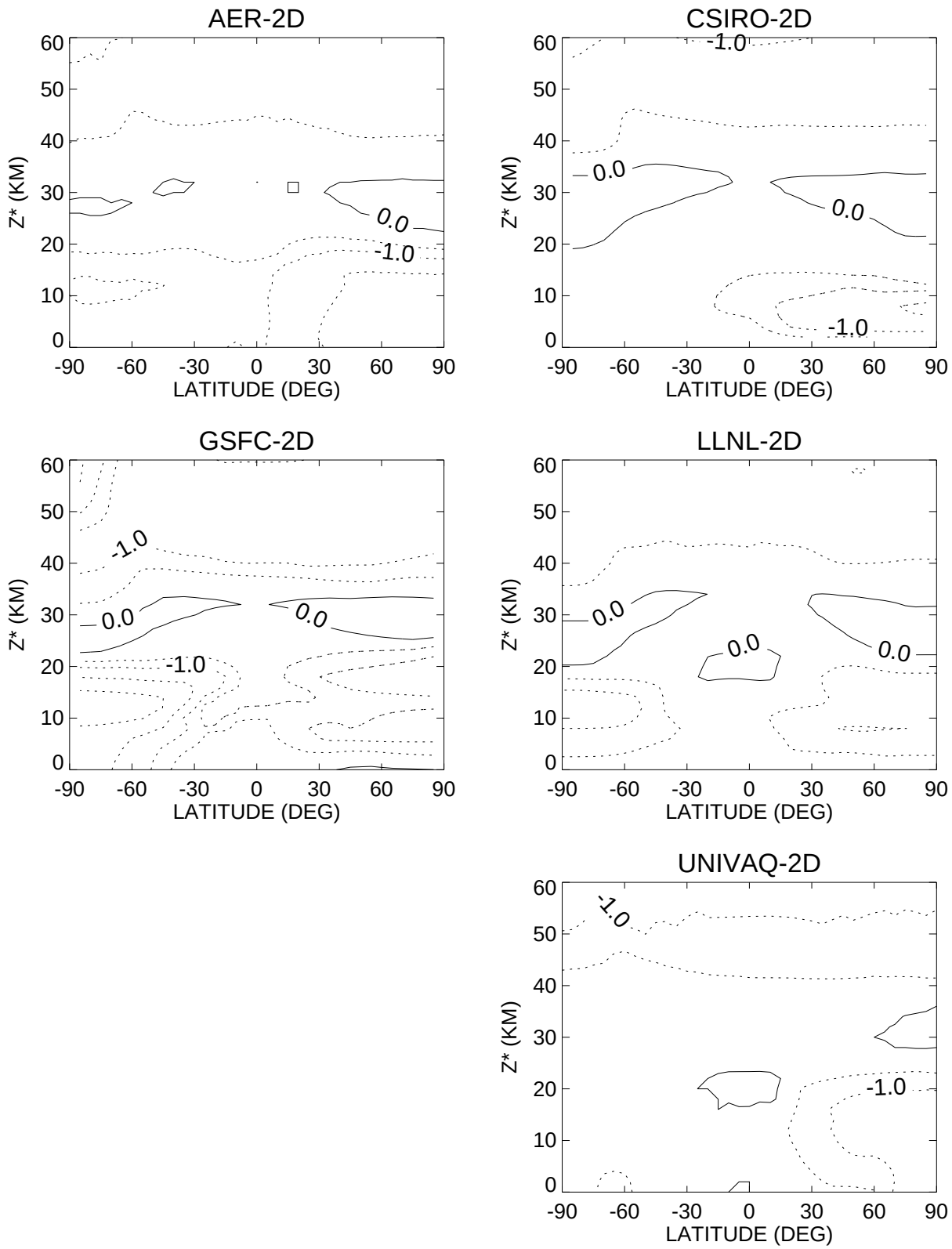

Figure 4.63: Calculated perturbations to O_3 (percent) as a function of latitude and altitude in June of 2015 due to emissions from a fleet of 500 HSCT aircraft with EI(NO_x)=0 under Scenario S1b relative to Scenario D. Contours are -3, -2, -1, -0.5, 0.

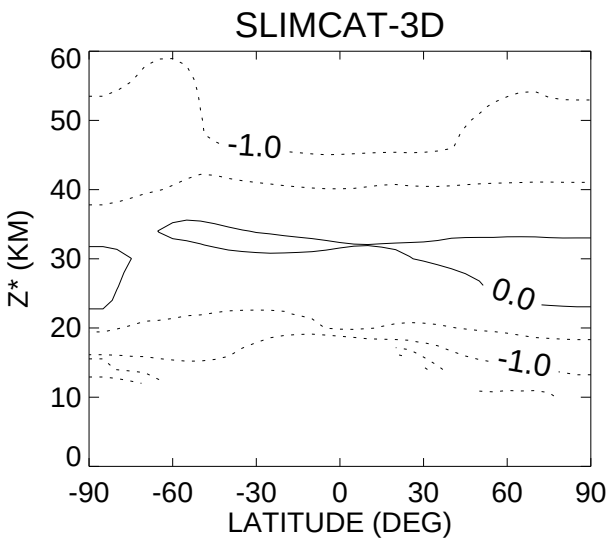

Figure 4.63: continued

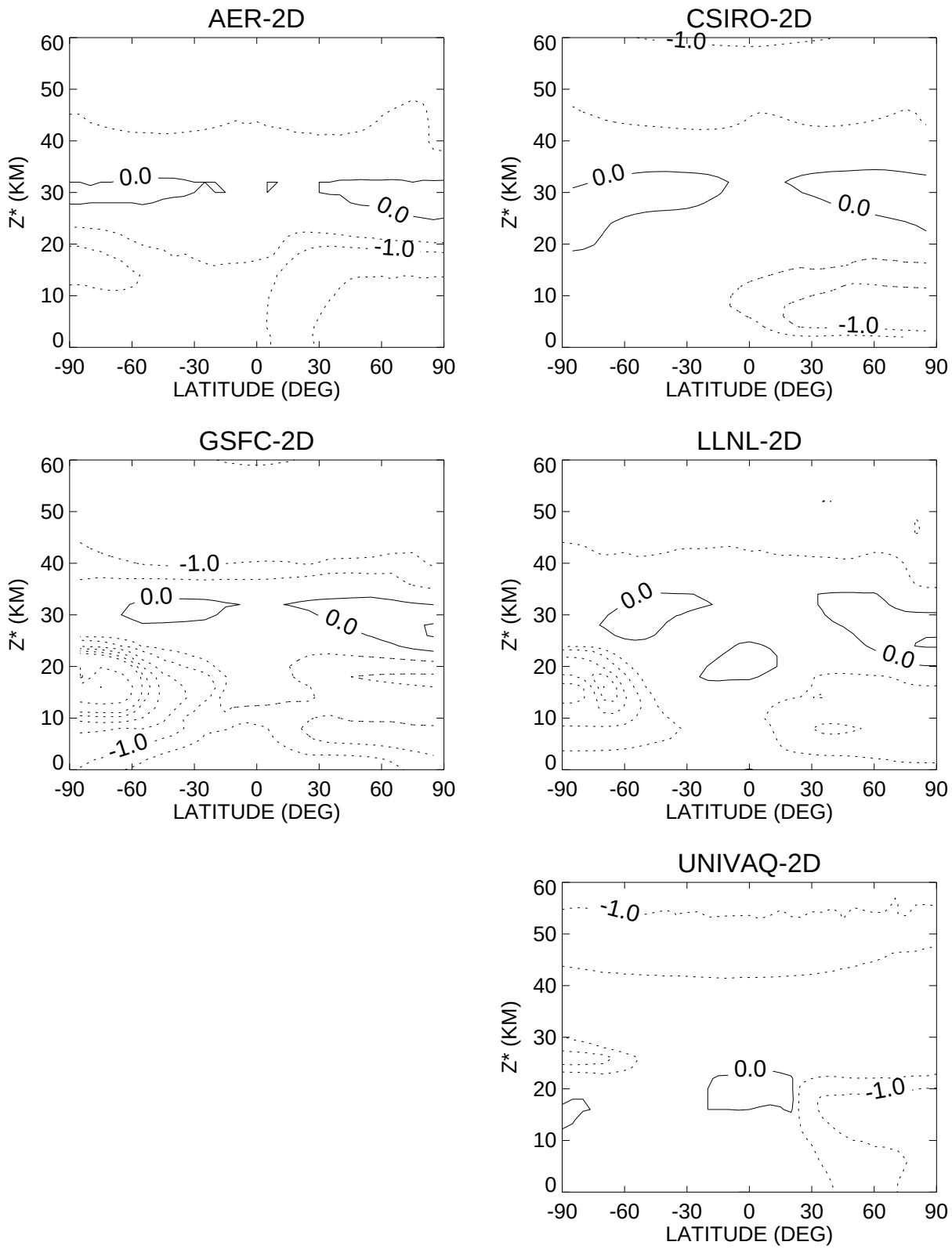

Figure 4.64: Calculated perturbations to O_3 (percent) as a function of latitude and altitude in October of 2015 due to emissions from a fleet of 500 HSCT aircraft with EI(NO_x)=0 under Scenario S1b relative to Scenario D. Contours are -15, -10, -5, -4, -3, -2, -1, -0.5, 0, 0.5.

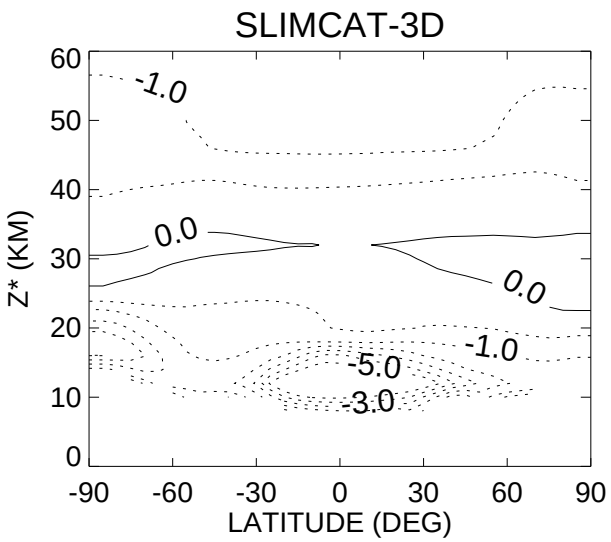

Figure 4.64: continued

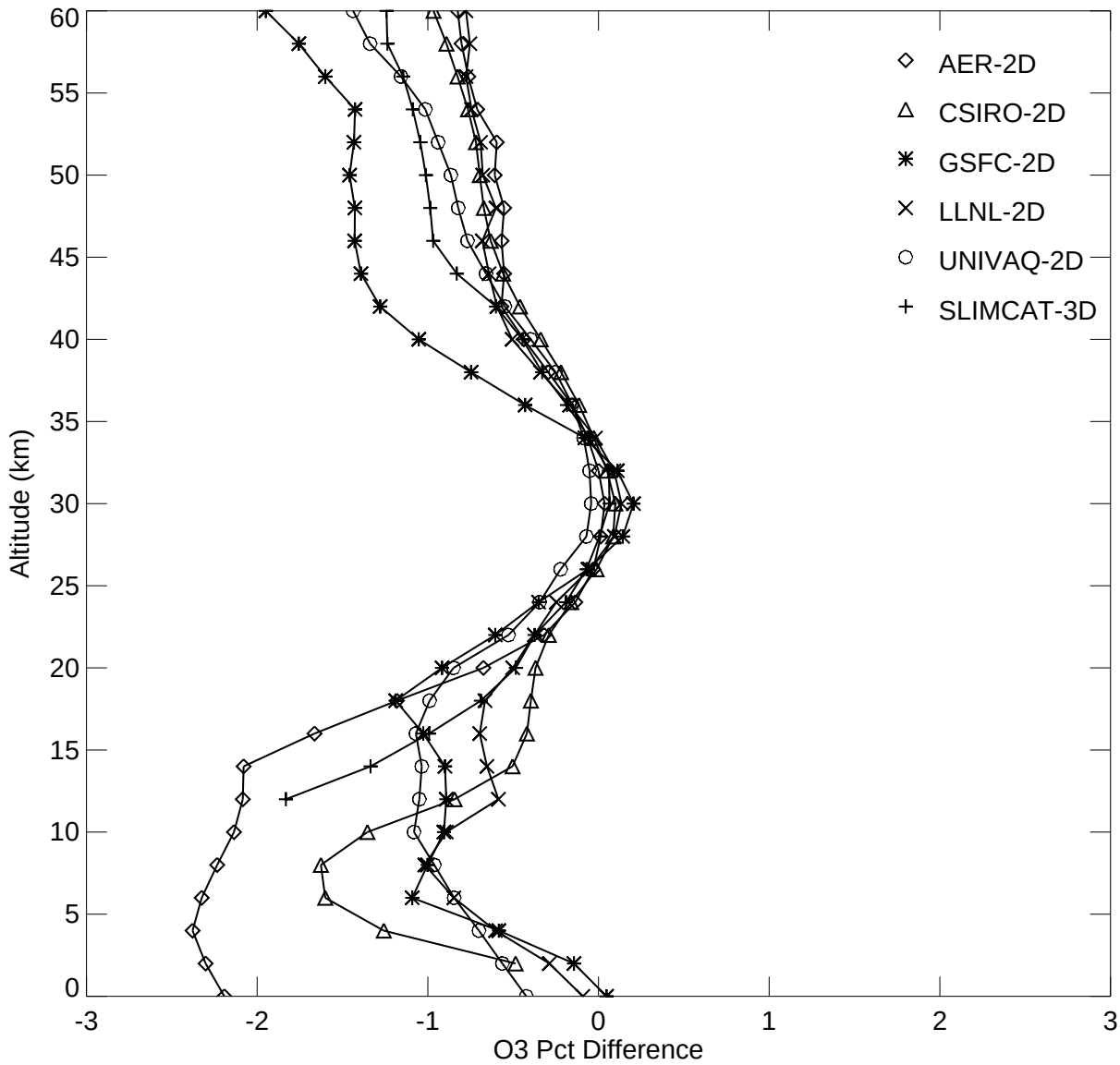

Figure 4.65: Calculated perturbations to O_3 (percent) as a function of altitude at 45°N in June of 2015 due to emissions from a fleet of 500 HSCT aircraft with EI(NO_x)=0 under Scenario S1b relative to Scenario D.

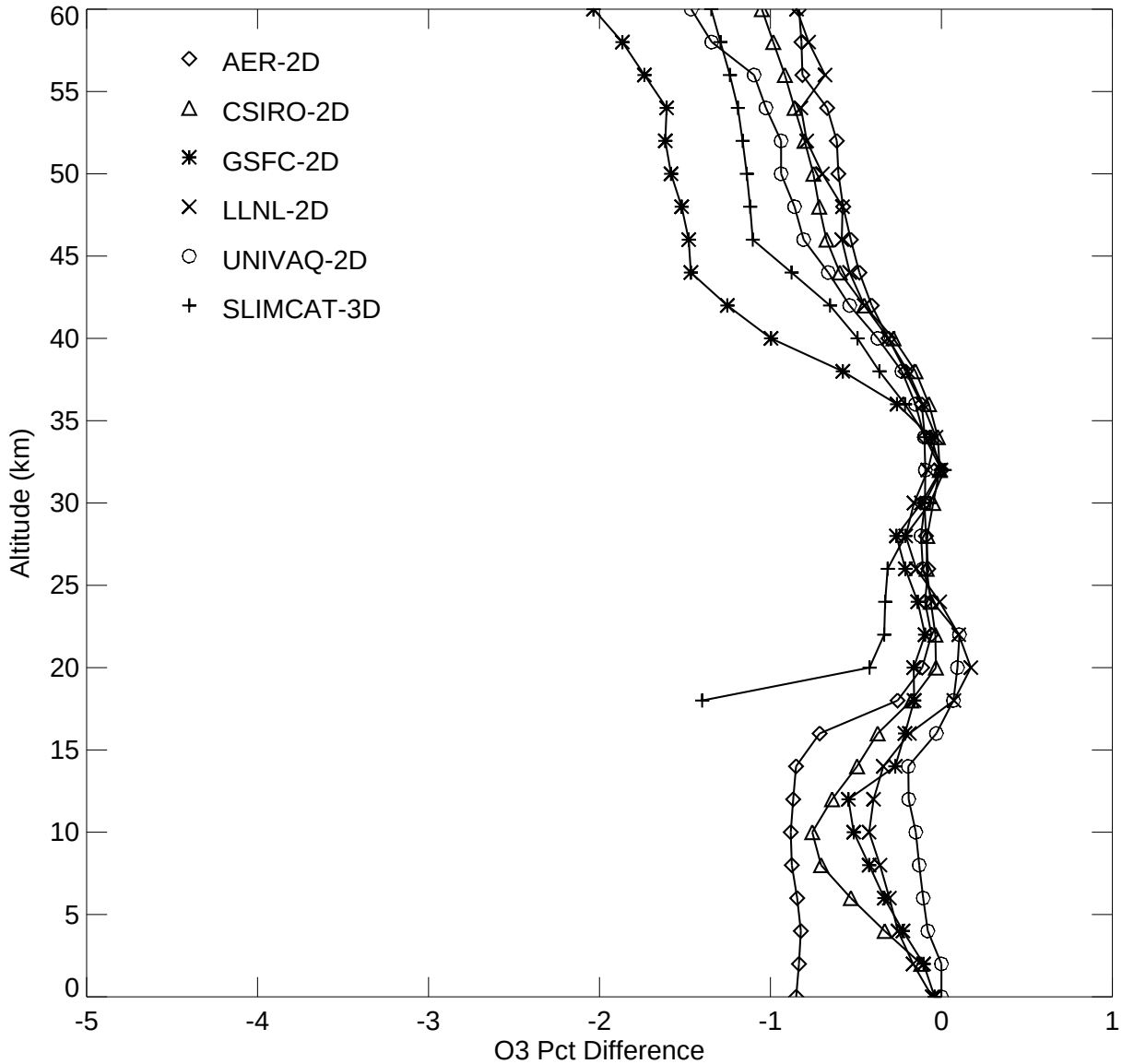

Figure 4.66: Calculated perturbations to O_3 (percent) as a function of altitude at the equator in June of 2015 due to emissions from a fleet of 500 HSCT aircraft with EI(NO_x)=0 under Scenario S1b relative to Scenario D.

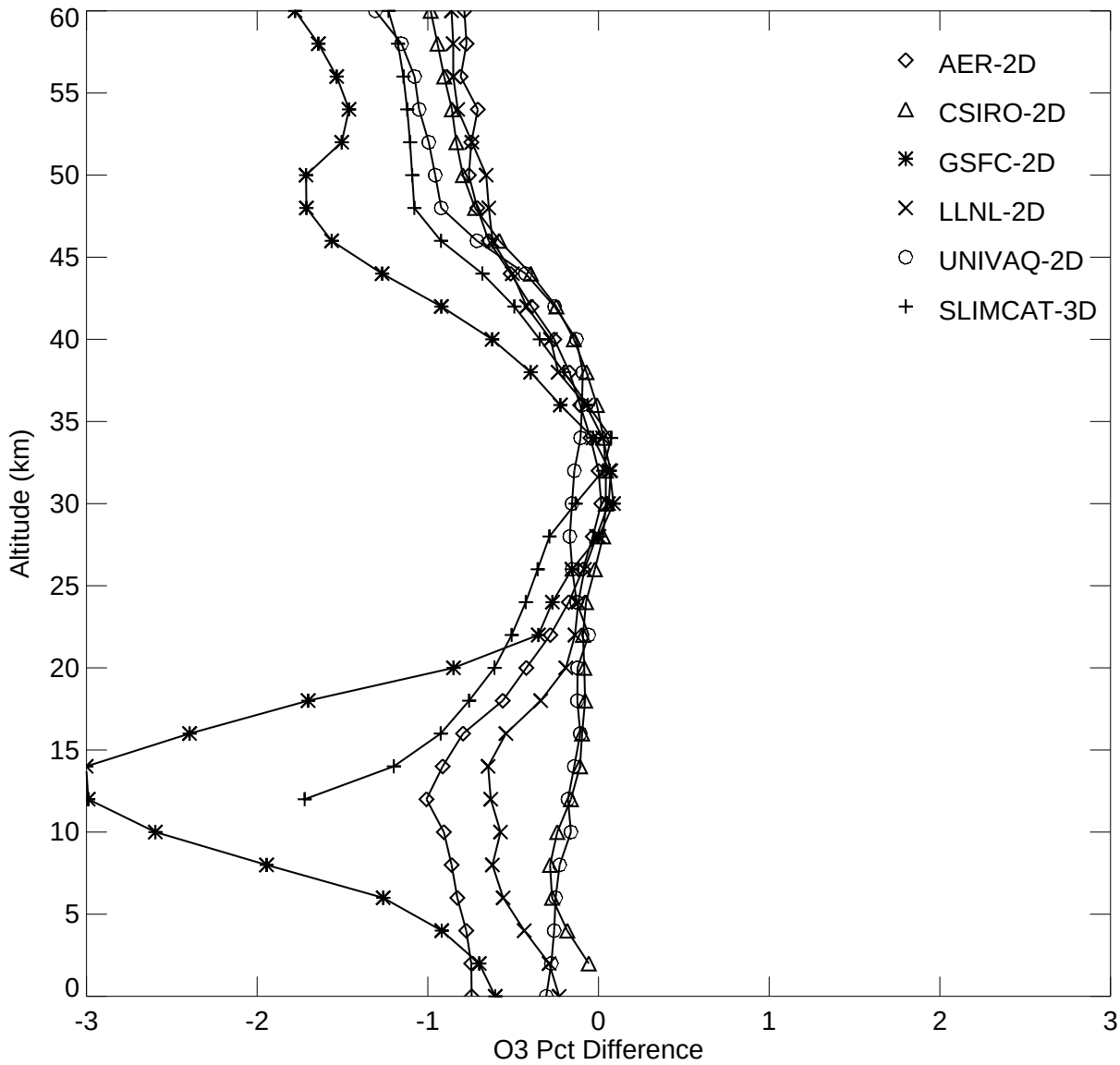

Figure 4.67: Calculated perturbations to O_3 (percent) as a function of altitude at 45^oS in June of 2015 due to emissions from a fleet of 500 HSCT aircraft with EI(NO_x)=0 under Scenario S1b relative to Scenario D.

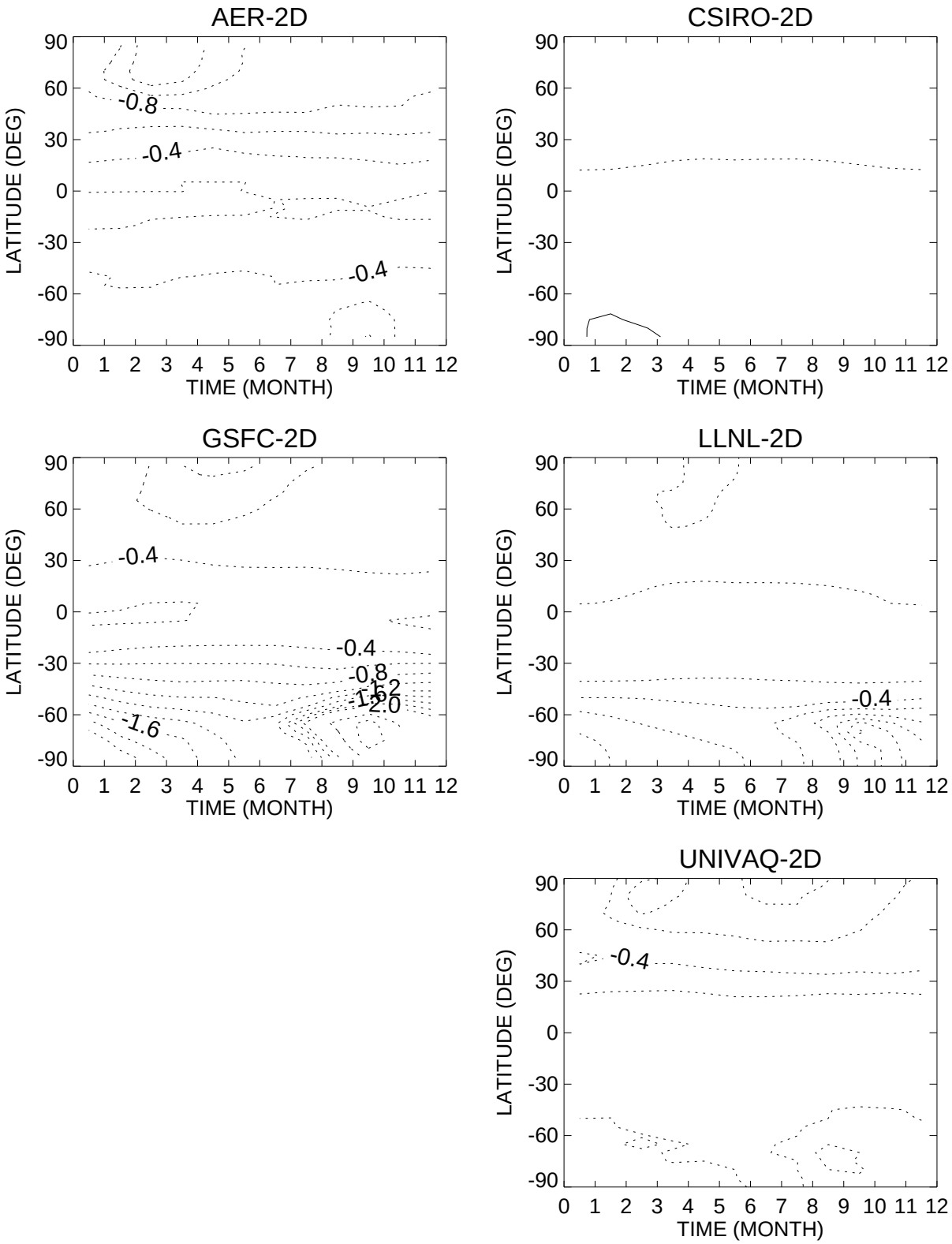

Figure 4.68: Calculated perturbations to column O_3 (percent) as a function of latitude and season in 2015 due to emissions from a fleet of 500 HSCT aircraft with EI(NO_x)=0 under Scenario S1b relative to Scenario D. Contours are -4, -3, and -2.0 to 0 by 0.2.

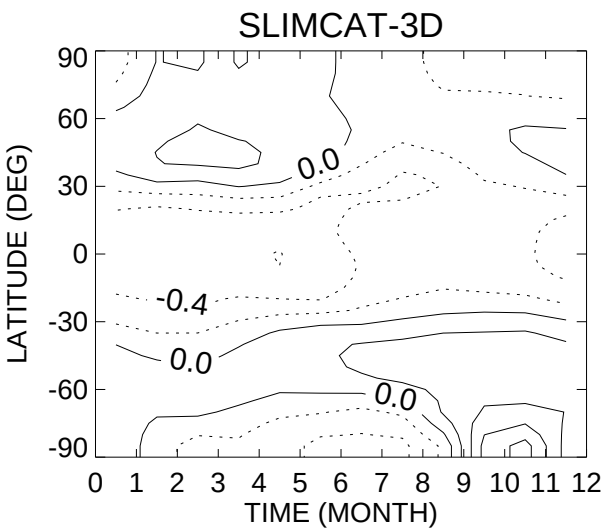

Figure 4.68: continued

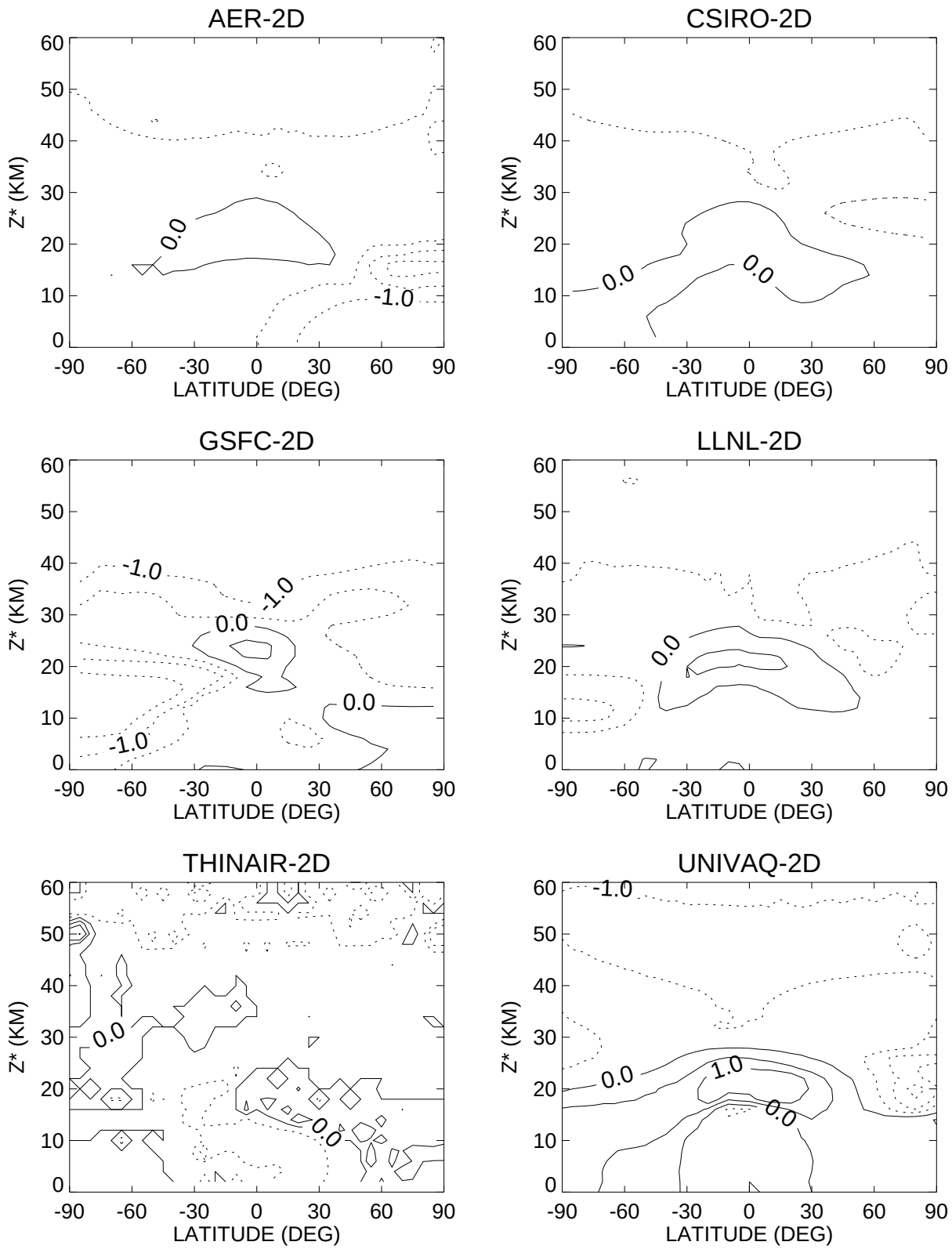

Figure 4.69: Calculated perturbations to O_3 (percent) as a function of latitude and altitude in March of 2015 due to emissions from a fleet of 500 HSCT aircraft with EI(NO_x)=5 under Scenario S1c relative to Scenario D. Contours are -10, -5, -4, -3, -2, -1, -0.5, 0, 0.5, 1.

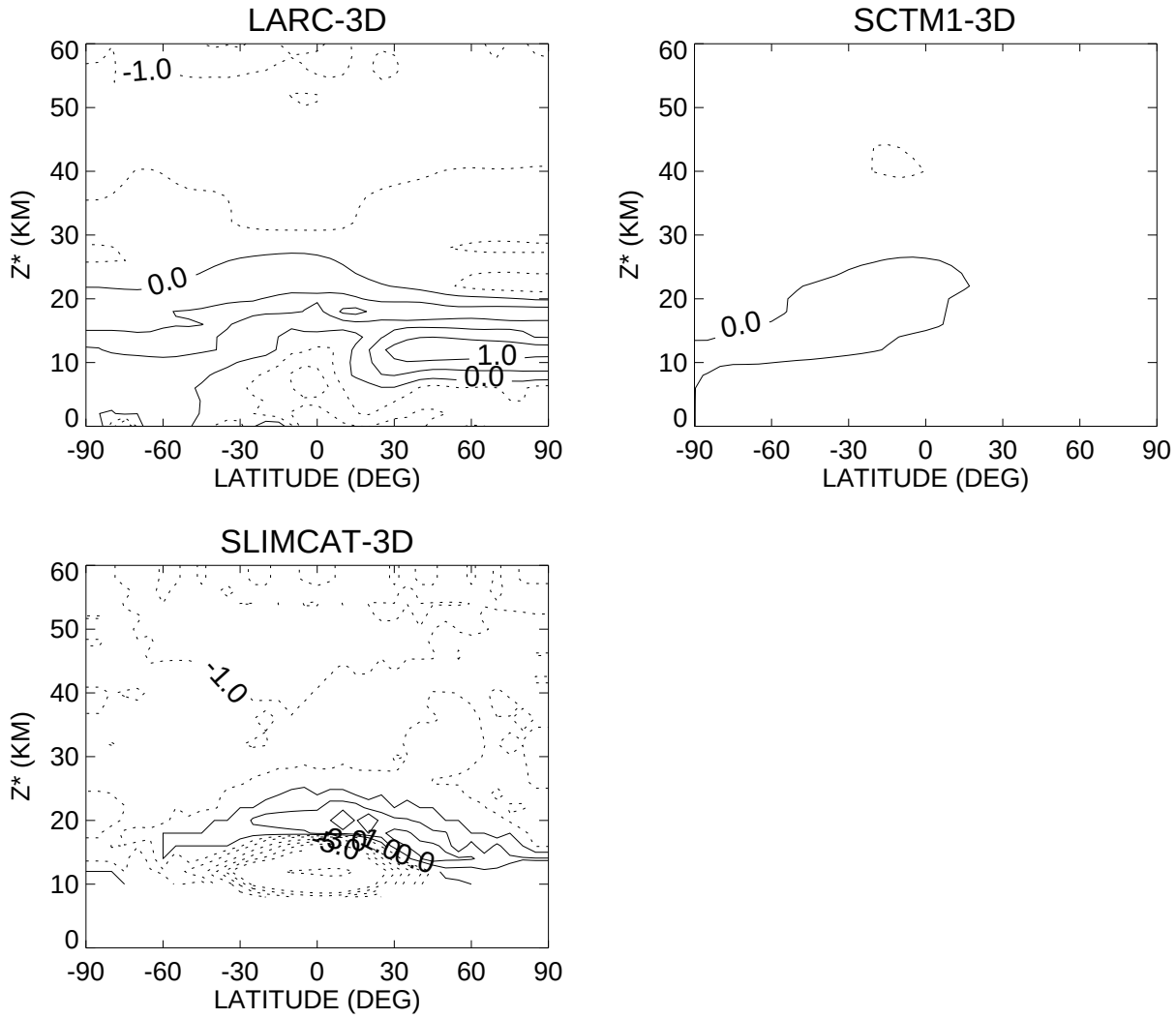

Figure 4.69: continued

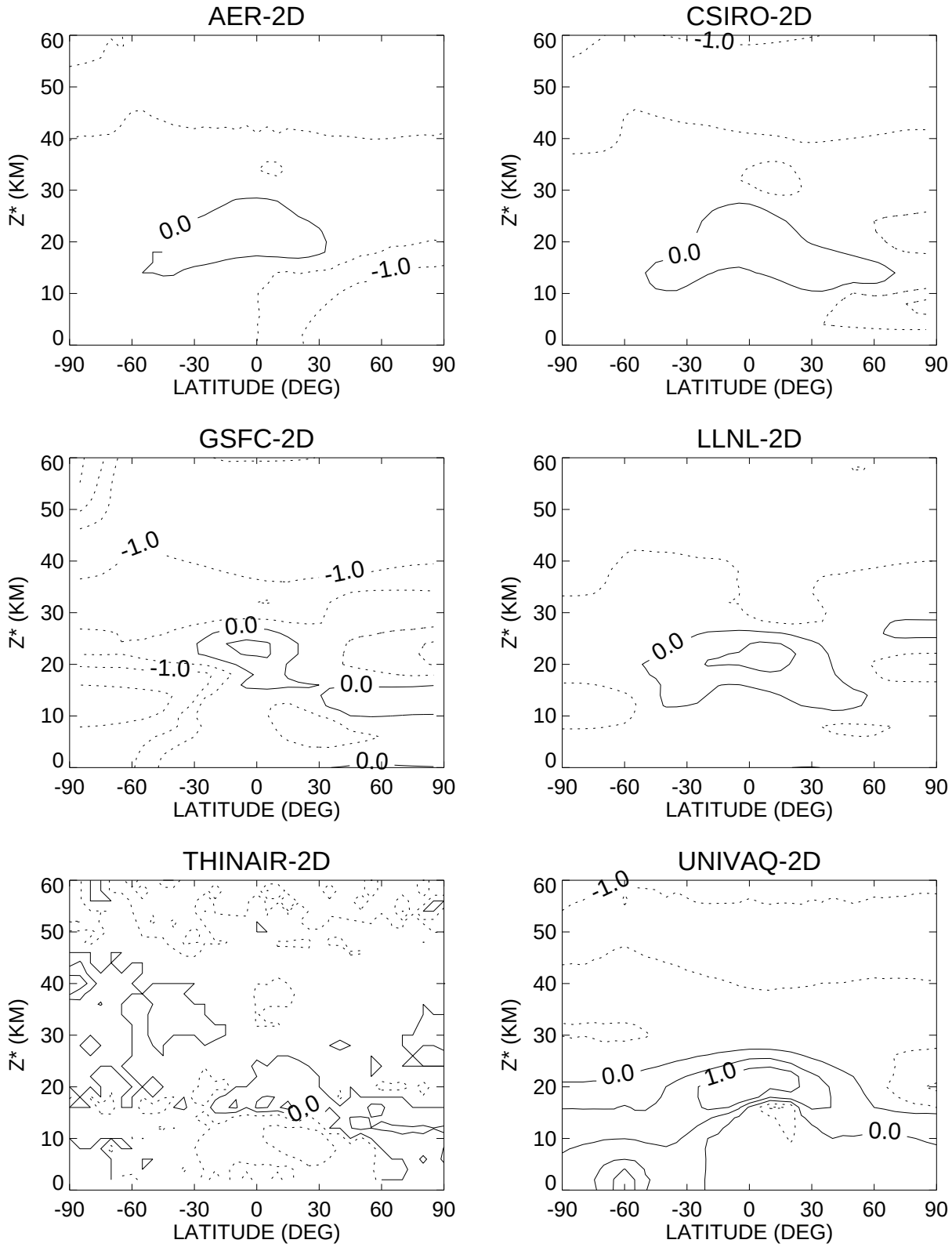

Figure 4.70: Calculated perturbations to O_3 (percent) as a function of latitude and altitude in June of 2015 due to emissions from a fleet of 500 HSCT aircraft with EI(NO_x)=5 under Scenario S1c relative to Scenario D. Contours are -10, -5, -4, -3, -2, -1, -0.5, 0, 0.5, 1, 2.

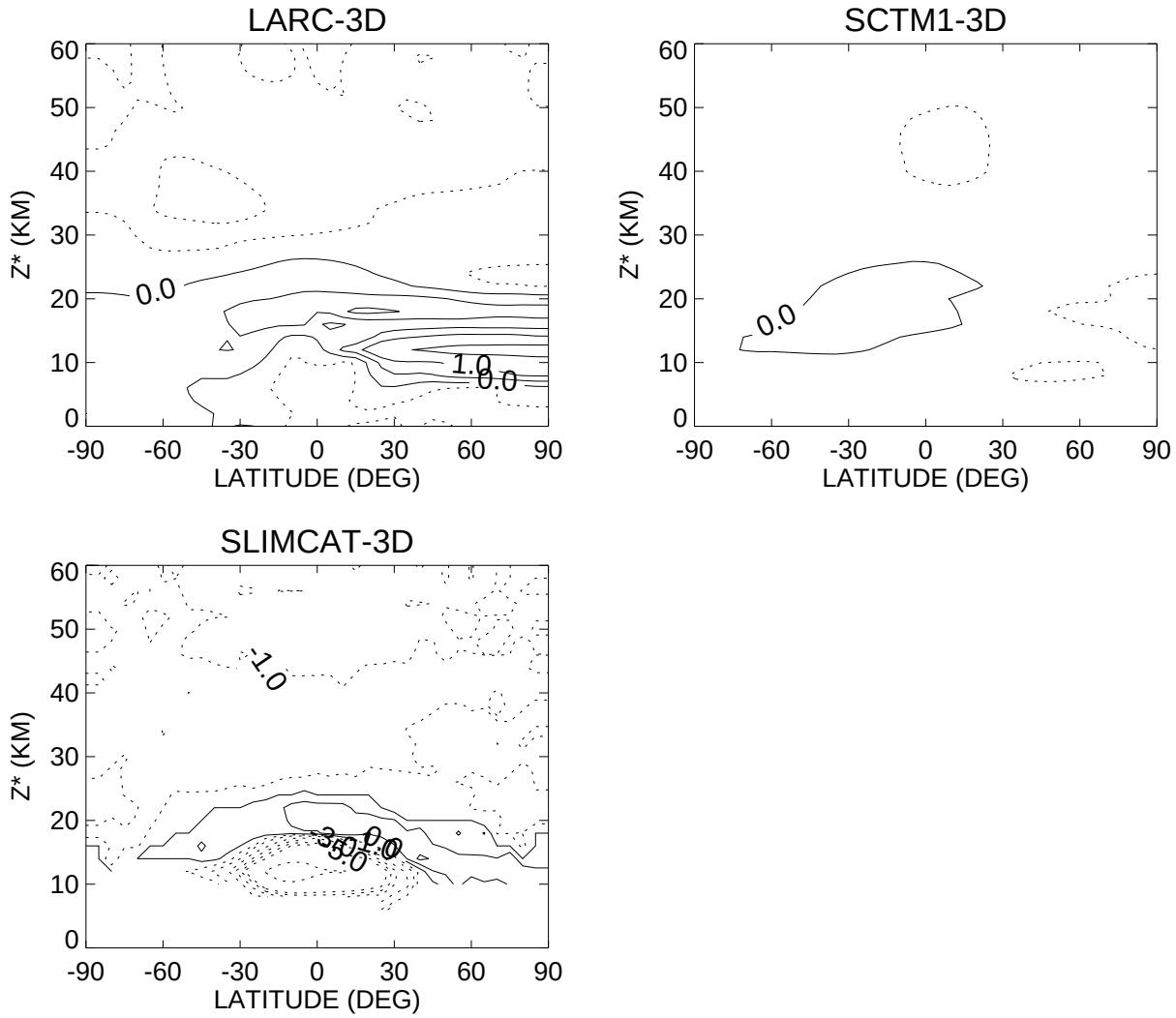

Figure 4.70: continued

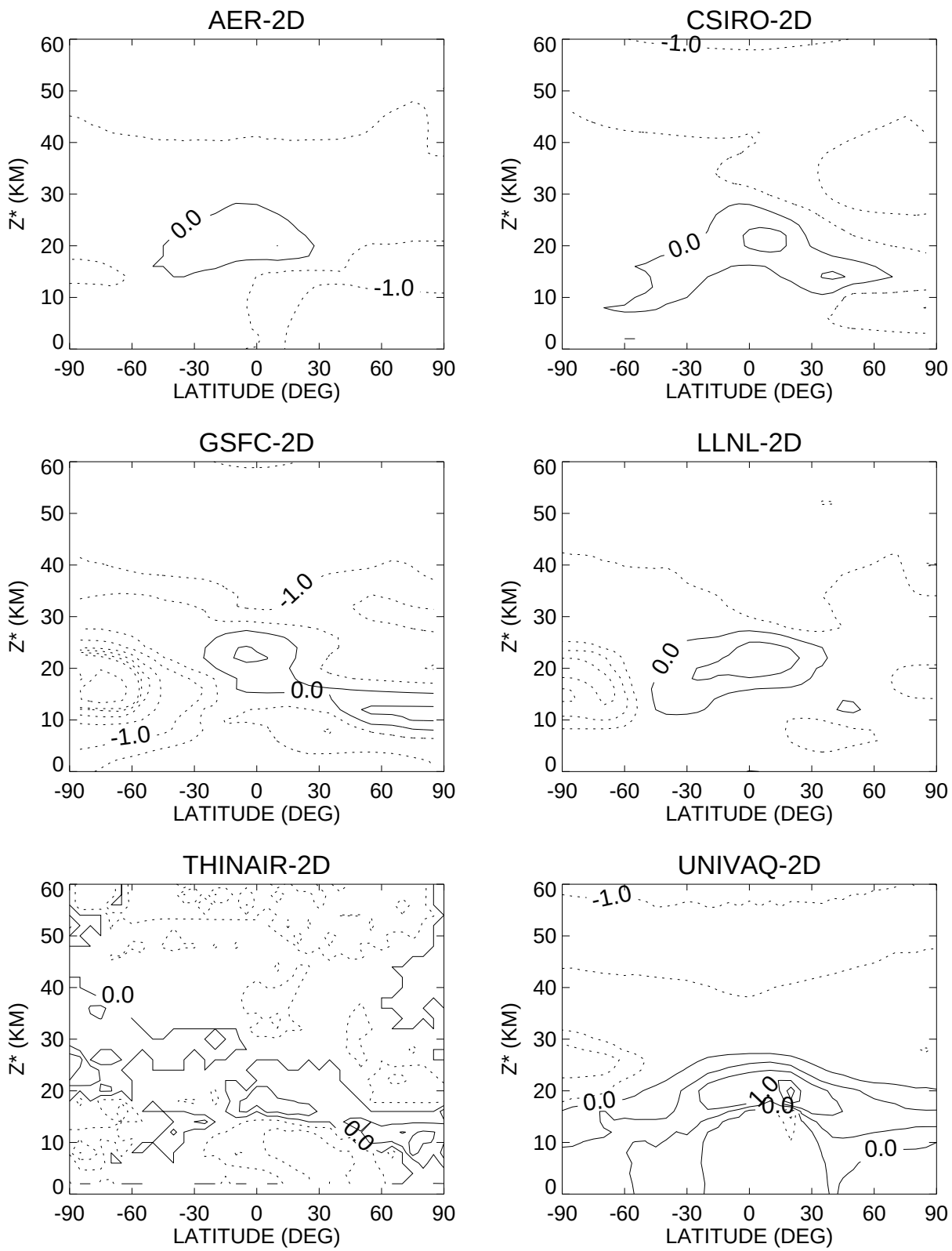

Figure 4.71: Calculated perturbations to O_3 (percent) as a function of latitude and altitude in October of 2015 due to emissions from a fleet of 500 HSCT aircraft with EI(NO_x)=5 under Scenario S1c relative to Scenario D. Contours are -10, -5, -4, -3, -2, -1, -0.5, 0, 0.5, 1, 2, 3.

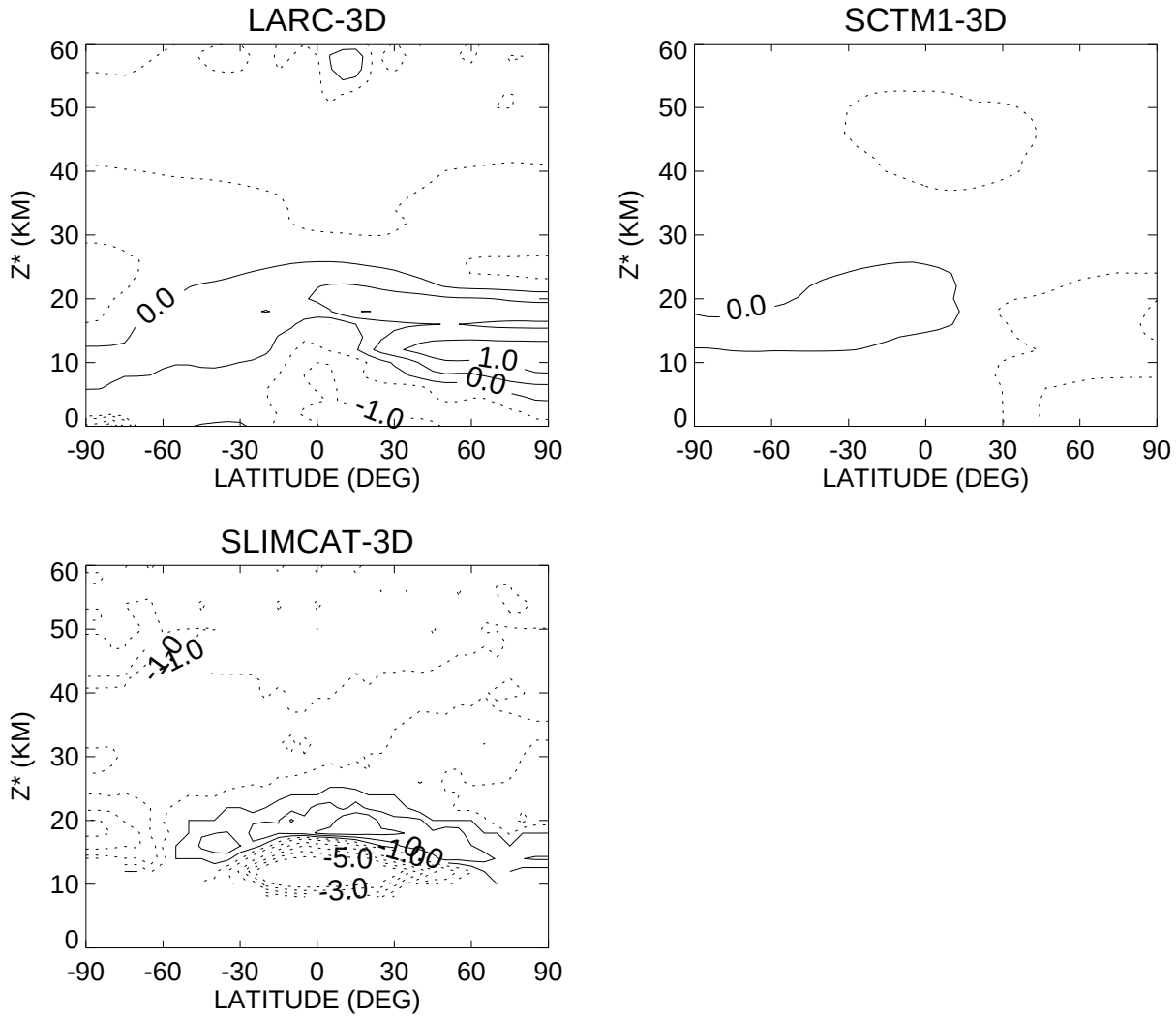

Figure 4.71: continued

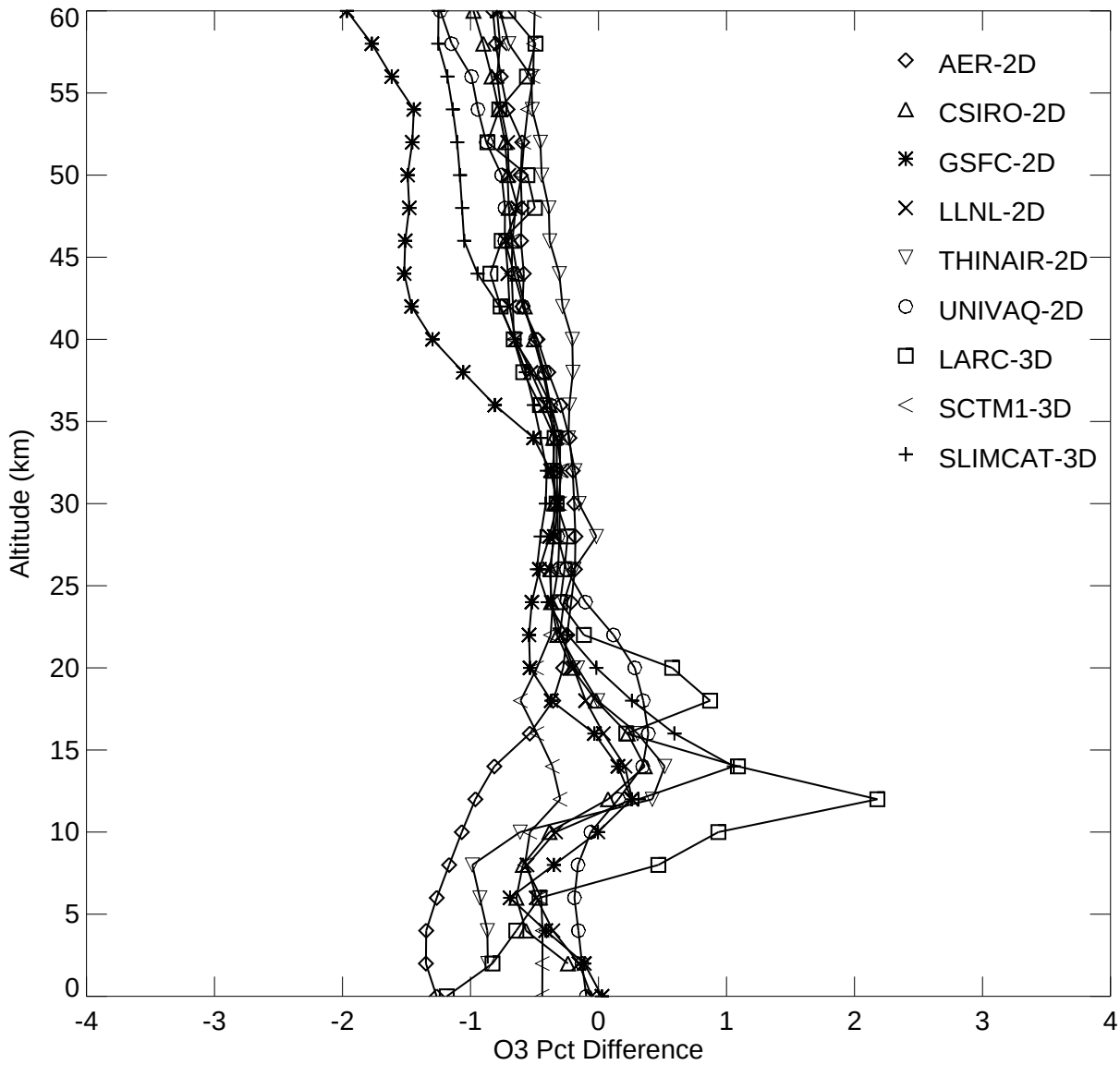

Figure 4.72: Calculated perturbations to O_3 (percent) as a function of altitude at 45°N in June of 2015 due to emissions from a fleet of 500 HSCT aircraft with EI(NO_x)=5 under Scenario S1c relative to Scenario D.

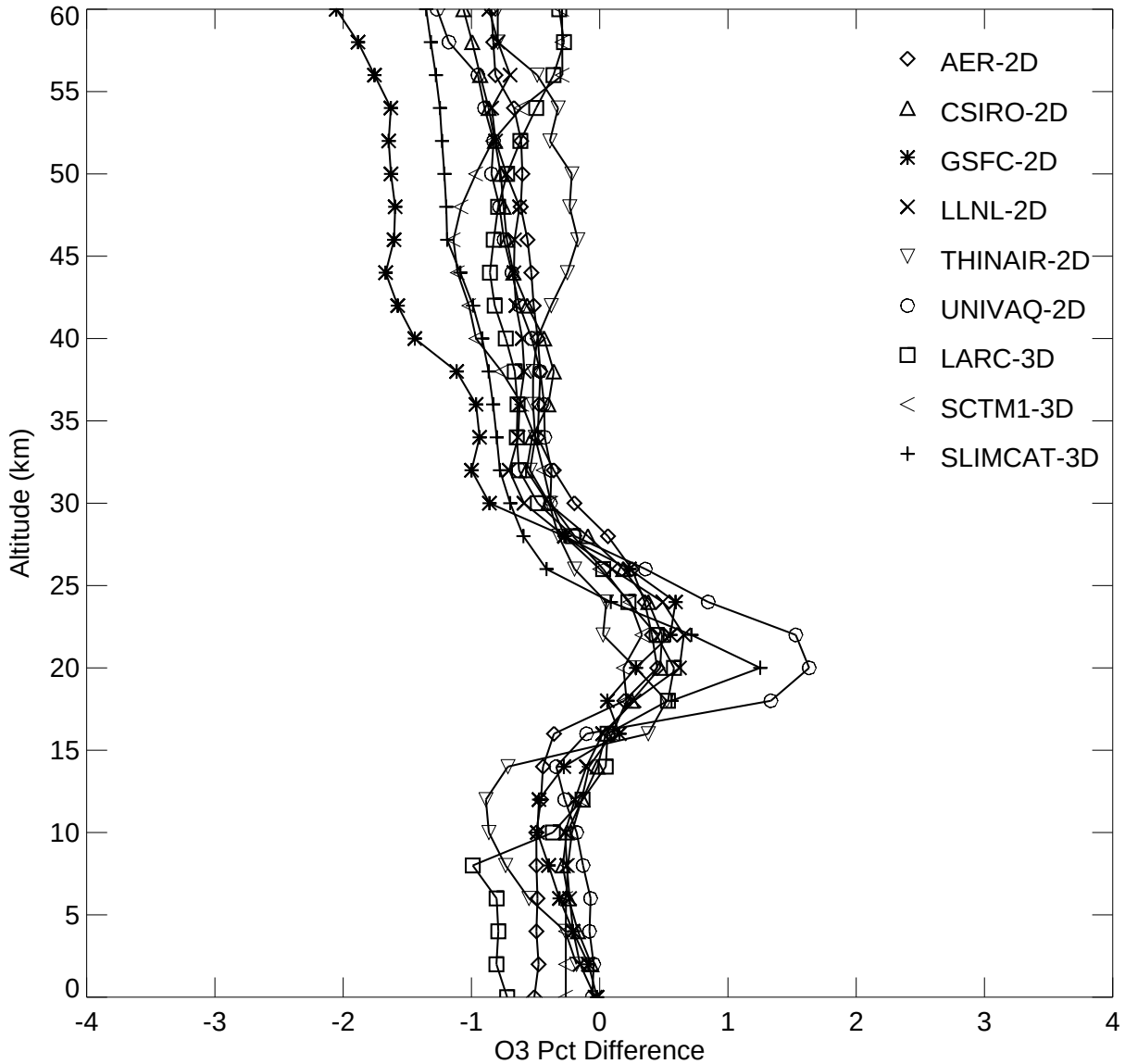

Figure 4.73: Calculated perturbations to O_3 (percent) as a function of altitude at the equator in June of 2015 due to emissions from a fleet of 500 HSCT aircraft with EI(NO_x)=5 under Scenario S1c relative to Scenario D.

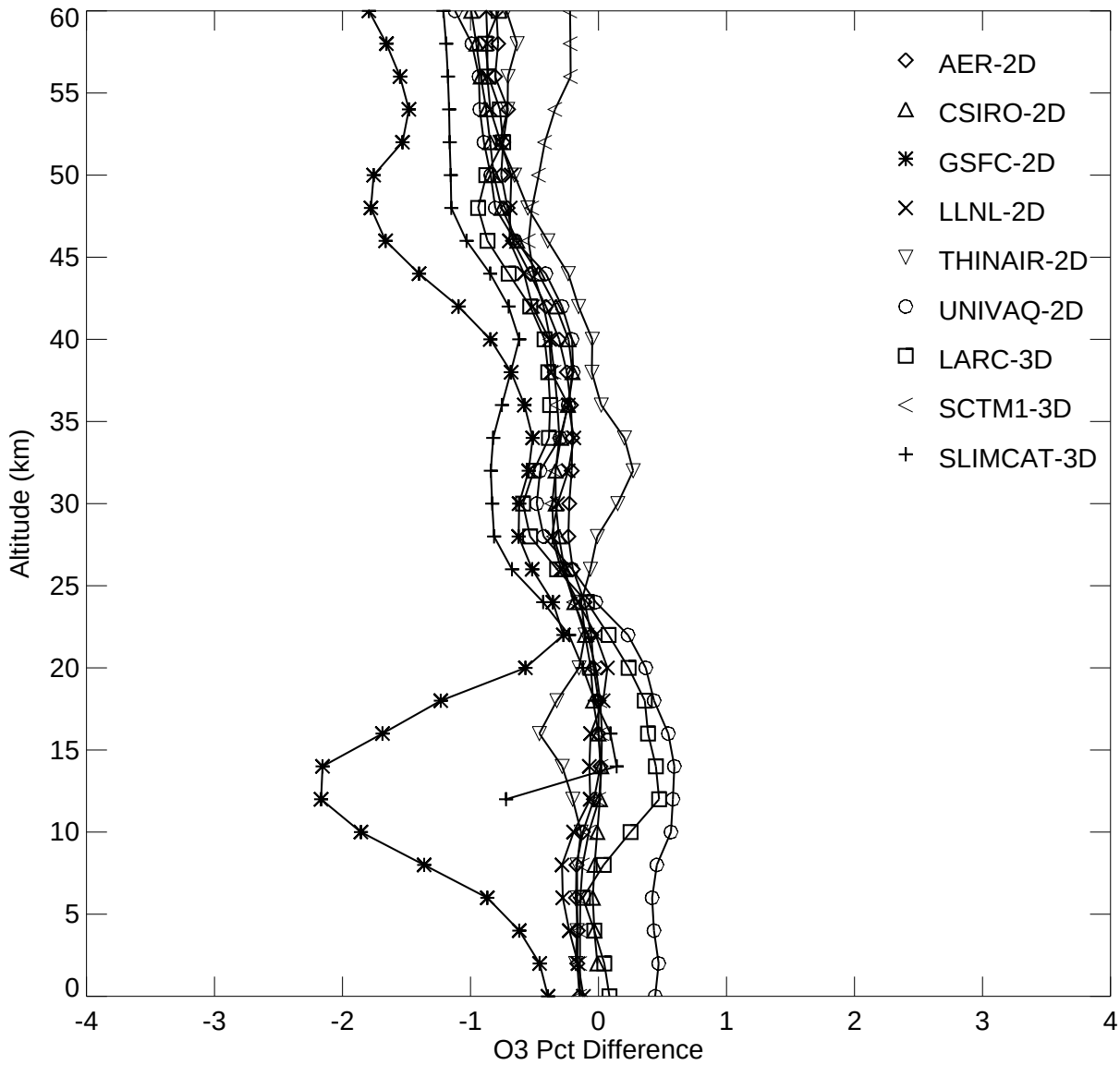

Figure 4.74: Calculated perturbations to O_3 (percent) as a function of altitude at 45^oS in June of 2015 due to emissions from a fleet of 500 HSCT aircraft with EI(NO_x)=5 under Scenario S1c relative to Scenario D.

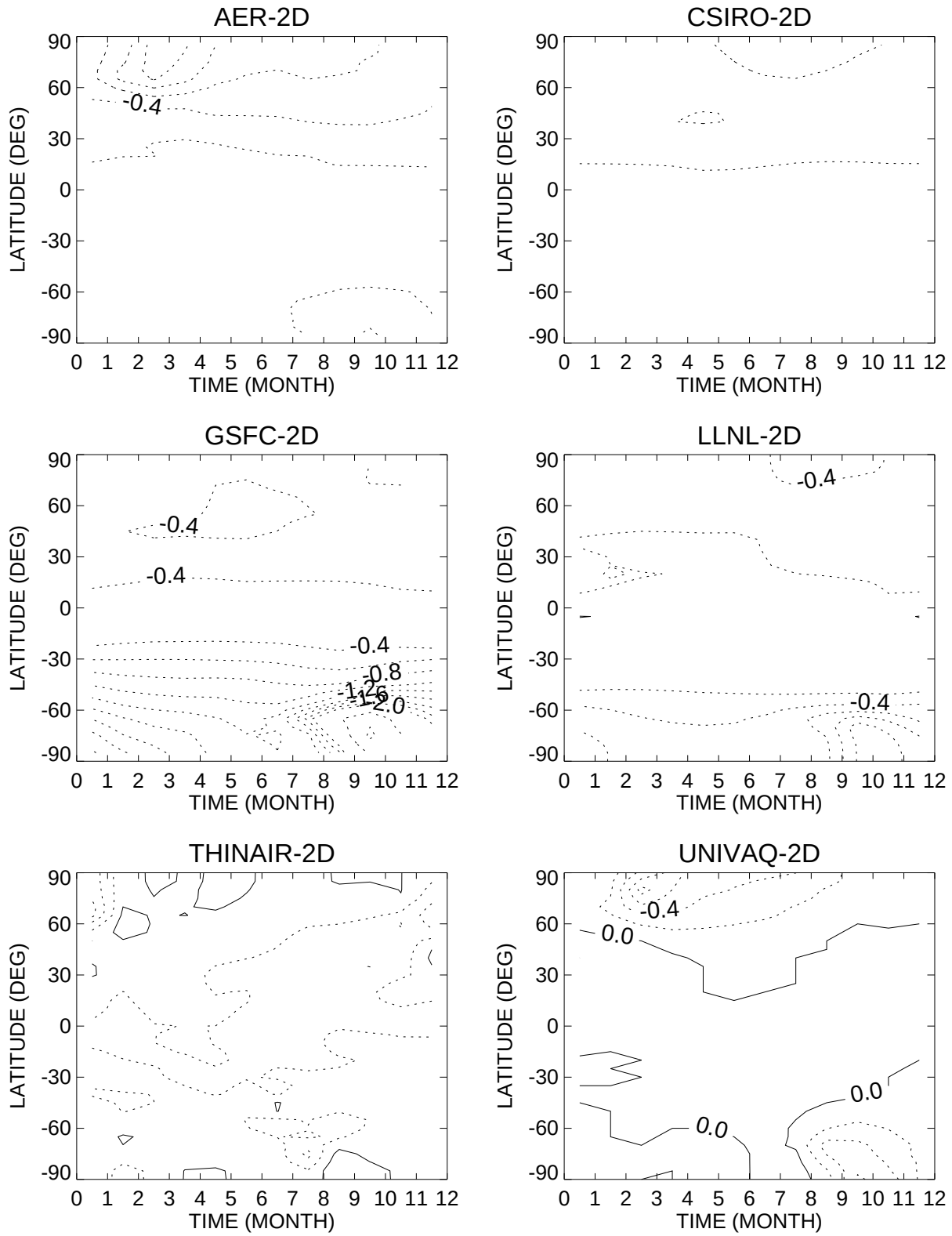

Figure 4.75: Calculated perturbations to column O_3 (percent) as a function of latitude and season in 2015 due to emissions from a fleet of 500 HSCT aircraft with EI(NO_x)=5 under Scenario S1c relative to Scenario D. Contours are -4, -3, and -2.0 to 0.2 by 0.2.

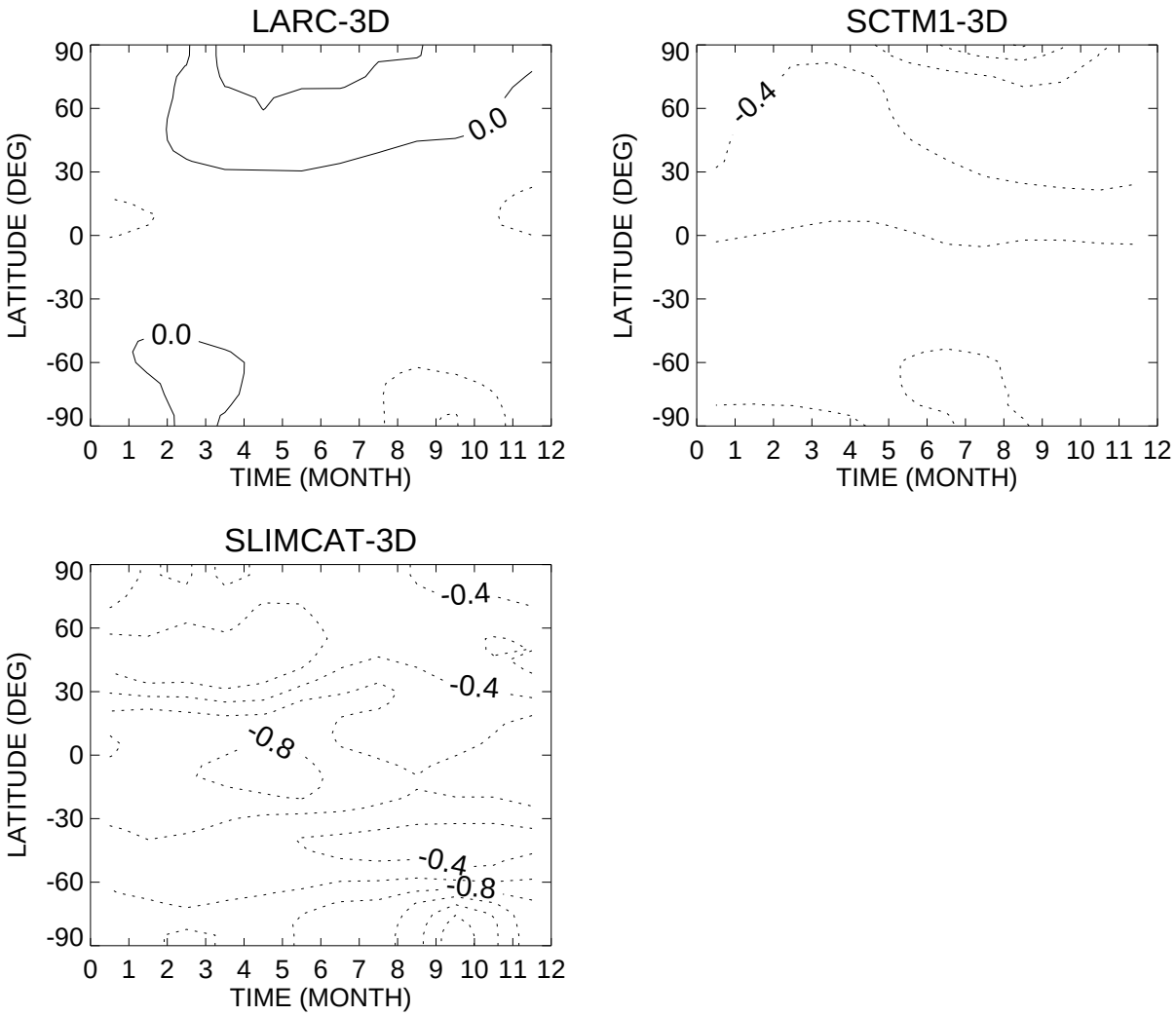

Figure 4.75: continued

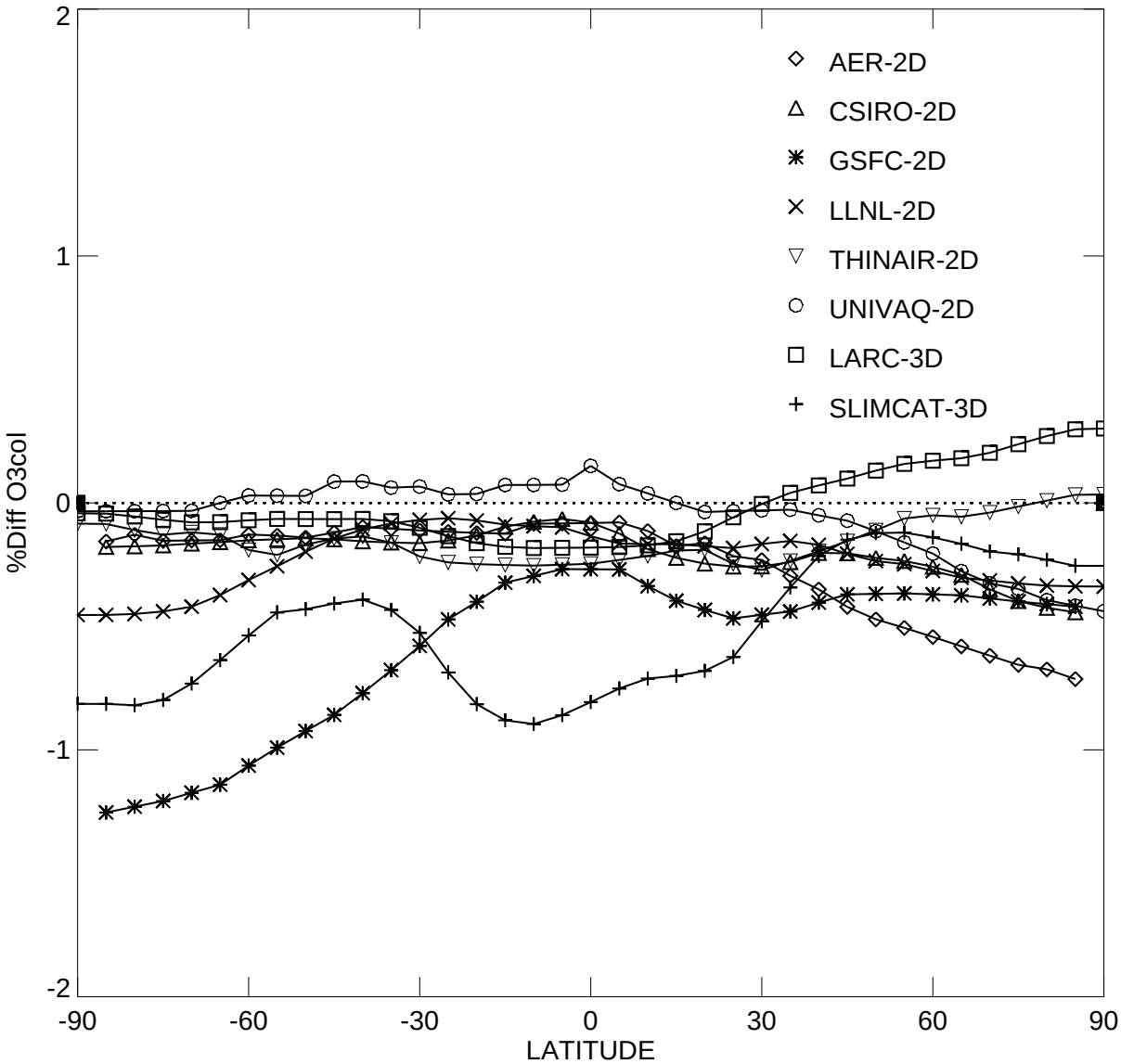

Figure 4.76: Calculated perturbations to total O_3 (percent) in June as function of latitude due to emissions from a fleet of 500 HSCT aircraft operating in 2015 (Scenario S1c - Scenario D) with EI(NO_x)=5.

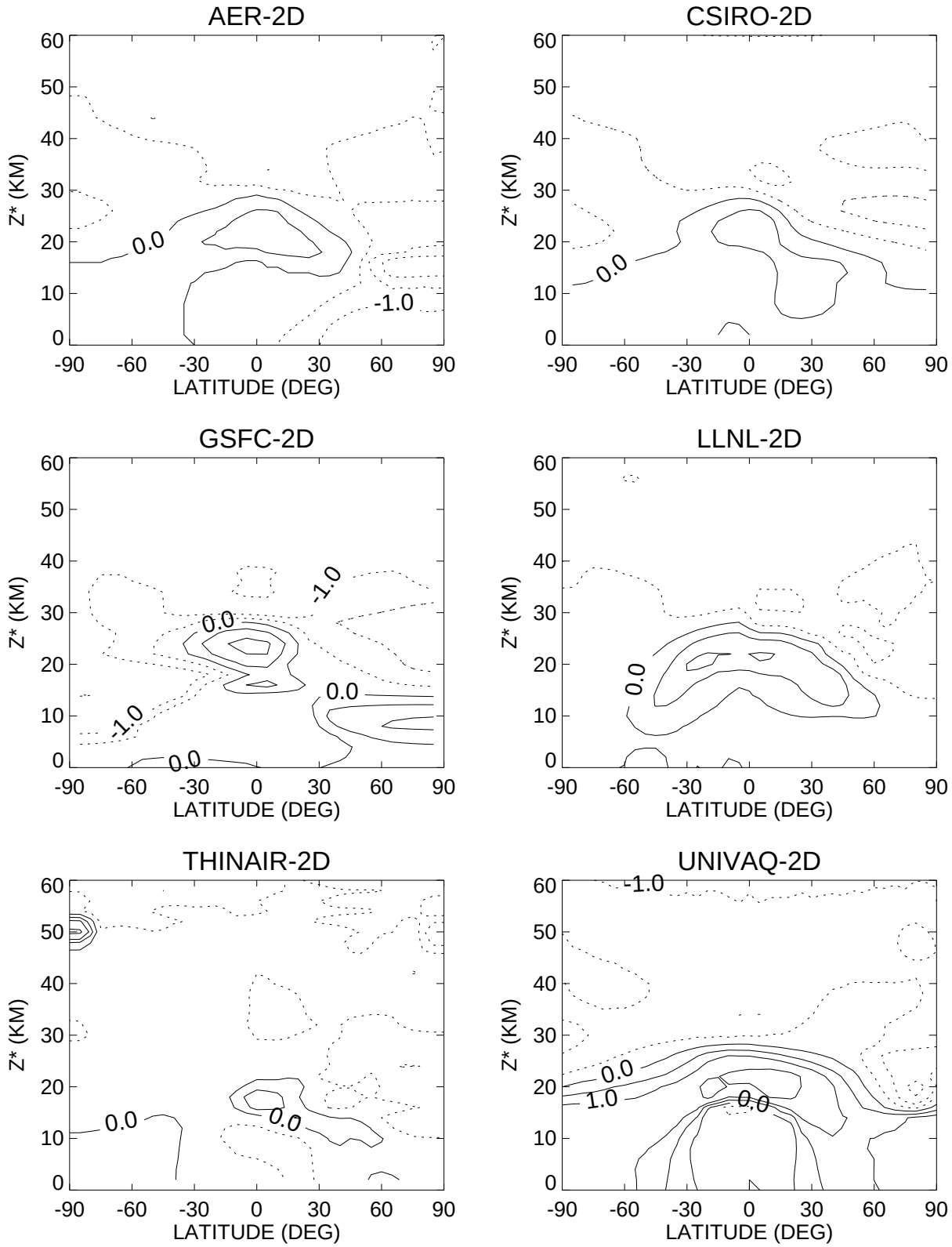

Figure 4.77: Calculated perturbations to O_3 (percent) as a function of latitude and altitude in March of 2015 due to emissions from a fleet of 500 HSCT aircraft with EI(NO_x)=10 under Scenario S1d relative to Scenario D. Contours are -2, -1, -0.5, 0, 0.5, 1, 2, 3.

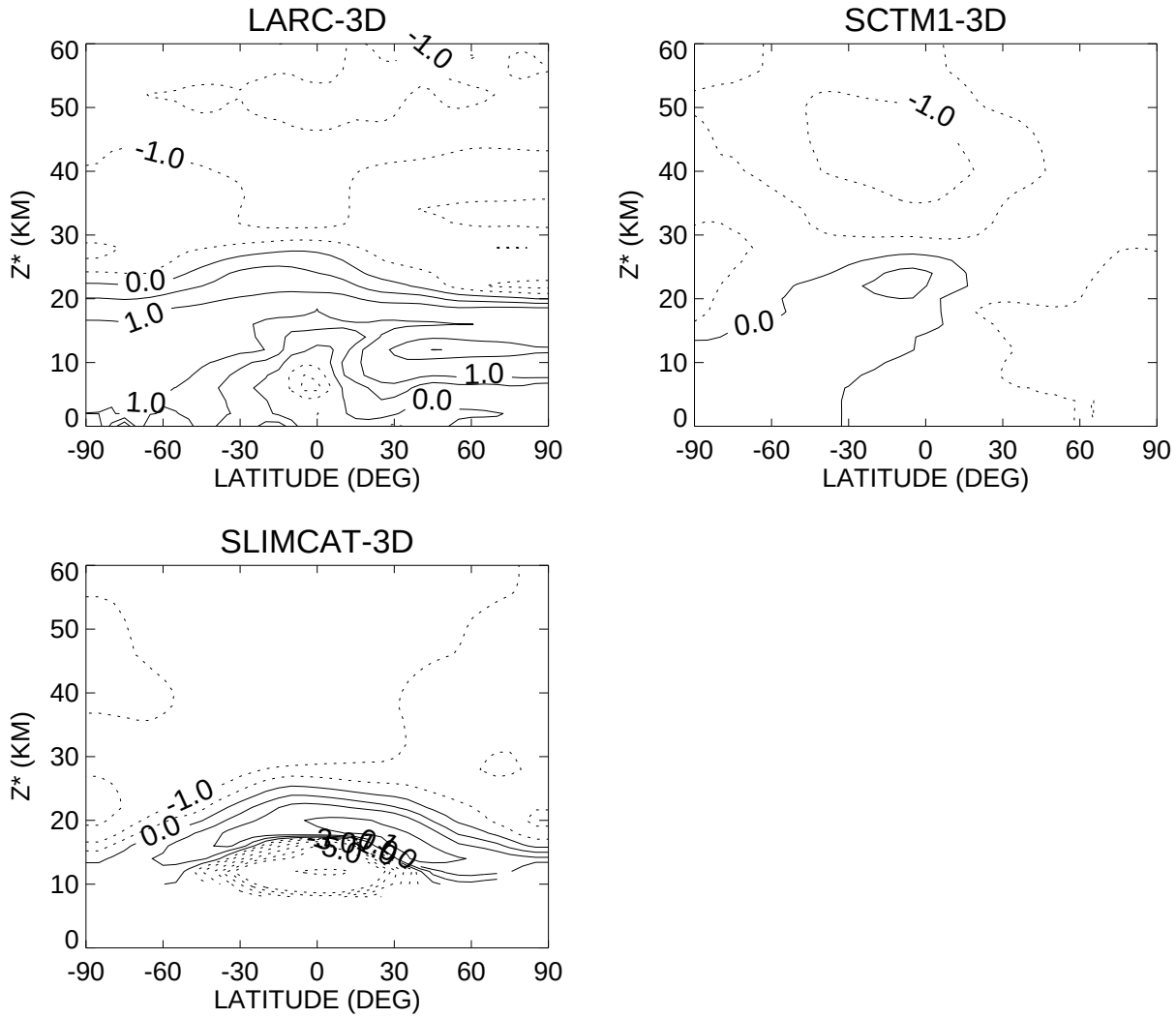

Figure 4.77: continued

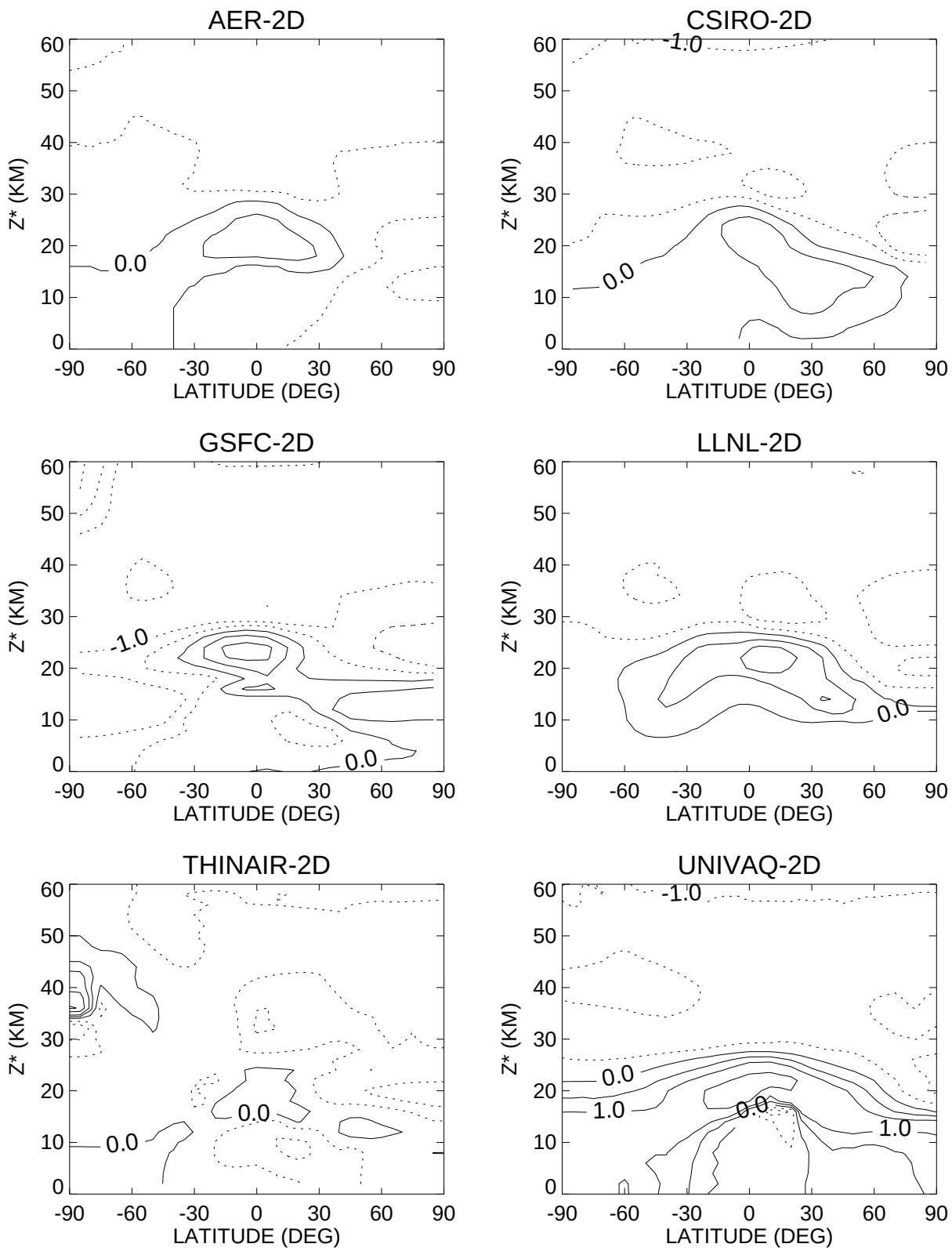

Figure 4.78: Calculated perturbations to O_3 (percent) as a function of latitude and altitude in June of 2015 due to emissions from a fleet of 500 HSCT aircraft with EI(NO_x)=10 under Scenario S1d relative to Scenario D. Contours are -2, -1, -0.5, 0, 0.5, 1, 2, 3, 4.

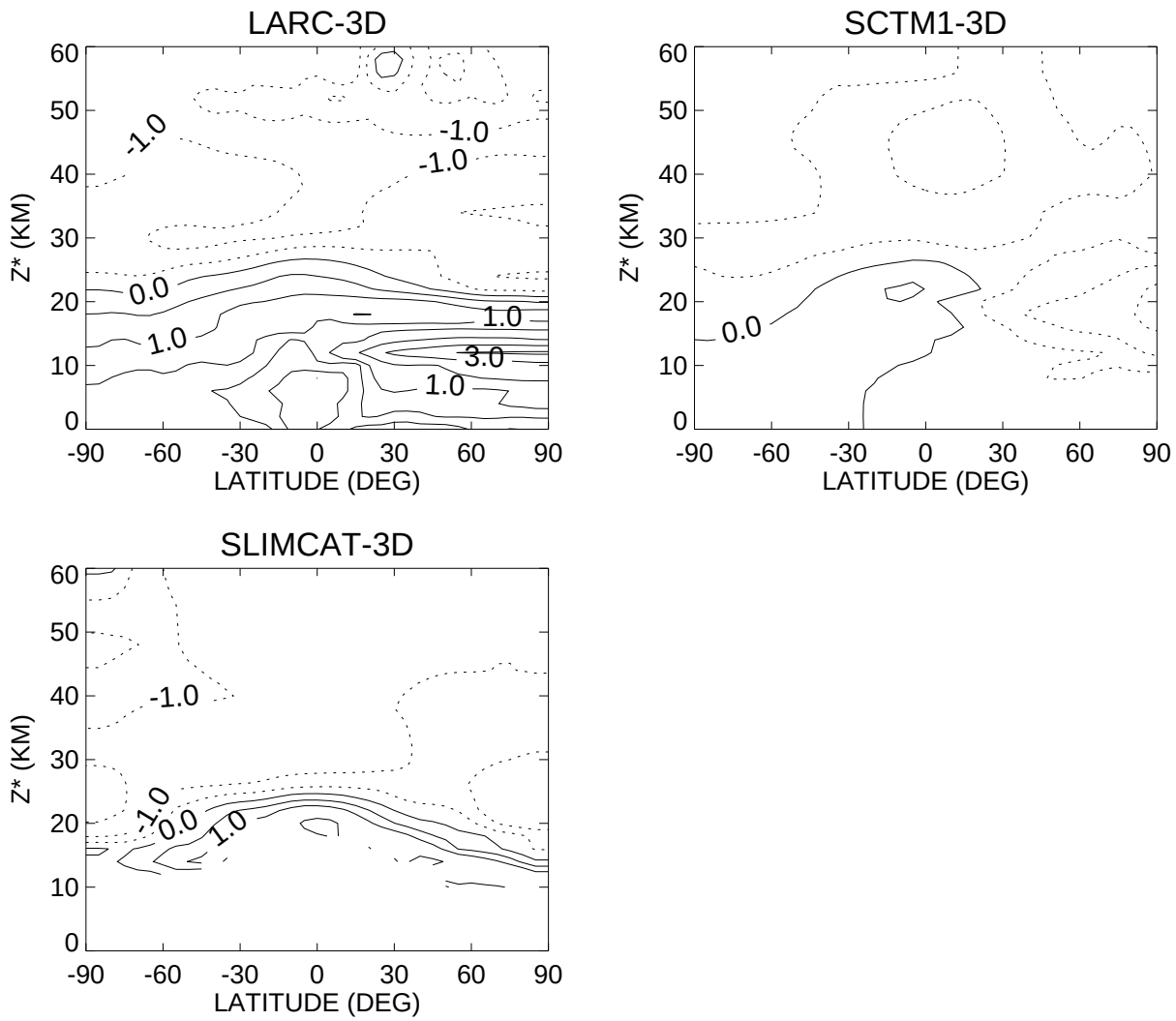

Figure 4.78: continued

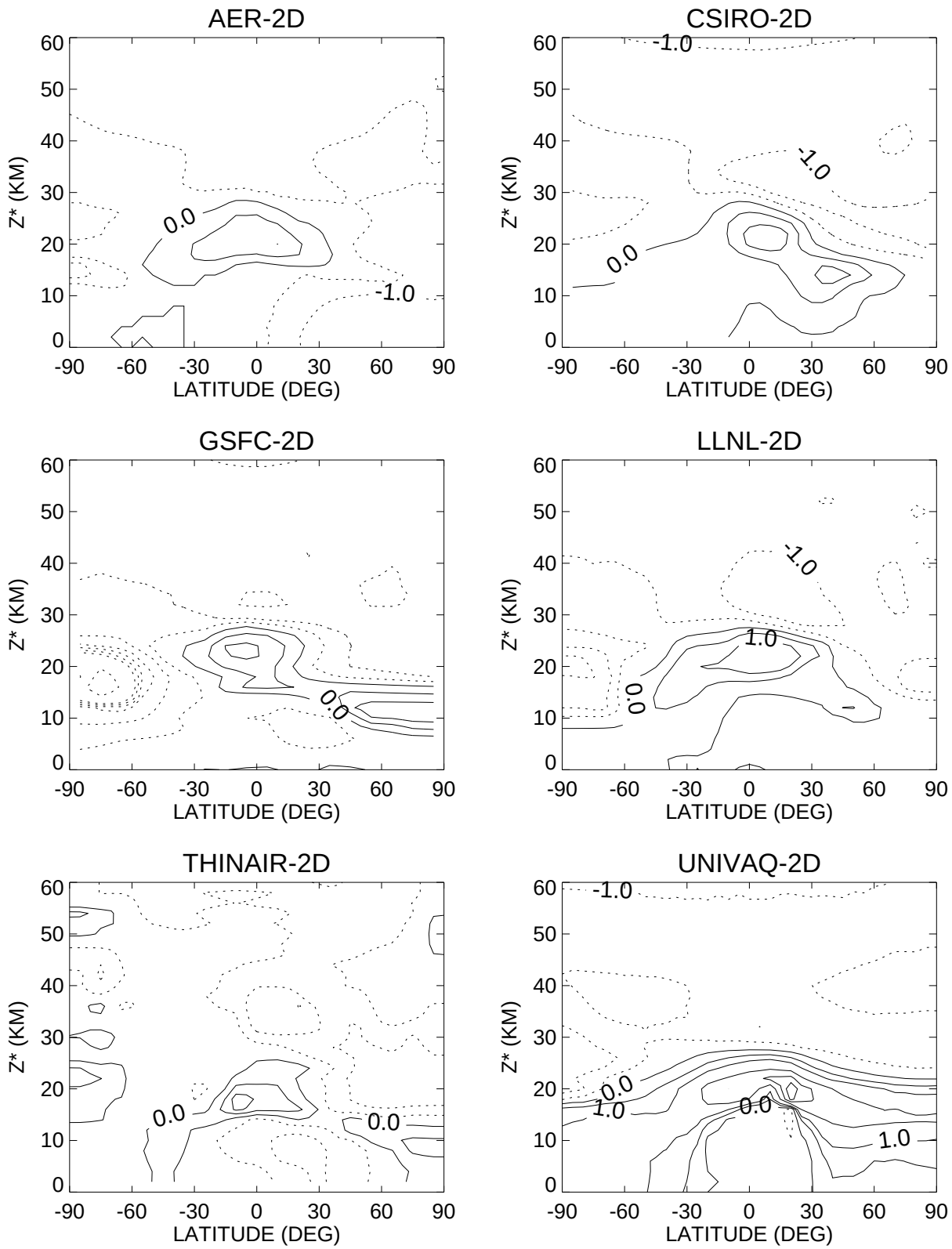

Figure 4.79: Calculated perturbations to O_3 (percent) as a function of latitude and altitude in October of 2015 due to emissions from a fleet of 500 HSCT aircraft with EI(NO_x)=10 under Scenario S1d relative to Scenario D. Contours are -10, -5, -4, -3, -2, -1, -0.5, 0, 0.5, 1, 2, 3, 4.

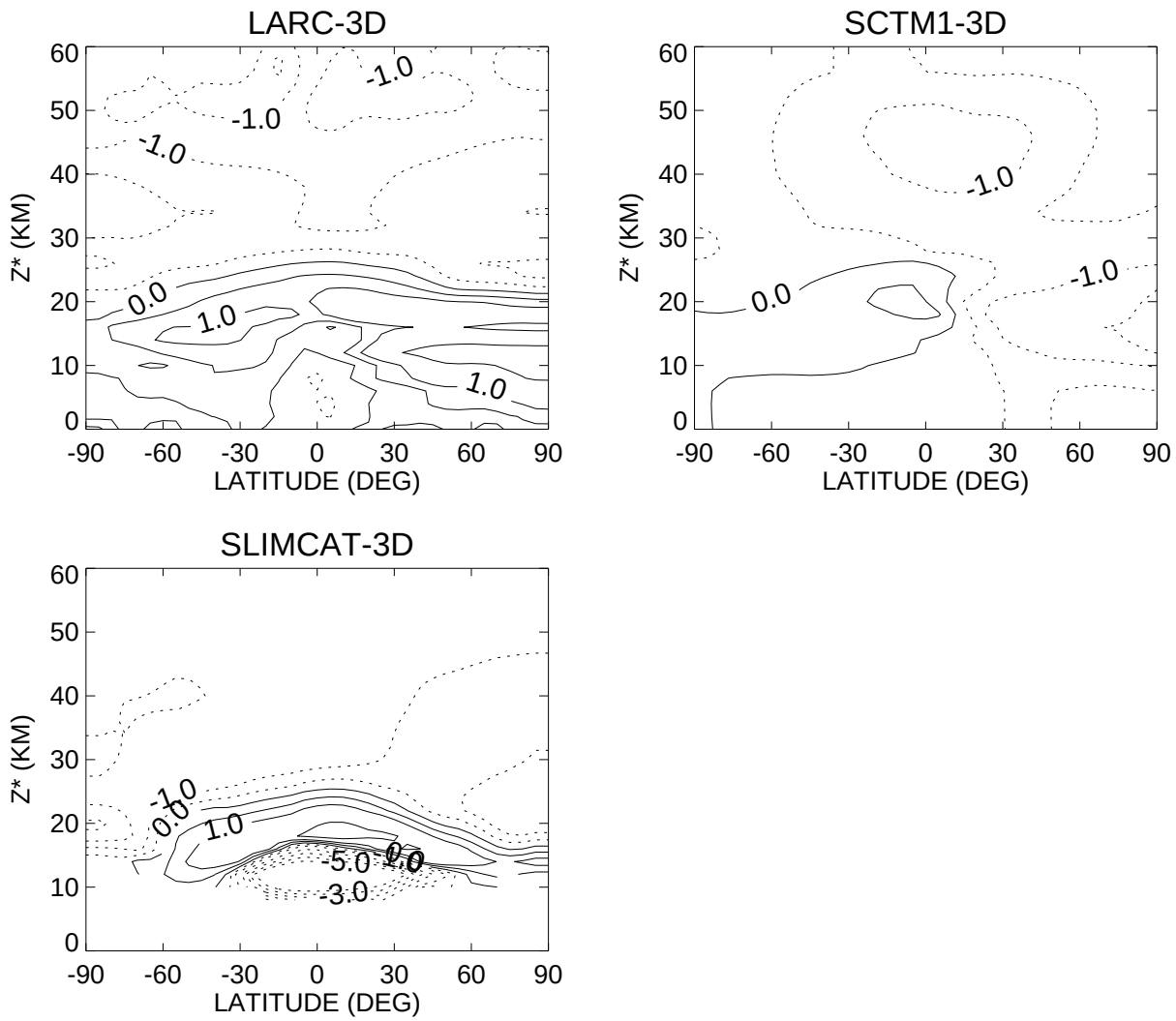

Figure 4.79: continued

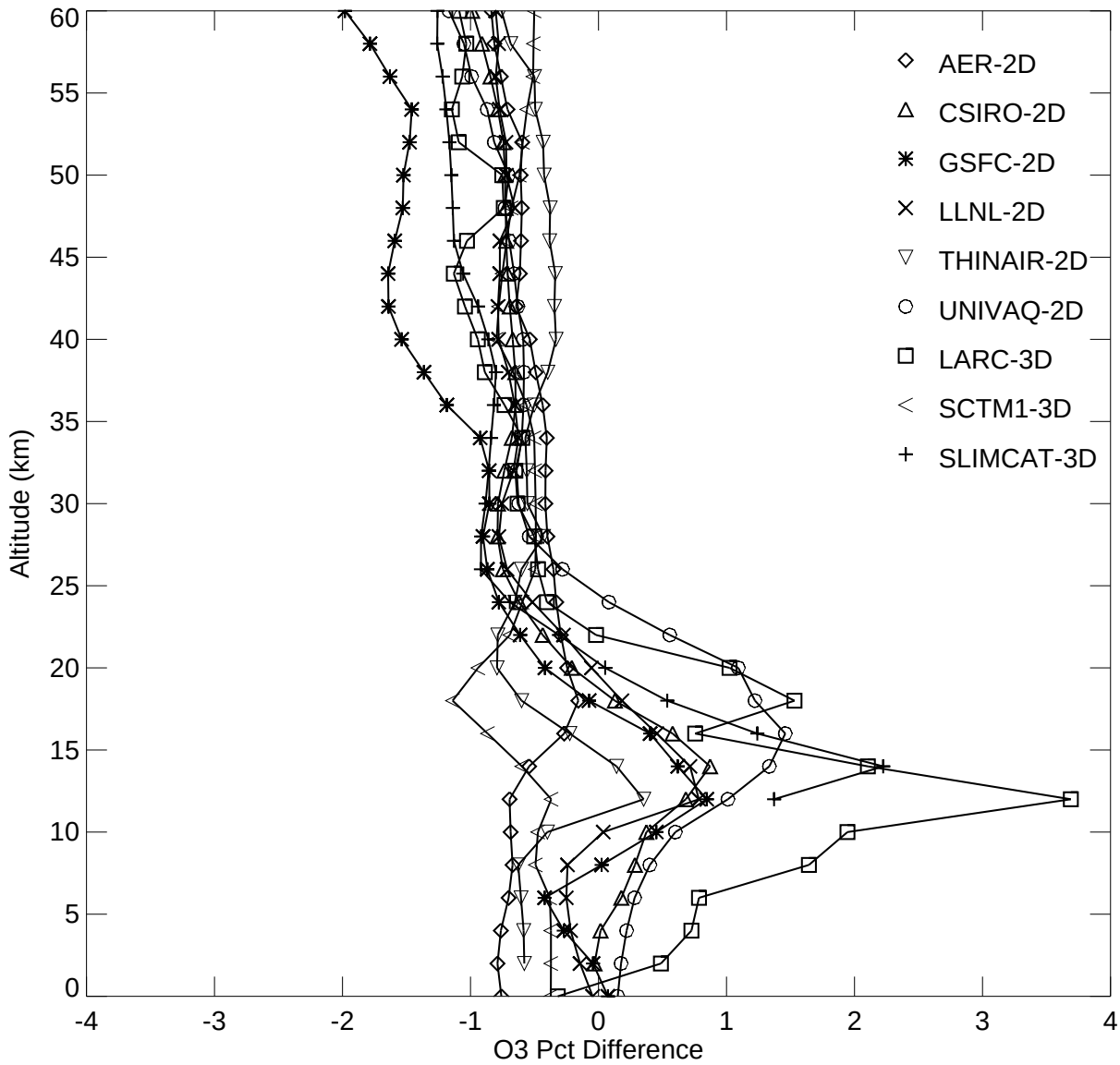

Figure 4.80: Calculated perturbations to O_3 (percent) as a function of altitude at 45°N in June of 2015 due to emissions from a fleet of 500 HSCT aircraft with EI(NO_x)=10 under Scenario S1d relative to Scenario D.

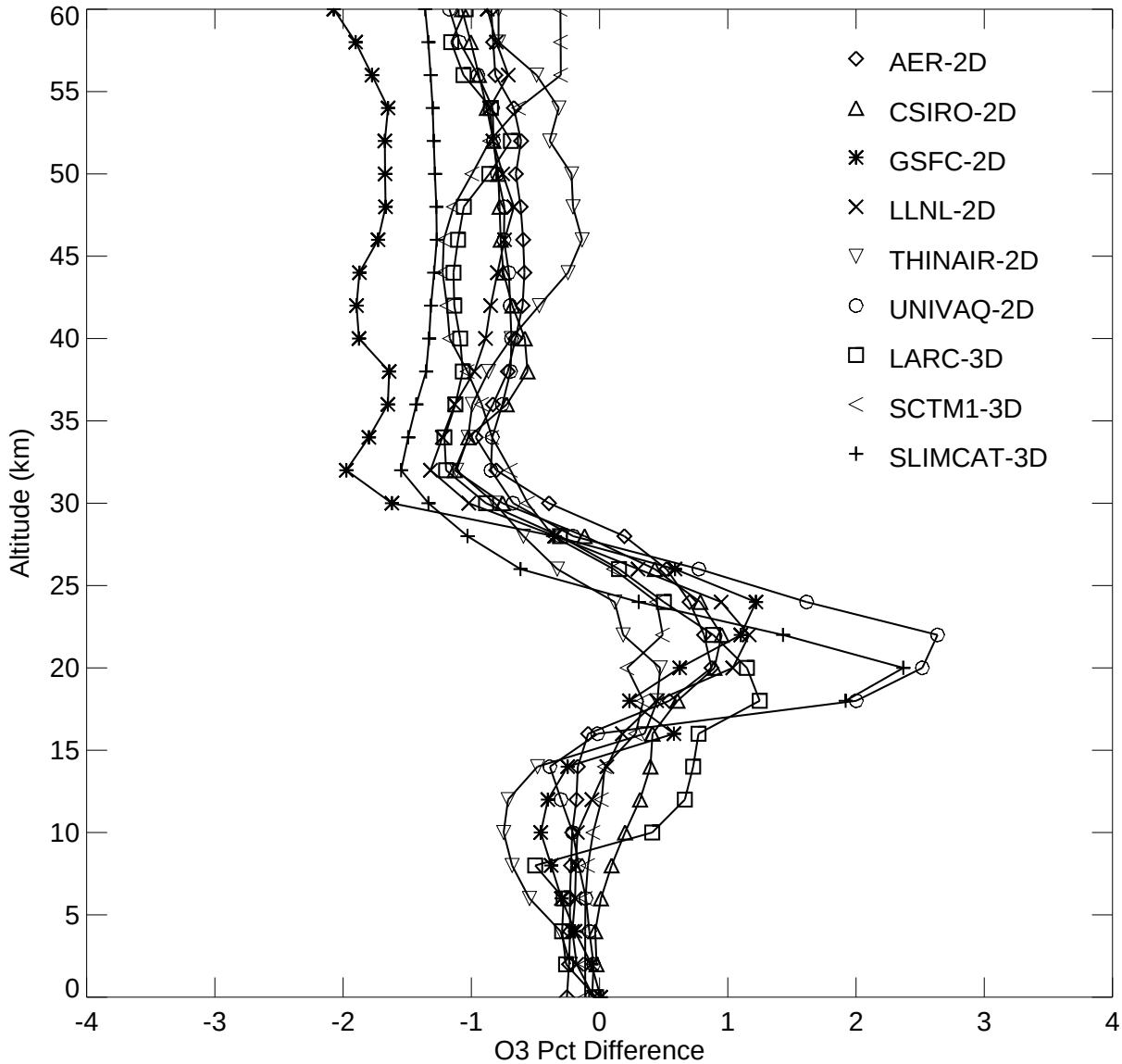

Figure 4.81: Calculated perturbations to O_3 (percent) as a function of altitude at the equator in June of 2015 due to emissions from a fleet of 500 HSCT aircraft with EI(NO_x)=10 under Scenario S1d relative to Scenario D.

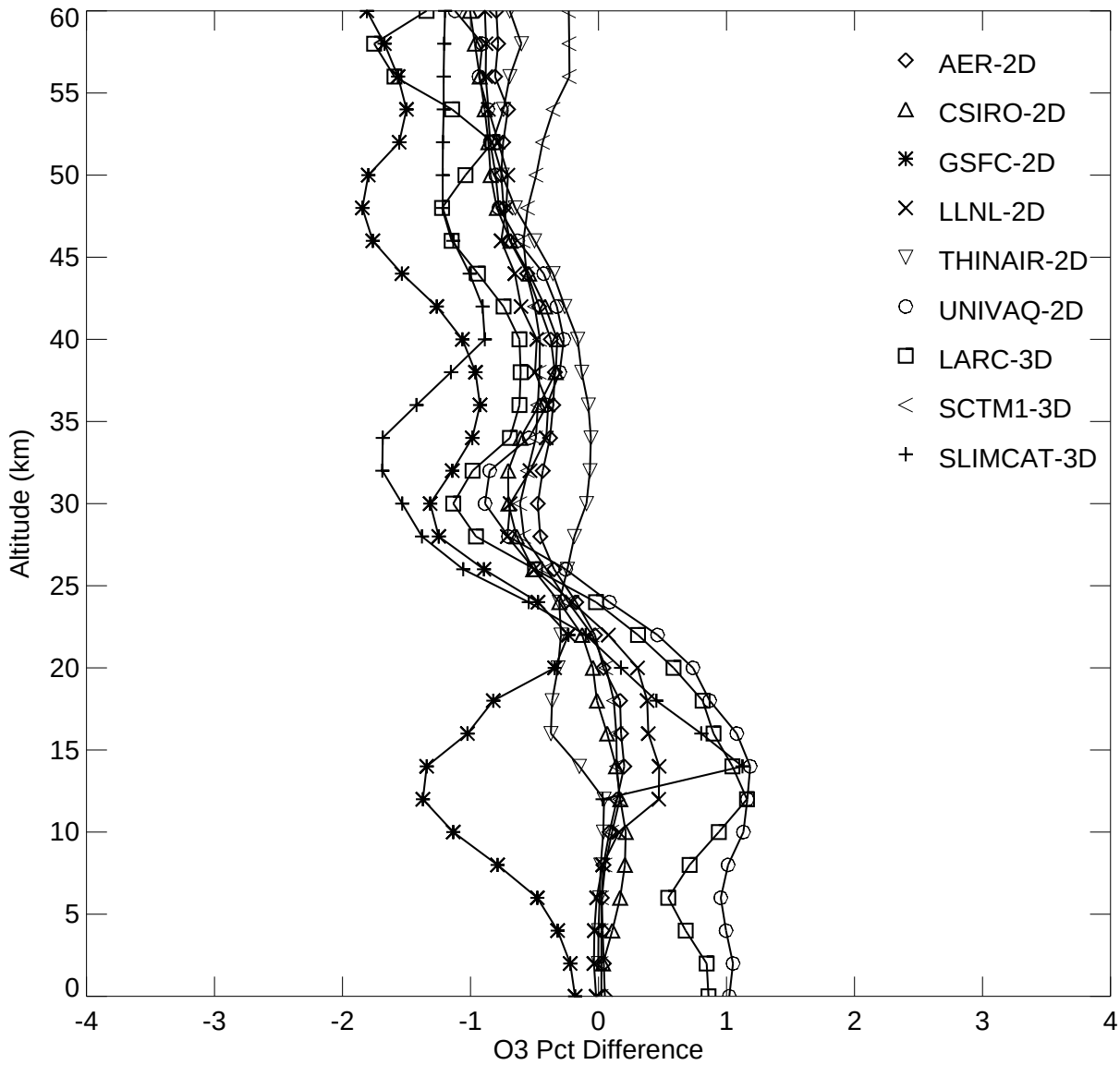

Figure 4.82: Calculated perturbations to O_3 (percent) as a function of altitude at 45^oS in June of 2015 due to emissions from a fleet of 500 HSCT aircraft with EI(NO_x)=10 under Scenario S1d relative to Scenario D.

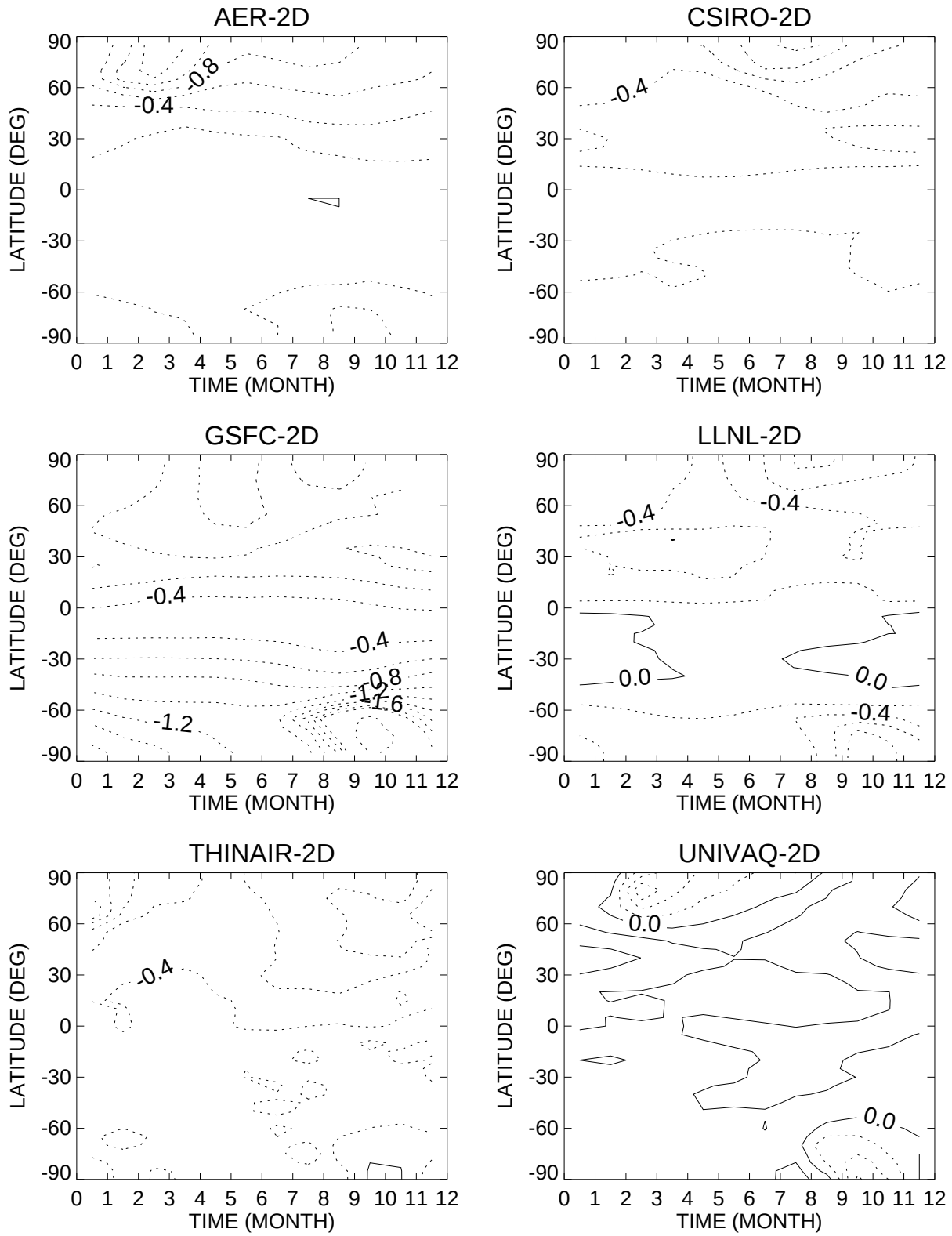

Figure 4.83: Calculated perturbations to column O_3 (percent) as a function of latitude and season in 2015 due to emissions from a fleet of 500 HSCT aircraft with EI(NO_x)=10 under Scenario S1d relative to Scenario D. Contours are -3 and -2.0 to 0.6 by 0.2.

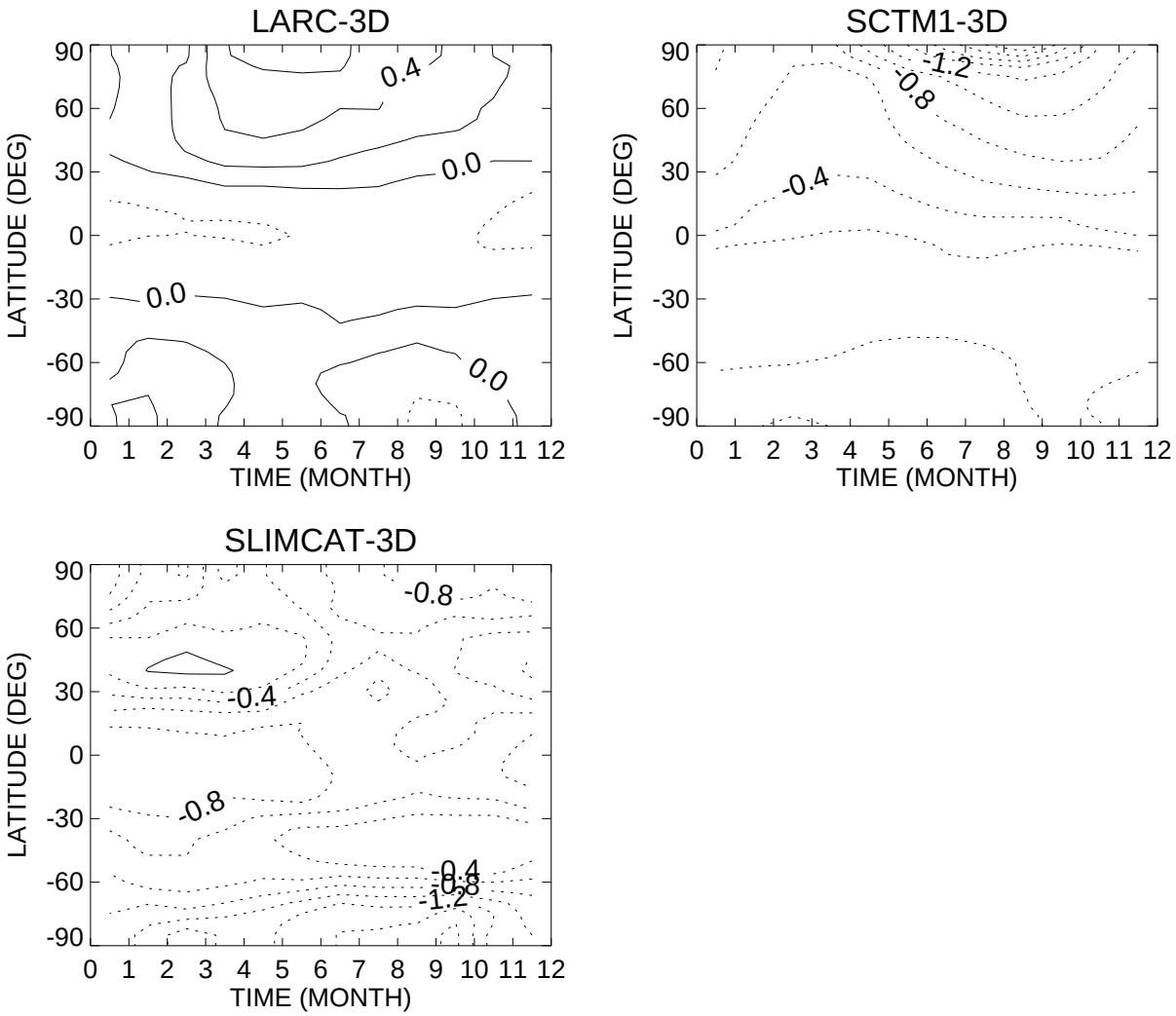

Figure 4.83: continued

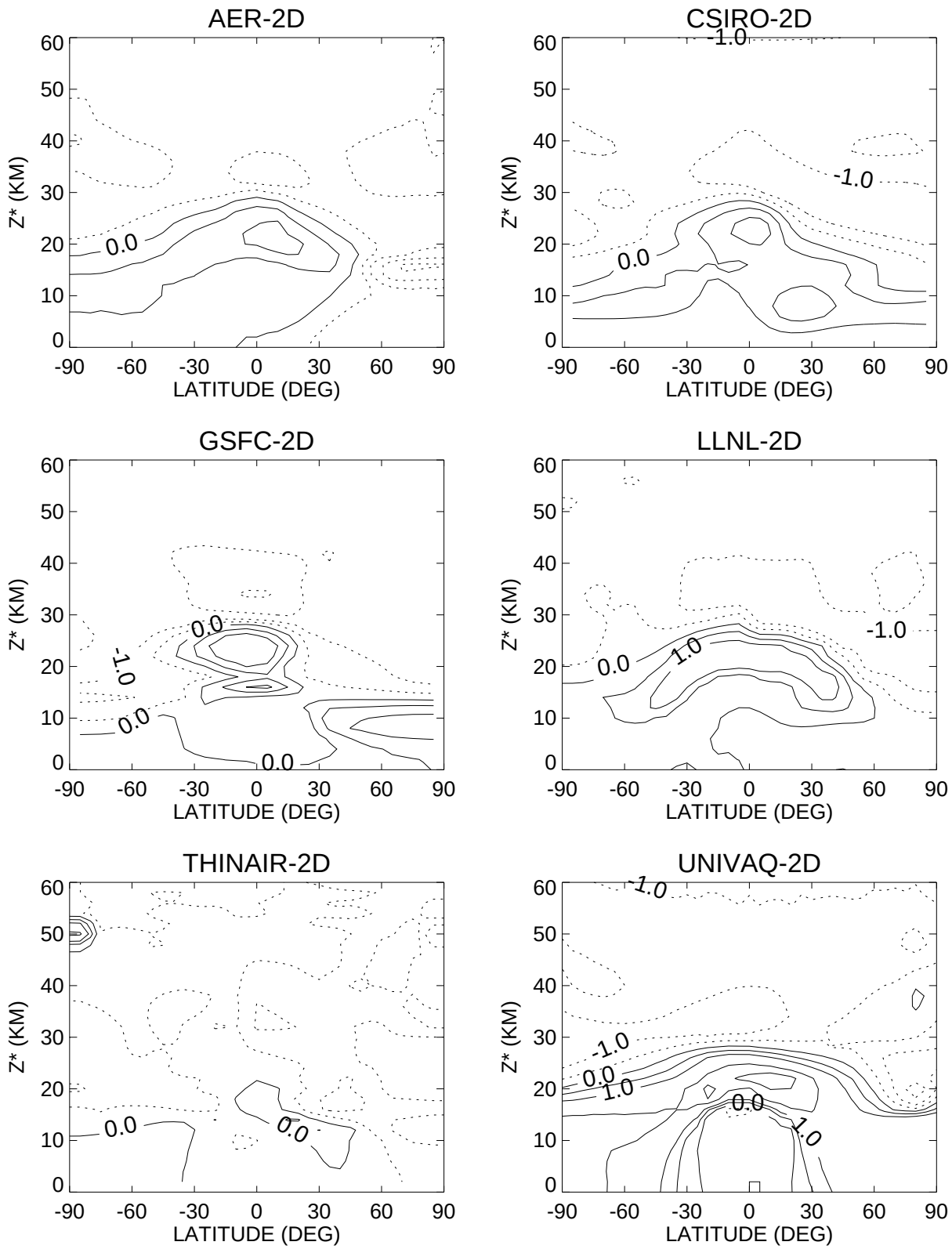

Figure 4.84: Calculated perturbations to O_3 (percent) as a function of latitude and altitude in March of 2015 due to emissions from a fleet of 500 HSCT aircraft with EI(NO_x)=15 under Scenario S1e relative to Scenario D. Contours are -3, -2, -1, -0.5, 0, 0.5, 1, 2, 3.

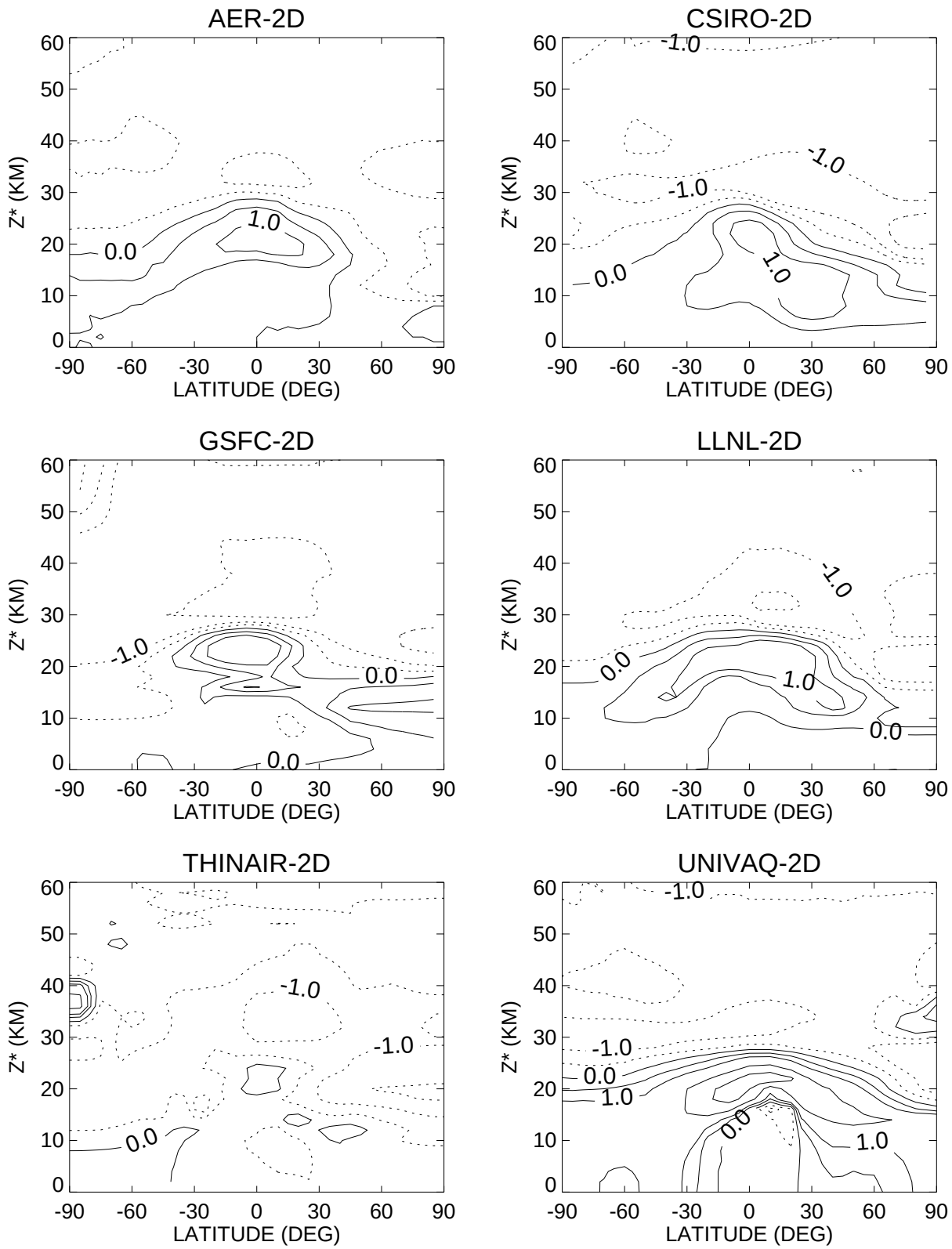

Figure 4.85: Calculated perturbations to O_3 (percent) as a function of latitude and altitude in June of 2015 due to emissions from a fleet of 500 HSCT aircraft with EI(NO_x)=15 under Scenario S1e relative to Scenario D. Contours are -2, -1, -0.5, 0, 0.5, 1, 2, 3.

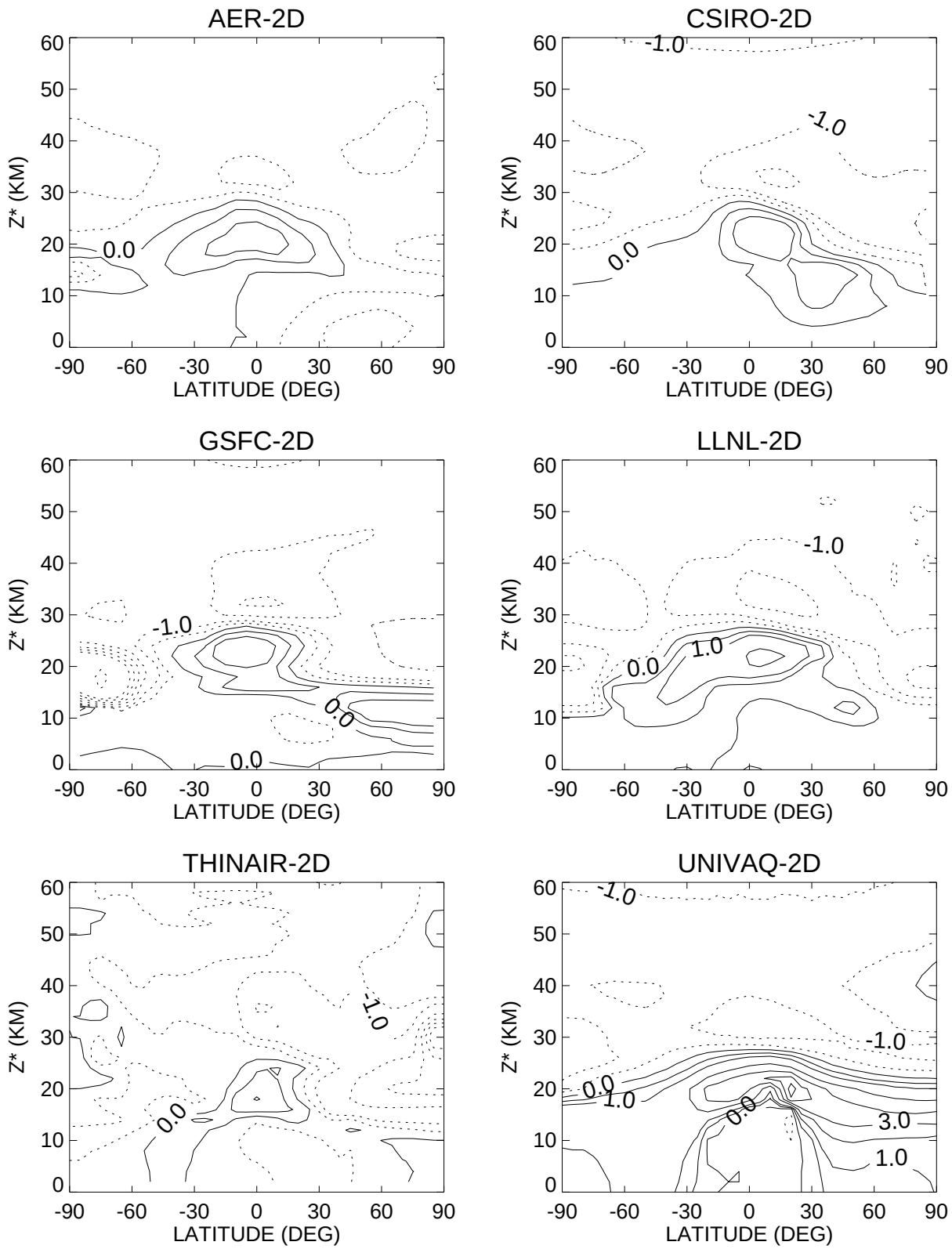

Figure 4.86: Calculated perturbations to O_3 (percent) as a function of latitude and altitude in October of 2015 due to emissions from a fleet of 500 HSCT aircraft with EI(NO_x)=15 under Scenario S1e relative to Scenario D. Contours are -10, -5, -4, -3, -2, -1, -0.5, 0, 0.5, 1, 2, 3, 4, 5.

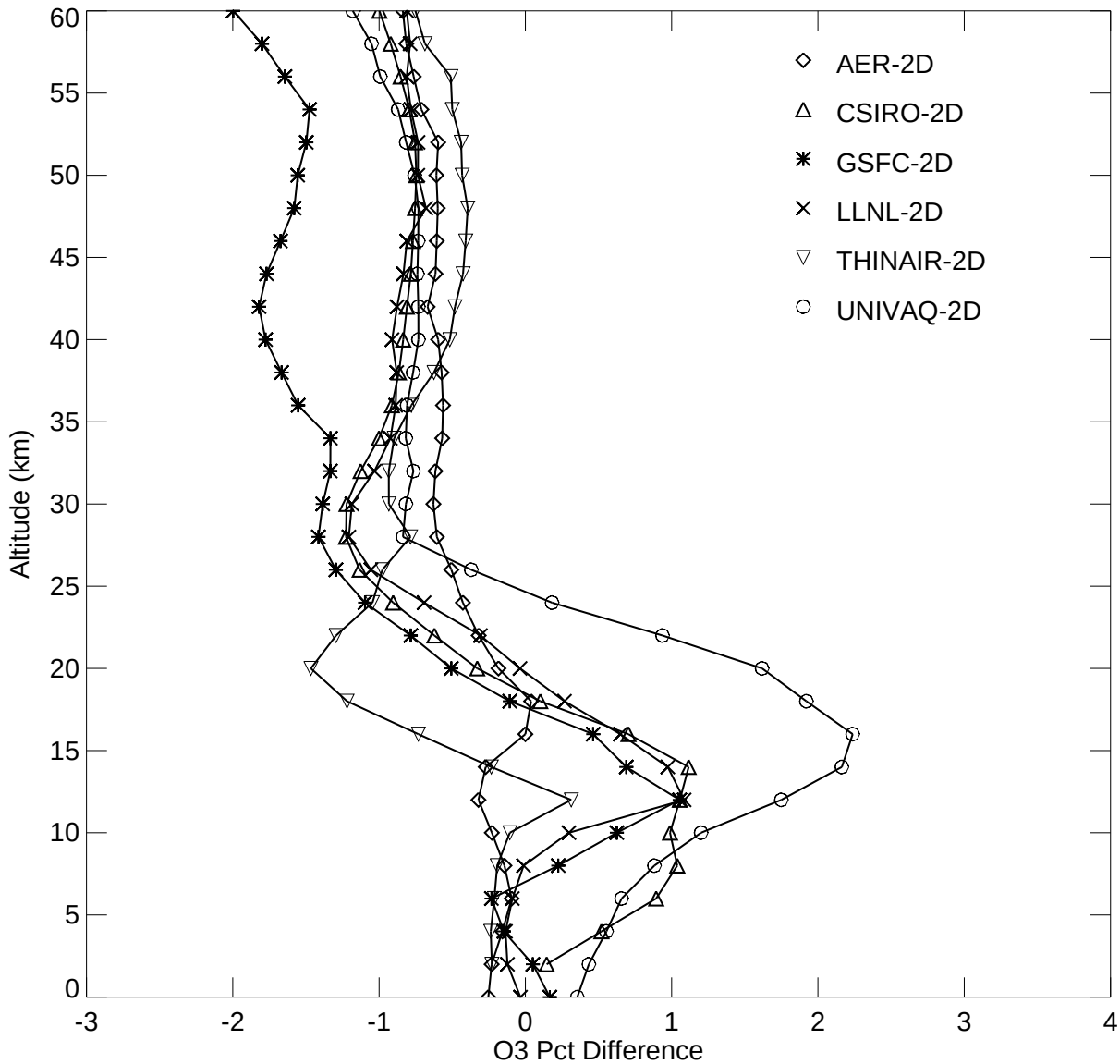

Figure 4.87: Calculated perturbations to O_3 (percent) as a function of altitude at 45°N in June of 2015 due to emissions from a fleet of 500 HSCT aircraft with EI(NO_x)=15 under Scenario S1e relative to Scenario D.

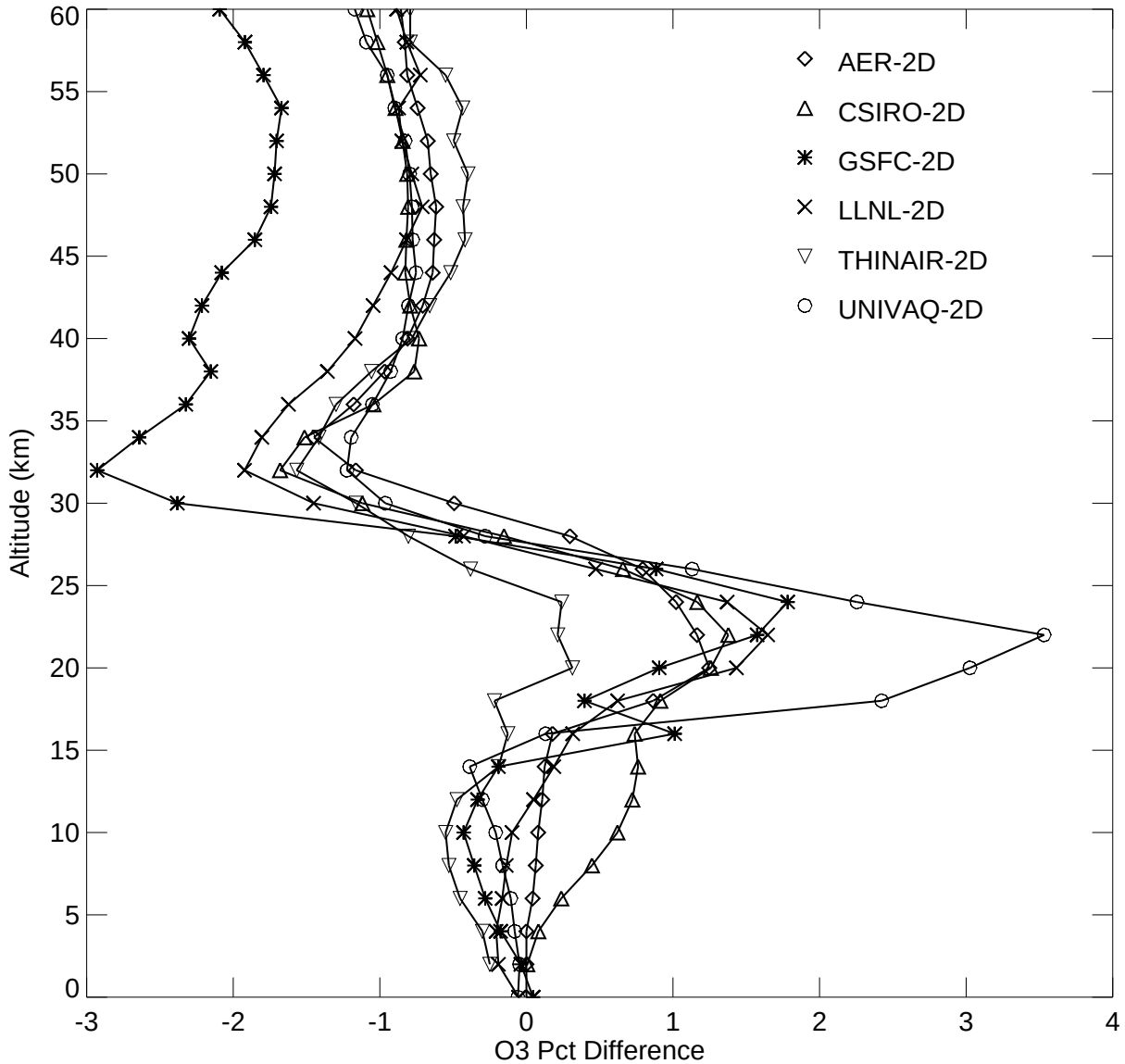

Figure 4.88: Calculated perturbations to O_3 (percent) as a function of altitude at the equator in June of 2015 due to emissions from a fleet of 500 HSCT aircraft with EI(NO_x)=15 under Scenario S1e relative to Scenario D.

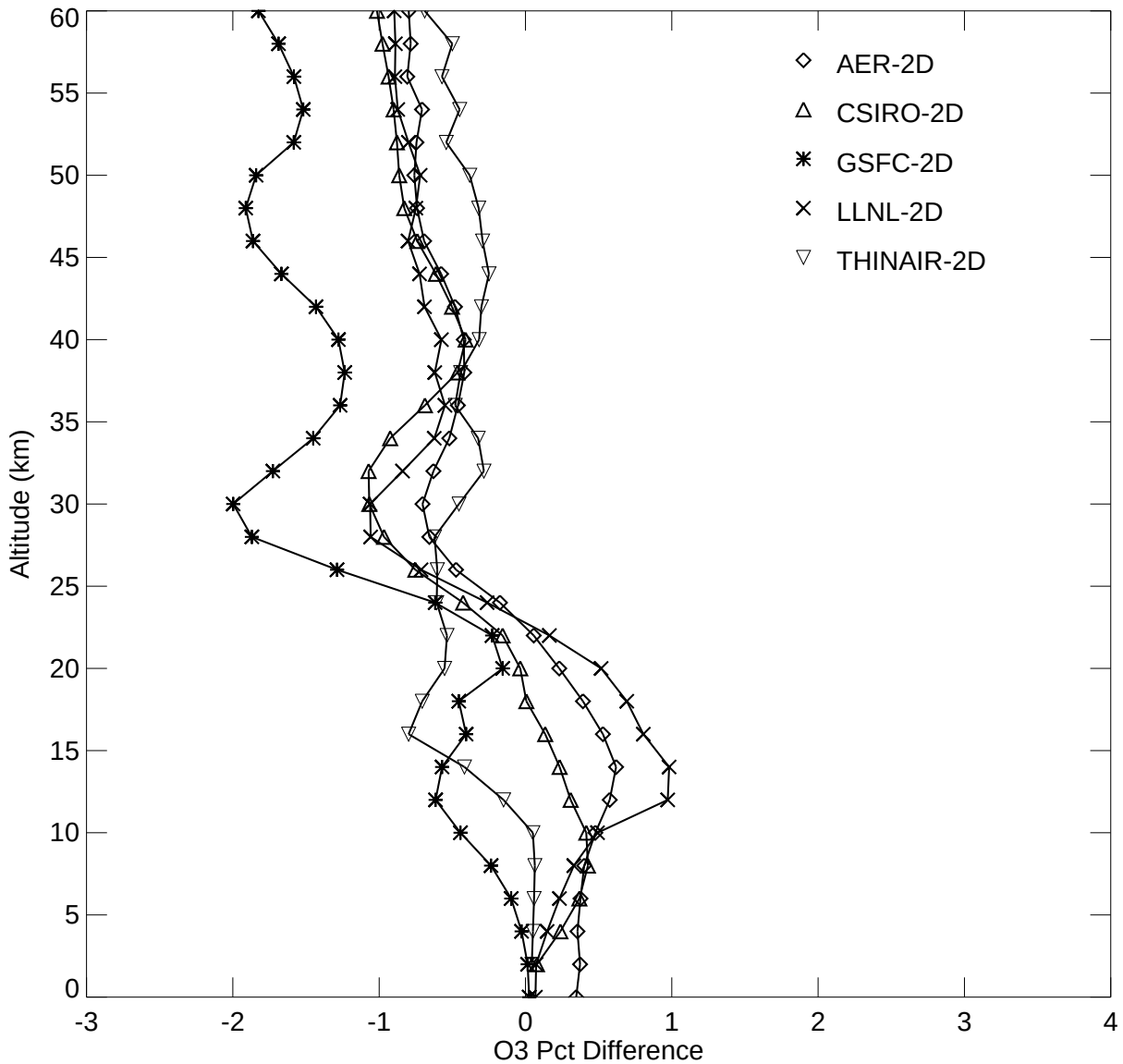

Figure 4.89: Calculated perturbations to O_3 (percent) as a function of altitude at 45^oS in June of 2015 due to emissions from a fleet of 500 HSCT aircraft with EI(NO_x)=15 under Scenario S1e relative to Scenario D.

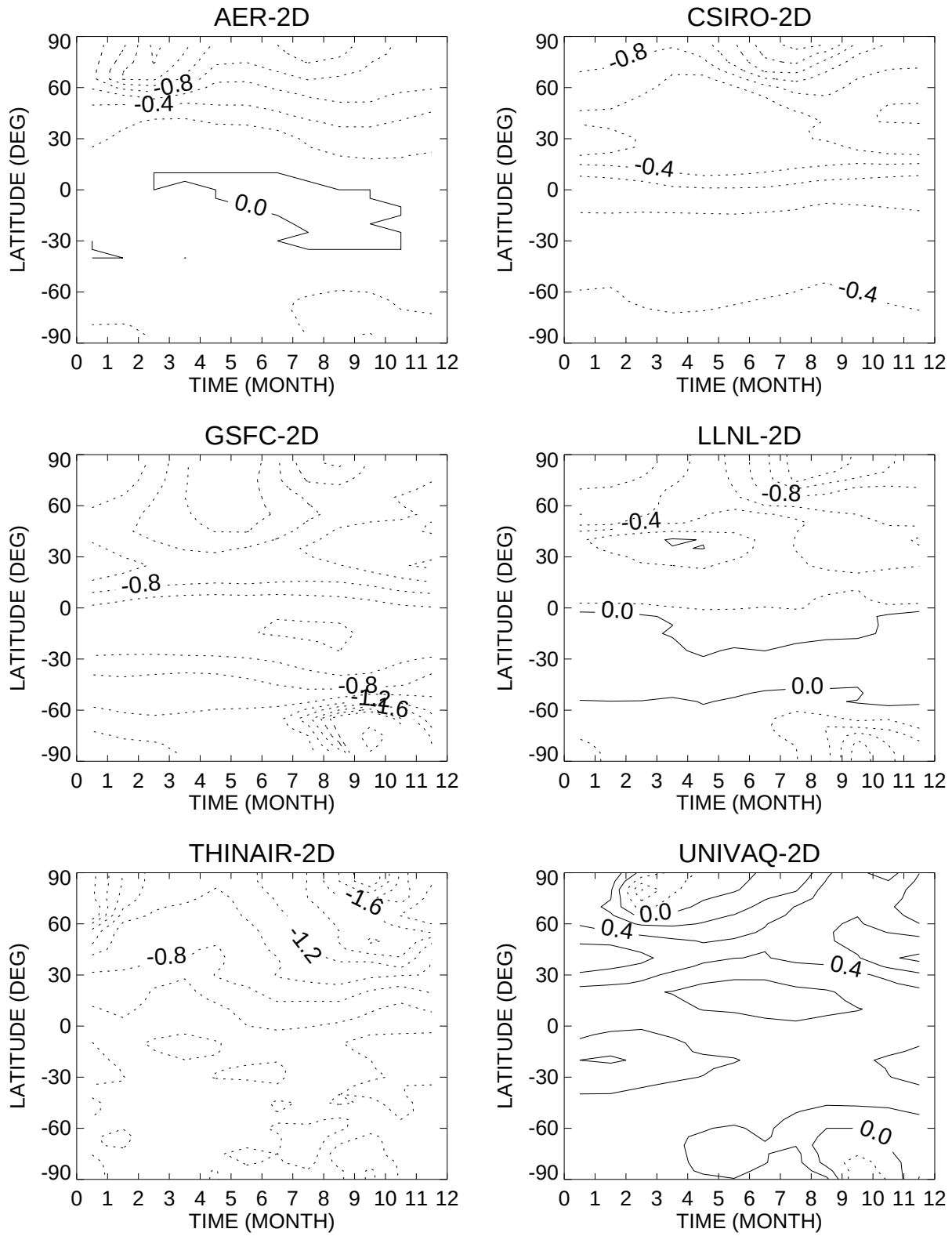

Figure 4.90: Calculated perturbations to column O_3 (percent) as a function of latitude and season in 2015 due to emissions from a fleet of 500 HSCT aircraft with EI(NO_x)=15 under Scenario S1e relative to Scenario D. Contours are -3 and -2.0 to 0.6 by 0.2.

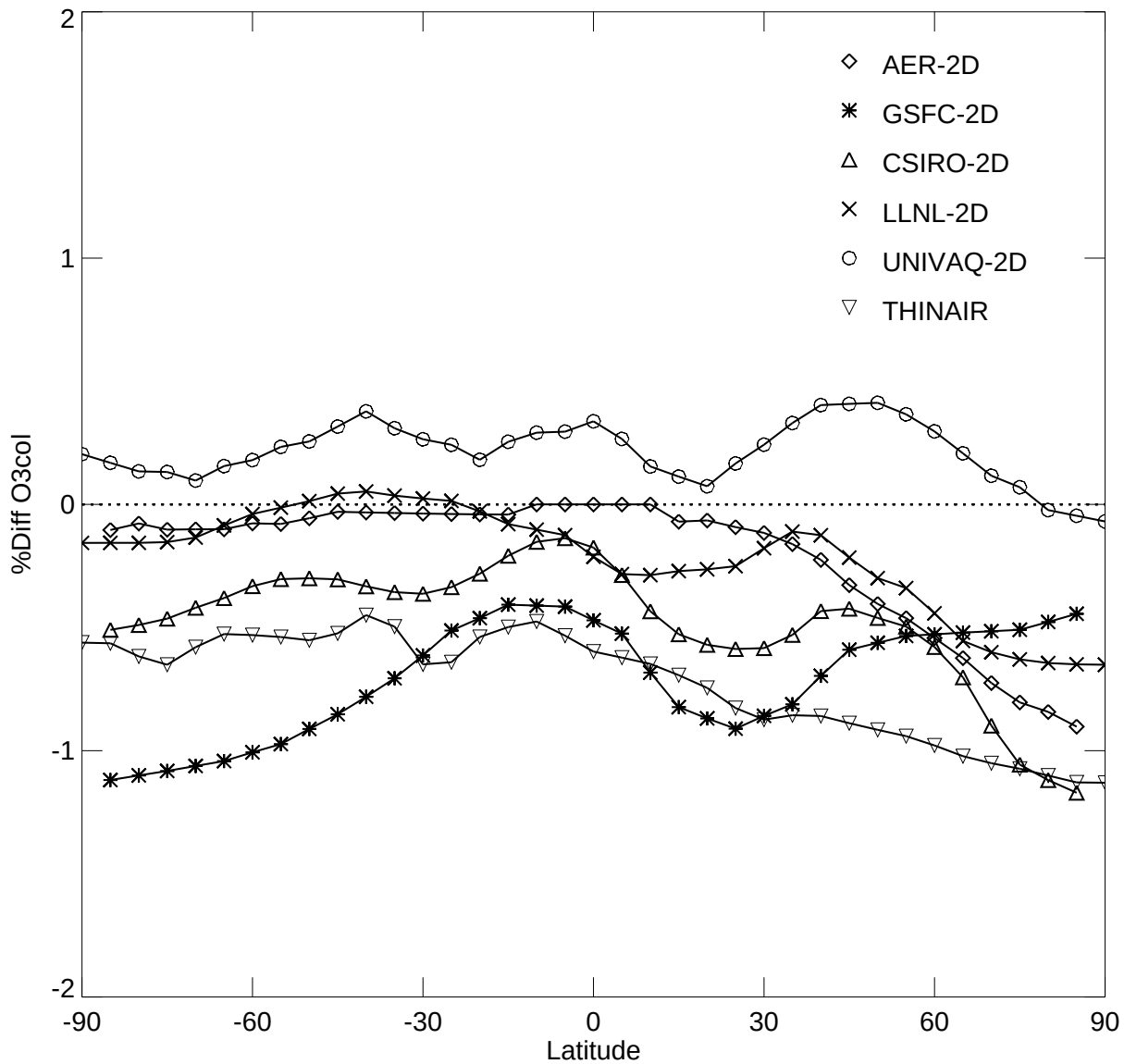

Figure 4.91: Calculated perturbations to total O_3 (percent) in June as a function of latitude due to emissions from a fleet of 500 HSCT aircraft operating in 2015 (Scenario S1e - Scenario D) with EI(NO_x)=15.

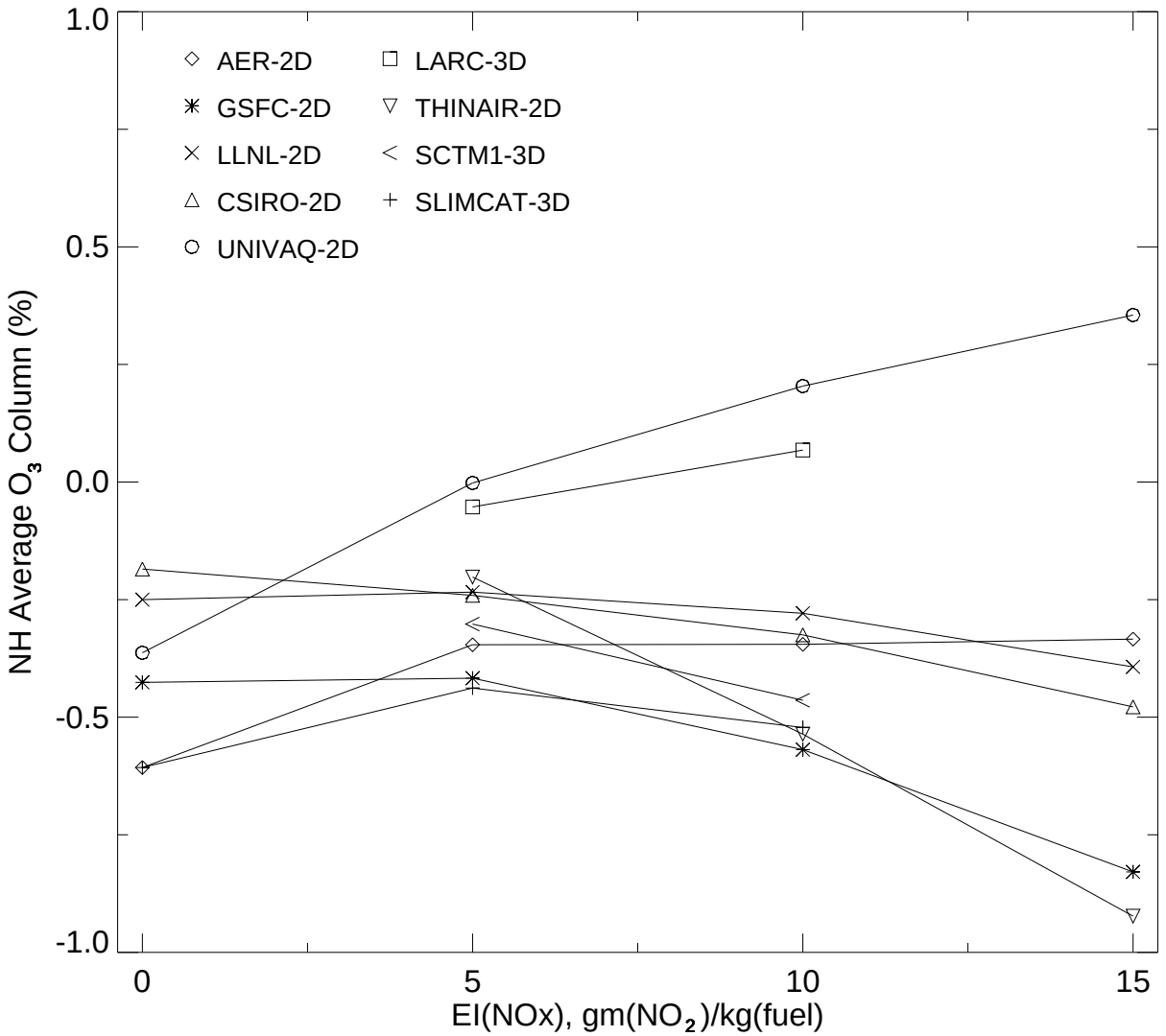

Figure 4.92: Northern hemisphere annual average total O_3 column change (percent) as a function of EI(NO_x) for an HSCT fleet of 500 aircraft operating in 2015 with SA0 sulfate surface area density.

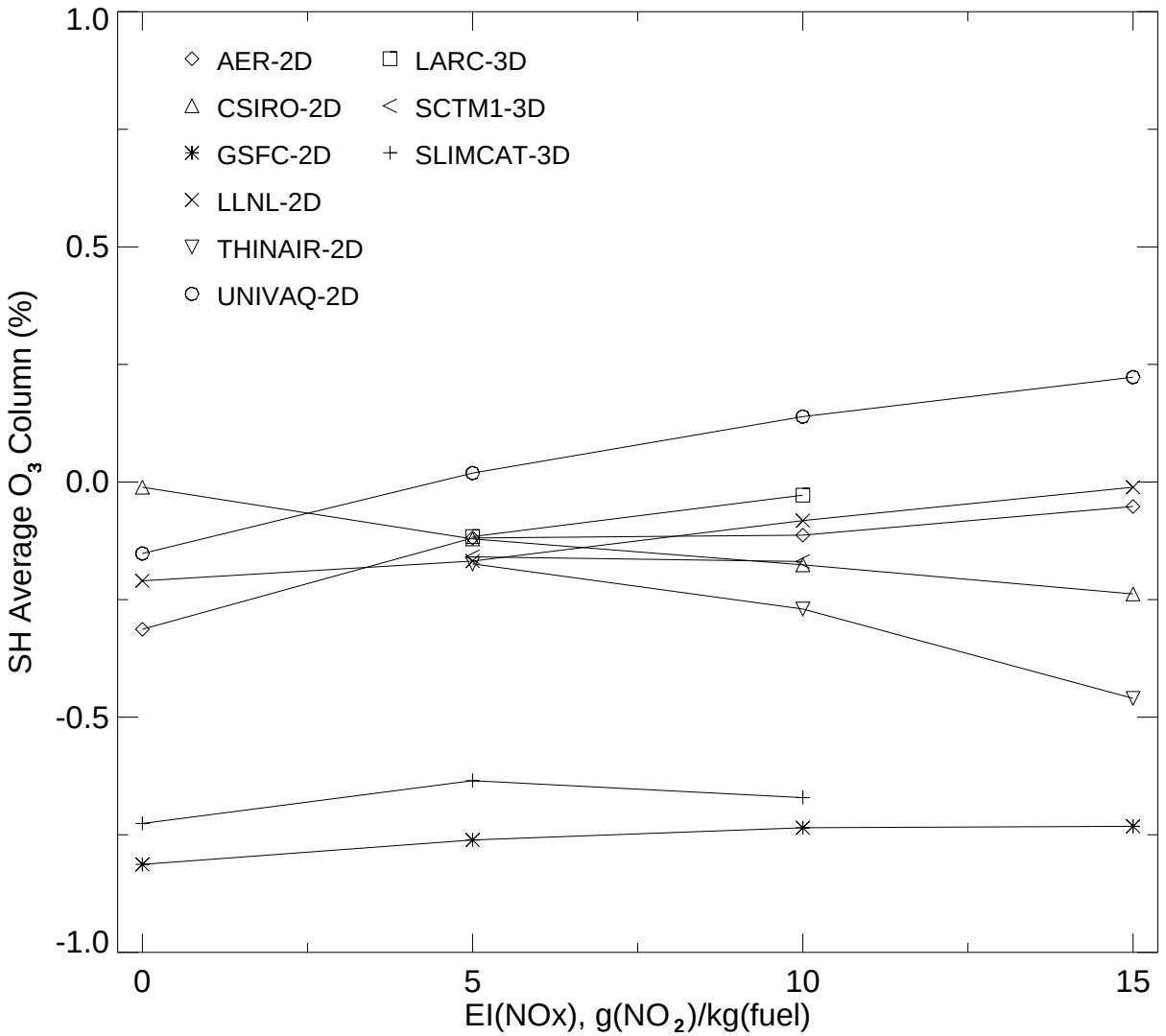

Figure 4.93: Southern hemisphere annual average total O_3 column change (percent) as a function of EI(NO_x) for an HSCT fleet of 500 aircraft operating in 2015 with SA0 sulfate surface area density.

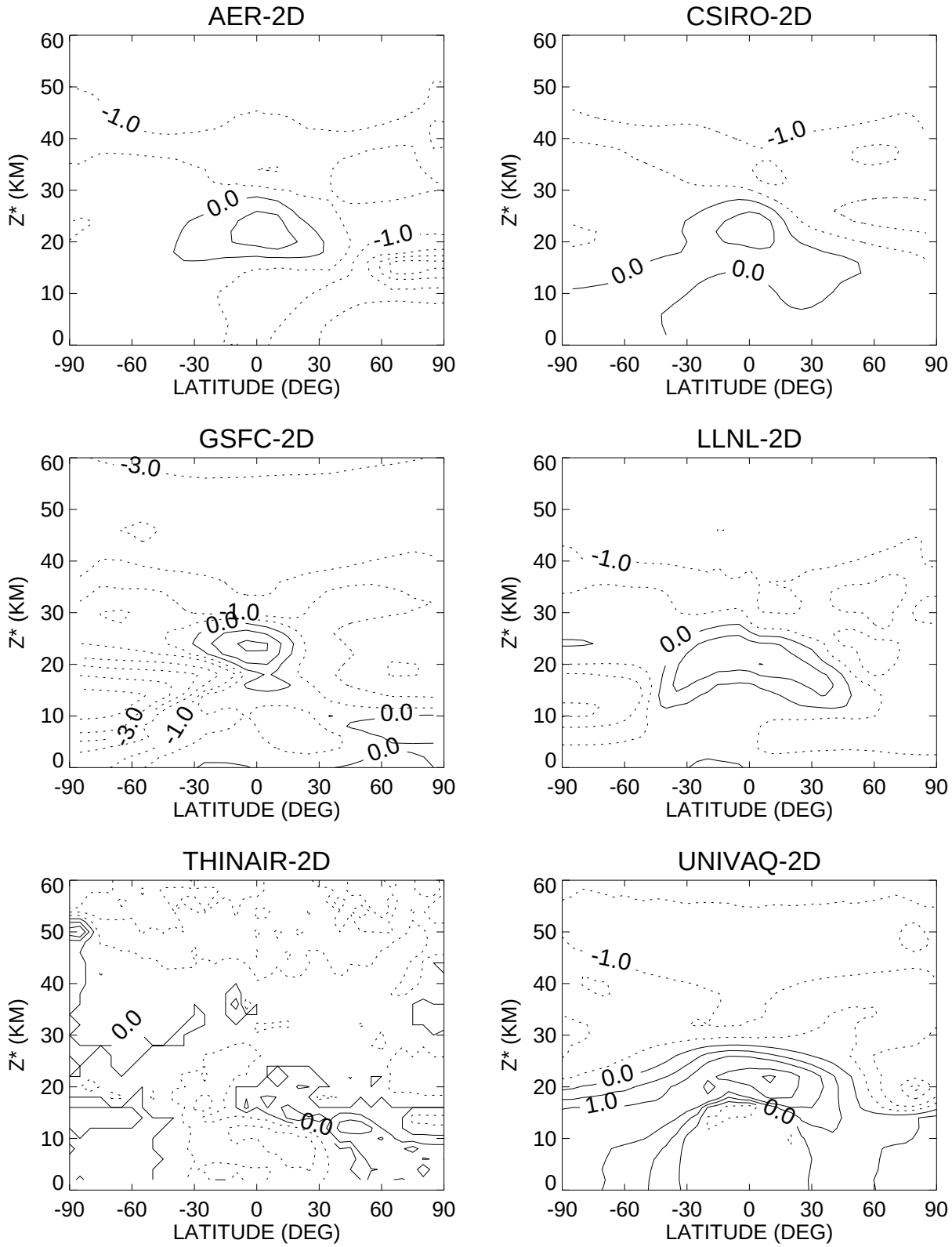

Figure 4.94: Calculated perturbations to O_3 (percent) as a function of latitude and altitude in March of 2015 due to emissions from a fleet of 1000 HSCT aircraft with EI(NO_x)=5 under Scenario S1i relative to Scenario D. Contours are -5, -4, -3, -2, -1, -0.5, 0, 0.5, 1, 2, 3.

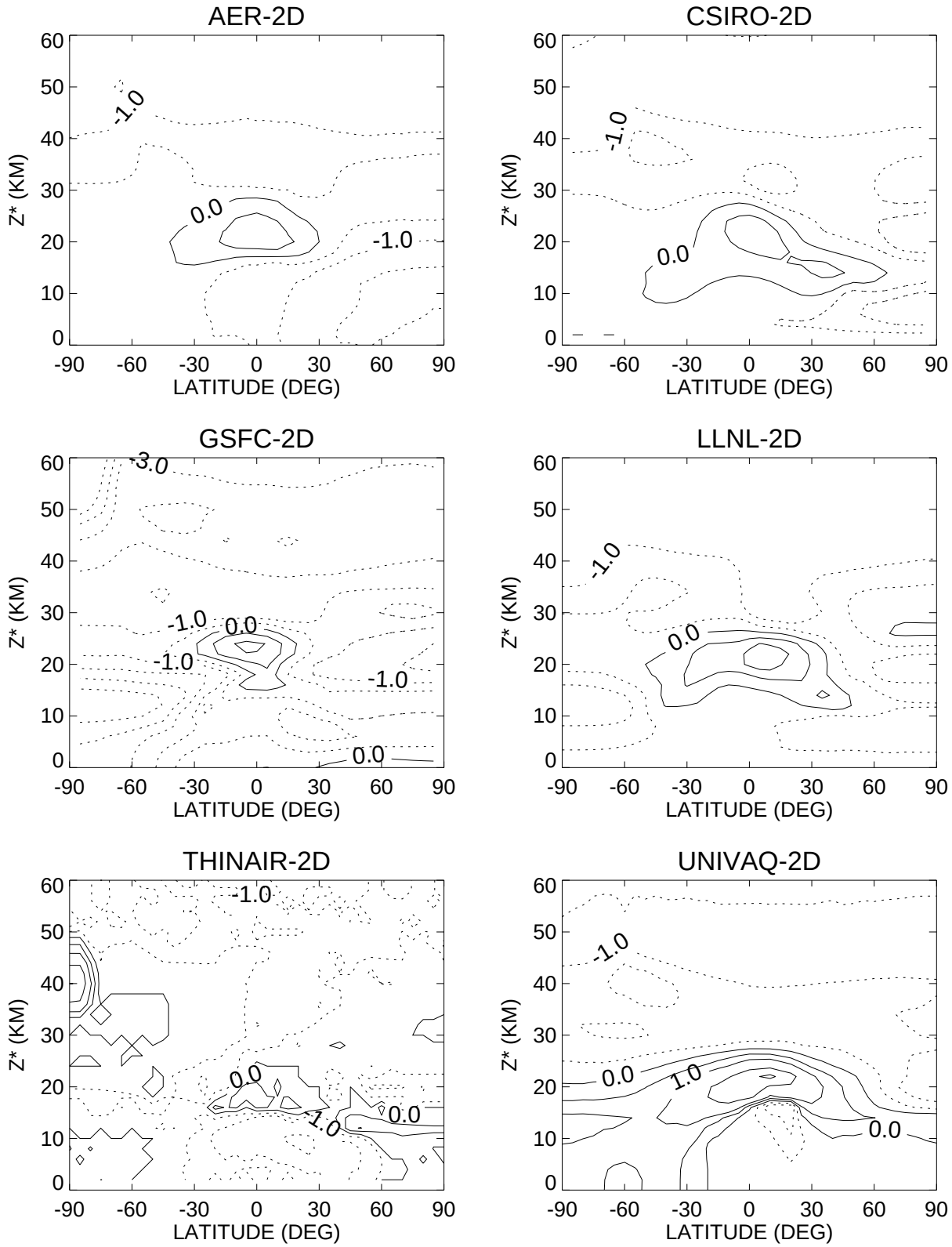

Figure 4.95: Calculated perturbations to O_3 (percent) as a function of latitude and altitude in June of 2015 due to emissions from a fleet of 1000 HSCT aircraft with EI(NO_x)=5 under Scenario S1i relative to Scenario D. Contours are -4, -3, -2, -1, -0.5, 0, 0.5, 1, 2, 3.

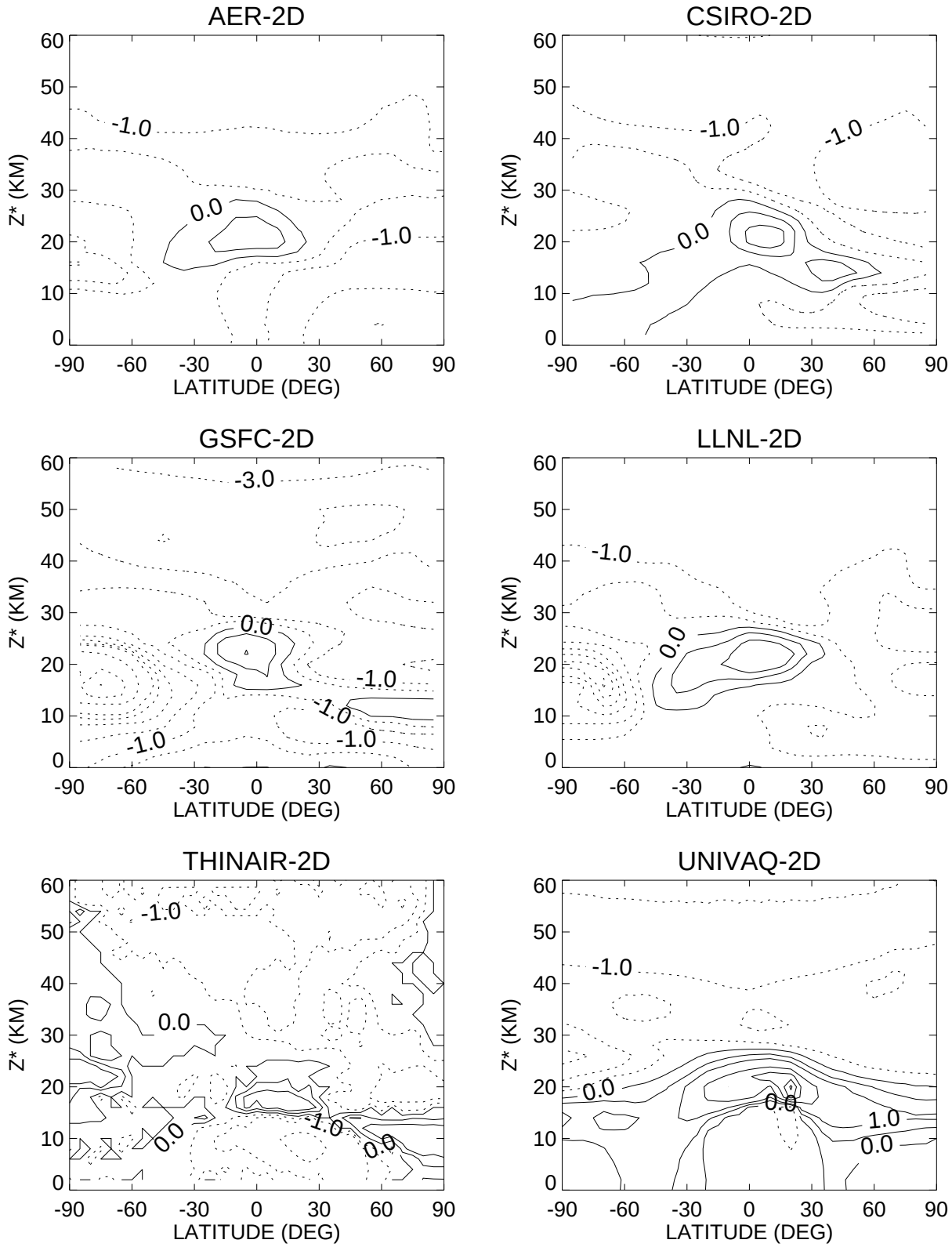

Figure 4.96: Calculated perturbations to O_3 (percent) as a function of latitude and altitude in October of 2015 due to emissions from a fleet of 1000 HSCT aircraft with EI(NO_x)=5 under Scenario S1i relative to Scenario D. Contours are -20, -15, -10, -5, -4, -3, -2, -1, -0.5, 0, 0.5, 1, 2, 3, 4, 5.

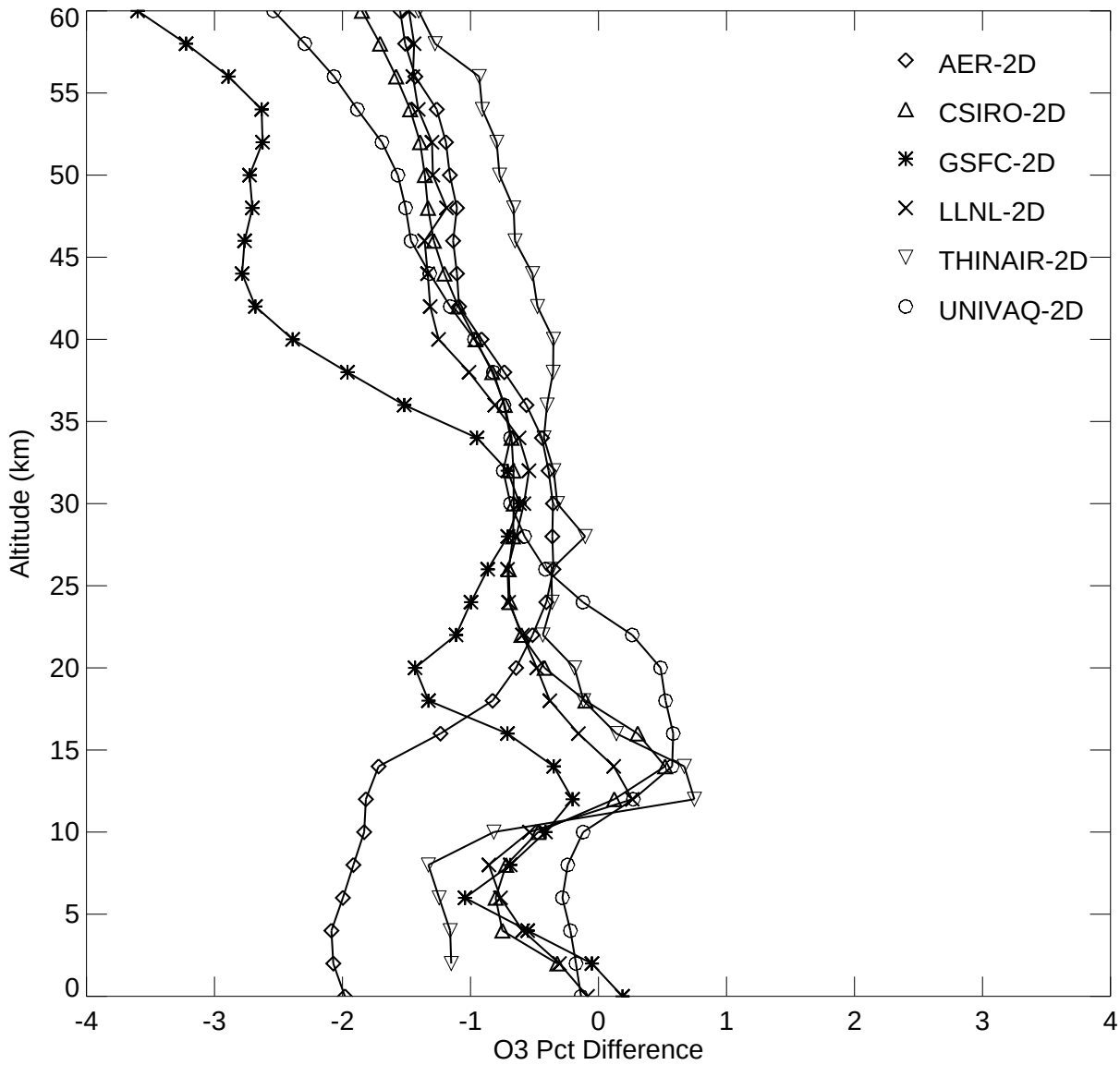

Figure 4.97: Calculated perturbations to O_3 (percent) as a function of altitude at 45°N in June of 2015 due to emissions from a fleet of 1000 HSCT aircraft with EI(NO_x)=5 under Scenario S1i relative to Scenario D.

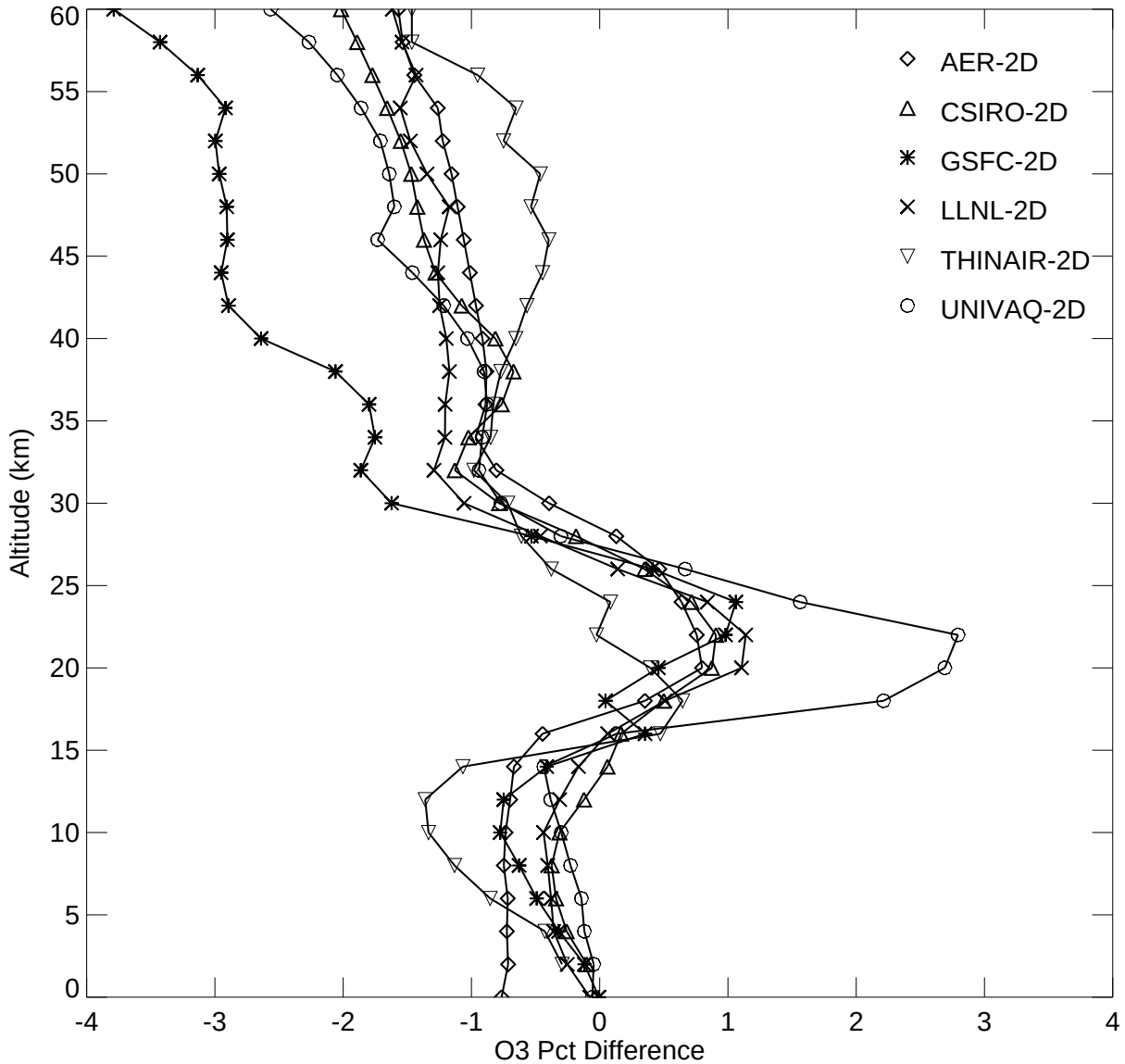

Figure 4.98: Calculated perturbations to O_3 (percent) as a function of altitude at the equator in June of 2015 due to emissions from a fleet of 1000 HSCT aircraft with EI(NO_x)=5 under Scenario S1i relative to Scenario D.

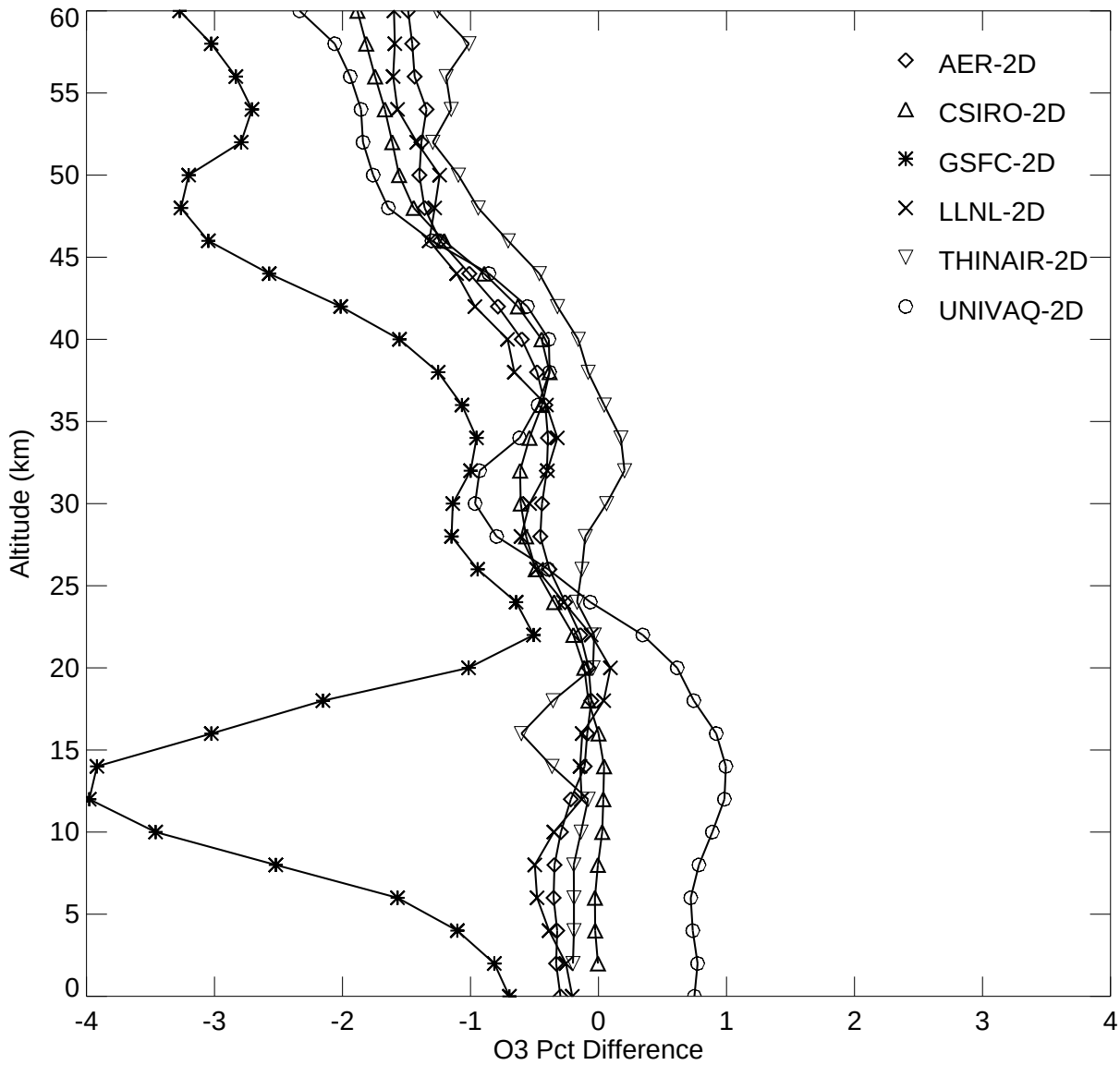

Figure 4.99: Calculated perturbations to O_3 (percent) as a function of altitude at 45^oS in June of 2015 due to emissions from a fleet of 1000 HSCT aircraft with EI(NO_x)=5 under Scenario S1i relative to Scenario D.

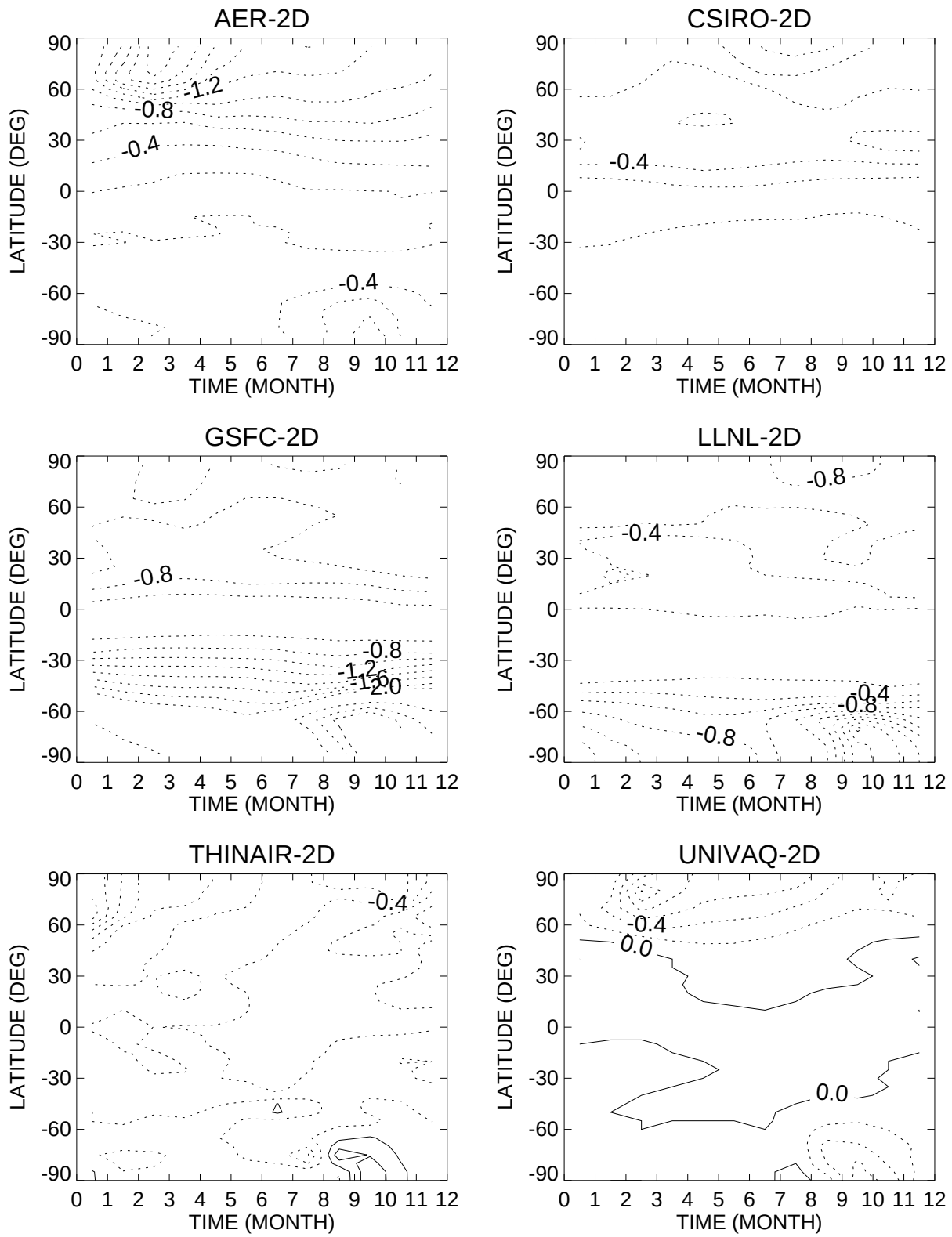

Figure 4.100: Calculated perturbations to column O_3 (percent) as a function of latitude and season in 2015 due to emissions from a fleet of 1000 HSCT aircraft with EI(NO_x)=5 under Scenario S1i relative to Scenario D. Contours are -5, -4, -3, and -2.0 to 0.2 by 0.2.

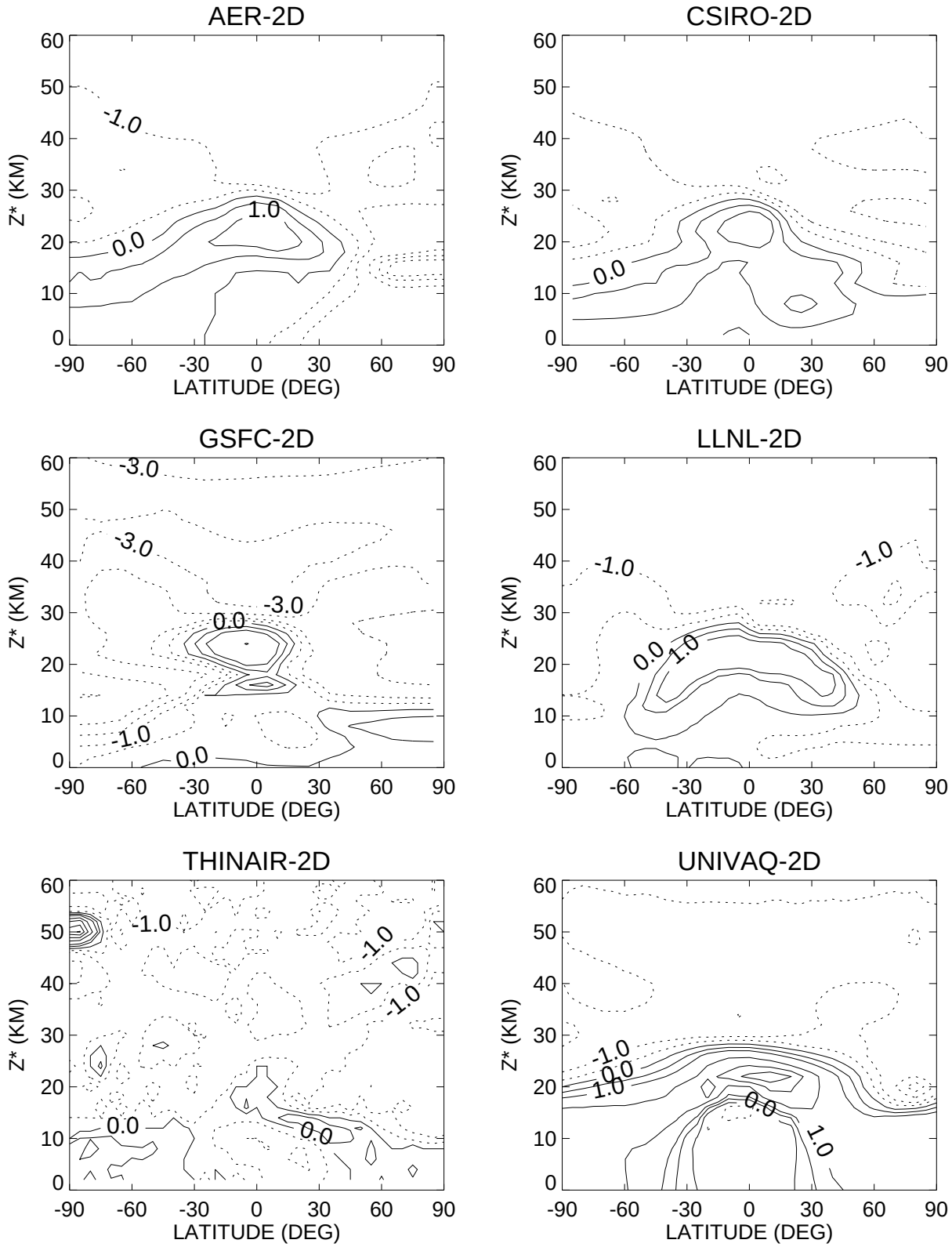

Figure 4.101: Calculated perturbations to O_3 (percent) as a function of latitude and altitude in March of 2015 due to emissions from a fleet of 1000 HSCT aircraft with EI(NO_x)=10 under Scenario S1j relative to Scenario D. Contours are -4, -3, -2, -1, -0.5, 0, 0.5, 1, 2, 3, 4.

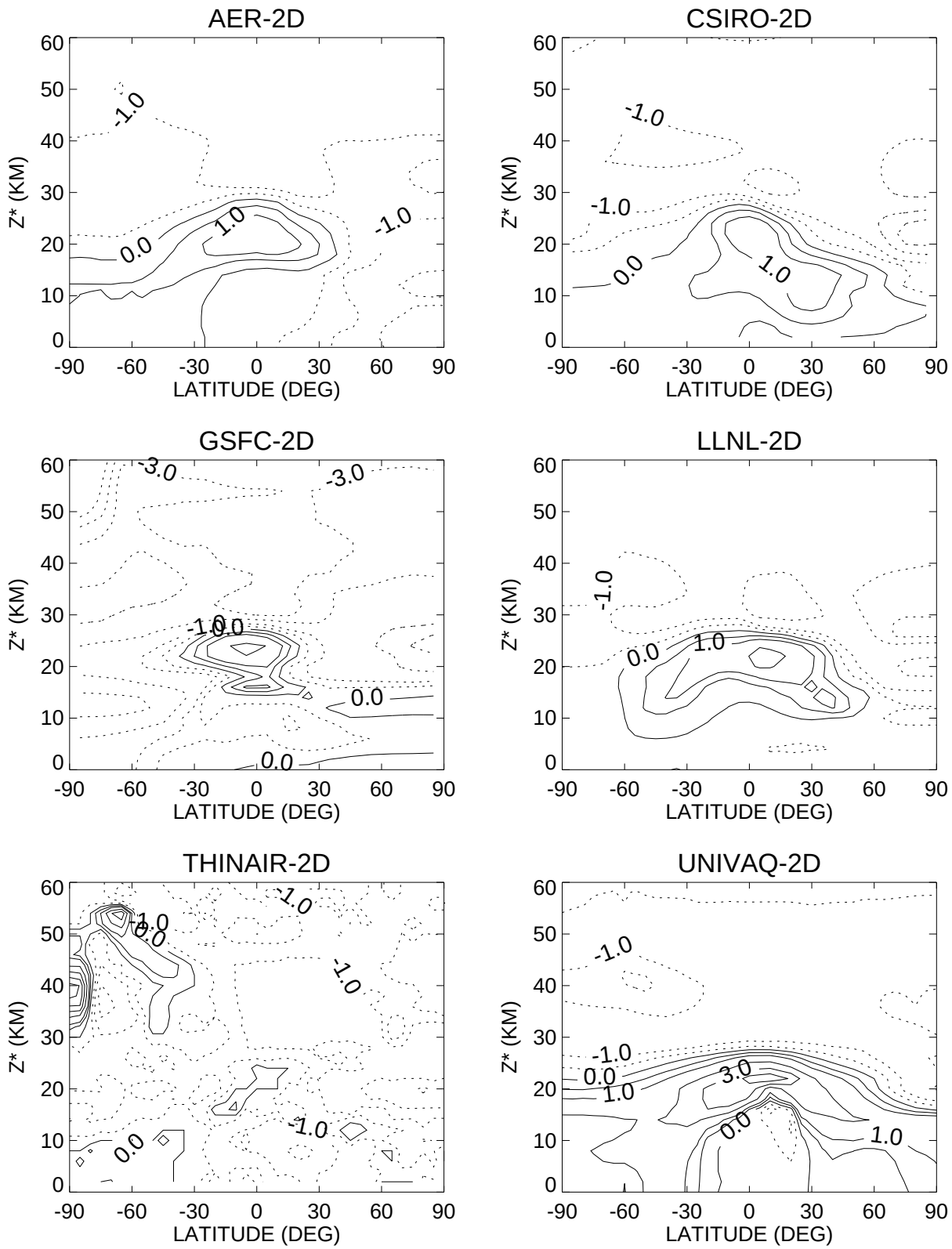

Figure 4.102: Calculated perturbations to O_3 (percent) as a function of latitude and altitude in June of 2015 due to emissions from a fleet of 1000 HSCT aircraft with EI(NO_x)=10 under Scenario S1j relative to Scenario D. Contours are -3, -2, -1, -0.5, 0, 0.5, 1, 2, 3, 4, 5.

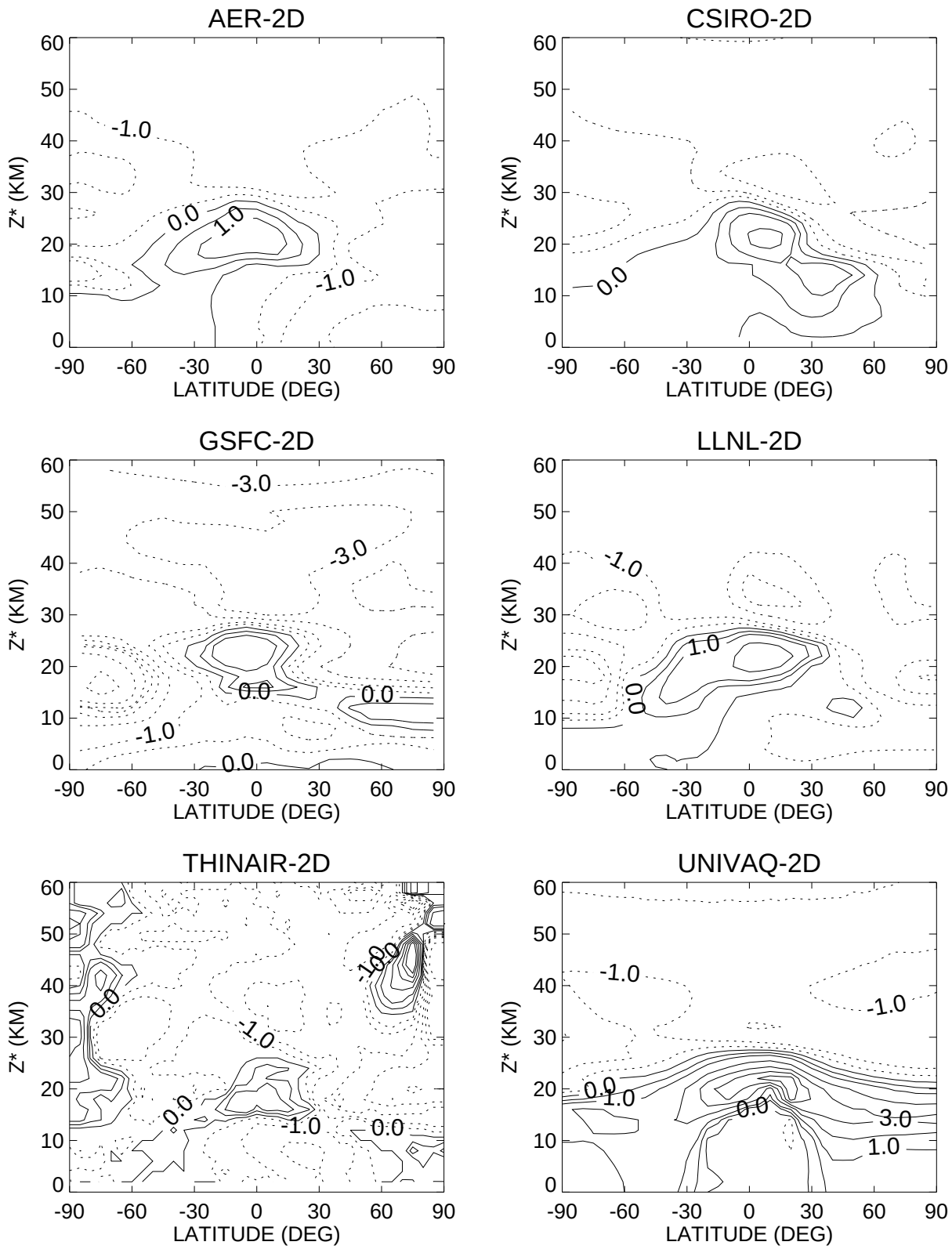

Figure 4.103: Calculated perturbations to O_3 (percent) as a function of latitude and altitude in October of 2015 due to emissions from a fleet of 1000 HSCT aircraft with EI(NO_x)=10 under Scenario S1j relative to Scenario D. Contours are -15, -10, -5, -4, -3, -2, -1, -0.5, 0, 0.5, 1, 2, 3, 4.

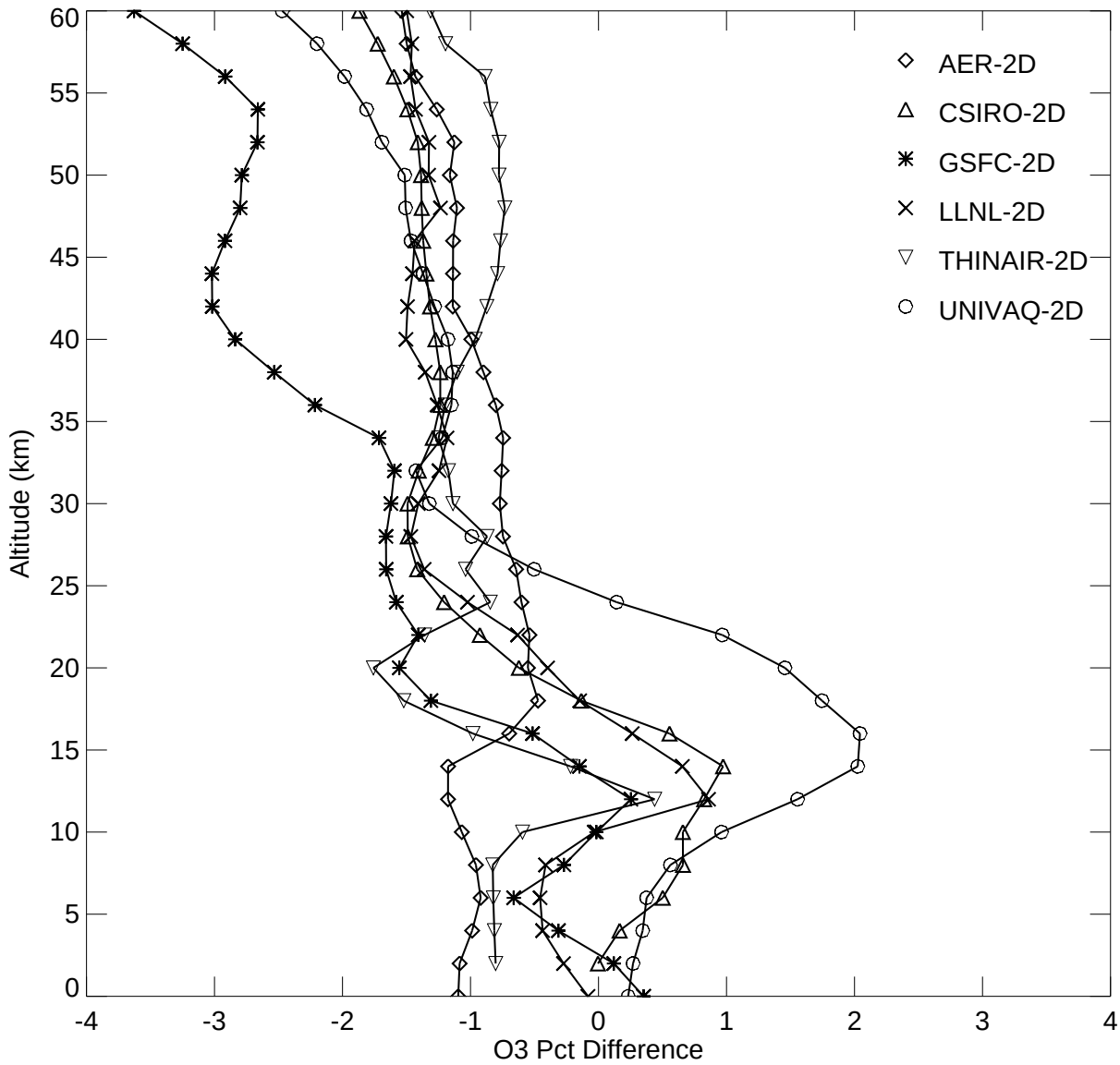

Figure 4.104: Calculated perturbations to O_3 (percent) as a function of altitude at 45^oN in June of 2015 due to emissions from a fleet of 1000 HSCT aircraft with EI(NO_x)=10 under Scenario S1j relative to Scenario D.

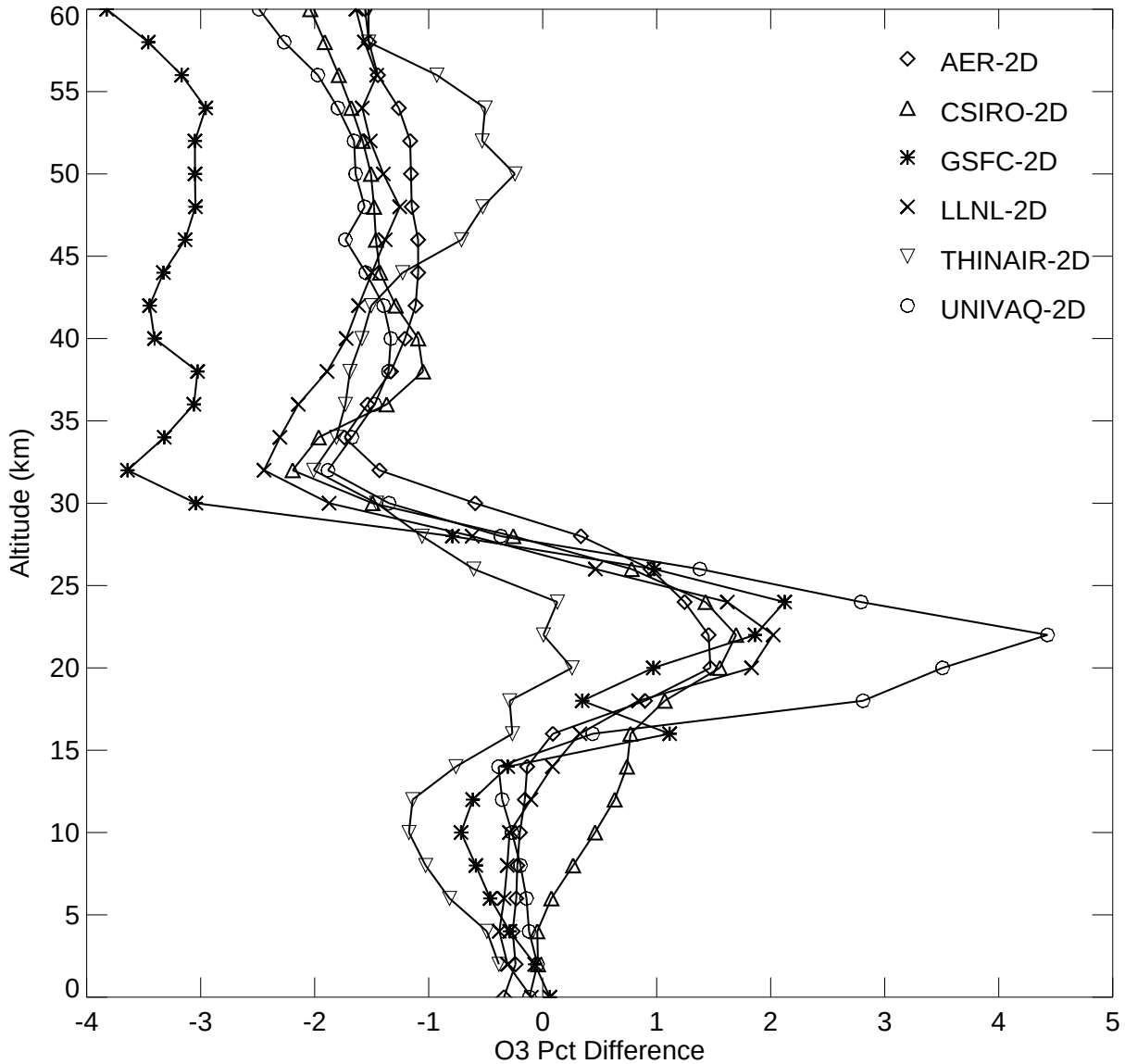

Figure 4.105: Calculated perturbations to O_3 (percent) as a function of altitude at the equator in June of 2015 due to emissions from a fleet of 1000 HSCT aircraft with EI(NO_x)=10 under Scenario S1j relative to Scenario D.

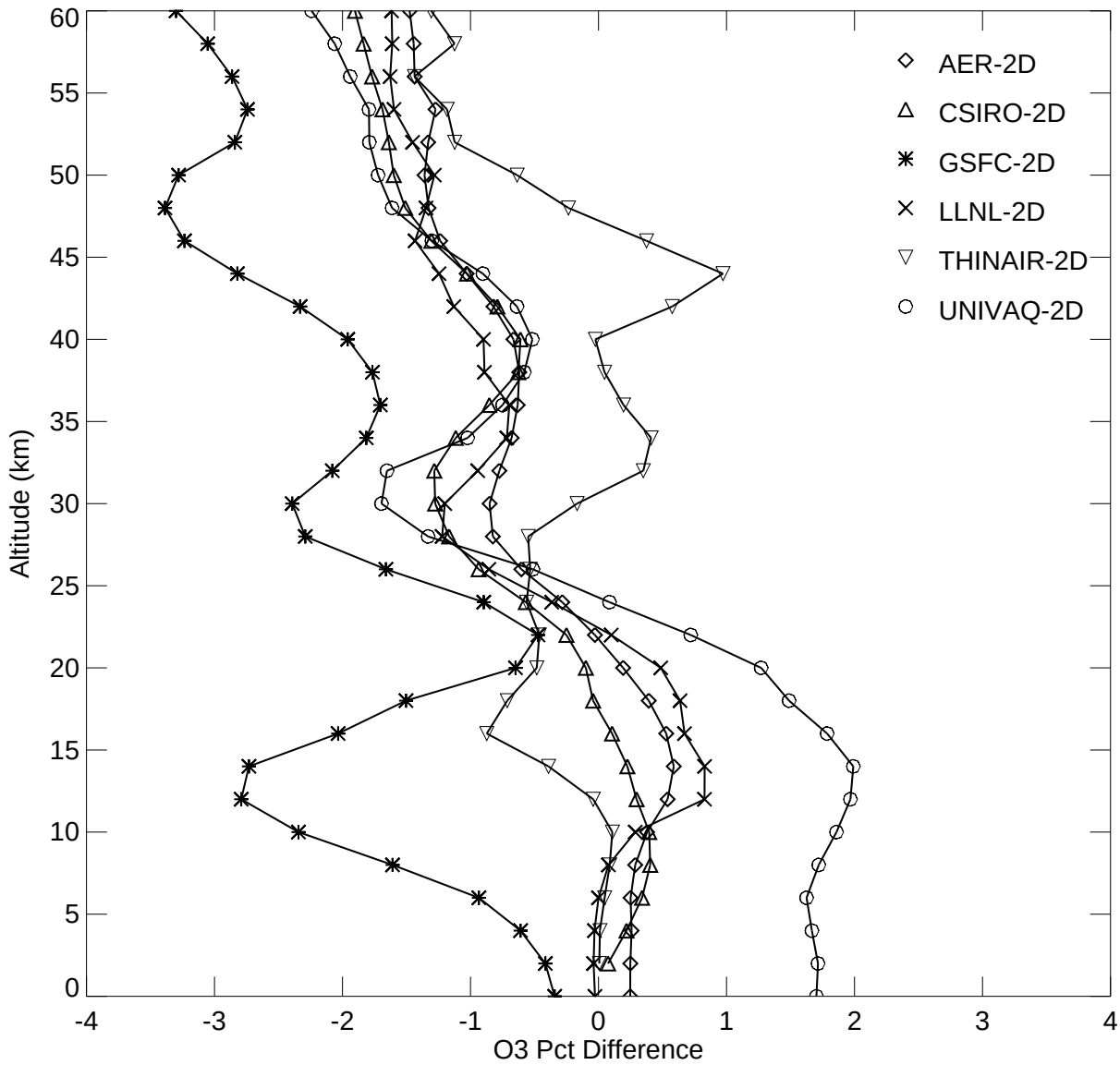

Figure 4.106: Calculated perturbations to O_3 (percent) as a function of altitude at 45°S in June of 2015 due to emissions from a fleet of 1000 HSCT aircraft with EI(NO_x)=10 under Scenario S1j relative to Scenario D.

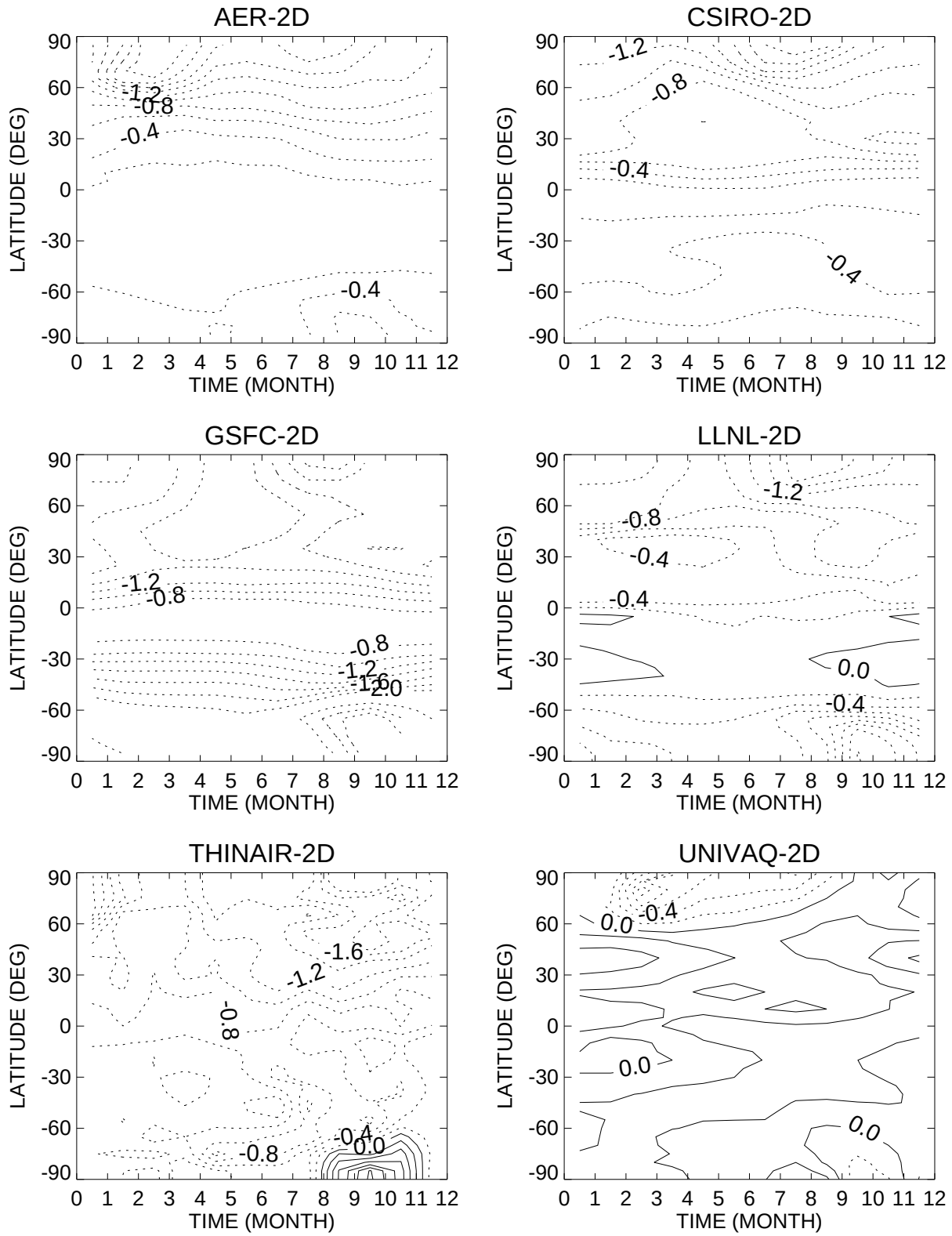

Figure 4.107: Calculated perturbations to column O_3 (percent) as a function of latitude and season in 2015 due to emissions from a fleet of 1000 HSCT aircraft with EI(NO_x)=10 under Scenario S1j relative to Scenario D. Contours are -5, -4, -3, and -2.0 to 1.0 by 0.2.

4.3.2 Scenarios with Sulfur Emissions (S1f-h,k,l)

Scenarios S1f, S1g, S1h, S1k, and S1l include emission of sulfur from a fleet of 500 HSCT aircraft, along with H_2O and NO_x emissions, in 2015. The sulfur emission scenarios are described in Section 2.3. They all assume an EI(SO_2) of 0.4 gm/(kg fuel) and that the new particles created in the plume reach a uniform radius of 10 nm when plume processing is complete. The fraction of sulfur emissions converted to particles within the plume is varied from 0% to 100%, with 10% taken as the most likely scenario and 50% a likely upper limit to the uncertainty. Aerosol surface area densities are specified as scenario input, based on calculations from the AER 2-D microphysical model. Table 2.3 describes the SAD designations used in these scenarios. Figures 2.12-2.16 show the SAD perturbations as a function of latitude and altitude for each of the scenarios. Aerosol surface area density for the subsonic-only background case (Scenario D) is SA0.

Scenario S1f uses the SA1 surface area density, which assumes 50% particle conversion, and EI(NO_x)=5. Changes in ozone relative to Scenario D for March, June, and October are shown in Figures 4.108, 4.109, and 4.110 as a function of latitude and altitude. Relative to Scenario S1c without sulfur emissions, ozone depletion is enhanced in all models below 25 km at middle and high latitudes. The AER and LLNL models show a region of ozone increase at near 25-30 km at high latitudes in October which were not present in Scenario S1c. The effect of added aerosol particles is to suppress NO_x and enhance HO_x, ClO_x, and BrO_x. The suppression of NO_x accounts for the ozone increase at 25 km in the AER and LLNL models, where the NO_x cycle represents a dominant removal cycle for ozone. Increases in HO_x, ClO_x, and BrO_x account for the additional ozone depletion below 25 km, where the HO_x cycle dominates ozone loss.

Figures 4.111, 4.112, and 4.113 show changes in ozone profile at 45^oN, the equator, and 45^oS for June. Local ozone depletions at 45^oN in June are as much as 3.5% for the AER and GSFC models for Scenario S1f, though they were below 1.5% for Scenario S1c. Changes at 45^oS are less dramatic. Changes in total ozone for Scenario S1f relative to Scenario D are shown in Figure 4.114. These column depletions are significantly larger than those for Scenario S1c without sulfur emissions. The UNIVAQ and LARC models, which showed mostly positive ozone change for Scenario S1c, show mostly negative ozone changes for Scenario S1f. The AER and GSFC models calculated northern hemisphere average ozone depletion of 1.0% and 1.1%, respectively, for this scenario.

Scenario S1g also uses SA1 aerosol surface area density, but with EI(NO_x)=10. Ozone change as a function of latitude and altitude for this scenario is shown in Figures 4.115-4.117. Ozone depletion below 25 km is somewhat reduced from Scenario S1f. Ozone depletion in the 25-30 km region is somewhat increased. Figures 4.118-4.120 show vertical profiles of ozone change for this scenario in June at 45^oN, the equator, and 45^oS. Changes in ozone column for Scenario S1g relative to Scenario D are shown in Figure 4.121. The AER and UNIVAQ models show less ozone depletion in the northern hemisphere with EI(NO_x)=10 than with EI(NO_x)=5 using SA1 surface area. The THINAIR model shows more ozone depletion with EI(NO_x)=10, and the GSFC, CSIRO, and LLNL models show little change with EI(NO_x).

The SA3 surface area distribution, representing 100% gas-to-particle conversion in the aircraft plume, is used in Scenario S1h, along with EI(NO_x)=5. Changes in ozone as a function of latitude and altitude for March, June, and October are shown in Figures 4.122, 4.123, and 4.124. The ozone depletion below 25 km is greater than that from Scenario S1f. Vertical profiles of ozone change are shown in Figures 4.125, 4.126, and 4.127 for 45^oN, the equator, and 45^oS, respectively, for this scenario. Ozone column changes, shown in Figure 4.128, are somewhat larger than for Scenario S1f for most models, though the CSIRO model shows little change.

An SO_2 gas-to-particle conversion ratio of 10% (SA5) is used in Scenario S1k, along with EI(NO_x)=5. Changes in ozone column for Scenario S1k relative to Scenario D are shown in Figures 4.129, 4.130, and 4.131 for March, June, and October. Vertical profiles of ozone change are shown in Figures 4.132, 4.133, and 4.134 for 45^oN, the equator, and 45^oS. Ozone depletion falls between that of Scenario S1c and Scenario S1f. Changes in total ozone are shown in Figure 4.135 as a function of latitude and season. Even for the SO_2 gas-to-particle conversion rate of 10%, ozone depletion is substantially increased over the case with no sulfur emissions (S1c). For the AER, LLNL, and CSIRO models, northern hemisphere average ozone depletion for Scenario S1k is double that for Scenario S1c.

A scenario with no SO_2 gas-to-particle conversion, ie. with all sulfur emitted as $SO2_2$ gas, was run by the AER model. Ozone changes for this scenario, designated S1l, are shown in Figures 4.136, 4.137, and 4.138 relative to Scenario D. Column ozone changes are shown in Figure 4.139. The average northern hemisphere

ozone depletion is -0.6% and the average southern hemisphere ozone depletion of -0.3%. This shows that sulfur emissions may have a significant though reduced effect on ozone depletion from HSCT aircraft even if there is no gas-to-particle conversion in the plume.

The sensitivity of northern hemisphere ozone change to aircraft sulfur emissions is depicted graphically in Figure 4.140. The abscissa show percentage increase in SAD in the 14-21 km, 33-90^{o}N region due to HSCT emissions of sulfur relative to an SA0 background. Scenario S1c is used for the 0% change in SAD. Scenario S1l, with no gas-to-particle conversion, corresponds to a 27% increase in SAD. Scenario S1k, with 10% gas to particle conversion, corresponds to a 38% increase in SAD. Scenarios S1f and S1h, with 50% and 100% gas to particle conversion, correspond to 82% and 111% increases in SAD, respectively. All models show increased ozone depletion for increased SAD perturbations. The slopes are also fairly consistent among the models.

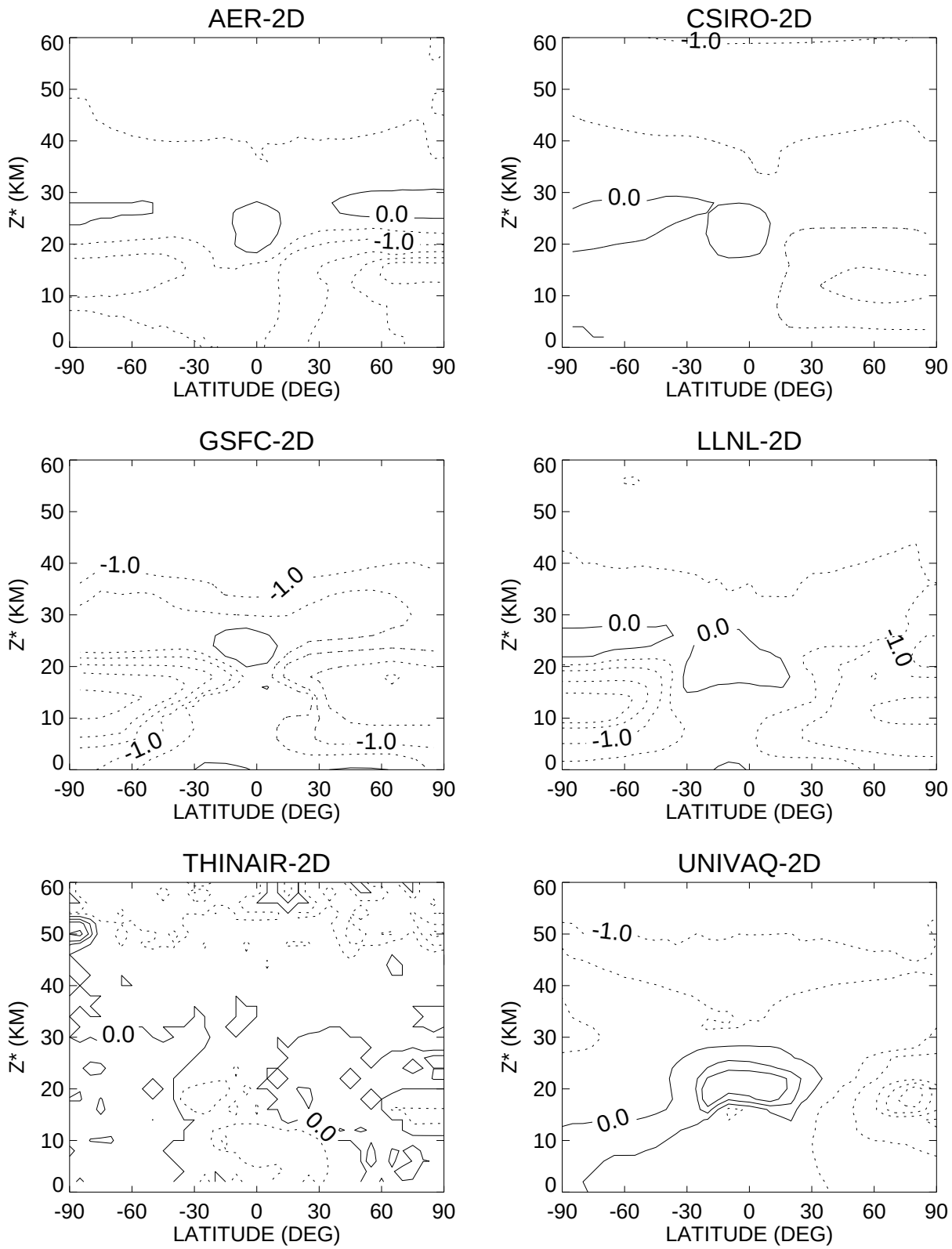

Figure 4.108: Calculated perturbations to O_3 (percent) as a function of latitude and altitude in March of 2015 due to emissions from a fleet of 500 HSCT aircraft with EI(NO_x)=5 and SA1 sulfate surface area under Scenario S1f relative to Scenario D. Contours are -4, -3, -2, -1, -0.5, 0, 0.5, 1.

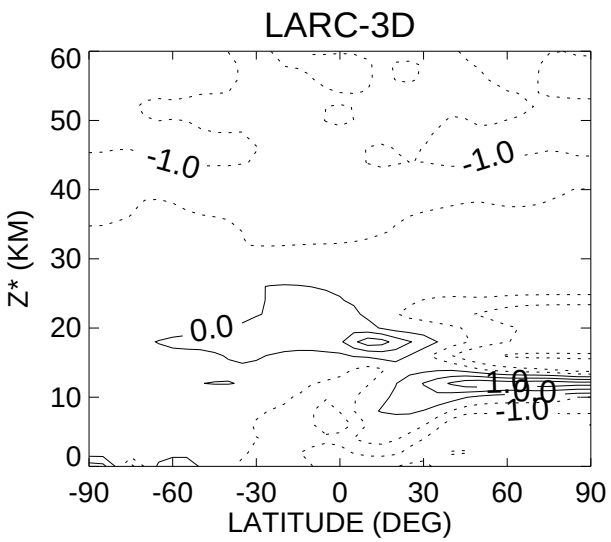

Figure 4.108: continued

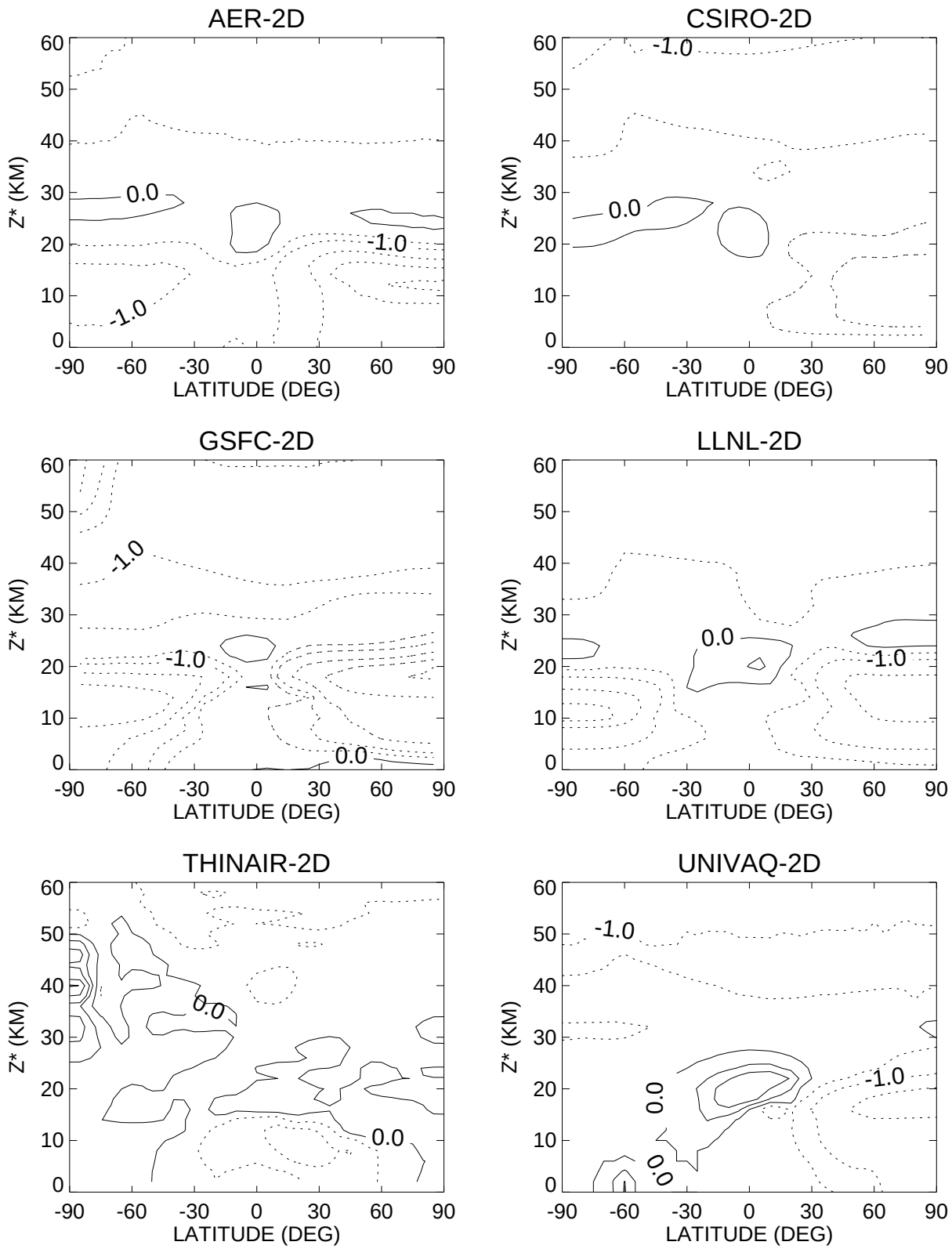

Figure 4.109: Calculated perturbations to O_3 (percent) as a function of latitude and altitude in June of 2015 due to emissions from a fleet of 500 HSCT aircraft with EI(NO_x)=5 and SA1 sulfate surface area under Scenario S1f relative to Scenario D. Contours are -4, -3, -2, -1, -0.5, 0, 0.5, 1.

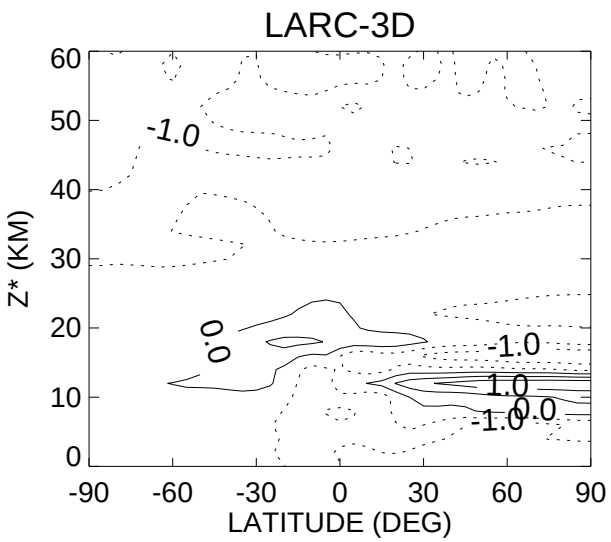

Figure 4.109: continued

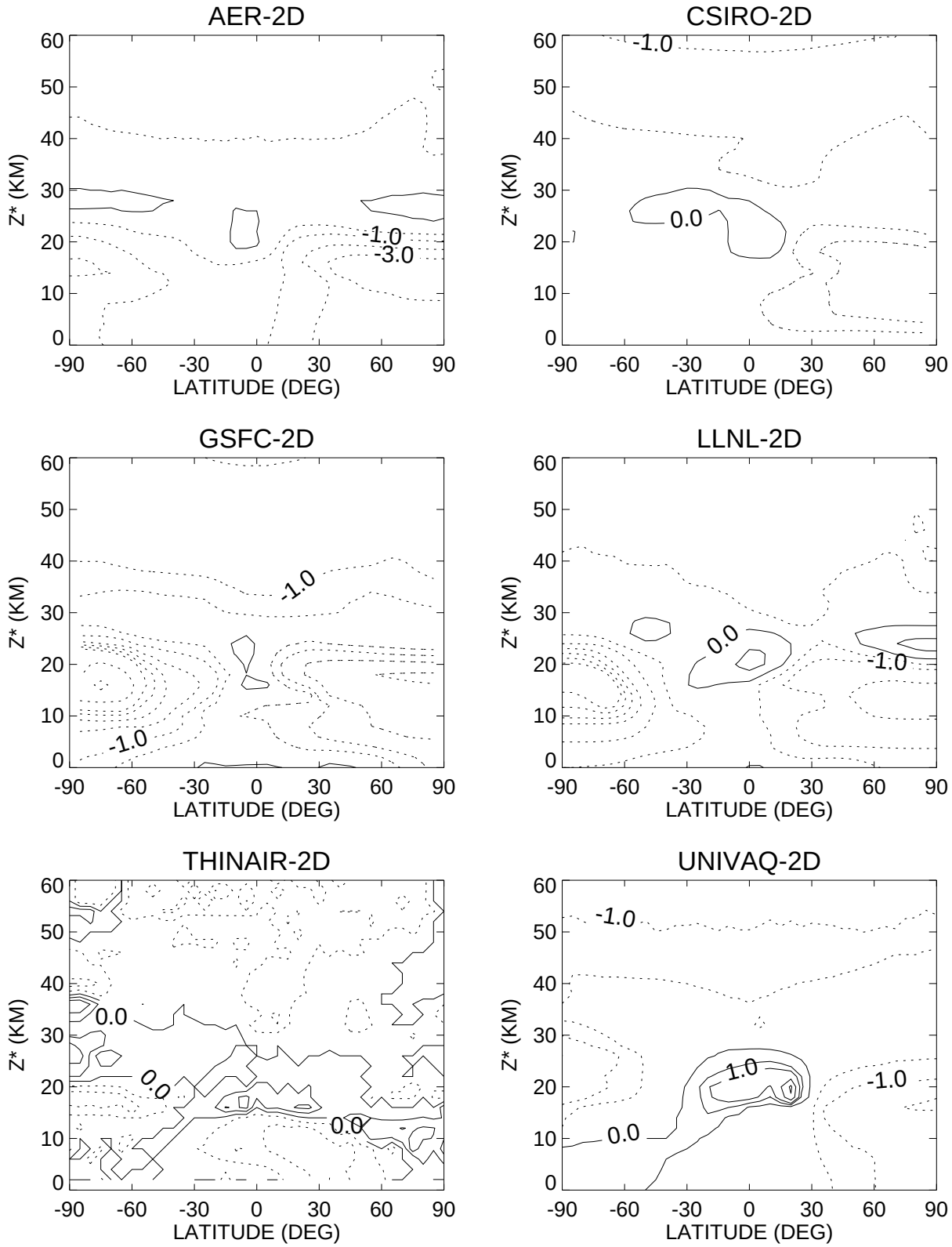

Figure 4.110: Calculated perturbations to O_3 (percent) as a function of latitude and altitude in October of 2015 due to emissions from a fleet of 500 HSCT aircraft with EI(NO_x)=5 and SA1 sulfate surface area under Scenario S1f relative to Scenario D. Contours are -15, -10, -5, -4, -3, -2, -1, -0.5, 0, 0.5, 1, 2, 3.

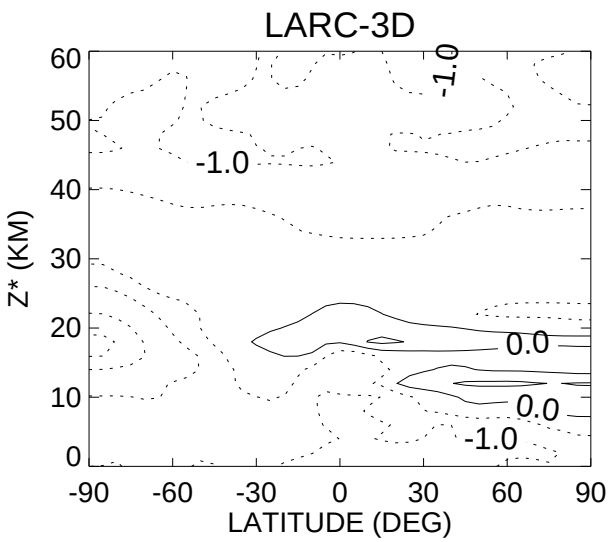

Figure 4.110: continued

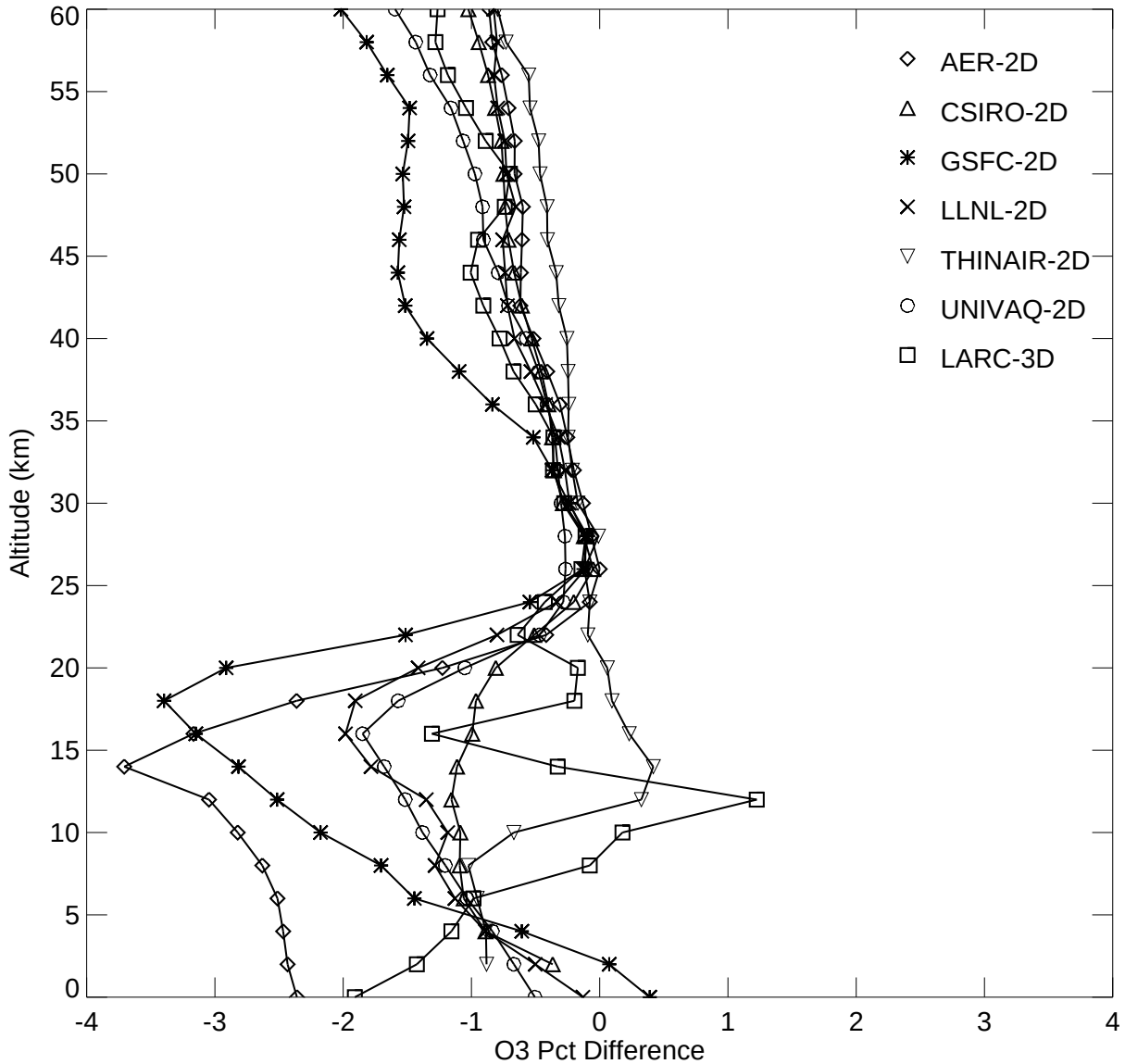

Figure 4.111: Calculated perturbations to O_3 (percent) as a function of altitude at 45^oN in June of 2015 due to emissions from a fleet of 500 HSCT aircraft with EI(NO_x)=5 and SA1 sulfate surface area under Scenario S1f relative to Scenario D.

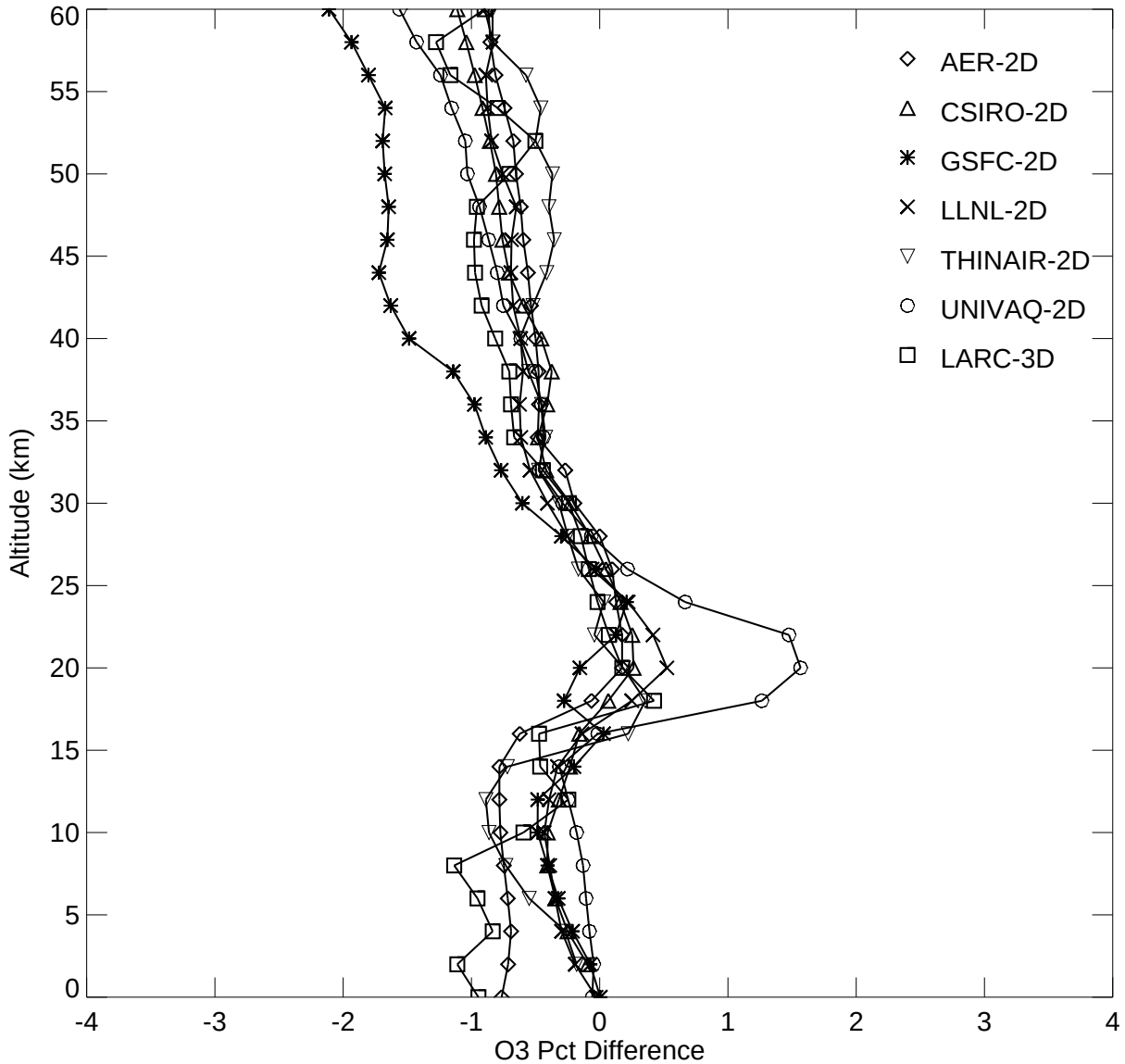

Figure 4.112: Calculated perturbations to O_3 (percent) as a function of altitude at the equator in June of 2015 due to emissions from a fleet of 500 HSCT aircraft with EI(NO_x)=5 and SA1 sulfate surface area under Scenario S1f relative to Scenario D.

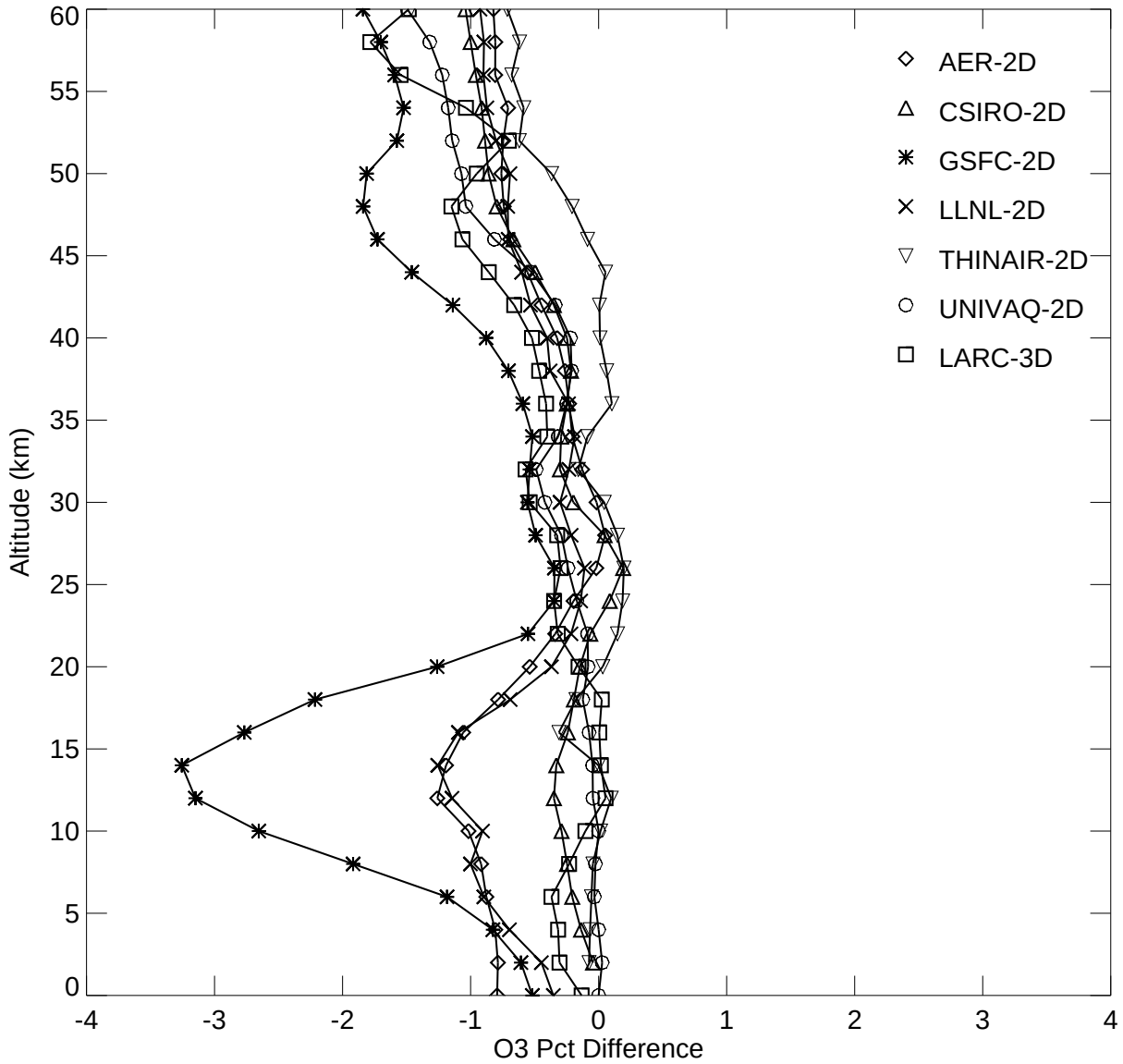

Figure 4.113: Calculated perturbations to O_3 (percent) as a function of altitude at 45°S in June of 2015 due to emissions from a fleet of 500 HSCT aircraft with EI(NO_x)=5 and SA1 sulfate surface area under Scenario S1f relative to Scenario D.

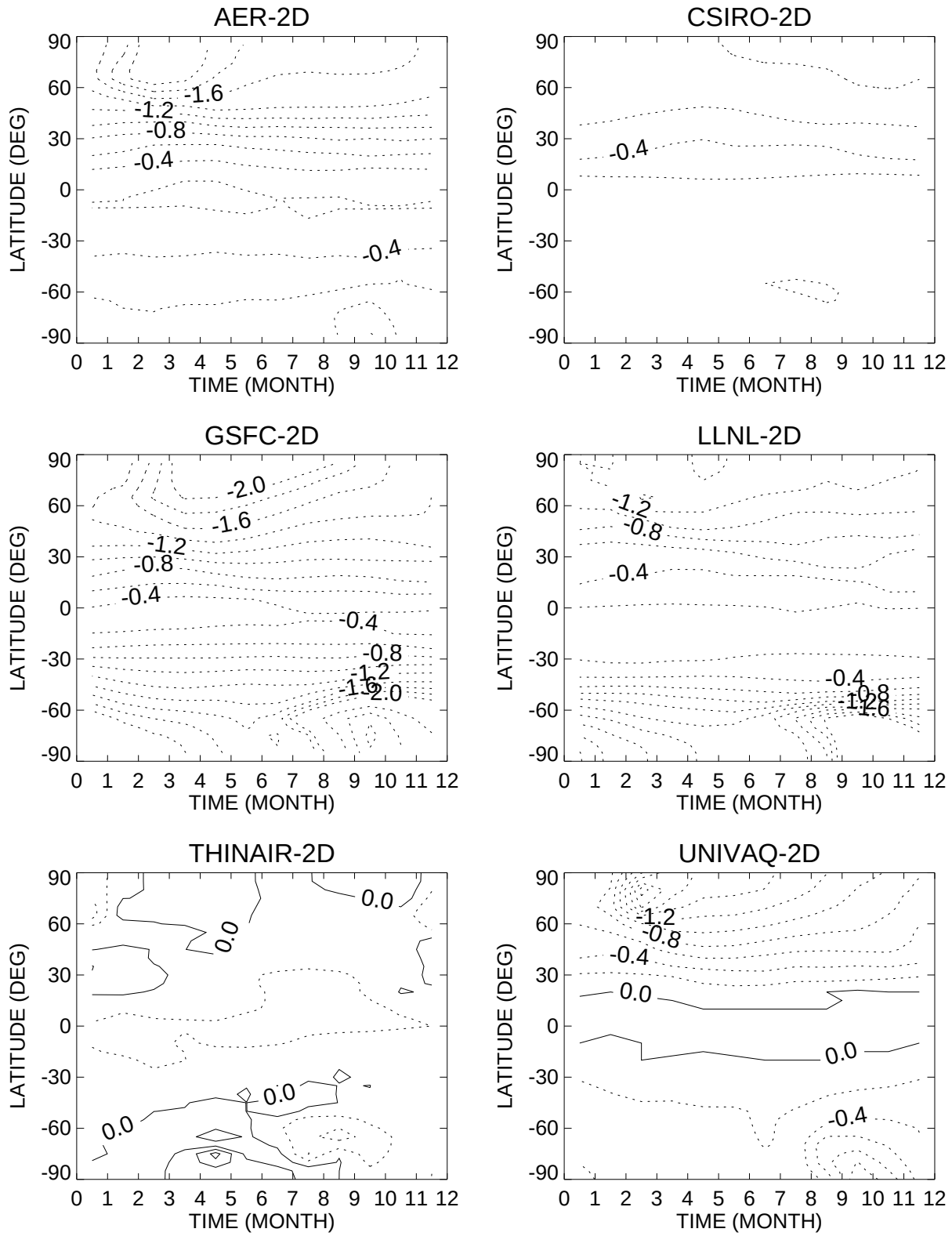

Figure 4.114: Calculated perturbations to column O_3 (percent) as a function of latitude and season in 2015 due to emissions from a fleet of 500 HSCT aircraft with EI(NO_x)=5 and SA1 sulfate surface area under Scenario S1f relative to Scenario D. Contours are -5, -4, -3, and -2.0 to 0.2 by 0.2.

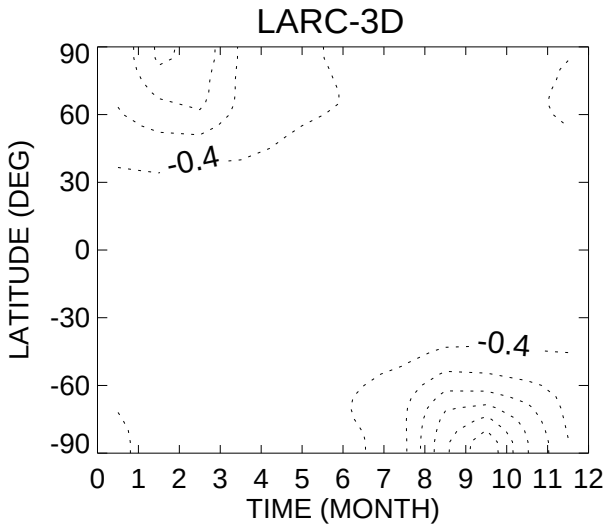

Figure 4.114: continued

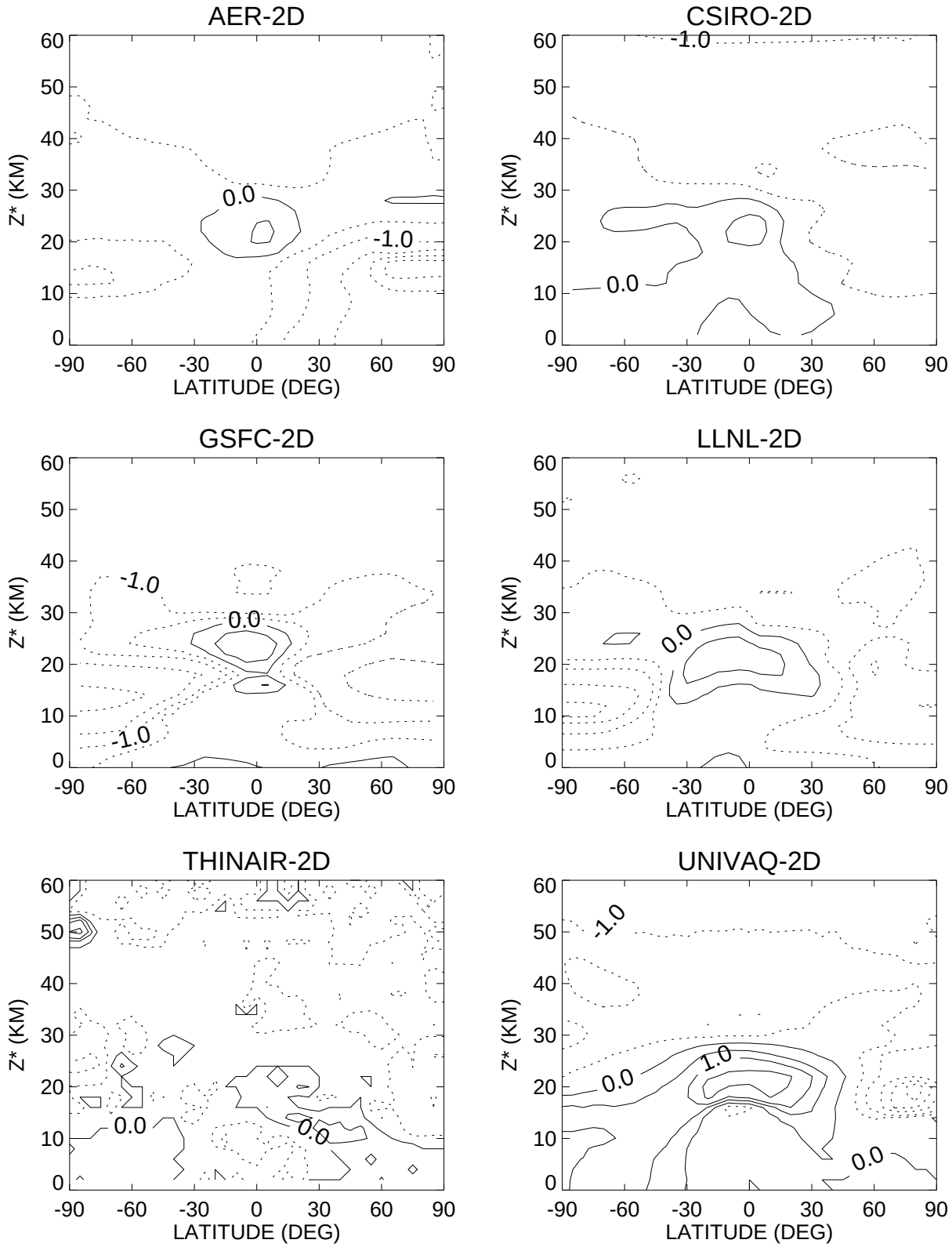

Figure 4.115: Calculated perturbations to O_3 (percent) as a function of latitude and altitude in March of 2015 due to emissions from a fleet of 500 HSCT aircraft with EI(NO_x)=10 and SA1 sulfate surface area under Scenario S1g relative to Scenario D. Contours are -4, -3, -2, -1, -0.5, 0, 0.5, 1, 2.

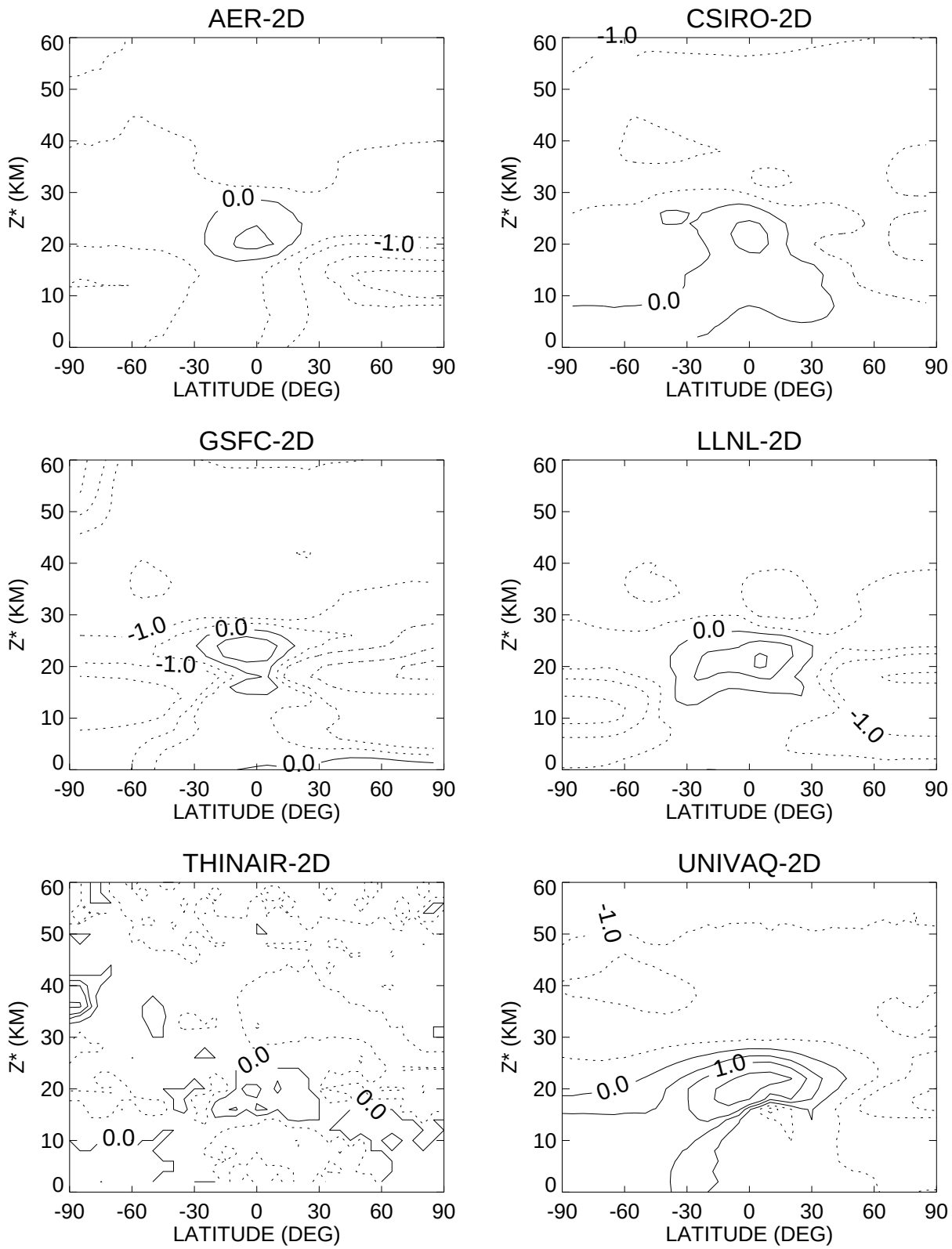

Figure 4.116: Calculated perturbations to O_3 (percent) as a function of latitude and altitude in June of 2015 due to emissions from a fleet of 500 HSCT aircraft with EI(NO_x)=10 and SA1 sulfate surface area under Scenario S1g relative to Scenario D. Contours are -3, -2, -1, -0.5, 0, 0.5, 1, 2.

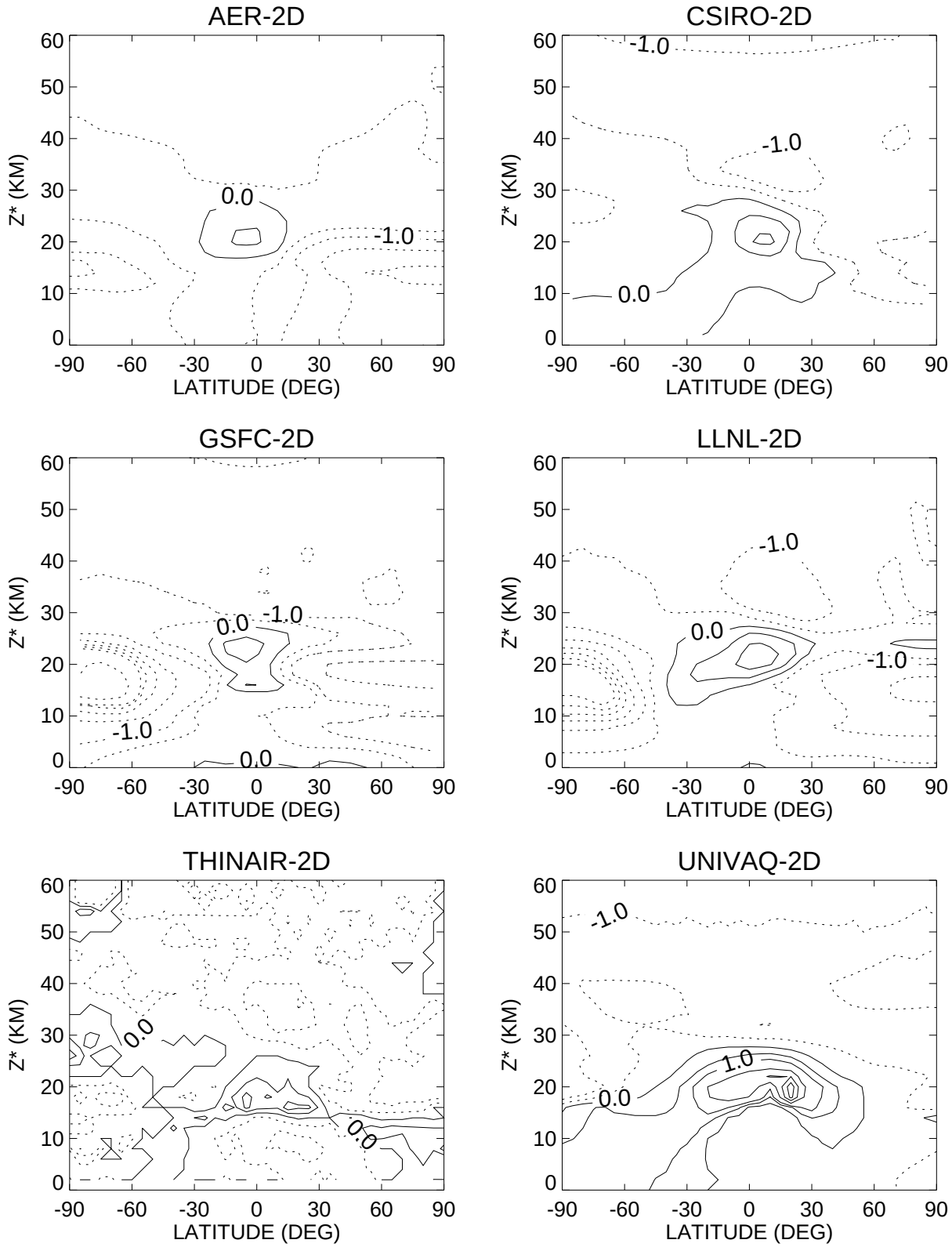

Figure 4.117: Calculated perturbations to O_3 (percent) as a function of latitude and altitude in October of 2015 due to emissions from a fleet of 500 HSCT aircraft with EI(NO_x)=10 and SA1 sulfate surface area under Scenario S1g relative to Scenario D. Contours are -10, -5, -4, -3, -2, -1, -0.5, 0, 0.5, 1, 2, 2, 3, 4.

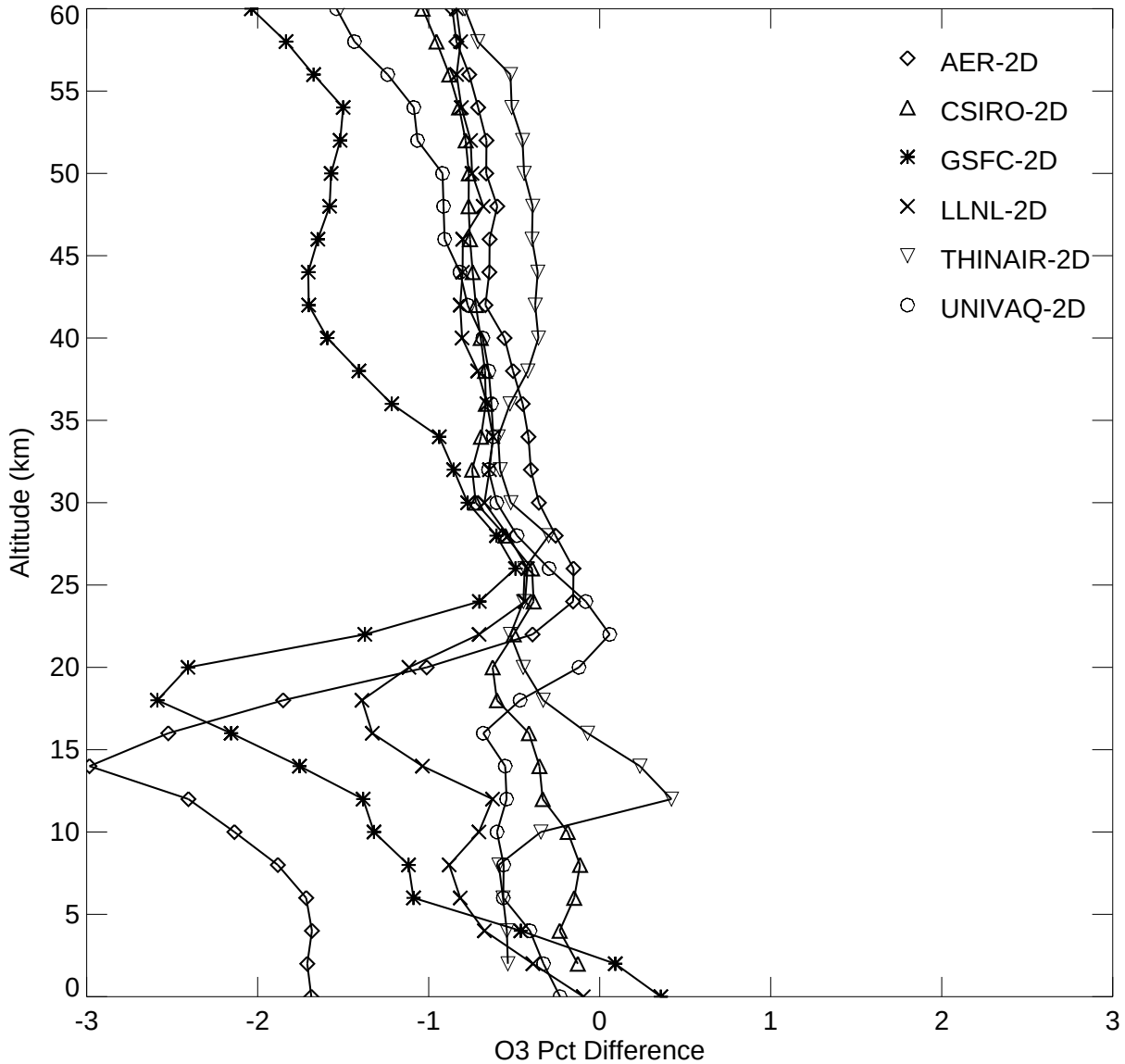

Figure 4.118: Calculated perturbations to O_3 (percent) as a function of altitude at 45°N in June of 2015 due to emissions from a fleet of 500 HSCT aircraft with EI(NO_x)=10 and SA1 sulfate surface area under Scenario S1g relative to Scenario D.

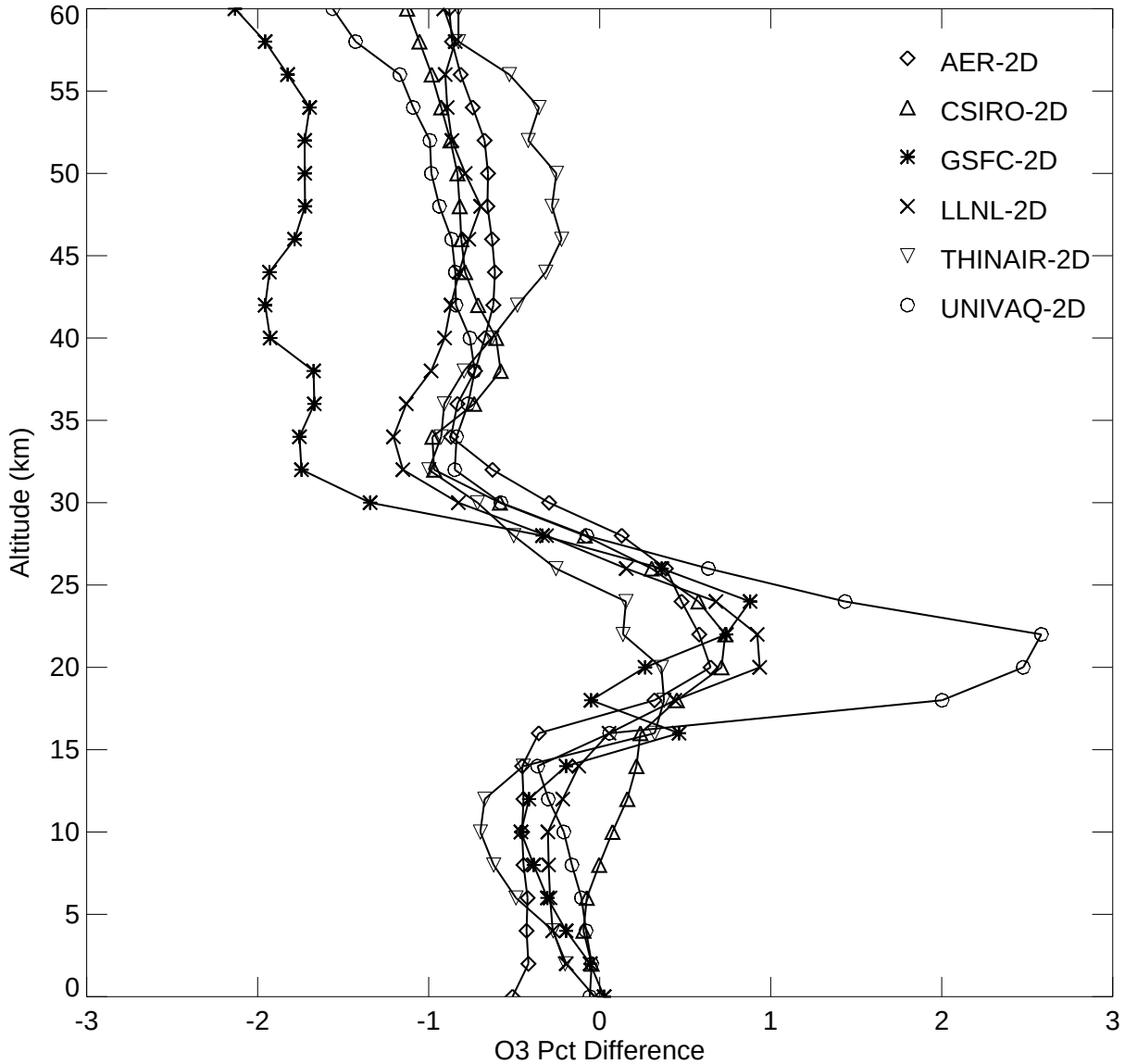

Figure 4.119: Calculated perturbations to O_3 (percent) as a function of altitude at the equator in June of 2015 due to emissions from a fleet of 500 HSCT aircraft with EI(NO_x)=10 and SA1 sulfate surface area under Scenario S1g relative to Scenario D.

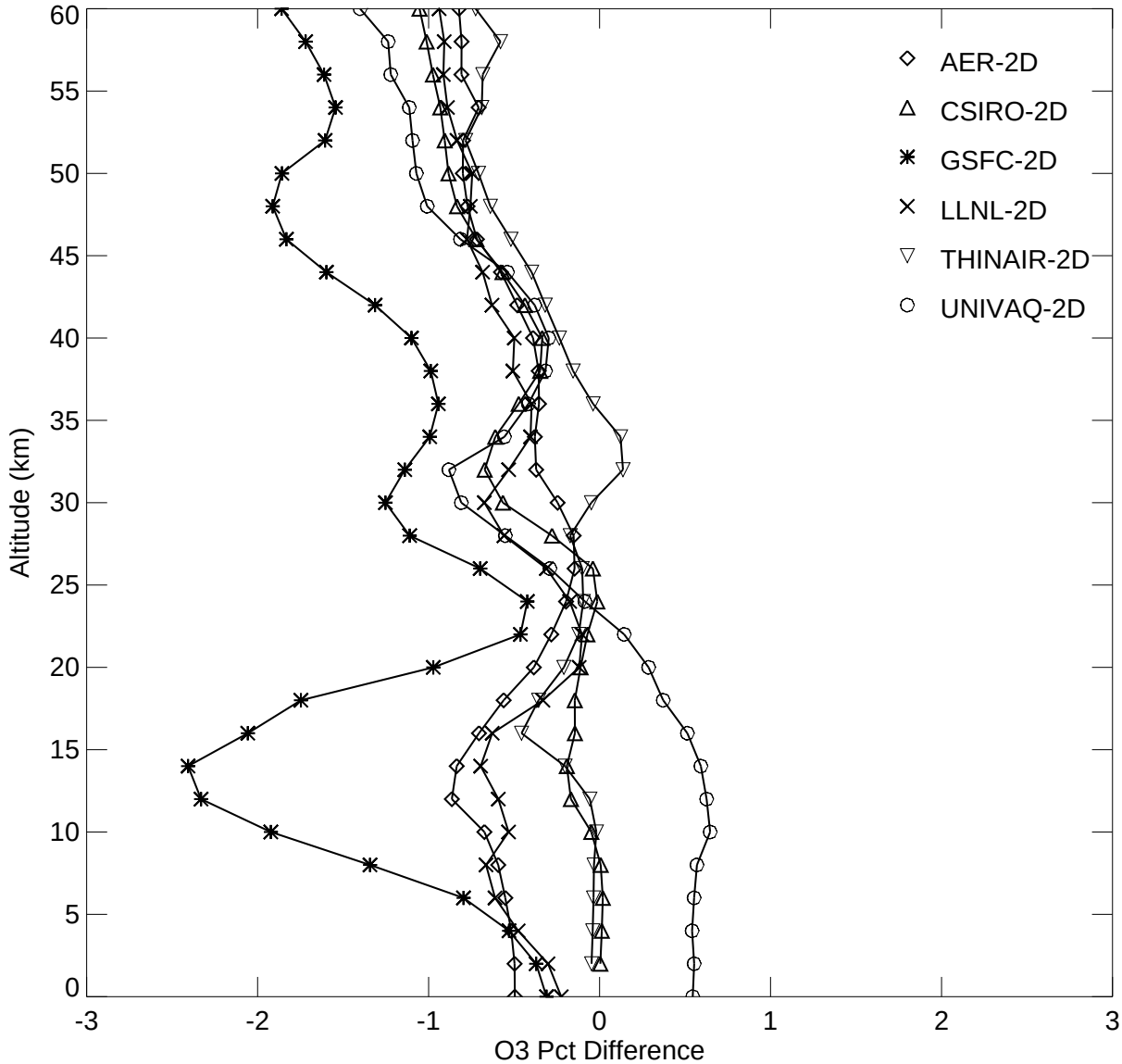

Figure 4.120: Calculated perturbations to O_3 (percent) as a function of altitude at 45^oS in June of 2015 due to emissions from a fleet of 500 HSCT aircraft with EI(NO_x)=10 and SA1 sulfate surface area under Scenario S1g relative to Scenario D.

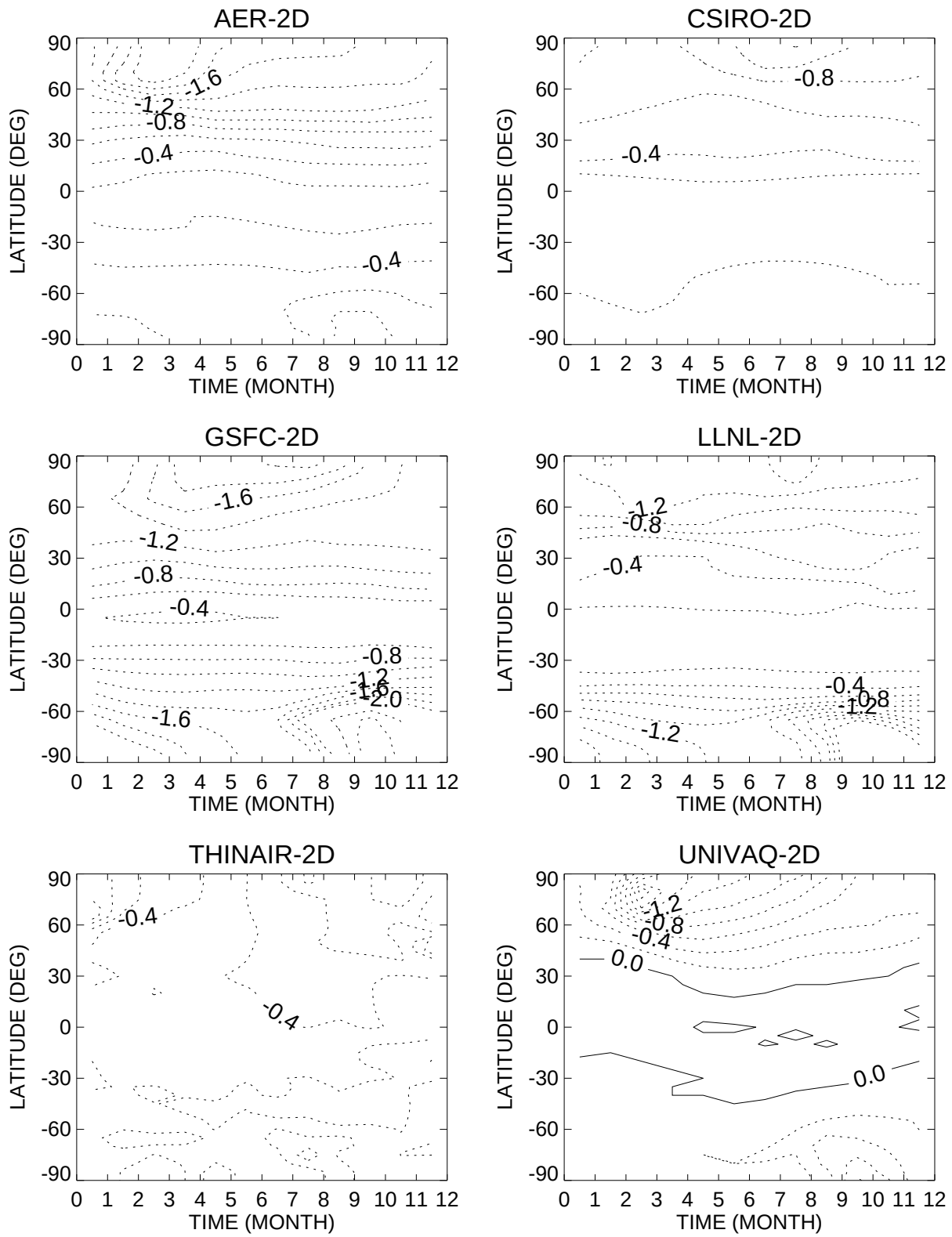

Figure 4.121: Calculated perturbations to column O_3 (percent) as a function of latitude and season in 2015 due to emissions from a fleet of 500 HSCT aircraft with EI(NO_x)=10 and SA1 sulfate surface area under Scenario S1g relative to Scenario D. Contours are -4, -3, and -2.0 to 0.2 by 0.2.

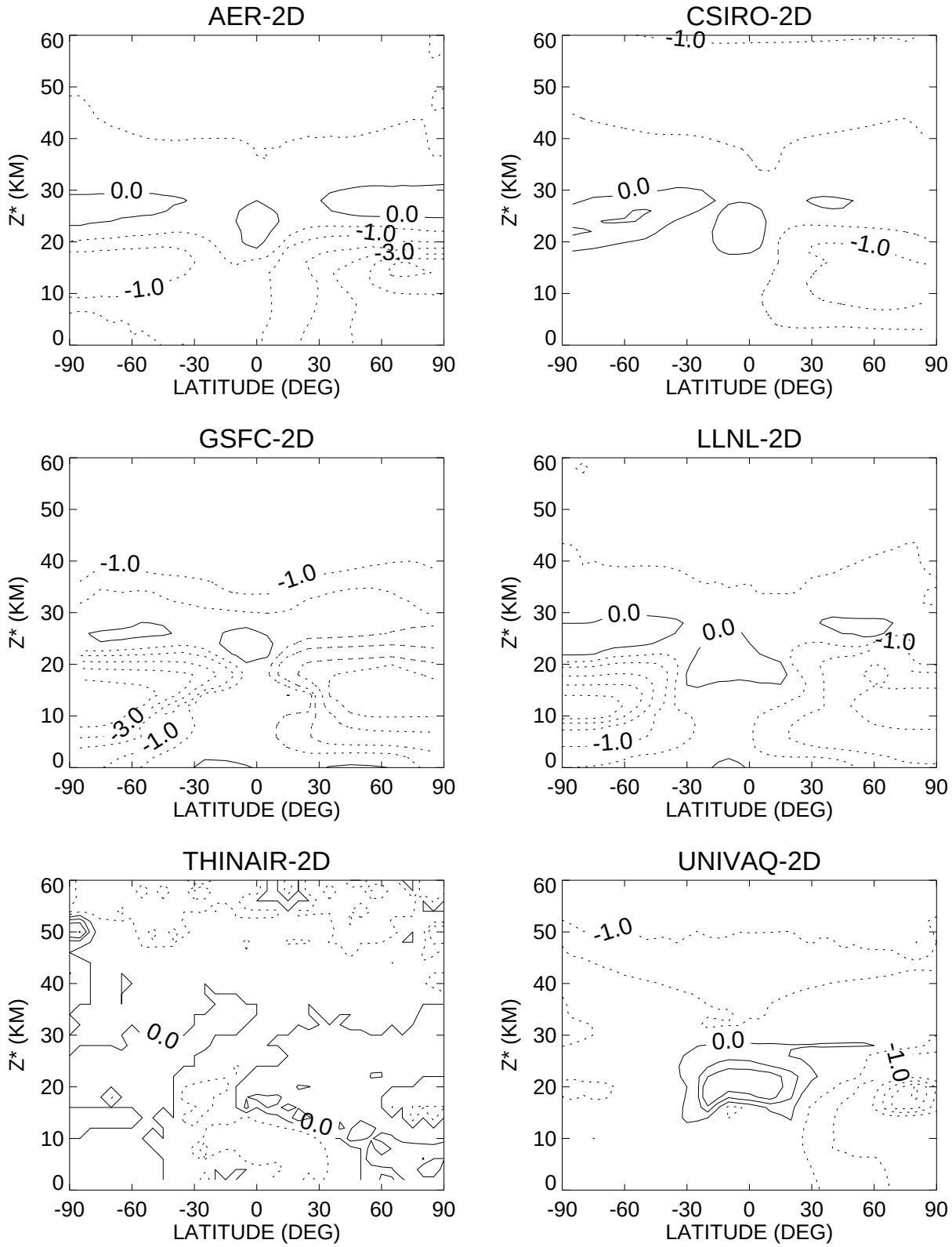

Figure 4.122: Calculated perturbations to O_3 (percent) as a function of latitude and altitude in March of 2015 due to emissions from a fleet of 500 HSCT aircraft with EI(NO_x)=5 and SA3 sulfate surface area under Scenario S1h relative to Scenario D. Contours are -5, -4, -3, -2, -1, -0.5, 0, 0.5, 1.

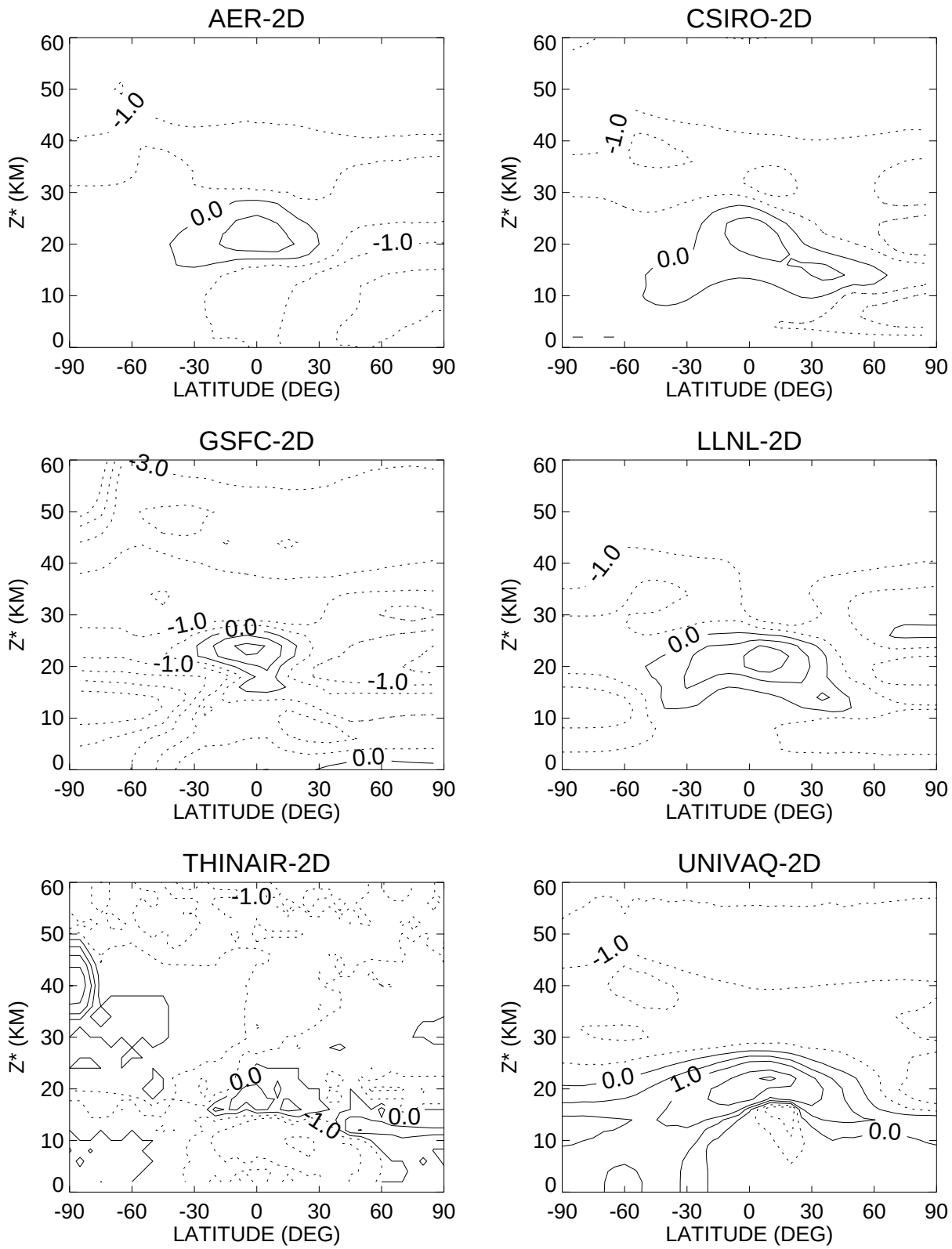

Figure 4.123: Calculated perturbations to O_3 (percent) as a function of latitude and altitude in June of 2015 due to emissions from a fleet of 500 HSCT aircraft with EI(NO_x)=5 and SA3 sulfate surface area under Scenario S1h relative to Scenario D. Contours are -4, -3, -2, -1, -0.5, 0, 0.5, 1, 2, 3.

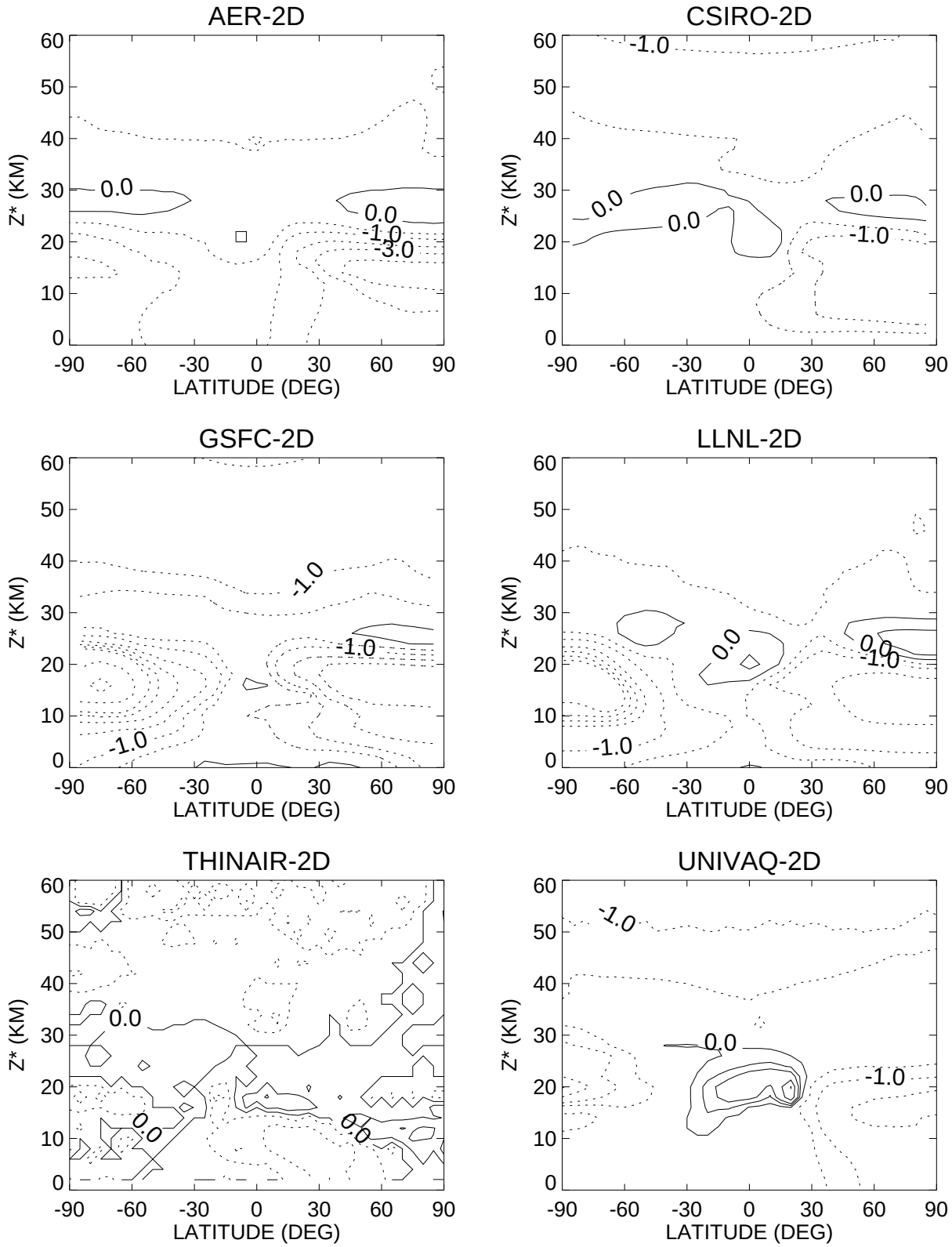

Figure 4.124: Calculated perturbations to O_3 (percent) as a function of latitude and altitude in October of 2015 due to emissions from a fleet of 500 HSCT aircraft with EI(NO_x)=5 and SA3 sulfate surface area under Scenario S1h relative to Scenario D. Contours are -15, -10, -5,-4, -3, -2, -1, -0.5, 0, 0.5, 1, 2, 3.

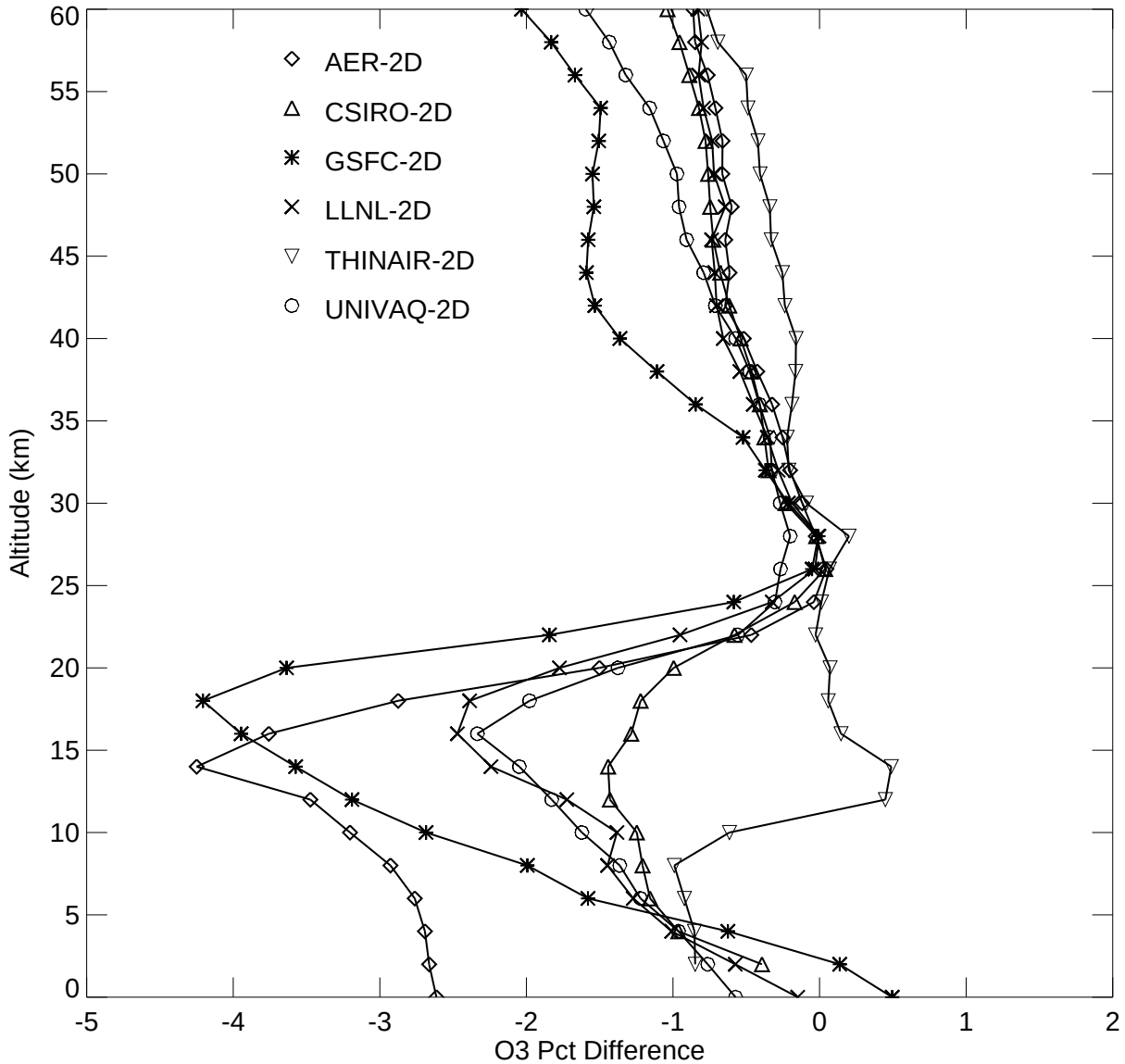

Figure 4.125: Calculated perturbations to O_3 (percent) as a function of altitude at 45^oN in June of 2015 due to emissions from a fleet of 500 HSCT aircraft with EI(NO_x)=5 and SA3 sulfate surface area under Scenario S1h relative to Scenario D.

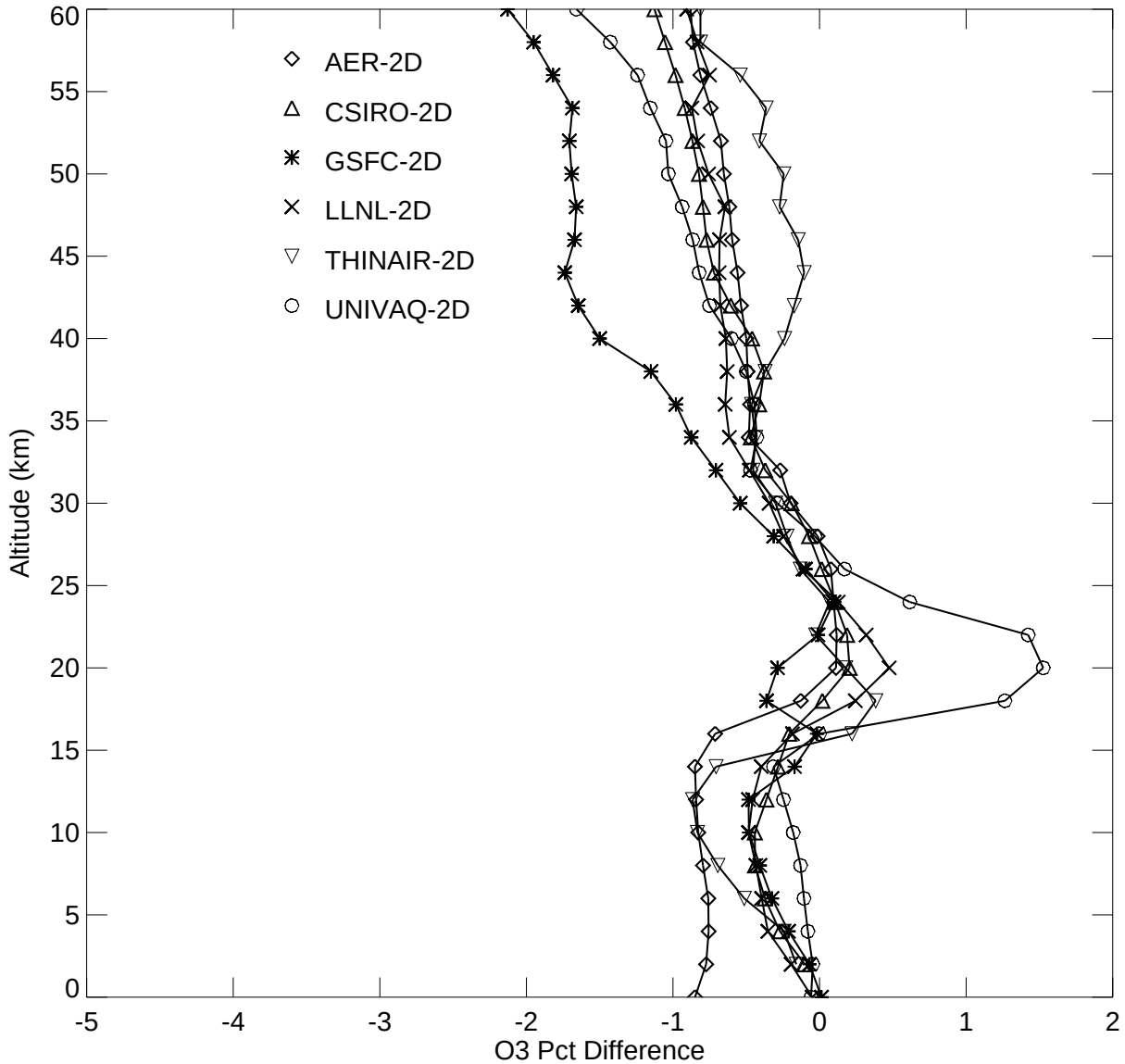

Figure 4.126: Calculated perturbations to O_3 (percent) as a function of altitude at the equator in June of 2015 due to emissions from a fleet of 500 HSCT aircraft with EI(NO_x)=5 and SA3 sulfate surface area under Scenario S1h relative to Scenario D.

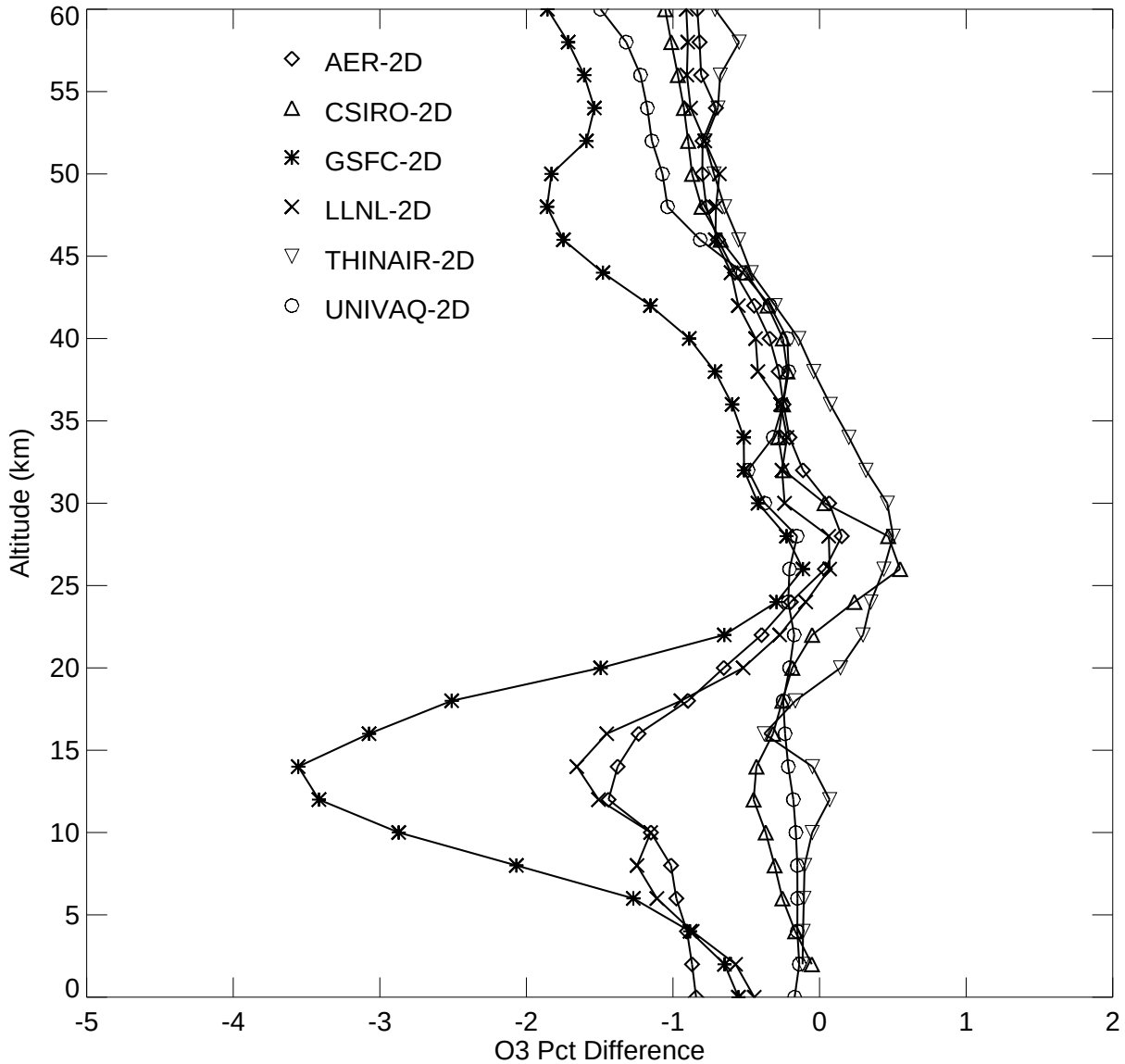

Figure 4.127: Calculated perturbations to O_3 (percent) as a function of altitude at 45°S in June of 2015 due to emissions from a fleet of 500 HSCT aircraft with EI(NO_x)=5 and SA3 sulfate surface area under Scenario S1h relative to Scenario D.

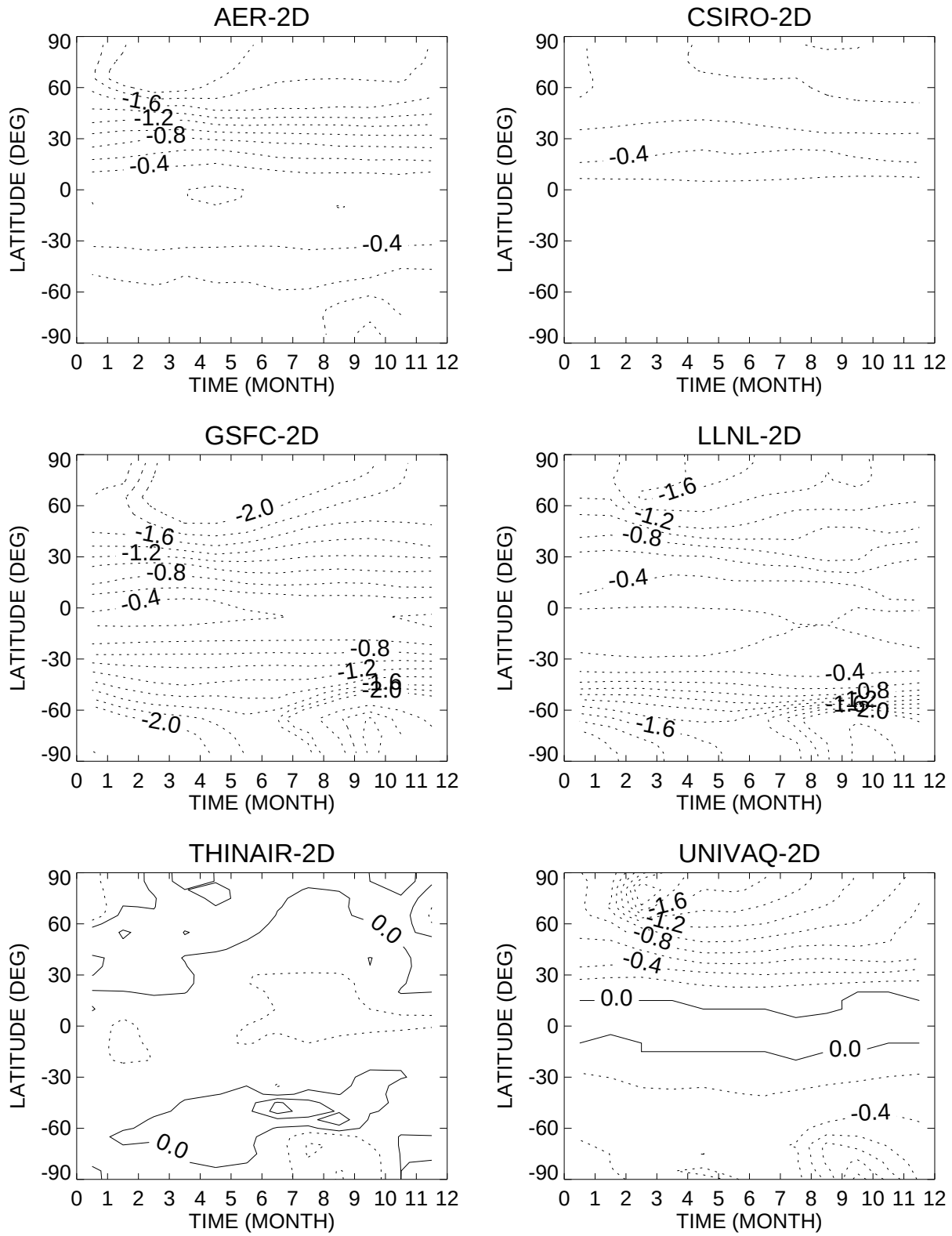

Figure 4.128: Calculated perturbations to column O_3 (percent) as a function of latitude and season in 2015 due to emissions from a fleet of 500 HSCT aircraft with EI(NO_x)=5 and SA3 sulfate surface area under Scenario S1h relative to Scenario D. Contours are -5, -4, -3, and -2.0 to 0.4 by 0.2.

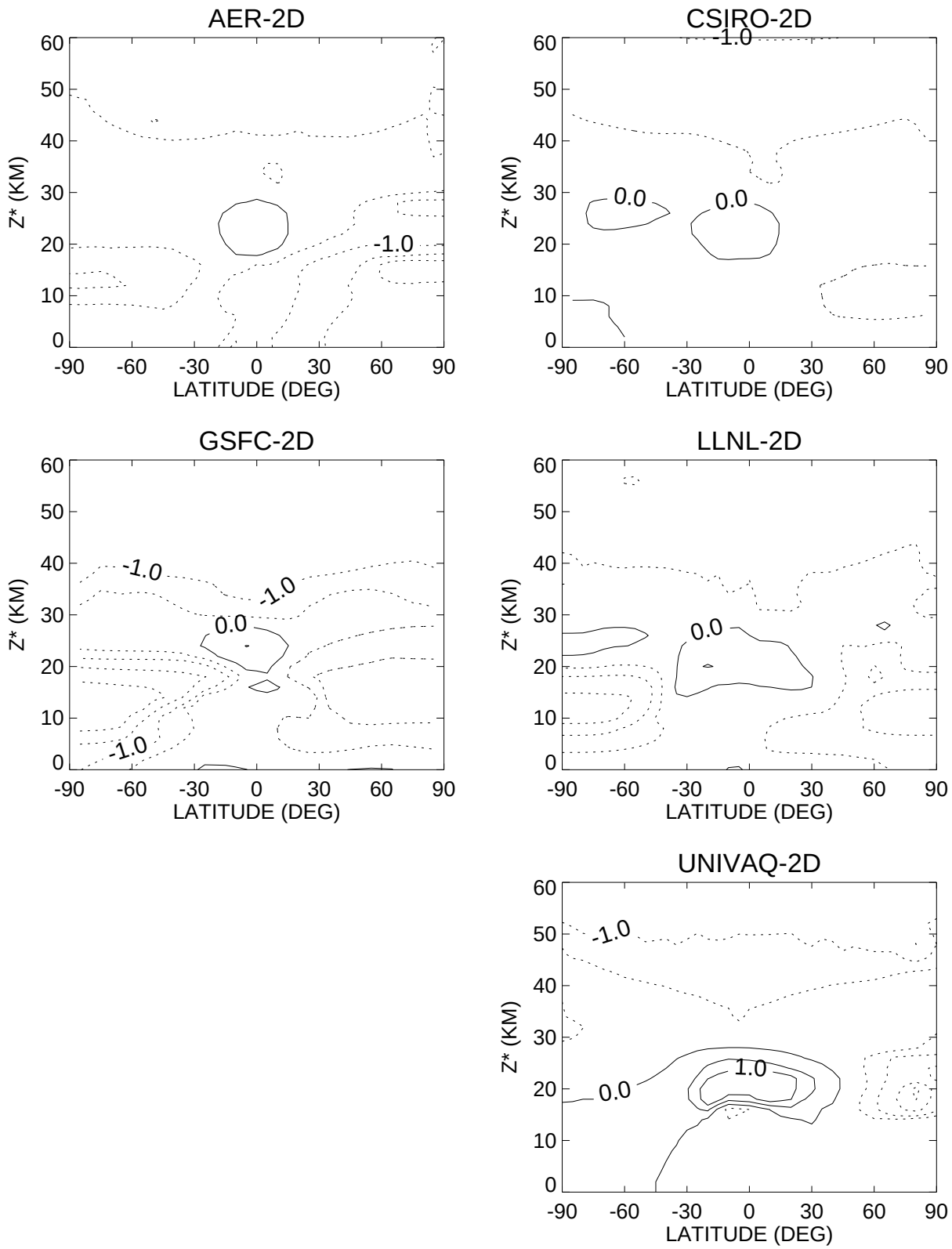

Figure 4.129: Calculated perturbations to O_3 (percent) as a function of latitude and altitude in March of 2015 due to emissions from a fleet of 500 HSCT aircraft with EI(NO_x)=5 and SA5 sulfate surface area under Scenario S1k relative to Scenario D. Contours are -3, -2, -1, -0.5, 0, 0.5, 1.

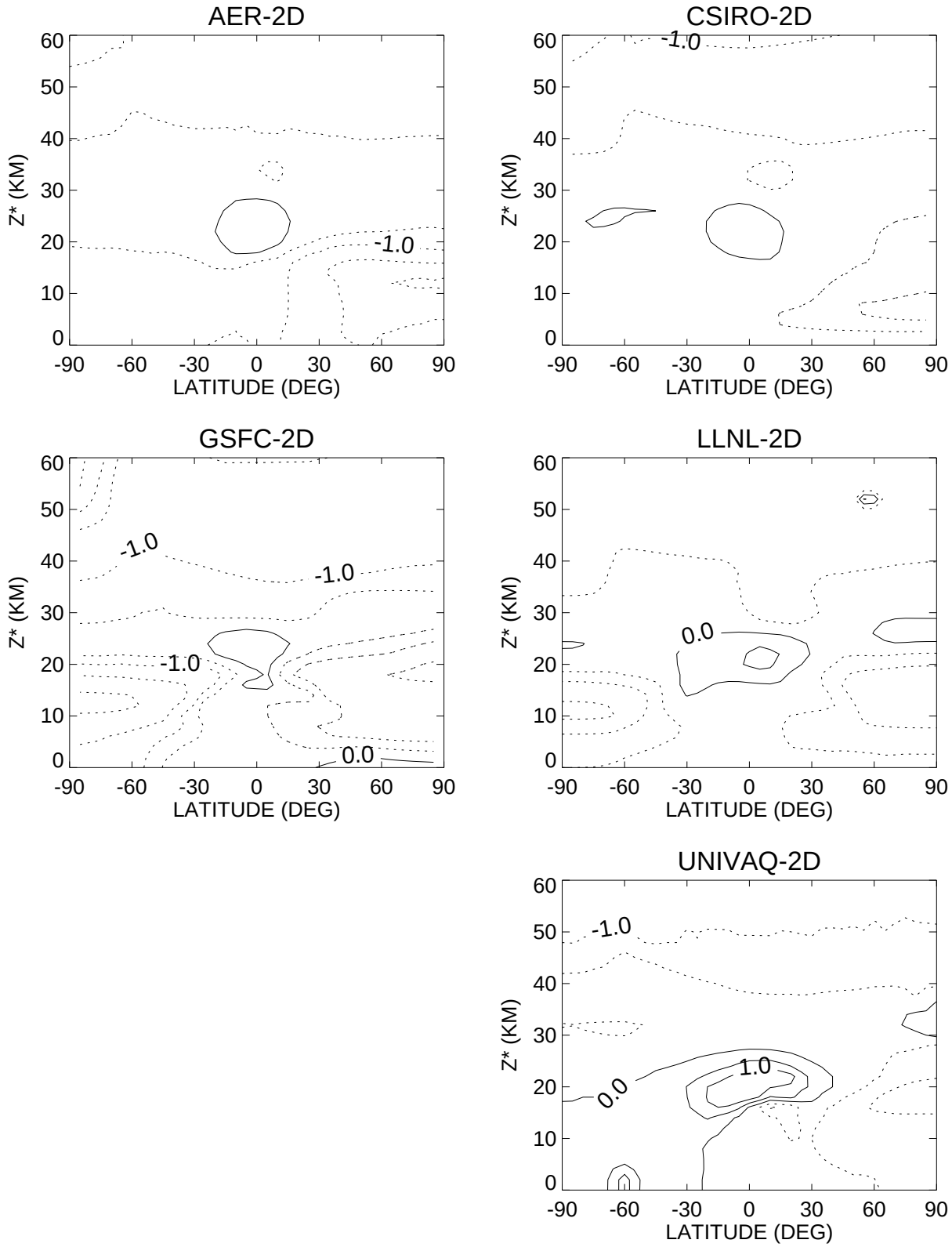

Figure 4.130: Calculated perturbations to O_3 (percent) as a function of latitude and altitude in June of 2015 due to emissions from a fleet of 500 HSCT aircraft with EI(NO_x)=5 and SA5 sulfate surface area under Scenario S1k relative to Scenario D. Contours are -3, -2, -1, -0.5, 0, 0.5, 1.

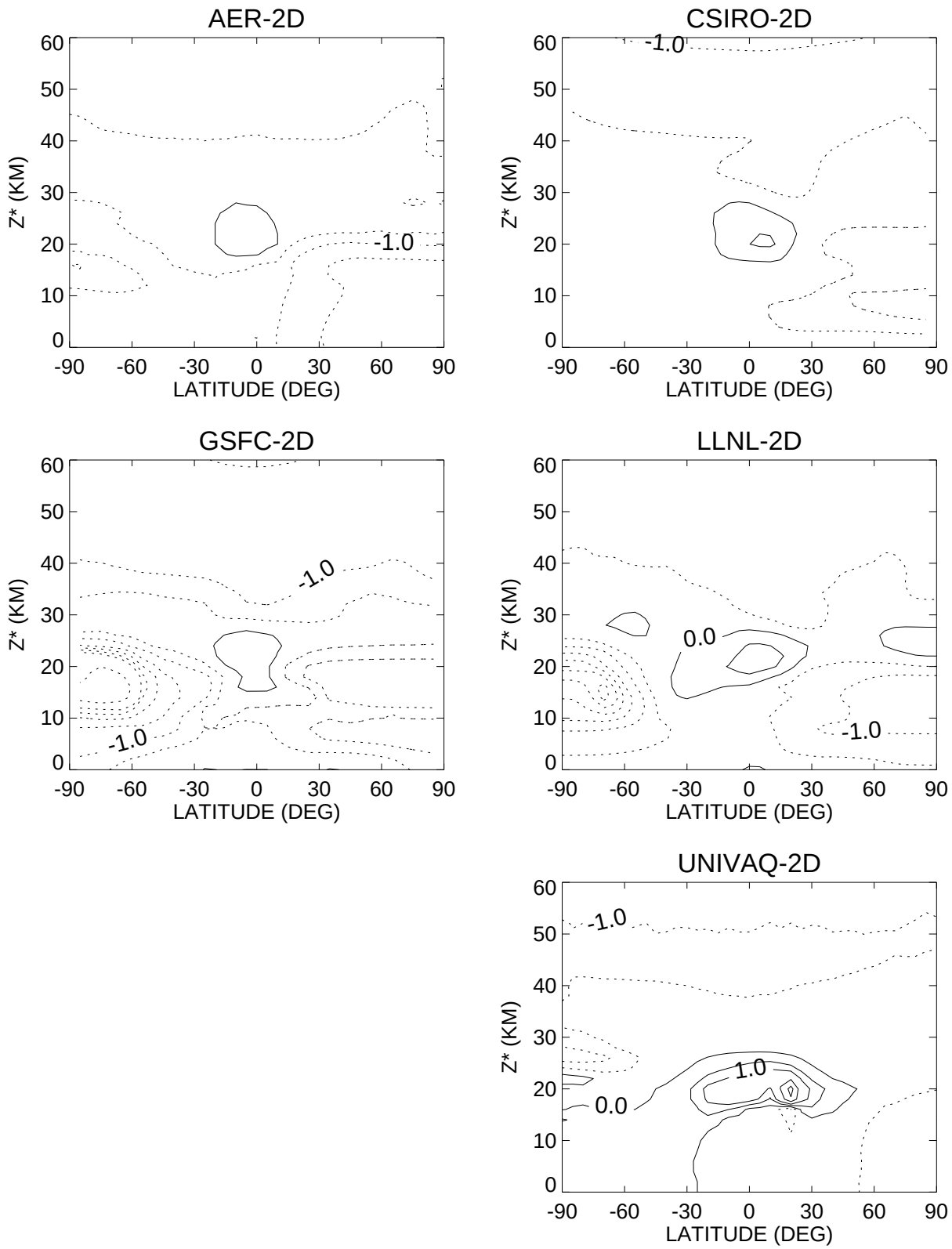

Figure 4.131: Calculated perturbations to O_3 (percent) as a function of latitude and altitude in October of 2015 due to emissions from a fleet of 500 HSCT aircraft with EI(NO_x)=5 and SA5 sulfate surface area under Scenario S1k relative to Scenario D. Contours are -10, -5, -4, -3, -2, -1, -0.5, 0, 0.5, 1, 2, 3.

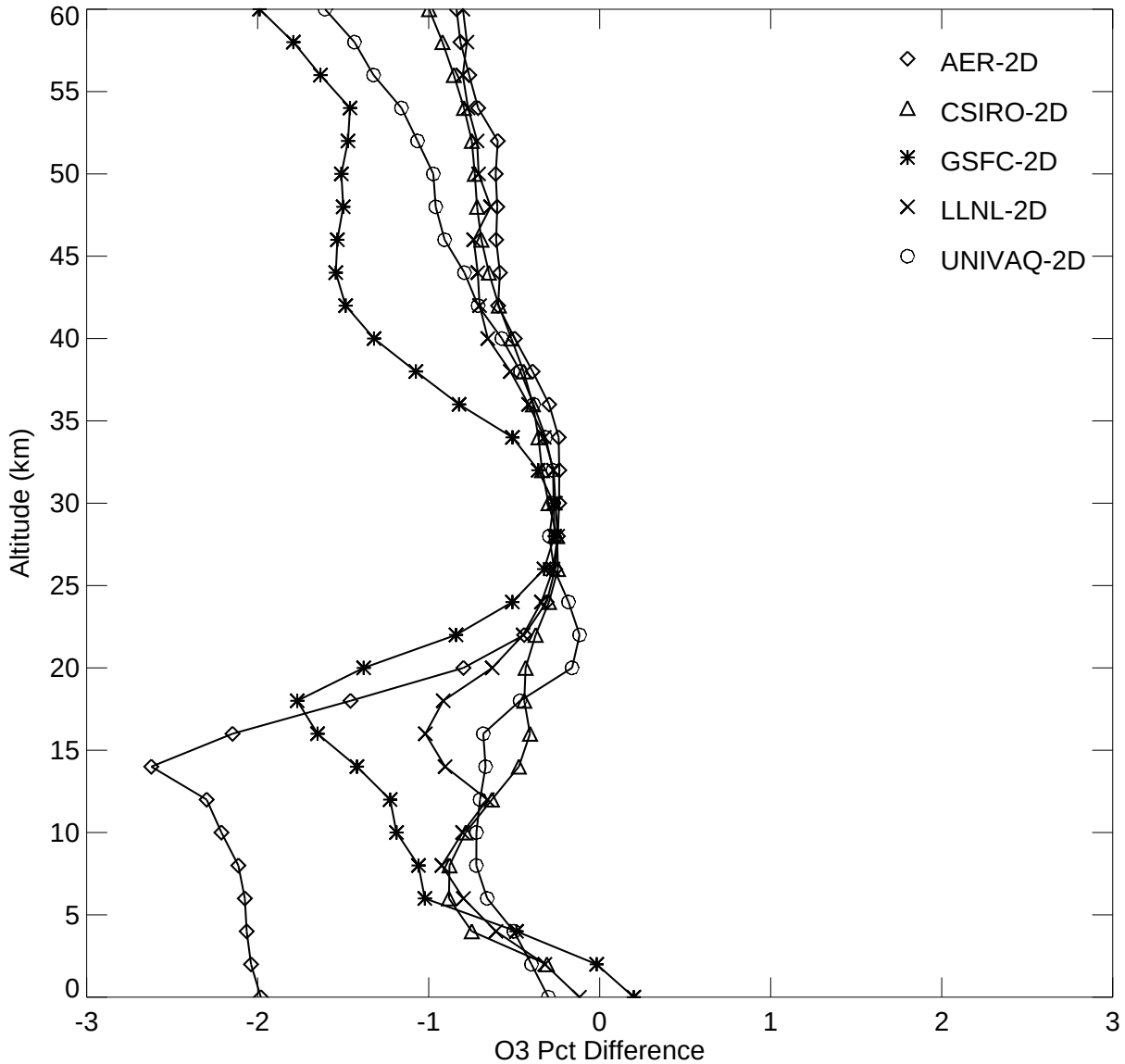

Figure 4.132: Calculated perturbations to O_3 (percent) as a function of altitude at 45^oN in June of 2015 due to emissions from a fleet of 500 HSCT aircraft with EI(NO_x)=5 and SA5 sulfate surface area under Scenario S1k relative to Scenario D.

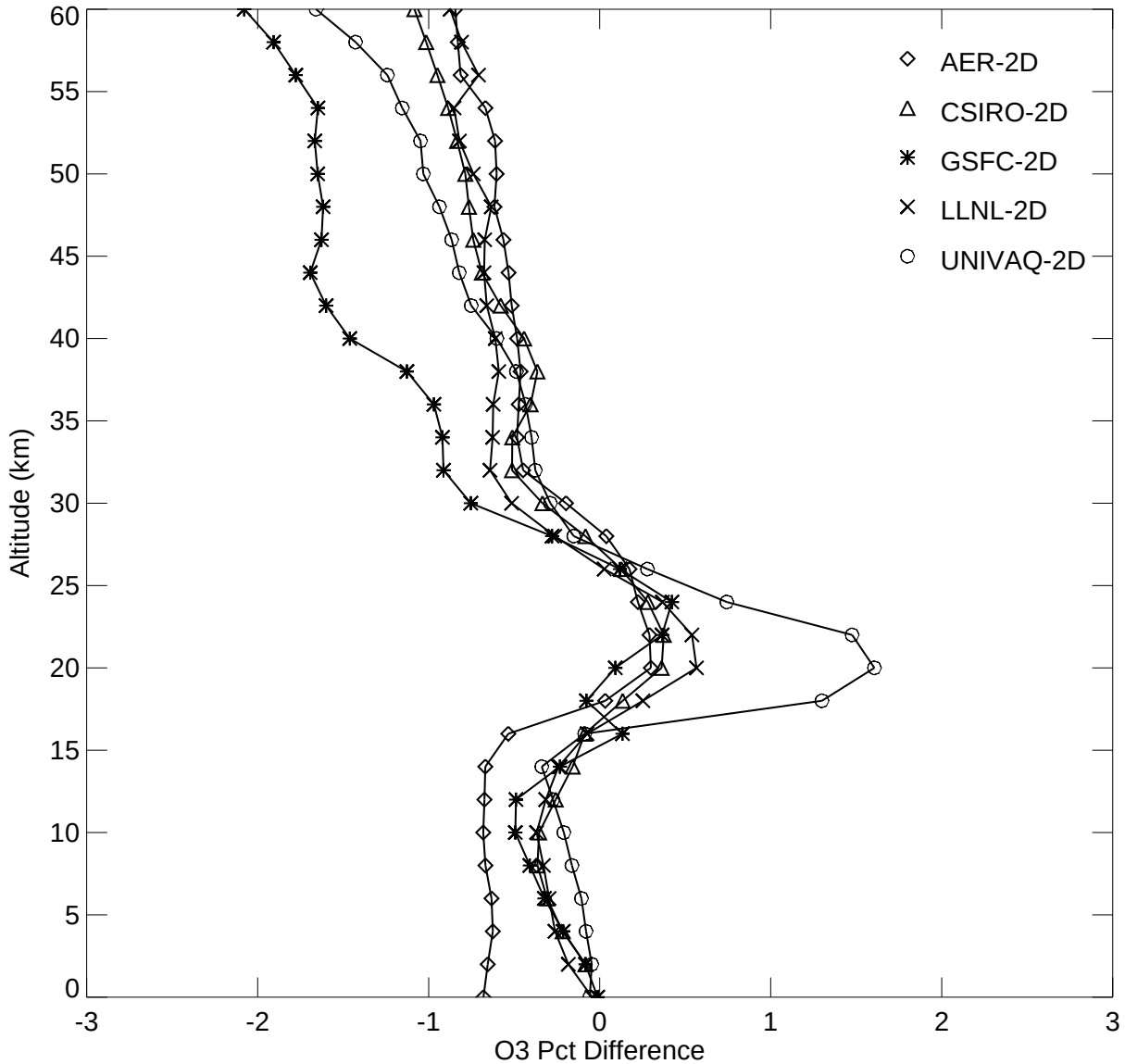

Figure 4.133: Calculated perturbations to O_3 (percent) as a function of altitude at the equator in June of 2015 due to emissions from a fleet of 500 HSCT aircraft with EI(NO_x)=5 and SA5 sulfate surface area under Scenario S1k relative to Scenario D.

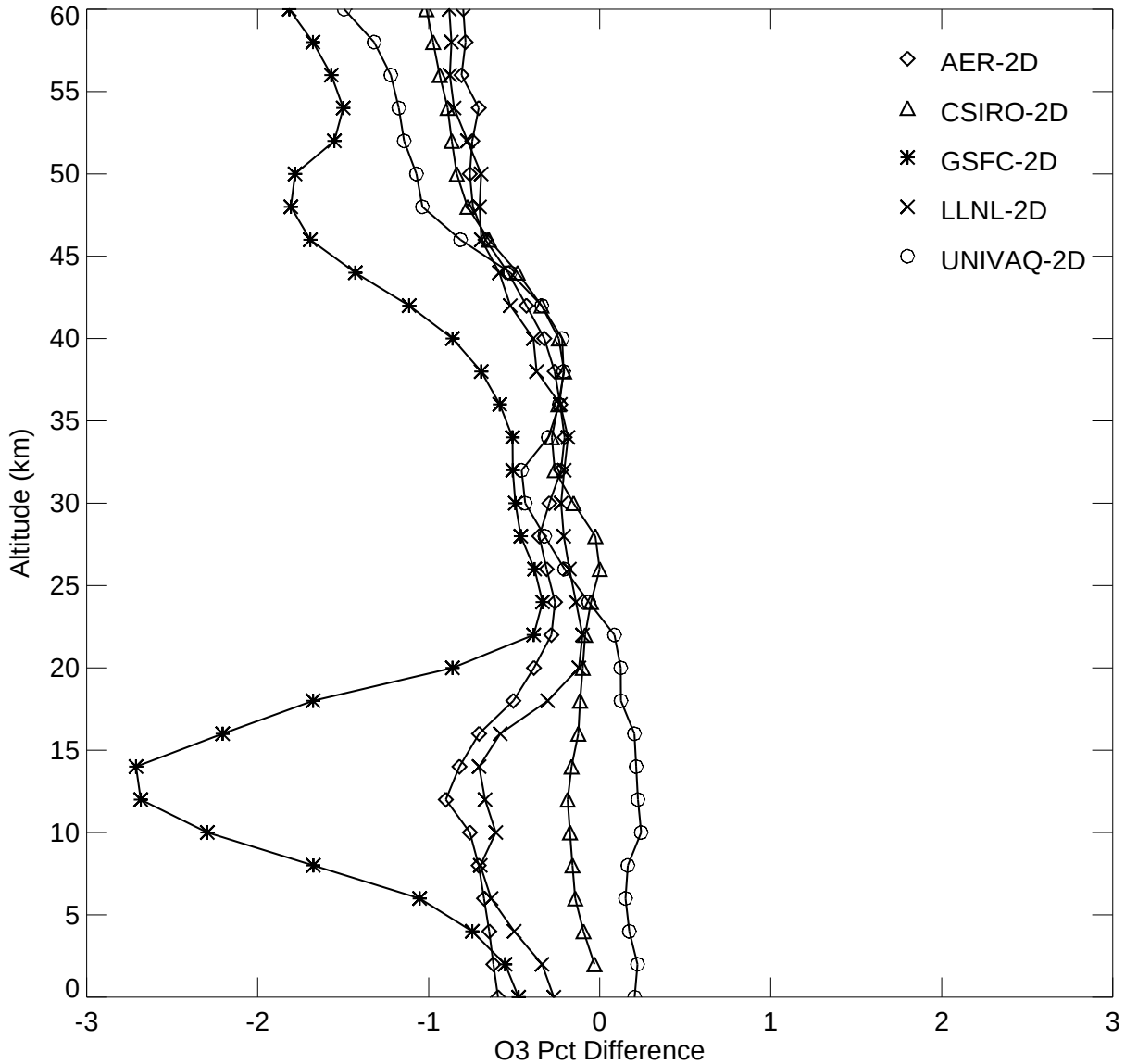

Figure 4.134: Calculated perturbations to O_3 (percent) as a function of altitude at 45°S in June of 2015 due to emissions from a fleet of 500 HSCT aircraft with EI(NO_x)=5 and SA5 sulfate surface area under Scenario S1k relative to Scenario D.

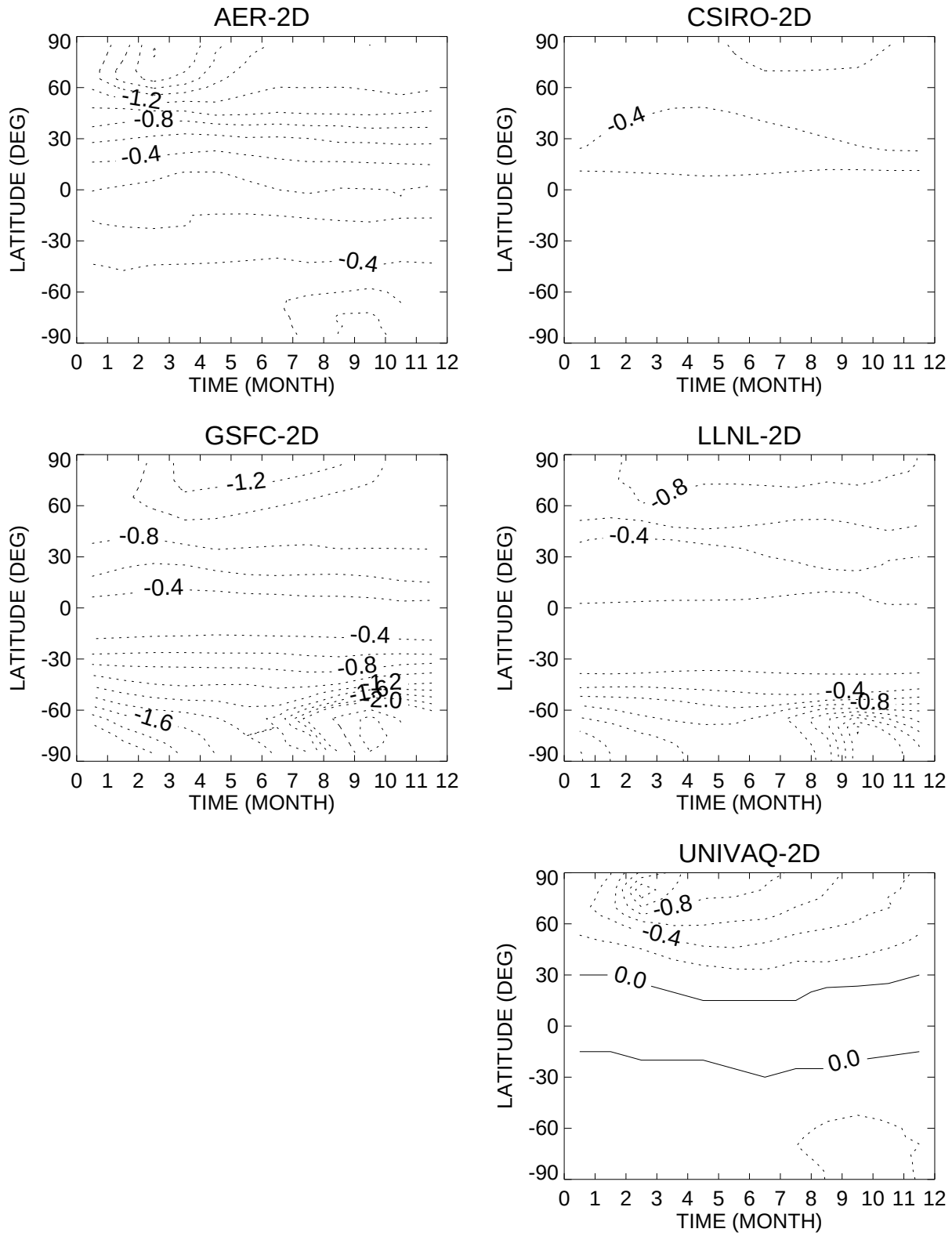

Figure 4.135: Calculated perturbations to column O_3 (percent) as a function of latitude and season in 2015 due to emissions from a fleet of 500 HSCT aircraft with EI(NO_x)=5 and SA5 sulfate surface area under Scenario S1k relative to Scenario D. Contours are -4, -3, and -2 to 0 by 0.2.

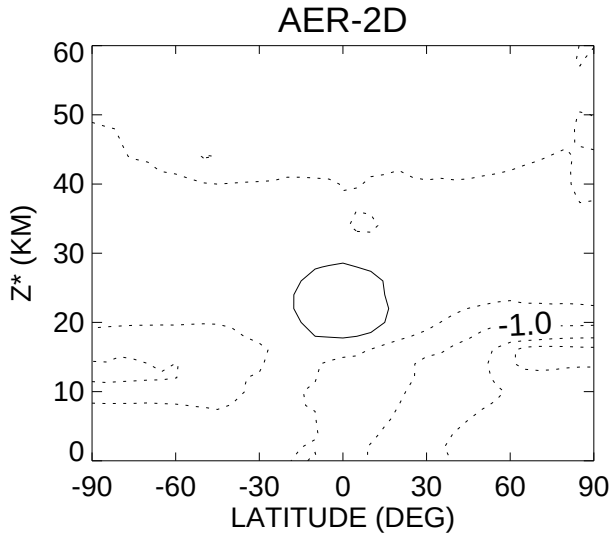

Figure 4.136: Calculated perturbations to O_3 (percent) as a function of latitude and altitude in March of 2015 due to emissions from a fleet of 500 HSCT aircraft with EI(NO_x)=5 and SA7 sulfate surface area under Scenario S1l relative to Scenario D. Contours are -3, -2, -1, -0.5, 0.

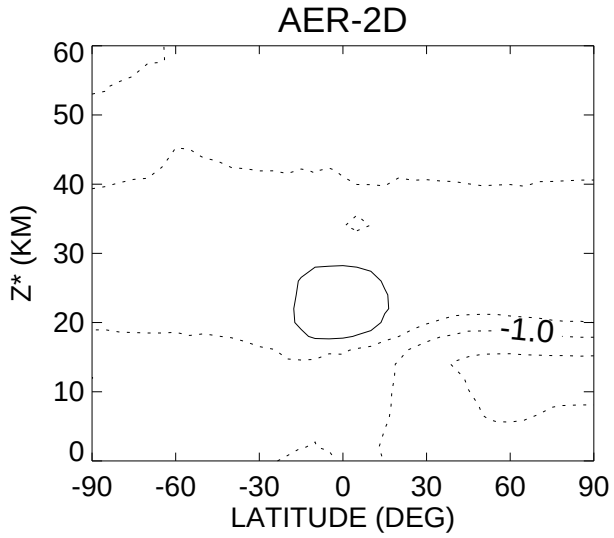

Figure 4.137: Calculated perturbations to O_3 (percent) as a function of latitude and altitude in June of 2015 due to emissions from a fleet of 500 HSCT aircraft with EI(NO_x)=5 and SA7 sulfate surface area under Scenario S1l relative to Scenario D. Contours are -2, -1, -0.5, 0.

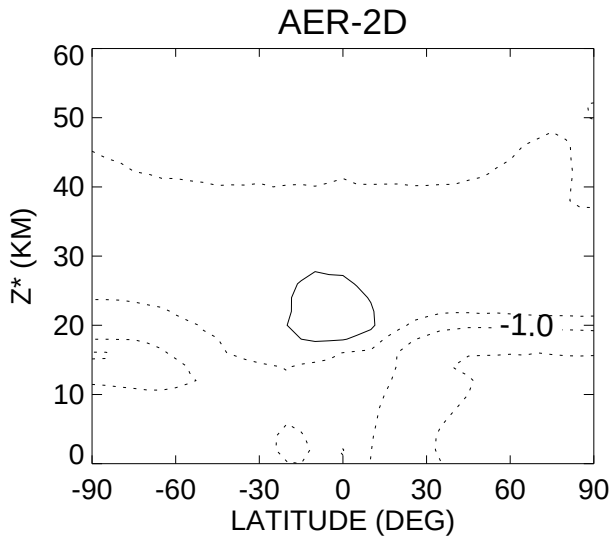

Figure 4.138: Calculated perturbations to O_3 (percent) as a function of latitude and altitude in October of 2015 due to emissions from a fleet of 500 HSCT aircraft with EI(NO_x)=5 and SA7 sulfate surface area under Scenario S1l relative to Scenario D. Contours are -2, -1, -0.5, 0.

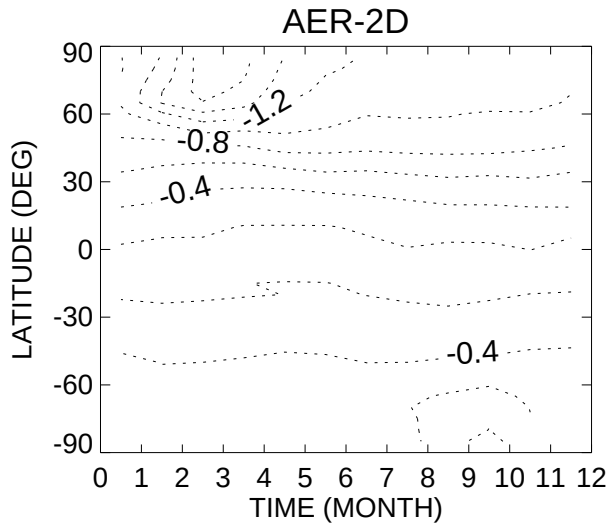

Figure 4.139: Calculated perturbations to column O_3 (percent) as a function of latitude and season in 2015 due to emissions from a fleet of 500 HSCT aircraft with EI(NO_x)=5 and SA7 sulfate surface area under Scenario S1l relative to Scenario D. Contours are -1.6 to -0.2 by 0.2.

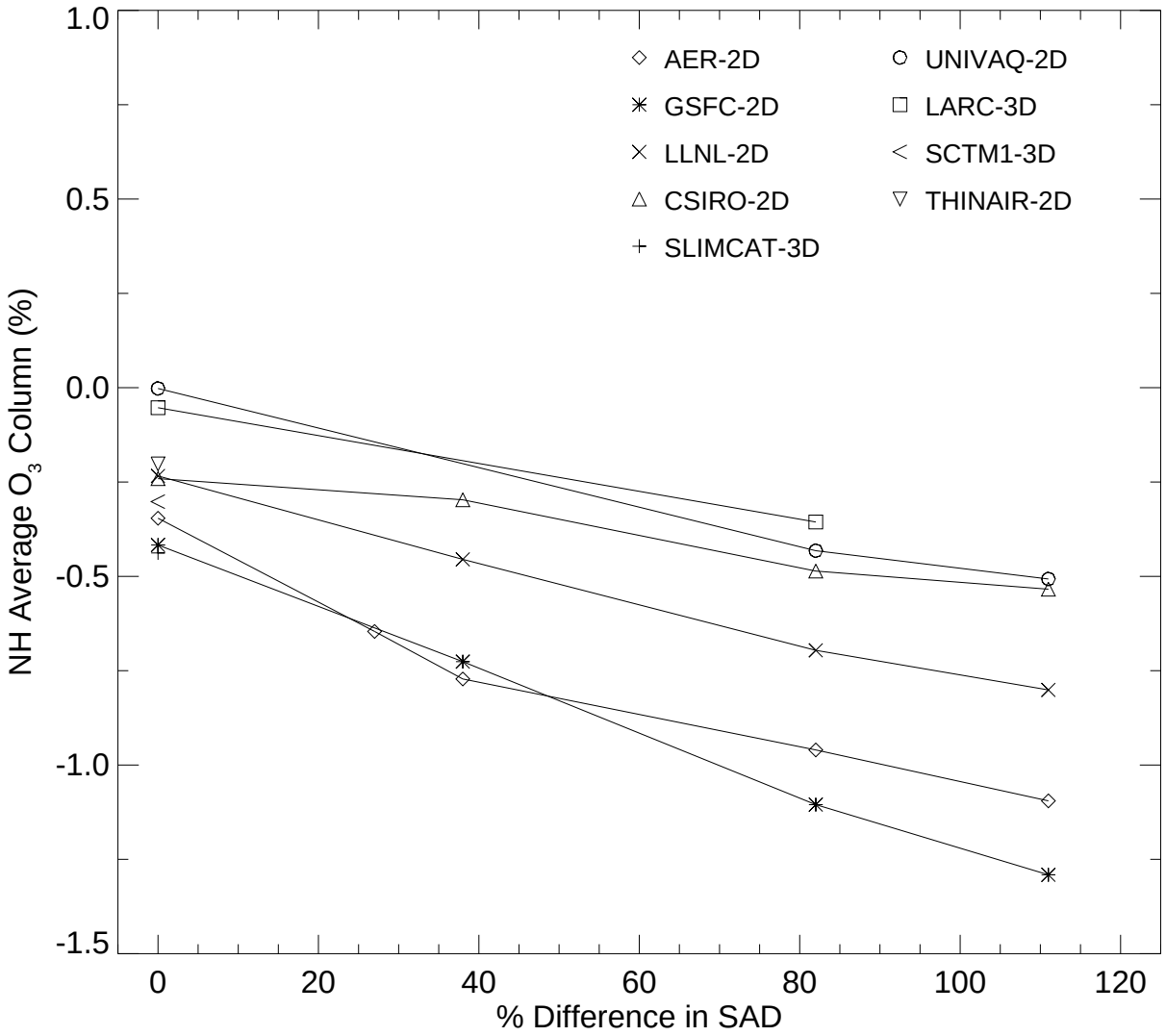

Figure 4.140: Northern hemisphere annual average total O_3 column change (percent) as a function of the percent change in aerosol surface area density in the region from 14 to 21 km and from 33^oN to 90^oN. The HSCT fleet consisted of 500 aircraft operating in 2015 with EI(NO_x)=5 and SA0 as the background surface area density.

4.3.3 Scenarios with Modified Cruise Altitude (S2a-e)

The impact of variations in cruise altitude on HSCT ozone perturbation is explored in this set of scenarios. Scenario S2a has the cruise altitude raised by 2 km, while Scenarios S2b-S2e have the cruise altitude lowered by 2 km. Based on the increased H_2O and NO_y perturbations found at higher cruise altitudes, the ozone response to HSCT should be larger for higher cruise altitudes and smaller for lower cruise altitudes.

Figures 4.141, 4.142, and 4.143 show ozone change as a function of latitude and altitude for March, June, and October for Scenario S2a relative to Scenario D. Scenario S2a includes 500 HSCT aircraft operating in 2015 with SA0 sulfate surface area density, no sulfur emissions, and a cruise altitude raised by 2 km above that used in the standard scenarios (S1a-S1l). Ozone depletion is increased in all models relative to Scenario S1c in both the lower and upper stratosphere. Figures 4.144, 4.145, and 4.146 show vertical profiles of ozone perturbation at 45^oN, the equator, and 45^oS in June. Changes in ozone column for Scenario S2a are shown in Figure 4.147. Ozone column depletion for Scenario S2a is greater than for Scenario S1c, though the THINAIR and UNIVAQ models still show regions of total ozone increase. For the AER, GSFC, LLNL, and CSIRO models, the northern hemisphere annual average percentage ozone depletion for Scenario S2a is more than double that of Scenario S1c.

Scenario S2b includes 500 HSCT aircraft in 2015 operating at 2 km below the standard cruise altitude with EI(NO_x)=5. This scenario produced smaller perturbations in H_2O and NO_y than a similar scenario (S1c) at the standard cruise altitude. Figures 4.148- 4.150 show ozone perturbations as a function of latitude and altitude for 3 months. Ozone depletion is considerably reduced compared with Scenario S1c. The CSIRO and LLNL models show depletion less than 0.5% everywhere in the stratosphere and ozone increases near the tropopause at all latitudes. Ozone changes as a function of altitude only for 45^oN, the equator, and 45^oS are shown in Figures 4.151-4.153. The large southern hemisphere ozone depletion calculated by the GSFC model is greatly reduced. Figure 4.154 shows changes in ozone column for Scenario S2b relative to Scenario D. Ozone column changes are less than 0.5% everywhere for all models except GSFC, which show a maximum 1% depletion near the south pole in September-October.

The sensitivity of ozone response to HSCT to changes in cruise altitude is depicted in Figures 4.155 and 4.156 for the northern and southern hemispheres, respectively. The annual average hemispheric ozone column perturbation is plotted against cruise altitude changes of -2 km (S2b-D), 0 km (S1c-D), and +2 km (S2a-D) with 500 HSCT aircraft, EI(NO_x)=5, and SA0. All models show a substantially more negative ozone response for higher cruise altitude in the northern hemisphere. For lower cruise altitudes, a reduced (near zero for -2 km cruise altitude) ozone response is seen. In the southern hemisphere, the GSFC model show a large sensitivity to cruise altitude and the LLNL model a moderate sensitivity. The other models show small sensitivity.

Scenario S2c is similar to Scenario S2b but with EI(NO_x)=10. Only the AER, CSIRO, GSFC, and LLNL models performed calculations for this case. Figures 4.157, 4.158, and 4.159 show changes in ozone as a function of latitude and altitude for this scenario for March, June, and October. The CSIRO, GSFC, and LLNL models show ozone increases in the troposphere due to substantial NO_x emissions at low altitude. Changes in ozone column for Scenario S2c relative to Scenario D are shown in Figure 4.160. All models show some areas of ozone increase. Ozone column depletion is greater than 0.5% only for the AER model at the springtime northern pole and the GSFC model at the springtime southern pole.

Scenario S2d is similar to S2b and S2c but with EI(NO_x)=15. Only the GSFC model performed this calculation. Figures 4.161, 4.162, and 4.163 show changes in ozone for March, June, and October from the GSFC model. Tropospheric ozone increases are as much as 6%. Stratospheric ozone depletions are up to 1%. Change in column ozone, shown in Figure 4.164, are mostly positive.

Sensitivity to aircraft NO_x emission index with 500 HSCT aircraft operating at 2 km below the standard cruise altitude in 2015 with SA0 sulfate surface area density is shown in Figures 4.165 and 4.166. These plots show annual average hemispheric ozone perturbation as a function of EI(NO_x) for Scenarios S2b-S2d. The AER model shows slightly greater ozone depletion at EI(NO_x)=10 than at EI(NO_x)=5 in both hemispheres. The LLNL and CSIRO models show slightly less depletion or no change between EI(NO_x)=5 and EI(NO_x)=10. The GSFC model show a substantial reduction in ozone depletion from EI(NO_x)=5 to EI(NO_x)=15. In contrast, the GSFC model showed the opposite trend at the standard cruise altitude in the northern hemisphere.

Scenario S2e represents a fleet of 1000 HSCT aircraft operating at 2 km below the nominal cruise altitude

in 2015 with EI(NO_x)=5. Changes in ozone as a function of latitude and altitude are shown in Figures 4.167-4.169. The HSCT NO_x emissions for this scenario are similar to S2c with 500 aircraft and EI(NO_x)=10, but the H_2O emissions are twice as large as that case. Stratospheric ozone depletion is greater than for Scenario S2c, and tropospheric ozone increases are much reduced. Figure 4.170 shows changes in ozone column for Scenario S2e relative to Scenario D. Ozone column depletion is greater for both Scenario S2b and S2c.

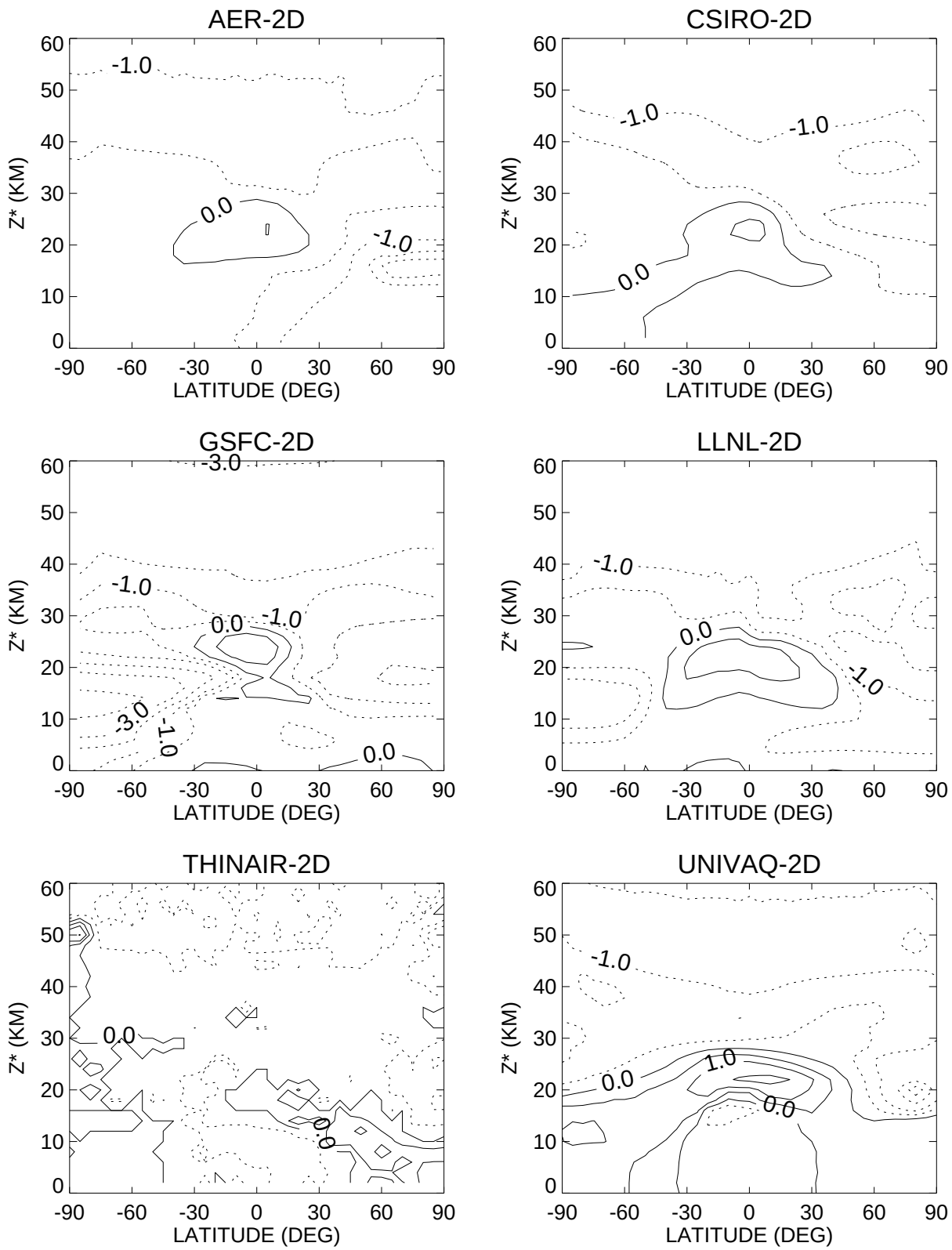

Figure 4.141: Calculated perturbations to O_3 (percent) as a function of latitude and altitude in March of 2015 due to emissions from a fleet of 500 HSCT aircraft operating at 2 km above nominal cruise altitude with EI(NO_x)=5 under Scenario S2a relative to Scenario D. Contours are -4, -3, -2, -1, -0.5, 0, 0.5, 1, 2.

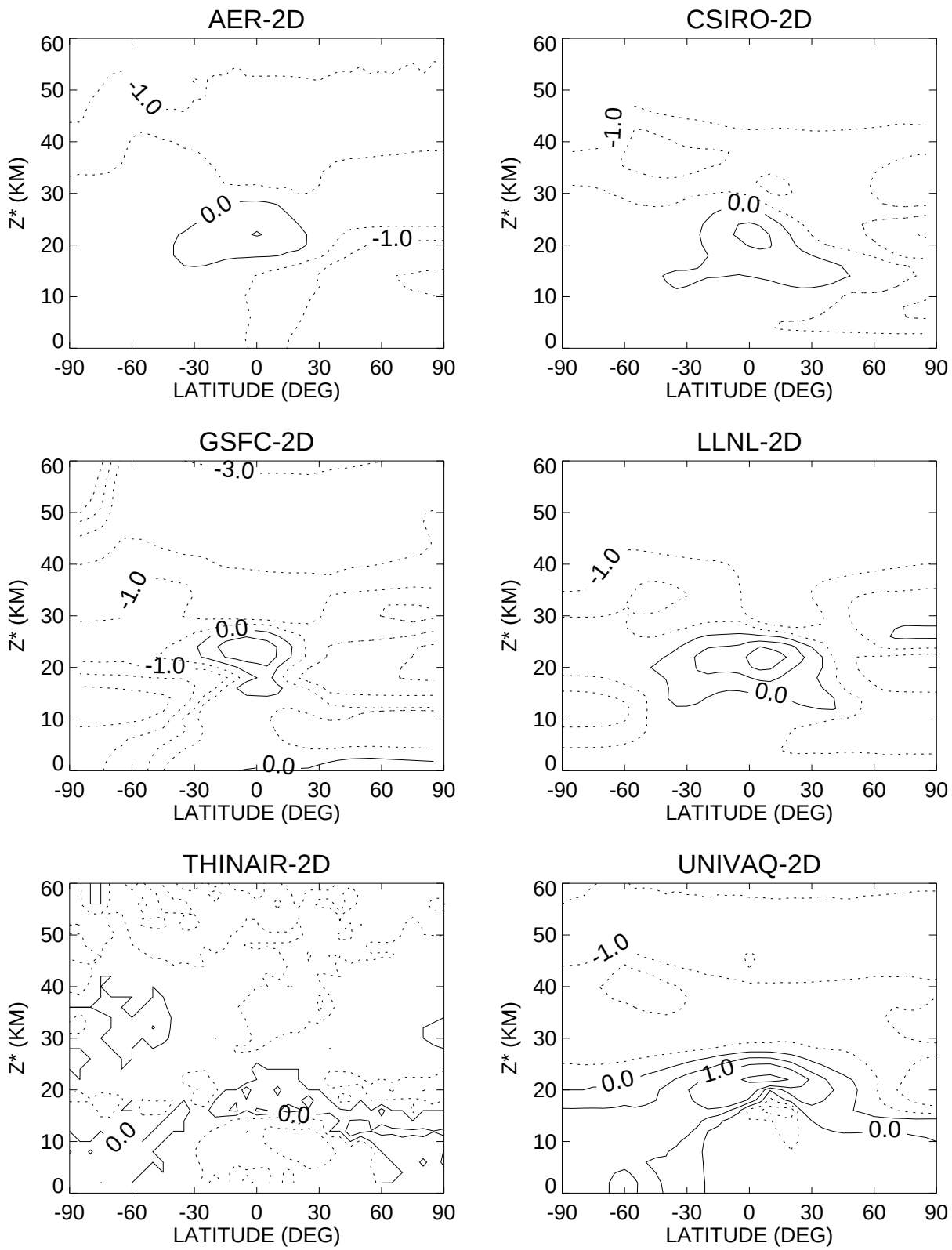

Figure 4.142: Calculated perturbations to O_3 (percent) as a function of latitude and altitude in June of 2015 due to emissions from a fleet of 500 HSCT aircraft operating at 2 km above nominal cruise altitude with EI(NO_x)=5 under Scenario S2a relative to Scenario D. Contours are -3, -2, -1, -0.5, 0, 0.5, 1, 2.

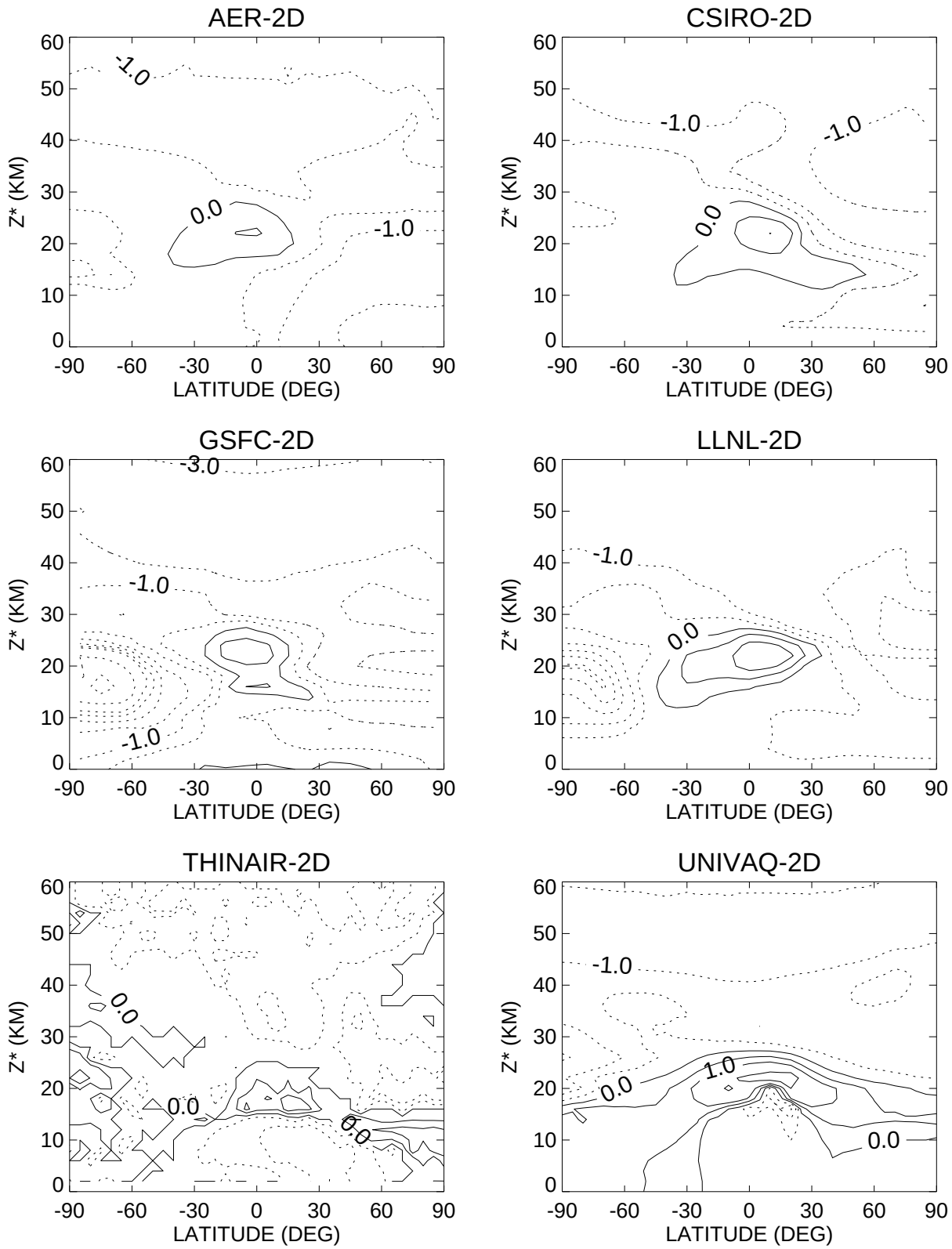

Figure 4.143: Calculated perturbations to O_3 (percent) as a function of latitude and altitude in October of 2015 due to emissions from a fleet of 500 HSCT aircraft operating at 2 km above nominal cruise altitude with EI(NO_x)=5 under Scenario S2a relative to Scenario D. Contours are -15, -10, -5, -4, -3, -2, -1, -0.5, 0, 0.5, 1, 2.

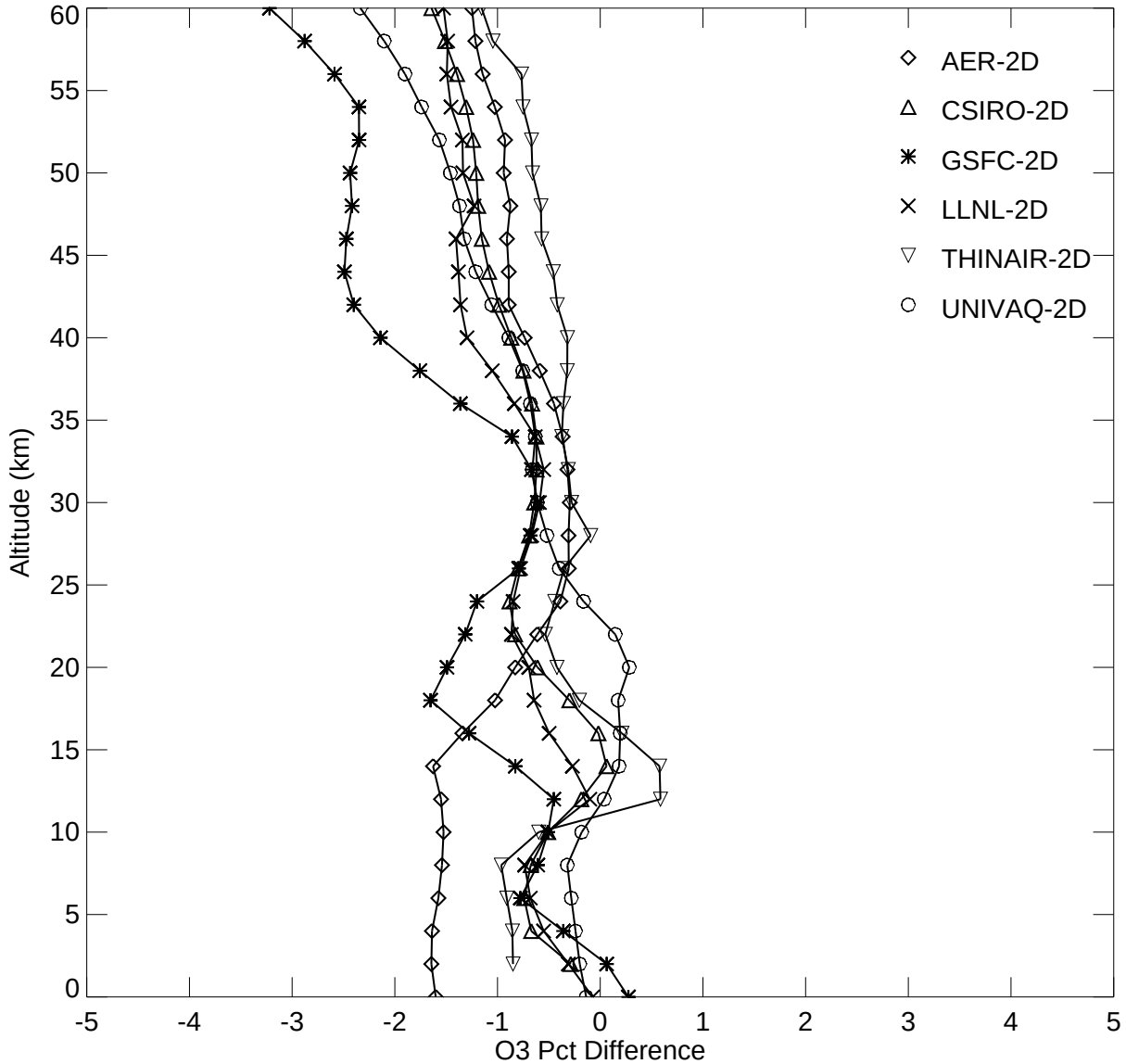

Figure 4.144: Calculated perturbations to O_3 (percent) as a function of altitude at 45°N in June of 2015 due to emissions from a fleet of 500 HSCT aircraft operating at 2 km above nominal cruise altitude with EI(NO_x)=5 under Scenario S2a relative to Scenario D.

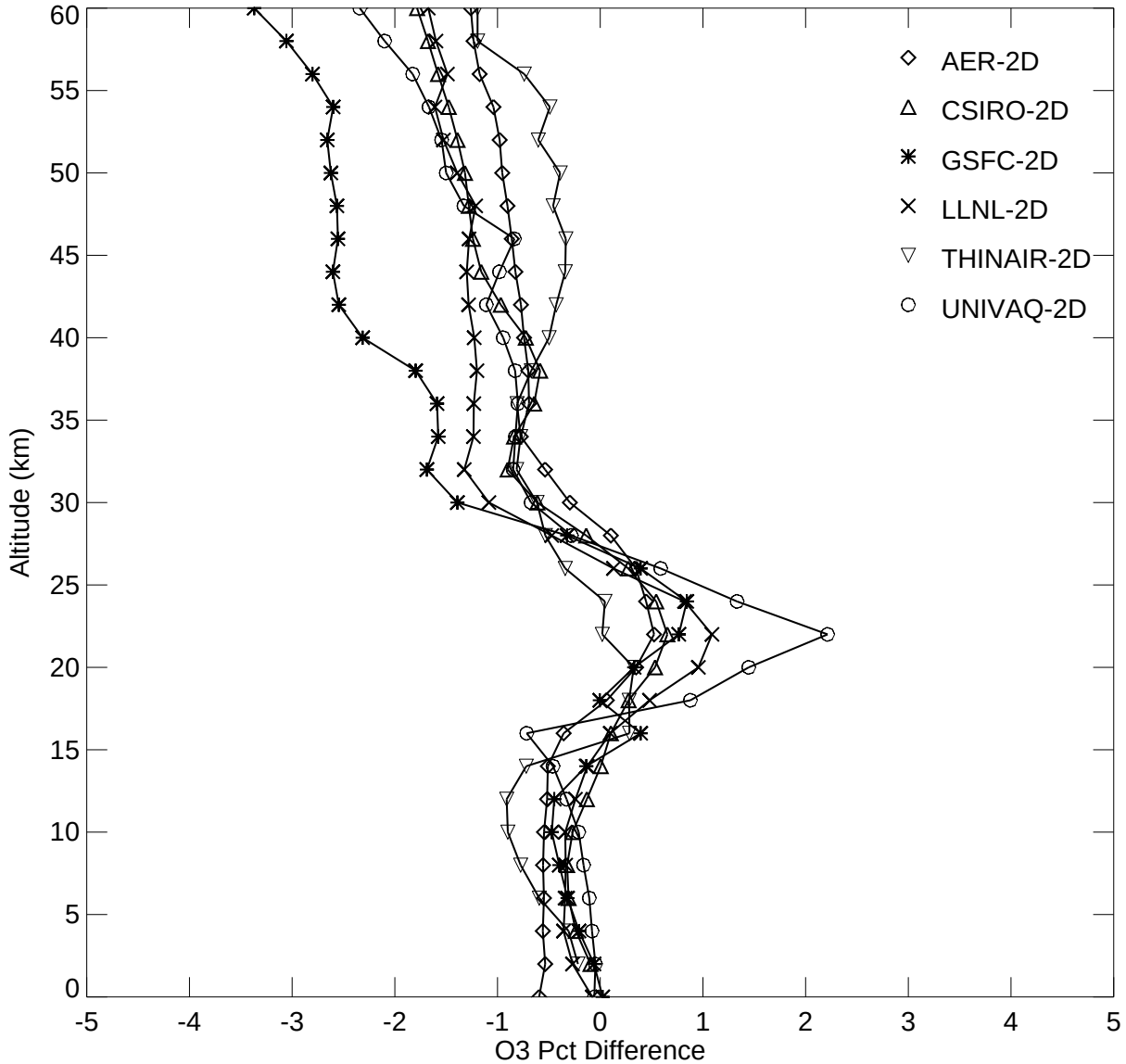

Figure 4.145: Calculated perturbations to O_3 (percent) as a function of altitude at the equator in June of 2015 due to emissions from a fleet of 500 HSCT aircraft operating at 2 km above nominal cruise altitude with EI(NO_x)=5 under Scenario S2a relative to Scenario D.

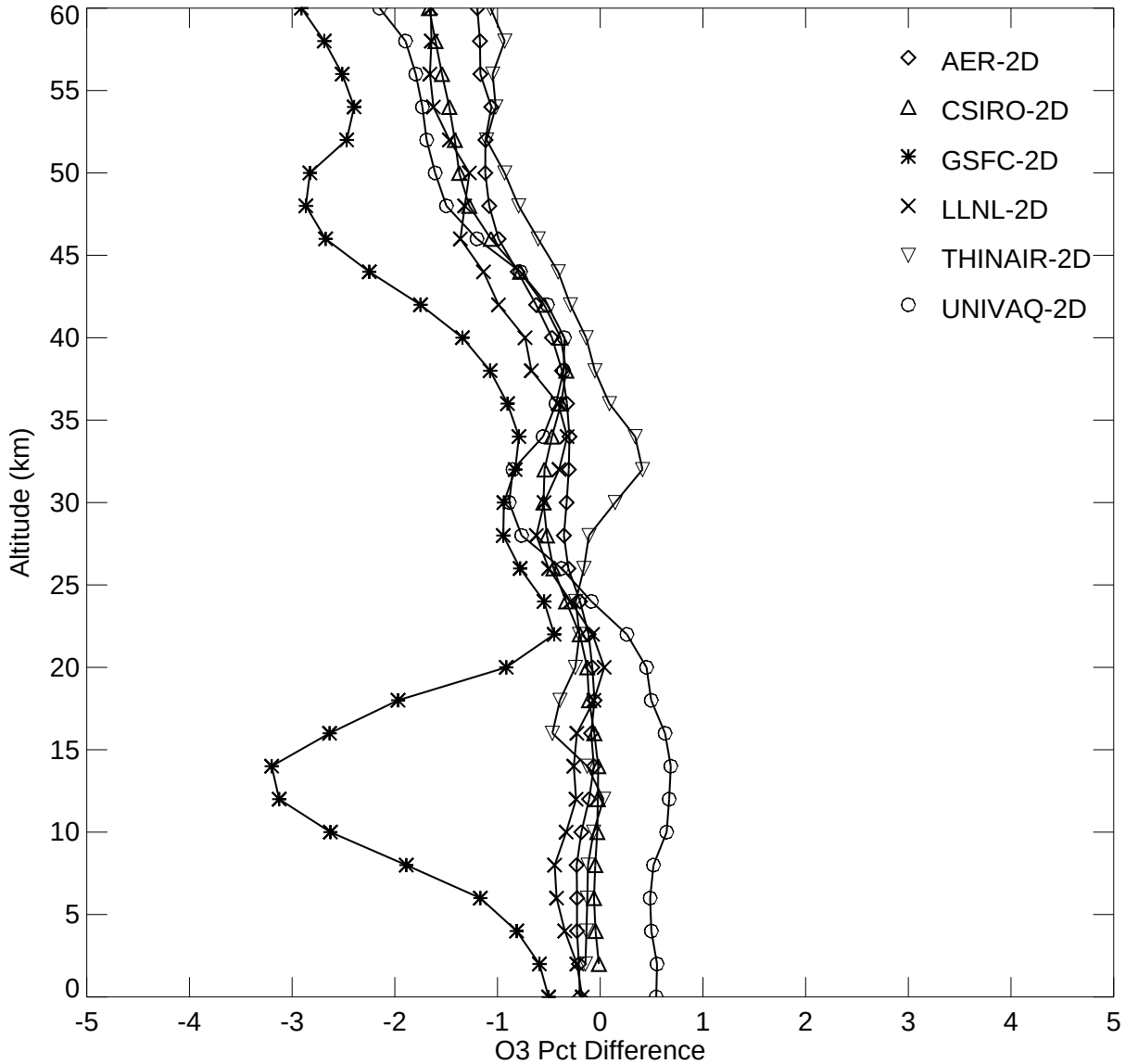

Figure 4.146: Calculated perturbations to O_3 (percent) as a function of altitude at 45°S in June of 2015 due to emissions from a fleet of 500 HSCT aircraft operating at 2 km above nominal cruise altitude with EI(NO_x)=5 under Scenario S2a relative to Scenario D.

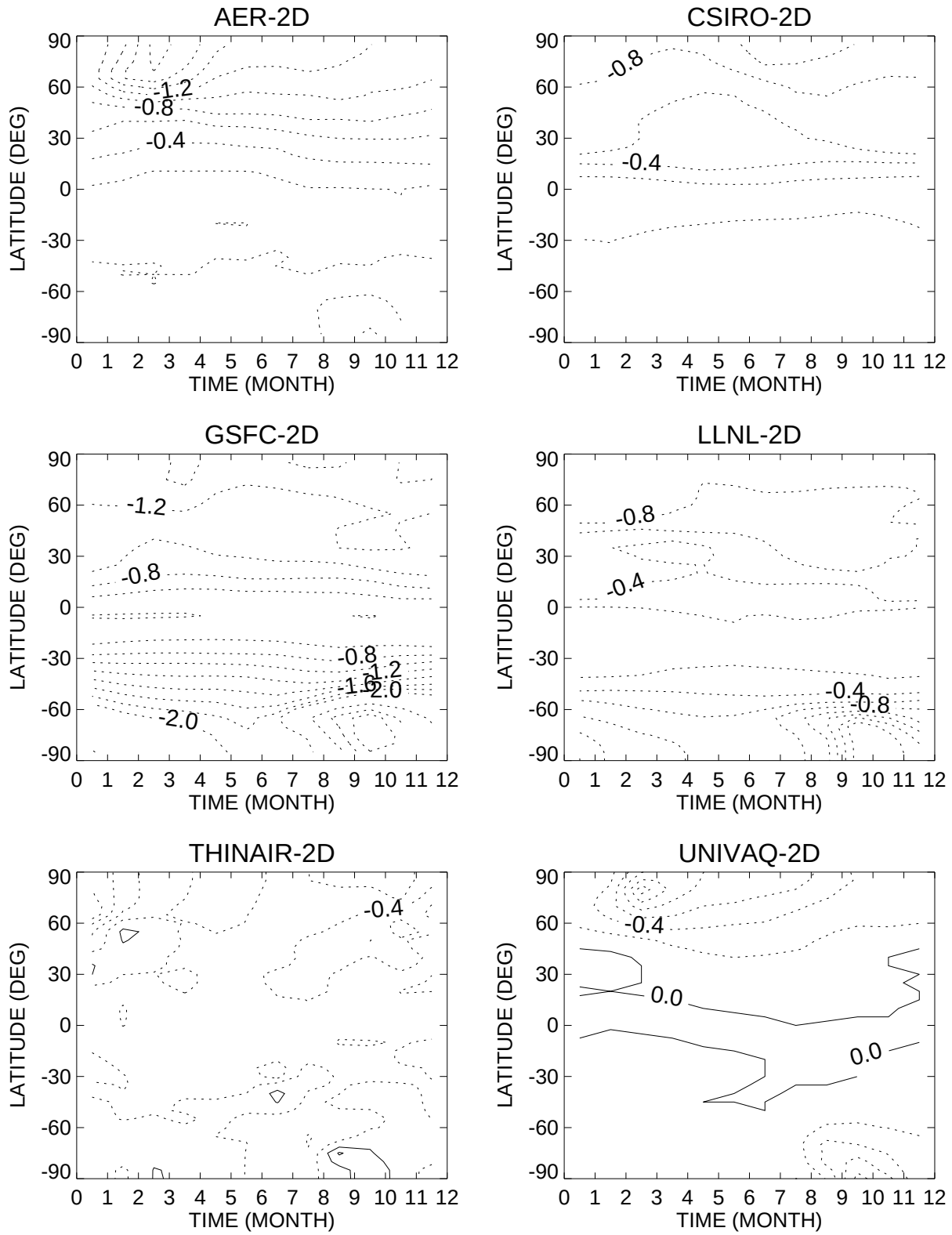

Figure 4.147: Calculated perturbations to column O_3 (percent) as a function of latitude and season in 2015 due to emissions from a fleet of 500 HSCT aircraft operating at 2 km above nominal cruise altitude with EI(NO_x)=5 under Scenario S2a relative to Scenario D. Contours are -5, -4, -3, and -2 to 0 by 0.2.

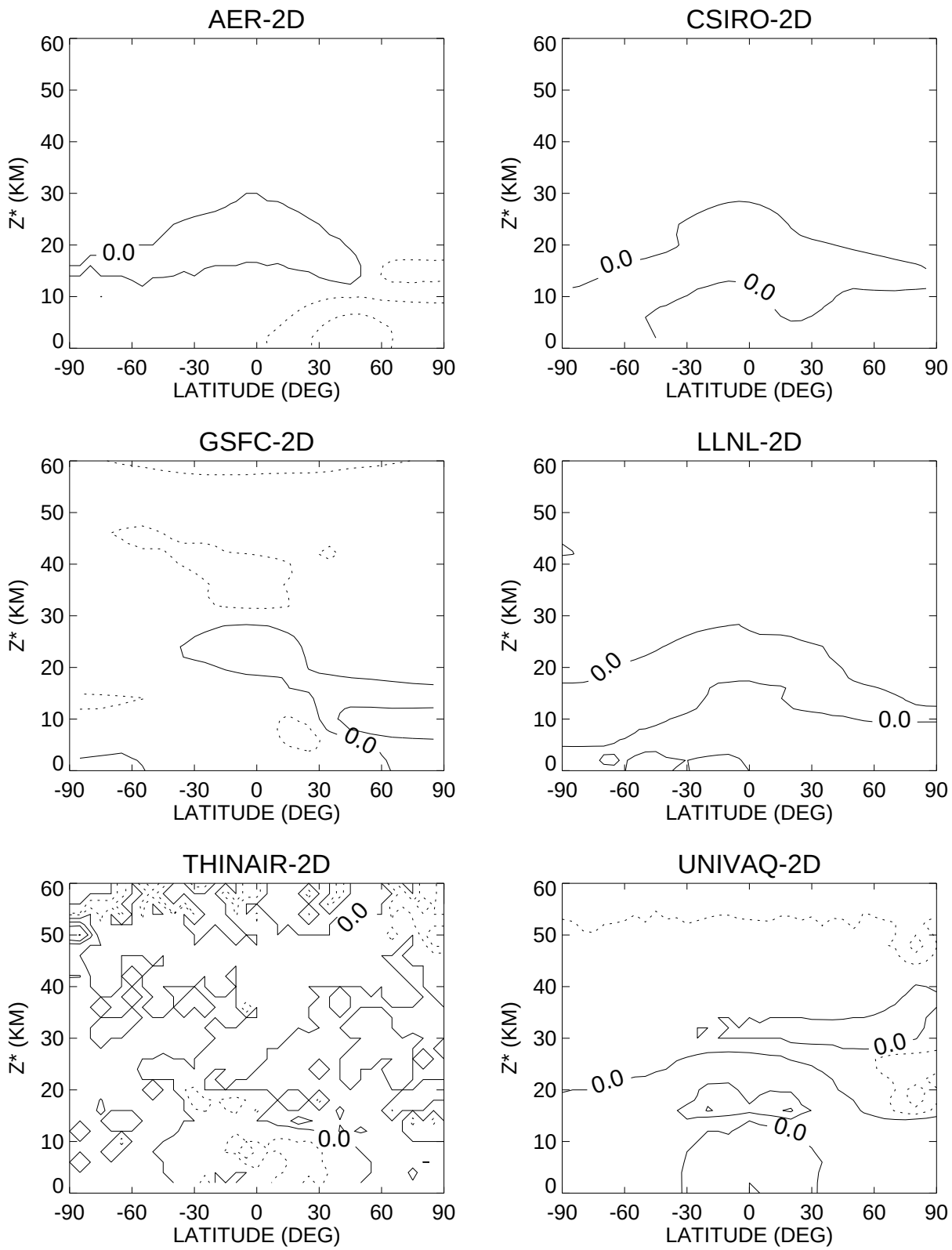

Figure 4.148: Calculated perturbations to O_3 (percent) as a function of latitude and altitude in March of 2015 due to emissions from a fleet of 500 HSCT aircraft operating at 2 km below nominal cruise altitude with EI(NO_x)=5 under Scenario S2b relative to Scenario D. Contours are -1, -0.5, 0, 0.5, 1.

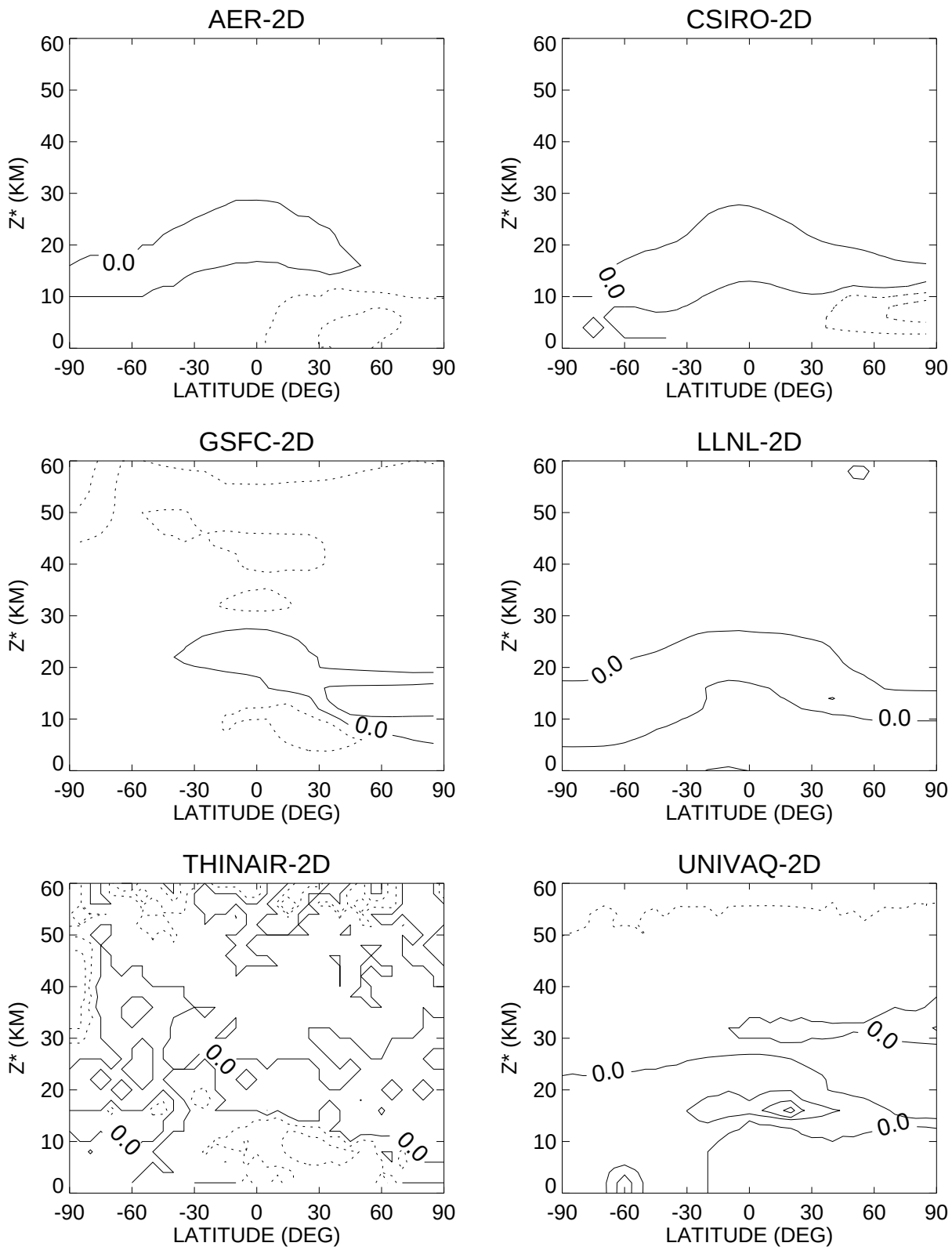

Figure 4.149: Calculated perturbations to O_3 (percent) as a function of latitude and altitude in June of 2015 due to emissions from a fleet of 500 HSCT aircraft operating at 2 km below nominal cruise altitude with EI(NO_x)=5 under Scenario S2b relative to Scenario D. Contours are -1, -0.5, 0, 0.5, 1, 2.

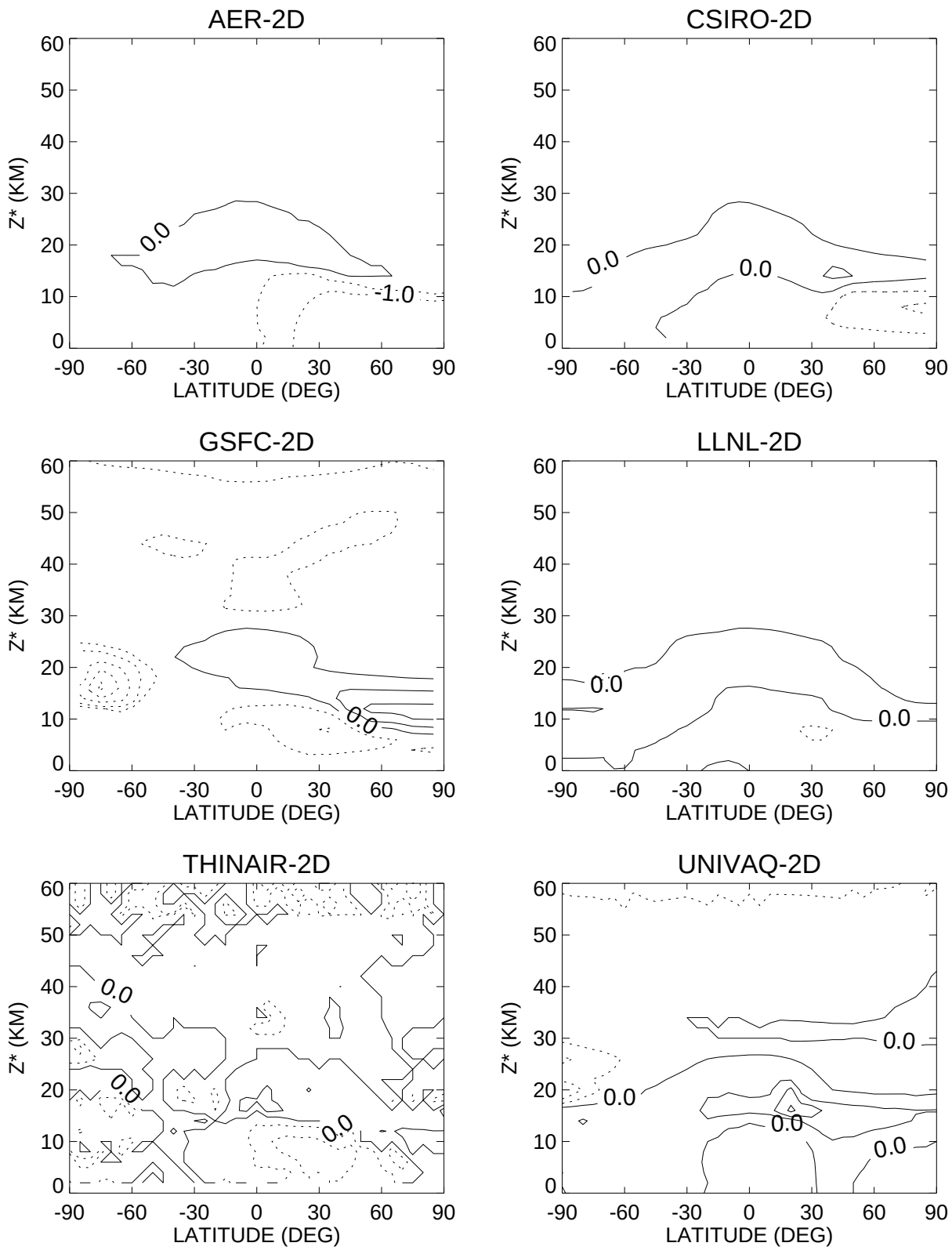

Figure 4.150: Calculated perturbations to O_3 (percent) as a function of latitude and altitude in October of 2015 due to emissions from a fleet of 500 HSCT aircraft operating at 2 km below nominal cruise altitude with EI(NO_x)=5 under Scenario S2b relative to Scenario D. Contours are -4, -3, -2,-1, -0.5, 0, 0.5, 1, 2.

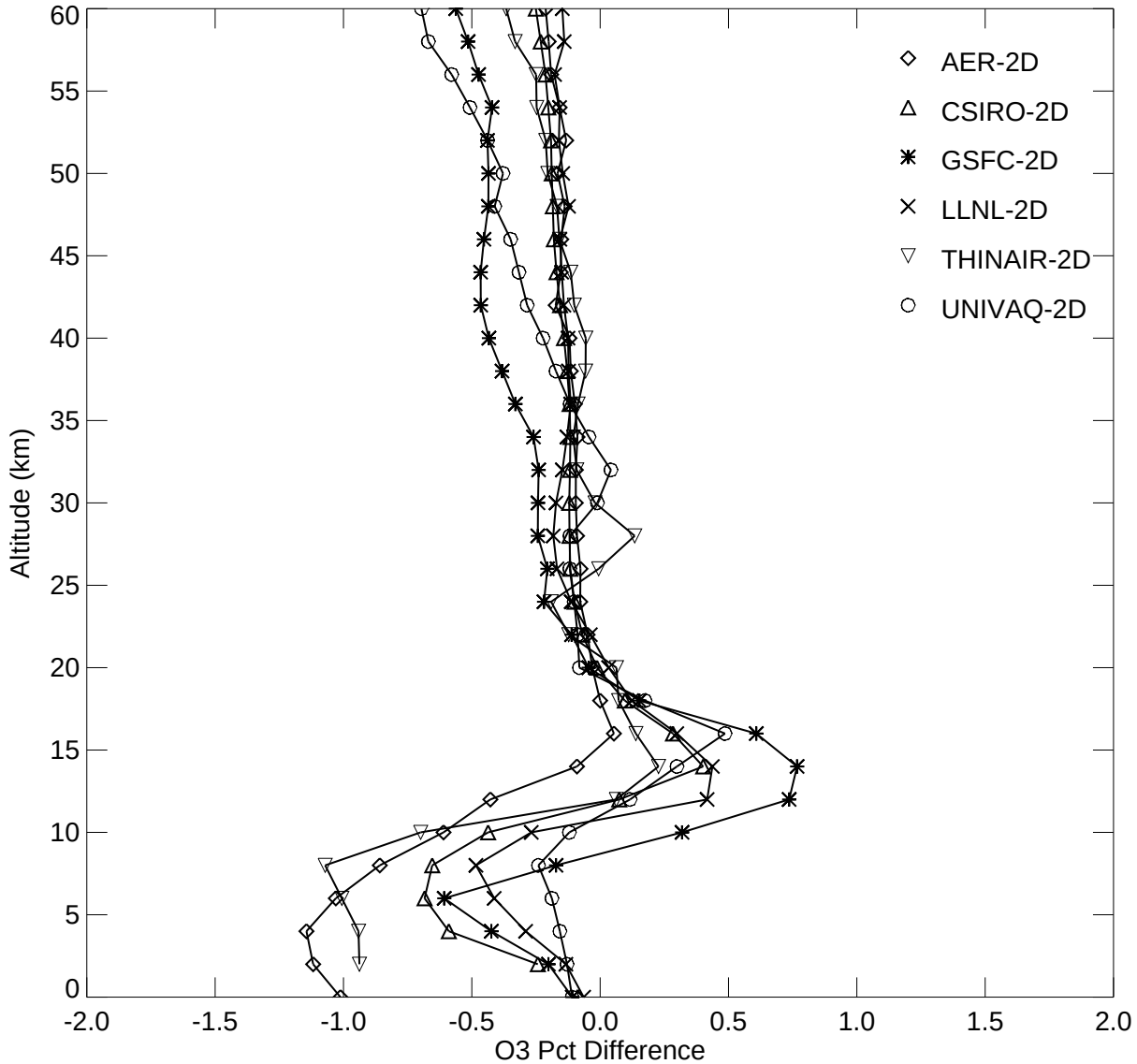

Figure 4.151: Calculated perturbations to O_3 (percent) as a function of altitude at 45^{o}N in June of 2015 due to emissions from a fleet of 500 HSCT aircraft operating at 2 km below nominal cruise altitude with EI(NO_x)=5 under Scenario S2b relative to Scenario D.

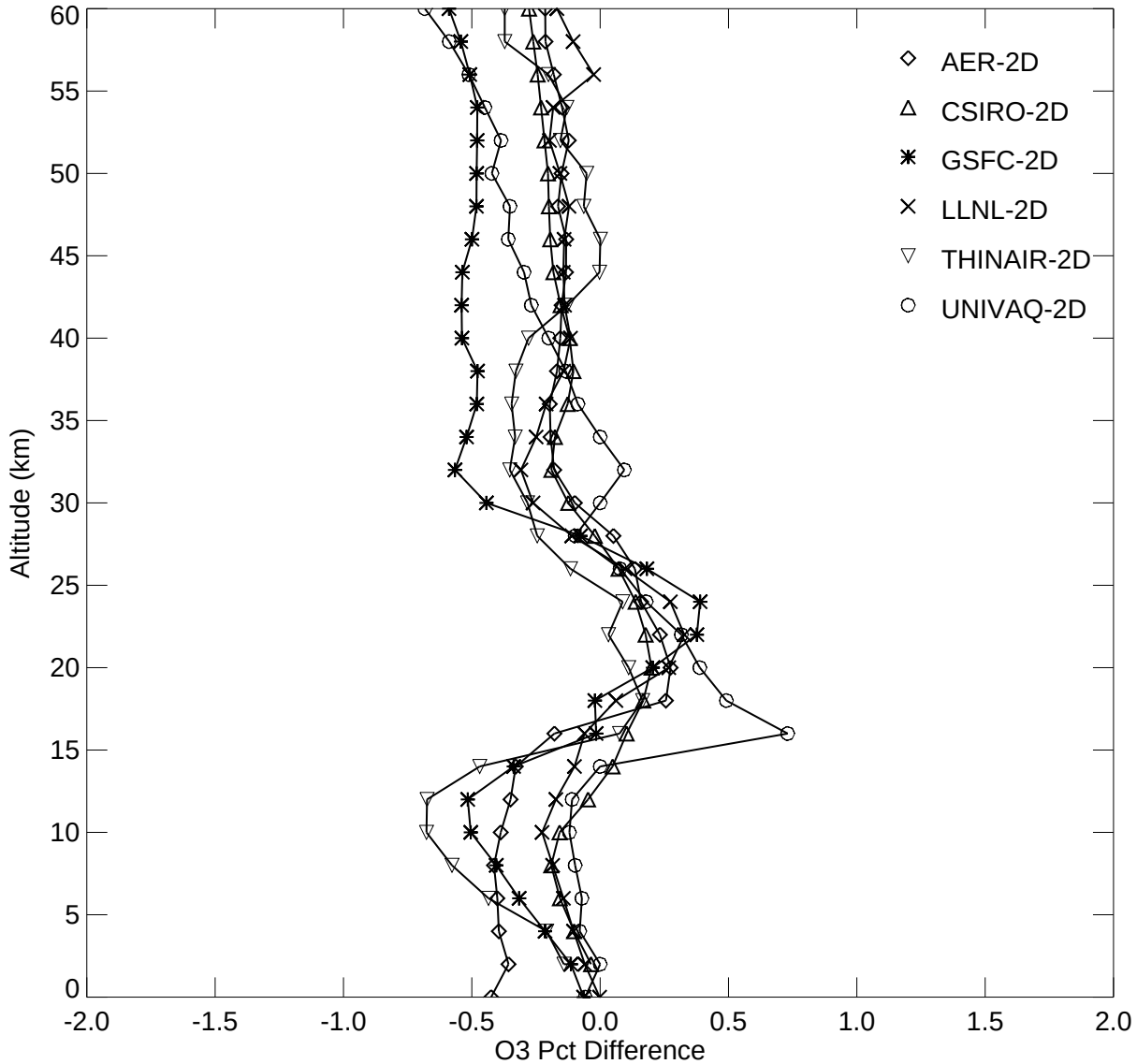

Figure 4.152: Calculated perturbations to O_3 (percent) as a function of altitude at the equator in June of 2015 due to emissions from a fleet of 500 HSCT aircraft operating at 2 km below nominal cruise altitude with EI(NO_x)=5 under Scenario S2b relative to Scenario D.

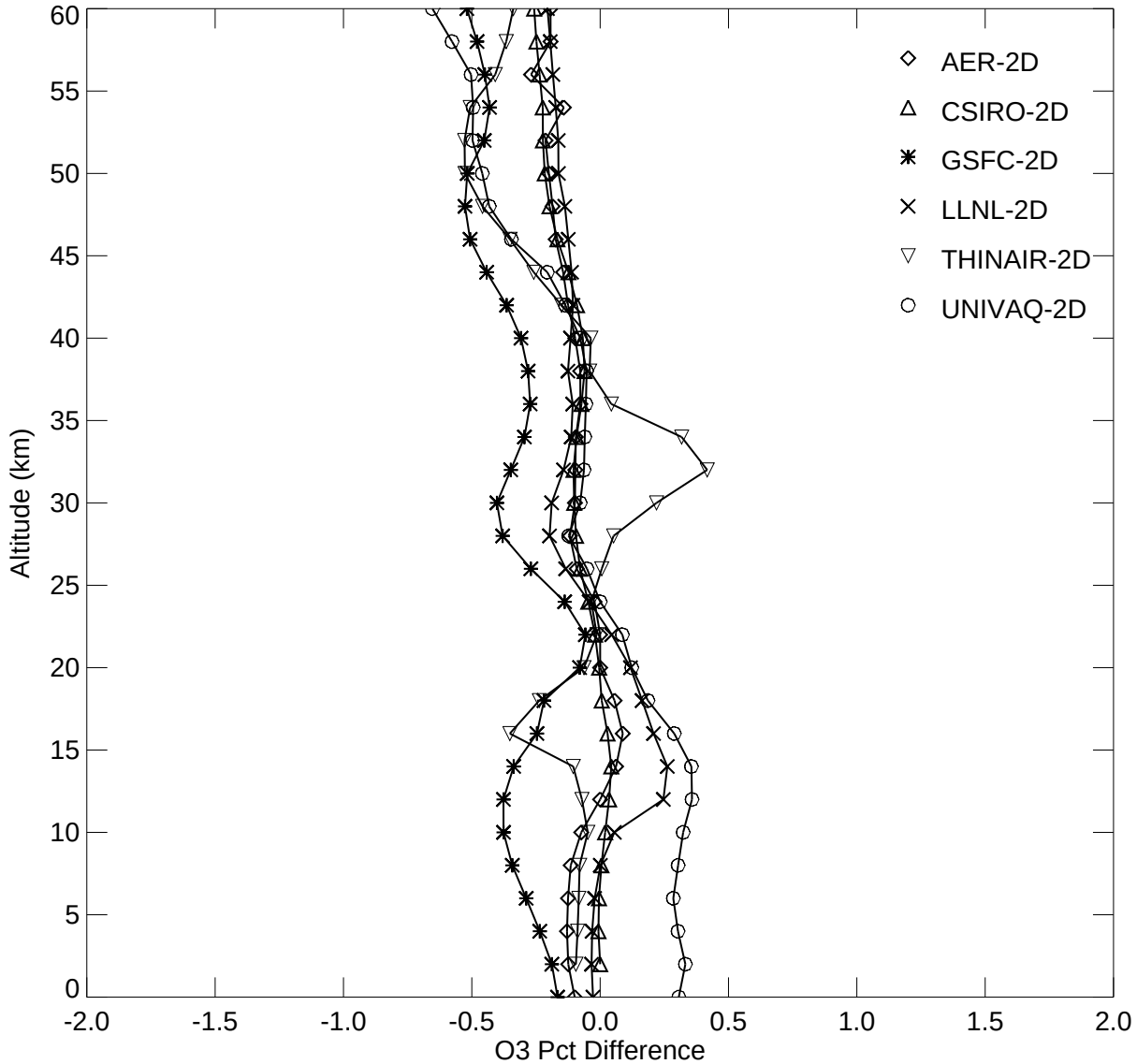

Figure 4.153: Calculated perturbations to O_3 (percent) as a function of altitude at 45^oS in June of 2015 due to emissions from a fleet of 500 HSCT aircraft operating at 2 km below nominal cruise altitude with EI(NO_x)=5 under Scenario S2b relative to Scenario D.

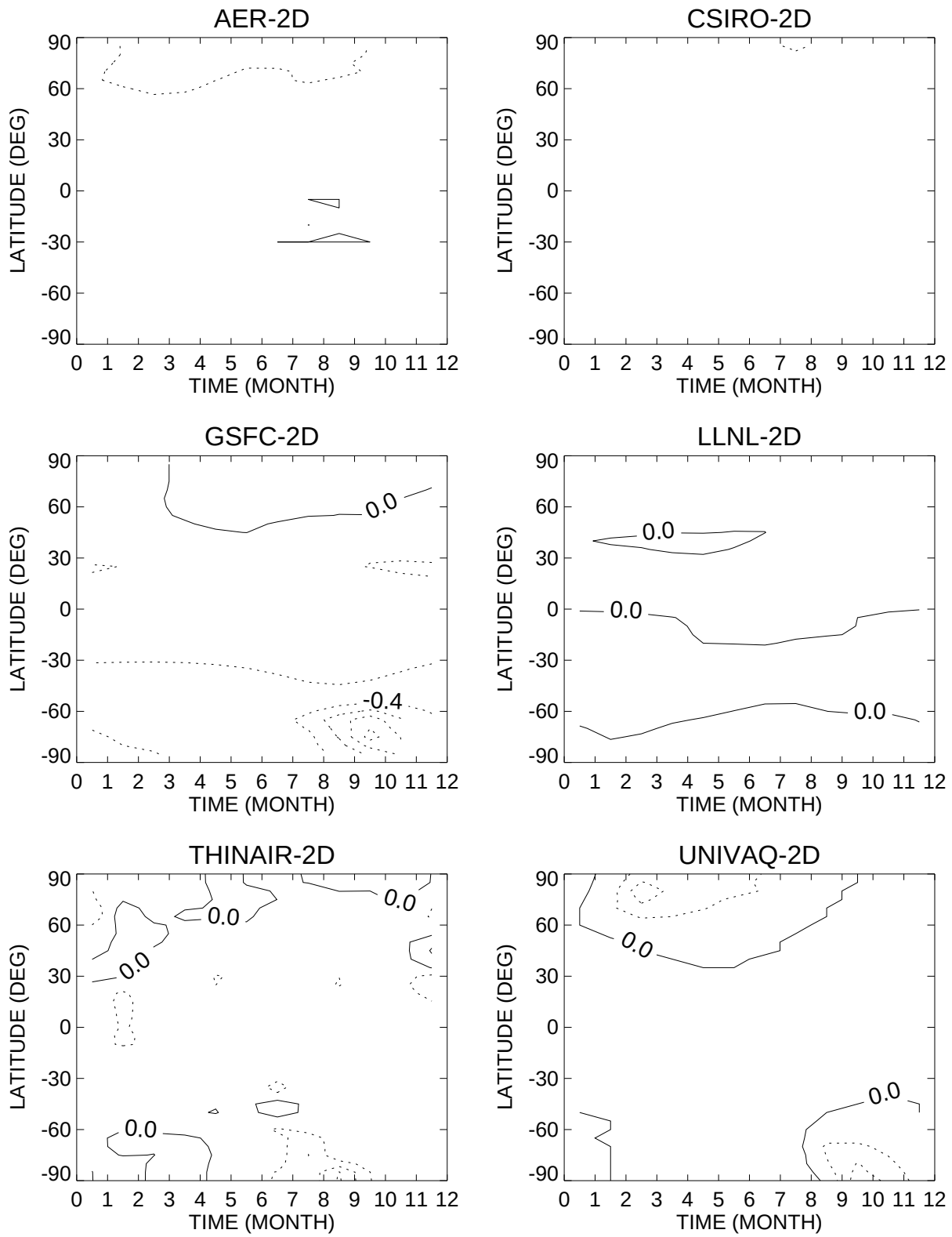

Figure 4.154: Calculated perturbations to column O_3 (percent) as a function of latitude and season in 2015 due to emissions from a fleet of 500 HSCT aircraft operating at 2 km below nominal cruise altitude with EI(NO_x)=5 under Scenario S2b relative to Scenario D. Contours are -1.0 to 0 by 0.2.

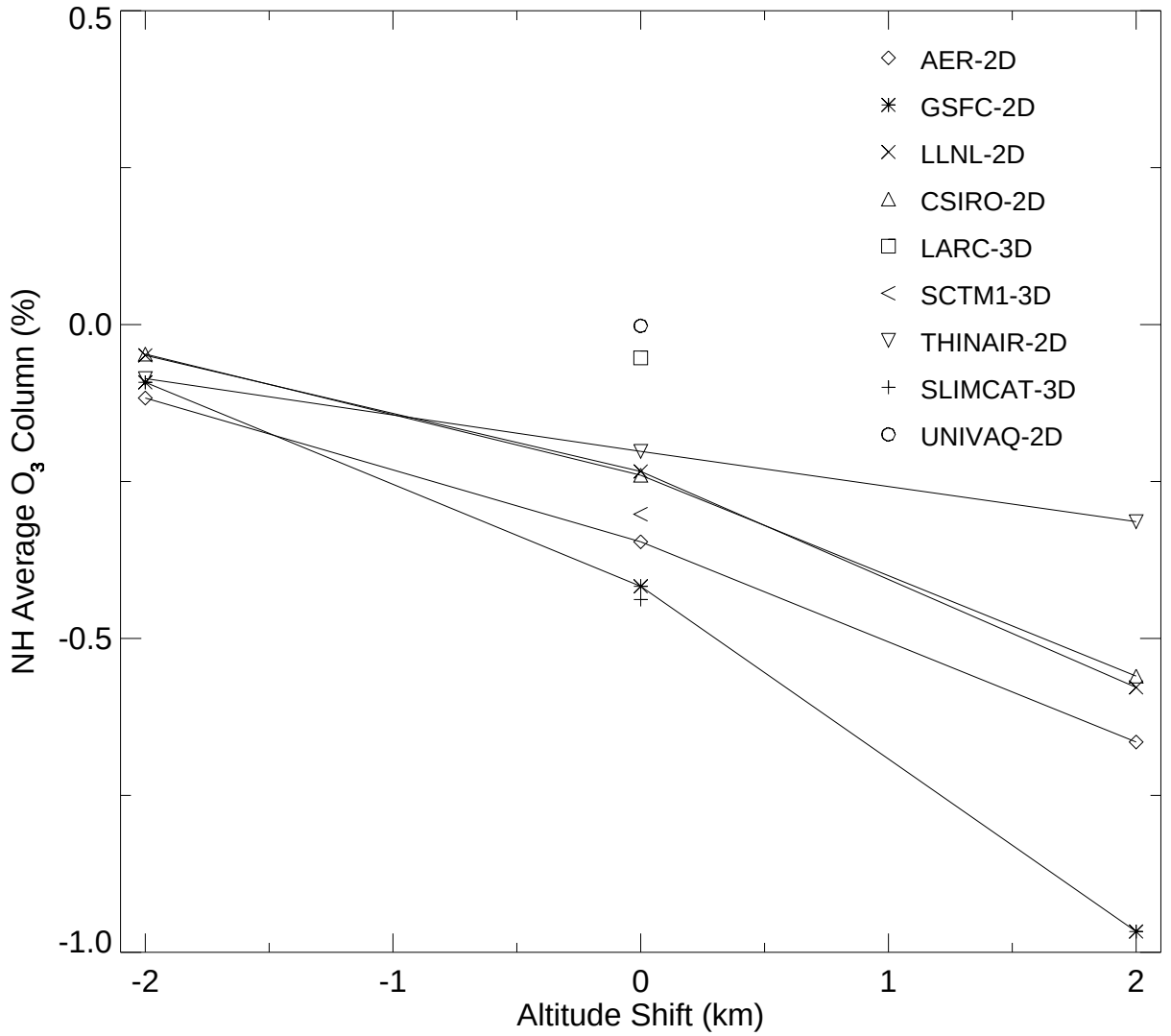

Figure 4.155: Northern hemisphere annual average total O_3 column change (percent) as a function of cruise altitude for an HSCT fleet of 500 aircraft operating in 2015 with EI(NO_x)=5 and SA0 sulfate surface area density.

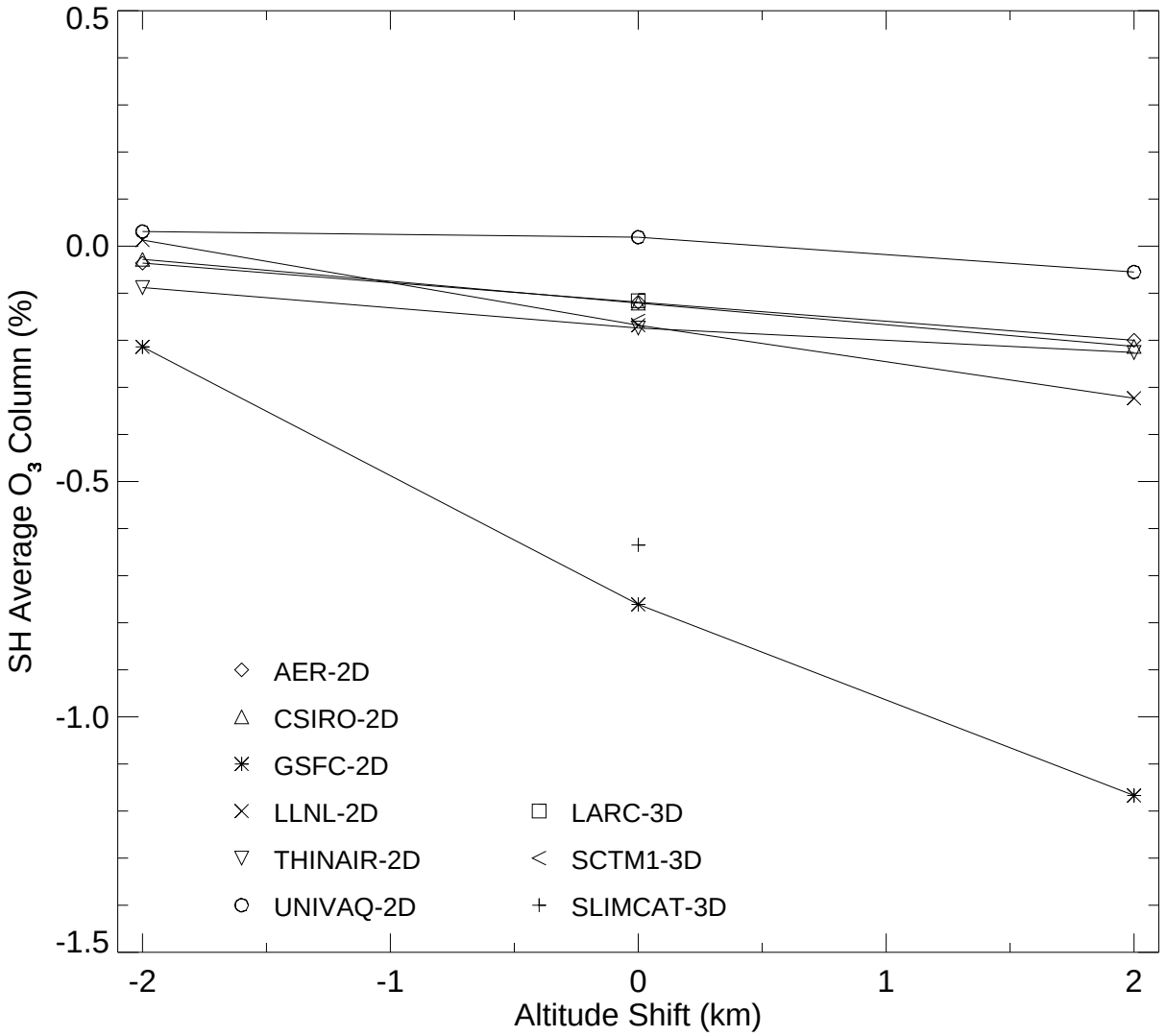

Figure 4.156: Southern hemisphere annual average total O_3 column change (percent) as a function of cruise altitude for an HSCT fleet of 500 aircraft operating in 2015 with EI(NO_x)=5 and SA0 sulfate surface area density.

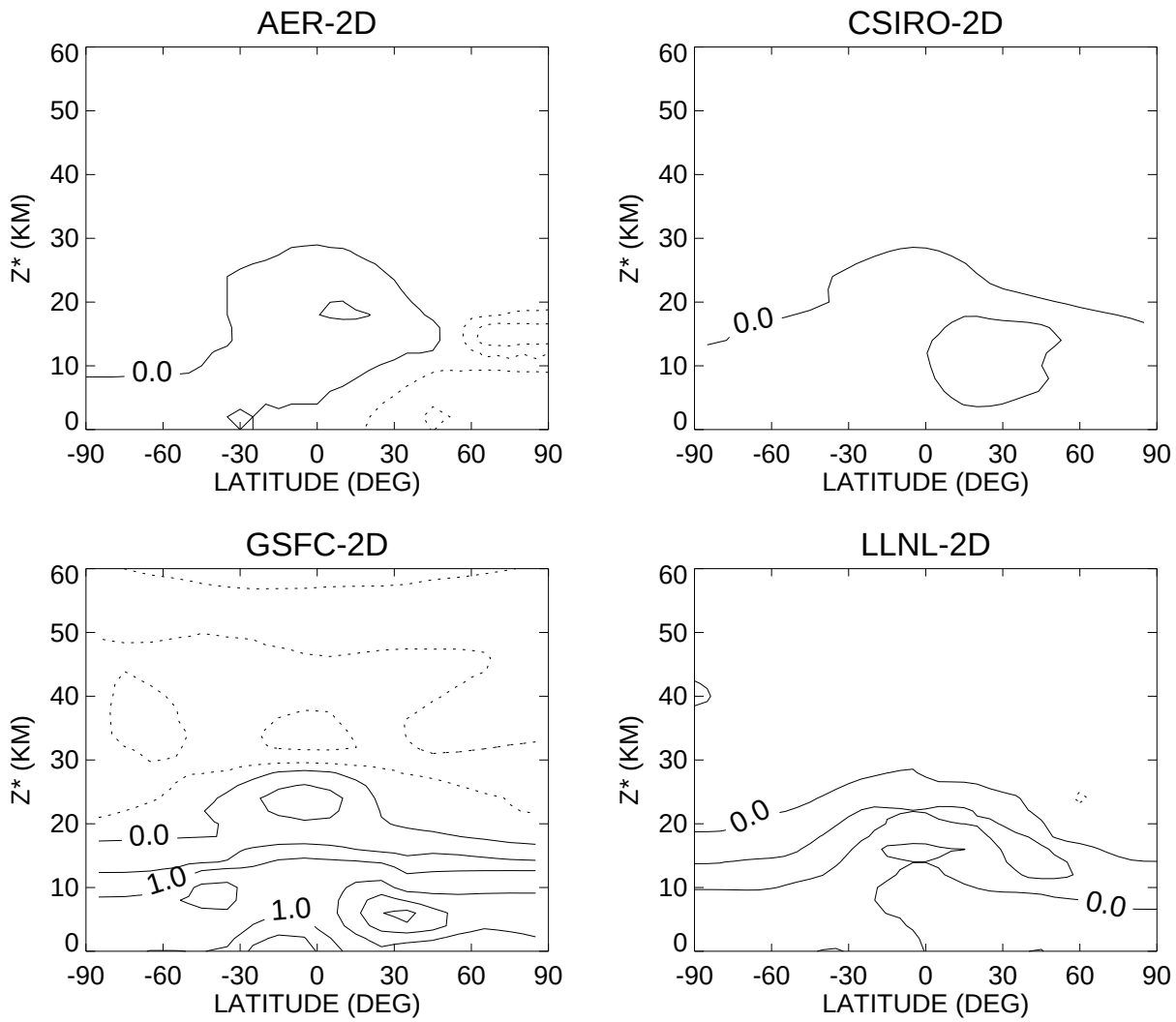

Figure 4.157: Calculated perturbations to O_3 (percent) as a function of latitude and altitude in March of 2015 due to emissions from a fleet of 500 HSCT aircraft operating at 2 km below nominal cruise altitude with EI(NO_x)=10 under Scenario S2c relative to Scenario D. Contours are -1, -0.5, 0, 0.5, 1, 2, 3, 4.

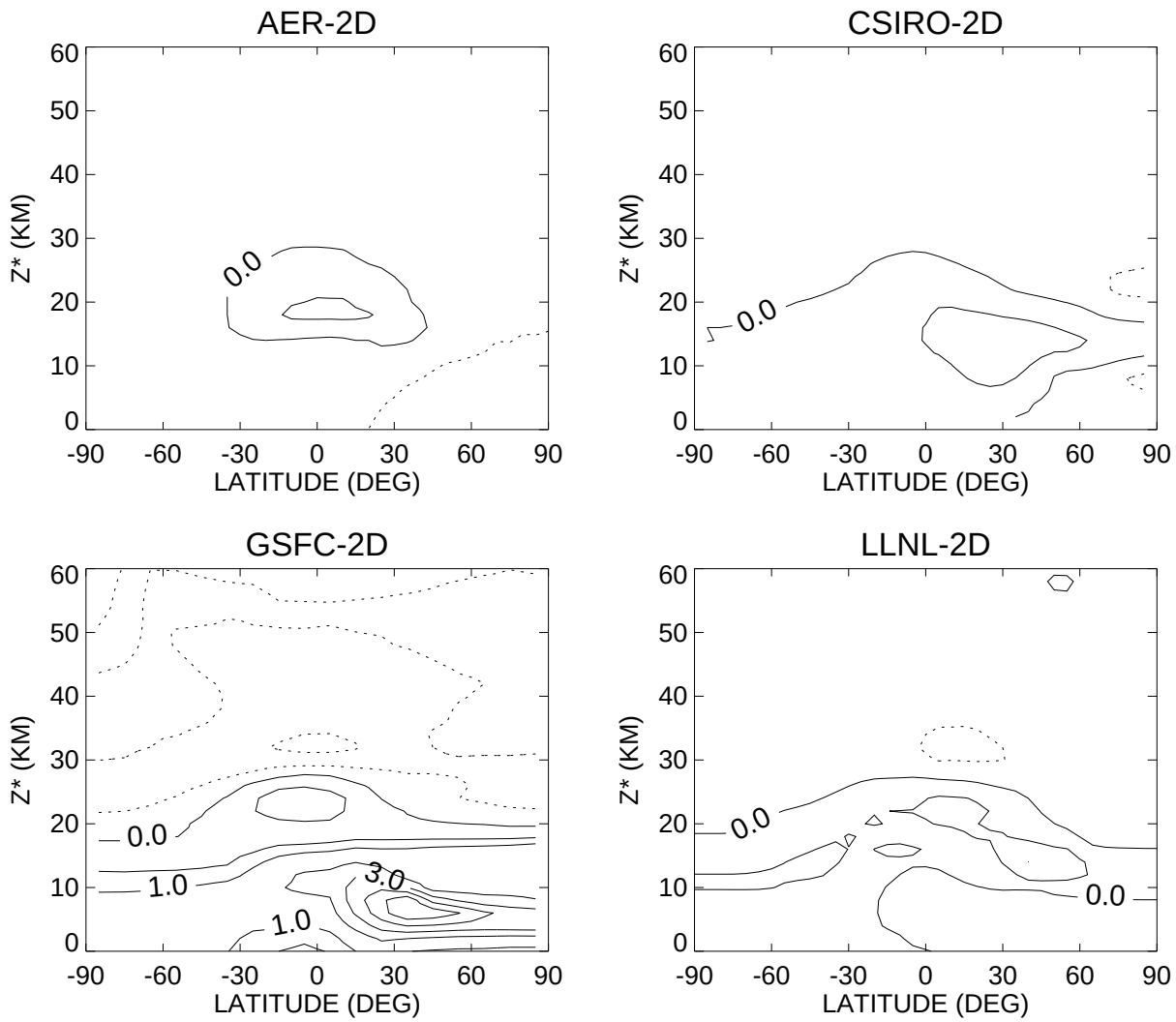

Figure 4.158: Calculated perturbations to O_3 (percent) as a function of latitude and altitude in June of 2015 due to emissions from a fleet of 500 HSCT aircraft operating at 2 km below nominal cruise altitude with EI(NO_x)=10 under Scenario S2c relative to Scenario D. Contours are -1, -0.5, 0, 0.5, 1, 2, 3, 4, 5.

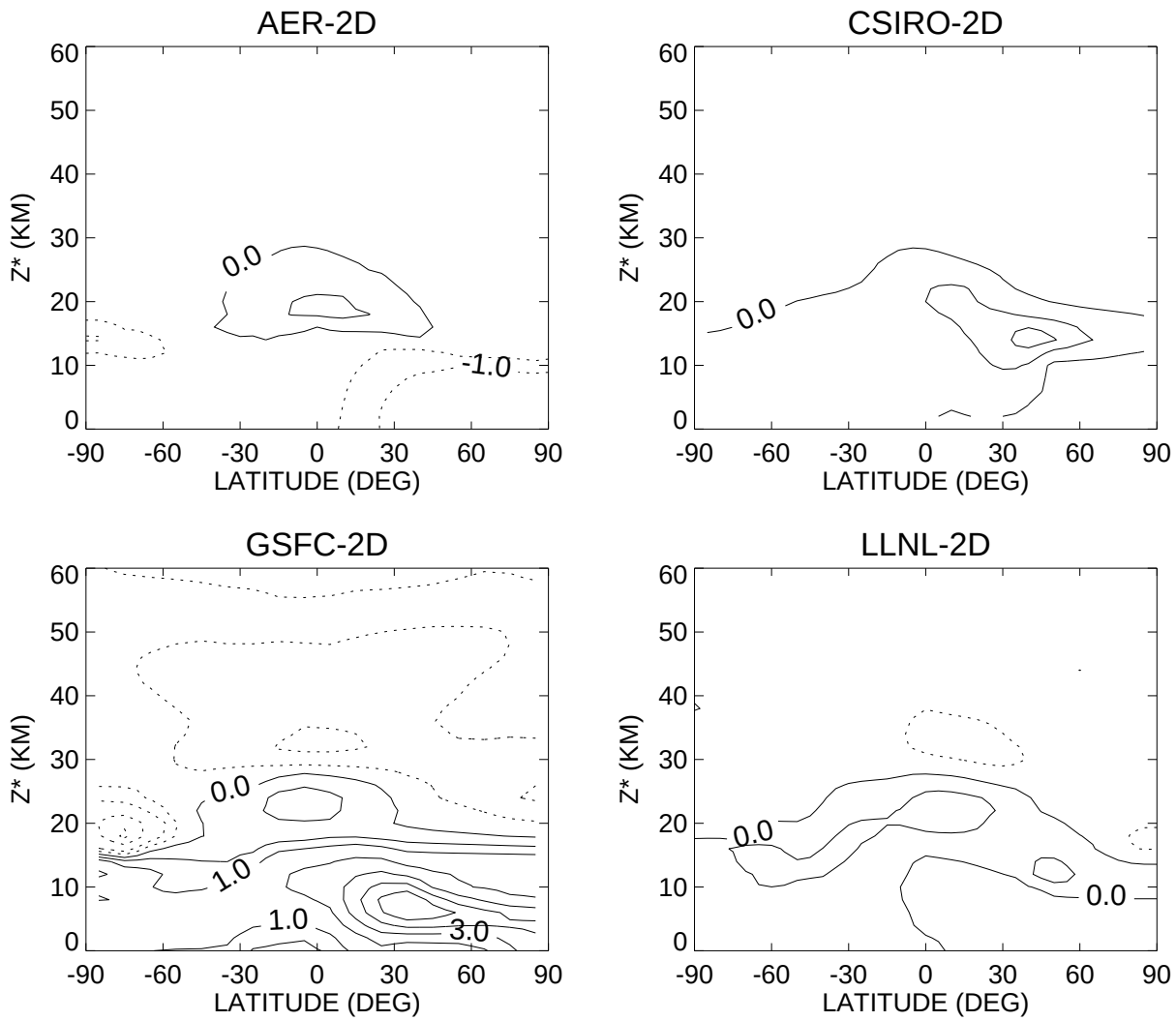

Figure 4.159: Calculated perturbations to O_3 (percent) as a function of latitude and altitude in October of 2015 due to emissions from a fleet of 500 HSCT aircraft operating at 2 km below nominal cruise altitude with EI(NO_x)=10 under Scenario S2c relative to Scenario D. Contours are -3, -2, -1, -0.5, 0, 0.5, 1, 2, 3, 4, 5.

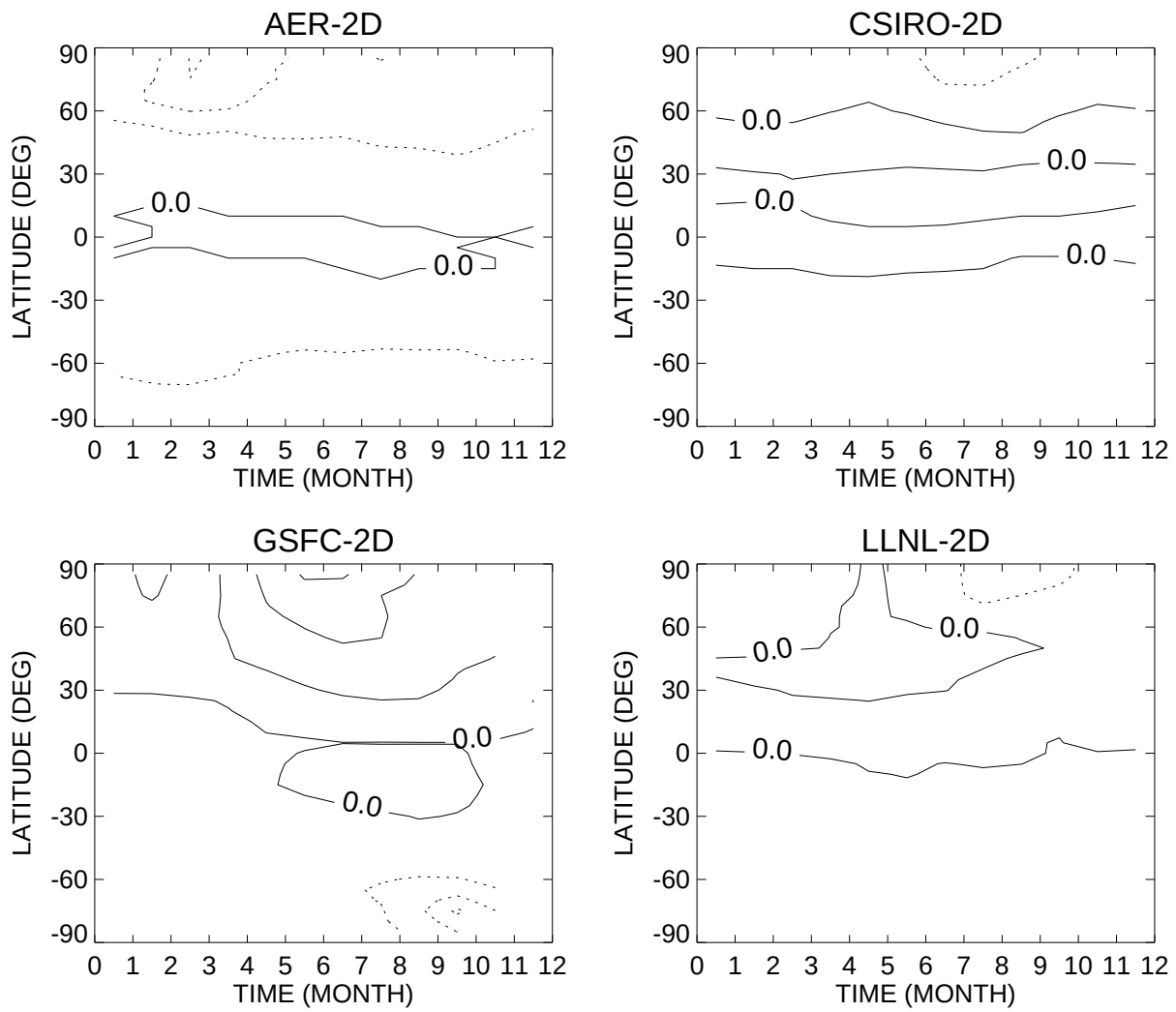

Figure 4.160: Calculated perturbations to column O_3 (percent) as a function of latitude and season in 2015 due to emissions from a fleet of 500 HSCT aircraft operating at 2 km below nominal cruise altitude with EI(NO_x)=10 under Scenario S2c relative to Scenario D. Contours are -0.6 to 0.6 by 0.2.

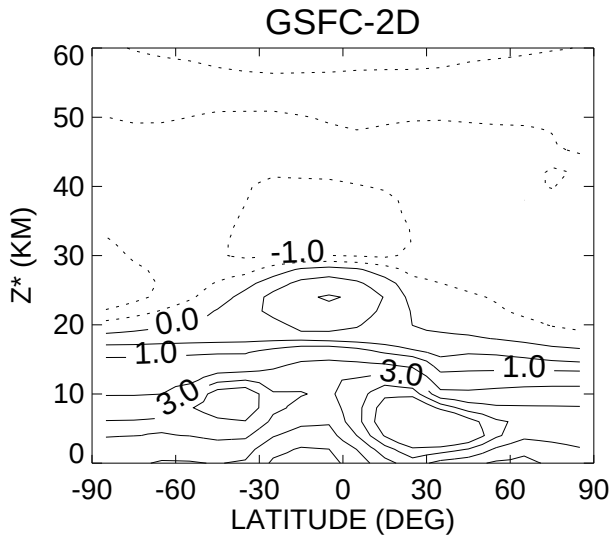

Figure 4.161: Calculated perturbations to O_3 (percent) as a function of latitude and altitude in March of 2015 due to emissions from a fleet of 500 HSCT aircraft operating at 2 km below nominal cruise altitude with EI(NO_x)=15 under Scenario S2d relative to Scenario D. Contours are -1, -0.5, 0, 0.5, 1, 2, 3, 4, 5.

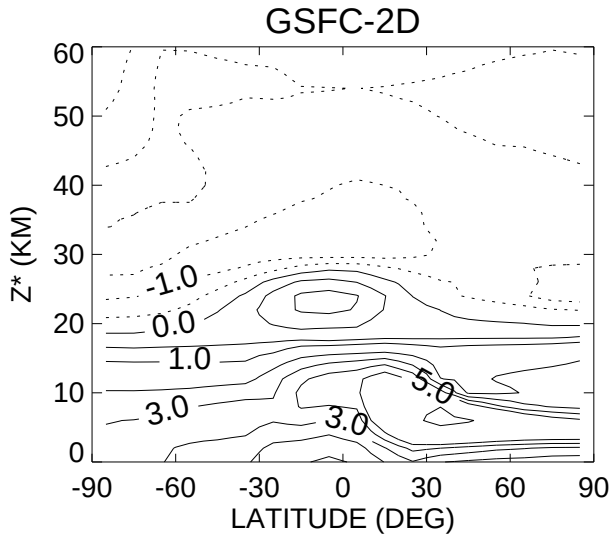

Figure 4.162: Calculated perturbations to O_3 (percent) as a function of latitude and altitude in June of 2015 due to emissions from a fleet of 500 HSCT aircraft operating at 2 km below nominal cruise altitude with EI(NO_x)=15 under Scenario S2d relative to Scenario D. Contours are -1, -0.5, 0, 0.5, 1, 2, 3, 4, 5, 10.

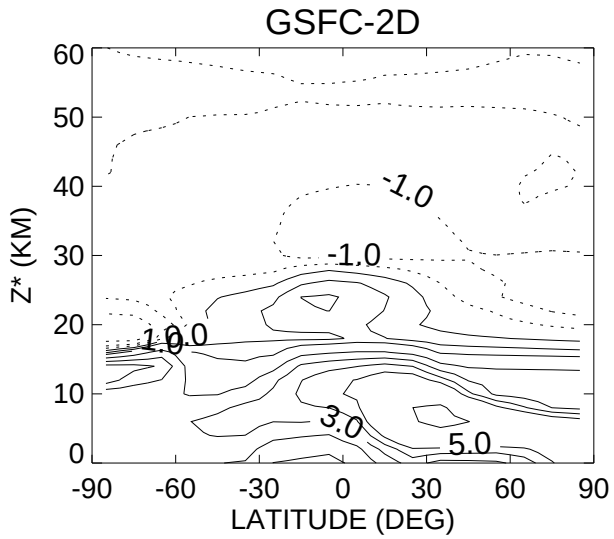

Figure 4.163: Calculated perturbations to O_3 (percent) as a function of latitude and altitude in October of 2015 due to emissions from a fleet of 500 HSCT aircraft operating at 2 km below nominal cruise altitude with EI(NO_x)=15 under Scenario S2d relative to Scenario D. Contours are -1, -0.5, 0, 0.5, 1, 2, 3, 4, 5, 10.

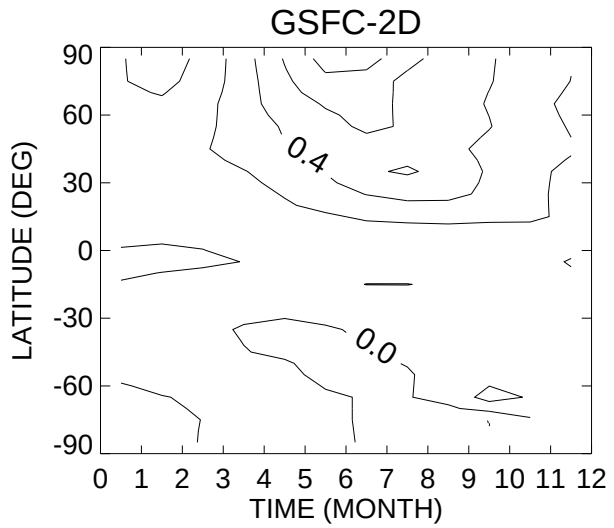

Figure 4.164: Calculated perturbations to column O_3 (percent) as a function of latitude and season in 2015 due to emissions from a fleet of 500 HSCT aircraft operating at 2 km below nominal cruise altitude with EI(NO_x)=15 under Scenario S2d relative to Scenario D. Contours are 0 to 0.8 by 0.2.

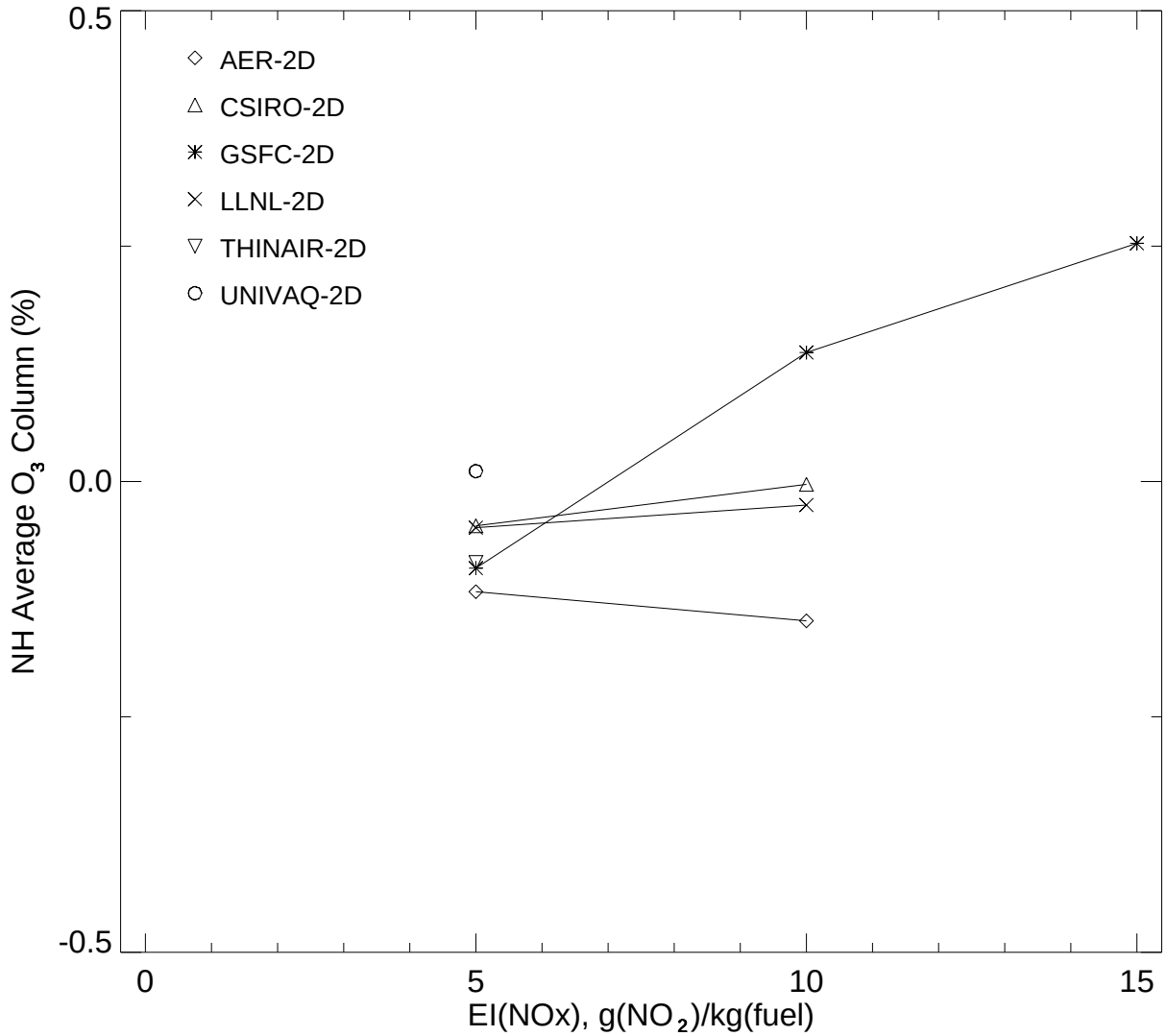

Figure 4.165: Northern hemisphere annual average total O_3 column change (percent) as a function of EI(NO_x) for an HSCT fleet of 500 aircraft operating in 2015 at 2 km below nominal cruise altitude with SA0 sulfate surface area density.

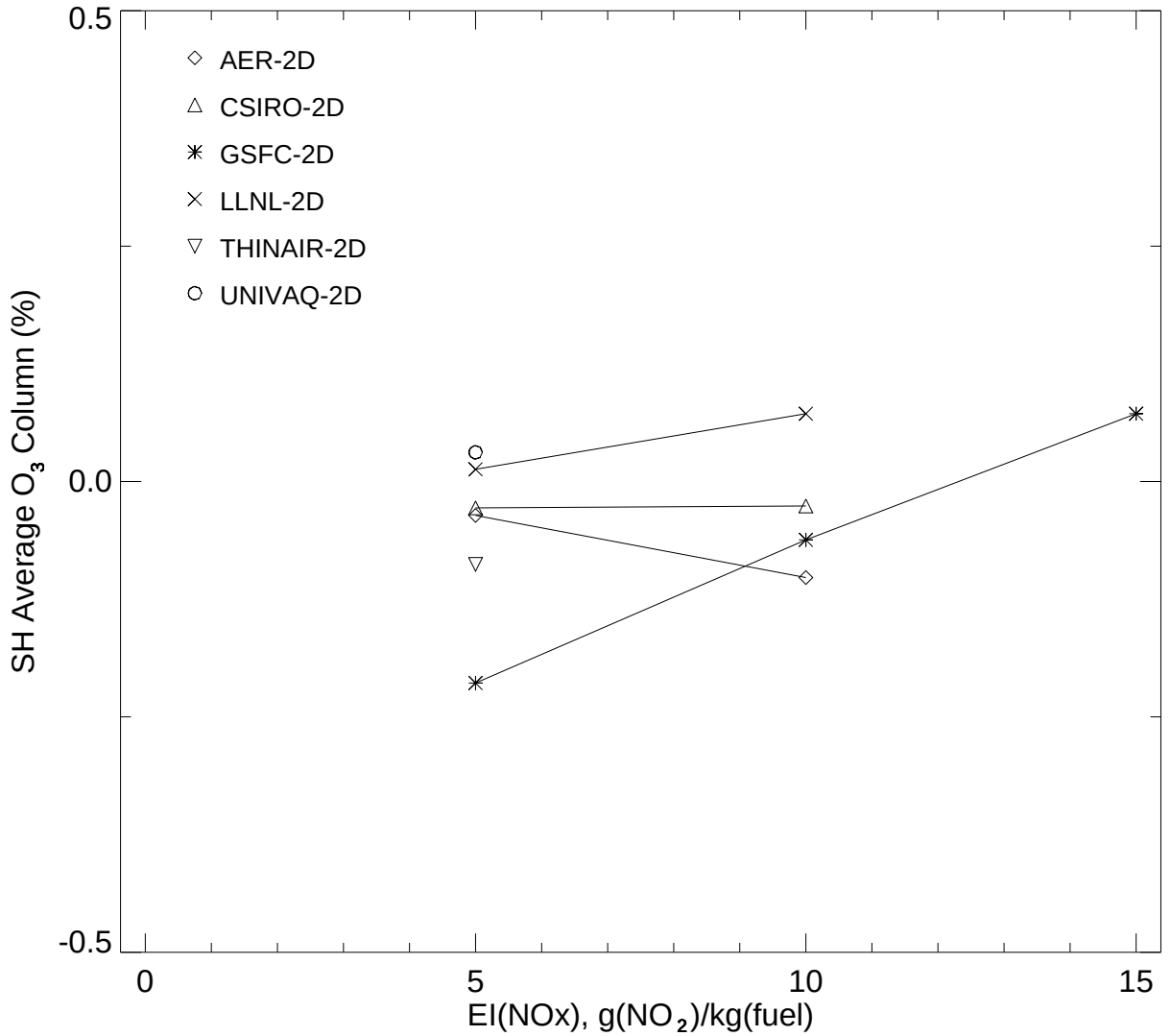

Figure 4.166: Southern hemisphere annual average total O_3 column change (percent) as a function of EI(NO_x) for an HSCT fleet of 500 aircraft operating in 2015 at 2 km below nominal cruise altitude with SA0 sulfate surface area density.

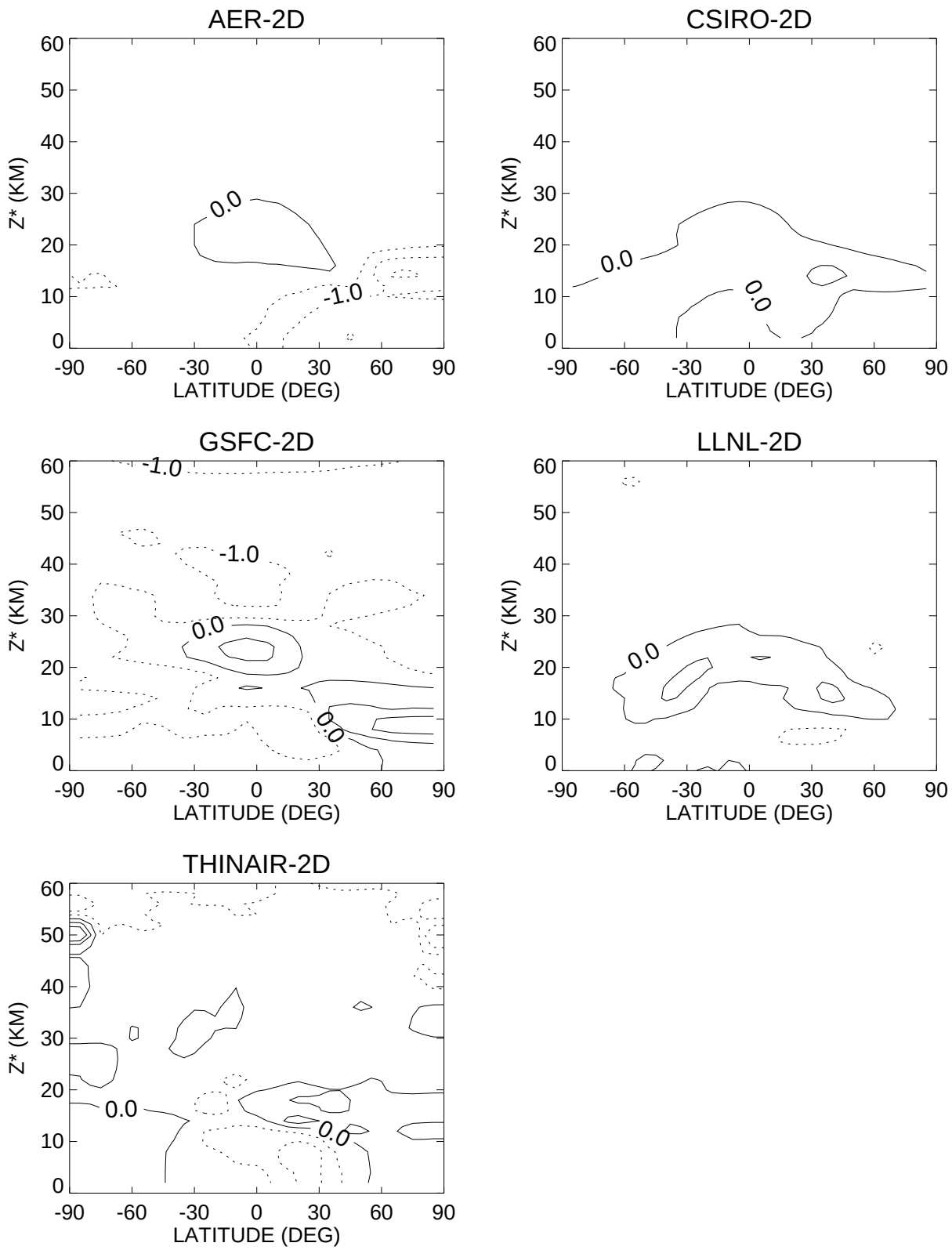

Figure 4.167: Calculated perturbations to O_3 (percent) as a function of latitude and altitude in March of 2015 due to emissions from a fleet of 1000 HSCT aircraft operating at 2 km below nominal cruise altitude with EI(NO_x)=5 under Scenario S2e relative to Scenario D. Contours are -2, -1, -0.5, 0, 0.5, 1.

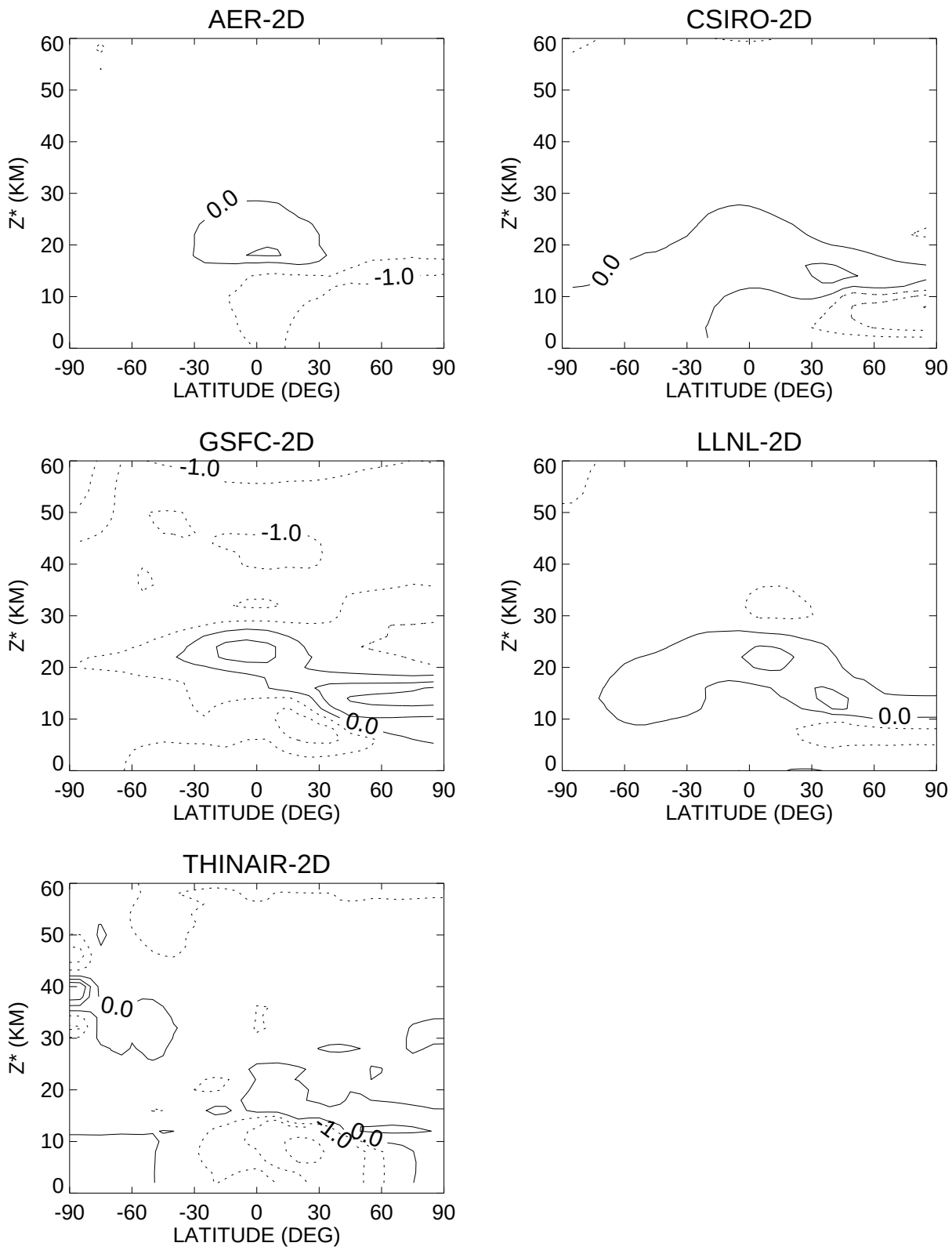

Figure 4.168: Calculated perturbations to O_3 (percent) as a function of latitude and altitude in June of 2015 due to emissions from a fleet of 1000 HSCT aircraft operating at 2 km below nominal cruise altitude with EI(NO_x)=5 under Scenario S2e relative to Scenario D. Contours are -1, -0.5, 0, 0.5, 1.

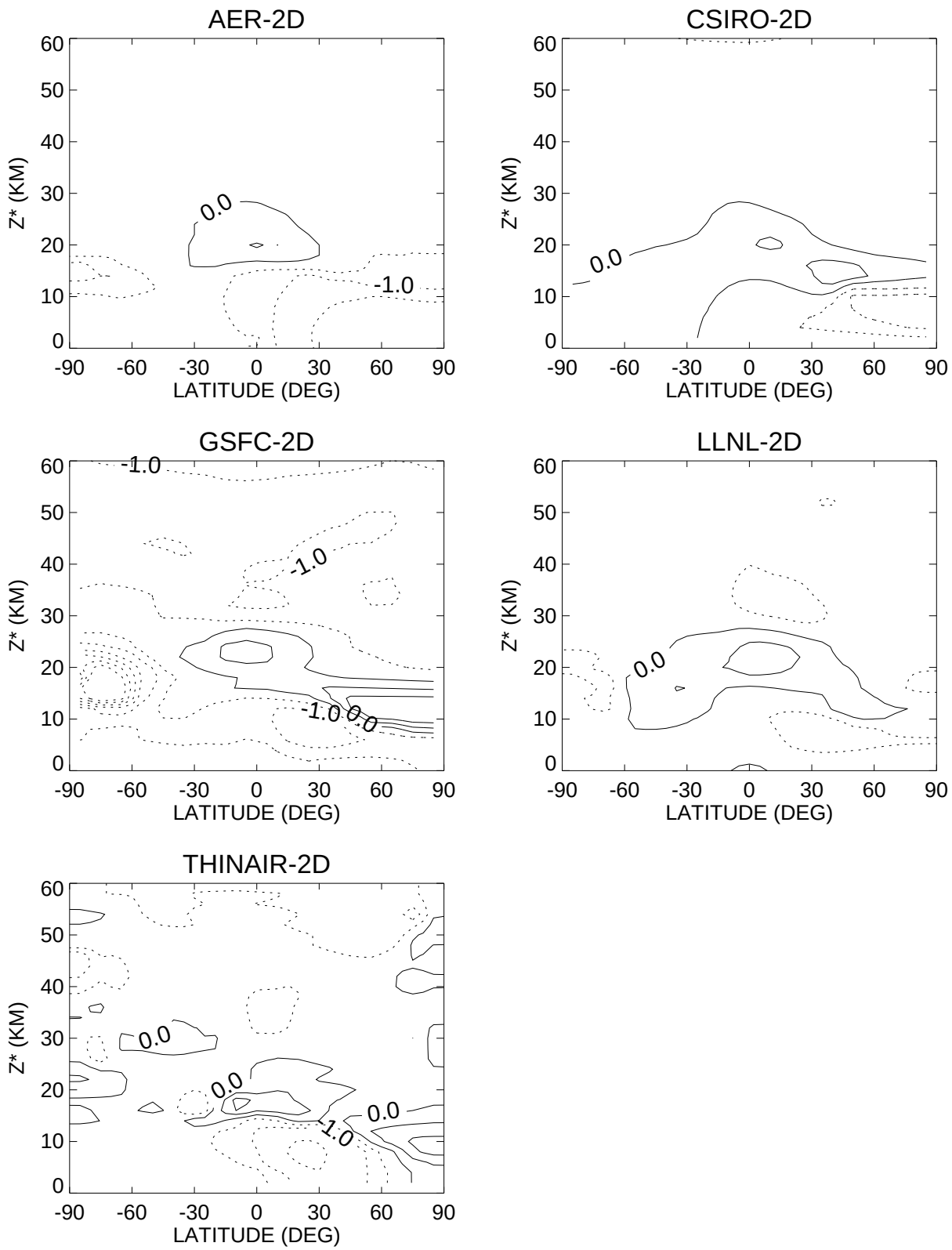

Figure 4.169: Calculated perturbations to O_3 (percent) as a function of latitude and altitude in October of 2015 due to emissions from a fleet of 1000 HSCT aircraft operating at 2 km below nominal cruise altitude with EI(NO_x)=5 under Scenario S2e relative to Scenario D. Contours are -5, -4, -3, -2, -1, -0.5, 0, 0.5, 1.

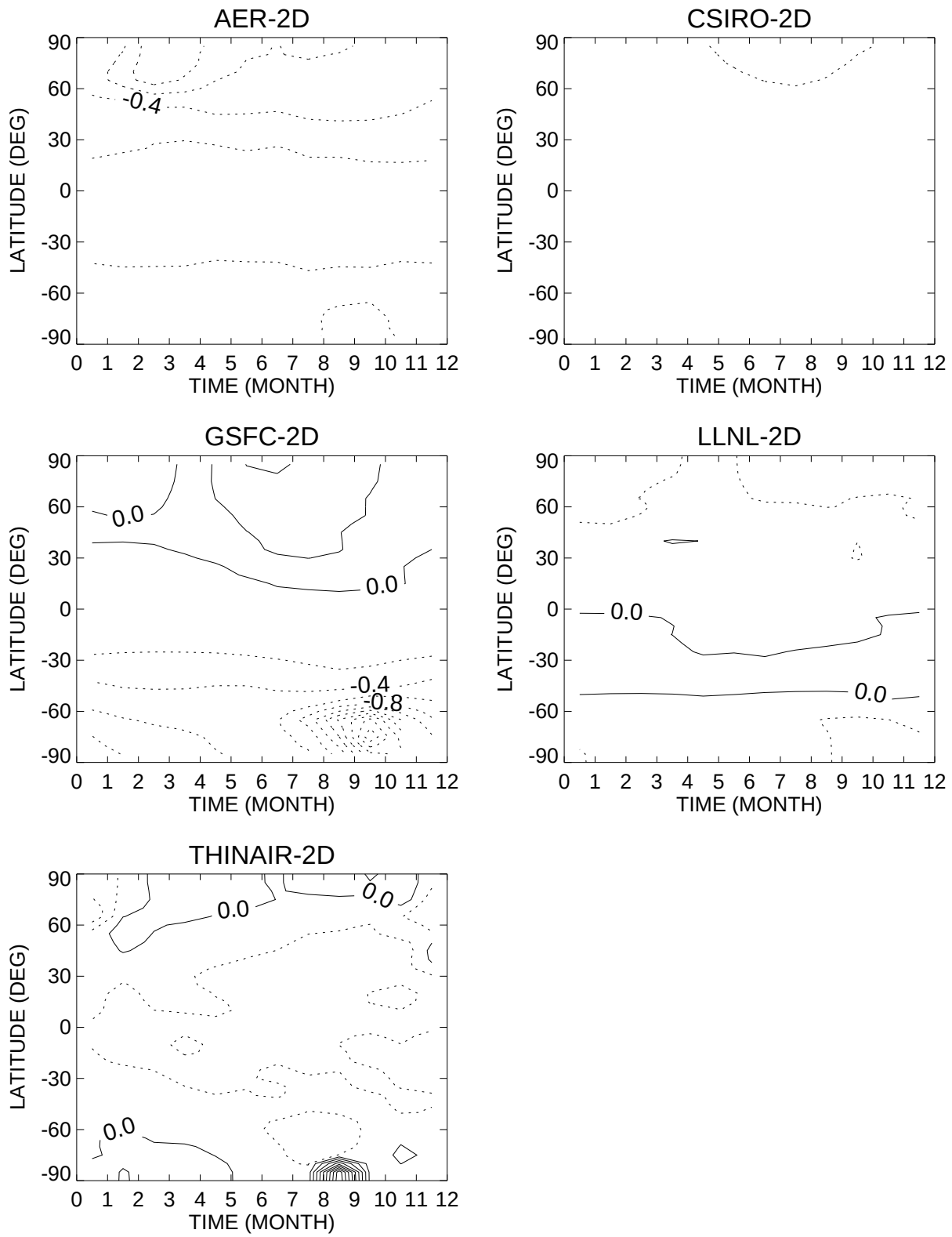

Figure 4.170: Calculated perturbations to column O_3 (percent) as a function of latitude and season in 2015 due to emissions from a fleet of 1000 HSCT aircraft operating at 2 km below nominal cruise altitude with EI(NO_x)=5 under Scenario S2e relative to Scenario D. Contours are -2.0 to 0.4 by 0.2.

4.3.4 Scenarios with Enhanced Background Aerosol (S3a-f)

This section will cover Scenarios S3a-S3f which use enhanced background surface area to simulate a volcanically active period. The background SAD is 4xSA0 for the HSCT scenarios in this section and the 2015 subsonic-only atmosphere (Scenario D3) with which they are compared. As discussed in Chapter 2.2, the increased aerosol SAD leads to reduced ozone below 20 km and increased ozone from 20-30 km for the D3 background atmosphere relative to Scenario D with SA0 sulfate surface area density. Total ozone amounts were several percent less with 4xSA0 than with SA0. For this sensitivity study, EI(NO_x) is varied from 0 to 15 in Scenarios S3a-S3d with no sulfur emitted by the 500 HSCT aircraft. Scenarios S3e and S3f do include aircraft sulfur emission with EI(NO_x)=5.

Scenario S3a represents 500 HSCT aircraft operating in 2015 with EI(NO_x)=0, no sulfur emissions, and a background sulfate surface area density of 4xSA0. Differences in ozone between this scenario and the 2015 background atmosphere with subsonic aircraft and sulfate surface area density of 4xSA0 (Scenario D3) are shown in Figures 4.171, 4.172, and 4.173 for March, June, and October. The models all show ozone depletion below 25 km and above 35 km due to the HSCT H_2O emissions. This is generally similar to the ozone response for Scenario S1b-D which includes the same HSCT fleet but for background surface area density of SA0. The GSFC show significantly less ozone depletion in the southern hemisphere lower stratosphere for this scenario than for S1b-D, while the LLNL model show somewhat more depletion in both hemispheres. Figure 4.174 shows changes in ozone column for Scenario S3a relative to Scenario D3. Ozone column depletions are less than 0.5% for the CSIRO model, up to 1% for the AER, LLNL, and UNIVAQ models, and up to 3% for the GSFC model.

Scenario S3b is identical to Scenario S1c except for the background sulfate SAD. This scenario includes 500 HSCTs operating in 2015 with EI(NO_x)=5 and background SAD of 4xSA0. Changes in ozone relative to background scenario D3 are shown in Figures 4.175, 4.176, and 4.177 for March, June, and October as functions of latitude and altitude. Again the GSFC model shows the greatest difference in ozone perturbation with elevated SAD (S3b-D3) versus with nonvolcanic SAD (S1c-D). The GSFC model shows a large region of ozone increase due to HSCT emissions under Scenario S3b, extending through the northern hemisphere and tropics near the tropopause. Other models also show some ozone increases in this region, and generally less depletion than in Scenario S1c. Changes in ozone for June at 45^{o}N, the equator, and 45^{o}S are shown in Figures 4.178, 4.179, and 4.180. Figure 4.181 shows changes in ozone column due to HSCT aircraft emissions for this scenario relative to Scenario D3. All models show less ozone depletion or more regions of ozone increase than for Scenario S1c, except for the LLNL model.

Scenario S3c uses an EI(NO_x) of 10 with background surface area density of 4xSA0. Calculated changes in ozone relative to Scenario D3 for March, June, and October are shown in Figures 4.182, 4.183, and 4.184. Ozone increases around the tropopause are of larger area and greater magnitude than for S3b-D3. Changes in total column ozone are shown in Figure 4.185 and reveal substantial ozone increases due to HSCT aircraft emissions for all models. The GSFC and LLNL models still show ozone reductions in the southern hemisphere, and the AER model shows ozone reductions in the northern polar region.

With EI(NO_x)=15, calculated ozone increases due to HSCT are even larger. Figures 4.186, 4.187, and 4.188 show ozone changes as a function of latitude and altitude for March, June, and October for Scenario S3d relative to Scenario D3. Ozone increases are as much as 5% in the GSFC model northern hemisphere lower stratosphere and up to 4% in the UNIVAQ model tropical lower stratosphere. Vertical profiles of ozone change are shown in Figures 4.189, 4.190, and 4.191 at 45^{o}N, the equator, and 45^{o}S in June. Changes in column ozone for this scenario are shown in Figure 4.192.

The sensitivity of the hemispheric annual average ozone column to EI(NO_x) in the 2015 environment with elevated sulfate SAD is shown in Figures 4.193 and 4.194. All models have a positive response to increases in EI(NO_x) in both the northern and southern hemispheres. This is in contrast to the sensitivity with nonvolcanic SAD (shown in Figures 4.92 and 4.93), in which some models showed positive sensitivity and some negative sensitivity. With EI(NO_x)=0, calculated changes in northern hemisphere column ozone range from -0.3% to -0.5%. With EI(NO_x)=15, calculated changes in northern hemisphere column ozone range from +0.1% to +0.6%. In the southern hemisphere, the spread among the models is larger. The GSFC and UNIVAQ models show the greatest positive sensitivity to EI(NO_x), while the CSIRO model shows almost no sensitivity.

The final two scenarios in this section include sulfur emission from HSCT aircraft with EI(NO_x)=5. The

SADs for Scenarios S3e and S3f were generated by adding the SAD perturbations calculated by the AER model for Scenarios S1f and S1h to the 4xSA0 elevated background SAD. The sulfate surface area density for S3e includes aircraft sulfur emissions assuming EI(SO_2)=0.4 and 50% gas to particle conversion in the plume and is designated 4xSA0+SA1-SA0. The sulfate surface area density for S3f assumes 100% gas to particle conversion and is designated 4xSA0+SA3-SA0.

Calculated changes in ozone as a function of latitude and altitude for March, June, and October for Scenario S3e relative to Scenario D3 are shown in Figures 4.195, 4.196, and 4.197. Ozone depletion is enhanced relative to S3b-D3 which does not include aircraft sulfur emissions. Vertical profiles of ozone change at 45^{o}N, the equator, and 45^{o}S in June are shown in Figures 4.198-4.200. Figure 4.201 shows changes in ozone column for Scenario S3e relative to Scenario D3. All models show more depletion in column ozone for this scenario than for a similar one without aircraft sulfur emissions. However, column ozone depletion is considerably less than (about half for most models) those for Scenario S1f-D, which included the same amount of sulfur emissions but with SA0 background SAD.

Calculated ozone perturbations for Scenario S3f are shown in Figures 4.202, 4.203, and 4.204 for March, June, and October. Results are not very different from S3e-D3. The change in ozone column for this scenario is shown in Figure 4.205. Ozone depletion is slightly larger than for S3e-D3. Figure 4.206 shows the sensitivity of northern hemisphere annual average column ozone response to HSCT to changes in sulfate surface area density in a background atmosphere with 4xSA0 surface area density. The abscissa shows the percent difference in SAD between the HSCT case and the baseline case in the 14-21 km, 33-90^{o}N region. All models show increases in ozone depletion with increasing SAD perturbation. The GSFC model shows the greatest sensitivity; the other models have similar sensitivities. Because the background SAD is elevated, the SAD perturbations are a factor of 4 smaller on a percentage basis than those shown in Figure 4.140 with SA0. The ozone sensitivities are similar to those for SA0 over the 0-28% SAD range.

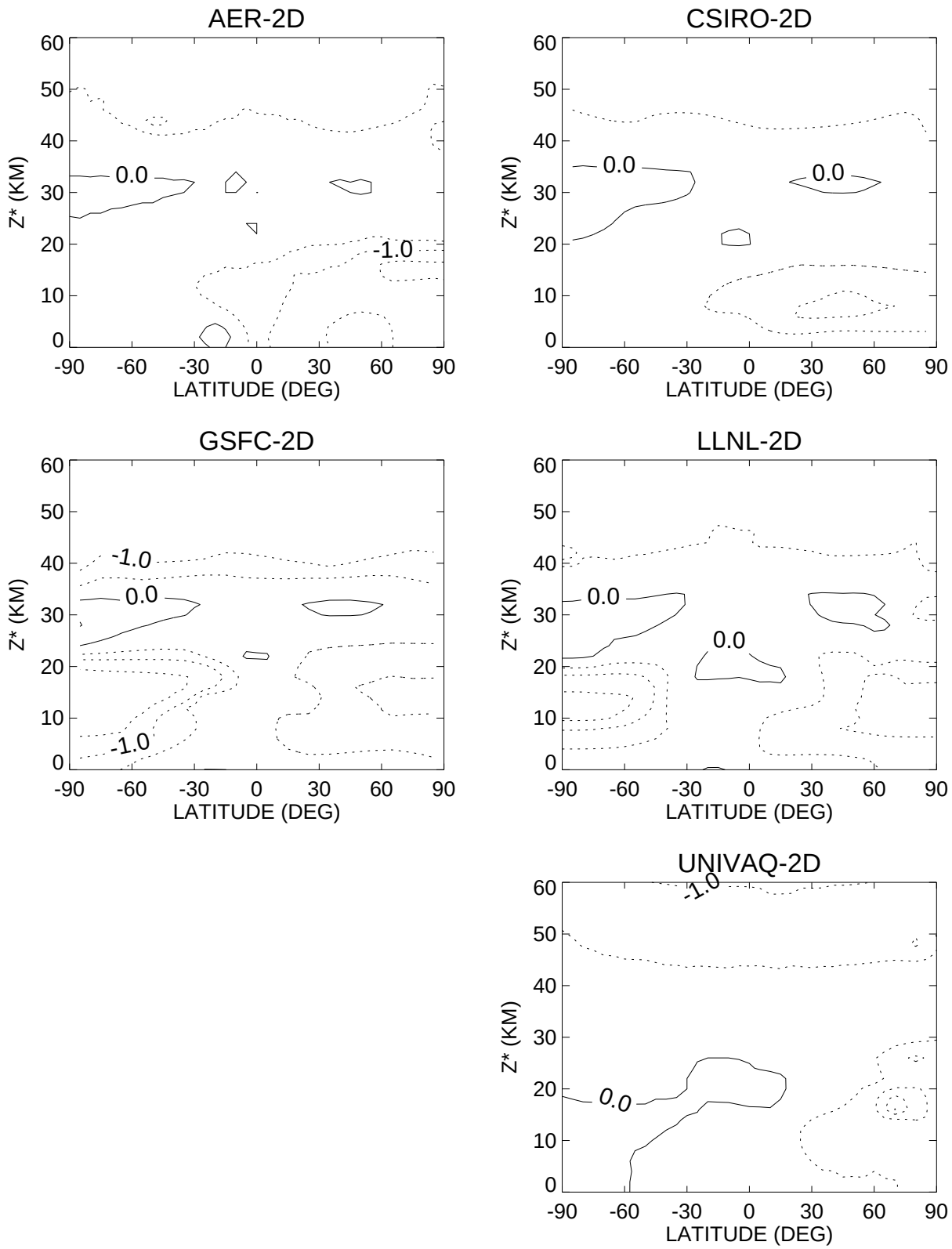

Figure 4.171: Calculated perturbations to O_3 (percent) as a function of latitude and altitude in March of 2015 due to emissions from a fleet of 500 HSCT aircraft with EI(NO_x)=0 and sulfate surface area of 4xSA0 under Scenario S3a relative to Scenario D3. Contours are -2, -1, -0.5, 0.

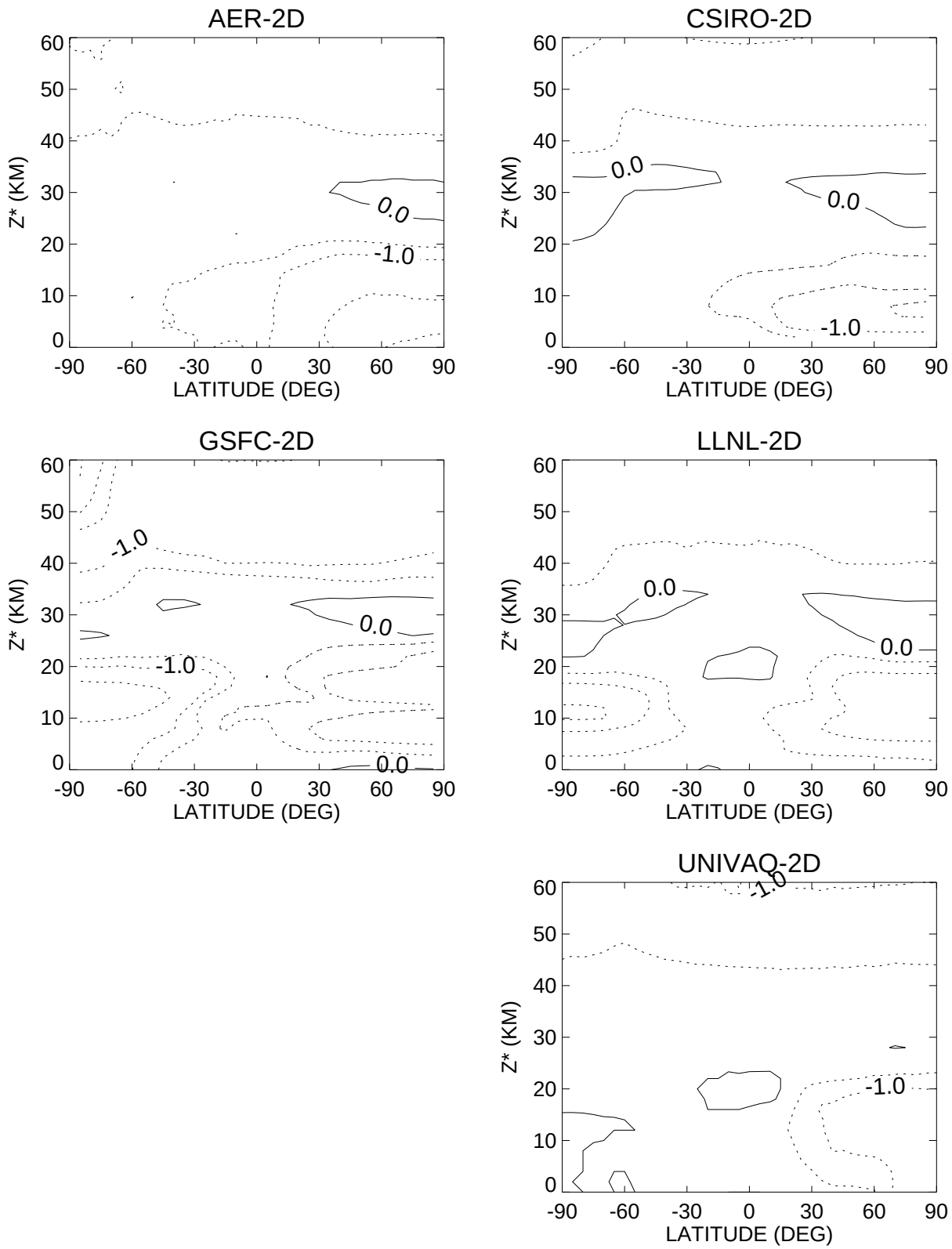

Figure 4.172: Calculated perturbations to O_3 (percent) as a function of latitude and altitude in June of 2015 due to emissions from a fleet of 500 HSCT aircraft with EI(NO_x)=0 and sulfate surface area of 4xSA0 under Scenario S3a relative to Scenario D3.. Contours are -3, -2, -1, -0.5, 0.

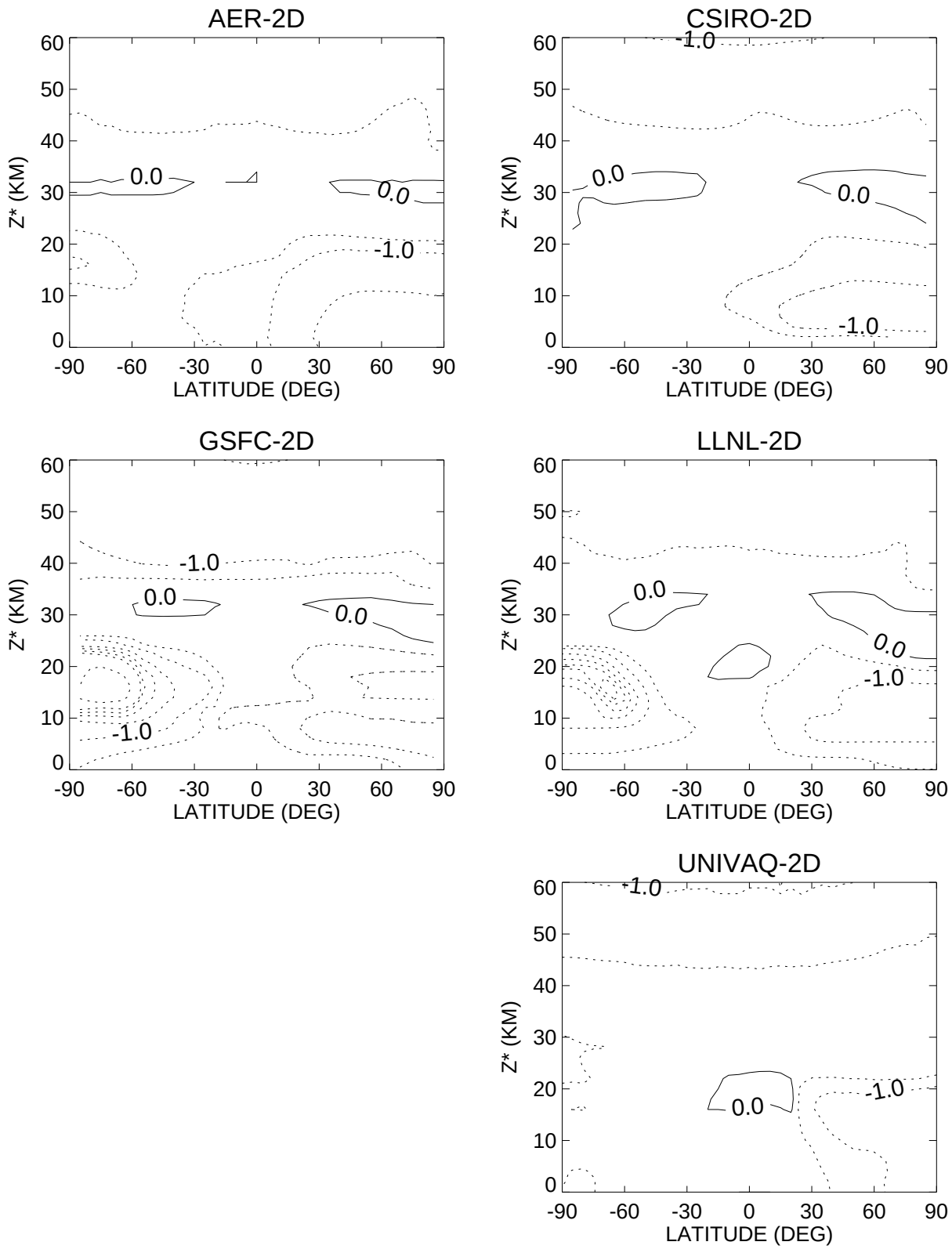

Figure 4.173: Calculated perturbations to O_3 (percent) as a function of latitude and altitude in October of 2015 due to emissions from a fleet of 500 HSCT aircraft with EI(NO_x)=0 and sulfate surface area of 4xSA0 under Scenario S3a relative to Scenario D3.. Contours are -10, -5, -4, -3, -2, -1, -0.5, 0.

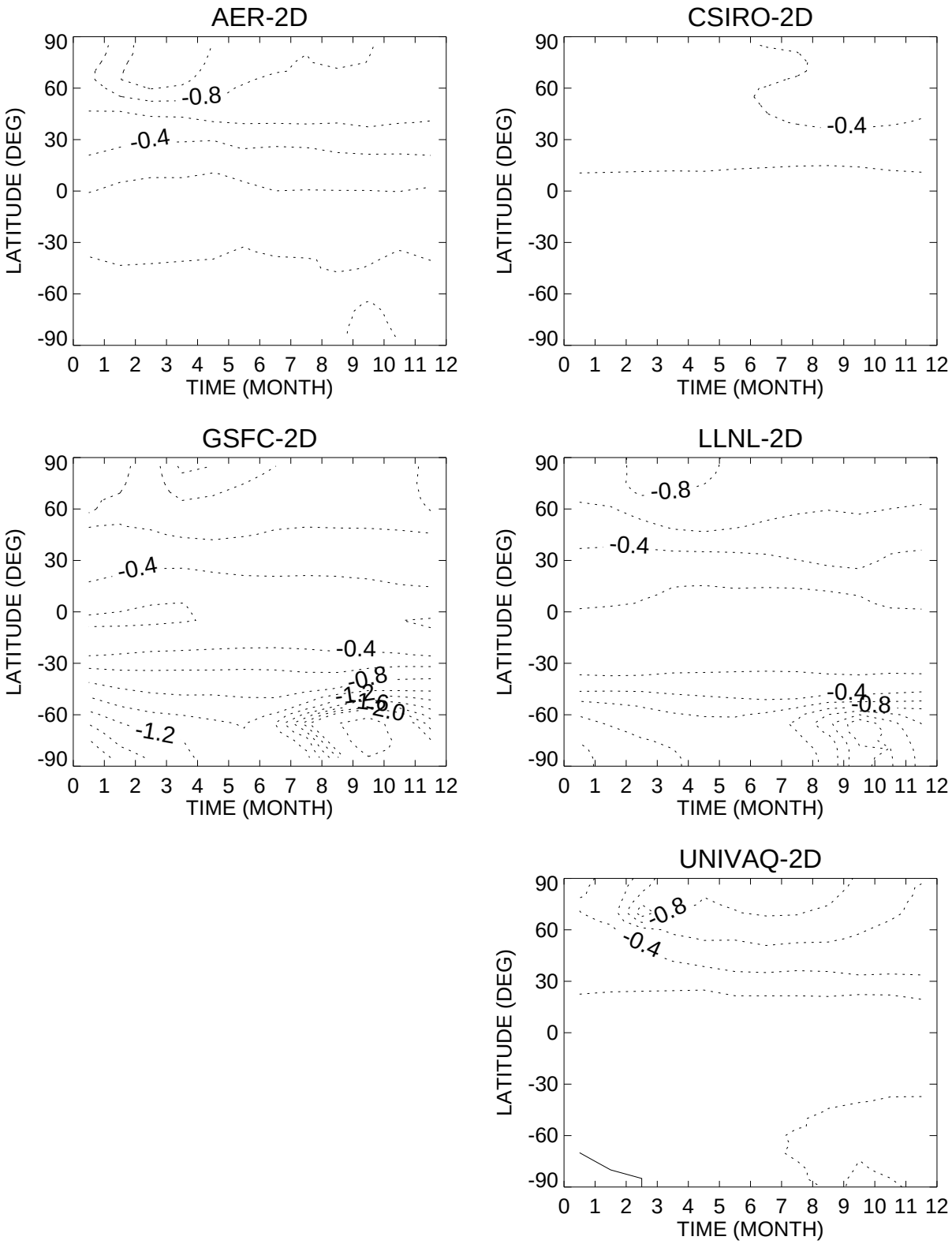

Figure 4.174: Calculated perturbations to column O_3 (percent) as a function of latitude and season in 2015 due to emissions from a fleet of 500 HSCT aircraft with EI(NO_x)=0 and sulfate surface area of 4xSA0 under Scenario S3a relative to Scenario D3. Contours are -3, and -2.0 to -0.2 by 0.2.

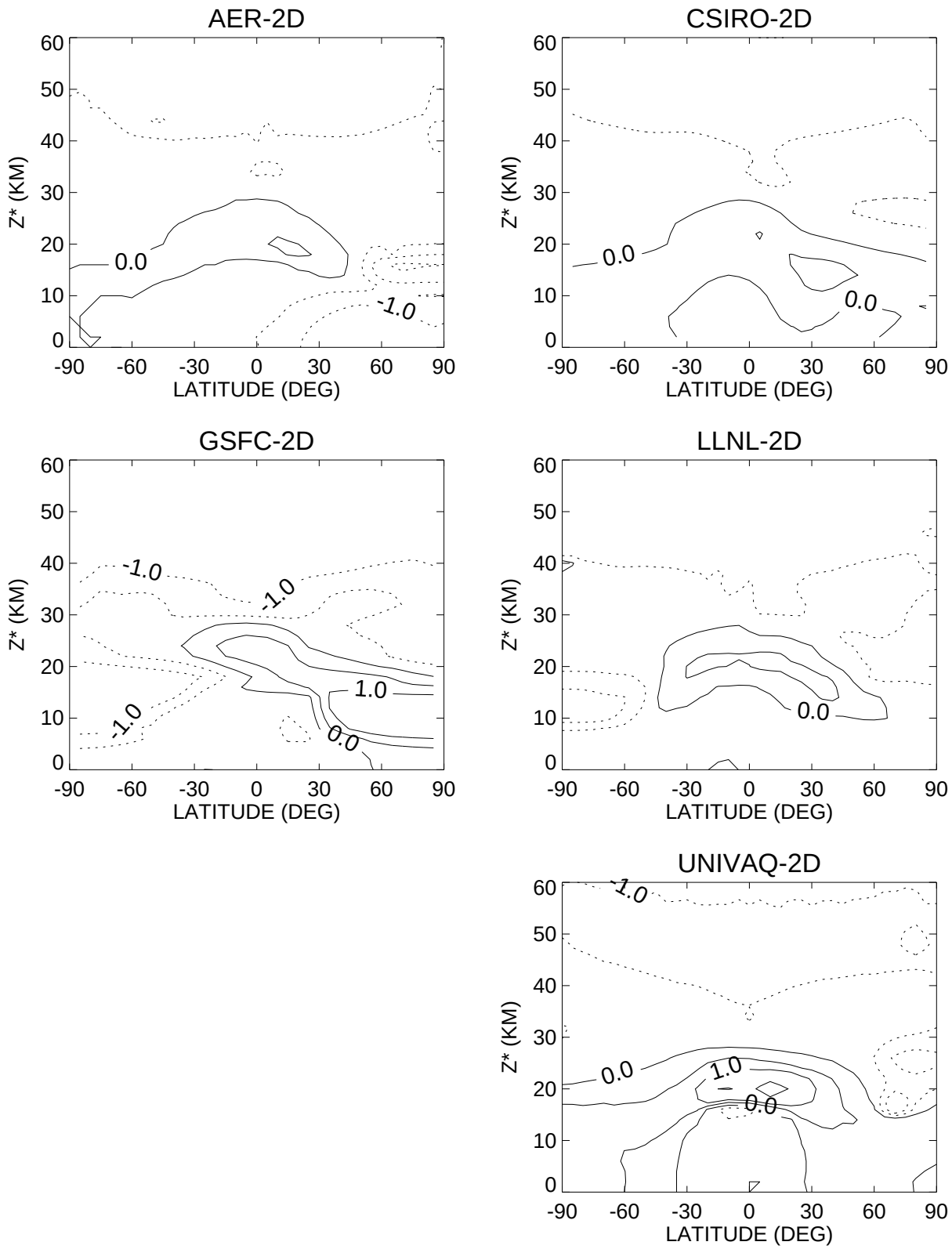

Figure 4.175: Calculated perturbations to O_3 (percent) as a function of latitude and altitude in March of 2015 due to emissions from a fleet of 500 HSCT aircraft with EI(NO_x)=5 and sulfate surface area of 4xSA0 under Scenario S3b relative to Scenario D3. Contours are -2, -1, -0.5, 0, 0.5, 1, 2.

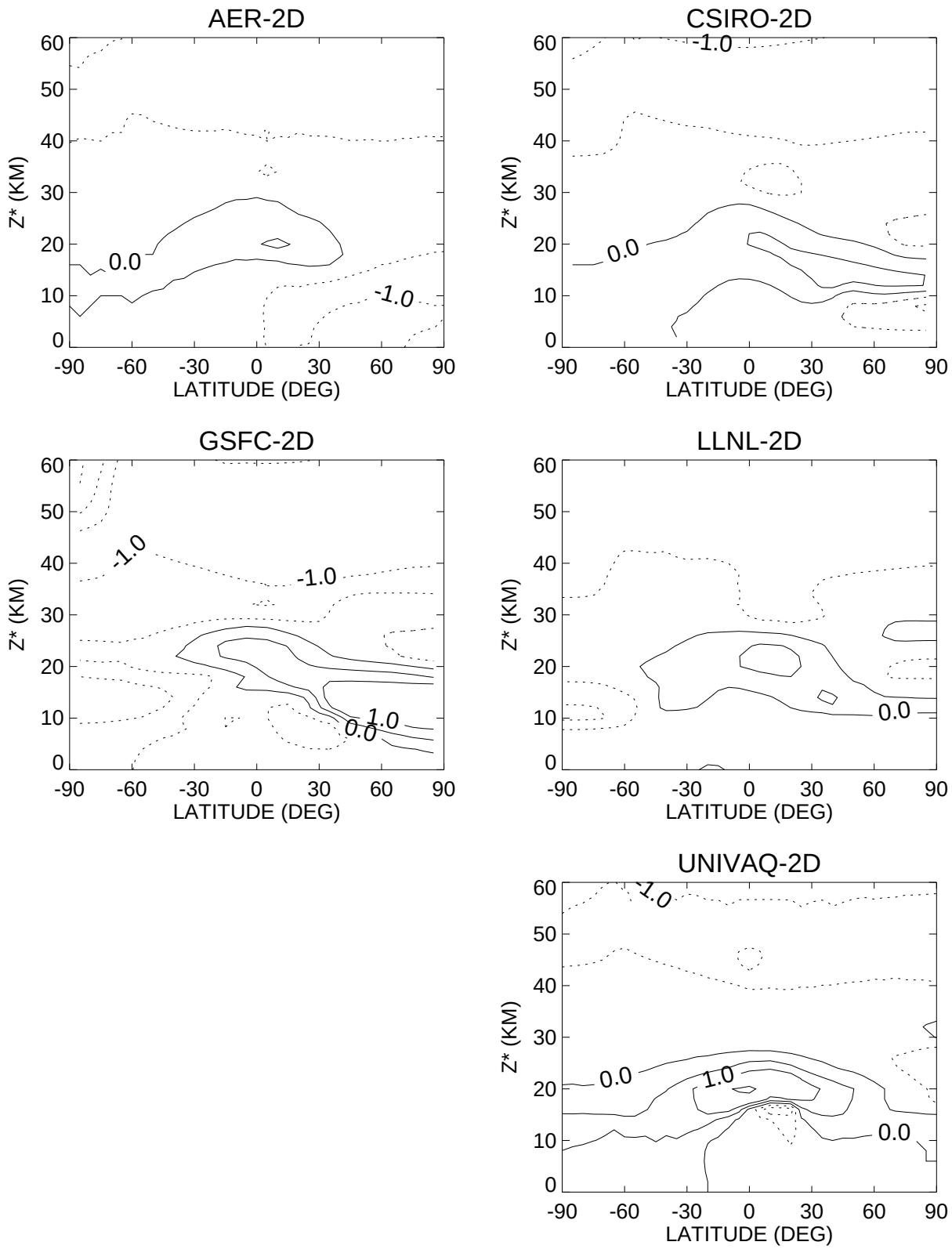

Figure 4.176: Calculated perturbations to O_3 (percent) as a function of latitude and altitude in June of 2015 due to emissions from a fleet of 500 HSCT aircraft with EI(NO_x)=5 and sulfate surface area of 4xSA0 under Scenario S3b relative to Scenario D3. Contours are -2, -1, -0.5, 0, 0.5, 1, 2.

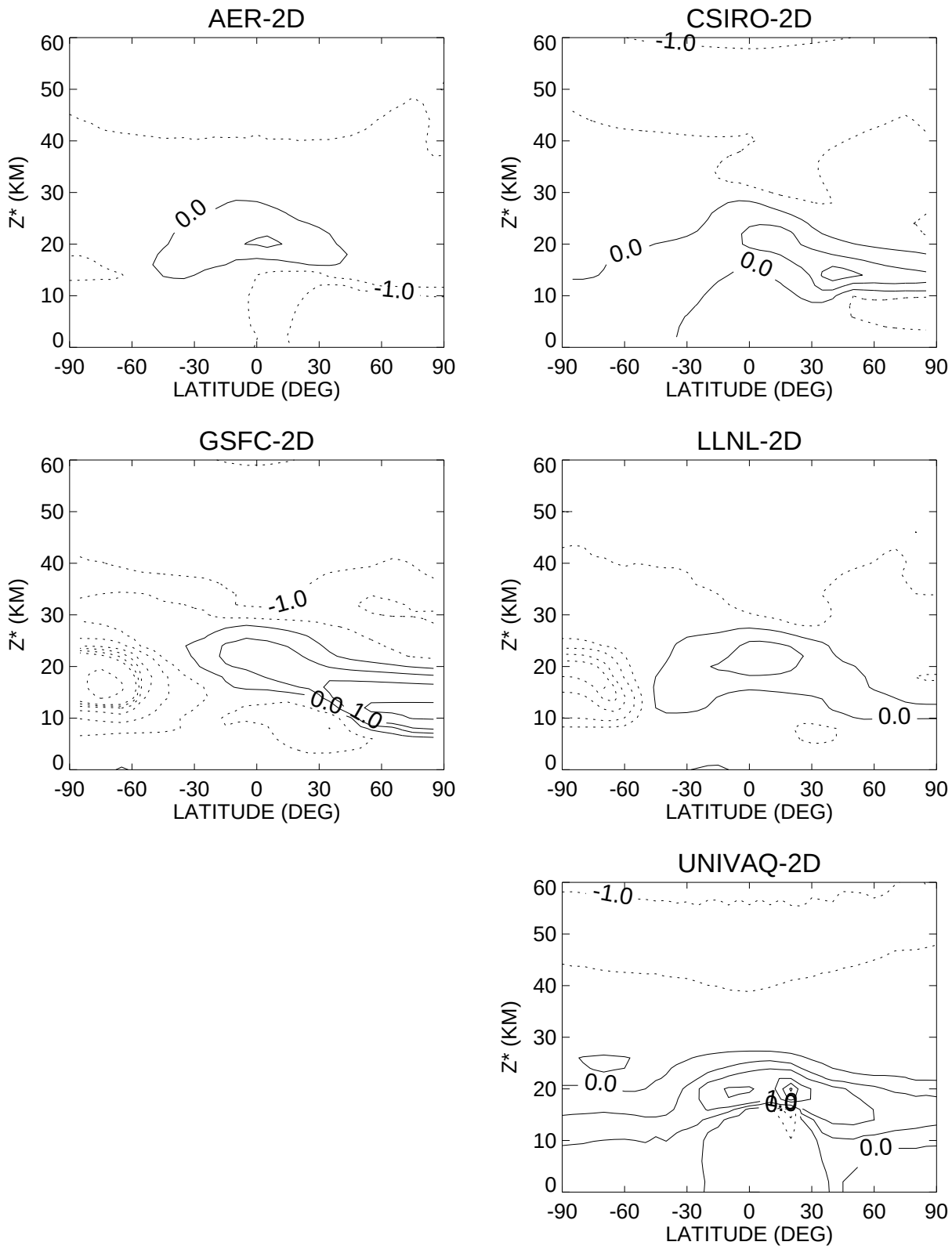

Figure 4.177: Calculated perturbations to O_3 (percent) as a function of latitude and altitude in October of 2015 due to emissions from a fleet of 500 HSCT aircraft with EI(NO_x)=5 and sulfate surface area of 4xSA0 under Scenario S3b relative to Scenario D3. Contours are -10, -5, -4, -3, -2, -1, -0.5, 0, 0.5, 1, 2, 3, 4.

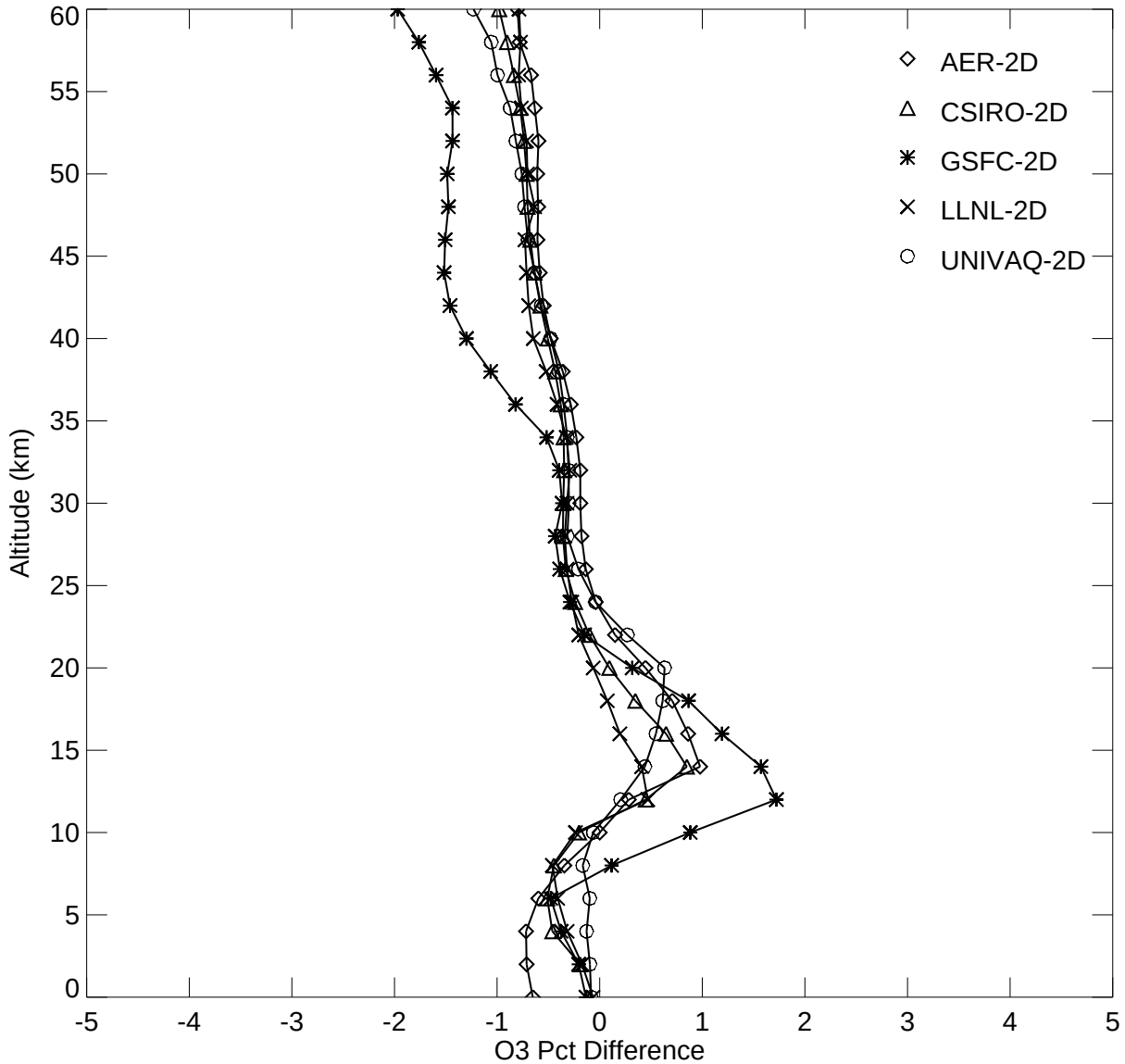

Figure 4.178: Calculated perturbations to O_3 (percent) as a function of altitude at 45°N in June of 2015 due to emissions from a fleet of 500 HSCT aircraft with EI(NO_x)=5 and sulfate surface area of 4xSA0 under Scenario S3b relative to Scenario D3.

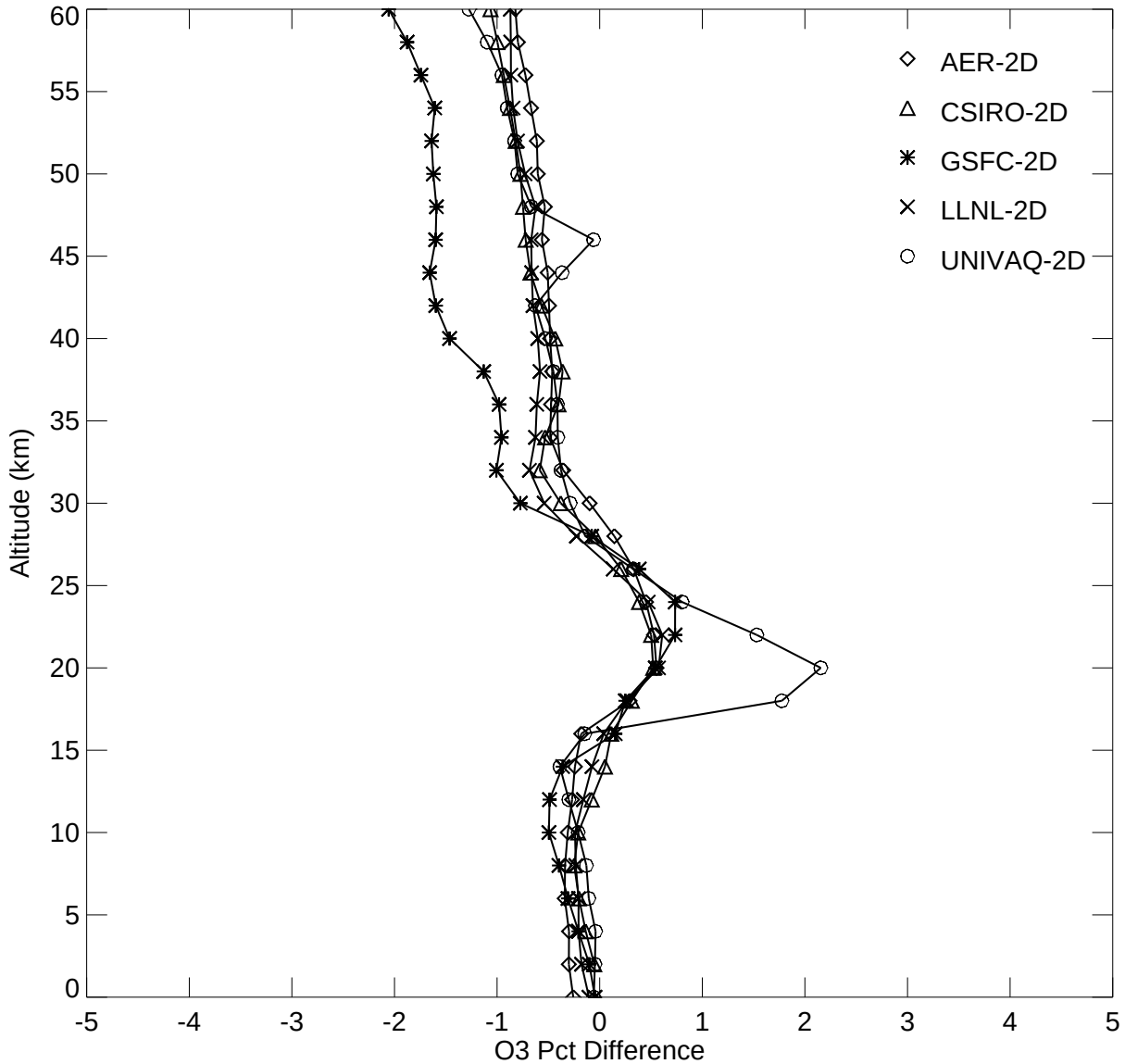

Figure 4.179: Calculated perturbations to O_3 (percent) as a function of altitude at the equator in June of 2015 due to emissions from a fleet of 500 HSCT aircraft with EI(NO_x)=5 and sulfate surface area of 4xSA0 under Scenario S3b relative to Scenario D3.

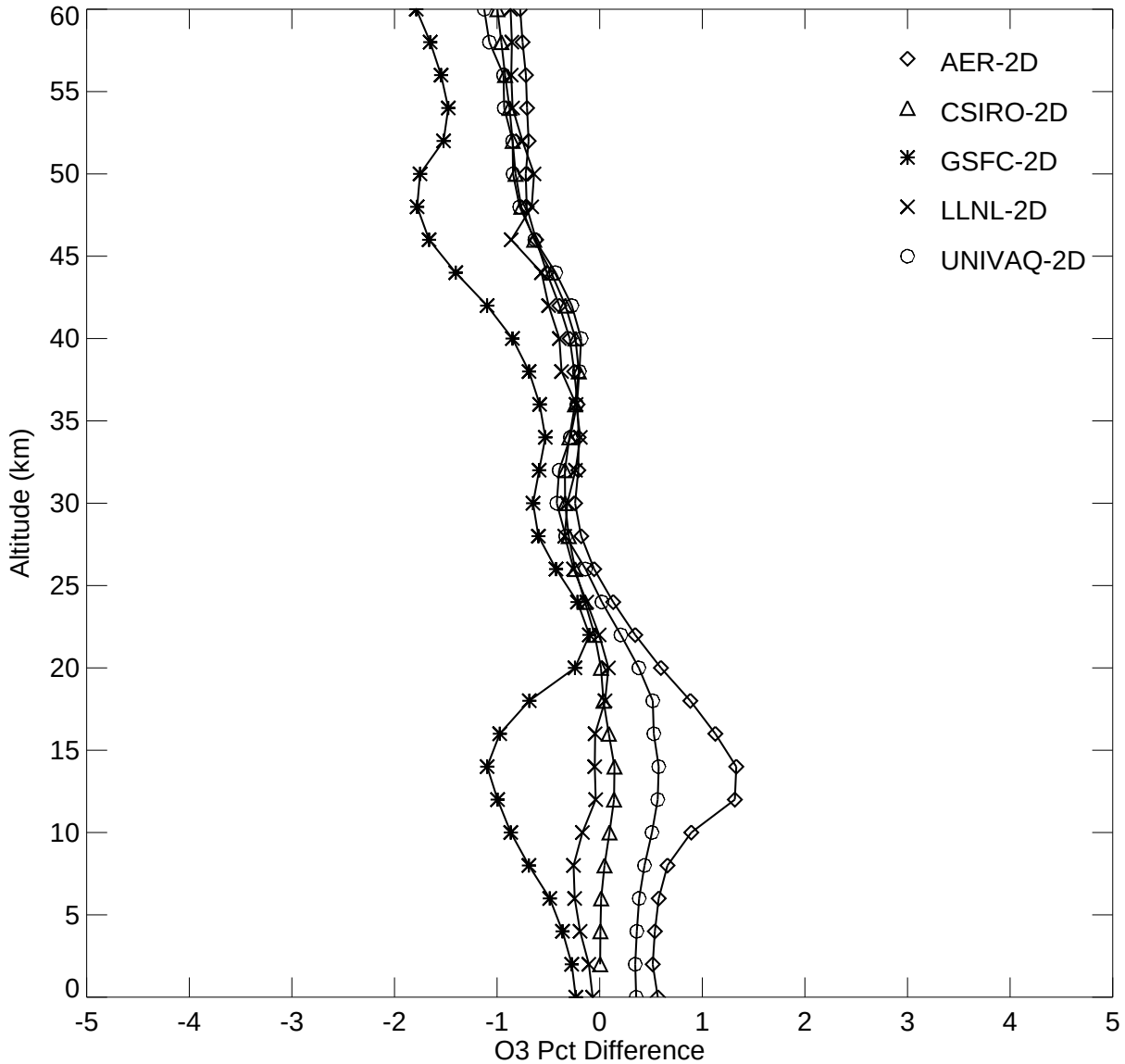

Figure 4.180: Calculated perturbations to O_3 (percent) as a function of altitude at 45°S in June of 2015 due to emissions from a fleet of 500 HSCT aircraft with EI(NO_x)=5 and sulfate surface area of 4xSA0 under Scenario S3b relative to Scenario D3.

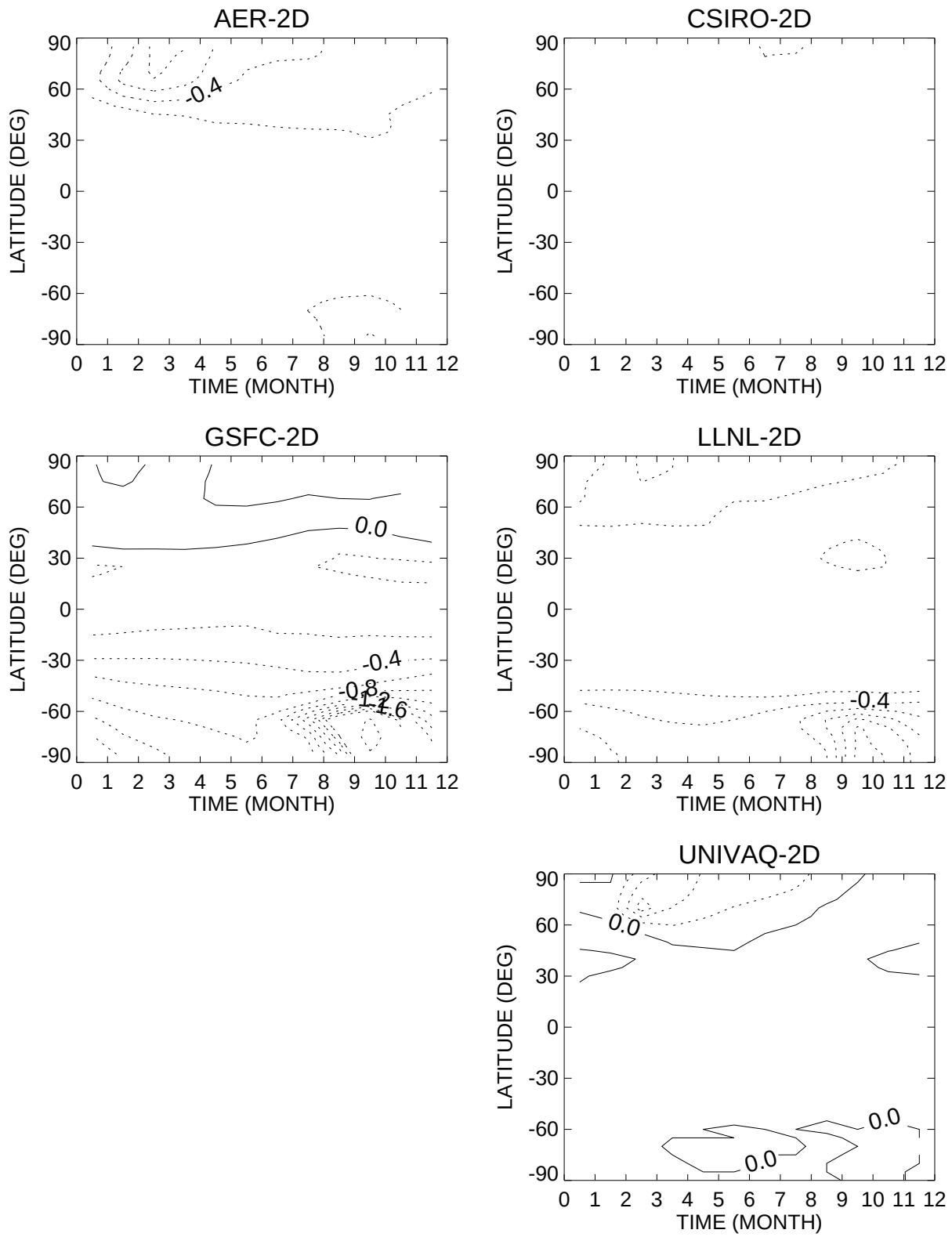

Figure 4.181: Calculated perturbations to column O_3 (percent) as a function of latitude and season in 2015 due to emissions from a fleet of 500 HSCT aircraft with EI(NO_x)=5 and sulfate surface area of 4xSA0 under Scenario S3b relative to Scenario D3. Contours are -3 and -2.0 to 0.2 by 0.2.

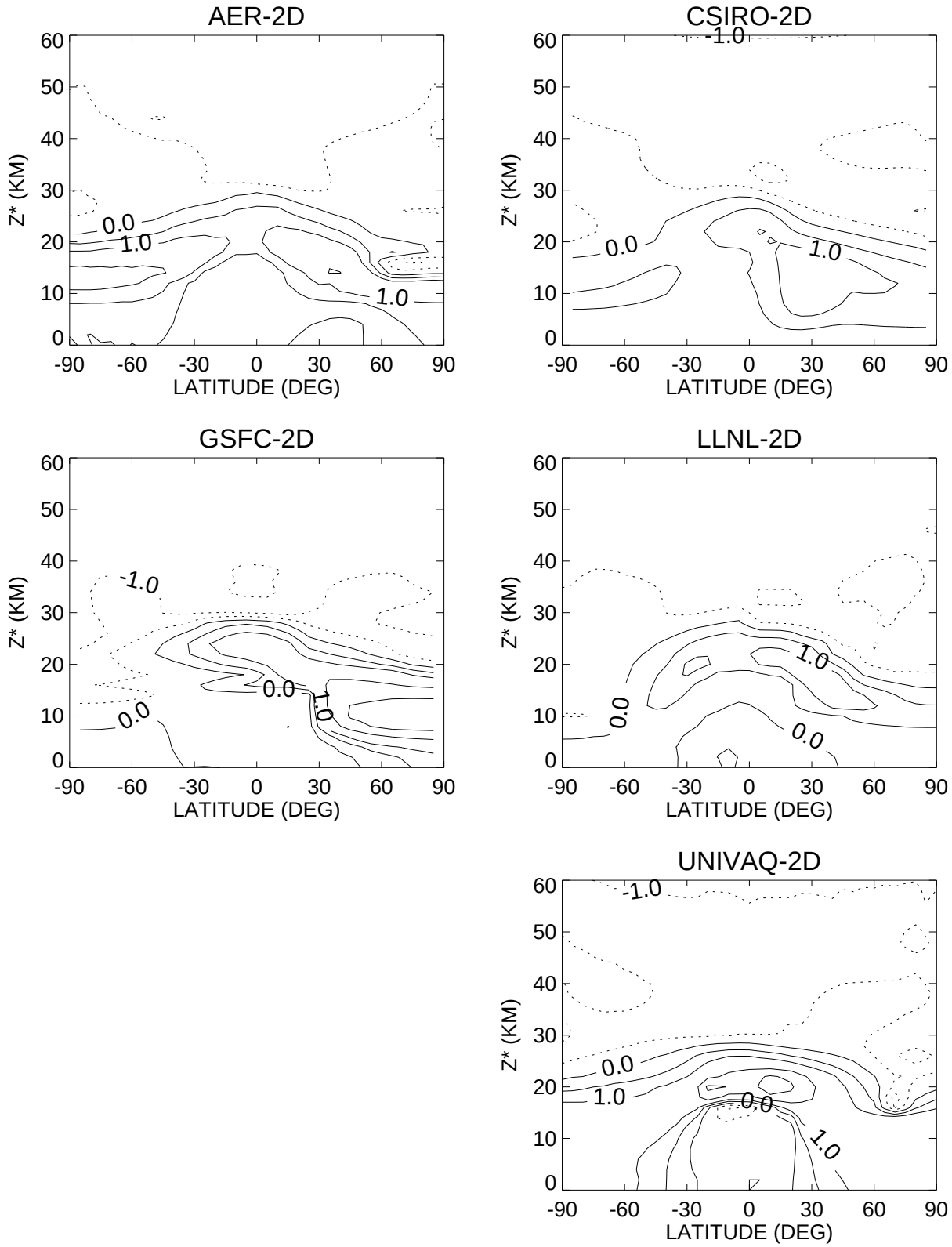

Figure 4.182: Calculated perturbations to O_3 (percent) as a function of latitude and altitude in March of 2015 due to emissions from a fleet of 500 HSCT aircraft with EI(NO_x)=10 and sulfate surface area of 4xSA0 under Scenario S3c relative to Scenario D3. Contours are -2, -1, -0.5, 0, 0.5, 1, 2, 3.

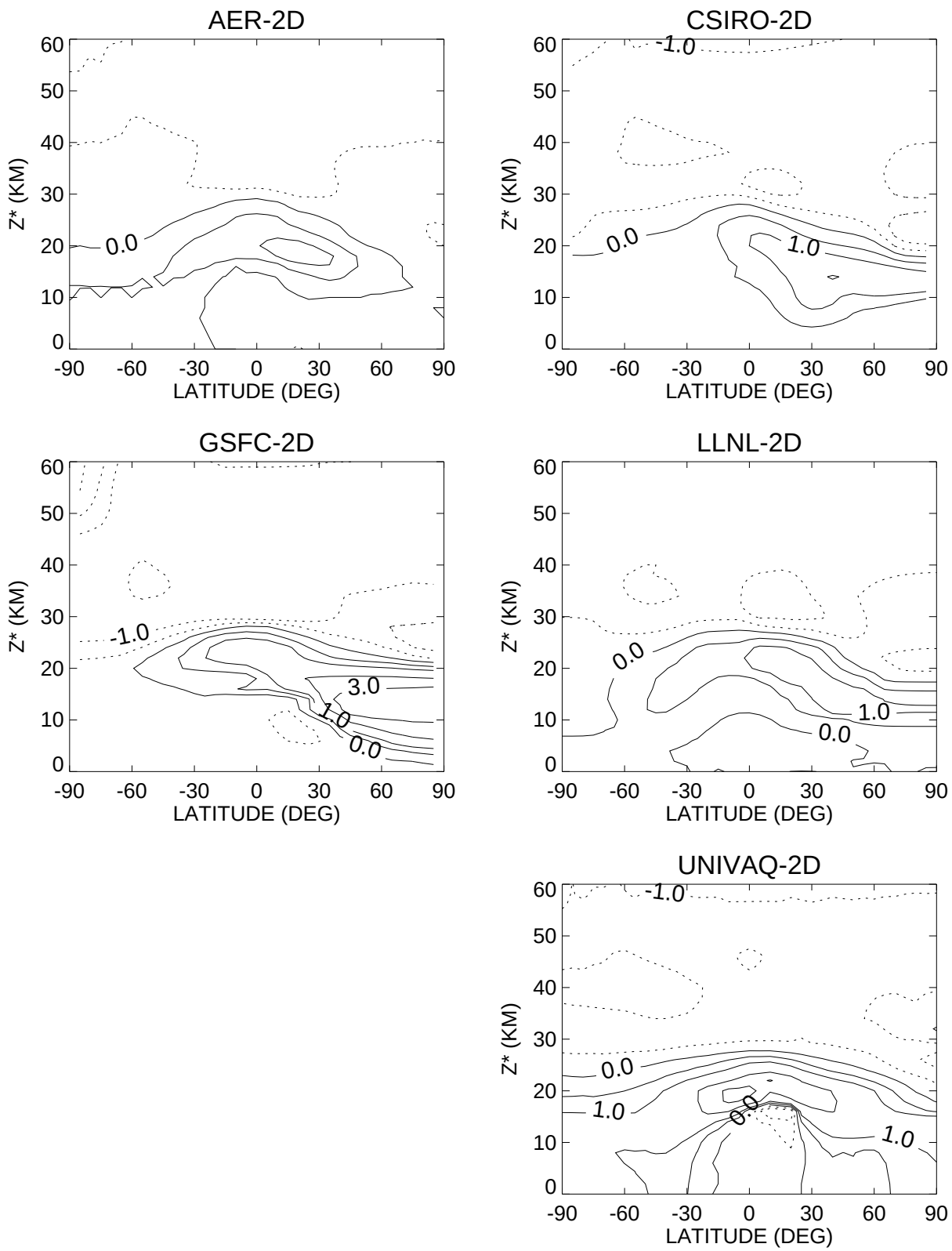

Figure 4.183: Calculated perturbations to O_3 (percent) as a function of latitude and altitude in June of 2015 due to emissions from a fleet of 500 HSCT aircraft with EI(NO_x)=10 and sulfate surface area of 4xSA0 under Scenario S3c relative to Scenario D3. Contours are -2, -1, -0.5, 0, 0.5, 1, 2, 3.

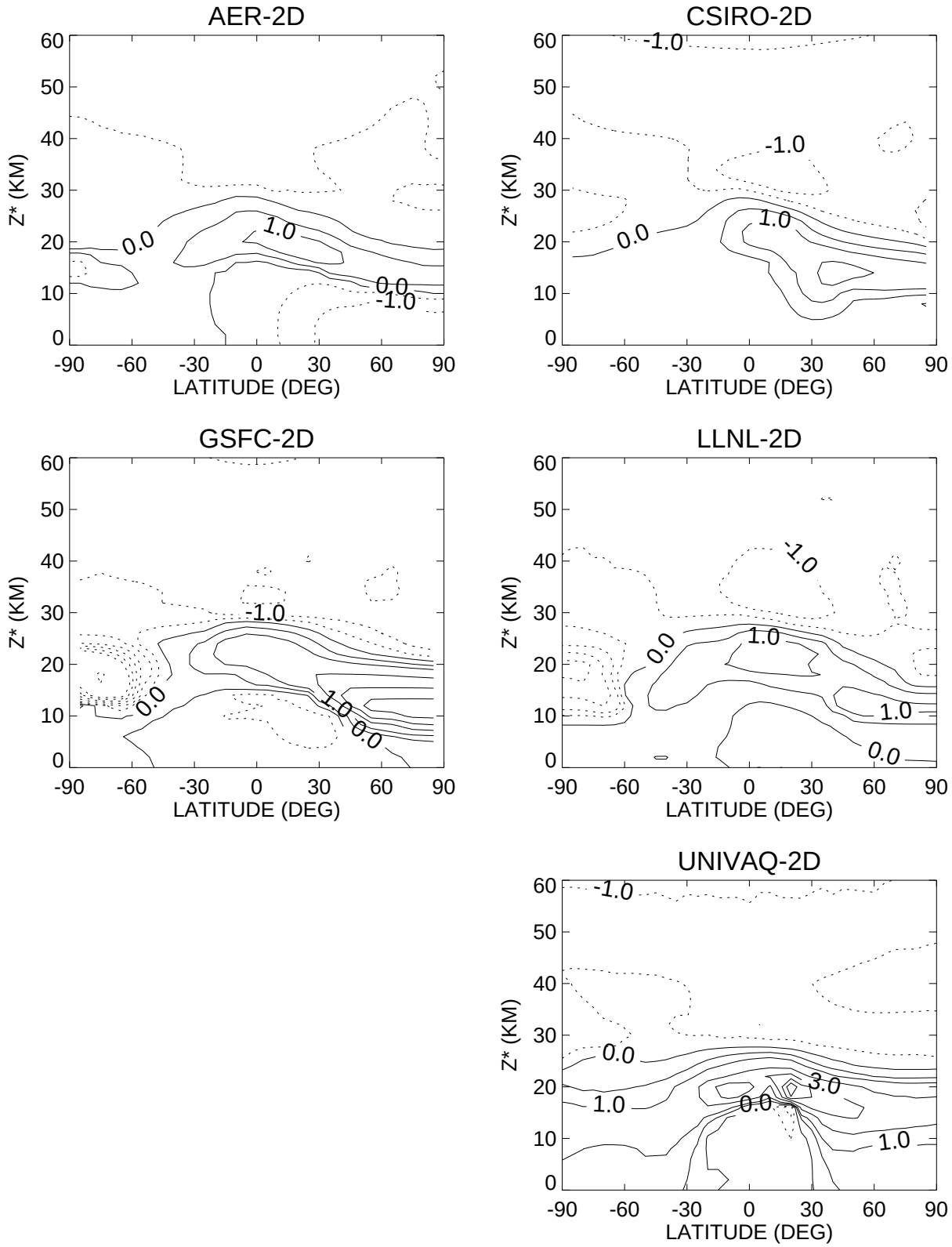

Figure 4.184: Calculated perturbations to O_3 (percent) as a function of latitude and altitude in October of 2015 due to emissions from a fleet of 500 HSCT aircraft with EI(NO_x)=10 and sulfate surface area of 4xSA0 under Scenario S3c relative to Scenario D3. Contours are -10, -5, -4, -3, -2, -1, -0.5, 0, 0.5, 1, 2, 3, 4, 5.

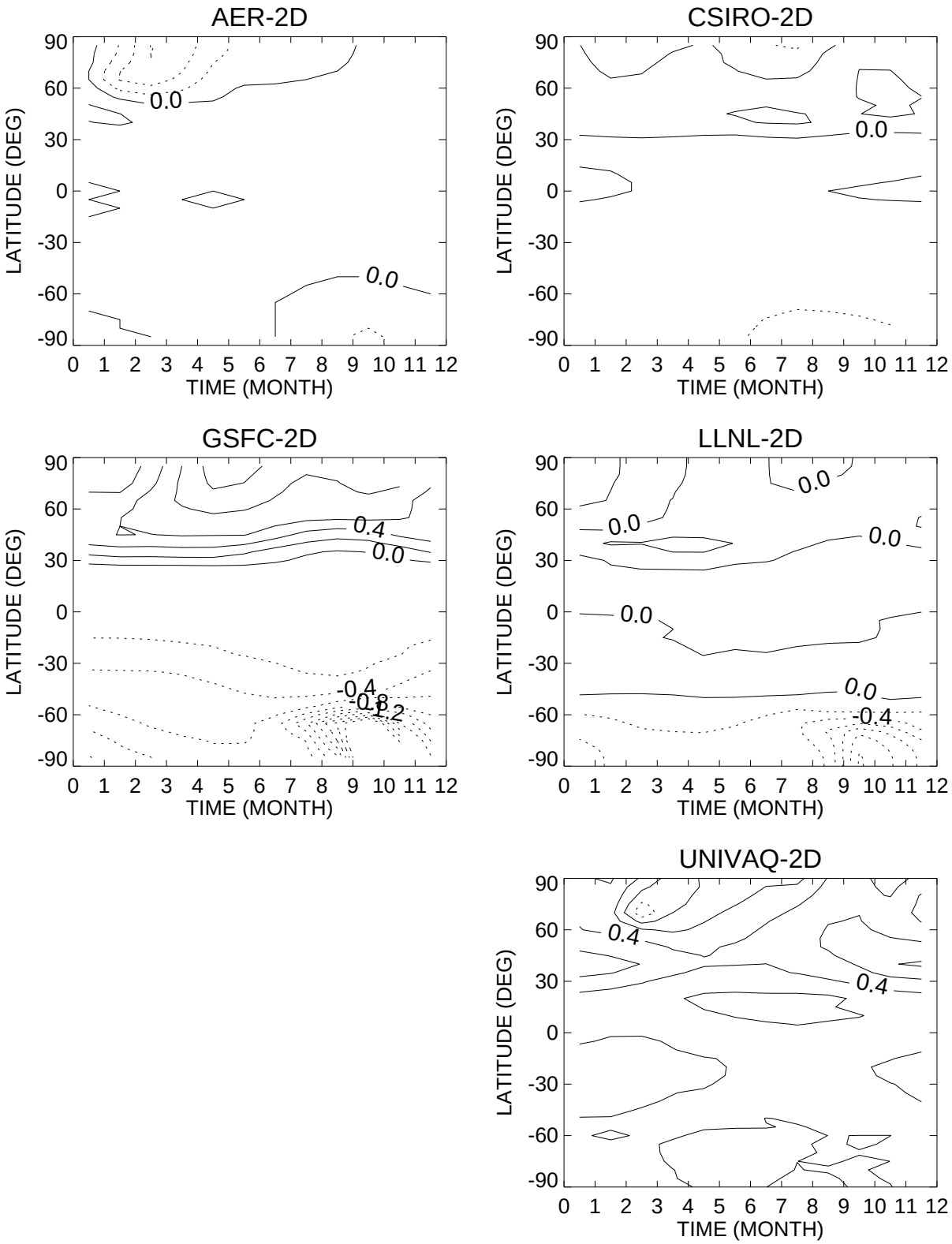

Figure 4.185: Calculated perturbations to column O_3 (percent) as a function of latitude and season in 2015 due to emissions from a fleet of 500 HSCT aircraft with EI(NO_x)=10 and sulfate surface area of 4xSA0 under Scenario S3c relative to Scenario D3. Contours are -2.0 to 1.0 by 0.2.

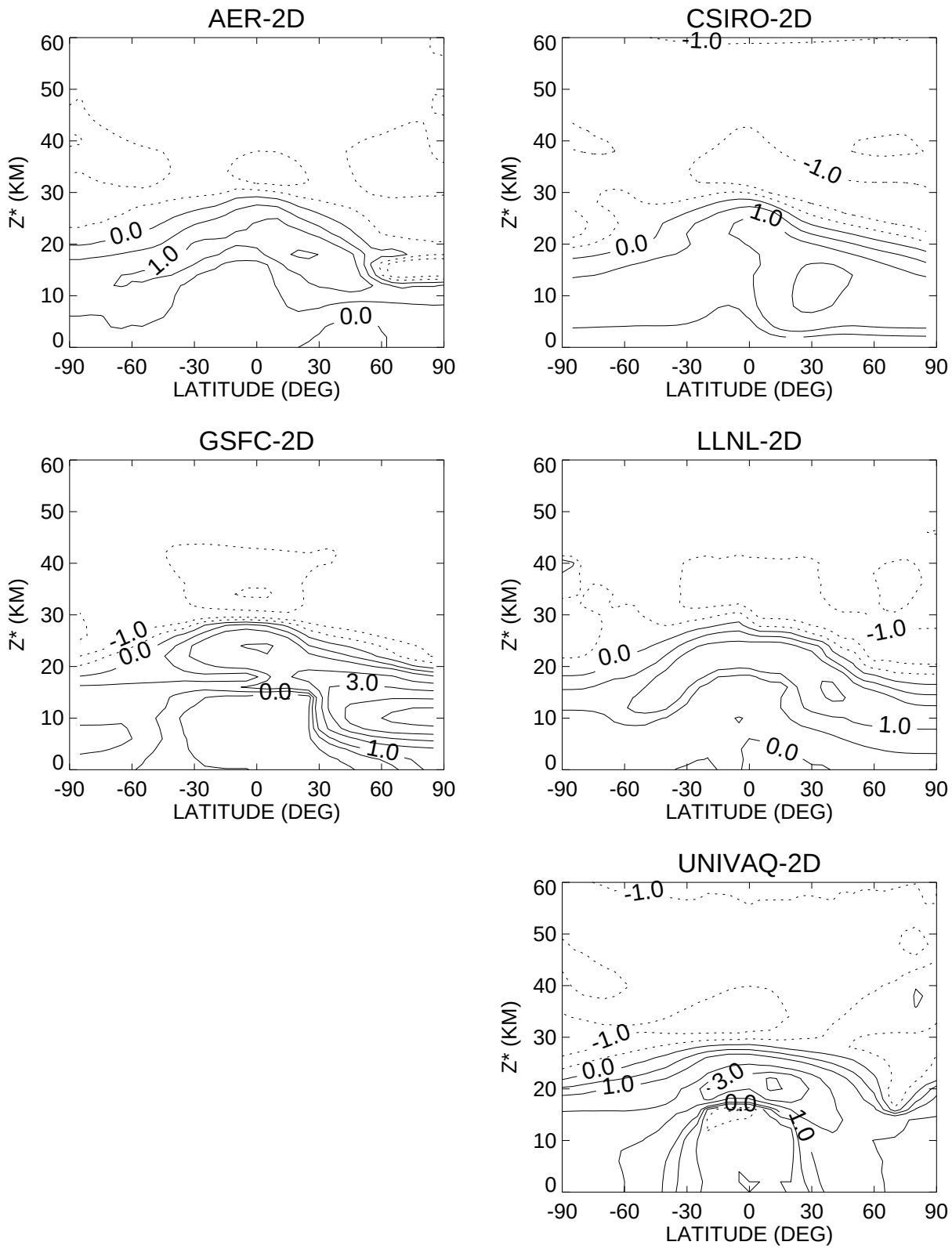

Figure 4.186: Calculated perturbations to O_3 (percent) as a function of latitude and altitude in March of 2015 due to emissions from a fleet of 500 HSCT aircraft with EI(NO_x)=15 and sulfate surface area of 4xSA0 under Scenario S3d relative to Scenario D3. Contours are -3, -2, -1, -0.5, 0, 0.5, 1, 2, 3, 4, 5.

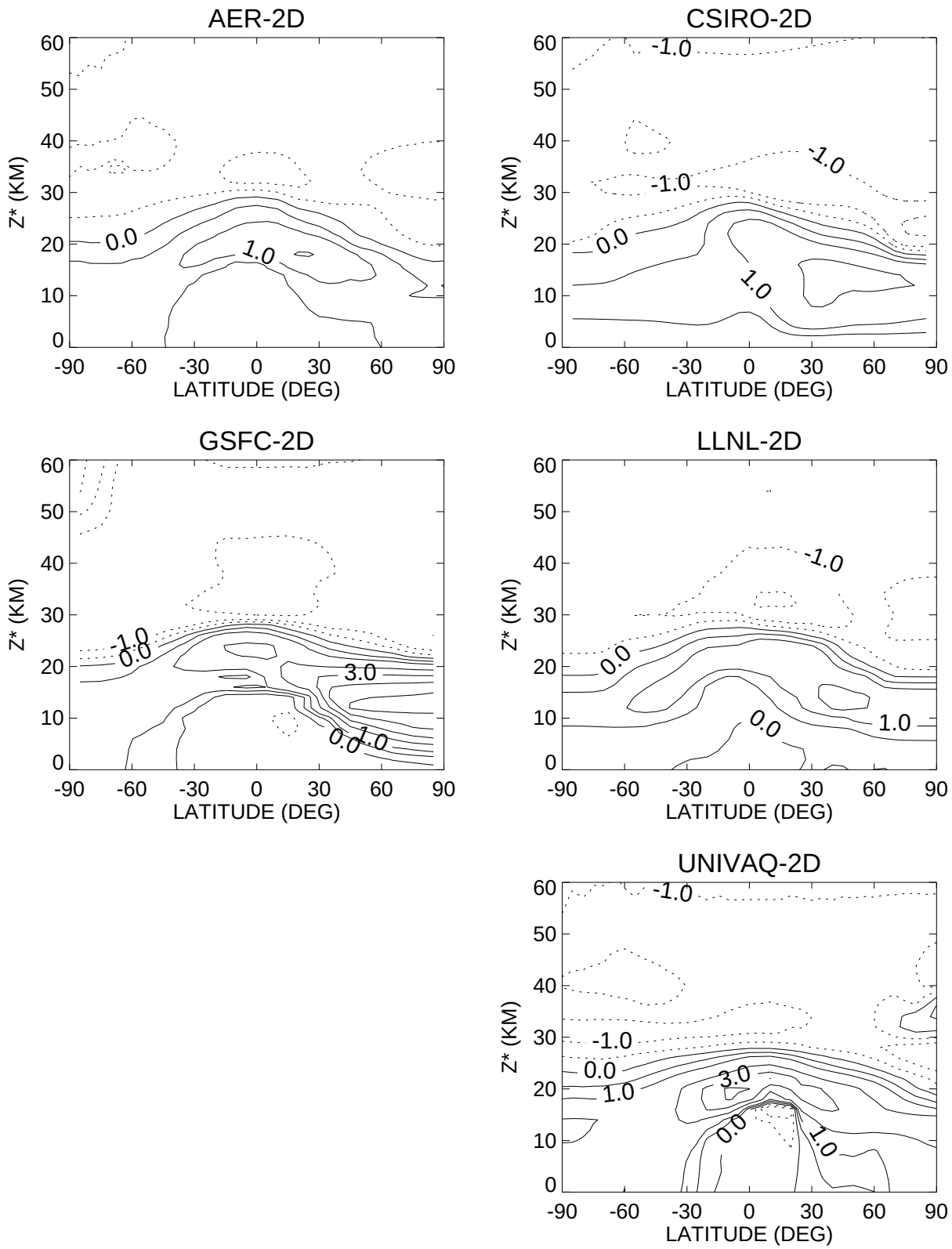

Figure 4.187: Calculated perturbations to O_3 (percent) as a function of latitude and altitude in June of 2015 due to emissions from a fleet of 500 HSCT aircraft with EI(NO_x)=15 and sulfate surface area of 4xSA0 under Scenario S3d relative to Scenario D3. Contours are -2, -1, -0.5, 0, 0.5, 1, 2, 3, 4, 5.

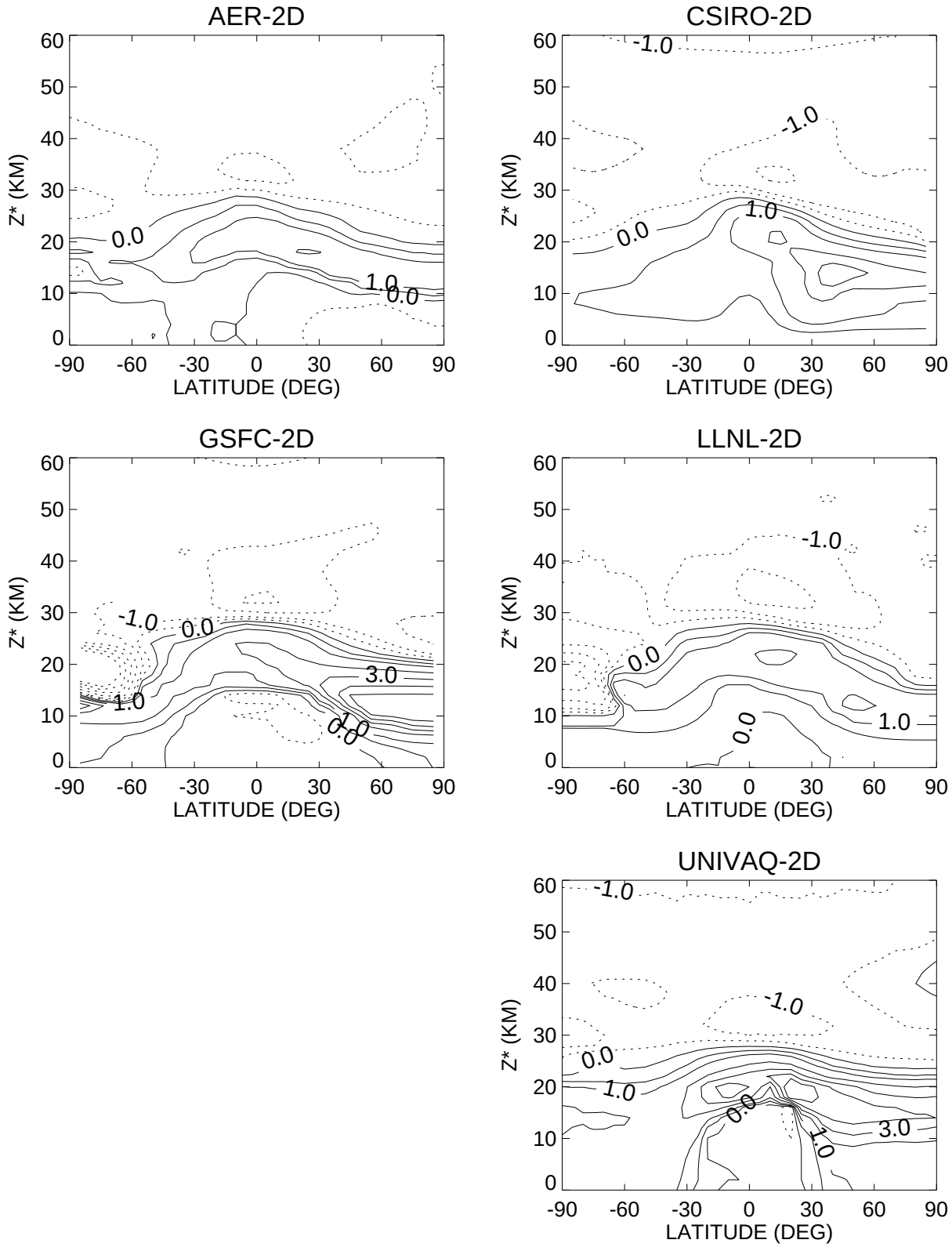

Figure 4.188: Calculated perturbations to O_3 (percent) as a function of latitude and altitude in October of 2015 due to emissions from a fleet of 500 HSCT aircraft with EI(NO_x)=15 and sulfate surface area of 4xSA0 under Scenario S3d relative to Scenario D3. Contours are -5, -4, -3, -2, -1, -0.5, 0, 0.5, 1, 2, 3, 4, 5.

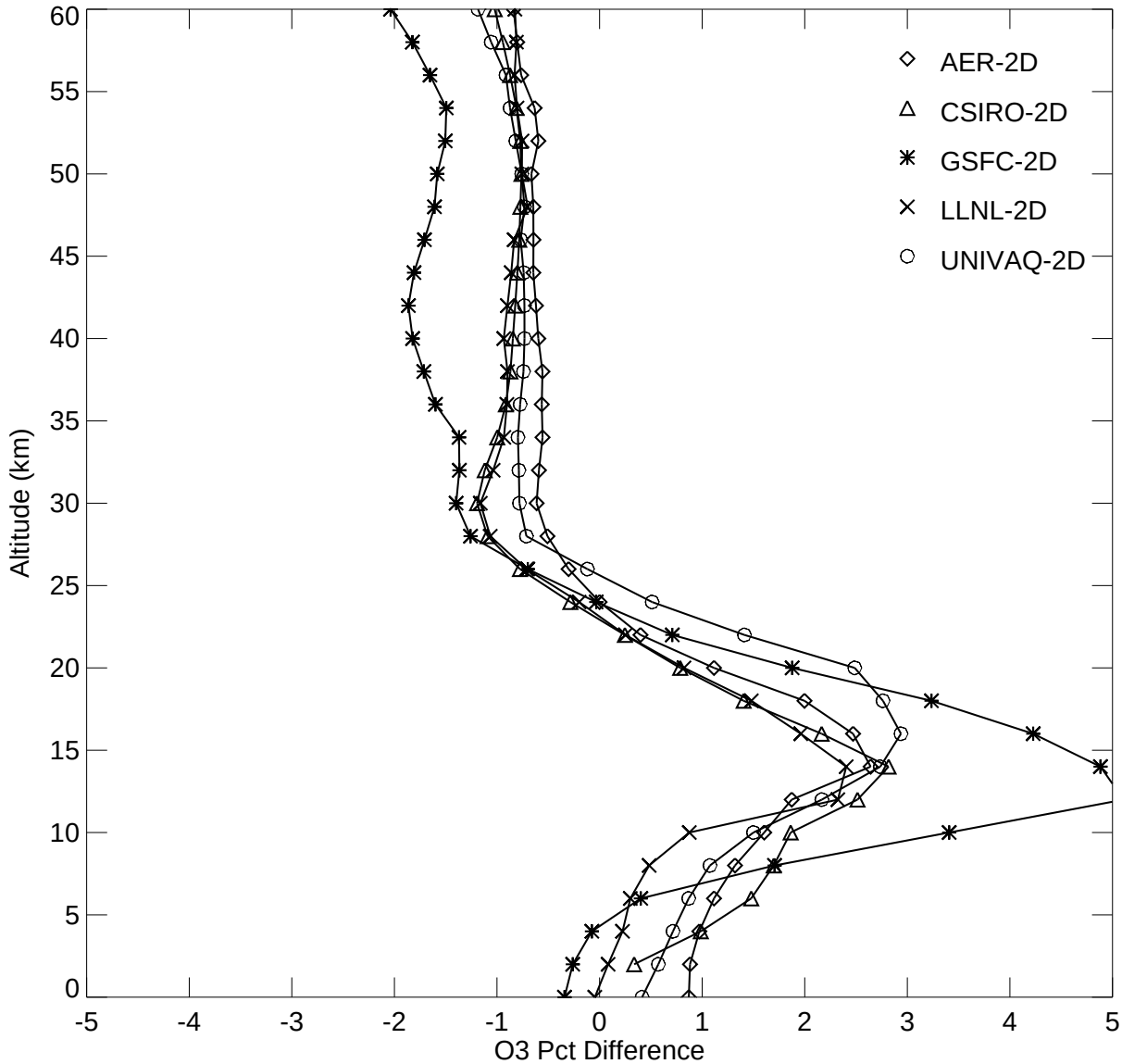

Figure 4.189: Calculated perturbations to O_3 (percent) as a function of altitude at 45^{o}N in June of 2015 due to emissions from a fleet of 500 HSCT aircraft with EI(NO_x)=15 and sulfate surface area of 4xSA0 under Scenario S3d relative to Scenario D3.

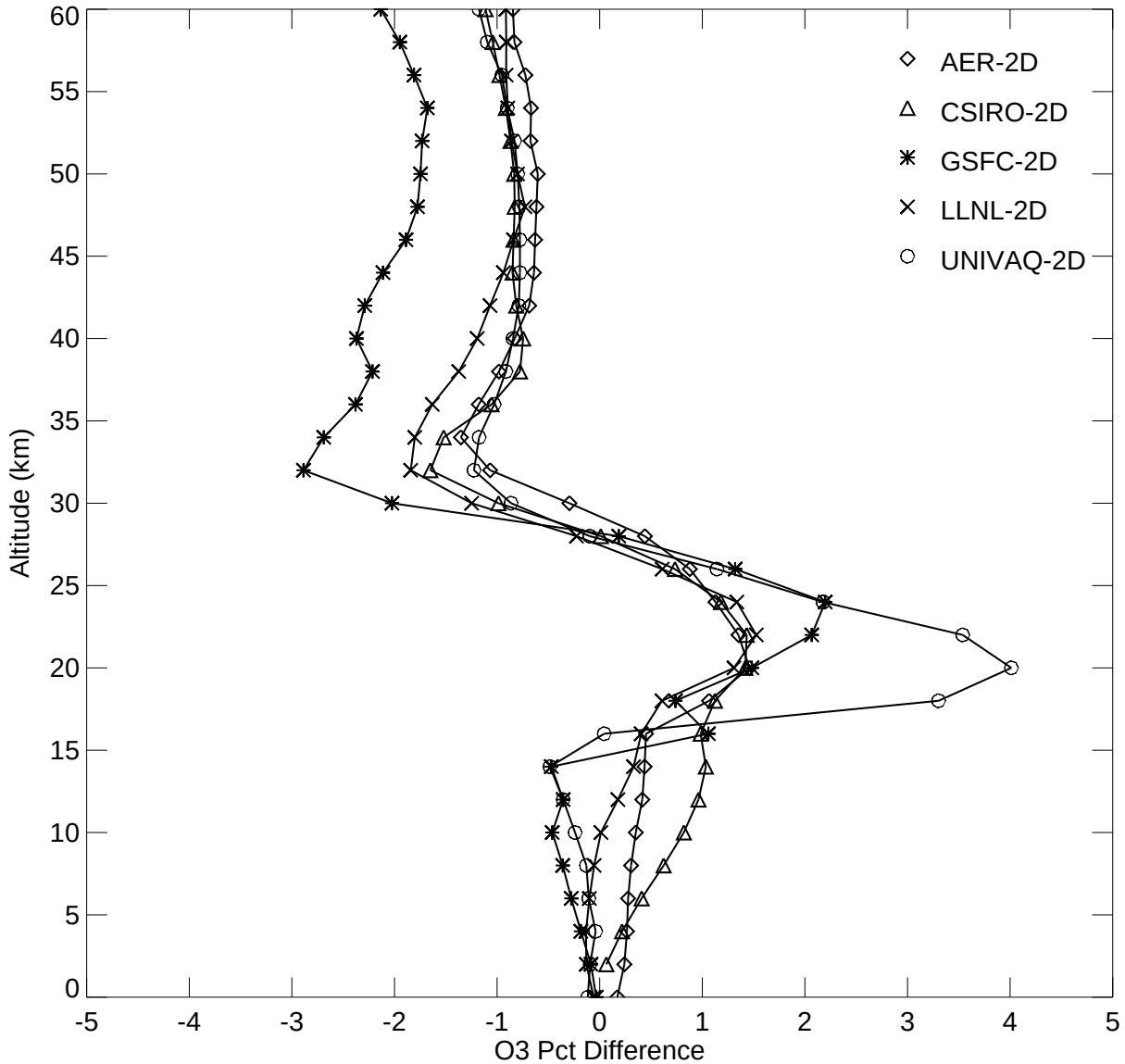

Figure 4.190: Calculated perturbations to O_3 (percent) as a function of altitude at the equator in June of 2015 due to emissions from a fleet of 500 HSCT aircraft with EI(NO_x)=15 and sulfate surface area of 4xSA0 under Scenario S3d relative to Scenario D3.

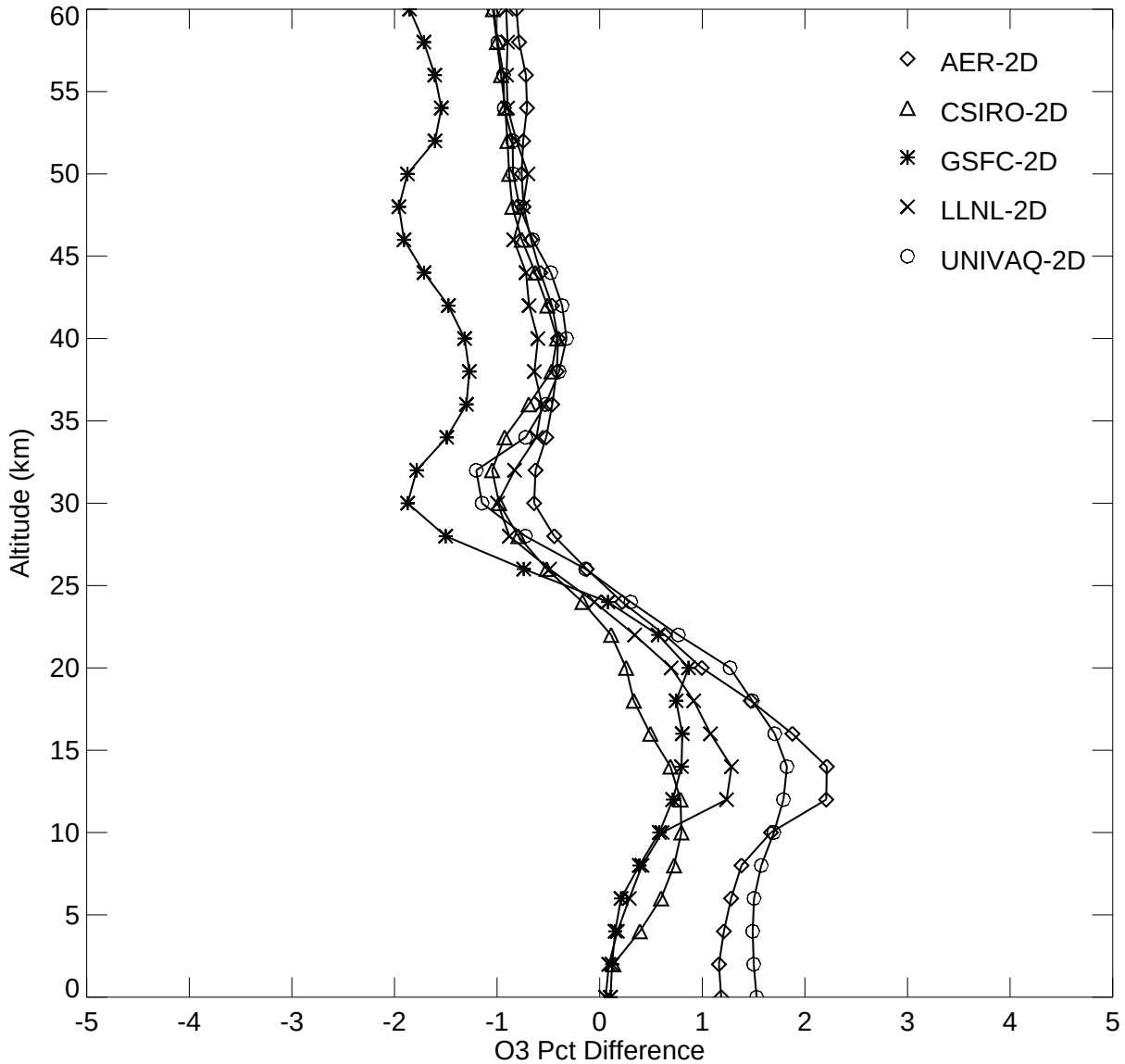

Figure 4.191: Calculated perturbations to O_3 (percent) as a function of altitude at 45°S in June of 2015 due to emissions from a fleet of 500 HSCT aircraft with EI(NO_x)=15 and sulfate surface area of 4xSA0 under Scenario S3d relative to Scenario D3.

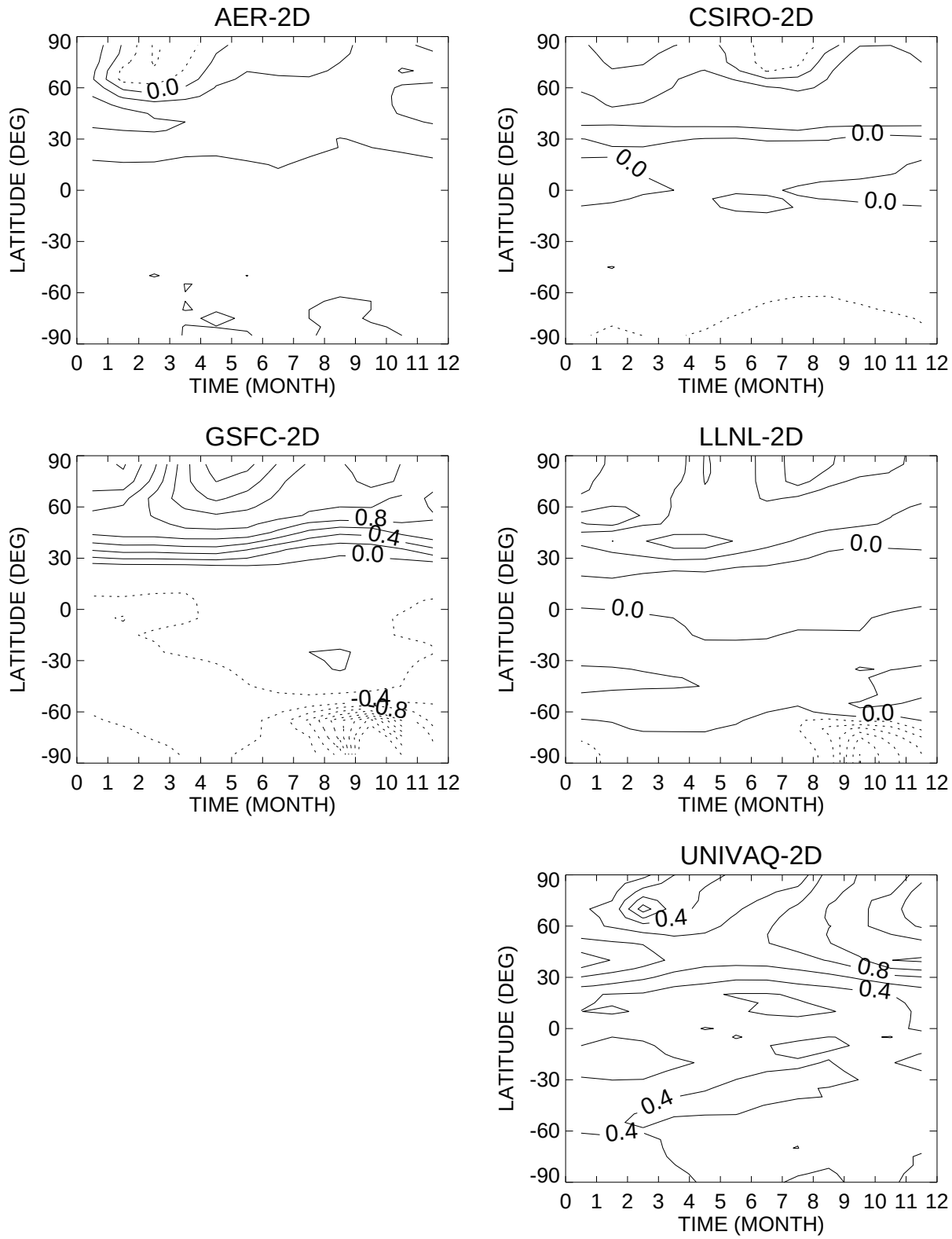

Figure 4.192: Calculated perturbations to column O_3 (percent) as a function of latitude and season in 2015 due to emissions from a fleet of 500 HSCT aircraft with EI(NO_x)=15 and sulfate surface area of 4xSA0 under Scenario S3d relative to Scenario D3. Contours are -2.0 to 1.6 by 0.2.

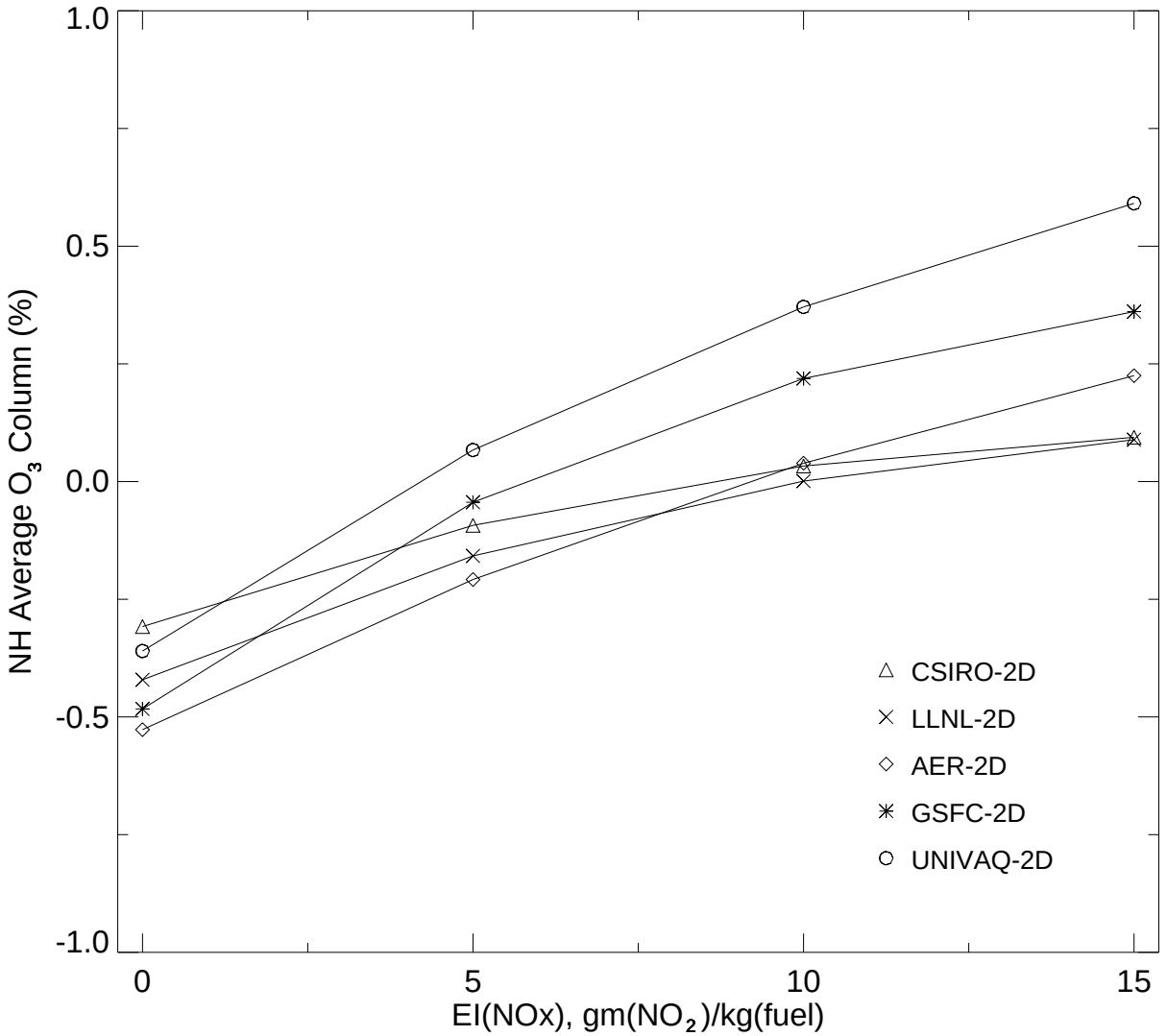

Figure 4.193: Northern hemisphere annual average total O_3 column change (percent) as a function of EI(NO_x) for an HSCT fleet of 500 aircraft operating in 2015 with 4xSA0 sulfate surface area density.

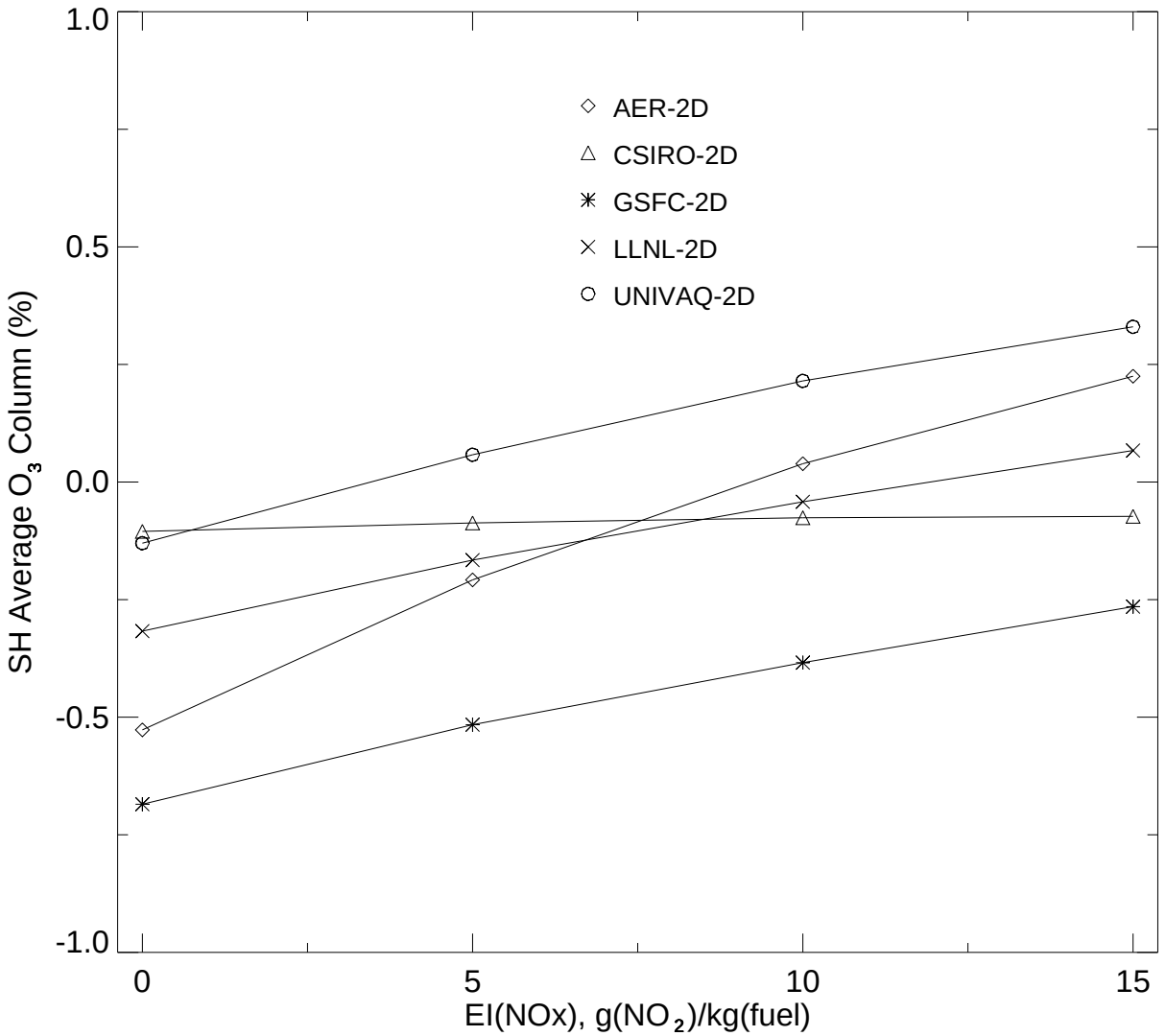

Figure 4.194: Southern hemisphere annual average total O_3 column change (percent) as a function of EI(NO_x) for an HSCT fleet of 500 aircraft operating in 2015 with 4xSA0 sulfate surface area density.

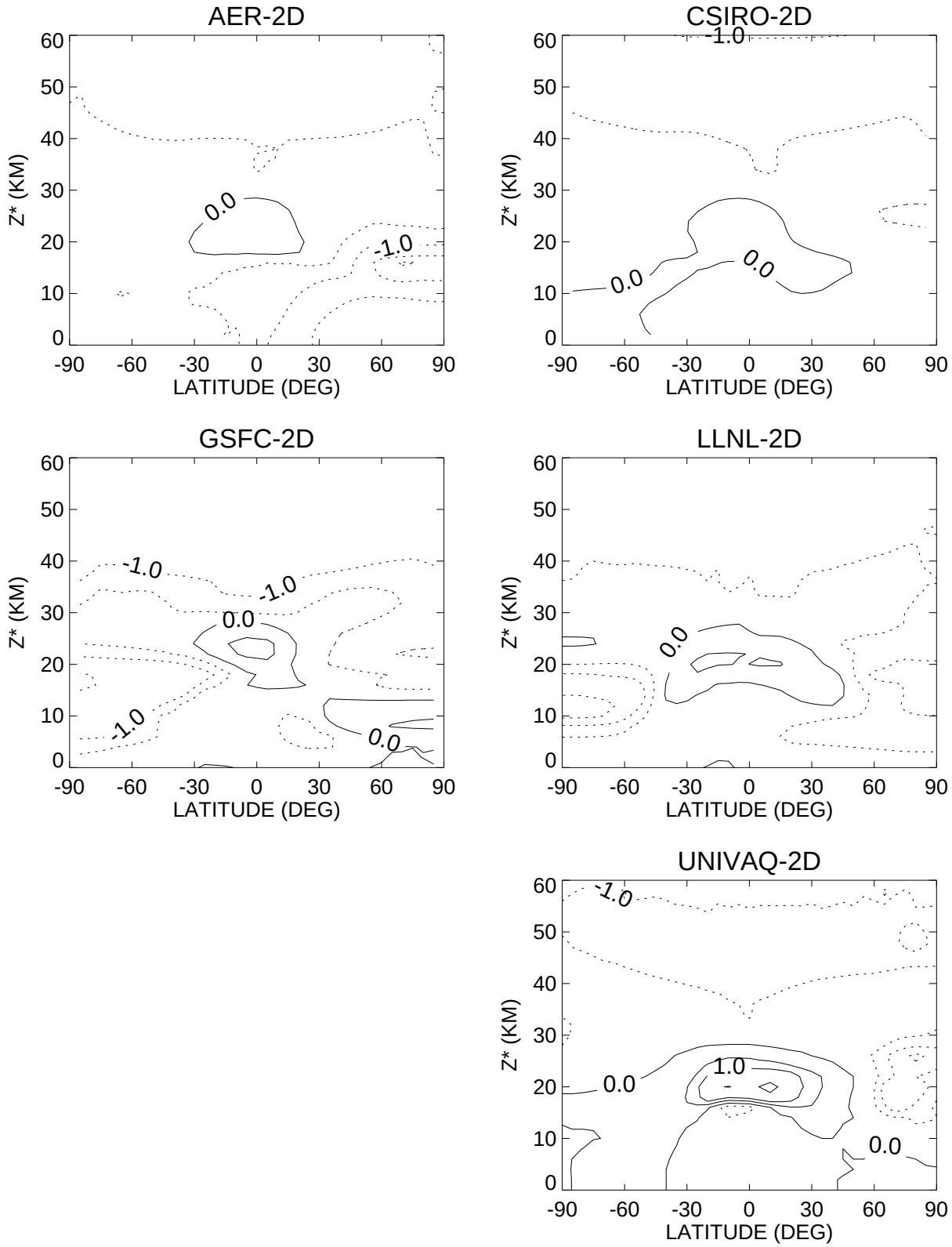

Figure 4.195: Calculated perturbations to O_3 (percent) as a function of latitude and altitude in March of 2015 due to emissions from a fleet of 500 HSCT aircraft operating with EI(NO_x)=5 and sulfate surface area of 4xSA0+SA1-SA0 under Scenario S3e relative to Scenario D3. Contours are -3, -2, -1, -0.5, 0, 0.5, 1, 2.

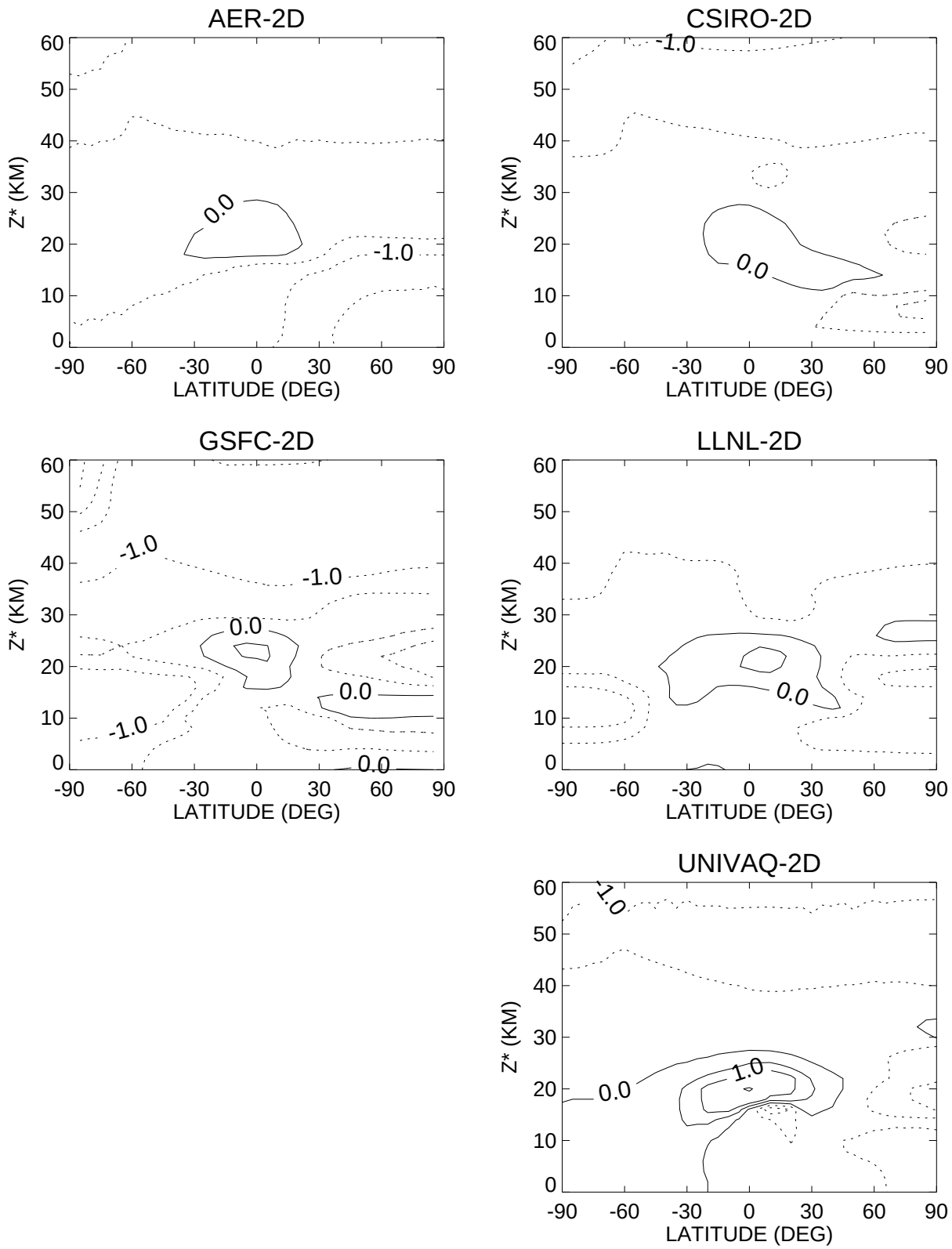

Figure 4.196: Calculated perturbations to O_3 (percent) as a function of latitude and altitude in June of 2015 due to emissions from a fleet of 500 HSCT aircraft with EI(NO_x)=5 and sulfate surface area of 4xSA0+SA1-SA0 under Scenario S3e relative to Scenario D3. Contours are -2, -1, -0.5, 0, 0.5, 1, 2.

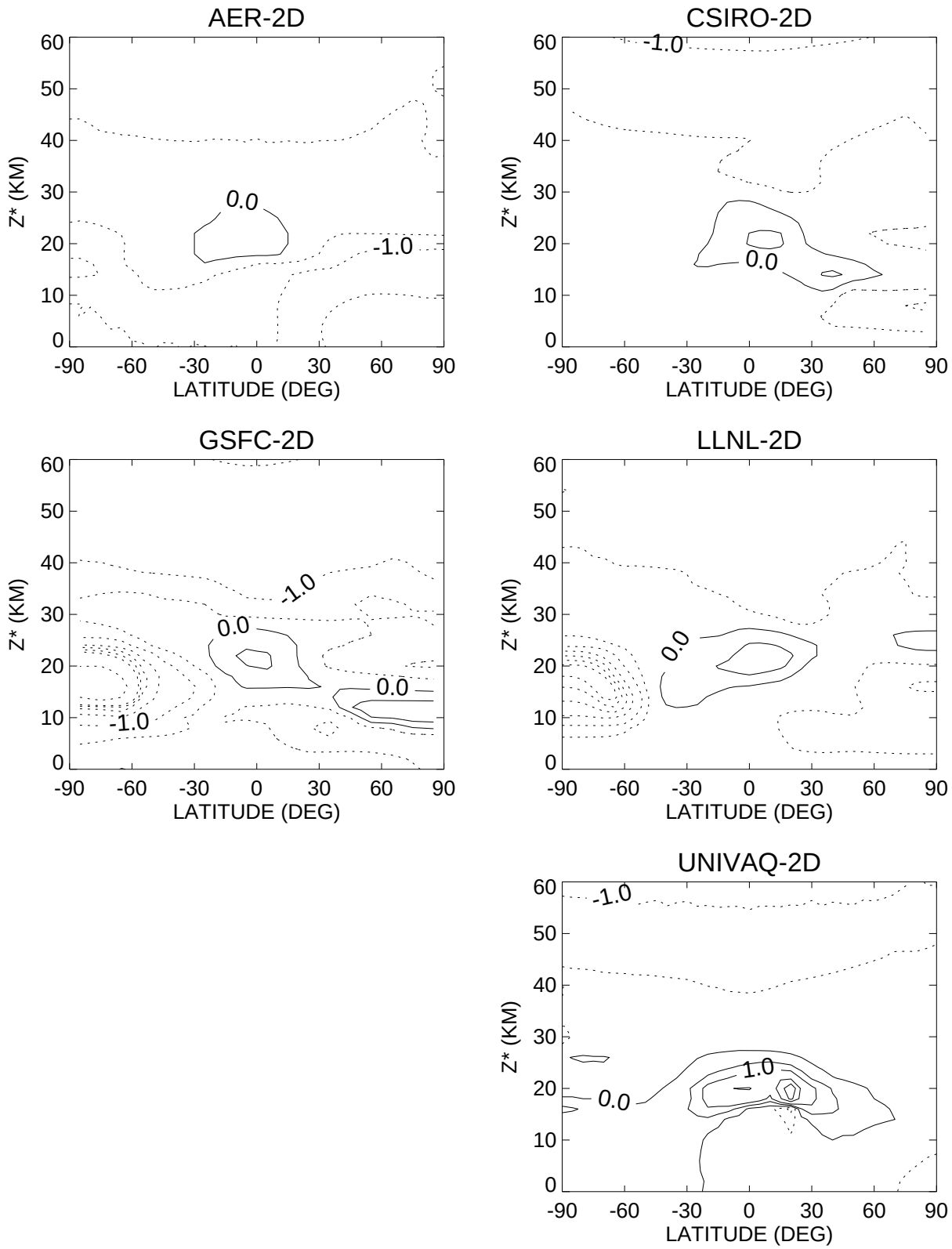

Figure 4.197: Calculated perturbations to O_3 (percent) as a function of latitude and altitude in October of 2015 due to emissions from a fleet of 500 HSCT aircraft with EI(NO_x)=5 and sulfate surface area of 4xSA0+SA1-SA0 under Scenario S3e relative to Scenario D3. Contours are -10, -5, -4, -3, -2, -1, -0.5, 0, 0.5, 1, 2, 3.

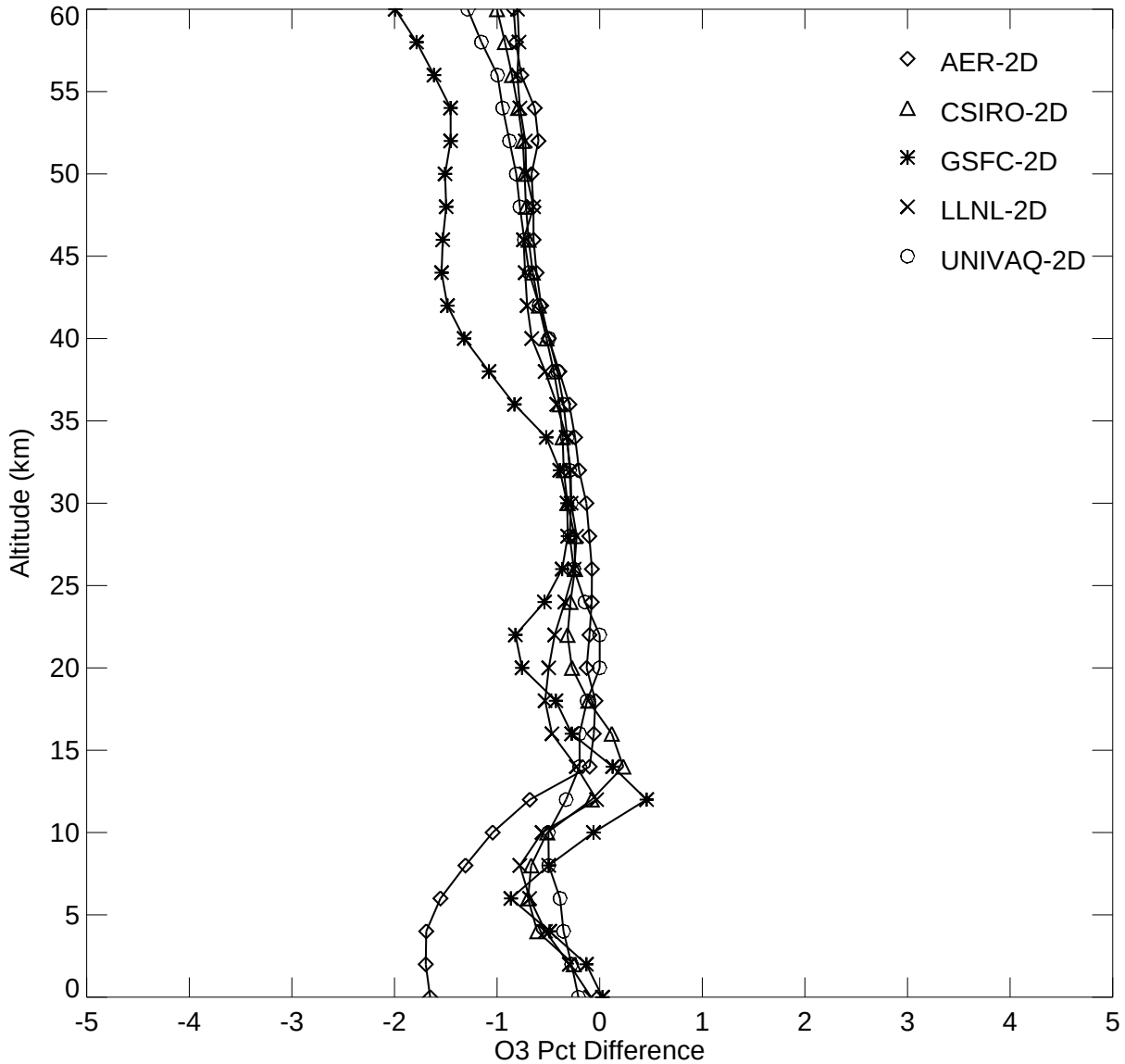

Figure 4.198: Calculated perturbations to O_3 (percent) as a function of altitude at 45^oN in June of 2015 due to emissions from a fleet of 500 HSCT aircraft with EI(NO_x)=5 and sulfate surface area of 4xSA0+SA1-SA0 under Scenario S3e relative to Scenario D3.

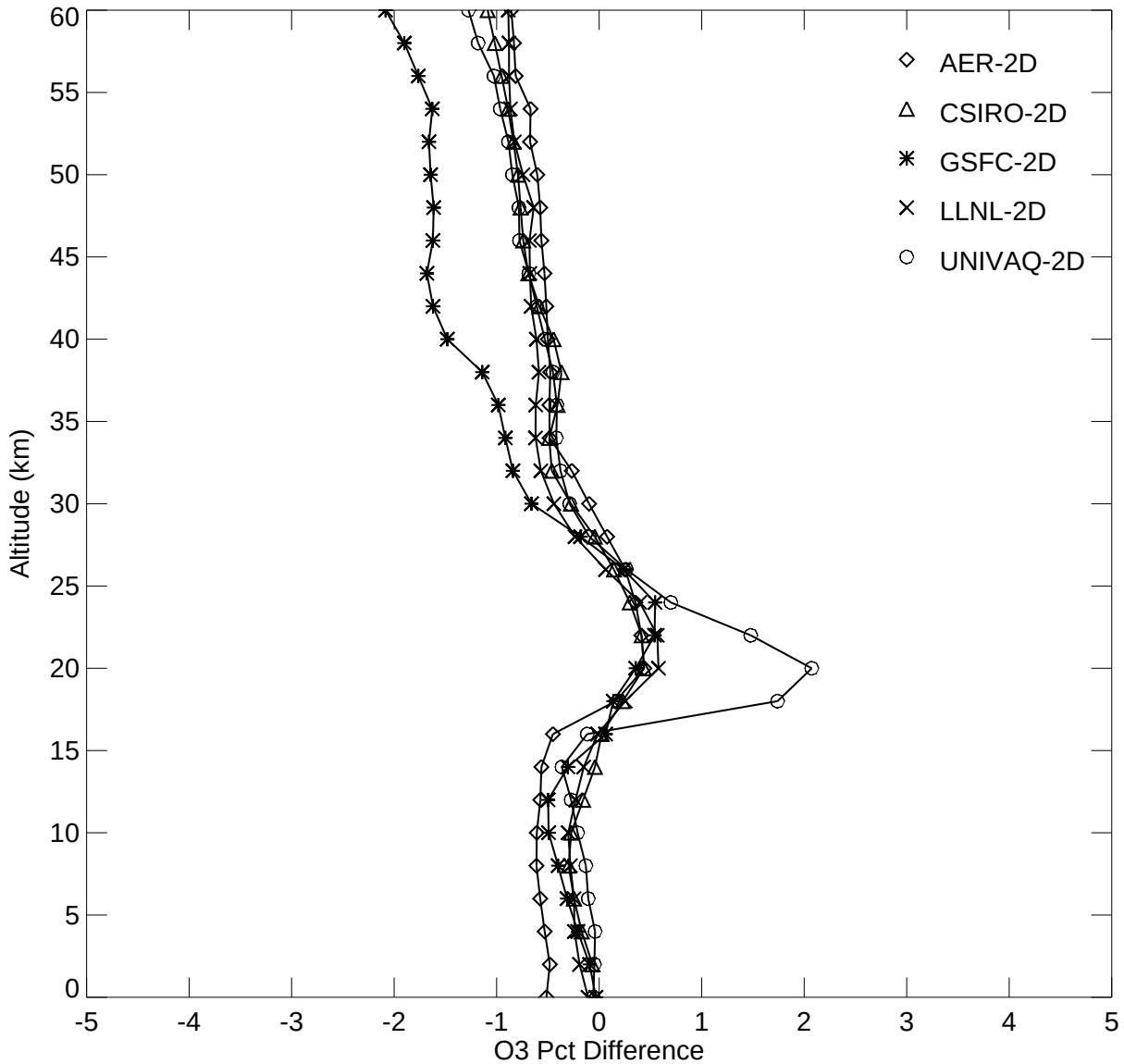

Figure 4.199: Calculated perturbations to O_3 (percent) as a function of altitude at the equator in June of 2015 due to emissions from a fleet of 500 HSCT aircraft with EI(NO_x)=5 and sulfate surface area of 4xSA0+SA1-SA0 under Scenario S3e relative to Scenario D3.

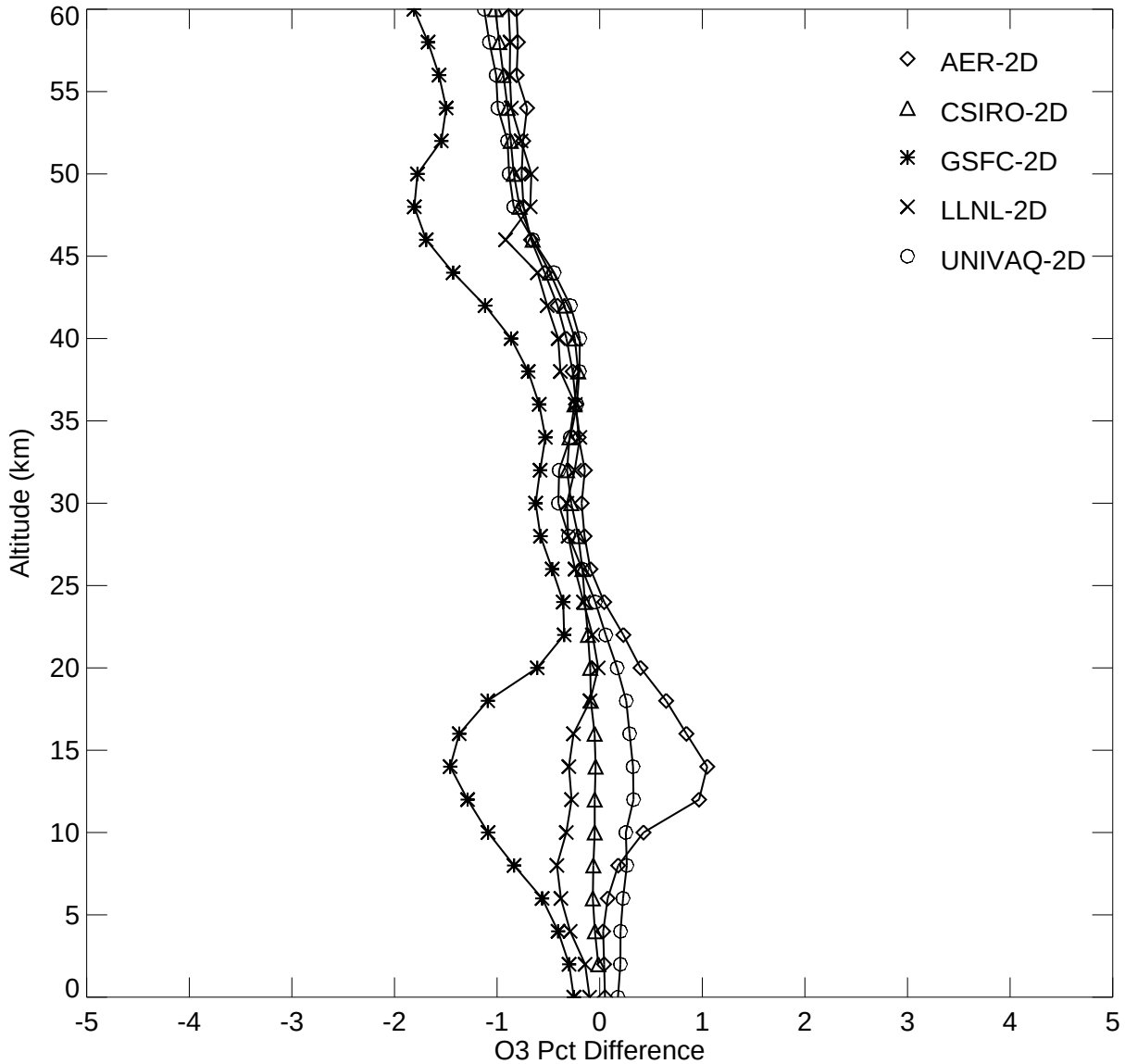

Figure 4.200: Calculated perturbations to O_3 (percent) as a function of altitude at 45°S in June of 2015 due to emissions from a fleet of 500 HSCT aircraft with EI(NO_x)=5 and sulfate surface area of 4xSA0+SA1-SA0 under Scenario S3e relative to Scenario D3.

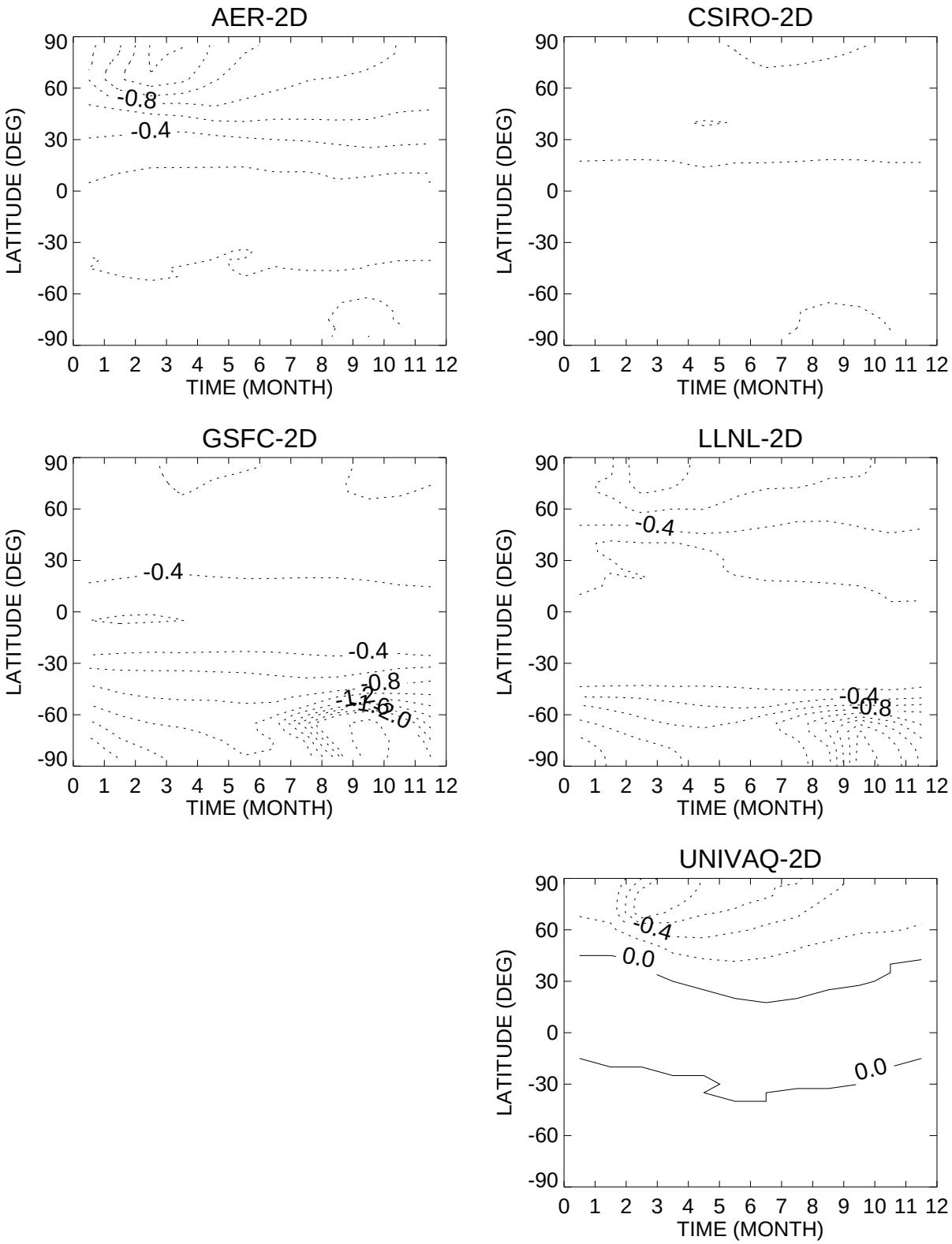

Figure 4.201: Calculated perturbations to column O_3 (percent) as a function of latitude and season in 2015 due to emissions from a fleet of 500 HSCT aircraft with EI(NO_x)=5 and sulfate surface area of 4xSA0+SA1-SA0 under Scenario S3e relative to Scenario D3. Contours are -3 and -2 to 0 by 0.2.

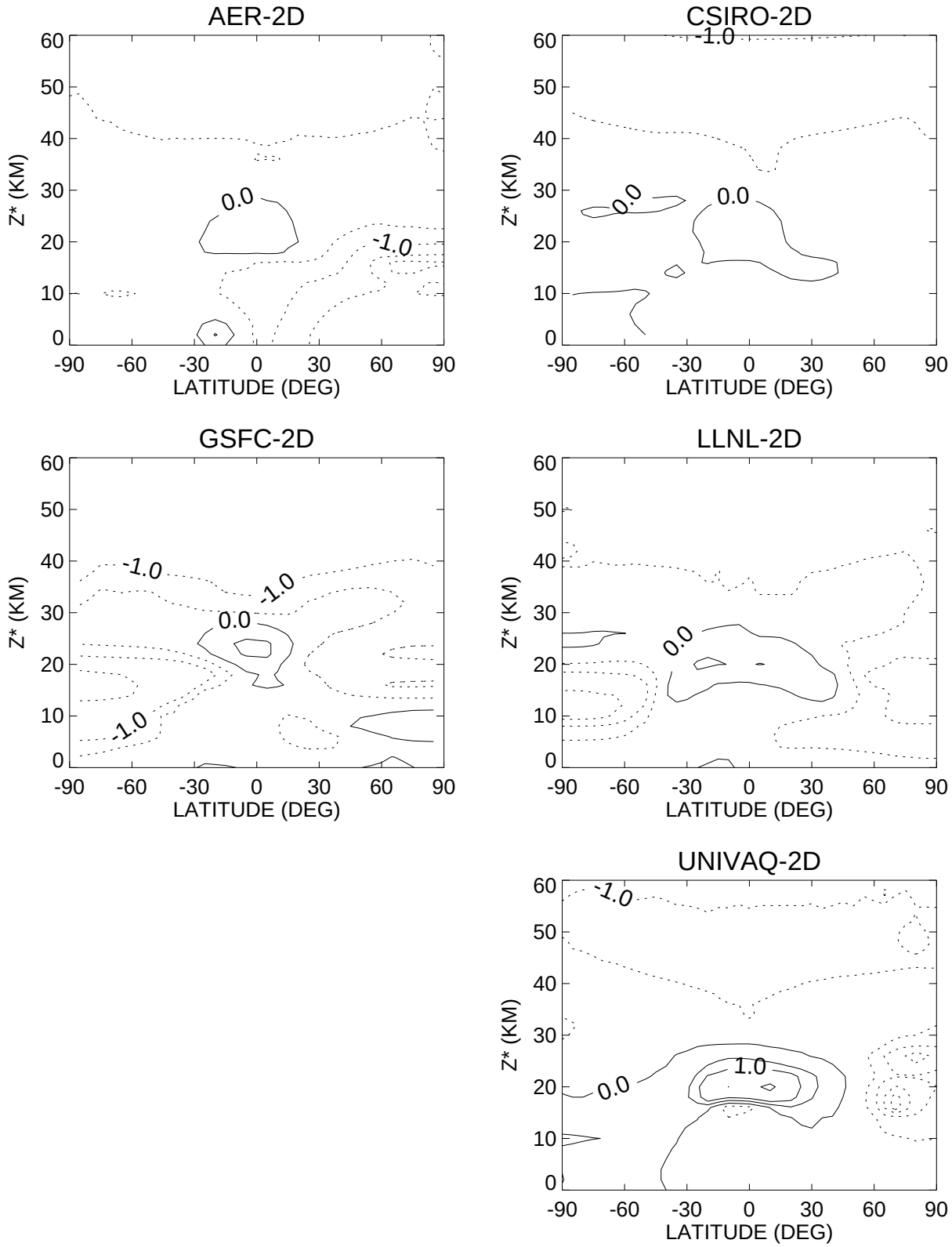

Figure 4.202: Calculated perturbations to O_3 (percent) as a function of latitude and altitude in March of 2015 due to emissions from a fleet of 500 HSCT aircraft with EI(NO_x)=5 and sulfate surface area of 4xSA0+SA3-SA0 under Scenario S3f relative to Scenario D3. Contours are -3, -2, -1, -0.5, 0, 0.5, 1, 2.

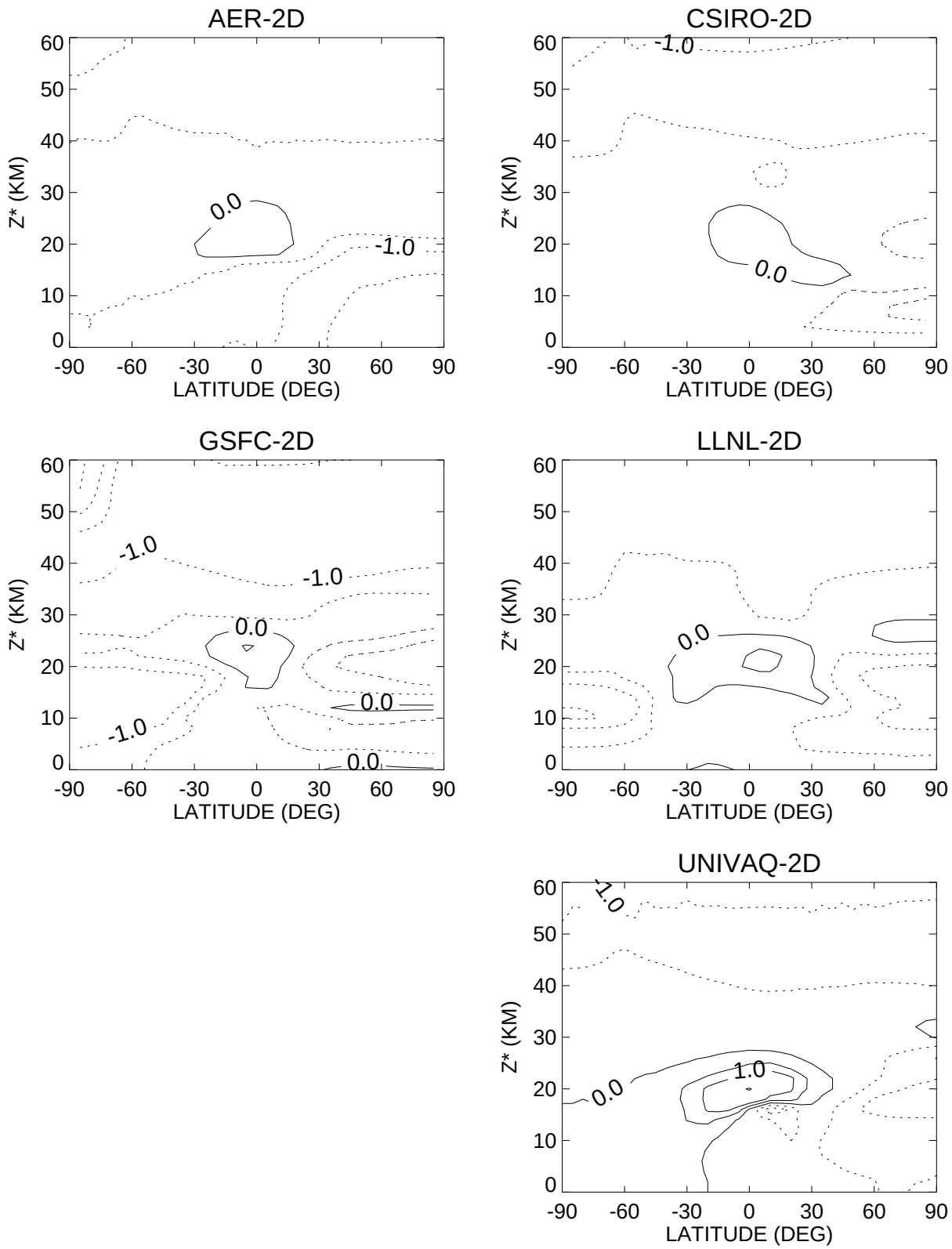

Figure 4.203: Calculated perturbations to O_3 (percent) as a function of latitude and altitude in June of 2015 due to emissions from a fleet of 500 HSCT aircraft with EI(NO_x)=5 and sulfate surface area of 4xSA0+SA3-SA0 under Scenario S3f relative to Scenario D3. Contours are -2, -1, -0.5, 0, 0.5, 1, 2.

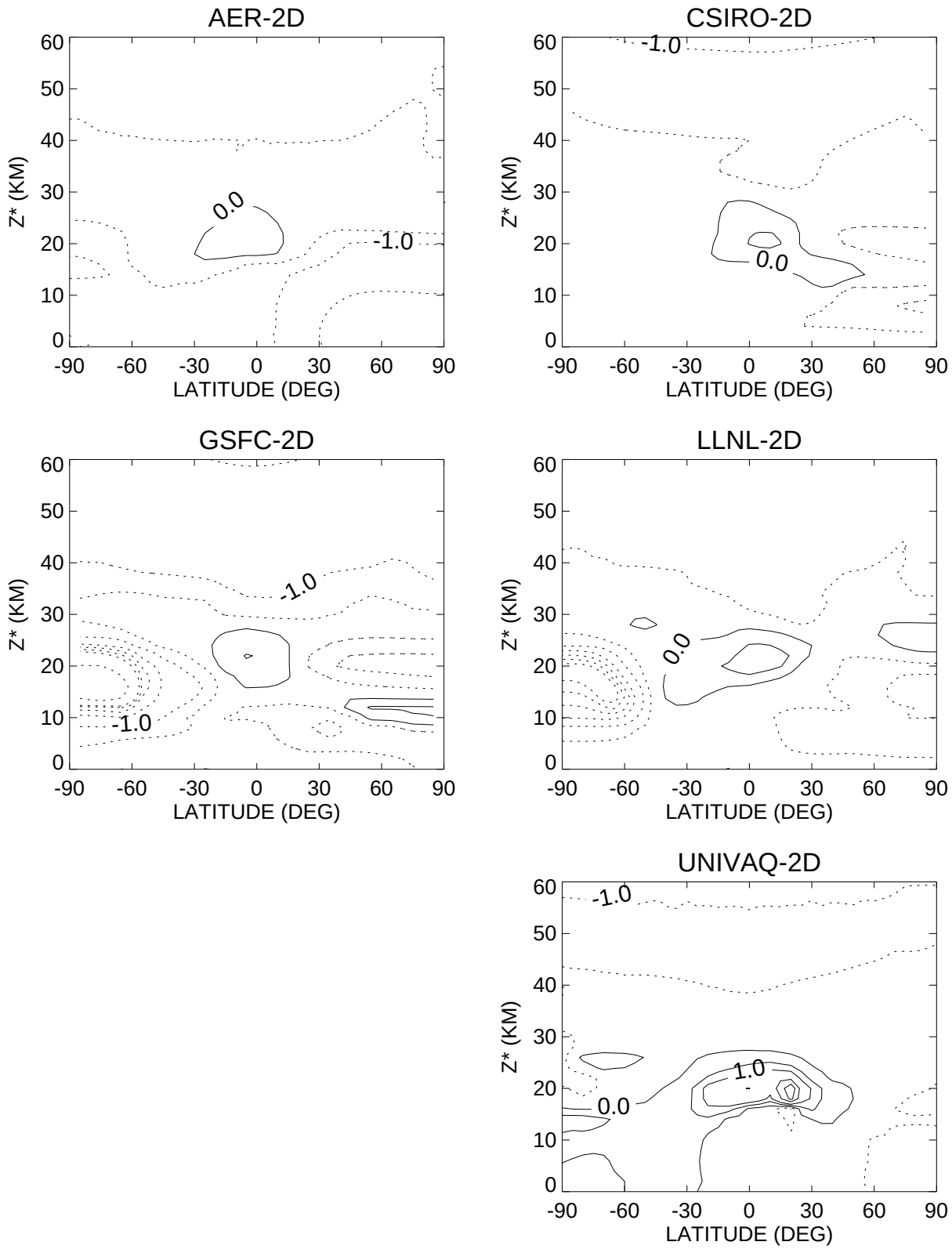

Figure 4.204: Calculated perturbations to O_3 (percent) as a function of latitude and altitude in October of 2015 due to emissions from a fleet of 500 HSCT aircraft with EI(NO_x)=5 and sulfate surface area of 4xSA0+SA3-SA0 under Scenario S3f relative to Scenario D3. Contours are -10, -5, -4, -3, -2, -1, -0.5, 0, 0.5, 1, 2, 3.

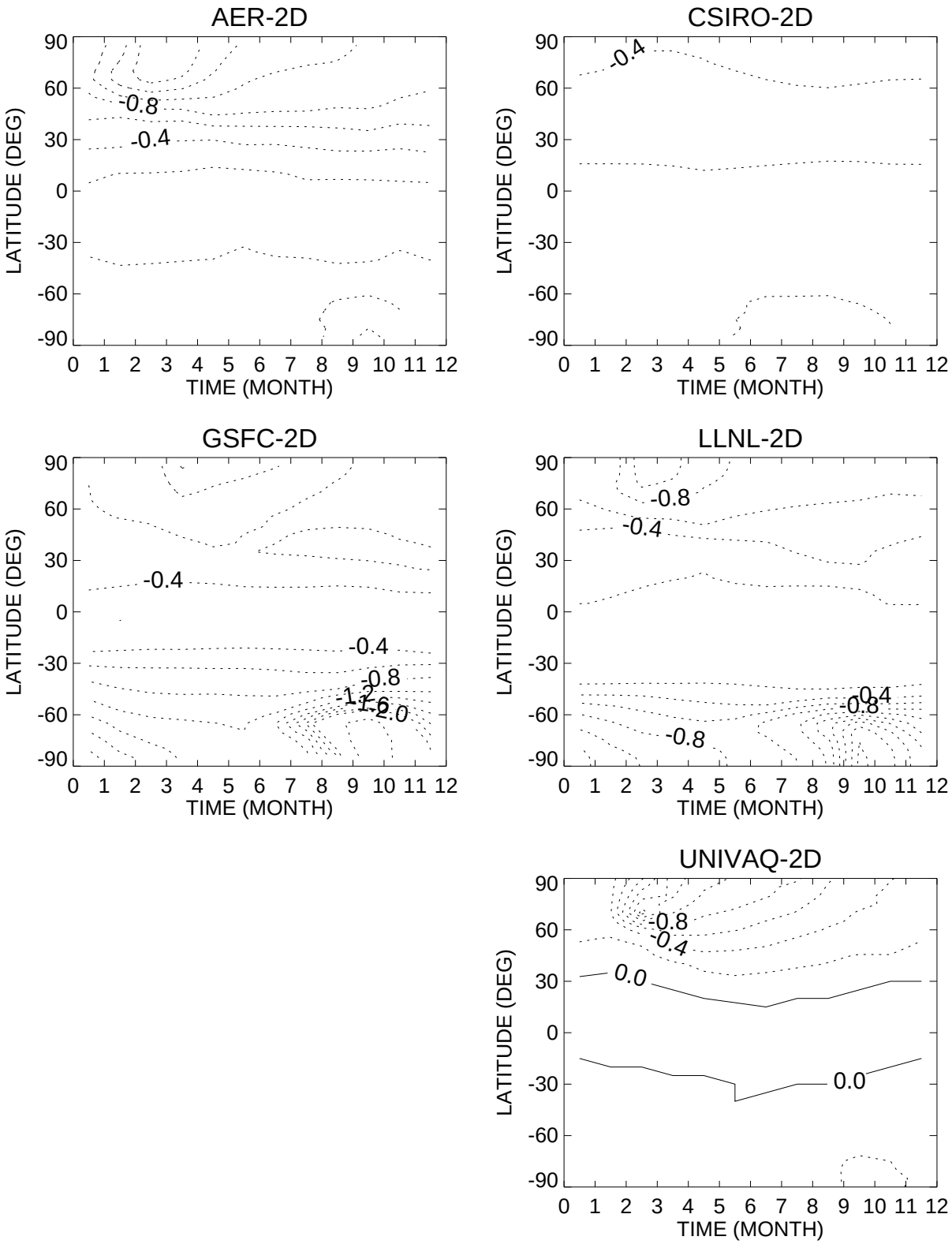

Figure 4.205: Calculated perturbations to column O_3 (percent) as a function of latitude and season in 2015 due to emissions from a fleet of 500 HSCT aircraft with EI(NO_x)=5 and sulfate surface area of 4xSA0+SA3-SA0 under Scenario S3f relative to Scenario D3. Contours are -3 and -2 to 0 by 0.2.

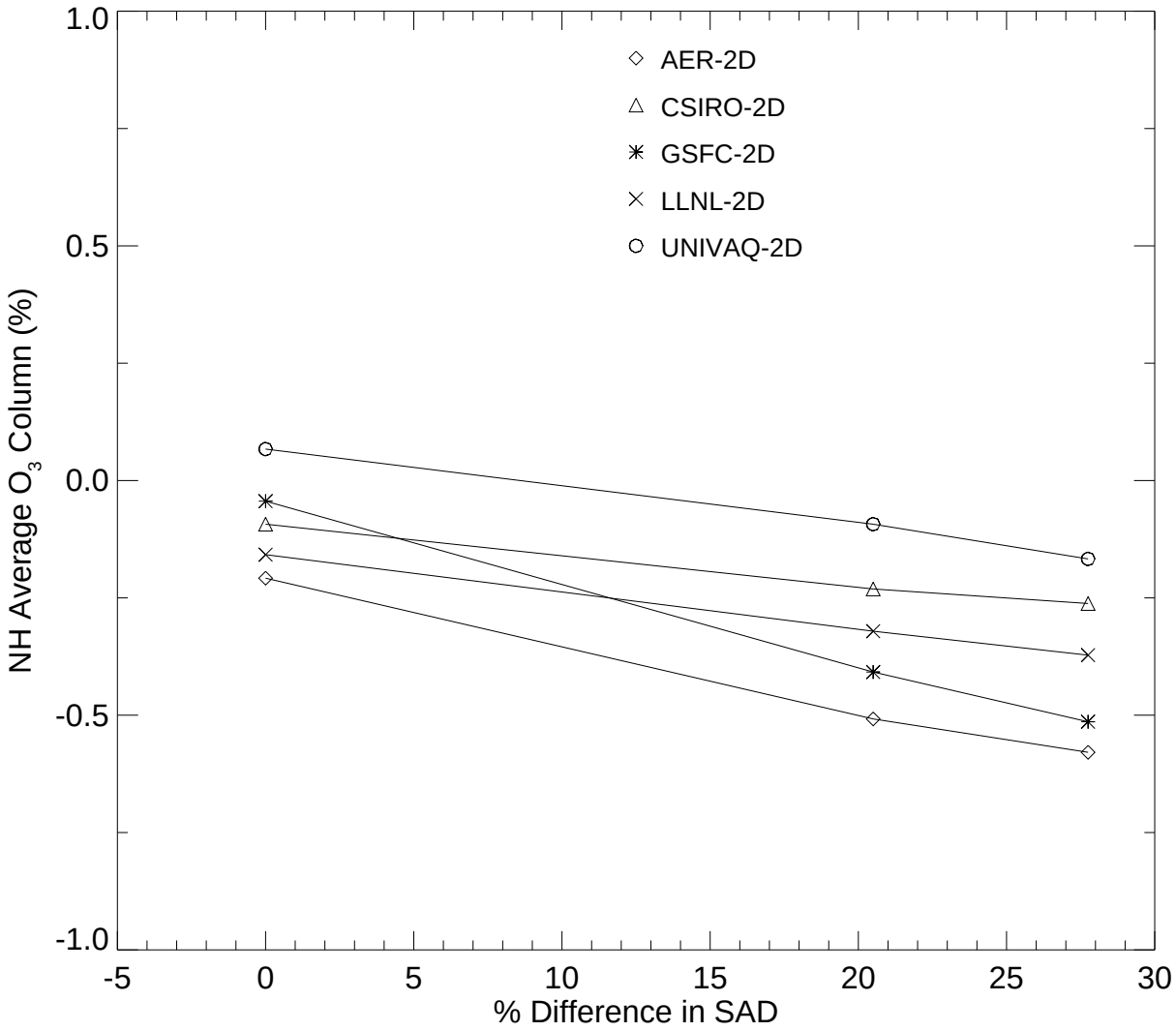

Figure 4.206: Northern hemisphere annual average total O_3 column change (percent) as a function of the percent change in aerosol surface area density in the region from 14 to 21 km and from 33^{o}N to 90^{o}N. The HSCT fleet consisted of 500 aircraft operating in 2015 with EI(NO_x)=5 and 4xSA0 as the background surface area density.

4.3.5 Scenarios without PSC Formulations (S4a-c)

This section will cover Scenarios S4a-S4c which omit the model PSC representation. Because the models use different representations of PSC processes, this is one aspect of modeling which may contribute substantially to intermodel differences. Removal of the PSC representations is found to considerably reduce the intermodel differences. It also allows us to evaluate the impact of each model's PSC representation on calculated ozone perturbation due to HSCT emissions. And it helps to provide a measurement of model uncertainty in evaluating HSCT impacts. Note that the CSIRO model does not include PSCs in its formulation, so Scenarios S1b, S1c, and S1a are identical to Scenarios S4a, S4b, and S4c, respectively.

Scenario S4a uses a 500 HSCT fleet with EI(NO_x)=0 in 2015 with nonvolcanic background sulfate surface area density SA0 and no aircraft sulfur emissions. This scenario is the same as Scenario S1b except that the PSC representations are omitted from the models. Changes in ozone for this scenario relative to background scenario D4 are shown in Figures 4.207, 4.208, and 4.209 for March, June, and October. The AER model is quite similar with and without PSCs for this scenario, but with northern hemisphere ozone depletion slightly smaller. The GSFC model shows much less ozone depletion in the southern hemisphere below 20 km without PSCs. The northern hemisphere also shows less ozone depletion below 20 km, but the 25-35 km region in both hemispheres shows more ozone depletion with PSCs. The UNIVAQ model shows slightly lower ozone depletion in both hemispheres without PSCs. Changes in ozone column as a function of latitude and season for S4a-D4 are shown in Figure 4.210.

Scenario S4b includes HSCT emissions with EI(NO_x)=5 and SA0 background SAD. Calculated ozone changes are shown in Figures 4.211, 4.212, and 4.213 for March, June, and October for S4b-D4. Ozone depletion is reduced relative to S4a-D4 in the AER, CSIRO, and UNIVAQ models below 25 km, but increased around 30 km. The GSFC model shows virtually no change due to the added HSCT NO_x emissions. Figure 4.214 shows changes in ozone column for Scenario S4b-D4. By comparison with Scenario S1c-D, ozone depletion is seen to be reduced in the southern hemisphere for the GSFC model when the PSC parameterizations are removed. Northern hemisphere ozone depletion is reduced for the AER model without PSCs.

Scenario S4c includes HSCT emissions of NO_x only (no H_2O emissions) with EI(NO_x)=5. Changes in ozone for S4c-D4 are shown in Figures 4.215-4.217. Ozone changes in the upper stratosphere are greatly reduced relative to S2b-D4 with H_2O emissions. All models show reduced ozone depletion relative to S2b-D4 in the troposphere and lower stratosphere as well, with the CSIRO, GSFC, and UNIVAQ models showing ozone increases relative to D4 in this region. Column ozone changes for S4c-D4 are shown in Figure 4.218. Ozone column changes are quite small for all models, between -0.4% and +0.4%. From comparison with S1a-D, which includes PSCs, we conclude that the PSC parameterizations have little impact without H_2O emissions.

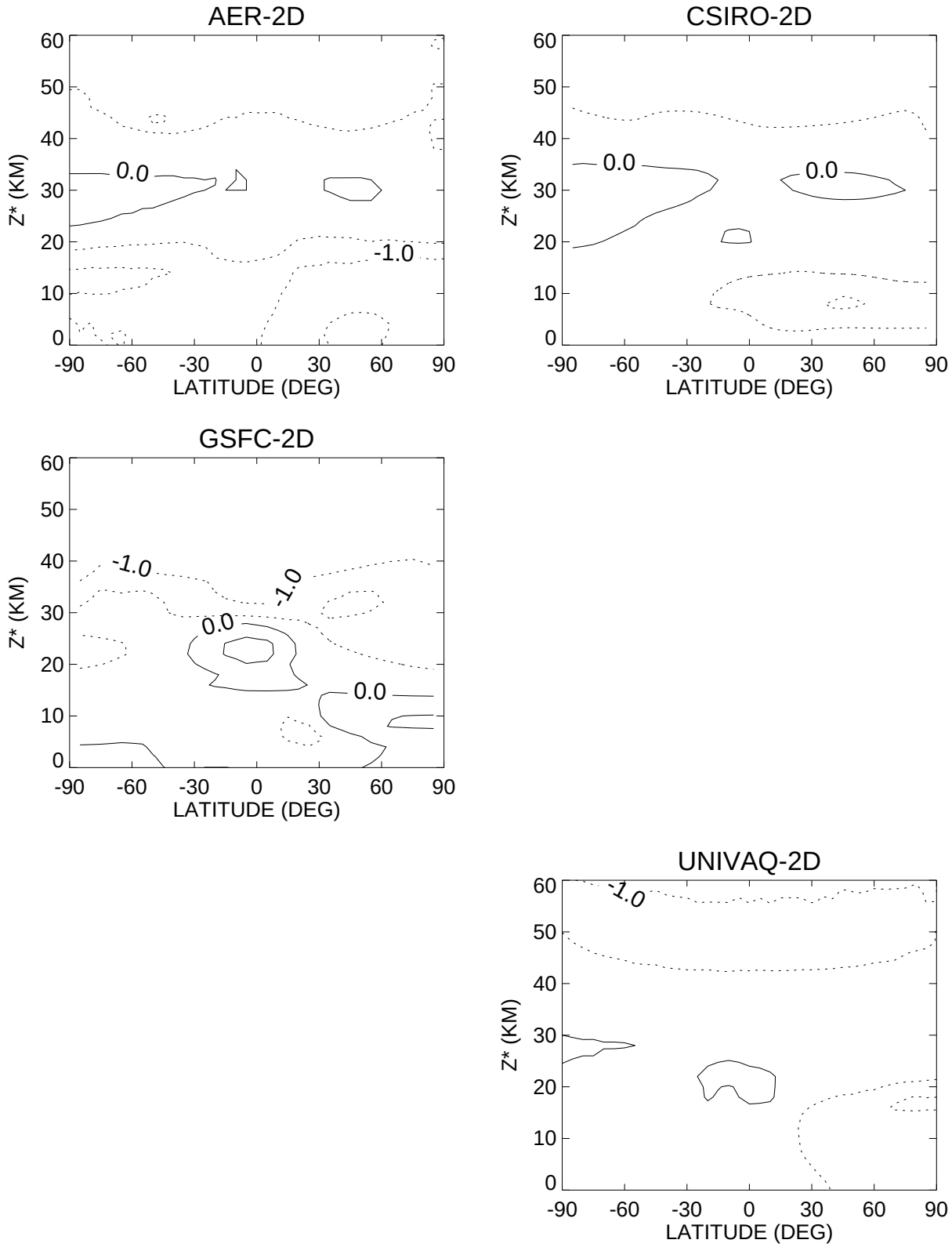

Figure 4.207: Calculated perturbations to O_3 (percent) as a function of latitude and altitude in March of 2015 due to emissions from a fleet of 500 HSCT aircraft with EI(NO_x)=0 and the model PSC parameterization removed under Scenario S4a relative to Scenario D4. Contours are -2, -1, -0.5, 0, 0.5.

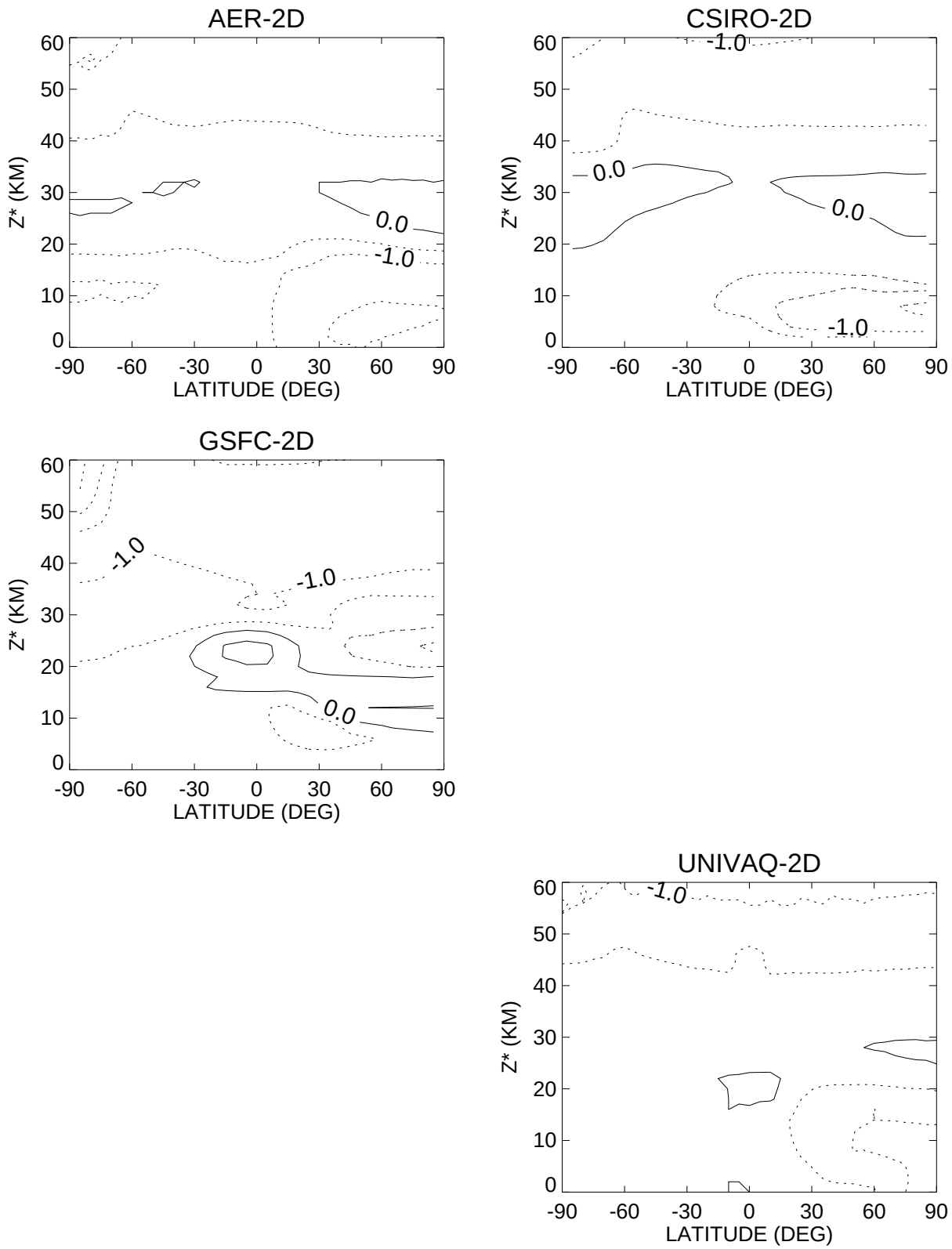

Figure 4.208: Calculated perturbations to O_3 (percent) as a function of latitude and altitude in June of 2015 due to emissions from a fleet of 500 HSCT aircraft with EI(NO_x)=0 and the model PSC parameterization removed under Scenario S4a relative to Scenario D4. Contours are -2, -1, -0.5, 0, 0.5.

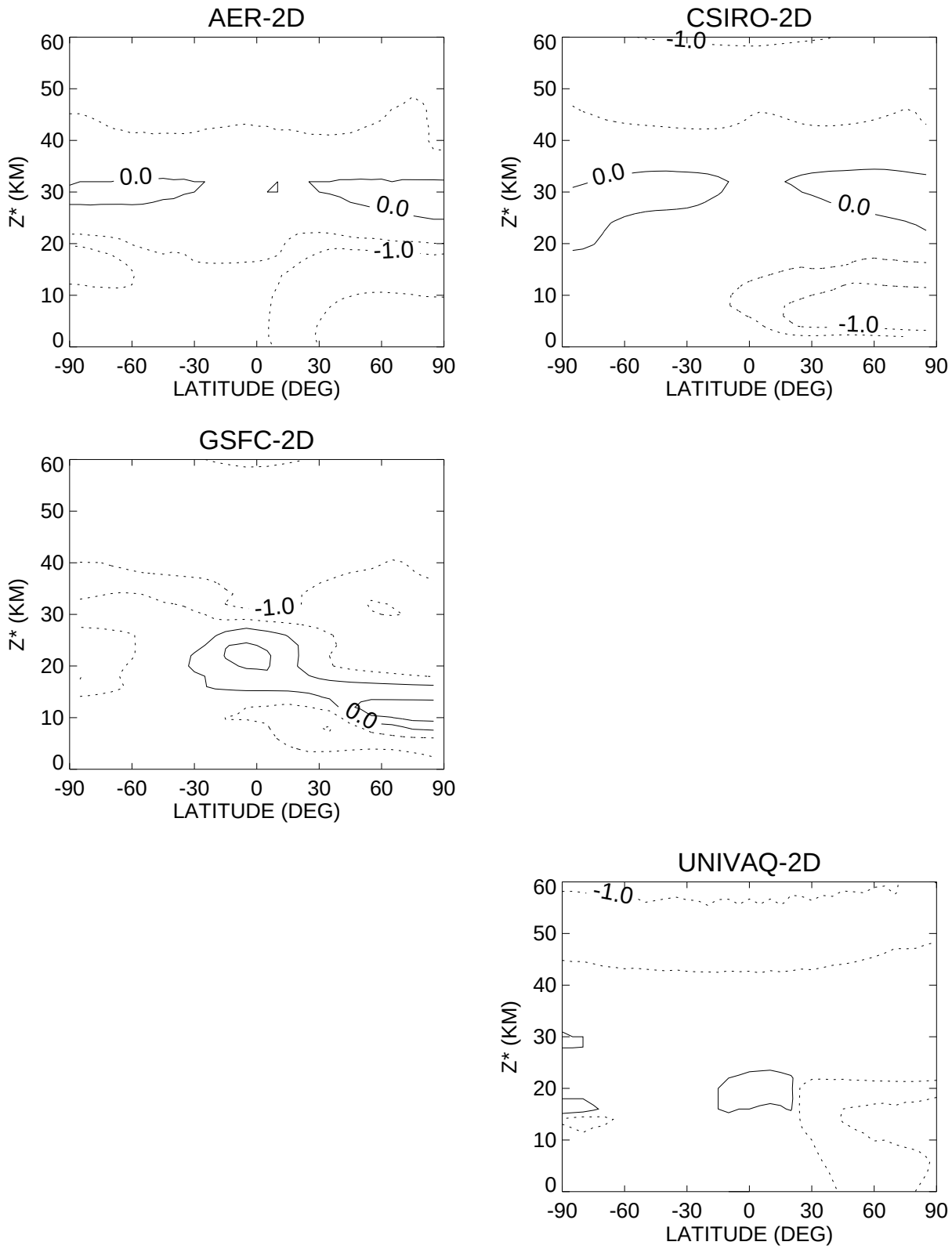

Figure 4.209: Calculated perturbations to O_3 (percent) as a function of latitude and altitude in October of 2015 due to emissions from a fleet of 500 HSCT aircraft with EI(NO_x)=0 and the model PSC parameterization removed under Scenario S4a relative to Scenario D4. Contours are -5, -4, -3, -2, -1, -0.5, 0, 0.5.

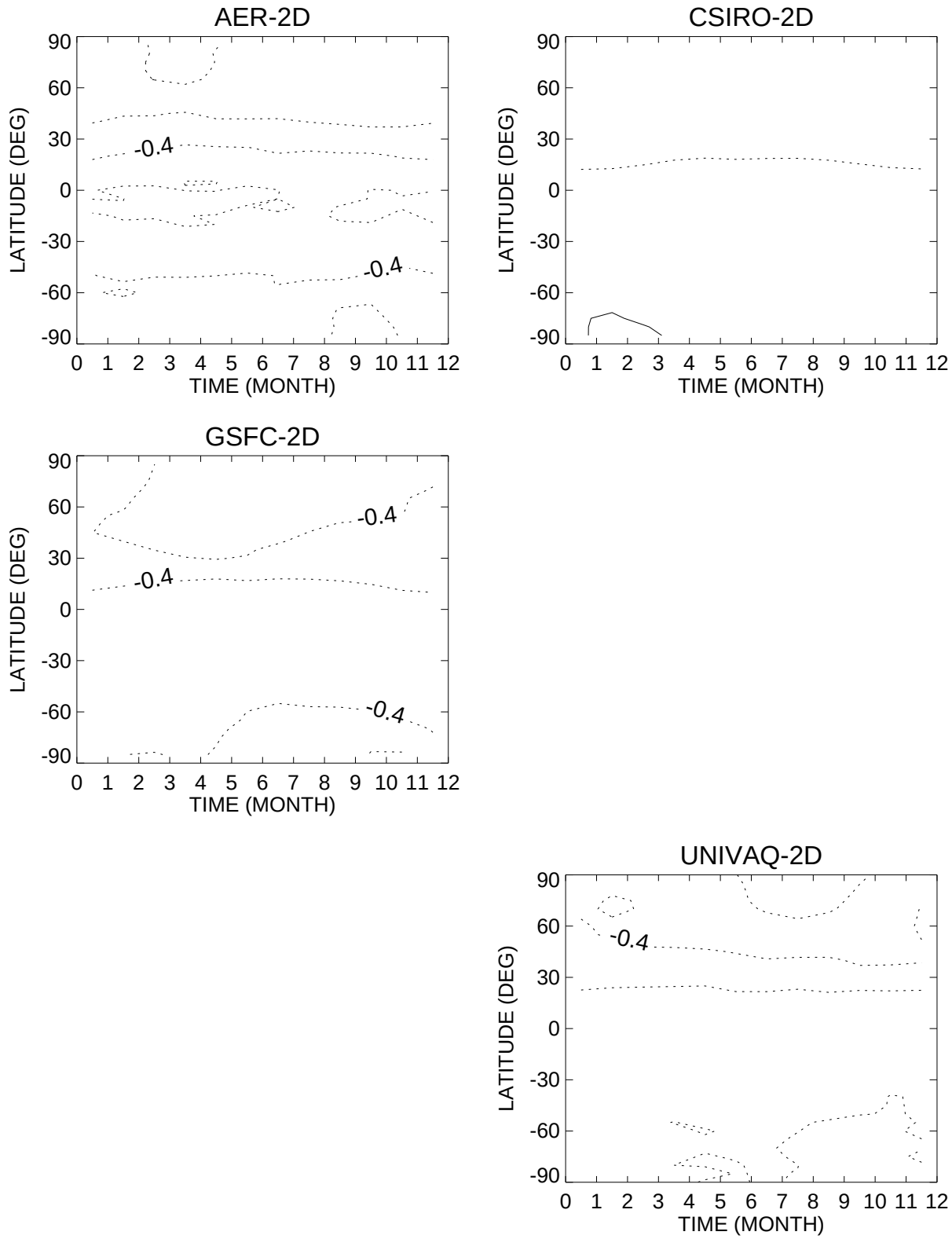

Figure 4.210: Calculated perturbations to column O_3 (percent) as a function of latitude and season in 2015 due to emissions from a fleet of 500 HSCT aircraft with EI(NO_x)=0 and the model PSC parameterization removed under Scenario S4a relative to Scenario D4. Contours are -1.2 to -0.2 by 0.2.

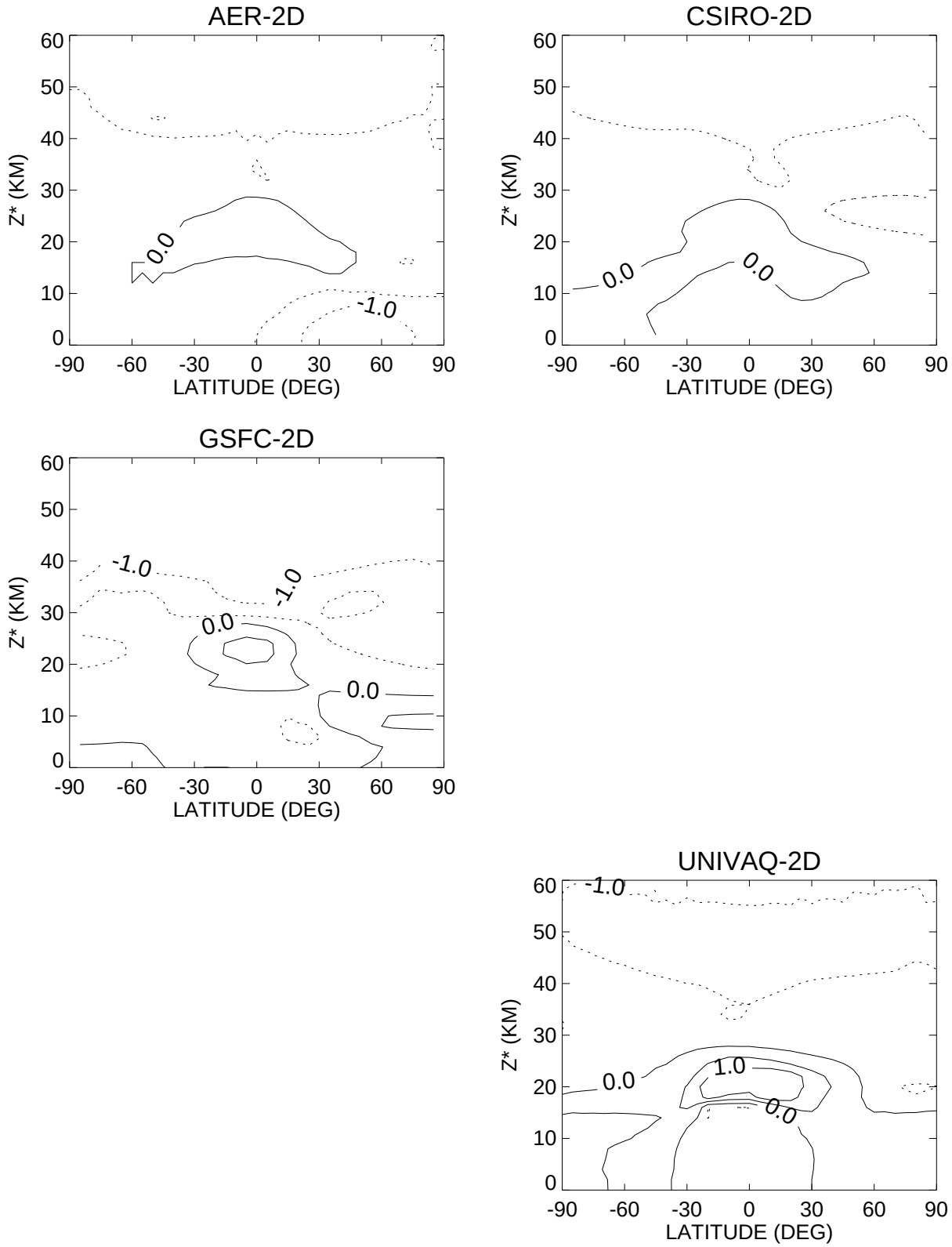

Figure 4.211: Calculated perturbations to O_3 (percent) as a function of latitude and altitude in March of 2015 due to emissions from a fleet of 500 HSCT aircraft with EI(NO_x)=5 and the model PSC parameterization removed under Scenario S4b relative to Scenario D4. Contours are -1, -0.5, 0, 0.5, 1.

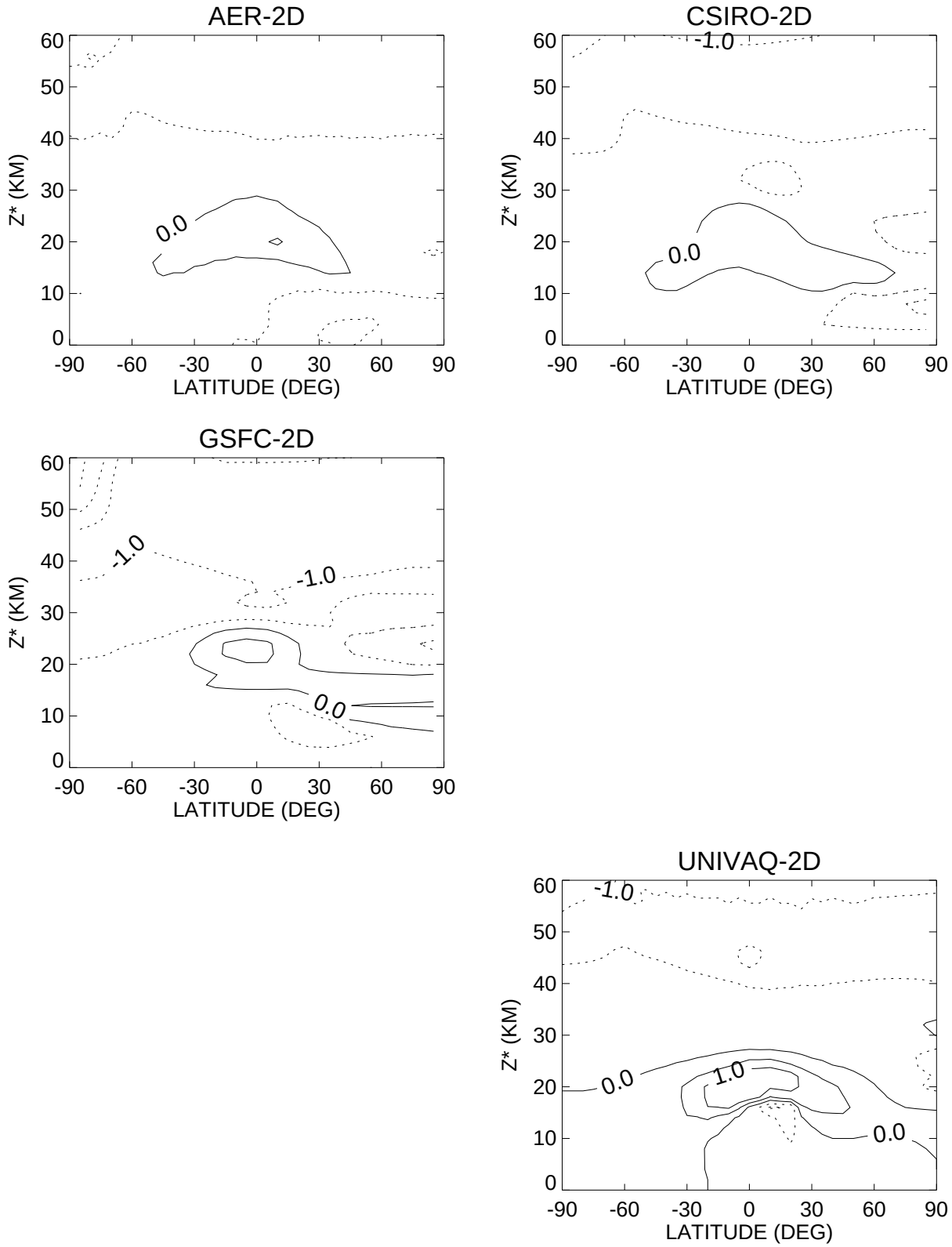

Figure 4.212: Calculated perturbations to O_3 (percent) as a function of latitude and altitude in June of 2015 due to emissions from a fleet of 500 HSCT aircraft with EI(NO_x)=5 and the model PSC parameterization removed under Scenario S4b relative to Scenario D4. Contours are -2, -1, -0.5, 0, 0.5, 1.

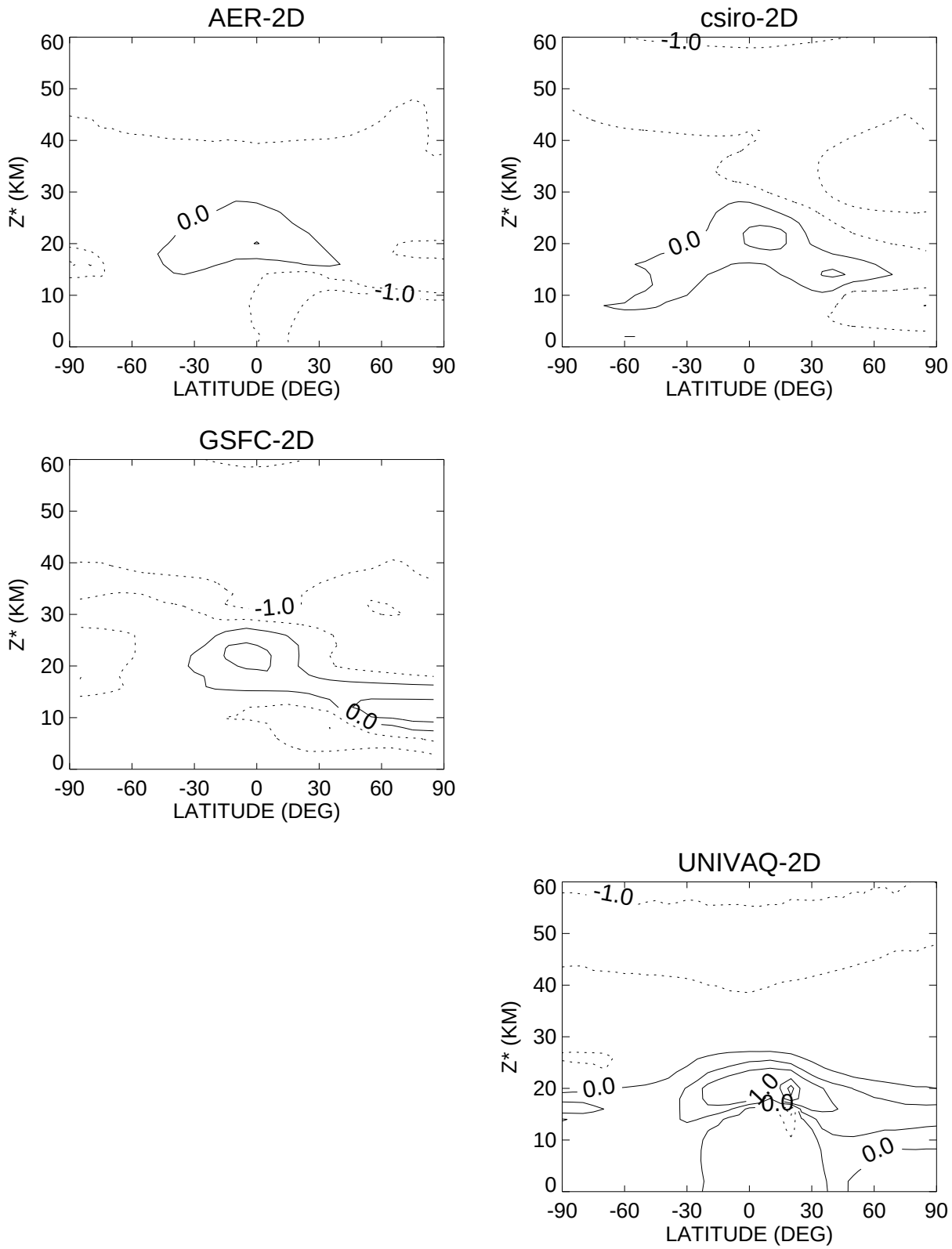

Figure 4.213: Calculated perturbations to O_3 (percent) as a function of latitude and altitude in October of 2015 due to emissions from a fleet of 500 HSCT aircraft with EI(NO_x)=5 and the model PSC parameterization removed under Scenario S4b relative to Scenario D4. Contours are -3, -2, -1, -0.5, 0, 0.5, 1, 2, 3.

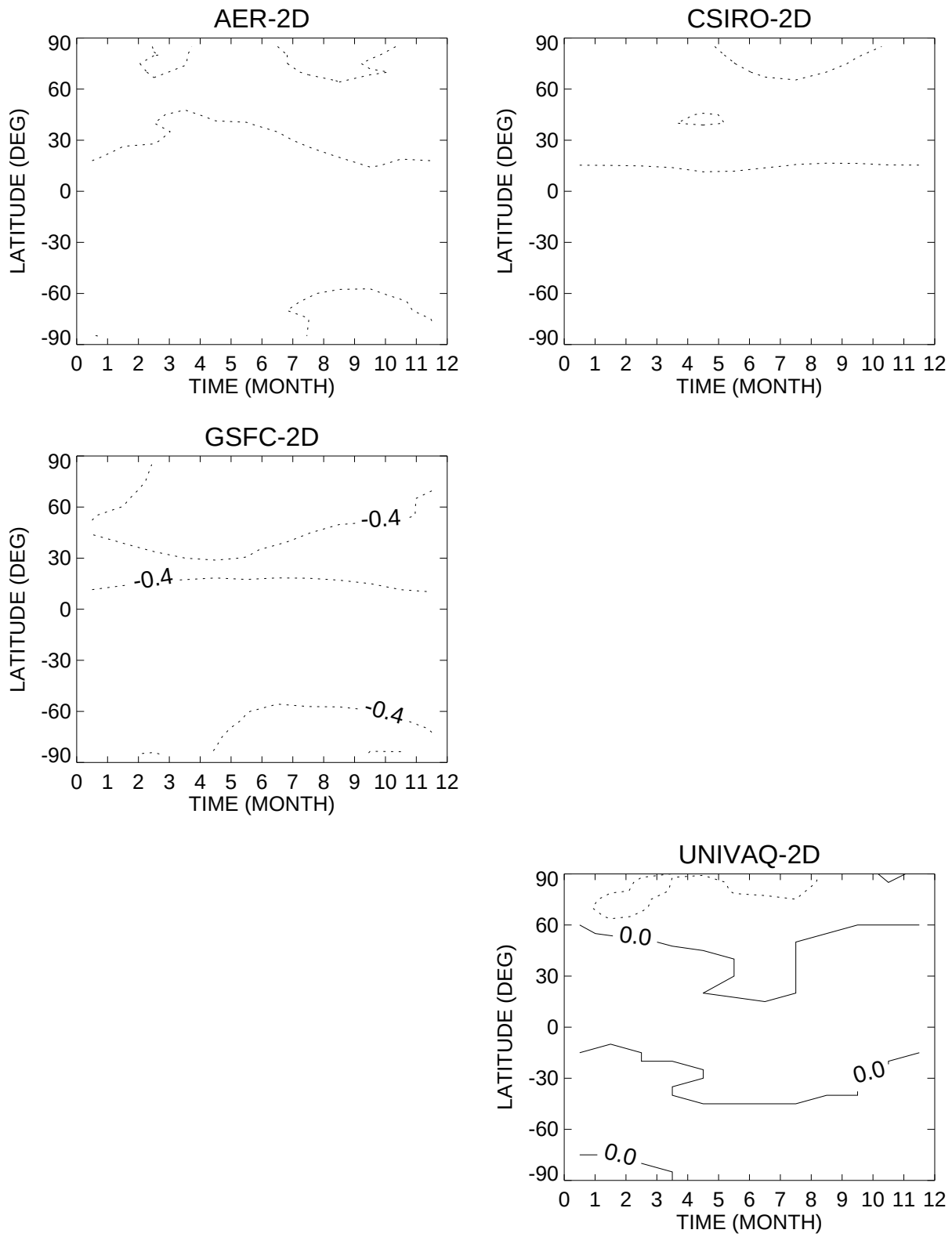

Figure 4.214: Calculated perturbations to column O_3 (percent) as a function of latitude and season in 2015 due to emissions from a fleet of 500 HSCT aircraft with EI(NO_x)=5 and the model PSC parameterization removed under Scenario S4b relative to Scenario D4. Contours are -0.6 to 0 by 0.2.

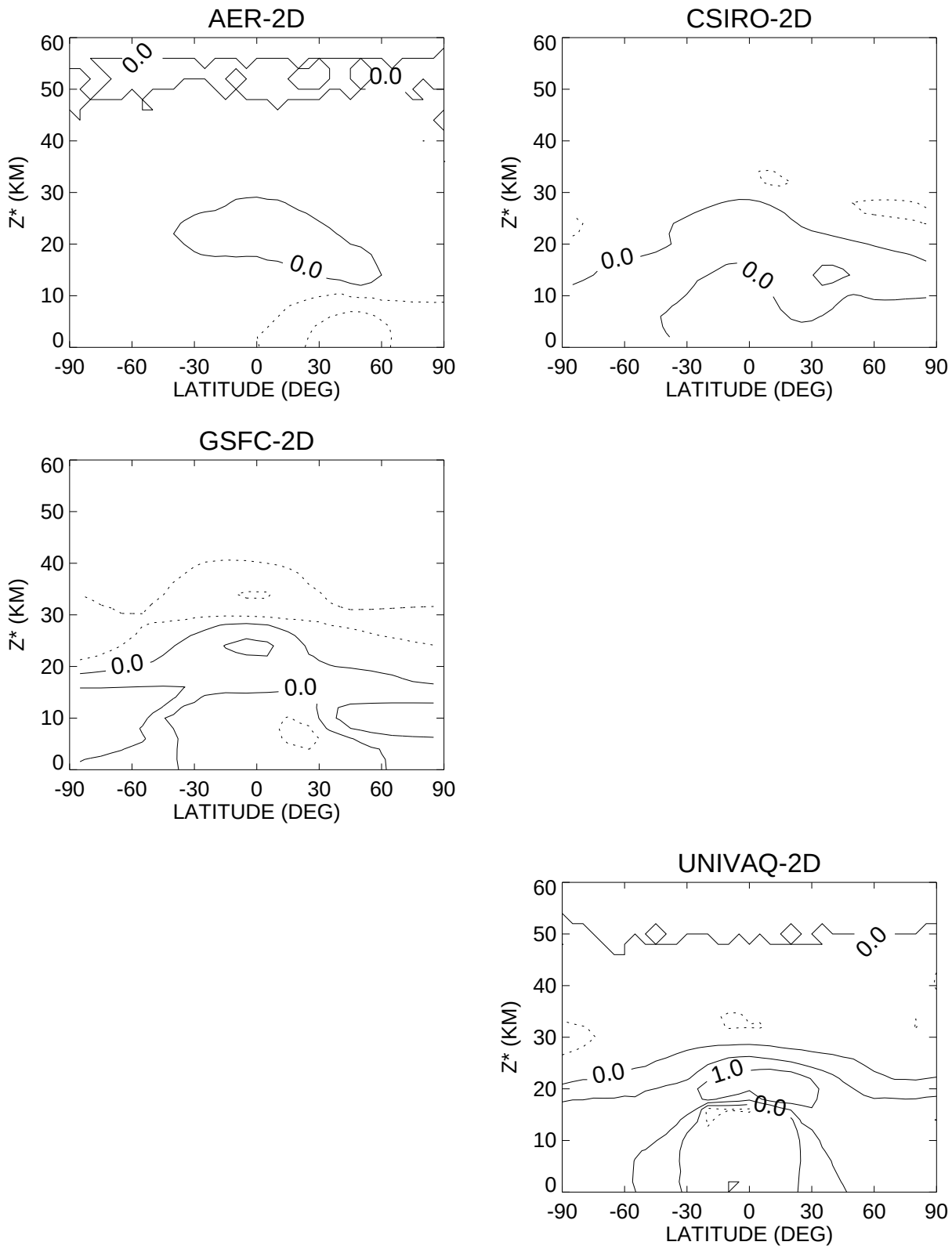

Figure 4.215: Calculated perturbations to O_3 (percent) as a function of latitude and altitude in March of 2015 due to emissions from a fleet of 500 HSCT aircraft with EI(NO_x)=5, no H_2O emissions, and the model PSC parameterization removed under Scenario S4c relative to Scenario D4. Contours are -1, -0.5, 0, 0.5, 1.

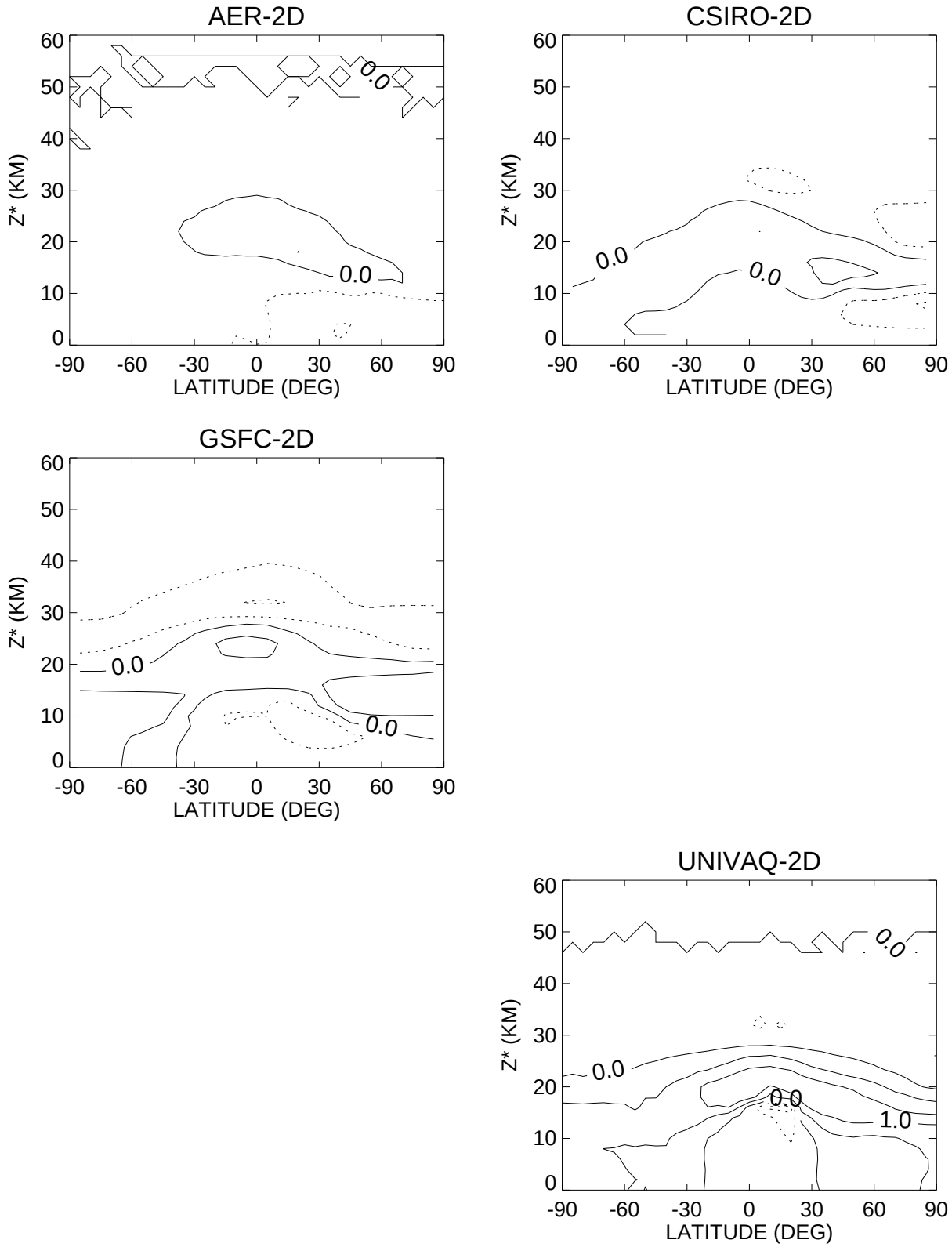

Figure 4.216: Calculated perturbations to O_3 (percent) as a function of latitude and altitude in June of 2015 due to emissions from a fleet of 500 HSCT aircraft with EI(NO_x)=5, no H_2O emissions, and the model PSC parameterization removed under Scenario S4c relative to Scenario D4. Contours are -1, -0.5, 0, 0.5, 1.

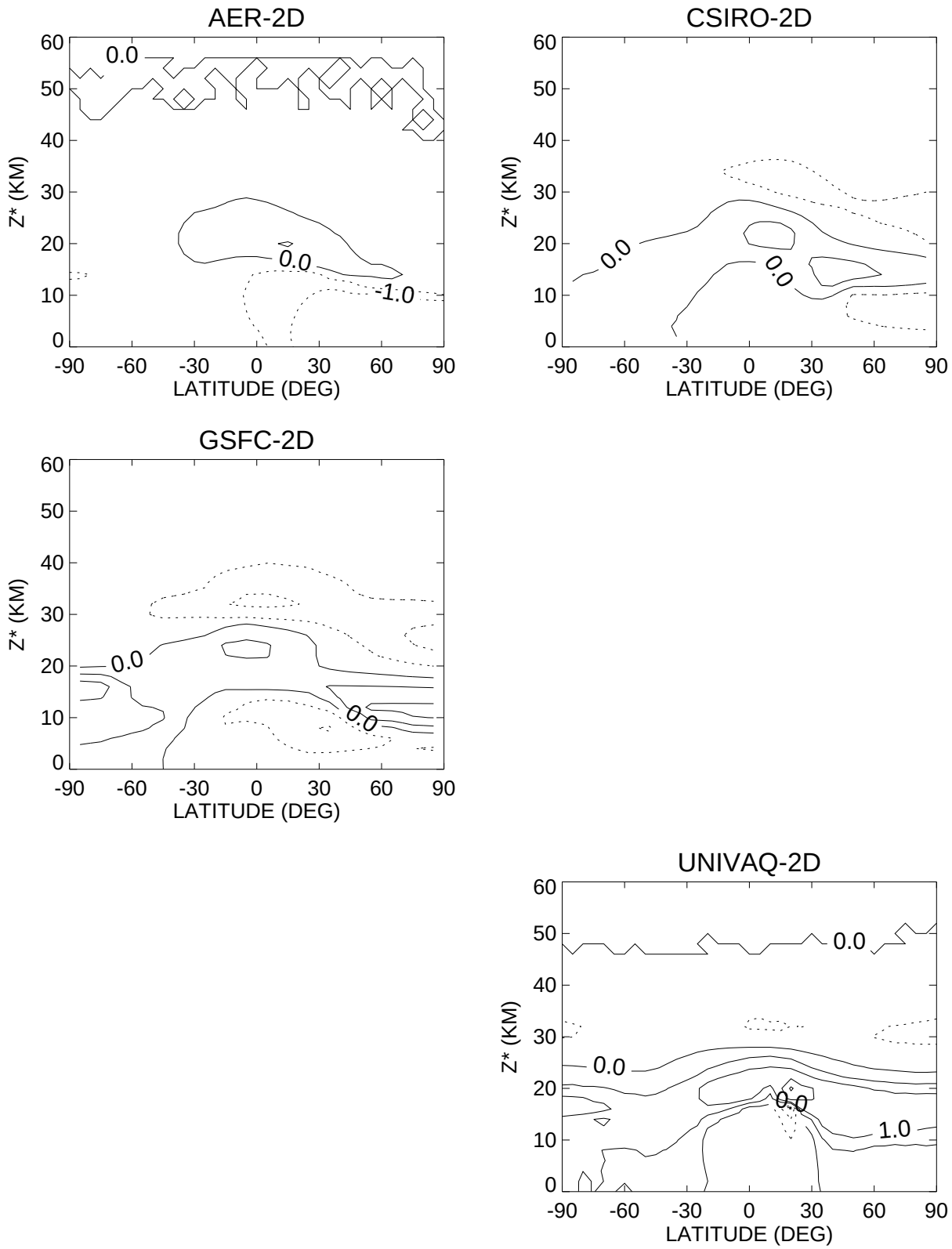

Figure 4.217: Calculated perturbations to O_3 (percent) as a function of latitude and altitude in October of 2015 due to emissions from a fleet of 500 HSCT aircraft with EI(NO_x)=5, no H_2O emissions, and the model PSC parameterization removed under Scenario S4c relative to Scenario D4. Contours are -1, -0.5, 0, 0.5, 1, 2, 3.

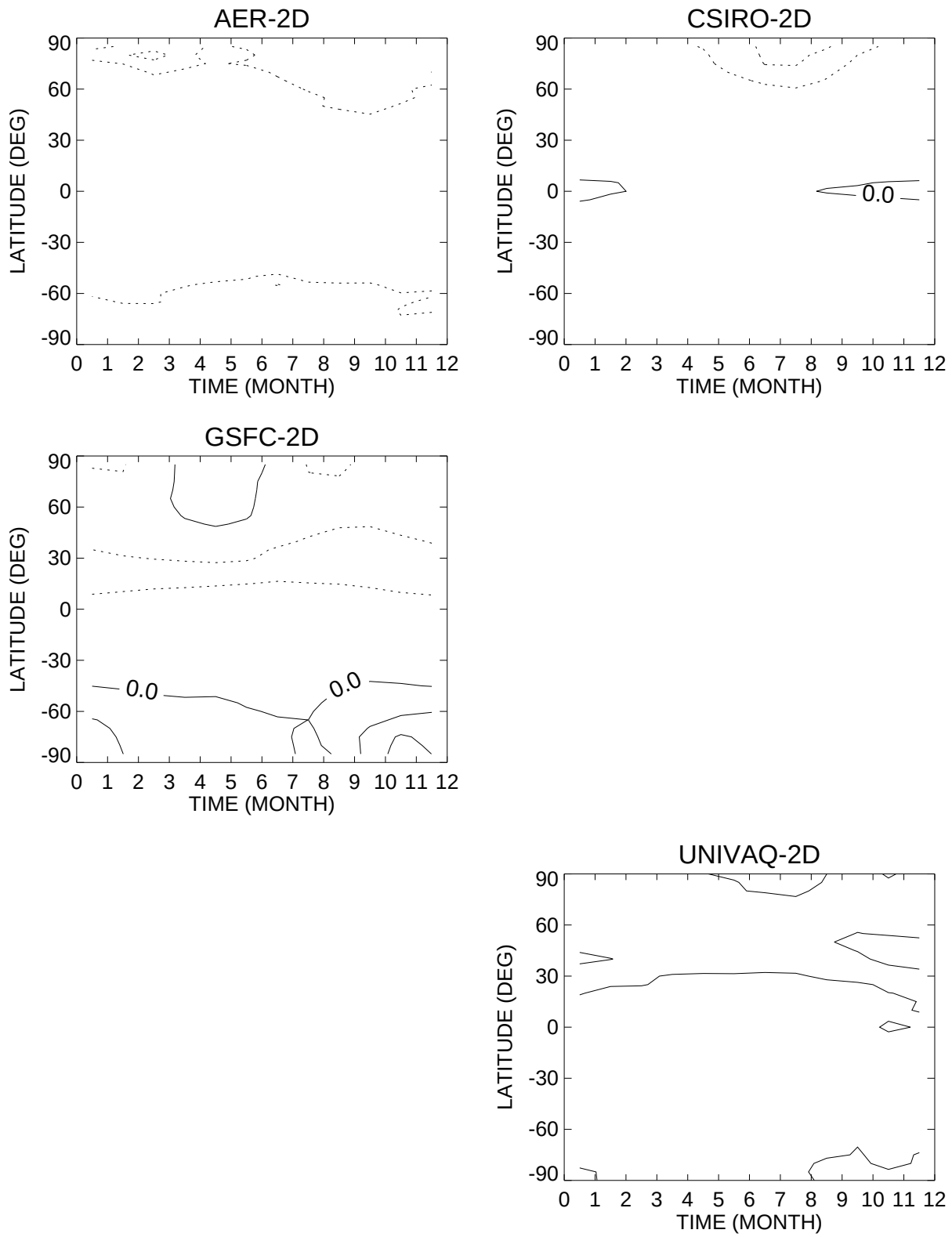

Figure 4.218: Calculated perturbations to column O_3 (percent) as a function of latitude and season in 2015 due to emissions from a fleet of 500 HSCT aircraft with EI(NO_x)=5, no H_2O emissions, and the model PSC parameterization removed under Scenario S4c relative to Scenario D4. Contours are -0.4 to 0.4 by 0.2.

4.3.6 Scenarios with Different Cl_y Loadings (S5a,b, S6a,b)

This section will cover Scenarios S5a-S6b which contain modified Cl_y background concentrations. Scenario S5a-S5b use 1.0 ppbv of Cl_y. Scenarios S6a-S6b use 4.0 ppbv of Cl_y. The standard 2015 scenarios use 3.0 ppbv of Cl_y and the 2050 scenarios use 2.0 ppbv of Cl_y. With these 4 alternate Cl_y loading levels, we can investigate the sensitivity of HSCT ozone impact to Cl_y loading, with and without aircraft sulfur emissions. The AER, GSFC, and UNIVAQ models performed these calculations.

Scenario S5a is identical to S1c except that the Cl_y loading is 1.0 ppbv instead of 3.0 ppbv. The scenario represents 500 HSCT aircraft with EI(NO_x)=5 and no sulfur emissions. Changes in ozone concentration for March, June, and October for S5a relative to D5 are shown in Figures 4.219, 4.220, and 4.221. The models show somewhat less ozone depletion in the extratropical lower stratosphere with S5a-D5 than with S1c-D, except for October, when the GSFC and UNIVAQ models show more depletion in the northern hemisphere lower stratosphere with S5a-D5. Figure 4.222 shows changes in ozone column for Scenario S5a relative to D5. The GSFC model shows much less springtime ozone column depletion in the southern polar region with 1 ppbv of Cl_y than with 3 ppbv of Cl_y. In the northern hemisphere, the GSFC model shows somewhat more depletion. The AER and UNIVAQ models show slightly less ozone column depletion in both hemispheres at high latitudes.

Scenario S5b includes sulfur emissions from HSCT aircraft assuming 50% gas to particle conversion (ie. using the SA1 surface area density) along with a Cl_y loading is 1 ppbv. The HSCT fleet includes 500 aircraft with EI(NO_x)=5. Changes in ozone relative to background scenario D5 are shown in Figures 4.223, 4.224, and 4.225 for March, June, and October. Ozone column depletion is increased relative to S5a-D5 by the addition of aircraft-emitted sulfur. However, the increase in ozone depletion is not as great as with a Cl_y loading of 3 ppbv (Scenarios S1c-D, S1f-D). Figure 4.226 shows changes in ozone column for this scenario. The ozone depletion calculated for S5b-D5 is reduced by 40-50% relative to S1f-D for the AER and GSFC models and by a lesser amount for the UNIVAQ model.

Scenarios S6a and S6b use a Cl_y loading of 4.0 ppbv. Both include HSCT fleets of 500 aircraft with EI(NO_x)=5. Scenario S6a includes no aircraft sulfur emissions. Ozone changes for Scenario S6a relative to D6 are shown in Figures 4.227, 4.228, and 4.229. The results for the AER and GSFC models with 4.0 ppbv of Cl_y are very similar to those with 3.0 ppbv of Cl_y. The UNIVAQ model results show less ozone depletion in the high latitude lower stratosphere and less of an ozone increase in the high latitude troposphere than for S1c-D. Changes in column ozone for S6a-D6 are shown in Figure 4.230. The AER and GSFC models show ozone column depletions at high latitudes which are slightly greater than for Scenario S1c-D. The UNIVAQ model shows slightly reduced ozone column depletion.

Sulfur emissions with 50% gas to particle conversion are included in Scenario S6b, using the SA1 surface area density. Figures 4.231, 4.232, and 4.233 show changes in ozone for Scenario S6b relative to Scenario D6. Compared with Scenario S1f-D, ozone depletion is about the same for the AER model, smaller for the GSFC model in the southern hemisphere, and slightly smaller at high latitudes in the lower stratosphere for the UNIVAQ model. Changes in column ozone for S6b-D6 are shown in Figure 4.234. The AER and GSFC models show slightly more ozone depletion in the southern polar springtime compared with S1f-D. The UNIVAQ model shows a bit less depletion in both hemispheres at high latitudes.

The sensitivity of ozone response to Cl_y loading without aircraft sulfur emissions is shown graphically in Figures 4.235 and 4.236 for the northern and southern hemisphere annual average ozone columns, respectively. The 2 ppb Cl_y loadings are from Scenarios S9a and S9c for 2050. These scenarios use the 2050 boundary conditions for N_2O and CH_4, and so differ slightly from the other scenarios included in the plots. Sensitivity to Cl_y is minor over the 1 ppb to 4 ppb range plotted, except for the GSFC model in the southern hemisphere, which shows greater ozone depletion at at 2 ppbv of Cl_y than at 1 ppbv.

Figures 4.237 shows Cl_y sensitivity in the northern hemisphere with aircraft sulfur emissions (SA1) included. In this case, all models show greater ozone depletion at 3 ppbv of Cl_y than at 2 ppbv of Cl_y. The AER model also shows a change in ozone depletion between 1 and 2 ppbv of Cl_y. Cl_y sensitivity in the southern hemisphere with sulfur emissions is shown in Figure 4.238. All models show a modest increase in ozone depletion between 2 ppbv and 3 ppbv of Cl_y. The GSFC and AER models also show increases in ozone depletion between 1 ppbv and 2 ppbv of Cl_y. In both hemispheres, increasing Cl_y from 3 ppbv to 4 ppbv has no influence on calculated ozone depletion.

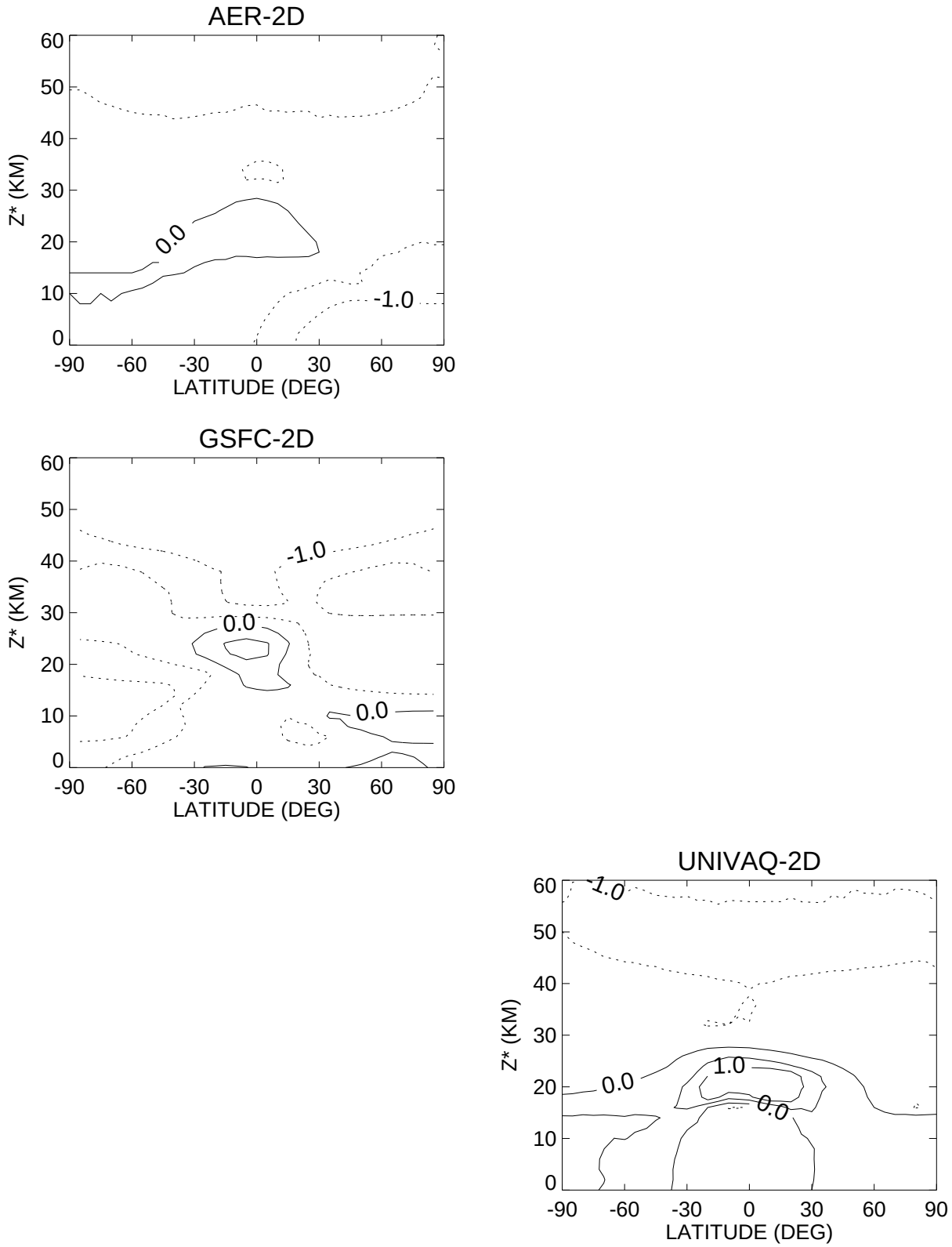

Figure 4.219: Calculated perturbations to O_3 (percent) as a function of latitude and altitude in March of 2015 due to emissions from a fleet of 500 HSCT aircraft with EI(NO_x)=5 and a background Cl_y concentration of 1.0 ppbv under Scenario S5a relative to Scenario D5. Contours are -1, -0.5, 0, 0.5, 1.

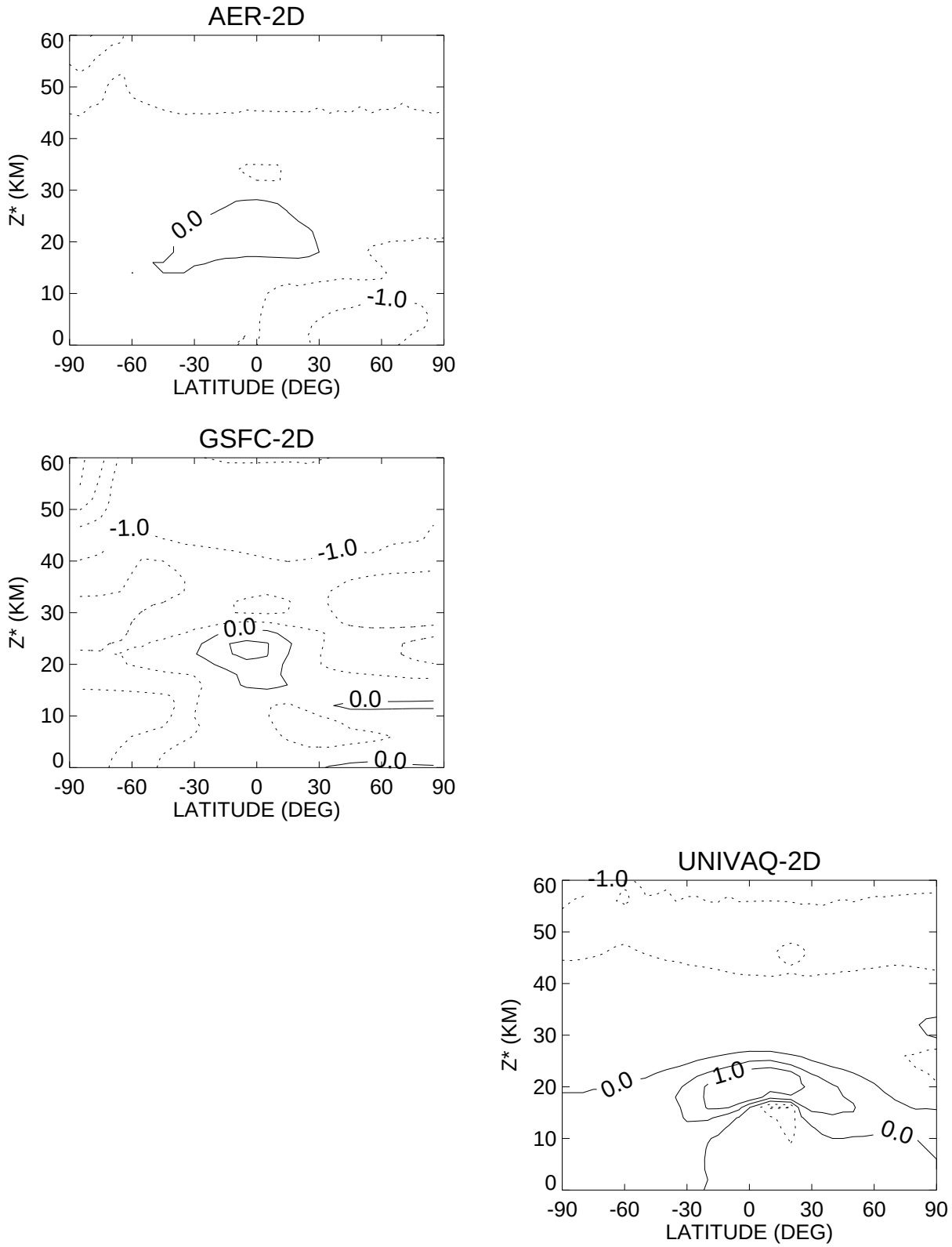

Figure 4.220: Calculated perturbations to O_3 (percent) as a function of latitude and altitude in June of 2015 due to emissions from a fleet of 500 HSCT aircraft with EI(NO_x)=5 and a background Cl_y concentration of 1.0 ppbv under Scenario S5a relative to Scenario D5. Contours are -1, -0.5, 0, 0.5, 1.

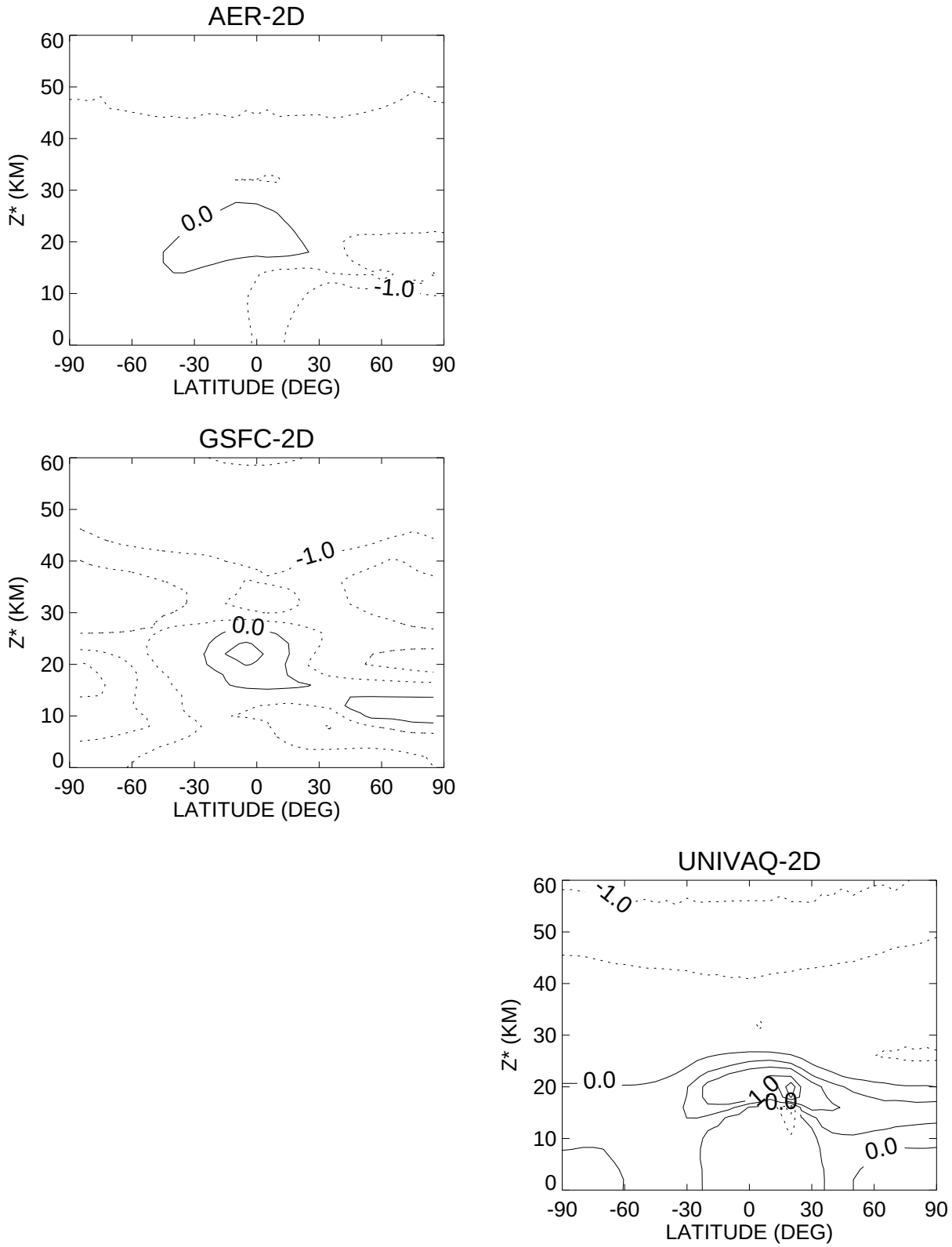

Figure 4.221: Calculated perturbations to O_3 (percent) as a function of latitude and altitude in October of 2015 due to emissions from a fleet of 500 HSCT aircraft with EI(NO_x)=5 and a background Cl_y concentration of 1.0 ppbv under Scenario S5a relative to Scenario D5. Contours are -2, -1, -0.5, 0, 0.5, 1, 2, 3.

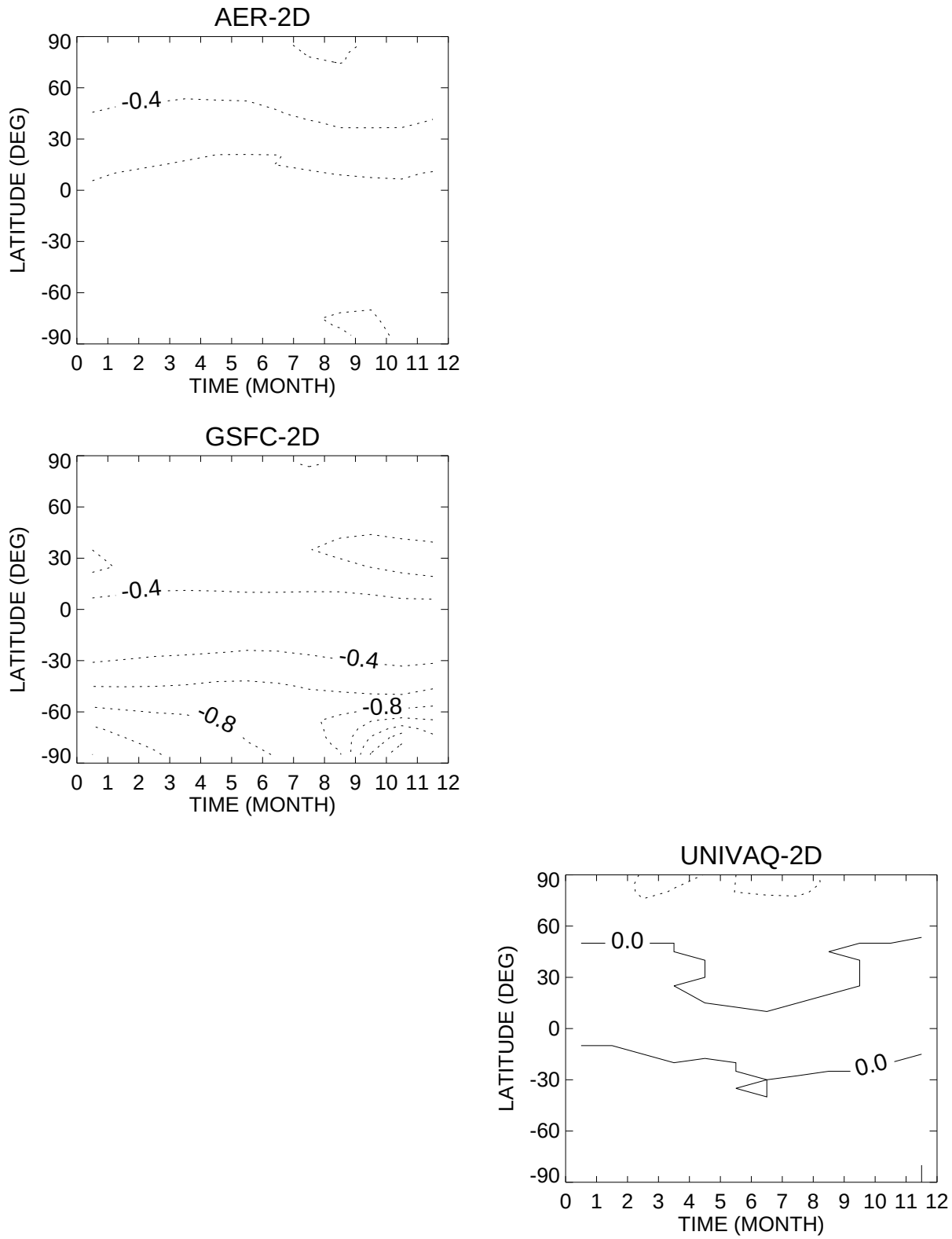

Figure 4.222: Calculated perturbations to column O_3 (percent) as a function of latitude and season in 2015 due to emissions from a fleet of 500 HSCT aircraft with EI(NO_x)=5 and a background Cl_y concentration of 1.0 ppbv under Scenario S5a relative to Scenario D5. Contours are -1.6 to 0 by 0.2.

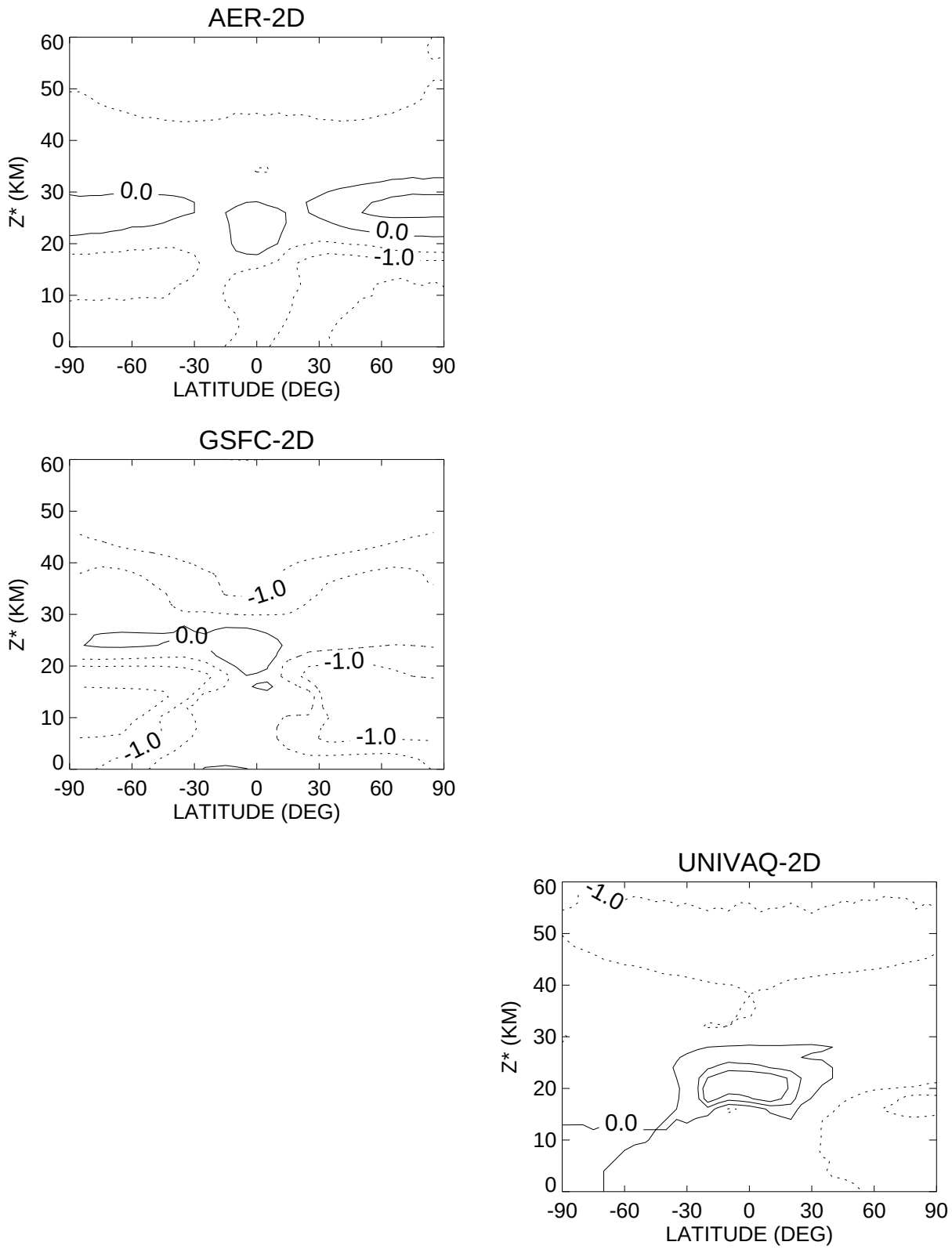

Figure 4.223: Calculated perturbations to O_3 (percent) as a function of latitude and altitude in March of 2015 due to emissions from a fleet of 500 HSCT aircraft with EI(NO_x)=5, SA1 sulfate surface area, and a background Cl_y concentration of 1.0 ppbv under Scenario S5b relative to Scenario D5. Contours are -2, -1, -0.5, 0, 0.5, 1.

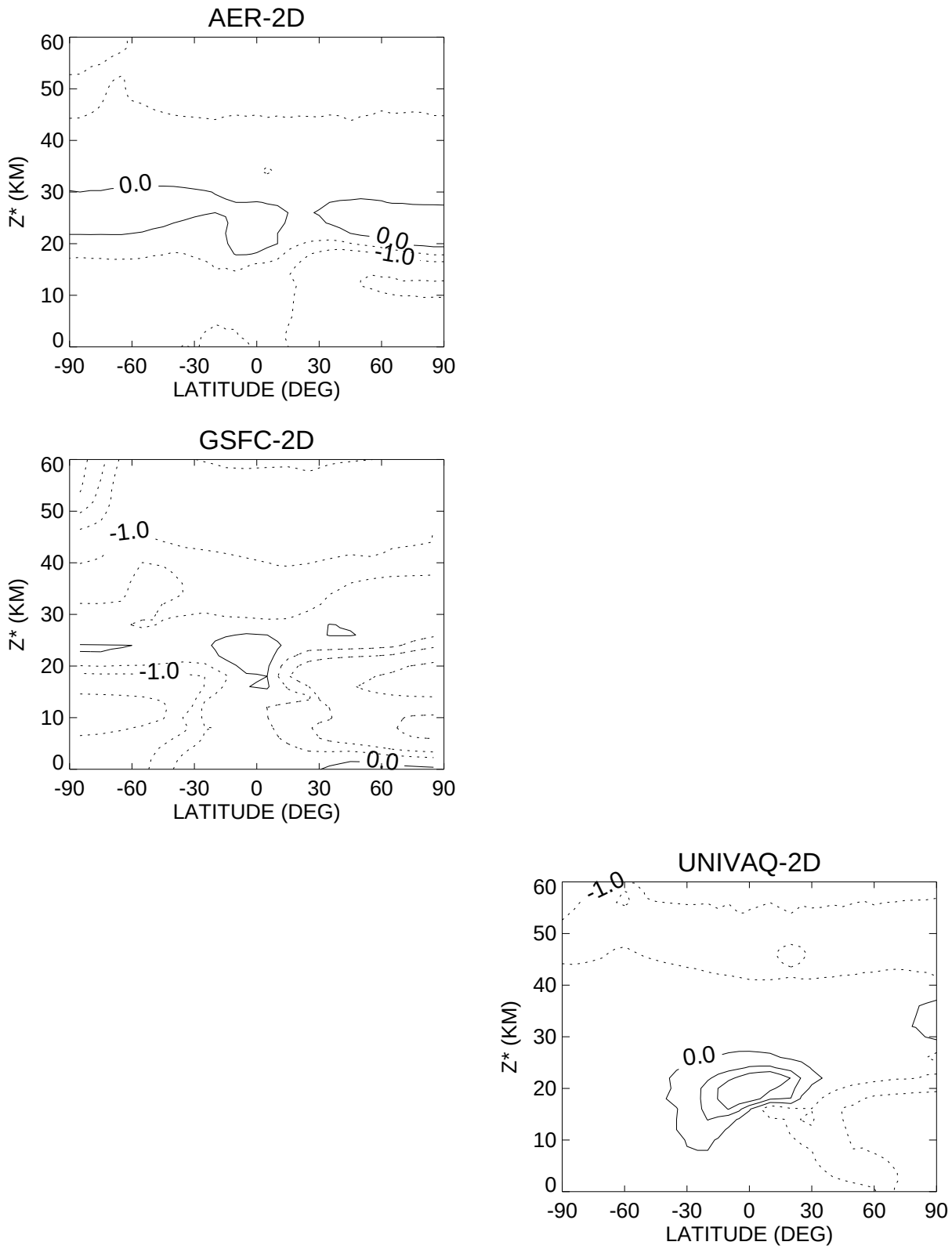

Figure 4.224: Calculated perturbations to O_3 (percent) as a function of latitude and altitude in June of 2015 due to emissions from a fleet of 500 HSCT aircraft with EI(NO_x)=5, SA1 sulfate surface area, and a background Cl_y concentration of 1.0 ppbv under Scenario S5b relative to Scenario D5. Contours are -2, -1, -0.5, 0, 0.5, 1.

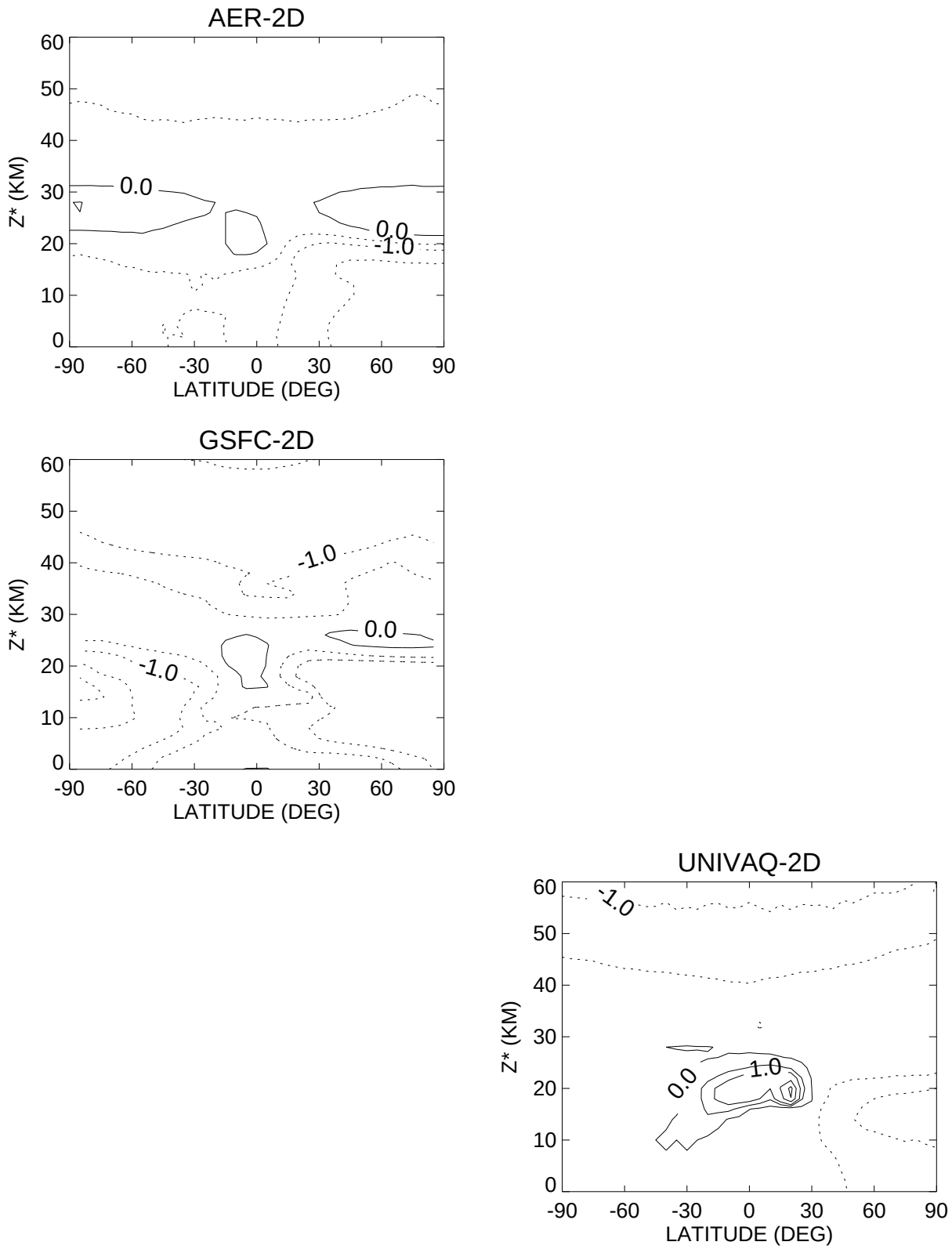

Figure 4.225: Calculated perturbations to O_3 (percent) as a function of latitude and altitude in October of 2015 due to emissions from a fleet of 500 HSCT aircraft with EI(NO_x)=5, SA1 sulfate surface area, and a background Cl_y concentration of 1.0 ppbv under Scenario S5b relative to Scenario D5. Contours are -3, -2, -1, -0.5, 0, 0.5, 1, 2, 3.

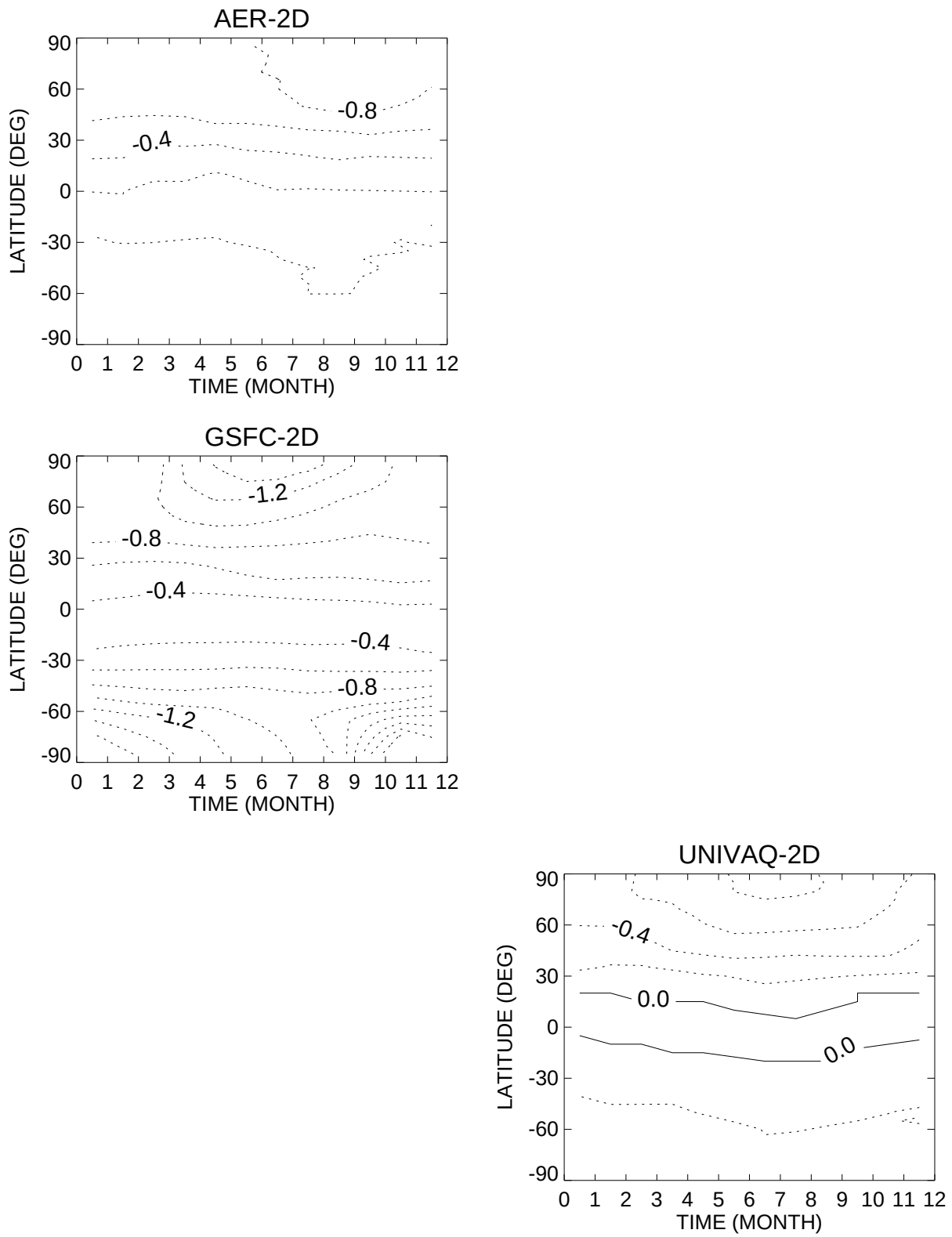

Figure 4.226: Calculated perturbations to column O_3 (percent) as a function of latitude and season in 2015 due to emissions from a fleet of 500 HSCT aircraft with EI(NO_x)=5, SA1 sulfate surface area, and a background Cl_y concentration of 1.0 ppbv under Scenario S5b relative to Scenario D5. Contours are -2.0 to 0 by 0.2.

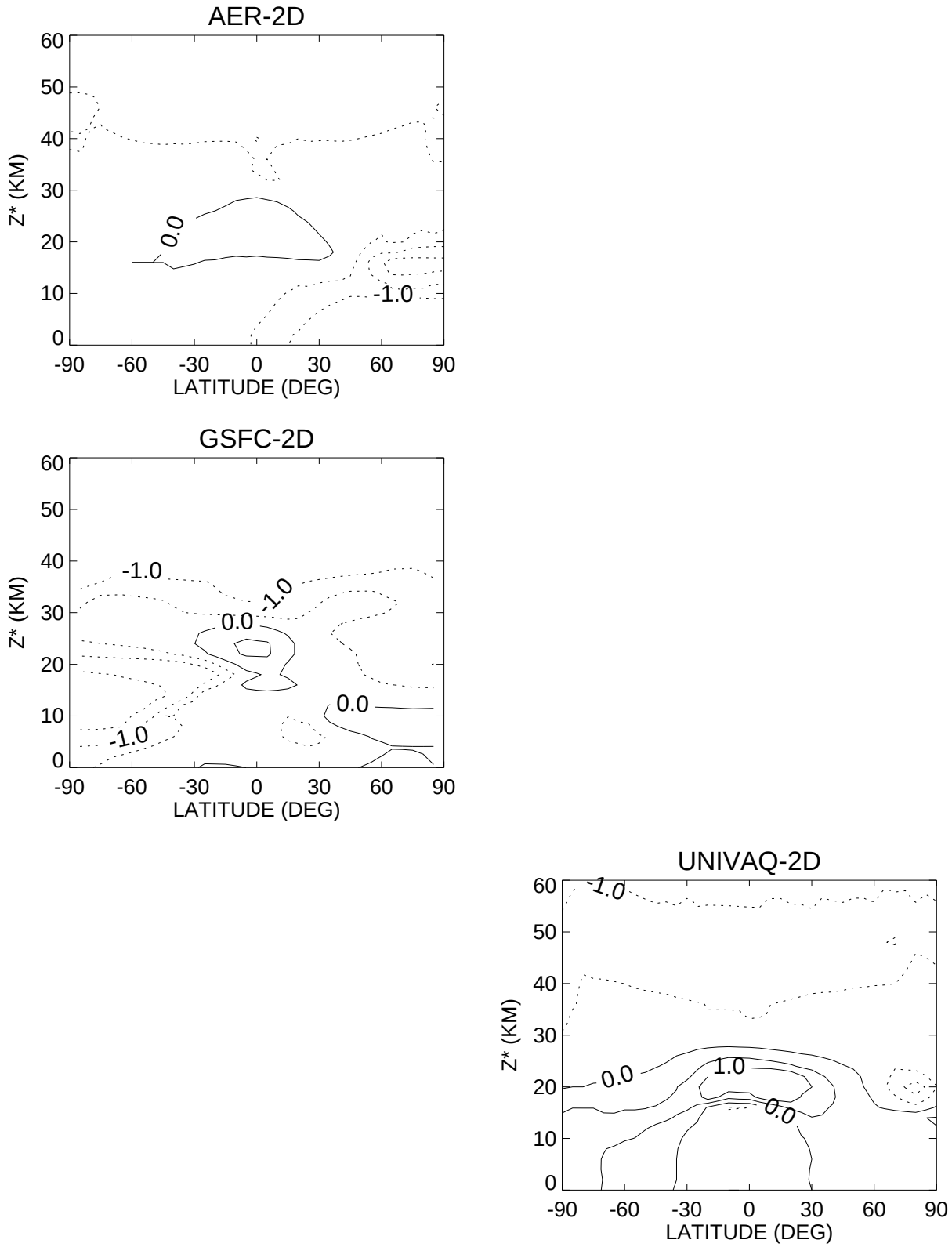

Figure 4.227: Calculated perturbations to O_3 (percent) as a function of latitude and altitude in March of 2015 due to emissions from a fleet of 500 HSCT aircraft with EI(NO_x)=5 and a background Cl_y concentration of 4.0 ppbv under Scenario S6a relative to Scenario D6. Contours are -2, -1, -0.5, 0, 0.5, 1.

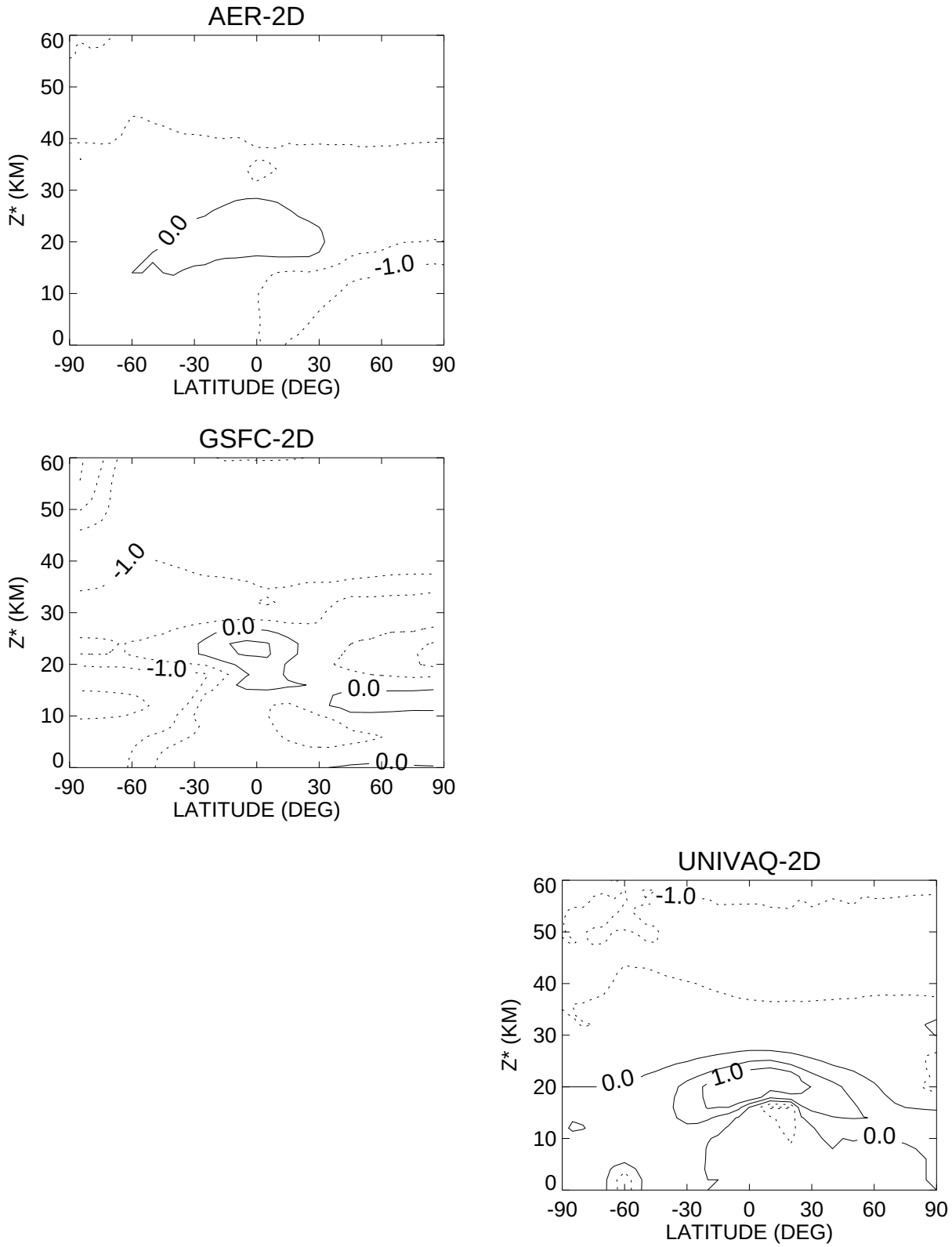

Figure 4.228: Calculated perturbations to O_3 (percent) as a function of latitude and altitude in June of 2015 due to emissions from a fleet of 500 HSCT aircraft with EI(NO_x)=5 and a background Cl_y concentration of 4.0 ppbv under Scenario S6a relative to Scenario D6. Contours are -2, -1, -0.5, 0, 0.5, 1.

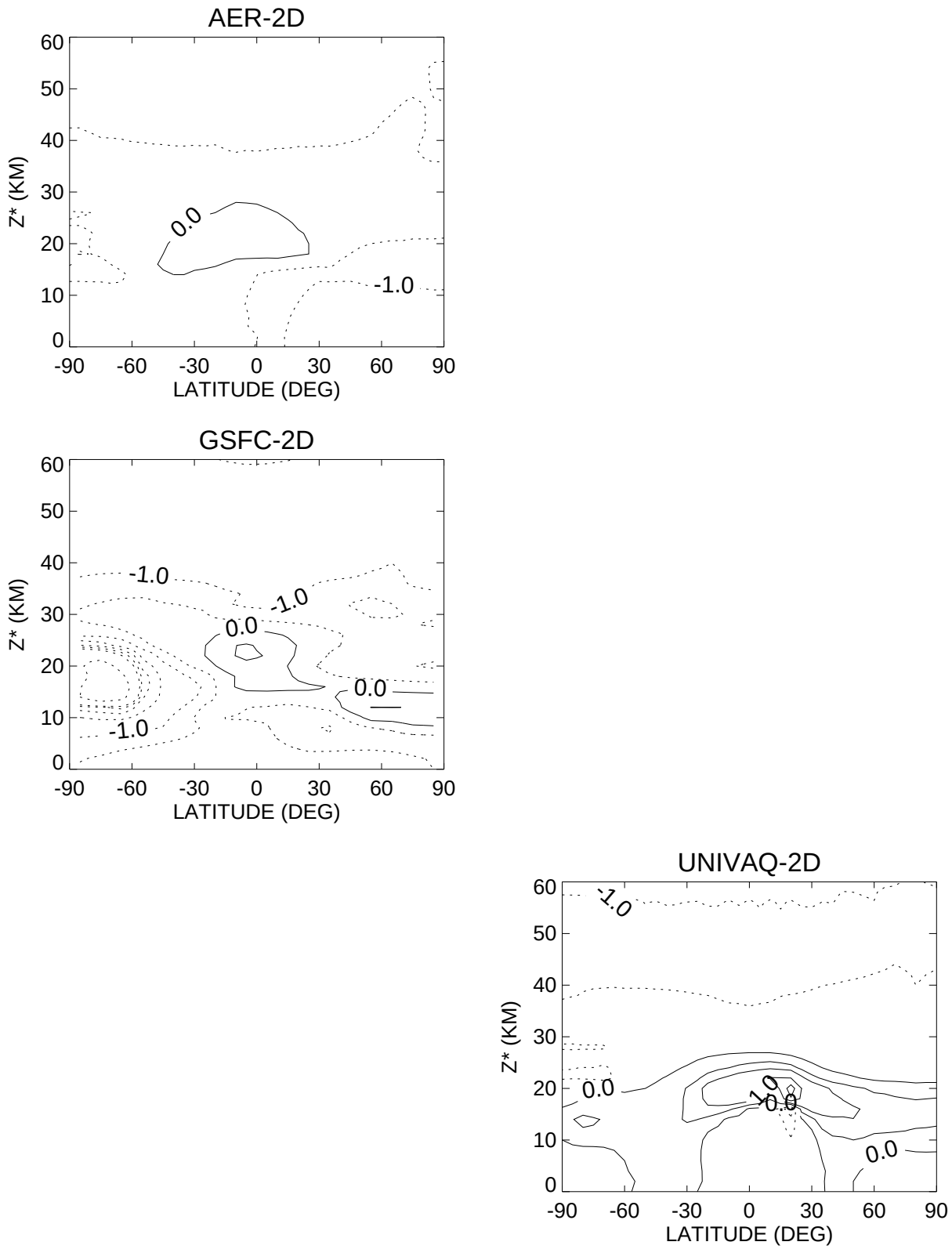

Figure 4.229: Calculated perturbations to O_3 (percent) as a function of latitude and altitude in October of 2015 due to emissions from a fleet of 500 HSCT aircraft with EI(NO_x)=5 and a background Cl_y concentration of 4.0 ppbv under Scenario S6a relative to Scenario D6. Contours are -10, -5, -4, -3, -2, -1, -0.5, 0, 0.5, 1, 2, 3.

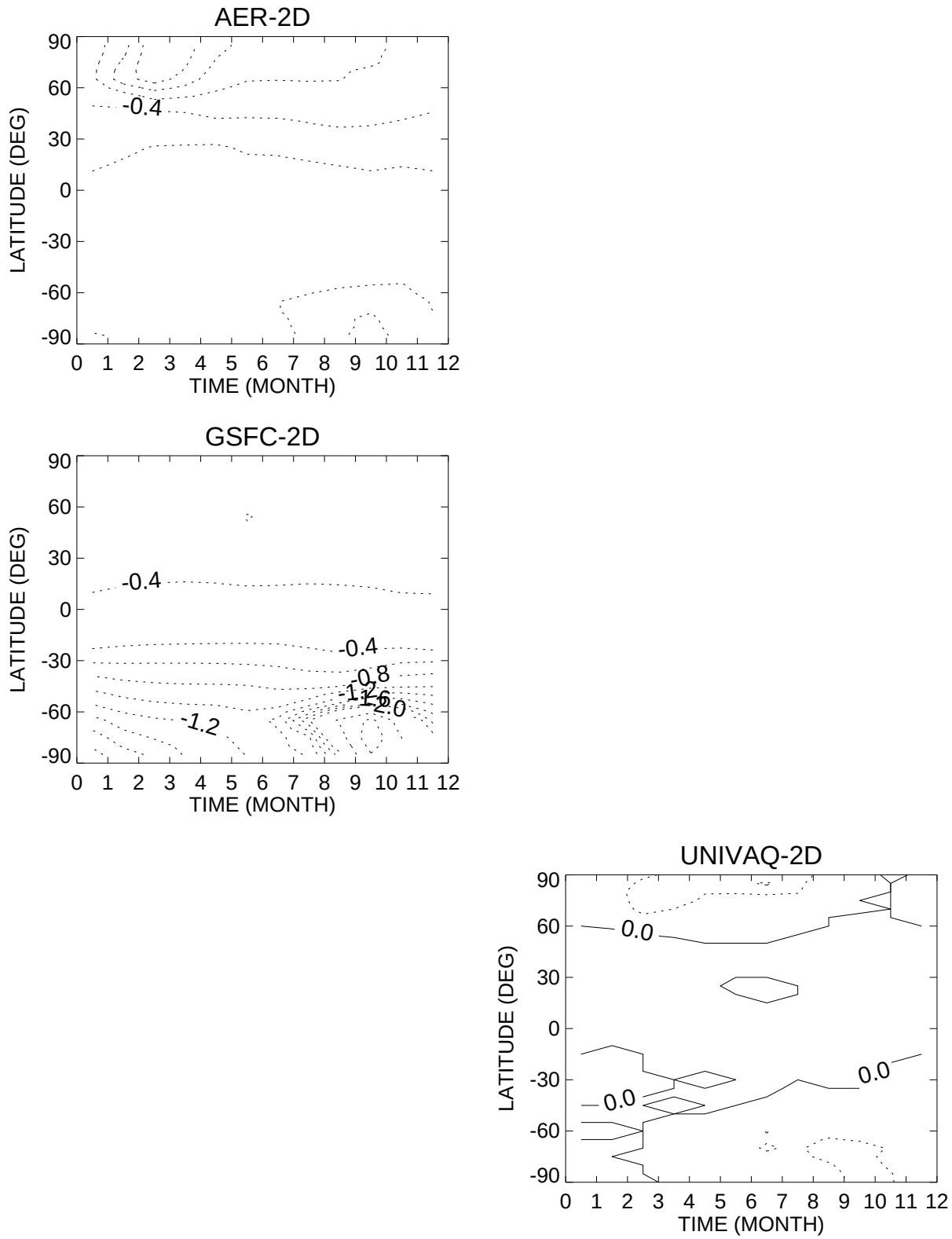

Figure 4.230: Calculated perturbations to column O_3 (percent) as a function of latitude and season in 2015 due to emissions from a fleet of 500 HSCT aircraft with EI(NO_x)=5 and a background Cl_y concentration of 4.0 ppbv under Scenario S6a relative to Scenario D6. Contours are -4, -3 and -2 to 0.2 by 0.2.

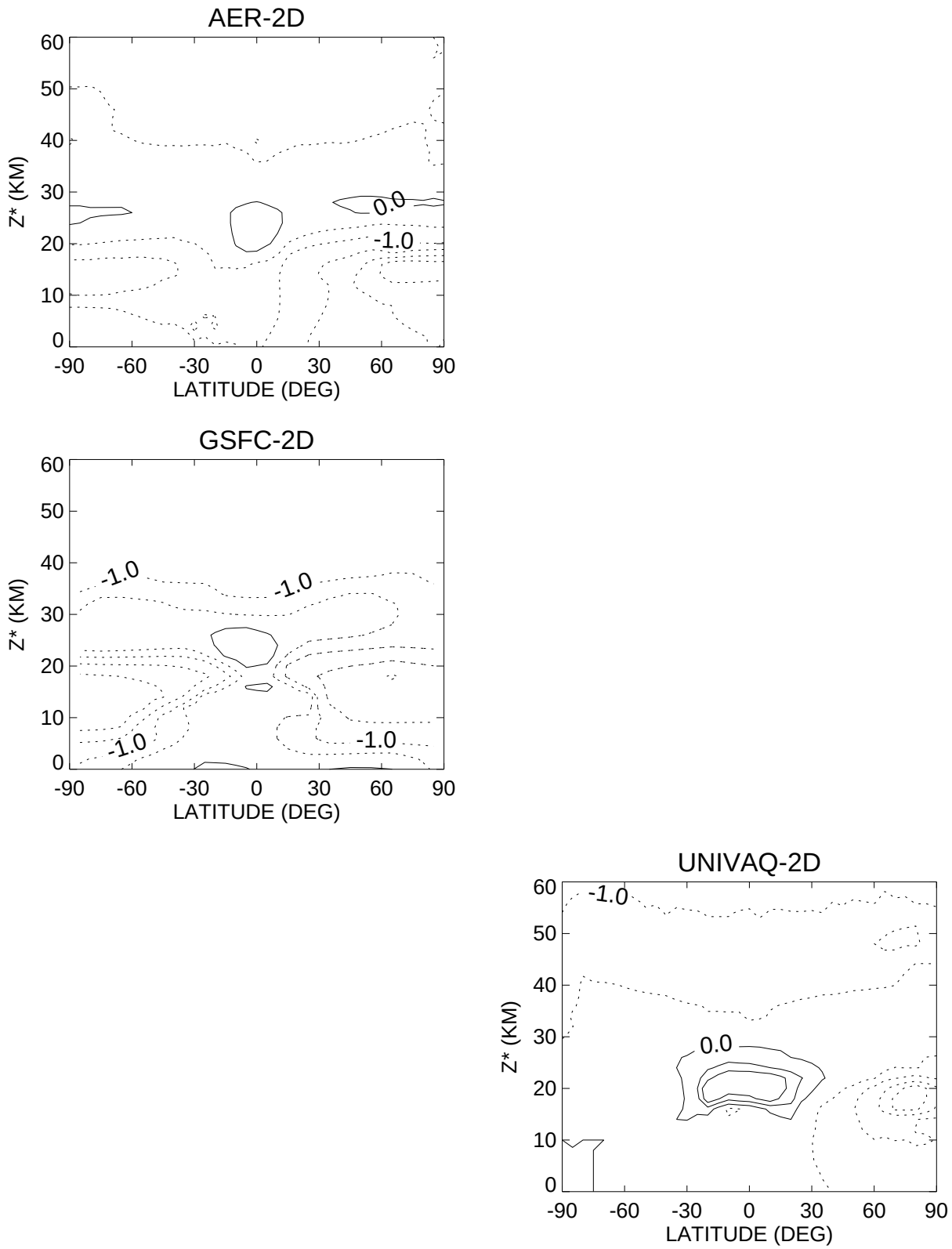

Figure 4.231: Calculated perturbations to O_3 (percent) as a function of latitude and altitude in March of 2015 due to emissions from a fleet of 500 HSCT aircraft with EI(NO_x)=5, SA1 sulfate surface area, and a background Cl_y concentration of 4.0 ppbv under Scenario S6b relative to Scenario D6. Contours are -4, -3, -2, -1, -0.5, 0, 0.5, 1.

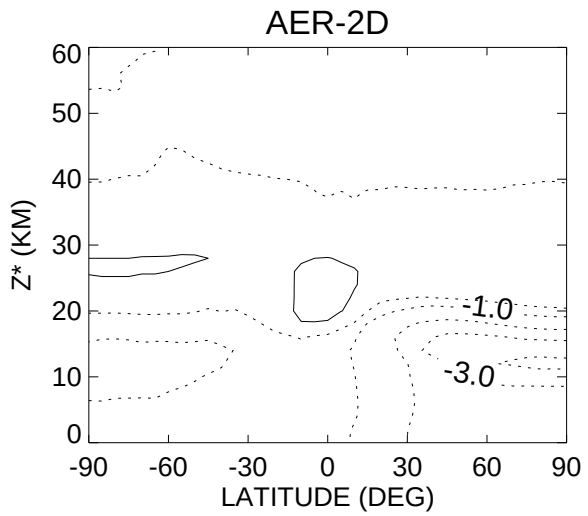

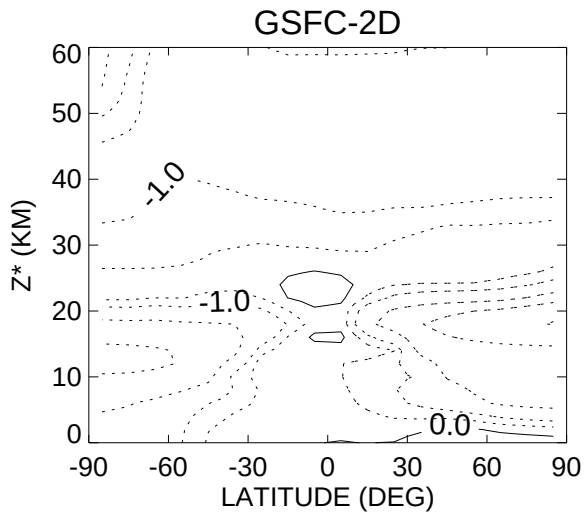

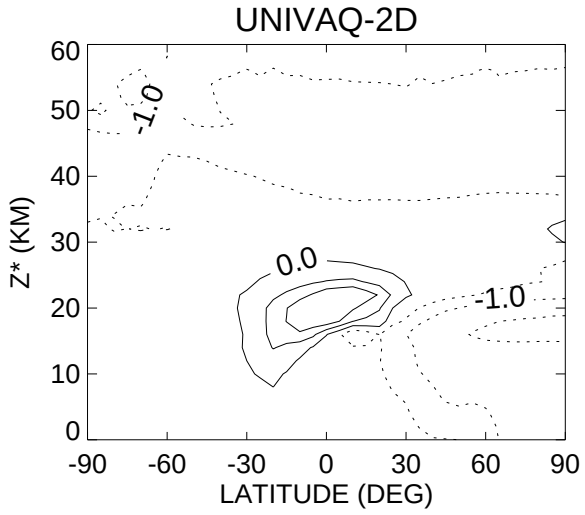

Figure 4.232: Calculated perturbations to O_3 (percent) as a function of latitude and altitude in June of 2015 due to emissions from a fleet of 500 HSCT aircraft with EI(NO_x)=5, SA1 sulfate surface area, and a background Cl_y concentration of 4.0 ppbv under Scenario S6b relative to Scenario D6. Contours are -4, -3, -2, -1, -0.5, 0, 0.5, 1.

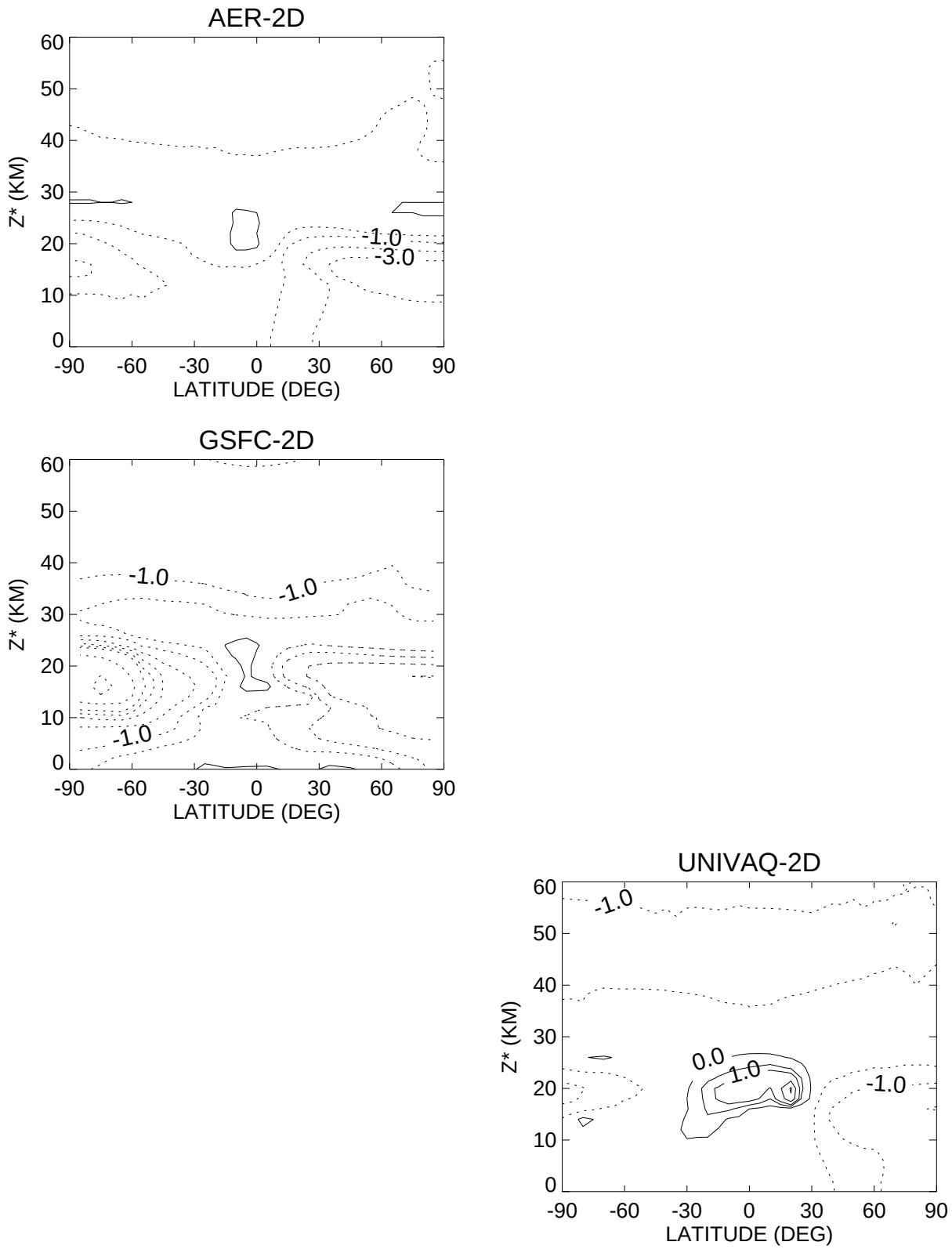

Figure 4.233: Calculated perturbations to O_3 (percent) as a function of latitude and altitude in October of 2015 due to emissions from a fleet of 500 HSCT aircraft with EI(NO_x)=5, SA1 sulfate surface area, and a background Cl_y concentration of 4.0 ppbv under Scenario S6b relative to Scenario D6. Contours are -15, -10, -5, -4, -3, -2, -1, -0.5, 0, 0.5, 1, 2, 3.

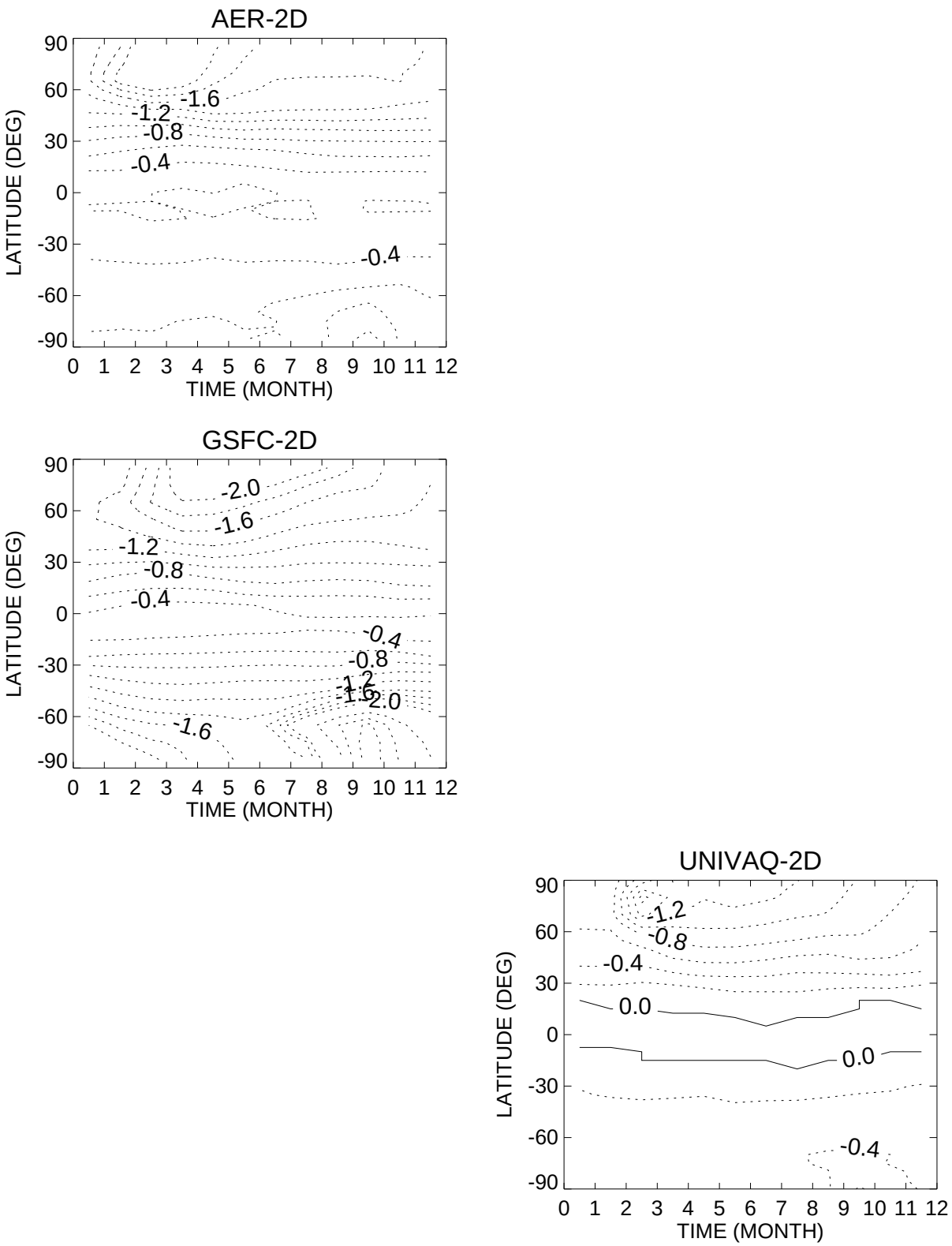

Figure 4.234: Calculated perturbations to column O_3 (percent) as a function of latitude and season in 2015 due to emissions from a fleet of 500 HSCT aircraft with EI(NO_x)=5, SA1 sulfate surface area, and a background Cl_y concentration of 4.0 ppbv under Scenario S6b relative to Scenario D6. Contours are -5, -4, -3 and -2 to 0 by 0.2.

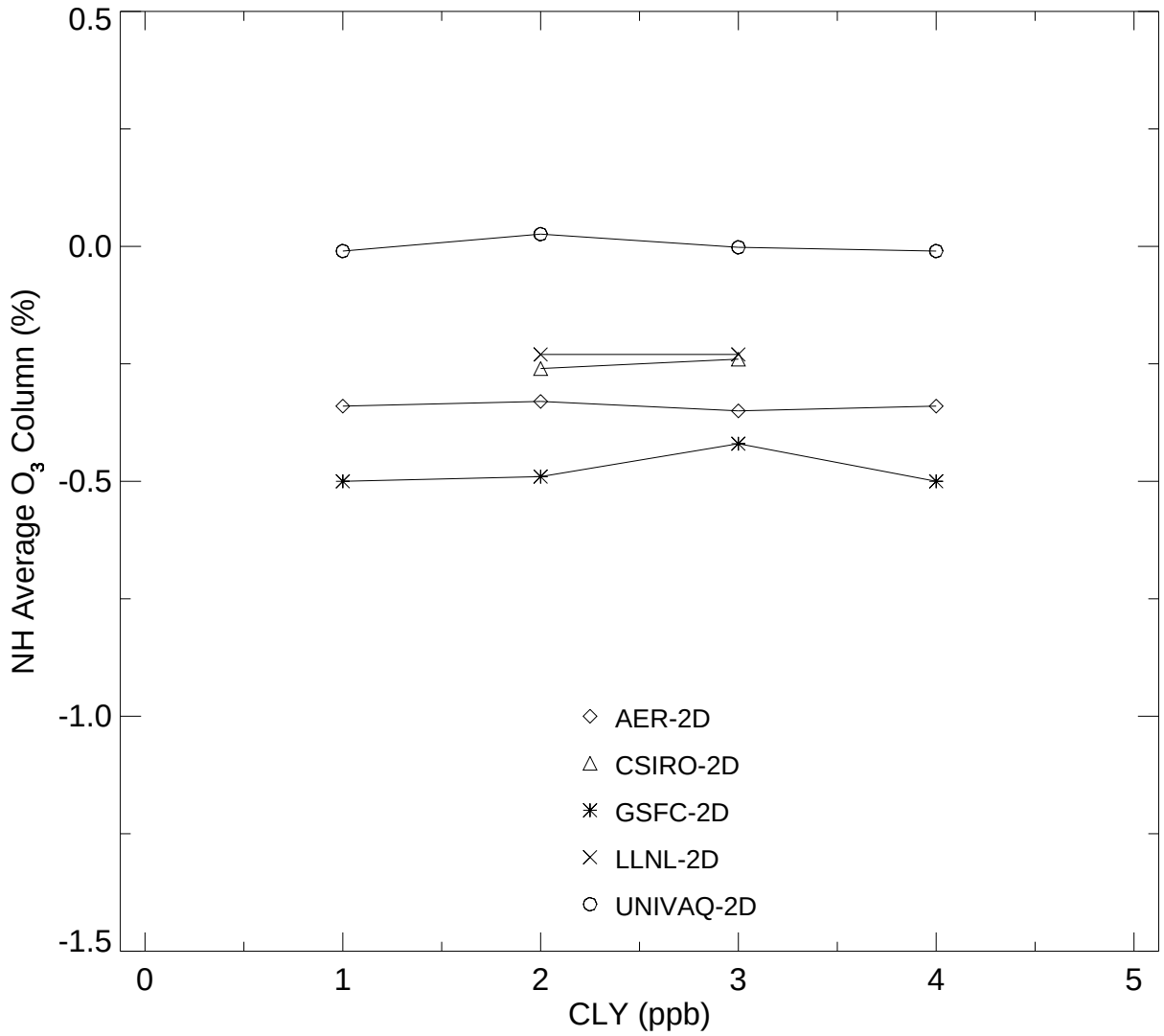

Figure 4.235: Northern hemisphere annual average total O_3 column change (percent) as a function of Cl_y loading for an HSCT fleet of 500 aircraft operating in 2015 with EI(NO_x)=5, no aircraft sulfur emissions, and SA0 sulfate surface area density. The 2 ppbv Cl_y scenarios use 2050 boundary conditions while the 1, 3, and 4 ppb Cl_y scenarios use 2015 boundary conditions.

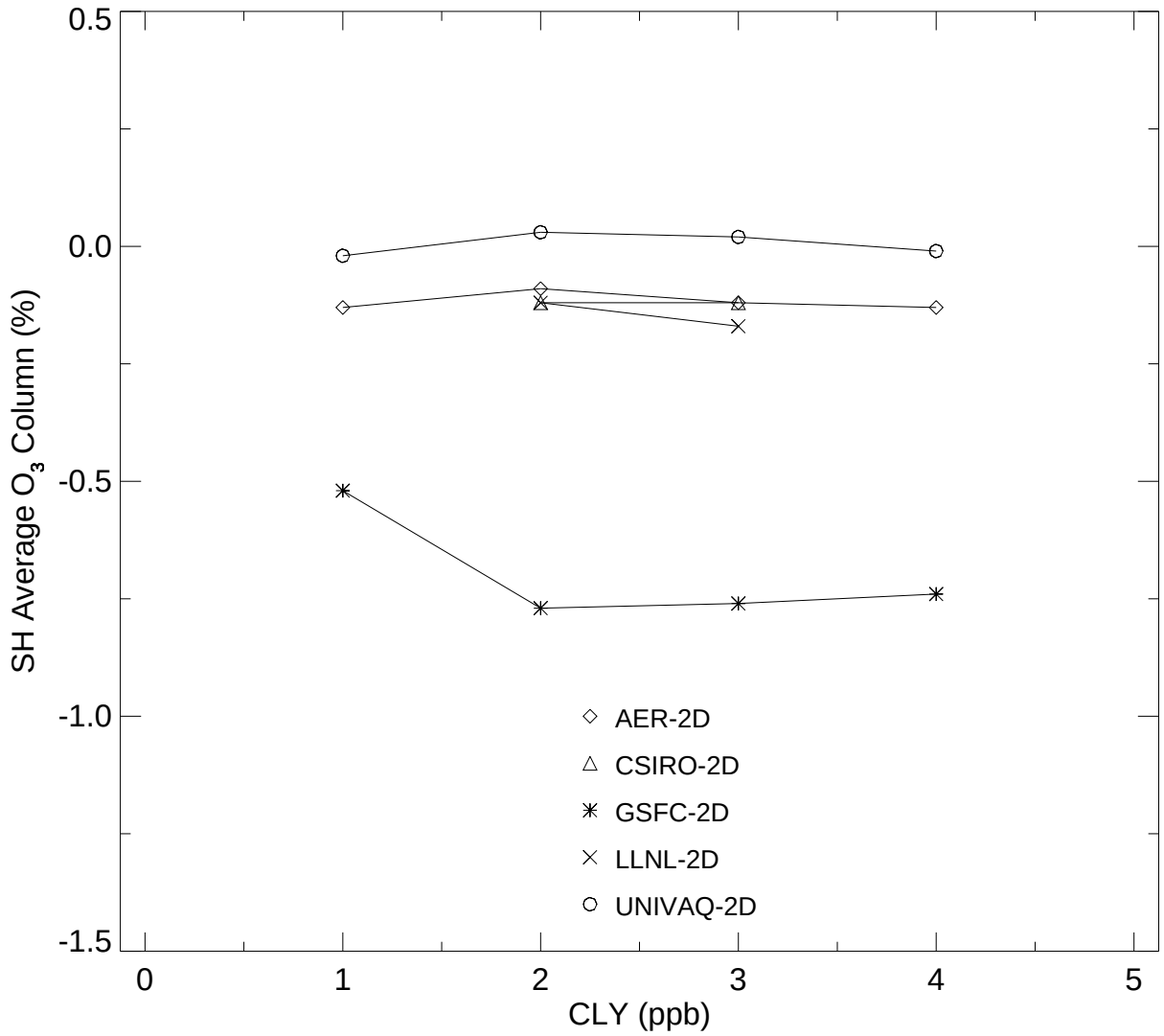

Figure 4.236: Southern hemisphere annual average total O_3 column change (percent) as a function of Cl_y loading for an HSCT fleet of 500 aircraft operating in 2015 with EI(NO_x)=5, no aircraft sulfur emissions, and SA0 sulfate surface area density. The 2 ppbv Cl_y scenarios use 2050 boundary conditions while the 1, 3, and 4 ppb Cl_y scenarios use 2015 boundary conditions.

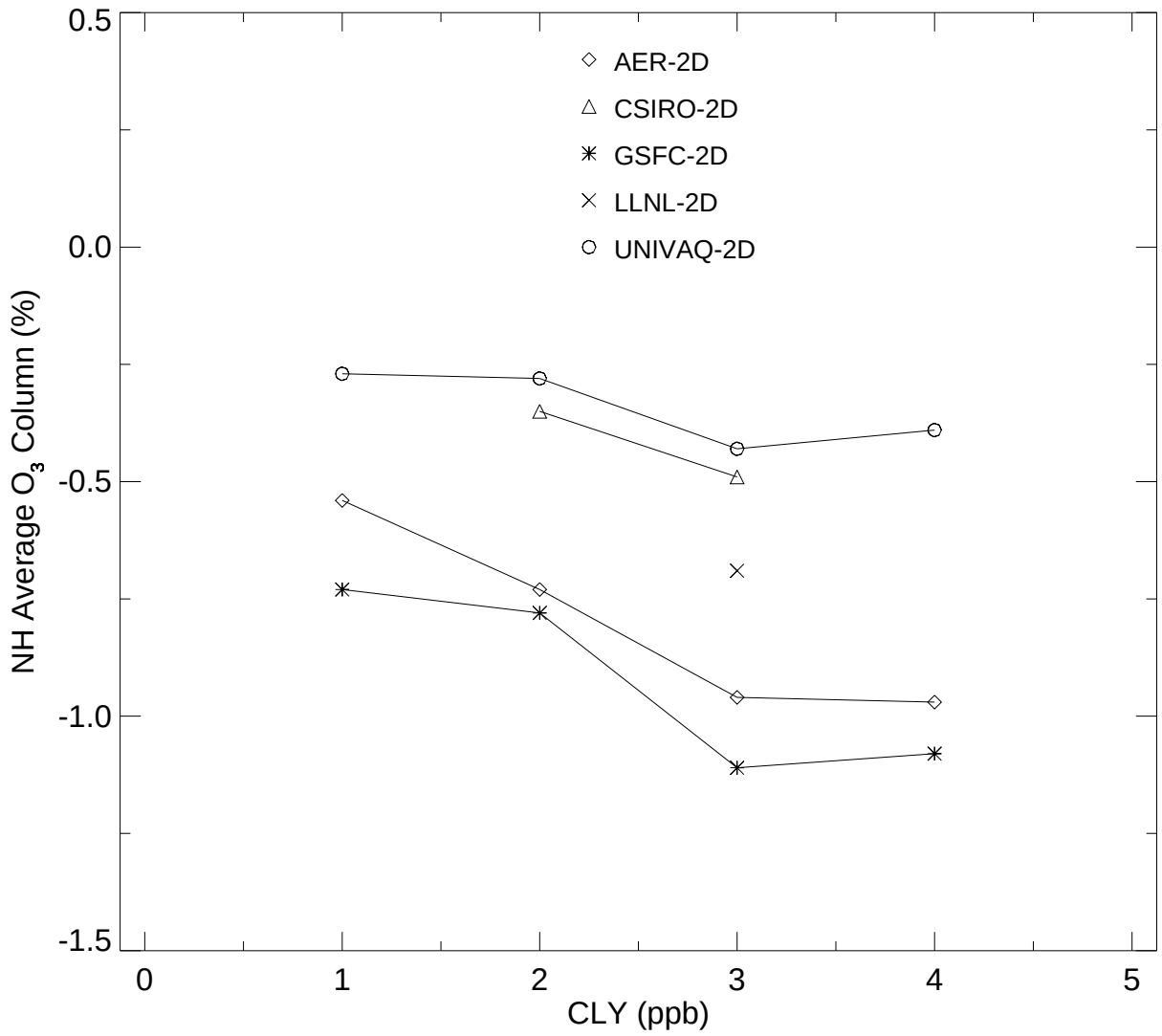

Figure 4.237: Northern hemisphere annual average total O_3 column change (percent) as a function of Cl_y loading for an HSCT fleet of 500 aircraft operating in 2015 with EI(NO_x)=5 and SA1 sulfate surface area density. The 2 ppbv Cl_y scenarios use 2050 boundary conditions while the 1, 3, and 4 ppb Cl_y scenarios use 2015 boundary conditions.

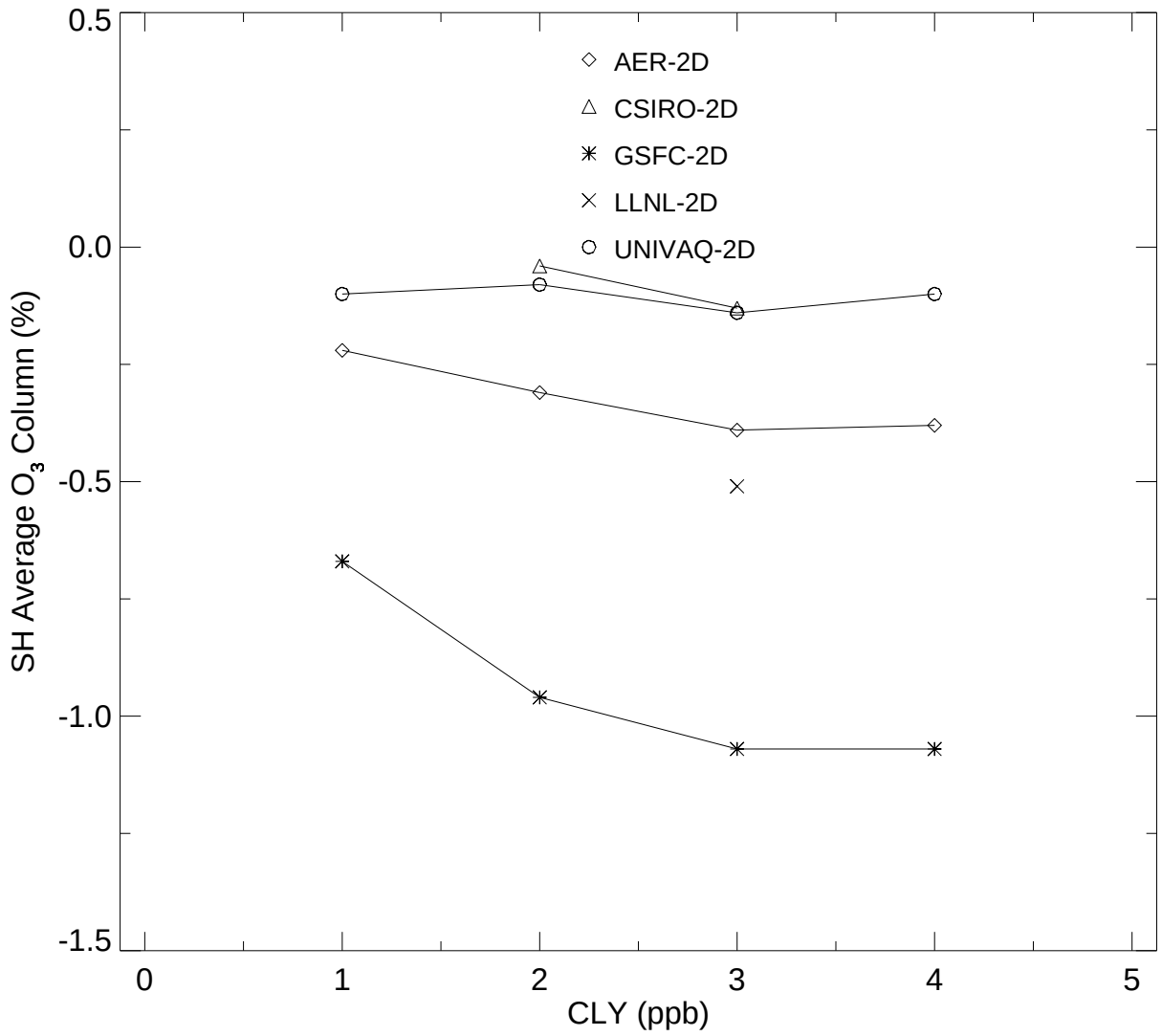

Figure 4.238: Southern hemisphere annual average total O_3 column change (percent) as a function of Cl_y loading for an HSCT fleet of 500 aircraft operating in 2015 with EI(NO_x)=5 and SA1 sulfate surface area density. The 2 ppbv Cl_y scenarios use 2050 boundary conditions while the 1, 3, and 4 ppb Cl_y scenarios use 2015 boundary conditions.

4.3.7 Scenarios with Interactive Microphysics (S7a-d, S8a)

This section will cover Scenarios S7a-S7d and S8a which include interactive sulfate aerosol microphysics. Only the AER and UNIVAQ models performed these simulations, as they were the only models with microphysics capabilities. The AER model calculations did not include aircraft emissions of sulfur below 13 km, due to uncertainties in modeling tropospheric sulfur. The UNIVAQ model did include these emissions, though they should have little impact on the perturbation which subtracts the HSCT+subsonic case from the subsonic-only case.

Scenario S7a includes 500 HSCT aircraft in 2015 with EI(NO_x)=5, EI(SO_2)=0.4, and 50% gas to particle conversion. It is identical to Scenario S1f except that instead of using the SA1 surface area density for the HSCT case, the SAD was calculated interactively by these models. Calculated perturbations in SAD are shown in Figure 4.239. Since the AER model provided the calculation of SA1, the only difference for AER is that the SAD perturbation is relative to the AER model's calculated background SAD rather than the SA0 surface area density provided by UNEP, and the values change monthly rather remaining fixed for 6 months at a time. Figures 4.240, 4.241, and 4.242 show changes in ozone between Scenario S7a and Scenario D7 (with subsonic aircraft only) for March, June, and October. The AER results is very similar to the AER results for S1f-D. The UNIVAQ result is quite different in the extra-tropical lower stratosphere. The ozone perturbation is zero at 30 km at all latitudes. In the 10-20 km region at mid and high latitudes, ozone depletion from S7a-D7 is somewhat larger than from S1f-D. Figure 4.243 shows the change in ozone column for this scenario. Both models show ozone depletion of up to 2% in the northern hemisphere high latitudes and up to 1% in the southern hemisphere high latitudes. This is slightly more depletion than was seen with S1f-D.

Scenario S7b is similar to S7a but with the HSCT emission altitude shifted upward by 2 km. The calculated surface area perturbation for this scenario is shown in Figure 4.244 for the AER model only. The peak surface area density perturbation has the same value as for S7a-D7, but occurs at a higher altitude. Figures 4.245, 4.246, and 4.247 show changes in ozone for Scenario S7b relative to Scenario D7 for March, June, and October. Ozone depletion for this scenario is greater than for S7a-D7 in both the upper and lower stratosphere, as the stratospheric residence time of H_2O, NO_y, and sulfur is increased by the higher altitude of emission. Changes in column ozone for this scenario are shown in Figure 4.248. Ozone depletions of up to 3% are seen at high northern latitudes for both models. Northern hemisphere annual average ozone depletion is 1.4% for the AER model and 0.7% for the UNIVAQ model. This is 40% greater than at the standard cruise altitude (S7a-D7) and double the depletion seen in Scenario S2a-D, which used the increased cruise altitude but no sulfur emissions.

Scenario S7c includes a downward shift of 2 km in the HSCT cruise altitude, but is otherwise similar to S7a and S7b. Figure 4.249 shows the change in aerosol surface area calculated by the AER model for this scenario. Ozone changes for this scenario are shown in Figures 4.250, 4.251, and 4.252. Ozone perturbations are significantly smaller than for S7a-D7, especially in the upper stratosphere and around 10-20 km in the mid to high latitudes. However, ozone depletion is significantly larger than for S2b-D, which includes HSCT emissions at the same altitude but without sulfur emissions. Figure 4.253 shows changes in ozone column as a function of latitude and season for this scenario. Ozone column changes range from -1.2% to -0.2% for the AER model and from -1.0% to 0% for the UNIVAQ model, with the UNIVAQ model showing larger column depletions in the southern springtime polar region. These results indicate the possible importance of aircraft sulfur emissions even with HSCT aircraft operating at reduced cruise altitude.

The sensitivity of annual average hemispheric ozone column change to cruise altitude for a fleet of 500 HSCT aircraft operating in 2015 with EI(NO_x)=5, EI(SO_2)=0.4, and 50% gas to particle conversion is shown in Figures 4.254 and 4.255. The change is calculated hemispheric ozone depletion over the -2 km to +2 km cruise altitude range is much greater than that seen without aircraft sulfur emissions (Figures 4.155 and 4.156), and the magnitude of the ozone depletion is larger for all altitudes.

Scenario S7d uses an EI(NO_x) of 10 with 50% gas to particle conversion and HSCT operation at the nominal cruise altitude. Figures 4.250, 4.251, and 4.252 show calculated ozone perturbations for this scenario. Ozone depletion is smaller than for S7a-D7 except near 30 km, where the depletion is larger with higher NO_x emissions. Changes in ozone column for this scenario are shown in Figure 4.259. Ozone depletion is slightly smaller than for S7a-D7 for both models. In the UNIVAQ model, northern hemisphere annual average ozone depletion is reduced from 0.5% for S7a-D7 to 0.2% for S7d-D7.

Scenario S8a includes 500 HSCT aircraft with EI(NO_x)=5 and EI(SO_2)=0.4. Sulfur emissions are assumed to be 100% particles of 10 nm radius. Figure 4.260 shows the change in aerosol surface area density calculated by the AER and UNIVAQ models for this scenario. SAD perturbations are 50% larger than for S7a-D7. Changes in calculated ozone for S8a-D8 are shown in Figures 4.261, 4.262, and 4.263. Due to the greater aerosol surface area perturbation with 100% gas to particle conversion in the plume, the models shows slightly greater ozone depletion in the lower stratosphere for this scenario than for S7a-D7. Ozone column perturbations, shown in Figure 4.264, are almost identical to S7a-D7 for the UNIVAQ model and just slightly greater for the AER model.

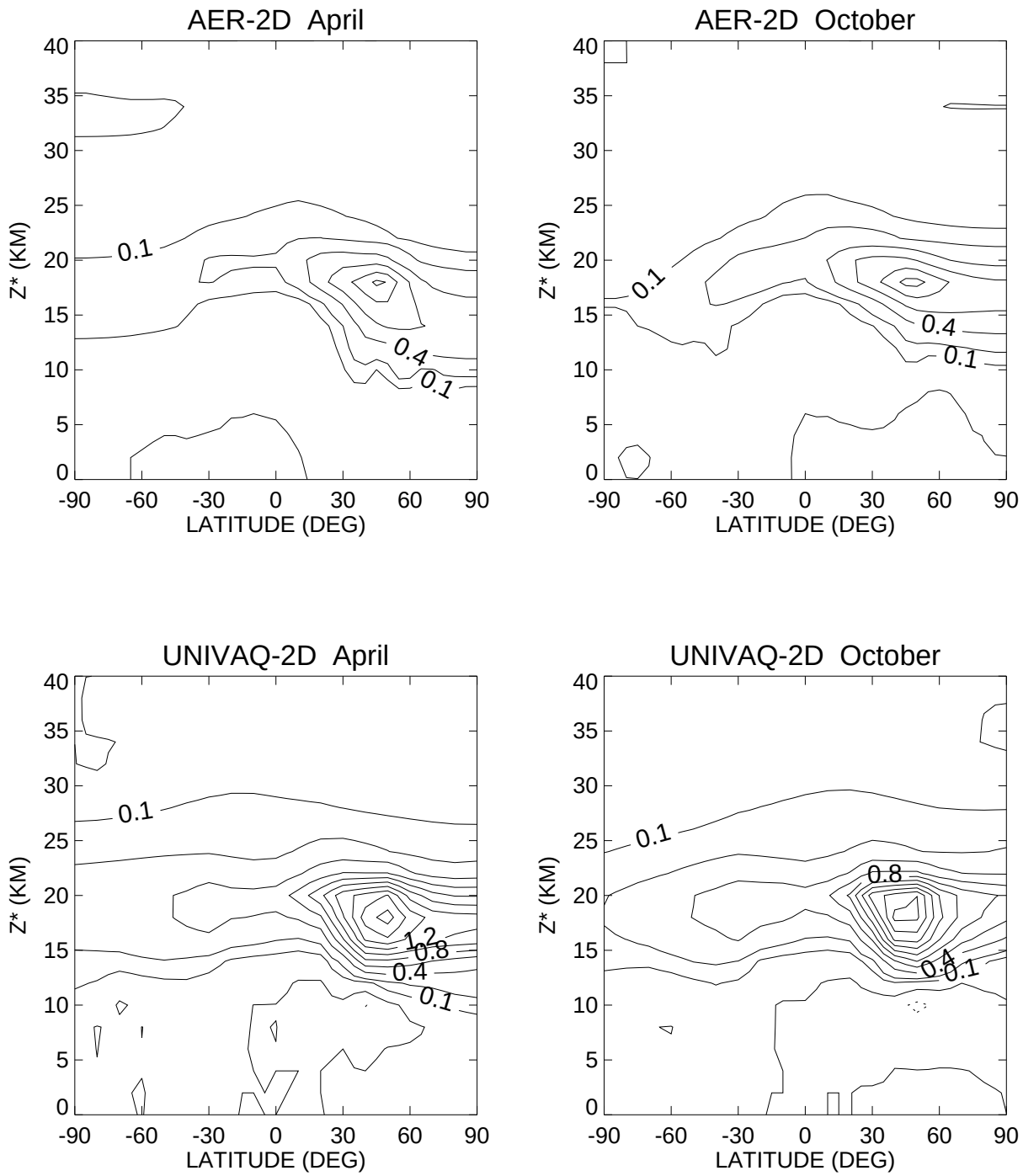

Figure 4.239: Calculated perturbations to aerosol surface area density ($\mu m^2/cm^3$) as a function of latitude and altitude in April and October due to emissions from a fleet of 500 HSCT aircraft with EI(SO_2)=0.4 and 50% gas to particle conversion under Scenario S7a relative to Scenario D7. Contours are -0.1, 0, 0.1, and 0.2 to 1.8 by 0.2.

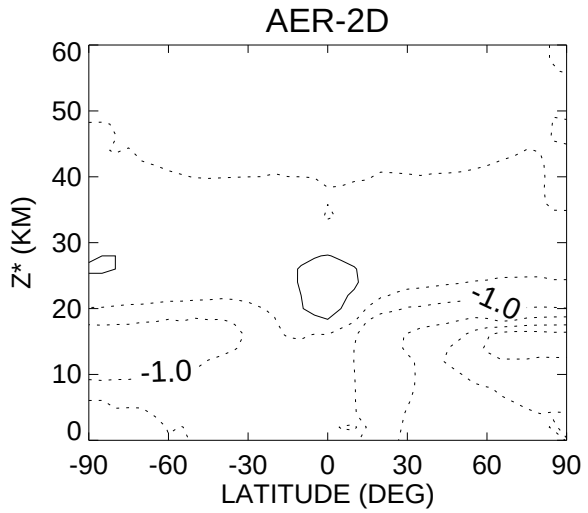

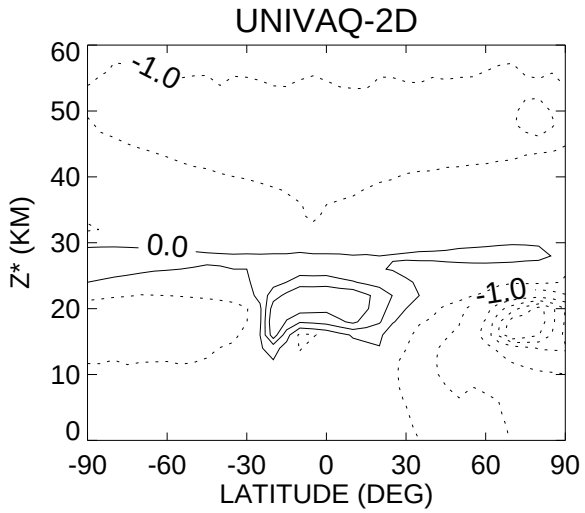

Figure 4.240: Calculated perturbations to O_3 (percent) as a function of latitude and altitude in March of 2015 due to emissions from a fleet of 500 HSCT aircraft with EI(NO_x)=5, EI(SO_2)=0.4, and 50% gas to article conversion under Scenario S7a relative to Scenario D7. Contours are -5, -4, -3, -2, -1, -0.5, 0, 0.5, 1.

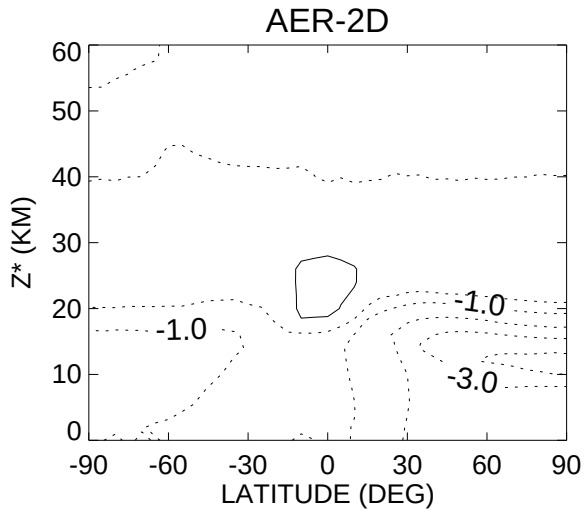

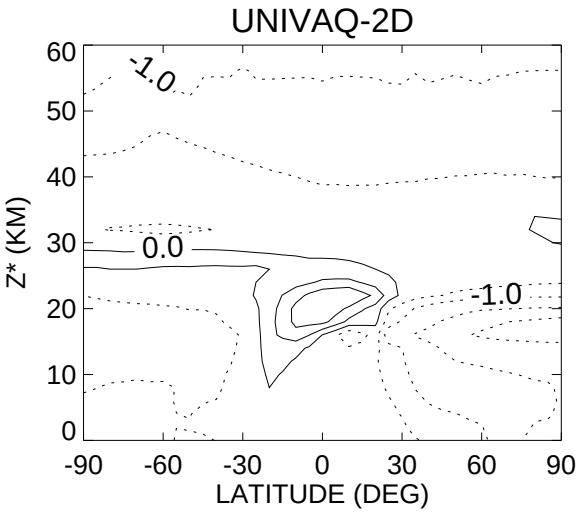

Figure 4.241: Calculated perturbations to O_3 (percent) as a function of latitude and altitude in June of 2015 due to emissions from a fleet of 500 HSCT aircraft with EI(NO_x)=5, EI(SO_2)=0.4, and 50% gas to particle conversion under Scenario S7a relative to Scenario D7. Contours are -4, -3, -2, -1, -0.5, 0, 0.5, 1.

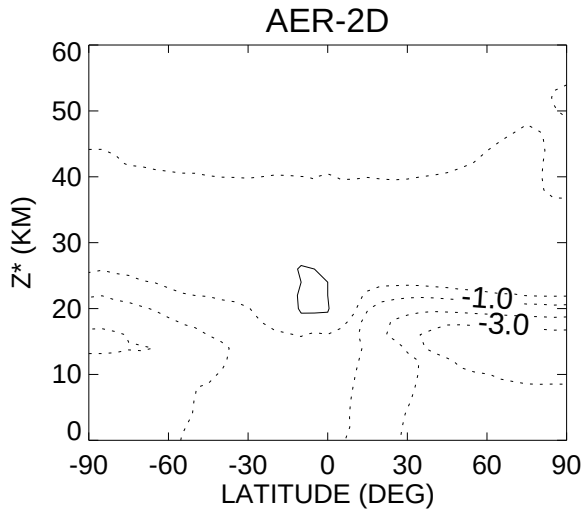

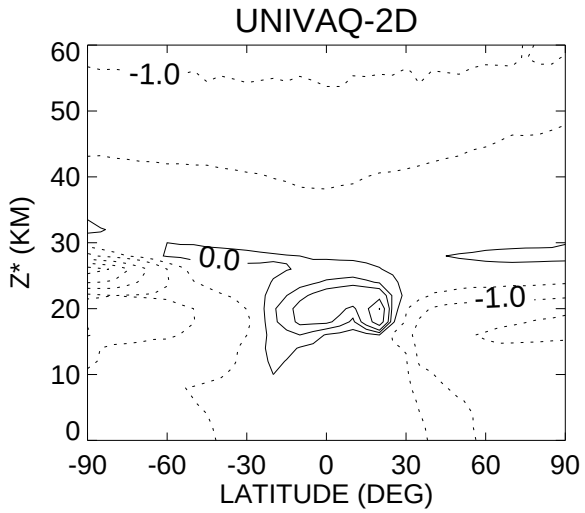

Figure 4.242: Calculated perturbations to O_3 (percent) as a function of latitude and altitude in October of 2015 due to emissions from a fleet of 500 HSCT aircraft with EI(NO_x)=5, EI(SO_2)=0.4, and 50% gas to particle conversion under Scenario S7a relative to Scenario D7. Contours are -3, -2, -1, -0.5, 0, 0.5, 1, 2, 3.

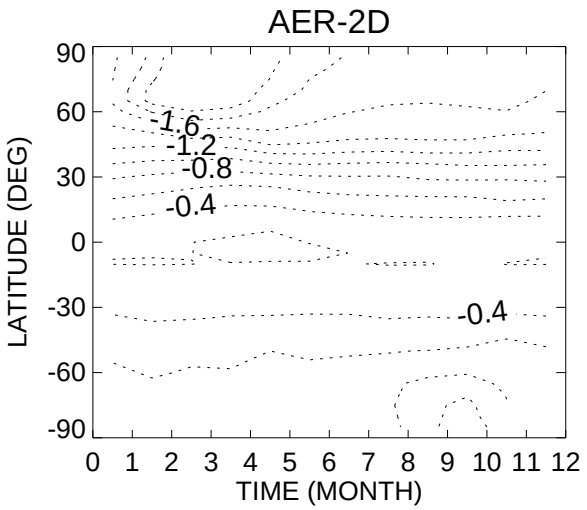

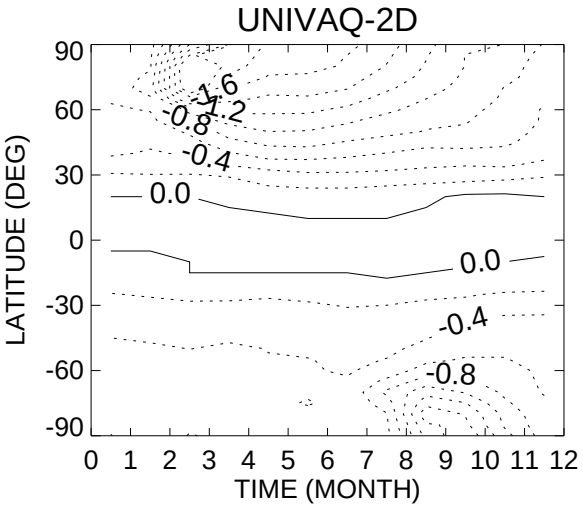

Figure 4.243: Calculated perturbations to column O_3 (percent) as a function of latitude and season in 2015 due to emissions from a fleet of 500 HSCT aircraft with EI(NO_x)=5, EI(SO_2)=0.4, and 50% gas to particle conversion under Scenario S7a relative to Scenario D7. Contours are -2 to 0 by 0.2.

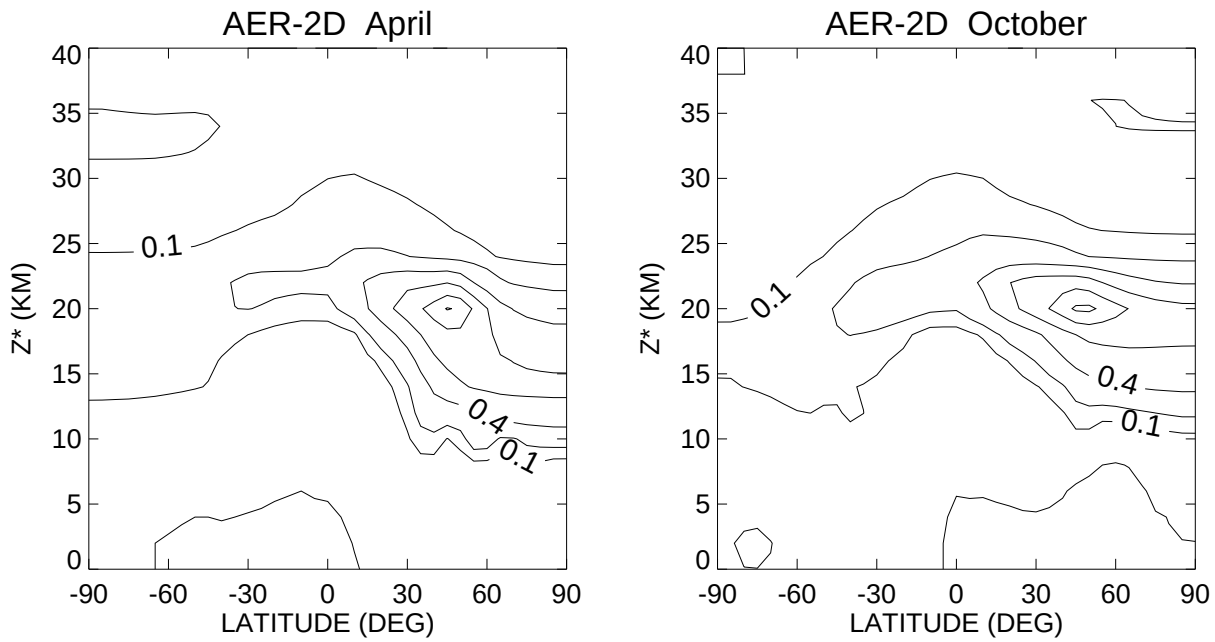

Figure 4.244: Calculated perturbations to aerosol surface area density ($\mu m^2/cm^3$) as a function of latitude and altitude in April and October due to emissions from a fleet of 500 HSCT aircraft operating at 2 km above the nominal cruise altitude with EI(SO_2)=0.4 and 50% gas to particle conversion under Scenario S7b relative to Scenario D7. Contours are -0.1, 0, 0.1, and 0.2, 0.4, 0.6, 0.8.

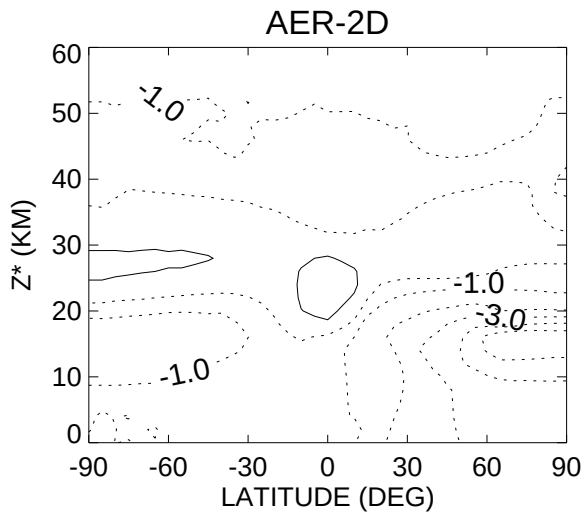

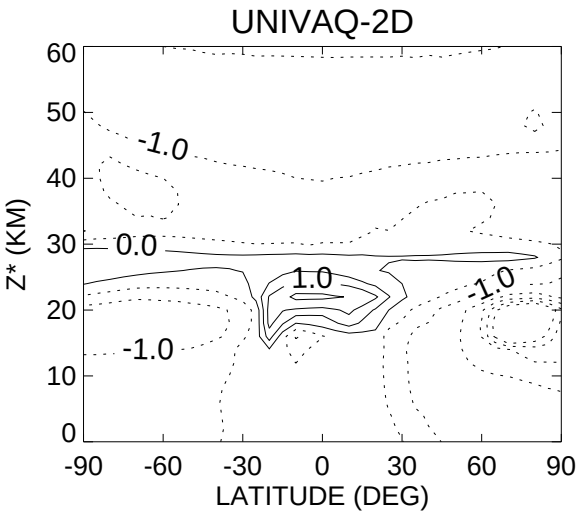

Figure 4.245: Calculated perturbations to O_3 (percent) as a function of latitude and altitude in March of 2015 due to emissions from a fleet of 500 HSCT aircraft operating at 2 km above the nominal cruise altitude with EI(NO_x)=5, EI(SO_2)=0.4, and 50% gas to particle conversion under Scenario S7b relative to Scenario D7. Contours are -5, -4, -3, -2, -1, -0.5, 0, 0.5, 1, 2.

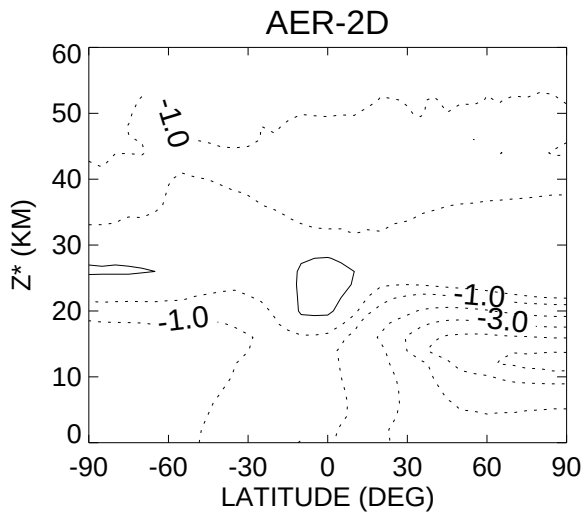

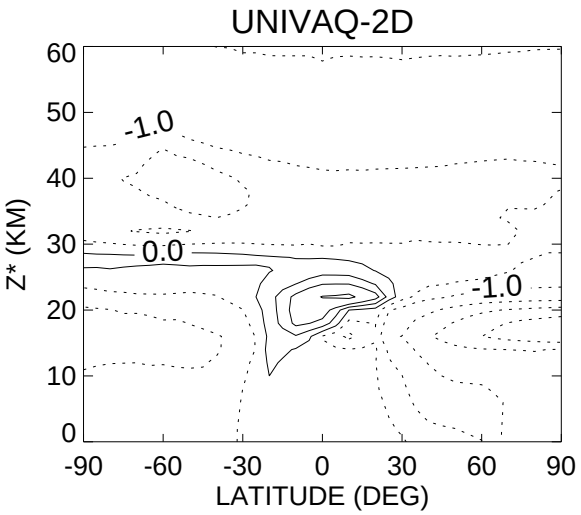

Figure 4.246: Calculated perturbations to O_3 (percent) as a function of latitude and altitude in June of 2015 due to emissions from a fleet of 500 HSCT aircraft operating at 2 km above the nominal cruise altitude with EI(NO_x)=5, EI(SO_2)=0.4, and 50% gas to particle conversion under Scenario S7b relative to Scenario D7. Contours are -5, -4, -3, -2, -1, -0.5, 0, 0.5, 1, 2.

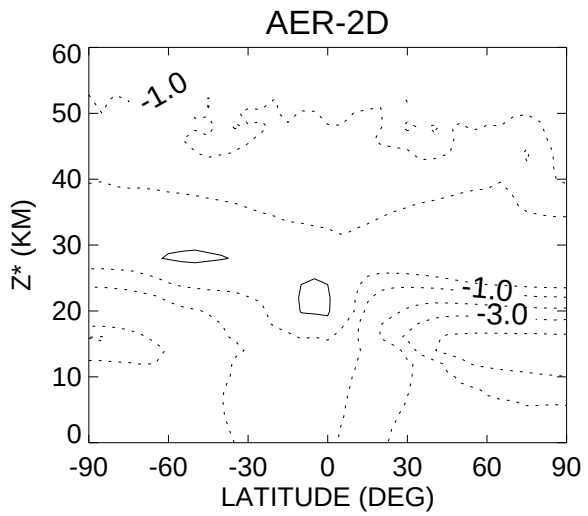

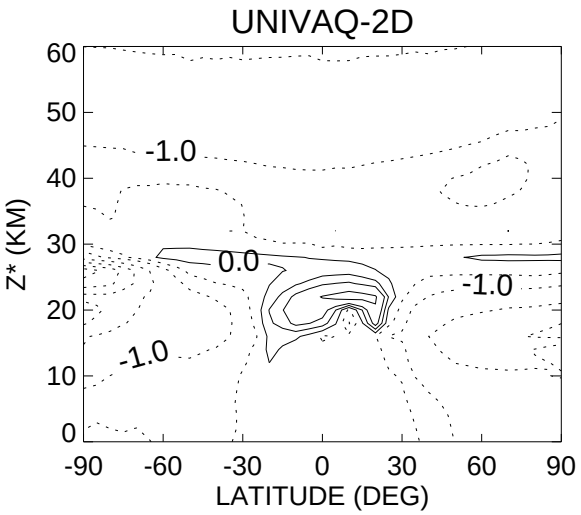

Figure 4.247: Calculated perturbations to O_3 (percent) as a function of latitude and altitude in October of 2015 due to emissions from a fleet of 500 HSCT aircraft operating at 2 km above the nominal cruise altitude with EI(NO_x)=5, EI(SO_2)=0.4, and 50% gas to particle conversion under Scenario S7b relative to Scenario D7. Contours are -5, -4, -3, -2, -1, -0.5, 0, 0.5, 1, 2.

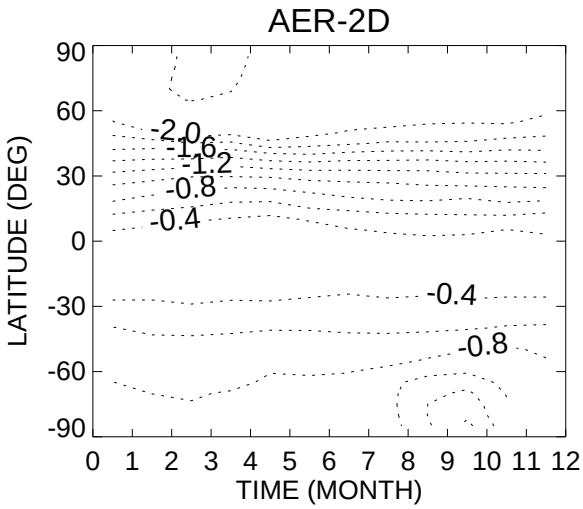

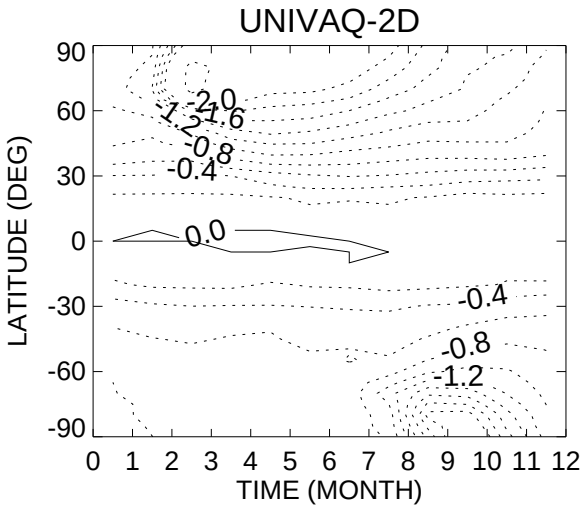

Figure 4.248: Calculated perturbations to column O_3 (percent) as a function of latitude and season in 2015 due to emissions from a fleet of 500 HSCT aircraft operating at 2 km above the nominal cruise altitude with EI(NO_x)=5, EI(SO_2)=0.4, and 50% gas to particle conversion under Scenario S7b relative to Scenario D7. Contours are -3 and -2 to 0 by 0.2.

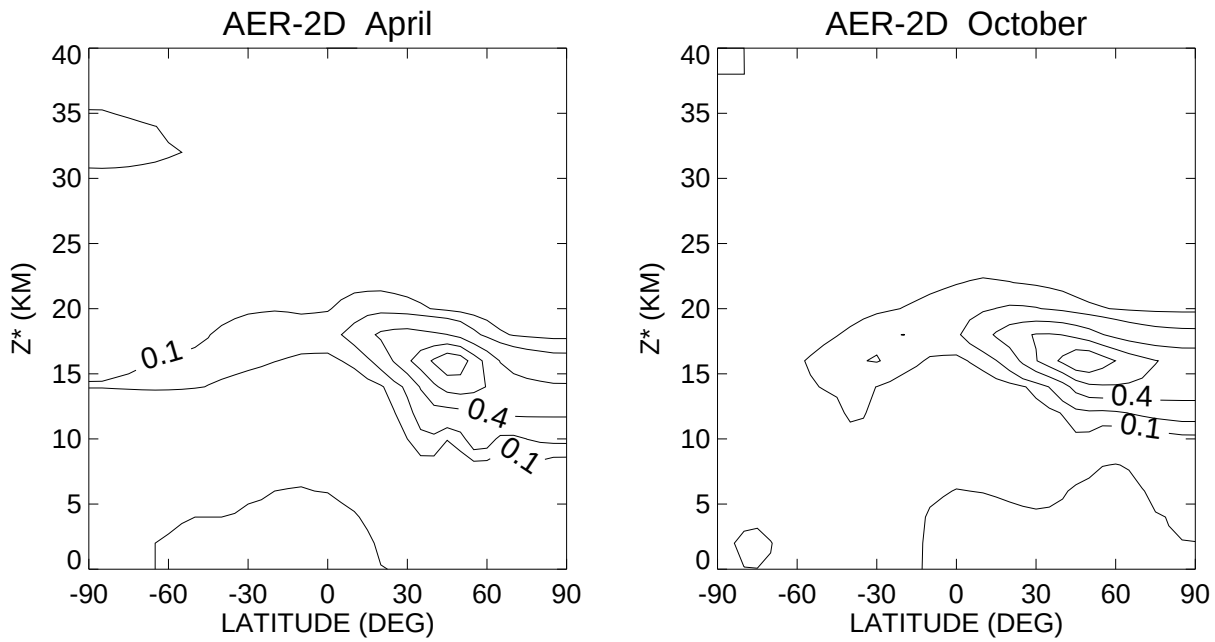

Figure 4.249: Calculated perturbations to aerosol surface area density ($\mu m^2/cm^3$) as a function of latitude and altitude in April and October due to emissions from a fleet of 500 HSCT aircraft operating at 2 km below the nominal cruise altitude with EI(SO_2)=0.4 and 50% gas to particle conversion under Scenario S7c relative to Scenario D7. Contours are -0.1, 0, 0.1, and 0.2, 0.4, 0.6, 0.8.

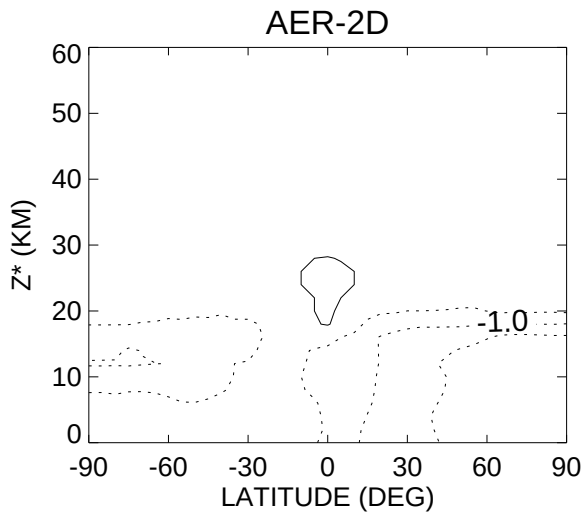

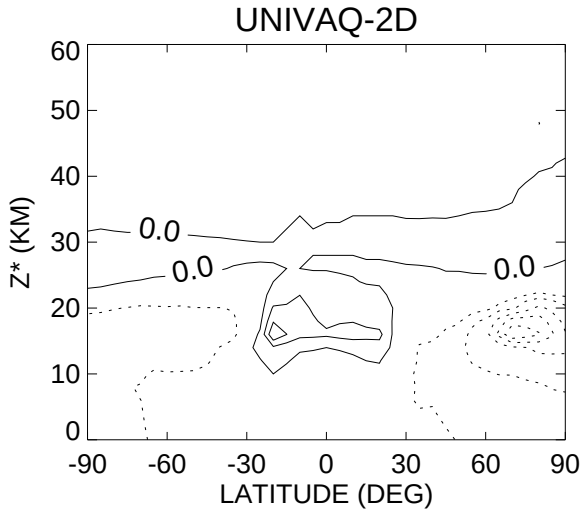

Figure 4.250: Calculated perturbations to O_3 (percent) as a function of latitude and altitude in March of 2015 due to emissions from a fleet of 500 HSCT aircraft operating at 2 km below the nominal cruise altitude with EI(NO_x)=5, EI(SO_2)=0.4, and 50% gas to particle conversion under Scenario S7c relative to Scenario D7. Contours are -4, -3, -2, -1, -0.5, 0, 0.5, 1.

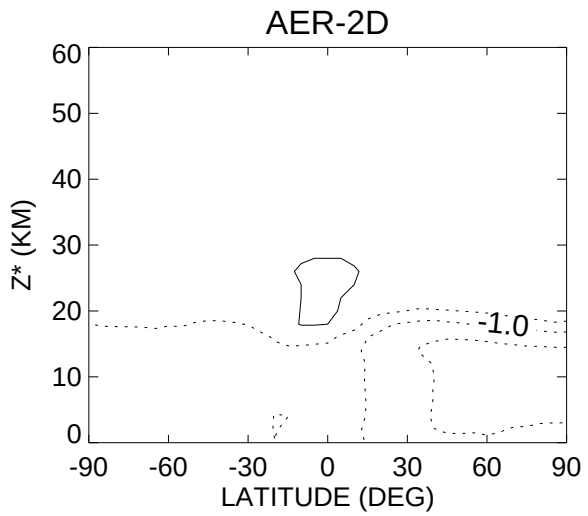

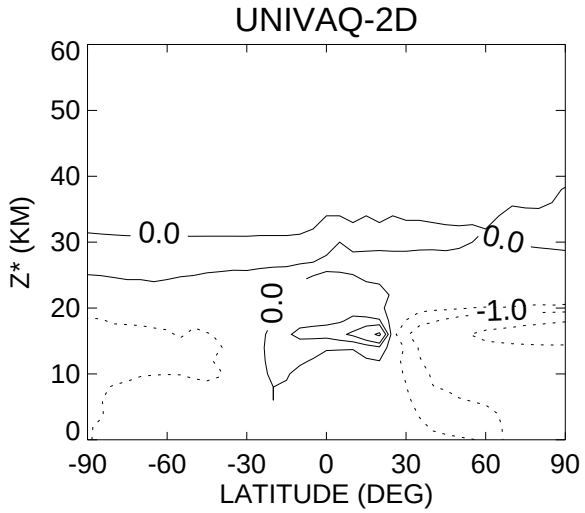

Figure 4.251: Calculated perturbations to O_3 (percent) as a function of latitude and altitude in June of 2015 due to emissions from a fleet of 500 HSCT aircraft operating at 2 km below the nominal cruise altitude with EI(NO_x)=5, EI(SO_2)=0.4, and 50% gas to particle conversion under Scenario S7c relative to Scenario D7. Contours are -2, -1, -0.5, 0, 0.5, 1, 2.

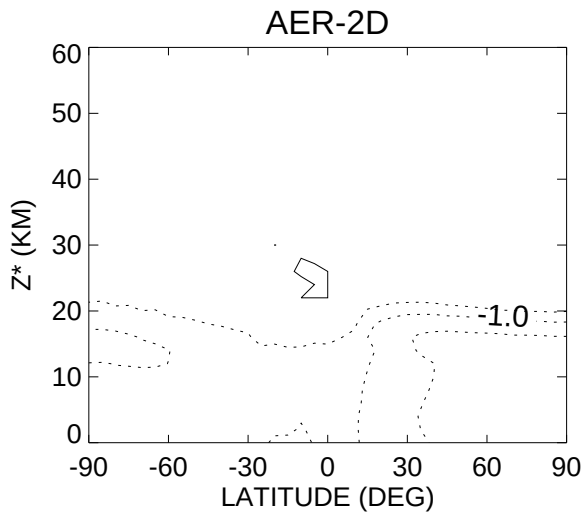

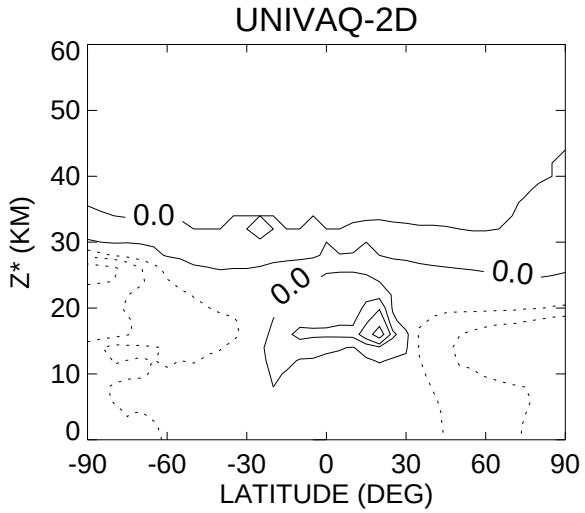

Figure 4.252: Calculated perturbations to O_3 (percent) as a function of latitude and altitude in October of 2015 due to emissions from a fleet of 500 HSCT aircraft operating at 2 km below the nominal cruise altitude with EI(NO_x)=5, EI(SO_2)=0.4, and 50% gas to particle conversion under Scenario S7c relative to Scenario D7. Contours are -2, -1, -0.5, 0, 0.5, 1, 2.

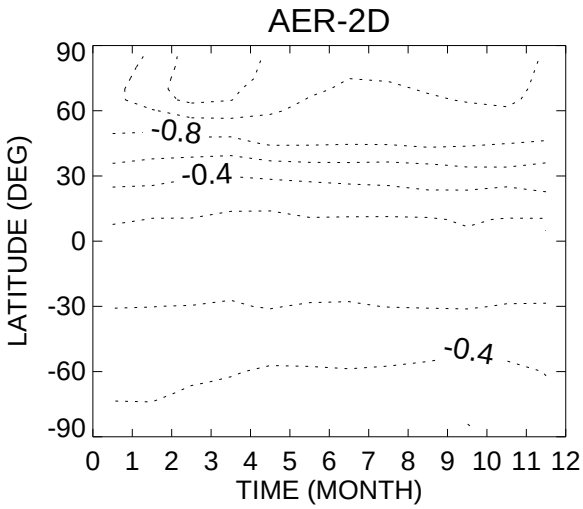

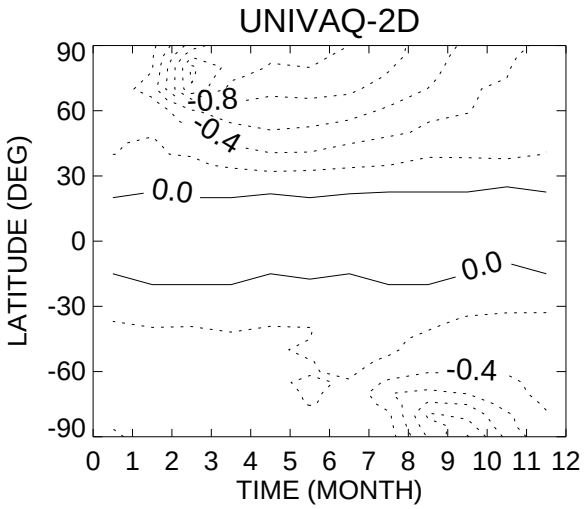

Figure 4.253: Calculated perturbations to column O_3 (percent) as a function of latitude and season in 2015 due to emissions from a fleet of 500 HSCT aircraft operating at 2 km below the nominal cruise altitude with EI(NO_x)=5, EI(SO_2)=0.4, and 50% gas to particle conversion under Scenario S7c relative to Scenario D7. Contours are -1.2 to 0 by 0.2.

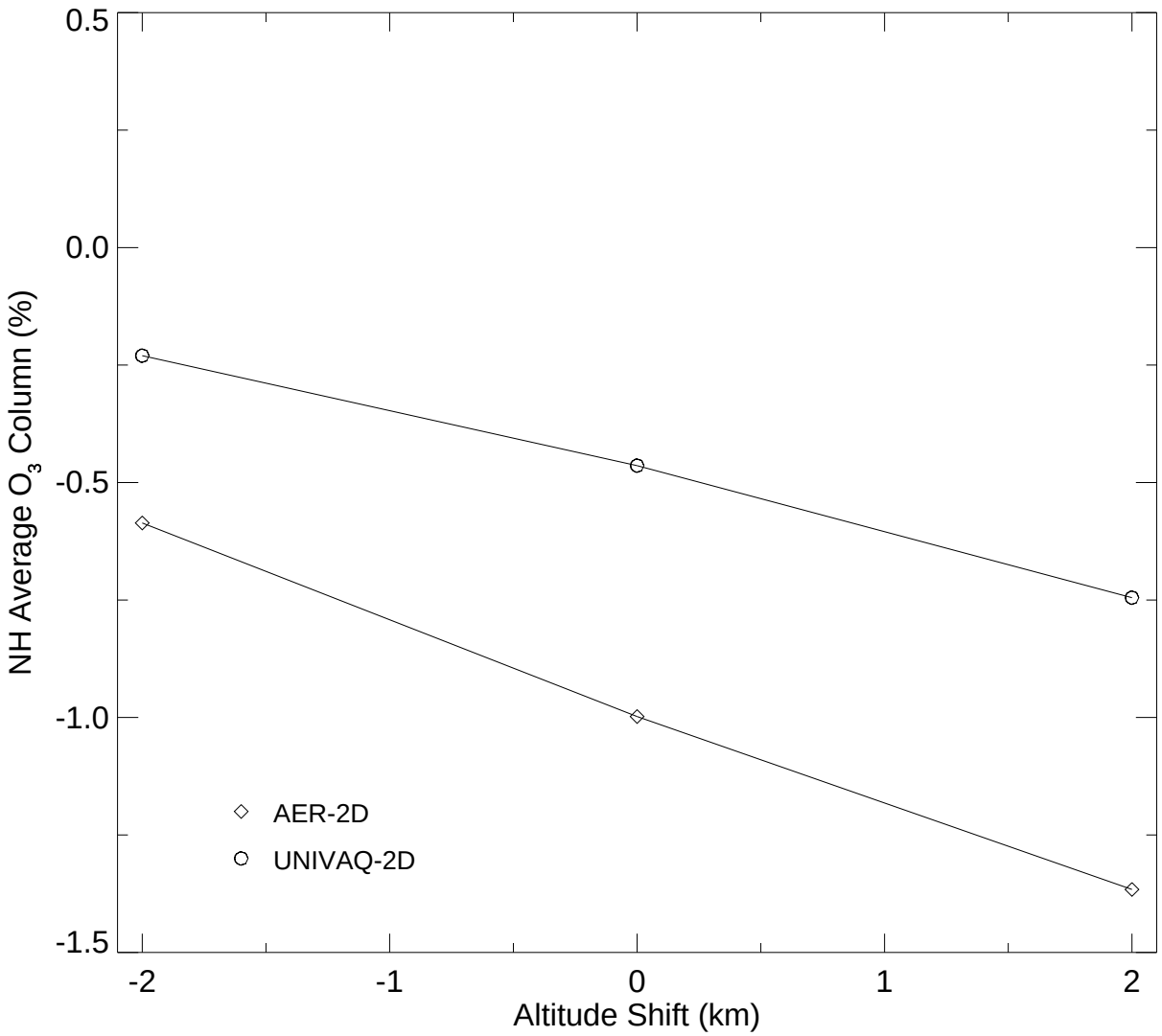

Figure 4.254: Northern hemisphere annual average total O_3 column change (percent) as a function of cruise altitude for an HSCT fleet of 500 aircraft operating in 2015 with EI(NO_x)=5 and sulfur emissions from aircraft assuming EI(SO_2)=0.4 and 50% particle conversion. These calculations were performed by the AER and UNIVAQ models with interactive microphysics.

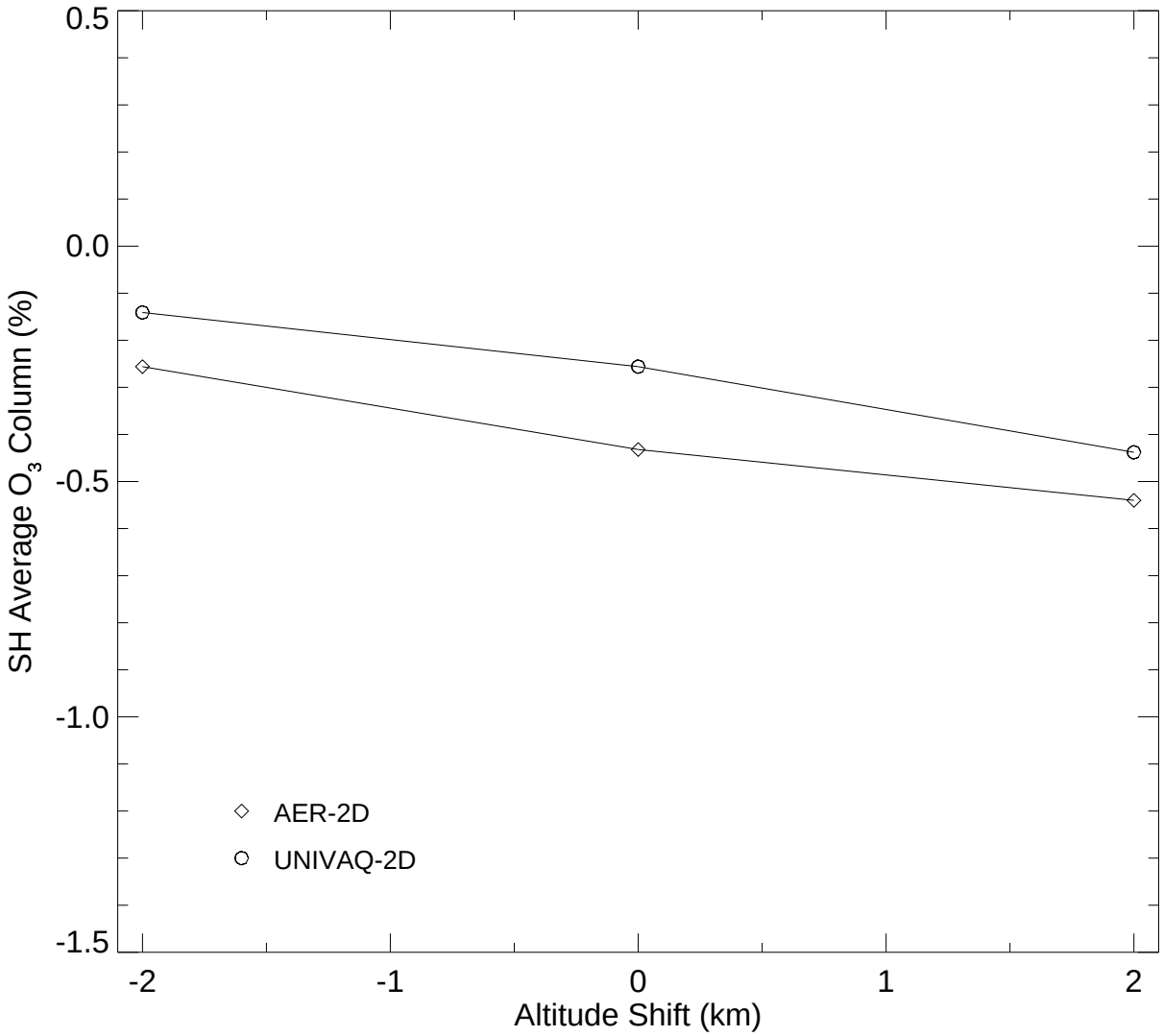

Figure 4.255: Southern hemisphere annual average total O_3 column change (percent) as a function of cruise altitude for an HSCT fleet of 500 aircraft operating in 2015 with EI(NO_x)=5 and sulfur emissions from aircraft assuming EI(SO_2)=0.4 and 50% particle conversion. These calculations were performed by the AER and UNIVAQ models with interactive microphysics.

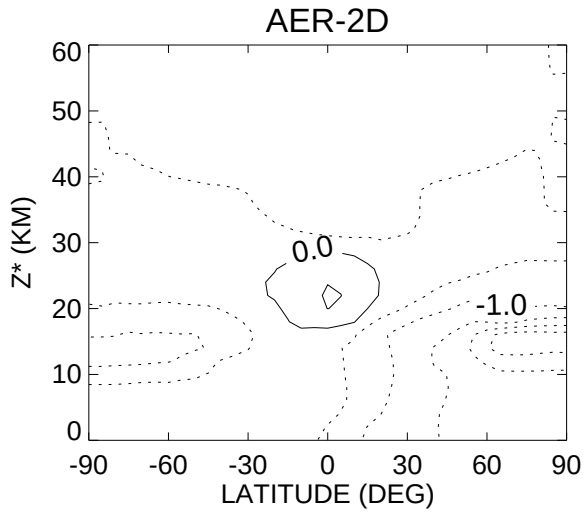

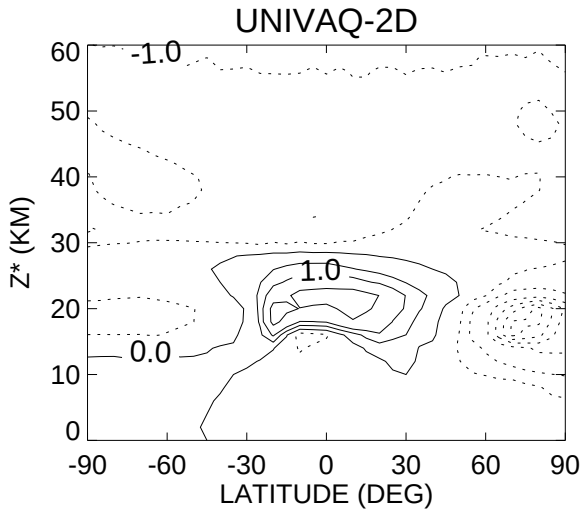

Figure 4.256: Calculated perturbations to O_3 (percent) as a function of latitude and altitude in March of 2015 due to emissions from a fleet of 500 HSCT aircraft with EI(NO_x)=10, EI(SO_2)=0.4, and 50% gas to particle conversion under Scenario S7d relative to Scenario D7. Contours are -3, -2, -1, -0.5, 0, 0.5, 1, 2.

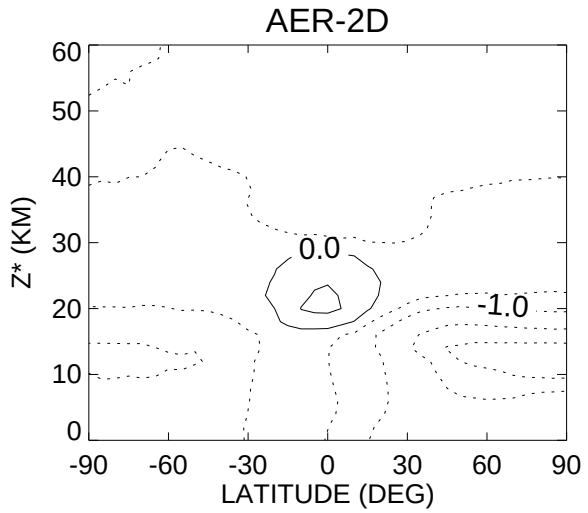

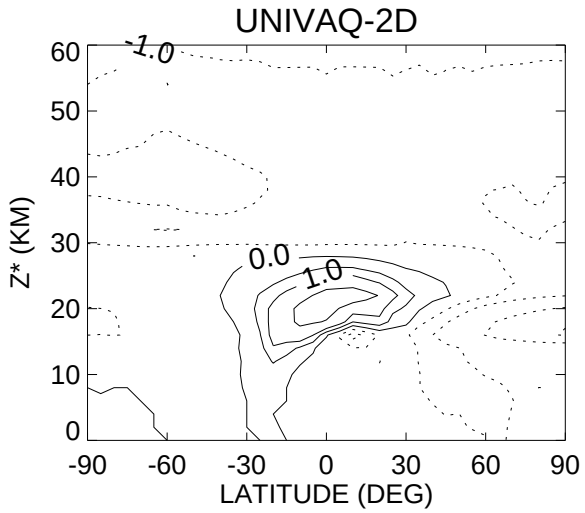

Figure 4.257: Calculated perturbations to O_3 (percent) as a function of latitude and altitude in June of 2015 due to emissions from a fleet of 500 HSCT aircraft with EI(NO_x)=10, EI(SO_2)=0.4, and 50% gas to particle conversion under Scenario S7d relative to Scenario D7. Contours are -3, -2, -1, -0.5, 0, 0.5, 1, 2.

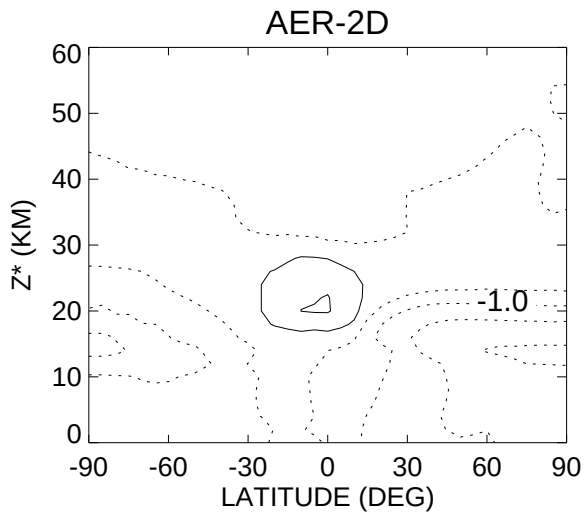

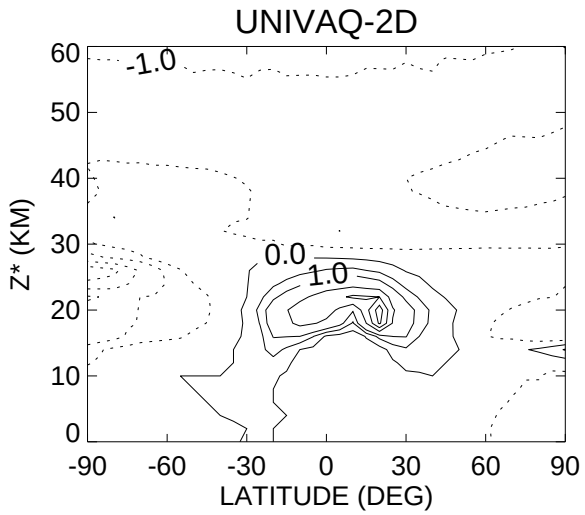

Figure 4.258: Calculated perturbations to O_3 (percent) as a function of latitude and altitude in October of 2015 due to emissions from a fleet of 500 HSCT aircraft with EI(NO_x)=10, EI(SO_2)=0.4, and 50% gas to particle conversion under Scenario S7d relative to Scenario D7. Contours are -3, -2, -1, -0.5, 0, 0.5, 1, 2, 3, 4.

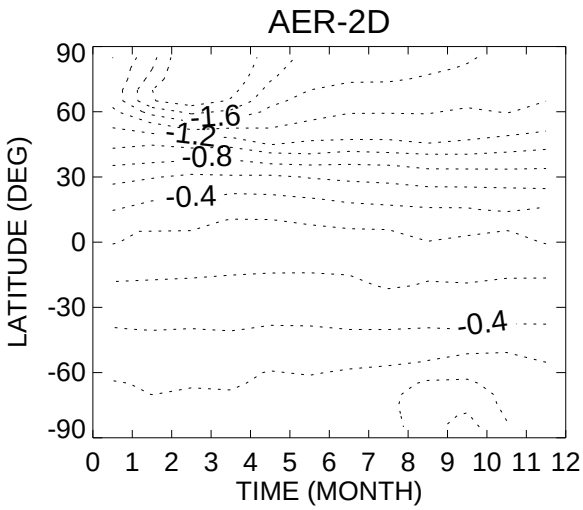

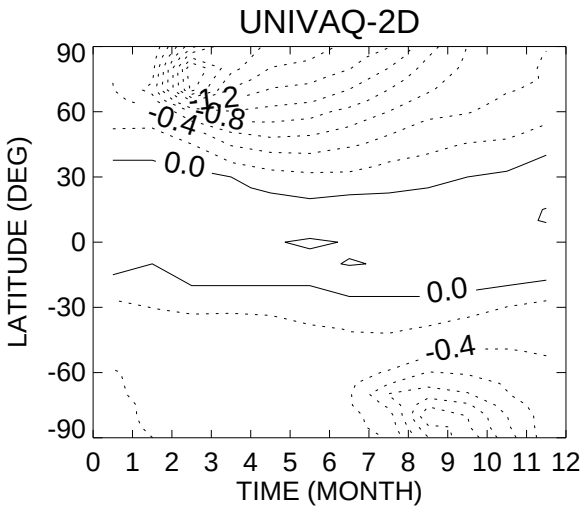

Figure 4.259: Calculated perturbations to column O_3 (percent) as a function of latitude and season in 2015 due to emissions from a fleet of 500 HSCT aircraft with EI(NO_x)=10, EI(SO_2)=0.4, and 50% gas to particle conversion under Scenario S7d relative to Scenario D7. Contours are -2 to +0.2 by 0.2.

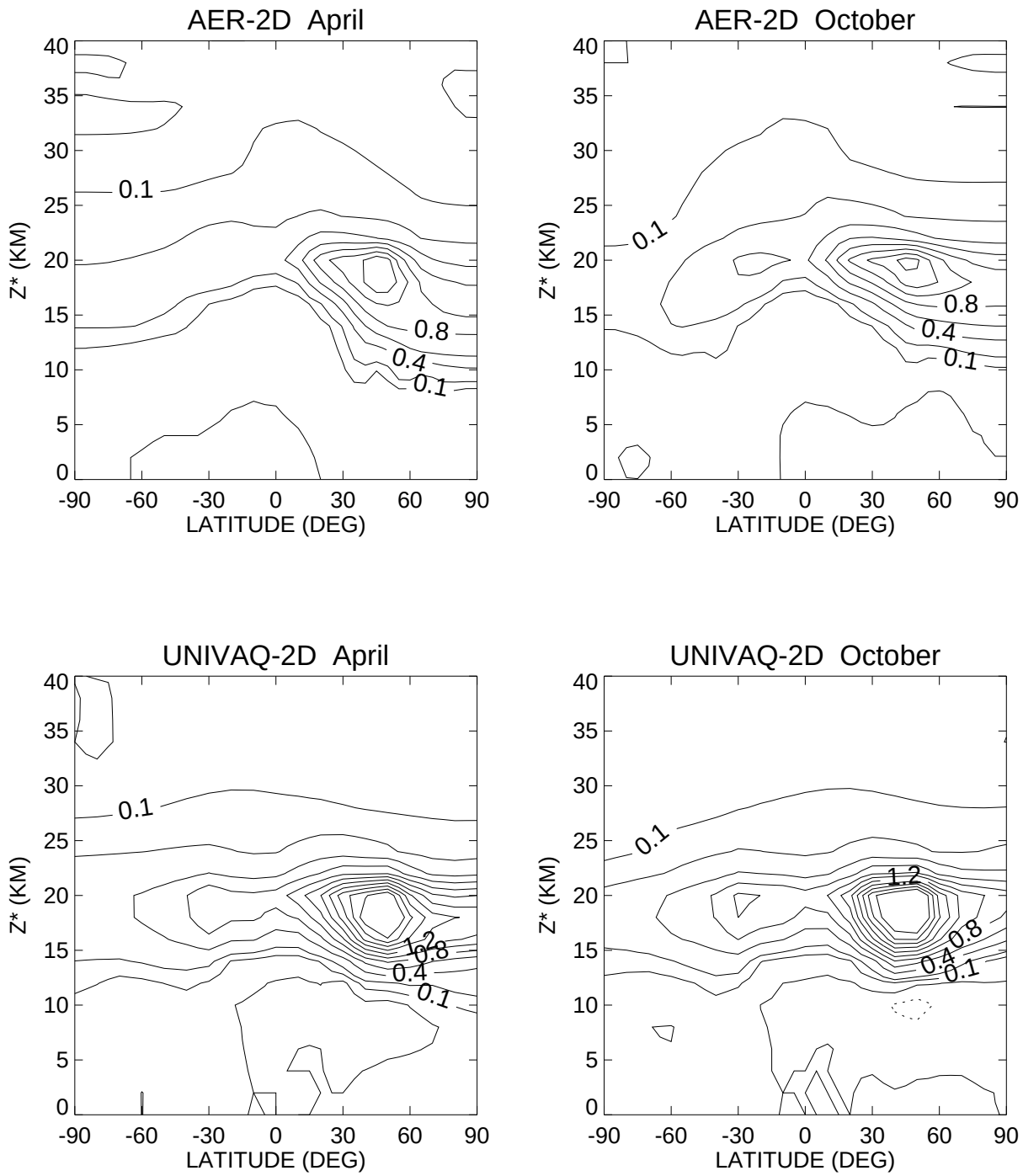

Figure 4.260: Calculated perturbations to aerosol surface area density ($\mu m^2/cm^3$) as a function of latitude and altitude in April and October due to emissions from a fleet of 500 HSCT aircraft with EI(SO_2)=0.4 and 100% gas to particle conversion under Scenario S8a relative to Scenario D8. Contours are -0.1, 0, 0.1, and 0.2 to 2.0 by 0.2.

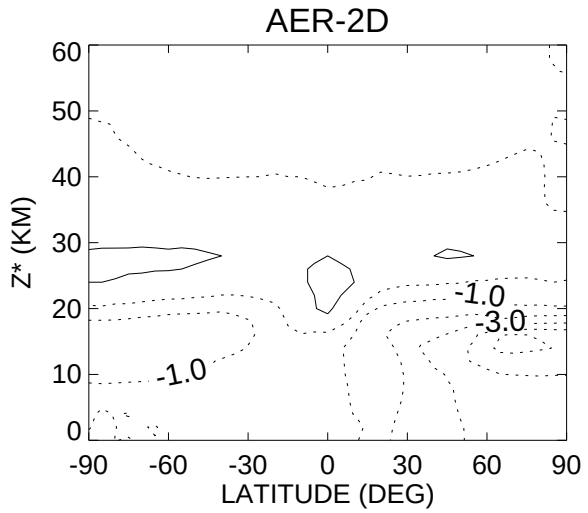

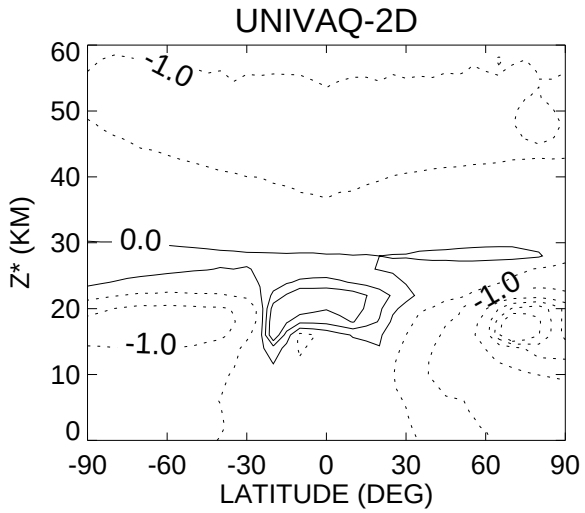

Figure 4.261: Calculated perturbations to O_3 (percent) as a function of latitude and altitude in March of 2015 due to emissions from a fleet of 500 HSCT aircraft with EI(NO_x)=5, EI(SO_2)=0.4, and 100% gas to particle conversion under Scenario S8a relative to Scenario D8. Contours are -5, -4, -3, -2, -1, -0.5, 0, 0.5, 1.

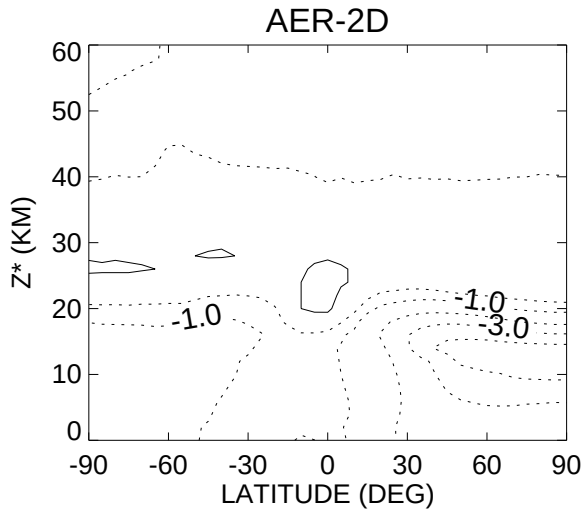

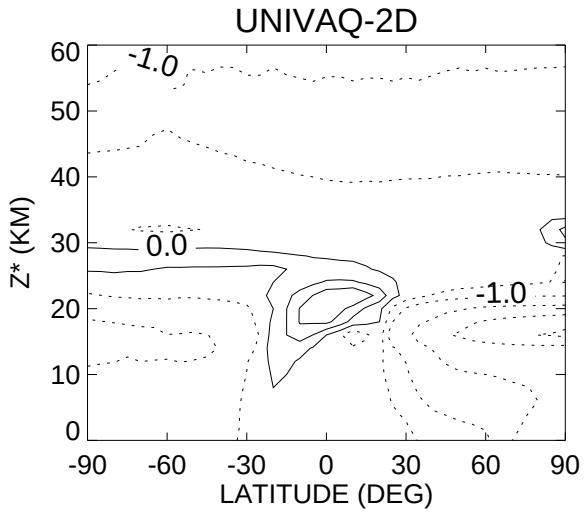

Figure 4.262: Calculated perturbations to O_3 (percent) as a function of latitude and altitude in June of 2015 due to emissions from a fleet of 500 HSCT aircraft with EI(NO_x)=5, EI(SO_2)=0.4, and 100% gas to particle conversion under Scenario S8a relative to Scenario D8. Contours are -4, -3, -2, -1, -0.5, 0, 0.5, 1.

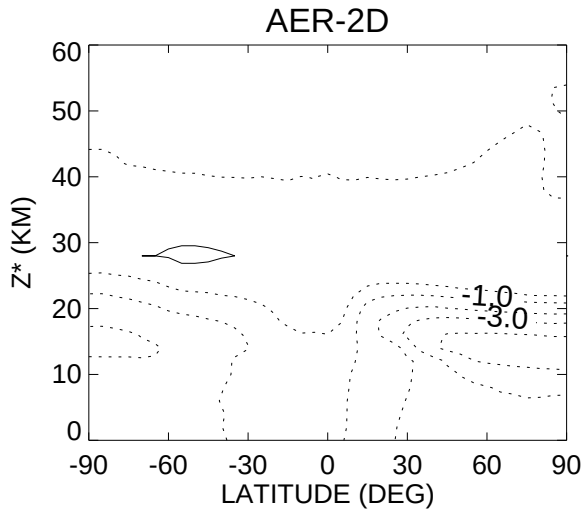

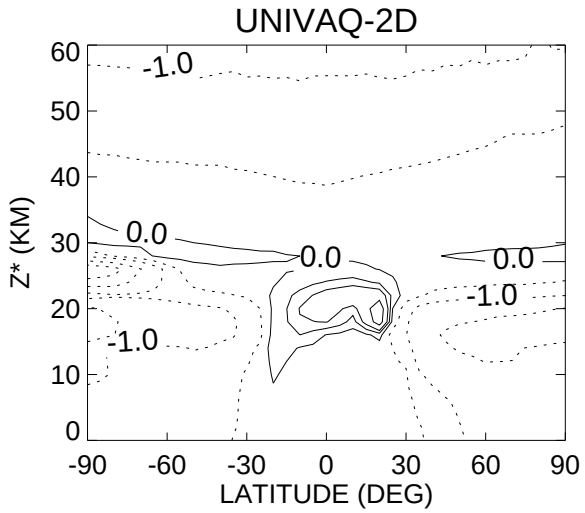

Figure 4.263: Calculated perturbations to O_3 (percent) as a function of latitude and altitude in October of 2015 due to emissions from a fleet of 500 HSCT aircraft with EI(NO_x)=5, EI(SO_2)=0.4, and 100% gas to particle conversion under Scenario S8a relative to Scenario D8. Contours are -4, -3, -2, -1, -0.5, 0, 0.5, 1, 2.

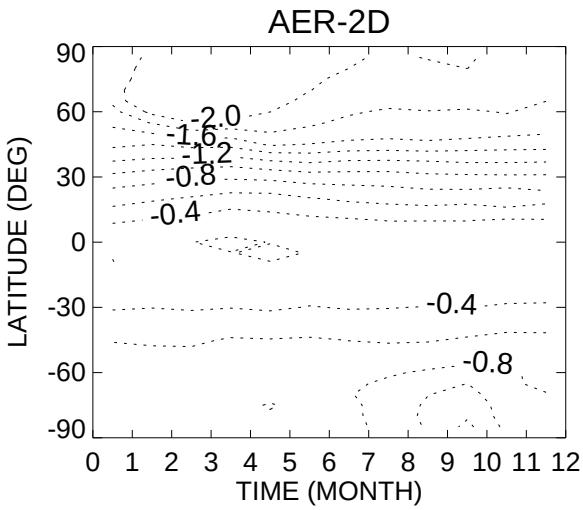

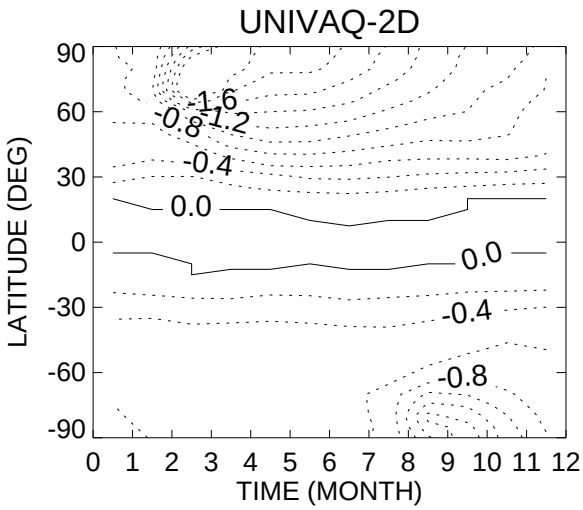

Figure 4.264: Calculated perturbations to column O_3 (percent) as a function of latitude and season in 2015 due to emissions from a fleet of 500 HSCT aircraft with EI(NO_x)=5, EI(SO_2)=0.4, and 100% gas to particle conversion under Scenario S8a relative to Scenario D8. Contours are -2 to 0 by 0.2.

Chapter 5

HSCT Perturbations for 2050

A total of 14 scenarios for the 2050 atmosphere were used in the IPCC supersonic aircraft assessment. Only 2-D models performed these scenario calculations. The scenarios were chosen to explore the effects of parametric modifications in the HSCT aircraft fleet, such as EI(NO_x), fleet size, cruise altitude, EI(SO_2), and SO_2 gas-to-particle conversion fraction. Most scenarios assumed the same subsonic fleet as was used for 2015. However, two scenarios (S11a and S12a) explored the effect of modifying the subsonic fleet, since projecting the fleet to 2050 is highly uncertain. The HSCT fleets consisted of either 500 or 1000 aircraft and were identical to those for 2015, though the larger fleet size was used for a majority of 2050 scenarios. A summary of the scenarios considered, along with the scenario designations, is given in Table 5.1. The reference atmosphere for each scenario is also listed in the table. Perturbations are given relative to these reference scenarios, which include identical boundary conditions and the same model formulation but omit the HSCT fleet.

Table 5.1: Specifications for Supersonic Aircraft Emission Scenarios in 2050

Scenario	Cl_y (ppbv)	Fleet Size	EI(NO_x)	Cruise Alt.	SAD Desc.	Special	Ref. Atm.
S9a	2.0	500	5	Std	SA0		D9
S9b	2.0	500	10	Std	SA0		D9
S9c	2.0	500	5	Std	SA1		D9
S9d	2.0	1000	5	Std	SA0		D9
S9e	2.0	1000	5	Std	SA2		D9
S9f	2.0	1000	5	Std	SA4		D9
S9g	2.0	1000	10	Std	SA0		D9
S9h	2.0	1000	5	Std	SA6		D9
S10a	2.0	1000	5	-2 km	SA0		D9
S10b	2.0	1000	10	-2 km	SA0		D9
S10c	2.0	1000	5	-2 km	SA6-2km		D9
S10d	2.0	1000	5	-2 km	SA2-2km		D9
S11a	2.0	1000	5	Std	SA0	2050 Subsonic IS92a	F
S12a	2.0	1000	5	Std	SA0	2050 Subsonic IS92e High Demand	G

5.1 H_2O Perturbations

Calculated changes to H_2O vapor due to HSCT emissions in 2050 are shown in Figure 5.1 for Scenario S9a relative to Scenario D9. These results are very similar to those for S1c-D, which includes the same 500 HSCT fleet but in 2015. Only the UNIVAQ model shows noticeable differences between 2015 and 2050 for this comparison. Figure 5.2 show perturbations to H_2O for Scenario S9d relative to D9, which includes a 1000 HSCT fleet. Perturbations in this case are double those from S9a-D9. Scenario S10a represent a 1000 HSCT fleet in 2050 with the cruise altitude shifted downward by 2 km. H_2O perturbations for this case are shown in Figure 5.3. The peak H_2O perturbation in this case is reduced by 50% (for AER and CSIRO), by 30% (for GSFC and UNIVAQ) and by 20% (for LLNL) relative to emissions at the standard cruise altitude.

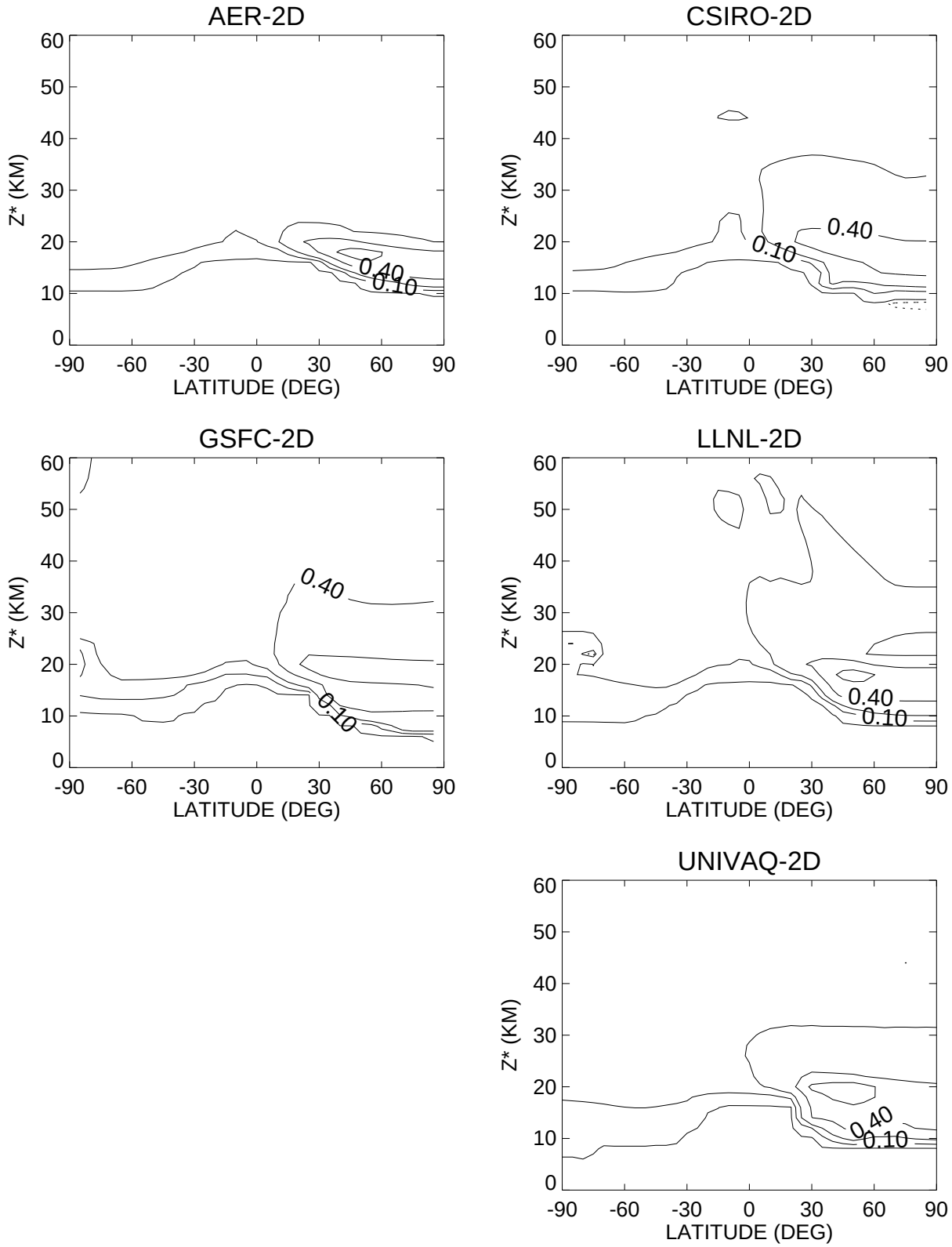

Figure 5.1: Calculated perturbation to H_2O (ppmv) as a function of latitude and altitude in June of 2050 due to H_2O emissions from a fleet of 500 HSCT aircraft under Scenario S9a relative to Scenario D9. Contours are 0, 0.1, 0.2, 0.4, 0.6 ppmv.

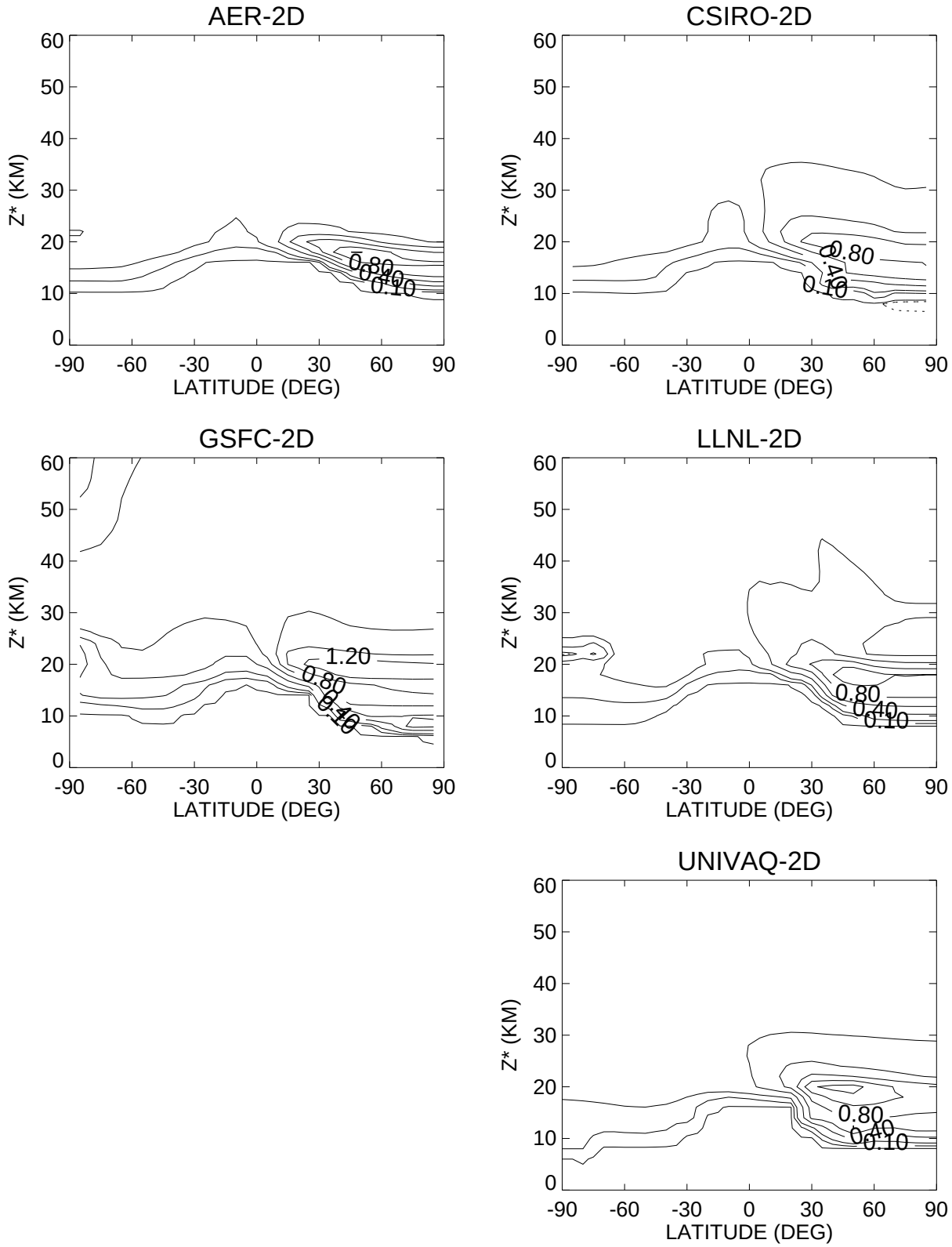

Figure 5.2: Calculated perturbation to H_2O (ppmv) as a function of latitude and altitude in June of 2050 due to H_2O emissions from a fleet of 1000 HSCT aircraft under Scenario S9d relative to Scenario D9. Contours are 0, 0.1 and 0.2 to 1.2 by 0.2 ppmv.

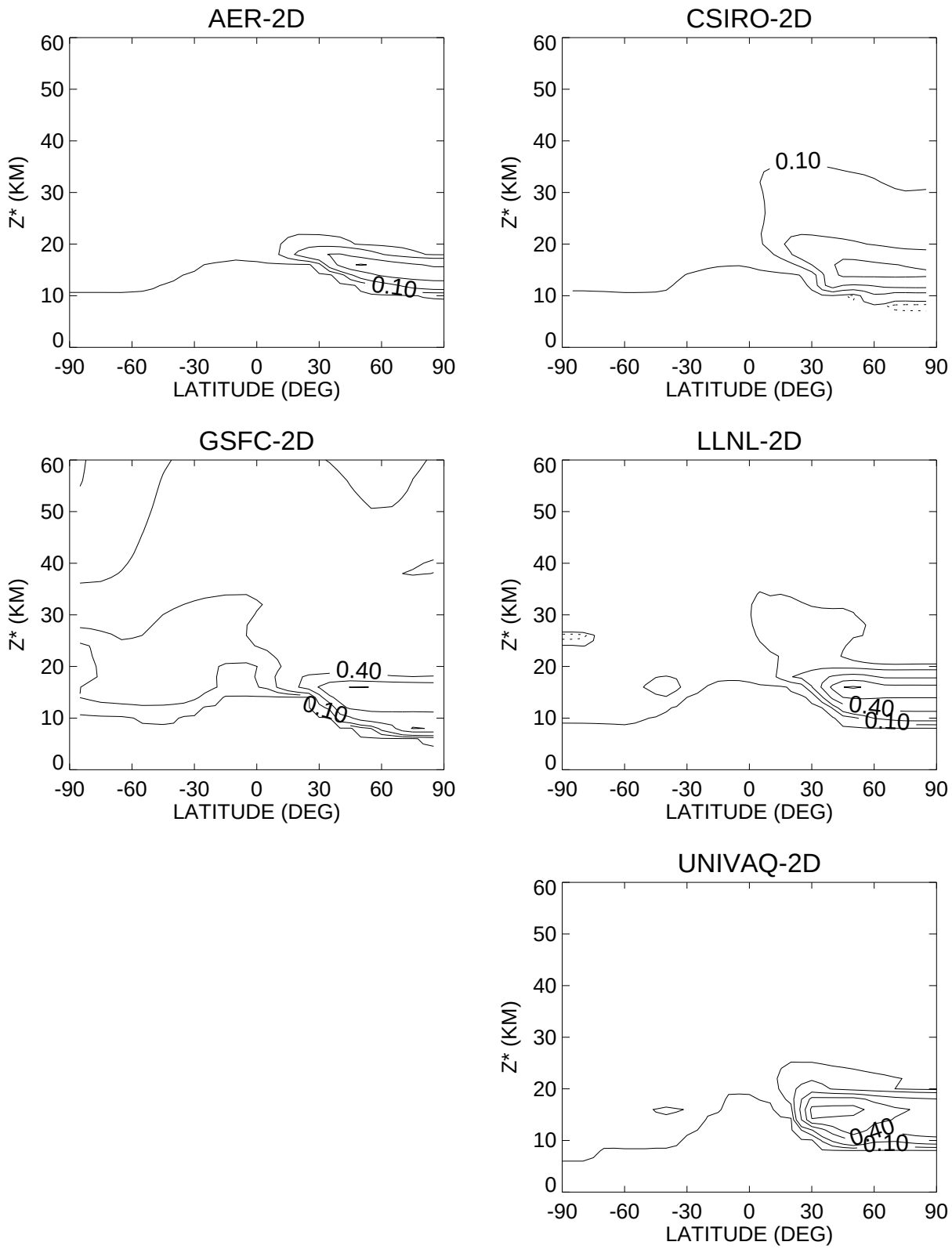

Figure 5.3: Calculated perturbation to H_2O (ppmv) as a function of latitude and altitude in June of 2050 due to H_2O emissions from a fleet of 1000 HSCT aircraft operating at 2 km below the nominal cruise altitude under Scenario S10a relative to Scenario D9. Contours are 0, 0.1 and 0.2 to 0.8 by 0.2 ppmv.

5.2 NO_y Perturbations

This section discusses calculated perturbation to NO_y for 2050. NO_x emission indices of 5 and 10 are used in the 2050 scenarios. Figure 5.4 shows the calculated perturbation to NO_y due to HSCT emissions from a fleet of 500 HSCTs with EI(NO_x)=5 in 2050 (Scenario S9a-D9). Differences from the similar 2015 perturbation (S1c-D) are small and mainly evident in the southern polar region where denitrification is calculated. For EI(NO_x)=10 with a 500 HSCT fleet (Scenario S9b-D9), NO_y perturbations are shown in Figure 5.5. These perturbations are roughly double those of S9a-D9 in the lower stratosphere.

Calculated NO_y perturbations for fleets of 1000 HSCTs in 2050 are shown in Figure 5.6 for an EI(NO_x) of 5 (S9d-D9) and in Figure 5.7 for an EI(NO_x) of 10 (S9g-D9). The NO_y perturbations are roughly twice those seen for the 500 HSCT fleet with the same EI(NO_x). In addition, the 1000 HSCT fleet with EI(NO_x)=5 has a similar NO_y perturbation to the 500 HSCT fleet with EI(NO_x)=10. Calculated maximum NO_y perturbations with EI(NO_x)=10 and 1000 aircraft range up to 2 or 3 ppbv in the models, which represents relative increases in NO_y of 20% or more at 45^oN and 20 km.

Scenario S10a and S10b represent 1000 HSCTs operating in 2050 at 2 km below the nominal cruise altitude with EI(NO_x)=5 and 10, respectively. Calculated NO_y perturbations for these scenarios are shown in Figures 5.8 and 5.9. NO_y perturbations are considerably reduced (by 50% in some cases) relative to similar scenarios at the standard cruise altitude.

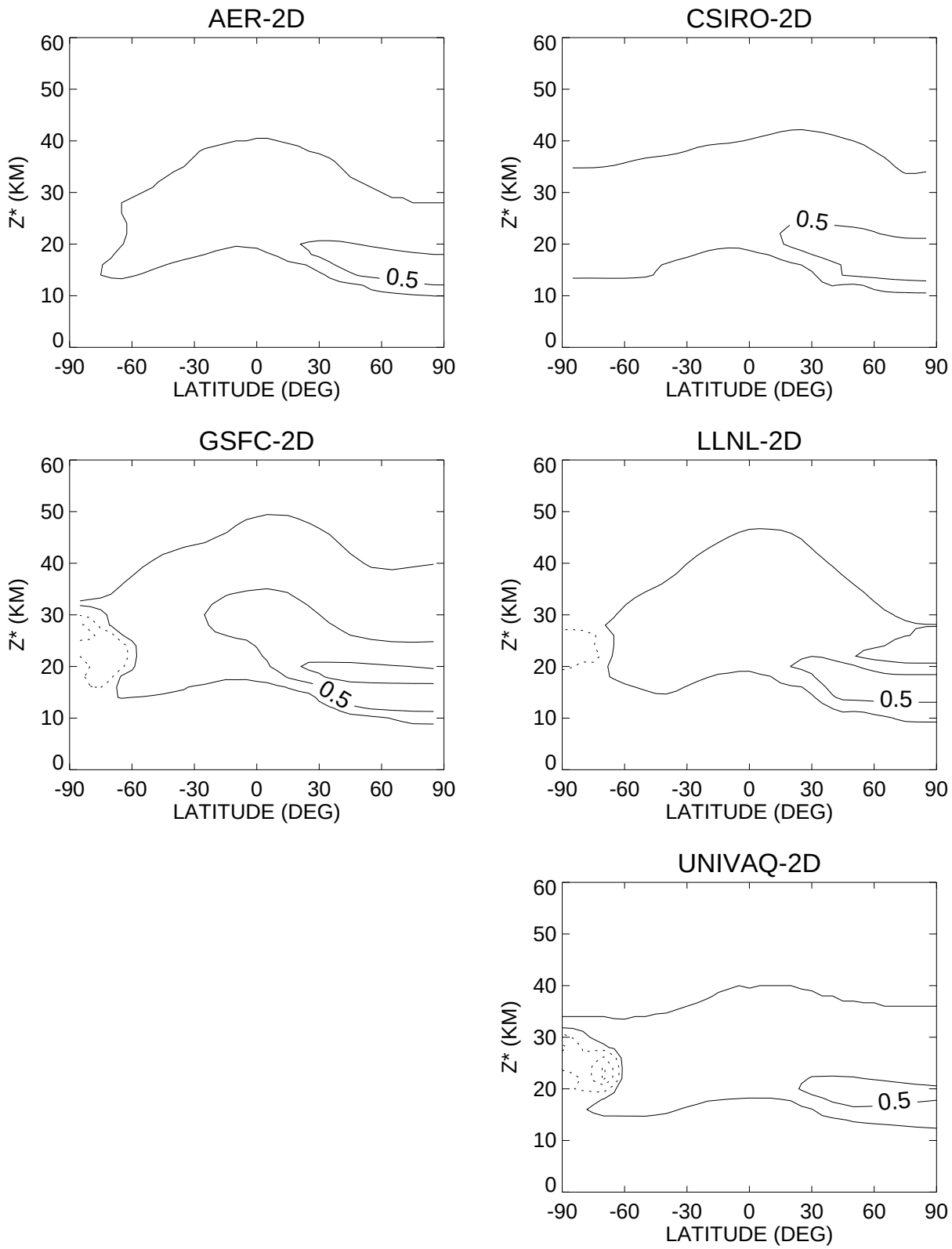

Figure 5.4: Calculated perturbations to NO_y (ppbv) as a function of latitude and altitude in June of 2050 due to NO_x emissions from a fleet of 500 HSCT aircraft with EI(NO_x)=5 under Scenario S9a relative to Scenario D9. Contours are -1, -0.5, 0, 0.5, 1.0 ppbv.

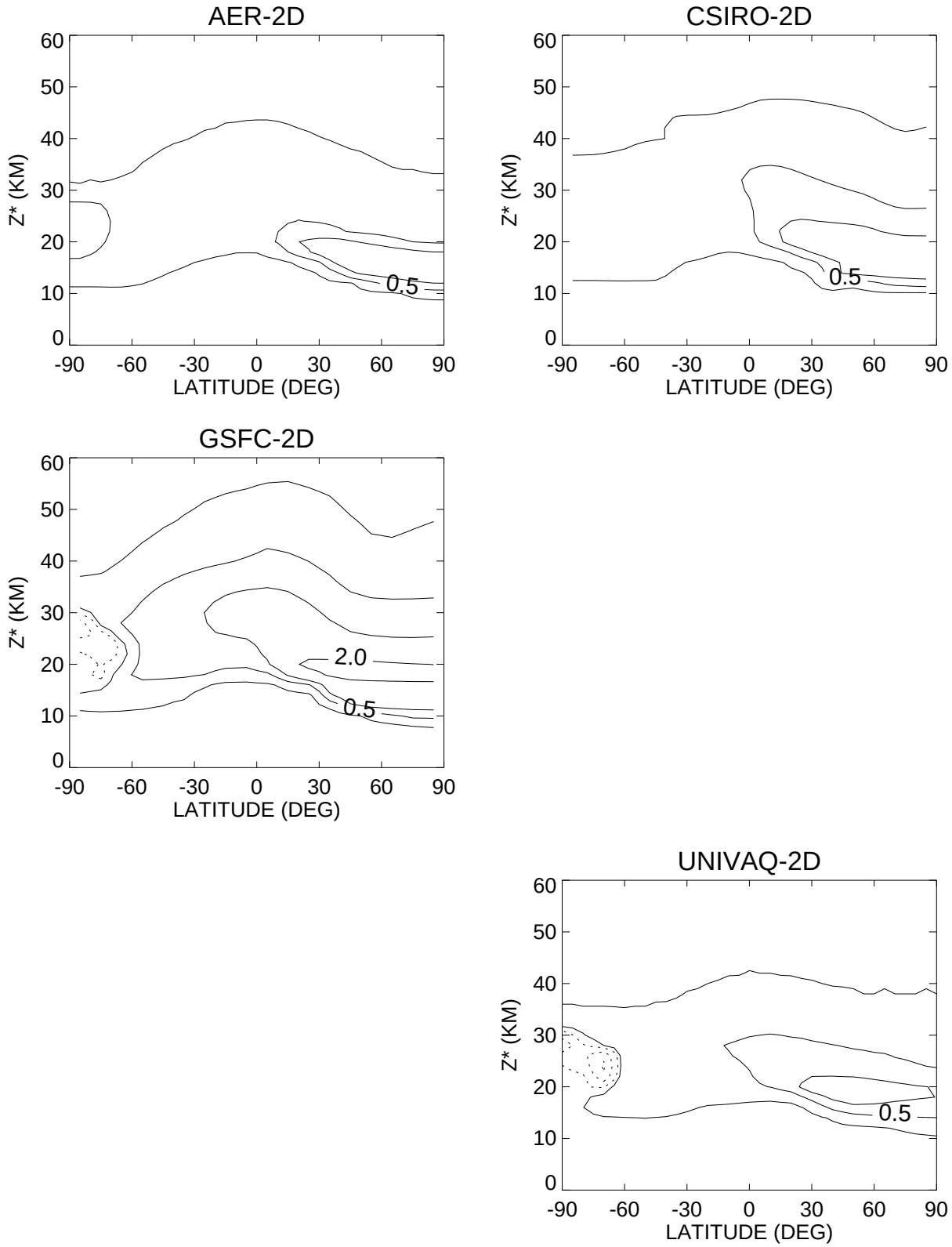

Figure 5.5: Calculated perturbations to NO_y (ppbv) as a function of latitude and altitude in June of 2050 due to NO_x emissions from a fleet of 500 HSCT aircraft with EI(NO_x)=10 under Scenario S9b relative to Scenario D9. Contours are -2, -1, -0.5, 0, 0.5, 1, 2 ppbv.

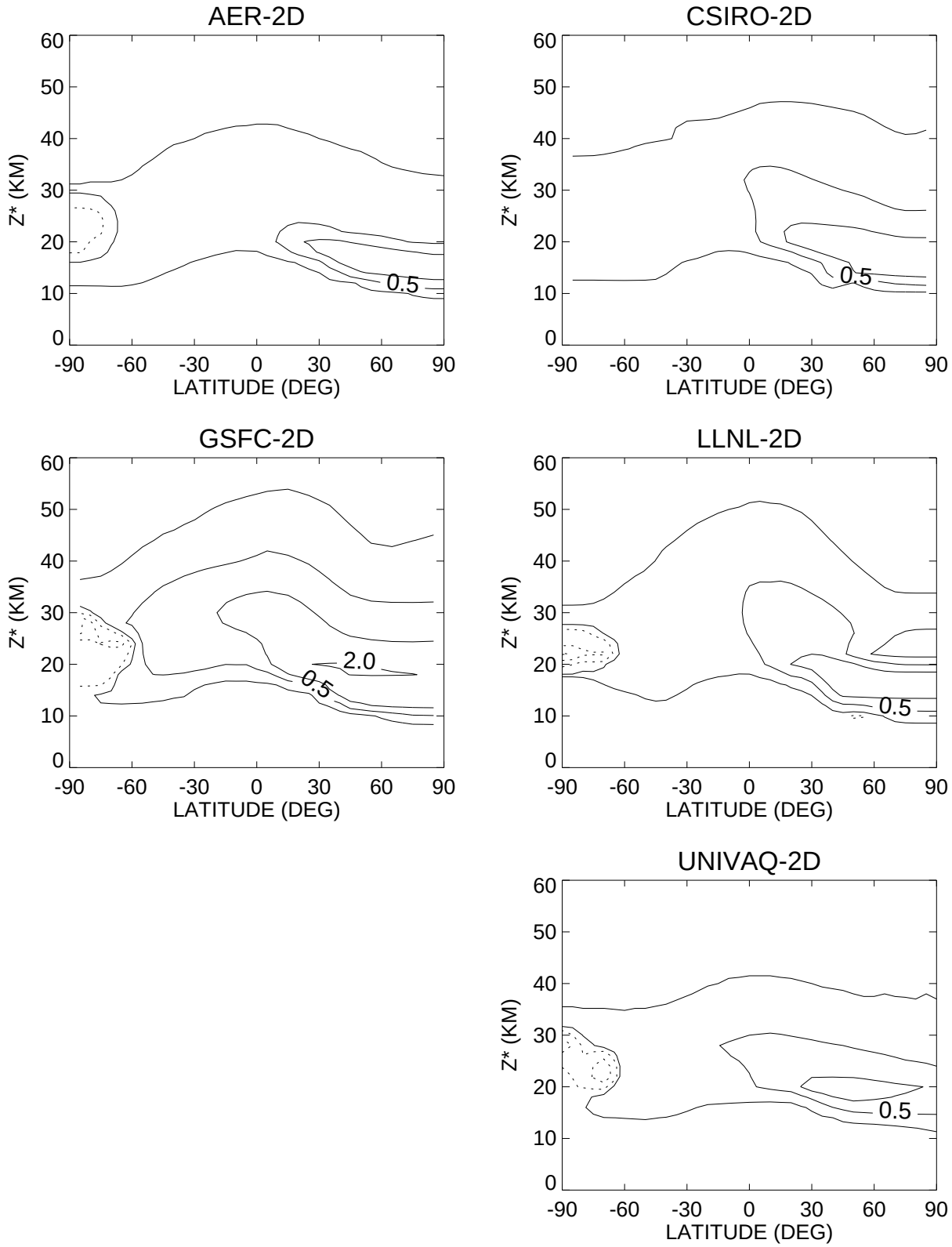

Figure 5.6: Calculated perturbations to NO_y (ppbv) as a function of latitude and altitude in June of 2050 due to NO_x emissions from a fleet of 1000 HSCT aircraft with EI(NO_x)=5 under Scenario S9d relative to Scenario D9. Contours are -1, -0.5, 0, 0.5, 1, 2 ppbv.

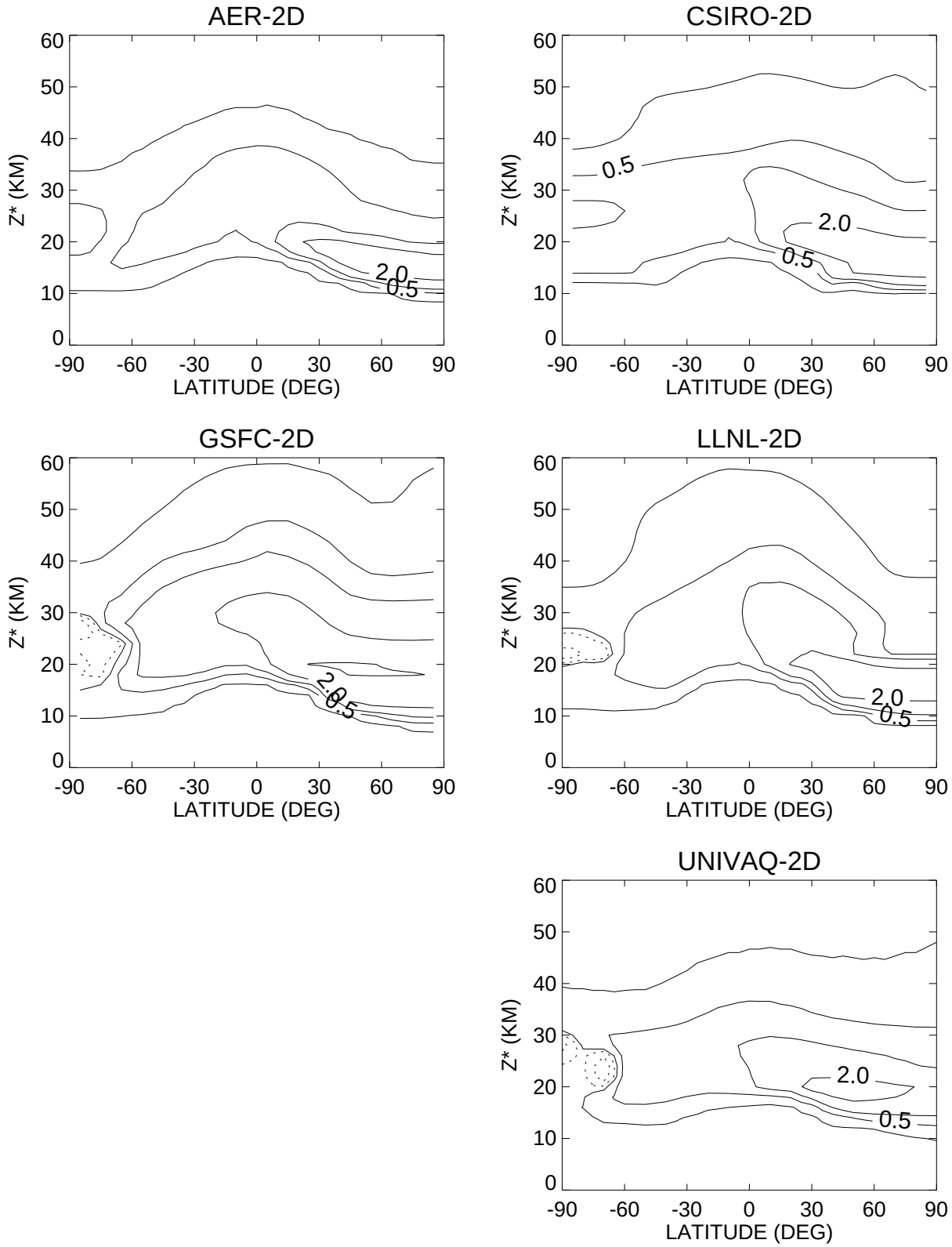

Figure 5.7: Calculated perturbations to NO_y (ppbv) as a function of latitude and altitude in June of 2050 due to NO_x emissions from a fleet of 1000 HSCT aircraft with EI(NO_x)=10 under Scenario S9g relative to Scenario D9. Contours are -1, -0.5, 0, 0.5, 1, 2, 3 ppbv.

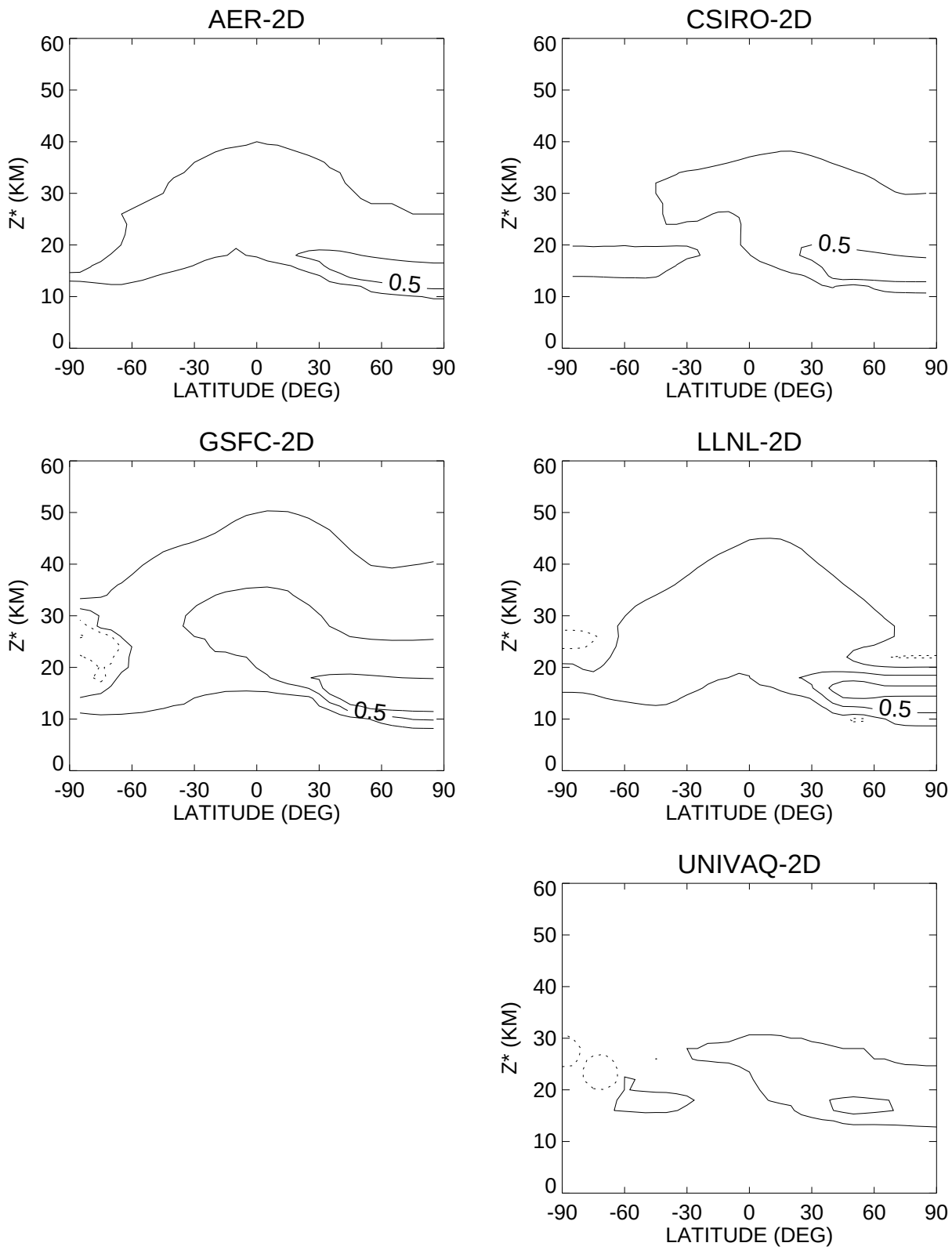

Figure 5.8: Calculated perturbations to NO_y (ppbv) as a function of latitude and altitude in June of 2050 due to NO_x emissions from a fleet of 1000 HSCT aircraft operating at 2 km below the nominal cruise altitude with EI(NO_x)=5 under Scenario S10a relative to Scenario D9. Contours are -0.5, 0, 0.5, 1 ppbv.

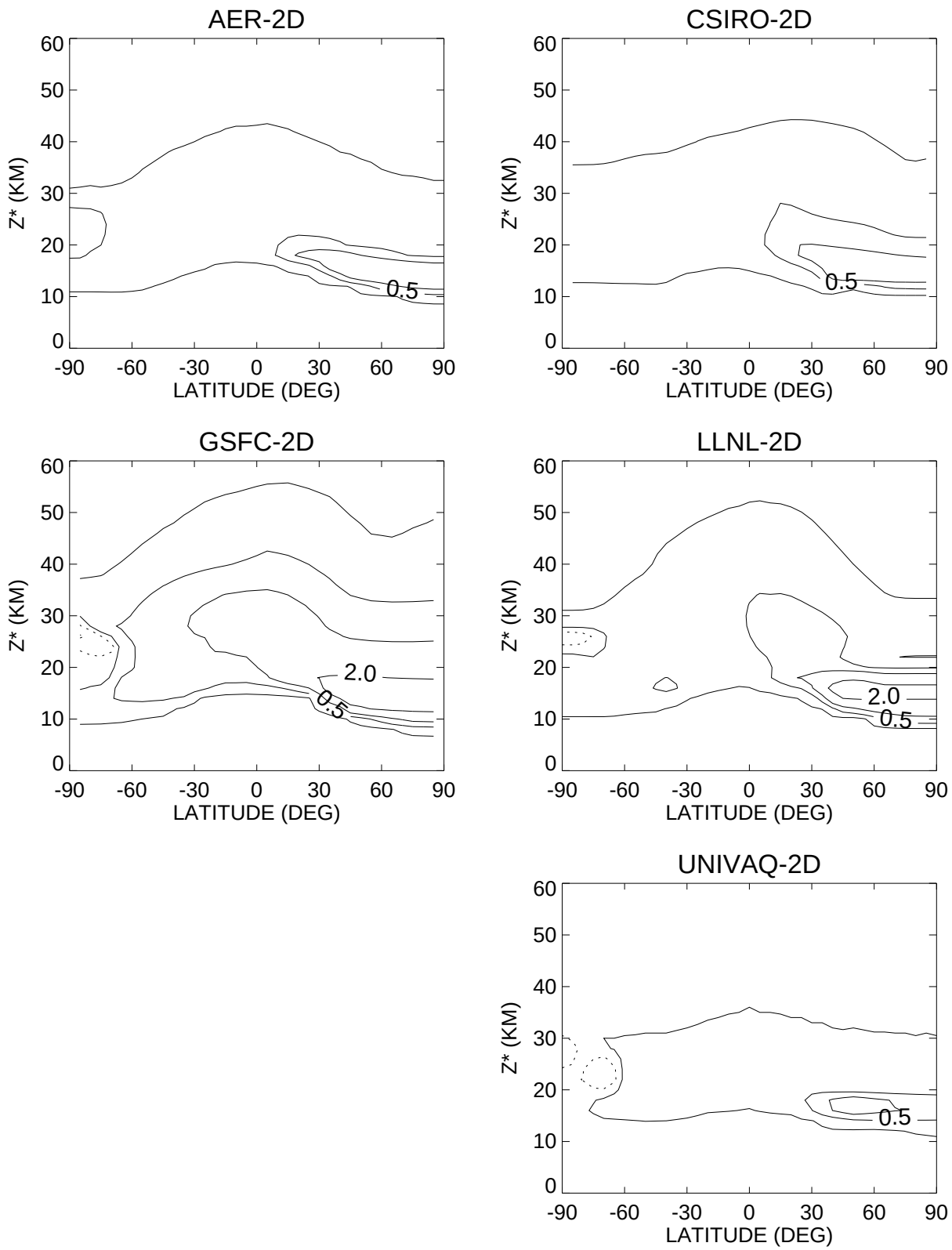

Figure 5.9: Calculated perturbations to NO_y (ppbv) as a function of latitude and altitude in June of 2050 due to NO_x emissions from a fleet of 1000 HSCT aircraft operating at 2 km below the nominal cruise altitude with EI(NO_x)=10 under Scenario S10b relative to Scenario D9. Contours are -0.5, 0, 0.5, 1, 2 ppbv.

Table 5.2: Annual Average Ozone Column Perturbations (in percent) for Each Model for the Northern Hemisphere (top number) and Southern Hemisphere (bottom number) in 2050

Scen -ario	Fleet Size	EI NO_x	SAD Desc.	Special	AER	GSFC	UNI-VAQ	LLNL	CSI -RO	THIN -AIR
S9a	500	5	SA0		-0.3	-0.5	0.03	-0.2	-0.3	-
					-0.1	-0.8	0.03	-0.1	-0.1	-
S9b	500	10	SA0		-0.4	-0.8	0.1	-	-0.4	-
					-0.09	-0.8	0.08	-	-0.2	-
S9c	500	5	SA1		-0.5	-0.8	-0.3	-	-0.4	-
					-0.2	-1	-0.08	-	-0.04	-
S9d	1000	5	SA0		-0.6	-1	-0.08	-0.5	-0.5	-
					-0.2	-1.4	-0.03	-0.3	-0.2	-
S9e	1000	5	SA2		-0.8	-1.3	-0.5	-0.8	-0.6	-
					-0.3	-1.7	-0.2	-0.6	-0.09	-
S9f	1000	5	SA4		-0.9	-1.4	-0.6	-0.9	-0.6	-
					-0.3	-1.8	-0.2	-0.6	-0.07	-
S9g	1000	10	SA0		-0.7	-1.6	0.02	-0.8	-0.9	-
					-0.2	-1.5	0.08	-0.2	-0.4	-
S9h	1000	5	SA6		-0.8	-1.1	-0.3	-0.6	-0.6	-
					-0.3	-1.5	-0.09	-0.4	-0.2	-
S10a	1000	5	SA0	Cruise -2 km	-0.2	-0.3	0.05	-0.1	-0.1	-
					-0.05	-0.5	0.05	-0.02	-0.05	-
S10b	1000	10	SA0	Cruise -2 km	-0.2	-0.6	0.2	-0.2	-0.09	-
					+0.01	-0.5	0.1	0.04	-0.05	-
S10c	1000	5	SA6-2km	Cruise -2 km	-0.4	-0.5	-0.1	-0.3	-0.2	-
					-0.1	-0.6	0.001	-0.2	-0.04	-
S10d	1000	5	SA2-2km	Cruise -2 km	-0.5	-0.6	-0.1	-0.4	-0.2	-
					-0.1	-0.6	-0.02	-0.2	-0.03	-
S11a	1000	5	SA0	Subsonic IS92a	-0.5	-0.9	-0.1	-	-0.5	-
					-0.2	-1.4	-0.03	-	-0.2	-
S12a	1000	5	SA0	Subsonic High Demand	-0.5	-0.9	-0.1	-	-0.5	-
					-0.2	-1.4	-0.03	-	-0.2	-

5.3 O_3 Perturbations

A synopsis of ozone column changes calculated for the 2050 scenarios is listed in Table 5.2 for the northern and southern hemisphere annual averages for each model. In the following sections, changes in ozone are plotted for each scenario. Changes in ozone as a function of altitude and latitude are shown for March, June, and October. These months were chosen to present both polar regions in their respective springtimes, since the northern and southern polar regions often respond differently to perturbations in H_2O and NO_x. Changes in total ozone as a function of latitude and season are also shown, since total column ozone is related to uv radiation which reaches the ground.

5.3.1 Base Scenarios (S9a,b,d,g)

These 2050 scenarios represent either 500 or 1000 aircraft HSCT fleets with EI(NO_x) of 5 or 10, no aircraft sulfur emissions, and sulfate surface area densities of SA0. The background Cl_y for 2050 is 2.0 ppbv, and boundary conditions are as listed in Table 3.1.

Scenario S9a represents 500 HSCT aircraft with EI(NO_x)=5 and SA0 sulfate surface area density. Ozone changes for this scenario are shown in Figures 5.10, 5.11, and 5.12 for March, June, and October, respectively. Ozone changes are similar to or somewhat less than those for S1c-D, which represents the same aircraft fleet in 2015. The GSFC model, however, calculated more ozone depletion for this scenario in the southern hemisphere lower stratosphere in March and June. Changes in column ozone are shown in Figure 5.13. The UNIVAQ model shows positive ozone changes over most of the globe. The CSIRO and LLNL models show ozone depletions of less than 0.5% over most of the globe.

The NO_x emission index is increased to 10 in Scenario S9b, which represents 500 HSCT aircraft and SA0 sulfate surface area density. Figures 5.14, 5.15, and 5.16 show changes in ozone for this scenario relative to Scenario D9. Compared with S9a-D9, the ozone perturbations are smaller in the lower stratosphere and larger near 30 km. Column ozone changes, shown in Figure 5.17, are similar to S9a-D9, except for the CSIRO model, which shows increase depletion in the northern hemisphere.

Scenario S9d represents 1000 HSCT aircraft operating in 2050 with EI(NO_x)=5, no sulfur emissions, and sulfate surface area density of SA0. Calculated ozone changes for this scenario, which are shown in Figures 5.18-5.20, are approximately twice those found with 500 HSCT aircraft (Scenario S9a-D9). The GSFC model calculated ozone depletion in the southern hemisphere lower stratosphere of over 5%. Changes in column ozone for S9d-D9 are shown in Figure 5.21. Column ozone changes are also roughly double those of S9a-D9.

Scenario S9g also represents 1000 HSCT aircraft but with EI(NO_x)=10. Figures 5.22-5.24 show changes in ozone for this scenario relative to Scenario D9. Ozone depletions are significantly larger than for S9d-D9 in both the lower and middle stratosphere, though the GSFC and LLNL models show less ozone depletion in the southern hemisphere lower stratosphere. Changes in ozone column are shown in Figure 5.25. Annual average northern hemisphere ozone depletion is greater than 0.7% for 4 of the 5 models that performed this simulation.

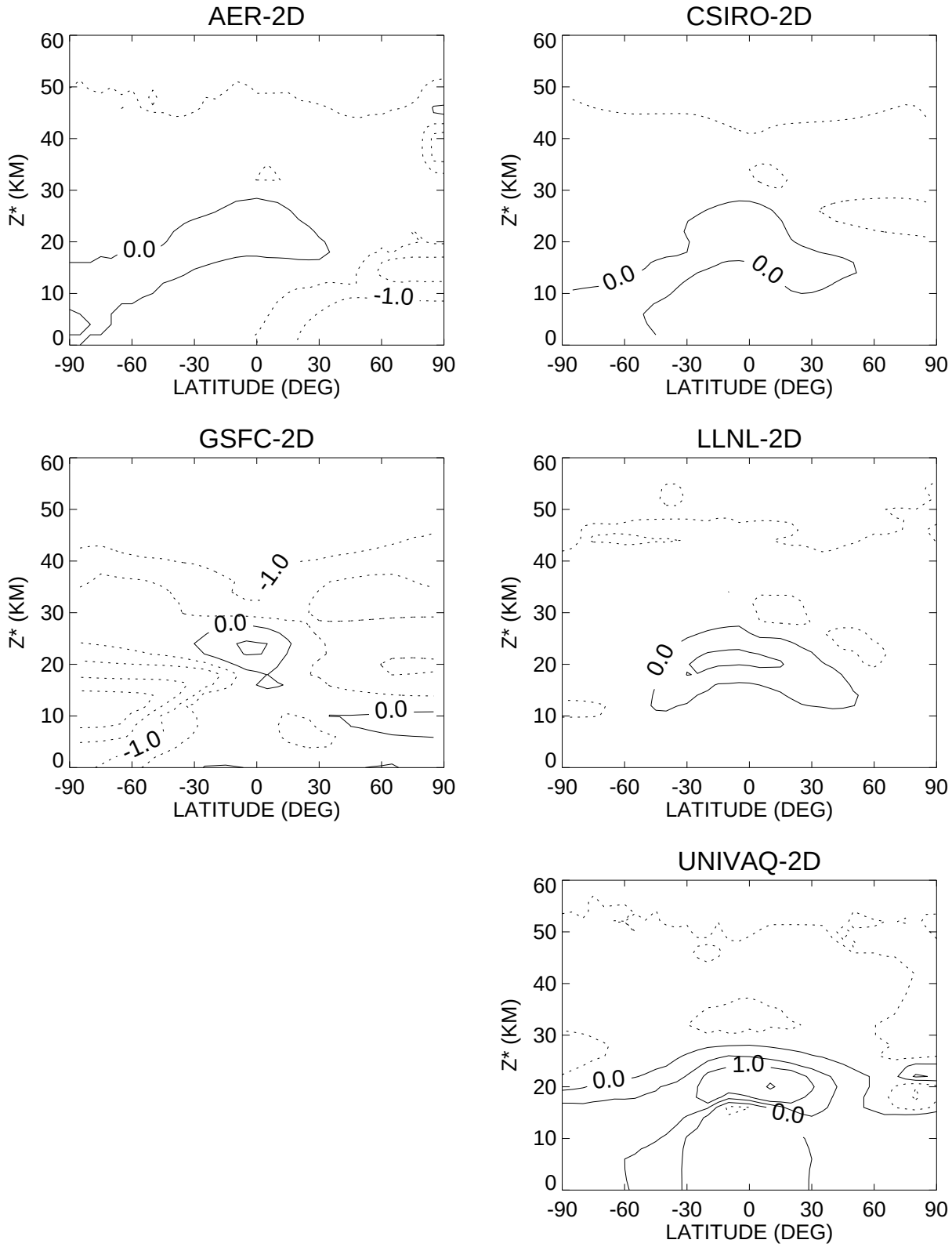

Figure 5.10: Calculated perturbations to O_3 (percent) as a function of latitude and altitude in March of 2050 due to emissions from a fleet of 500 HSCT aircraft with EI(NO_x)=5 under Scenario S9a relative to Scenario D9. Contours are -3, -2, -1, -0.5, 0, 0.5, 1, 2.

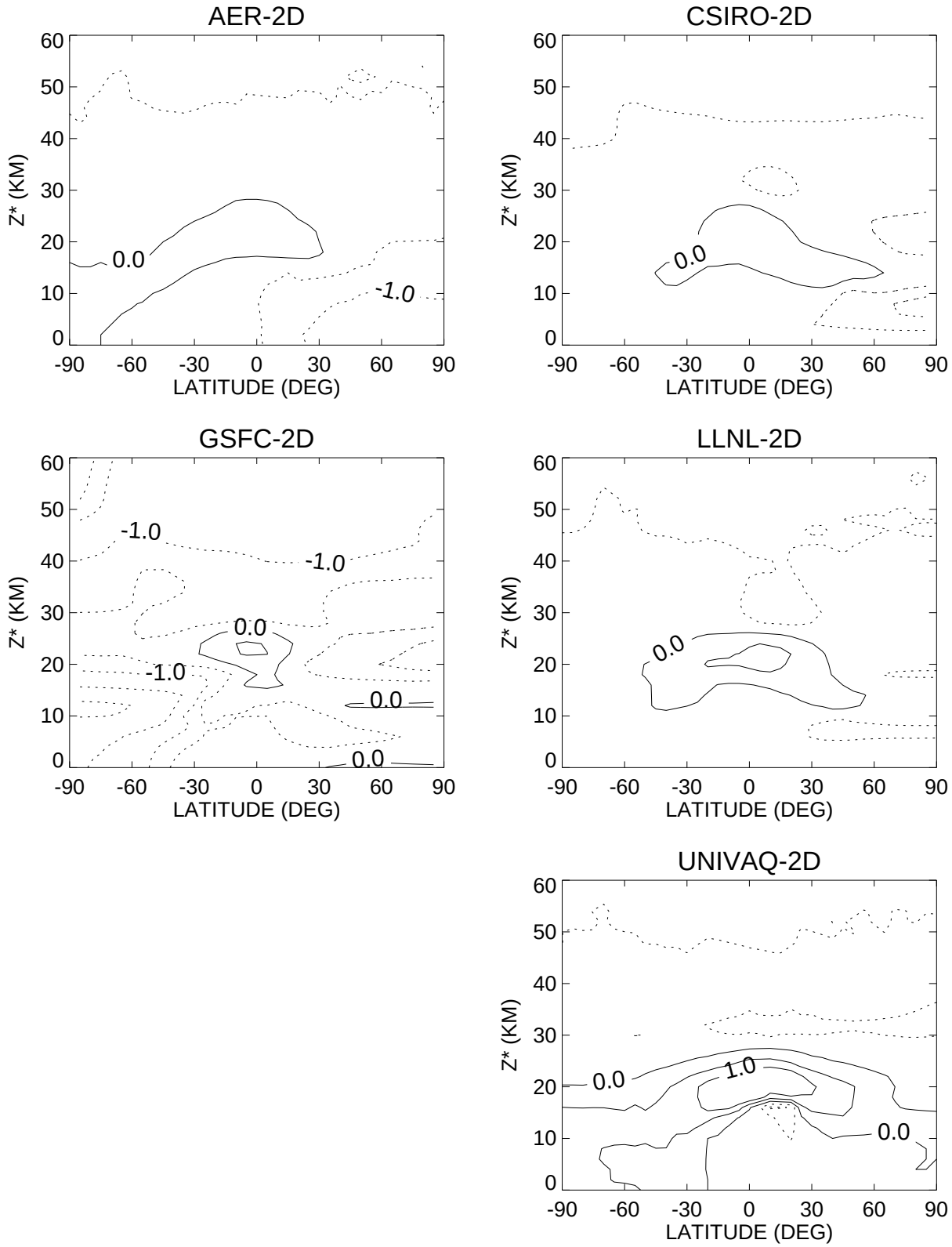

Figure 5.11: Calculated perturbations to O_3 (percent) as a function of latitude and altitude in June of 2050 due to emissions from a fleet of 500 HSCT aircraft with EI(NO_x)=5 under Scenario S9a relative to Scenario D9. Contours are -3, -2, -1, -0.5, 0, 0.5, 1.

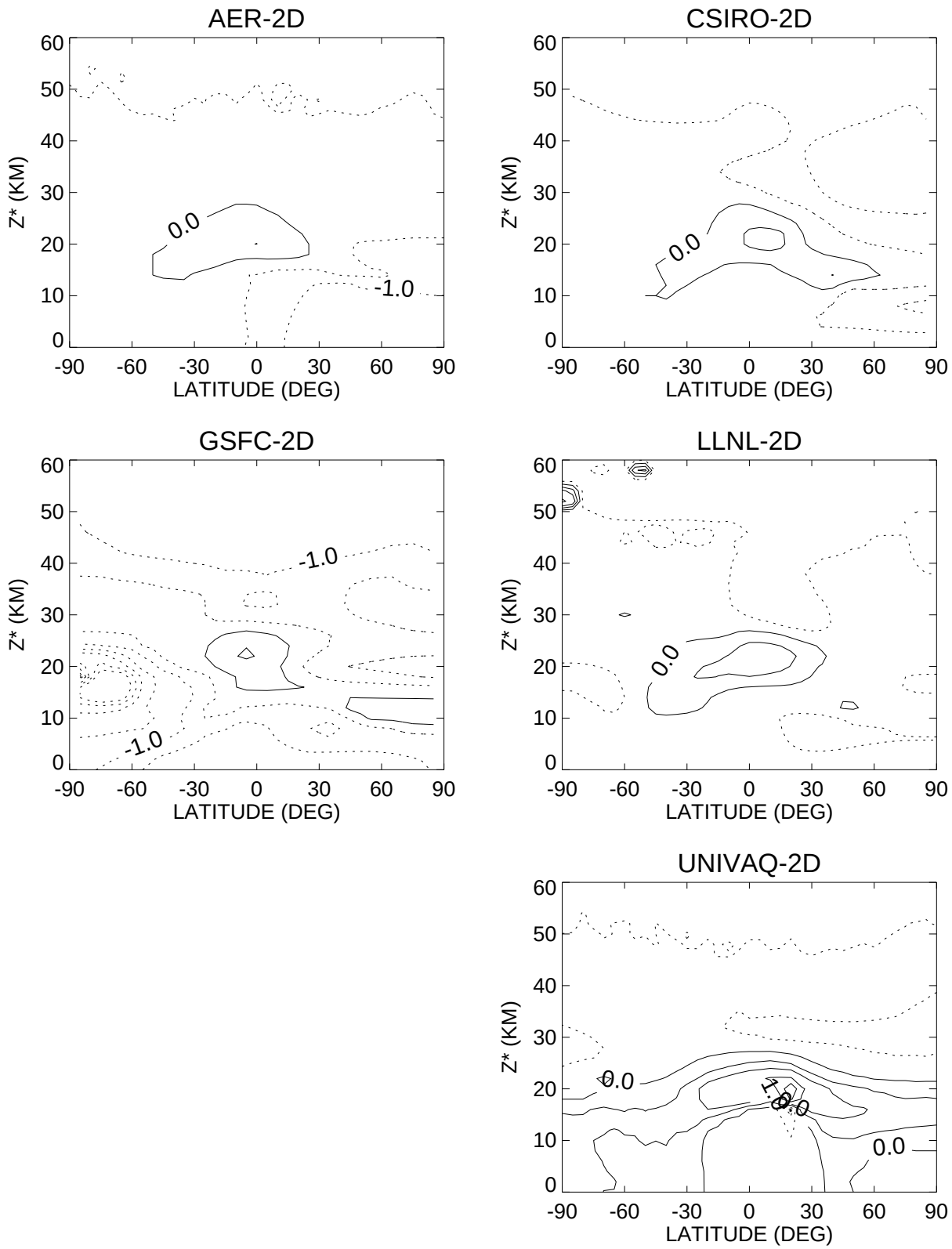

Figure 5.12: Calculated perturbations to O_3 (percent) as a function of latitude and altitude in October of 2050 due to emissions from a fleet of 500 HSCT aircraft with EI(NO_x)=5 under Scenario S9a relative to Scenario D9. Contours are -5, -4, -3, -2, -1, -0.5, 0, 0.5, 1, 2, 3.

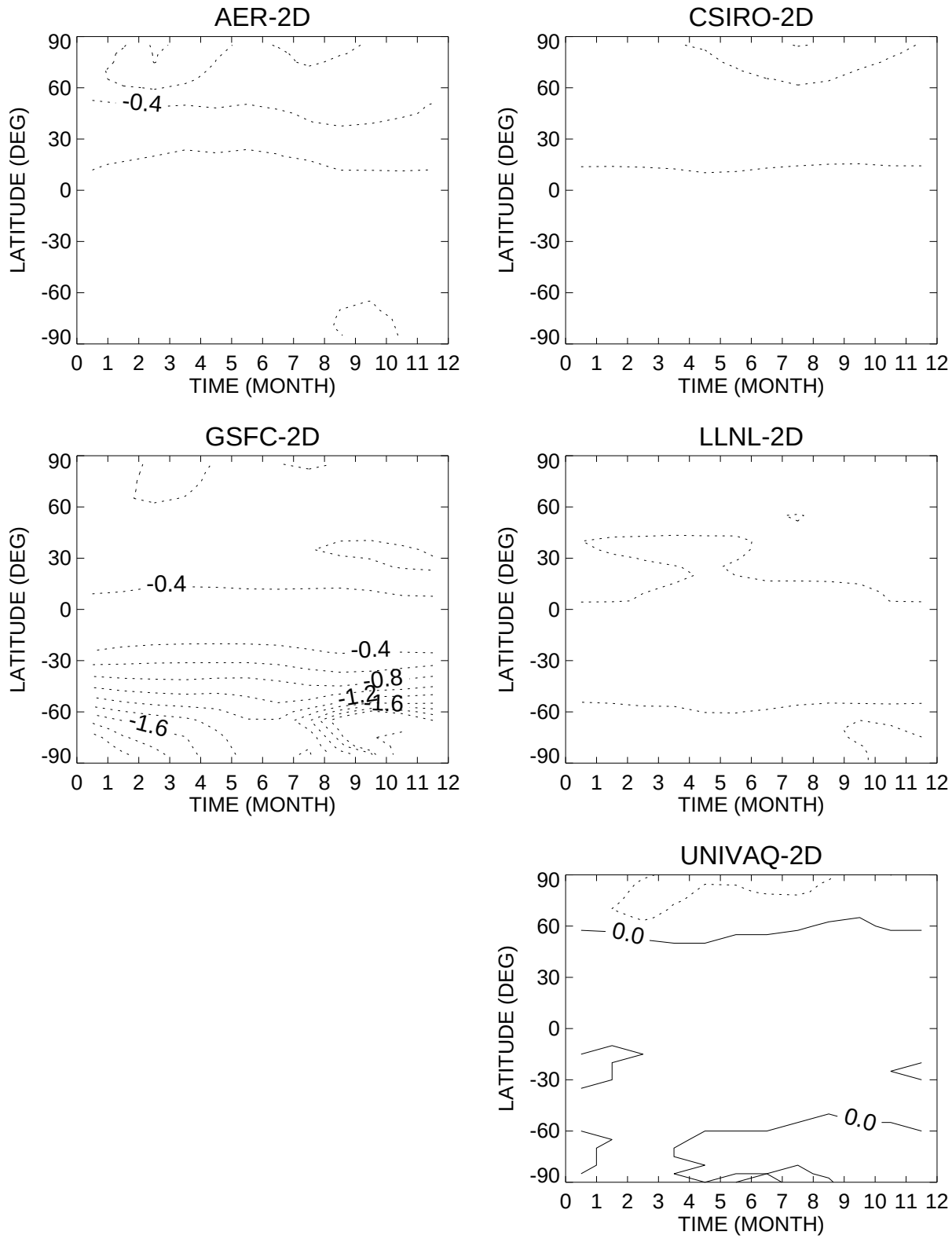

Figure 5.13: Calculated perturbations to column O_3 (percent) as a function of latitude and season in 2050 due to emissions from a fleet of 500 HSCT aircraft with EI(NO_x)=5 under Scenario S9a relative to Scenario D9. Contours are -3 and -2 to 0 by 0.2.

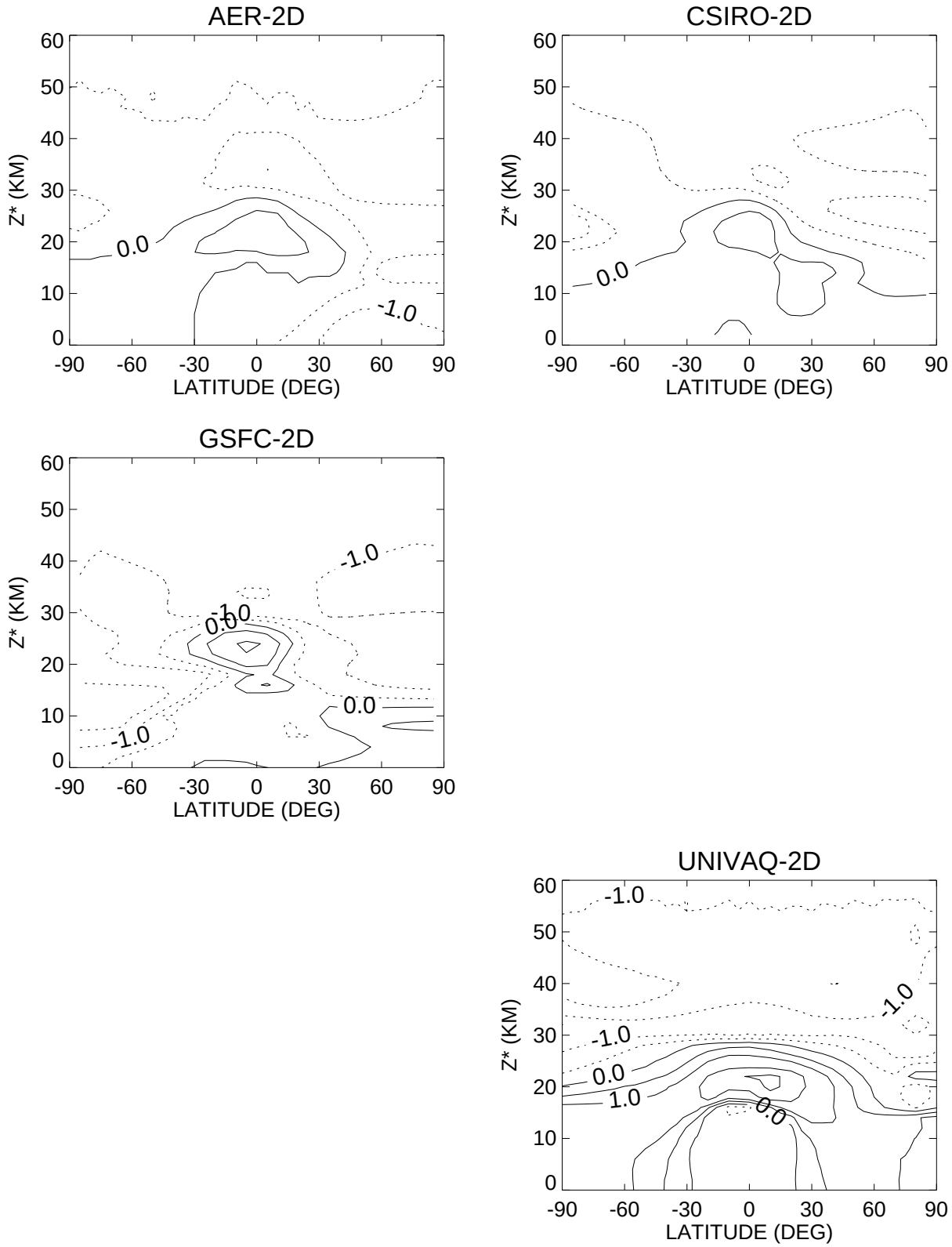

Figure 5.14: Calculated perturbations to O_3 (percent) as a function of latitude and altitude in March of 2050 due to emissions from a fleet of 500 HSCT aircraft with EI(NO_x)=10 under Scenario S9b relative to Scenario D9. Contours are -2, -1, -0.5, 0, 0.5, 1, 2, 3.

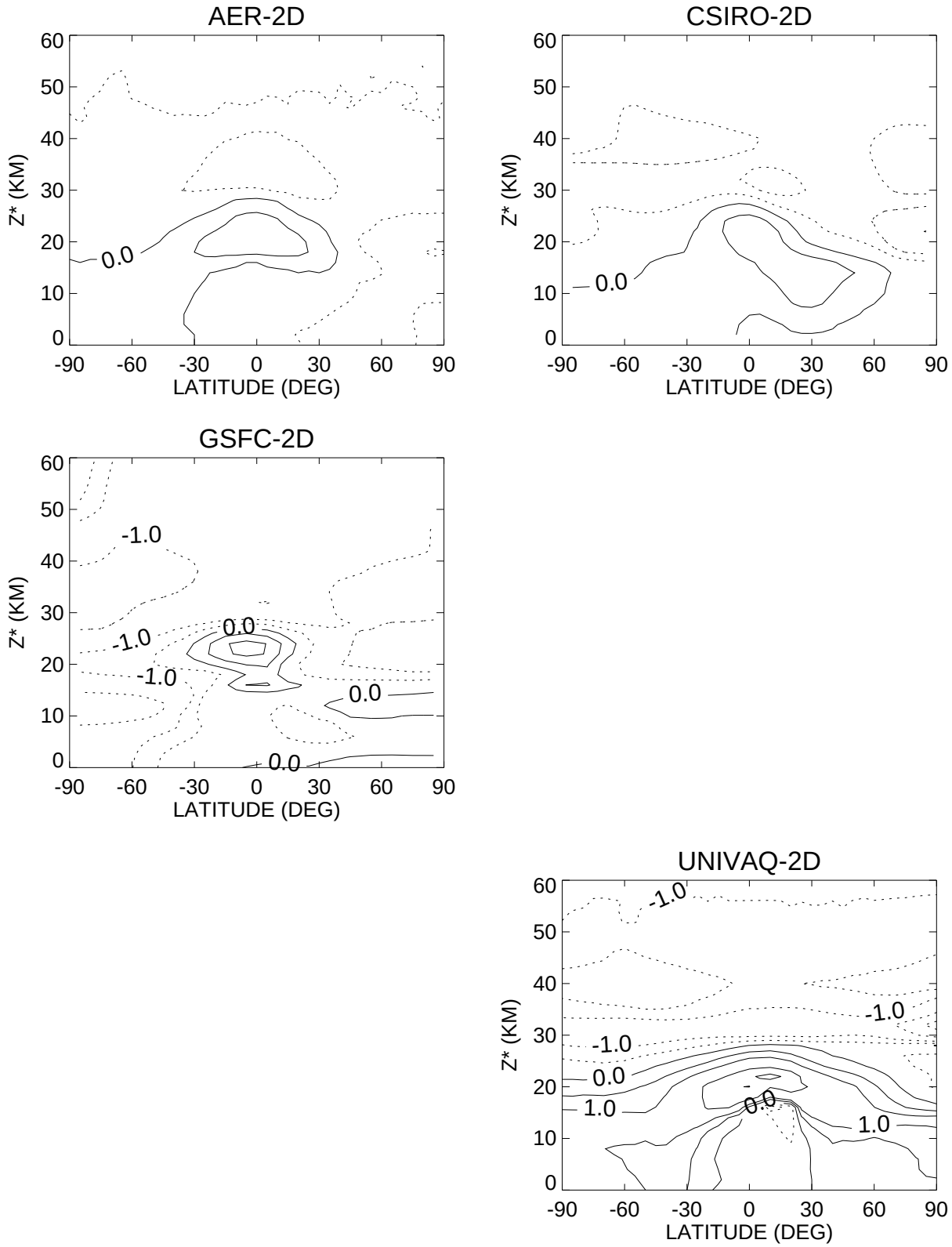

Figure 5.15: Calculated perturbations to O_3 (percent) as a function of latitude and altitude in June of 2050 due to emissions from a fleet of 500 HSCT aircraft with EI(NO_x)=10 under Scenario S9b relative to Scenario D9. Contours are -2, -1, -0.5, 0, 0.5, 1, 2, 3.

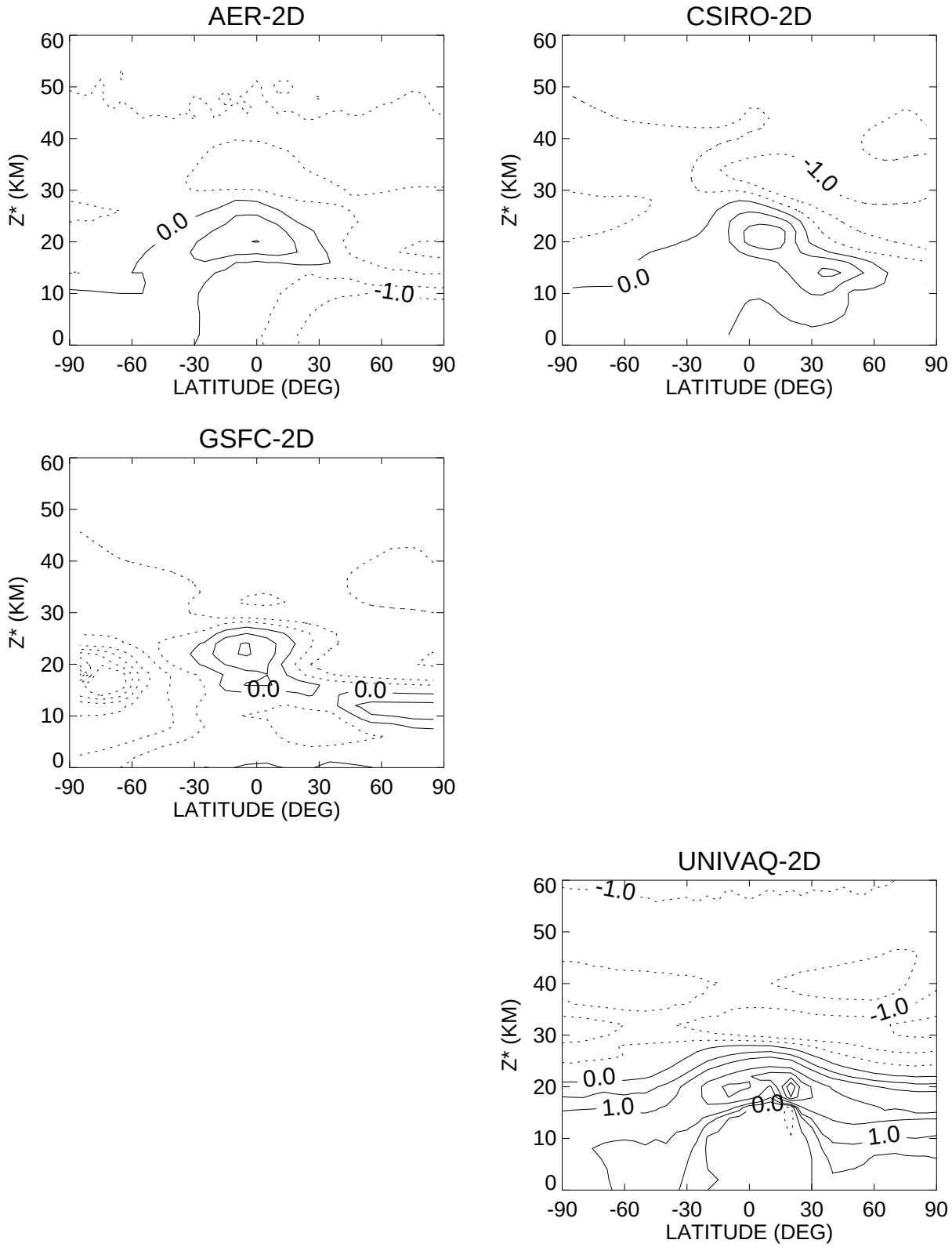

Figure 5.16: Calculated perturbations to O_3 (percent) as a function of latitude and altitude in October of 2050 due to emissions from a fleet of 500 HSCT aircraft with EI(NO_x)=10 under Scenario S9b relative to Scenario D9. Contours are -5, -4, -3, -2, -1, -0.5, 0, 0.5, 1, 2, 3, 4, 5.

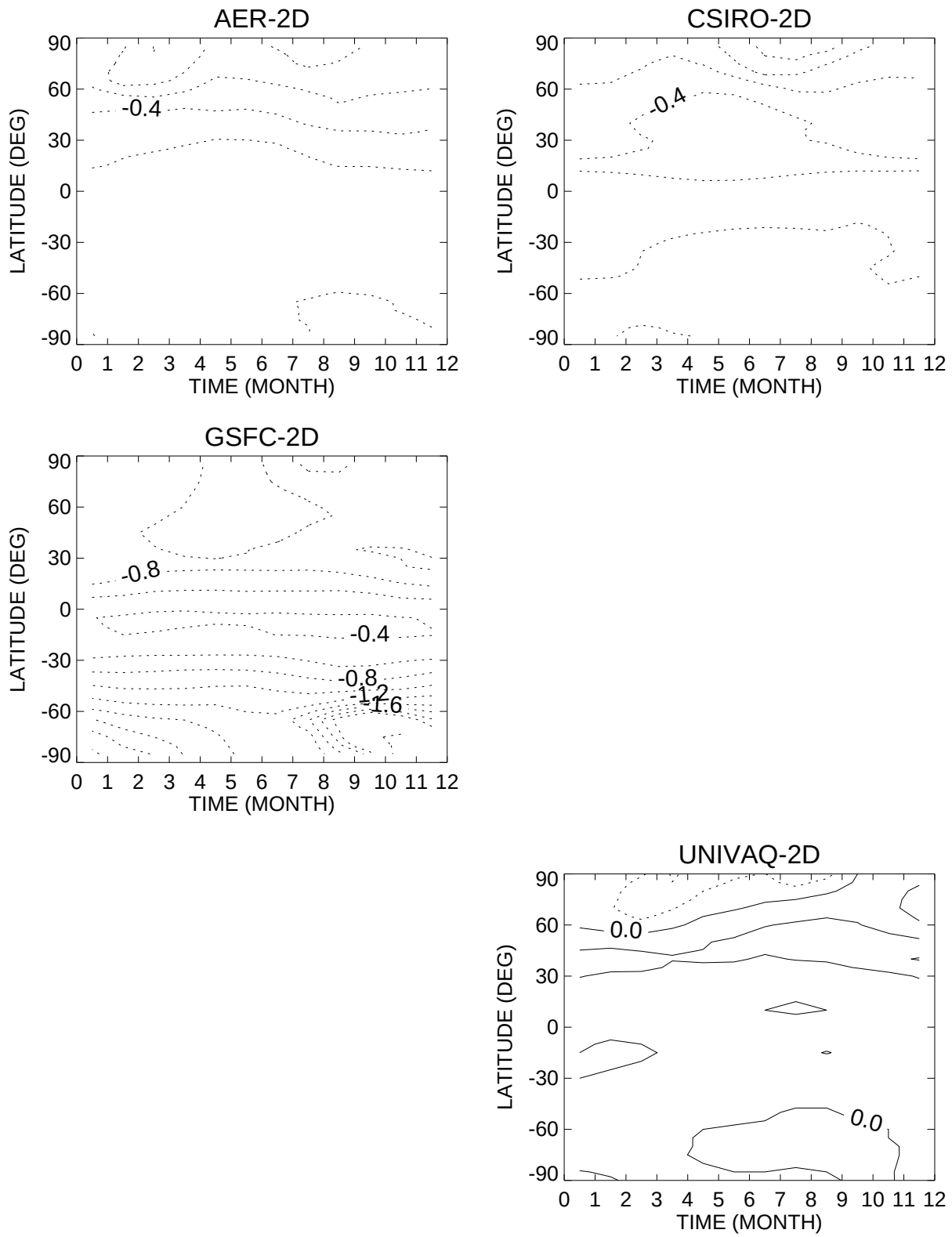

Figure 5.17: Calculated perturbations to column O_3 (percent) as a function of latitude and season in 2050 due to emissions from a fleet of 500 HSCT aircraft with EI(NO_x)=10 under Scenario S9b relative to Scenario D9. Contours are -3 and -2 to 0.2 by 0.2.

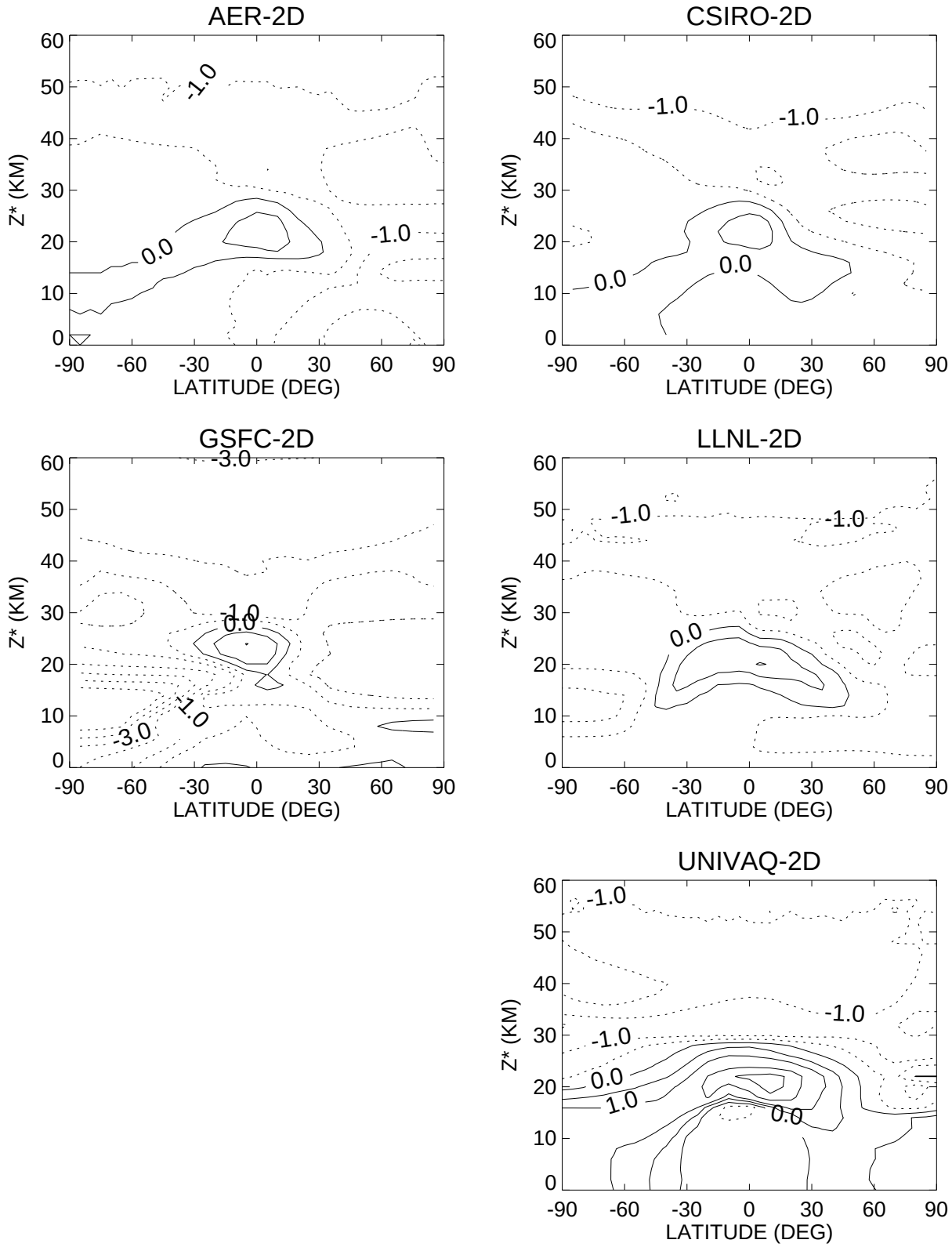

Figure 5.18: Calculated perturbations to O_3 (percent) as a function of latitude and altitude in March of 2050 due to emissions from a fleet of 1000 HSCT aircraft with EI(NO_x)=5 under Scenario S9d relative to Scenario D9. Contours are -5, -4, -3, -2, -1, -0.5, 0, 0.5, 1, 2, 3.

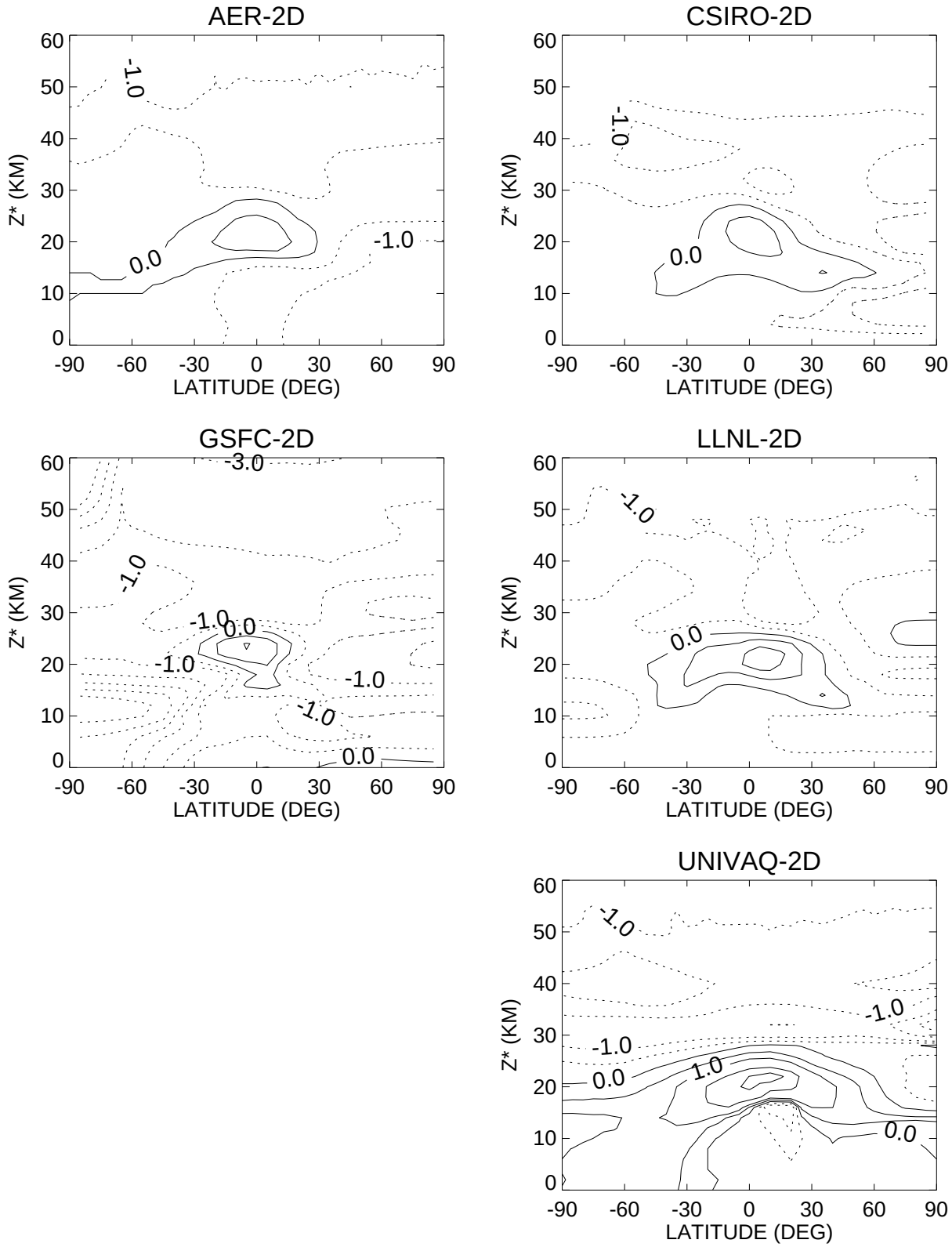

Figure 5.19: Calculated perturbations to O_3 (percent) as a function of latitude and altitude in June of 2050 due to emissions from a fleet of 1000 HSCT aircraft with EI(NO_x)=5 under Scenario S9d relative to Scenario D9. Contours are -5, -4, -3, -2, -1, -0.5, 0, 0.5, 1, 2, 3.

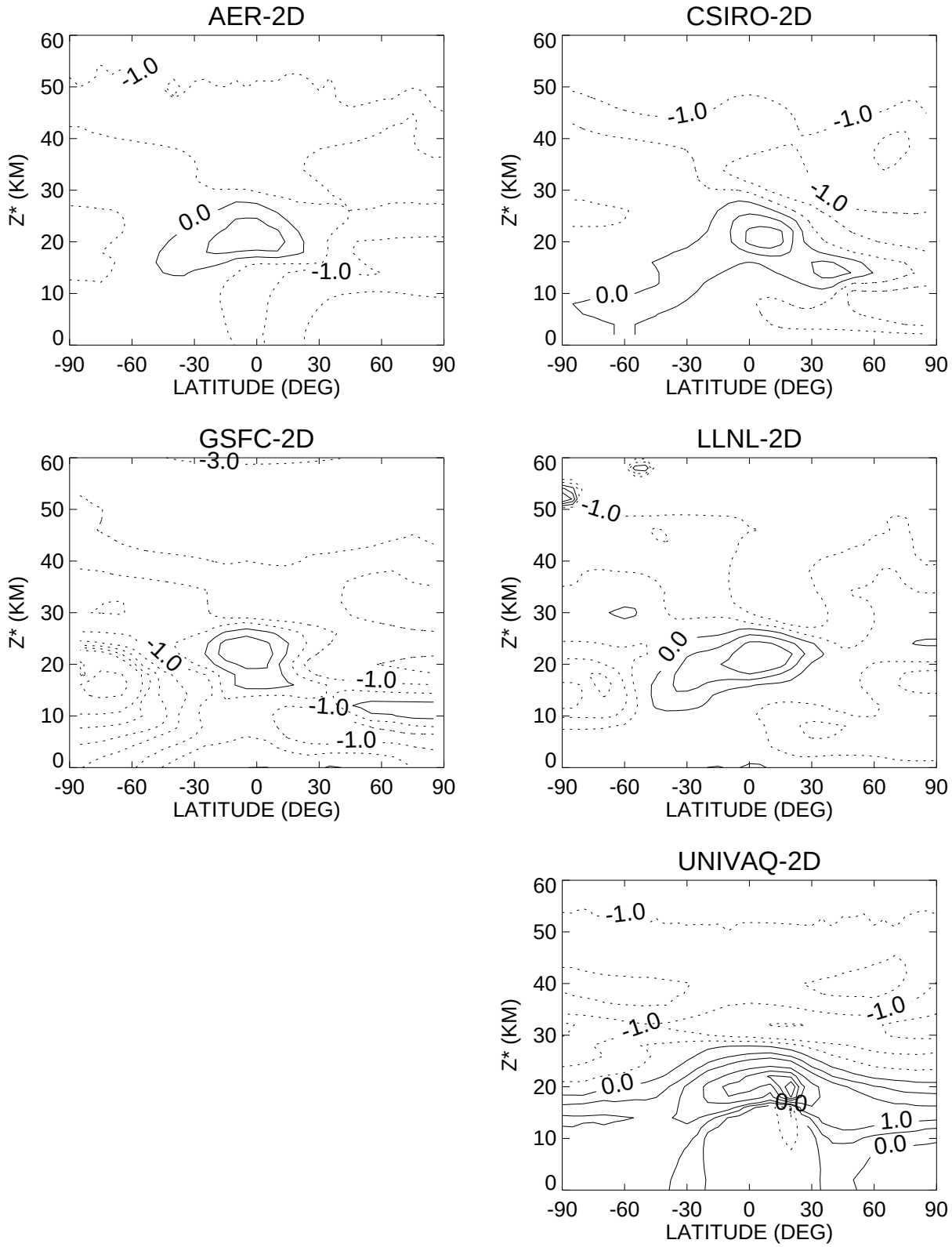

Figure 5.20: Calculated perturbations to O_3 (percent) as a function of latitude and altitude in October of 2050 due to emissions from a fleet of 1000 HSCT aircraft with EI(NO_x)=5 under Scenario S9d relative to Scenario D9. Contours are -10, -5, -4, -3, -2, -1, -0.5, 0, 0.5, 1, 2, 3, 4, 5.

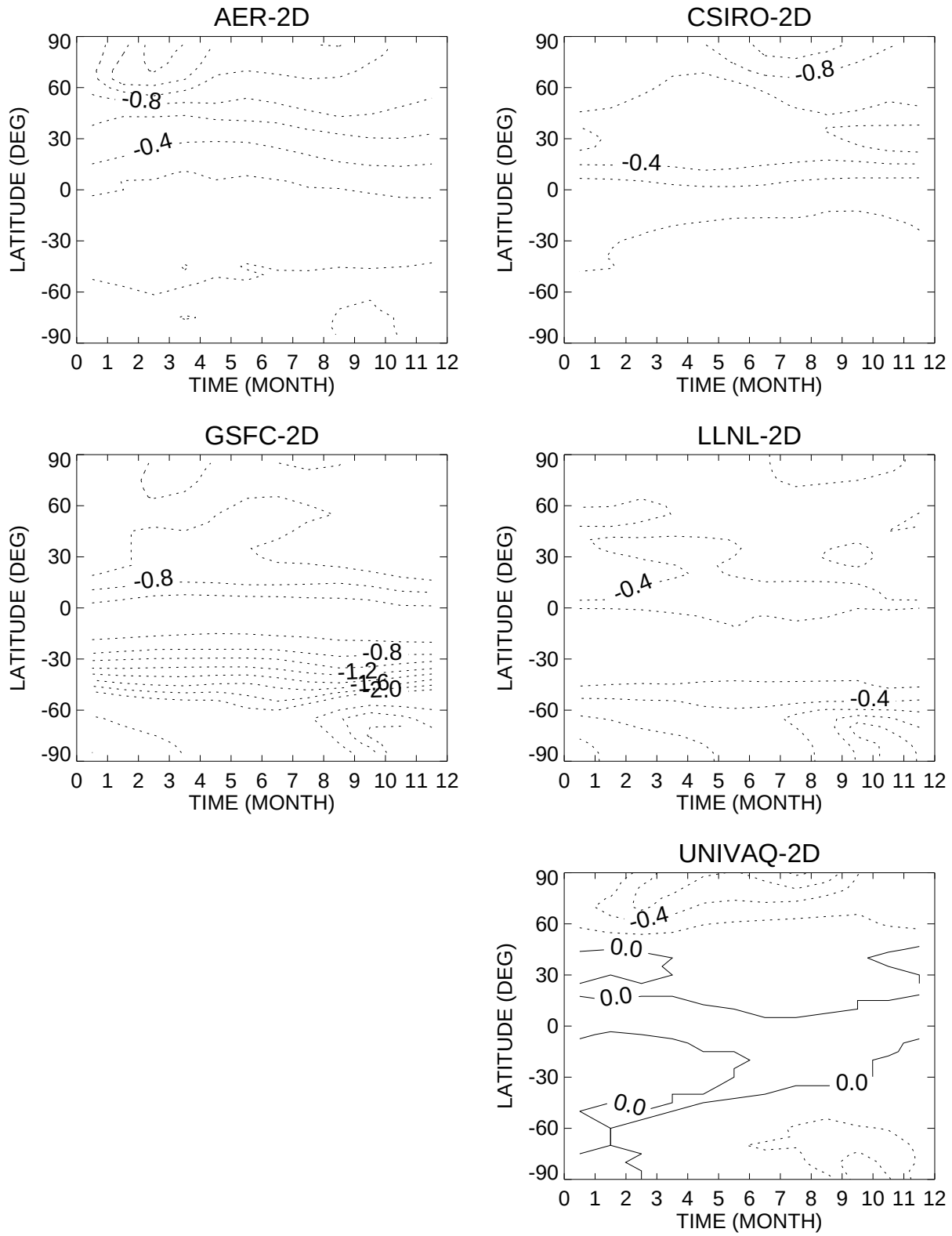

Figure 5.21: Calculated perturbations to column O_3 (percent) as a function of latitude and season in 2050 due to emissions from a fleet of 1000 HSCT aircraft with EI(NO_x)=5 under Scenario S9d relative to Scenario D9. Contours are -5, -4, -3 and -2 to 0 by 0.2.

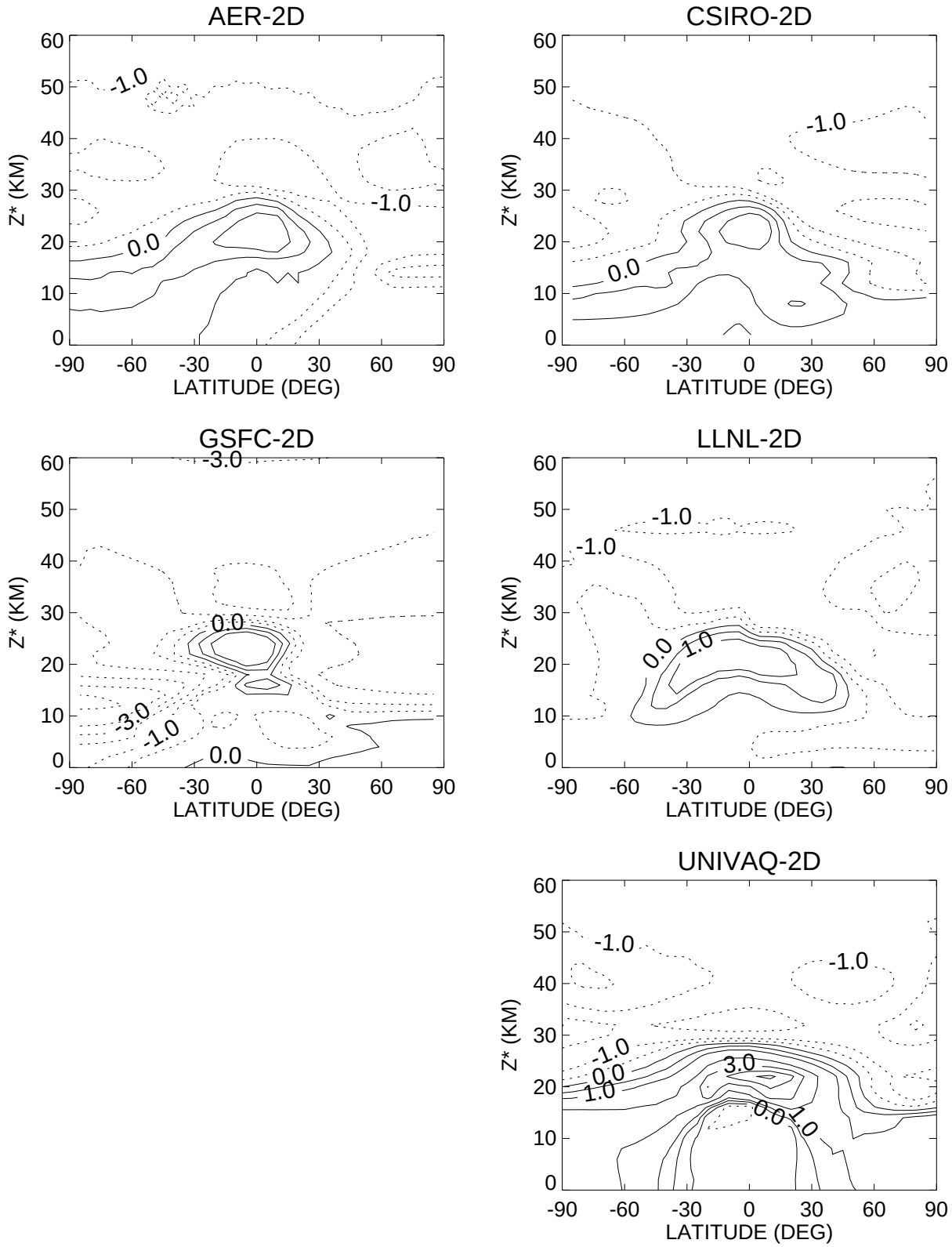

Figure 5.22: Calculated perturbations to O_3 (percent) as a function of latitude and altitude in March of 2050 due to emissions from a fleet of 1000 HSCT aircraft with EI(NO_x)=10 under Scenario S9g relative to Scenario D9. Contours are -5, -4, -3, -2, -1, -0.5, 0, 0.5, 1, 2, 3, 4, 5.

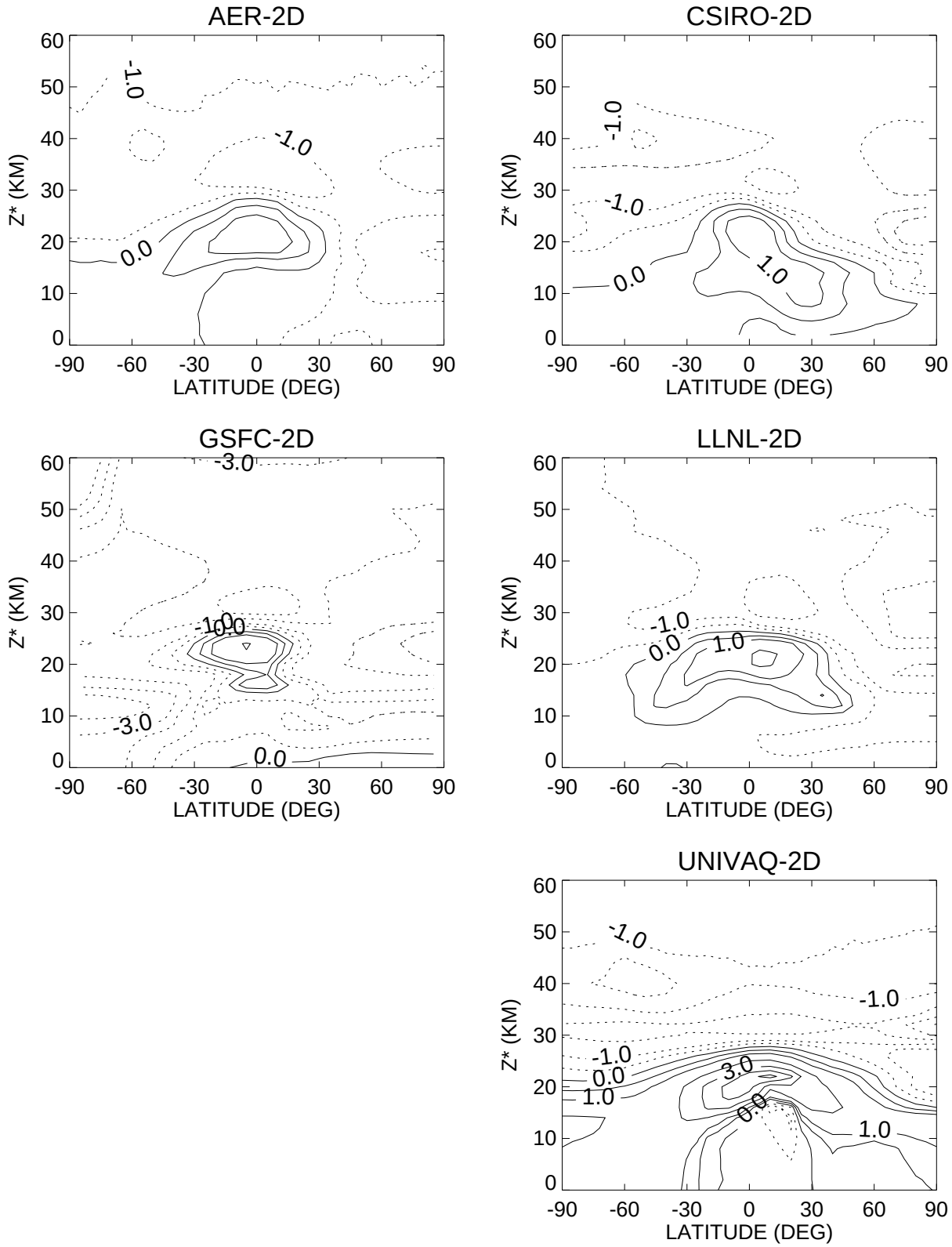

Figure 5.23: Calculated perturbations to O_3 (percent) as a function of latitude and altitude in June of 2050 due to emissions from a fleet of 1000 HSCT aircraft with EI(NO_x)=10 under Scenario S9g relative to Scenario D9. Contours are -4, -3, -2, -1, -0.5, 0, 0.5, 1, 2, 3, 4, 5.

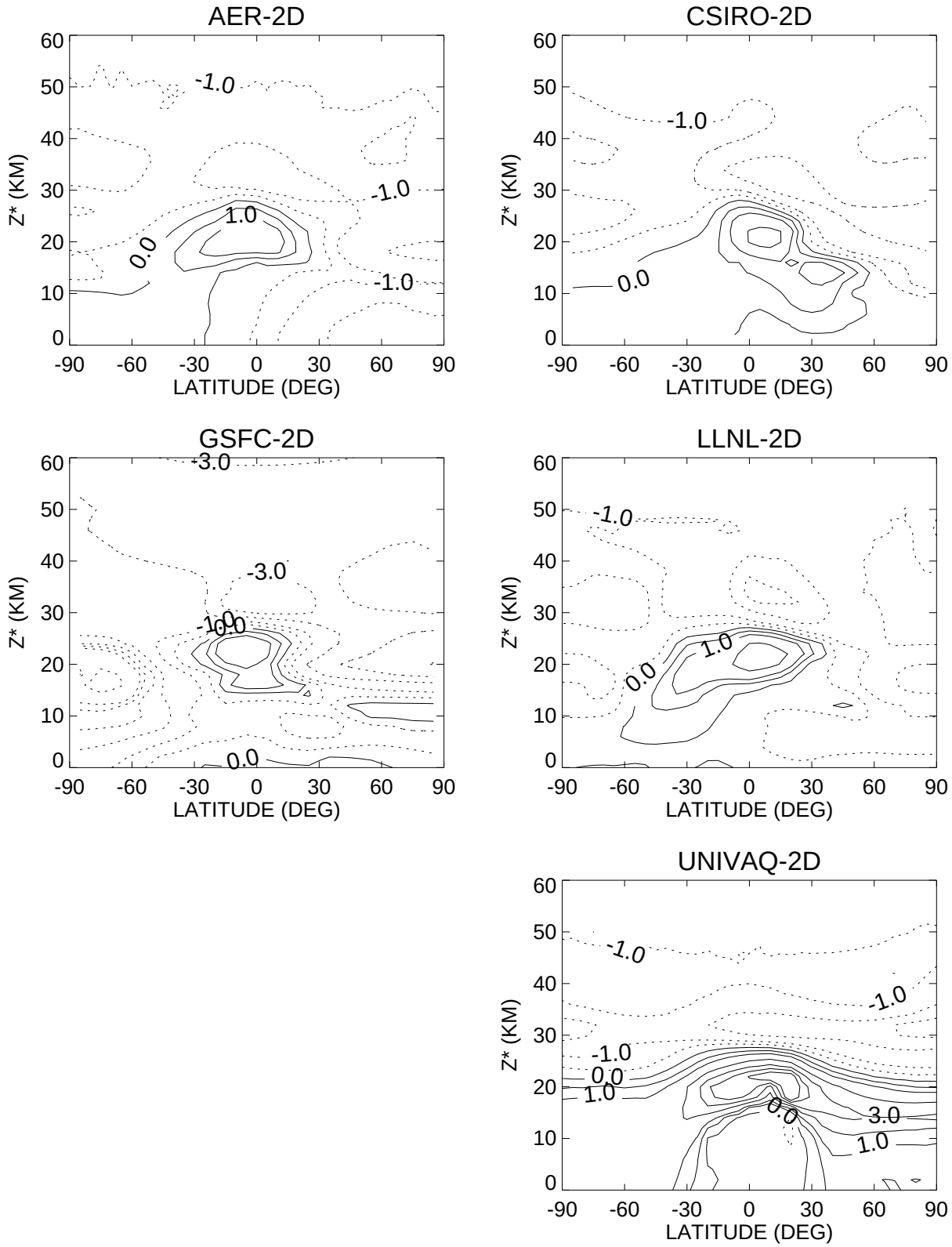

Figure 5.24: Calculated perturbations to O_3 (percent) as a function of latitude and altitude in October of 2050 due to emissions from a fleet of 1000 HSCT aircraft with EI(NO_x)=10 under Scenario S9g relative to Scenario D9. Contours are -10, -5, -4, -3, -2, -1, -0.5, 0, 0.5, 1, 2, 3, 4, 5.

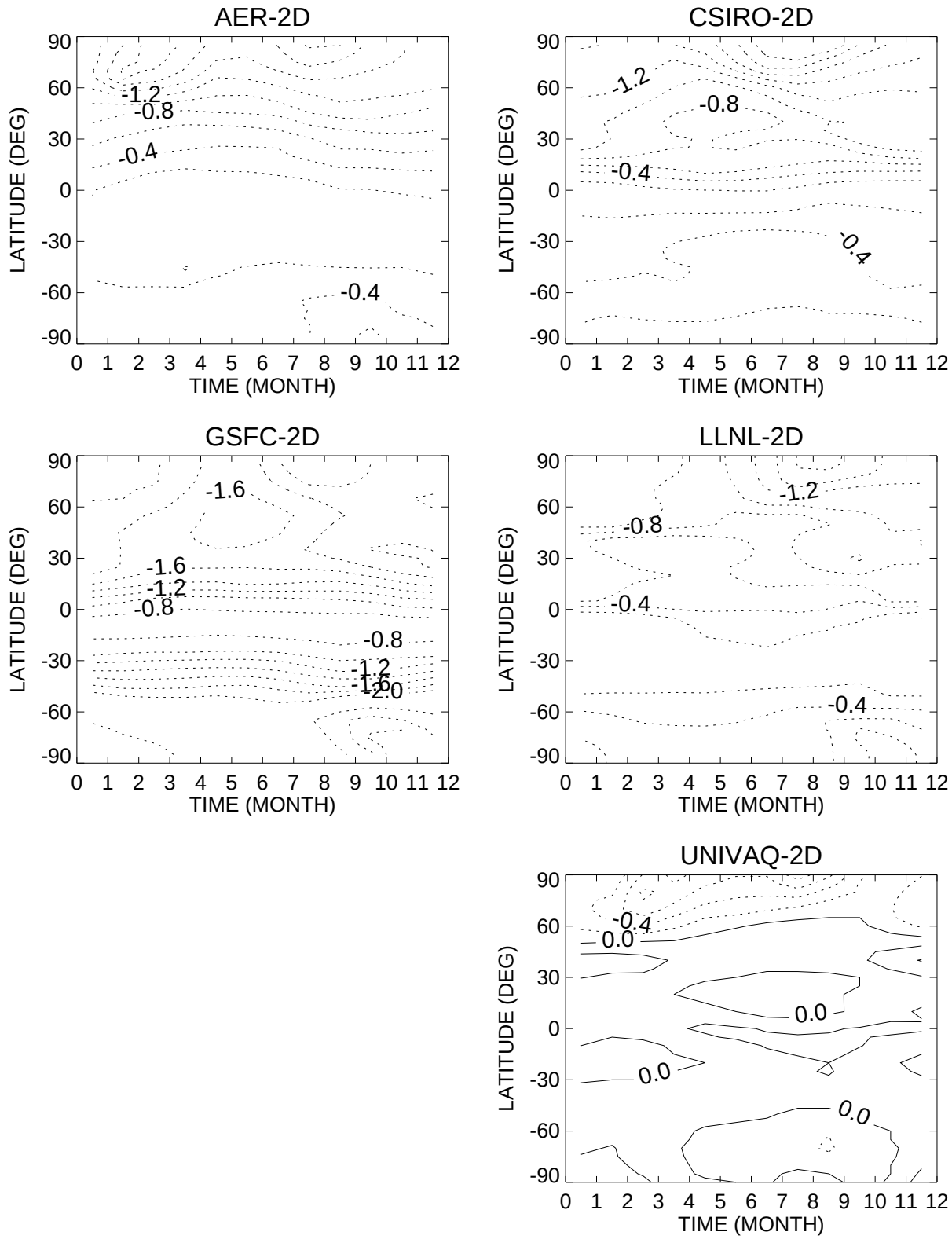

Figure 5.25: Calculated perturbations to column O_3 (percent) as a function of latitude and season in 2050 due to emissions from a fleet of 1000 HSCT aircraft with EI(NO_x)=10 under Scenario S9g relative to Scenario D9. Contours are -5, -4, -3 and -2 to 0.2 by 0.2.

5.3.2 Scenarios with Sulfur Emissions (S9c,e,f,h)

Scenarios S9c, S9e, S9f, and S9h include sulfur emission from HSCT aircraft in 2050. S9c uses a 500 HSCT fleet while the others use a 1000 HSCT fleet. All these scenarios employ an EI(NO_x) of 5 and an EI(SO_2) of 0.4. The gas to particle conversion fraction varies from 10% to 100%.

Scenario S9c uses sulfate surface area SA1, which assumes 50% gas to particle conversion in the plume. The aircraft fleet contains 500 HSCTs with EI(NO_x)=5. Changes in ozone for this scenario relative to scenario D9 are shown in Figures 5.26, 5.27, and 5.28 for March, June, and October, respectively. Compared to Scenario S9a-D9 which omits aircraft sulfur emissions, the ozone change is more negative below 20 km and more positive above. Compared with a similar scenario (S9f-D) in 2015, the ozone depletion is reduced. Figure 5.29 shows changes in ozone column for this scenario. The CSIRO model shows ozone increases in much of the southern hemisphere and ozone decreases of up to 0.6% in the northern hemisphere high latitudes. The AER model shows ozone decreases of greater than 0.8% in the northern hemisphere poleward of 60^{o}N. The GSFC model shows depletions of up to 1.6% in the northern high latitudes and over 2% in the southern high latitudes. The UNIVAQ model shows ozone increases in the tropics and depletions of up to 0.8% in the northern high latitudes.

Scenario S9e uses a 1000 HSCT fleet and SA2 surface area density, which assumes 50% gas to particle conversion. Figures 5.30, 5.31, and 5.32 show calculated changes in ozone for March, June, and October. Lower stratospheric ozone depletion peaks around 15 km in the northern hemisphere, with up to 3% depletion in the AER and GSFC models, 2% in the LLNL and UNIVAQ models, and 1% in the CSIRO Model. The AER, CSIRO, and LLNL models show ozone increases around 25 km at some extratropical latitudes, due to a decrease in NO_x-catalyzed ozone loss when aerosols are added. Ozone column changes are shown in Figure 5.33. All models calculate more than 1% ozone column depletion in parts of the northern hemisphere, with the AER and UNIVAQ models maximizing at 1.8% and the GSFC model at over 2%.

Scenario S9f uses surface area density SA4, which assumes 100% gas to particle conversion to calculate the maximum possible effect of aircraft sulfur emissions. The fleet consists of 1000 HSCTs. Calculated changes in ozone for this scenario relative to Scenario D9 are shown in Figures 5.34, 5.35, and 5.36. Ozone perturbations are slightly larger than those for S9e-D9. Figure 5.37 shows changes in ozone column. All models show slightly greater ozone column depletion for S9f-D9 than for S9e-D9.

Scenario S9h uses the 1000 HSCT fleet with surface area density SA6. SA6 assumes 10% gas to particle conversion in the plume. Calculated ozone changes for this scenario are shown in Figures 5.38, 5.39, and 5.40 for March, June, and October. Ozone reductions are somewhat greater than for S9d-D9 with SA0, but less than S9e-D9 with SA2. Figure 5.41 shows changes in column ozone for this scenario. Maximum column ozone depletions in the northern hemisphere are 1.8% for GSFC, 1.6% for AER, 1% for CSIRO and UNIVAQ, and 0.8% for LLNL.

The sensitivity of northern hemisphere ozone change to aircraft sulfur emissions in 2050 is depicted graphically in Figure 5.42. The abscissa show percentage increase in SAD in the 14-21 km, 33-90^{o}N region due to emission of sulfur from 1000 HSCTs relative to an SA0 background. Scenario S9d is used for the 0% change in SAD. Scenario S9h, with 10% gas to particle conversion, corresponds to a 74% increase in SAD. Scenarios S9e and S9f, with 50% and 100% gas to particle conversion, correspond to 124% and 164% increases in SAD, respectively. These scenarios all employ an EI(NO_x) of 5. All models show increasing ozone depletion with increasing SAD perturbation, and the slopes are fairly consistent among the AER, GSFC, LLNL, and UNIVAQ models. The CSIRO model shows a smaller response to aircraft sulfur emissions. The sensitivity to SAD perturbation in 2050 is considerably less than in 2015 (by factors of 2-4) due to the reduced Cl_y concentration.

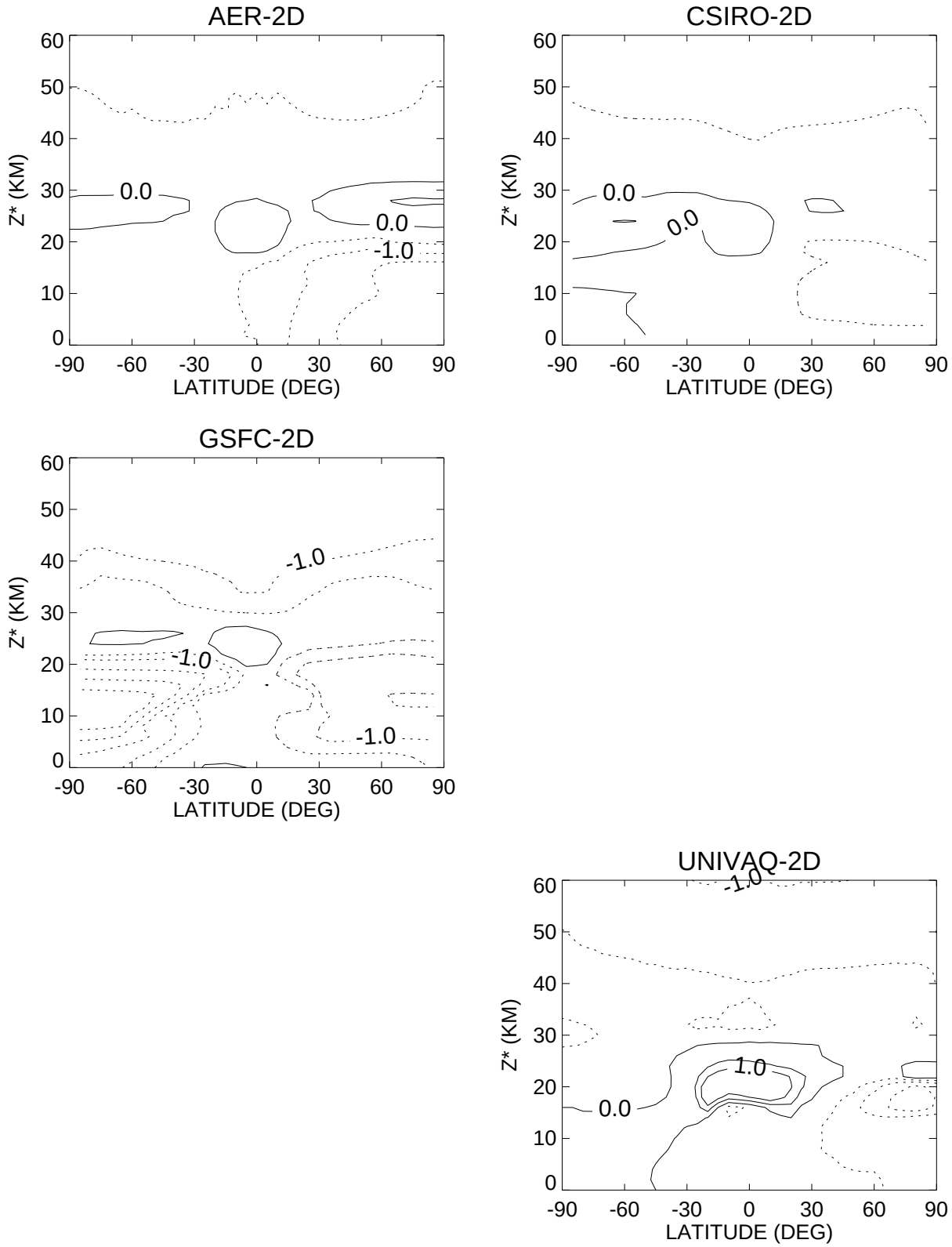

Figure 5.26: Calculated perturbations to O_3 (percent) as a function of latitude and altitude in March of 2050 due to emissions from a fleet of 500 HSCT aircraft with EI(NO_x)=5 and SA1 sulfate surface area density under Scenario S9c relative to Scenario D9. Contours are -4, -3, -2, -1, -0.5, 0, 0.5, 1.

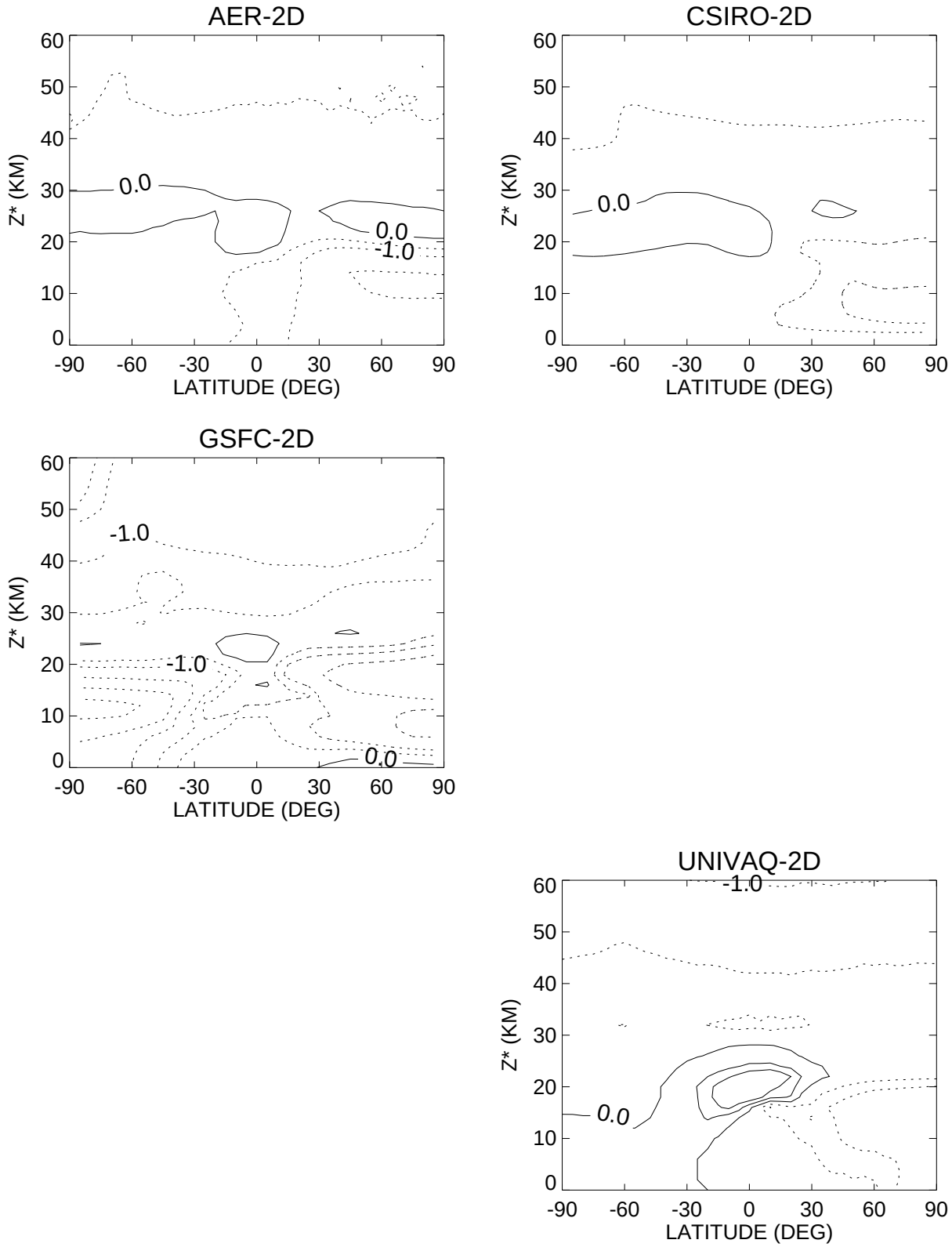

Figure 5.27: Calculated perturbations to O_3 (percent) as a function of latitude and altitude in June of 2050 due to emissions from a fleet of 500 HSCT aircraft with EI(NO_x)=5 and SA1 sulfate surface area density under Scenario S9c relative to Scenario D9. Contours are -4, -3, -2, -1, -0.5, 0, 0.5, 1.

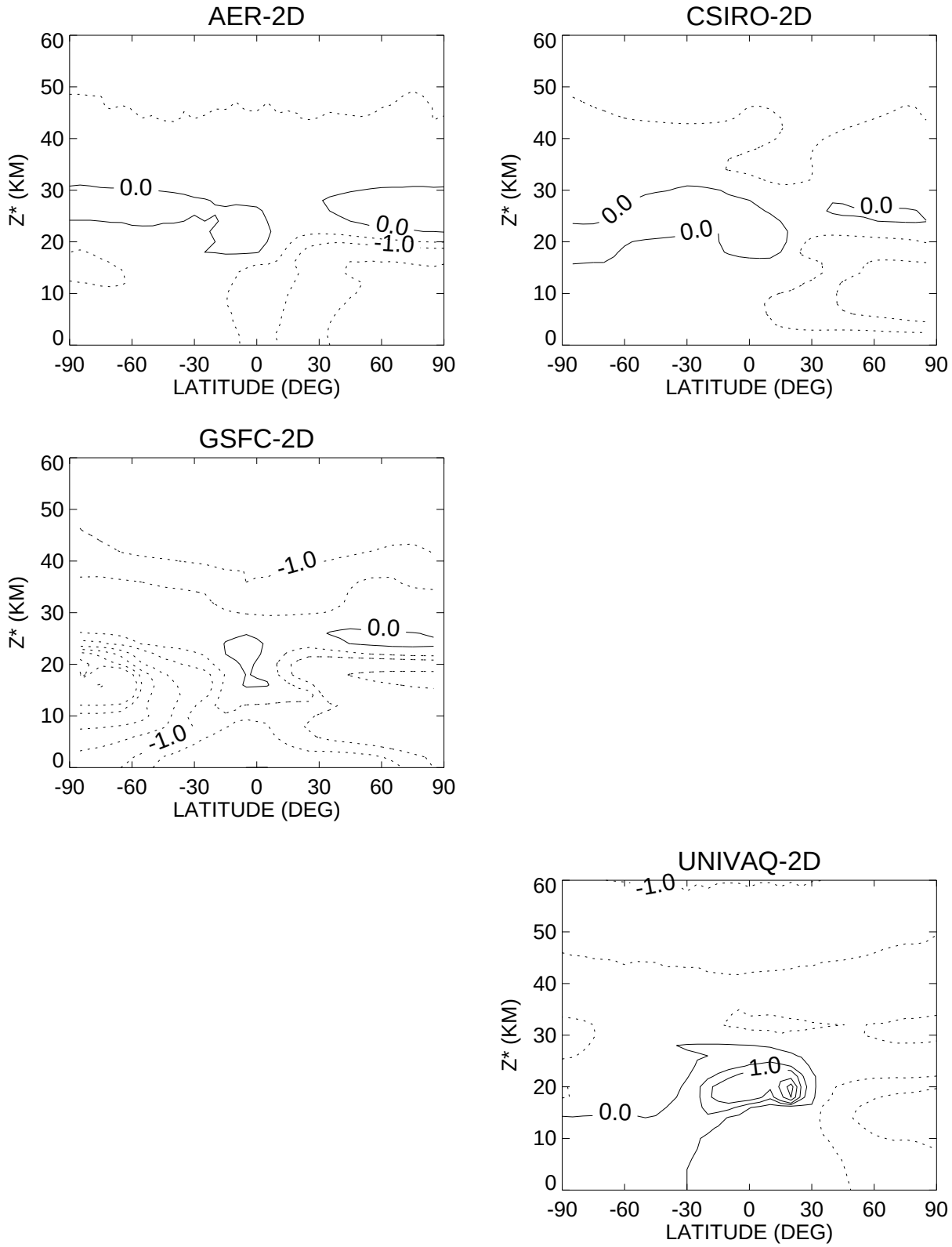

Figure 5.28: Calculated perturbations to O_3 (percent) as a function of latitude and altitude in October of 2050 due to emissions from a fleet of 500 HSCT aircraft with EI(NO_x)=5 and SA1 sulfate surface area density under Scenario S9c relative to Scenario D9. Contours are -10, -5, -4, -3, -2, -1, -0.5, 0, 0.5, 1, 2, 3.

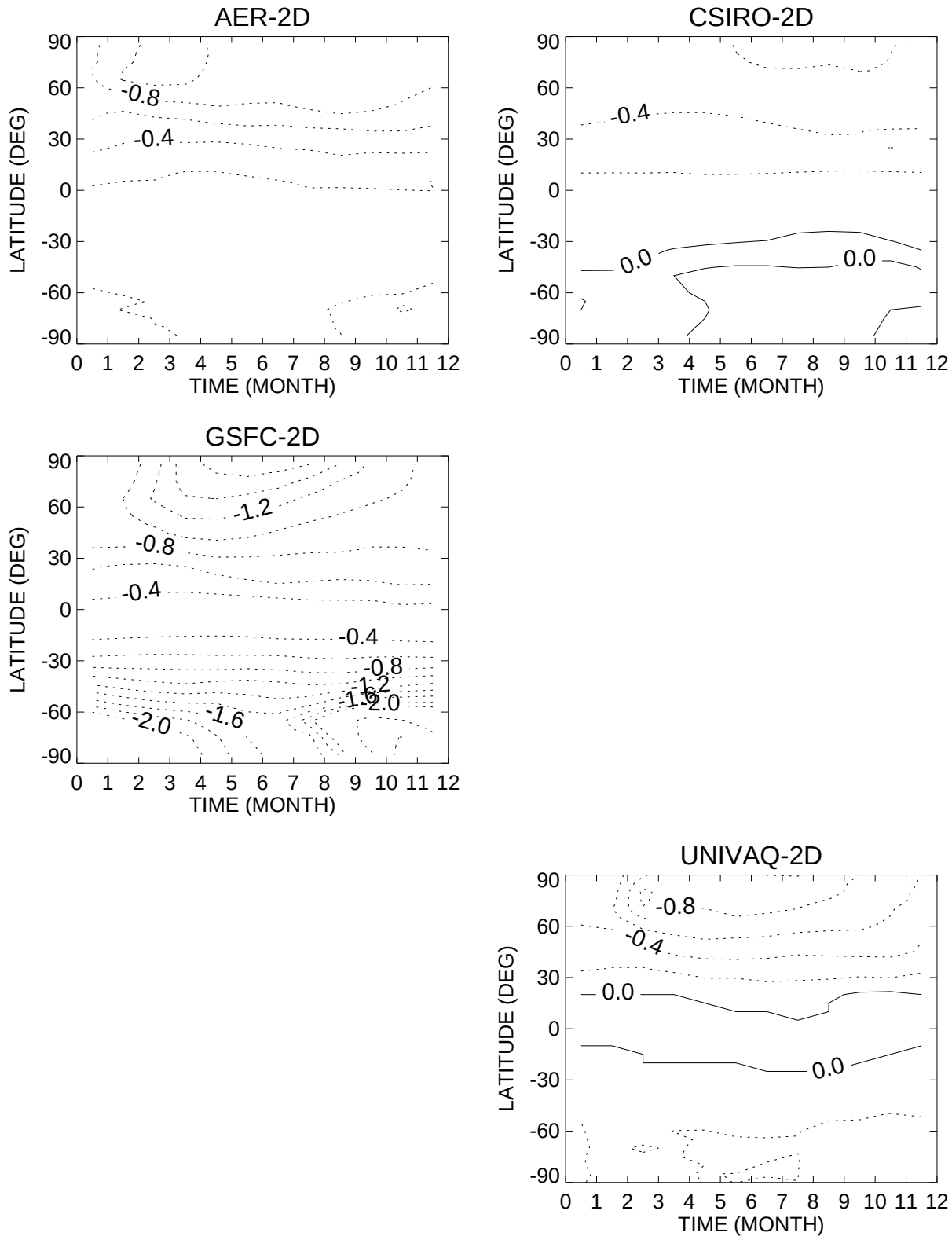

Figure 5.29: Calculated perturbations to column O_3 (percent) as a function of latitude and season in 2050 due to emissions from a fleet of 500 HSCT aircraft with EI(NO_x)=5 and SA1 sulfate surface area density under Scenario S9c relative to Scenario D9. Contours are -4, -3 and -2 to 0.2 by 0.2.

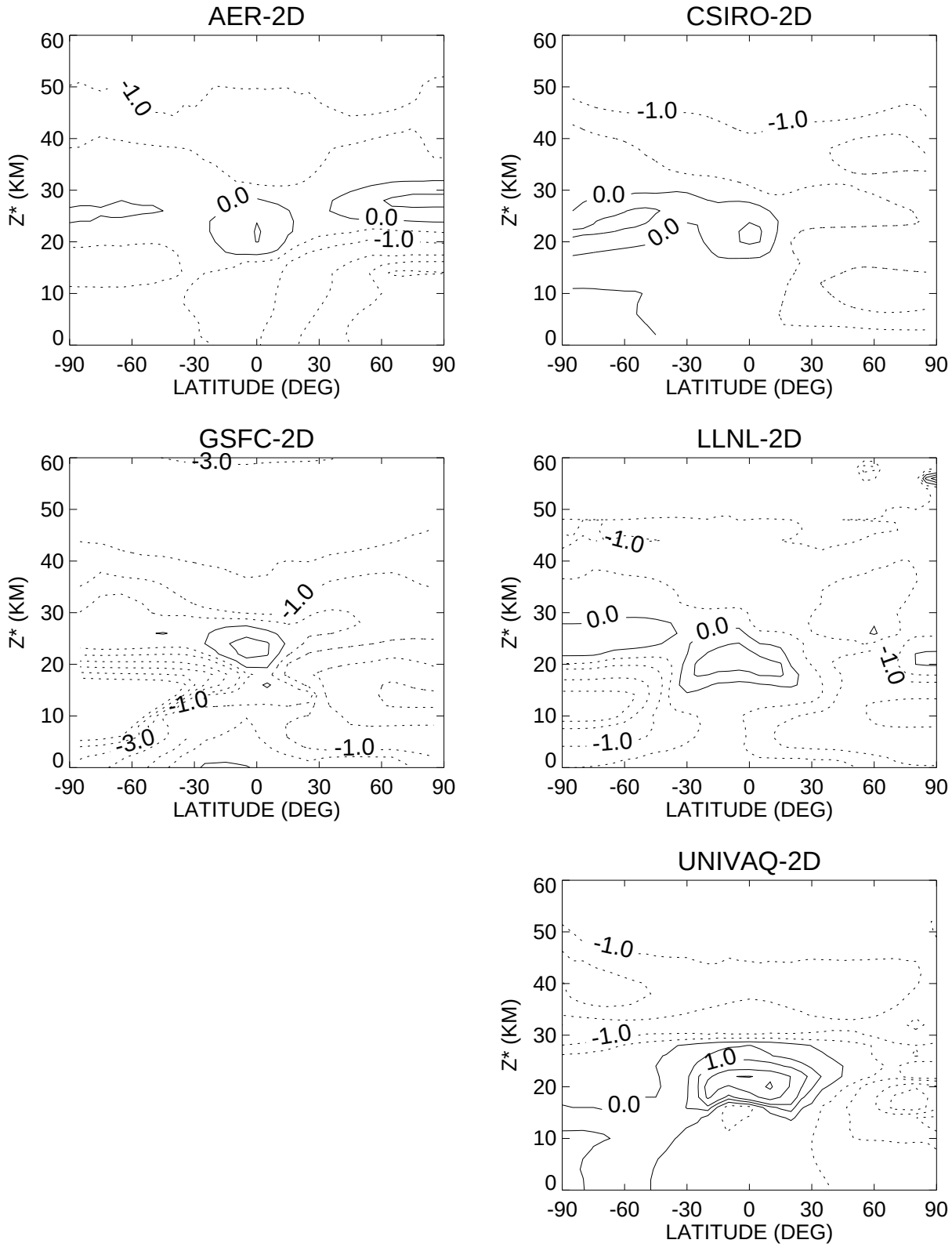

Figure 5.30: Calculated perturbations to O_3 (percent) as a function of latitude and altitude in March of 2050 due to emissions from a fleet of 1000 HSCT aircraft with EI(NO_x)=5 and SA2 sulfate surface area density under Scenario S9e relative to Scenario D9. Contours are -5, -4, -3, -2, -1, -0.5, 0, 0.5, 1, 2, 3.

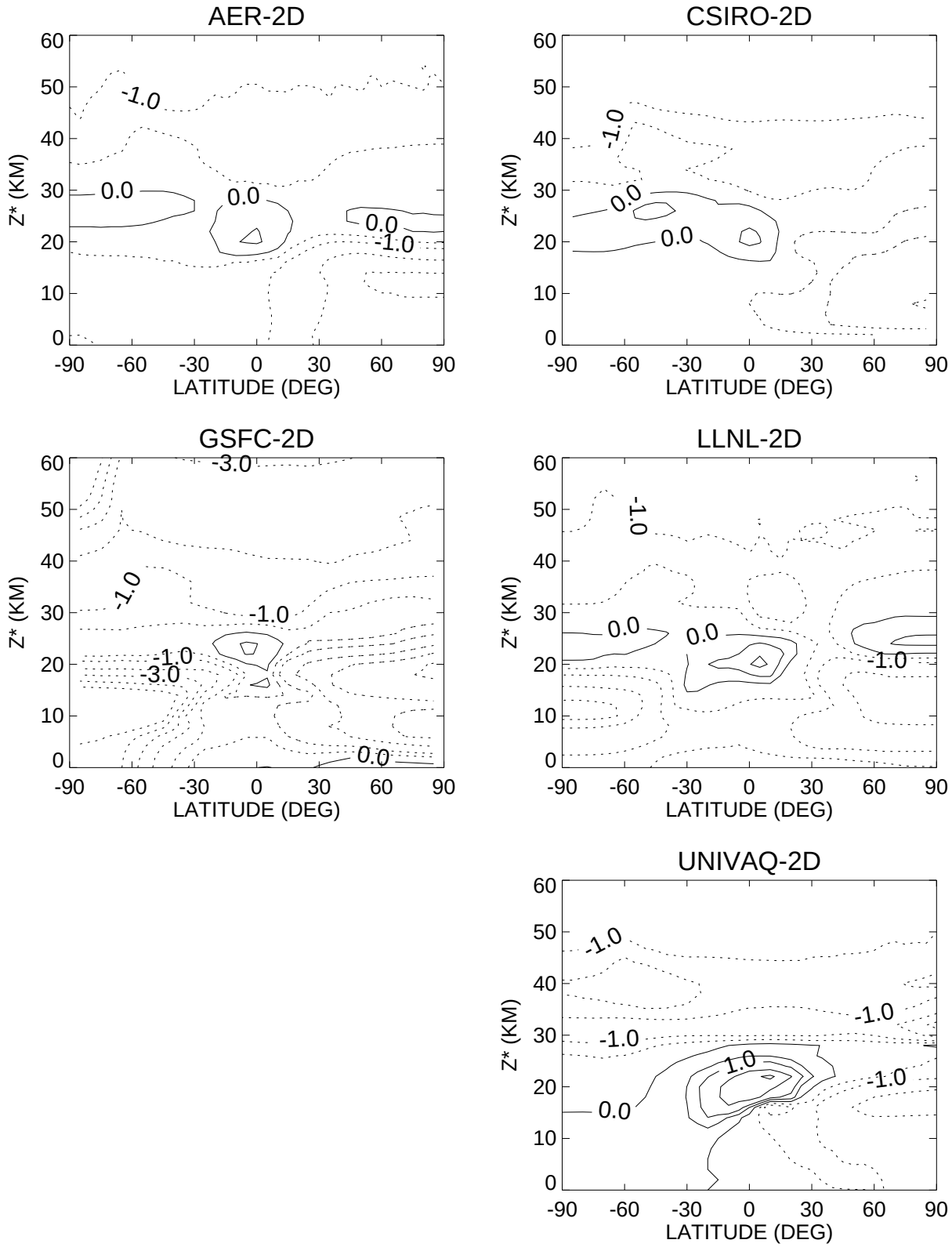

Figure 5.31: Calculated perturbations to O_3 (percent) as a function of latitude and altitude in June of 2050 due to emissions from a fleet of 1000 HSCT aircraft with EI(NO_x)=5 and SA2 sulfate surface area density under Scenario S9e relative to Scenario D9. Contours are -5, -4, -3, -2, -1, -0.5, 0, 0.5, 1, 2, 3.

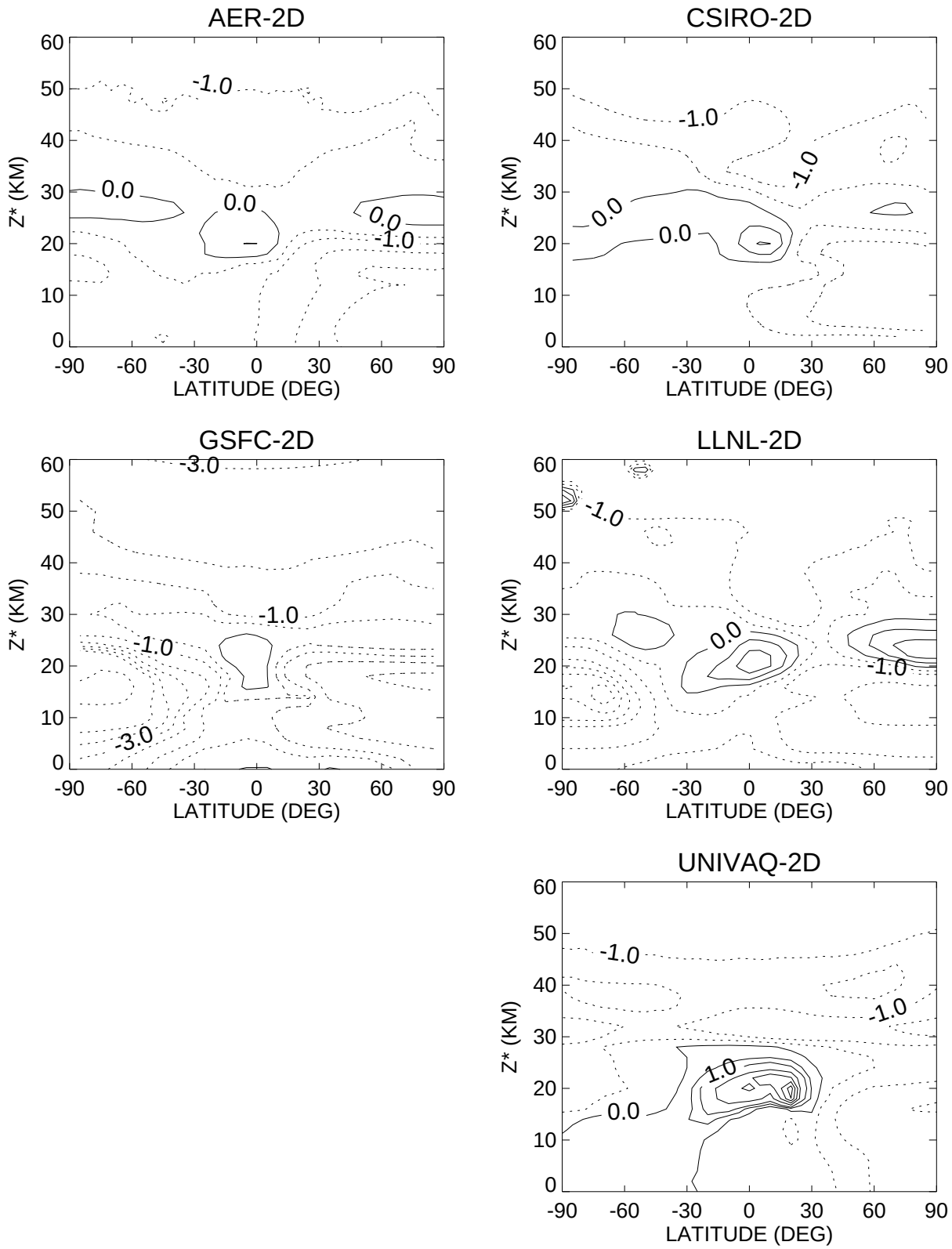

Figure 5.32: Calculated perturbations to O_3 (percent) as a function of latitude and altitude in October of 2050 due to emissions from a fleet of 1000 HSCT aircraft with EI(NO_x)=5 and SA2 sulfate surface area density under Scenario S9e relative to Scenario D9. Contours are -10, -5, -4, -3, -2, -1, -0.5, 0, 0.5, 1, 2, 3, 4, 5.

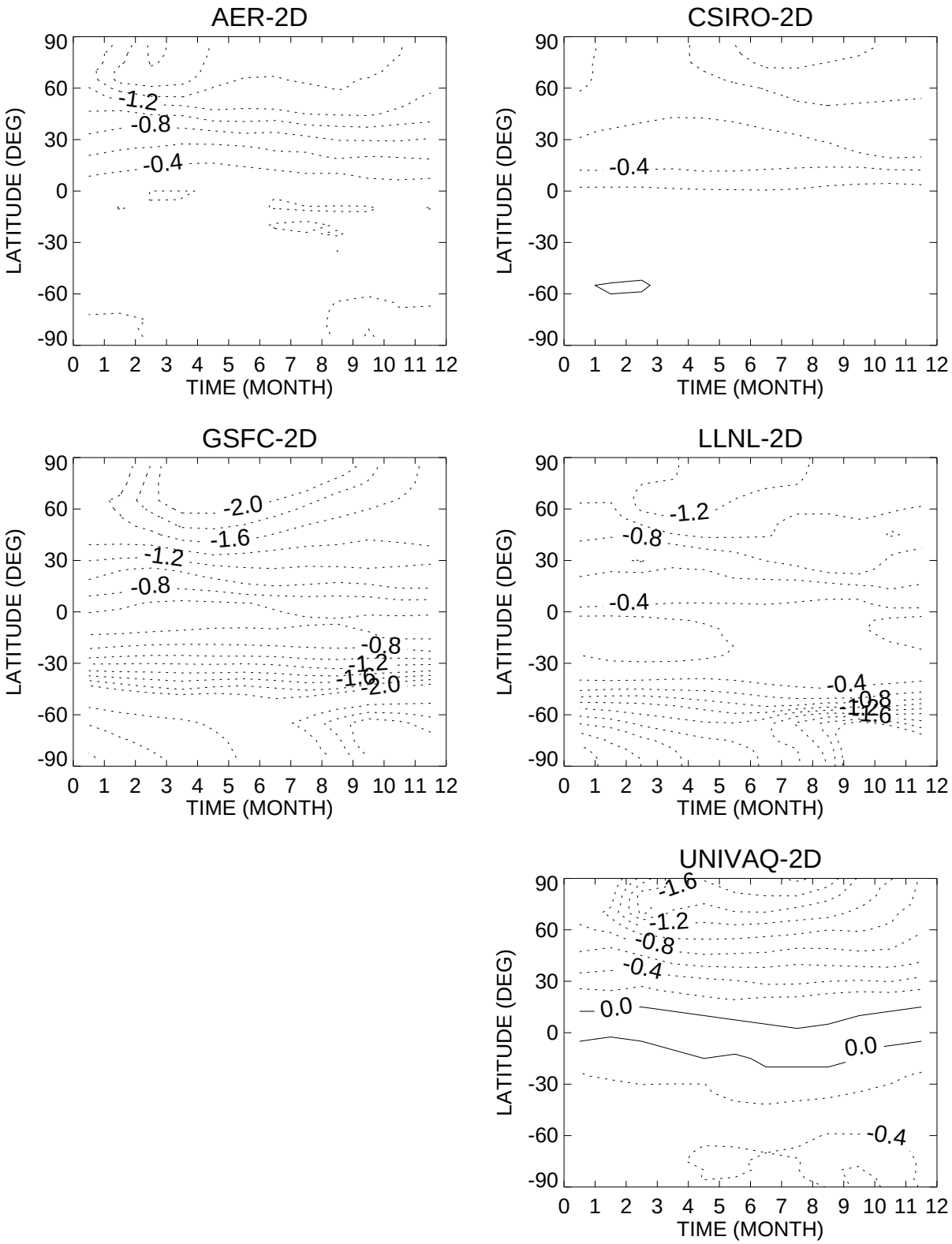

Figure 5.33: Calculated perturbations to column O_3 (percent) as a function of latitude and season in 2050 due to emissions from a fleet of 1000 HSCT aircraft with EI(NO_x)=5 and SA2 sulfate surface area density under Scenario S9e relative to Scenario D9. Contours are -5, -4, -3 and -2 to 0 by 0.2.

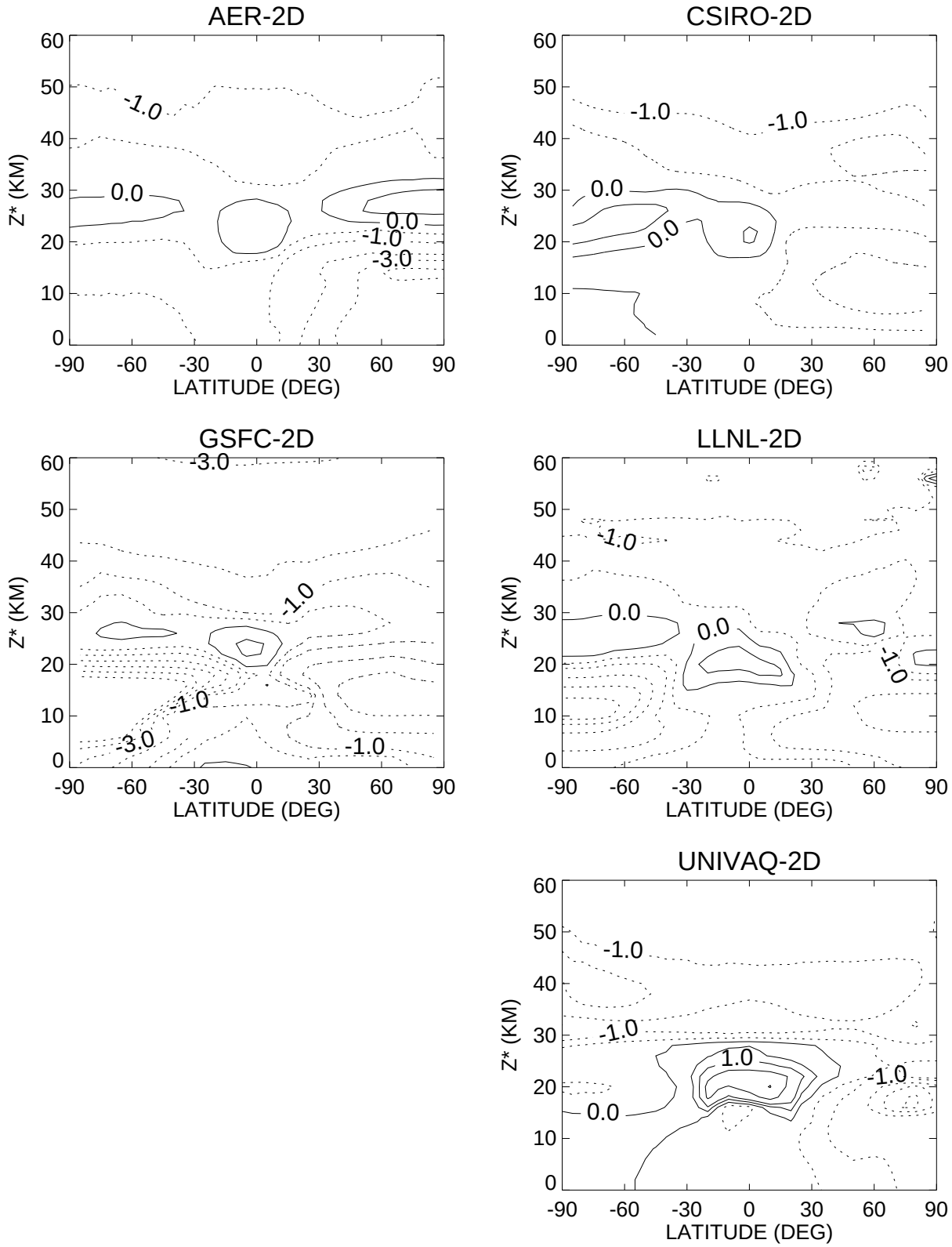

Figure 5.34: Calculated perturbations to O_3 (percent) as a function of latitude and altitude in March of 2050 due to emissions from a fleet of 1000 HSCT aircraft with EI(NO_x)=5 and SA4 sulfate surface area density under Scenario S9f relative to Scenario D9. Contours are -5, -4, -3, -2, -1, -0.5, 0, 0.5, 1, 2, 3.

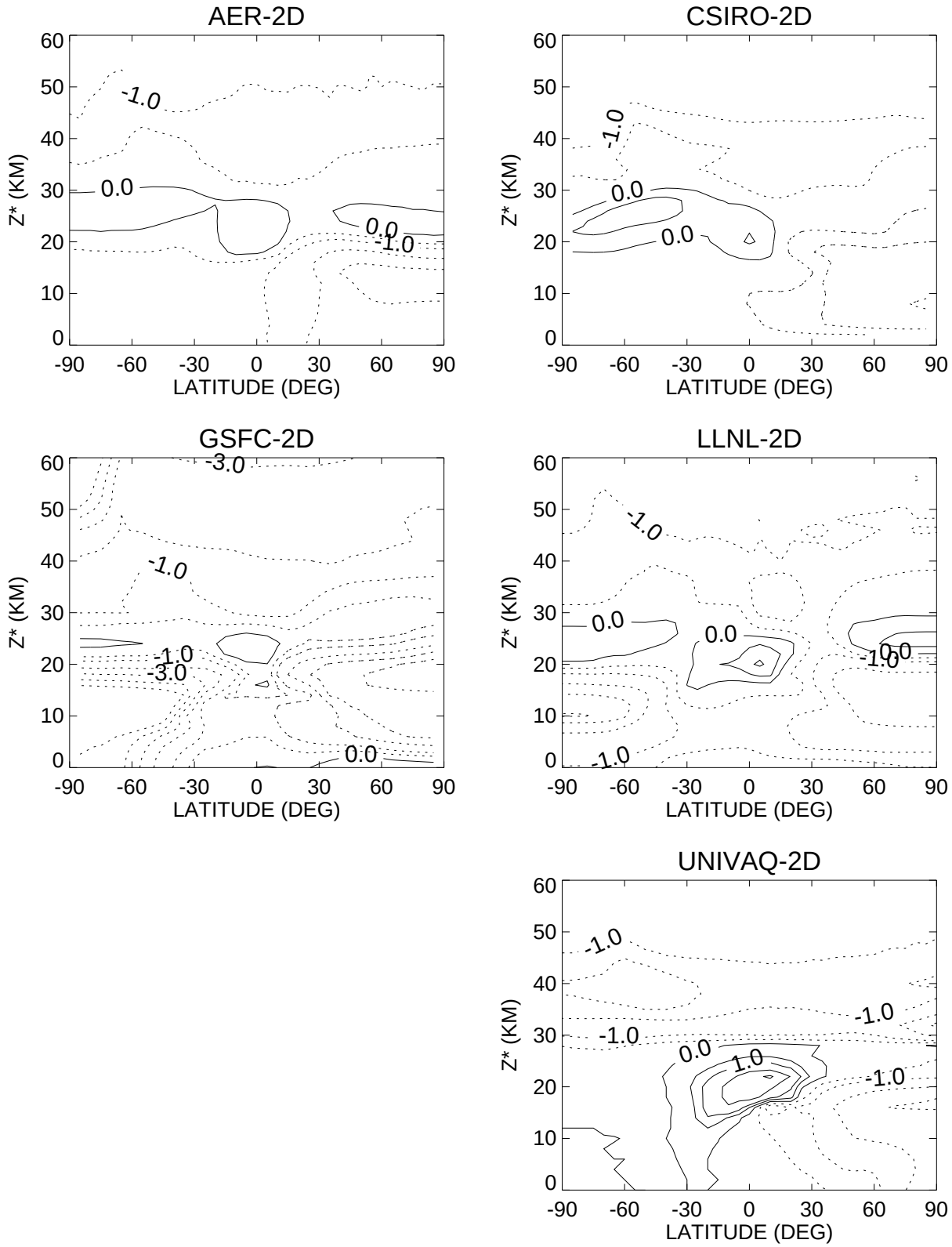

Figure 5.35: Calculated perturbations to O_3 (percent) as a function of latitude and altitude in June of 2050 due to emissions from a fleet of 1000 HSCT aircraft with EI(NO_x)=5 and SA4 sulfate surface area density under Scenario S9f relative to Scenario D9. Contours are -5, -4, -3, -2, -1, -0.5, 0, 0.5, 1, 2, 3.

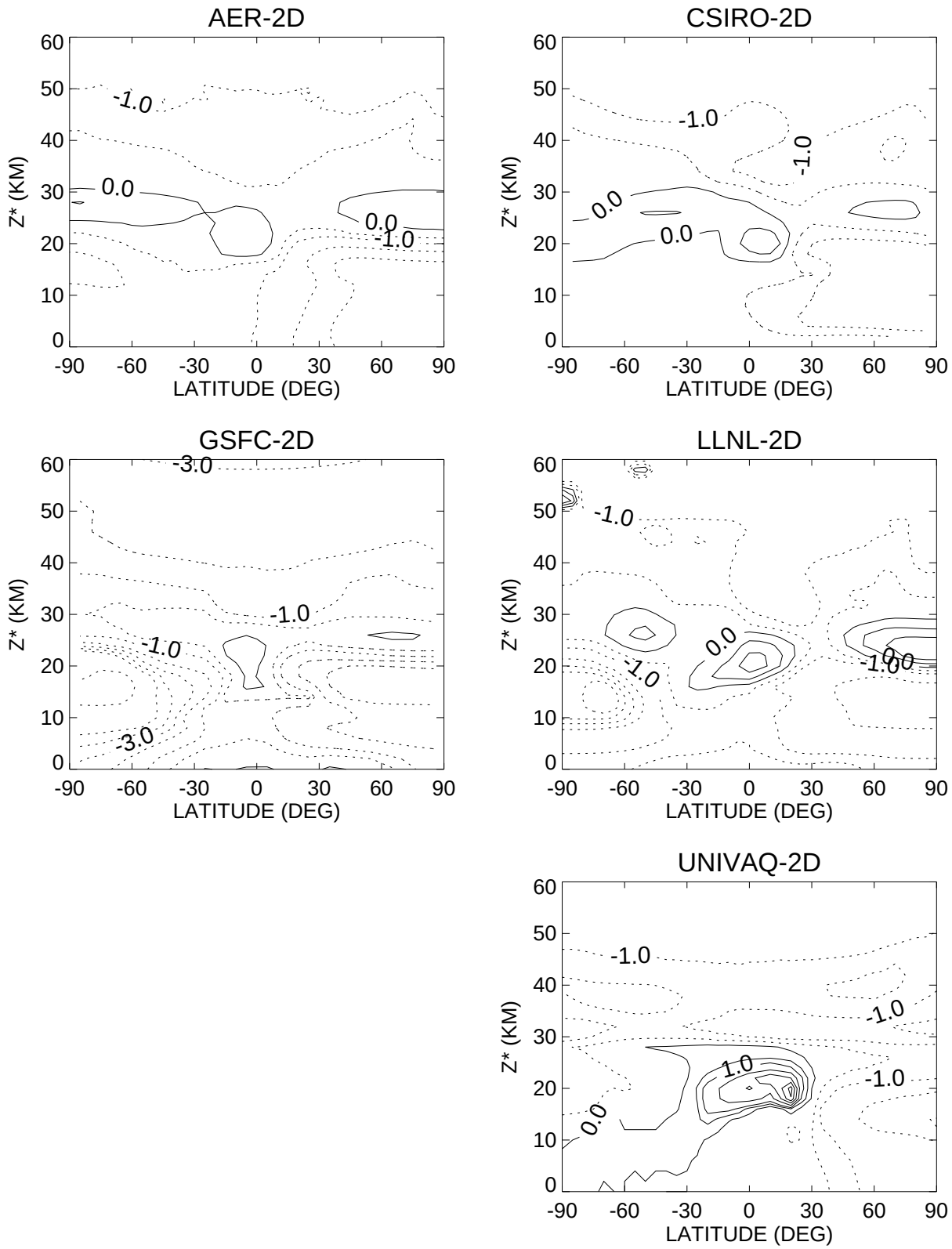

Figure 5.36: Calculated perturbations to O_3 (percent) as a function of latitude and altitude in October of 2050 due to emissions from a fleet of 1000 HSCT aircraft with EI(NO_x)=5 and SA4 sulfate surface area density under Scenario S9f relative to Scenario D9. Contours are -10, -5, -4, -3, -2, -1, -0.5, 0, 0.5, 1, 2, 3, 4, 5.

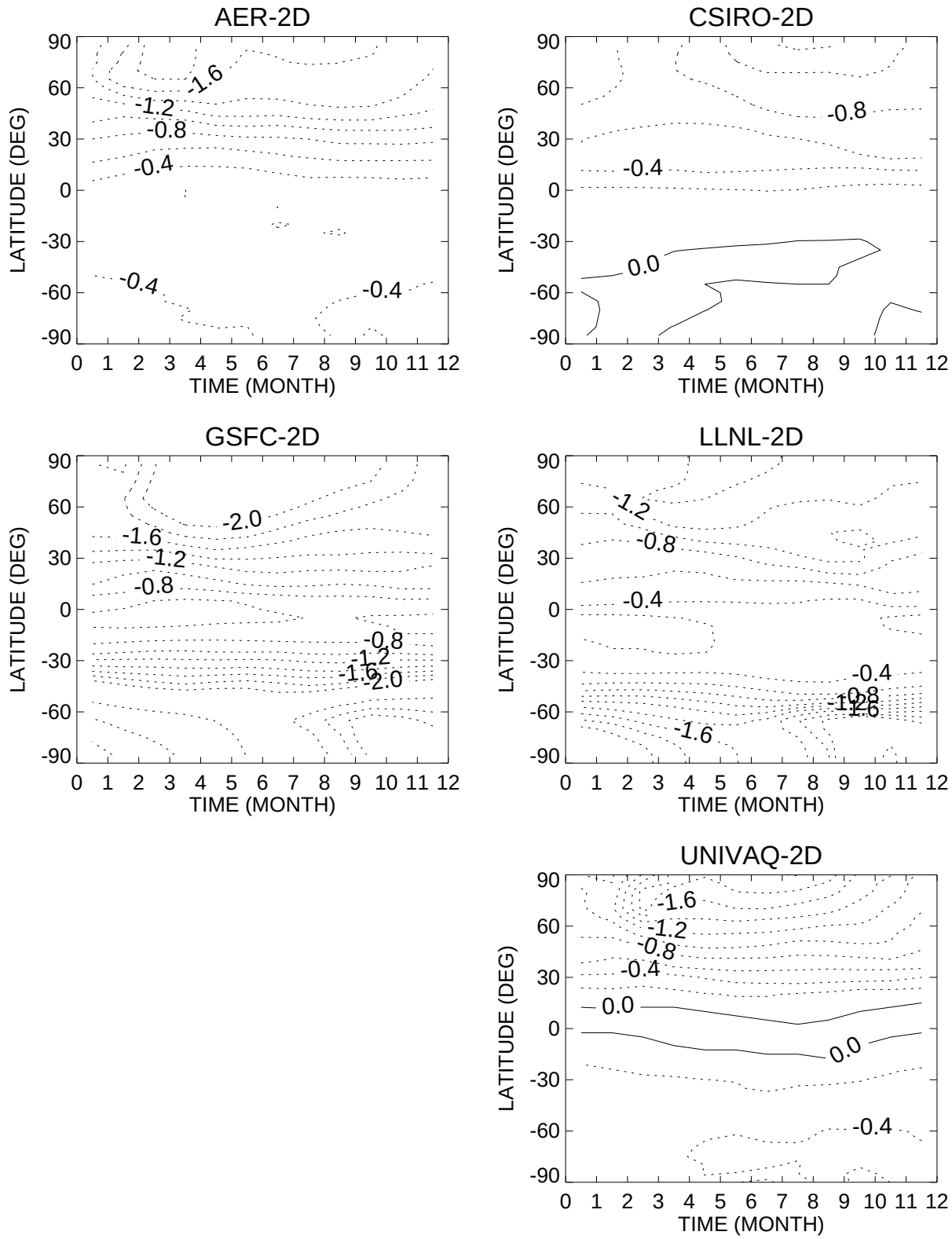

Figure 5.37: Calculated perturbations to column O_3 (percent) as a function of latitude and season in 2050 due to emissions from a fleet of 1000 HSCT aircraft with EI(NO_x)=5 and SA4 sulfate surface area density under Scenario S9f relative to Scenario D9. Contours are -5, -4, -3 and -2 to 0 by 0.2.

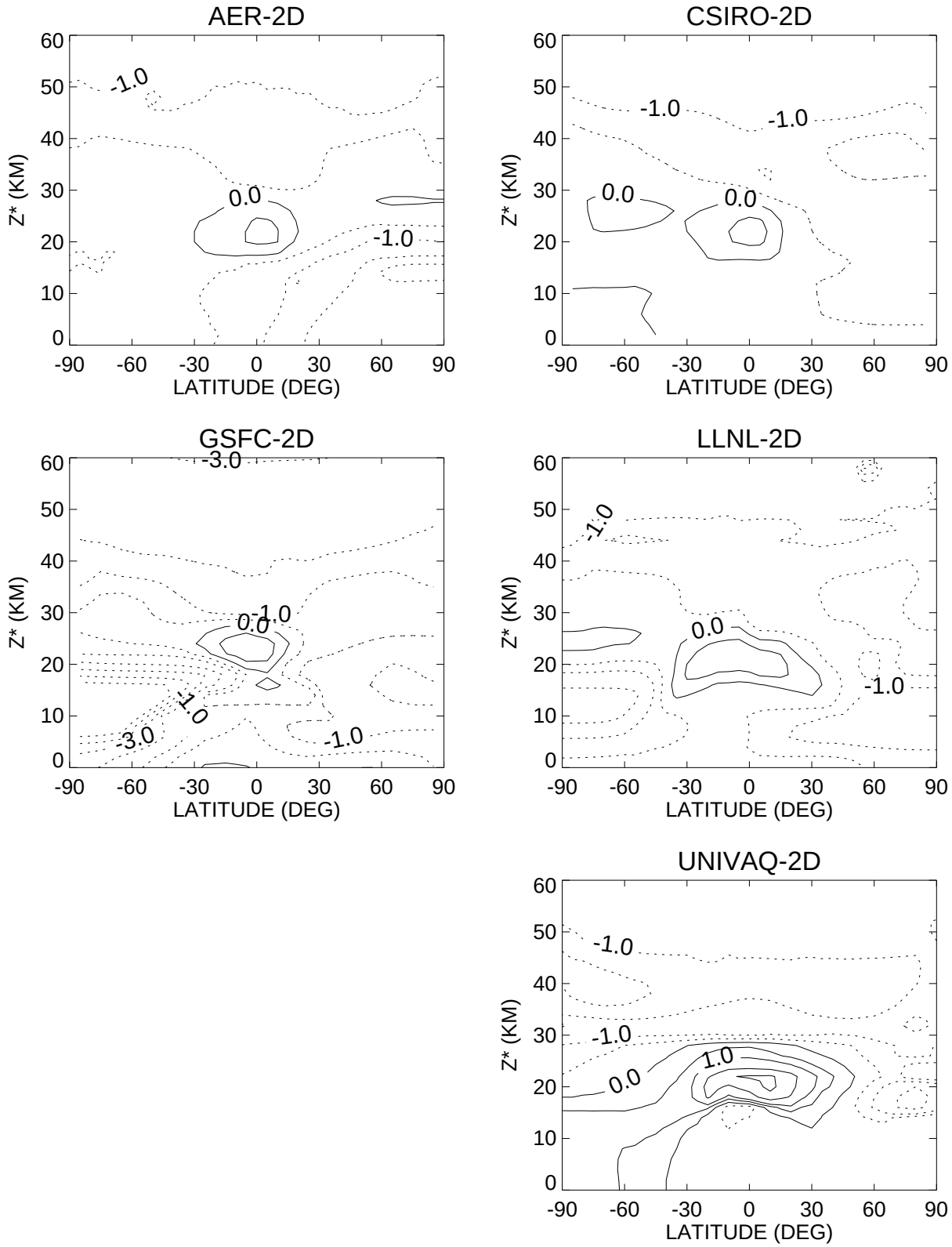

Figure 5.38: Calculated perturbations to O_3 (percent) as a function of latitude and altitude in March of 2050 due to emissions from a fleet of 1000 HSCT aircraft with EI(NO_x)=5 and SA6 sulfate surface area density under Scenario S9h relative to Scenario D9. Contours are -5, -4, -3, -2, -1, -0.5, 0, 0.5, 1, 2, 3.

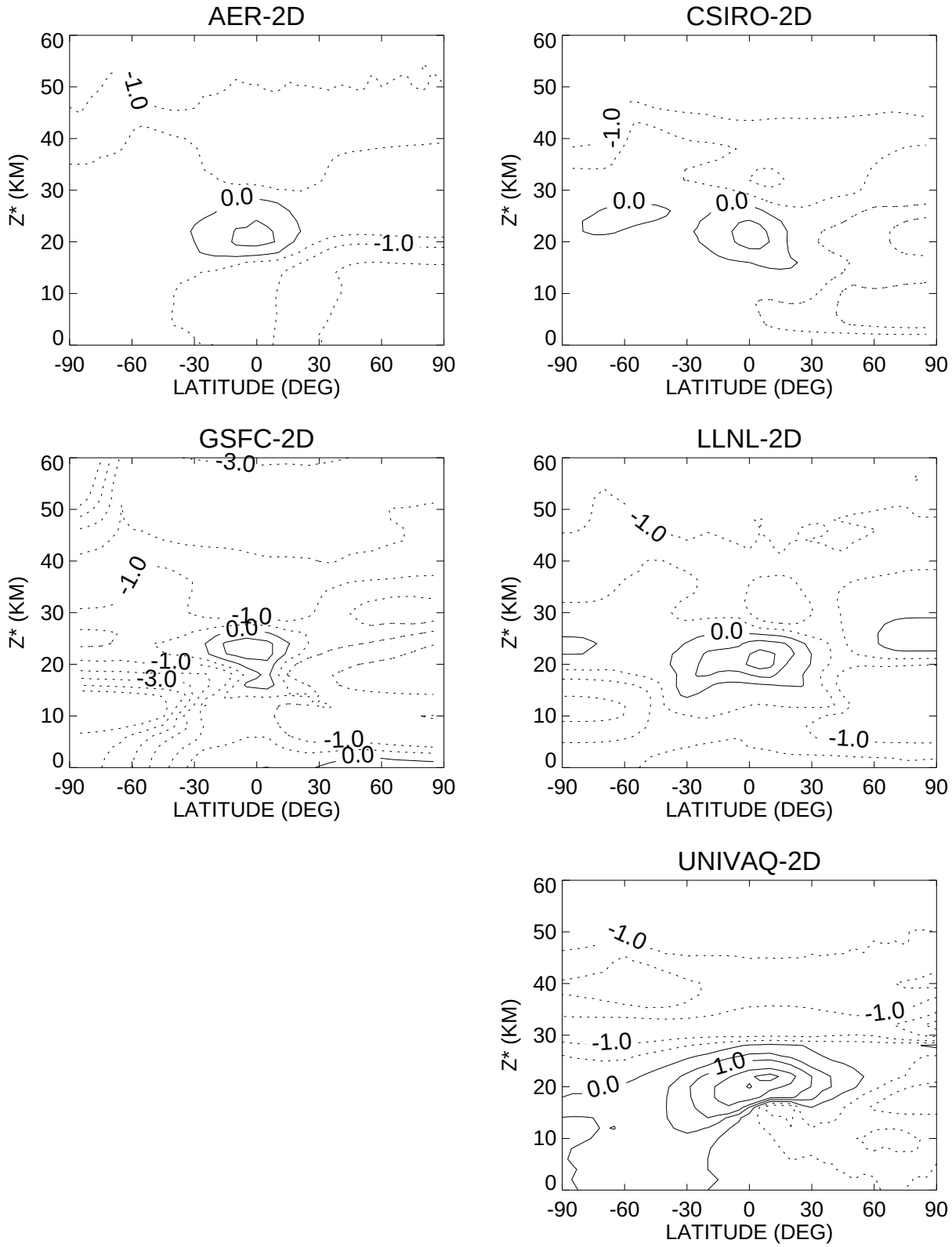

Figure 5.39: Calculated perturbations to O_3 (percent) as a function of latitude and altitude in June of 2050 due to emissions from a fleet of 1000 HSCT aircraft with EI(NO_x)=5 and SA6 sulfate surface area density under Scenario S9h relative to Scenario D9. Contours are -5, -4, -3, -2, -1, -0.5, 0, 0.5, 1, 2, 3.

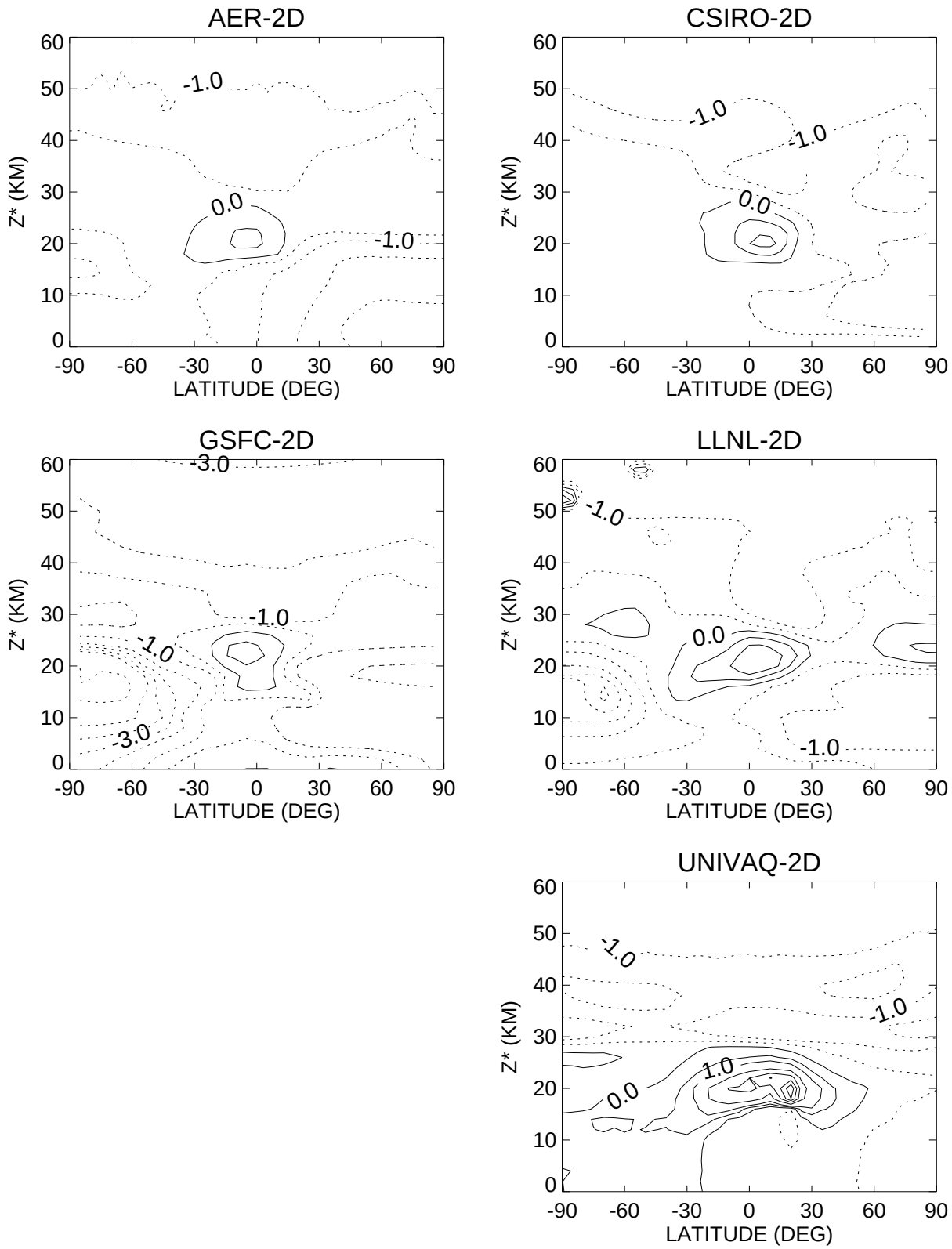

Figure 5.40: Calculated perturbations to O_3 (percent) as a function of latitude and altitude in October of 2050 due to emissions from a fleet of 1000 HSCT aircraft with EI(NO_x)=5 and SA6 sulfate surface area density under Scenario S9h relative to Scenario D9. Contours are -10, -5, -4, -3, -2, -1, -0.5, 0, 0.5, 1, 2, 3, 4, 5.

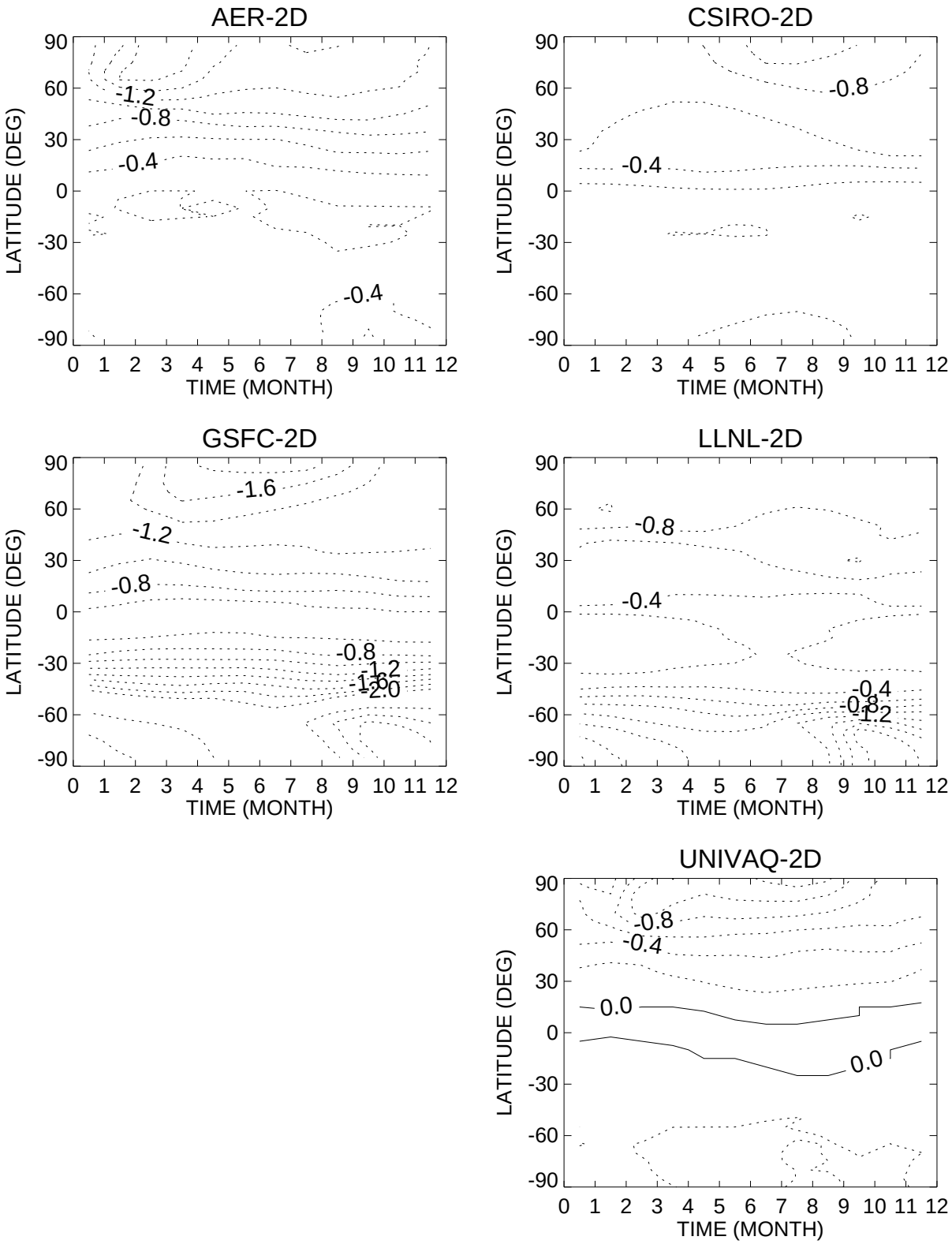

Figure 5.41: Calculated perturbations to column O_3 (percent) as a function of latitude and season in 2050 due to emissions from a fleet of 1000 HSCT aircraft with EI(NO_x)=5 and SA6 sulfate surface area density under Scenario S9h relative to Scenario D9. Contours are -5, -4, -3 and -2 to 0 by 0.2.

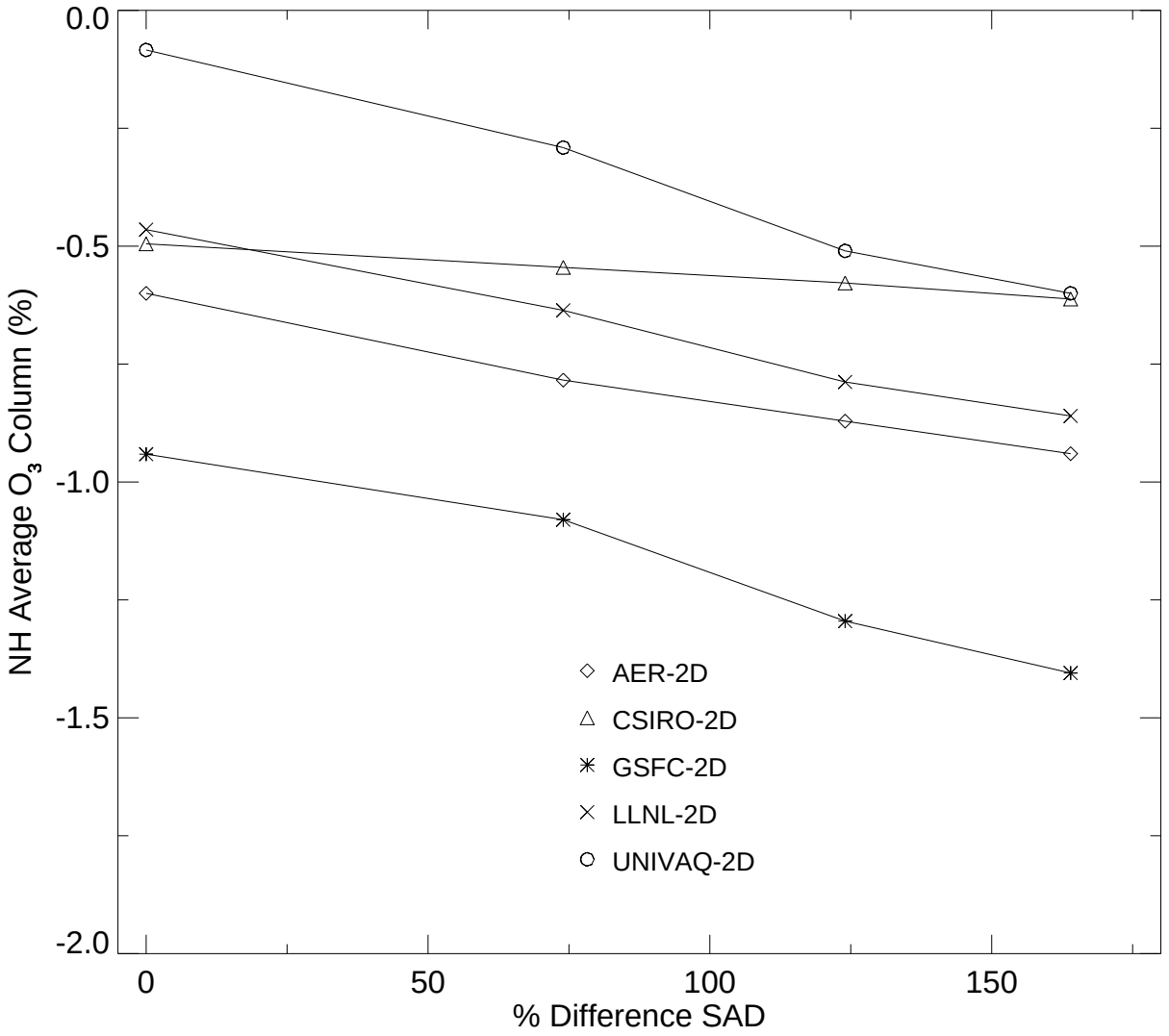

Figure 5.42: Northern hemisphere annual average total O_3 column change (percent) as a function of the percent change in aerosol surface area density in the region from 14 to 21 km and from 33^oN to 90^oN. The HSCT fleet consisted of 1000 aircraft with EI(NO_x)=5 operating in 2050 and assuming a background surface area density of SA0.

5.3.3 Scenarios with Modified Cruise Altitude (S10a-d)

Scenarios with modified cruise altitude are covered in this section. These 4 scenarios all use a supersonic fleet for which the cruise altitude is shifted downward by 2 km. Scenario S10a represents a fleet of 1000 HSCTs in 2015 with EI(NO_x)=5. Calculated changes in ozone as a function of latitude and altitude for March, June, and October are shown in Figures 5.43, 5.44, and 5.45. These ozone perturbations are similar to those for Scenario S2e-D, which represents the same aircraft fleet in 2015. Major differences are seen only in the October plot at high southern latitudes and in the GSFC model northern hemisphere lowermost stratosphere. And as with the 2015 scenarios, reducing the HSCT cruise altitude decreases the calculated ozone perturbation in the stratosphere very substantially. Changes in ozone column for Scenario S10a relative to Scenario D9 are shown in Figure 5.46. The CSIRO, LLNL, and UNIVAQ models show ozone column changes of 0.2% or less everywhere. The AER model shows maximum ozone column changes of -0.4% in the northern high latitudes, while the GSFC model shows ozone column changes of up to -1.6% in the high southern latitudes.

Scenario S10b represents 1000 HSCTs operating in 2050 at 2 km below the nominal cruise altitude with EI(NO_x)=10. Figures 5.47, 5.48, and 5.49 show calculated changes in ozone for this scenario relative to Scenario D9 for March, June, and October. Calculated changes in column ozone are shown in Figure 5.50. The AER, CSIRO and LLNL models show more of an ozone increase in the tropics and southern hemisphere and more of an ozone decrease at high latitudes for this scenario than for S10a. The GSFC model shows an increase in ozone depletion near 30^oN and a decrease in the southern hemisphere poleward of 60^oN. The UNIVAQ model show ozone column increases due to HSCT emissions over most latitudes and seasons with this scenario.

Scenarios S10c and S10d include aircraft sulfur emissions along with emissions of H_2O and NO_x with EI(NO_x)=5. S10c uses aerosol scenario SA6-2km, which assumes 10% gas to particle conversion for a fleet of 1000 HSCTs cruising at 2 km below the nominal cruise altitude. Ozone perturbations for this scenario relative to Scenario D9 are shown in Figures 5.51, 5.52, and 5.53. The effect of the aircraft SO_x emissions is to increase ozone depletion (or reduce ozone increases) in the extratropics below 20 km (compare with S10a-D9). Calculated perturbations to ozone column for Scenario 10c are shown in Figure 5.54. Ozone column depletions are larger than for S10a-D9.

Aerosol scenario SA2-2km is used for Scenario S10d. This scenario assumes 50% gas to particle conversion from 1000 HSCTs cruising at 2 km below the nominal altitude. Figures 5.55, 5.56, and 5.57 show calculated ozone changes for March, June, and October. Compared with S10c, ozone depletions are larger in the extratropics below 20 km and smaller from 20-30 km. Ozone column changes are shown in Figure 5.58. Ozone column depletion is increased slightly over S10c-D9, with the GSFC model showing the largest northern hemisphere increases due to the additional particle production.

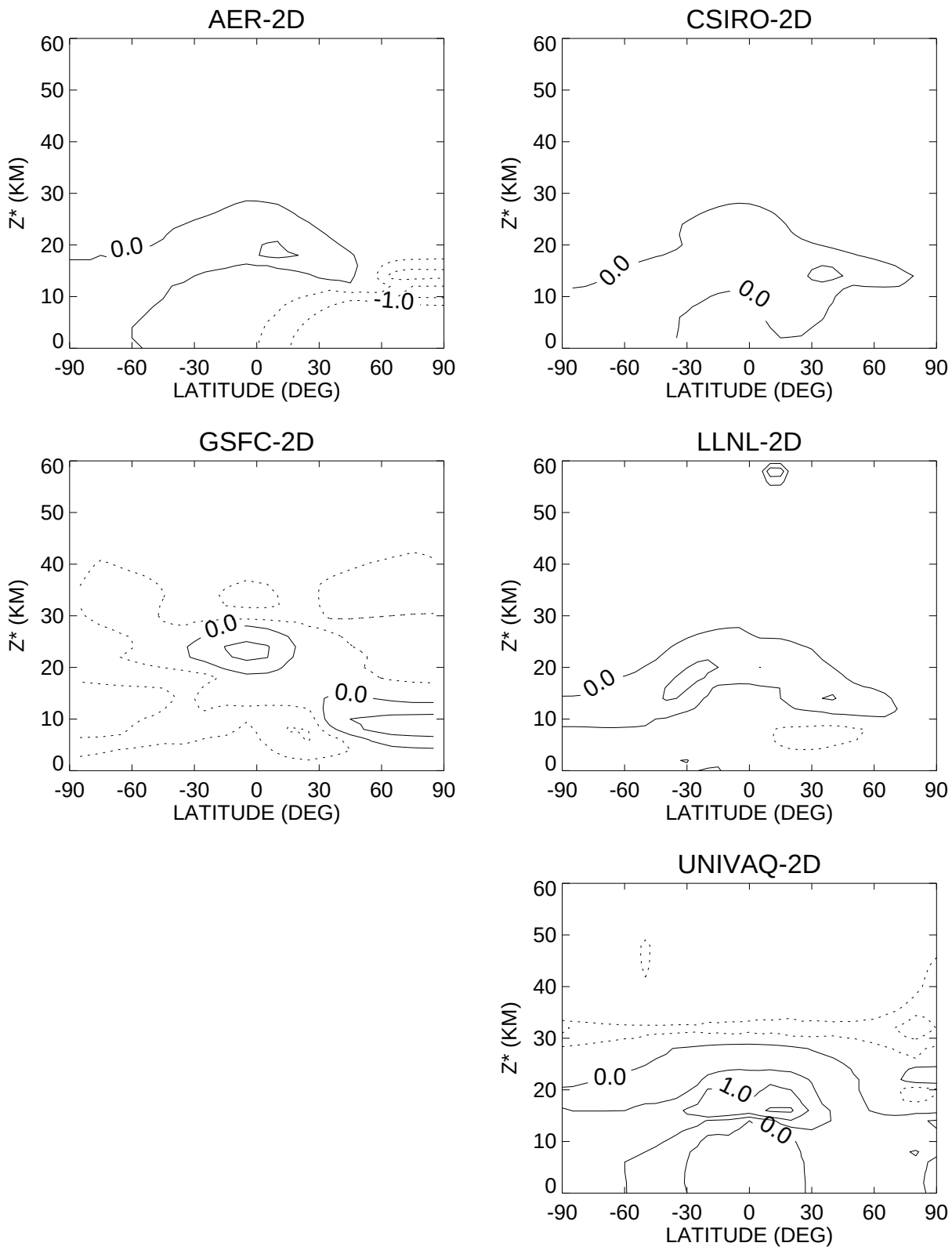

Figure 5.43: Calculated perturbations to O_3 (percent) as a function of latitude and altitude in March of 2050 due to emissions from a fleet of 1000 HSCT aircraft operating at 2 km below nominal cruise altitude with EI(NO_x)=5 under Scenario S10a relative to Scenario D9. Contours are -1, -0.5, 0, 0.5, 1, 2.

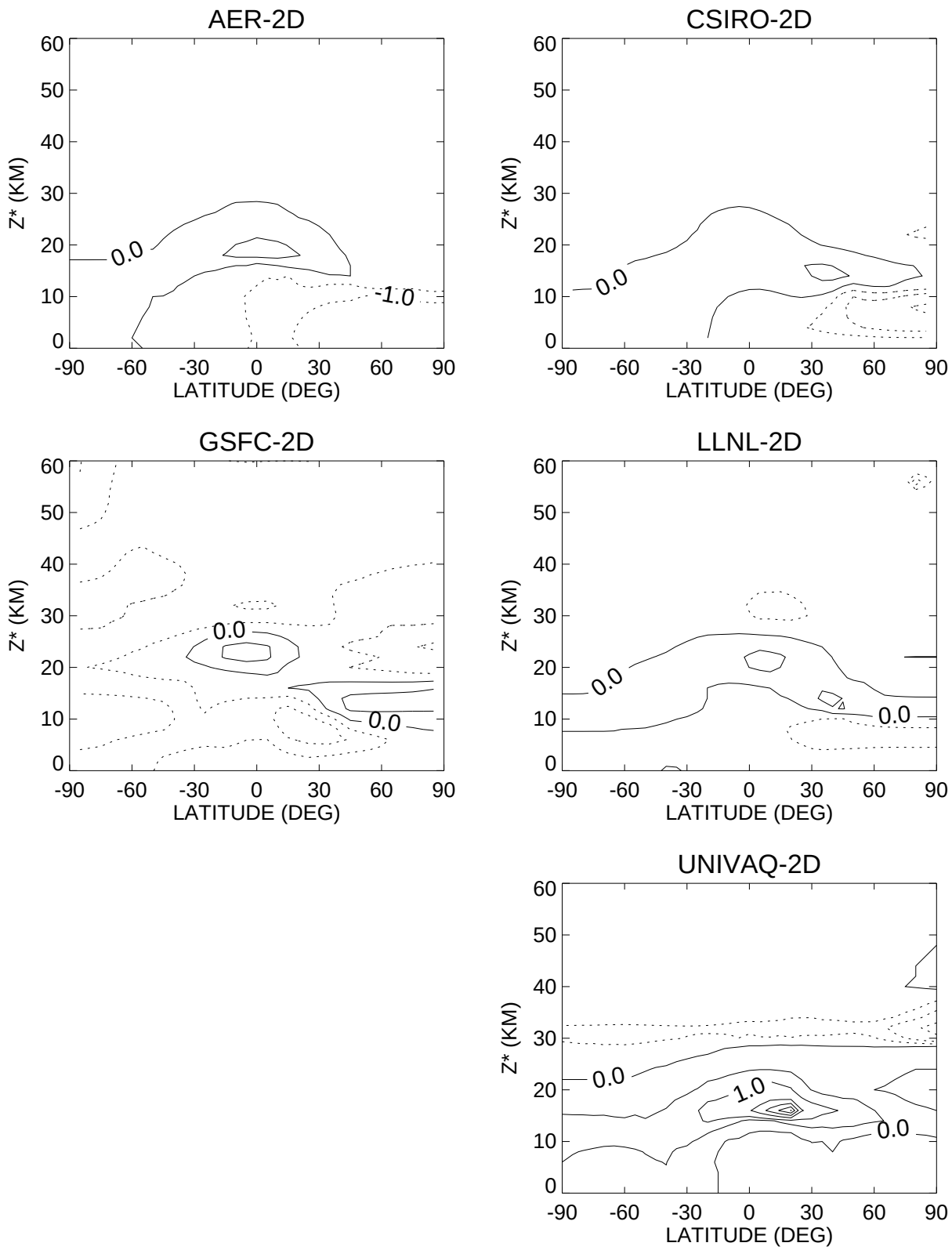

Figure 5.44: Calculated perturbations to O_3 (percent) as a function of latitude and altitude in June of 2050 due to emissions from a fleet of 1000 HSCT aircraft operating at 2 km below nominal cruise altitude with EI(NO_x)=5 under Scenario S10a relative to Scenario D9. Contours are -2, -1, -0.5, 0, 0.5, 1, 2, 3, 4, 5.

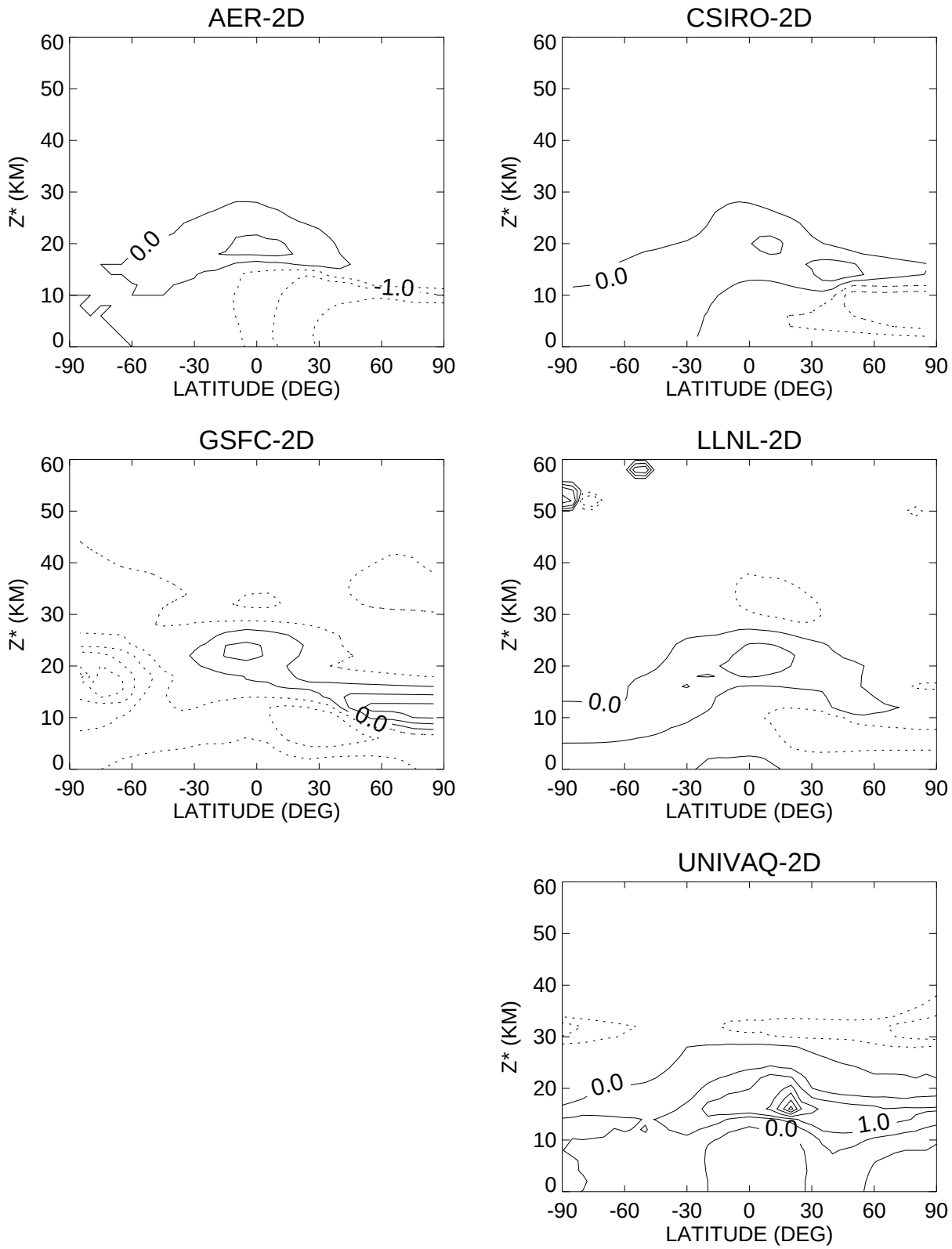

Figure 5.45: Calculated perturbations to O_3 (percent) as a function of latitude and altitude in October of 2050 due to emissions from a fleet of 1000 HSCT aircraft operating at 2 km below nominal cruise altitude with EI(NO_x)=5 under Scenario S10a relative to Scenario D9. Contours are -3, -2, -1, -0.5, 0, 0.5, 1, 2, 3, 4, 5.

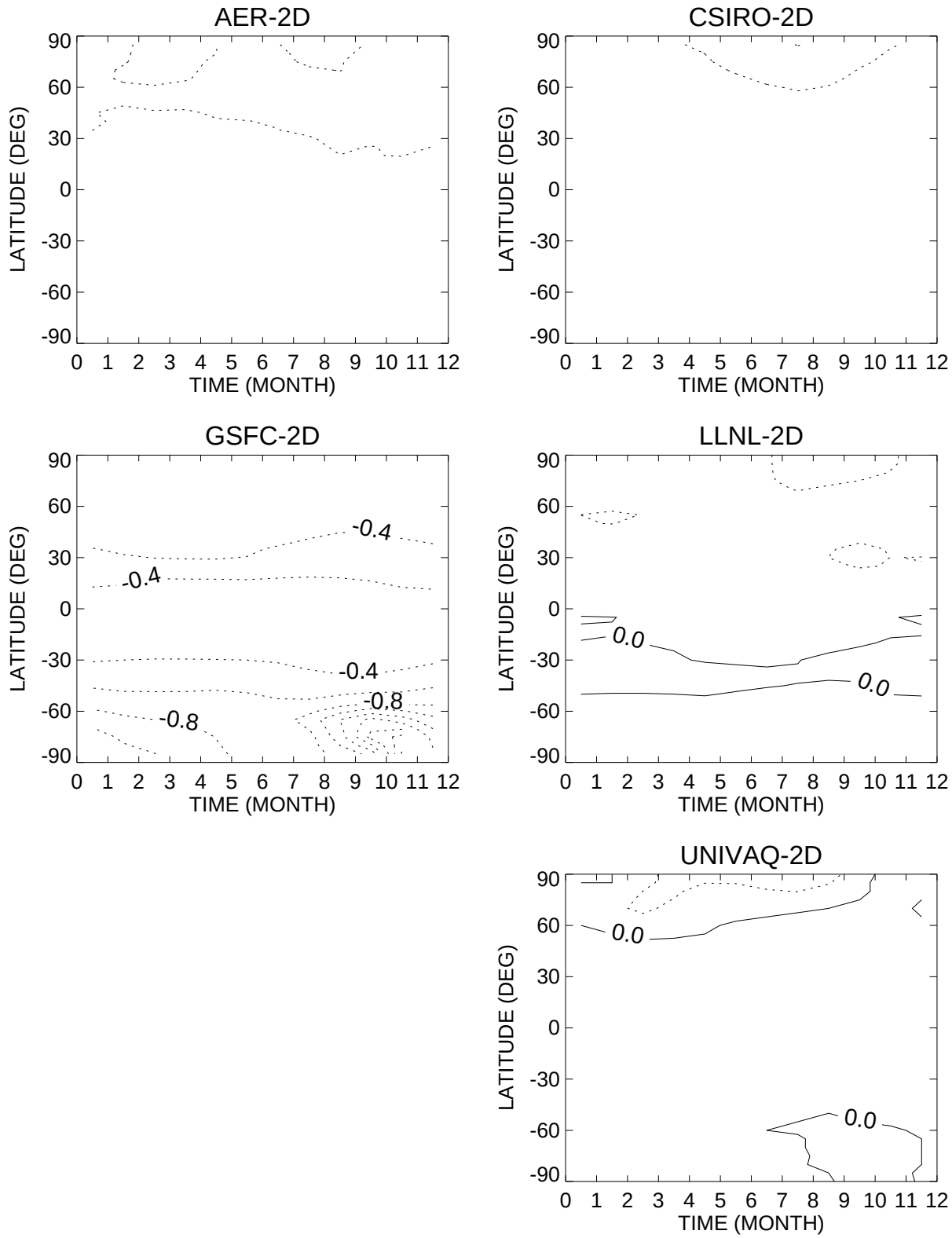

Figure 5.46: Calculated perturbations to column O_3 (percent) as a function of latitude and season in 2050 due to emissions from a fleet of 1000 HSCT aircraft operating at 2 km below nominal cruise altitude with EI(NO_x)=5 under Scenario S10a relative to Scenario D9. Contours are -1.6 to 0 by 0.2.

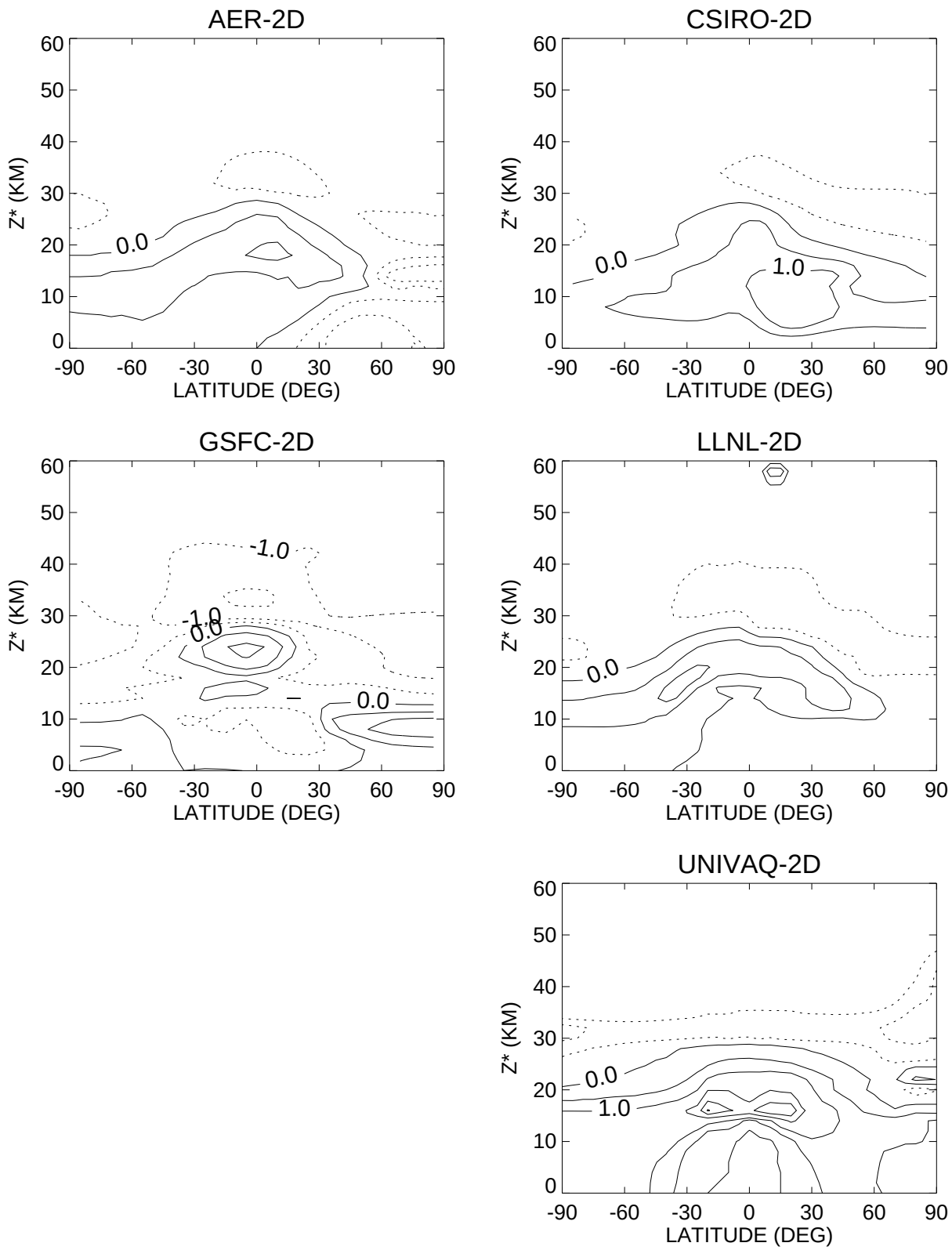

Figure 5.47: Calculated perturbations to O_3 (percent) as a function of latitude and altitude in March of 2050 due to emissions from a fleet of 1000 HSCT aircraft operating at 2 km below nominal cruise altitude with EI(NO_x)=10 under Scenario S10b relative to Scenario D9. Contours are -2, -1, -0.5, 0, 0.5, 1, 2, 3, 4.

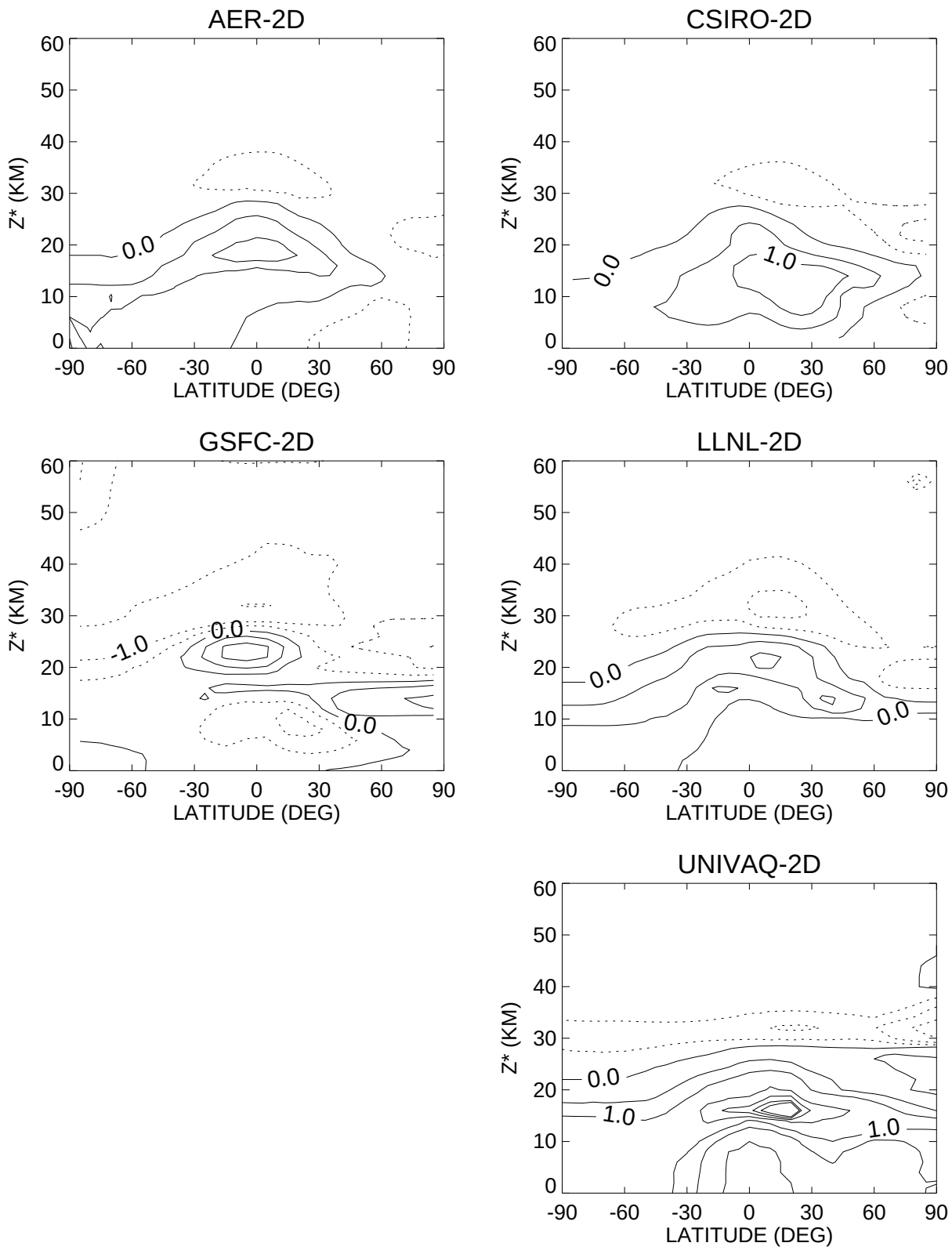

Figure 5.48: Calculated perturbations to O_3 (percent) as a function of latitude and altitude in June of 2050 due to emissions from a fleet of 1000 HSCT aircraft operating at 2 km below nominal cruise altitude with EI(NO_x)=10 under Scenario S10b relative to Scenario D9. Contours are -2, -1, -0.5, 0, 0.5, 1, 2, 3, 4, 5.

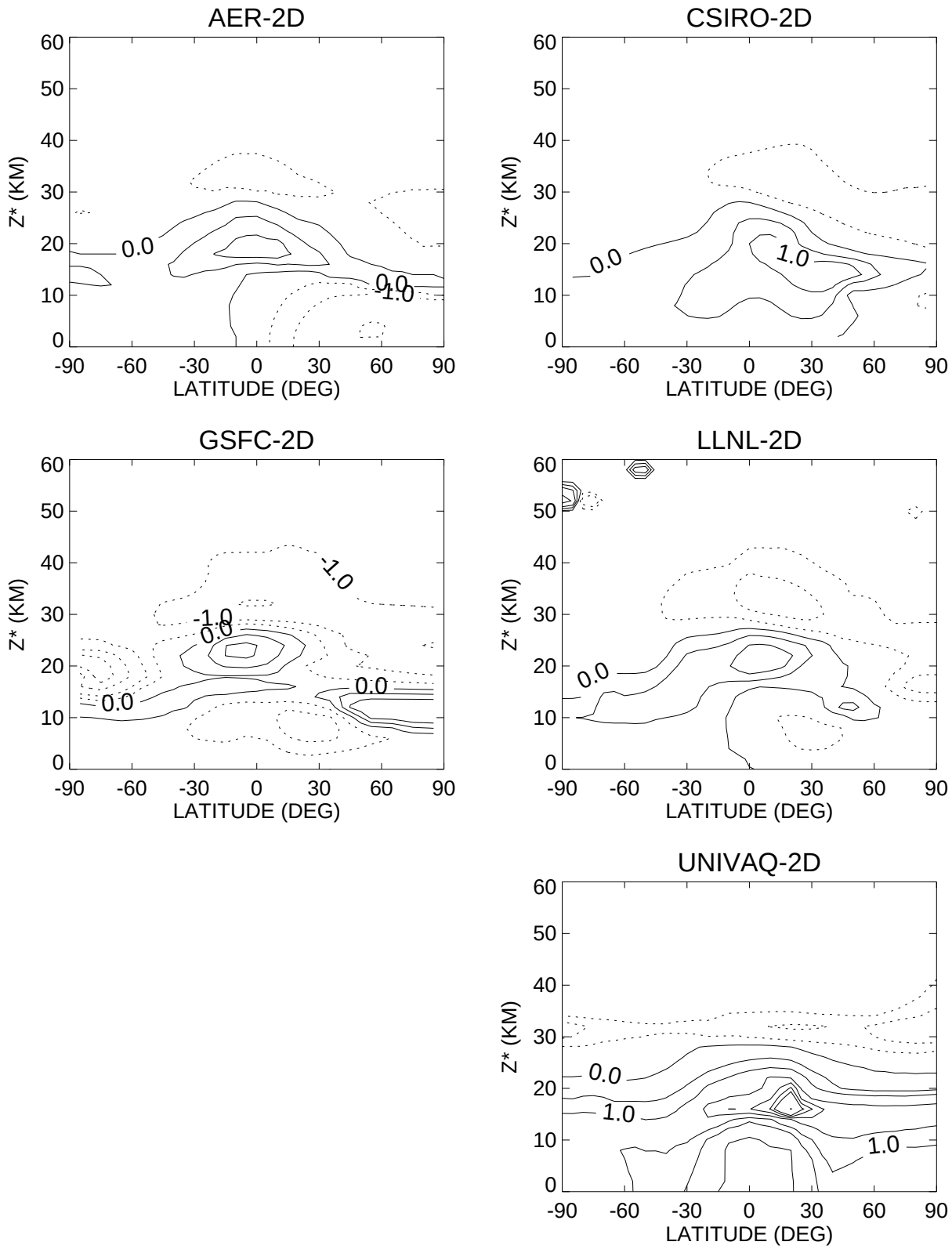

Figure 5.49: Calculated perturbations to O_3 (percent) as a function of latitude and altitude in October of 2050 due to emissions from a fleet of 1000 HSCT aircraft operating at 2 km below nominal cruise altitude with EI(NO_x)=10 under Scenario S10b relative to Scenario D9. Contours are -3, -2, -1, -0.5, 0, 0.5, 1, 2, 3, 4, 5, 6.

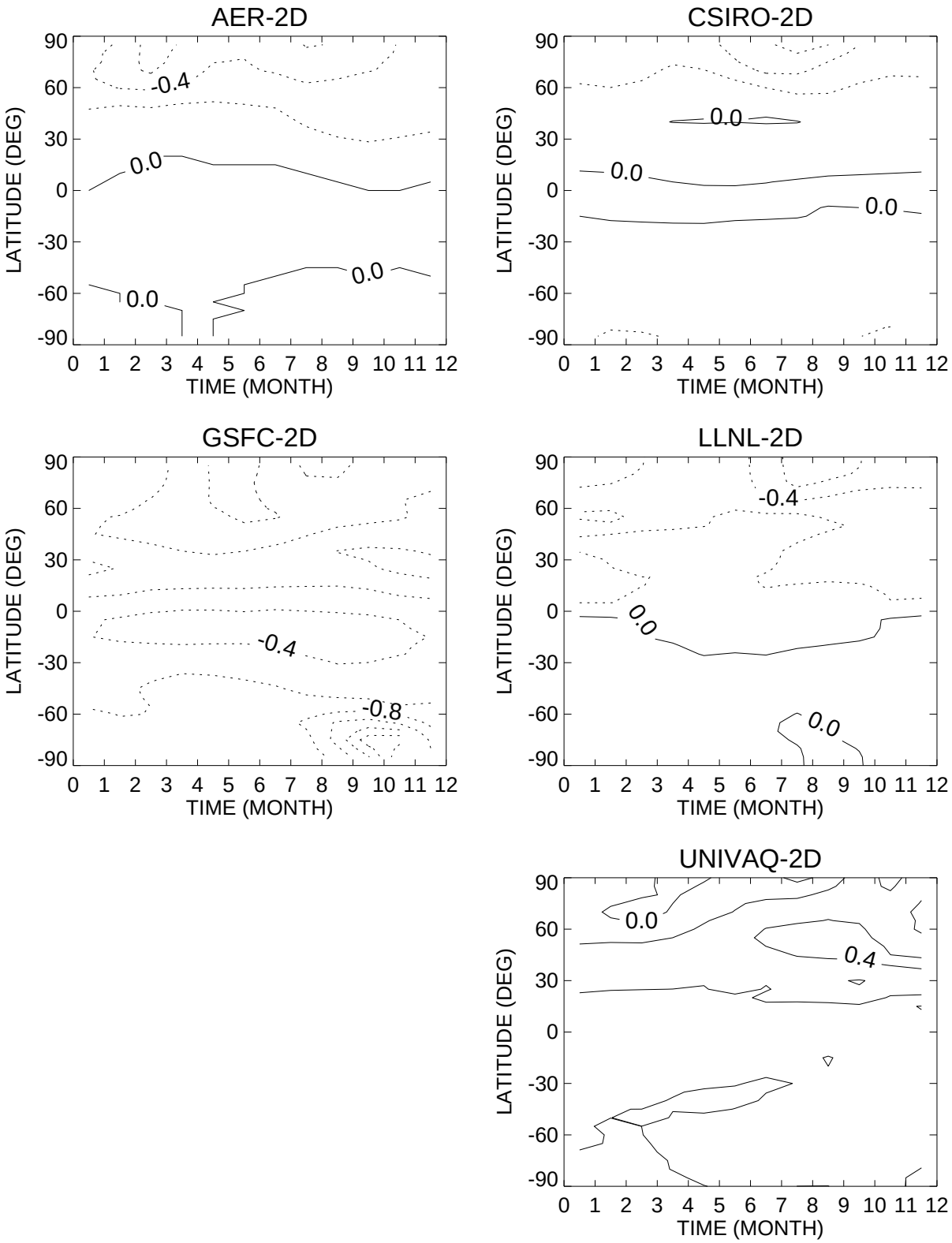

Figure 5.50: Calculated perturbations to column O_3 (percent) as a function of latitude and season in 2050 due to emissions from a fleet of 1000 HSCT aircraft operating at 2 km below nominal cruise altitude with EI(NO_x)=10 under Scenario S10b relative to Scenario D9. Contours are -1.4 to 0.4 by 0.2.

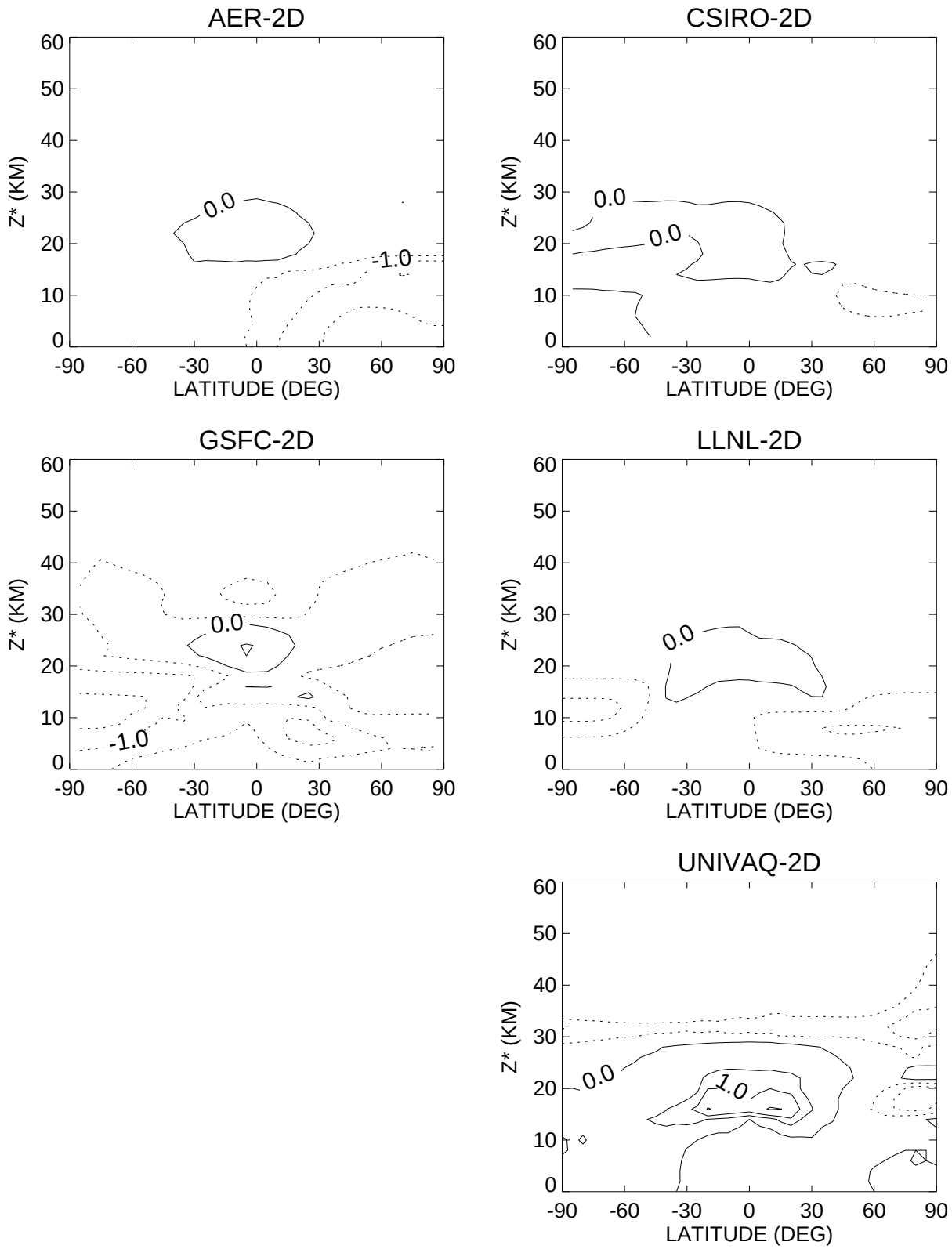

Figure 5.51: Calculated perturbations to O_3 (percent) as a function of latitude and altitude in March of 2050 due to emissions from a fleet of 1000 HSCT aircraft operating at 2 km below nominal cruise altitude with EI(NO_x)=5 with SA6-2km sulfate surface area density under Scenario S10c relative to Scenario D9. Contours are -2, -1, -0.5, 0, 0.5, 1, 2.

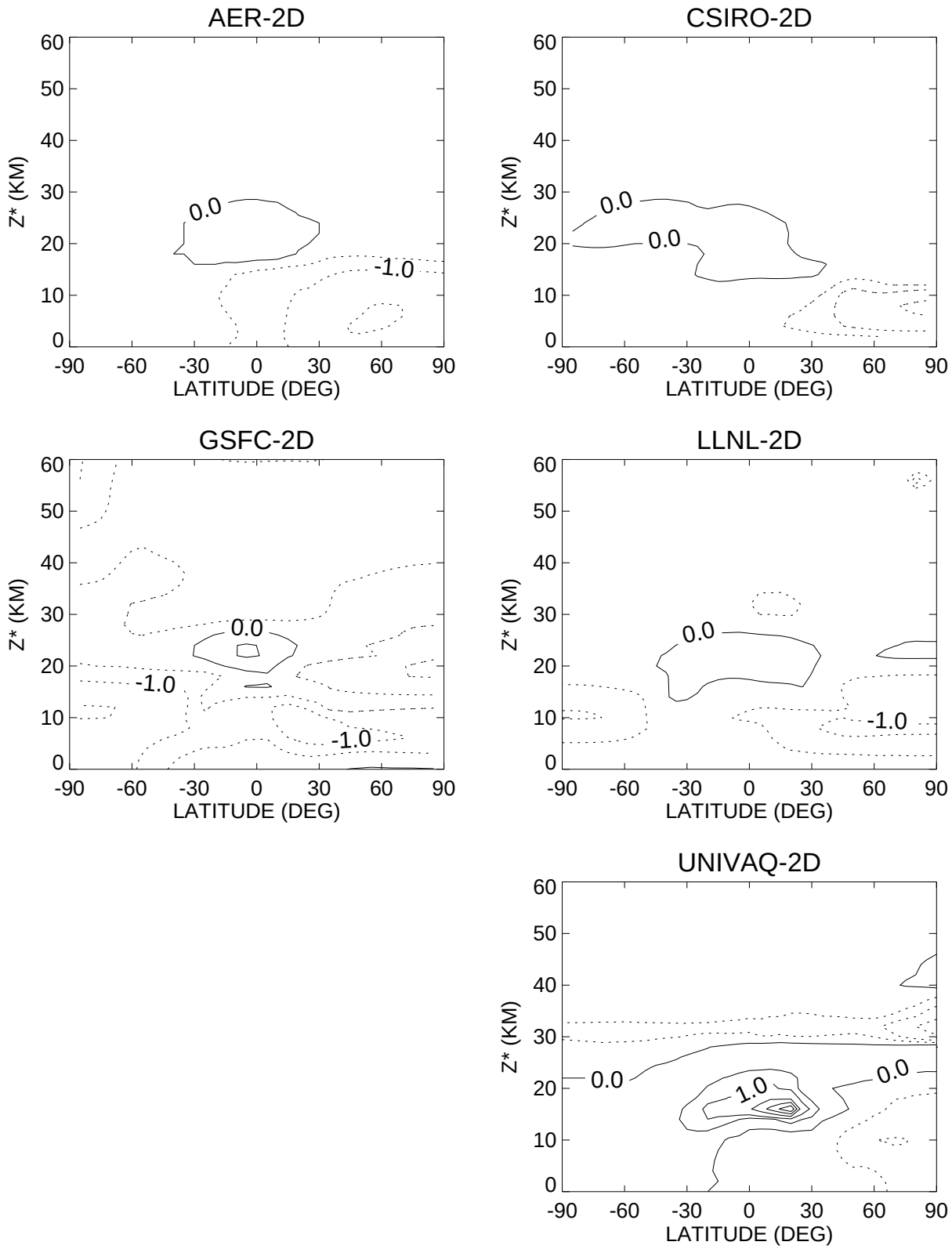

Figure 5.52: Calculated perturbations to O_3 (percent) as a function of latitude and altitude in June of 2050 due to emissions from a fleet of 1000 HSCT aircraft operating at 2 km below nominal cruise altitude with EI(NO_x)=5 with SA6-2km sulfate surface area density under Scenario S10c relative to Scenario D9. Contours are -2, -1, -0.5, 0, 0.5, 1, 2, 3, 4.

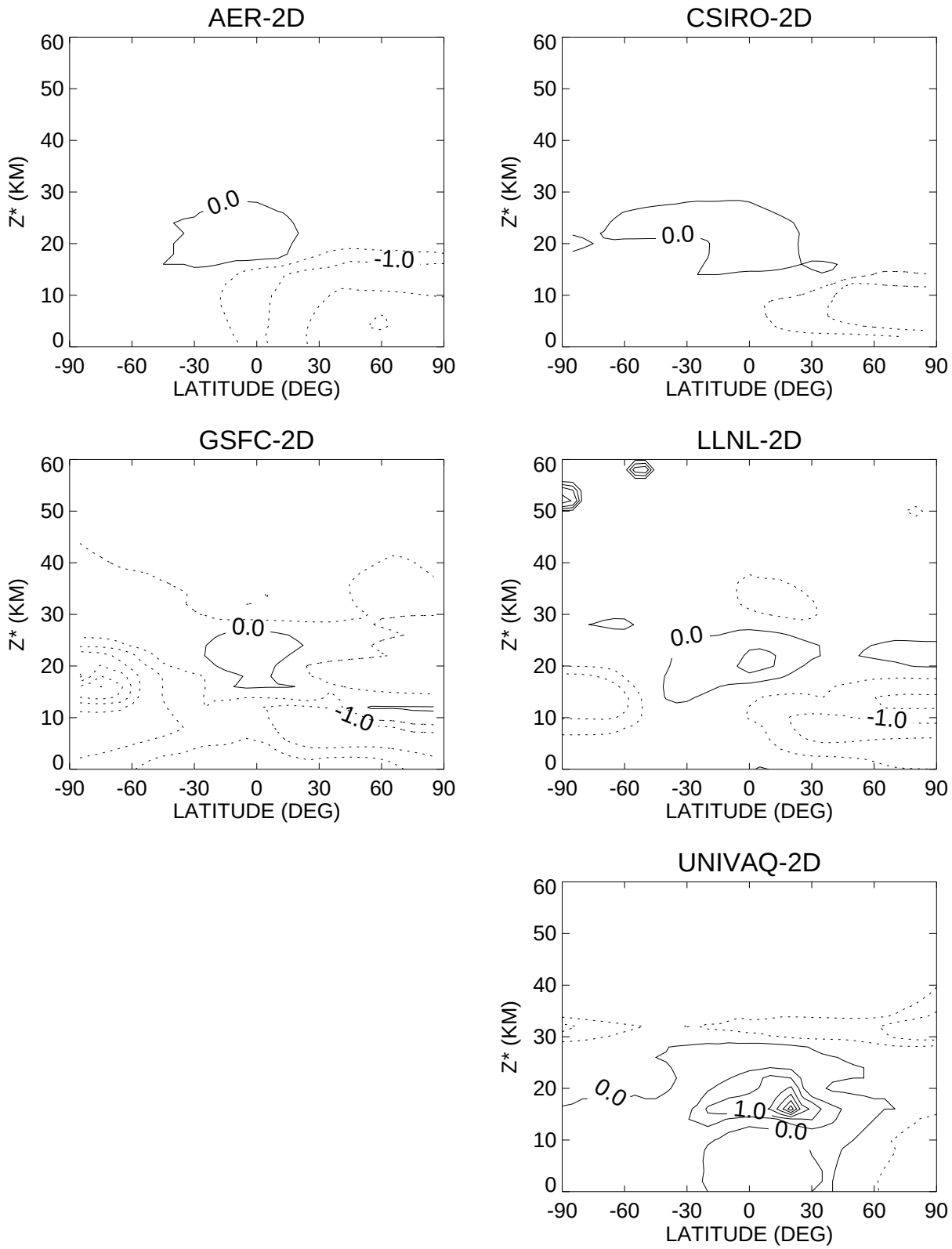

Figure 5.53: Calculated perturbations to O_3 (percent) as a function of latitude and altitude in October of 2050 due to emissions from a fleet of 1000 HSCT aircraft operating at 2 km below nominal cruise altitude with EI(NO_x)=5 with SA6-2km sulfate surface area density under Scenario S10c relative to Scenario D9. Contours are -5, -4, -3, -2, -1, -0.5, 0, 0.5, 1, 2, 3, 4, 5.

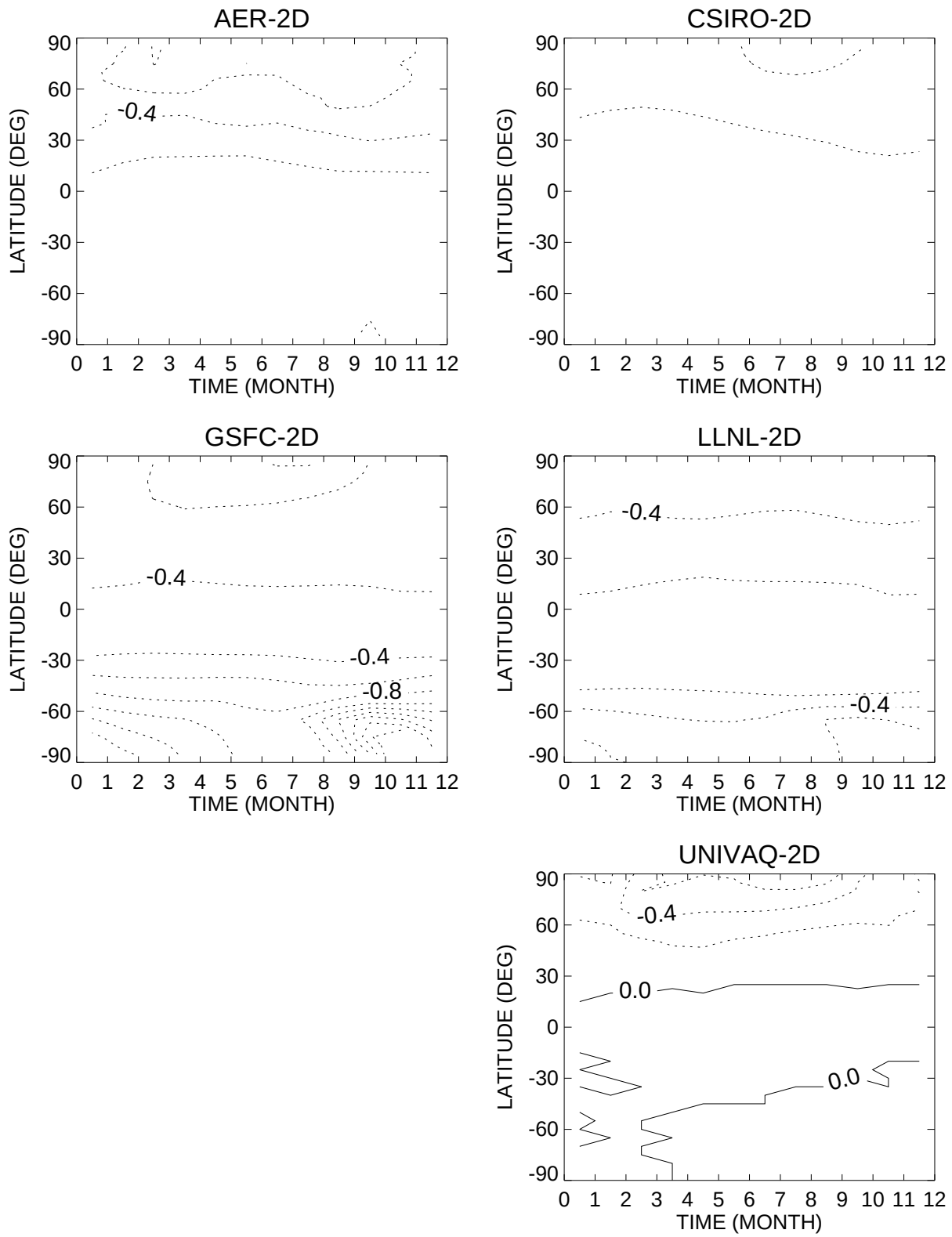

Figure 5.54: Calculated perturbations to column O_3 (percent) as a function of latitude and season in 2050 due to emissions from a fleet of 1000 HSCT aircraft operating at 2 km below nominal cruise altitude with EI(NO_x)=5 with SA6-2km sulfate surface area density under Scenario S10c relative to Scenario D9. Contours are -2.0 to 0 by 0.2.

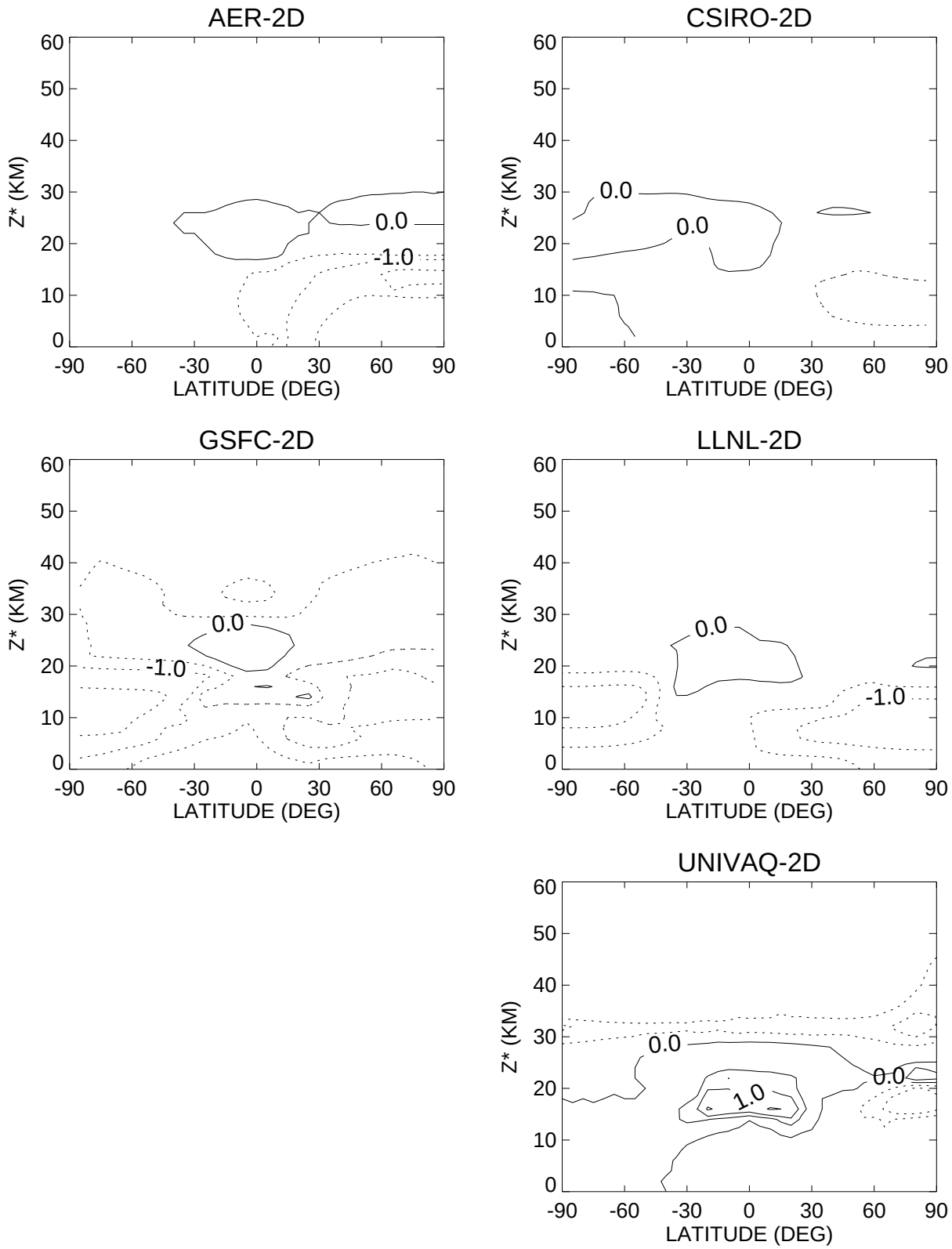

Figure 5.55: Calculated perturbations to O_3 (percent) as a function of latitude and altitude in March of 2050 due to emissions from a fleet of 1000 HSCT aircraft operating at 2 km below nominal cruise altitude with EI(NO_x)=5 with SA2-2km sulfate surface area density under Scenario S10d relative to Scenario D9. Contours are -2, -1, -0.5, 0, 0.5, 1, 2.

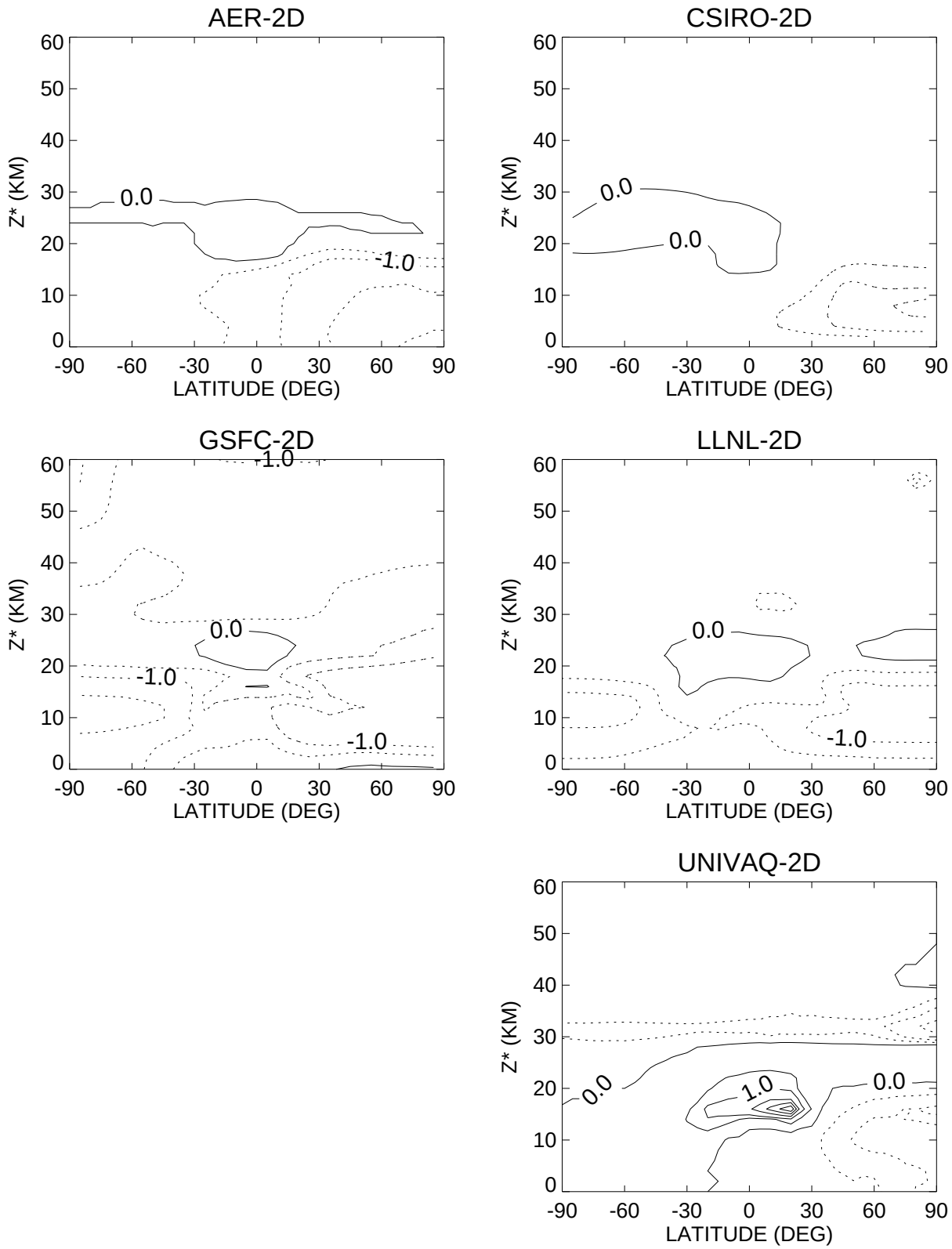

Figure 5.56: Calculated perturbations to O_3 (percent) as a function of latitude and altitude in June of 2050 due to emissions from a fleet of 1000 HSCT aircraft operating at 2 km below nominal cruise altitude with EI(NO_x)=5 with SA2-2km sulfate surface area density under Scenario S10d relative to Scenario D9. Contours are -3, -2, -1, -0.5, 0, 0.5, 1, 2, 3, 4.

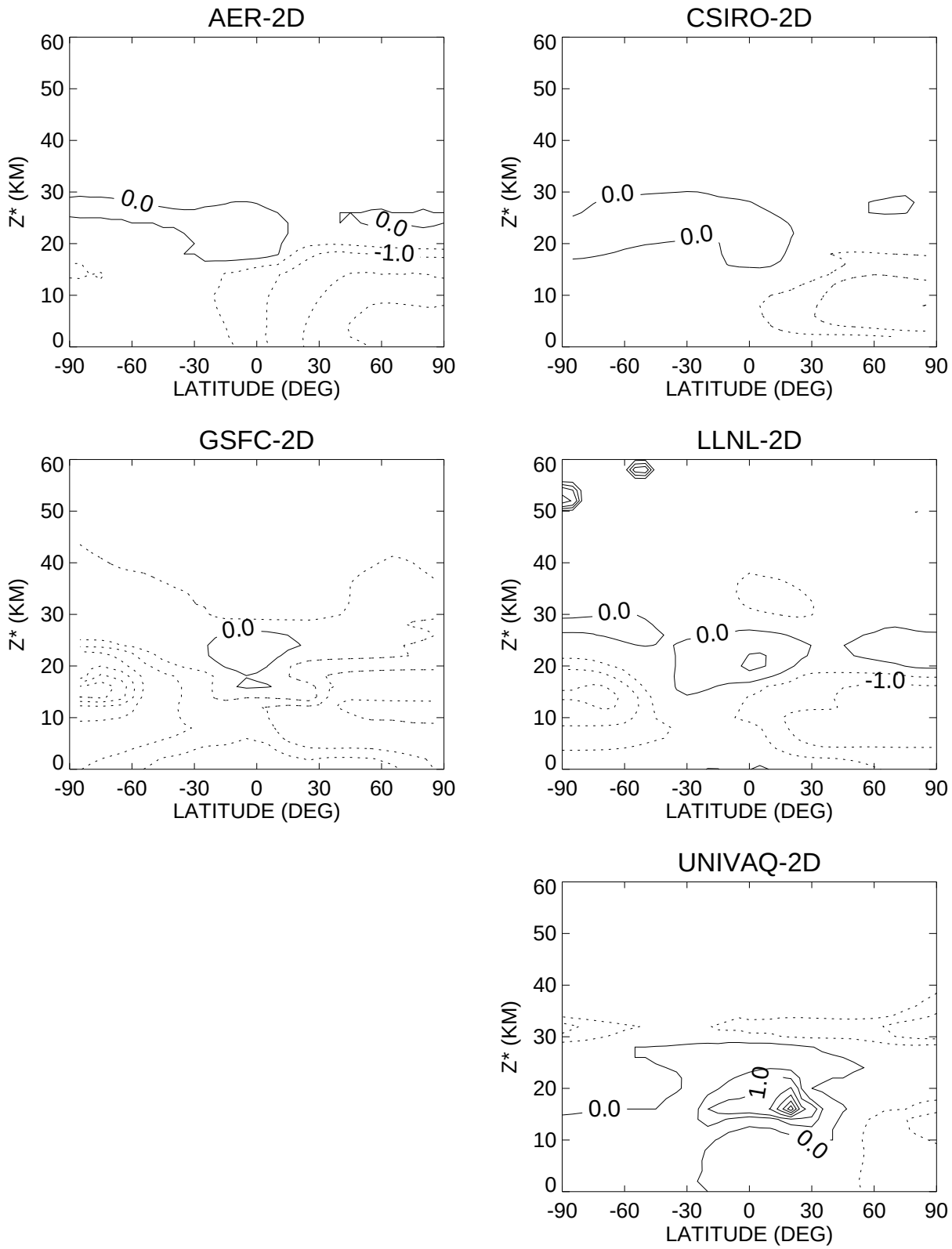

Figure 5.57: Calculated perturbations to O_3 (percent) as a function of latitude and altitude in October of 2050 due to emissions from a fleet of 1000 HSCT aircraft operating at 2 km below nominal cruise altitude with EI(NO_x)=5 with SA2-2km sulfate surface area density under Scenario S10d relative to Scenario D9. Contours are -5, -4, -3, -2, -1, -0.5, 0, 0.5, 1, 2, 3, 4, 5.

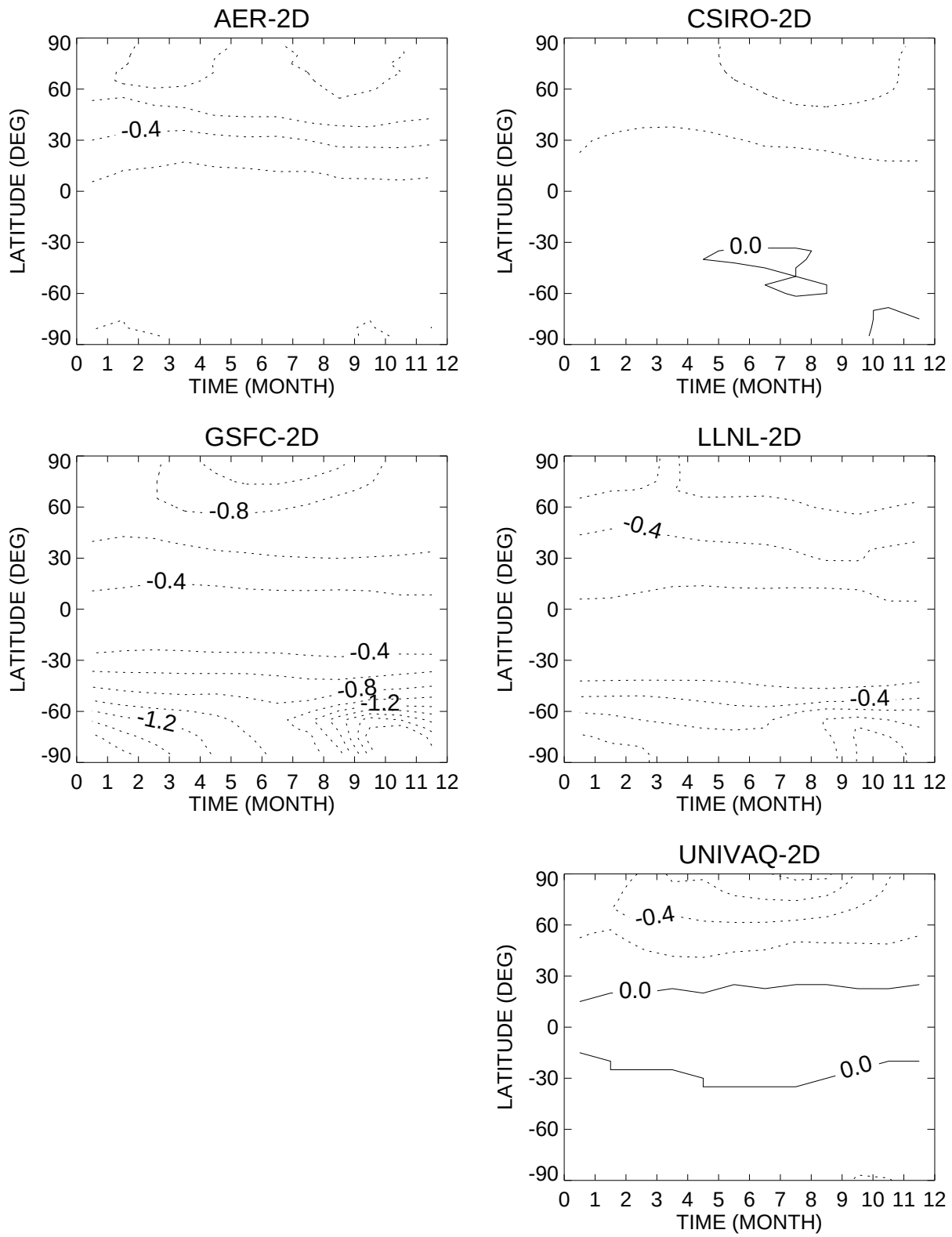

Figure 5.58: Calculated perturbations to column O_3 (percent) as a function of latitude and season in 2050 due to emissions from a fleet of 1000 HSCT aircraft operating at 2 km below nominal cruise altitude with EI(NO_x)=5 with SA2-2km sulfate surface area density under Scenario S10d relative to Scenario D9. Contours are -2.0 to 0 by 0.2.

5.3.4 Scenarios with Modified Subsonic Fleets (S11a, S12a)

Scenarios S11a and S12a use subsonic fleets projected to 2050 based on various assumptions regarding economic growth in the intervening years. The other scenarios for 2050 used the same subsonic fleet as was used for the 2015 scenarios. The IS92a subsonic fleet is used for Scenario S11a which includes 1000 HSCTs and for Scenario F which uses only subsonic aircraft. The IS92a subsonic fleet uses 50% more fuel per year than the 2015 subsonic fleet. Calculated ozone depletions for Scenario S11a relative to Scenario F are shown in Figures 5.59, 5.60, and 5.61. Differences due to the subsonic fleet are found mostly below 10 km, as can be seen by comparing this results with that for Scenario S10d-D9. Perturbations to column ozone for S11a are shown in Figure 5.62. Differences between this result and S10d-D9 are small.

Scenario S12a uses the IS92e high demand subsonic scenario. Subsonic fuel usage for IS92e high demand is a factor of 2.4 times greater than for the 2015 subsonic scenario. Figures 5.63, 5.64, and 5.65 show calculated changes in ozone for Scenario S12a relative to Scenario G. Stratospheric ozone perturbations are changed very little by the greatly increased subsonic fleet. Figure 5.66 shows changes in calculated column ozone. These column ozone changes are virtually identical to those for S11a-F and S10d-D9.

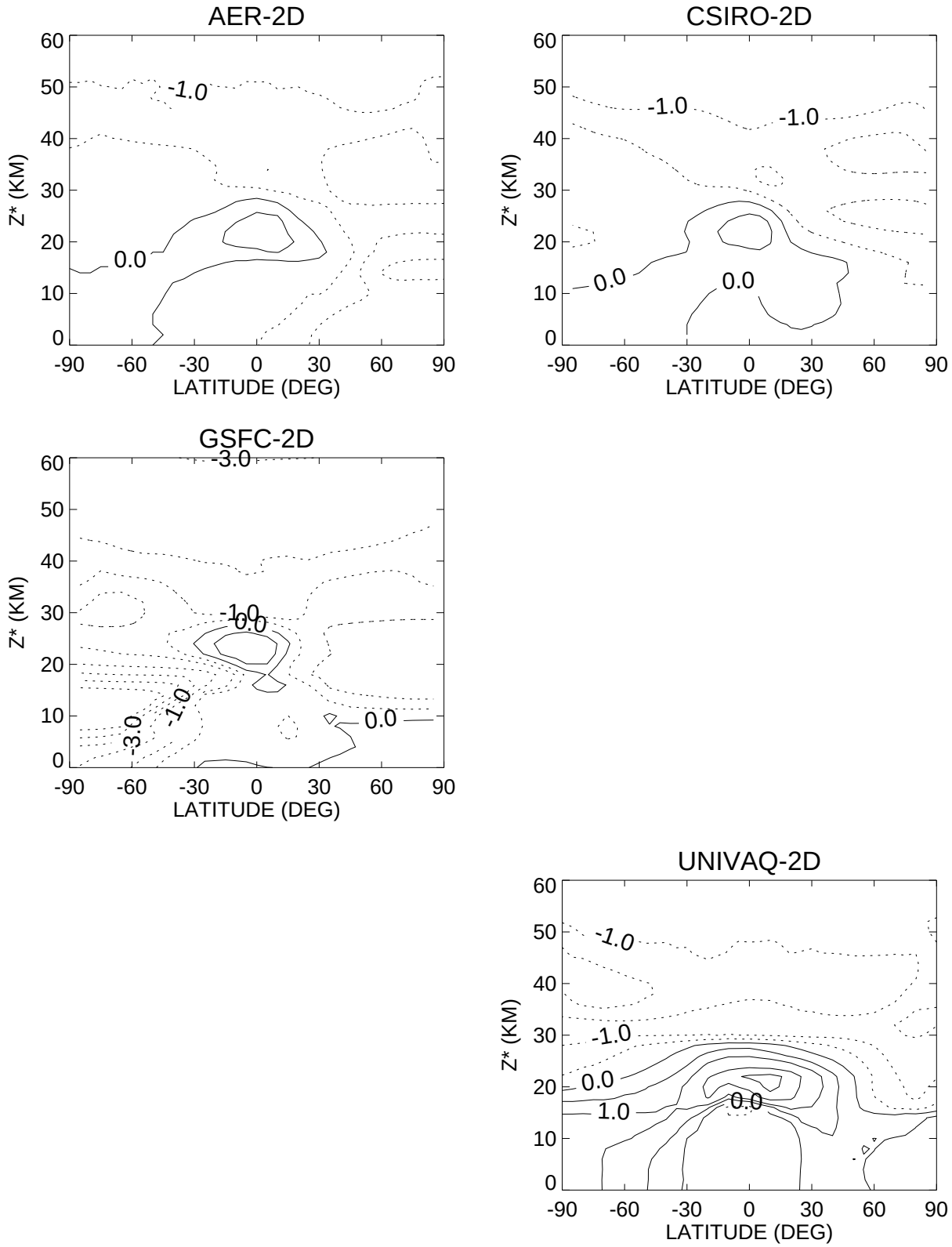

Figure 5.59: Calculated perturbations to O_3 (percent) as a function of latitude and altitude in March of 2050 due to emissions from a fleet of 1000 HSCT aircraft with EI(NO_x)=5 and utilizing the IS92a subsonic fleet under Scenario S11a relative to Scenario F. Contours are -5, -4, -3, -2, -1, -0.5, 0, 0.5, 1, 2, 3.

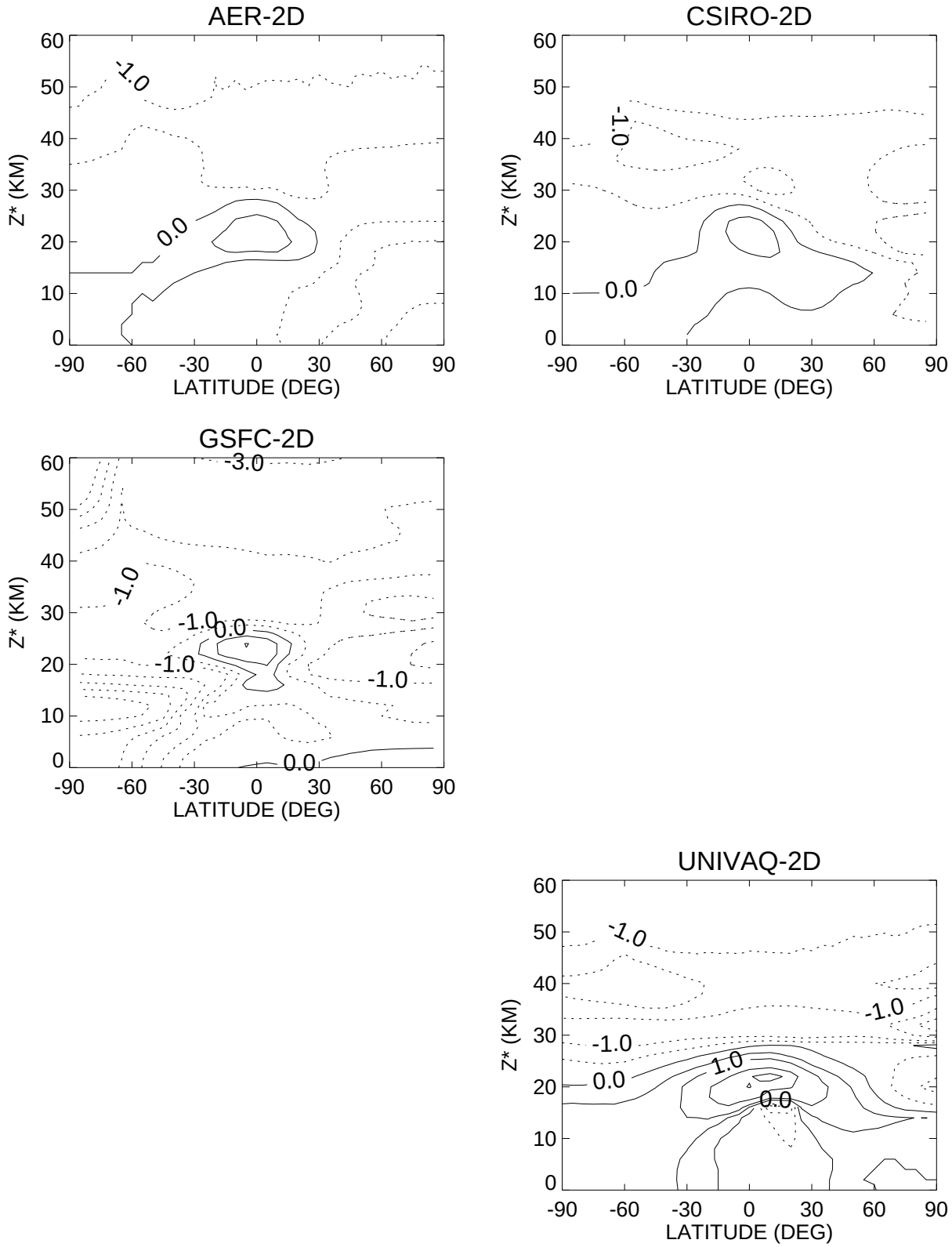

Figure 5.60: Calculated perturbations to O_3 (percent) as a function of latitude and altitude in June of 2050 due to emissions from a fleet of 1000 HSCT aircraft with EI(NO_x)=5 and utilizing the IS92a subsonic fleet under Scenario S11a relative to Scenario F. Contours are -5, -4, -3, -2, -1, -0.5, 0, 0.5, 1, 2, 3.

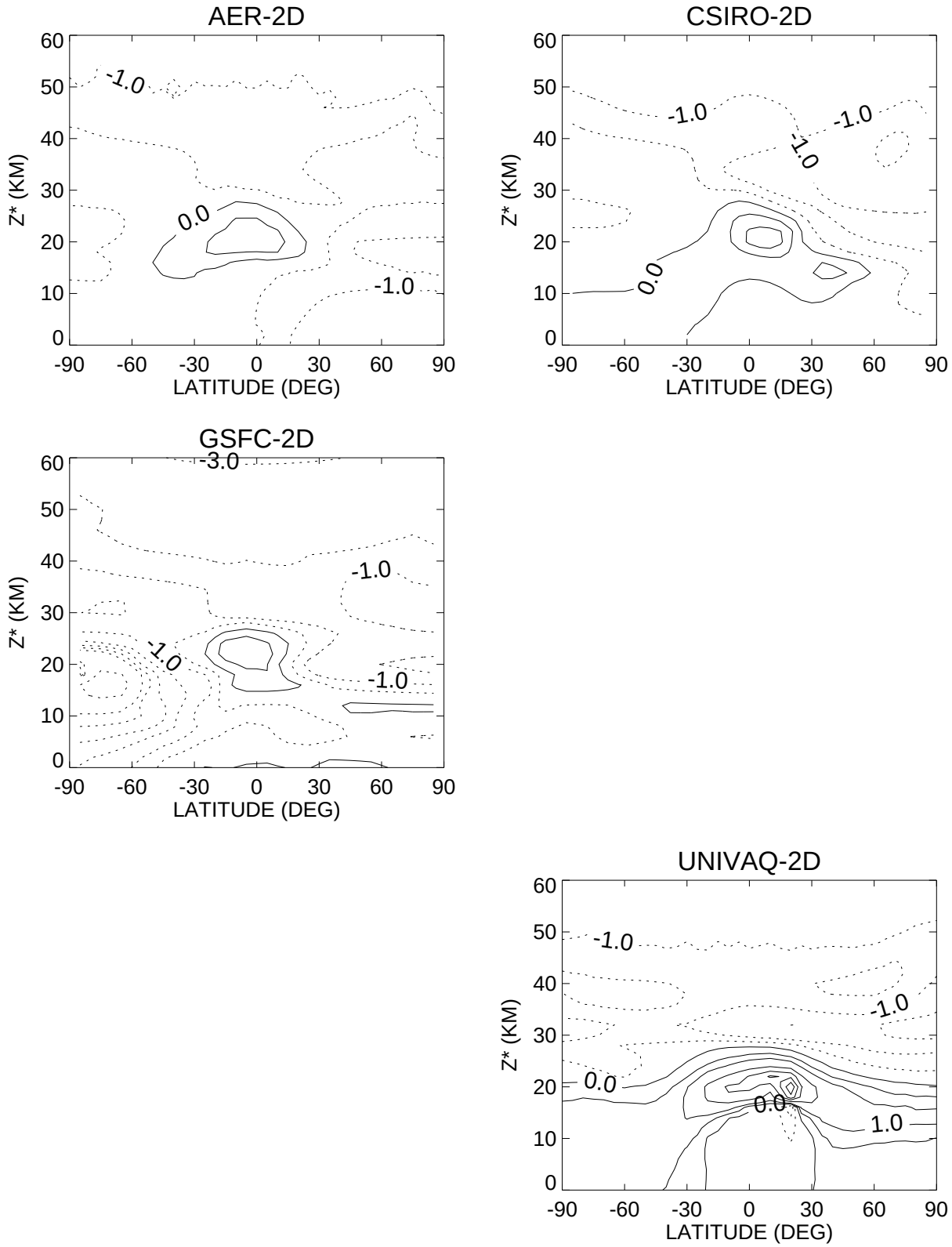

Figure 5.61: Calculated perturbations to O_3 (percent) as a function of latitude and altitude in October of 2050 due to emissions from a fleet of 1000 HSCT aircraft with EI(NO_x)=5 and utilizing the IS92a subsonic fleet under Scenario S11a relative to Scenario F. Contours are -10, -5, -4, -3, -2, -1, -0.5, 0, 0.5, 1, 2, 3, 4, 5.

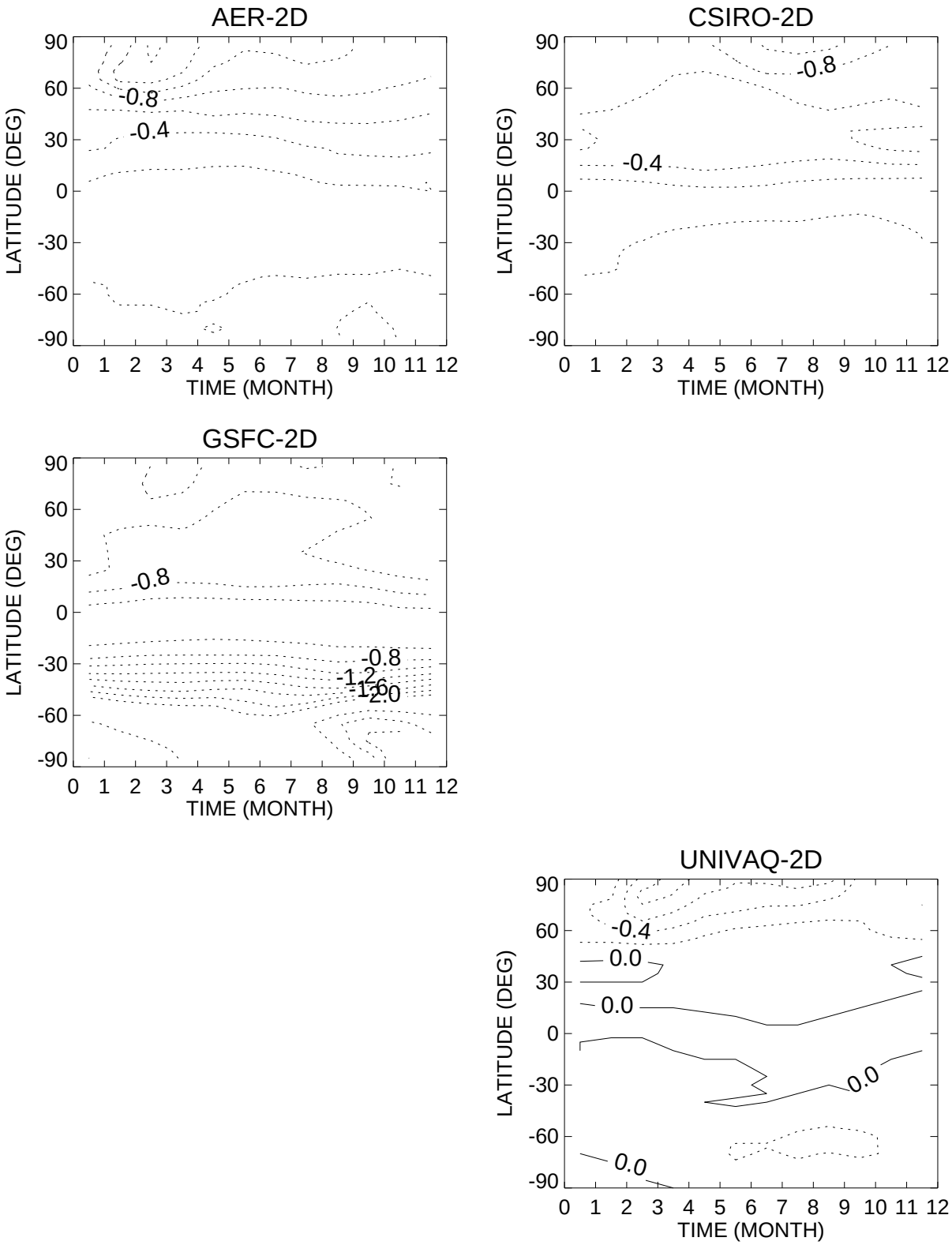

Figure 5.62: Calculated perturbations to column O_3 (percent) as a function of latitude and season in 2050 due to emissions from a fleet of 1000 HSCT aircraft with EI(NO_x)=5 and utilizing the IS92a subsonic fleet under Scenario S11a relative to Scenario F. Contours are -5, -4, -3, and -2.0 to 0 by 0.2.

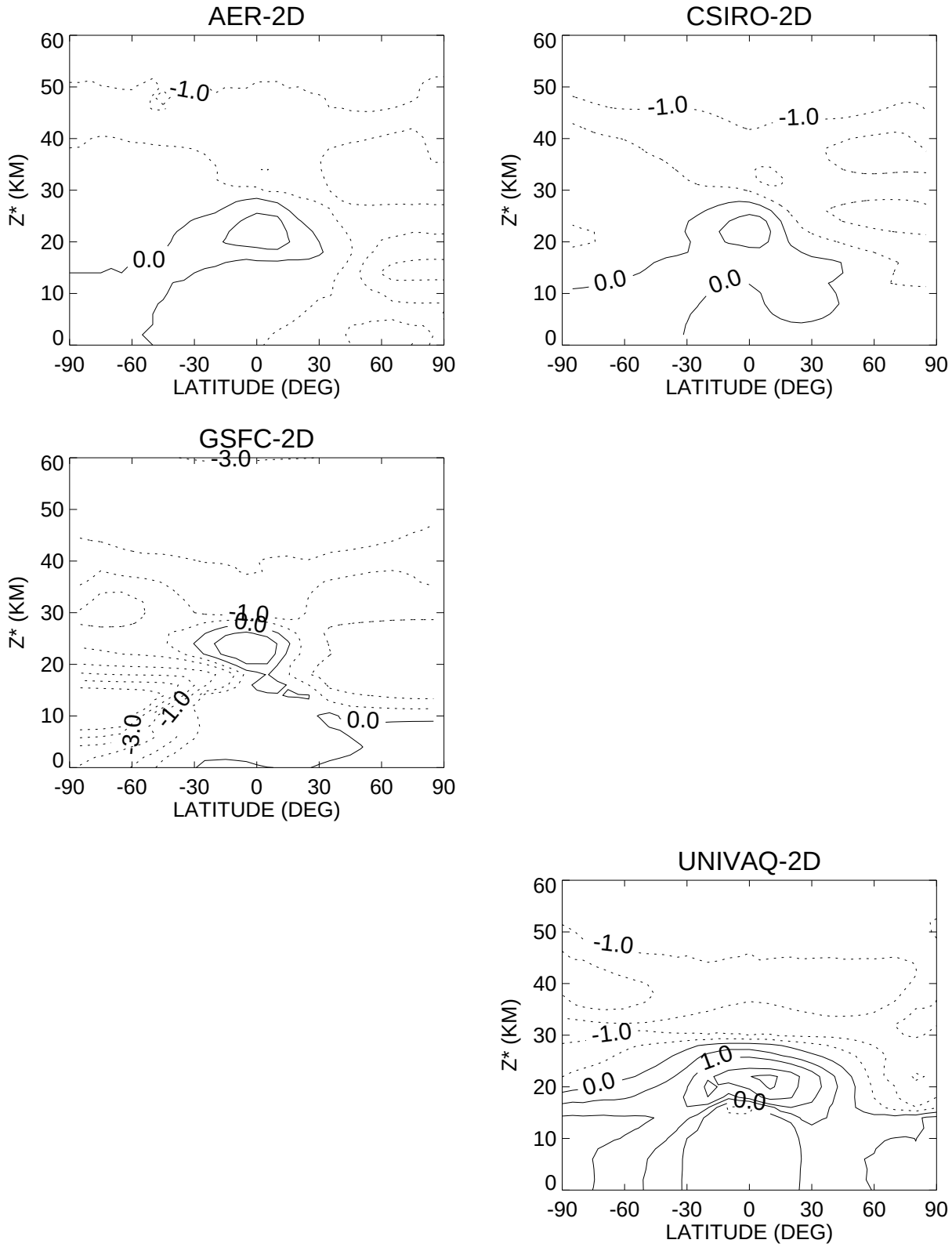

Figure 5.63: Calculated perturbations to O_3 (percent) as a function of latitude and altitude in March of 2050 due to emissions from a fleet of 1000 HSCT aircraft with EI(NO_x)=5 and utilizing the IS92e high demand subsonic fleet under Scenario S12a relative to Scenario G. Contours are -5, -4, -3, -2, -1, -0.5, 0, 0.5, 1, 2, 3.

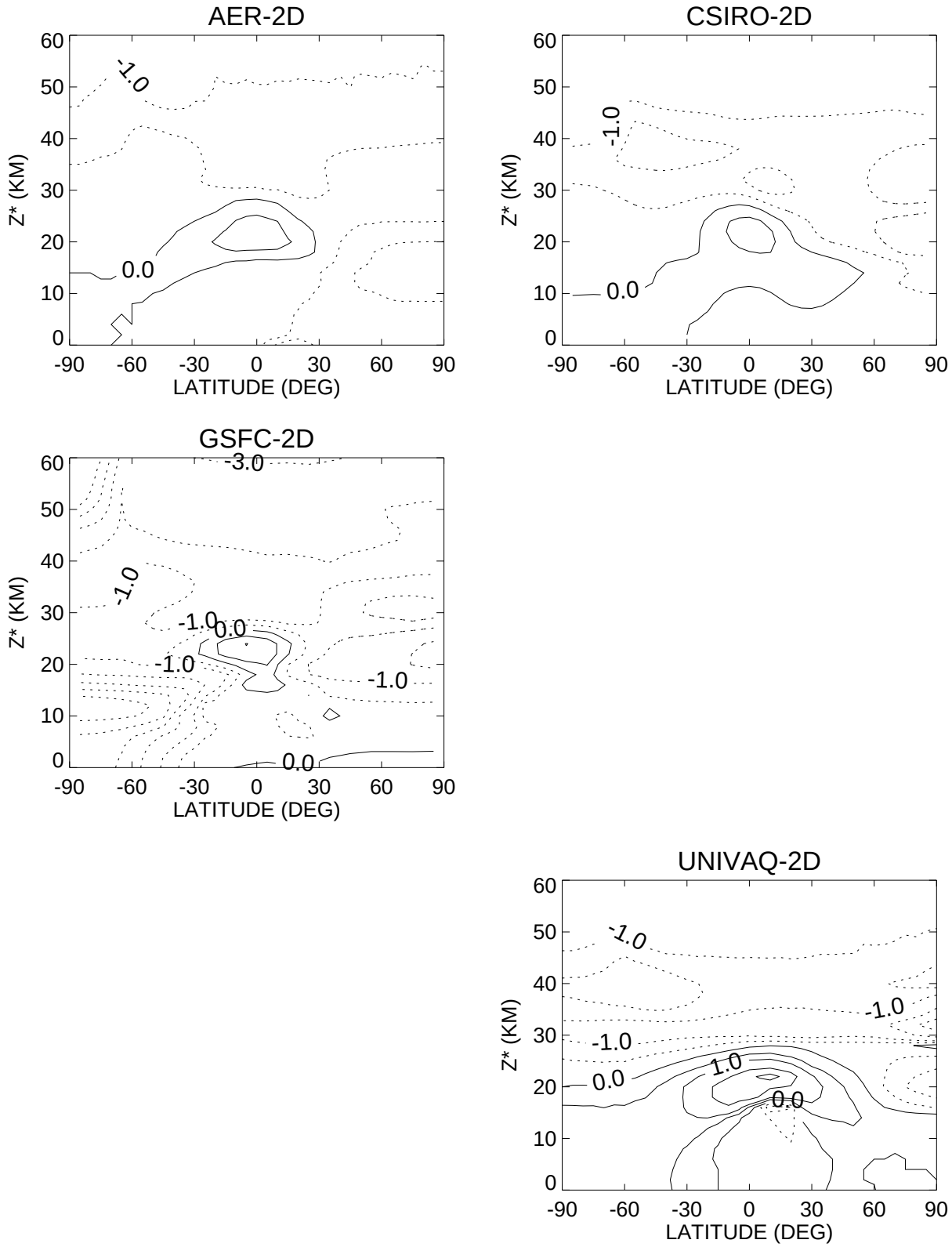

Figure 5.64: Calculated perturbations to O_3 (percent) as a function of latitude and altitude in June of 2050 due to emissions from a fleet of 1000 HSCT aircraft with EI(NO_x)=5 and utilizing the IS92e high demand subsonic fleet under Scenario S12a relative to Scenario G. Contours are -5, -4, -3, -2, -1, -0.5, 0, 0.5, 1, 2, 3.

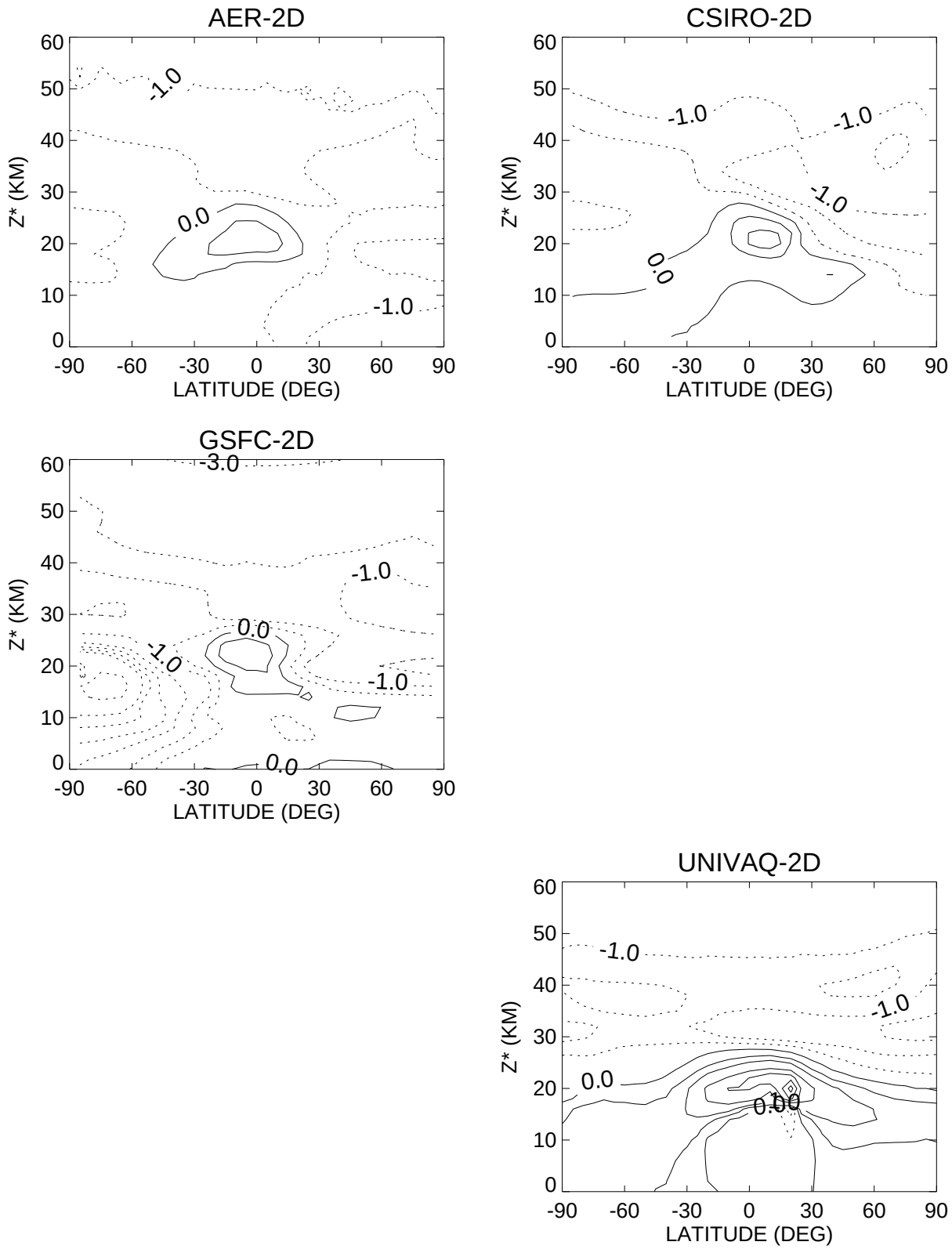

Figure 5.65: Calculated perturbations to O_3 (percent) as a function of latitude and altitude in October of 2050 due to emissions from a fleet of 1000 HSCT aircraft with EI(NO_x)=5 and utilizing the IS92e high demand subsonic fleet under Scenario S12a relative to Scenario G. Contours are -10, -5, -4, -3, -2, -1, -0.5, 0, 0.5, 1, 2, 3, 4, 5.

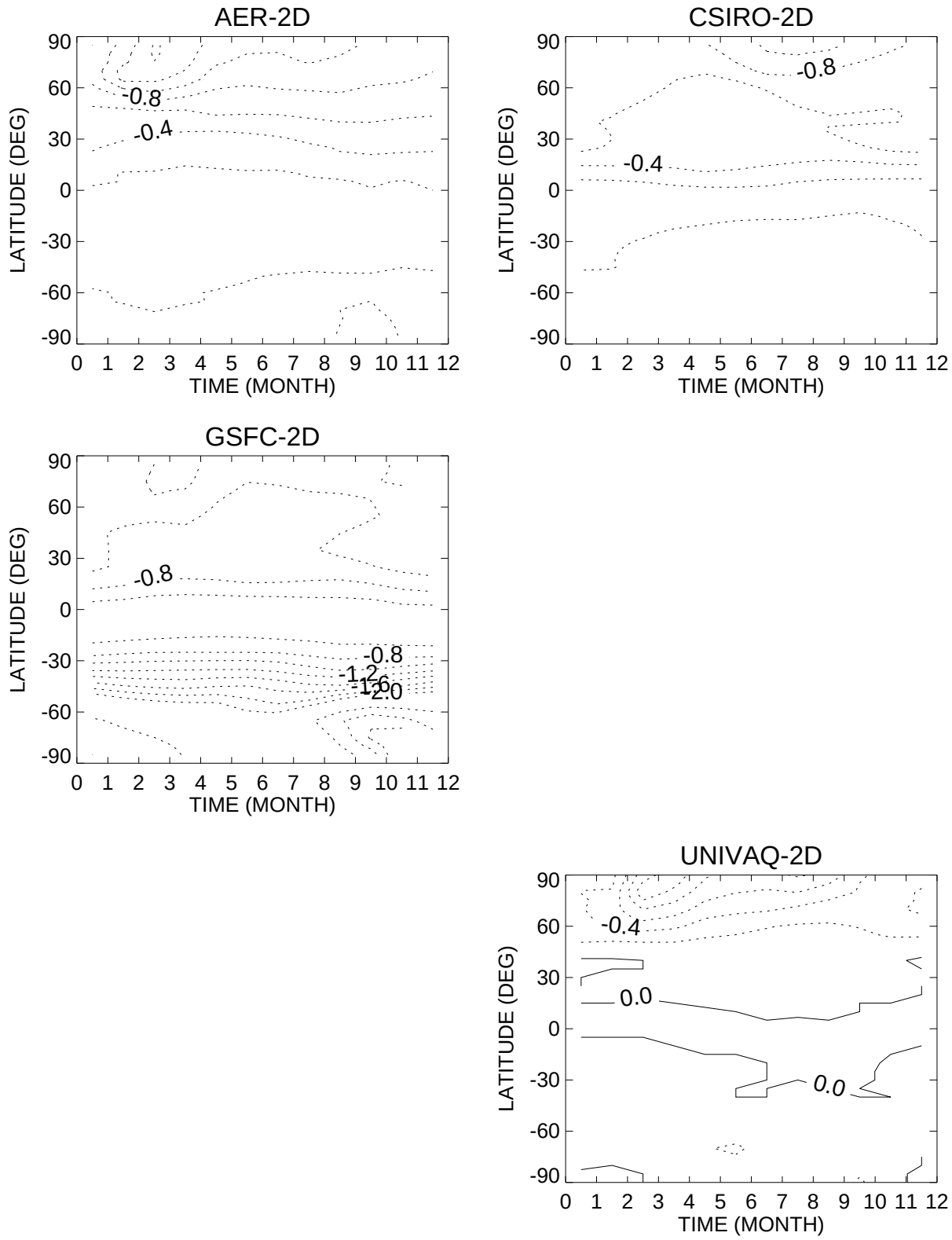

Figure 5.66: Calculated perturbations to column O_3 (percent) as a function of latitude and season in 2050 due to emissions from a fleet of 1000 HSCT aircraft with EI(NO_x)=5 and utilizing the IS92e high demand subsonic fleet under Scenario S12a relative to Scenario G. Contours are -5, -4, -3, and -2.0 to 0 by 0.2.